

ARO 35016.2 ms-CF



MATERIALS
RESEARCH
SOCIETY

SYMPOSIUM PROCEEDINGS

Volume 395

Gallium Nitride and Related Materials

EDITORS:

F.A. Ponce

R.D. Dupuis

S. Nakamura

J.A. Edmond

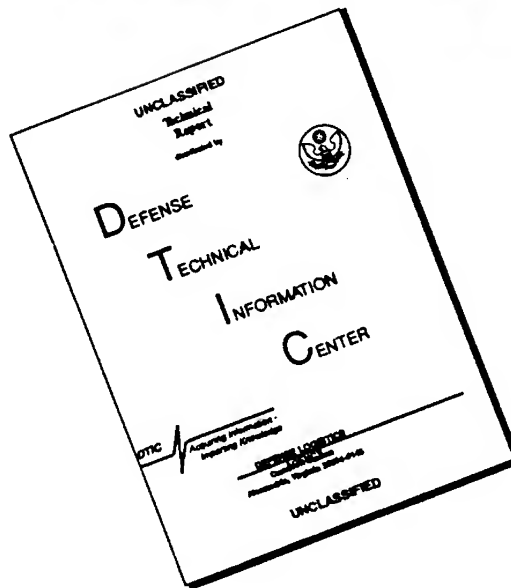
CONFIDENTIAL - NOT FOR DISTRIBUTION

ALL INFORMATION CONTAINED HEREIN IS UNCLASSIFIED

DATE 10/10/01 BY 1045 JRS/STP

EXEMPT FROM AUTOMATIC DOWNGRADING AND DECLASSIFICATION

DISCLAIMER NOTICE



THIS DOCUMENT IS BEST QUALITY AVAILABLE. THE COPY FURNISHED TO DTIC CONTAINED A SIGNIFICANT NUMBER OF PAGES WHICH DO NOT REPRODUCE LEGIBLY.

REPORT DOCUMENTATION PAGE

Form Approved
OMB NO. 0704-0188

Public reporting burden for this collection of information is estimated to average 1 hour per response, including the time for reviewing instructions, searching existing data sources, gathering and maintaining the data needed, and completing and reviewing the collection of information. Send comment regarding this burden estimate or any other aspect of this collection of information, including suggestions for reducing this burden, to Washington Headquarters Services, Directorate for Information Operations and Reports, 1215 Jefferson Davis Highway, Suite 1204, Arlington, VA 22202-4302, and to the Office of Management and Budget, Paperwork Reduction Project (0704-0188), Washington, DC 20503.

1. AGENCY USE ONLY (Leave blank)		2. REPORT DATE Sept 96		3. REPORT TYPE AND DATES COVERED Final 29 Sep 95 - 28 Sep 96	
4. TITLE AND SUBTITLE Gallium Nitride and Related Materials, Vol 395, 1995 Fall Meeting of the Materials Research Society				5. FUNDING NUMBERS DAAH04-95-1-0646	
6. AUTHOR(S) Robert H. Pachavis					
7. PERFORMING ORGANIZATION NAMES(S) AND ADDRESS(ES) Materials Research Society Pittsburgh, PA 15237-6005				8. PERFORMING ORGANIZATION REPORT NUMBER	
9. SPONSORING / MONITORING AGENCY NAME(S) AND ADDRESS(ES) U.S. Army Research Office P.O. Box 12211 Research Triangle Park., NC 27709-2211				10. SPONSORING / MONITORING AGENCY REPORT NUMBER ARO 35016.2-MS-CF	
11. SUPPLEMENTARY NOTES The views, opinions and/or findings contained in this report are those of the author(s) and should not be construed as an official Department of the Army position, policy or decision, unless so designated by other documentation.					
12a. DISTRIBUTION / AVAILABILITY STATEMENT Approved for public release; distribution unlimited.				12b. DISTRIBUTION CODE	
13. ABSTRACT (Maximum 200 words) The current excitement in the scientific community about the III-V nitrides was reflected in this First International Symposium on Gallium Nitride and Related Materials (ISGN-1). The symposium consisted of nine half-day oral sessions (25 invited and 54 contributed talks) and four poster sessions (113 presentations). The attendance was very high for all sessions, with an estimated peak of over 550 attendees at one of the sessions. The symposium reflected the large amount of work that has taken place since the field exploded about two years ago with the announcement of commercial blue light emitting devices. The invited talk program was designed to give a thorough review of the state of the art in the field. The large number of contributions, in the form of talks and poster presentations, showed much progress in understanding III-V nitrides, and in the production of optoelectronic devices based on these materials. These proceedings represent the current state of understanding in the field, reflecting about 75% of the work presented at the symposium.					
14. SUBJECT TERMS				15. NUMBER OF PAGES	
				16. PRICE CODE	
17. SECURITY CLASSIFICATION OR REPORT UNCLASSIFIED		18. SECURITY CLASSIFICATION OF THIS PAGE UNCLASSIFIED		19. SECURITY CLASSIFICATION OF ABSTRACT UNCLASSIFIED	
				20. LIMITATION OF ABSTRACT UL	

**MATERIALS RESEARCH SOCIETY
SYMPOSIUM PROCEEDINGS VOLUME 395**

Gallium Nitride and Related Materials

The First International Symposium on Gallium Nitride and Related Materials
held November 27-December 1, 1995, Boston, Massachusetts, U.S.A.

EDITORS:

F.A. Ponce

*Xerox Palo Alto Research Center
Palo Alto, California, U.S.A.*

R.D. Dupuis

*The University of Texas
Austin, Texas, U.S.A.*

S. Nakamura

*Nichia Chemical Industries
Tokushima, Japan*

J.A. Edmond

*Cree Research, Inc.
Durham, North Carolina, U.S.A.*



PITTSBURGH, PENNSYLVANIA

19961023 260

DTIC QUALITY INSPECTED 1

This work was supported in part by the Army Research Office under Grant Number DAAH04-95-1-063. The views, opinions, and/or findings contained in this report are those of the author(s) and should not be construed as an official Department of the Army position, policy, or decision, unless so designated by other documentation.

This material is based upon work supported by the National Science Foundation under Grant No. DMR-9526060. Any opinions, findings, and conclusions or recommendations expressed in this materials are those of the author(s) and do not necessarily reflect the views of the National Science Foundation.

This work relates to Department of Navy Grant N00014-95-1-0857 issued by the Office of Naval Research. The United States Government has a royalty-free license throughout the world in all copyrightable material contained herein.

Single article reprints from this publication are available through University Microfilms Inc., 300 North Zeeb Road, Ann Arbor, Michigan 48106

CODEN: MRSPDH

Copyright 1996 by Materials Research Society.
All rights reserved.

This book has been registered with Copyright Clearance Center, Inc. For further information, please contact the Copyright Clearance Center, Salem, Massachusetts.

Published by:

Materials Research Society
9800 McKnight Road
Pittsburgh, Pennsylvania 15237
Telephone (412) 367-3003
Fax (412) 367-4373
Website: <http://www.mrs.org/>

Library of Congress Cataloging in Publication Data

Gallium nitride and related materials : first international symposium held November 27- December 1, 1995, Boston, Massachusetts, U.S.A. / editors, F. A. Ponce, R.D. Dupuis, S. Nakamura, J.A. Edmond
p. cm—(Materials Research Society symposium proceedings ; v. 395)
Includes bibliographical references and index.
ISBN 1-55899-298-7 (alk. paper)
1. Semiconductors—Materials—Congresses. 2. Electroluminescent devices—Materials Congresses. 3. Gallium nitride—Congresses. 4. Epitaxy—Congresses. I. Ponce, F.A. II. Dupuis, R.D. III. Nakamura, S. IV. Edmond, J.A. V. Series: Materials Research Society symposium proceedings ; v. 395.

TK7871.15.G33I57 1996
621.3815'2—dc20

96-21894
CIP

Manufactured in the United States of America

CONTENTS

Preface	xix
Acknowledgments	xxi
Materials Research Society Symposium Proceedings	xxii

PART I: CRYSTAL GROWTH - SUBSTRATES AND EARLY STAGES

*Issues and Examples Regarding Growth of AlN, GaN and Al _x Ga _{1-x} N Thin Films Via OMVPE and Gas Source MBE	3
<i>Robert F. Davis, T.W. Weeks, Jr., M.D. Bremser, S. Tanaka, R.S. Kern, Z. Sitar, K.S. Ailey, W.G. Perry, and C. Wang</i>	
*Growth and Properties of Bulk Single Crystals of GaN	15
<i>T. Suski, P. Perlin, M. Leszczyński, H. Teisseyre, I. Grzegory, J. Jun, M. Boćkowski, S. Porowski, K. Pakuła A. Wyszomerek, and J.M. Baranowski</i>	
*Growth of Cubic GaN on (001) GaAs	27
<i>O. Brandt, H. Yang, A. Trampert, and K.H. Ploog</i>	
*Lattice-Matching Growth of InGaAlN Systems	39
<i>Takashi Matsuoka</i>	
ScAlMgO ₄ : An Oxide Substrate for GaN Epitaxy	51
<i>E.S. Hellman, C.D. Brandle, L.F. Schneemeyer, D. Wiesmann, I. Brener, T. Siegrist, G.W. Berkstresser, D.N.E. Buchanan, and E.H. Hartford, Jr.</i>	
Epitaxial Growth of GaN on Lattice-Matched Hafnium Substrates	55
<i>R. Beresford, K.S. Stevens, C. Briant, R. Bal, and D.C. Paine</i>	
Properties of GaN Epitaxial Layer Grown by MOVPE on MgAl ₂ O ₄ Substrate	61
<i>A. Kuramata, K. Horino, K. Domen, R. Soejima, H. Sudo, and T. Tanahashi</i>	
Gallium Nitride Epitaxy on Silicon: Importance of Substrate Preparation	67
<i>G.A. Martin, B.N. Sverdlov, A. Botchkarev, H. Morkoç, D.J. Smith, S.-C.Y. Tsen, W.H. Thompson, and M.H. Nayfeh</i>	
Hydrazoic Acid: A Potent 'Active Nitrogen' Precursor for Group III Nitride Growth	73
<i>Andrew Freedman and Gary N. Robinson</i>	

*Invited Paper

Growth of GaN on (100)Si Using a New C-H and N-H Free Single-Source Precursor	79
<i>John Kouvetakis, Jeffrey McMurran, David B. Beach, and David J. Smith</i>	
A New Single Source Precursor Approach to Gallium and Aluminum Nitride	85
<i>Deborah A. Neumayer, C.J. Carmalt, M.F. Arendt, J.M. White, A.H. Cowley, R.A. Jones, and J.G. Ekerdt</i>	
The Surface Chemistry of Triallylamine on Si(111) and its Coadsorption with Triethylgallium	91
<i>Dirk Freundt, Georg Landmesser, Angela Rizzi, and Hans Lüth</i>	
Gas Phase Adduct Reactions in MOCVD Growth of GaN	97
<i>A. Thon and T.F. Kuech</i>	
Parasitic Reactions Between Alkyls and Ammonia in OMVPE	103
<i>C.H. Chen, H. Liu, D. Steigerwald, W. Imler, C.P. Kuo, and M.G. Craford</i>	

PART II: MOLECULAR BEAM GROWTH TECHNIQUES

*Epitaxial Growth of GaN Films Produced by ECR-Assisted MBE	111
<i>T.D. Moustakas</i>	
*Growth and Properties of III-V Nitride Films, Quantum Well Structures and Integrated Heterostructure Devices	123
<i>J.F. Schetzina</i>	
NH₃ as Nitrogen Source in MBE Growth of GaN	135
<i>M. Kamp, M. Mayer, A. Pelzmann, A. Thies, H.Y. Chung, H. Sternschulte, O. Marti, and K.J. Ebeling</i>	
Gallium Incorporation Kinetics During GSMBE of GaN	141
<i>Charles R. Jones, Ting Lei, Ron Kaspi, and Keith R. Evans</i>	
ECR-MBE and GSMBE of Gallium Nitride on Si(111)	145
<i>U. Rossner, J.-L. Rouviere, A. Bourret, and A. Barski</i>	
Growth and Doping of GaN Directly on 6H-SiC by MBE	151
<i>D. Korakakis, A. Sampath, H.M. Ng, G. Morales, I.D. Goepfert, and T.D. Moustakas</i>	
Plasma-Assisted MBE of GaN and AlGa_xN on 6H SiC(0001)	157
<i>S. Sinharoy, A.K. Agarwal, G. Augustine, L.B. Rowland, R.L. Messham, M.C. Driver, and R.H. Hopkins</i>	

* Invited Paper

Growth of InGaN Films by MBE at the Growth Temperature of GaN	163
---	-----

R. Singh and T.D. Moustakas

P-type Mg-Doped GaN Grown by Molecular Beam Epitaxy Using Ammonia as the Nitrogen Source	169
--	-----

Z. Yang, L.K. Li, and W.I. Wang

Defect Microstructure of Thin Wurtzite GaN Films Grown by MBE	175
---	-----

B.N. Sverdlov, A. Botchkarev, G.A. Martin, A. Salvador, H. Morkoç, S.-C.Y. Tsen, and David J. Smith

PART III: CHEMICAL VAPOR PHASE GROWTH TECHNIQUES

High-Quality III-V Nitrides Grown by Metalorganic Chemical Vapor Deposition	183
---	-----

R.D. Dupuis, A.L. Holmes, P.A. Grudowski, K.G. Fertitta, and F.A. Ponce

Optoelectronic and Structural Properties of High-Quality GaN Grown by Hydride Vapor Phase Epitaxy	189
---	-----

R.J. Molnar, R. Aggarwal, Z.-L. Liau, E.R. Brown, I. Melngailis, W. Götz, L.T. Romano, and N.M. Johnson

Growth and Doping of $\text{Al}_x\text{Ga}_{1-x}\text{N}$ Deposited Directly on $\alpha(6\text{H})\text{-SiC}(0001)$ Substrates Via Organometallic Vapor Phase Epitaxy	195
--	-----

M.D. Bremser, W.G. Perry, N.V. Edwards, T. Zheleva, N. Parikh, D.E. Aspnes, and R.F. Davis

MOVPE Growth of High Electron Mobility AlGaIn/GaN Heterostructures	201
--	-----

J.M. Redwing, J.S. Flynn, M.A. Tischler, W. Mitchel, and A. Saxler

Growth Kinetics and Structural Quality in GaN Epitaxy by Low Pressure MOVPE	207
---	-----

O. Briot, J.P. Alexis, B. Gil, and R.L. Aulombard

Low-Temperature Growth of High Quality $\text{In}_x\text{Ga}_{1-x}\text{N}$ by Atomic Layer Epitaxy	213
---	-----

K.S. Boutros, J.C. Roberts, F.G. McIntosh, E.L. Piner, N.A. El-Masry, and S.M. Bedair

AlGaInN Quaternary Alloys by MOCVD	219
--	-----

F.G. McIntosh, E. Piner, K. Boutros, J.C. Roberts, Y. He, M. Moussa, N. El-Masry, and S.M. Bedair

A Study of the Effect of Growth Rate and Annealing on GaN Buffer Layers on Sapphire	225
---	-----

J.C. Ramer, K. Zheng, C.F. Kranenberg, M. Banas, and S.D. Hersee

The Effect of a GaN Nucleation Layer on GaN Film Properties Grown by Metalorganic Chemical Vapor Deposition	231
<i>W. Van der Stricht, I. Moerman, P. Demeester, J.A. Crawley, E.J. Thrush, P.G. Middleton, C. Trager-Cowan, and K.P. O'Donnell</i>	
An Atomic Force Microscopy Study of the Initial Nucleation of GaN on Sapphire	237
<i>M. Richards-Babb, S.L. Buczowski, Zhonghai Yu, and T.H. Myers</i>	
Halide Vapor Phase Epitaxy of Gallium Nitride Films on Sapphire and Silicon Substrates	243
<i>M.R. Perkins, M.N. Horton, Z.Z. Bandic, T.C. McGill, and T.F. Kuech</i>	
AlN Films Deposited by LP-MOCVD Atomic Layer Deposition at Lower Temperatures Using DMEAA and Ammonia	249
<i>J.N. Kidder, Jr., J.S. Kuo, T.P. Pearsall, and J.W. Rogers, Jr.</i>	
A Modeling Study of GaN Growth by MOVPE	255
<i>S.A. Safvi, J.M. Redwing, M.A. Tischler, and T.F. Kuech</i>	
Effect of Carrier Gas on the Surface Morphology and Mosaic Dispersion for GaN Films by Low-Pressure MOCVD	261
<i>T.J. Kistenmacher, D.K. Wickenden, M.E. Hawley, and R.P. Leavitt</i>	
Facets Formation Mechanism of GaN Hexagonal Pyramids on Dot-Patterns Via Selective MOVPE	267
<i>Kazumasa Hiramatsu, Shota Kitamura, and Nobuhiko Sawaki</i>	
Growth of High Quality InGaN Films by Metalorganic Chemical Vapor Deposition	273
<i>J.C. Roberts, F.G. McIntosh, K.S. Boutros, S.M. Bedair, M. Moussa, E.L. Piner, Y. He, and N.A. El-Masry</i>	
Low Resistivity Aluminum Nitride: Carbon (AlN:C) Films Grown by Metalorganic Chemical Vapor Deposition	279
<i>K. Wongchotikul, N. Chen, D.P. Zhang, X. Tang, and M.G. Spencer</i>	

PART IV: ALLOYS AND NOVEL GROWTH TECHNIQUES

*GaAsN Alloys and GaN/GaAs Double-Heterostructures	285
<i>Michio Sato</i>	
GaN Three Dimensional Nanostructures	295
<i>V. Dmitriev, K. Irvine, A. Zubrilov, D. Tsvetkov, V. Nikolaev, M. Jakobson, D. Nelson, and A. Sitnikova</i>	

* Invited Paper

Supersonic Jet Epitaxy: An Improved Method for Nitride Deposition	301
<i>Peter E. Norris, Long D. Zhu, H. Paul Maruska, Willson Ho, Scott Ustin, and L. Lauhon</i>	
New Buffer Layers for GaN on Sapphire by Atomic Layer and Molecular Stream Epitaxy	307
<i>E.L. Piner, Y.W. He, K.S. Boutros, F.G. McIntosh, J.C. Roberts, S.M. Bedair, and N.A. El-Masry</i>	
Low Temperature Epitaxial Growth of AlN and GaN Thin Films by the Method of Ion Beam Assisted Deposition	313
<i>Ig-Hyeon Kim, Chan-Wook Jeon, and Seon-Hyo Kim</i>	
Single Crystal Wurtzitic Aluminum Nitride Growth on Silicon Using Supersonic Gas Jets	319
<i>S.A. Ustin, L. Lauhon, K.A. Brown, D.Q. Hu, and W. Ho</i>	
Epitaxial Growth of AlN Thin Films on Silicon and Sapphire by Pulsed Laser Deposition	325
<i>R.D. Vispute, H. Wu, K. Jagannadham, and J. Narayan</i>	
Deposition of Gallium Nitride Films Using Ammonia and Triethylgallium Seeded Helium Beams	331
<i>J.J. Sumakeris, R.K. Chilukuri, R.F. Davis, and H.H. Lamb</i>	
Alternative Routes to the MOVPE Growth of GaN and AlN	337
<i>V. Roberts, J.S. Roberts, A.C. Jones, and S. Rushworth</i>	
Low Temperature Growth of Oriented Gallium Nitride Using Pulsed Laser Deposition	343
<i>Robert Leuchtner, W. Brock, Y. Li, and L. Hristakos</i>	

PART V: STRUCTURAL PROPERTIES

*Structural Defects in Heteroepitaxial and Homoepitaxial GaN	351
<i>Zuzanna Liliental-Weber, S. Ruvimov, Ch. Kisielowski, Y. Chen, W. Swider, J. Washburn, N. Newman, A. Gassmann, X. Liu, L. Schloss, E.R. Weber, I. Grzegory, M. Bockowski, J. Jun, T. Suski, K. Pakula, J. Baranowski, S. Porowski, H. Amano, and I. Akasaki</i>	
High-Precision Characterization of III-Nitride Semiconductor Alloys with Secondary Ion Mass Spectrometry (SIMS)	363
<i>J.W. Erickson, Y. Gao, and R.G. Wilson</i>	
Photoluminescence and SIMS Studies of Hydrogen Passivation of Mg-Doped P-Type Gallium Nitride	369
<i>Y. Li, Y. Lu, H. Shen, M. Wraback, C.-Y. Hwang, M. Schurman, W. Mayo, T. Salagaj, and R.A. Stall</i>	

* Invited Paper

XPS Measurement of the SiC/AlN Band-Offset at the (0001) Interface	375
<i>Sean W. King, Mark C. Benjamin, Robert J. Nemanich, Robert F. Davis, and Walter R.L. Lambrecht</i>	
A Microscopic Evaluation of the Surface Structure of OMVPE Deposited α-GaN Epilayers	381
<i>G.S. Rohrer, J. Payne, W. Qian, M. Skowronski, K. Doverspike, L.B. Rowland, and D.K. Gaskill</i>	
The Microstructural Study of Aluminum Nitride Thin Films: Epitaxy on the Two Orientations of Sapphire and Texturing on Si	387
<i>K. Dovidenko, S. Oktyabrsky, J. Narayan, and M. Razeghi</i>	
Understanding the Pyramidal Growth of GaN	393
<i>J.-L. Rouviere, M. Arlery, A. Bourret, R. Niebuhr, and K.-H. Bachem</i>	
Elastic Constants and Related Properties of the Group III-Nitrides	399
<i>Kwiseon Kim, Walter R.L. Lambrecht, and B. Segall</i>	
Analysis of Strain in GaN on Al₂O₃ and 6H-SiC: Near-Bandedge Phenomena	405
<i>N.V. Edwards, M.D. Bremser, T.W. Weeks, Jr., R.S. Kern, H. Liu, R.A. Stall, A.E. Wickenden, K. Doverspike, D.K. Gaskill, J.A. Freitas, Jr., U. Rossow, R.F. Davis, and D.E. Aspnes</i>	
Strain Effects in GaN on Sapphire: Towards a Quantitative Comprehension	411
<i>O. Briot, J.P. Alexis, B. Gil, and R.L. Aulombard</i>	
Defect Studies of GaN Under Large Hydrostatic Pressure	417
<i>C. Wetzel, S. Fischer, W. Walukiewicz, J. Ager, III, E.E. Haller, I. Grzegory, S. Porowski, and T. Suski</i>	
The Phonon Densities of States of AlN and ZnN	423
<i>C.-K. Loong</i>	
Structure and Quasiparticle Energies of Cubic, Wurtzite and Hexagonal BN	429
<i>Giancarlo Cappellini, Vincenzo Fiorentini, Katrin Tenelsen, and Friedhelm Bechstedt</i>	
Simulated Thermal Effects on Structural and Electronic Properties of GaN	435
<i>S. Serra, L. Miglio, and Vincenzo Fiorentini</i>	

PART VI: ELECTRONIC PROPERTIES

*Shallow and Deep Level Defects in GaN	443
<i>W. Götz, N.M. Johnson, D.P. Bour, C. Chen, H. Liu, C. Kuo, and W. Imler</i>	

* Invited Paper

*Electronic and Optical Properties of the Group-III Nitrides, Their Heterostructures and Alloys	455
<i>Walter R.L. Lambrecht, Kwiseon Kim, Sergey N. Rashkeev, and B. Segall</i>	
Conductivity Measurements of GaN Grown by OMVPE and HVPE	467
<i>M. Ben-Chorin, J. Diener, B.K. Meyer, M. Drechsler, D. Volm, H. Amano, I. Akasaki, T. Detchprohm, and K. Hiramatsu</i>	
Electronic Structures of Wide Band-Gap (AlN)_m(GaN)_n(001) Superlattices	473
<i>Z.-J. Tian, M.W.C. Dharma-Wardana, and L.J. Lewis</i>	
Monte Carlo Calculation of Hole Transport in Bulk Zincblende Phase of GaN Including a Pseudopotential Calculated Band Structure	479
<i>I.H. Oguzman, J. Kolnik, K.F. Brennan, R. Wang, and P.P. Ruden</i>	
Excitonic Recombination Processes in Undoped and Doped Wurtzite GaN Films Deposited on Sapphire Substrates	485
<i>J.A. Freitas, Jr., K. Doverspike, and A.E. Wickenden</i>	
Identification of Transition Metals In GaN	491
<i>K. Pressel, R. Heitz, L. Eckey, I. Loa, P. Thurian, A. Hoffmann, B.K. Meyer, S. Fischer, C. Wetzel, and E.E. Haller</i>	
Magnesium Doping of GaN by Metalorganic Chemical Vapor Deposition	497
<i>Hongqiang Lu and Ishwara Bhat</i>	
Hydrogen, Acceptors, and H-Acceptor Complexes in GaN	503
<i>Andrea Bosin, Vincenzo Fiorentini, and David Vanderbilt</i>	
Electronic Structure of a Nitrogen Vacancy in Cubic Gallium Nitride	509
<i>V.A. Gubanov, A.F. Wright, J.S. Nelson, C.Y. Fong, and B.M. Klein</i>	
Structural and Electronic Properties of AlN, GaN and InN, and Band Offsets at AlN/GaN (101$\bar{0}$) and (0001) Interfaces	515
<i>A. Satta, Vincenzo Fiorentini, Andrea Bosin, F. Meloni, and David Vanderbilt</i>	
The Role of Impurities in LP-MOCVD Grown Gallium Nitride	521
<i>C.-Y. Hwang, Y. Li, M.J. Schurman, W.E. Mayo, Y. Lu, and R.A. Stall</i>	
*Optical Properties of Mg-GaN, GaN/AlGa_{0.5}N SCH Structures, and GaN on ZnO Substrates	527
<i>H. Morkoç, W. Kim, Ö. Aktas, A. Salvador, A. Botchkarev, D.C. Reynolds, D.C. Look, M. Smith, G.D. Chen, J.Y. Lin, H.X. Jiang, T.J. Schmidt, X.H. Yang, W. Shan, J.J. Song, B. Goldenberg, C.W. Litton, and K. Evans</i>	

*Invited Paper

PART VII: OPTICAL PROPERTIES

Growth and Optical Properties of GaN Grown by MBE on Novel Lattice-Matched Oxide Substrates	535
<i>J.F.H. Nicholls, H. Gallagher, B. Henderson, C. Trager-Cowan, P.G. Middleton, K.P. O'Donnell, T.S. Cheng, C.T. Foxon, and B.H.T. Chai</i>	
Electroreflectance from Gallium Nitride Using Second-Harmonic Generation	541
<i>Joseph Miragliotta and Dennis K. Wickenden</i>	
Optical Properties of Wurtzite-and Zincblende-GaN Films Grown by RF Plasma-MBE	547
<i>F. Semendy, N. Bambha, J.G. Kim, H. Liu, and R.M. Park</i>	
Temperature Dependence of the Absorption Band Gap Edge of GaN	553
<i>M.O. Manasreh and A.K. Sharma</i>	
Near-Bandgap Photoluminescence Decay Time in GaN Epitaxial Layers Grown on Sapphire	559
<i>A. Hangleiter, J.S. Im, T. Forner, V. Härle, and F. Scholz</i>	
Picosecond Raman Studies of Electron-Phonon Interactions in the Wide Bandgap Semiconductor GaN	565
<i>K.T. Tsen, D.K. Ferry, A. Botchkarev, B. Sverdlov, A. Salvador, and H. Morkoç</i>	
Fine Structure of the 3.42 eV Emission Band in GaN	571
<i>S. Fischer, C. Wetzel, W. Walukiewicz, and E.E. Haller</i>	
Spatially-Resolved Photoluminescence and Raman Study on the GaN/Substrate Interface	577
<i>H. Siegle, P. Thurian, L. Eckey, A. Hoffmann, C. Thomsen, B.K. Meyer, T. Detchprohm, K. Hiramatsu, H. Amano, and I. Akasaki</i>	
Excitation Wavelength and Saturation Effects on Gallium Nitride Photoluminescence	583
<i>Mike Banas, Guangtian Liu, Jeff Ramer, Kang Zheng, Steve Hersee, and Kevin Malloy</i>	
Selective Dynamical Study of Luminescences Near the Surface and the Interface of Epitaxial GaN	589
<i>L. Eckey, A. Hoffmann, R. Heltz, I. Broser, B.K. Meyer, T. Detchprohm, K. Hiramatsu, H. Amano, and I. Akasaki</i>	
Photoluminescence Related to the 2-Dimensional Electron Gas in Modulation Doped GaN/AlGaIn Structures	595
<i>J.P. Bergman, T. Lundström, B. Monemar, H. Amano, and I. Akasaki</i>	

Dielectric Functions of Wurtzite and Zincblende Structure GaN	601
<i>R. Wang, P.P. Ruden, J. Kolnik, I. Oguzman, and K.F. Brennan</i>	
Exciton Luminescence of Single-Crystal GaN	607
<i>J.R. Müllhäuser, O. Brandt, H. Yang, and K.H. Ploog</i>	
Transition Metal Luminescence in AlN Crystals	613
<i>K. Pressel, R. Heltz, S. Nilsson, P. Thurian, A. Hoffmann, and B.K. Meyer</i>	
2.2 eV Luminescence in GaN	619
<i>D.M. Hofmann, D. Kovalev, G. Steude, D. Volm, B.K. Meyer, C. Xavier, T. Monteiro, E. Pereira, E.N. Mokov, H. Amano, and I. Akasaki</i>	
Growth of GaN Without Yellow Luminescence	625
<i>X. Zhang, P. Kung, D. Walker, A. Saxler, and M. Razeghi</i>	

PART VIII: POINT DEFECTS

*Light Generating Carrier Recombination and Impurities in Wurtzite GaN/Al₂O₃ Grown by MOCVD	633
<i>U. Kaufmann, M. Kunzer, C. Merz, I. Akasaki, and H. Amano</i>	
*Theory of Point Defects and Complexes in GaN	645
<i>Jörg Neugebauer and Chris G. Van de Walle</i>	
*Spin-Dependent Transport in GaN Light Emitting Diodes	657
<i>M.S. Brandt, N.M. Reinacher, O. Ambacher, and M. Stutzmann</i>	
Detection of Magnetic Resonance on Shallow Donor - Shallow Acceptor and Deep (2.2 eV) Recombination from GaN Films Grown on 6H-SiC	667
<i>E.R. Glaser, T.A. Kennedy, S.W. Brown, J.A. Freitas, Jr., W.G. Perry, M.D. Bremser, T.W. Weeks, Jr., and R.F. Davis</i>	
Magnetic Resonance Studies of Recombination Processes in GaN-Based Light Emitting Diodes	673
<i>W.E. Carlos, E.R. Glaser, T.A. Kennedy, and S. Nakamura</i>	
On Compensation and Impurities in State-of-the-Art GaN Epilayers Grown on Sapphire	679
<i>A.E. Wickenden, D.K. Gaskill, D.D. Koleske, K. Doverspike, D.S. Simons, and P.H. Chi</i>	
Role of C, O and H in III-V Nitrides	685
<i>C.R. Abernathy, S.J. Pearton, J.D. MacKenzie, J.W. Lee, C.B. Vartuli, R.G. Wilson, R.J. Shul, J.C. Zolper, and J.M. Zavada</i>	

*Invited Paper

Infrared Absorption and Electron Spin Resonance Studies of Nanocrystalline Cubic Boron Nitride/Amorphous Hydrogenated Boron Nitride Mixed Phase Thin Films	691
<i>Shu-Han Lin, Ian M. Brown, and Bernard J. Feldman</i>	

Magneto-Optic Studies of GaN Films and GaN/AlGaN Heterostructures	697
<i>Y.J. Wang, H.K. Ng, R. Kaplan, K. Doverspike, D.K. Gaskill, T. Ikeda, H. Amano, and I. Akasaki</i>	

Deep States in GaN Studied by Thermally Stimulated Current Spectroscopy	703
<i>Z.C. Huang, J.C. Chen, and D.B. Mott</i>	

Exciton Lifetimes in GaN	709
<i>J.P. Bergman, C. Harris, B. Monemar, H. Amano, and I. Akasaki</i>	

PART IX: HYDROGEN, ETCHING AND OTHER MATERIALS PROCESSES

*Dry Etching of III-V Nitrides	717
<i>S.J. Pearton, R.J. Shul, G.F. McLane, and C. Constantine</i>	

*Hydrogen in GaN	723
<i>N.M. Johnson, W. Götz, J. Neugebauer, and C.G. Van de Walle</i>	

Theoretical Study of Electron Initiated Impact Ionization Rate in Bulk GaN Using a Wave Vector Dependent Numerical Transition Rate Formulation	733
<i>J. Kolnik, I.H. Oguzman, K.F. Brennan, R. Wang, and P.P. Ruden</i>	

Ex Situ and In Situ Methods for Oxide and Carbon Removal from AlN and GaN Surfaces	739
<i>Sean W. King, Laura L. Smith, John P. Barnak, Ja-Hum Ku, Jim A. Christman, Mark C. Benjamin, Michael D. Bremser, Robert J. Nemanich, and Robert F. Davis</i>	

The Effect of Hydrogen-Based, High Density Plasma Etching on the Electronic Properties of Gallium Nitride	745
<i>C.R. Eddy, Jr. and B. Molnar</i>	

Plasma Chemistry Dependent ECR Etching of GaN	751
<i>R.J. Shul, C.I.H. Ashby, D.J. Rieger, A.J. Howard, S.J. Pearton, C.R. Abernathy, C.B. Vartuli, P.A. Barnes, and P. Davis</i>	

Reactive Ion Etching of AlN, AlGaIn, and GaN Using BCl₃	757
<i>W.C. Hughes, W.H. Rowland, Jr., M.A.L. Johnson, J.W. Cook, Jr., and J.F. Schetzina</i>	

Electron Cyclotron Resonance Etching Characteristics of GaN in Plasmas with and without Hydrogen	763
<i>L. Zhang, J. Ramer, J. Brown, K. Zheng, L.F. Lester, and S.D. Hersee</i>	

*Invited Paper

**Effects of Reactive Ion Etching on the Electrical Properties
of n-GaN Surfaces 769**

A.T. Ping, A.C. Schmitz, M. Asif Khan, and I. Adesida

PART X: SURFACES AND METAL CONTACTS

***(Negative) Electron Affinity of AlN and AlGaN Alloys 777**

*R.J. Nemanich, M.C. Benjamin, S.P. Bozeman, M.D. Bremser,
S.W. King, B.L. Ward, R.F. Davis, B. Chen, Z. Zhang, and J. Bernholc*

**Negative Differential Resistivity in GaN
Metal-Semiconductor-Metal Photoconductors 789**

Z.C. Huang, J.C. Chen, Youdou Zheng, and D.B. Mott

Properties of Zn Implanted GaN 795

S. Strite, P.W. Epperlein, A. Dommann, A. Rockett, and R.F. Broom

**Ion Implantation Doping and High Temperature
Annealing of GaN 801**

*J.C. Zolper, M. Hagerott Crawford, A.J. Howard, S.J. Pearton,
C.R. Abernathy, C.B. Vartuli, C. Yuan, R.A. Stall, J. Ramer,
S.D. Hersee, and R.G. Wilson*

**Ion Damage and Annealing of Epitaxial Gallium Nitride
and Comparison with GaAs/AlGaAs Materials 807**

H.H. Tan, J.S. Williams, C. Yuan, and S.J. Pearton

**Annealing Study of Ion Implanted MOCVD and MBE
Grown GaN 813**

*E. Silkowski, Y.K. Yeo, R.L. Hengehold, M.A. Khan, T. Lei, K. Evans,
and C. Cerny*

Interfacial Reactions Between Metal Thin Films and p-GaN 819

J.T. Trexler, S.J. Miller, P.H. Holloway, and M.A. Khan

Thermal Stability of Ohmic Contacts to n-In_xGa_{1-x}N 825

*A. Durbha, S.J. Pearton, C.R. Abernathy, J.W. Lee, P.H. Holloway,
and F. Ren*

Schottky Barrier Heights of Ni, Pt, Pd, and Au on n-type GaN 831

A.C. Schmitz, A.T. Ping, M. Asif Khan, and I. Adesida

Schottky Barriers on p-GaN 837

N.I. Kuznetsov, E.V. Kalinina, V.A. Soloviev, and V.A. Dmitriev

Metallurgical Study of Contacts to Gallium Nitride 843

S.E. Mohny, B.P. Luther, T.N. Jackson, and M.A. Khan

*Invited Paper

Calculations of the Specific Resistance of Contacts to III-V Nitride Compounds	849
<i>P.A. Barnes, X-J Zhang, M.L. Lovejoy, T.J. Drummond, H.P. Hjalmarson, M. Crawford, R.J. Shul, and J.C. Zolper</i>	
Ohmic Contacts to Si-implanted and Un-implanted n-type GaN	855
<i>J. Brown, J. Ramer, K. Zheng, L.F. Lester, S.D. Hersee, and J. Zolper</i>	
Ohmic Contact Formation to Doped GaN	861
<i>L.L. Smith, M.D. Bremser, E.P. Carlson, T.W. Weeks, Jr., Y. Huang, M.J. Kim, R.W. Carpenter, and R.F. Davis</i>	

PART XI: DEVICES

*Fabrication and Properties of AlGaIn/GaN Double Heterostructure Grown on 6H-SiC(0001) _{Si}	869
<i>Hiroshi Amano, Shigetoshi Sota, Masaki Nishikawa, Masato Yoshida, Makoto Kawaguchi, Masahiro Ohta, Hiromitsu Sakai, and Isamu Akasaki</i>	
InGaIn Light-Emitting Diodes with Quantum-Well Structures	879
<i>Shuji Nakamura</i>	
*Light-Emitting Devices Based on Gallium Nitride and Related Compound Semiconductors	889
<i>M. Koike, N. Shibata, S. Yamasaki, S. Nagai, S. Asami, H. Kato, N. Koide, H. Amano, and I. Akasaki</i>	
*Growth of Silicon-Doped and High Quality, Highly Resistive GaN for FET Applications	897
<i>K. Doverspike, A.E. Wickenden, S.C. Binari, D.K. Gaskill, and J.A. Freitas, Jr.</i>	
*AlGaIn/GaN/AlGaIn Double-Heterojunction Blue LEDs on 6H-SiC Substrates	903
<i>Hua-Shuang Kong, Michelle Leonard, Gary Bulman, Gerry Negley, and John Edmond</i>	
Electric Breakdown in Nitride PN Junctions	909
<i>V.A. Dmitriev, N.I. Kuznetsov, K.G. Irvine, and C.H. Carter, Jr.</i>	
*Recent Progress in AlGaIn/GaN Based Optoelectronic Devices	913
<i>M.A. Khan, Q. Chen, C.J. Sun, J.W. Yang, and M.S. Shur</i>	
Optically Pumped GaN-AlGaIn Double-Heterostructure Lasers Grown by ECR-GSMBE and HVPE	919
<i>P.A. Maki, R.J. Molnar, R.L. Aggarwal, Z-L. Liao, and I. Melngailis</i>	

*Invited Paper

Analysis of Wurtzite GaN/AlGa_N Quantum Well Lasers from First-Principles Calculations	925
<i>T. Uenoyama and M. Suzuki</i>	
Room-Temperature Life Test of Nichia AlGa_N/InGa_N/Ga_N Blue Light Emitting Diodes	931
<i>Marek Osⁿⁱski, Christopher J. Helms, Niel Berg, Daniel L. Barton, and B. Scott Phillips</i>	
Electrical Properties of Nichia AlGa_N/InGa_N/Ga_N Blue LEDs in a Wide Current/Temperature Range	937
<i>Joachim Zeller, Petr G. Eliseev, Philippe Sartori, Piotr Perlin, and Marek Osⁿⁱski</i>	
Correlation of Surface Morphology and Optical Properties of Ga_N by Conventional and Selective-Area MOCVD	943
<i>X. Li, A.M. Jones, S.D. Roh, D.A. Turnbull, E.E. Reuter, S.Q. Gu, S.G. Bishop, and J.J. Coleman</i>	
Light Emission Properties of Ga_N-Based Double Heterostructures and Quantum Wells	949
<i>D.A.S. Loeber, J.M. Redwing, N.G. Anderson, and M.A. Tischler</i>	
Spectral Response of Ga_N P-N Junction Photovoltaic Structures	955
<i>D. Walker, X. Zhang, P. Kung, A. Saxler, J. Xu, and M. Razeghi</i>	
Author Index	961
Subject Index	967

PREFACE

The current excitement in the scientific community about the III-V nitrides was reflected in this First International Symposium on Gallium Nitride and Related Materials (ISGN-1). The symposium consisted of nine half-day oral sessions (25 invited and 54 contributed talks) and four poster sessions (113 presentations). The attendance was very high for all sessions, with an estimated peak of over 550 attendees at one of the sessions.

The symposium reflected the large amount of work that has taken place since the field exploded about two years ago with the announcement of commercial blue light emitting devices. The invited talk program was designed to give a thorough review of the state of the art in the field. The large number of contributions, in the form of talks and poster presentations, showed much progress in understanding III-V nitrides, and in the production of optoelectronic devices based on these materials. These proceedings represent the current state of understanding in the field, reflecting about 75% of the work presented at the symposium.

The procedures for the second gathering in this series was decided during the week of the symposium. It was agreed that every effort should be made to unify the community. The suggestion of the Japanese delegation was to unite the efforts of the ISGN-1 with those of the Topical Workshop on GaN, held in Nagoya in October 1995, and to produce a single unified international conference series with the second meeting to be held in Japan in 1997. It was decided that this series of meetings would alternate between the United States, Japan and Europe. Thus, the Second International Conference on Nitride Semiconductors, ICNS'97, is currently being planned to be held in Tokushima, Japan, in October 1997, and will be chaired by Professor I. Akasaki, and organized together with Professors S. Yoshida, S. Sakai, K. Kishino, S. Nakamura, and K. Hiramatsu.

It is with much enthusiasm for the future of III-V nitrides that we present these proceedings for publication by the Materials Research Society.

F. A. Ponce
R. D. Dupuis
S. Nakamura
J. A. Edmond

December 1995

ACKNOWLEDGMENTS

We wish to thank the following organizations for their generous financial support of the symposium:

Advanced Research Projects Agency
Air Products and Chemicals Incorporated
AIXTRON
Akzo Chemicals Inc.
Army Research Office
Cree Research, Inc.
Crystal Systems
EMCORE Corporation
Hewlett-Packard OED
JEOL USA
Morton International
National Science Foundation
Office of Naval Research
Rockwell International

We would also like to thank our invited speakers, who with their talks and participation as session chairs, contributed greatly to the success of this symposium:

H. Amano	H.-S. Kong
M.S. Brandt	W.R.L. Lambrecht
O. Brandt	Z. Liliental-Weber
M.G. Craford	T. Matsuoka
R.F. Davis	H. Morkoc
K. Doverspike	T.D. Moustakas
B.L. Goldenberg	R.J. Nemanich
W. Götz	J. Neugebauer
N.M. Johnson	S.J. Pearton
U. Kaufmann	M. Sato
M.A. Khan	J.F. Schetzina
M. Koike	T. Suski

We would especially like to thank all of the authors for the high quality of the oral and poster presentations, and for submitting manuscripts in a timely manner. In addition, we are very grateful to all of the referees for their conscientious review of the manuscripts. We are also very grateful to the staff of MRS for their efficient support.

MATERIALS RESEARCH SOCIETY SYMPOSIUM PROCEEDINGS

- Volume 377—Amorphous Silicon Technology—1995, M. Hack, E.A. Schiff, M. Powell, A. Matsuda, A. Madan, 1995, ISBN: 1-55899-280-4
- Volume 378—Defect- and Impurity-Engineered Semiconductors and Devices, S. Ashok, J. Chevallier, I. Akasaki, N.M. Johnson, B.L. Soporl, 1995, ISBN: 1-55899-281-2
- Volume 379—Strained Layer Epitaxy—Materials, Processing, and Device Applications, J. Bean, E. Fitzgerald, J. Hoyt, K-Y. Cheng, 1995, ISBN: 1-55899-282-0
- Volume 380—Materials—Fabrication and Patterning at the Nanoscale, C.R.K. Marrian, K. Kash, F. Cerrina, M.G. Lagally, 1995, ISBN: 1-55899-283-9
- Volume 381—Low-Dielectric Constant Materials—Synthesis and Applications in Microelectronics, T-M. Lu, S.P. Murarka, T.S. Kuan, C.H. Ting, 1995, ISBN: 1-55899-284-7
- Volume 382—Structure and Properties of Multilayered Thin Films, T.D. Nguyen, B.M. Lairson, B.M. Clemens, K. Sato, S-C. Shin, 1995, ISBN: 1-55899-285-5
- Volume 383—Mechanical Behavior of Diamond and Other Forms of Carbon, M.D. Drory, M.S. Donley, D. Bogy, J.E. Field, 1995, ISBN: 1-55899-286-3
- Volume 384—Magnetic Ultrathin Films, Multilayers and Surfaces, A. Fert, H. Fujimori, G. Guntherodt, B. Heinrich, W.F. Egelhoff, Jr., E.E. Marinero, R.L. White, 1995, ISBN: 1-55899-287-1
- Volume 385—Polymer/Inorganic Interfaces II, L. Drzal, N.A. Peppas, R.L. Opila, C. Schutte, 1995, ISBN: 1-55899-288-X
- Volume 386—Ultraclean Semiconductor Processing Technology and Surface Chemical Cleaning and Passivation, M. Liehr, M. Hirose, M. Heyns, H. Parks, 1995, ISBN: 1-55899-289-8
- Volume 387—Rapid Thermal and Integrated Processing IV, J.C. Sturm, J.C. Gelpey, S.R.J. Brueck, A. Kermani, J.L. Regolini, 1995, ISBN: 1-55899-290-1
- Volume 388—Film Synthesis and Growth Using Energetic Beams, H.A. Atwater, J.T. Dickinson, D.H. Lowndes, A. Polman, 1995, ISBN: 1-55899-291-X
- Volume 389—Modeling and Simulation of Thin-Film Processing, C.A. Volkert, R.J. Kee, D.J. Srolovitz, M.J. Fluss, 1995, ISBN: 1-55899-292-8
- Volume 390—Electronic Packaging Materials Science VIII, R.C. Sundahl, K.A. Jackson, K-N. Tu, P. Børgesen, 1995, ISBN: 1-55899-293-6
- Volume 391—Materials Reliability in Microelectronics V, A.S. Oates, K. Gadepally, R. Rosenberg, W.F. Filter, L. Greer, 1995, ISBN: 1-55899-294-4
- Volume 392—Thin Films for Integrated Optics Applications, B.W. Wessels, S.R. Marder, D.M. Walba, 1995, ISBN: 1-55899-295-2
- Volume 393—Materials for Electrochemical Energy Storage and Conversion—Batteries, Capacitors and Fuel Cells, D.H. Doughty, B. Vyas, J.R. Huff, T. Takamura, 1995, ISBN: 1-55899-296-0
- Volume 394—Polymers in Medicine and Pharmacy, A.G. Mikos, K.W. Leong, M.L. Radomsky, J.A. Tamada, M.J. Yaszemski, 1995, ISBN: 1-55899-297-9
- Volume 395—Gallium Nitride and Related Materials—The First International Symposium on Gallium Nitride and Related Materials, R.D. Dupuis, J.A. Edmond, F.A. Ponce, S.J. Nakamura, 1996, ISBN: 1-55899-298-7
- Volume 396—Ion-Solid Interactions for Materials Modification and Processing, D.B. Poker, D. Ila, Y-T. Cheng, L.R. Harriott, T.W. Sigmon, 1996, ISBN: 1-55899-299-5
- Volume 397—Advanced Laser Processing of Materials—Fundamentals and Applications, D. Norton, R. Singh, J. Narayan, J. Cheung, L.D. Laude, 1996, ISBN: 1-55899-300-2
- Volume 398—Thermodynamics and Kinetics of Phase Transformations, J.S. Im, B. Park, A.L. Greer, G.B. Stephenson, 1996, ISBN: 1-55899-301-0

MATERIALS RESEARCH SOCIETY SYMPOSIUM PROCEEDINGS

- Volume 399— Evolution of Epitaxial Structure and Morphology, R. Clarke, A. Zangwill, D. Jesson, D. Chambliss, 1996, ISBN: 1-55899-302-9
- Volume 400— Metastable Metal-Based Phases and Microstructures, R.D. Shull, G. Mazzone, R.S. Averbach, R. Bormann, R.F. Ziolo, 1996 ISBN: 1-55899-303-7
- Volume 401— Epitaxial Oxide Thin Films II, J.S. Speck, D.K. Fork, R.M. Wolf, T. Shiosaki, 1996, ISBN: 1-55899-304-5
- Volume 402— Silicide Thin Films—Fabrication, Properties, and Applications, R. Tung, K. Maex, P.W. Pellegrini, L.H. Allen, 1996 ISBN: 1-55899-305-3
- Volume 403— Polycrystalline Thin Films II—Structure, Texture, Properties, and Applications, H.J. Frost, C.A. Ross, M.A. Parker, E.A. Holm, 1996 ISBN: 1-55899-306-1
- Volume 404— *In Situ* Electron and Tunneling Microscopy of Dynamic Processes, R. Sharma, P.L. Gai, M. Gajdardziska-Josifovska, R. Sinclair, L.J. Whitman, 1996, ISBN: 1-55899-307-X
- Volume 405— Surface/Interface and Stress Effects in Electronic Material Nanostructures, R.C. Cammarata, S.M. Prokes, K.L. Wang, A. Christou, 1996, ISBN: 1-55899-308-8
- Volume 406— Diagnostic Techniques for Semiconductor Materials Processing, S.W. Pang, O.J. Glemboczi, F.H. Pollack, F. Celii, C.M. Sotomayor Torres, 1996, ISBN 1-55899-309-6
- Volume 407— Disordered Materials and Interfaces—Fractals, Structure, and Dynamics, H.E. Stanley, H.Z. Cummins, D.J. Durian, D.L. Johnson, 1996, ISBN: 1-55899-310-X
- Volume 408— Materials Theory, Simulations, and Parallel Algorithms, E. Kaxiras, P. Vashishta, J. Joannopoulos, R.K. Kalia, 1996, ISBN: 1-55899-311-8
- Volume 409— Fracture—Instability Dynamics, Scaling, and Ductile/Brittle Behavior, R. Blumberg Selinger, J. Mecholsky, A. Carlsson, E.R. Fuller, Jr., 1996, ISBN: 1-55899-312-6
- Volume 410— Covalent Ceramics III—Science and Technology of Non-Oxides, A.F. Hepp, A.E. Kaloyeros, G.S. Fischman, P.N. Kumta, J.J. Sullivan, 1996, ISBN: 1-55899-313-4
- Volume 411— Electrically Based Microstructural Characterization, R.A. Gerhardt, S.R. Taylor, E.J. Garboczi, 1996, ISBN: 1-55899-314-2
- Volume 412— Scientific Basis for Nuclear Waste Management XIX, W.M. Murphy, D.A. Knecht, 1996, ISBN: 1-55899-315-0
- Volume 413— Electrical, Optical, and Magnetic Properties of Organic Solid State Materials II, L.R. Dalton, A.K.Y. Jen, M.F. Rubner, C.C.Y. Lee, G.E. Wnek, L.Y. Chiang, 1996, ISBN: 1-55899-316-9
- Volume 414— Thin Films and Surfaces for Bioactivity and Biomedical Applications, C. Cotell, S.M. Gorbalkin, G. Grobe, A.E. Meyer, 1996, ISBN: 1-55899-317-7
- Volume 415— Metal-Organic Chemical Vapor Deposition of Electronic Ceramics II, D.B. Beach, S.B. Desu, P.C. Van Buskirk, 1996, ISBN: 1-55899-318-5
- Volume 416— Diamond for Electronic Applications, D. Dreifus, A. Collins, K. Das, T. Humphreys, P. Pehrsson, 1996, ISBN: 1-55899-319-3
- Volume 417— Optoelectronic Materials - Ordering, Composition Modulation, and Self-Assembled Structures, E.D. Jones, A. Mascarenhas, P. Petroff, R. Bhat, 1996, ISBN: 1-55899-320-7
- Volume 418— Decomposition, Combustion, and Detonation Chemistry of Energetic Materials, T.B. Brill, W.C. Tao, T.P. Russell, R.B. Wardle, 1996 ISBN: 1-55899-321-5
- Volume 419— Spectroscopy of Heterojunctions, N. Tolk, G. Margaritondo, E. Viturro, 1996, ISBN: 1-55899-322-3

Part I

Crystal Growth - Substrates and Early Stages

ISSUES AND EXAMPLES REGARDING GROWTH OF AlN, GaN AND $\text{Al}_x\text{Ga}_{1-x}\text{N}$ THIN FILMS VIA OMVPE AND GAS SOURCE MBE

Robert F. Davis, T. W. Weeks, Jr., M. D. Bremser, S. Tanaka, R. S. Kern,
Z. Sitar, K. S. Ailey, W. G. Perry and C. Wang
North Carolina State University, Department of Materials Science and Engineering,
Raleigh, NC 27695-7907

ABSTRACT

Organometallic vapor phase epitaxy (OMVPE) and molecular beam epitaxy (MBE) are the most common methods for the growth of thin films of AlN and GaN. Sapphire is the most common substrate; however, a host of materials have been used with varying degrees of success. Both growth techniques have been employed by the authors to grow AlN, GaN and $\text{Al}_x\text{Ga}_{1-x}\text{N}$ thin films primarily on 6H-SiC(0001). The mismatch in atomic layer stacking sequences along the growth direction produces double positioning boundaries in AlN and the alloys at the SiC steps; this sequence problem appears to discourage the two-dimensional nucleation of GaN. Films of these materials grown by MBE at 650°C are textured; monocrystalline films are achieved between 850°C (pure GaN) and 1050°C (pure AlN) by this technique and OMVPE. Donor and acceptor doping of GaN has been achieved via MBE without post growth annealing. Acceptor doping in CVD material requires annealing to displace the H from the Mg and eventually remove it from the material. High brightness light emitting diodes are commercially available; however, numerous concerns regarding metal and nitrogen sources, heteroepitaxial nucleation, the role of buffer layers, surface migration rates as a function of temperature, substantial defect densities and their effect on film and device properties, ohmic and rectifying contacts, wet and dry etching and suitable gate and field insulators must and are being addressed. Selected issues surrounding the growth of these materials with particular examples drawn from the authors' research are presented herein.

DISCUSSION OF III-N DEPOSITION ISSUES

The growth of III-N thin films have been achieved primarily via several configurations of organometallic vapor phase epitaxy (OMVPE) [1-7] and molecular beam epitaxy (MBE) [8-14]. There are numerous growth-related issues both generally and specifically associated with each of these techniques which have and continue to emerge and receive attention. These problems have not, however, been sufficiently deleterious to prevent the development and commercialization of very bright light emitting diodes over a wide range of wavelengths (see e.g., [15]) and the fabrication of field effect transistors with good properties [16].

The most substantive issue, at present, is the lack of single crystal nitride wafers. Sapphire(0001) is the most commonly used substrate. However, its lattice parameters and coefficients of thermal expansion are substantially different from that of any of nitrides. The same is true for GaAs and Si which have also been employed; only SiC and AlN have atom-atom distances in the closest packed planes which differ by ~1%—a not insignificant amount. These differences, the termination of sapphire with O, the likelihood of a larger surface energy for AlN (and perhaps for GaN) than for sapphire, the differences in stacking sequences along [0001] between SiC and the nitrides and the formation of strong Si-N bonds on Si-terminated SiC(0001) surfaces make difficult the nucleation of AlN and $\text{Al}_x\text{Ga}_{1-x}\text{N}$ alloys on sapphire and GaN on all substrates at high temperatures.

It has been shown by Yoshida [17] and by Amano et al. [18] for MBE and OMVPE growth, respectively, of GaN on sapphire that a thin AlN buffer layer deposited initially at low temperature improves the microstructure and reduces the n-type electrical conductivity of the undoped GaN. The AlN is amorphous or partially crystalline when deposited via OMVPE and some MBE processes; annealing results in crystallization. However, as shown by Hiramatsu et al. [19] and Qian et al. [20], the resulting films are preferentially oriented along [0001], misoriented by <3° in the basal plane and contain low-angle boundaries. The initial crystallites of the GaN epilayer reportedly undergo geometric selection via grain orientation competition until an oriented domain structure emerges, as shown in Fig. 1 [19]. The same is believed to be true for GaN buffer layers

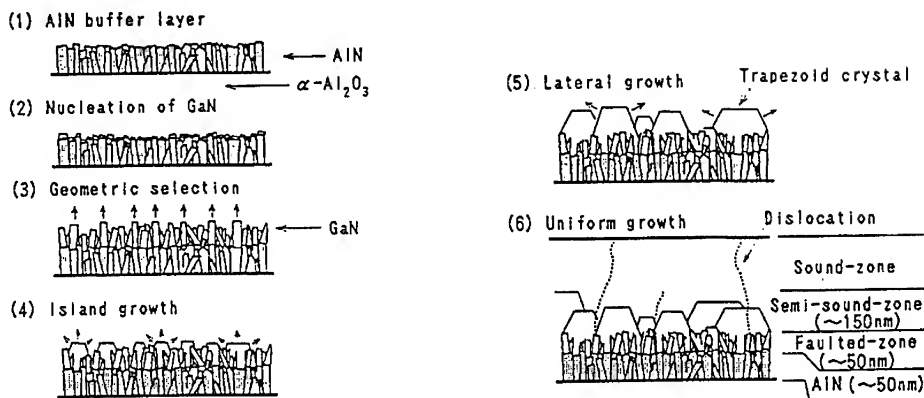


Figure 1. Growth sequence of GaN films deposited on AlN previously deposited on sapphire (from Ref. 19).

deposited at similar temperatures on sapphire [21, 22] using the same respective deposition techniques. The orientation relationships after annealing are $\text{AlN/GaN}(0001)\parallel\text{Al}_2\text{O}_3(0001)$ and $\text{AlN/GaN}[1\bar{2}10]\parallel\text{Al}_2\text{O}_3[10\bar{1}0]$. This two-step approach has been adopted almost universally for OMVPE and MBE deposition on sapphire.

In contrast, Weeks et al.[7] have shown that AlN or GaN deposited via OMVPE on 6H-SiC(0001) wafers in the range of 500-950°C resulted in random *polycrystalline* material, with the GaN being electrically conductive. The sequential deposition of AlN or $\text{Al}_x\text{Ga}_{1-x}\text{N}$ and GaN at $\geq 1100^\circ\text{C}$ and 1050°C , respectively, on this substrate resulted in monocrystalline and electrically insulating films of all materials. However, defects form at the SiC steps as a result of different metal/nonmetal stacking arrangements along [0001] in the SiC and the AlN (or $\text{Al}_x\text{Ga}_{1-x}\text{N}$ alloys), as described below. This is likely to be even more serious at a SiC/GaN interface because of the larger atom-atom distance in the GaN. This may be the primary factor which tends to discourage the nucleation of GaN on SiC to a greater degree than AlN. That this is true is indicated by the research of Hughes et al.[14] who employed GaN(0001) films deposited via OMVPE on 6H-SiC(0001) as the substrate for subsequent MBE growth of GaN in the temperature range of 600-800°C. The structural and optical properties of the MBE GaN were improved relative to that grown on AlN at the same temperature via this process; however, the growth rate was markedly less ($\sim 0.25 \mu\text{m/hr}$) than normally achieved via OMVPE.

The difficulty of achieving two-dimensional nucleation on GaN may also be caused by the fact that 6H-SiC(0001) has the lower surface energy. If the sum of the surface energy of the substrate and that of the substrate/film interface (usually the much smaller quantity) is less than the surface energy of the film, the film will undergo nucleation of three dimensional islands which will continue to grow as islands until material fills the spaces between them. The resulting film is almost invariably strongly textured and polycrystalline, at least at the outset of growth. The present authors have found that the addition of five per cent (the lowest concentration so far investigated) or more of AlN to GaN results in the nucleation of two-dimensional islands directly on the SiC substrates at a growth temperature $\geq 1050^\circ\text{C}$. As in the case of pure AlN, these islands quickly coalesce and the mode of growth changes to layer-by-layer. This indicates that the addition of the AlN lowers the surface energy of the film below that of the SiC. This is unlikely to be caused by the small reduction in lattice parameter which is affected by the addition of the AlN.

Finally, it is also likely that the rates of desorption of Ga and N from foreign surfaces and/or the rate of decomposition (sublimation) of islands of GaN at elevated temperatures markedly exceed those from the surface of a contiguous two-dimensional GaN film. Thus, while nucleation is difficult, the growth of a two-dimensional GaN film, having formed, is more easily facilitated even at $T > 1000^\circ\text{C}$. These phenomena would be closely coupled with the much lower bond energy of GaN relative to AlN which does not sublime at the temperatures used for thin film growth of

either material. This would explain the difficulty of achieving nucleation on any substrate (except another nitride) at elevated temperatures.

Given the situation described in the previous paragraph, it is not surprising that there is considerable research to lower the nitride film growth temperature, to improve the rate of nucleation and to reduce the surface volatility but achieve monocrystalline nitride films. This is especially true for GaN, InN and their alloys. This is usually manifest in the use of various plasma techniques to decompose one or more of the reactants in both OMVPE and MBE processes. However, surface migration rates of the reactant species and/or their products diminishes exponentially with substrate temperature, and this reduction in thermal energy may not be fully compensated by energetic reactants from the plasma or ion bombardment of the surfaces, even if were desired. This invariably results in textured polycrystalline films. High temperature growth should result in monocrystalline films. A negative factor in the case of SiC substrates is that the larger coefficient of thermal expansion of the nitrides relative to SiC often results in cracking of thick ($\geq 5\mu\text{m}$) nitride films. This potential for cracking is increased with an increase in growth temperature on this substrate. A final factor which tends to discourage low temperature growth is the dramatically reduced rate of the decomposition of ammonia, the principal N source in OMVPE and therefore, the reduced rate of thin film growth. Additional concerns regarding ammonia under particular growth situations are noted below.

The conversion of Si and GaAs to a Si_xN_y material and GaN, respectively, have also been employed with marginal success, relative to the use of sapphire and SiC. The reasons for this lie in the material which is formed and its relationship either to the subsequently grown GaN film or the underlying substrate. The Si_xN_y material is amorphous which compounds the problem of nucleation of a monocrystalline III-N film. By contrast, GaN forms on the GaAs; however, the mismatches in the lattice parameters and coefficients of thermal expansion are considerable and very high densities of line and planar defects (especially if cubic GaN is formed) and significant stresses occur in the film at temperature and on cooling. Moreover, the temperatures of significant vaporization of As from GaAs as well as the components of ZnO are well below the desired growth temperatures for AlN, GaN and most of the III-N alloys.

Another topic of considerable concern and debate is the choice of metal and N sources. A host of metal sources have been examined for use in OMVPE and MOMBE, again commonly to reduce growth temperature or enhance nucleation. However, trimethyl- or triethyl- species remain the sources of choice because of purity and availability. Ammonia is the leading nitrogen source for OMVPE and MOMBE. However, several interesting challenges are encountered in the use of this gas for the growth and doping of the nitride films. One of these is encountered in low temperature growth such as might be used for MOMBE and for some of the studies noted above. By analogy with GaAs-based materials, the presence of As on the growing surface assists in the decomposition of the Ga (or other metal)-containing metallorganics, and the surface mobilities of both Ga and As are sufficient such that low temperature growth of monocrystalline films is readily achieved. However, the N on the growing surface of GaN (or other nitrides) films does not assist in the decomposition of the metallorganics, at least to anywhere near the degree that As does in GaAs. Thus, to achieve respectable rates of film growth, one must elevate the substrate temperature to greater than 800°C . As such, the temperature of MOMBE and gas source MBE of the nitrides are approaching those of MOCVD as a function of time.

In previous times of intense study of III-N film growth, oxygen doping via the thermal decomposition of water vapor contained in the ammonia and the formation of H-Mg complexes (and those of other p-type dopants such as Zn) on the growing surface of GaN (and very likely on other nitrides) were a significant problem in MOVPE and the metal hydride process routes. The ammonia produced at this writing is significantly cleaner than even that produced even three years ago, but continued reduction in water vapor must be achieved and new, more effective purifiers for this gas must be developed. The problem of the formation of H-Mg complexes is much more difficult, as the reactive H from the ammonia will always be on the surface at the sites of thermal decomposition. The use of H scavengers such as Cl would result in significant etching of the growing film. As such, the use of species containing both N and the desired metal species as single source dopants well as RF plasma decomposition of N_2 have been and continue to be studied in attempts to surmount the aforementioned difficulties with ammonia in MOVPE deposition processes.

In contrast, there has been a concerted effort to avoid the use of ammonia in MBE deposition. Electron cyclotron resonance (ECR) plasma units and a growing number of RF plasma systems are, at present, the most commonly used for producing reactive nitrogen species. However, film damage from these energetic N sources is being reported with greater frequency. Modifications to the MBE system including positively charged grids surrounding the substrate and shrouds adjacent to the ECR source to deflect the energetic species have been used with success. Azides have also been used; however, due to their considerable instability, this employment is not likely to grow. As such, and despite the aforementioned problems, the use of ammonia for MBE growth is being more frequently reported.

The following sections describe research in MBE and OMVPE of nitrides within the authors' laboratories which is pertinent to some of the topics noted above.

EXPERIMENTAL PROCEDURES

Molecular Beam Epitaxy

Films of AlN(0001) have been deposited at NCSU in the range 650-1050°C on vicinal α (6H)-SiC(0001) cut 3-4° toward $\langle 11\bar{2}0 \rangle$ and at 650°C on sapphire. The substrates were degreased, dipped into a 10% HF solution to remove the thermally grown oxide layer, placed in the MBE system having a base pressure of $\geq 10^{-9}$ Torr and desorbed at 700-1000°C prior to deposition. Reactive nitrogen species were produced from purified N₂ in a compact ECR plasma source at a pressure of $\approx 1.5 \times 10^{-4}$ Torr and 50 - 100 W. Aluminum (99.999% pure) was evaporated from a standard effusion cell held at 1260°C. The growth rate was ≈ 60 nm/min. Films of GaN have been deposited on ≈ 15 nm AlN buffer layers at substrate temperatures in the range of 650 - 850°C using Ga evaporated at 990°C and a similar ECR-derived source of N. The growth rates (final thicknesses) of the AlN buffer layers and the GaN films were 1000 Å/hr (150-200 Å) and 1700 Å/hr (4000-5000 Å), respectively. Donor and acceptor doping of the GaN were achieved by the evaporation of Si or Ge and Mg, respectively. No post-growth annealing was necessary to achieve p-type character.

Organometallic Vapor Phase Epitaxy

Buffer layers and films of AlN(0001) and GaN(0001), respectively, as well as Al_xGa_{1-x}N alloy films have been grown via this technique only on vicinal 6H-SiC(0001) wafers held on a SiC-coated graphite susceptor contained in an RF heated, cold-wall, vertical, pancake-style, diffusion pumped deposition system. The continuously rotating susceptor was heated to the AlN deposition temperature of 1100°C in 3 SLM of flowing H₂ diluent. Hydrogen was also used as the carrier gas for the various metalorganic precursors. Deposition of ≈ 100 nm AlN was initiated by flowing triethylaluminum (TEA) and ammonia (NH₃) into the reactor at 23.6 μ mol/min and 1.5 SLM, respectively. The system pressure was 45 Torr. The TEA flow was subsequently terminated, the substrate temperature decreased to 950°C and the system pressure increased to 90 Torr for GaN growth. The flow rate of triethylgallium (TEG) was maintained at 24.8 μ mol/min. The growth rate for GaN was ≈ 0.9 μ m/hr. The Al_xGa_{1-x}N alloys were achieved by changing the ratios of the flow rates of the Al and Ga metallorganics while keeping the ammonia flow rate constant. Silicon doped n-type GaN and Al_xGa_{1-x}N were achieved via the addition of SiH₄ (8.2 ppm in a balance of N₂) at flow rates between 0.05 nmol/min and 15 nmol/min. Magnesium doped, p-type samples of GaN were accomplished via the incorporation of bis-cyclopentadienylmagnesium (Cp₂Mg) at a flow rate of 0.2 μ mol/min. The latter were subsequently annealed at 700°C and 900°C at 700 Torr in 3 SLM of N₂ for 20 minutes at each temperature.

Characterization

The structural, microstructural, optical and electrical characteristics of the epitaxial AlN and/or the GaN thin films and those of the alloys were analyzed using scanning electron microscopy (SEM), conventional and high resolution transmission electron microscopy (TEM), double-crystal x-ray rocking curve (DCXRC) measurements and photoluminescence (PL) (15 mW He-Cd laser ($\lambda = 325$ nm)) at 8K (GaN only). Each TEM sample was examined along either the $\langle 1100 \rangle$ or the

$\langle\bar{2}110\rangle$ zone axes to observe the structure of the substrate surface or the deposited films, respectively. Thermally evaporated Al served as the ohmic contacts for the electrical measurements of the GaN.

RESULTS AND DISCUSSION

Aluminum Nitride

The monocrystalline AlN grown on both vicinal and on-axis 6H-SiC(0001) surfaces simultaneously at 1050°C using MBE received extensive examination via HRTEM in terms of initial growth mode and interface defects. It is believed that these results are similar for the AlN films deposited via OMVPE at 1100°C. All films exhibited a sharp interface. Essentially atomically flat AlN surfaces, indicative of the two dimensional growth discerned in earlier NCSU research were obtained using on-axis substrates. Island-like and 'valley' features were observed on the vicinal surface, as shown in Fig. 2. The latter formed perpendicular to the substrate surface when the boundaries of coalescence between the island-like areas occurred at a step due to the misalignment between the islands. Coalescence via two-dimensional growth of the islands features at Si/C bilayer steps gave rise to double positioning boundaries (DPBs) as a result of the misalignment of these steps with the AlN bilayers in the growing film. The film thickness within these features varied from 3-4 to 7-8 AlN bilayers. The quality of thicker AlN films was strongly influenced by the concentration of DPBs formed at the outset of growth, as shown by the low angle boundaries oriented perpendicular to the growth surface in Fig. 3. No other line or planar defects were observed. The films deposited on sapphire at 650°C were columnar but with a smooth surface. The RHEED patterns of the final surfaces were highly streaked with easily observed Kikuchi lines. The potential for AlN as an active electronic semiconductor materials is considerable and is enhanced by the availability of SiC substrates. However, research regarding the optimum growth conditions and the repetitive achievement of n- and p-type doping are necessary before the material can be considered as a host for active devices.

The characteristics of the AlN films deposited via MOVPE on 6H-SiC were essentially the same in the first several monolayers in microstructure and surface smoothness as those deposited via GSMBE. The double position boundaries observe in Fig. 2 stopped after a few tens of monolayers, and growth to ≥ 1000 Å resulted in the much improved films suitable for the deposition of high quality monocrystalline GaN(0001) films as described below.

Gallium Nitride

RHEED analysis of the GaN films grown via GSMBE showed Kikuchi lines indicating good crystal quality. SEM observations revealed the surface morphology to be smooth and featureless. Cross-section HRTEM revealed sharp interfaces between the substrate and buffer layer and buffer layer and GaN. The GaN also showed low-angle grain boundaries propagating from the interface. Observation along different diffraction vectors also revealed inversion domain boundaries and dislocations. Resistivity and Hall measurements of these 0.5 µm films could not be made owing to their high resistivity. However, they were found to be easily doped n- and p-type with Si and Mg, respectively, without any post deposition processing.

Research concerned with the deposition of AlN/GaN layered structures on 6H-SiC substrates has also been achieved by GSMBE. Coherent interfaces (no relaxation by misfit dislocations) were observed for bilayer periods smaller than 6 nm. By contrast, completely relaxed individual layers of GaN and AlN with respect to each other were present for bilayer periods >20 nm. Cathodoluminescence showed a shift in the emission peak from 3.42 eV for a sample with individual 10 nm thick GaN wells and AlN barriers to 4.11 eV due to the quantum size effect for samples having 1 nm thick individual layers. These last studies also showed that there exists a constant offset of 170 meV between the experimental and calculated values. Since this offset is present only for the pseudomorphic structures, it has been related to the strain-induced band gap shift of the two materials.

GaN films deposited via OMVPE directly on 6H-SiC(0001) substrates at 900°C and 45 Torr had columnar grains, faceted surfaces and net carrier concentrations ($n_D - n_A > 1 \times 10^{19} \text{ cm}^{-3}$). In

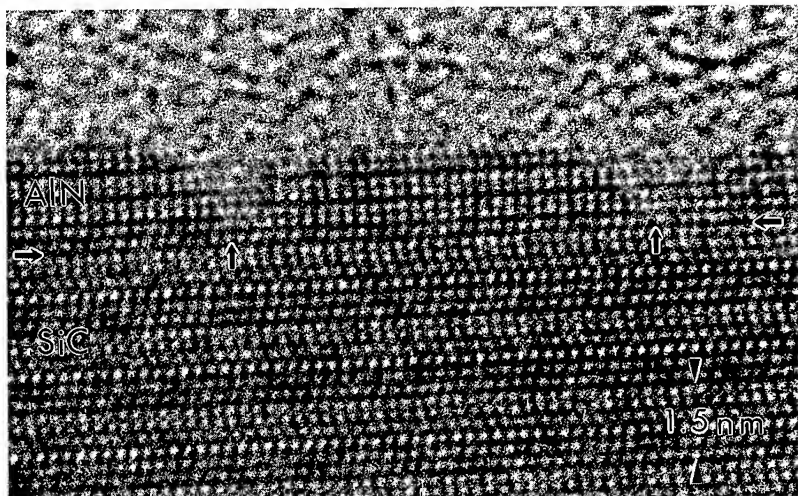


Figure 2. Initial stages of growth of AlN films on vicinal 6H-SiC(0001) substrates. The formation of double positioning boundaries is strongly coupled to the presence of surface steps in the off-axis substrate, as shown by the arrows.

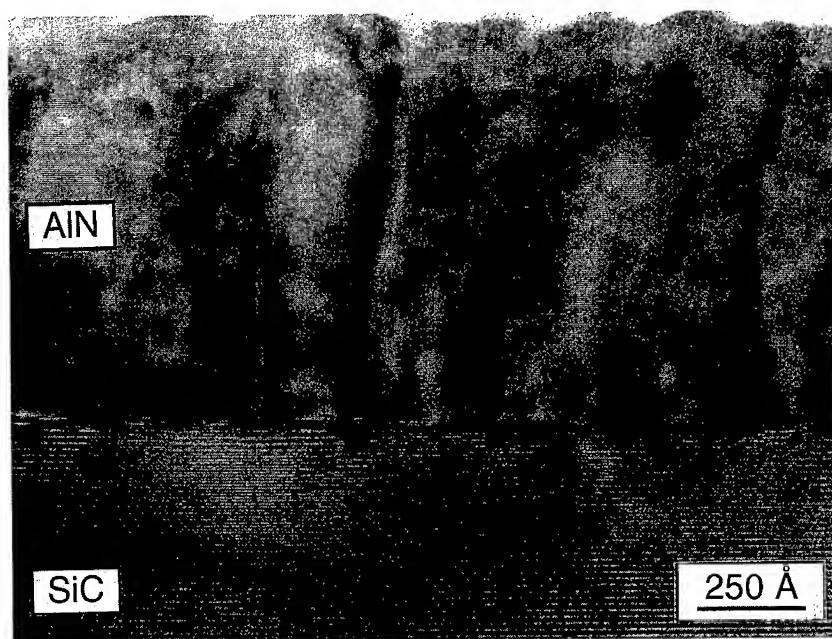


Figure 3. TEM of AlN thin film grown directly on vicinal 6H-SiC substrate showing low angle boundaries originating from and oriented perpendicular to the substrate

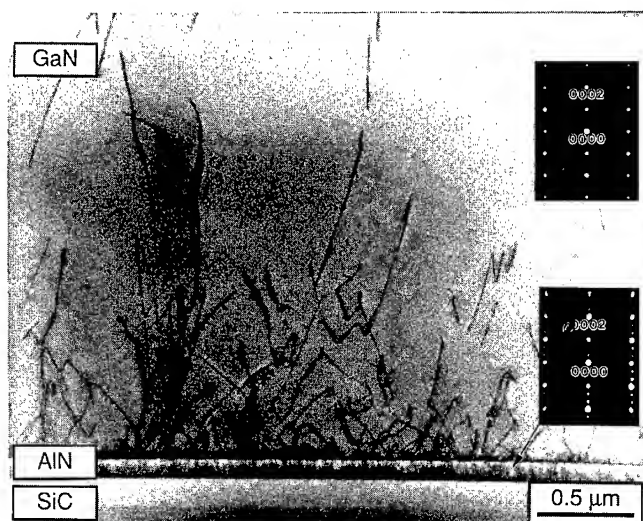


Figure 4. Cross-sectional TEM micrograph of a 2.7 μm GaN(0001) film deposited at 950°C and 90 Torr via OMVPE on a high temperature (1100°C) monocrystalline AlN buffer layer previously deposited on a vicinal 6H-SiC substrate.

contrast, both the AlN buffer layers and the subsequently grown GaN films deposited on similar SiC substrates were monocrystalline with no misorientation or low-angle grain boundaries, as determined by selected area diffraction (SAD) and microstructural analysis via TEM. The stacking fault density was also very low. These results are apparent in the representative cross-sectional TEM micrograph shown in Fig. 4. Inserts in the micrograph show SAD patterns from the top layer of GaN and the GaN/AlN interface. Overlapping spots from the 6H-SiC substrate are seen in the latter SAD pattern. The growth of GaN on the HT-AlN buffer layer was two-dimensional after the initial coalescence of GaN islands which occurred within the first several hundred angstroms of growth. The dislocation density within the first 0.5 μm of the GaN was approximately $1 \times 10^9 \text{ cm}^{-2}$, as determined from plan-view TEM analysis by counting the number of dislocations per unit area. This defect density is about an order of magnitude lower than that for thicker GaN films deposited on sapphire(0001) substrates using low-temperature buffer layers.

The low-temperature (8K) PL spectra of the undoped OMVPE-derived GaN films revealed an intense near band-edge emission at 357.4 nm (3.47 eV). The FWHM value of this bound exciton peak was 4 meV. A very weak donor-acceptor (DA) defect peak was observed at 379 nm (3.26 eV) with two associated LO-phonon replicas only after a 250X magnification of the spectrum. Two LO-phonon replicas of the bound exciton peak and a broad peak centered at $\approx 545 \text{ nm}$ (2.2 eV), commonly associated with deep-levels (DL) in the band gap, were observed at this magnification. The PL intensity of the blue emission from the p-type samples was increased by the 700°C anneal and was dramatically decreased by the subsequent 900°C anneal.

Undoped high quality GaN films grown on HT-AlN buffer layers on vicinal 6H-SiC(0001) were too resistive for measurements. The controlled introduction of SiH₄ allowed the reproducible achievement of donor carrier concentrations within the range of $\approx 1 \times 10^{17} \text{ cm}^{-3}$ to $\approx 1 \times 10^{20} \text{ cm}^{-3}$. The room temperature mobility of the former = 375 $\text{cm}^2/\text{V}\cdot\text{s}$. Similar measurements made on the annealed Mg-doped samples revealed p-type GaN with a net hole carrier concentration of $n_A - n_D \approx 3 \times 10^{17} \text{ cm}^{-3}$, a resistivity $\approx 7 \Omega\cdot\text{cm}$ and a hole mobility of $\approx 3 \text{ cm}^2/\text{V}\cdot\text{s}$. Four-point probe and Hg-probe C-V measurements verified p-type GaN.

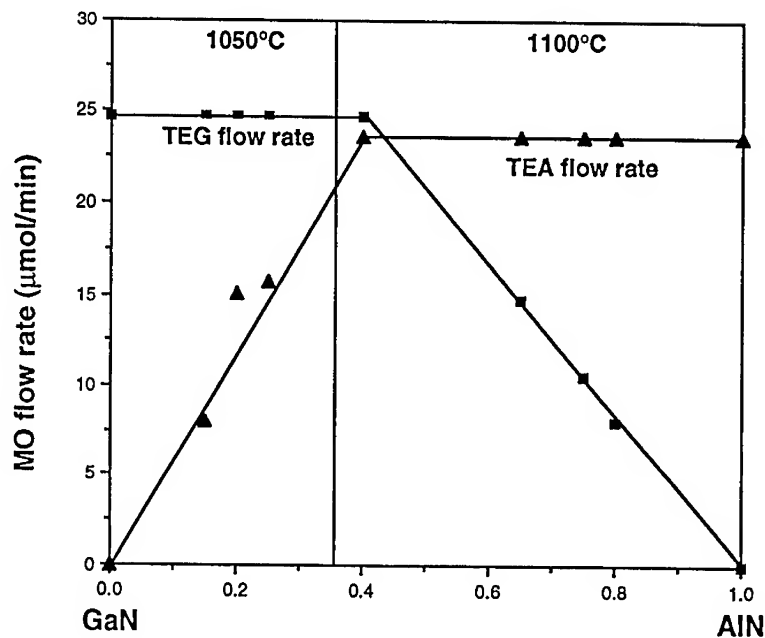


Figure 5. TEA and TEG flow rates as a function of $\text{Al}_x\text{Ga}_{1-x}\text{N}$ alloy composition

$\text{Al}_x\text{Ga}_{1-x}\text{N}$

$\text{Al}_x\text{Ga}_{1-x}\text{N}$ films have been grown for Al mole fractions of $0 \leq x \leq 1$, as shown in Fig. 5. The alloy concentrations were determined via AES by depth profiling through multi-layer heterostructures, one of which is shown in Fig. 6. GaN and AlN served as the necessary standards. $\text{Al}_x\text{Ga}_{1-x}\text{N}$ films for $0 < x < 0.3$ were then simultaneously deposited directly on vicinal and on-axis 6H-SiC(0001) substrates without the use of the customary high-temperature AlN buffer layers. These films were electrically insulating as-grown. The Al mole fractions were determined by low-temperature CL measurements as described below. Similar to findings for GaN film growth, the DCXRC measurements revealed smaller FWHM values for $\text{Al}_x\text{Ga}_{1-x}\text{N}$ films grown on the on-axis substrates as compared to simultaneously deposited films grown on vicinal substrates. Also, the FWHM values expand with increasing Al mole fraction. These results are shown in Fig. 7 where FWHM values are plotted versus alloy concentration for $\text{Al}_x\text{Ga}_{1-x}\text{N}$ films simultaneously deposited on vicinal and on-axis 6H-SiC(0001) substrates.

The low-temperature (8K) CL spectra of the $\text{Al}_x\text{Ga}_{1-x}\text{N}$ films with $x < 0.5$ showed strong near band-edge emission. As expected, the energy positions of these peaks shifted towards higher energy with increasing x , as shown in Fig. 8. The dashed line in the graph shows the peak position for $\text{Al}_x\text{Ga}_{1-x}\text{N}$ where $x = 0$. Al mole fractions were assigned from the near band-edge peak positions using a bowing parameter of $b = 0.98$ eV, as determined by Khan et al. [46].

Apparent in Fig. 8 is the increased FWHM values of the energy peaks with increasing values of x . $\text{Al}_x\text{Ga}_{1-x}\text{N}$ films grown on the on-axis substrates showed a similar trend. The broadening of the near band-edge peak is possibly due to increased fluctuations in the alloy compositions of $\text{Al}_x\text{Ga}_{1-x}\text{N}$ films for increasing values of x [46]. Also, the CL peak intensities were 0.1 to 1 order of magnitude stronger for undoped AlGa_{1-x}N films grown on vicinal substrates than for films grown on the on-axis substrates. This phenomenon is being further investigated.

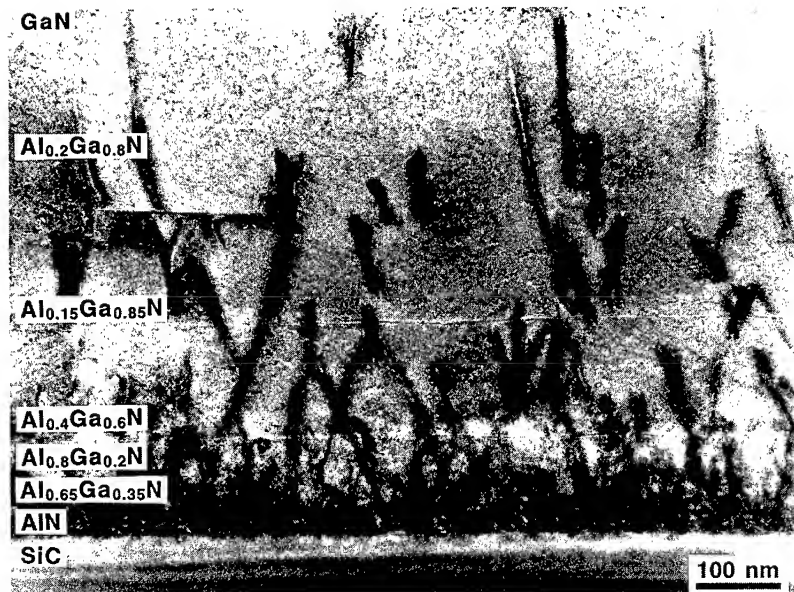


Figure 6. Cross-section TEM micrograph of a 7-layer $\text{Al}_x\text{Ga}_{1-x}\text{N}$ heterostructure.

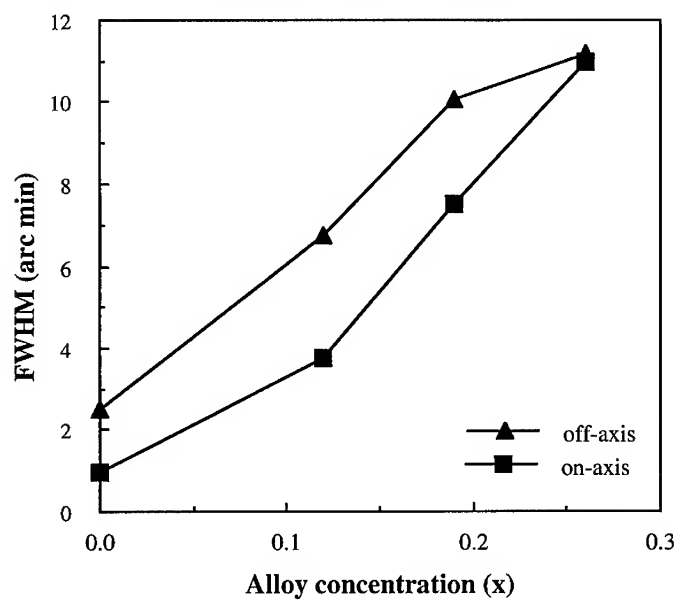


Figure 7. DCXRC FWHM values versus alloy concentration for $\text{Al}_x\text{Ga}_{1-x}\text{N}$ films simultaneously deposited on vicinal and on-axis 6H-SiC(0001) substrates.

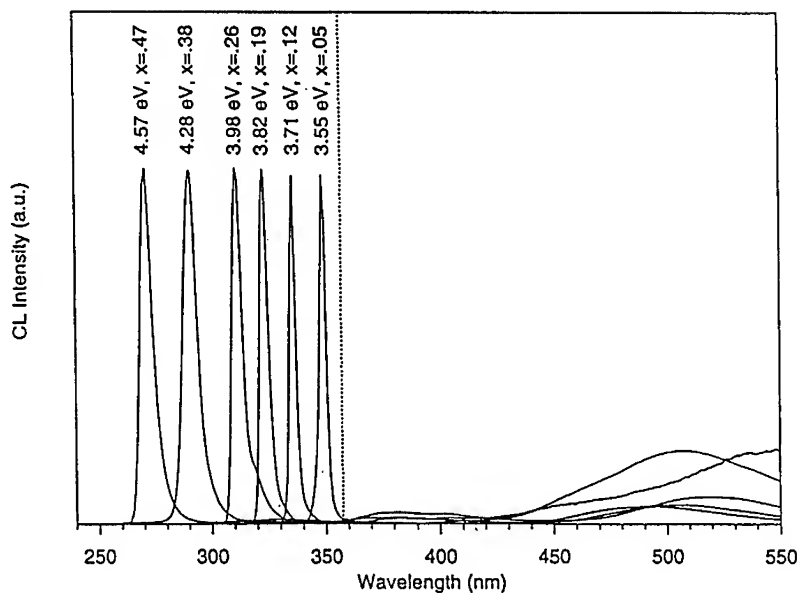


Figure 8. Low-temperature (8K) CL of $\text{Al}_x\text{Ga}_{1-x}\text{N}$ films with $x < 0.5$.

CONCLUSIONS

The two most primary methods for the deposition of III-N thin films are OMVPE and gas source MBE, with the former being the more commonly employed. Numerous research issues related to thin film growth by these techniques as well as device preparation remain including metal and nitrogen sources, heteroepitaxial nucleation, the role of buffer layers, surface migration rates as a function of temperature, substantial defect densities and their effect on film and device properties, ohmic and rectifying contacts, wet and dry etching and suitable gate and field insulators. The authors have deposited monocrystalline epitaxial thin films of both AlN and GaN by both techniques on 6H-SiC(0001) substrates at elevated temperatures using an AlN buffer layer for the latter material. Misalignment of the steps heights at the SiC surface results in the formation of double positioning boundaries in the AlN; however, these defects do not extend into the GaN films. The line defect density in the GaN is approximately one order of magnitude less than is found in material grown on sapphire. The optical, microstructural and electrical characteristics of the GaN films are equal to those reported for material deposited on sapphire. $\text{Al}_x\text{Ga}_{1-x}\text{N}$ films ($0 \leq x \leq 1$) were grown directly these substrates at 1050 or 1100°C. Chemically abrupt heterojunctions were demonstrated. All films possessed a smooth surface morphology and were free of low-angle grain boundaries and associated oriented domain microstructures. The PL spectra of the GaN films deposited on both vicinal and on-axis substrates revealed strong bound exciton emission with a FWHM value of 4 meV. The spectra of these films on the vicinal substrates were shifted to a lower energy, indicative of films containing residual tensile stresses. DCXRC measurements revealed smaller FWHM values for the $\text{Al}_x\text{Ga}_{1-x}\text{N}$ films grown on on-axis 6H-SiC(0001) substrates compared to simultaneously deposited films grown on vicinal substrates. These values increased with increasing values of x . The CL spectra of the $\text{Al}_x\text{Ga}_{1-x}\text{N}$ films for $x < 0.5$ showed strong near band-edge emission. FWHM values of the main energy peak increased with increasing Al mole fraction. Controlled n-type Si-doping in GaN was achieved for net carrier concentrations ranging from approximately $2 \times 10^{17} \text{ cm}^{-3}$ to $1 \times 10^{20} \text{ cm}^{-3}$. Mg-doped, p-type GaN was achieved with $n_{\text{A}}-n_{\text{D}} \approx 3 \times 10^{17} \text{ cm}^{-3}$, $\rho \approx 7 \Omega\text{-cm}$ and $\mu \approx 3 \text{ cm}^2/\text{V-s}$.

ACKNOWLEDGMENTS

This work was supported by the Office of Naval Research on Contracts N00014-92-J-1720 and N00014-92-J-1477. Appreciation is expressed to Cree Research for the SiC wafers and for their assistance in performing the C-V measurements, N. Doyle of the Westinghouse Science and Technology Center for the DCXRC measurements and to Prof. K. Hiramatsu of Nagoya University and S. Tanaka and A. D. Bachelor of NCSU for many helpful discussions.

REFERENCES

1. I. Akasaki, H. Amano, Y. Koide, K. Hiramatsu and N. Sawaki, *J. Cryst. Growth* **98**, 209 (1989).
2. S. Nakamura, *Jpn. J. Appl. Phys.* **30**, L1705 (1991).
3. K. Hiramatsu, S. Itoh, H. Amano, I. Akasaki, N. Kuwano, T. Shiraishi and
4. Oki, *J. Cryst. Growth* **115**, 628 (1991).
5. M.A. Khan, J.N. Kuznia, D.T. Olson and R. Kaplan, *J. Appl. Phys.* **73**, 3108 (1993).
6. J.N. Kuznia, M.A. Khan, D.T. Olson, R. Kaplan and J. Freitas, *J. Appl. Phys.* **73**, 4700 (1993).
7. T. W. Weeks, Jr., M. D. Bremser, K. S. Ailey, E. Carlson, W. G. Perry and R. F. Davis, *Appl. Phys. Lett.* **67**, 401 (1995).
8. S. Strite, J. Ruan, Z. Li, A. Salvador, J. Chen, D. J. Smith, W. J. Choyke, and H. Morkoç, *J. Vac. Sci. Technol. B* **9**, 1924 (1991).
9. T. Lei, T. D. Moustakas, R. J. Graham, Y. He and S. J. Berkowitz, *J. Appl. Phys.* **71**, 4933 (1992).
10. H. Okumura, S. Misawa, and S. Yoshida, *Appl. Phys. Lett.* **59**, 1058 (1991).
11. R. C. Powell, N. E. Lee, Y. W. Kim and J. E. Greene, *J. Appl. Phys.* **73**, 189 (1993).
12. M. J. Paisley and R. F. Davis, *J. Crystal Growth* **127**, 136 (1993).
13. C. Wang and R. F. Davis, *Appl. Phys. Lett.* **63**, 990 (1993).
14. W. C. Hughes, W. H. Rowland, Jr., M. A. L. Johnson, S. Fujita, J. W. Cook, Jr., and J. F. Schetzina, *J. Vac. Sci. Technol. B* **13**, 1571 (1995).
15. S. Nakamura, M. Senoh, N. Iwasa and S. Nagahama, *Jpn. J. Appl. Phys.* **34**, Pt 2, L 797 (1995).
16. M.A. Khan, J.N. Kuznia, A. R. Bhattarai and D.T. Olson, *Appl. Phys. Lett.* **62**, 1786 (1993).
17. S. Yoshida, S. Misawa and S. Gonda, *Appl. Phys. Lett.* **42**, 427 (1983).
18. H. Amano, N. Sawaki, I. Akasaki and Y. Toyoda, *Appl. Phys. Lett.* **48**, 353 (1986).
19. K. Hiramatsu, S. Itoh, H. Amano, I. Akasaki, N. Kuwano, T. Shiraishi and K. Oki, *J. Cryst. Growth* **115**, 628 (1991).
20. W. Qian, M. Skowronski, M. De Graef, K. Dovrespike, L. B. Rowland and D. K. Gaskill, *Appl. Phys. Lett.* **66**, 1252 (1995).
21. T. D. Moustakas, T. Lei and R. J. Molnar, *Physica B* **185**, 36 (1993).
22. S. Nakamura, *Jpn. J. Appl. Phys.* **30**, L1705 (1991).

GROWTH AND PROPERTIES OF BULK SINGLE CRYSTALS OF GaN

T. Suski*[#], P. Perlin*⁺, M. Leszczyński*, H. Teisseyre*, I. Grzegory*, J. Jun*,
M. Boćkowski*, S. Porowski*, K. Pakuła**, A. Wyszomirski**, and J.M. Baranowski*^{***}

*UNIPRESS, High Pressure Research Center, 01-142 Warszawa, POLAND,
tadek@iris.unipress.waw.pl; tadek@ux5.lbl.gov

**Institute of Experimental Physics, Warsaw University, 00-681 Warszawa, POLAND

ABSTRACT

In this paper we review recent developments in the growth of bulk GaN crystals by a high-pressure, high-temperature method. We also provide information on various physical properties of bulk GaN material. Then, some preliminary results on the homoepitaxial growth of GaN are given. In the second part of this paper we discuss the following problems: the possible origin of the large free electron concentration in undoped GaN material, the parasitic effect of yellow luminescence and the nature of Zn- and Mg-acceptors.

INTRODUCTION

A successful fabrication of the superbright green and blue (InGaAl)N light emitting diodes (LEDs) confirms that III-V nitrides play a dominant role with respect to other semiconductor families in the development of short-wavelength optoelectronics [1]. The short life time of II-VI - based devices, due mainly to the low energy of defects formation in these compounds, currently prevents commercialization. The performance of GaN-based LEDs, on the other hand, despite large lattice mismatch and differences in thermal expansion between the sapphire substrate and constituent epitaxial layers, is surprisingly high. This finding suggests that the presence of a large number of extended defects, e.g. dislocations, need not be detrimental to the development of LED-related applications for nitrides.

Semiconductor lasers operating in the blue and ultraviolet range of the spectrum represent the next goal to be achieved. It is a common belief that the inadequate structural quality of III-V nitride epitaxial films is the main limitation here. Different approaches to the solution of the above problem have been proposed very recently. Low/high temperature buffer layers made of GaN or AlN films lead to a significant improvement in the quality of heteroepitaxially grown layers of various nitrides [2-6]. Another idea consists of using new substrates with properties well matched with the nitride compounds. For example, LiGaO₂, LiAlO₂ [7] or AlMg₂O₄ [8] have been found very promising. However, the use of GaN single crystals as substrates for the homoepitaxial growth of GaN represents the most natural way to overcome difficulties caused by a large lattice mismatch and differences in thermal expansion between the substrate and an epitaxial film. Homoepitaxy has become possible owing to the growth of wurtzite GaN crystals in the form of platelets with dimensions of a few millimeters. A high-pressure, high-temperature method has been employed for this purpose [9].

The other important aspect of the existence of well-characterized bulk single crystals of GaN consists in the opportunity of using them as a standard and reference material. Strain effects, present in GaN layers grown on lattice mismatched substrates with a different thermal expansion, modify various properties of GaN films. For example, excitonic transitions studied by photoluminescence exhibit not only a broadening of the related bands but also a shift of their energetic positions [10].

The purpose of this review paper is to describe the method used for the growth of GaN bulk, single crystals. Properties of this material will be also discussed. Then, we will present some preliminary results on the homoepitaxial growth of a GaN-film on a GaN-substrate. The second part of this paper is devoted to studies which were undertaken with the purpose of answering some basic questions about the nature of GaN which have implications for devices, in particular: i) an origin of a dominant donor in undoped GaN material, ii) a radiative recombination mechanism leading to the parasitic effect of a yellow luminescence, and iii) optical properties of Zn- and Mg-acceptors.

HIGH-PRESSURE, HIGH-TEMPERATURE GROWTH OF GaN CRYSTALS

Due to the very high melting temperature of GaN (the estimated value is 2800K) at a corresponding equilibrium pressure of nitrogen (about 4 GPa) [9], bulk crystals of GaN cannot be obtained by typical equilibrium methods, e.g. the Czochralski or Bridgman methods in which stoichiometric melts are used. Therefore, the lower-temperature method consisting of growth from a solution should be applied. The Synthesis Solid Diffusion method was chosen for the crystal growth of GaN [9]. The formation of a thin polycrystalline film of GaN on the Ga surface, its dissolution and transport into the cooler part of the solution results in the nucleation and growth of GaN single crystals on the internal surface of the film. Growth should be carried out under conditions where GaN is still stable. Use of high temperature (which requires applying high pressure of nitrogen) ensures a maximum solubility of nitrogen in the liquid gallium. Usually, it means that the temperature and pressure of N_2 should be between 1500-1900K and 1-2 GPa, respectively. In every experiment a large number of crystals (20-50) was grown, of size 0.1-10 mm. We have not yet succeeded in finding a relation between growth conditions and crystal quality. Instead, the density of extended defects depends on crystal size. Platelets of bulk GaN are oriented perpendicularly to the hexagonal c-axis and one surface is usually flat with a low concentration of extended defects in the neighboring area. This surface is suitable for homoepitaxial growth.

The bulk GaN crystals possess a high concentration of free electrons, n_H , caused by an individual type or a group of point defects. n_H values between 10^{19} - 10^{20} cm^{-3} have been measured by means of the Hall method, infrared reflectivity and Raman spectroscopy [11] (undamped plasmon-phonon modes). The blue shift of the absorption edge has been assigned to this high electron concentrations via the Burstein-Moss effect [12]. Mobilities of conducting electrons range from 30 to 90 cm^2/Vs .

HOMOEPITAXIAL GROWTH OF GaN

The most popular form of GaN crystals is an epitaxial layer grown on a foreign substrate (sapphire, SiC, and others). The lattice mismatch induces a high concentration of unwelcome defects. Moreover, the difference in the thermal expansion between a layer and a substrate induces thermal strains during cooling of the grown GaN film. These strains are not relaxed at low temperatures. Thus, the knowledge of thermal expansion coefficients (TECs) is especially important in epitaxial growth. We will illustrate this problem below, comparing TECs of bulk GaN and epitaxial films of GaN grown by molecular beam epitaxy (MBE) on sapphire. The following results have been obtained [13] (Figure 1):

- a) the c -lattice constant values of the GaN layer and the bulk crystal are identical within the experimental error (at the 300-760K temperature range);
- b) the lattice constant a is smaller for the layer at room temperature. The difference decreases down to zero at about 800K (by extrapolation);
- c) the lattice mismatch between the substrate and the layer decreases at elevated temperatures. At higher temperatures a change of concentration of misfit defects takes place. This result is unexpected, as for GaAs on Si [14] and InP on GaAs [15], the similar thermal strains remain unrelaxed. However, the crystallographic structure of these compounds is similar. In the case of GaN on sapphire the crystallographic structures are different. Additionally, the presence (in the epitaxial sample studied) of an AlN buffer layer, which has a smaller lattice constant and TEC than those of GaN, can influence the process of stress relaxation in the GaN layer.

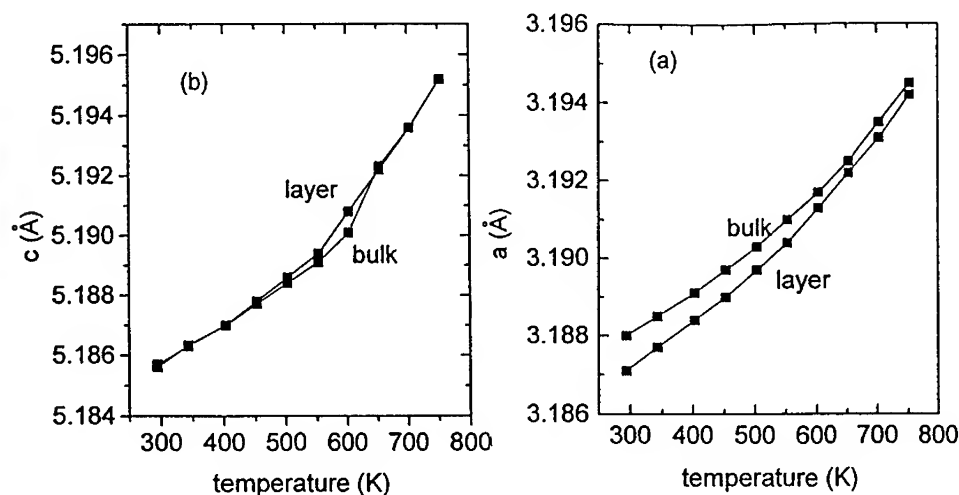


Fig. 1. Temperature dependence of GaN lattice constants for bulk crystal and MBE grown layer on sapphire. (a) lattice constant a parallel to the interface and (b) lattice constant c perpendicular to the interface.

The above discussion illustrates how important and useful is the idea of homoepitaxial growth of GaN film on GaN bulk crystal. Both MOCVD (metalorganic chemical vapor deposition)[16] and MBE methods have been successfully applied. We will describe the results obtained very recently in Warsaw. Bulk GaN substrate crystals were grown by the high-pressure, high-temperature method described above. The GaN platelets (the hexagonal c-axis perpendicular to the surface) had areas of a few mm² and relatively flat surfaces which were used for the MOCVD growth without any mechanical or chemical treatment. The growth temperature was close to 1000°C and the deposited films were 1.5 µm thick. GaN layers were grown directly on single crystal substrates without deposition of a low temperature nucleation layer.

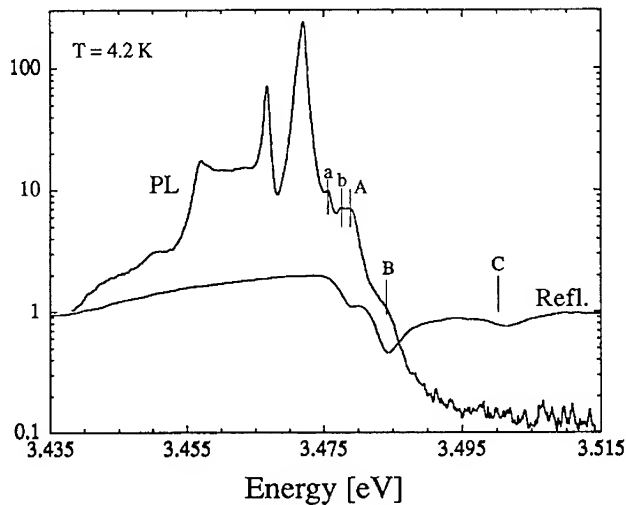


Fig. 2. The photoluminescence and reflectance measured on the same surface of the homoepitaxially (MOCVD) grown GaN film on the bulk GaN crystal.

The photoluminescence and reflectance of the layers were studied in a variable temperature range. Figure 2 illustrates the results characteristic of the exciton region at $T=4.2\text{K}$. The spectrum is dominated by two strong and narrow lines at energies of 3.4666(2) and 3.4719(2) eV. These lines are likely related to donor and acceptor bound excitons. Since their FWHM are 1.0 meV and 1.8 meV respectively, these lines are the most narrow ones observed to date in GaN. Moreover, four weak lines a, b, A, B with energies $E_a = 3.4755(2)$ eV, $E_b = 3.4774(3)$ eV, $E_A = 3.4780(3)$ eV, and $E_B = 3.4835(5)$ eV are observed. The two luminescence lines A and B correspond exactly with the reflectance dispersion lines (see Fig. 2). In addition, in the reflectance spectrum, there is a third line at $E_C = 3.502(1)$ eV. These

are the free exciton lines formed with participation of holes originating from the crystal-field and spin-orbit split valence band. Comparison of these results with positions of free excitons in MOCVD layers grown on sapphire [17] shows that the center of gravity of the exciton lines in the latter case is shifted to higher energies: $E_A = 3.485$ eV, $E_B = 3.493$ eV and $E_C = 3.518$ eV. This effect would be an indication of a strain existing in GaN layers grown on sapphire. It is important to note that the homoepitaxially grown sample studied here exhibited negligible yellow luminescence, usually present in bulk GaN crystals.

DOMINANT DONOR IN UNDOPED GaN

One of the fundamental questions concerning basic properties of GaN material concerns the origin of n-type conductivity in undoped crystals. In the bulk samples, the concentration of conduction electrons ranges from 10^{19} to 10^{20} cm^{-3} . In undoped MBE or MOCVD grown epitaxial films the electron concentrations are of the order 10^{17} cm^{-3} . Maruska and Tietjen [18] and Ilegems and Montgomery [19] suggested that the autodoping is due to native defects, since concentrations of contaminants are lower by a few orders of magnitude than the highest observed electron concentrations.

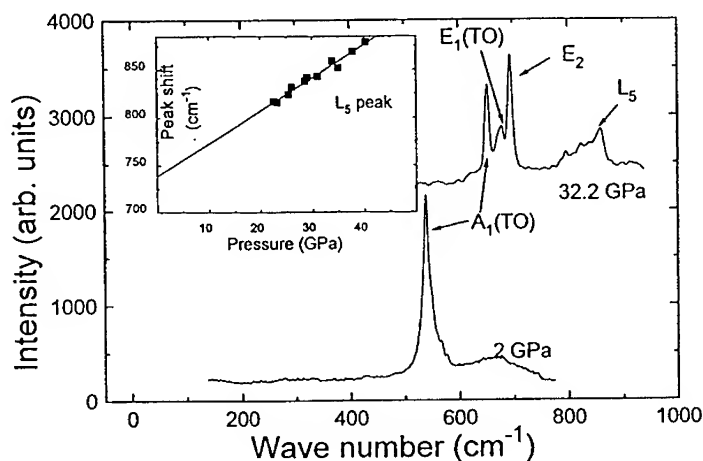


Fig. 3. Raman spectra of bulk, single crystal of GaN at two values of pressure. The peaks labelled $A_1(\text{TO})$, $E_1(\text{TO})$, and E_2 correspond to the phonon modes. Their appearance results from a depolarization of the laser light due to strain in the diamond anvils. The peak L_5 appears above 20 GPa. The inset shows the pressure dependence of the L_5 peak energy. The solid line represents a linear extrapolation of the peak energy to ambient pressure.

The residual donor was tentatively assigned to the nitrogen vacancy, V_N [18-21]. Technologically, it is likely that V_N appears during the growth because of the very high nitrogen equilibrium pressure at the growth temperatures. This implies that the growth occurs under Ga-rich conditions. So far, however, the dominant donor has not been positively identified with a nitrogen vacancy.

Recently, ab initio calculations of electronic structure of GaN native defects were performed by Boguslawski et al. [22] and Neugebauer and Van de Walle [23]. They showed that V_N introduces a resonant level inside the conduction bands at about 0.8 eV above the band minimum. Idea of the verification of the above theoretical prediction is based on the fact that the pressure coefficient of the bottom of the conduction band is usually higher than that of the resonance. Consequently, at sufficiently high pressures a crossover should occur between the two levels. The resonance should become a genuine gap state that traps conducting electrons. After the crossover, free electrons would disappear from the conduction band and would occupy this deep state located in the band gap of GaN. A number of experiments verifying this expectation have been performed [24,25]. For example, a decay of the infrared absorption at pressures higher than 20 GPa was observed. One expects at this spectral region only absorption due to the free electrons and phonons. The latter contribution should change weakly with pressure. Therefore, the observed drastic decrease of infrared absorption at high pressures is related to a decrease of the conducting electron concentration.

Raman scattering measurements were also performed. Figure 3 shows the difference between the spectra taken at low and high pressures. It can be seen that the spectrum corresponding to 32.2 GPa contains additional peaks. Especially significant is the presence of the longitudinal-optical mode (L_5), which was suppressed at lower pressures by a high free-electron concentration (phonon-plasmon interaction [12]). To justify the proposed interpretation of the role of nitrogen vacancy, its electronic structure under hydrostatic pressure has been calculated [24]. The results show that the vacancy-induced resonance, located at 0.8 eV above the bottom of the conduction band (at ambient pressure), moves down with pressure at a rate of 5 meV/GPa. The resonance crosses the bottom of the conduction band at about 18 GPa.

Another explanation of the experimental findings was considered. The interstitial Ga also introduces a resonance which crosses the bottom of the conduction band at about 20 GPa. However, the formation energy of a nitrogen vacancy is significantly lower than that of a Ga-interstitial [23] which suggests that the nitrogen vacancy is the defect more likely responsible for high concentration of the conducting electrons.

YELLOW LUMINESCENCE

Luminescence spectra for many GaN materials (bulk and epitaxial films) contain in addition to the band-edge luminescence, the band of a yellow luminescence. The origin and nature of this parasitic effect is still not clear. The yellow luminescence peak has a broad and symmetrical shape and is centered usually at about 2.2-2.3 eV. A basic question which arises

concerns the mechanism of the radiative recombination producing the yellow luminescence. Two qualitatively different approaches have been proposed. According to the model discussed by Ogino and Aoki [26], the initial state of the considered transition is a shallow donor (with a level depth of 25 meV) and the final state is a deep acceptor (about 0.86 eV above the valence band). A competitive model has been introduced very recently by Glaser et al. [27]. They proposed a scheme of radiative transition of electrons between a deep double donor of A_1 character (with a depth of about 0.8 eV) and an acceptor state of effective mass character. This transition is preceded by a nonradiative transfer of an electron between a shallow donor and the A_1 state. Both approaches predict a strong electron-lattice interaction associated with the localized defect state involved in the yellow emission.

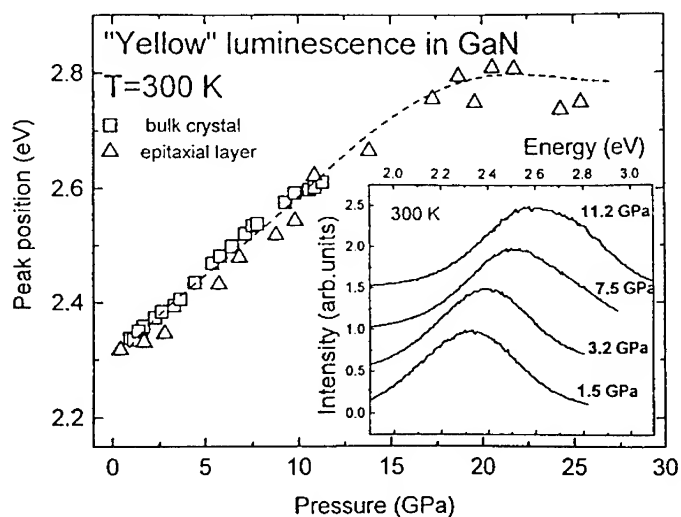


Fig. 4. Pressure dependence of the *yellow*-luminescence band energy in two different samples of GaN : bulk, single crystal (open squares) and epitaxial layer grown by MBE method (open triangles). The broken line is drawn to guide the eye. Insert shows spectra of the yellow luminescence of the bulk GaN sample for different hydrostatic pressure magnitudes.

According to the second model, the appearance of the localized level in the upper part of the band gap does not influence the pressure variation of the yellow luminescence energy. The experiment performed by us [28] supports the first model. The saturation of the luminescence shift at pressures above about 20 GPa can be clearly seen on Figure 4. Very recent results of time resolved photoluminescence studies in GaN epitaxial layers confirm our experimental finding [29]. However, the microscopic nature of the defect responsible for the yellow luminescence remains an open question.

Zn AND Mg ACCEPTOR STATES IN GaN

For a long time the most serious stumbling block to GaN applications was a very high intrinsic electron concentration. Recently, p-type conductivity in GaN, AlGaIn, and InGaIn alloys has been achieved by means of Mg doping [1,30]. Mg acceptor is responsible for the luminescence band observed at energies exceeding 3 eV. Zn is a particularly useful dopant which increases the brightness of the luminescence in GaN material. GaN:Zn exhibits an efficient blue luminescence band with a maximum centered at about 2.9 eV [31]. Introducing Zn into GaN crystal may produce a semi-insulating material [19].

At present, MOCVD is the superior growth technique for devices based on III-V nitrides. All devices obtained by this method require post-growth treatment to electrically activate Mg-acceptor dopant. Formation of electrically inactive hydrogen-acceptor complexes during MOCVD growth is the widely accepted explanation of the observed low p-type doping efficiency in as-grown GaN [32]. The other factor limiting this efficiency might result from the high value of Zn- and Mg- acceptor activation energies. As follows from the experimental studies, the Zn-acceptor level is situated at about 0.3 eV and the Mg-acceptor level only about 0.15 eV above the valence band maximum (VBM) [33]. The increased distance to the VBM for the Zn-level suggests stronger localization of the related acceptor state with respect to Mg-dopant. However, since the estimated location of the hydrogenic-like acceptor state in GaN is about 0.1 above the VBM, the question arises as to what extent the Mg-related state represents an effective mass acceptor. The experiment described below [34] was performed to answer this question.

Temperature- and pressure-induced evolution of the photoluminescence bands originating from the radiative recombination of electrons to acceptor-related states were examined. Mg and Zn were introduced to a GaN host during the high-pressure, high-temperature growth. The concentration of zinc was estimated to be around 10^{19} cm^{-3} . The concentration of Mg was higher, which resulted in the red-shift (up to 0.2 eV) of the GaN energy gap. Samples doped by both impurities exhibited n-type conductivity with a small decrease in electron concentration with respect to the undoped bulk GaN material.

With application of pressure, photoluminescence bands related to Mg and Zn shift to higher energies at a rate similar to the change of the GaN band gap. This is in agreement with the radiative recombination models for which the initial state consists of a conduction band state or a shallow donor state. The luminescence in GaN:Zn does not change its position with temperature. In contrast, the temperature evolution of the luminescence in our highly doped GaN:Mg sample resembles the change of the GaN band gap (Figure 5). This fact may be attributable to the shallow character of the acceptor state formed by Mg. Zn-related states have more localized character and exhibit a stronger electron-lattice coupling effect. Results of the theoretical calculations [34] confirm these experimental findings. The wave function of VBM at Γ point is composed about 90% of p-states of nitrogen (p(N)) and 10% of d- and p-states of Ga. The Mg-acceptor state has a contribution of the 83% of p(N) and thus, it has the character of the shallow acceptor state. A deeper location of this state with respect to the effective-mass acceptor state may be due to the chemical shift contribution. On the other hand, the Zn-state contains 42% p(N), 48% d(Zn), and 8% p(Zn), which corresponds to the much more localized

character of Zn acceptor state. It has been suggested [34] that variation of electron-lattice coupling might be responsible for the lack of Zn-luminescence shift with temperature.

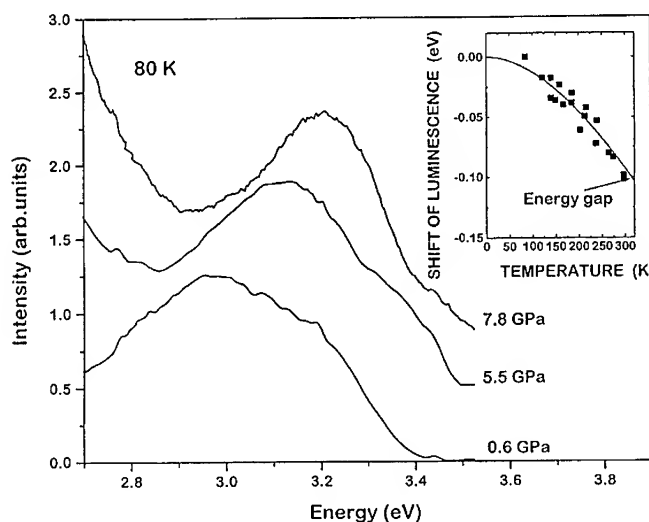


Fig. 5. Photoluminescence spectra of Mg doped bulk, single GaN crystal for different pressure magnitude ($T=80\text{K}$). Increase of the luminescence intensity at the low energy part of the plot (seen at 5.5 and 7.8 GPa) is due to the yellow luminescence band. Insert: the temperature dependence of the shift of Mg-related luminescence band energy. The solid line illustrates changes of GaN band gap with temperature.

SUMMARY

One of the main purposes of this paper was to demonstrate that GaN bulk, single crystals of a few mm^2 size can be obtained through high-pressure, high-temperature growth. Platelets with dimensions up to 3 mm represent homogeneous crystals with very narrow X-ray rocking curves (less than 40 arc sec). At present, crystals with dimensions up to 5 mm, though of lower crystallographic quality, can be used as substrates in the homoepitaxial growth of GaN films. A significant improvement in the quality of photoluminescence (excitonic lines of 1 meV FWHM!) and reduction in the concentration of extended defects with respect to the heteroepitaxial films of GaN have been observed for MOCVD grown layers of GaN on the GaN substrates.

Further development of the high-pressure, high-temperature growth of GaN bulk single crystals with perfect homogeneity and larger dimensions is expected.

Studies of basic properties of GaN crystals have supplied valuable information which bring us nearer to a complete identification and understanding of the role of defects responsible for n-type character of undoped GaN and the yellow luminescence effect. With respect to highly efficient p-type doping, it will be worthwhile looking for an acceptor which forms a more shallow state than that introduced by magnesium.

ACKNOWLEDGEMENT

This work was partially supported by KBN Grant PBZ-101.12.

REFERENCES

#present adress: Lawrence Berkeley Laboratory, MS: 66-200, Berkeley, CA 94720

*present adress: Center for High Technology Materials, University of New Mexico, Albuquerque, NM 87131-6081.

1. S. Nakamura, M. Senoh, N. Iwasa, S. Nagahama, T. Yamada, and T. Mukai, Jpn. J. Appl. Phys. **34** (to be published).
2. M.A. Khan, J.N. Kuznia, D.T. Olson, and R. Kaplan, J. Appl. Phys. **73**, 108 (1993).
3. I. Akasaki, H. Amano, Y. Koide, K. Hiramatsu, and N. Sawaki, J. Cryst. Growth **98**, 209 (1989).
4. S. Nakamura, Jpn. J. Appl. Phys. **30**, L1705 (1991).
5. T.W. Weeks, Jr., M.D. Bremser, K.S. Ailey, E. Carlson, W.G. Perry, and R.F. Davis, Appl. Phys. Lett. **67**, 401 (1995).
6. F.A. Ponce, B.S. Krusor, J.S. Major, Jr., W.E. Plano, and D.F. Welch, Appl. Phys. Lett. **67**, 410 (1995).
7. B.H.T. Chai, unpublished.
8. A. Kuramata, K. Horino, K. Domen, K. Shinohara, and T. Tanahashi, Appl. Phys. Lett. **67**, 2521 (1995).
9. S. Porowski, I. Grzegory, and J. Jun in High Pressure Chemical Synthesis edited by B. Baranowski and J. Jurczak (Elsevier Science, Amsterdam, 1989) p. 21.
10. C.I. Harris, B. Monemar, H. Amano, and I. Akasaki, Appl. Phys. Lett. **67**, 840 (1995).
11. P. Perlín, J. Camassel, W. Knap, T. Talericio, J.C. Chervin, T. Suski, I. Grzegory, and S. Porowski, Appl. Phys. Lett. **67**, 2524 (1995).
12. H. Teisseyre, P. Perlín, M. Leszczynski, T. Suski, I. Grzegory, J. Jun, S. Porowski, and T.D. Moustakas, J. Appl. Phys. **76**, 2429 (1994).
13. M. Leszczynski, T. Suski, H. Teisseyre, P. Perlín, I. Grzegory, J. Jun, S. Porowski, and T.D. Moustakas, J. Appl. Phys. **76**, 4909 (1994).
14. S.F. Fang, K. Adoni, S. Iyer, H. Morkoc, H. Zabel, C. Choi, and N. Otsuka, J. Appl. Phys. **68**, R31 (1990).
15. K. Bickmann and J. Hauck, Mater. Lett. **11**, 236 (1991).
16. K. Pakula, J.M. Baranowski, R. Stepniowski, A. Wyszomolek, I. Grzegory, J. Jun, M. Sawicki, S. Porowski, K. Starowiejski, Acta Phys. Polon. (to be published).

17. W. Shan, T.J. Smith, X.H. Yang, S.J. Hwang, J.J. Song, and B. Goldenberg, *Appl. Phys. Lett.* **66**, 985 (1995).
18. H.P. Maruska and J.J. Tietjen, *Appl. Phys. Lett.* **15**, 327 (1969).
19. M. Ilegems and M.C. Montgomery, *J. Phys. Chem. Solids* **34**, 885 (1973).
20. B. Monemar and O. Lagerstedt, *J. Appl. Phys.* **50**, 6480 (1979).
21. T.L. Tansley and R.J. Egan, *Phys. Rev.* **B45**, 10942 (1992).
22. P. Boguslawski, E. Briggs, and J. Bernholz, *Phys. Rev.* **B51**, 17255 (1995).
23. J. Neugebauer and C.G. Van de Walle, *Phys. Rev.* **B50**, 8067 (1994).
24. P. Perlin, T. Suski, H. Teisseyre, M. Leszczynski, I. Grzegory, J. Jun, S. Porowski, P. Boguslawski, J. Bernholz, J.C. Chervin, A. Polian, and T.D. Moustakas, *Phys. Rev. Lett.* **75**, 296 (1995).
25. C. Wetzel, W. Walukiewicz, E.E. Haller, J. Ager III, I. Grzegory, S. Porowski, and T. Suski, *Phys. Rev. B* (to be published).
26. T. Ogino and M. Aoki, *Jpn. J. Appl. Phys.* **19**, 2395 (1980).
27. E.R. Glaser, T.A. Kennedy, K. Doverspike, L.B. Rowland, D.K. Gaskill, J.A. Freitas, W. A. Khan, D.T. Olson, J.N. Kuznia, and D.K. Wickenden, *Phys. Rev.* **B51**, 13362 (1995).
28. T. Suski, P. Perlin, H. Teisseyre, M. Leszczynski, I. Grzegory, J. Jun, M. Bockowski, S. Porowski, and T.D. Moustakas, *Appl. Phys. Lett.* **67**, 2188 (1995).
29. D.F. Hofmann, D. Kovalev, G. Steude, B.K. Mayer, A. Hoffmann, L. Eckey, R. Heitz, T. Detchprom, H. Amano, and I. Akasaki, (to be published).
30. H. Amano, M. Kito, K. Hiramatsu, and I. Akasaki, *Jpn. J. Appl. Phys.* **28**, L2112 (1989).
31. M. Ilegems and R. Dingle, *J. Appl. Phys.* **43**, 3797 (1972); B. Monemar, O. Lagerstedt, and H.P. Gislason, *J. Appl. Phys.* **51**, 625 (1980).
32. S. Nakamura, N. Iwasa, M. Senoh, and T. Mukai, *Jpn. J. Appl. Phys.* **31**, 1258 (1992).
33. S. Strite and H. Morkoc, *J. Vac. Sci. Technol.* **B10**, 1237 (1992).
34. H. Teisseyre, T. Suski, P. Perlin, I. Gorczyca, M. Leszczynski, I. Grzegory, J. Jun, and S. Porowski, in *Proc. of the 18th Int. Conf. on Defects in Semiconductors*, Sendai, Japan, 1995, (to be published).

GROWTH OF CUBIC GAN ON (001) GAAS

O. BRANDT*, H. YANG*, A. TRAMPERT**, AND K. H. PLOOG*

* *Paul-Drude-Institut für Festkörperelektronik, Hausvogteiplatz 5–7, D-10117 Berlin, Germany, E-mail: brandt@pdi.wias-berlin.de*

** *Max-Planck-Institut für Festkörperforschung, Heisenbergstraße 1, D-70569 Stuttgart, Germany*

ABSTRACT

We present a study of the growth of cubic GaN films on (001) GaAs by molecular beam epitaxy. Our investigations focus on the nucleation stage as well as on the subsequent growth of GaN. The phenomenon of epitaxial growth at this extreme mismatch (20%) is demonstrated to arise from a coincidence lattice between GaAs and GaN. The presence of a high-density of stacking faults in the GaN layer is explained within this understanding as being a natural consequence of the coalescence of perfectly relaxed nuclei. We furthermore analyze the growth kinetics of GaN via the surface reconstruction transitions observed upon an impinging Ga flux, from which we obtain both the desorption rate of Ga as well as the diffusion coefficient of Ga adatoms on the Ga-stabilized GaN surface. The diffusivity of Ga is found to be very low at the growth temperatures commonly used during molecular beam epitaxy, which provides an explanation for the microscopic surface roughness observed on our samples.

INTRODUCTION

Epitaxial layers of GaN and the related InGaN/AlGaIn heterostructures are now routinely fabricated in device quality on both Al_2O_3 and SiC substrates. In fact, the current throughput of GaN-based blue light-emitting diodes, which became commercially available in 1993, reportedly exceeds a million per month.¹ Despite this achievement, severe technological problems still exist. For the case of Al_2O_3 substrates, these problems mainly result from the incompatible cleavage planes of the substrate and GaN, paired with the extreme hardness and chemical inertness of Al_2O_3 as well as its insulating properties. SiC, on the other hand, suffers from its comparatively poor quality and high cost. In either case, the resulting device is still too expensive to be acceptable for true mass-applications such as full-color displays. These technological problems could, in principle, be circumvented by the use of substrates compatible with the established technology such as Si or GaAs. Indeed, several groups have achieved epitaxial growth of cubic and hexagonal GaN films on these substrates, although the quality of the resulting GaN films is still much inferior compared to that of their counterparts on Al_2O_3 or SiC.²

Here, we review our investigation of the growth of cubic GaN films on (001) GaAs by plasma-assisted molecular beam epitaxy (MBE). We present detailed studies of the nucleation stage as well as of the subsequent growth of GaN. For achieving epitaxial growth, nucleation of the first monolayers of GaN has to take place under N rich conditions, which gives rise to the formation of a connected epitaxial cubic template after deposition of a few monolayers. The phenomenon of epitaxial growth at this extreme mismatch (20%) is demonstrated to arise from a coincidence lattice between GaAs and

GaN. During the subsequent growth, a well-controlled surface stoichiometry is required for preserving the phase purity of the GaN film. The surface reconstructions of cubic GaN allow the *in situ* measurement and control of the effective V/III ratio impinging onto the growth front. Furthermore, we quantitatively analyze the reconstruction transitions observed upon an impinging Ga flux, from which we obtain both the desorption rate of Ga and the diffusion coefficient of Ga adatoms on the Ga-stabilized GaN surface. The low diffusion coefficient obtained is in quantitative agreement with that expected from the cohesive strength of GaN, and explains the microscopic surface roughness observed by atomic force microscopy for our GaN films.

EXPERIMENTAL

GaN films are grown on exactly oriented ($<0.1^\circ$ off) GaAs (001) substrates using a custom-made MBE system equipped with a DC glow-discharge plasma source for dissociating molecular N_2 . The source is operating at a power of $1.5\text{ kV} \times 20\text{ mA}$ and a pressure of $1\text{--}5 \times 10^{-4}$ Torr in the growth chamber. Nucleation and growth are monitored *in situ* by reflection high-energy electron diffraction (RHEED), using an incident angle of $1\text{--}3^\circ$ and an acceleration voltage of 15 kV. The RHEED patterns are recorded by a CCD camera and analyzed by an image processing system. Substrate temperatures used in this work range from 500°C to 800°C . (All temperature values quoted in this paper are thermocouple readings following a three-point calibration, assuming (i) the $(2 \times 4)\text{-c}(4 \times 4)$ reconstruction transition of GaAs to occur under an As_4 flux of 8×10^{-6} Torr at 490°C , (ii) the desorption of the native oxide of GaAs to take place at 580°C , and (iii) the growth rate of GaAs as measured by RHEED intensity oscillations to drop at temperatures above 630°C .) The Ga flux used in this study, as determined by RHEED intensity oscillations during the GaAs buffer layer growth, ranges from 3.0×10^{13} to 1.5×10^{14} atoms/ cm^2s , corresponding to nominal growth rates of $0.03\text{--}0.15$ monolayers (ML)/s for GaN. The morphology of the samples is examined *ex situ* by atomic force microscopy (AFM). The microstructure is studied by cross-sectional high-resolution electron microscopy (HREM) using a JEOL 4000 FX microscope operating at 400 kV. The $\langle 110 \rangle$ -oriented cross-sections are prepared using conventional ion-milling techniques.

RESULTS AND DISCUSSION

Prior to the growth of GaN, an atomically smooth surface is established by the deposition of a 100 nm thick GaAs buffer layer at $580\text{--}620^\circ\text{C}$ followed by a 2 min annealing at the growth temperature. The nucleation of GaN is initiated on the (2×4) reconstructed GaAs surface by closing the arsenic shutter and opening the Ga and N shutters. The RHEED pattern then invariably switches to an apparently N-induced (3×3) reconstruction, the atomic configuration of which is as yet unknown. The substrate temperature is set to $580\text{--}620^\circ\text{C}$ at the beginning of GaN growth and increased after deposition of a few (typically 5) ML to $620\text{--}680^\circ\text{C}$ without interrupting the growth. Simultaneously, the Ga flux is increased from about 3.0×10^{13} to 1.5×10^{14} atoms/ cm^2s . The RHEED pattern observed at this stage consists of diffuse transmission spots at the position for cubic GaN. These spots elongate and transform into streaks within about 10

nm of growth. Depending on the V/III ratio used, either a (2×2) or a $c(2\times 2)$ surface reconstruction becomes visible during growth.

Figure 1 shows both a HREM (a) and an AFM (B) micrograph of GaN layers obtained in this way.

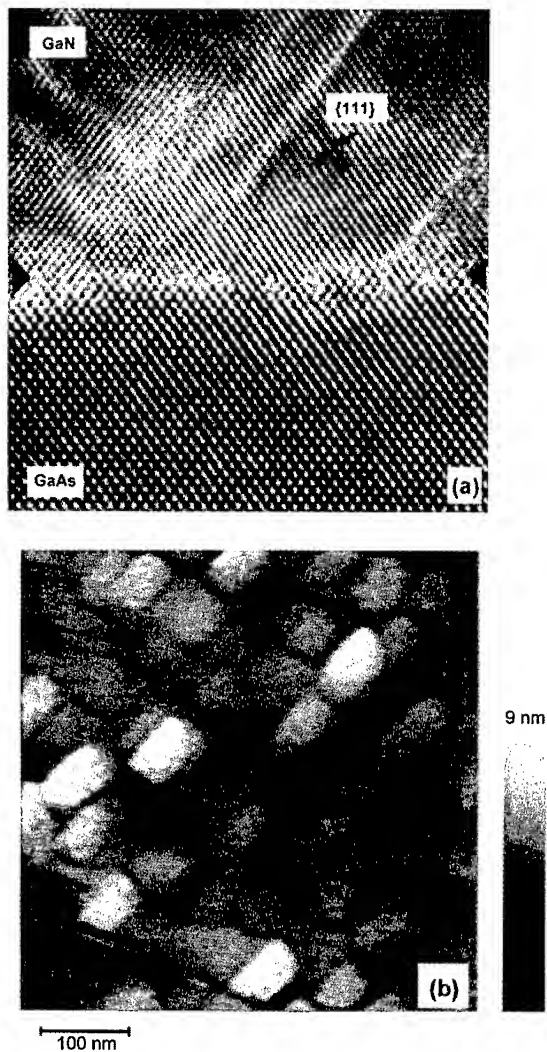


Figure 1 (a) HREM micrograph of the interface region between a GaN layer and the (001) GaAs buffer layer. Note the sharp heterointerface and the periodic array of Lomer dislocations at the interface. (b) AFM micrograph of a 100 nm thick GaN layer on (001) GaAs. The rms roughness measured is 0.5 nm. The edges of the rectangular features on the surface run along the $\langle 110 \rangle$ directions.

The HREM micrograph (a) demonstrates that epitaxial growth of GaN on (001) GaAs has been obtained. In fact, despite the lattice mismatch of 20% between GaN and GaAs, the layer is single-crystal in the sense that a grain structure is detected neither on the scale displayed in Fig. 1 (a) nor on the largest scale accessible by transmission electron microscopy (not shown here). The interface between GaN and GaAs is remarkably well-defined and exhibits only monolayer fluctuations. A high density array of Lomer (90°) dislocations appear at the interface. Secondly, stacking faults of a much lower density, which apparently originate from the interface, run through the GaN layer. Some of these stacking faults mutually terminate when intersecting. The AFM micrograph (b) shows the surface of a GaN layer grown under the $c(2\times 2)$ surface reconstruction, corresponding to a N/Ga ratio of one. The surface, while being quite smooth on a macroscopic scale, is microscopically rather rough, and consists of a densely-packed array of highly regular rectangular features. In fact, although the rms roughness measured from this and similar surfaces over a lateral scale of $1\ \mu\text{m}^2$ is impressively low (0.5 nm), peak-to-valley values of up to 4 nm are observed between adjacent rectangles. It has to be pointed out that these rectangular features on the GaN surface do not correspond to a grain or columnar structure of the layer.

Two important questions arise from the micrographs displayed in Fig. 1. First of all, which factors determine the epitaxial nucleation of GaN on GaAs, and which are the primary defects created in this stage? Secondly, which factors determine the surface morphology of a cubic GaN layer, and how can we possibly improve it? These two questions will be considered separately in the following two paragraphs.

Nucleation

Empirically, we found that the epitaxial growth of GaN on (001) GaAs is by no means trivial to achieve, but is critically depending on the growth conditions in the very first stage of deposition, i.e., during nucleation. For example, the deposition of the first GaN MLs with the same Ga flux used for growth (i.e., a N/Ga ratio of one) results in the formation of comparatively large three-dimensional (3D) nuclei with large rotational misorientations to each other due to a high density of 60° dislocations. Further growth onto this kind of template leads to a polycrystalline GaN deposit with grain sizes on the order of 10 nm. On the other hand, the *brute force* concept of depositing an amorphous GaN layer to avoid formation of 3D nuclei, which is used with much success for the growth of wurtzite GaN on (0001) Al_2O_3 ,³ also does not suffice for our purpose. Recrystallization of this amorphous deposit at 680°C leads to randomly oriented grains with predominantly wurtzite structure within a highly disordered polycrystalline matrix, and further deposition onto this kind of template results in the well-known columnar growth of hexagonal GaN. It is clear that, for achieving solid phase epitaxy, a higher temperature is needed than that we can reach in view of the limited thermal stability of our substrate. These problems led us to the concept of depositing a very thin nucleation layer under conditions which, while strongly limiting adatom kinetics, still allow formation of crystalline GaN. The conditions used for this purpose are those detailed above. In Fig. 2, we show the AFM (a) and HREM (b) micrographs obtained from such a nucleation layer.

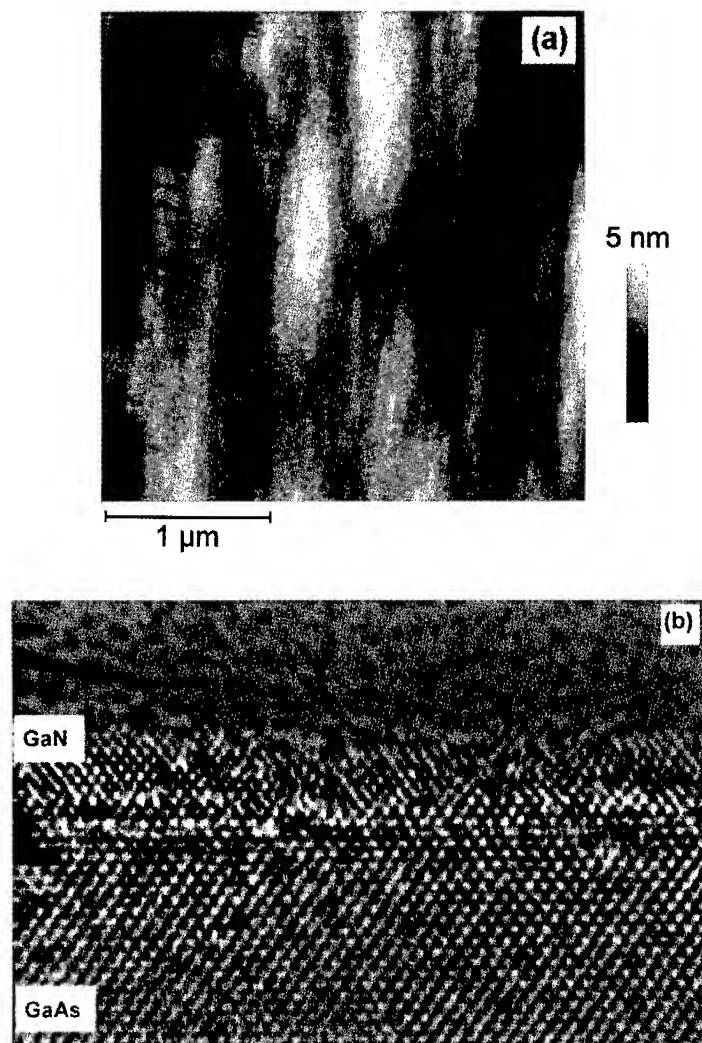


Figure 2 (a) AFM micrograph of a 5 ML thick GaN deposit on (001) GaAs. The rms roughness measured is 1 nm. **(b)** HREM micrograph of the 5 ML thick GaN film whose surface morphology is shown in (a). The GaN deposit is highly connected and forms indeed an epitaxial layer. Lomer dislocations are formed each 5 interatomic distances.

The AFM micrograph (a) reveals a quite smooth surface (rms roughness 1 nm), particularly on a microscopic scale, with large, highly anisotropic terrace-like features. The edges of these terraces run along the $\langle 110 \rangle$ directions, and they are thus supposed to originate from the anisotropic step structure of our GaAs buffer layer. 3D nuclei are not

observed. The HREM micrograph (b) of this nucleation layer most impressively shows that the 5 ML GaN deposit forms a connected, epitaxial layer. The mismatch between GaN and GaAs is seen to be relieved by Lomer dislocation formed each 5 interatomic distances. The phenomenon of a regular periodic spacing of these dislocations is observed along both $\langle 110 \rangle$ directions and for all of our epitaxial GaN layers [see also Fig. 1(a)]. The periodicity is broken just at those locations from which stacking faults originate.

These observations lead us to the following understanding of the epitaxial growth of GaN on GaAs. Coincidentally, the lattice misfit between these materials almost exactly corresponds to a ratio of integers (5/4), i.e., the *residual* misfit $f = (na_{\text{GaN}} - ma_{\text{GaAs}}) / ma_{\text{GaAs}}$ between GaN and GaAs is essentially zero if and only if $n=5$ and $m=4$. In fact, taking the most accurate values for the lattice constants available at *growth temperature*, namely, $a_{\text{GaN}} = 0.455 \pm 0.01$ nm and $a_{\text{GaAs}} = 0.568886$ nm, we obtain $f = -0.02 \pm 0.2\%$. Thus, an array of Lomer dislocations with a period of 5 GaN lattice planes will essentially account for the entire misfit. Individual nuclei supposedly relax by the direct nucleation of Lomer dislocations during lateral growth, as suggested by Fig. 2(b), making these dislocations the *primary* defect at the interface with no immediately obvious reason for generating other defects. However, the spacing of these individual nuclei will not necessarily be in phase with respect to their dislocation array, and upon their coalescence the periodicity of the dislocation array will thus, in general, be broken. These locations are centers of very high local strain (a 6/5 ratio, for example, corresponds to a residual misfit f of -4%), and we believe that these local strain concentrations are responsible for the *secondary* defects in our layers, namely, the stacking faults. The occurrence of a "magic mismatch" between GaN and GaAs provides an explanation of the phenomenon of epitaxial growth for a strain for which epitaxy of covalently bonded materials is usually no longer achieved. This "magic mismatch" also helps to understand why the structural quality of our GaN films rivals that of GaN layers grown on (001) SiC and (001) MgO, substrates which both have a considerably smaller lattice mismatch to GaN. However, the remaining problem of the generation of a high density of secondary defects, which is an inevitable consequence of the statistical nature of nucleation, seems difficult to overcome, since its solution would amount to a spatial synchronization of the dislocation arrays formed independently in individual nuclei. Attempts in this direction, which are based on the idea of regular step arrays with a distance of 4 GaAs interatomic spacings [here provided by (711) surfaces], are underway in this laboratory.

Growth kinetics

We now turn to the question which factors determine the surface morphology of GaN layers on (001) GaAs. As described in detail elsewhere,⁴ we have found that the most important factor for determining the phase purity of cubic GaN films is the N/Ga ratio during growth. A high N/Ga ratio leads to the formation of hexagonal domains within the layer, which subsequently deteriorates the structural and morphological quality of the layer. A low N/Ga ratio gives rise to smooth films of high structural quality, which are, however, intersected by large (~ 1 μm) GaN crystals formed within Ga droplets on the surface of the growing film. Macroscopically smooth ("mirrorlike") films are only obtained with a N/Ga ratio close to one.

We have also demonstrated that the surface reconstructions of GaN and their transitions upon an impinging Ga and/or N flux provide a means for controlling the surface stoichiometry during growth.⁴ The N/Ga flux ratio required to grow smooth films was shown to correspond to the region between the (2×2) and the c(2×2) surface reconstructions.

Here, we go one step further and analyze the surface reconstruction transitions quantitatively. For this purpose, we develop a simple model of the surface kinetics which accounts for the basic processes involved, namely, adsorption, diffusion, desorption, and incorporation of the surface species present on the GaN (001) surface. The basic equations of our model are given by

$$\begin{aligned}\left[\frac{d\theta_1(t)}{dt}\right] &= 2j_{\text{Ga}}(1/2 - \theta_1) + \hat{D}_{\text{Ga}} \frac{(1/2 - \theta_1)}{\theta_1} n + \gamma_N(1/2 - \theta_1) - j_N\theta_1, \\ \left[\frac{d\theta_2(t)}{dt}\right] &= 2j_{\text{Ga}}(\theta_1 - \theta_2) + \hat{D}_{\text{Ga}} \frac{(\theta_1 - \theta_2)}{\theta_2} n - \gamma_{\text{Ga}}\theta_2 - j_N\theta_2, \\ \left[\frac{dn(t)}{dt}\right] &= 2j_{\text{Ga}}\theta_2 + \hat{D}_{\text{Ga}} \frac{(1/2 - \theta_2)}{\theta_2} n - 2k_n n^{2/3},\end{aligned}$$

where θ_1 and θ_2 denote the Ga dimer coverage related to (2×2) and c(2×2) domains, n the amount of excess (liquid) Ga, j_{Ga} and j_N the Ga and N flux, \hat{D}_{Ga} the diffusion rate of excess Ga adatoms impinging onto θ_2 , γ_{Ga} and γ_N the rates of Ga and N desorption, and k_n the rate coefficient of excess Ga desorption. The first term of each equation accounts for adsorption of Ga, building up the θ_1 phase and subsequently the accompanying phases θ_2 and n . In much the same way, the second terms account for diffusion of Ga adatoms impinging onto θ_2 domains having a size proportional to the coverage. In other words, the diffusion rate is defined as the ratio of diffusion coefficient D_{Ga} and domain size L^2 . The third terms describe the desorption of N, Ga dimers (θ_2) and excess Ga (n), where the latter phase has been assumed to eventually form hemispherical droplets where desorption takes place from the droplets' surface which is of order 2/3. The last terms, finally, stand for the incorporation of Ga and N adatoms into the crystal, i.e., actual growth.

Finally, we have to relate the surface coverage calculated by means of the above equations to the quantity experimentally observed, namely, the RHEED intensity of the half-order beam. Although the intensity in RHEED is, in general, to be calculated by dynamical diffraction theory, there are certain instances for which the use of the kinematical approximation is justified.⁵ These instances include the present case of the half-order beam related to the (2×2) reconstruction. Within the kinematical approximation, we thus write for the intensity of the half-order reconstruction streak along a $\langle 110 \rangle$ azimuth⁶

$$I(t) = [\theta_1(t) - \theta_2(t)]^2.$$

Figure 3 shows RHEED transients at (a) 620°C and (b) 680°C upon the supply of 1.5 ML Ga onto a (2×2) reconstructed surface on a logarithmic scale.

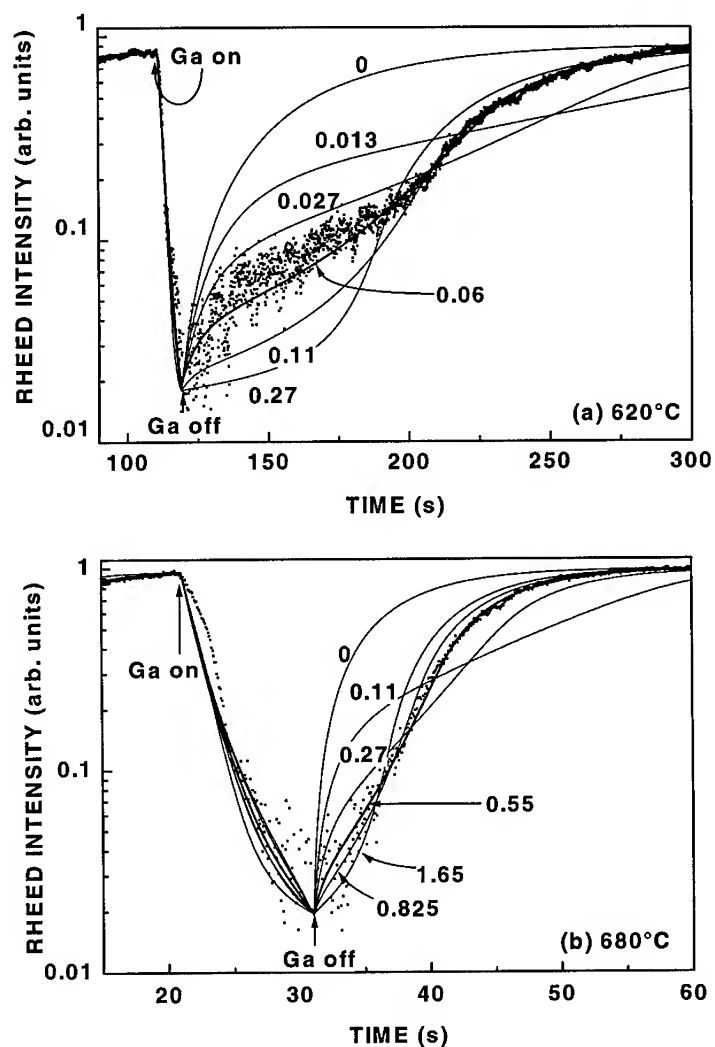


Figure 3 Logarithmic display of RHEED intensity transients upon a 1.5 monolayer Ga dose at (a) 620°C and (b) 680°C. The points represent experimental data, and the bold solid lines show the best fit of our model using diffusion rates of (a) 0.06/s and (b) 0.55/s.

The maximum intensity corresponds in each case to that of the (2×2) reconstruction, while the intensity drop is associated to the transition towards the c(2×2) reconstructed surfaces. It is obvious from these experiments that the half-order streak first vanishes upon the impinging flux of Ga, but recovers in a finite time once the supply has ceased. Note that the recovery time is substantially shorter at higher temperature. The simplest explanation for this effect consists in the initial adsorption of Ga, thus forming the c(2×2) surface phase which is distinct in coverage and symmetry from the (2×2) surface phase, followed by the isothermal desorption of the species building up these phases. The amount of Ga supplied exceeds the maximum coverage of 1 ML reached for the c(2×2) reconstruction, and, thus, the influence of the diffusion of excess Ga (n) is quite important. The experimental data are compared to simulations of our model where all parameters have been kept constant except for the diffusion rate \hat{D}_{Ga} . The sensitive dependence of the transient behavior on this parameter is evident.

To go further, we next extract the actual diffusion coefficient D_{Ga} from these measurements of the diffusion rate. The determination of $D_{Ga} = \hat{D}_{Ga} L^2$ requires knowledge of the domain size L , which is acquired here by scanning tunneling microscopy investigations of our GaN films. These studies show that the surface reconstruction is disordered on an atomic scale. As a worst-case approximation, the surface domain size L^2 has been assumed to be on the order of one unit cell.

In Fig. 4, we present the temperature dependence of the diffusion coefficient D_{Ga} .

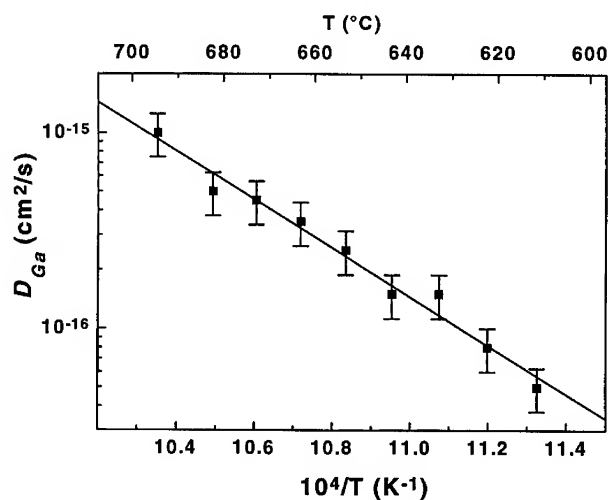


Figure 4 Arrhenius representation of the diffusion coefficient D_{Ga} . The solid squares are experimental data. The solid line is a least-square fit of an exponential to the data. For the diffusion coefficient $D_{Ga} = D_0 \exp(-E_D/k_B T)$ we obtain $D_0 = 0.007 \text{ cm}^2/\text{s}$ and $E_D = 2.48 \text{ eV}$.

Our assumptions results in a preexponential factor of $0.007 \text{ cm}^2/\text{s}$, which is in fact consistent with the expected "universal" $D_0 = v/4N_0$, where v is the frequency of thermal

vibrations and N_0 is the surface site density. The diffusivity is characterized by an activation energy of 2.48 eV, i.e., twice that obtained for GaAs.⁷ This finding is consistent with the theoretically expected scaling of the surface diffusivity with the cohesive strength of the material.⁸ Note that this activation energy may originate from the temperature dependence of the domain size L^2 , which is determined by diffusion of Ga on the (2×2) reconstructed surface, rather than by \hat{D}_{Ga} which accounts for diffusion of excess Ga on the c(2×2) domains. In any case, it is clear that the diffusion coefficient for Ga adatoms on the Ga stabilized (001) GaN surface is too low to obtain a truly smooth surface.

SUMMARY AND CONCLUSION

We have shown that the phenomenon of epitaxial growth of GaN on (001) GaAs arises from a coincidence lattice between GaAs and GaN. The presence of a high-density of stacking faults within the GaN layer is thus understood as being a natural consequence of the coalescence of perfectly relaxed nuclei. We have furthermore analyzed the growth kinetics of GaN via the surface reconstruction transitions observed upon an impinging Ga flux, from which we have obtained both the desorption rate of Ga and the diffusion coefficient of Ga adatoms on the Ga-stabilized GaN surface. The low diffusivity of Ga provides an explanation for the microscopic surface roughness observed on our samples.

Possible remedies for these two major problems identified in this work, namely, the high stacking fault density and the microscopic surface roughness, include the following strategies. Firstly, in order to avoid the coalescence of "out of phase" nuclei and thus the formation of the consequential stacking faults, it is required to synchronize the formation of dislocation arrays in spatially separated nuclei. This task might be achieved by a surface with a highly uniform array of steps four interatomic distances apart. If, for example, the step array runs straight along a $\langle 110 \rangle$ direction, such a surface would be formed by a $\{711\}$ -plane. However, the inevitable statistical fluctuation of the terrace widths on such surfaces might render this simplified view as being rather too idealistic. Secondly, the most straightforward way for enhancing the diffusivity of surface adatoms is a higher growth temperature. Since the temperatures used in this work are actually limited by the thermal stability of the GaAs substrate, Si seems an attractive candidate in that it shares most of the advantages of GaAs while simultaneously offering additional ones, such as, particularly, a higher thermal stability. However, the growth of a III-V compound on a group IV substrate brings about also additional complications related to the formation of antiphase domain boundaries, and it is, at present, not clear which of these factors will eventually be most important for the quality of the GaN layer.

ACKNOWLEDGEMENT

The authors are much indebted to M. Wassermeier for the AFM images, and to H. P. Schönher for his expert technical help regarding the MBE setup. This work was financially supported by the Bundesministerium für Forschung und Bildung (BMBF) of the Federal Republic of Germany.

REFERENCES

- ¹ R.A. Metzger, in *Compound Semiconductor*, edited by M. Meyer, Vol. 1, (Franklin Publishing, Saint Paul, 1995), p. 28.
- ² M.J. Paisley, Z. Sitar, J.B. Posthill, and R.F. Davis, *J. Vac. Sci. Technol. A* **7**, 701 (1989); S. Strite, J. Ruan, Z. Li, A. Salvador, H. Chen, D.J. Smith, W.J. Choyke, and H. Morkoç, *J. Vac. Sci. Technol. B* **9**, 1924 (1991); T. Lei, T.D. Moustakas, R.J. Graham, Y. He, and S.J. Berkowitz, *J. Appl. Phys.* **71**, 4933 (1992); R.C. Powell, N.-E. Lee, Y.-W. Kim, and J.E. Greene, *J. Appl. Phys.* **73**, 189 (1993); H. Liu, A.C. Vrenkel, J.G. Kim, and R.M. Park, *J. Appl. Phys.* **74**, 6124 (1993), T.S. Cheng, L.C. Jenkins, S.E. Hooper, C.T. Foxon, J.W. Orton, and D.E. Lacklison, *Appl. Phys. Lett.* **66**, 1509 (1995).
- ³ S. Yoshida, S. Misawa and S. Gonda, *Appl. Phys. Lett.* **42**, 427 (1983); H. Amano, N. Sawaki, I. Akasaki and Y. Toyoda, *Appl. Phys. Lett.* **48**, 353 (1986); M. J. Paisley and R. F. Davis, *J. Crystal Growth* **127**, 136 (1993); J. N. Kuznia, M. Asif Khan, D. T. Olson, R. Kaplan and J. Freitas, *J. Appl. Phys.* **73**, 4700 (1993).
- ⁴ O. Brandt, H. Yang, B. Jenichen, Y. Suzuki, L. Däweritz, and K.H. Ploog, *Phys. Rev. B* **52**, R2253 (1995).
- ⁵ L.M. Peng and M.J. Whelan, *Acta. Cryst. A* **47**, 95 (1991).
- ⁶ M.G. Lagally, D.E. Savage, and M.C. Tringides, in *Reflection high-energy electron diffraction and reflection electron imaging of surfaces*, edited by P.K. Larsen and P.J. Dobson, (Plenum Press, New York, 1988), NATO ASI Series B Vol. 188, p. 139; W. Moritz, *ibid.*, p. 175.
- ⁷ J.H. Neave, P.J. Dobson, B.A. Joyce, and J. Zhang, *Appl. Phys. Lett.* **47**, 100 (1985).
- ⁸ M.H. Yang and C.P. Flynn, *Phys. Rev. Lett.* **62**, 2476 (1989).

LATTICE-MATCHING GROWTH OF InGaAlN SYSTEMS

Takashi Matsuoka

NTT Opto-electronics Labs., 3-1 Morinosato Wakamiya, Atsugi-shi, Kanagawa, 243-01 Japan,
matsuoka@aecl.ntt.jp

ABSTRACT

The development and device applications of the InGaAlN system have progressed dramatically with improvements in crystalline quality by achieved through a buffer layer, the realization of p-type doping, and the growth of ternary alloys. As a substrate, sapphire is mainly used for epitaxial growth because of the lack of a GaN bulk crystal. However, many cracks in GaN film can still be observed and its X-ray rocking curve width is less than 100 arc seconds. This is are thought to be due to the lattice constants and thermal expansion coefficients of GaN and sapphire differ by 13.8% and by -34.2%, respectively. These values are extremely large in comparison with the corresponding values for InP and GaAs. Lattice-matching growth thus remains a basic problem in growing the high-quality epitaxial films necessary for high-performance devices.

This paper reviews attempts at lattice-matching growth. Lattice-matching growth of InGaN on a house-made ZnO substrate and near-lattice-matching growth of GaN on SiC and NdGaO₃ substrates have been proposed and performed, and the effects of lattice-matching have been confirmed. Various types of surface planes commercially available sapphire substrates are also discussed.

INTRODUCTION

Recent progress in research on an InGaAlN system has been remarkable since the InGaAlN quaternary system has proposed as a promising material in the fabrication of high performance optical devices in wavelength regions shorter than orange. High-quality GaN films have been grown on (0001) sapphire substrates by using buffer layers of AlN [1] and GaN [2] grown at low temperatures by metalorganic vapor phase epitaxy (MOVPE), because unfortunately no substrate for the homoepitaxial growth of InGaAlN systems exists yet. In molecular beam epitaxy (MBE), high quality GaN has been grown using nitrogen radicals as the nitrogen source [3,4].

Conduction type control has also been carried out. N-type GaN has been obtained by Si-doping using silane [5]. P-type GaN has been obtained by Mg-doping, and post-growth treatment, that is, through the low-energy electron-beam irradiation (LEEBI) [6] and thermal annealing [7]. In MBE, conduction type control has been achieved without the use of any post-growth treatment [4].

The most difficult part of growing an InGaAlN system is InN growth because the equilibrium vapor pressure of nitrogen is several orders of magnitude higher than AlN and GaN [8]. A single

crystal of InN has been successively grown under high flow rate ratios of group V to group III sources [8]. This success has made composition control possible. The quality of InGa_N has improved at a growth temperature of 800°C such that photoluminescence has been observed. At present, using the growth methods mentioned above, an InGa_N/AlGa_N double-heterostructure (DH structure) has been fabricated and a candela-class DH light-emitting-diode (LED) has been obtained [9]. Optically pumped stimulated emission from a GaN/AlGa_N DH structure has also been demonstrated [10]. However, no laser diode (LD) with an InGa_N system exists which oscillates with current injection. Present demand requires an LD with an InGa_N system to be fabricated. To achieve this, much higher quality material through lattice-matching growth on a substrate needs to be attained. Of course, the lattice matching between respective layers of configuring devices is also important. This has not been as large a problem in the device lifetimes of InGa_N LEDs up to now, however, the strain due to lattice-mismatch may decrease lifetime in devices such as ZnSe-based blue-green LDs and LEDs. Lattice-matching growth has been a basic technique of epitaxial growth throughout its history.

In this paper, lattice-matching growth is reviewed. The substrate materials suitable for complete and near lattice-matching growth are described. The control of composition of InGa_N which is important for light emitting devices and lattice-matching growth is also shown.

SUBSTRATE FOR InGa_N SYSTEM

The relationship between the lattice constant and band-gap energy is a basic consideration in device fabrication and substrate selection. Figure 1 shows this relationship and the lattice constants of some candidate substrate materials for the InGa_N system are indicated by the dotted lines [11]. We can see from this figure that DH structures can be configured using lattice-matching. Although sapphire is similar to GaN, it does not have a wurtzite structure. The lattice-mismatch between GaN and (0001) sapphire is 13.8% as shown in Table 1. In addition, this table also includes thermal expansion mismatch which is as important as lattice constant for epitaxial growth. In particular, sapphire with various types of commercially available planes are compared in Table 2. This table shows the relationship of orientation, lattice-mismatch and crystallographic symmetry between a GaN epitaxial film and a sapphire substrate. From the viewpoints of lattice-mismatch and crystallographic symmetry, (01 $\bar{1}$ 0) sapphire seems the most suited to GaN growth. The c-axis of a GaN film grown on a (01 $\bar{1}$ 0) sapphire substrate inclines to that of this substrate. This means that twins may generate in an epitaxial film. This is the only disadvantage of a (01 $\bar{1}$ 0) plane in comparison with a (0001) plane. Lattice-mismatch of NdGaO₃ with an orthorhombic crystal structure is calculated in Table 1. This structure has been regarded as pseudo-cubic because the lattice constants along with the a- and b-axes are almost the same [12]. NdGaO₃ has been used in the epitaxial growth of super-conductive oxide material [13]. Lattice mismatching of (0001) 6H-SiC and (101) NdGaO₃ to GaN is smaller than that of GaAs to Si. The use of (111) MgAl₂O₄ has recently been proposed [14]. This material can be cleaved and this property is useful in fabricating

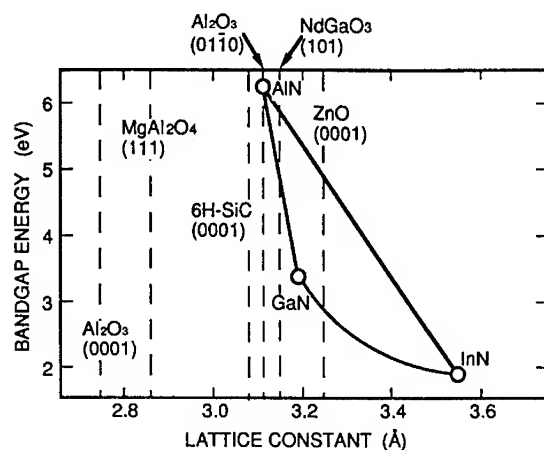


Figure 1 Relationship between bandgap energy and lattice constant. Dotted lines show atomic spaces in-plane corresponding to GaN.

Table 1 Lattice and thermal mismatch between GaN and substrates.

SUBSTRATE	LATTICE MISMATCH (%)	THERMAL EXPANSION MISMATCH (%)
(0001) SAPPHIRE	13.8	-25.5
(0110) SAPPHIRE	-1.9, 2.6	9, 62
(0001) 6H-SiC	3.4	25
(101) NdGaO ₃	1.2	20.6
(111) MgAl ₂ O ₄	9.5

$$\text{MISMATCH} = \frac{\text{GaN} - \text{SUBSTRATE}}{\text{GaN}}$$

Table 2 Relationships of orientation, lattice mismatch and crystallographic symmetry between GaN epitaxial film and sapphire substrate. After ref. 15.

INTERFACE PLANE GaN / Al ₂ O ₃	IN - PLANE GaN // Al ₂ O ₃	LATTICE MISMATCH (%)	CRYSTALLOGRAPHIC SYMMETRY
(0113) / (0110)	[0332] // [2110]	- 2.6	COINCIDENCE
	[2110] // [0001]	1.9	
(0001) / (0001)	[2110] // [0110]	13.8	COINCIDENCE
	[0110] // [2110]	13.8	
(0001) / (2110)	[0110] // [0110]	- 0.4	NON COINCIDENCE
	[2110] // [0001]	1.9	
(2110) / (0112)	[0110] // [2110]	13.8	COINCIDENCE
	[0001] // [0111]	1.1	

(0110);M-PLANE, (0001);C-PLANE, (2110);A-PLANE, (0112);R-PLANE

laser cavities. In this table, there is no difference in thermal expansion mismatch between materials.

EXPERIMENTAL RESULTS AND DISCUSSION

Epitaxial films were grown by metalorganic vapor phase epitaxy (MOVPE). The source gases were trimethylindium (TMI), triethylgallium (TEG), and purified ammonia. Both carrier and bubbling gases were purified hydrogen and nitrogen for GaN and InGaN growth, respectively. The reactor pressure was held at 76 Torr.

GaN GROWTH ON (01 $\bar{1}$ 0) SAPPHIRE SUBSTRATE

Sapphire substrates were degreased with organic solvents. Next, these substrates were cleaned in hydrogen at 1150 °C for 10 minutes and then their surfaces were nitrided in-situ in an ambient of ammonia at 1150 °C for 5 minutes just before growth. Ammonia was introduced into the reactor at 2.5 standard liters per minute (slm). The flow rate ratio of ammonia to triethylgallium (TEG) (V/III ratio) was 5.5×10^3 , and the growth temperature was 1000°C.

The surface morphology of GaN films simultaneously grown on (0001) and (01 $\bar{1}$ 0) sapphire substrates was examined using the differential interference micrographs [15]. The GaN film on the (01 $\bar{1}$ 0) substrate had no characteristic patterns or projections, and only a relatively flat surface was observed. On the other hand, GaN on the (0001) substrate exhibits peculiar hexagonal patterns. The surface roughness of approximately a 1- μ m thick piece of film was measured with a surface profilometer. The magnitude of the surface roughness of GaN on a (01 $\bar{1}$ 0) substrate was about 50 nm on one order of magnitude smaller than that on the (0001) substrate.

Electron concentration and the mobility of undoped GaN films was evaluated by Hall measurements at room temperature. The dependence of both characteristics on growth temperature are shown in Fig. 2 in comparison with the (01 $\bar{1}$ 0), (0001), (01 $\bar{1}$ 2), and (2 $\bar{1}$ 10) substrates. Both characteristics improved by using high growth temperatures. GaN on the (01 $\bar{1}$ 0) substrate showed the best characteristics.

The photoluminescence (PL) spectra of GaN films on both (01 $\bar{1}$ 0) and (0001) substrates are compared in Fig. 3. Excitation was carried out using a helium-cadmium laser with a wavelength of 325 nm. The PL intensity of the film on the (01 $\bar{1}$ 0) substrate was more than three times greater than that on the (0001) substrate, despite the fact that the film grown on the (0001) substrate had approximately four times higher carrier concentration.

The above results suggest that the crystalline quality of GaN film grown on sapphire (01 $\bar{1}$ 0) substrates is better than that grown on (0001) substrates, and that (01 $\bar{1}$ 0) substrates are more suitable for GaN growth.

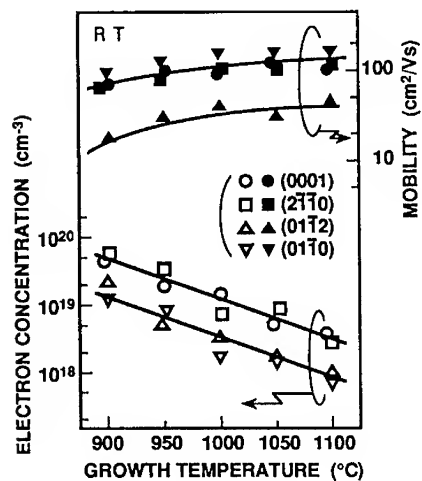


Figure 2 Dependence of electron mobility and carrier concentration on growth temperature in comparison with the (0110), (0001), (0112), and (2110) substrates.

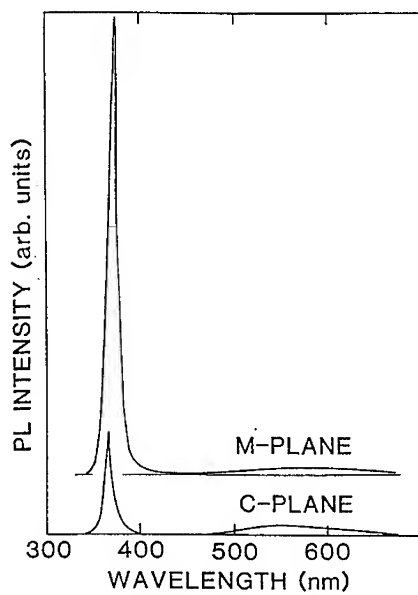


Figure 3 Room temperature PL spectra of GaN grown on (0110) (M-plane) and (0001) (C-plane) sapphire substrates.

GaN GROWTH ON (0001) 6H-SiC SUBSTRATE

(0001) 6H-SiC not only has a lattice constant closer to GaN than sapphire, but it is also vastly different from sapphire in terms of crystallographic structures. In contrast to the centrosymmetric structure of sapphire, SiC has polarity along the [0001] axis. The polarity of GaN has been overlooked because most researchers have used the nonpolar substrate of sapphire. GaN polarity can be expected to appear on the polar planes of SiC.

The substrates used were low-resistivity n-type (0001) 6H-SiC grown by the Acheson method. As SiC has a chemically stable nature, the substrates were prepared for epitaxial growth [16]. Degreasing in organic solvents, oxidizing in oxygen ambient at 1100°C over 10 hours, and removing oxide with hydrofluoric acid were performed. The substrates were then heated in hydrogen at 1150°C for 10 minutes just before growth. The substrate polarity of SiC substrates was discriminated by the dependence of oxidation rate on the polarity [17]. To study the substrate polarity dependence of GaN films, they were simultaneously grown on (0001)_C and (0001)_{Si} SiC substrates. As a comparison, sapphire substrates were used in the same run.

Surface morphologies of GaN films were observed through a scanning electron microscope. The film on (0001)_{Si} SiC showed a featureless, rather smooth surface in contrast that the film on (0001)_C SiC. The latter had prominent hexagonal pyramids similar to the film on (0001) sapphire. PL spectra at room temperature consisted on three emission peaks: near-edge emission at 365 nm and two broad deep bands near 425 and 560 nm as shown in Fig. 4. Although the near-edge emission intensity is almost constant in these films, the broad emission near 425 nm of GaN on (0001)_{Si} SiC is much smaller than those of GaN on (0001)_C SiC and on (0001) sapphire.

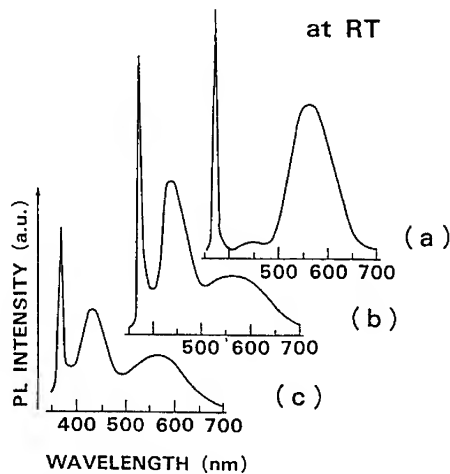


Figure 4 Room temperature PL spectra of GaN on (0001)_{Si} SiC (a), (0001)_C SiC (b) and (0001) sapphire (c).

The polarity of GaN was determined from X-ray photoelectron spectroscopy (XPS) using Frommer's method [18]. This method has been proposed to discriminate GaP polarity, and it is based in principle on the dependency of the chemical shift in the XPS signal of Ga atoms on Ga-P and Ga-O bonds. Frommer reported that additional higher-energy peak appeared in the Ga 2p_{3/2} spectrum from {111}_{Ga} GaP. This higher-energy peak was assigned to surface Ga-O bonds. When this peak was observed, the surface of GaP was thought to have terminated by Ga. The Ga 2p_{3/2} photoelectron spectra from GaN are shown in Fig. 5. It should be noticed that the spectra from the film on (0001)_C SiC shift towards higher energy. For the XPS spectra of GaN, the electronegativity difference between nitrogen and oxygen are significantly smaller than the difference between phosphorus and oxygen. This inadequate difference in electronegativity between nitrogen and oxygen leads to small binding-energy shift and makes it difficult to resolve the present spectra based on the contribution from Ga-N and Ga-O bonds. From Fig. 5, GaN films on (0001)_{Si} and (0001)_C SiC substrates were terminated with gallium and nitrogen, respectively. The details describing this determination process are reported in ref. [16].

Currently, bulk single crystals of SiC are grown using a modified-Lely method. High quality SiC substrates with diameter over one inch have been fabricated. GaN homojunction LEDs have been fabricated on SiC substrates [19].

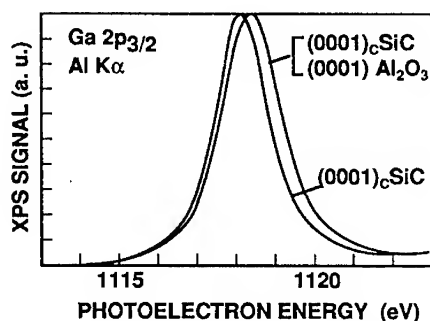


Figure 5 Ga 2p_{3/2} photoelectron spectra from GaN on (0001)_{Si} and (0001)_C SiC.

GaN GROWTH ON (011) NdGaO₃ SUBSTRATE

GaN films were grown on NGO (011) substrates by the hydride VPE at 810 and 850°C using NH₃ and HCl as source gases, and N₂ as a carrier gas [12]. GaN film quality depended on growth conditions and the best results were obtained for a film grown at a low growth rate after nitridation of the substrate surface by the NH₃ gas. GaN (0001) films had been confirmed to be grown on substrates from the X-ray diffraction measurement and to be grown along the c-axis with good lattice-matching to substrates from the TEM observation. PL spectra measured at room

temperature from GaN films grown on a NGO (011) and a (0001) sapphire are shown in Fig. 6 [12]. The near-band edge emission were observed for both films. This emission for the GaN film on a NGO substrate is sharper than that of the GaN film on a sapphire and the emission of a longer wavelength region for the GaN film on a NGO substrate is much weaker. These results show NGO substrates is effective for the growth of high quality GaN film.

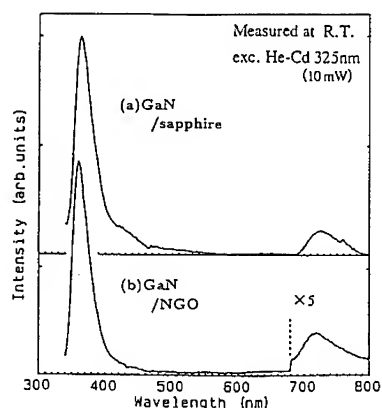


Figure 6 Comparison of room-temperature PL spectra of GaN films (a) on (011) NGO and (b) on (0001) sapphire.

GaN GROWTH ON (111) MgAl_2O_4 SUBSTRATE

GaN films were grown by MOVPE with a low-pressure horizontal chamber [14]. The source gases were TMG and NH_3 . The 30 nm thick GaN buffer layer grown at 500°C was used. After annealing this layer at 1030°C , the thick GaN film was grown. The morphology of GaN on (111) MgAl_2O_4 was specular, while the morphology of GaN on (001) MgAl_2O_4 was very rough. From X-ray diffraction measurement, the GaN film was found to be (0001) oriented. The crystallographic orientation relationships between the GaN film and the MgAl_2O_4 substrate are as follows: $(0001)\text{GaN} // (111)\text{MgAl}_2\text{O}_4$, $(1\bar{1}00)\text{GaN} // (\bar{2}11)\text{MgAl}_2\text{O}_4$. The full width of half-maximum (FWHM) value of X-ray rocking curves for GaN are shown in Fig. 7 [14], in comparison with MgAl_2O_4 and sapphire substrates. The FWHM decreased as the thickness increased. The dependence was nearly the same for both substrates, although the very narrow FWHM value of 36 arcseconds has been reported on sapphire substrates. The FWHM value for a $3.6\text{ }\mu\text{m}$ thick GaN grown on MgAl_2O_4 was 310 arcseconds, comparably to the typical data for the GaN grown on the sapphire substrate. PL characteristics were also investigated and were the same spectra for both MgAl_2O_4 and sapphire substrates. Therefore, MgAl_2O_4 is found to be suitable for the substrate of GaN growth.

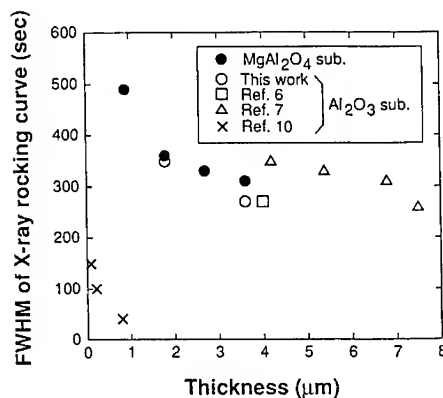


Figure 7 Comparison of room-temperature PL spectra of GaN films (a) on (0001) sapphire and (b) on (111) MgAl₂O₄.

LATTICE-MATCHING GROWTH OF InGaN ON (0001) ZnO SUBSTRATE

InGaN growth, which is important in lattice-matching growth on a ZnO substrate, is first described. The flow rate ratio of ammonia to the sum of group III sources was increased from 2,000 to 20,000, and the growth temperature was varied from 500 to 800°C. InGaN films were grown on (0001) plane sapphire substrates treated with the same method used for GaN growth as explained above.

The relationship between the indium mole fraction and the group III flow rate ratio of TMI to the sum of TMI and TEG ($TMI/(TMI+TEG)$) as a function of growth temperature is shown in Fig. 8 [20]. The ammonia flow rate was fixed at 20 l/min throughout. At growth temperatures of 500°C and 700°C, the V/III flow rate ratio (mole ratio) was kept at 20000 because indium droplets appeared on the surface when V/III flow rate ratios were less than 15000. However, for growth at 800°C, TEG was supplied at 17 μmol/min and the V/III flow rate ratio reached about 4000. This figure shows that the indium mole fraction varied linearly with $TMI/(TMI+TEG)$ at a growth temperature of 500°C. At 800°C, the indium mole fraction increased steeply with $TMI/(TMI+TEG)$ when that ratio was more than 0.8. From this figure, the incorporation efficiency of indium can be found to decrease with increasing temperature from 500°C to 800°C, probably because the vapor pressure of indium is higher than that of gallium. InGaN with an indium content of 22 % can be lattice-matched to (0001) ZnO substrate as shown by Fig. 1.

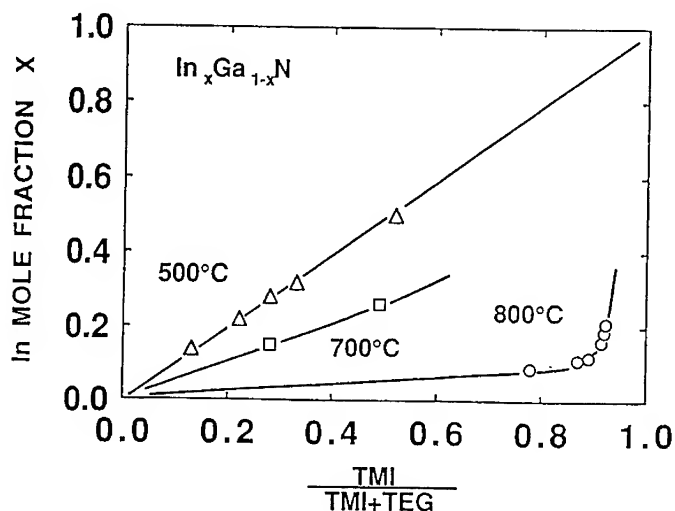


Figure 8 Relationship between indium mole fraction of InGa_N and flow rate ratio of indium to the sum of group III sources.

ZnO bulk crystals were grown by the flux method and its wafers were fabricated in our laboratory because ZnO wafers are not commercially available. The treatment of ZnO substrates just before InGa_N growth was briefly investigated because no clear report have yet been published. The Zn-surface was smoothed by etching with nitric acid for 10 minutes except for the groove created by slicing and polishing. The O-surface was quite rough. Therefore, the Zn-surface was used for epitaxial growth. To avoid degradation of the substrate surface in reduced atmospheres such as ammonia, the substrate was kept in a nitrogen atmosphere until growth, and the substrate temperature was gradually raised to the growth temperature. At the growth temperature, the nitrogen in the reactor was exchanged for ammonia and group III sources.

The X-ray diffraction of InGa_N with an indium content of 22 % grown at 500°C on the Zn-surface of a (0001) plane ZnO substrate are shown in Fig. 9 [20]. Only diffraction from the (0002) planes of InGa_N and ZnO could be observed. The difference in diffraction angle between both peaks was 0.44 degrees. This coincides with the lattice-constant difference along with the c-axis between the ZnO substrate and the InGa_N film which is lattice-matched along with the a-axis, thus confirming the lattice-matching in-plane between InGa_N and ZnO. The InGa_N on ZnO had a spotty pattern under reflection high energy electron diffraction (RHEED). For comparison, InGa_N was also grown on sapphire grown without surface nitridation at the same time. This InGa_N on sapphire showed rings, which indicated that the film was polycrystalline. X-ray rocking curve width was also compared between InGa_N on ZnO and on sapphire having nitrided surfaces at growth temperatures from 500 to 800°C. All the films were from 0.3 to 0.5 μm thick. For growth

temperatures greater than 500°C, an initial 20 nm layer of InGa_N was grown at 500°C for surface protection. Thick InGa_N was successively grown at higher temperatures. X-ray diffraction line width narrowed for growth at higher temperatures. The X-ray diffraction line width of InGa_N grown on ZnO was about 20 % smaller than that of films grown on sapphire substrates. Thus, using lattice-matched substrates was shown to improve the crystalline quality of InGa_N. However, the minimum width of 30 arc minutes was still quite large in comparison with state-of-the-art III-V material such as GaAs, because of the poor crystalline quality of ZnO, insufficient surface treatment and the nonoptimized growth conditions of InGa_N. Further improvement of the crystalline quality of InGa_N films is expected as these factors are removed.

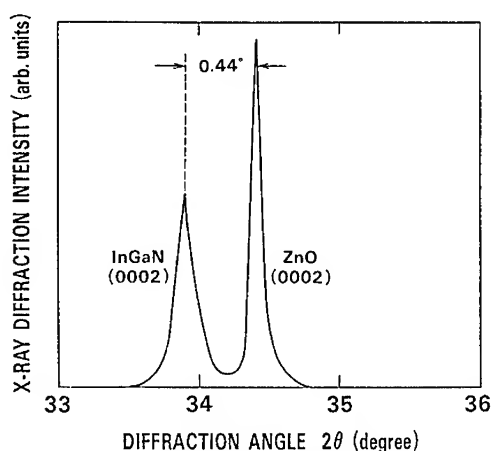


Figure 9 X-ray diffraction line of InGa_N grown on a (0001) ZnO substrate. The composition of InGa_N was selected to lattice-match with ZnO.

CONCLUSIONS

Near and complete lattice-matching growth to (01 $\bar{1}$ 0) sapphire, (0001) 6H-SiC and house-made ZnO substrates was reviewed. Effects of lattice-matching were described such as the ready growth of single crystals and improvements in electrical and optical characteristics. The surface polarity of epitaxially grown GaN on SiC substrates with polarity was also discussed.

These InGaAlN films with higher quality than present films are expected to achieve high performance in light-emitting-devices such as LDs and allow device fabrication with high yields. For these purposes, lattice-matching growth is essential. Currently, it is impossible to fabricate a GaN wafer because the equilibrium nitrogen vapor pressure over GaN is extremely high [21]. Therefore, we will have to examine the usefulness of various crystals in lattice-matching growth in the literature and to grow bulk crystals.

ACKNOWLEDGMENTS

I greatly appreciate the contribution of Dr. Tohru Sasaki for his discussion on crystallography between substrates and epitaxial films, and his explanations on the growth mechanism. I would also like to thank Dr. Hidetoshi Iwamura and Dr. Yutaka Matsuoka for giving me the chance to write this review.

REFERENCES

1. H. Amano, N. Sawaki and I. Akasaki, *Appl. Phys. Lett.* **48**, 353 (1986).
2. S. Nakamura, *Jpn. J. Appl. Phys.* **30**, L1705 (1991).
3. R. C. Powell, G. A. Tomasch, Y.-W. Kim, J. A. Thornton and J. E. Green, *Mater. Res. Soc. Symp. Proc.* **162**, 525 (1990).
4. T. D. Moustakas and R. J. Molnar, *Mat. Res. Soc. Symp. Proc.* **281**, 753 (1993).
5. M. E. Lin, B. Sverdlov, G. L. Zhou and H. Morkoç, *Appl. Phys. Lett.* **62**, 3479 (1993).
6. H. Amano, M. Kito, K. Hiramatsu and I. Akasaki, *Jpn. J. Appl. Phys.* **28**, L2112 (1989).
7. S. Nakamura, T. Mukai, M. Senoh and N. Iwasa, *Jpn. J. Appl. Phys.* **31**, L139 (1992).
8. T. Matsuoka, H. Tanaka, T. Sasaki and A. Katsui, in: *Proc. 16th Intern. Symp. on GaAs and Related Compounds*, Karuizawa, 1989, *Inst. Phys. Conf. Ser.* **106**, Eds. T. Ikoma and H. Watanabe (*Inst. Phys.*, Bristol, 1990) p.141.
9. S. Nakamura, T. Mukai and M. Senoh, *Appl. Phys. Lett.* **64**, 1687 (1994).
10. I. Akasaki, H. Amano, N. Koide, M. Kotaki and K. Manabe, *Physica B* **185**, 428 (1993).
11. T. Matsuoka, A. Ohki, T. Ohno and Y. Kawaguchi, *J. Crystal Growth* **138**, 727 (1994).
12. H. Okazaki, A. Arakawa, T. Asahi, O. Oda and K. Aiki, in *Abstract Topical Workshop on III-V Nitrides*, Nagoya, 1995, SP. 8.
13. M. Mukaida, S. Miyazawa, M. Sasaura, K. Kuroda, *Jpn. J. Appl. Phys.* **29**, L936 (1990).
14. A. Kuramata, K. Horino, K. Domen, K. Shinohara and T. Tanahashi, *Appl. Phys. Lett.* **67**, 2521 (1995).
15. T. Matsuoka, T. Sasaki and A. Katsui, *Optoelectronics Device & Technologies (OP-DET)* **5**, 53 (1990).
16. T. Sasaki and T. Matsuoka, *J. Appl. Phys.* **64**, 4531 (1988).
17. W. von Münch and I. Pfaffeneder, *J. Electrochem Soc.* **122**, 642 (1975).
18. M. H. Frommer, *J. Appl. Phys.* **62**, 657 (1987).
19. J. Edmond, H. S. Kong, M. Leonard and G. Bulman, *Tech. Digest. Int. Conf. SiC and Related Mater.*, Kyoto, Japan, 1995, 431.
20. T. Matsuoka, N. Yoshimoto, T. Sasaki and A. Katsui, *J. Electron. Mater.* **21**, 157 (1992).
21. T. Matsuoka, *J. Crystal Growth* **124**, 433(1992).

ScAlMgO₄: AN OXIDE SUBSTRATE FOR GaN EPITAXY

E. S. HELLMAN, C. D. BRANDLE, L. F. SCHNEEMEYER, D. WIESMANN, I. BRENER, T. SIEGRIST, G. W. BERKSTRESSER, D. N. E. BUCHANAN, E. H. HARTFORD, JR. AT&T Bell Laboratories, P. O. Box 636, Murray Hill, New Jersey 07974, USA.

ABSTRACT

We report the use of ScAlMgO₄ as a substrate for the epitaxial growth of wurzitic GaN. The low misfit (+1.8%) allows coherent epitaxy of GaN, as observed by RHEED. The congruent melting of ScAlMgO₄ makes Czochralski growth possible, suggesting that large, high quality substrates can be realized. Boules about 17mm in diameter are reported. We have used nitrogen-plasma molecular beam epitaxy to grow GaN epitaxial films onto ScAlMgO₄ substrates. Band-gap photoluminescence has been observed from some of these films, depending primarily on the deposition conditions. A 3x3 superstructure has been observed by RHEED on the GaN surfaces. Structural analysis by x-ray diffraction indicates very good in-plane alignment of the GaN films. We also report thermal expansion measurements for ScAlMgO₄.

INTRODUCTION

The availability of an appropriate substrate for epitaxial growth is crucial to the practical application of new semiconductor materials. The factors determining appropriateness include crystallographic, physical, chemical, and economic parameters. For the wide band-gap semiconductor GaN, the most appropriate substrate for practical applications such as light-emitting-diodes (LED's) has proven to be c-plane sapphire.[1] However, sapphire has one drawback: a huge lattice mismatch with GaN. The -13% misfit results in a very large dislocation density in GaN epitaxial films on sapphire[2]. For epitaxial growth, 13% is almost the largest misfit that can be tolerated while still getting a well-aligned film. The surprisingly high quality of GaN films that have been obtained on sapphire may be due to an interfacial AlN reaction layer.[3, 4]

In this paper, we report epitaxial growth of GaN on a material with is the YbFe₂O₄ structure.[5] This structure-type is a rhombohedral layered structure, with hexagonal *a*-lattice constants between 3.236 (ScMgAlO₄)[6] and 3.489Å (YFeZnO₄).[6] The structure can be considered to be a superlattice of rock-salt-like layers and wurtzite-like layers. The oxygen lattice is near to close-packed. The smallest of the known YbFe₂O₄-type materials, ScAlMgO₄ is well matched (+1.8%) to the hexagonal face of wurtzite-structure GaN. A more complete report of this work has been published elsewhere.[7]

PREPARATION AND CHARACTERIZATION OF ScAlMgO₄ CRYSTALS

Two types of ScAlMgO₄ substrate crystals were prepared and used for epitaxial growth. Platelets as large as 1 cm across were grown by slow cooling of a stoichiometric melt. A 50g batch prepared from stoichiometric amounts of MgO, Sc₂O₃ and Al₂O₃ was placed in an Ir crucible. The sample was melted using RF induction heating under an N₂ atmosphere. The sample was then cooled slowly to yield crystals approaching 1 cm diameter and 1 mm thick, although many of these had low angle grain boundaries. Flat flakes were peeled from the micaceous crystal mass and soldered with indium to molybdenum heater blocks for epitaxial growth.

A compelling reason to consider ScAlMgO₄ as a potentially practical substrate for GaN epitaxial films is that it can be grown by the Czochralski method. Thus, the techniques needed to produce large diameter, high quality crystals on an industrial scale are already well established. A melt of stoichiometric composition was prepared by mixing 44.01g MgO and 75.31g Sc₂O₃, forming the mixture into a pellet, placing the pellet into a conventional iridium crucible together with 55.68g Al₂O₃, and heating the charged crucible under N₂ in a conventional RF induction furnace. The starting materials were commercially available, and of at least 99.99% purity.

The charge was completely molten at about 1900°C. At this point, a thin iridium rod was dipped into the liquid and a button of polycrystalline ScAlMgO₄ was formed on the tip of the rod.

The rod with solidified ScAlMgO_4 thereon was slowly raised (initially at 2.5 mm/hr) and rotated at 15 rpm. After about 1.5 hours the pull rate was gradually increased to 4 mm/hr. Pull conditions were regulated under computer control by maintaining weight gain to yield a boule having a neck (about 7mm in diameter, about 60mm long) that blended smoothly into the main body of the boule, about 60mm long. This was done to favor the growth of a limited number of relatively large crystals in the boule. Away from the seed end of the boule, the crystallites were large enough to separate with a razor blade into 20mm diameter near-single crystal slices. The slices were then mounted on a polishing block with black wax and polished with emery paper until they were flat on a cleavage plane. The slices were flipped and the process repeated on the reverse side, followed by polishing of the intended growth surface with LINDE A® and LINDE B® polishing compound. The surface chips rather easily, so considerable care is required during this stage, so as not to gouge the surface. After a final polish using Syton® on polishing paper, the slices were soldered to heater blocks with indium.

The substrates are somewhat flexible, but will break into flakes rather than cleave, as expected from a micaceous material. They are clear and insulating. Low angle grain boundaries were visible in some substrates

GaN EPITAXIAL GROWTH

Nitride growth was done in a Riber molecular beam epitaxy (MBE) system with a custom nitrogen plasma source. The plasma source is described in Reference [8]. The substrates were heated to 700°C in vacuum, then exposed to the nitrogen plasma at a temperature between 600 and 650°C briefly before starting the GaN deposition. The nitrogen plasma is excited with 10-20 watts of RF power in nitrogen at 65-85 mTorr. The RHEED (reflection high energy electron diffraction) pattern was observed through the whole process. Exposure to nitrogen resulted in a marked improvement in the RHEED pattern of the substrate. The substrate was then exposed to a Ga beam by opening the Ga furnace shutter, starting the growth. The Ga furnace temperature was set to obtain GaN growth rates between 350 and 5000 Å/hr. The RHEED pattern remains bright at the start of GaN growth, in contrast to growth on Al_2O_3 , for which the RHEED pattern is sharply reduced in intensity at the start of growth. For low growth rates, the streaks become brighter and sharper to the end of the growth, as seen in Figure 1. Figure 1 shows the RHEED pattern we observe in films of high quality after cooling to 250°C in vacuum. This 3x3 reconstruction, which we have confirmed by low energy electron diffraction (LEED) and also observe in the best of our films on sapphire, may be a result of nitrogen loss at the surface.

GaN FILM CHARACTERIZATION

After the films are removed from the growth chamber they are un-soldered from the heater block. The films are smooth as seen under a Nomarski microscope, although under some growth conditions gallium droplets can form. No peeling is observed, although our first film had some surface chipping remaining from the surface preparation. The films are further characterized by x-ray diffraction, optical transmittance, and by photoluminescence. The film crystallinity was examined using a 4-circle x-ray diffractometer using monochromated $\text{Cu K}\alpha$ radiation. In addition to the usual θ - 2θ and ω scans, scans on in-plane diffraction peaks of the film and substrate were used to measure the azimuthal order. This measurement is a particularly relevant to large misfit epitaxial systems, as discussed in Reference [9]. The diffractometer resolution was insufficient to resolve the θ - 2θ peak widths. ω (rocking) scans on the substrate (0 0 18) peak revealed two crystallites in the measured region with a 0.3° difference in orientation, each with ω peak widths of 0.5°. The (0 0 4) rocking curve for the film showed 0.8° wide peaks. These numbers are to be compared with the 0.37° rocking curve width measured for GaN grown concurrently on sapphire, which had an ω peak width limited instrumentally to 0.22°. The ϕ scans of substrate and GaN azimuthal peaks indicated only the 3 peaks spaced at 120° intervals for the rhombohedral sapphire and ScAlMgO_4 , and the 6 expected peaks in the hexagonal GaN. Figure 2 shows the ϕ scan peaks in detail. The ScAlMgO_4 substrate again reveals two crystallites, misoriented in ϕ by 0.4°; the sapphire peak again exhibits the instrumental resolution. The azimuthal broadening of the GaN peaks is clearly apparent, and is similar for growth on sapphire and growth on ScAlMgO_4 . The Matthews theory of island rotations for large misfit systems [10] predicts that the ϕ width on

sapphire should be a factor of 3 larger than that on ScAlMgO₄, which we do not see in the data. This suggests that island nucleation is not the principle source of the azimuthal broadening in this film.

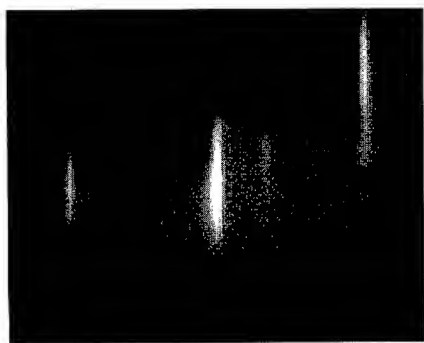


Figure 1. RHEED pattern along the $\langle 1\ 1\ \bar{2}\ 0 \rangle$ azimuth of ScAlMgO₄, showing the 3x3 superstructure observed after cooling in vacuum to 250°C.

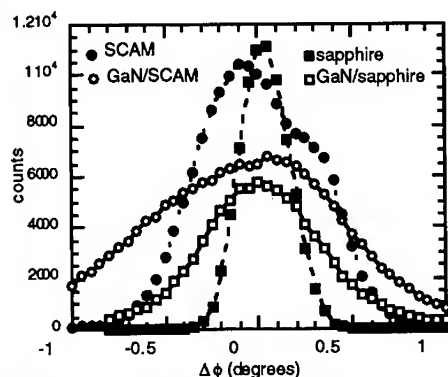


Figure 2. Azimuthal scans on in-plane diffraction peaks for GaN films on sapphire and on ScAlMgO₄. The peak width for the sapphire (1 1 6) peak is essentially the instrumental resolution. GaN peaks rotated 60° from the substrate peaks are used to avoid interference.

A comparison of the photoluminescence (PL) spectra of 0.16 μm thick GaN films grown on ScAlMgO₄ and on sapphire in the same growth run was made. The emission spectra of both samples look very similar for both temperatures and the intensity is roughly the same. These spectra are dominated by the donor-acceptor pair transition at 3.26 eV and its phonon replicas. At room temperature we observe a band edge peak at 3.37 eV although the main emission features are broad bands with their maximums around 2.0 and 1.7 eV.

The PL results show that the band edge emission from thin GaN films grown on ScAlMgO₄ and on sapphire is roughly comparable. Films of superior quality have been grown on sapphire by MOCVD; these films are typically an order of magnitude thicker than our MBE films. We find that, between sapphire and ScAlMgO₄, the luminescence intensity is much more dependent on growth conditions than on the substrate type. Considering the crystal quality of the substrate, which has to be improved, the luminescent properties of GaN films grown on ScAlMgO₄ look very promising.

DISCUSSION

What should be clear from our results is that ScAlMgO₄ is a very promising substrate material for epitaxial growth. What should also be clear is that ScAlMgO₄ substrates are not the magic solution to all problems facing the realization of practical high performance GaN based devices. Although we can expect further improvement in film properties when truly single crystal ScAlMgO₄ substrates are available, we do not observe the dramatic improvements that we might naively expect from an order of magnitude reduction of misfit. This could indicate either that misfit dislocations are not the primary limitation to, for example, luminescence properties in our films, or that new types of defects are introduced by the substrate.

We note that since a small fraction of InN will increase the film lattice constant, substrates with positive misfits to GaN can be perfectly lattice matched to alloys in the (In,Ga,Al)N system. Thus the +1.8% misfit for ScAlMgO₄ should be perfectly lattice matched to In_{0.16}Ga_{0.84}N and In_{0.30}Al_{0.70}N, while the -3% misfit to 6H-SiC cannot be eliminated in this manner.

CONCLUSION

The initial results reported here indicate that ScAlMgO₄ is a promising substrate material for GaN epitaxial growth. Although growth conditions for GaN on ScAlMgO₄ may have to be re-optimized to benefit from the order-of-magnitude reduction in the misfit, we anticipate that when large, high quality single crystals are available, growth on ScAlMgO₄ will result in epitaxial films surpassing the quality of those currently produced on sapphire. This may be a crucial step towards the realization of high-performance GaN-based opto-electronic devices.

ACKNOWLEDGMENTS

The authors would like to thank A. J. Valentino for assistance in the substrate growth.

REFERENCES

1. S. Nakamura, Mat. Res.Soc. Symp. Proc. **339**, 173 (1994).
2. S. D. Lester, F. A. Ponce, M. G. Craford and D. A. Steigerwald, Appl. Phys. Lett. **66**, 1249 (1995).
3. M. E. Lin, B. N. Sverdlov and H. Morkoç, J. Appl. Phys. **74**, 5038 (1993).
4. T. D. Moustakas, T. Lei and R. J. Molnar, Physica B **185**, 36 (1993).
5. K. Kato, I. Kawada, N. Kimizuka and T. Katsura, Z. Kristallog. **141**, 314 (1975).
6. N. Kimizuka and T. Mohri, J. Sol. St. Chem. **78**, 78 (1989).
7. E. S. Hellman, C. D. Brandle, L. F. Schneemeyer, D. Wiesmann, I. Brener, T. Siegrist, G. W. Berkstresser, D. N. E. Buchanan and E. H. Hartford Jr., MRS Internet J. Nitride Semicond. Res. **1**, 1 (1995).
8. R. J. Spah, H. F. Hess, H. L. Stormer, A. E. White and K. T. Short, Appl. Phys. Lett **53**, 441 (1988).
9. E. S. Hellman and E. H. Hartford Jr., Appl. Phys. Lett **64**, 1341 (1994).
10. J. W. Matthews, in Epitaxial Growth, Part B J. W. Matthews, Eds. (Academic Press, New York, 1975), pp. 566.

EPITAXIAL GROWTH OF GaN ON LATTICE-MATCHED HAFNIUM SUBSTRATES

R. BERESFORD, K.S. STEVENS, C. BRIANT, R. BAI, and D.C. PAINE
Box D, Division of Engineering, Brown University, Providence, RI 02912

ABSTRACT

A method of producing epitaxial GaN on single-crystal Hf has been developed. The metal substrate is formed by a strain-anneal process yielding macroscopic (5-mm) grain sizes, followed by polishing, chemical etching, and Ar ion sputtering at elevated temperature in ultrahigh vacuum. The growth is conducted by plasma-assisted molecular beam epitaxy using an initial passivation layer deposited at low temperature and subsequent growth at 700 °C. The resulting films are in registry with the hcp substrate lattice as observed by reflection high-energy electron diffraction during growth and verified by plan-view transmission electron microscopy. High-resolution x-ray rocking curve linewidths of the GaN and Hf [10 $\bar{1}$ 2] peaks are as narrow as 900 and 180 arc seconds, respectively. The [0002] peak separation confirms the approximately 2.7% mismatch in the *c* axis spacing. Initial photoluminescence observations at 20 K of a (donor-bound exciton) peak at 3.467 eV are consistent with the assumption of a nearly strain-free film resulting from the exact basal-plane lattice match and close thermal coefficient match between GaN and Hf.

INTRODUCTION

The goals of optoelectronic device development in the III-N materials system require high-crystal-quality strain-free films, first for the advancement of fundamental understanding of the materials and second for the fabrication of high-performance devices such as laser diodes. It is by now widely appreciated that the "device-quality" CVD-grown GaN on sapphire has a very high dislocation density [1] and in general will be under compressive stress due to the thermal coefficient mismatch, although special processing techniques apparently allow substantial relaxation of the thermal strain. In contrast, films grown on SiC or Si are put in tension during the cool-down from growth temperatures. In the absence of any viable bulk GaN growth technology, there is a compelling incentive to develop lattice-matched heteroepitaxial substrates. The group-IVB refractory metals Ti, Zr, and especially Hf comprise an intriguing alternative that has been under development by the present authors.

The characteristics of these metals that suit them particularly well for the present applications can be summarized as follows:

- Hexagonal close-packed lattice (induces wurtzite-structure nitride films).
- Exact basal-plane lattice match between Hf and GaN.
- Small mismatch along the *c* axis (2.7%).
- Solid solutions can match a range of AlGa_xN and InGa_xN lattice parameters.
- Close thermal expansion coefficient match between Hf and GaN (about 4.6% mismatch).
- Low vapor pressure at nitride growth temperatures.
- High thermal and electrical conductivity (built-in ohmic contact and heat sink).

Along with these notable advantages come several challenges, principally the facts that single-crystal Hf is not readily available and GaN is not thermodynamically stable on Hf. The former problem is addressed in the present work with a strain-anneal process of grain growth that produces macroscopic (cm-sized) grains exhibiting crystal quality (as measured by x-ray diffraction) that substantially exceeds what is available from pulled or deposited Hf crystals. In the future, the bulk crystal growth methods will be improved, particularly as the present work demonstrates an incentive for doing so. The second problem has been overcome via a plasma-assisted molecular-beam epitaxial growth process. These advances and the resulting GaN materials properties are the subject of this report.

SUBSTRATE PREPARATION

The conventional approach to the growth of single-crystal metals usually involves pulling the crystal from a melt using an oriented seed crystal. However, in the case of Ti, Zr, and Hf, this approach is difficult because these molten metals are extremely reactive and cannot easily be contained in a crucible. Many researchers have employed the zone-melting approach and have produced reasonably large single crystals of Ti and Zr. These crystals, however, are of little use for our application because they contain large densities of defects as a result of the bcc-to-hcp transformation that occurs via a mechanical shear process upon cooling from the melt. The temperatures of this transformation in Ti, Zr, and Hf are, respectively, 1155, 1139, and 2016 K.

An alternative, the strain-anneal method, requires that the sample receive a small, though critical, amount of deformation. The level of this critical deformation varies depending on the material, but 1% to 5% is typical. If less than this critical amount of strain is applied, no grain growth will occur, while for amounts greater than this critical amount the grain size is increasingly refined. The mechanism by which strain-annealing grain growth occurs is usually described in the following way [2, 3, 4]. The application of a small level of strain provides a general level of deformation throughout the sample. It is inevitable, however, that this strain will not be uniform on a microscopic scale and, as a consequence, some grains will contain more strain energy than others. When the sample is heated to a temperature that is sufficient to allow grain boundary motion, boundaries that separate regions of higher strain from those with lower strain will move such that a few strain-free grains grow at the expense of the highly strained ones.

It is known from investigations of recrystallization that the difference in strain energy between the two grains has to be greater than a critical amount in order to obtain this strain-induced grain boundary motion. The key to obtaining very large grains by this method is to have this process begin at only a few points throughout the sample. If there are too many nucleation sites then the final grain size will be smaller. Consequently, successful implementation of this process for the formation of large oriented grains requires careful control of the amount of deformation introduced. Also, recrystallization during the temperature ramp-up must be avoided. Factors such as the purity of the material and the temperature of deformation can have substantial influence on the final grain size that is obtained. Deformation in excess of the critical amount results in a higher nucleation rate of strain-free material and hence the final grain size decreases with increasing deformation.

Using this approach, Ti and Zr treatments have been developed that result in grain sizes of 1 cm or greater. To date, other than our own success reported here, we are not aware of any attempts to grow large grains of hafnium. Large-grain polycrystals of titanium have been prepared by both the strain-anneal method and the phase-change method (repeated cycling through

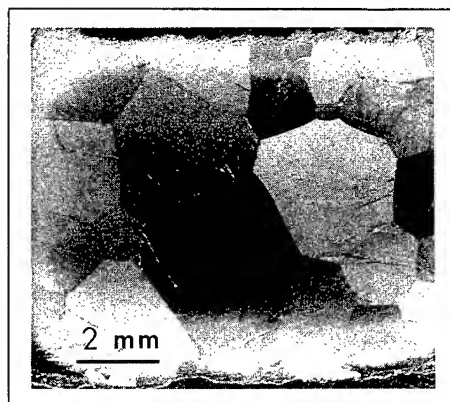


Figure 1. Optical micrograph of the grain structure in a strain-annealed Hf sample. The largest grains are about 5 mm in diameter.

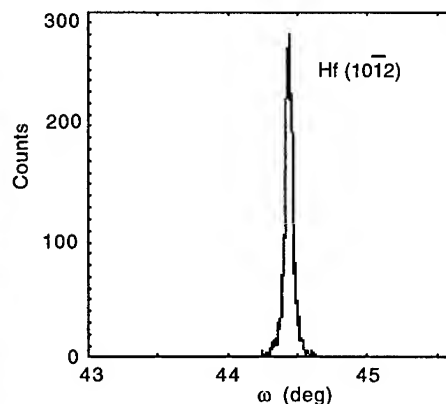


Figure 2. High-resolution x-ray rocking curve of the Hf $[10\bar{1}2]$ peak showing a full-width of 180 arc seconds.

the transformation temperature). Churchman prepared samples by deforming and then annealing at 860 °C for up to 200 hours; the individual crystals were greater than 1 cm in diameter [5]. Anderson *et al.* prepared samples with individual grains up to 5 cm in diameter using the phase-change method [6]. The samples were heated at 1200 °C for 4 hr and then cooled to 850 °C where they were held for 3 to 5 days to grow the large grains of the hcp phase. This process was repeated at least three times before the final grains were formed. In all of these experiments, high-purity titanium was used and care was taken during heat treatment not to introduce any oxygen or nitrogen. Large-grain Zr has been obtained using similar approaches [7, 8].

Our typical strain-anneal Hf process begins with 99.999% Hf polycrystalline ingots (the quoted purity does not necessarily consider Zr, which is commonly present at the percent level). Bar-shaped samples are deformed by rolling from 950 °C to various strains. Annealing in vacuum is carried out at 1700 °C, slightly below the transformation temperature, for up to 8 hr. Wafers are sliced from the bar and polished by conventional metallographic methods. A polishing etch of HF + HNO₃ reveals the grain structure as in Figure 1. In this case the largest grains are approximately 5 mm in diameter.

To make use of such a sample for epitaxial growth experiments, it is essential to determine the orientation of individual grains. Furthermore, use of the strain-anneal technique for demonstration devices will entail some means to control the grain orientation as well as to increase the grain size. The orientation is determined by electron back-scattering diffraction patterns (EBSP), a well-established technique in scanning electron microscopy in which computerized algorithms automatically detect the Kikuchi bands in the patterns of back-scattered electrons [9, 10]. By this means, individual grain orientations have been established in order to conduct high-resolution x-ray diffraction scans. A rocking curve of the Hf $[10\bar{1}2]$ diffraction is given in Figure 2, showing a full-width of approximately 180 arc seconds. This value is about 4 times better than that of the deposited bulk crystals obtained to date.

It will be appreciated that the benefits of lattice matching accrue only for near-basal-plane oriented grains, since there exists about 2.7% mismatch along the *c* axis (with the GaN lattice spacing the larger one). Direct control of the strain-anneal grain orientation has not been

attempted yet, but in principle can be effected by orientation and controlled deformation during the annealing cycles. Another less direct approach has also given usable results. Because of the elastic anisotropy of the crystallized material, the texture changes with deformation. For low levels of strain, the annealed material tends to have grains with their basal-plane normals perpendicular to the rolling direction, but otherwise with no apparent preferential direction. However, if the strain is greater than a critical amount (on the order of 20%), the annealed material basal planes evolve further, toward parallelism with the rolling plane. Taking advantage of this effect has produced large-grained samples with a distribution of vicinal orientations from 2° – 15° from the basal plane. The GaN growths are conducted on these and other samples.

EPITAXIAL GROWTH

Chemical reactivity of the substrate represents the greatest challenge to the use of Hf for growth of the group-III nitrides. This reactivity suggests that MBE is the preferred growth technique since the alternative, MOCVD, offers less direct control of the flux of the reactive species to the substrate. Like Si, the hexagonal refractory metals have a strong affinity for oxygen, which means that regardless of the cleaning procedure, any Hf substrate placed in the MBE system will have a surface layer of native oxide. This oxide must be removed *in situ* before the Hf lattice can act as a template for epitaxial growth. Unlike Si, whose native oxide decomposes at high temperature into a volatile sub-oxide species via the reaction $\text{Si} + \text{SiO}_2 = 2\text{SiO}(\text{g})$, the refractory hexagonal metals do not have a volatile sub-stoichiometric oxide. Thus, the oxides of Hf must be removed either by ensuring that the oxygen partial pressure in the UHV chamber is below the equilibrium oxidation potential or via a physical process such as sputtering.

The equilibrium oxygen potential needed to cause the chemical breakdown of hafnium oxide via the reverse formation reaction $\text{HfO}_2 \rightarrow \text{Hf} + \text{O}_2(\text{g})$ at reasonable temperatures is extremely low, for example, 10^{-30} atm at 1200°C . An alternative would be to use (at a higher pressure) dry hydrogen to effect the chemical reduction of the oxide. At 1200°C , HfO_2 can be chemically reduced via the reaction $\text{HfO}_2 + 2\text{H}_2(\text{g}) = \text{Hf} + 2\text{H}_2\text{O}(\text{g})$ by ensuring that the $\text{H}_2\text{O}:\text{H}_2$ ratio is below 10^{-10} . The chemical reduction approach has the drawback that at the total pressures and maximum heater temperature that are used in the MBE growth chamber, the kinetics of the reaction will be extremely slow. This problem may be partially alleviated by using plasma-activated hydrogen, possibly in combination with Ar ion sputtering of the surface.

Satisfactory results have been obtained with Ar sputtering alone, although possible surface damage has not yet been analyzed. The electron-cyclotron-resonance source used to activate nitrogen for the GaN growth process is operated at 100 W with an Ar gas flow of 2 sccm to produce ions. The growth stage is isolated from its mounting flange and the chamber walls so that electrostatic biasing is possible. Because the substrate is conducting, a dc bias of approximately -500 V can be used to accelerate the ions. Using this technique for 15 min with the substrate at 800°C , we have obtained clear electron diffraction patterns of Hf substrates as in Figure 3a. The bright and streaky RHEED patterns indicate a reasonably flat and crystalline surface.

Another aspect of the surface chemistry challenge is the reactivity of the substrate with the deposited nitride. A simple thermodynamic analysis shows that GaN is not stable on Hf and will react to form HfN and one of a series of Ga_mHf_n intermetallic compounds. Therefore, it is required to control the growth temperature and reactant flux in such a way as to preserve a kinetically stable interface. One approach that has been successful is to deposit a monolayer of N on the sputter-cleaned Hf surface. This layer is thought to protect the clean Hf surface from reaction

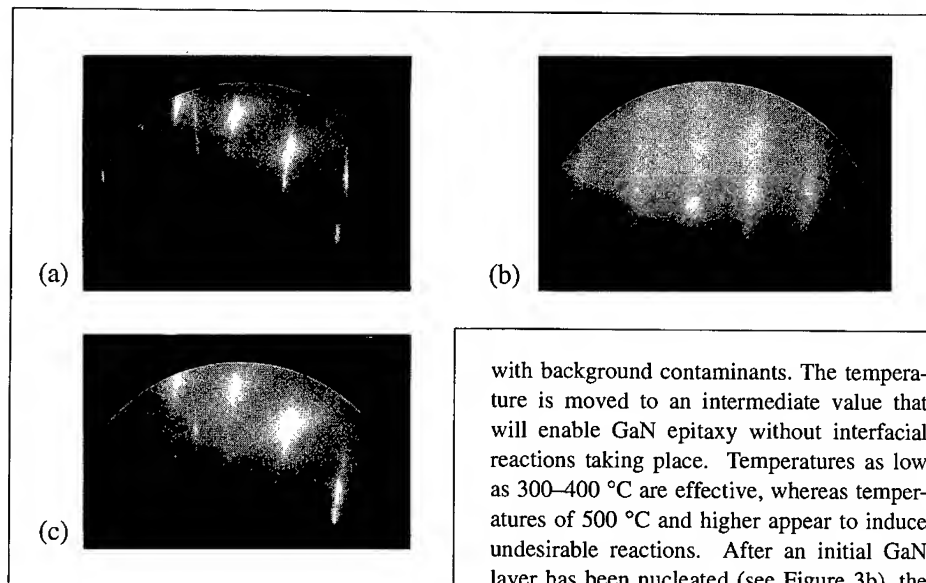


Figure 3. RHEED patterns (10 kV) obtained from an Ar sputter-cleaned Hf surface showing basal texture (a); after nucleation of the 300 °C passivation layer (b); and at the end of a 1.2- μm GaN growth, showing replication of the initial grain structure (c).

with background contaminants. The temperature is moved to an intermediate value that will enable GaN epitaxy without interfacial reactions taking place. Temperatures as low as 300–400 °C are effective, whereas temperatures of 500 °C and higher appear to induce undesirable reactions. After an initial GaN layer has been nucleated (see Figure 3b), the temperature is raised to 700 °C and growth is carried out at approximately 0.1 μm / hr. We have demonstrated that specular GaN, 1.0- μm thick, can be grown on single-crystal Hf substrates by such low-temperature passivation methods. An example of the RHEED pattern

obtained after a 12-hr growth is shown in Figure 3c. The pattern is single-crystal and predominantly two-dimensional.

MATERIALS CHARACTERIZATION

X-ray diffraction studies of this material revealed no obvious interfacial reaction products, that is, no strong diffraction peaks except those belonging to GaN and Hf. High-resolution x-ray rocking curve linewidths of the GaN [0002] peak are in the range of 15 arc minutes, about 2 times greater than the “standard” MBE-grown material on a non-native substrate (sapphire). At this point, the crystal quality is believed to be limited by the Hf substrate quality—both crystallinity and surface topography, which is still being analyzed. The separation of the GaN and Hf [0002] diffraction peaks is consistent with the *c*-axis mismatch value quoted above, confirming that the intended epitaxial relation actually occurs. Plan-view TEM study confirms that the material is single crystal, even when the substrate orientation is well away from the basal plane, where optimum lattice matching occurs. In all cases observed, the film is in registry with the substrate lattice and there is no extended microstructure (except that due to the substrate grain structure itself).

Low-temperature photoluminescence of not-intentionally-doped GaN/Hf films shows several features in the near-band-edge region, as well as lower energy peaks that could represent transitions related to unintentional acceptor or deep-donor levels. The principal near-band-edge peak occurs at 3.467 eV with a full-width of about 14 meV at 20 K. The spectral position appears to

match that of the shallow-donor-bound exciton observed in GaN grown on thick ($>50\text{ }\mu\text{m}$) relaxed quasibulk GaN produced by vapor-phase transport growth. This observation would support the claim that the present films are largely strain-free. Further details of the optical characterization will be presented subsequently.

CONCLUDING DISCUSSION

It is important to note that the elimination of misfit strain by lattice matching GaN to Hf will promote layer-by-layer growth. If lower temperature epitaxy can be achieved, the N-stoichiometry problem that has plagued MBE-grown GaN can be alleviated because the N supersaturation is increased. On the other hand, the surface mobility required to maintain a two-dimensional growth mode generally requires higher temperatures. These trade-offs involved in optimizing the GaN/Hf growth process have not yet been documented. However, the present work has demonstrated for the first time the feasibility of epitaxial growth of GaN on Hf, including methods for preparing single crystals of Hf, cleaning them *in situ*, and nucleating metastable GaN layers that enable growth of good quality GaN films.

ACKNOWLEDGMENTS

The cooperation and materials provided by Dr. John Haygarth of Teledyne Wah Chang are warmly appreciated. Portions of this work are supported by the National Science Foundation Materials Research Grant DMR-9121747.

REFERENCES

1. S.D. Lester, F.A. Ponce, M.G. Craford, and D.A. Steigerwald, Appl. Phys. Lett. **66**, 1249 (1995).
2. K.T. Aust, in *The Art and Science of Growing Crystals*, edited by J.J. Gilman (John Wiley and Sons, New York, 1963), p. 452.
3. R.A. Laudise, *The Growth of Single Crystals* (Prentice-Hall, Englewood Cliffs, 1970), p. 114.
4. P.A. Beck and P.B. Sperry, J. Appl. Phys. **21**, 150 (1959).
5. A.T. Churchman, Nature **171**, 706 (1953); Proc. Roy. Soc. **226**, 216 (1954).
6. E.A. Anderson, D.C. Jillson, and S.R. Dunbar, Trans. AIME **197**, 1191 (1953).
7. E.J. Rapperport, Acta Met. **3**, 208 (1955).
8. J.P. Langeron and P. Lehr, Revue Met. **55**, 901 (1958).
9. S.I. Wright and B.L. Adams, Metall. Trans. **23A**, 759 (1992).
10. N.C. Krieger Lassen, D. Juul Jensen, and K. Conradsen, Scanning Microscopy **6**, 115 (1992).

PROPERTIES OF GaN EPITAXIAL LAYER GROWN BY MOVPE ON MgAl_2O_4 SUBSTRATE

A. KURAMATA, K. HORINO, K. DOMEN, R. SOEJIMA, H. SUDO and T. TANAHASHI
Fujitsu Laboratories Ltd., 10-1 Morinosato-Wakamiya, Atsugi 243-01, Japan
Tel : +81-462-48-3111, Fax : +81-462-48-5193

ABSTRACT

We propose a MgAl_2O_4 substrate for GaN-based laser diodes. We grew GaN epitaxial layers using metal-organic vapor phase epitaxy on a MgAl_2O_4 substrate. The GaN on the MgAl_2O_4 showed a narrow X-ray diffraction peak of 310 arcsec, a photoluminescence dominated by the band-edge emission, and good electronic properties. The optical cavity was fabricated by cleaving the GaN on the MgAl_2O_4 , and the stimulated emission from the cavity using optical pumping was observed. We also fabricated a light emitting diode (LED) with a AlGaIn/InGaIn double-heterostructure. The electroluminescence was dominated by the band-edge emission of InGaIn with a narrow FWHM of 13.5 nm. The characteristics of LED on the MgAl_2O_4 were comparable to that on a Al_2O_3 substrate. MgAl_2O_4 is feasible as a substrate for laser applications.

INTRODUCTION

GaN and related alloy compounds of InGaIn and AlGaIn have a direct band-gap that is suitable for making optical devices. The band-gap energy can also be varied in a wide range, from the 1.9 eV of InN to the 6.2 eV of AlN. GaN devices are more tolerant of higher operating temperatures, due to their larger band-gap when compared with other III-V semiconductors and Si. The growth techniques for GaN have recently made progress, and high quality GaN devices can be fabricated [1]. For example, high-intensity blue to yellow light emitting diodes (LEDs) have been fabricated [2-3]. However, a laser diode using these materials has not yet been made.

The important challenge for realizing GaN-based laser diodes is the fabrication of optical cavity. It is difficult to make a cavity by cleavage when epitaxial layers are grown on a sapphire (Al_2O_3) substrate. This is because sapphire has little tendency toward cleavage and the cleavage direction of sapphire is different from that of GaN. One way to make a cavity mirror is polish, but it is not suitable for a commercial production. For this reason, it is necessary to develop a new technique such as the use of a different cleavable substrate, dry etching, and selective growth. We think that the use of a cleavable substrate is the best way, because the method is simple and the cleaved facet has an ideal flatness for a cavity mirror. If we use metal-organic vapor phase epitaxy (MOVPE) as the growth method, the substrate material requirements are as follows: 1) It must be stable both thermally and chemically, because MOVPE growth of GaN is conducted at about 1000°C in a reducing atmosphere of ammonia and hydrogen. 2) The lattice constant and thermal expansion coefficient should match GaN. 3) The cleavage direction must match with that of GaN.

6H-SiC is known to be a good material as the substrate for GaN growth [4-6]. It can be cleaved in the same direction as GaN, and high-quality GaN epitaxial layers have been grown on it. However, cracks are easily generated in the GaN layer on 6H-SiC. We investigated the feasibility of other cleavable substrates and found that spinel (MgAl_2O_4) was an attractive material [7]. Other researchers have reported similar findings [8].

In this paper, we evaluated spinel as a substrate for laser applications. We investigated the surface morphology, X-ray diffraction, and the optical and electrical properties of GaN on spinel. We fabricated an optical cavity using cleavage and performed a stimulated emission experiment using optical pumping from the cavity. We also fabricated LEDs that consisted of an AlGaIn/InGaIn double-heterostructure. The characteristics of LEDs on the spinel and the sapphire were compared.

EXPERIMENT

GaN epitaxial layers were grown by low-pressure MOVPE on a (111) oriented spinel substrate. The growth pressure was 200 torr, and the growth temperature was between 1000°C and 1040°C. Ammonia (NH₃) and trimethyl-gallium (TMG) were used as the source gases, with respective flow rates of 2 standard liters per minute and 1 standard cubic centimeter per minute. Hydrogen was used as the carrier gas. The growth rate was 1.8 μm per hour. The low-temperature buffer layer was deposited at 500°C for 1 minute before the growth. The n-type and p-type doping were done using SiH₄ and Cp₂Mg, respectively. We annealed the p-type GaN after growth at 800°C for 10 minutes in a nitrogen atmosphere to activate the acceptor [9-10].

RESULTS

Quality of GaN on Spinel

We investigated the surface morphology using an interference microscope. GaN surface was specular, which shows that the spinel has sufficient stability to resist the severe GaN growth environment. No cracks were observed in the GaN layer. This is probably because the thermal expansion coefficient of spinel is larger than that of GaN, which causes the compressive residual stress in the GaN layer. When the residual stress is tensile, as in the case of SiC and Si, the tendency for the GaN layer to crack becomes large.

The X-ray diffraction measurements showed that the GaN on the (111) spinel was single crystal and was (0001)-oriented. Figure 1 shows the full width at half maximum (FWHM) values of X-ray rocking curve at the (0002) diffraction peak of GaN. We compared the FWHM on the spinel and the sapphire substrate [1,11-13]. The FWHM of a 3.6-μm-thick GaN layer on the spinel substrate was 310 arcsec, and was comparable to the typical value on the sapphire substrate. Very narrow FWHMs have been recently reported on sapphire substrates. We believe that the same results can be obtained on the spinel if the growth conditions are optimized.

Photoluminescence measurements were performed at room temperature using a He-Cd laser operating at 10 mW. The excitation intensity was 0.4 kW/cm². The photoluminescence was dominated by band-edge emission at 363 nm, but weak deep-level emission bands were also observed at around 440 nm and 550 nm. When we compared the spectra of GaN on the spinel and the sapphire, the relative deep-level emission intensity to the band-edge emission was comparable around 440 nm, but weaker around 550 nm for the spinel. Although we do not know the exact origin of these deep-level emissions, it is clear that using a spinel substrate does not increase these deep-level emissions. We evaluated the band-edge emission intensity using a pulsed nitrogen laser at an excitation intensity of about 100 kW/cm², to avoid the intensity change due to the fluctuation of the residual carrier concentration. When we changed the GaN layer thickness, the shapes of the photo-luminescence spectra did not vary. But, the photoluminescence intensities decreased drastically for an epitaxial layer thickness of less than 3 μm, indicating the presence of high-density non-radiative recombination centers in the GaN epitaxial layer near the spinel substrate. This phenomenon was not observed on the sapphire substrate. Secondary ion mass spectrometry (SIMS) showed that only

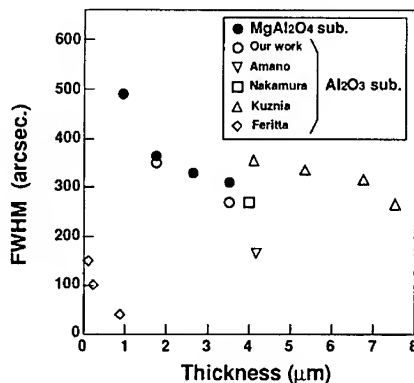


Fig. 1. FWHM of X-ray rocking curves for GaN on spinel and sapphire substrates.

magnesium diffused into the GaN epitaxial layer among the elements composing the spinel. The diffusion reached to about 1.2 μm from the interface. It is our view that magnesium diffusion caused the non-radiative recombination centers near the interface, and that they gradually disappeared as the growth proceeded. For practical purposes, the reduction of emission intensity can be avoided by growing a buffer layer with a thickness greater than 3 μm .

We investigated the electrical properties using Hall measurement for the undoped, n-doped, and p-doped GaN on the spinel and the sapphire substrates. The thickness of the GaN layer was about 3.2 μm . The undoped GaN was semi-insulating on both substrates. The electron mobility of the GaN with the n-type carrier concentration of $2 \times 10^{18} \text{ cm}^{-3}$ was 250 cm^2/Vs on spinel, and 220 cm^2/Vs on sapphire. The hole mobility of the GaN with the p-type carrier concentration of $1 \times 10^{17} \text{ cm}^{-3}$ was 10 cm^2/Vs on both substrates. No differences were seen in the GaN electrical properties between the spinel and the sapphire.

We found that many characteristics for spinel were comparable to those for sapphire. This shows that spinel may be a good alternative for sapphire substrate.

Optical Cavity

The cleavage direction between the epitaxial layer and the substrate must coincide to make a cavity mirror using a cleaved facet. The cleavage direction of GaN is deduced from the direction of epitaxial layer cracks to be $[11\bar{2}0]$, and that of spinel is $[1\bar{1}0]$. The epitaxial relationships, which were investigated using asymmetric X-ray diffraction, told us that the cleavage direction of GaN is the same as that of spinel. We cleaved the 3.6- μm -thick GaN and a 100- μm -thick spinel substrate wafer, and obtained a smooth cleaved GaN facet. The GaN was cleaved on the $(1\bar{1}00)$ plane, which was normal to the surface. The spinel was cleaved on the (100) plane, which was inclined at 55 degrees from the surface, although an uncleaved part of the spinel was also observed near the interface. We consider that the uncleaved part is formed due to the difference in the angle between the cleaved facet of the GaN and that of the spinel.

To investigate whether the cleaved facet of the GaN on spinel acts as the cavity mirror, we performed the stimulated emission experiment using optical pumping in the edge emitter configuration. The cavity was formed by cleavage, and its length was 600 μm . A pulsed nitrogen laser was used as the pumping light. The pulse width of the nitrogen laser was 10 ns with operating frequency of 14 Hz, while the intensity of each pulse was about 0.5 mJ. The pumping light was perpendicular to the surface. This yielded the maximum power density of 1.2 MW/cm^2 . Then, the light emitted from the cleaved facet

was measured at room temperature. Figure 2 shows the change in emission intensity with an increase in incident power. The emission intensity increased super-linearly. The spectrum was broad at low incident power, and the peak wavelength of this spontaneous emission was 370 nm. A narrow peak appeared at a longer wavelength of 380 nm when the incident power exceeded the threshold. These results indicate that the narrow emission that appeared above threshold is the stimulated emission. The threshold value which was decided from the spectrum change was about 0.2

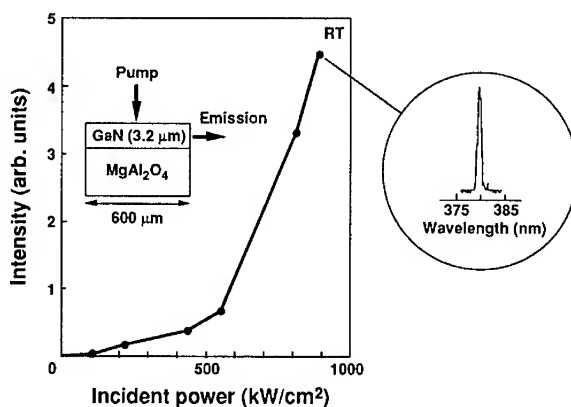


Fig. 2. Stimulated emission by optical pumping in edge emitter configuration at room temperature.

MW/cm². We also observed the stimulated emission in the surface emitter configuration, which was the same as reported one on the sapphire substrate [14], and the threshold value was about 1 MW/cm². The threshold value in the edge emitter configuration was about 1/5 that of the surface emitter configuration. Although we did not get direct proof of the lasing, such as the Fabry-Perot mode and the far field pattern, the reduction in the threshold value indicates that the light is coupled with the cavity. This shows that the cleaved facet of GaN on the spinel substrate acts as a cavity mirror. Previous reports on the observations of the stimulated emission from the GaN layer in the edge emitting configuration were done on a sapphire substrate [15-16], and on a SiC substrate [4]. Their threshold values were 0.6 MW/cm² and 0.8 MW/cm² on the sapphire, and 3.4 MW/cm² on the SiC substrate. Our threshold value is comparable to these reported ones, indicating the high-quality of the epitaxial layer and the cavity mirror.

LED Characteristics

We fabricated LEDs consisting of AlGaIn/InGaIn double-heterostructure on a spinel substrate. Figure 3 shows the structure of the LED. Low-temperature GaN buffer, undoped Al_{0.05}Ga_{0.95}N, n-doped Al_{0.05}Ga_{0.95}N, n-doped GaN, undoped In_{0.05}Ga_{0.95}N, p-doped Al_{0.05}Ga_{0.95}N, and p-doped GaN were sequentially grown on the spinel substrate, with a respective thickness of 30 nm, 1.2 μ m, 2.2 μ m, 60 nm, 30 nm, 0.6 μ m, and 0.2 μ m. Carrier concentration of the n-doped and p-doped layer was 2×10^{18} cm⁻³ and 1×10^{17} cm⁻³, respectively. Electrodes were formed in a stripe pattern. Part of the epitaxial layers was dry-etched to expose n-doped GaN layer. An n-type Ti/Pt/Au electrode was formed on the exposed n-doped GaN layer. Ni/Ti was used as the p-type electrode. The width of p-type electrode was 80 μ m, and the length of the diode was about 600 μ m. The electroluminescence measurements was performed using a pulsed current with the pulse duration of 10 μ s and a repeating frequency of 5 kHz. Figure 4 shows the electroluminescence of the LED at room temperature operated at 50 mA to 200 mA, with a corresponding current density of 104 A/cm² to 417 A/cm². The inset shows the current-voltage characteristics. The LED showed clear rectifying characteristics. The turn on voltage was about 4 V. The peak wavelength and FWHM in the electro-

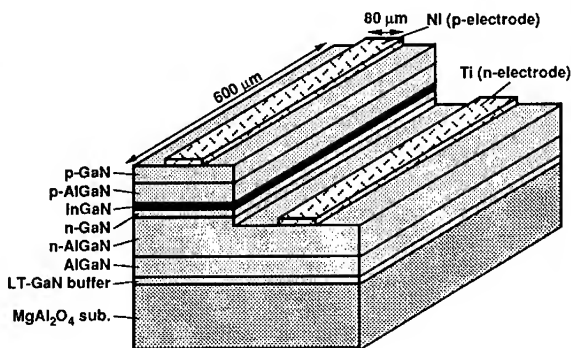


Fig. 3. AlGaIn/InGaIn double-heterostructure LED.

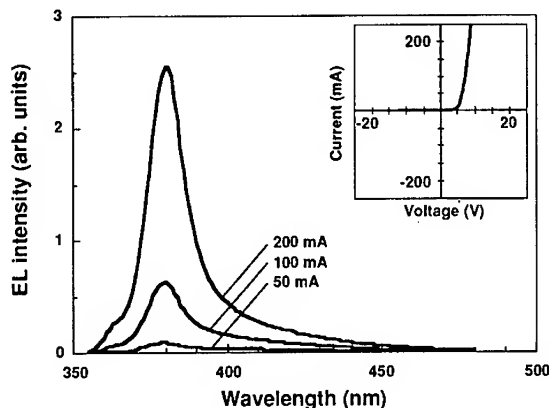


Fig. 4. Electroluminescence of LED at room temperature. Inset shows the I-V characteristics.

luminescence was 380 nm and 13.5 nm, respectively. When we increased the operating current, the peak wavelength did not varied. This indicate that the emission originated in the near-band-edge transition of $\text{In}_{0.05}\text{Ga}_{0.95}\text{N}$, such as band-to-band, band-to-acceptor, and donor-to-band transition. We believe that the lasing will be achieved if we succeed in increasing the current density by making a better p-type contact. We also compared the electroluminescence of LEDs fabricated on the spinel with that on the sapphire substrate, as shown in Figure 5. The LED structures were simultaneously grown on spinel and sapphire in the

same growth run. The intensity on spinel was comparable to that on the sapphire. The peak wavelength for sapphire was about 8 nm longer than that for spinel. This is probably due to the temperature inhomogeneity in the susceptor which was used in the growth. The magnitude of wavelength shift corresponds to the temperature difference of 5°C. The current-voltage characteristics were also almost the same. From these results, we conclude that the problem does not exist with using the spinel substrate.

CONCLUSION

We proposed spinel as a substrate for laser applications. We investigated the surface morphology, X-ray diffraction, and the optical and electrical properties of GaN on spinel. From the results, it was shown that there were no serious problems in terms of GaN quality with using spinel as the substrate material. We fabricated the optical cavity using cleavage and observed the stimulated emission using optical pumping from the cavity. The threshold value in the edge emitter configuration was about 1/5 that of the surface emitter configuration, which indicates that the cleaved facets act as cavity mirrors. We also fabricated AlGaIn/InGaIn double-heterostructure LEDs on the spinel substrate. The electroluminescence was dominated by the band-edge emission of InGaIn with a narrow FWHM of 13.5 nm. The LED fabricated on the spinel showed the comparable characteristics to those on the sapphire substrate. We believe that it is possible to achieve current injection lasing on the spinel substrate.

REFERENCES

- [1] H. Amano, N. Sawaki, I. Akasaki, and Y. Toyoda, *Appl. Phys. Lett.* **48**, 353 (1986).
- [2] S. Nakamura, T. Mukai, and M. Senoh, *Appl. Phys. Lett.* **64**, 1687 (1994).
- [3] S. Nakamura, M. Senoh, N. Iwasa, and S. Nagahama, *Jpn. J. Appl. Phys.* **34**, L797 (1995).
- [4] A. S. Zubrilov, V. I. Nikolaev, D. V. Tsvetkov, V. A. Dmitriev, K. G. Irvine, J. A. Edmond, and C. H. Carter, Jr., *Appl. Phys. Lett.* **67**, 533 (1995).
- [5] F. A. Ponce, B. S. Krusor, J. S. Major, Jr., W. E. Plano, and D. F. Welch, *Appl. Phys. Lett.* **67**,

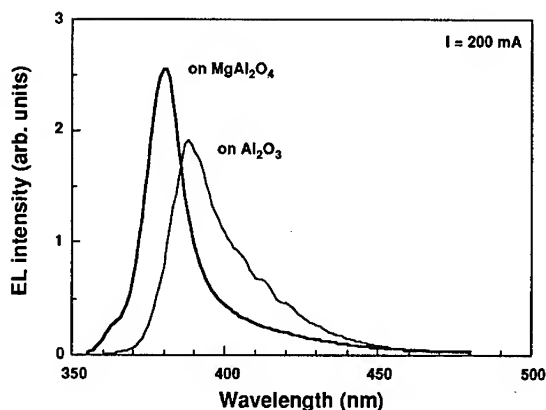


Fig. 5. Comparison of electroluminescence for LED fabricated on spinel and sapphire substrates.

410 (1995).

[6] T. W. Weeks, Jr., M. D. Bremser, K. S. Ailey, E. Carlson, W. G. Perry, and R. F. Davis, *Appl. Phys. Lett.* **67**, 401 (1995).

[7] A. Kuramata, K. Horino, K. Domen, K. Shinohara, and T. Tanahashi, *Appl. Phys. Lett.* **67**, 2521 (1995).

[8] Q. Chen, J. W. Yang, C. J. Sun, and M. Asif Khan, in 37th Electronic Materials Conference (1995).

[9] H. Amano, M. Kito, K. Hiramatsu, and I. Akasaki, *Jpn. J. Appl. Phys.* **28**, L2112 (1989).

[10] S. Nakamura, T. Mukai, M. Senoh, and N. Iwasa, *Jpn. J. Appl. Phys.* **31**, L139 (1992).

[11] S. Nakamura, *Jpn. J. Appl. Phys.* **30**, L1705 (1991).

[12] J. N. Kuznia, M. Asif Khan, and D. T. Olson, *J. Appl. Phys.* **73**, 4700 (1993).

[13] K. G. Feritta, A. L. Holmes, J. G. Neff, F. J. Ciuba, and R. D. Dupuis, *Appl. Phys. Lett.* **65**, 1823 (1994).

[14] M. Asif Khan, D. T. Olsen, J. M. Van Hove, and N. Kuznia, *Appl. Phys. Lett.* **58**, 1515 (1991).

[15] H. Amano, T. Asahi, and I. Akasaki, *Jpn. J. Appl. Phys.* **29**, L205 (1990).

[16] X. H. Yang, T. J. Schmidt, W. Shan, J. J. Song, and B. Goldenberg, *Appl. Phys. Lett.* **66**, 1 (1995).

GALLIUM NITRIDE EPITAXY ON SILICON: IMPORTANCE OF SUBSTRATE PREPARATION

G. A. MARTIN *, B. N. SVERDLOV *, A. BOTCHKAREV *, H. MORKOÇ *,
D. J. SMITH **, S.-C. Y. TSEN **, W. H. THOMPSON ***, M. H. NAYFEH ***

* Coordinated Science Laboratory and Materials Research Laboratory, University of Illinois
at Urbana-Champaign, Urbana, IL 61801

** Department of Physics and Astronomy and Center for Solid State Science, Arizona State
University, Tempe, AZ 85287

*** Department of Physics, University of Illinois at Urbana-Champaign, Urbana, IL 61801

ABSTRACT

Hexagonal GaN films grown on non-isomorphic substrates are usually characterized by numerous threading defects which are essentially boundaries between wurtzite GaN domains where the stacking sequences do not align. One origin of these defects is irregularities on the substrate surface such as surface steps. Using Si <111> substrates and a substrate preparation procedure that makes wide atomically flat terraces, we demonstrate that reduction of these irregularities greatly improves the crystalline and luminescent quality of GaN films grown by plasma-enhanced molecular beam epitaxy. X-ray rocking curve width decreases from over 1 degree to less than 20 minutes, while PL halfwidth decreases from over 15 meV to less than 10 meV.

INTRODUCTION

The Group III nitrides have great potential for optoelectronic devices operating across the entire visible spectrum and into the ultra-violet [1]. However, growth of nitride materials has been plagued by dense networks of threading defects in almost all nitride epitaxial layers grown to date by molecular beam epitaxy (MBE) [2] and metal-organic chemical vapor deposition (MOCVD) [3]. The threading defects are generally identified as stacking mismatch boundaries (SMBs), originating from the intersection of two domains where the stacking sequences are not aligned. Recent work demonstrated that in wurtzite epitaxy on non-isomorphic substrates each substrate surface step has a high probability of leading to an SMB [4]. A natural avenue for exploration is to reduce the number of surface steps and observe whether the density of threading defects decreases. Unfortunately, most substrates, whether mechanically or chemically polished, are far from atomically smooth and contain a very high density of surface steps. Previous attempts to grow wurtzite GaN on Si have generally yielded unsatisfactory results [5-7]. However, the Si <111> surface, when treated with certain etches, is reported to exhibit atomically flat terraces extending for thousands of angstroms [8-10], greatly increasing the distance between surface steps and thus decreasing their density. In this work we have systematically investigated substrate preparation procedures for improving the growth of GaN on Si <111> by decreasing the density of substrate steps.

EXPERIMENT

Three-inch n-type 50 ohm-cm $\langle 111 \rangle \pm 0.10^\circ$ silicon substrates from Virginia Semiconductor were used in this work. All substrate preparations began with a standard RCA cleaning procedure [11] (without thermal oxide growth). Later substrate preparations produced H-termination through immersion in a 1% HF solution for 20 seconds. Successful H-termination was evidenced by a hydrophobic surface afterwards. Substrates with extended atomically flat terraces were prepared using solutions of 7:1 $\text{NH}_4\text{F}:\text{HF}$ (buffered oxide etch) mixed with NH_4OH to raise the pH to various values from 6.5 to 9.25. Atomic force microscopy (AFM) was performed on the silicon substrates under ambient conditions using a TopoMetrix Explorer in contact mode to assess the effects of various substrate preparation schemes. GaN growth was performed by plasma-enhanced MBE using a Perkin Elmer 430 system previously described elsewhere [12,13]. Buffer layers of AlN, GaN, or InN were deposited as the substrate temperature was ramped from 400°C to 760°C. GaN films were grown to final thicknesses of 1-2 microns. X-ray double-crystal rocking curves (DCRC) were measured to assess crystal quality through the mosaic model. Photoluminescence (PL) was employed to assess the presence of defects through the effects on carrier recombination processes. Samples were prepared for transmission electron microscopy (TEM) using the rod-and-tube method by first mechanically thinning to a thickness of about 20 microns and then ion-milling to electron transparency with 4.5 keV argon ions. The samples were observed in cross-section with a JEM-4000EX high-resolution electron microscope (HREM) operated at 400 keV.

RESULTS

Preparation of Si $\langle 111 \rangle$ substrates for GaN epitaxy went through three stages of development. The first stage was epitaxial growth on a standard RCA-cleaned Si surface. GaN growth on such surfaces was immediately polycrystalline as shown by reflection high-energy electron diffraction (RHEED). The x-ray DCRC exhibited a full-width-at-half-maximum (FWHM) value of over 1.1 arcdegrees, while the PL halfwidth was 15 meV (4K). Reference values for GaN grown on sapphire substrates under similar conditions are 7 arcminutes and 6 meV (4K), respectively. TEM revealed that the GaN was extremely faulted, and that the Si starting surface contained hills and valleys, sometimes on the scale of many tens of angstroms. AFM was used to examine the Si starting surface after the RCA cleaning procedure, and it was found to have a roughness of 50-100 angstroms. This roughness could have been decreased somewhat with a thermal oxidation step prior to RCA cleaning [14]. The polycrystalline growth of GaN was attributed to an oxide layer left on the Si surface by the last stage of the RCA cleaning procedure. The absence of an ordered starting surface led immediately to polycrystalline growth since the amorphous oxide did not provide a crystal lattice for subsequent GaN epitaxy. The difficulties experienced with obtaining a RHEED pattern before growth support this idea.

In the next stage of silicon substrate preparation, all oxide was removed after the RCA cleaning procedure. Oxide removal was accomplished by a brief dip in dilute HF, leaving the sample with a H-terminated surface [15]. This surface is very resistant to subsequent oxidation [9]. After the substrate was heated to 800°C in the growth chamber, the H was desorbed and the 7×7 reconstruction of the Si surface was observed by RHEED. This indicated a clean Si surface free from oxide. According to RHEED, subsequent GaN growth was single-crystal and the x-ray DCRC FWHM decreased dramatically to 28 arcminutes.

The final stage of Si substrate preparation, after RCA cleaning, oxide removal, and H-termination, utilized $\text{NH}_4\text{F}:\text{HF}:\text{NH}_4\text{OH}$ solutions to produce Si surfaces with extended atomically flat regions and widely spaced substrate steps. There were many solution mixtures and immersion times that produced flat terraces, and many that did not. One successful formula was to mix commercial 7:1 $\text{NH}_4\text{F}:\text{HF}$ (buffered oxide etch) with NH_4OH to reach a final pH of 9.25 (approximately 3:1 mixture), and then immerse the substrate for 3 seconds. Afterwards the surface was hydrophobic, implying H-termination, and RHEED showed 7×7 reconstruction of the Si surface. AFM images demonstrated the presence of extended flat terraces as shown in Figure 1. This most recent stage of surface preparation achieved considerable improvement over the previous results. X-ray DCRC FWHM decreased to just under 20 arcminutes, and PL halfwidth decreased to just under 10 meV (4K).

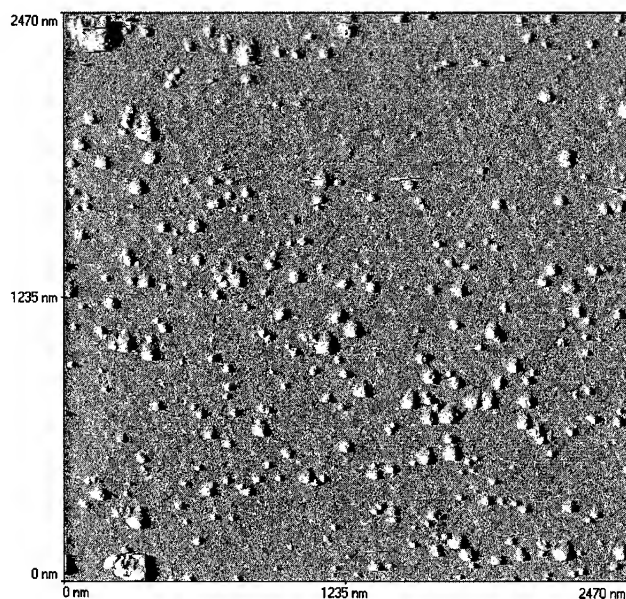


FIGURE 1: AFM image of the Si $\langle 111 \rangle$ surface after RCA cleaning, oxide removal, H-termination, and $\text{NH}_4\text{F}:\text{HF}:\text{NH}_4\text{OH}$ etching. The lines are atomic bilayer steps and exhibit 60° angles characteristic of the Si $\langle 111 \rangle$ surface. The bumps are approximately 40-70 angstroms high, and their origin is currently unexplained.

The progression of x-ray DCRC FWHM is shown in Figure 2. The greatest improvement was from stage one to stage two where the growth became single crystal. However, there was a significant improvement from stage two to stage three, suggesting that the decrease in the surface step density led to improvement in the GaN quality. The improvement in the PL halfwidths from stage one to stage three is demonstrated in Figure 3.

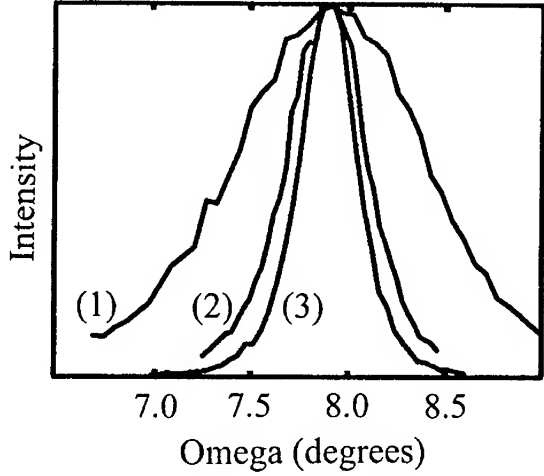


FIGURE 2: X-ray double-crystal rocking curves for MBE-grown GaN on Si $\langle 111 \rangle$ with substrate surface preparation consisting of: (1) RCA cleaning; (2) RCA cleaning, oxide removal, and H-termination; (3) RCA cleaning, oxide removal, H-termination, and $\text{NH}_4\text{F}:\text{HF}:\text{NH}_4\text{OH}$ etching.

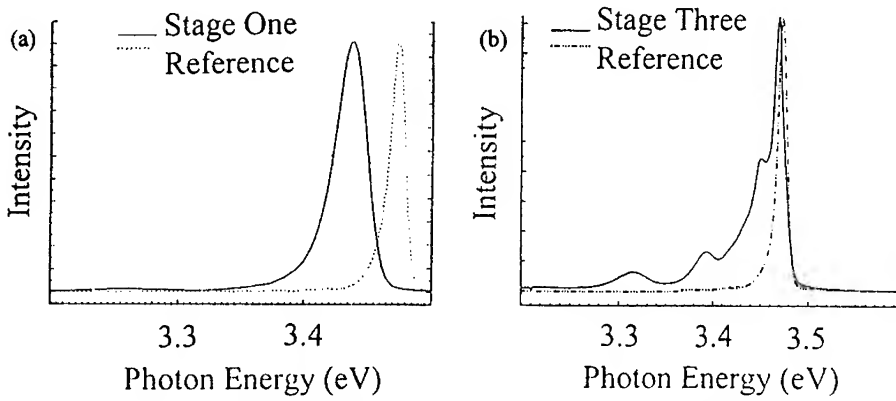


FIGURE 3: PL (4K) of MBE-grown GaN on Si $\langle 111 \rangle$ with substrate surface preparation consisting of: (a) RCA cleaning; (b) RCA cleaning, oxide removal, H-termination, and $\text{NH}_4\text{F}:\text{HF}:\text{NH}_4\text{OH}$ etching.

The goal of an unblemished surface with maximum distance between substrate steps has not yet been reached. The Si surfaces displayed extended terraces, but they also contained unexplained bumps approximately 40-70 angstroms high and of varying sub-micron diameters. The origin of these bumps has not been satisfactorily explained, and they are the subject of ongoing debate in the literature [16]. Our efforts to remove (water rinsing) or avoid [17] the bumps have proven unsuccessful. These bumps are certainly detrimental to growth, and occur

with a density on the order of 10^{10} cm^{-2} , which is the same density of threading defects observed in GaN grown by MOCVD on traditional substrates [3].

Figure 4 is an HREM micrograph of wurtzite GaN grown by MBE on Si $\langle 111 \rangle$, illustrating the successes and limitations of the current work. The Si substrate is atomically flat in this region. The thin buffer layer is heavily faulted, and it absorbs the lattice mismatch. Buffer layer optimization (including whether even to use a buffer layer) is the subject of ongoing work. The grown GaN is ordered, and is single-crystal from RHEED. The GaN contains a high density of domain boundaries near the interface, but other micrographs show that the domain boundary density decreases considerably with increasing distance from the interface. Many of the domains are slightly tilted, suggesting broadening contributions to the x-ray DCRC FWHM in the mosaic model. The GaN interface-region domains in this micrograph are much smaller than those observed in the best GaN grown on SiC and sapphire.

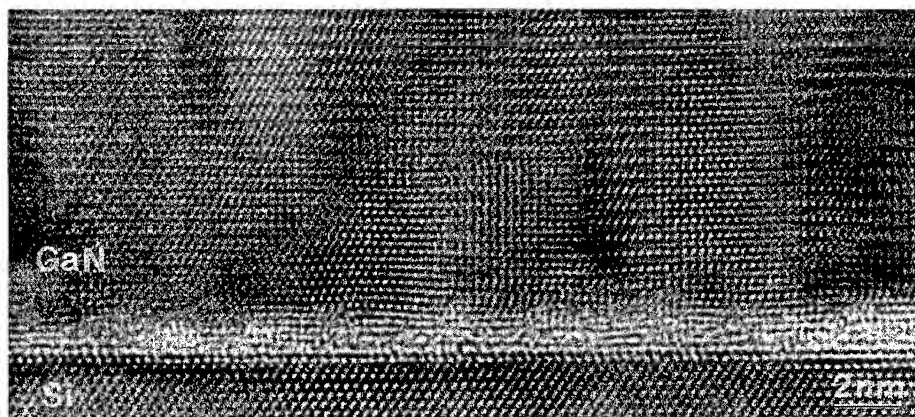


FIGURE 4: High-resolution electron micrograph of wurtzite GaN grown on an atomically flat region of Si $\langle 111 \rangle$ with a thin buffer layer.

CONCLUSIONS

Despite the marked improvements in the quality of MBE-grown GaN on Si $\langle 111 \rangle$ resulting from modified surface treatments, the results have not approached those achieved on sapphire and SiC. X-ray DCRC FWHM of 20 arcminutes and PL linewidth of 10 meV (4K) are, however, substantial improvements over previous results for MBE growth of GaN on Si. It may be that other factors such as lattice mismatch and thermal mismatch will ultimately limit the possibilities for GaN epitaxy on Si, but there is still room for improvement in buffer layer optimization and Si $\langle 111 \rangle$ surface preparation, particularly in producing an unblemished terraced surface. Producing even better Si $\langle 111 \rangle$ surfaces still holds promise for further reduction of defect density and improvement in GaN crystallinity.

ACKNOWLEDGMENTS

Electron microscopy was conducted at the Center for High Resolution Electron Microscopy at Arizona State University supported by the National Science Foundation under Grant No. DMR-93-1426. The work at the University of Illinois was sponsored by the Office of Naval Research under the direction of Max Yoder. G. A. Martin wishes to thank W. Kim, K. Ritley, and A. K. E. Fleming for timely assistance.

REFERENCES

1. S. Strite and H. Morkoç, *J. Vac. Sci. Technol. B* **10**, 1287 (1992).
2. D. J. Smith, D. Chandrasekhar, B. Sverdlov, A. Botchkarev, A. Salvador, and H. Morkoç, *Appl. Phys. Lett.* **67**, 1830 (1995).
3. S. D. Lester, F. A. Ponce, M. G. Crawford, and D. A. Steigerwald, *Appl. Phys. Lett.* **66**, 1249 (1995).
4. B. N. Sverdlov, G. A. Martin, H. Morkoç, and D. J. Smith, *Appl. Phys. Lett.* **67**, 2063 (1995).
5. T. Lei and T. D. Moustakas, *J. Appl. Phys.* **71**, 4933 (1992).
6. A. Ohtani, K. S. Stevens, and R. Beresford, *Appl. Phys. Lett.* **65**, 61 (1994).
7. P. Kung, A. Saxler, X. Zhang, D. Walker, T. C. Wang, I. Ferguson, and M. Razeghi, *Appl. Phys. Lett.* **66**, 2958 (1995).
8. G. S. Higashi, R. S. Becker, Y. J. Chabal, and A. J. Becker, *Appl. Phys. Lett.* **58**, 1656 (1991).
9. U. Neuwald, H. E. Hessel, A. Feltz, U. Memmert, and R. J. Behm, *Appl. Phys. Lett.* **60**, 1307 (1992).
10. M. Kageshima, H. Yamada, Y. Morita, H. Tokumoto, K. Nakayama, and A. Kawazu, *Jpn. J. Appl. Phys.* **32**, L1321 (1993).
11. W. Kern, *Semiconductor International* April 1984, 94.
12. S. Strite, J. Ruan, Z. Li, N. Manning, A. Salvador, H. Chen, D. J. Smith, W. J. Choyke, and H. Morkoç, *J. Vac. Sci. Technol. B* **9**, 124 (1991).
13. S. Strite, D. Chandrasekhar, D. J. Smith, J. Sarel, H. Chen, N. Teraguchi, and H. Morkoç, *J. Cryst. Growth* **127**, 204 (1993).
14. Y. J. Chabal, P. Dumas, P. Guyot-Sionnest, and G. S. Higashi, *Surf. Sci.* **242**, 524 (1991).
15. G. S. Higashi, Y. J. Chabal, G. W. Trucks, and K. Raghavachari, *Appl. Phys. Lett.* **56**, 656 (1990).
16. M. Niwano, K. Kurita, Y. Takeda, and N. Miyamoto, *Appl. Phys. Lett.* **62**, 1003 (1993).
17. S.-K. Yang, S. Peter, and C. G. Takoudis, *J. Appl. Phys.* **76**, 4107 (1994).

HYDRAZOIC ACID: A POTENT 'ACTIVE NITROGEN' PRECURSOR FOR GROUP III NITRIDE GROWTH

ANDREW FREEDMAN and GARY N. ROBINSON

Aerodyne Research, Inc., 45 Manning Road, Billerica, MA 01821

af@aerodyne.com, robinson@aerodyne.com

ABSTRACT

Hydrazoic acid, HN_3 , was shown to be an extremely reactive molecule and an effective precursor species for 'active nitrogen'. At room temperature, hydrazoic acid dissociatively chemisorbed on GaAs (110) surfaces to form the NH radical and N_2 . At 473 K, the NH fragment reacted with the substrate, broke Ga-As bonds and formed GaN and AsN species. At 673 K, an anionic exchange mechanism commenced; the surface became completely depleted of As and a thin film of GaN formed. When the surface was dosed at 773 K, a 20 Å thick GaN film was grown. This evidence demonstrates that hydrazoic acid is highly reactive at comparatively low surface temperatures and offers a viable alternative to ammonia as a nitrogen precursor gas.

INTRODUCTION

The III-V nitrides of Al, Ga and In are direct band gap semiconductors which form complete solid solutions with each other and are candidate materials for high frequency microelectronic and optoelectronic devices. The latter devices would be operative within the orange (InN) to ultraviolet (GaN and AlN) range of the spectrum. However, these materials, particularly GaN and InN, possess a high vapor pressure at the growth temperatures of vapor phase epitaxy (VPE) (800 - 1100°C) and molecular beam epitaxy (MBE) (500 - 700°C). The primary experimental problem is the difficulty of maintaining sufficient reactive N in the vicinity of the growing film to counteract the tendency for nitrogen loss. The use of electron cyclotron resonance plasmas has allowed the deposition temperature to be decreased in the MBE technique, but the flux of reactive N species is limited. In the case of VPE, the presence of a substantial partial pressure of ammonia, especially in the case of InN deposition, allows the growth temperature to be increased, but with a concomitant increase in the N vapor pressure from the growing nitride. The desired alternative is a system which allows for the production of copious amounts of reactive N species and deposition at reduced temperatures where the rate of vaporization is low.

We are investigating the use of HN_3 , hydrazoic acid, as such a nitrogen precursor species. Its major advantage over other precursors, such as molecular nitrogen and ammonia, is that its bond energy to produce the highly active radical species NH is only 0.5 eV (compared to bond dissociation energies of 9.8 and 4.5 eV for nitrogen and ammonia respectively).[1] In order to investigate the reactivity of hydrazoic acid, the non-polar (110) surface of single crystal wafers of GaAs was dosed with controlled exposures of HN_3 . The subsequent reactions of the crystal with HN_3 were studied as a function of crystal temperature using x-ray photoelectron spectroscopy as the main diagnostic tool.

EXPERIMENT

The microchemistry of hydrazoic acid interactions with GaAs crystal surfaces was studied in an ultrahigh vacuum apparatus which comprises a turbomolecular pumped, liquid nitrogen trapped ultrahigh vacuum cell interfaced to an ion-pumped analysis chamber. The diagnostics available in the analysis chamber are x-ray photoelectron spectroscopy (XPS) and low energy electron diffraction (LEED). The sample is transferred between chambers using a linear motion feedthrough with sample heating (1200 K) and cooling (130 K) capabilities. We utilized a commercially available pulsed beam source, the General Valve Iota-1, to dose the surface. The pulse length was set such that an individual pulse of gas delivered a dose of approximately 10^{15} molecules cm^{-2} of HN_3 to the substrate surface during each pulse.

Hydrazoic acid, HN_3 , was synthesized according to the procedure described by Setzer in which HN_3 was made by the reaction of sodium azide with a slight excess of stearic acid in a thick-walled Pyrex vessel.[2] A stainless steel cylinder was used to collect the hydrazoic acid vapor using a Teflon and stainless steel gas handling system. The cylinder was subsequently back-filled to a pressure of one atmosphere with argon or helium in order to stabilize the acid. Mass spectra of the gas samples indicated the presence of an oxygen contaminant.

The GaAs (110) substrates were mounted in the chamber, Ar^+ etched for 30 minutes at 1 keV to remove any traces of carbon or oxygen contamination, and annealed at 580 °C for 60 minutes. X-ray photoelectron spectroscopy (XPS) and low energy electron diffraction (LEED) patterns of the samples indicated that surface order had been restored and a gallium rich reconstruction ($\text{Ga/As} \approx 1.3$) had formed.[3] The samples were then exposed to doses of hydrazoic acid that were determined by setting both the pulse length and number of pulses. XPS spectra were taken using PHI 15 keV Mg and Al $K\alpha$ X-ray sources and a PHI double-pass cylindrical mirror electron energy analyzer operated at a bandpass of 25 and 50 eV depending on the particular transition being studied. All spectra are referenced to the As 3d transition at 41.5 ± 0.2 eV.

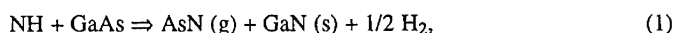
RESULTS

Figures 1-3 present a series of XPS spectra showing the reactions of GaAs (110) with hydrazoic acid as a function of substrate temperature during the dosing cycle. Each individual experiment shown involved exposure to doses sufficiently high to saturate any possible reaction path ($\sim 10^{18} \text{ cm}^{-2}$). Figure 1 presents the N 1s spectra. At 310 K (slightly above room temperature), only one peak is observed which is indicative of the presence of NH and N_2 species adsorbed on the surface. This assignment has been made by and confirmed by groups led by Lin [4,5] and White [6,7]. The absence of a peak above 400 eV indicates that there is no undissociated hydrazoic acid present on the surface at these temperatures. The Ga and As $2p_{3/2}$ spectra shown in Figures 2 and 3 show no indication of any nitride formation since the recorded spectra are identical with those recorded on clean GaAs surfaces. From the poor signal-to-noise ratios of the nitrogen spectra, we estimate that at 310 K, a monolayer of hydrazoic acid dissociatively chemisorbs to form dinitrogen and amido radicals on the surface. There is no evidence for any breakage of Ga-As bonds. Furthermore, most of these nitrogen adspecies desorb from the surface when it is heated to 473 K and within our ability to detect them, they are completely desorbed by 573 K.

At 473 K, a different situation obtains. The nitrogen spectrum shown in Figure 1 shows evidence of a slight shoulder to lower binding energies compared to the previous NH/N_2 peaks. This shoulder occurs precisely where one would expect to find a peak for GaN and AsN.[4-7]

Comparing the intensity of the shoulder to the main peak, we estimate that no more than a monolayer of GaN/AsN is formed. The Ga 2p peak shows a slight shift upward of ~ 0.2 - 0.3 eV and the As 2p peak shows slight evidence of a shoulder at higher binding energies; this data is consistent with the formation of both AsN and GaN. It should also be noted that the ratio of arsenic to gallium remains constant throughout the dosing process.

A radical transition in the observed chemistry takes place when the sample is dosed at 673 K. Note that the N 1s peak corresponding to NH/N_2 has disappeared and been totally replaced by a peak corresponding to GaN/AsN. Furthermore, the integrated intensity of this peak is several times greater than that of the nitrogen peak found at 310 K and is thus indicative of a nitride film that is several layers thick. The Ga 2p spectrum has also shifted 0.5 eV to higher binding energy from clean GaAs indicating the formation of several layers of GaN. The As 2p spectrum shows two distinct peaks; one at that found for bulk GaAs and one which corresponds to AsN which is at ~ 2.3 eV higher binding energy. But even more illuminating is the loss of integrated intensity of the As peak and growth in the Ga peak intensity. The Ga intensity has increased by 50% while the As intensity has fallen by over half. This trend is indicative of an anionic exchange mechanism where the NH radical reacts with the arsenic to form volatile AsN:



leaving behind the thermally more stable gallium nitride. This same behavior is observed in the reactions of GaAs with fluorine atoms and molecules to form GaF_3 thin films, albeit at lower temperatures.[3,8,9] The observation of some AsN residue is the result of the fact that the GaN layer, at sufficient thickness, acts as a diffusion barrier to the volatilization of the AsN species.

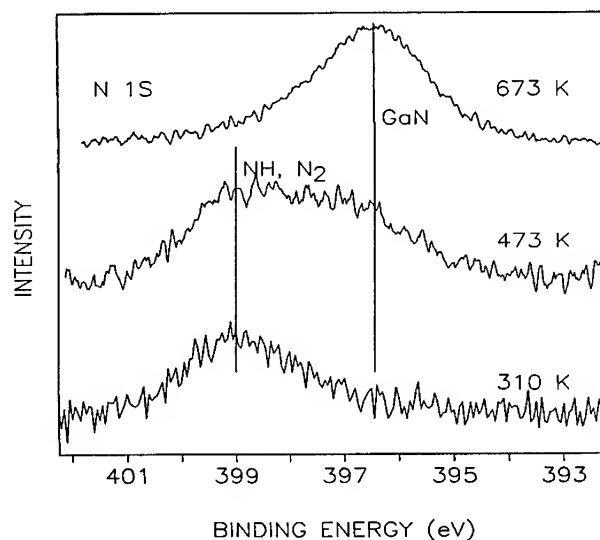


Figure 1. N 1s transition XPS spectra of GaAs(110) substrates after having been dosed to saturation with hydrazoic acid as a function of substrate temperature.

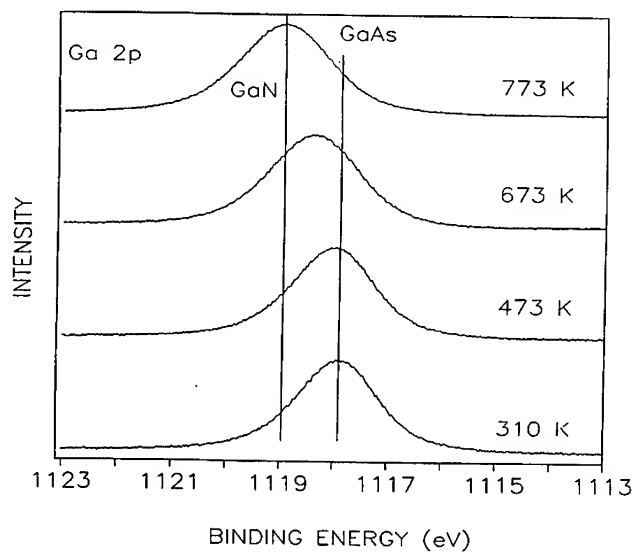


Figure 2. Ga $2p_{3/2}$ transition XPS spectra of GaAs(110) substrates after having been dosed to saturation with hydrazoic acid as a function of substrate temperature.

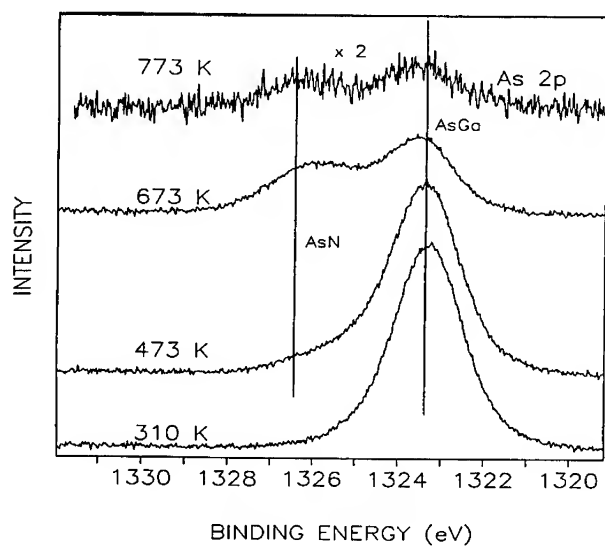


Figure 3. As $2p_{3/2}$ transition XPS spectra of GaAs(110) substrates after having been dosed saturation with hydrazoic acid as a function of substrate temperature.

As deposition takes place at higher temperatures, one expects the film to grow thicker before the reaction product layer acts as a diffusion barrier. We observe precisely this behavior! The integrated intensity of the nitrogen spectrum of GaAs dosed at 773 K (not shown) is several times that found at 673 K. Furthermore, the Ga 2p peak has completely shifted to higher binding energies consistent with the formation of a GaN thin film which is on the order of three times the escape depth of this transition or 20-25 Å. The arsenic peak has almost completely disappeared indicating that it has been completely replaced in this reaction product region. Note that there is still a trace of some AsN which must reside at the interface of the GaN and GaAs.

Figure 4 summarizes the data by presenting a graph showing the thickness of the GaN film formed by dosing with hydrazoic acid as a function of substrate temperature. At 310 K, no GaN film is formed; HN_3 dissociatively chemisorbs, but does not break any GaAs bonds. At 473 K, a monolayer of GaN/AsN is formed before the reaction stops. At 673 K, a GaN layer ~ 6 Å thick forms with an AsN layer found at the GaN/GaAs interface. At 773 K, the GaN layer can be grown to a thickness of 20 Å before the anionic exchange mechanism is cut off by the inability of the AsN to diffuse to the surface. We estimate that the thickness of the GaN/GaAs interface region which contains undesorbed AsN to be ~ 5 Å.

DISCUSSION

Gallium arsenide surfaces were found to be surprisingly reactive towards hydrazoic acid. Lin and co-workers [4,5] had shown that when gallium arsenide was dosed with hydrazoic acid at low temperatures, the HN_3 desorbed from the surface below 200 K with no trace of any reaction. Apparently, at room temperature and above, the surface becomes reactive and HN_3 dissociatively chemisorbs upon adsorption. As the substrate temperature is increased to 473 K, Ga-As bonds are broken and GaN and AsN species are formed. But even at this temperature, the reaction is limited to the topmost layer. At 673, on the other hand, a preferential etching process leading to anionic exchange occurs. Subsurface arsenic is removed by the formation and desorption of volatile AsN, leaving behind GaN. This behavior is similar to that found for the fluorination reactions of GaAs which lead to the formation of GaF_3 thin films.[3,8,9] The thickness of the thin film that can be formed in this fashion is extremely temperature sensitive. At 673 K, the thin film is limited to 5-6 Å; at 773 K, a 20 Å GaN film can be formed. This temperature effect is caused by the fact that the forming GaN film acts as a diffusion barrier to the inward path of the active nitrogen species and to the desorption of subsurface AsN.

This observed reactivity of hydrazoic acid at relatively low temperatures indicates that HN_3 is an excellent source of neutral forms of 'active nitrogen' which does not require any sort of discharge or excitation. Recent work of John Russell at the Naval Research Laboratory has indicated that HN_3 will also readily react with crystalline aluminum surfaces to form epitaxial layers of AlN as well.[10] Thus, it would seem that if a low temperature form of metallic gallium or aluminum is provided at the surface, binary or ternary metal nitride films could be readily grown on arbitrary surfaces at reduced temperatures. Organometallic species, such as diethyl gallium and aluminum, are excellent choices of metal atom precursors. They decompose at temperatures well below that required for metal nitride growth (< 750 K). It would seem that film growth could readily be accomplished using heated pulsed nozzles of both metal and nitrogen precursor molecules such as diethylgallium and hydrazoic acid. We note that Lin and co-workers have grown epitaxial α -GaN films on sapphire using a low pressure chemical vapor deposition system using hydrazoic acid and triethylgallium at 850 K.[11]

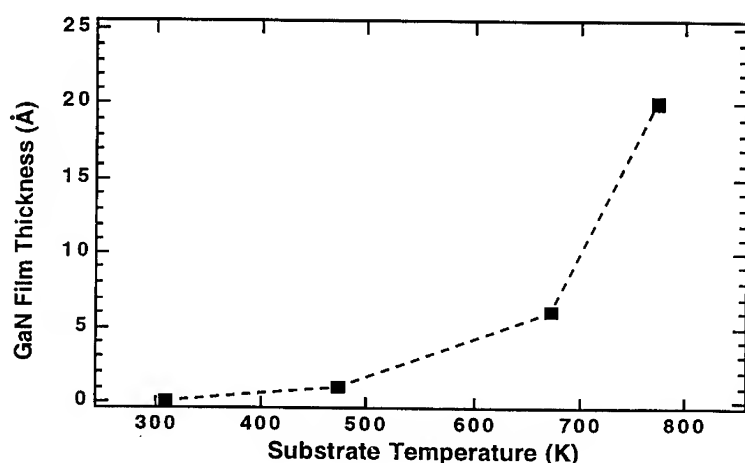


Figure 4. GaN film thickness as a function of substrate temperature during deposition.

ACKNOWLEDGMENTS

This project was supported by funding from the Office of Naval Research under the Small Business Technology Transfer program.

REFERENCES

1. A. Freedman and C.D. Stinespring, *J. Phys. Chem.* **96**, 2253 (1992)
2. J. Haabadas, S. Wategaonkar, and D.W. Setser, *J. Phys. Chem.* **91**, 451 (1987)
3. H. Okabe, *Photochemistry of Small Molecules*, Wiley, New York, 1978
4. Y. Bu and M.C. Lin, *Surf. Sci.* **317**, 152 (1994)
5. Y. Bu, J.C.S. Chu, and M.C. Lin, *Surf. Sci. Lett.* **264**, L154 (1992)
6. X.Y. Zhu, M. Wolf, T. Huett and J.M. White, *J. Chem. Phys.* **97**, 5856 (1992)
7. Y.M. Sun, D.W. Sloan, M. McEllistrem, A.L. Schwaner and J.M. White, *J. Vac. Sci. Technol.* **A13**, 1455 (1995)
8. A.S. Barrière, G. Couturier, H. Guégan, T. Séguelond, A. Thabti, P. Alnot and J. Chazelas, *Appl. Surf. Sci.* **41/42**, 383 (1990)
9. A.S. Barrière, B. Desbat, H. Guégan, L. Lozano, T. Séguelond, A. Tressaud and P. Alnot, *Thin Solid Films*, **170**, 259 (1989)
10. John Russell, Naval Research Laboratory, personal communication.
11. Y. Y. Bu, M.C. Lin, L.P. Fu, D.G. Chetchekine, Y. Chen, S.E. Ralph, and S.R. Stock, *Appl. Phys. Lett.* **66**, 2433 (1995)

GROWTH OF GaN ON (100)Si USING A NEW C-H AND N-H FREE SINGLE-SOURCE PRECURSOR

JOHN KOUVETAKIS AND JEFFREY McMURRAN

Department of Chemistry and Biochemistry, Arizona State University, Tempe, AZ 85287-1604

DAVID B. BEACH

Chemical and Analytical Science Division, Oak Ridge National Laboratory, Oak Ridge, TN 37831

DAVID J. SMITH

Center for Solid State Science and Department of Physics and Astronomy, Arizona State University, Tempe, AZ 85287

ABSTRACT

We have demonstrated growth of crystalline GaN on Si substrates by using, for the first time, a novel inorganic precursor Cl_2GaN_3 and ultra-high-vacuum chemical vapor deposition techniques. Cross-sectional electron microscopy of the highly conformal films showed columnar growth of wurtzite GaN while Auger and RBS oxygen- and carbon-resonance spectroscopies showed that the films were pure and highly homogeneous. In addition to the high growth rates of 70-500 Å per minute, the low deposition temperature of 550-700 °C, and the nearly perfect GaN stoichiometry that we obtain, another notable advantage of our method is that it provides a carbon-free growth environment which is compatible with p-doping processes.

INTRODUCTION

The potential of the group III nitrides, InN, GaN, and AlN, for microelectronic and optoelectronic applications is well recognized [1]. In principle, bandgap variation ranging from 1.8 eV (InN) to 6.3 eV AlN can be achieved by suitable alloy combinations. The use of GaN in the fabrication of light emitting diodes has been demonstrated [2], but fabrication of blue-laser diodes and other high-power, high-frequency and high-temperature GaN-based devices has not yet been realized. A major reason is that the growth of good quality epitaxial nitride films is hindered by the lack of suitable substrate material, and achieving p-type doping is another serious difficulty. A further problem is the high background of n-type carrier concentration caused primarily by nitrogen deficiencies.

Much attention has recently been given to the nature of the structural defects present in wurtzite GaN films grown by CVD [3] and molecular beam epitaxy [4] methods, and it is clear that such factors as the substrate orientation and the nature of any buffer layers have a major influence on the thin-film microstructure. Moreover, it has recently been concluded that a high density of threading defects originating at the substrate-film interface must be considered as inevitable whenever materials that are nonisomorphic with GaN are used as the substrate [5]. Consequently, not only is there a pressing need to develop GaN films of better quality but alternative substrates also need to be investigated.

We are exploring new ways to grow nitride films using novel synthetic approaches. Our primary aim is to utilize simple inorganic precursors that would allow us to grow stoichiometric materials (no nitrogen vacancies), in a carbon-free environment which should not interfere with p-doping processes. The ultimate objective is to grow defect-free layers on suitable substrate materials that would promote crystalline perfection. In this report we describe our first synthetic approach which primarily involves surface decomposition of a unimolecular precursor, Cl_2GaN_3 , with a "preformed" strong GaN bond, at very low pressures in a custom-built UHV-CVD system.

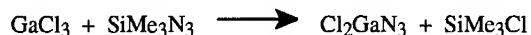
We have prepared this single source inorganic precursor which is free of C and H via single-step synthesis at nearly quantitative yields.

Previous synthetic routes to GaN utilizing single source precursors with preformed GaN bonds include decompositions of $\text{Et}_3\text{Ga}\cdot\text{NH}_3$ and related adducts [6], Et_2GaN_3 [7], $(\text{Me}_2\text{GaN}_3)_n$ and $((\text{Me}_2\text{GaNH}(\text{NMe}_2))_2$ [8]. The major disadvantages of these methods is carbon incorporation in the films and low growth rates. The precursor synthesis and characterization as well as the deposition procedure to obtain highly conformal films of stoichiometric GaN are discussed below.

SYNTHESIS AND GROWTH

Precursor synthesis

We have prepared azidodichlorogallane in nearly quantitative yields from a convenient single step synthesis involving the reaction of GaCl_3 with trimethylsilyl azide as shown below.



The compound is a colorless, air-sensitive solid that sublimates readily and melts with some decomposition at 210 °C. It is not as air-sensitive as GaCl_3 and the trimethyl gallium or triethyl gallium precursors currently used in GaN CVD processes. It reacts rapidly but in a remarkably mild manner with liquid water and it is not sensitive to shock. The FTIR spectrum reveals the strong azide stretch at 2184 cm^{-1} and the characteristic Ga-N and Ga-Cl stretches at 450 and 385 cm^{-1} respectively. Additional vibrations at 350 and 250 indicate bridging N-Ga-N stretching and bending modes respectively. Electron impact mass spectroscopic analysis shows $(\text{Cl}_2\text{GaN}_3)_3 - \text{Cl}$ as the highest mass peak at 511 amu and a fragmentation pattern that is consistent with a trimeric presumably six-membered Ga-N ring structure as shown in figure 1.

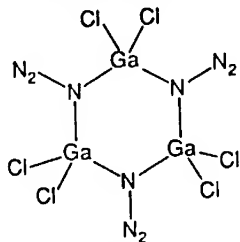


Figure 1. Proposed trimeric structure of dichlorogallium azide

Synthetic procedure for azidodichlorogallane.

To a frozen solution of GaCl_3 (15.0 g, 85.2 mmol) in CH_2Cl_2 (80 mL) at -196 °C was added Me_3SiN_3 (11.3 mL, 85.1 mmol) by syringe. The mixture was allowed to slowly warm to room temperature and stirred for 18 h. The CH_2Cl_2 was removed under reduced pressure and the residue was sublimed (100 °C, 10^{-3} mm Hg) to give 14.5 g (79.5 mmol, 93%) of Cl_2GaN_3 as a white powder. MP 209-211 °C. IR (Nujol): 3359 (w, $\nu_{\text{as}}\text{N}_3 + \nu_{\text{s}}\text{N}_3$), 2403 (m, $2\nu_{\text{s}}\text{N}_3$), 2184 (vs, $\nu_{\text{as}}\text{N}_3$), 1205 (vs, $\nu_{\text{s}}\text{N}_3$), 1097 (w, comb), 759 (s, δN_3), 551 (m, γN_3), 452 (s, νMN), 429 (s, νMN), 383 (s, νMCl), 348 (m, δMNM), 250 (s, δMNM) cm^{-1} . EIMS: 511 $\{(\text{Cl}_2\text{GaN}_3)_3 - \text{Cl}\}$. Anal. calcd. for Cl_2GaN_3 : Cl, 38.8. Found: Cl, 37.96

Deposition Procedure

The UHV reactor used in this study consists of a cold-wall, inductively heated 3-inch quartz tube equipped with a water jacket connected to a recirculator bath filled with ethylene glycol. The bath can provide wall temperatures ranging from -20 to 80 °C. The temperature of the susceptor was measured by an optical pyrometer through a quartz window. The reaction tube is attached to a load-locked UHV stainless-steel chamber equipped with a differentially pumped Inficon PPC mass spectrometer capable of in situ gas sampling through several micrometer size orifices. The pumping system consists of a high-capacity corrosion resistant turbomolecular pump that was used to obtain ultrahigh-vacuum (approximately $7\text{--}9 \times 10^{-9}$ Torr) before and after each deposition. It was also used as a process pump during deposition. In a typical experiment, the susceptor and the substrates were loaded on a quartz boat, pumped in the load lock to 10^{-7} torr and then passed into the reactor using a magnetically coupled manipulator. The pumping was switched to the process turbopump and the temperature of the susceptor was adjusted to 650 °C while the reactor wall temperature was maintained at 70 °C by circulating preheated ethylene glycol. The precursor was held 70 °C in a quartz reservoir directly connected to the reaction chamber and transported into the reactor by sublimation at a pressure of $1\text{--}2 \times 10^{-4}$. The reaction pressure remains remarkably constant throughout the deposition and can be increased or decreased proportionally by increasing or decreasing the precursor reservoir temperature. The pressure in the reactor is constantly monitored with a cold cathode gauge. The gaseous precursor decomposes thermally at temperatures as low as 550 °C and pressures of 10^{-4} Torr to grow GaN films on silicon substrates. Most depositions, however, were carried out at 650-700 °C because the lower temperature depositions resulted in substantial chlorine incorporation (3-4 at. %) in the films. At 700 °C the deposition time was typically 30 minutes giving thicknesses ranging from 2000-15000 Å and the growth rate increased from 70 Å per minute to 500 Å per minute as the reaction pressure increased from 1×10^{-4} to 1×10^{-3} Torr. This clearly suggests that the growth rate is dependent on the amount of gaseous precursor available during deposition. There was no obvious film formation or precursor degradation on the warm reactor walls during growth. It appears, however, that the heated wall ensured complete transport of the vaporized precursor through the hot zone and that eventually the entire precursor supply was vaporized from the reservoir. We never observed any nonvolatile residues that might have originated from precursor degradation during sublimation. Decomposition of the precursor occurred only on the hot substrate and the graphite susceptor. No solid byproduct residues were observed down-stream from the deposition zone indicating that virtually no precursor remains undecomposed, and all byproducts were in the form of gaseous species which were constantly removed by the process turbopump. Mass spectroscopic analysis of the byproducts showed that only elemental nitrogen and GaCl₃ were formed at all deposition temperatures and pressures.

CHARACTERIZATION

Depositions of Ga-N materials from dichlorogallium azide in the UHV reactor were performed at 550-700 °C. Rutherford backscattering spectroscopy (RBS) in the random mode was routinely used to determine the gallium and nitrogen concentration and the film thickness. Elastic carbon and oxygen resonance reactions were also used to check for carbon and oxygen impurities. Auger electron spectroscopy depth profiles were used to obtain the gallium and nitrogen distribution and also to show the absence of oxygen or any other impurities. The microstructure of all materials was characterized by cross-sectional transmission electron microscopy (TEM).

RBS analyses of the films deposited at 550 °C revealed a slight excess more nitrogen relative to gallium and the films also contained 2-4 at. % of chlorine. Cross-sectional TEM images showed columnar GaN growth and selected area electron diffraction patterns indicated that the material had the wurtzite structure. *In situ* annealing of the samples between 800-1000 °C under high vacuum resulted in stoichiometric wurtzite GaN having chlorine content of less

than 1 at. %. The crystallinity of the annealed samples was substantially improved and the columnar grains extended, as shown in Fig. 2, from the interface through the entire length of the layer.



Figure 2. Cross-sectional electron micrograph showing columnar growth of wurtzite GaN

Higher annealing temperatures at 10^{-8} Torr resulted in a slight increase in grain size but also caused substantial surface roughness as was observed from examinations of the surface morphology by atomic force microscopy (AFM). Figure 3 shows AFM images of the as-deposited and annealed samples illustrating the significant increase in surface roughness that resulted from a high temperature (1000°C) heat treatment at 10^{-8} Torr.

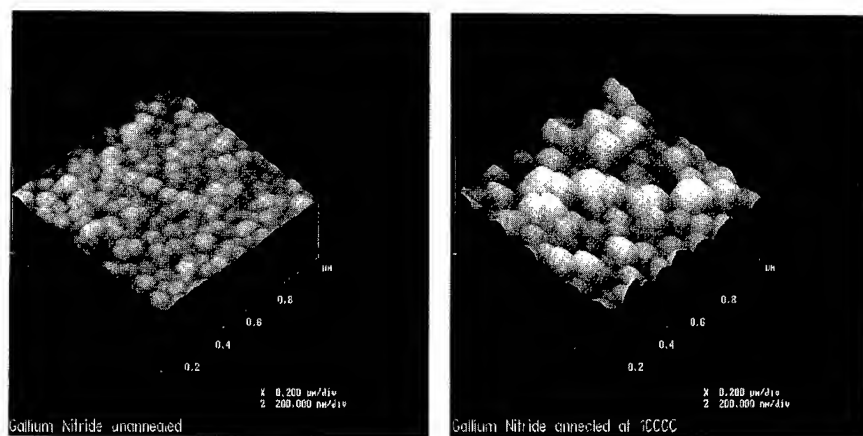


Figure 3. GaN film as-deposited at 650°C (left) and GaN film annealed at 1000°C

RBS analyses of 2000 to 15000 Å films deposited at 700 °C revealed stoichiometric GaN with chlorine contents less than 1 at. %. High resolution transmission electron microscopy showed that this material was also columnar and that the columns were significantly larger than those obtained at 550 °C. In fact, the column size is virtually identical to that of the annealed samples described previously. These results imply that the Cl impurity content is lower and the crystallinity is better for films produced at higher deposition temperatures and that the GaN stoichiometry is independent of the deposition temperature and film growth rate. Annealing of the films grown at 700 °C GaN improved the crystallinity slightly and resulted in an increase of the surface roughness. RBS carbon and oxygen resonance analyses did not show any carbon or oxygen impurities and Auger (Fig. 4) depth profiles revealed constant elemental content through the layer. Ellipsometric scans of samples obtained at 500 °C and at 700 °C indicated a bandgap of 3.4 eV.

Decomposition reaction mechanism

We chose Cl_2GaN_3 for thermal CVD precursor of GaN because the azide group should eliminate nitrogen and the chloride ligands could potentially eliminate Cl_2 . The intended overall reaction is



However, mass spectroscopic examination of the volatile byproducts showed that only nitrogen and GaCl_3 formed in depositions between 500-700 °C from the decomposition of Cl_2GaN_3 . Controlled pyrolysis experiments of this compound in a horizontal hot-wall reactor produced only solid byproducts which were collected in a liquid nitrogen trap and were identified by infrared spectroscopy and by melting point measurements as gallium trichloride. Although N_2 was produced from the controlled pyrolysis of Cl_2GaN_3 , we again did not detect any other byproducts such as chlorine gas. The lack of Cl_2 elimination and the production of substantial quantities of GaCl_3 suggest a disproportionation reaction of the gaseous $(\text{Cl}_2\text{GaN}_3)_3$ trimer as shown in Fig. 4.

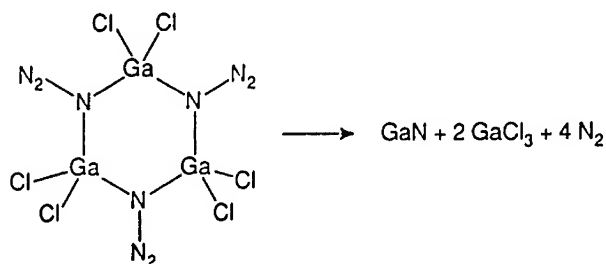


Figure 4. Probable decomposition pathway of $(\text{Cl}_2\text{GaN}_3)_3$ to yield GaN, N_2 and GaCl_3

SUMMARY

We have achieved synthesis of stoichiometric GaN by thermal low-pressure decomposition of Cl_2GaN_3 in a cold wall UHV CVD reactor. Our inorganic precursor is conveniently prepared in nearly quantitative yields and is not as air-sensitive as the trimethyl gallium and triethyl gallium molecules which are currently used in GaN CVD processes. More importantly, it incorporates the stoichiometry of the nitride phase and decomposes readily at 500-700 °C at extraordinarily high rates of 70-500 Å/minute to produce films with thickness up to 15000 Å on Si substrates. The most striking advantages of our method are the high deposition

rates, the stoichiometric character of the films and the simplicity of the deposition process. Next we will focus our efforts on growing defect-free epitaxial films on sapphire, SiC and other structurally consistent substrates.

ACKNOWLEDGMENTS

This work was primarily supported by the National Science Foundation DMR 9458047. One of us, DBB was supported by the Division of Materials Sciences, Office of Basic Energy Sciences, U.S. Department of Energy under contract No. DE-AC05-84OR21400 with Lockheed Martin Energy Systems Inc. Electron microscopy was conducted at the Center for High Resolution Electron Microscopy supported by the National Science Foundation under Grant DMR-9115680.

REFERENCES

- [1] H. Morkoc, S. Strite, G. B. Gao, M. E. Lin, B. Sverdlov and M. Burns, *J. Appl. Phys.* **76**, 1763 (1994).
- [2] S. Nakamura, M. Senoh, N. Iwasa and S. Nagahama, *Jap. J. Appl. Phys.* **34**, L797 (1995).
- [3] S. D. Lester, F. A. Ponce, M. G. Crawford and D. A. Steigerwald, *Appl. Phys. Lett.* **66**, 1249 (1995) 1249.
- [4] D. J. Smith, D. Chandrasakher, B. Sverdlov, A. Botchkarev, A. Salvador and H. Morkoc, *Appl. Phys. Lett.* **67**, 1830 (1995).
- [5] B. N. Sverdlov, G. A. Martin, H. Morkoc and D. J. Smith, *Appl. Phys. Lett.* **67**, 2063 (1995).
- [6] J. E. Andrews, M. A. Little John, *J. Electrochem. Soc.* **122**, 1273 (1975).
- [7] J. Kouvetakis and D. B. Beach, *Chem. Mat.* **1**, 476 (1989).
- [8] V. Lakhotia, D. A. Neumayer, A. H. Cowley, R. A. Jones, and J. G. Ekerdt, *Chem. of Mat.* **3**, 441 (1995).

A NEW SINGLE SOURCE PRECURSOR APPROACH TO GALLIUM AND ALUMINUM NITRIDE

*Deborah A. Neumayer, **C.J. Carmalt, **M.F. Arendt, **J.M. White, **A.H. Cowley, **R.A. Jones, **J.G. Ekerdt

**Science and Technology Center for Synthesis, Growth and Analysis of Electronic Materials, University of Texas, Austin, TX.

ABSTRACT

Single source precursors which contain preformed gallium-nitrogen and aluminum-nitrogen bonds are being considered for the growth of gallium and aluminum nitride because of their potential for overcoming problems associated with conventional precursors. Presented is the evaluation of dimethylgallium azide, Me_2GaN_3 (1), bisdimethylamidogallium azide, $(\text{Me}_2\text{N})_2\text{GaN}_3$ (2), and bisdimethylamidoaluminum azide, $(\text{Me}_2\text{N})_2\text{AlN}_3$ (3) as potential precursors for AlN and GaN film growth. The compounds were evaluated for stability, ease of transport, temperature of decomposition and quality of film deposited. Amorphous thin films of GaN with a band gap of 3.4 eV were deposited with 2 at 250 °C. Increasing the substrate temperature to 580 °C resulted in the deposition of epitaxial GaN films. Polycrystalline AlN films were grown with 3 at 600 °C.

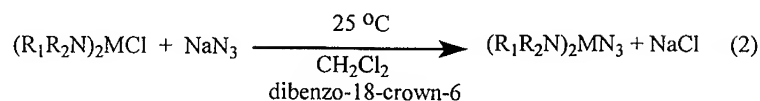
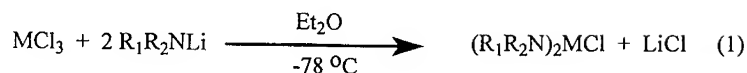
INTRODUCTION

The AlGaInN quaternary alloy system is uniquely suited for numerous device applications because the band gap can be varied from 1.9 to 6.2 eV by changing the alloy composition.¹ Growth of epitaxial group III (Al, Ga, In) nitride films has been hindered by a lack of suitably lattice matched substrates, the large equilibrium dissociation temperature pressure of N_2 from the nitrides at typical growth temperatures and predeposition reactions with the commonly employed metal-organic chemical vapor deposition (MOCVD) precursors. The most successful films have been grown at temperatures in excess of 900 °C by MOCVD. However, high growth temperatures may limit compatibility and incorporation of group III nitrides with existing fabrication technologies and devices. Attempts to lower deposition temperature include activated nitrogen sources and alternative precursors. While the use of alternate nitrogen or gallium sources has resulted in lower deposition temperatures, the deposited films are usually polycrystalline. We have devised a new class of single-source group III nitride precursors that embodies labile amido substituents and an azide nitrogen source. One such precursor 2, has been examined in detail and found to deposit epitaxial films of GaN at 580 °C.²

EXPERIMENTAL

Solid 1 was prepared from dimethylgallium chloride and sodium azide (eq 2). Solids 2 and 3 were prepared in high yields by means of the two-stage procedure summarized below (eq 1 and 2). Complete details on synthesis and structure of compounds 1,⁴ and 2² have been published previously.

* Current address is IBM, Watson Research Center, Yorktown Heights, NY 10598



2: $\text{R}_1 = \text{R}_2 = \text{Me}$ $\text{M} = \text{Ga}$

3: $\text{R}_1 = \text{R}_2 = \text{Me}$ $\text{M} = \text{Al}$

Film growth experiments with compounds 1, 2, and 3 were conducted in a low pressure hot wall reactor MOCVD reactor (Analysis Reactor) attached to a X-ray photoelectron spectroscopy (XPS) tool to enable in-situ sample transfer without exposure to ambient conditions. GaN and AlN films were grown on Si [001] substrates which were mounted on molybdenum stubs with indium foil. Substrates were cleaned with methanol and acetone before use. Precursors were sublimed from a glass saturator at 65-84 °C. Ultra-high purity nitrogen was used as the carrier gas flowing at 250 sccm. The N_2 was prewarmed and scrubbed by a Puratrem metal alloy getter operating at 250 °C. Substrate deposition temperatures varied between 480-500 °C, reactor pressure was maintained at 10 torr for all depositions. XPS analyses were performed using a VG ESCALAB Mark I spectrometer with Mg $\text{K}\alpha$ (1253.6 eV) and Al $\text{K}\alpha$, (1486.6 eV) x-rays as the excitation sources, operating at 275 W and 450 W, respectively. The base pressure of the analysis chamber was 6×10^{-11} Torr and during sample irradiation never exceeded 5×10^{-10} Torr. Sputter cleaned Ag[100] was used for calibration of the spectrometer. The Ag(3d_{5/2}) peak had a full width at half maximum value of 1.7 eV and a binding energy of 368.2 eV when the spectrometer is operated at a pass energy of 50 eV. The GaN standard was grown by atmospheric pressure MOCVD ex-situ of the Analysis Reactor with triethylgallium and ammonia at 1050 °C.⁵

RESULTS

Compounds 1,⁴ and 2² are colorless nonpyrophoric solids (m.p. = 60 °C). They do not enflame in air, but slowly decompose when exposed to ambient conditions. Compound 1 is a polymer in the solid state. The basic repeating unit $(\text{CH}_3)_2\text{GaN}_3$ forms a spiral along the a-axis of the orthorhombic unit cell. The gallium atoms in the chain are bridged by a single nitrogen of the azide group. Compound 2 which combines labile amido ligands and an azide nitrogen delivering substituent is a polymeric chain of dimers with the azide substituent bridging two gallium centers. Compound 2 (0.01 Torr at 90 °C) has a lower vapor pressure than compound 1 (0.05 Torr at 60 °C). Compound 3 is a colorless solid with a low melting point, 65-67 °C, and is readily decomposed. Careful Schlenk technique is necessary during synthesis and handling to prevent premature decomposition. A dimeric structure for compound 3 is suggested by similarity arguments with compound 2, the detection of the dimer by mass spectroscopy and the equivalence of the ^1H and $^{13}\text{C}\{^1\text{H}\}$ resonances.³

Pyrolysis experiments with compounds 1,⁶ and 2² were conducted. The azide ligand of compound 1 was observed to decompose at 375 °C and the methyl-gallium bond to cleave at 425 °C. Decomposition of 2 was observed at 250 °C with cleavage of the Ga-NMe₂ bond.

Film growth experiments with compounds 1,⁵ 2² and 3 were conducted in a chemical beam epitaxy (CBE) reactor at low growth pressures (10^{-4} to 10^{-5} Torr). A minimum film

growth temperature of 450 °C with compound 1 was utilized to ensure cleavage of the methyl-gallium bond. Crystalline quality of the GaN films grown with compound 1 is independent of the substrate template. Highly oriented wurzitic (0002) polycrystalline GaN films were deposited on sapphire, (100) and (111) GaAs, and amorphous quartz. In agreement with thermolysis results, amorphous GaN was grown at 250 °C with compound 2. Epitaxial growth of GaN on (0001) sapphire was observed at higher deposition temperatures. Film growth at 600 °C with 3 was observed by scanning electron microscopy but no discernible x-ray diffraction pattern was obtained.

The crystalline quality of the films deposited in the Analysis Reactor was poor relative to the films grown in the CBE reactor. However, no attempt was made to optimize deposition conditions in the Analysis Reactor. XPS results are summarized in Figures 1-4.

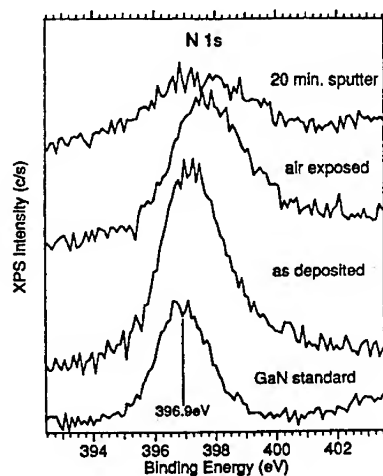
DISCUSSION

The GaN and AlN films deposited with 1, 2, and 3 in the Analysis reactor and the GaN standard had a surface contamination layer consisting primarily of carbon and oxygen. The surface of the films were cleaned by sputter etching with argon for 30 minutes. A reduction in both carbon and oxygen is observed after etching of the film surface. However, sputter etching of the nitride films resulted in preferential removal of nitrogen as evidenced by a marked decrease in N(1s) signal intensity making quantitative assessment of the nitride films difficult (Fig. 1).

The as deposited GaN films grown with 1 and 2 had a Ga 3d binding energy of 19.9 eV. After a 3 hour air exposure of a GaN film grown with 1, the Ga/O ratio decreased from 1.0 to 0.69 and the maxima of the Ga 3d spectra shifted to a higher binding energy 20.2 eV (Fig. 2 and 3) implicative of Ga₂O₃ formation on the surface. Sputter etching of the GaN films grown with 1 and 2 shifted the maxima of the Ga 3d peak to lower binding energy of 18.7 eV (Fig. 2) suggesting the formation of metallic gallium. Only a small 0.1 eV shift from 19.6 to 19.5 eV was observed in the Ga 3d peak after sputtering the GaN standard. The GaN films appear to decompose during sputter etching with loss of nitrogen and formation of metallic Ga. The resultant films are composed of metallic Ga and GaN (Fig. 3). This degradation of GaN film quality during sputter etching has been previously observed.⁷

The as deposited GaN films grown with 1 and 2 had a Ga/N peak area ratio of 1.0 and 2.0, respectively. The as deposited GaN standard had a Ga/N peak area ratio of 0.40. After sputter etching and loss of nitrogen, the Ga/N ratio of the GaN standard doubled to 0.80 as did the Ga/N ratio of the GaN films grown with 1 and 2 to ~1.8 and 2.5, respectively. The nitrogen present in the GaN films grown with 1 and 2 and in the GaN standard is bound as the nitride (Fig. 4). A small shift from 397.3 to 396.9 eV is observed in the N(1s) binding energy after sputtering (Fig. 2). In literature, the N(1s) binding energy on silicon surfaces is 397.4-397.7 and is 396.6 eV on metal surfaces.⁸ The shift to lower binding energy observed for the GaN films grown with 1 and 2 is consistent with the formation of metallic Ga after sputtering.

1.)



2.)

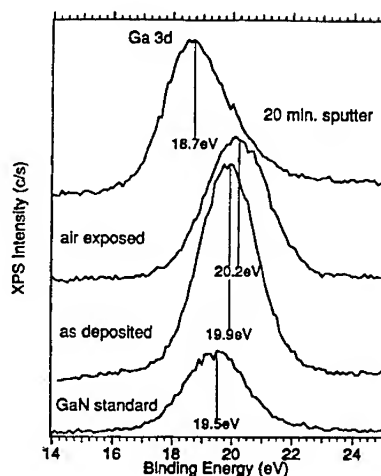
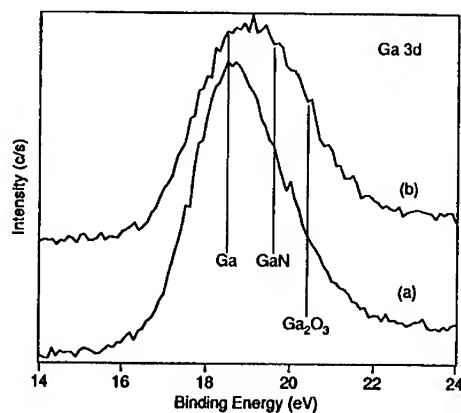


Figure 1.) N 1s X-ray photoelectron spectra from GaN standard after sputtering and GaN films grown with 1 as deposited, after 3 h air exposure and after sputtering. Figure 2.) Ga 3d X-ray photoelectron spectra from GaN standard after sputtering and GaN films grown with 1 as deposited, after 3 h air exposure and after sputtering.

3.)



4.)

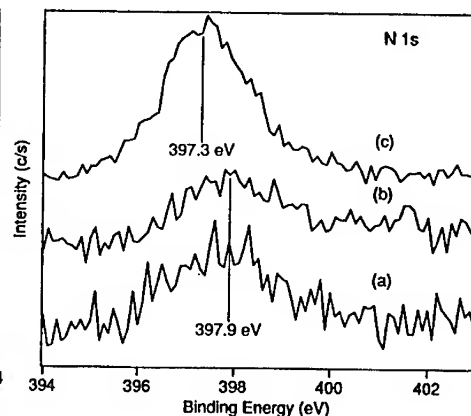


Figure 3.) Comparison of Ga 3d spectra from GaN films grown with (a) 1 and (b) 2 after sputtering. Figure 4.) Comparison of N 1s spectra from GaN films grown with (a) 1, (b) 2, and (c) 3 after sputtering.

The XPS results for AlN film growth with compound **3** differs from the GaN results. The as deposited films grown with compound **3** contain relatively large amounts of aluminum (45.5%), carbon (21.6%), and oxygen (17.8%) relative to nitrogen (15.1 %). In contrast to the GaN films, sputter etching improved the Al (60.5%) to nitrogen (24.1 %) ratio. A reduction in carbon to 12.6% and oxygen to 2.7% was observed as well. After sputter etching, a small shift (0.2 eV) from 396.5 to 396.7 eV to higher binding energy in the N(1s) spectrum is observed indicative of the improved Al/N ratio.

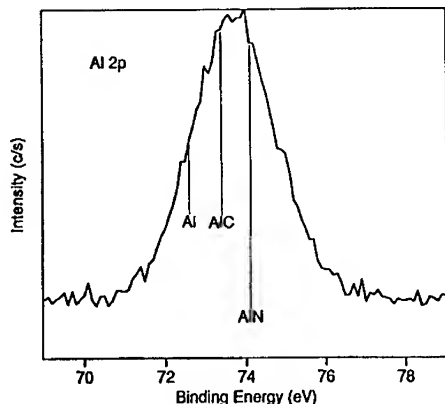


Figure 5.) Al 2p spectra from AlN film grown with **3** after sputtering.

The Al 2p peak at 73.6 eV (Fig. 5) is a mixture of AlN (74.1) eV⁹ and aluminum carbide or methyl aluminum at (73.4). The binding energies for these two types of carbon (methyl or carbide) bound to aluminum are known to be nearly identical. The C (1s) peak at 281.7 eV attributed to aluminum carbide, because the carbon binding energy is observed at a lower binding energy than methyl carbon bonded to aluminum at 283.4 eV or bulk carbon at 285 eV.¹⁰

CONCLUSIONS

In summary, a new class of GaN and AlN single-source precursors has been developed which feature labile amido leaving groups and an azide nitrogen delivering moiety. These precursors were successfully used to deposit GaN and AlN films in a CBE reactor and by low pressure MOCVD.

ACKNOWLEDGMENTS

This work was supported by the Science and Technology Program of the National Science Foundation NSF grant CHE 8921120, NSF Grant CHE-9108228, and the State of Texas Advanced Technology Program. The authors gratefully acknowledge Sandra R. Whaley, Peter M. Blass, and Beth A. Walden for their assistance with the XPS results.

REFERENCES

1. Comprehensive reviews have been recently published. (a) Morkoc, H.; Mohammad, S.N.; *Science* **1995**, 267, 51. (b) Morkoc, H.; Strite, S.; Gao, G.B.; Lin, M.E.; Sverdlov, B.; Burns, M. *J. Appl. Phys.* **1994**, 76(3), 1363. (c) Strite, S.; Morkoc, H. *J. Vac. Sci. Technol. B* **1992**, 10(4), 1237.
2. Neumayer, D.A.; Cowley, A.H.; Decken, A.; Jones, R.A.; Lakhota, V.; Ekerdt, J.G. *J. Am. Chem. Soc.* **1995**, 117, 5893.
3. Compound 3, mp 65-67 °C, ^1H NMR (300.15 MHz, C_6D_6) δ 2.71 (s, 6H, N-CH₃), $^{13}\text{C}\{^1\text{H}\}$ NMR (75.48 MHz, C_6D_6) δ 42.0 (s, N-CH₃), MS (CI⁺, M = C₈H₂₅N₁₀Al₂): 314 (M), 274 (M-N₃), IR (NaCl plates) 2955 (s), 2922 (s), 2851 (s), 2820 (s), 2768 (s), 2497, (w), 2141 (s), 1461 (s), 1409 (w), 1376 (m), 1308 (w), 1266 (s), 1231 (m), 1156 (s), 1114 (m), 1069 (m), 1037 (s), 977 (s), 897 (s), 825 (w), 722 (w), 670 (s), 609 (m).
4. Atwood, D.A.; Jones, R.J.; Cowley, A.H.; Atwood, J.L.; Bott, S.G. *J. Organomet. Chem.* **1990**, 394, C6.
5. GaN film supplied by R.D. DuPuis. Film preparation detailed in Fertitta, K.G.; Holmes, A.L.; Ciuba, F.J.; Dupuis, R.D. *J. Electron. Mater.* **1995**, 24, 257.
6. Lakhota, V.; Neumayer, D.A.; Cowley, A.H.; Jones, R.A.; Ekerdt, J.G. *Chemistry of Materials* **1995**, 7, 546.
7. Carin, R.; Deville, J.P.; Werckmann, J. *Surf. Interface Anal.* **1990**, 16, 65.
8. Zhu, X.-Y.; Wolf, M.; Huett, T.; White, J.M. *J. Chem Phys.* **1992**, 97, 5856 and references cited therein.
9. (a) Baier, H.U.; Monch, W. *J. Appl. Phys.* **1990**, 68, 586 and references cited therein. (b) Kovaich, J.A.; Kasperkiewicz, J.; Lichtman, D.; Aita, C.R. *J. Appl. Phys.* **1984**, 55, 2935. (c) Sung, M.M.; Jung, H.D.; Lee, J.-K.; Kim, S.; Park, J.T.; Kim, Y. *Bull. Korean Soc.* **1994**, 15, 79.
10. Maruyama, B.; Ohuchi, F.S.; Rabbenberg *J. Mater. Sci. Lett.* **1990**, 9, 864.

THE SURFACE CHEMISTRY OF TRIALLYLAMINE ON Si(111) AND ITS COADSORPTION WITH TRIETHYLGALLIUM

Dirk FREUNDT, Georg LANDMESSER, Angela RIZZI[#] and Hans LÜTH

Institut für Schicht- und Ionentechnik (ISI), Forschungszentrum Jülich, 52425 JÜLICH, Germany

[#]Dipartimento di Fisica, Università di Modena, via Campi 213/A, 41100 MODENA, Italy, rizzi@unimo.it

ABSTRACT

The surface chemistry of Triallylamine (TAA), $(C_3H_5)_3N$ on Si(111) has been studied by adsorption under UHV conditions and *in-situ* characterization. High Resolution Electron Energy Loss Spectroscopy (HREELS) yields the spectrum of vibration modes at the surface, and X-ray Photoelectron Spectroscopy (XPS) yields the chemical bonding and the partial concentration of the different adsorbates in the near surface region. The tertiary amine TAA physisorbs at RT without dissociation. Successive annealing steps of the physisorbed phase induce the dissociation of the amine at 400 °C. At higher temperatures the allyl groups are partially desorbed and the rest fully dissociated at 600 °C, where the hydrogen leaves the surface and the nitrogen and carbon start to diffuse into the Si substrate. A very similar behaviour is observed for the adsorption of TAA on a heated Si substrate. The coadsorption with Triethylgallium (TEG) in the temperature range 500-800 °C does not induce significant changes in the reaction at the Si surface. A negligible quantity of Ga is detected at the surface after codeposition in the whole investigated temperature range. The growth of a GaN phase has not been observed, neither on Si(111) nor on $Al_2O_3(0001)$ substrates.

INTRODUCTION

The growth of III-Nitride semiconductor materials represents a difficult task, as compared with the other III-V compounds, due to the poor efficiency in the incorporation of N. In fact, the high equilibrium vapor pressure of nitrogen requires either the use of a large throughput and high substrate temperatures for the thermal dissociation of ammonia, as in MOCVD growth processes, or a plasma generation to get highly reactive N, as in ECR- or RF-plasma assisted MBE. In the latter growth processes, especially in ECR sources energetic ions are created which degrade the material quality by introducing point defects. A further intrinsic disadvantage in the MOCVD growth of nitrides is the large H background pressure during growth, which has been shown to passivate Mg acceptor dopants.

Reduced substrate temperatures, a hydrogen free process, impinging molecules of thermal energy together with the possibility for selective growth could be achieved by MOMBE if new precursors can be identified as replacement for the more stable NH_3 . The substitution of organic radicals for each hydrogen in the ammonia results in the formation of amines, whose stability decreases by increasing the number of replaced H, from primary (RNH_2) down to tertiary (R_3N) amines. A further important point is the stability of the attached organic rests, after the N-R bond has been broken; favourable for a carbon free nitride layer growth is that the R complexes possibly leave the surface without further dissociation, *i.e.* they should be stable at typical growth temperatures.

Triallylamine is a tertiary amine and the allyl radical which is formed after dissociation from the N atom is more stable than *e.g.* alkyl radicals with single C bonds. Each carbon in the allyl radical $\text{CH}_2=\text{CH}-\text{CH}_2$ is sp^2 hybridized, giving rise to σ -bonds with each neighbor atom; the remaining three p electrons contribute to a 'one and a half' π -bond among the C atoms (mesomery or delocalized C=C bond). TAA has been successfully employed in MOCVD for the doping of II-VI semiconductors [1].

In a MOMBE process, due to the reduced gas pressures as compared with MOCVD, the reactions among the different precursors take place at the substrate surface rather than in the gas phase. Surface analysis methods are therefore particularly suited to follow the reaction/dissociation paths and the incorporation at the growing surface. After each deposition step, *in-situ* High Resolution Electron Energy Loss Spectroscopy (HREELS) yields the spectrum of vibration modes at the surface and X-ray Photoelectron Spectroscopy (XPS) the chemical bonding and the partial concentration of the different adsorbates in the near surface region. Due to its conductive properties and the absence of any spectral feature in the infra-red region, a silicon substrate has been chosen for the adsorption experiments. The insulating sapphire has been investigated at the end of this study to verify the potential of TAA as a precursor in the GaN growth, which is known to give the best results on this substrate so far.

EXPERIMENTAL

The experiments were carried out in a three-unit UHV system, equipped with a deposition and two analysis chambers [2]. The gases (TAA and TEG) were introduced into the deposition unit through separated Baratron controlled gas lines. The HREELS spectra are all measured under reflection geometry (dipole scattering regime) with a primary beam energy $E=5$ eV, an incidence angle $\theta=60^\circ$ and a resolution (FWHM) of 3 meV for the electron beam in the spectrometer. For the XPS analysis monochromatized Al-K α radiation ($h\nu=1486.6$ eV) was used with different pass energies corresponding to overall resolutions of 1.6, 0.56 and 0.42 eV, chosen depending on the intensity of the different measured core levels. The Si(111) substrates were prepared *in-situ* by annealing at 820 °C for 15 minutes giving a (7x7) surface reconstruction as confirmed by Low Energy Electron Diffraction and HREELS.

TAA ADSORPTION ON Si(111)

Fig. 1 shows the HREEL spectrum after 1 minute exposure to triallylamine. Two main spectral regions are identified. The stretching bands of CH_x complexes at 2700-3300 cm^{-1} and a broad band between 900 and 1500 cm^{-1} . On both sides of this latter region at 750 cm^{-1} and at 1650 cm^{-1} two small structures are also observed. For comparison the IR absorption spectrum of TAA is superimposed as a shaded area [3] and an overall good agreement is found, which gives evidence of molecular adsorption at RT. Assignments for each of the single bands are also given in the figure. A few points should be mentioned which are as follows. The presence of the broad band on the lower energy side is a fingerprint of the molecular adsorption of TAA. The shoulder at 2800 is due to a $>\text{CH}$ stretching mode under the assumption that this group is bonded to $\text{N}-\text{CH}_2$ and therefore reveals the presence of the N-allyl bond. The stretching mode at 1650 cm^{-1} ($\nu \text{ C}=\text{C}$) is a hint for the existence of the allyl group. The vibration at 750 cm^{-1} corresponds to the Si-C stretching mode.

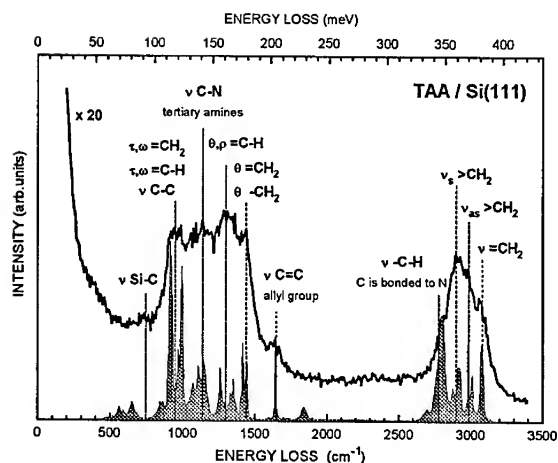


FIG. 1 - HREEL spectrum (continuous line) measured after the adsorption of TAA on Si(111) at RT (1 minute, $p_{\text{TAA}} = 2.5 \cdot 10^{-5}$ Torr). The IR absorption spectrum (shaded) is reported for comparison and the assignment of the principal vibration modes is also indicated. (ν : stretching mode; ρ : rotation mode; τ, ω : twisting mode; θ : scissor mode).

The core level XPS (not reported) also confirm the molecular physisorption of TAA on Si(111) at RT. The N-1s experimental spectrum is fitted with just one component at 399.7 eV which corresponds to the bonding of nitrogen in organic compounds; the C-1s core level shows a two component structure at 284.9 eV and 286.2 eV assigned to the C-C and C-N bonds, respectively.

After RT adsorption the thermally induced dissociation of TAA has been studied by successive annealing and characterization cycles. Fig. 2 shows the HREEL spectra measured at RT after each annealing step. Up to 300 °C the main loss features characterizing the TAA molecular physisorption are retained. The Si-C stretching mode at 750 cm^{-1} gains intensity which shows that N-allyl bonds are increasingly broken and the allyl radicals chemisorb at the Si surface. At 400 °C the fingerprint loss region for molecular TAA adsorption is no more recognized and also the typical shoulder on the low energy loss side of the CH_x band is missing. Partial dissociation together with desorption of the allyl groups are observed: elemental hydrogen remains at the surface (ν Si-H at 2100 cm^{-1}) and the overall intensity of the loss spectrum decreases as is seen from the increasing magnification factor. The spectra are all normalized to the elastic peak intensity at zero energy loss (not shown). At 500 °C the trend to desorption and further dissociation of the allyl groups continues and at 600 °C the surface is nearly free of hydrogen and carbon hydrides. The evolution of the Si-C stretching band with its shift towards higher loss energies is a hint for carbon diffusing into the Si substrate at increasing temperatures. In fact, the only structure that is left at 800 °C shows an energy loss very close to that of

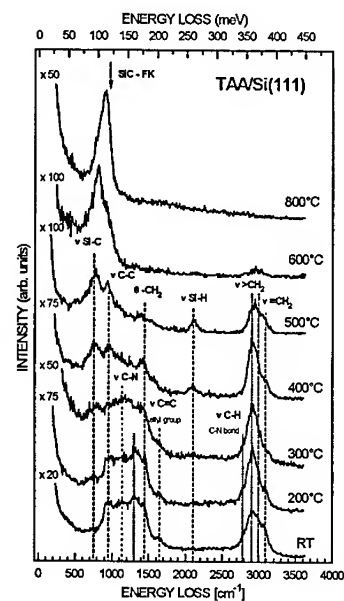


FIG. 2 - Normalized HREEL spectra measured after the adsorption of TAA on Si(111) at RT and after successive annealing steps (5 min) at the indicated temperature.

the Fuchs Kliewer phonon vibration in SiC. The HREEL spectra do not give information about the nitrogen at the highest annealing temperatures, since no further losses can be identified, once the TAA molecule is broken or it happens to be superimposed to the Si-C mode. It will be shown in the following that XPS reveals, even if in very small quantity, N incorporation with the formation of a $\text{Si}_x\text{C}_{1-x}\text{N}_x$ matrix at 800 °C.

After having studied the thermally induced dissociation of TAA, adsorbed on Si(111) at room temperature, deposition of the triallylamine on the substrate held at elevated temperatures has been performed. The deposition time amounts to 5 minutes and the amine pressure is $p_{\text{TAA}}=2.5 \times 10^{-5}$ Torr. Each deposition is performed on a freshly prepared Si surface and the temperature range 500-800 °C is chosen to be of interest for a nitride growth process. The HREEL spectra measured after each deposition resemble those reported in Fig. 2 at the corresponding temperature, showing that the gas molecules arriving at the heated substrate first adsorb and then dissociate, by following the same path as before.

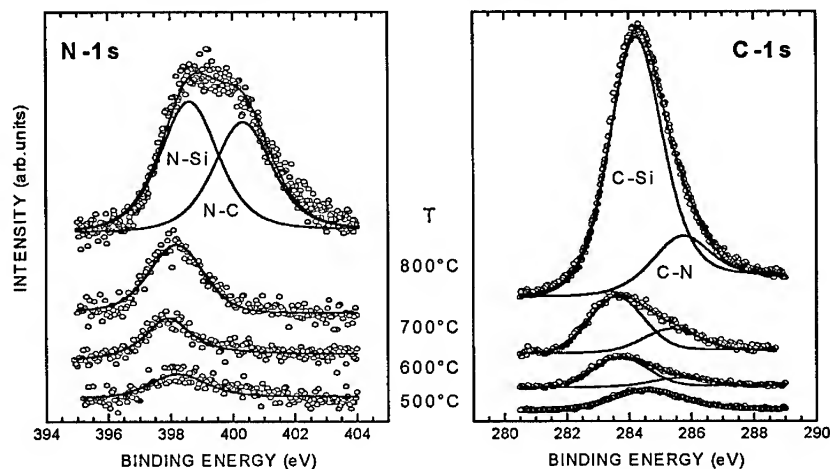


FIG. 3 - Core level photoelectron spectra measured after the adsorption of TAA on Si(111) heated at the indicated temperature (circles). The adsorption time is 5 min and $p_{\text{TAA}}=2.5 \times 10^{-5}$ Torr. The left panel shows the N-1s and the right one the C-1s core level excitation. The single components and the model spectra resulting from the fitting procedure are indicated as continuous lines.

Fig. 3 shows the N-1s and C-1s core level spectra measured by XPS after each deposition. Relative intensities have to be considered only within one core level series and not between different core levels. At increasing deposition temperatures, the relative amount of N and C deposited at the surface increases. Up to 700 °C the N-1s core level shows a component at about 398 eV binding energy which is attributed to the N-Si chemical bond and its shift to higher binding energy at increasing temperature is a sign of N diffusing into the Si matrix [4]. The new component at 400.3 eV appearing at 800 °C corresponds to the N-C bonding state. The C-1s core level shows a similar development with the deposition temperature. The component at the lower binding energy corresponds to the Si-C bond, it shifts towards higher energies with increasing temperatures up to 284.2 eV at 800 °C. A similar shift has been observed in amorphous $\text{Si}_{1-x}\text{C}_x$ at increasing carbon concentration [5]. The N-1s component developing at higher binding energy, 285.7 eV at 800 °C, is attributed to the N-C bonding state.

Both core level spectra in Fig. 3 indicate the tendency of nitrogen and carbon incorporation in the Si substrate with increasing temperature. The relative concentrations calculated from the

XPS core level intensities show the formation of a SiC like phase with about 5% of N at 800 °C. These concentrations are determined within the photoelectron escape depth which is about 20 Å. It should be mentioned that the XPS spectra measured during the thermally induced dissociation of TAA at the Si surface give one and the same picture.

The results discussed so far show that triallylamine is easily dissociated at the Si(111) surface heated to typical growth temperatures between 500 and 800 °C. However, on Si the carbon incorporation is very high and a C:N intensity ratio of 11:1 is calculated from the XPS results. This value is very close to the one in the molecule, 9:1, suggesting that TAA completely dissociates so that the allyl groups do not effectively desorb. This is not surprising by considering the relatively high bond strengths of C-Si and N-Si, 104 and 105 kcal mol⁻¹, respectively, as compared with typical carbon hydrides bonds, *e.g.* 104 kcal mol⁻¹ for the dissociation of the first C-H bond in CH₄. This means that substrate materials other than Si have to be considered in order to verify the potential of TAA for nitride growth. Before addressing this point the surface reaction after the codeposition of triallylamine and triethylgallium on Si(111) has been studied.

TAA/TEG CODEPOSITION ON Si(111)

Triethylgallium, (C₂H₅)₃Ga, is the typical gallium source used in III-V growth processes by MOMBE. In this experiment, TEG and TAA are deposited on a heated Si(111) surface in the temperature range 500-800 °C. The reported results are obtained with a partial pressure ratio $p_{\text{TAA}}:p_{\text{TEG}} = 5 \times 10^{-5} : 5 \times 10^{-6}$ Torr = 10:1; no significant difference has been observed by applying other ratios in the range from 1:1 up to 100:1.

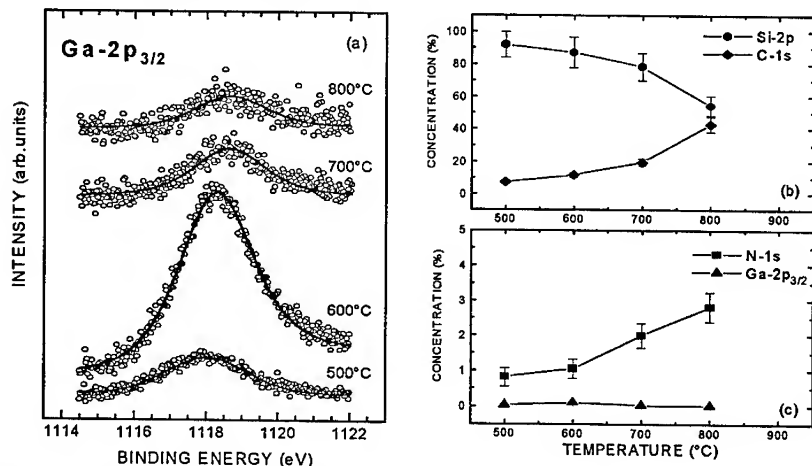


FIG. 4 - (a) Ga-2p_{3/2} core level excitation spectra measured after the codeposition of TAA and TEG on Si(111) at the indicated temperatures. The single components resulting from the fitting procedure are given as continuous lines. Relative concentrations, within the photoelectron escape depth, $\lambda \sim 20$ Å, as calculated from the XPS core level intensities for (b) silicon and carbon, (c) nitrogen and gallium.

The HREEL spectra and the XPS N-1s and C-1s core level spectra, not reported for space reasons, resemble in their behavior those observed in the previous section (Fig. 2 and Fig. 3). The presence of TEG does not induce significant differences with respect to the adsorption picture for TAA, and it is this latter which predominantly contributes to the measured spectral features. Fig. 4 shows the Ga-2p_{3/2} core level excitation together with the relative concentrations of the different

chemical species involved, as determined by the XPS core level intensity. The binding energy of 1118 eV at 500 °C agrees with the literature data for TEG on Si [6]; a maximum in intensity is revealed at 600 °C. However the relative concentration of Ga in the near surface region is almost negligible in the whole temperature range, Fig.4c. The codeposition experiment results in the formation of a SiC like phase (Fig. 4b) containing a small percent of nitrogen, as in the case of only TAA deposition.

A possible explanation for the negligible sticking coefficient of TEG in this experiment is that the Si surface is nearly saturated with carbon atoms and complexes and no sites are available for the adsorption of Ga, leaving TEG mostly in the gas phase. No trace of GaN formation has been revealed in the investigated temperature range, even at 600 °C where TEG is known to dissociate at the surface and still has a desorption rate low enough to allow growth of III-V compounds in a MOMBE process [7].

CONCLUSIONS

It might be possible that the Si substrate chosen for the study of the surface reaction is not the best choice for the growth of nitride phases by the used source materials. In fact it is known that mask materials like SiN_x are not able to catalyze the metal alkyl source and for this reason allow selective growth in MOMBE. Many codeposition runs with TAA and TEG have therefore been performed in the temperature range 600-800 °C on Al₂O₃(0001) substrates, which is known to be the best substrate for GaN growth so far. However even on this substrate we did not succeed in growing GaN with TEG and TAA sources and the substrate remained completely free of any adsorbate, independent of the chosen growth parameters. A steric effect might be the cause of the observed lack of adsorption and growth; furthermore the formation of C=N bonds during the dissociation of these amines might not be excluded. It should be mentioned, in conclusion, that to our knowledge the only gas processes which successfully showed the growth of GaN either use atomic Ga in combination with e.g. ammonia [8] or TEG with activated nitrogen [9]. In the first case the presence of Ga at the surface catalyzes the dissociation of NH₃, whereas in the other case enough reactive nitrogen is provided by the plasma source, which catalyzes the dissociation of the alkyl metal.

ACKNOWLEDGMENTS

We are grateful to our chemist colleagues Hilde Hardtdegen and Manfred Müller for interesting discussions.

REFERENCES

1. W.Taudt, B.Wachtendorf, F.Sauerländer, S.Lampe, H.Hamadeh, H.Heuken, DPG Berlin (1995)
2. A.Rizzi, B.N.E.Rösen, D.Freundt, Ch.Dieker, D.Gerhsen and H.Lüth, Phys. Rev. B 51, 17780 (1995)
3. K.G.R. Pachler, F.Matlok, H.U.Gremlich, *Merk FT-IR Atlas* (VCH GmbH, Weinheim, 1988), p. 733
4. R.Kärcher, L.Ley, R.L.Johnson, Phys. Rev. B 30, 1896 (1984)
5. R.C.Fang and L.Ley, Phys. Rev. B 40, 3818 (1989)
6. H.Hirayama, C.Sasaoka, T.Tasumi, Y.Ohshita, Appl. Phys. Lett. 54, 126 (1988)
7. C.R.Abernathy, in *Handbook of Thin Film Process Technology*, Eds. D.A.Glocker, S.Ismat Shah, A2.1 (IOP Publishing Ltd, 1995)
8. R.C.Powell, N.-E. Lee, J.E.Greene, Appl. Phys. Lett. 60, 2505 (1992)
9. C.R.Abernathy, J. Vac. Sci. Technol. A 11, 869 (1993)

GAS PHASE ADDUCT REACTIONS IN MOCVD GROWTH OF GaN

A. THON, T.F. KUECH

Department of Chemical Engineering, University of Wisconsin, 1415 Engineering Drive, Madison, WI 53706, thon@quiche.che.wisc.edu

ABSTRACT

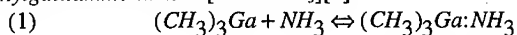
Gas phase reactions between trimethylgallium (TMG) and ammonia were studied at high temperatures, characteristic to MOCVD of GaN reactors, by means of insitu mass spectroscopy in a flow tube reactor. It is shown, that a very fast adduct formation followed by elimination of methane occurs. The decomposition of TMG and the adduct - derived compounds are both first order and have similar apparent activation energy. The pre-exponential factor of the adduct decomposition is smaller, and hence is responsible for the higher full decomposition temperature of the adduct relative to that of TMG.

INTRODUCTION

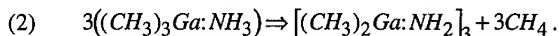
The emergence of metal organic vapor phase epitaxy (MOVPE) as the major technique for the growth of GaN for device structures[1], has resulted in an increased activity in understanding the growth process. The growth of device-quality GaN is complicated by gas phase interactions between *trimethylgallium* (TMG or $(\text{CH}_3)_3\text{Ga}$) and ammonia, NH_3 . These interactions can lead to changes in the nature, or the gas phase depletion of growth nutrients, leading to a degradation in the growth uniformity, quality and efficiency[2]. The main gas phase reaction is a strong adduct formation between NH_3 and TMG[3]. In this study, we have directly monitored this gas phase reaction in order to better understand its impact on the growth process. The reactions have been monitored over the temperature range of 200-800°C which is typically encountered in the gas phase environment of the MOVPE reactor, as the growth nutrients are transported to the growth front.

The gas phase reactions of both TMG and NH_3 , individually, are relatively understood. The decomposition temperature of TMG was found to be 370 - 500°C[4,5,6,7] under most experimental conditions. It is decomposed in stepwise first order reactions, where at each step one CH_3 -Ga bond is broken. The reaction products are dependent on the ambient gas, but it is agreed, however, in all studies, that methane is the main product released in the decomposition. The apparent activation energy measured for the first methyl group is ~58-60 kcal/mol and 35.4 kcal/mol for the second[4]. Under similar conditions of temperature, ammonia is quite stable. The gas phase decomposition of NH_3 is generally second order with a high activation energy[8].

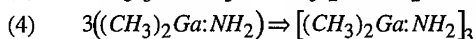
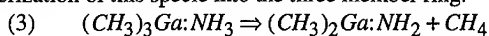
At low temperatures, a Lewis acid - Lewis base interactions between TMG (electron acceptor) and NH_3 (electron donor) can form the intermediate adduct compound, *Trimethylgalliummonamine* $[\text{TMG}:\text{NH}_3]$ [3]:



The structure and thermodynamic of this adduct at low temperature have been intensely studied[9,10,11]. It has a moderate melting point of 31°C and has a low vapor pressure of about 1 Torr at room temperature. The strength of the Ga-N coordination bond was estimated to be 21 kcal/mol [12]. Recent studies[13] show that above 90°C one methane molecule per one Ga atom is eliminated, and a six member ring *Cyclo(triamido-hexamethyltrigallium)* $[(\text{CH}_3)_2\text{Ga}:\text{NH}_2]_3$ is formed in the reaction:



This overall reaction has been suggested to proceed in two steps. The first step is the hydrogen-elimination reaction with the subsequent release of a CH_4 [12]. The second step is the oligimerization of this specie into the three member ring.



The estimated energy required for the elimination process is 49 kcal/mol [12].

The gas phase reaction between $(CH_3)_3Ga$ and NH_3 at elevated temperatures, characteristic of MOVPE growth environments ($\sim 200^\circ C$ - $1100^\circ C$) is still not understood. The actual significance of adduct formation at these higher process temperatures has not been determined, despite the potential impact it may have on reactor modeling and optimization and on process design.

EXPERIMENT

We studied the high temperature gas phase reactions between TMG and NH_3 by means of *in situ* mass spectrometry within a flow tube isothermal reactor [15], shown in fig. 1. The gas phase decomposition of TMG, NH_3 , and the combined TMG- NH_3 systems in H_2 and D_2 were studied over the temperature range of 200-800°C. A two temperature zone reaction furnace was used. This reactor circumvents any premature decomposition of the TMG prior to mixing and reaction with the NH_3 , and avoids any unintentional adduct formation at room temperature. The two primary reactants, TMG and NH_3 , were allowed to mix in the first hot zone of the reactor, that was kept in 150°C. This adduct and its initial reaction products are transported to the second

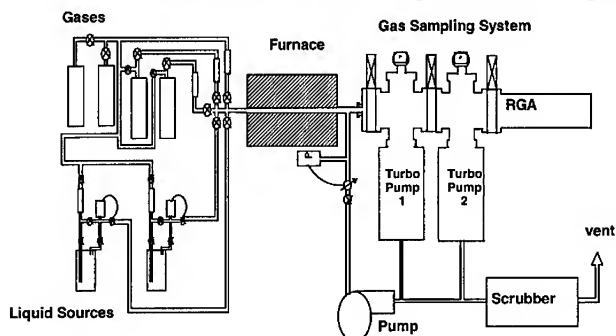


Figure 1: Schematic of the experimental system

temperature zone where they undergo decomposition. The reacted stream was sampled from within the hot isothermal regions of the reactor through $\sim 75 \mu m$ diameter quartz nozzle. The gas was further expanded in molecular flow and sampled by a residual gas analyzer (RGA). The inlet gas stream always contained 0.5% of Ar during all experiments, to allow for data normalization and to avoid gas expansion artifacts. Data were obtained as function of temperature through the continuous ramping of the reactor temperature. The TMG mole fraction in the inlet of the reactor was 0.015 - 0.05. Measurements of the co-pyrolysis of TMG and ammonia utilized both NH_3 , as well as deuterated ammonia (ND_3), in order to label the products and to distinguish between possible reaction pathways. All experiments were done at a pressure of 76 Torr. Peaks at m/e

values of 16, 17, 20, 30, 69, 84 and 99 were monitored corresponding to molecular fragments CH_4 , CH_3D , ND_3 , C_2H_6 , Ga, CH_3Ga and $(\text{CH}_3)_2\text{Ga}$ respectively.

RESULTS

The gas phase homolysis of TMG in H_2 and D_2 was carried out and compared to previous FTIR measurements of TMG decomposition in H_2 [7] as a reference, and served as a base line for understanding the decomposition of TMG in H_2/NH_3 . Since the electron impact in the RGA immediately breaks the adduct Ga-N bond[14], the peaks at $m/e = 69, 84$ and 99 , characteristic of TMG decomposition, are also indicative of the primary adduct $(\text{CH}_3)_3\text{Ga}:\text{NH}_3$ and the downstream product $(\text{CH}_3)_2\text{Ga}:\text{NH}_2$. However, as shown in fig. 2, differences between the reaction in H_2 and in H_2/NH_3 ambients were found in the ratio of the $m/e = 69$ and 84 to that of $m/e = 99$ peaks. This constant ratio in the peak height between the TMG/ H_2 and TMG/ H_2/NH_3 cases indicates that there is a gas phase reaction occurring, leading to a thermally stable product, presumably an adduct, up to temperatures of 500°C .

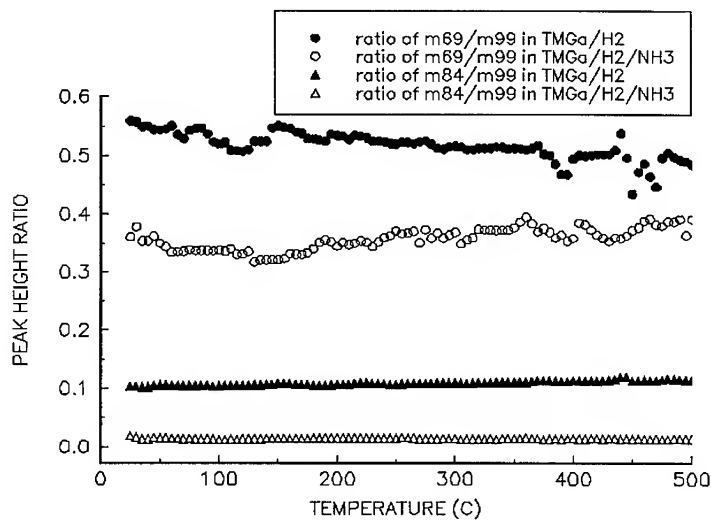


Figure 2: The relative peak height of TMG decomposition in hydrogen and hydrogen / ammonia ambients

The temperature dependence of decomposition, within the TMG/ H_2 and TMG/ H_2/ND_3 systems is presented in fig. 3. The decomposition of TMG in H_2 follows trends previously reported[4,5,6,7]. The principal reaction product is methane, CH_4 , with ethane, C_2H_6 , being found at higher temperatures. For the second case, several trends are readily noted. There is reaction between TMG and ND_3 resulting in the elimination of a single CH_3D molecule over the temperature range of 200°C to $\sim 500^\circ\text{C}$. No further reaction, beyond this initial release of methane is noted until a temperature of $\sim 500^\circ\text{C}$. Also noted is the decrease in the TMG (adduct) - derived

peaks that occurs at about 50°C higher than the TMG/H₂ mixture. The full decomposition results in the stepwise elimination of CH₃D. A total of three CH₃D per one TMG molecule are formed at high temperatures. In both cases, the simple mass balance between the calibrated peak heights of all carbon based peaks accounts for all of the initial carbon in the form of CH₄ and C₂H₆. Another important observation is the 1:1 release of methane, CH₃D (deuterated methane, m/e=17), to TMG feed upon mixing TMG and ND₃ at high temperature. A single methane molecule is immediately released over the relatively lower temperature range. This result most likely represents high temperature adduct formation followed by very fast elimination reaction, similar to that proposed for the low temperatures [12]. Fig. 4 shows Arrhenius plots of the decay of the m/e=99 signal for both systems, fitted to first order reaction. The apparent activation energy for the TMG/H₂ is 48.7±3 very close to that calculated from FTIR measurements. For the case of TMG/H₂/NH₃ the overall apparent activation energy for the elimination of the last two methyl groups is 50.5±1 kcal/mol. This value is very close to the previously measured for the homolysis of TMG in H₂.

DISCUSSION

While a complete reaction model for the high temperature decomposition of TMG:ND₃ species can not be obtained from these measurements, several conclusions can be made concerning the gas phase chemistry within a MOVPE growth environment. The formation of a gas phase adduct occurs at an extremely high rate within our flow tube reactor. The gas phase species, presumably TMG:ND₃ adduct follows the same reaction path as adducts formed at lower temperature, and immediately self-eliminates a CH₃D molecule at all temperatures monitored. The isotopically tagged ND₃ clearly identifies that this reaction occurs through the transfer of a deuterium from the ND₃ to a CH₃ on the TMG. The formation of the trimeric cyclic compound is predicted at low temperatures, however our experimental system would not be capable of determining these high molecular weight species. This methane-eliminated species is quite stable

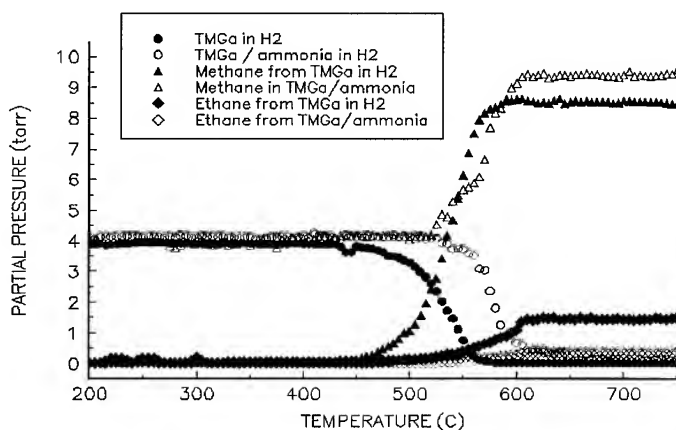


Figure 3: Temperature dependence of TMG decomposition in hydrogen and hydrogen / ammonia ambient

over the temperature range of 200-500°C. The shift in decomposition temperature, while possessing a similar activation energy to the TMG/H₂ pyrolysis, indicates that the reduction in the value of the pre-exponential factor in the kinetic rate expression is responsible for the higher stability of the adduct compared to that of TMG. Unlike TMG/H₂-based pyrolysis, we see very little C₂H₆ in the reaction products, even at high temperatures. The predominance CH₃D and the lack of C₂H₆ or CH₄ both indicate that the homolysis of methyl radicals with their subsequent reaction with excess ND₃ or H₂ in the gas phase is unlikely. The self-elimination of CH₃D from the initial adduct reaction product, appears to be the dominant reaction pathway. Decomposition proceeds until three CH₃D molecules are removed per initial (CH₃)₃Ga molecule. Final downstream reaction products have not been identified up to this point.

The implication of these studies for the design and operation of MOVPE reactors for GaN growth is several fold. In most or all MOVPE growth systems operating at conventional pressures (1-760

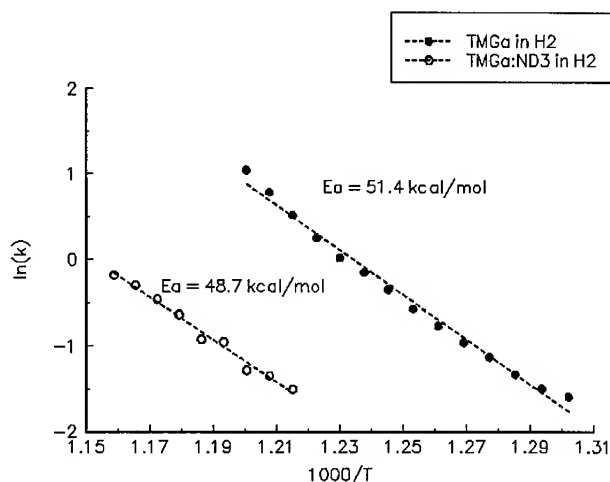


Figure 4: Arrhenius plots of TMG decomposition in hydrogen and hydrogen / ammonia

Torr), little (CH₃)₃Ga exists in the growth environment during NH₃ - based GaN growth. The rapid adduct formation reaction, together with the immediate release of a single methane molecule, implies that the dominant gas phase species within the reactor is ((CH₃)₂GaNH₂)_x. The reactions of this specie in the gas phase, through decomposition or further oligimerization, should be the principal mechanism by which the growth rate and growth rate uniformity is affected by the specific reactor design. Larger molecules, and eventually particles, will affect the growth rate through differences in the transport rate to the surface, due to a difference in diffusion and thermal diffusion coefficients. The further decomposition of this species can be suppressed by an appropriate design of the MOVPE reactor. The reaction kinetics and chemical pathways determined in this study are currently being used to provide a realistic model of the gas phase chemistry and growth rate behavior within our working MOVPE reactor. Further work is

currently in progress, aiming to understand how the above gas phase reactions can be controlled to allow for high quality growth.

ACKNOWLEDGMENTS

The authors would like to thank Anwar S. Safvi for discussion. Funding from the NSF-MRG on CVD mechanisms and the ARPA-URI on visible light emitters are acknowledged.

REFERENCES

1. I. Akasaki and H. Amano, *J. Crystal Growth* **146**, 455 (1995).
2. R. H. Moss, *J. Crystal Growth* **68**, 78 (1984).
3. B. S. Sywe, J. R. Schlup and J. H. Edgar, *Chem. Mater.* **3**(4), 737 (1991).
4. M. G. Jacko and S. J. W. Price, *Canadian Journal of Chemistry* **41**, 1560 (1963).
5. C. A. Larsen, N. I. Buchan, S. H. Li and G. B. Stringfellow, *J. Crystal Growth* **102**, 103 (1990).
6. M. Yoshida, H. Watanabe and F. Uesugi, *J. Electrochem. Soc.* **132**(3), 677 (1985).
7. S. P. DenBaars, B. Y. Maa, P.D. Dapkus, A. D. Danner and H. C. Lee, *J. Crystal Growth* **77**, 188 (1986).
8. J. E. Dove and U. S. Nip, *Canadian Journal of Chemistry* **57**, 689 (1979).
9. J. R. Durig, C. B. Bradly and J. D. Odom, *Inorg. Chem.* **21**, 1466 (1982).
10. M. J. Almond, C. E. Jenkins, D. A. Rice and K. Hagen, *J. Organomet. Chem.* **439**, 251 (1992).
11. G. E. Coates, *J. Chem. Soc.* , 2003 (1951).
12. A. Zaouk, E. Salvétat, J. Sakaya, F. Maury and G. Constant, *J. Crystal Growth* **55**, 135 (1981).
13. M. J. Almond, M. G. B. Drew, C. E. Jenkins and D. A. Rice, *J. Chem Soc. DALTON TRANS.* , 5 (1992).
14. F. H. Field and J. L. Franklin, *Electron Impact Phenomena*, Academic Press Inc, New York, 1957, pp. 53-79.
15. J.M. Redwing, T.F. Kuech, D. Saulys and D.F. Gaines, *J. Crystal Growth* **135**, 423 (1994).

PARASITIC REACTIONS BETWEEN ALKYLs AND AMMONIA IN OMVPE

C.H. CHEN, H. LIU, D. STEIGERWALD, W. IMLER, C.P. KUO, M.G. CRAFT
Hewlett-Packard Optoelectronics Division, San Jose, CA 95131; changhua_chen@sj.hp.com

Abstract

The parasitic reactions between ammonia and commonly used alkyls have been studied in a horizontal OMVPE reactor. The results indicate that parasitic reactions between TMAI and NH_3 is severe, leading to the necessity to grow AlN at low reactor pressure. On the other hand, parasitic reactions between $\text{TMGa}+\text{NH}_3$ and $\text{TMin}+\text{NH}_3$ are not significant and it is possible to grow GaN and GaInN at any reactor pressure.

Introduction

Gas phase parasitic reactions between group III and group V precursors have been troublesome in the development of OMVPE growth of III-V materials [1-4], especially when triethyl alkyls are used as the group III precursors at atmospheric pressure for the growth of In-containing materials [1-3]. The group III Lewis-acid reacts readily with the Lewis-base hydride to form adduct [5-6]. Usually, the adduct breaks up when it passes through the hot zone of the susceptor and has no adverse effect on crystal growth. In some cases, however, the adduct undergoes severe elimination reaction to produce less volatile polymers upstream of the susceptor and depletes the precursors for crystal growth [3, 6].

One of the most efficient techniques to reduce parasitic reactions (both adduct formation and elimination reaction) has been the use of low pressure growth, as was pioneered by Duchemin et al [7]. Reactor pressure is an effective parameter because the parasitic reaction is a bi-molecular reaction. As the reactor pressure is reduced, both reactant's concentrations are reduced. In addition, the flow velocity is increased at low reactor pressure, leading to a reduction in residence time of the reactants.

In this paper, the pressure dependence of GaN, AlN, and GaInN growth efficiencies are used to study the parasitic reactions between the NH_3 hydride and trimethylgallium (TMGa), trimethylaluminum (TMAI), and trimethylindium (TMin). The results indicate that while TMAI reacts strongly with NH_3 to deplete reactants when the reactor pressure is high, the reaction between NH_3 and other alkyls are minimal, even at atmospheric pressure.

Experimental

The OMVPE growth was done in a horizontal quartz reactor with a rectangular liner, which is placed inside a circular quartz tube. The cross-section of the rectangular tube is 7 cm wide and 4 cm high. The N source is 100% ammonia and the carrier gas is Pd-diffused H_2 . The substrate is (0001)-oriented Al_2O_3 . The group III and V precursors are separated in the gas manifold and mixed before they enter the quartz reactor. The distance between reactor entrance and substrate is about 15 cm.

The epilayer thickness was measured using an optical interferometer. The light source is a halogen lamp and the spectrum was detected with an Inspec IV CCD detector. The interference wavelength is used to calculate the layer thickness. The results of the optical

thickness measurements have been confirmed by cross-sectional scanning electron microscopy. X-ray measurement was done using a QCI double crystal x-ray diffractometer using a wide area detector. The x-ray source is Cu. The primary crystal is GaAs. The measured X-ray peaks are (0004) peak for Wurtzite structures.

Results

This horizontal reactor has been used to grow GaN and other related nitride materials. The x-ray rocking curve's FWHM of several μm thick GaN epilayers varies between 150 arc-sec to 400 arc-sec. The electron background carrier concentration typically is in the low 10^{16} cm^{-3} . The highest electron mobility is about $600 \text{ cm}^2/\text{V}\cdot\text{sec}$ at room temperature and the bound exciton FWHM at 2K PL measurement is 2.4 meV. Indium concentration as high as 25% has also been obtained in this reactor. These results indicate that the material quality grown using this reactor is high and the observations to be discussed later represent what is actually happening in a real OMVPE reactor (rather than a reactor designed to do decomposition study, for example).

Atmospheric growth of GaN has been done easily using TMGa and NH_3 . Fig1 shows the growth efficiency [3] as a function growth temperature at two reactor pressure. The growth efficiencies show the typical kinetically limited regime at low growth temperature and the diffusion-limited regime at moderate temperature [8]. At growth temperatures above 1000°C , GaN growth at atmospheric pressure becomes extremely difficult and no thickness data can be obtained. This is probably due to the strong thermal convection at atmospheric pressure and high growth temperature. At a low growth pressure of 85 torr, however, GaN can be easily grown with growth temperature up to 1075°C (the highest temperature achievable by the RF generator) with high quality. The slight drop in growth efficiency at high temperature for GaN grown at 85 torr is likely due to pre-deposition of GaN on the reactor wall at such a high growth temperature [9].

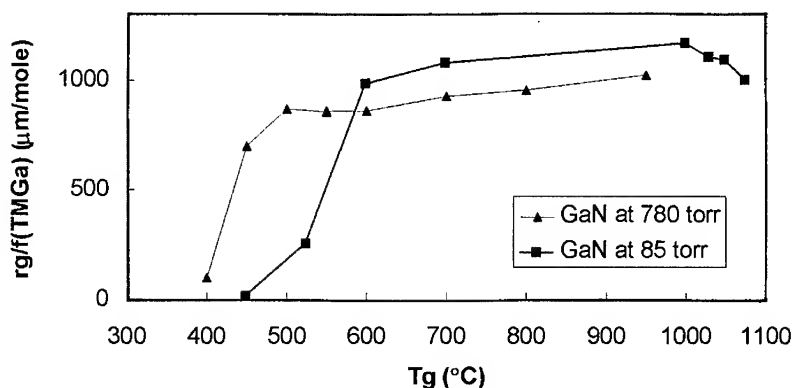


Fig.1: Growth efficiencies for GaN as a function of growth temperature. The reactor pressure is either 780 torr or 85 torr.

Atmospheric pressure AlN growth has been attempted at 500 °C, 600 °C, and 700 °C. No epilayer was grown even after using a long growth time and high TMAI flow rate. The growth efficiency of AlN at atmospheric pressure is estimated to be less than 100 $\mu\text{m}/\text{mole}$. This low level of unmeasurable growth efficiency indicates that TMAI and NH_3 might undergo parasitic reaction at atmospheric pressure to deplete the reactants. Indeed, white deposits are observed near the reactor entrance where TMAI and NH_3 are mixed.

The growth of AlN is possible only at low reactor pressure. Fig.2 shows the GaN and AlN growth efficiency dependences as a function of reactor pressure. In the experiments, the mass flow rates of the gases are fixed and only the reactor pressure is changed. This means that the flow velocity and reactant concentrations are varied as reactor pressure is varied [10-11]. Reactor pressure dependence of growth efficiency without parasitic reactions has been discussed in the literature [10-12]. Using a boundary layer model, it has been predicted that the growth efficiency does not depend on reactor pressure [10-11]. This has been confirmed experimentally [11-12]. A recent calculation using kinetic and transport modeling for InP growth also shows that the growth efficiency is almost pressure independent [13]. For GaN growth, the growth efficiency is almost constant at different reactor pressures, consistent with the conclusion that parasitic reaction is minimal between TMGa and NH_3 . On the other hand,

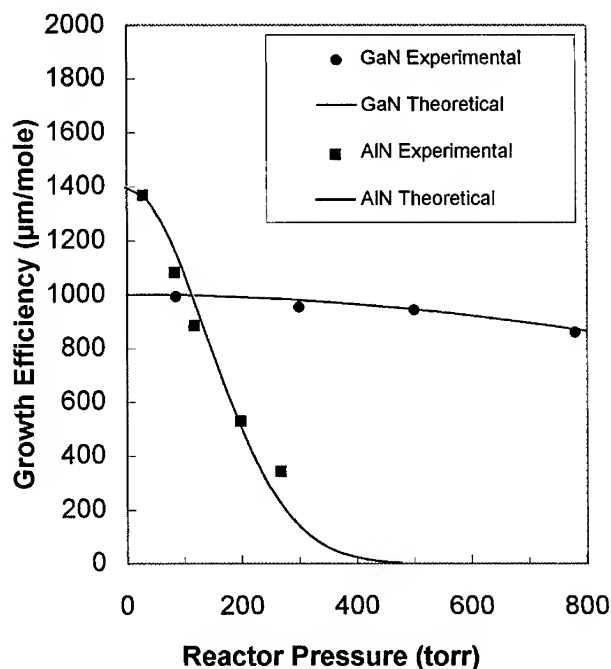
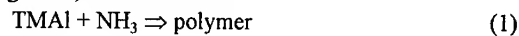


Fig.2: Growth efficiencies for GaN and AlN as a function of reactor pressure. The data points are experimental results. The curves are results from theoretical calculations, assuming that parasitic reactions cause the growth efficiency to decrease at higher reactor pressure. The growth temperature is 600 °C.

AlN growth efficiency shows a strong dependence on reactor pressure and the result confirms the conclusion that TMAI and NH₃ parasitic reaction is severe.

The parasitic reaction is a bi-molecular process between group III and group V precursors. In the case of AlN growth, the reaction is:



and the rate equation can be written as follows

$$\frac{d[\text{polymer}]}{dt} = k_1 * [\text{TMAI}] * [\text{NH}_3] \quad (2)$$

where k_1 is the reaction rate constant for equation (1) and [species] denotes concentration of the species. Because the increase in polymer concentration is equal to the decrease in TMAI concentration and because [NH₃] is almost constant, equation (2) produces

$$[\text{TMAI}] = [\text{TMAI}]_0 \text{EXP}\{-k_1[\text{NH}_3]t\} \quad (3)$$

where $[\text{TMAI}]_0$ is the initial TMAI concentration or TMAI concentration at $p=0$. Since [NH₃] and residence time t are proportional to reactor pressure, p , equation (3) can be re-written as

$$[\text{TMAI}] = [\text{TMAI}]_0 \text{EXP}\left\{-\left(\frac{p}{p_0}\right)^2\right\} \quad (4)$$

where p_0 is related to reactor geometry, NH₃ concentration, and reaction rate constant k_1 . Since growth efficiency in the diffusion-limited regime is proportional to input group III concentration, the pressure dependence of growth efficiency can be expressed as follows:

$$\text{G.E.} = [\text{G.E.}]_0 \text{EXP}\left\{-\left(\frac{p}{p_0}\right)^2\right\} \quad (5)$$

where G.E. denotes growth efficiency and $[\text{G.E.}]_0$ is the growth efficiency when parasitic reaction is absent.

It is possible to use equation (5) to fit the experimental data in Fig.2 to get quantitative values for the two parameters. The best fit is obtained by using the following equations for GaN and AlN, respectively:

$$\text{G.E.}_{\text{TMAI}} = 1400 \text{EXP}\left\{-\left(\frac{p}{200}\right)^2\right\} \quad (6)$$

$$\text{G.E.}_{\text{TMGa}} = 1000 \text{EXP}\left\{-\left(\frac{p}{2100}\right)^2\right\} \quad (7)$$

It is seen that the $[\text{G.E.}]_0$ for GaN is 1000 $\mu\text{m}/\text{mole}$, smaller than the value of 1400 $\mu\text{m}/\text{mole}$ for AlN. The reason is not clear. The parameter p_0 for GaN growth is much larger than that for AlN growth. Thus, GaN parasitic reaction is unlikely for this reactor since the parameter p_0 is as high as 2100 torr. On the other hand, AlN parasitic reaction will become a problem at reactor pressures higher than 200 torr. In other words, the parasitic reaction rate constant k_1 for AlN is approximately 100 times faster. This may seem surprising at first glance because one might think that the parasitic reaction is more severe for a gallium precursor than for an aluminum precursor [6]. However, it has been reported that while $\text{TEGa}+\text{AsH}_3$ does not show parasitic reaction, $\text{TEAl}+\text{AsH}_3$ does [14].

It is worthwhile to note that the above results are reactor-specific and other reactor geometry may produce a different degree of parasitic reactions. For example, it is possible to grow AlN even in an atmospheric reactor if the flow velocity of the reactants is high and the

residence time is short [15]. However, the relative ratios of parasitic reaction rates elucidated in this paper should still be valid.

The parasitic reactions between TMIn and NH_3 is harder to study. It is well known that one of the difficulties in growing InN and GaInN is that In-N bond is weak and InN dissociates easily. Because of this complication, it is difficult to use the growth temperature and reactor pressure dependences of InN growth efficiency and In incorporation in InGaIn to determine the parasitic reactions between TMIn and NH_3 . Thus, one can only draw conclusions about the parasitic reactions between TMIn and NH_3 from somewhat limited experimental results. Fig.3 shows the PL and transmission results for GaInN grown at atmospheric pressure. The growth temperature is 700 °C and the TMIn/TMGa molar ratio is about 1. Both the PL and transmission measurements show that the as-grown GaInN contains fair amount of In. The PL spectrum is distorted by thickness interference which leads to difficulty in determining the exact peak position. The left-most peak has a wavelength 438 nm, which would corresponds to about 26% of In in the GaInN solid [16]. The results suggest that parasitic reaction between TMIn and NH_3 is not severe.

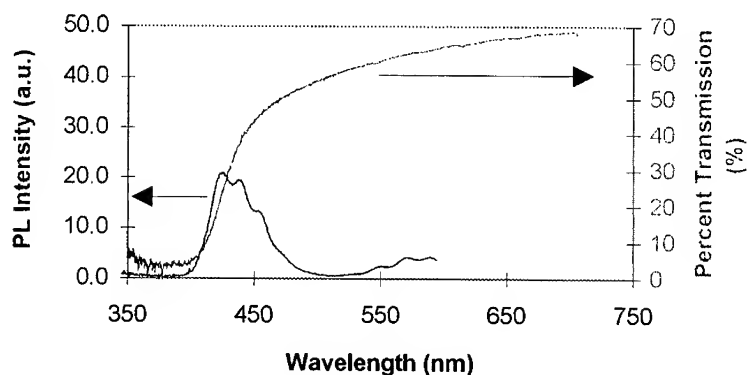


Fig.3 Room temperature PL and transmission for a GaInN layer. The light spot size for the transmission measurement is much larger than the laser excitation spot size for PL measurement. That is why interference fringes are observed in the PL spectrum and not in the transmission spectrum.

Replacing TMGa with the same molar flow rate of TEGa for the growth of GaInN does not produce any significant change in the In solid composition in GaInN. Thus, the parasitic reaction between TEGa and NH_3 is also not severe as compared to that between TMAI and NH_3 .

Summary

In summary, the OMVPE growth efficiencies of GaN, AlN and AlGaIn have been studied as a function of growth temperature and reactor pressure. For GaN growth, the growth efficiency is almost independent of growth temperature and reactor pressure. This

indicates that mixing TMGa with NH_3 results in minimal parasitic reaction. For AlN growth, the growth efficiency decreases at higher reactor pressure. The results indicate that TMAI reacts strongly with NH_3 to deplete the reactants. Thus, it is better to grow Al containing nitride materials at low reactor pressure to minimize parasitic reaction.

Acknowledgments

The authors like to thank the technical supports provided by Shari Owen-Balassa for the OMVPE growth and characterization. The authors also appreciate the help and discussions from Tim Osentowski, M. Peanasky, D. DeFevere, and S. Rudaz, S. Lester, M. Ludowise, and J. Amano.

References:

1. J.P. Noad and A.J. SpringThorpe, *J. Electron. Mater.* **9**, 601 (1980).
2. S.J. Bass, C. Pickering and M.L. Young, *J. Cryst. Growth* **64**, 68 (1983).
3. C.P. Kuo, J.S. Yuan, R.M. Cohen, J. Dunn, and G.B. Stringfellow, *Appl. Phys. Lett.* **44**, 550 (1984).
4. M. Ludowise, *J. Appl. Phys.* **58**, R31 (1985), and references therein.
5. G.B. Stringfellow, Organometallic Vapor Phase Epitaxy: Theory and Practice, (Associated Press, San Diego, 1989), Section 2.3.
6. G.E. Coates, M.L.H. Green and K. Wade, Organometallic Compounds: The Main Group Elements (3rd ed. Meuthen & Co., LTD, London, 1967), Vol. I.
7. J.P. Duchemin, J.P. Hirtz, M. Razaghi, M. Bonnet, and S.D. Hersee, *J. Cryst. Growth* **55**, 64 (1981).
8. G.B. Stringfellow, Organometallic Vapor Phase Epitaxy: Theory and Practice, (Associated Press, San Diego, 1989), Chapter 6.
9. G.B. Stringfellow, Organometallic Vapor Phase Epitaxy: Theory and Practice, (Associated Press, San Diego, 1989), p265.
10. G.B. Stringfellow, Organometallic Vapor Phase Epitaxy: Theory and Practice, (Associated Press, San Diego, 1989), section 6.3.
11. H. Heinecke, E. Veuhoff, N. Putz, M. Heyyen, and P. Balk, *J. Electron. Mater.* **13**, 815 (1984).
12. R.J. Field and S.K. Ghandhi, *J. Cryst. Growth* **69**, 581 (1984).
13. C. Theodoropoulos, N.K. Ingle, T.J. Mountziaris, Z.-Y. Chen, P. Liu, G. Kioseoglou, and A. Petrou, *J. Electrochem. Soc.* **142**, 2086 (1995).
14. T.F. Kuech, E. Veuhoff, T.S. Kuan, V. Deline, and R. Potemski, *J. Cryst. Growth* **77**, 257 (1986).
15. I. Akasaki, H. Amano, Y. Koide, K. Hiramatsu, and N. Sawaki, *J. Cryst. Growth* **98**, 209 (1989).
16. S. Nakamura, T. Mukai, M. Senoh, S. Nagahama, *J. Appl. Phys.* **74**, 3911 (1993).

Part II

Molecular Beam Growth Techniques

EPITAXIAL GROWTH OF GaN FILMS PRODUCED BY ECR-ASSISTED MBE

T.D.MOUSTAKAS

Molecular Beam Epitaxy Laboratory, Department of Electrical Engineering and Center for Photonics Research, Boston University, Boston , MA 02215

ABSTRACT

The epitaxial growth of wurtzite and zincblende GaN on (0001) sapphire and (001) Si by the Electron Cyclotron Resonance-assisted Molecular Beam Epitaxy (ECR-MBE) method is discussed. We show that films can be grown in the layer-by-layer mode when growth occurs in Ga-rich regime. Surface roughening mechanisms are addressed. The similarity of photoluminescence data of Mg-doped wurtzite GaN films with those of undoped zincblende GaN films suggests that Mg doping facilitates the formation of stacking faults in the wurtzite structure which are nucleation sites for zincblende domains.

INTRODUCTION

The full exploitation of III-V nitrides for various opto-electronic applications requires significant progress in a number of science areas. Such include, for example, the study of heteroepitaxial growth, the crystal structure and microstructure, impurity doping, formation of defects, alloying phenomena and formation of homojunction and heterojunction structures.

Some of these phenomena are further being complicated by the fact that the III-V nitrides can exist in various polymorphs. All three binaries (InN, GaN, AlN) were found to exist in the wurtzite and zincblende structures [1]. In addition, AlN was found to transform to the sodium chloride structure under high pressure [2]. The evidence suggests that the cohesive energies of the wurtzite and zincblende GaN are comparable [3]. The two structures are analogous to the HCP and FCC structures in their stacking sequences. Since bulk GaN substrates are not available, films must be grown heteroepitaxially on foreign substrates. The majority of GaN films reported have been grown in the wurtzite structure, most commonly with the basal planes parallel to the substrate. However, epitaxial stabilization of the zincblende phase has been obtained on substrates having cubic symmetry [1].

Examination of these crystal structures by θ -2 θ XRD scans generally indicate that the films are of perfect crystalline quality. However, any stacking faults along the growth direction of the GaN film cannot be easily detected in the normal θ -2 θ scans. It should be stressed that such stacking faults are very common defects in material with FCC and HCP structures growing along the (111) and (0002) directions. Such stacking faults, if exist in the wurtzite GaN films, should give rise to a certain amount of cubic GaN component with the (111) planes parallel to the substrate. Since the cohesive energies of the two structures are comparable the energy of formation of stacking faults

must be negligible, and their formation may be instigated by many factors such as strain, impurities and various growth parameters which affect the kinetics of growth.

The transport, optical and recombination properties must also be influenced significantly by the coexistence of the two phases in the same film. This is because the wurtzite and zincblende structures of GaN are direct bandgap semiconductors with room temperature energy gaps of 3.4 eV and 3.2 eV respectively [1].

In this paper we review the epitaxial growth of GaN in the wurtzite and zincblende structures and discuss evidence that certain experimental results may be related to the coexistence of both phases in the same film.

EXPERIMENTAL METHODS

A. Thin Film Growth

GaN films were grown by the Electron Cyclotron Resonance microwave-plasma assisted Molecular Beam Epitaxy method (ECR-MBE). The deposition system is schematically illustrated in Fig. 1. It consists of a Varian GenII MBE unit with an ASTeX compact ECR source mounted in one of the effusion cell ports. The base pressure of the overall system is 10^{-11} Torr. A reflection high energy electron diffraction (RHEED) setup is an integral part of the apparatus. Conventional Knudsen effusion cells are used for the evaporation of the group III elements as well as the dopants (Si and Mg). Active nitrogen is produced by passing molecular nitrogen through the ECR source at a flow rate, which produces a downstream pressure of 10^{-5} to 10^{-4} Torr.

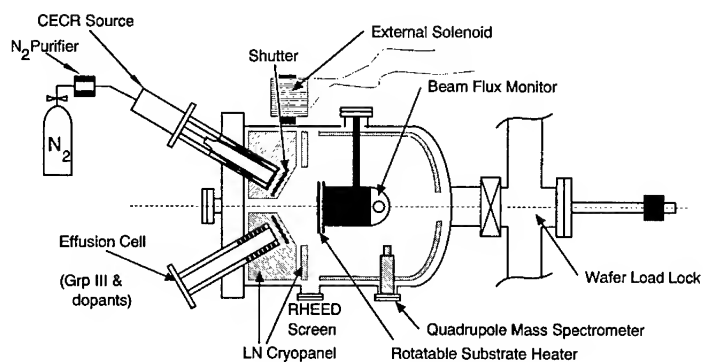


Fig. 1 Schematic of the ECR-MBE System

The wurtzite GaN films were grown on (0001) sapphire substrates while the zincblende GaN films were grown on (001) Si substrates. The sapphire substrates were degreased and etched in $\text{H}_3\text{PO}_4\text{:H}_2\text{SO}_4$ (1:3) for the removal of surface contaminants and mechanical damage due to polishing and finally were rinsed in de-ionized water. The Si-substrates were degreased and etched in buffered HF and outgassed to 800 °C in the MBE preparation chamber. RHEED studies of such Si wafer at 400 °C indicate that the (001) Si surface is unreconstructed (ie. 1x1). We found that such an unreconstructed surface is required for the growth of cubic GaN.

B. Design and Characterization of the ECR source

The ASTeX ECR source is designed with an axial solenoid to generate the magnetic field required for ECR operation. The design of this source promotes efficient electron/gas collisions and results in high density plasma with gas ionization efficiencies as high as 10%. This efficient resonant coupling allows the source to be stably operated with growth chamber pressure as low as 10^{-5} Torr. Due to the large mean free path of the gaseous species at these low background pressures (~ 1 m at 10^{-4} Torr), the growth is carried out in the molecular flow regime, where the transport of atoms or molecules in both thermal beams from the effusion cells as well as the beam of activated nitrogen from the ECR source occurs in a collisionless manner. This low collision rate coupled with the axial magnetic field effects on the charged species (electrons, ions) can have profound effect on the operation of this source and the diffusional behavior of the charged species. Generally, the electrons in the plasma are well confined to the magnetic field lines by their Larmor gyration around these fields lines and are guided down the divergence of the magnetic field and charge the substrate negatively. The ions, on the other hand, are poorly confined due to their comparatively larger mass, however they do reach the substrate because of the coulombic interaction with the negatively charged substrate [4]. The gain in ion translational kinetic energy along the magnetic field lines can effect the kinetics of film growth by depositing additional energy in the surface of the growing film and thus influence the adatom surface diffusion. If the ion kinetic energy is high then displacement of bulk atoms becomes important. The damage threshold of GaN was estimated to be 24 eV [5].

Two different methods have been developed in our laboratory to control the ion species arriving at the substrate. One method employs an off-axis external solenoid which modifies the magnetic field lines in the substrate region and extracts charged species away from the substrate [6]. The second method uses a flow limiting orifice in front of the ECR source [5]. The exit aperture results in a pressure increase in the discharge region which reduces the kinetic energy of the charged species through collisional losses with the background gas species. The ECR plasmas in these two methods were investigated by Langmuire probe measurements and optical emission spectroscopy [5,6]. These studies clearly indicate that the relative ion density at the substrate decrease with the strength of the magnetic field in the external solenoid and with reduction in the size of the ECR exit aperture.

EXPERIMENTAL RESULTS AND DISCUSSION

A. Growth of Wurtzite GaN Films

GaN films having the wurtzite structure were grown on (0001) sapphire substrates. As discussed previously, the growth on sapphire involves three steps [3,7,8]. The first step is the conversion of the surface of the Al_2O_3 substrate to AlN by exposing the substrate to an ECR nitrogen plasma at 800 °C for approximately 10 min. The exact mechanism of this nitridation is not well understood yet. However, the thin AlN film is a single crystal with atomically smooth surface morphology as indicated by the streakiness of the RHEED pattern in Fig. 2a. The broadness of the diffraction lines suggest that the AlN film is very thin and highly strained. It is also very likely that this film is not continuous but it consists of isolates AlN islands. We believe that the nitridated sapphire substrate is a better substrate for the growth of GaN because of the smaller lattice mismatch between AlN and GaN. The second step involves the deposition of a thin GaN-buffer (200-300 Å thick) at 550 °C. This thin GaN film is single crystal with atomically smooth surface morphology as indicated by the RHEED pattern of Fig. 2b. The diffraction lines of this film are sharper than that of the AlN film. The third step involves the deposition of the rest of the GaN film at 800 °C. The growth during this step is close to homoepitaxy. The RHEED pattern upon the completion of approximately 1 µm thick film is shown in Fig. 2c. The streakiness and sharpness of the diffraction lines suggest that the film has atomically smooth surface morphology with excellent crystalline quality.

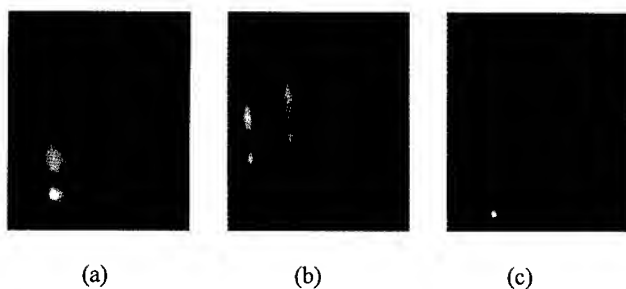


Fig 2. RHEED data (a) after substrate nitridation, (b) after deposition of 300 Å buffer, (c) after the growth of 1 µm GaN film at 800 °C.

The RHEED patterns of the GaN films were found to depend strongly on the microwave power in the ECR discharge. Fig 3 shows the RHEED diffraction patterns for three films grown at 18W, 20W and 25W. This data indicates that films grown at relatively low microwave power have atomically smooth surface morphology, while those grown at 25W or higher have a rough surface morphology (3 dimensional diffraction)

Postgrowth SEM studies of the three films, discussed in Fig 3, are shown in Fig 4, and their surface morphologies are consistent with the RHEED diffraction data. The films grown at the lowest power show a strong columnar morphology consistent with initial island growth. The surface of the partially connected columns are atomically smooth, which leads to streaky RHEED diffraction pattern (Fig 3a). The films grown at intermediate power (20W) show no evidence of columnar morphology and their surface morphology appears to be atomically smooth. On the contrary, films grown at higher microwave power (25W) have a characteristic surface roughness. The Ga-flux during the growth of the three films was the same and the growth rate was about 2500 Å/h. We have observed that if the Ga-flux increases in proportion to the power in the ECR discharge the surface morphology of the films remain smooth. Thus, the observed roughening is not directly related to the power in the ECR discharge but is related to the ratio of group III to group V fluxes [9].

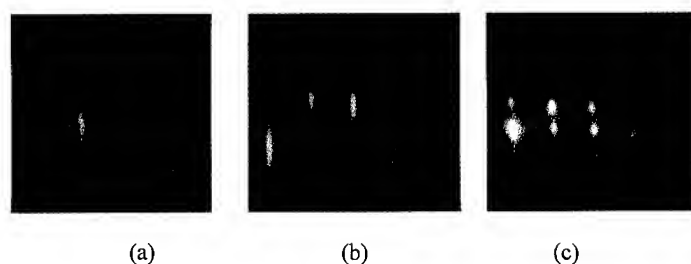


Fig. 3 RHEED patterns of GaN films grown at the following ECR microwave powers: (a) 18W, (b) 20W, (c) 25W

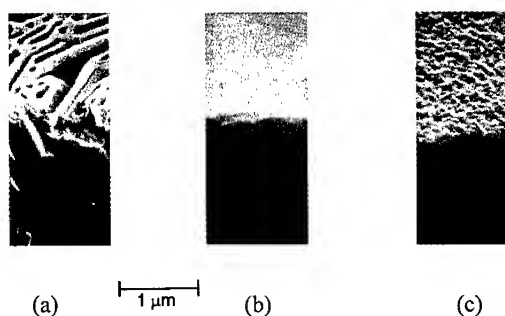


Fig. 4 SEM surface morphology of the GaN films discussed in Fig. 3

The observed surface modification with the power in the ECR discharge shows the effect of ion assistance on the film's "growth modes". A discussion of the growth modes can be found in a recent review by Peercy et al. [10]. The morphology of Fig 4a is consistent with island growth (Volmer-Weber mode), the morphology of Fig 4b is consistent with layer by layer growth (Frant-vand der Merwe mode), and the morphology of Fig 4c is consistent with formation of three dimensional clusters on a microscopically thin uniform layer (Stanski-Krastanov mode).

The origin of the observed layer by layer growth is not understood yet. According to Bauer [11] if the deposited material has larger surface energy than the substrate, the growth mode will be three dimensional. More recently Bruinsman and Zangwill [12] developed a phenomenological analysis based on continuous elasticity, which predict that in the presence of lattice misfit the layer by layer growth is never the equilibrium morphology but rather is metastable with respect to cluster formation on a thin wetting layer. Atomistic simulations by Grabow and Gilmer [13] support the conclusion that layer by layer growth is the ground state only for zero misfit. The observation of a layer by layer growth of GaN on (0001) sapphire is probably related to the existence of the GaN buffer, which acts as the wetting layer.

The observed surface roughening with the power in the discharge may result from two different process. In one process the extra kinetic energy supplied by the energetic plasma increases the surface diffusion of the adatoms, which migrate and form clusters on the top of other clusters and thus give rise to three dimensional growth. The second process involves chemistry. Growth in nitrogen rich environments increases the nucleation rate due to the strength of the Ga-N bond. In other words, the Ga atoms will be bonded to N atoms before they complete their migration to step edges. The fact that we do not observe surface roughening when growth proceeds under Ga-rich conditions supports the chemical interpretation. Thus, Ga-rich conditions appear to promote step-flow growth in which condensing material must reach the growth ledges by surface diffusion before new islands nucleate; otherwise surface roughening occurs [10].

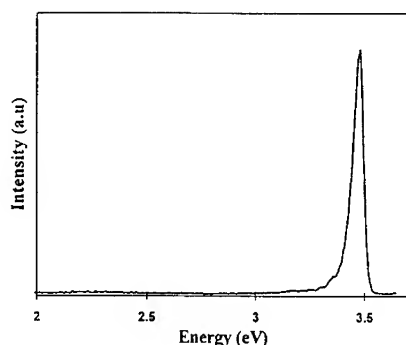


Fig. 5 Photoluminescence spectra for a GaN film grown under Ga-rich conditions.

GaN films grown under Ga-rich conditions on (0001) sapphire were found to have very high crystalline quality. RHEED studies indicate (2x2) surface reconstruction during film growth and the x-ray rocking curve has a full width a half maximum (FWHM) of 69 Arcsec. These structural data are discussed in another paper [9]. Photoluminescence measurements at 77 K in one such film is shown in Fig. 5. Recombination occurs at 3.48 eV, a transition associated with free exciton, with a FWHM of 50 meV.

B. Growth of Zincblende GaN Films

GaN films having the zincblende structure were grown on both n and p-type (001) silicon substrates. As discussed previously such films were grown in two temperature steps [14,15]. More specifically, a GaN buffer layer about 300 - 900 Å thick was deposited at temperature of 400 °C, and found by RHEED studies to have the zincblende structure with the [001] direction perpendicular to the substrate. The temperature of the substrate was then raised to 600 °C and the rest of the GaN film was grown. The zincblende structure of these films was confirmed by RHEED and ex-situ XRD and TEM [16,17].

The surface morphologies of the GaN films, grown under identical conditions, were found to be smoother on n-type rather than p-type Si-substrates. Fig 6 shows two characteristic surface morphologies observed on p-type substrates. The sample with the smoother surface was grown at lower nitrogen pressure. The surface of the sample shown in Fig 6a is roughened with many rectangular shaped "tiles" oriented along the [110] and [1-10] directions. This presumably arises because the GaN surface corresponding to these directions are more closely packed than the (100) and (010) surfaces and therefore have lower surface energies. The size of these "tiles" reveals the size of the domains. The smoother surface morphology of the films grown at lower pressure is consistent with ion assisted increased adatom surface diffusion.

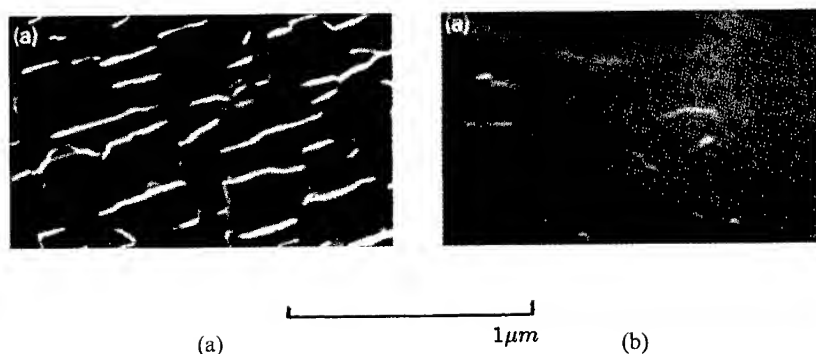


Fig. 6 Surface morphology of two zincblende GaN films grown at nitrogen pressures of (a) 1×10^{-4} Torr and (b) 5×10^{-5} .

From the data of Fig 6b we can estimate the two dimensional nucleation rate and the lateral growth rate [3]. Let J be the nucleation rate, S the average area of the plateaus, h the height of the plateaus and t the time for the plateaus to grow, which is limited by nucleation rate. Then we have:

$$\sqrt{S} = v_l t = \frac{v_l}{JS} \quad (1)$$

$$h = v_n t = \frac{v_n}{JS} \quad (2)$$

where v_l and v_n are the lateral and vertical growth rates respectively. Using data from Fig. 6b ($\sqrt{S} \approx 1 \mu\text{m}$, $h \approx 100 \text{ \AA}$) and the known growth rate ($v_n = 2000 \text{ \AA/h}$) we find from Eqs (1) and (2) $v_l \approx 100 v_n$ and $J = 20 \text{ nuclei / } (\mu\text{m}^2 \cdot \text{h})$.

These data clearly indicate that the two-step growth method leads to quasi-layer-by-layer growth with very small two dimensional nucleation rate and high lateral growth rate.

XRD [16] and TEM [17] studies on these films indicate that the films have the zincblende structure with approximately 1% wurtzite phase occurring primarily close to the Si-GaN interface. This is to be contrasted with wurtzite GaN films grown on Si (111) which were found to have approximately 25% zincblende component. This clearly suggest that stacking faults may be introduced much more easily when growth proceeds with the basal plane parallel to the substrate. We believe that this high concentration of stacking faults is instigated by the high interfacial strain between Si and GaN.

C. Doping Studies

Wurtzite GaN films grown by the ECR-MBE method were doped intentionally n- or p-type by incorporating Si or Mg respectively [8]. Films with hole or electron concentration between $10^{18} - 10^{19} \text{ cm}^{-3}$ have been obtained without requiring any post-growth treatment [8]. Si was found to contribute a shallow donor state ($\approx 20 \text{ meV}$) while Mg contributes a deep acceptor state ($\approx 150 \text{ meV}$). Comparing SIMS and Hall measurements we concluded that the Mg-doping efficiency is up to 10% [18]. The effect of hydrogen on p-type GaN was studied by post-growth hydrogenation [18]. We found that while hydrogen does not affect the carrier concentration of n-type sample, it reduces the carrier concentration of p-type samples by more than an order of magnitude. Infrared and Raman scattering studies in these samples suggest the formation of Mg-H complexes [19].

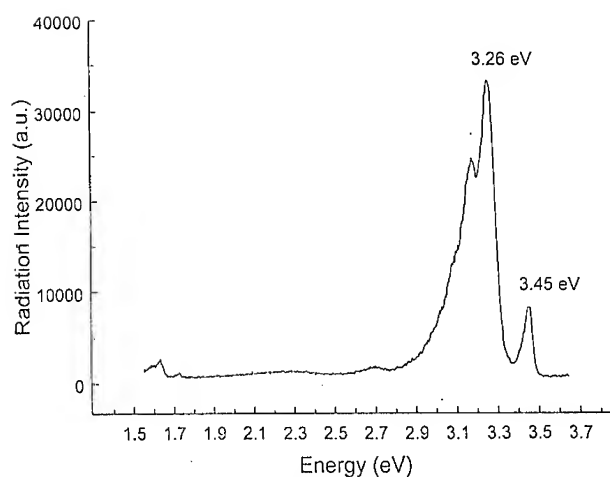


Fig. 7 Photoluminescence spectra at 77K of a lightly Mg-doped wurtzite GaN film.

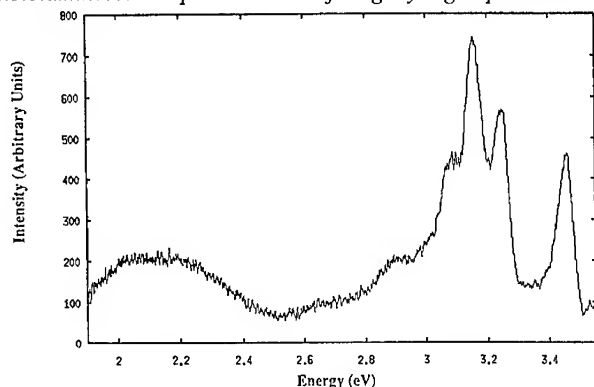


Fig 8. Photoluminescence spectra at 77K of an undoped zincblende GaN film.

The luminescence spectra of the Mg-doped films at 77K are shown in Fig. 7. Such data have been reported by other groups as well [1]. These spectra show a small peak at 3.46 eV associated with neutral donor bound excitons and a strong broad peak at 3.26 eV. At the low energy side of this peak one can distinguish two other peaks at 3.17 eV and 3.08 eV which can be accounted for as one optical and two optical phonon replicas of the 3.26 eV transition. These transitions were observed by Lagerstedt et al [20] and Ilegems et al [21] and the 3.26 eV peak was attributed to Donor-Acceptor transition and the lower energy peaks were attributed to phonon replicas.

Luminescence studies of undoped GaN film grown on β -SiC substrates are shown in Fig. 8. Structural studies of this film indicate that the film has primarily the zincblende structure however, a small diffraction peak associated with the wurtzite structure is also present. The data of Fig. 8 show the transitions at 3.45 eV, which is associated with the small concentration of the wurtzite structure and a broad feature with three peaks. These three peaks are identical with those of Fig. 7. This raises the question whether the peak at the 3.26 eV, which was associated with DA recombination, is instead due to a transition across the gap of the zincblende structure, whose gap at 77K is about 3.26 eV.

To account for the similarity of the data of Fig. 7 and 8 we propose that Mg-doping of wurtzite GaN instigates the formation of stacking faults, which are nucleation sites for zincblende- GaN domains. This is probably related to having a group II element in a wurtzite structure. The composite material of wurtzite GaN with randomly distributed microscopic domains of zincblende GaN or isolated stacking faults has a band diagram as illustrated in Fig. 9. The quantum wells in Fig. 9b represent domains of the zincblende structure. Transitions in these quantum wells give rise to the peak at 3.26 eV of the Mg doped films. Doping of wurtzite-GaN with high concentrations of Mg will introduce a high concentration of cubic domains and the Mg- doping of these domains will give rise to transitions in the blue part of the spectrum. This accounts for the observation that GaN p-n junction LEDs emit in the blue rather than the ultraviolet part of the spectrum. This model needs to be verified by conducting structural studies on both lightly and heavily Mg-doped GaN samples.

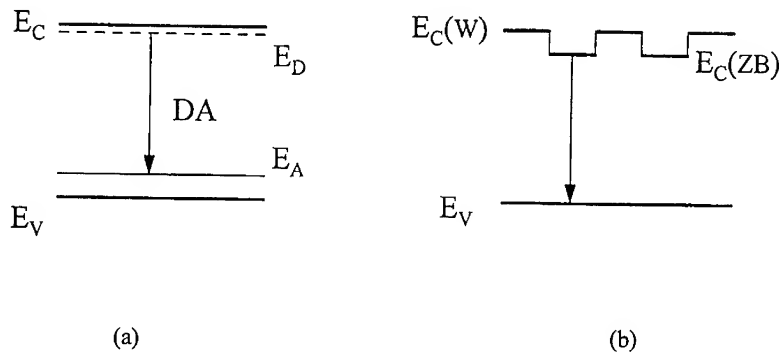


Fig. 9 Luminescence transitions in Mg-doped GaN in (a) wurtzite structure (b) mixed phase structure.

CONCLUSIONS

The heteroepitaxial growth of GaN in their wurtzite and zincblende structures on (0001) sapphire and (001) Si respectively by the ECR-MBE method has been discussed. We have demonstrated that layer-by-layer growth occurs in the Ga- rich regime of growth using the two temperature step growth process. We proposed a new model to account for the photoluminescence results of Mg-doped GaN. This model assumes that Mg-doping introduces stacking faults which are nucleation sites of cubic domains. The observed transitions at 3.26 eV are associated with transitions across the energy gap of the cubic domains.

ACKNOWLEDGMENT

The author is indebted to his current and past graduate students, R. Singh, D.Korakakis, A. Sampath, I. Goepfert, R. Molnar and T. Lei. The work was supported by ARPA.

REFERENCES

1. S. Strite and H. Morkoc , J. Vac. Sci. Tech. B 10, p. 1237 (1992)
2. H. Vollstadt, E. Ito, M. Akaishi, S. Akimoto, O. Fukunaga, Proc. Japan Acad. 66, Ser. B, p. 7 (1990)
3. T.D Moustakas, T. Lei and R.J. Molnar, Physica B 185, p. 36 (1993)
4. R.J. Molnar , R.Singh and T.D. Moustakas, J. of Electr. Mat. 24, p. 275 (1995)
5. K.W. Böer, Survey of Semiconductor Physics , vol I (New York , Van Nostrand Reinhold, 1990)
6. R.J. Molnar and T.D. Moustakas, J. App. Phys. 76, p. 4587 (1994)
7. T.D. Moustakas, R.J. Molnar, T. Lei, G. Menon and C.R. Eddy Jr, Mat. Res. Soc. Symp. Proc. Vol 242, p. 427 (1992)
8. T.D. Moustakas and R.J Molnar, Mat. Res. Soc. Symp. Proc. Vol 281, p. 753 (1993)
9. R. Singh, et al, App. Phys. Lett. (to be submitted)
10. P.S. Peercy et al, J. Mater. Res. 5, p. 852 (1990)
11. E. Bauer, Z. Krist. 100, p.372 (1958)

12. R. Bruinsman and A. Zangwill, *Europhys. Lett.* 4, 729 (1987)
13. M.H. Grabow and G.H. Gilmer, in *Layered Structures and Epitaxy*, edited by J.M Gibson, G.C. Osbourn and R.M Thompson (MRS Pittsburg, PA 1986) p.13
14. T. Lei, M. Fanciulli, R.J. Molnar, T.D. Moustakas, R.J. Graham, J. Scanlon, *App. Phys. Lett.* 59, p. 944 (1991)
15. T. Lei, T.D. Moustakas, R.J. Graham, Y. He and S.J. Berkowitz, *J. Appl. Phys.* 71, p. 4933 (1992)
16. T. Lei, K.F. Ludwig Jr. and T.D. Moustakas, *J. Appl. Phys.* 74, p. 4430 (1993)
17. S.N. Basu, T. Lei and T.D. Moustakas, *J. Mater. Res.* 9, p.2370 (1994)
18. M.S. Brandt, N.M. Johnson, R.J. Molnar, R.Singh and T.D Moustakas, *Appl. Phys. Lett.* 64, p.2264 (1994)
19. M.S. Brandt, J.W. Ager III, W. Götz, N.M. Johnson, J.S. Harris Jr., R.J. Molnar and T.D. Moustakas *Phys Rev B.* 49, p. 14758 (1994)
20. O. Lagerstedt and B. Monemar, *J. Appl. Phys.* 45, p. 2266 (1979)
- 21 M. Ilegems and R. Dingle, *J. Appl. Phys.* 39, p. 4234 (1973)

GROWTH AND PROPERTIES OF III-V NITRIDE FILMS, QUANTUM WELL STRUCTURES AND INTEGRATED HETEROSTRUCTURE DEVICES

J.F. SCHETZINA

Department of Physics, North Carolina State University, Raleigh N.C., 27695-8202

ABSTRACT

Growth of III-V nitrides by molecular beam epitaxy (MBE) is being studied at NCSU using an rf nitrogen plasma source. GaN/SiC substrates consisting of $\sim 3 \mu\text{m}$ thick GaN buffer layers grown on 6H-SiC wafers by MOVPE at Cree Research, Inc. are being used as substrates in the MBE film growth experiments. The MBE-grown GaN films exhibit excellent structural and optical properties -- comparable to the best GaN films grown by MOVPE--as determined from photoluminescence, x-ray diffraction, and vertical-cross-section TEM micrographs. Mg and Si have been used as dopants for p-type and n-type layers, respectively. $\text{Al}_x\text{Ga}_{1-x}\text{N}$ films ($x \sim 0.06\text{--}0.08$) and $\text{Al}_x\text{Ga}_{1-x}\text{N}/\text{GaN}$ multi-quantum-well structures have been grown which display good optical properties. Light-emitting diodes (LEDs) based on double-heterostructures of $\text{Al}_x\text{Ga}_{1-x}\text{N}/\text{GaN}$ which emit violet light at $\sim 400 \text{ nm}$ have also been demonstrated. Key issues that must be addressed before III-V nitride laser diodes can be demonstrated and commercialized are discussed. New integrated heterostructures are proposed for the development of a variety of vertical-transport devices such as light-emitting diodes, laser diodes, photocathodes, electron emitters based on the negative-electron-affinity of AlN, and certain transistor structures.

INTRODUCTION

The III-V nitrides are promising materials for high temperature electronic and UV/blue/green optoelectronic applications which would make use of the wide range of direct energy band gaps that these materials possess: from 1.9 eV (InN), to 3.4 eV (GaN), to 6.2 eV (AlN) as shown in Figure 1. This paper reports growth by molecular

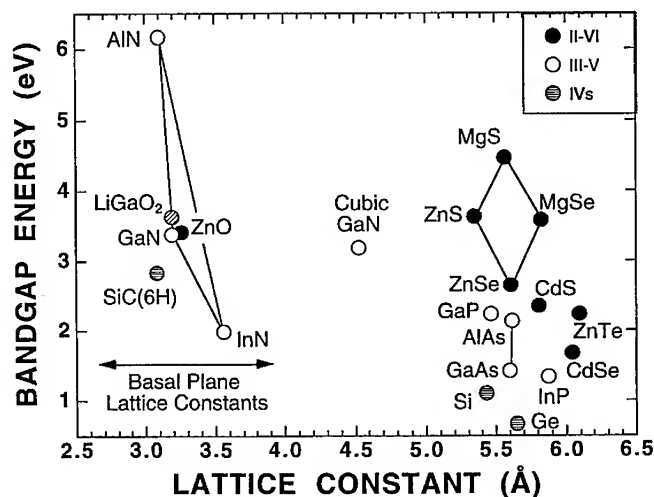


Figure 1. Energy bandgap versus lattice constant for selected semiconductors.

beam epitaxy (MBE) of high quality GaN, $\text{Al}_x\text{Ga}_{1-x}\text{N}$, and AlN films on GaN/SiC substrates. The GaN films were grown homoepitaxially by rf plasma-assisted MBE on 3 μm thick GaN buffer layers previously grown on 6H-SiC substrates prepared by MOCVD at Cree Research, Inc. By using this homoepitaxial approach, we have circumvented the problems associated with heteroepitaxial nucleation of GaN on highly lattice-mismatched substrates such as sapphire or SiC and have instead concentrated on the issues associated with the MBE growth process itself. We employed radio frequency (rf) plasma-assisted MBE instead of the commonly used ECR plasma-assisted MBE to generate beams of active nitrogen for film growth. Using an rf plasma source, MBE growth of very high quality GaN and $\text{Al}_x\text{Ga}_{1-x}\text{N}$ layers, $\text{Al}_x\text{Ga}_{1-x}\text{N}/\text{GaN}$ multiple quantum well (MQW) structures, and blue-violet light emitting diodes based on double-heterostructures of $\text{Al}_x\text{Ga}_{1-x}\text{N}/\text{GaN}$ have been achieved at growth rates of $\sim 0.3 \mu\text{m/hr}$.

Recently-measured valence band offsets for III-V nitride materials pose fundamental problems for vertical transport devices such as laser diodes. New approaches to deal with vertical transport are discussed. Integrated heterostructures are proposed, which incorporate graded nitride layers to eliminate band offsets, for the development of a variety of vertical transport devices such as light-emitting diodes, laser diodes, photocathodes, electron emitters based on the negative-electron-affinity of AlN, and certain transistor structures.

EXPERIMENTAL DETAILS

The III-V nitride films were grown using a three-chamber MBE system. The first chamber is equipped with an ECR plasma source for plasma cleaning of substrates using various gas mixtures. The second chamber is equipped for surface analysis of substrates and epilayers at temperature up to 800°C using Auger electron spectroscopy. The third chamber is the main MBE film growth chamber which accepts substrates up to 75 mm in diameter, has provisions for up to nine MBE source ovens, is equipped with reflection high energy electron diffraction (RHEED), and includes an optical pyrometer for measuring substrate temperatures.

An Oxford Applied Research MPD21 radio frequency (rf) plasma source was used to generate an active nitrogen flux. The plasma source was operated at nitrogen pressures ranging from 5×10^{-6} to 4×10^{-4} Torr using rf powers of 150 to 400 W. The nitride films synthesized by MBE during this study were grown on 2-3 μm thick high-quality GaN buffer layers prepared by MOCVD on basal plane 6H-SiC substrates at Cree Research, Inc. The best MOVPE-grown GaN layers exhibit photoluminescence (PL) spectra at 298 K dominated by near-edge emission at 3.41 eV and double-crystal x-ray rocking curves as narrow as 85 arc sec FWHM (0002). These GaN/SiC substrates were cleaned prior to MBE film growth using trichloroethylene, acetone, and methanol followed by plasma-cleaning using a 1:1 hydrogen/helium gas mixture to remove carbon. This was followed by thermal annealing at 600°C - 800°C . After cleaning, the GaN/SiC substrate surface showed little or no carbon or oxygen contamination [1]. The GaN films were monitored during MBE growth by RHEED. The GaN films displayed a streaky RHEED pattern with a (2×2) surface reconstruction, characteristic of two-dimensional layer growth [1]. Similar patterns were observed during the growth of the $\text{Al}_x\text{Ga}_{1-x}\text{N}$ films and $\text{Al}_x\text{Ga}_{1-x}\text{N}/\text{GaN}$ multilayer structures.

Selected MBE-grown film samples were also characterized by means of Nomarski interference-contrast microscopy, scanning electron microscopy (SEM), transmission electron microscopy (TEM), double-crystal x-ray diffraction, and variable-temperature PL. The PL measurements were obtained using a He-Cd laser for excitation and a SPEX double-grating monochromator equipped with a cooled GaAs photomultiplier for detection. Photon-counting instrumentation and a computer were

employed to collect, store and analyze the PL data. Double-crystal x-ray rocking curves were obtained using a Blake Industries double-crystal x-ray unit which employed $\text{Cu K}\alpha$ x-rays. The double-crystal rocking curves were measured in a standard fashion with the detector fully open (no aperture).

MBE FILM GROWTH: RESULTS AND DISCUSSION

GaN Films on GaN/SiC Substrates

A representative double-crystal x-ray rocking curve for a 3 μm thick MBE-grown GaN film is shown in Figure 2. Diffraction peaks from both the GaN film and the underlying 6H-SiC substrates are shown. It is seen that the GaN film exhibits a symmetric (0002) diffraction peak with a full-width at half-maximum (FWHM) of 156 arc sec. The (0002) GaN diffraction peak represents a superposition of diffraction peaks from the 3 μm thick MBE-grown layer and the underlying $\sim 3 \mu\text{m}$ thick MOCVD-grown GaN layer since diffraction from the SiC substrate is also observed.

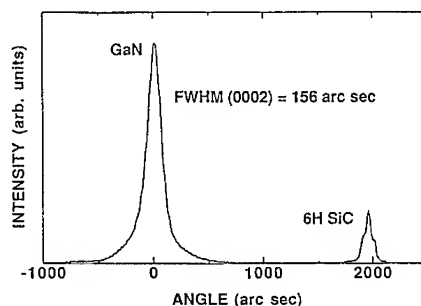


Figure 2. X-ray rocking curve.

Vertical cross-section TEM studies were also conducted on selected MBE-grown GaN epilayers on GaN/SiC substrates. The TEM photo in Figure 3 shows

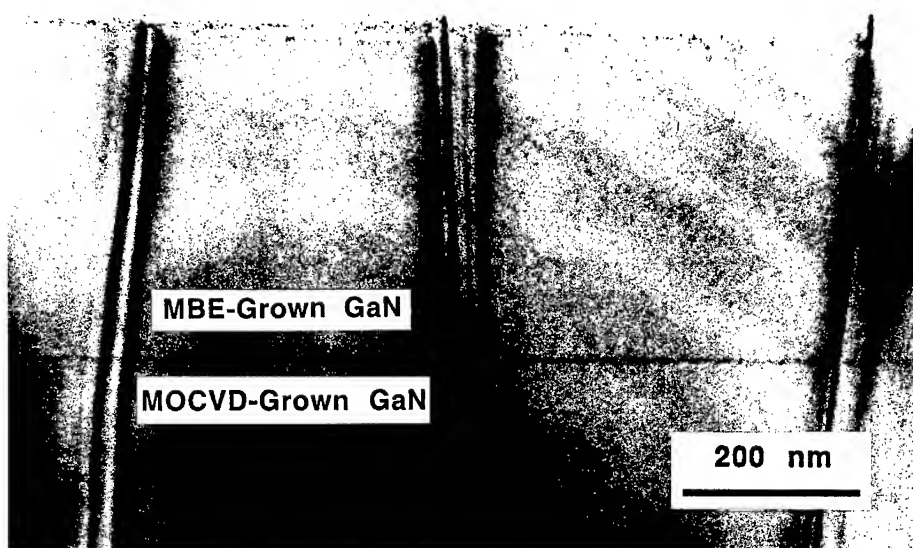


Figure 3. Vertical cross-section TEM photograph of MBE-grown GaN on GaN/SiC.

dislocation densities as low as 10^8 per cm^2 in both the MBE-grown GaN layers and the underlying MOCVD-grown GaN buffer layers. These results provide direct evidence that by using MBE it is possible to grow GaN which is comparable in structural quality to state-of-the-art MOCVD-grown GaN.

PL measurements of the GaN epilayers provide additional proof of their quality. Figure 4 shows representative PL spectra for an undoped MBE-grown GaN epilayer at 295 K, 77 K, and 4.2 K. The room temperature PL spectrum is dominated by band-edge emission at 3.409 eV. Note that this band-edge emission peak has a FWHM of only 29.7 meV -- remarkably close to the theoretical thermal-broadening limit at room temperature. There is also evidence in the PL spectrum at 300 K of deep level yellow-green emission near 2.2 eV. At 77 K, the deep level emission is no longer present and the band-edge emission peak has narrowed to 15.8 meV FWHM. When cooled to 4.2 K, the band-edge feature, due presumably to excitonic emission, splits into two sharp peaks having FWHMs of only 4-5 meV. The splitting between these two peaks roughly matches the exciton splitting observed by Dingle *et al.* [2,3].

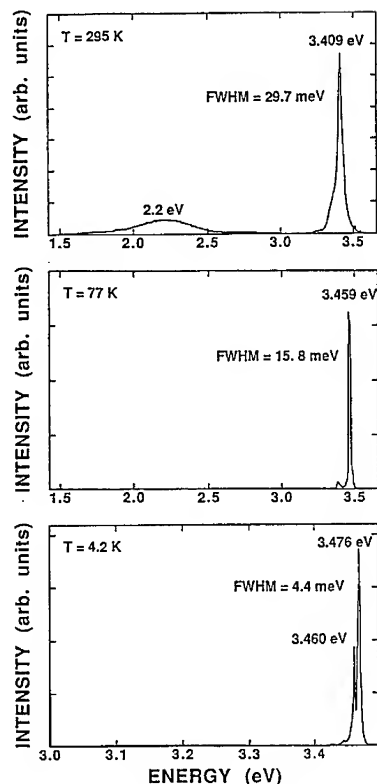


Figure 4. PL spectra of undoped GaN.

A representative room temperature PL spectrum for a $0.7\ \mu\text{m}$ thick MBE-grown p-type Mg-doped GaN film is shown in Figure 5(a). The PL emission peak at 3.25 eV is believed to be due to an electron-to-acceptor (e,A) optical transition associated with the Mg dopant. If this is the case, this would correspond to an acceptor ionization energy E_a for the Mg acceptor of about 160 meV in GaN. Near-band-edge emission from GaN:Mg at 3.39 eV, which may be associated with an unintentional donor, is also seen in the PL spectrum.

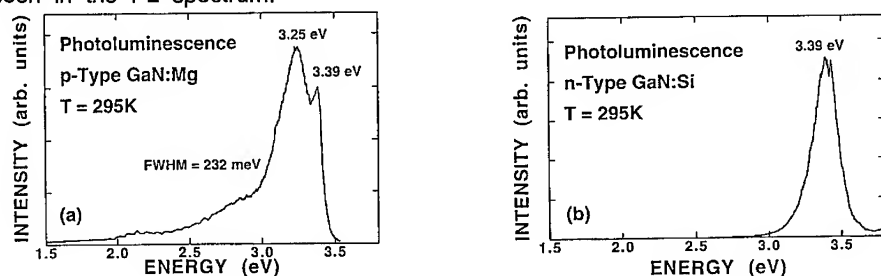


Figure 5. 295K PL spectra for (a) GaN:Mg and (b) GaN:Si films

For comparison, the PL spectrum of a 1 μm thick MBE-grown heavily-doped n-type GaN:Si is shown in Figure 5(b). In this case, the spectrum is dominated by a very intense peak at 3.39 eV due, we believe, to a donor-hole (D,h) optical transition associated with the Si donor. If this is the case, this would correspond to a donor activation energy E_d of about 19 meV for the Si donor in GaN. Hall effect measurements on this sample yielded a room temperature carrier concentration $n = 1.2 \times 10^{20} \text{ cm}^{-3}$ and an electron mobility $\mu_n = 65 \text{ cm}^2/\text{V}\cdot\text{s}$.

$\text{Al}_x\text{Ga}_{1-x}\text{N}$ Films and $\text{Al}_x\text{Ga}_{1-x}\text{N}/\text{GaN}$ Multi-Quantum-Well Structures

$\text{Al}_x\text{Ga}_{1-x}\text{N}$ layers ($x \sim 0.06\text{--}0.08$) were also grown by MBE on GaN/SiC substrates. Figure 6(a) shows a representative PL spectrum at 295 K for a 1.2 μm thick undoped MBE-grown $\text{Al}_x\text{Ga}_{1-x}\text{N}$ epilayer. The emission spectrum is dominated by a high intensity near-band-edge emission peak at 3.690 eV with a FWHM of 79.5 meV.

$\text{Al}_x\text{Ga}_{1-x}\text{N}/\text{GaN}$ multiple quantum-well (MQW) structures consisting of five 50 \AA GaN quantum wells separated by four 100 \AA $\text{Al}_x\text{Ga}_{1-x}\text{N}$ barriers were grown on GaN/SiC substrates by MBE under the same conditions. The structure was capped with a 500 \AA thick $\text{Al}_x\text{Ga}_{1-x}\text{N}$ layer. As shown in Figure 6(b), PL emission occurs from both the $\text{Al}_x\text{Ga}_{1-x}\text{N}$ capping layer and the GaN QWs. The relative PL peak intensities depend on the thickness of the $\text{Al}_x\text{Ga}_{1-x}\text{N}$ capping layer and the wavelength of the excitation source. Note that the emission peak associated with the GaN QWs occurs at 3.435 eV, corresponding to a shift to higher energy by about 36 meV from that of the bulk GaN value (see Fig. 4(a)). This energy shift, we believe, is due to the combined effects of strain and quantum confinement as has been reported by Krishnakutty *et al.* [4].

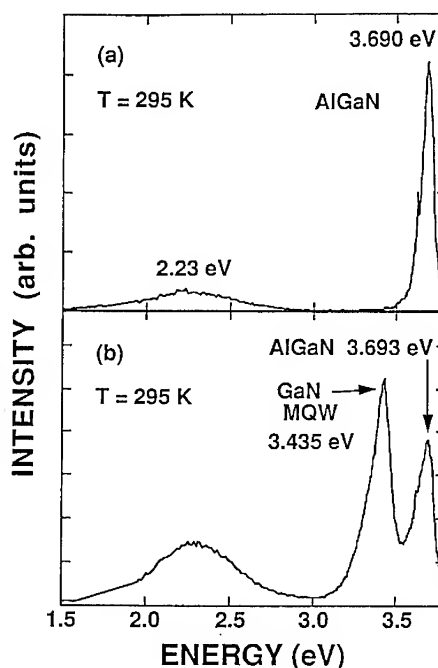


Figure 6. Photoluminescence at 295K from (a) an undoped MBE-grown $\text{Al}_x\text{Ga}_{1-x}\text{N}$ layer and (b) an $\text{Al}_x\text{Ga}_{1-x}\text{N}/\text{GaN}$ MQW structure.

$\text{Al}_x\text{Ga}_{1-x}\text{N}/\text{GaN}$ Double Heterostructure LEDs

Double heterostructure (DH) LEDs based on $\text{Al}_x\text{Ga}_{1-x}\text{N}/\text{GaN}$ were grown by MBE. The GaN active region was co-doped with Si and Mg to create an emission center based on donor-acceptor pair recombination. The LEDs were fabricated using photolithography and dry etching techniques to define 200 μm x 200 μm mesas. Electrical contacts to the p-type layer were obtained by evaporating 100 μm x 100 μm

Ni/Au contact pads. The bottom n-type layer was contacted by depositing Ni onto the backside of the conducting GaN/SiC substrate. Room temperature current - voltage (I-V) characteristics of a typical DH LED are shown in Figure 7. The device has a turn-on voltage of 3.2 V and a forward voltage of 4.7 V at 20 mA. The LED emits blue-violet light from 77K to room temperature. The peak wavelength of the electroluminescence (EL) occurs at 400 nm at 77 K, as shown in Figure 8. At 160 K, the peak wavelength shifts to 390 nm. At room temperature, however, the emission is quite broad and includes emission from deep level states. Additional work is underway at NCSU to improve the efficiency of MBE grown LED devices and to shift their EL spectrum into the blue/green region of the visible spectrum.

III-V NITRIDE CONDUCTION BAND AND VALENCE BAND OFFSETS.

Important advances in understanding the band structures and band offsets of III-V nitride materials have been made within the past two years by several research groups. Benjamin et al. [5] report convincing evidence based on ultraviolet photoemission spectroscopy (UPS) that AlN is a negative electron affinity (NEA) material. That is to say, the conduction band of AlN lies above the vacuum energy level implying that AlN can be used as an efficient emitter of electrons. Consistent with these findings, the above investigators also report the valence band offset between AlN(0001) and SiC(0001) to be approximately 0.8 eV.

Three other research groups have recently reported values for the valence band offset between AlN and GaN. Martin et al. [6] report a Type I heterojunction (valence band edge of AlN below that of GaN) with a valence band offset or discontinuity of $\Delta E_v = 0.8 \pm 0.3$ eV. Baur et al. report [7] a Type 1 heterojunction with a valence band discontinuity of $\Delta E_v = 0.5$ eV. Segall et al. [8] also report a valence band

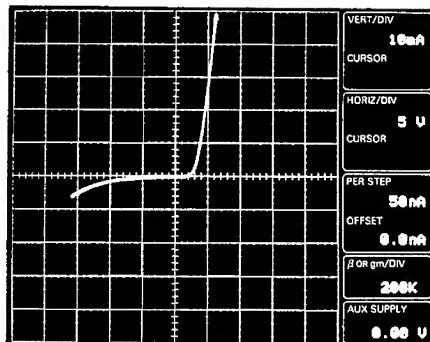


Figure 7. I - V characteristics of LED.

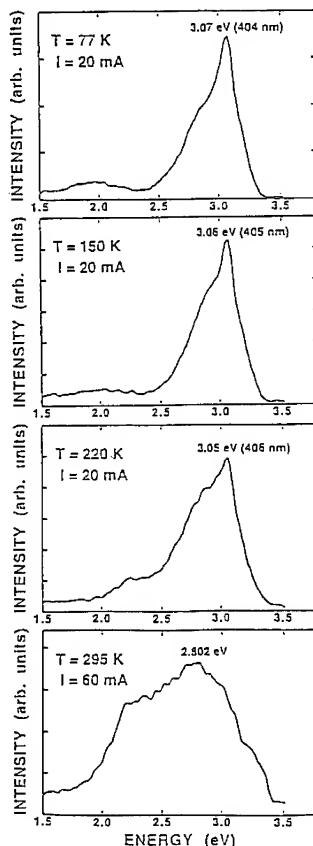


Figure 8. Emission from GaN LED.

offset between AlN and GaN of $\Delta E_v = 0.8$ eV. In addition, these researchers report a Type 1 interface between GaN and InN with $\Delta E_v = 0.5$ eV. These researchers also report a Type 1 interface between AlN and GaAs with $\Delta E_v = 2.0$ eV [8].

The above results for band offsets have important consequences concerning the transport of electrons and holes through interfaces involving III-V nitride materials. Figure 9 summarizes these results by illustrating schematically, in terms of an energy band diagram, how the conduction and valence bands of the binary III-V nitride semiconductors line up relative to one another and to other well-known semiconductor

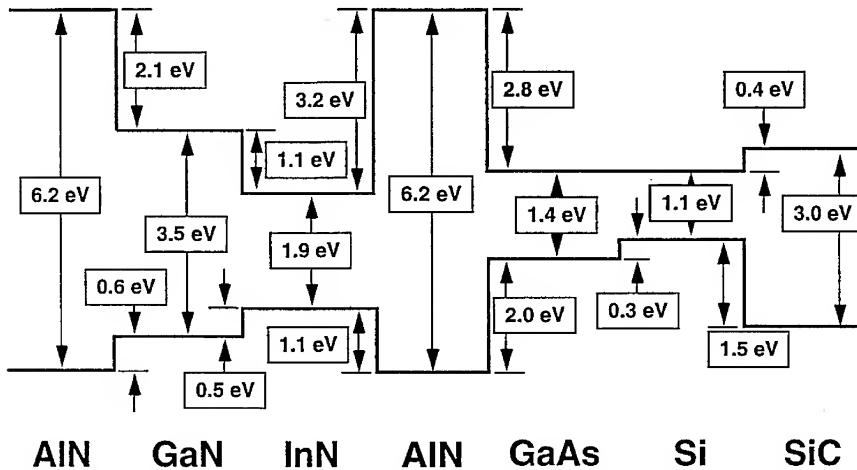


Figure 9. Approximate band lineups for selected semiconductors.

materials GaAs, Si, and SiC. It should be recognized that Figure 9 lists approximate band offsets among the various materials that are shown. That is to say, the band diagram of Figure 9 represents a best effort to illustrate band lineups of the materials shown as they are known from experiments performed to date. These band offsets may only be accurate to within ± 0.2 - 0.3 eV, based on the accuracy of current experimental measurement techniques. However, the band diagram of Figure 9 provides an important and essential guide for the design and implementation of "bandgap engineered" III-V nitride vertical-transport devices such as laser diodes.

It is well-known that heterojunction energy barriers in excess of about 0.3 eV can prevent the flow of carriers (electrons and/or holes) in thin film devices which require vertical transport of charged carriers across heterointerfaces [9]. Devices of this type include not only light emitting diodes and laser diodes but also certain transistor structures, and electron emitters based on NEA materials such as AlN, for example. The energy band diagram of Figure 9 clearly shows that there can be substantial energy barriers when these types of devices are based on III-V nitride heterostructures. To illustrate this point, let us consider current nitride LEDs: All nitride LEDs fabricated to date suffer from less-than-ideal current-voltage (I-V) characteristics as a result of high contact resistances, particularly with regards to contacts for p-type material. As a consequence, because of the much higher current densities required, it is expected that nitride laser diodes would exhibit high turn-on voltages -- similar to the problem that has plagued blue/green laser diodes based on II-VI materials.

The above analysis can be understood by referring to the energy band diagrams of Figure 10. The diagrams at the left of Figure 10 show how gold, typically used to contact p-type GaN, lines up with the valence band of GaN as determined using the band offset diagram of Figure 10. It might be noted that, coincidentally, the valence band of GaN is located at the same energy as the valence band of ZnSe [10]. Thus, there is an energy barrier of about 1.6 eV between gold and the GaN valence band. This 1.6 eV reversed-biased energy barrier prevents the flow of holes towards a forward-biased GaN p-n junction, as is shown by the band diagram at the right in Figure 10. As a consequence, high voltages will accompany the high current densities required for any future nitride laser -- if a gold electrode contacting scheme is employed.

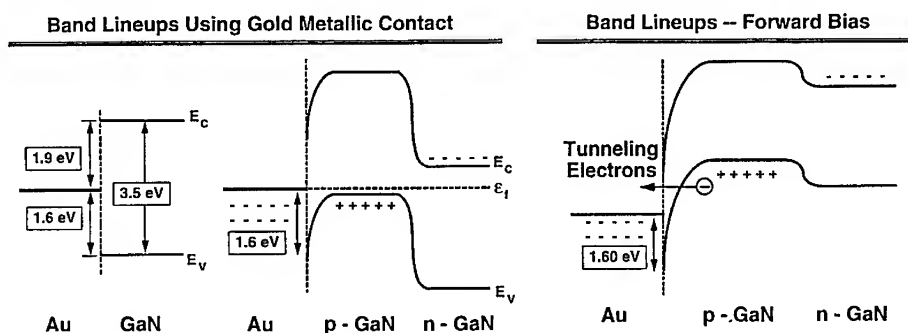


Figure 10. Band diagrams for gold on undoped GaN and for gold on a GaN p-on-n junction (left); gold on a forward-biased GaN p-n junction (right)

INTEGRATED HETEROSTRUCTURE DEVICES

The term integrated heterostructure or integrated heterostructure device (IHD) is here defined as a multilayered structure in which particular layers, or combination of layers, perform distinctly different functions. An example of an IHD is a semiconductor surface-emitting laser which contains (a) multilayers for optical mirrors, (b) an active light generation region which might consist of one or more additional layers or quantum wells, (c) p-type and n-type layers which supply the active light generation region with electron and holes under forward bias, and (d) additional top layers for optically and electrically coupling the laser output to the outside world. These various functions are integrated into a single epitaxial multilayered structure using sophisticated growth techniques such as molecular beam epitaxy (MBE) or metal-organic chemical vapor deposition (MOCVD).

IHDs composed of II-VI materials have been developed to specifically address the p-type ohmic contact problem associated with blue/green laser diodes and LEDs. These devices incorporate special graded/doped layers which eliminate band offsets between the metal/p-type semiconductor and which permit II-VI light emitters to operate at low voltages [10,11,12]. The basic principle behind the use of graded/doped layers to minimize or eliminate band offsets is illustrated by the band diagrams of Figure 11. At the left is shown a Type 1 heterojunction for which appreciable band offsets exist. If both semiconductors are doped n-type, then a large conduction band spike occurs at the heterointerface. This represents a large potential barrier which prevents the flow of electrons from left-to-right into the larger bandgap material under

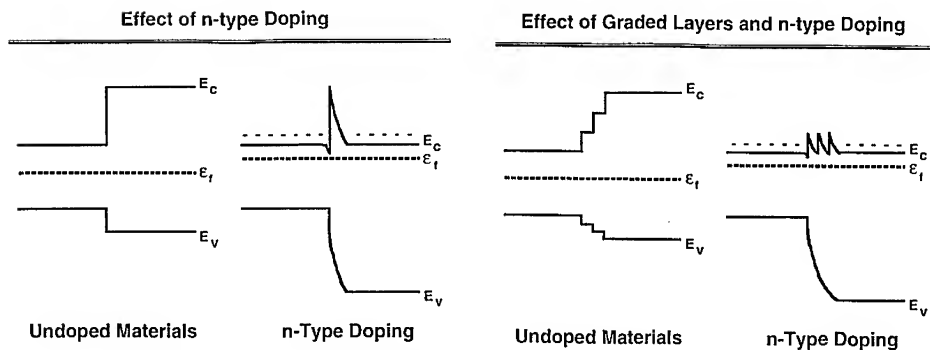


Figure 11. Effect of doping (left) combined with step-grading (right).

an appropriate electrical bias. As a consequence, the heterojunction will exhibit a large impedance to current flow in this direction.

However, doped alloy layers of intermediate bandgap can be deposited between the two semiconductor materials as shown at the right of Figure 11. A well-known property of the equilibrium state is that the Fermi level be constant over the entire system of layers. As a consequence, step-grading along with n-type doping together produce the triple-spiked heterointerface shown at the far right in Figure 11. Note, however, that the barrier heights are now only one-third of the original conduction band offset of the heterojunction.

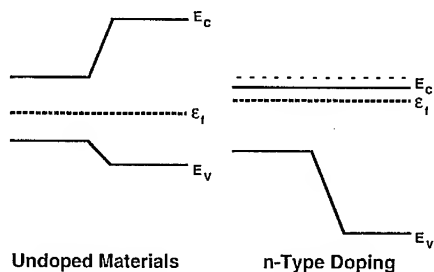


Figure 12. Continuous grading and doping.

Thus, it is clear that by combining n-type doping with a continuously graded intermediate layer, as is illustrated in Figure 12, the original conduction band offset associated with the heterojunction can be completely eliminated. Similar grading/doping procedures can be employed to eliminate band offsets between III-V nitride layers, as is illustrated in Figure 13 below

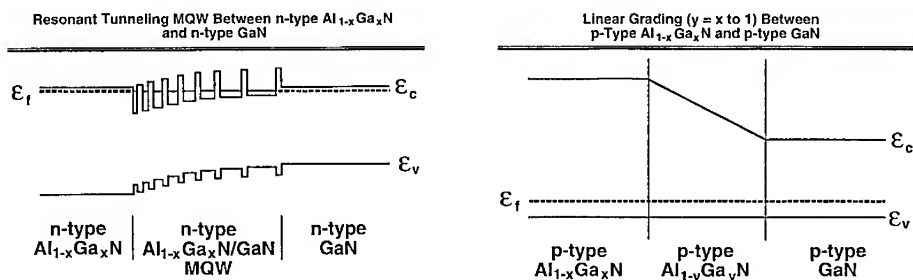


Figure 13. Examples of grading/doping to eliminate band offsets between nitrides.

III-V NITRIDE DEVICES ON SILICON CARBIDE

III-V Nitride Laser Diodes

Nitride lasers will most likely be vertical devices which require a conducting substrate. At present, the substrate of choice is SiC. However, growth of III-V nitrides on SiC introduces another heterointerface which can be the source of an additional barrier to electron and/or hole transport. This is so because of the large band offsets between SiC and the III-V nitrides, as shown in Figure 9. Because of differences in the lattice constant and thermal expansion characteristics of these materials, it has been found that a buffer layer of AlN or AlGa_{0.5}N must be deposited onto SiC prior to the growth of GaN.

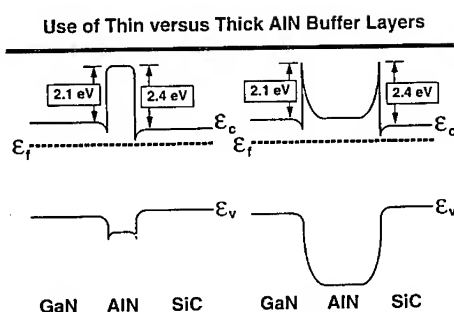


Figure 14. GaN/AlN/SiC heterointerfaces.

So far, all efforts throughout the world have involved the use of n-type SiC substrates onto which an n-type AlGa_{0.5}N or AlN buffer layer is deposited followed by a p-on-n GaN diode. Figure 14 illustrates why this approach generates a barrier with respect to electron flow from SiC into GaN. Note in particular, that an AlN buffer layer introduces a barrier of more than 2 eV for the flow of conduction band electrons from n-type SiC into n-type GaN. This extremely large barrier to electron conduction occurs whether a thin or a thick layer of AlN is used as a buffer, even when the AlN is doped n-type.

To further illustrate this point, consider the p-on-n diode of Al_{0.5}Ga_{0.5}N deposited onto an n-type SiC substrate. Figure 15 shows an energy band diagram of the SiC/Al_{0.5}Ga_{0.5}N heterointerface, consistent with Figure 9. Note that in this case, there is a conduction band offset of about 1.4 eV and a valence band offset of about 0.5 eV, as illustrated by the left diagram of Figure 15. As a consequence of the large conduction band offset between these two materials, a p-on-n diode of Al_{0.5}Ga_{0.5}N deposited onto n-type SiC would behave according to the band diagram at the right of Figure 15. Note that such a structure

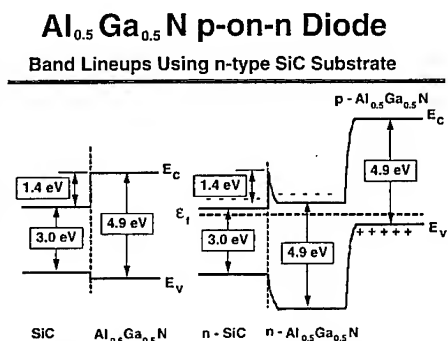


Figure 15. p-on-n diode on n-type SiC.

would generate a large (1.4 eV) energy spike at the heterointerface and this would severely impede the flow of electrons from SiC into n-type Al_{0.5}Ga_{0.5}N when the p-on-n nitride diode is forward biased.

Vertical transport between SiC and Al_{0.5}Ga_{0.5}N is greatly improved when a p-type SiC substrate is employed and an n-on-p nitride diode structure is deposited. This is illustrated by the energy band diagram of Figure 16. In this case, there is a valence band offset of about 0.5 eV at the heterointerface. As a consequence of this reduced

energy barrier, holes can flow relatively easily from p-type SiC into p-type $\text{Al}_{0.5}\text{Ga}_{0.5}\text{N}$ and the nitride diode should operate at low voltage. This situation is improved further if $\text{Al}_{1-x}\text{Ga}_x\text{N}$ alloys having higher x-values are employed. The n-on-p structure therefore addresses two major problems encountered in laser development: (1) The large conduction band offset between n-type SiC and AlGaN is not a factor, since a p-type AlGaN layer are grown epitaxially onto p-type SiC. By incorporating a intermediate graded and doped AlGaN layer it may be possible to

$\text{Al}_{0.5}\text{Ga}_{0.5}\text{N}$ n-on-p Diode on p-SiC

Band Lineups - Forward Bias ($V_{\text{BO}} = 500 \text{ meV}$)

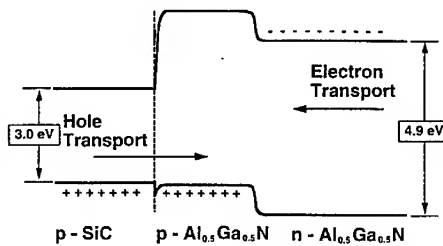
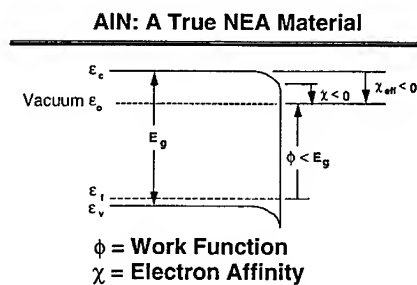


Figure 16. N-on-P diode on p-type SiC.

further reduce the valence band offset between the SiC substrate and the nitride device to $\leq 0.3 \text{ eV}$, so that hole transport under forward bias from the SiC substrate to the nitride device is essentially unimpeded. (2) The n-on-p structure does not require a metal contact to any p-type nitride layer. Rather, a metal contact is provided on the back of the p-type SiC substrate using standard techniques which employ Pt or Ti/Al metallizations. As a consequence, the nitride device can function at low voltage when operating under forward bias, even under the high current densities required for laser diodes.

AlN Negative-Electron-Affinity Electron Emitter

AlN is an attractive candidate for vacuum microelectronic applications because it is a true NEA material. That is, at the AlN surface the conduction band lies above the vacuum level as shown in Figure 17. One problem that a true NEA material faces is the difficulty in obtaining an ohmic contact to the material, particularly if it is doped n-type. Here we suggest a solution to this problem which employs the grading/doping scheme described above. A simple AlN electron emitter is shown in Figure 18 to illustrate the concept. The device is grown on an n-type SiC substrate. A graded and doped layer of AlGaN is employed to eliminate the conduction band offset between the n-type SiC substrate and the AlN overlayer (also presumed to be n-type). A surface layer may be added to enhance the NEA condition as shown, and each device may



- Potential Electron Emitter
- Need Electrons (n-type Doping)
- Need Backside Ohmic Contact

Figure 17. NEA property of AlN.

be processed into a sharp tip to further enhance electron emission. Electrical contact to the device consists of a standard metal contact such as Ni to the back surface of the SiC substrate. The device emits electrons in vacuum when the anode is positively

biased since the ~2.4 eV conduction band offset, which serves as a barrier to electron flow between SiC and AlN, has been eliminated by means of the graded/doped AlGaN layer.

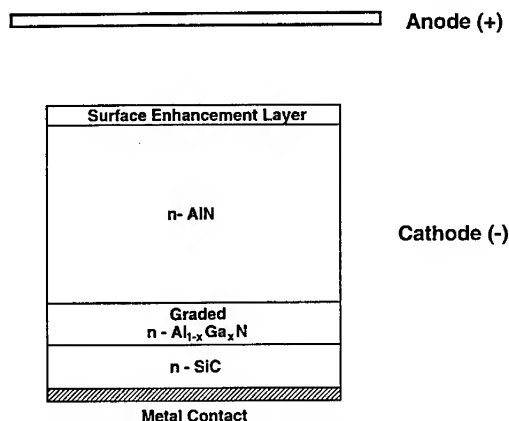


Figure 18. AlN electron emission device which employs an $\text{Al}_{1-x}\text{Ga}_x\text{N}$ grading layer.

ACKNOWLEDGMENTS

All of the authors listed in reference 1 below contributed to the NCSU MBE results.

REFERENCES

1. W. C. Hughes, W. H. Rowland, Jr., M. A. L. Johnson, Shizuo Fujita, J. W. Cook, Jr., J. F. Schetzina, J. Ren, and J. A. Edmond, *J. Vac. Sci. Technol.* **B 13**, 1571 (1995).
2. R. Dingle, D. D. Sell, S. E. Stokowski, M. Ilegems, *Phys. Rev.* **B 4**, 1211 (1971).
3. N.V. Edwards, T.W. Weeks, Jr., M.D. Bremser, R.F. Davis, and D.E. Aspnes, to be published.
4. S. Krishnankutty, R. M. Kolbas, M. A. Khan, J. N. Kuznia, J. M. Van Hove, and D. T. Olson, *J. Electron. Mater.* **21**, 609 (1992).
5. M.C. Benjamin, C. Wang, R.F. Davis, and R.J. Nemanich, *Appl. Phys. Lett.* **64**, 3288 (1994).
6. G. Martin, S. Strite, A. Botchkarev, A. Agarwal, A. Rockett, and H. Morcoç, *App. Phys. Lett.* **65**, 610 (1994).
7. G. Baur, K. Maier, M. Kunzer, U. Kaufmann, and J. Schneider, *Appl. Phys. Lett.* **65**, 2211 (1994).
8. B. Segal, E.A. Abanesi, K. Kim, and W.R. L. Lambrecht, Nitride Workshop, St. Louis, MO, (1994).
9. Z. Yang and J.F. Schetzina, *J. Electron. Mater.* **23**, 1071 (1994).
10. J. Ren, D.B. Eason, L.E. Churchill, Z. Yu, C. Boney, J.W. Cook, Jr., J.F. Schetzina, N.A. El-Masry, *J. Cryst. Growth* **138**, 455 (1994).
11. Y. Lansari, J. Ren, B. Sneed, K.A. Bowers, J.W. Cook, Jr., and J.F. Schetzina, *App. Phys. Lett.* **61**, 2554 (1992).
12. Y. Fan, J. Han, L. He, J. Saraie, M. Hagerott, H. Jeon, N.V. Nurmikko, G.C. Hua, N. Otsuka, *Appl. Phys. Lett.* **61**, 3160 (1992).
13. M.E. Lin, Z. Ma, F.Y. Huang, Z.F. Fan, L.H. Allen, and H. Morkoç, *Appl. Phys. Lett.* **64**, 1003, (1994).

NH₃ AS NITROGEN SOURCE IN MBE GROWTH OF GaN

M. Kamp, M. Mayer, A. Pelzmann, A. Thies, H. Y. Chung, H. Sternschulte*,
O. Marti** and K. J. Ebeling
Department of Optoelectronics, *Department of Semiconductor Physics,
**Department of Experimental Physics, University of Ulm, D-89069 Ulm, Germany

ABSTRACT

We report on the growth of GaN in GSMBE using NH₃ as nitrogen source. Special focus will be on the NH₃ cracking, where we applied an On Surface Cracking technique (OSC). Using OSC we achieve photoluminescence linewidths as narrow as 5.5meV (5K) and mobilities of 220 cm²/Vs at room temperature.

INTRODUCTION

Today, growth of GaN and its related compounds is dominated by MOVPE techniques [1,2]. This is mainly due to the fact that supply of atomic nitrogen seemed to be very difficult under MBE conditions. Commonly N₂ is used as nitrogen source, which due to the high binding energy of 9.5 eV requires the application of a plasma cracking source. However, using plasma sources such as DC, RF, ECR ion damage during growth is hard to avoid [3]. Furthermore, the self biased voltage of the plasma sources show sputtering effects leading to contamination of the epitaxial structures. Other serious challenges with plasma grown nitrides include reproducibility and homogeneity.

We report on the successful use of NH₃ as nitrogen precursor in MBE. For this purpose we employ an technique entitled On Surface Cracking (OSC) where uncracked ammonia is injected onto the growing GaN surface. We will work out that OSC of ammonia provide an excellent N source to MBE growth of GaN. It is economical, reliable, easy to maintain, highly reproducible, unsophisticated and does not require an expensive plasma source.

EXPERIMENT AND RESULTS

For our investigations we use an almost standard MBE system (Riber 32) adapted to group V gas sources. The system is turbo pumped, the attached gas control and handling system is home made. NH₃ is introduced into the system through a standard high temperature injector (Riber HTI 432). Effusion cells are used to supply the group III species Ga and Al. Unless otherwise mentioned GaN layers are grown at growth rates of 700 nm/h to a thickness of approximately 2 μm. By increasing the growth rate to 1.2 μm/h comparable crystal and optical properties are achieved.

Characterization of the grown structures is carried out by optical and scanning electron microscopy (SEM), atomic force microscopy (AFM), X-ray diffraction (XRD), photoluminescence (PL) and cathodoluminescence (CL). Electrical data are obtained from Hall and CV measurements. A quadrupole mass analyzer (QMA) is used for detection of background gas species and for the NH₃ cracking studies.

To evaluate the suitability of NH_3 as nitrogen source for MBE we first investigate the thermal cracking using a high temperature gas injector. Figure 1. reveals that the 4.8 eV binding energy of NH_3 despite being significant lower than that of N_2 still requires cracking temperatures above 600°C for thermal cracking (pyrolysis).

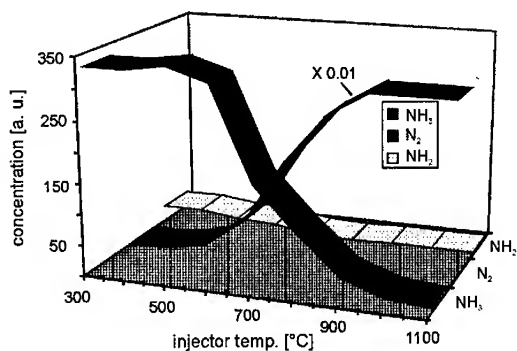
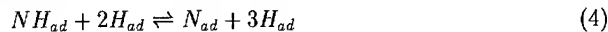
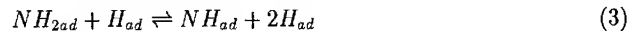


Figure 1: Concentration of NH_3 , N_2 and NH_2 at the QMA as a function of injector temperature

A more detailed study of the ammonia cracking was recently published by our group [4]. Therein thermodynamic equilibrium data are presented and possible dissociation processes on the surfaces are discussed. In quintessence, we assume that the dissociation steps on the surface can be described according to [5] :

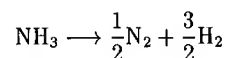


($g \hat{=}$ gaseous , $ad \hat{=}$ adsorpt)

with a decomposition rate (for $T \geq 550^\circ\text{C}$) given by

$$\nu = \frac{K_1 K_2 [\text{NH}_3]}{K_{-1} + K_2} \quad (7)$$

Clearly, cracking is described by the overall reaction



which is verified by our QMA data (fig.1).

We propose that applying OSC of ammonia on a GaN surface the NH_3 dissociation undergoes reactions similar to steps (1) to (4), but that at least one nitrogen species can chemically react with Ga atoms on the surface before being desorbed as N_2 . Therefore OSC of NH_3 succeeds whereas cracking in the injector fails.

Applying OSC for GaN growth we found that growth can be accomplished at temperatures as low as approx. 550°C . This is in reasonable agreement with the temperatures we found to be necessary for ammonia cracking (fig.1).

However, the best GaN crystal properties were achieved at substrate temperatures around 800°C using a beam equivalent NH_3 pressure of approx. 10^{-5} torr and a V/III ratio of approx. 20.

To produce high quality GaN films on sapphire substrate we apply a short nitridation step and use a thin AlN nucleation layer before growing the GaN layer. Fig. 2 shows

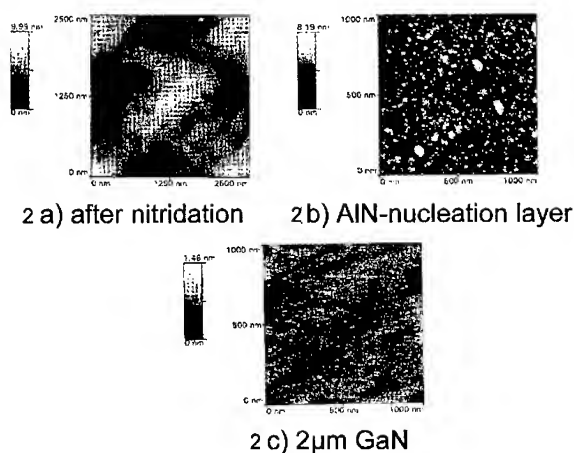


Figure 2: AFM-topography after different steps of growth

typical atomic force micrographs of the (0001) sapphire surface after nitridation, AlN nucleation layer formation, and $2\ \mu\text{m}$ GaN growth. Numerous tiny islands of about 50 nm width and 10 nm height appear in the AlN nucleation layer which are smoothened during growth of the GaN layer. The resulting $2\ \mu\text{m}$ thick GaN film is optically flat.

Fig. 3 shows photoluminescence spectra of a $2\ \mu\text{m}$ GaN layer. We find narrow near band edge emission with 5.5 meV linewidth at 5K which increases to 34 meV at room temperature. Yellow emission often present between 2 to 2.75 eV was so much suppressed that it could not be detected even at 300 K.

Electrical properties of the layers were obtained from Hall and CV measurements at 300K. We find carrier concentrations in the low $10^{17}\ \text{cm}^{-3}$ range with mobilities of $220\ \text{cm}^2/\text{Vs}$ at 300 K. Electron concentrations as low as $1 \times 10^{16}\ \text{cm}^{-3}$ were also measured with Hall and verified by CV measurements. However, since corresponding mobilities are about $160\ \text{cm}^2/\text{Vs}$ such layers are supposed to probably contain deep traps.

MBE grown $2\ \mu\text{m}$ thick GaN layers typically show 400 arcsec wide x-ray diffraction linewidths ((0002) reflex, $\text{Cu K}\alpha_1$ lines, omega scans). A significant improvement in crys-

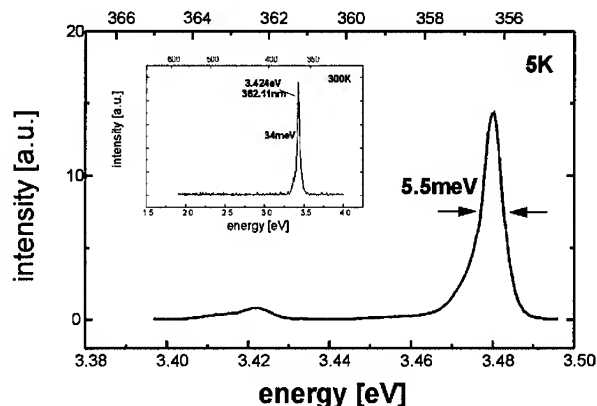


Figure 3: Photoluminescence spectra of a 2 μm thick GaN film at 5K and at 300 K in the inset

talline quality is observed when MBE growth is performed on 0.5 μm thick GaN layers grown on sapphire with our MOVPE system. The MBE growth process results in a linewidth reduction of the original MOVPE layers from 100 to 70 arcsec for the 2 μm thick MBE layers. Herefrom, we conclude that the crystalline quality of GaN films is essentially affected by the nitridation and nucleation process. Comparing our MBE and MOVPE results and their combination our data suggest, that in MBE we have to improve the first steps of growth (nitridation and nucleation). However, the excellent crystallinity obtained on top of the MOVPE layers reveal that the general growth conditions for our MBE bulk growth seems to be appropriate.

SUMMARY

We report on cracking of ammonia in a high temperature injector. Efficient cracking of NH_3 in a high temperature gas injector was verified at temperatures above 600 $^\circ\text{C}$ using QMA. The dominant cracking product is N_2 which is due its high binding energy not appropriate for growth of nitrides. However, on surface cracking (OSC) of NH_3 results in excellent GaN material quality. Photoluminescence at 5K reveals near band edge emission with linewidths of 5.5 meV at 3.48 eV. Electrical transport measurements show electron mobilities of 220 cm^2/Vs for concentrations of $2 \times 10^{17} \text{ cm}^{-3}$. GaN layers with background carrier concentrations in the $1 \times 10^{16} \text{ cm}^{-3}$ range are found to have high concentration on either traps or holes. X-ray data prove a FWHM of 450 arcsec.

From those promising data we conclude that OSC of ammonia offers an excellent N source for MBE growth of GaN. It is economical, reliable, easy to maintain, highly

reproducible, unsophisticated and the requirements to the injector are very low compared to every plasma source.

ACKNOWLEDGEMENTS

We like to acknowledge contributions from C. Kirchner, S. Menzel, D. Sowada, A. Fricke, T. Albrecht and S. Hild and financial support from BMBF.

REFERENCES

1. I. Akasaki and H. Amano, J. Cryst. Growth **146**, 455 (1995).
2. S. Nakamura, T. Mukai and M. Senoh, J. Appl. Phys. **76**, 8189 (1994).
3. R. J. Molnar, R. Singh and T. D. Moustakas, J. Electronic Materials **4**, 275 (1995).
4. M. Kamp, M. Mayer, A. Pelzmann, S. Menzel, H. Y. Chung, H. Sternschulte and K. J. Ebeling, in Proceedings of Topical Workshop on III-V Nitrides, Nagoya, Japan, 1995.
5. M. Weiss, G. Ertl and F. Nietschke, Appl. Surf. Sci., **2**, 614 (1979)

GALLIUM INCORPORATION KINETICS DURING GSMBE OF GaN

CHARLES R. JONES*, TING LEI**, RON KASPI*, and KEITH R. EVANS**

*Wright State University Research Center, Dayton, Ohio 45435

**Solid State Electronics Directorate, Wright Laboratory, Wright-Patterson Air Force Base, OH 45433

ABSTRACT

The kinetics of Ga incorporation during gas-source molecular beam epitaxy of GaN are investigated for varying substrate temperature and incident ammonia flux. Incident Ga atoms eventually either: 1) react with NH_3 to form GaN, 2) accumulate on the film surface, or 3) desorb. Low substrate temperatures lead to significant Ga surface accumulation due to the temperature-dependent reactivity of NH_3 towards Ga. High substrate temperatures give rise to significant Ga desorption. Increasing NH_3 flux retards both Ga surface accumulation and Ga desorption. The GaN formation rate variation with substrate temperature peaks near 750°C and increases with NH_3 flux. The observation of two distinct and very low activation energies for Ga desorption suggests a relatively complex surface chemistry and a strong likelihood that hydrogen is playing an important role.

INTRODUCTION

Group III-nitride semiconductor heterostructures show great potential for applications in ultraviolet/visible photonics and high temperature and high power electronics.¹ However, issues of substrate availability, limited growth rates, and high intrinsic point defect generation rates have slowed progress in developing these materials. It is likely that a fundamental understanding of the surface processes occurring during growth will pave the way towards the realization of higher growth rates and lower intrinsic defect generation rates.

In this study we investigate the kinetics of Ga incorporation, over a range of substrate temperature and incident NH_3 flux, during gas source MBE (GSMBE) growth of GaN. The in-situ sensor technique of desorption mass spectrometry² (DMS) is employed for real-time monitoring of the Ga desorption rate during GaN growth and for determination of the Ga surface accumulation rate via temperature-programmed desorption (TPD) measurements performed immediately upon growth interruption.³ The GaN formation rate is then determined by mass balance.

EXPERIMENTAL

Growths were performed on two-inch indium-bonded (0001) sapphire substrates in a highly modified Varian 360 MBE chamber, which is pumped by a 2400 l/s diffusion pump equipped with a liquid nitrogen-cooled optically opaque baffle. This system is capable of producing state-of-the-art GaN in terms of optical and structural properties.⁴ A contact thermocouple is used for substrate temperature sensing. Desorption monitoring is performed with a differentially pumped, shuttered, quadrupole mass spectrometer which has direct sight of approximately the center 1.5 inch diameter region of the substrate. A novel gas cracker cell⁵ is used in the uncracked mode to supply NH_3 as the nitrogen source; the NH_3 flux is controlled by a manual precision leak valve. Prior to the experiments, a suitable GaN buffer layer of thickness of ~ 500 nm is first deposited to ensure a reproducible starting surface.

The GaN formation rate (R_{GaN}), Ga surface accumulation rate ($J_{\text{Ga,accum}}$), and Ga desorption rate ($J_{\text{Ga,desorb}}$) during growth are determined for the substrate temperature (T_s) range of 625 to 875°C for three different NH_3 flux (J_{NH_3}) values: 1.0×10^{-6} torr, 1.0×10^{-5} torr, and 1.0×10^{-4} torr. The incident Ga flux (J_{Ga}) is held constant at 0.30 monolayers per second [(ML)/sec]. The corresponding V/III incident flux ratio ($J_{\text{NH}_3}/J_{\text{Ga}}$) then varies from ~ 10 to $\sim 10^3$.

The Ga desorption rate during growth is determined by DMS monitoring of the 69 amu peak. The Ga surface accumulation rate is determined by integrating the 69 amu peak during TPD analysis³ performed immediately after growth and normalizing by the growth time. The TPD

analysis is carried out in the absence of NH_3 flux in order to eliminate the possibility that surface Ga atoms, which accumulated during the growth cycle, can react during the TPD measurement to form GaN. Additionally, we have verified that the underlying GaN does not dissociate during TPD analysis, which is as expected based on its relatively high enthalpy of formation (-110.5 kJ/mol).⁶ The GaN formation rate is then determined by mass balance: $R_{\text{GaN}} = J_{\text{Ga}} - J_{\text{Ga,desorb}} - J_{\text{Ga,accum}}$.

RESULTS AND DISCUSSION

Figure 1 shows the variation of $J_{\text{Ga,desorb}}$ with time during the [GaN growth/TPD] sequence for $J_{\text{NH}_3} = 1.0 \times 10^{-6} \text{ torr}$. Data is shown for three T_s values: a) 650°C , b) 700°C , and c) 750°C . The Ga shutter is opened at $t = 120 \text{ sec}$, initiating GaN growth and Ga surface accumulation. The Ga desorption rate $J_{\text{Ga,desorb}}$ is significant for all three T_s and increases with increasing T_s . At $t = 135 \text{ sec}$ growth is interrupted by closing both the Ga and NH_3 shutters and closing off the NH_3 supply leak valve. TPD analysis is initiated immediately upon growth interruption by heating the sample at constant current, causing T_s to rise monotonically with time from the growth temperature to reach a final value of $\sim 875^\circ\text{C}$ at $t = 420 \text{ sec}$. All of the surface accumulated Ga desorbs between $t = 280$ and 420 sec , giving rise to the observed Ga TPD peak, the area under which provides a quantitative measure of the surface accumulated Ga population resulting from the GaN film growth. Visual inspection shows that the area of the TPD peak decreases with increasing T_s . Similar data obtained for other values of T_s and J_{NH_3} show the same qualitative behavior.

Note in Fig. 1 that, for the two lowest T_s values, $J_{\text{Ga,desorb}}$ drops with time during GaN growth. This reproducible phenomenon is not understood at present, although it may be due to a drop in surface temperature associated with the change in surface emissivity accompanying surface Ga accumulation. It also may be related to the relatively poor GaN surface morphology and the relatively high density of dislocations present due to the relatively large lattice mismatch between the GaN film and the sapphire substrate. Additional experiments are planned to discern the mechanism giving rise to this effect. For the analysis below we simply use the average value of $J_{\text{Ga,desorb}}$ observed during GaN growth.

In Fig. 2 the (average) magnitude of $J_{\text{Ga,desorb}}$ during GaN growth is plotted versus T_s for varying J_{NH_3} . As observed, the magnitude of $J_{\text{Ga,desorb}}$: 1) is finite for all conditions investigated, 2) grows monotonically with T_s , 3) increases rapidly near $T_s \sim 700^\circ\text{C}$, and 4) flattens out for the highest T_s values. The inset shows an Arrhenius plot [$\ln(J_{\text{Ga,desorb}})$ vs $1/T_s$] for $J_{\text{NH}_3} = 1.0 \times 10^{-4} \text{ torr}$. Two distinct activation energies are observed with two associated T_s regimes. The rate-limiting-step for Ga desorption is found to have an associated activation energy of $1.4 \pm 0.1 \text{ eV}$ for $625^\circ\text{C} < T_s < 740^\circ\text{C}$ and $0.4 \pm 0.1 \text{ eV}$ for $740^\circ\text{C} < T_s < 875^\circ\text{C}$. Similar plots (not shown) for the two lower values of J_{NH_3} show the same activation energy of 1.4 eV in the low T_s regime and a negligible energy barrier for desorption at higher T_s . The negligible barrier at higher T_s gives rise to the flat region in Fig. 2 for the two lower values of J_{NH_3} . We interpret this behavior as follows: The surface lifetimes of both Ga and NH_3 are so short for $T_s > 800^\circ\text{C}$ that they essentially desorb immediately after incidence unless they encounter each other at the time of incidence; if an encounter is made, reaction occurs. The likelihood of such an encounter would be relatively independent of T_s .

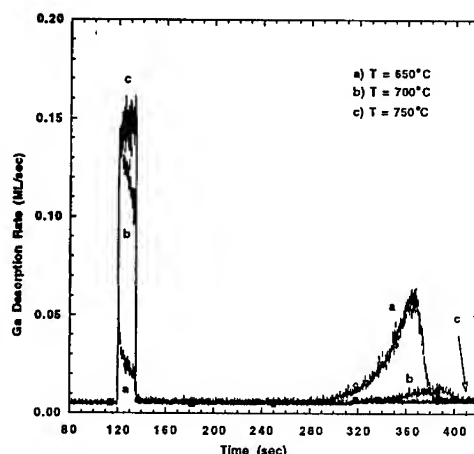


Fig. 1. Plot of Ga desorption rate vs time during the GaN growth/TPD sequence for three different growth temperatures. The incident NH_3 flux was $1.0 \times 10^{-6} \text{ torr}$.

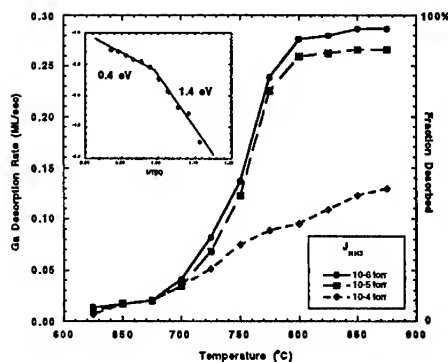


Fig. 2. Variation of Ga desorption rate with substrate temperature for varying incident NH_3 flux. The relative fraction of Ga desorbed is shown on the right axis. An Arrhenius plot for $J_{\text{NH}_3} = 1.0 \times 10^{-4}$ torr is shown in the inset.

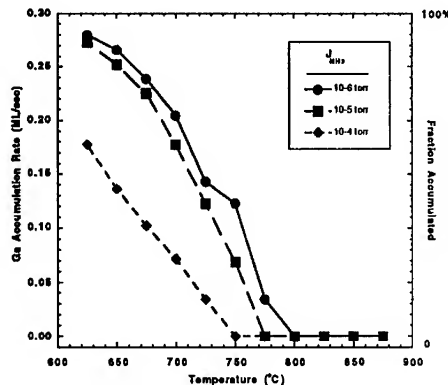


Fig. 3. Variation of Ga surface accumulation rate with substrate temperature for varying incident NH_3 flux. The relative fraction of Ga accumulated is shown on the right axis.

Integration of the area under the TPD peak (see Fig. 1) gives, when normalized by the growth time, the Ga surface accumulation rate, which is plotted in Fig. 3 as a function of T_s for the three values of J_{NH_3} . Significant Ga surface accumulation occurs at the lower T_s values investigated, with the tendency for Ga to accumulate at the surface increasing when J_{NH_3} is reduced. For instance, for growth at $T_s = 750^\circ\text{C}$, 44% of incident Ga atoms remain on the surface for $J_{\text{NH}_3} = 1.0 \times 10^{-6}$ torr, 24% of incident Ga atoms remain on the surface for $J_{\text{NH}_3} = 1.0 \times 10^{-5}$ torr, and negligible Ga accumulation occurs for $J_{\text{NH}_3} = 1.0 \times 10^{-4}$ torr. The tendency for Ga to accumulate at the growth surface at low T_s was previously reported⁷ on for the same growth system: GSMBE of GaN using NH_3 . The increase in accumulation rate for decreased NH_3 flux is consistent with simple mass action considerations.

By subtracting the Ga surface accumulation rate and the Ga desorption rate from the incident Ga flux, the GaN formation rate is determined. The dependence of the GaN formation rate on T_s is shown in Fig. 4 for the three different values of J_{NH_3} investigated. The GaN formation rate is seen to peak near $T_s = 750^\circ\text{C}$, with the exact peak temperature being larger for increased J_{NH_3} . At lower and higher T_s values the GaN formation rate is reduced due to effects of Ga surface accumulation and desorption, respectively. The GaN formation rate is seen to increase with J_{NH_3} at all T_s values, which is consistent with considerations of mass action. Note that these calculated GaN formation rates are consistent with ex-situ analyses on GaN films⁴ grown in the same GSMBE system.

The tendency to accumulate Ga at low T_s is explained by the relatively low reactivity of NH_3 towards Ga at low T_s values, as previously observed.⁷ The dependence of Ga desorption on T_s is more difficult to understand. The observed activation energies of 1.4 eV and 0.4 eV for Ga desorption are significantly lower than 2.8 eV, the enthalpy of vaporization of liquid Ga.⁵ The presence of two distinct activation energies suggests the presence of

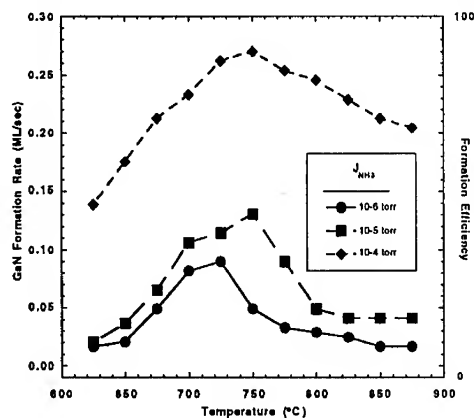


Fig. 4. Variation of GaN formation rate with substrate temperature for varying incident NH_3 flux. The relative GaN formation efficiency is shown on the right axis.

two different precursor states to desorption for the two respective T_s regimes, with both precursors significantly more weakly-bound than a Ga atom at the surface of liquid Ga. It is difficult to postulate a surface Ga species which would have such a small surface binding energy, unless the presence of hydrogen, which is abundant in this growth system, is invoked. Indeed, we believe that hydrogen is playing a role: Ga physisorbed to a hydrogen-terminated GaN surface would be expected to have a low surface binding energy. The presence of two different precursor states to desorption suggests two different hydrogen-terminated sites from which Ga atoms desorb. We speculate that the low temperature desorption precursor site, associated with a 1.4 eV desorption activation energy, is a hydrogen-terminated liquid Ga "pool" which is microscopic in size, the population of which becomes negligible above ~ 750 to 800°C (depending on the incident NH_3 flux), which corresponds to the temperatures above which negligible Ga surface accumulation occurs. We speculate that the high temperature desorption precursor site, associated with a 0.4 eV desorption activation energy, is a hydrogen-terminated GaN site.

Under the assumption that hydrogen is playing an important role in the Ga desorption kinetics, we would expect that those kinetics will change significantly for the case of non-hydrogen containing growth chemistries, such as ECR N_2 -based GSMBE growth. We plan to perform similar Ga desorption studies using alternate growth chemistries in the near future.

CONCLUSIONS

The gas source molecular beam epitaxy growth of GaN from atomic Ga and NH_3 beams is characterized by significant Ga surface accumulation at low growth temperatures and significant Ga desorption at high growth temperatures. These effects combine to produce a peaked dependence of the GaN formation rate on temperature. The GaN formation rate increases with increasing NH_3 flux, with a concomitant decrease in both the process of Ga surface accumulation and Ga desorption. Two distinct desorption activation energies, associated with differing growth temperature ranges, are observed and are consistent with the presence of two distinct desorption precursor states - one or both of which may involve hydrogen. These results are consistent with the relatively low reactivity of NH_3 towards Ga at low T_s and indicate a relatively complex surface chemistry.

ACKNOWLEDGMENT

We thank C. Huang, C. Litton, and G. McCoy for technical support and D. Braddock, S. Buchau, H. Morkoc and S. Ringel for technical discussions. This work was performed at Wright Laboratory, Solid State Electronics Directorate and was partially supported by the US Air Force Office of Scientific Research. Author TL was supported under the National Research Council Associateship Program. Authors CRJ and RK were supported by Air Force Contract No. F33615-95-C-1765.

REFERENCES

1. S. Strite and H. Morkoc, *J. Vac. Sci. Technol. B* **10**, 1237 (1992).
2. K. R. Evans, C. E. Stutz, D. K. Lorange, and R. L. Jones, *J. Vac. Sci. Technol. B* **7** (1989) 259.
3. K. R. Evans, R. Kaspi, J. E. Ehret, M. Skowronski, and C. R. Jones, *J. Vac. Sci. Tech. B* **13**, 1820 (1995).
4. T. Lei, C. R. Jones, and K. R. Evans, 1995 Spring Meeting of the Materials Research Society.
5. Supplied by EPI MBE Products Group, Saint Paul, MN, USA.
6. Lange's Handbook of Chemistry, Ed. John A. Dean, McGraw-Hill Book Company (1973) p. 9.
7. R. C. Powell, N. E. Lee and J. E. Greene, *Appl. Phys. Lett.* **60**, 2505 (1992).

ECR-MBE and GSMBE of Gallium nitride on Si(111)

U. ROSSNER, J.-L. ROUVIERE, A. BOURRET, A. BARSKI,
Département de Recherche Fondamentale sur la Matière Condensée/SP2M,
CEA/Grenoble - 17, Rue des Martyrs - 38054 Grenoble Cedex 9, France.

ABSTRACT

Electron Cyclotron Resonance Plasma Assisted Molecular Beam Epitaxy (ECR-MBE) and Gas Source Molecular Beam Epitaxy (GSMBE) have been used to grow hexagonal GaN on Si (111). In the ECR-MBE configuration high purity nitrogen has been used as nitrogen source. In GSMBE ammonia was supplied directly to the substrate to be thermally cracked in the presence of gallium.

By a combined application of in-situ reflection high-energy electron-diffraction (RHEED) and cross-sectional transmission electron microscopy (TEM) the growth mode and structure of GaN were determined. The growth mode strongly depends on growth conditions. Quasi two dimensional growth was observed in ECR-MBE configuration for a substrate temperature of 640°C while three dimensional growth occurred in GSMBE configuration in the temperature range from 640 to 800°C.

Low temperature (9 K) photoluminescence spectra show that for samples grown by ECR-MBE and GSMBE a strong near band gap emission peak dominates while transitions due to deep level states are hardly detectable. The best optical results (the highest near band gap emission peak intensity) have been observed for samples grown by GSMBE at high temperature (800°C). This could be explained by the increase of grain dimensions (up to 0,3 - 0,5 μm) observed in samples grown by GSMBE at 800°C.

INTRODUCTION

The group III nitrides are intensively investigated because of their particular physical properties. Among them much interest is devoted to gallium nitride : its band-gap ($E_g = 3.4$ eV) gives access to optoelectronics in the blue and ultraviolet range [1] and its high thermal stability makes it an advantageous material for devices working at high temperature [2]. However, during the growth of GaN we have to face serious problems : GaN can occur in either hexagonal (wurtzite) or cubic (zinc blende) structure, and often both polytypes appear in the same epitaxial layer, leading to stacking faults. Moreover, it has a large lattice mismatch with substrates currently used in microelectronics like Si and GaAs (16.6% and 19.9% respectively). Relatively little work has been done on other substrates than Al_2O_3 . Concerning silicon, Lei et al. [3] reported GaN growth on low temperature (400°C) GaN buffer layer, Watanabe et al. [4], Stevens et al. [5] and Meng et al. [6] reported GaN growth on AlN buffer layer on Si (111) by Electron Cyclotron Resonance Plasma assisted Molecular Beam Epitaxy (ECR-MBE) and Metal Organic Chemical Vapor Deposition (MOCVD).

In the present paper we report GaN growth on AlN buffer layer on Si (111) by ECR-MBE and Gas Source Molecular Beam Epitaxy (GSMBE). The aim of this work is to compare structural and optical properties of GaN grown by ECR-MBE with GaN grown by GSMBE on Si (111) substrates.

EXPERIMENT

The GaN and AlN films were grown in a RIBER MBE 2300 chamber. The home-made 2.45 GHz ECR plasma source used in this experiment was described elsewhere in detail [7]. In the ECR-MBE, molecular nitrogen (Air Liquide N 70) was supplied to produce active nitrogen species via the plasma source. In GSMBE high purity ammonia (Air Liquide ULSI grade) was supplied directly to the substrate and thermally cracked in the presence of gallium.

Conventional Knudsen effusion cells were used for the gallium and aluminium evaporation (Ga, Al 7 N). The substrates used in this study were p-type phosphorus-doped ($30 \Omega \text{ cm}^{-1}$) Si (111). The buffer AlN layers were grown by ECR-MBE at substrate temperatures ranging from 540°C to 800°C at growth rate of about 300 Å/h. The GaN layers were grown by ECR-MBE and GSMBE. The GaN growth rate in ECR-MBE configuration was 200 to 500 Å/h. In GSMBE the growth rate was about 0.5 µm/h. The in-situ characterization has been done by reflection high-energy electron diffraction (RHEED) at 15 keV, the ex-situ structural characterization by cross-sectional transmission electron microscopy (TEM) using a JEOL 4000 EX microscope. A He-Cd laser has been used for low temperature (9 K) photoluminescence observations.

AlN buffer layer growth

Prior to AlN buffer layer growth, silicon substrates were outgassed at 200°C and the protective oxide was desorbed at 850°C. The well known Si (111) 7x7 reconstruction was observed after oxide desorption. The RHEED patterns of the AlN films grown by ECR-MBE at 540°C, 640°C and 800°C are shown in Fig. 1. All films are monocrystalline in epitaxial relationship with the silicon substrate: $\alpha\text{-AlN}(0001) [11\bar{2}0] // \text{Si}(111) [1\bar{1}0]$.

GaN growth by ECR-MBE

GaN films have been grown by ECR-MBE at 640°C on AlN buffer layers prepared at three different temperatures: 540°C, 640°C and 800°C. As can be seen from Fig. 2 the AlN buffer layer growth temperature has a strong effect on GaN RHEED image. A GaN film deposited on AlN buffer layer grown at 640°C reveals almost two dimensional growth mode. For GaN deposited on AlN buffer layer grown at higher (800°C) and lower (540°C) temperatures the GaN growth mode is intermediate between two dimensional and three dimensional. Epitaxial relationship of GaN with AlN/Si (111) deduced from RHEED pattern observation is: $\alpha\text{-GaN}(0001) [11\bar{2}0] // \alpha\text{-AlN}(0001) [11\bar{2}0] // \text{Si}(111) [1\bar{1}0]$. The TEM images give more information on the structure of these layers. Low

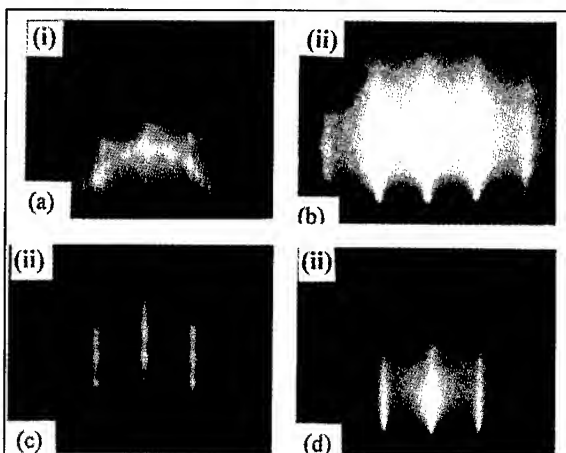


Fig. 1 : RHEED pattern of Si (111) and α - AlN grown by ECR-MBE on Si (111) (a): Si (111) 7x7 ; (b) (c) (d) : α - AlN grown on Si (111) at different substrate temperatures: (b) - 540°C, (c) - 640°C, (d) - 800°C ; (i) $[1\bar{1}0]$ e⁻ azimuth (ii) $[11\bar{2}0]$ e⁻ azimuth.

resolution TEM image of GaN / AlN / Si (111) is shown in Fig. 3. For this sample the AlN buffer layer has been grown at 640°C. High density of dislocations ($10^{11}/\text{cm}^2$) is clearly observed in AlN buffer layer. The first 250 Å contain stacking faults, dislocations and even some cubic zones. The surface of 600 Å AlN buffer layer is smooth and dislocations observed in AlN seems not to extend in GaN epilayer. The crystallinity of GaN films examined ex-situ by TEM indicates growth made by grain formation. The diameter of grains is in the range of 1200 to 1600 Å for GaN film thickness of 500/600 Å. The GaN surface roughness depends on AlN buffer layer growth temperature. For AlN grown at 540°C, 640°C and 800°C GaN surface roughness revealed by TEM investigations is respectively 150 Å, 100 Å, 200 Å.

GaN grown by GSMBE

Using ammonia instead of nitrogen plasma allows to increase the growth rate of GaN. The RHEED pattern of the GaN films grown at 640°C with a growth rate of 0.6 $\mu\text{m}/\text{h}$ on AlN/Si(111) are shown in Fig. 4. The GaN layer thickness is about 8000 Å. Unlike the GaN grown by ECR-MBE the RHEED image of GaN grown by GSMBE shows three dimensional growth mode even for sample thickness as high as 8000 Å.

This three dimensional growth mode has been observed for all growth temperatures under investigations from 640° to 800°C. The TEM investigations shown in Fig. 5 confirm columnar morphology of GaN epilayer and extremely rough surface. Many columns are terminated by (10 $\bar{1}$ 1) facets which give the triangular aspect of the GaN surface. Grain (column) dimensions increase with growth temperature. For the GaN grown at 640°C the size of the grain is 0.06-0.07 μm while for the GaN grown at 800°C grain size increase to 0.3-0.5 μm .

Optical properties of GaN

Photoluminescence is an extremely powerful tool used to determine the quality of the sample. Pure GaN exhibits a band edge low temperature photoluminescence (PL) with three free excitons at 3.475 eV, 3.482 eV

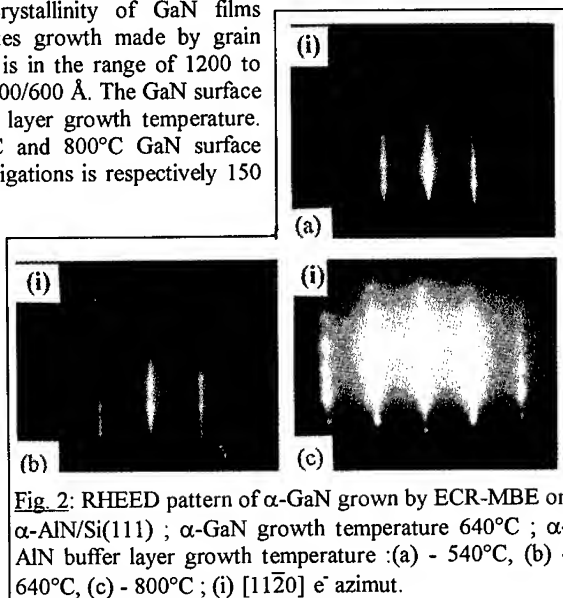


Fig. 2: RHEED pattern of α -GaN grown by ECR-MBE on α -AlN/Si(111) ; α -GaN growth temperature 640°C ; α -AlN buffer layer growth temperature : (a) - 540°C, (b) - 640°C, (c) - 800°C ; (i) $[11\bar{2}0]$ e $^-$ azimuth.

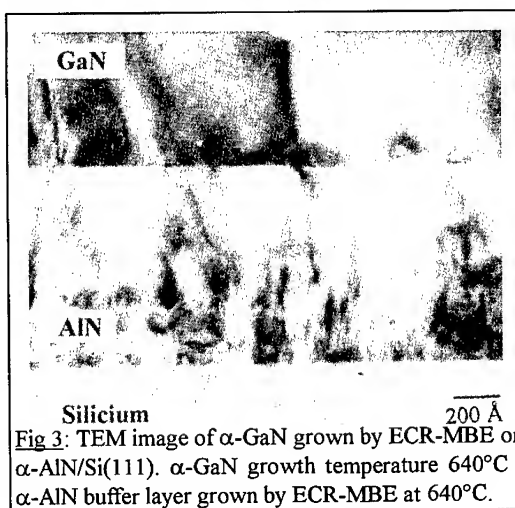


Fig 3: TEM image of α -GaN grown by ECR-MBE on α -AlN/Si(111). α -GaN growth temperature 640°C ; α -AlN buffer layer grown by ECR-MBE at 640°C.

and (3.493 - 3.498) eV [8]. The so called yellow band observed around 2.2 eV [9] appears in samples contaminated by carbon [10] however its origin is still unexplained. Fig. 6 shows low temperature (9 K) PL spectra of GaN elaborated by ECR-MBE and GSMBE. All spectra are dominated by near band edge transitions. PL spectra of GaN grown by ECR-MBE is dominated by a 3.462 eV peak which can be

attributed to exciton bound to neutral donor D^0X [11]. A weak free exciton peak could be observed at 3.497 eV and the 3.266 eV peak could be tentatively assigned as donor - acceptor transitions D^0A^0 [12].

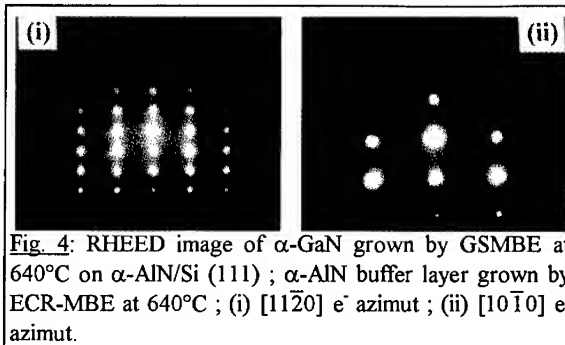


Fig. 4: RHEED image of α -GaN grown by GSMBE at 640°C on α -AlN/Si (111); α -AlN buffer layer grown by ECR-MBE at 640°C; (i) $[11\bar{2}0]$ e^- azimuth; (ii) $[10\bar{1}0]$ e^- azimuth.

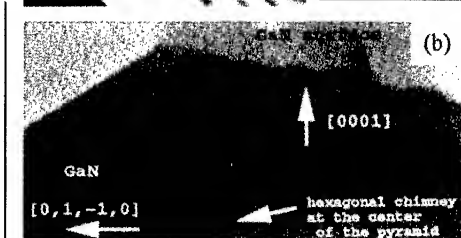
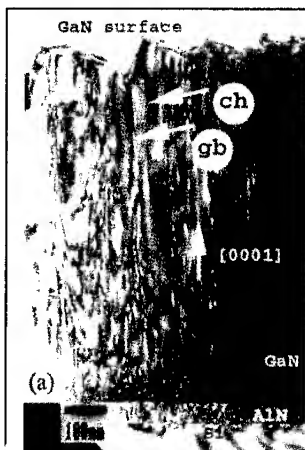


Fig. 5: TEM image of α -GaN grown by GSMBE on α -AlN/Si(111), α -GaN growth temperature 640°C; α -AlN buffer layer grown by ECR-MBE at 640°C; (a) - low resolution TEM image, ch - chimney, gb - grain boundaries; (b) - high resolution TEM image showing hexagonal chimney.

The same transitions are observed in low temperature PL spectrum of GaN grown by GSMBE at 750°C and 800°C. In PL spectrum of GaN grown at 800°C the transition at 3.455 eV (D^0X or A^0X) has the highest intensity of all samples under investigation in this work. However some new peaks appear in PL spectra of GaN grown by GSMBE compared to ECR-MBE. Transitions at 3.410 eV are not yet identified being probably related with radiative recombinations involving impurity levels.

The most striking observation is the extremely high quality of photoluminescence observed in all samples under investigation. No essential differences exist in PL spectra between GaN grown by ECR-MBE and GSMBE; however structural properties are drastically different. Almost two dimensional growth occurred in ECR-MBE; columnar morphology has been observed in GSMBE.

Comparing our TEM observation with PL data the increase of PL intensity for sample grown at 800°C by GSMBE could be attributed to high grain dimensions in this sample (0.3 - 0.5 μ m). For all samples under investigation the ratio of near band edge emission to the so called yellow band was extremely high being respectively 200, 300 and 1000 for α -GaN grown by ECR-MBE at 640°C and GSMBE at 750°C and 800°C.

CONCLUSION

ECR-MBE and GSMBE have been used to grow α - GaN on Si (111) substrates. Prior to GaN growth the AlN buffer layer has been deposited by ECR-MBE. Almost two

dimensional growth occurred in ECR-MBE while three dimensional columnar growth has been observed in GSMBE for all substrate temperatures under investigation (from 640°C to 800°C). The ammonia used in GSMBE considerably increases the growth rate of GaN. In our experiment the growth rate in ECR-MBE was about 300 Å/h ; in GSMBE the growth rate as high as 0,6 µm/h was easily achieved. Even higher growth rate (1 µm/h) has been reported by Z. Yang et al [13] for α-GaN grown on Al₂O₃ by GSMBE using α - GaN low temperature ECR-MBE grown buffer layer. Two dimensional growth has been observed even for substrate temperatures as low as 750°C. R.C. Powell et al [14] reported three dimensional to two dimensional transition for α - GaN grown on Si (111) by GSMBE at Ts ≥ 770°C. Clearly further work is necessary to explain why this transition was not observed in our experimental conditions. The influence of the nature of the buffer layer on α - GaN growth mode in GSMBE needs clearly to be investigated. The most striking observation in our experiment is the extremely high quality of low temperature photoluminescence spectra observed for our samples ; no essential differences exist in PL spectra between samples grown by ECR-MBE and GSMBE. The near band edge transition intensity increases with GaN grain dimensions and dominates the PL spectra despite the high density of dislocations and vertical faults observed inside the grains.

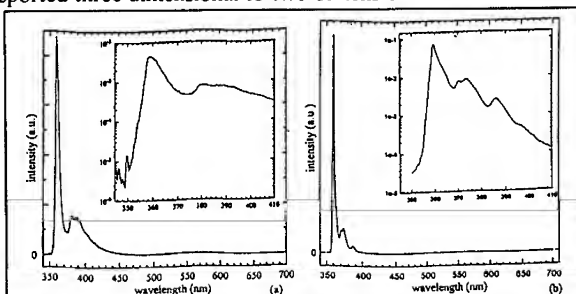


Fig. 6: Photoluminescence spectra at 9 K of α-GaN on α-AlN/Si(111) α-GaN grown by : (a) ECR-MBE at 640°C, (b) GSMBE at 800°C.

ACKNOWLEDGEMENTS

We would like to thank M. Leroux and N. Grandjean for low temperature photoluminescence observations. This work has been partly supported by the French CRG "Interface" Program at ESRF.

REFERENCES

1. N. Koide, H. Kato, M. Sassa, S. Yamasaki, K. Manabe, M. Hashimoto, H. Amano, K. Hiramatsu and I. Akasaki, *J. Cryst. Growth*, 115 (1991) 639.
2. R.F. Davis, Z. Sitar, B.E. Milliams, H.S. Kong, M.J. Kim, J.W. Palmour, J.A. Edmond, J. Ryn, J.T. Glass and C.H. Carter, *J. Mater. Sci. Eng.*, B1 (1988) 77.
3. T. Lei, K.F. Ludwig, T.D. Moustakas, *J. Appl. Phys.* 74 (7), 4430 (1993).
4. A. Watanabe, T. Takenchi, K. Hirose, H. Amano, K. Hiramatsu, I. Akasaki, *J. Cryst. Growth* 128, 391 (1993).
5. K.S. Stevens, A. Otani, A.F. Schwartzman, R. Beresford, *J. Vac. Sci. Technol.* B12 (2), 1186 (1994).

6. W.J. Meng, T.A. Perry, J. Appl. Phys. 76 (12), 7824 (1994).
7. U. Rössner, D. Brun-Le Cunff, A. Barski, B. Daudin, submitted to J. Vac. Sci. Technol.
8. B. Monemar, Phys. Rev. B, 10 (2), 676 (1974).
9. M.E. Lin, B.N. Sverdlov, H. Morkoç, Appl. Phys. Lett. 63 (26), 3625 (1993).
10. U. Rössner, PhD Thesis, Grenoble, 1995.
11. T. Oetchprohm, K. Hiramatsu, H. Amano, I. Akasaki, Appl. Phys. Lett. 61 (22), 2688 (1992).
12. S. Strite, H. Morkoç, J. Vac. Sci. Technol. B10 (4), 1237 (1992).
13. Z. Yang, L.K. Li, and W.I. Wang, Appl. Phys. Lett. 67 (12), 1686, (1995).
14. R.C. Powell, N.E. Lee, and J.E. Greene, Appl. Phys. Lett. 60 (20), 2505 (1992).

GROWTH AND DOPING OF GaN DIRECTLY ON 6H-SiC BY MBE

D. KORAKAKIS*, A. SAMPATH, H.M. NG, G. MORALES**, I.D. GOEPFERT and T.D. MOUSTAKAS
Molecular Beam Epitaxy Laboratory, Dept. of Electrical Engineering and Center for Photonics Research, Boston University, 44 Cummings St., Boston, MA 02215

*e-mail address: dimitris@engc.bu.edu

**Physics Department, Boston University, 590 Commonwealth Avenue, Boston MA 02215

ABSTRACT

We report on methods for the growth of GaN by MBE directly on 6H-SiC substrates. The films were doped p-type by the incorporation of Mg and the samples were characterized by studying their structure and morphology by RHEED, XRD and SEM and their recombination properties by photoluminescence measurements. The undoped films were found to be atomically smooth with 2x2 surface reconstruction and have an x-ray rocking curve with a FWHM of 3.5 arcmin. The photoluminescence spectra indicate that recombination is dominated by transition across the gap. The p-type doped films have a rocking curve with FWHM of 6.5 arcmin. and the majority of recombination occurs through D-A transitions at 3.26 eV.

INTRODUCTION

Employment of 6H-SiC substrates for the growth of GaN provides a number of advantages such as small lattice mismatch (~3%), compared to sapphire's (~13.8 %), as well as potential for the formation of Fabry-Perot cavities by cleaving. The epitaxial growth of GaN on 6H-SiC substrates generally follows the predeposition of an AlN buffer whose growth temperature was reported to vary from 500° - 1100 °C^{1,2}.

The epitaxial growth of the III-V nitrides directly on doped SiC is important for the fabrication of vertical devices. The direct growth of GaN on SiC for the fabrication of heterojunction bipolar transistors has been demonstrated³. However, for the fabrication of blue GaN LEDs an AlGaIn buffer was employed⁴. Still, for the realization of efficient devices it is desirable to eliminate any buffer layer since as such it hinders the operation of the device by introducing an additional series resistance. It is therefore of interest to identify conditions that allow AlGaIn epitaxial growth directly on 6H-SiC.

In this paper we report on the optimization of the growth of GaN directly on n-6H-SiC without the employment of an intermediate buffer. Furthermore, the films have been doped p-type and preliminary studies of the junction properties of the p-GaN/n-SiC heterojunctions were conducted.

EXPERIMENTAL METHODS

A Varian Gen II MBE unit equipped with an ASTEX compact ECR plasma source was used for the work reported in this paper. The apparatus has been described in detail elsewhere⁵.

The substrates employed in this study were Si-terminated (0001) 6H-SiC⁶. Prior to growth the substrates were chemically cleaned using the RCA procedure, passivated by immersing them

in buffered HF for 5 minutes, and mounted to a Mo blocks with Mo wires. The SiC substrates were degassed in the MBE buffer chamber at 400 °C and subsequently heated in the growth chamber to 900 °C just prior to growth. Although other workers¹ found that H-plasma cleaning is necessary to form a good SiC surface, we found that the procedure described previously lead to surfaces with good RHEED patterns, including Kikuchi lines (see Fig. 1).

All investigated films were grown at 800 °C measured by a thermocouple in the back of the Mo holder. The growth rates varied up to 0.5 $\mu\text{m/h}$ by adjusting the Ga flux and the microwave power in the ECR discharge. The films were doped p-type by subliming Mg from an effusion cell.

X-ray diffraction (XRD) studies were carried out in a four circle, double crystal diffractometer with Co- $K\alpha_1$ radiation as the excitation source. The incoming beam was monochromated using a single Ge crystal. Photoluminescence measurements were carried out with a 10 mW He-Cd laser. A 0.5 m grating spectrometer with a holographically blazed grating (1800 grooves/mm) was used to disperse the collected light.

EXPERIMENTAL RESULTS

Fig. 2 is a RHEED pattern of an undoped GaN sample. It is important to note that these data indicate (2x2) surface reconstruction occurring during the growth of the film. Our group reported previously surface reconstruction in GaN films grown on sapphire but only after the films were cooled down⁷. The surface morphology and the cross sectional view of the same film is shown in Fig. 3. These data indicate that the surfaces are atomically smooth with no evidence of

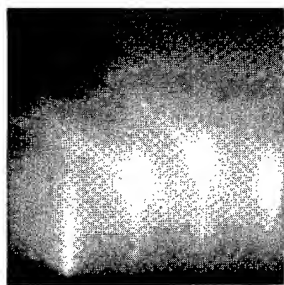


Fig. 1: RHEED pattern from the 6H-SiC substrate exhibiting Kikuchi lines. The electron beam is along the (11-20) azimuth.

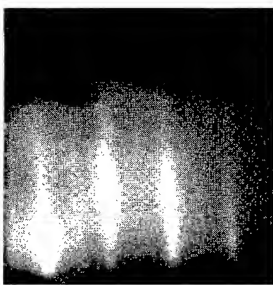


Fig. 2: RHEED pattern from the GaN film exhibiting (2x2) surface reconstruction. The electron beam is along the (11-20) azimuth.

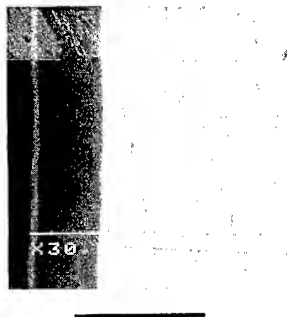


Fig. 3: SEM cross sectional view of a 0.5 μm thick GaN film.
Marker represents 1 μm

columnar morphology. In some areas, however, we have observed that the film maps out scratches on the SiC substrate. The surface morphology of the p-type films was similar to the undoped films however the RHEED pattern did not exhibit surface reconstruction.

The structure of the films was further investigated by XRD. The θ - 2θ scans of the (0002) peak of GaN was found to have a FWHM of less than 4 arcmin for films with thickness about 0.5 μm . The best FWHM of the XRD rocking curve was found to be 3.5 arcmin, as shown in Fig. 4. However, films grown under various growth conditions were found to have rocking curves with FWHM up to 9 arcmin. For p-type doped films we found that the best rocking curve has a FWHM of 6.5 arcmin. The samples were also investigated by conducting l -scans. This study is aiming at detecting any cubic domains. Fig. 5 shows one such scan in the (1-10 \bar{l}) direction where l was varied between 0.5 - 3.5 reciprocal lattice units. From these results we see no evidence of cubic domains. However, concentrations less than 1% cannot be detected by x-rays and TEM studies are required.

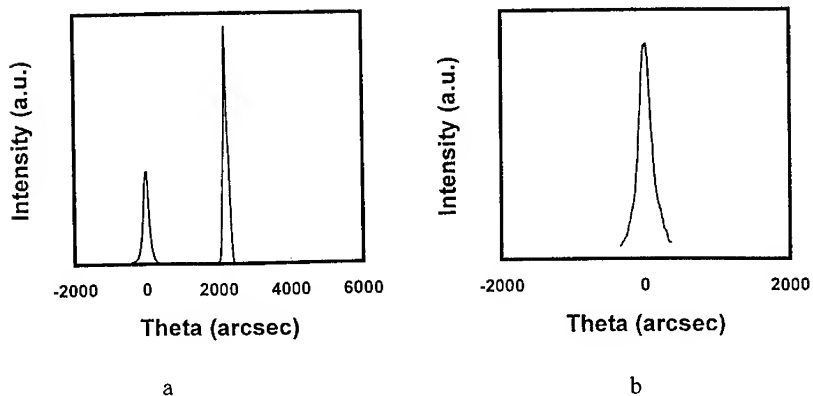


Fig 4: a) XRD θ - 2θ scan of the (0002) peak of GaN and the (0006) peak of 6H-SiC. The FWHM of the GaN peak is 2.5 arcmin. b) XRD rocking curve of the (0002) for an undoped film. FWHM is 3.5 arcmin.

The samples were not characterized by Hall effect measurements due to the conducting SiC substrate. However, the p-type conductivity of the films was ascertained by the hot probe method.

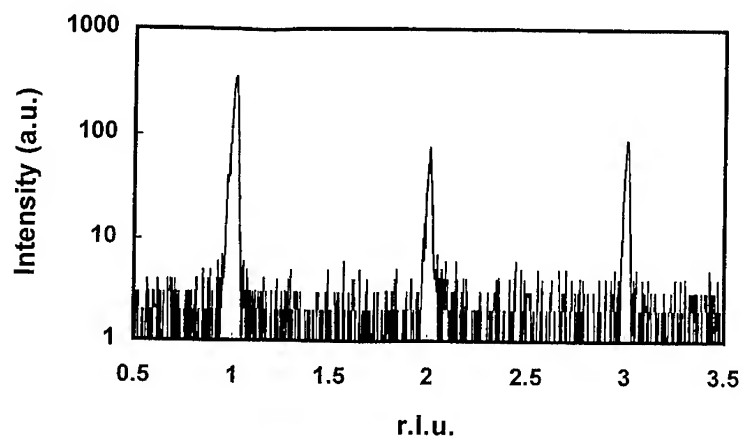


Fig. 5: l -scan along the $(1-10l)$ direction. There is no evidence of cubic domains.

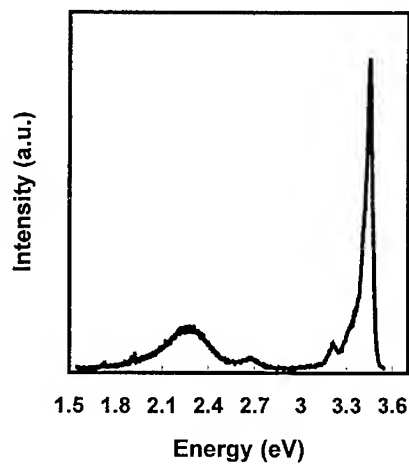


Fig. 6: Photoluminescence at 77K of an undoped GaN film. The FWHM at the 3.45eV peak is 50meV.

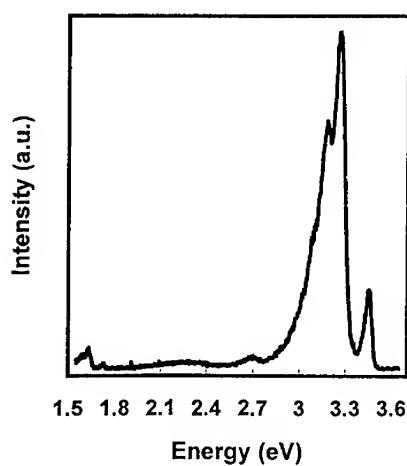


Fig. 7: Photoluminescence at 77K of a lightly doped p-GaN film.

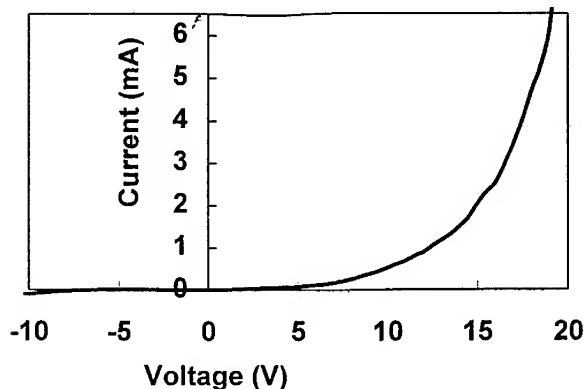


Fig. 8: I-V characteristics of the heterojunction between n-6H-SiC/p-GaN.

Photoluminescence studies of undoped GaN films, shown in Fig 6, indicate that the recombination is dominated by transitions at 3.45 eV with a smaller, broad peak at 2.2 eV. The photoluminescence of the p-type films shown in Fig 7 indicate that the recombination proceeds through the D-A transitions at 3.26 eV⁸.

The heterojunction between the p-GaN and the n-6H-SiC was also investigated. Ohmic contacts to SiC were formed by evaporating sequentially 10 nm of Cr and 100 nm of Al. Pressure contacts using a Au wire was employed on the GaN side. Typical I-V characteristics is shown in Fig. 8. The reverse breakdown voltage was about -10 V and the diode turn on voltage is between 2-3 V. These devices suffer from series resistance, however, they do emit blue light when biased at forward bias of about 7-8 V.

CONCLUSIONS

The studies reported in this paper demonstrated that good quality GaN can be grown directly on 6H-SiC without the employment of either AlN or GaN buffers. The films were found to have atomically smooth surface morphologies, exhibiting (2x2) surface reconstruction and XRD rocking curves with FWHM of 3.5 arcmin. Such films were doped with Mg p-type and heterojunctions between substrate and film was found to be rectifying and emit blue light in the forward direction.

ACKNOWLEDGMENTS

The authors acknowledge discussion and help from Prof. K. Ludwig and Mr. R. Singh. The work was funded by ARPA (Grant No MDA972-95-3-0008).

REFERENCES

- ¹ M.E. Lin, S. Sverdlov, L. Zhou, H. Morkoç, Appl. Phys. Lett. **62** (26), p. 3479 (1993)
- ² T.W. Warren, Jr., M.D. Bremser, K.S. Ailey, E. Carlson, W.G. Perry, R.F. Davis, Appl. Phys. Lett. **67** (3), p. 401 (1995)
- ³ J. Pankove, S.S. Chang, H.C. Lee, R.J. Molnar, T.D. Moustakas, B. Van Zeghbroeck, IEDM-94 p. 389 (1994)
- ⁴ CREE Research, Inc., U.S. Patent No. 5,393,993, "Buffer Structure between silicon carbide and gallium nitride and resulting semiconductor devices", February 28, 1995
- ⁵ T.D. Moustakas and R.J. Molnar, Mat. Res. Soc. Symp. Proc., Vol. 281, p. 753 (1993)
- ⁶ CREE Research, research grade.
- ⁷ R.J. Molnar, R. Singh and T.D. Moustakas, J. Elec. Mat, Vol. 24, p.275 (1995)
- ⁸ O. Lagerstedt, B. Monemar, J. Appl. Phys. **45**, p. 2266 (1974)

Plasma-Assisted MBE of GaN and AlGa_N on 6H SiC(0001)

S. Sinharoy, A. K. Agarwal, G. Augustine, L. B. Rowland, R. L. Messham, M. C. Driver, and R. H. Hopkins
Westinghouse Science & Technology Center, 1310 Beulah Road, Pittsburgh, PA 15235

ABSTRACT

The growth of undoped and doped GaN and AlGa_N films on off-axis 6H SiC substrates was investigated using plasma-assisted molecular beam epitaxy (MBE). Smooth and crack-free GaN and AlGa_N films were obtained; the best results occurred at the highest growth temperature studied (800°C) and with a 40 to 50 nm AlN buffer layer grown at the same temperature. Carrier concentrations of up to $n = 4 \times 10^{20} \text{ cm}^{-3}$ were accomplished with silicon, with a 40 to 50% activation rate as determined by secondary ion mass spectrometry (SIMS). Unintentionally doped Al_xGa_{1-x}N ($x \approx 0.1$) was n-type with a carrier concentration of $7 \times 10^{18} \text{ cm}^{-3}$. N-type AlGa_N ($x \approx 0.1$)/p-type 6H SiC (0001) heterostructures showed excellent junction characteristics with leakage currents of less than 0.1 nA at 5 V reverse bias at room temperature and 0.5 nA at 200°C operating temperature.

INTRODUCTION

There has been intense interest in the III-N semiconductors mainly for optoelectronics over the last several years. Blue light emitting InGa_N/AlGa_N diodes (LEDs) using metalorganic vapor phase epitaxy (MOVPE) grown layers on sapphire¹ have recently become commercially available. There have been recent reports²⁻⁴ of blue-violet emitting LEDs using molecular beam epitaxy (MBE)-grown material as well. In the area of high temperature, high speed electronic device applications using III-V nitrides, only experimental devices to date have been reported. MOVPE materials have been used to demonstrate GaN metal-semiconductor field-effect transistors (MESFETs)^{5,6} and modulation-doped field-effect transistors (MODFETs)⁷ on sapphire, whereas MBE grown materials have been used to fabricate MODFETs on sapphire⁸ and heterojunction bipolar transistors (HBT) on 6H SiC⁹.

It is not clear at this early stage which of the two film growth techniques (MOVPE and MBE) will ultimately provide better quality materials for high speed III-V nitride device development. While MOVPE provides a higher growth rate (up to 2.5 $\mu\text{m/hr}$), nitride films grown by this technique must be electron-beam or thermally annealed to activate the Mg p-dopant.¹⁰ Both n- and p-type doping is readily achievable in the MBE technique, but the growth rate is much slower (typically 0.1 $\mu\text{m/hr}$). Hughes et al.¹¹ have recently reported that GaN growth rates as high as 1.0 $\mu\text{m/hr}$ can be achieved by MBE, using radio frequency (rf) plasma source instead of an electron cyclotron resonance (ECR) source.

We have chosen MBE as the growth technique for our initial III-V nitride epitaxial film development work. SiC has been chosen as the substrate material, because our goal is to eventually integrate high temperature, high speed device technology based on III-V nitrides with the silicon carbide device technology already under development.¹² Silicon carbide is also a logical choice, because it is relatively closely lattice-matched (3.5% mismatch to GaN) and has the highest thermal conductivity among the available substrates for GaN and AlGa_N epitaxy.

EXPERIMENTAL

GaN films were grown on 6H SiC(0001) substrates with 3° tilt towards $\langle \bar{1}2\bar{1}0 \rangle$ (hereafter denoted "off axis"). High resistivity ($>1000 \Omega\text{-cm}$) substrates were used except for the n-p

structure described below. The experimental set up and the SiC substrate cleaning procedure have been described in a separate publication¹⁴ and will not be repeated here. GaN films were grown at temperatures ranging from 700°C to 850°C after thermal cleaning of the SiC substrate. Film growth experiments were performed with 100Å to 500Å AlN or GaN buffer layers grown at temperatures ranging from 450°C to 800°C. A thin (~400Å) layer of AlN grown at 800°C was found to provide the optimum buffer layer for the subsequent GaN film growth. GaN films grown at 800°C were found to be of the best structural and morphological quality. Other optimum growth parameters for these films were as follows: plasma power at 25 W, magnet current at 17 A, nitrogen flow rate of 2.5 sccm with chamber pressure at 2.5×10^{-4} mbar, Ga effusion cell at 900°C, and Al effusion cell at 950°C. The film growth rate ranged from 600 to 1000Å per hour. Typical film thickness was about 1 µm. The structural and morphological quality of the films were found to improve with increasing film thickness. Structural quality was determined by x-ray rocking curve measurement of the GaN (0002) reflection using CuKα radiation. Morphological quality was determined using optical microscopy and scanning electron microscopy (SEM). Secondary electron mass spectrometry (SIMS) was used to determine the compositional profile, including dopant and impurity concentrations. Hall effect measurements were performed in the van der Pauw configuration with indium contacts at the corners of each sample. In view of the success of Pankove et al.⁹ in fabricating an HBT on a 6H SiC substrate using GaN as the emitter, we have investigated the n-p junction characteristics of a n-Al_{0.1}Ga_{0.9}N/p-SiC diode. The test structure and the results are shown in the next section.

RESULTS AND DISCUSSION

SEM micrographs of 1 µm thick GaN films grown on an off-axis 6H-SiC substrate under the optimized conditions described in the previous section showed a smooth, crack-free surface. X-ray rocking curve full width at half maximum (FWHM) of the GaN(0002) reflection ranged between 9 and 20 arc-min. This is indicative of reasonably good crystalline quality, and is comparable to FWHM values reported for MBE-grown GaN films on 6H-SiC by other researchers.^{15,16} Hughes et al.¹¹ have recently reported a FWHM value of 156 arc-sec for the GaN(0002) reflection of a homoepitaxial GaN film on 6H-SiC by MBE. They reported that the GaN film quality depended on the type of nitrogen plasma source; a rf source providing better quality films than an ECR source. The FWHM value of 156 arcsec reported by Hughes et al.¹¹ is comparable to the value of 66 arc-sec reported recently by Weeks et al.¹⁷ for the GaN(0004) reflection of their MOVPE-grown GaN film on vicinal 6H-SiC.

Room temperature Hall effect measurements gave carrier concentration values of our undoped GaN films of $\leq 1 \times 10^{16}$ cm⁻³. The corresponding mobility value was unexpectedly low, in the range of 50 to 60 cm²/Vs. This may be due to difficulties in making Ohmic contacts to lightly doped or undoped material. Other contact materials as well as use of heavily Si-doped GaN contact layers will be investigated to improve Ohmic behavior for these Hall measurements. Films were intentionally Si doped over a wide range by varying the Si effusion cell temperature from 900-1200°C. Figure 1 shows the carrier concentration and Hall electron mobility as obtained from room temperature Hall measurements as a function of Si cell temperature. Carrier concentrations from 4×10^{17} to as high as 4×10^{20} cm⁻³ were obtained, with corresponding mobilities ranging from 130 to 20 cm²V⁻¹s⁻¹. The electron mobilities in this work are slightly lower for a given carrier concentration than those previously reported for MOVPE Si doping^{17,22}. However, carrier concentrations for intentionally doped material of above 1×10^{20} cm⁻³ have not previously been reported.

SIMS characterization of the Si-doped GaN films showed that the Si atomic concentration was constant throughout the film and increased abruptly once the SiC substrate is reached. Figure 2 shows the carrier concentration (as obtained from Hall measurements) and the atomic concentration of Si (as obtained by SIMS) in the doped GaN films as a function of Si cell temperature. Approximately 40-50% of the Si in the films was electrically active. This is within the range of electrical activation reported by other researchers for Si doping of GaN¹⁸⁻²².

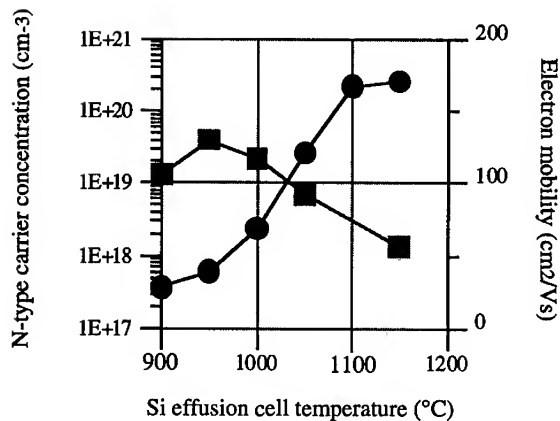


Figure 1: Results of room temperature Hall effect measurements of Si-doped GaN films grown on off-axis 6H-SiC, showing carrier concentration (filled circles) and mobility (filled squares) as a function of silicon effusion cell temperature.

SEM micrographs of undoped $\text{Al}_x\text{Ga}_{1-x}\text{N}$ films grown 6H-SiC substrates with the previously described AlN buffer layer showed smooth, crack-free surfaces similar to those of GaN. The aluminum concentration of an undoped film grown at 800°C, with the Al effusion cell at 950°C, was determined by two different techniques. The x values differed in each measurement, giving values of $x=0.13$ by electron microprobe analysis, and $x=0.07$ by SIMS analysis. A third technique, either photoluminescence or high resolution x-ray diffraction, will be used in the near future to determine the exact aluminum concentration in the alloy.

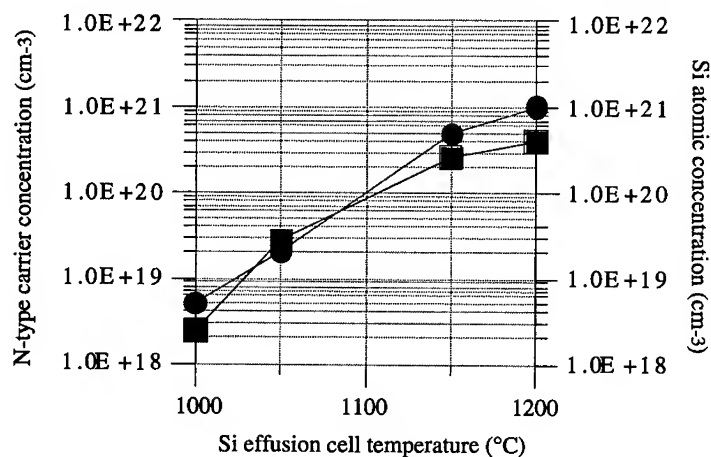


Figure 2: Atomic Si concentration (filled circles) obtained by SIMS and carrier concentration (filled squares) obtained by Hall effect measurements, plotted as a function of silicon effusion cell temperature, showing 40% to 50% activation of the Si dopant in the GaN films on off-axis 6H-SiC.

Room temperature Hall effect measurement showed that this $\text{Al}_x\text{Ga}_{1-x}\text{N}$ film was unintentionally n-doped, with a carrier concentration of $7 \times 10^{18}/\text{cm}^3$ and a mobility of $23 \text{ cm}^2/\text{V}\cdot\text{sec}$.

In order to investigate the n-AlGaIn/p-SiC junction characteristics, we fabricated the heterostructure junction diode shown in Figure 3 on a p/p+ 6H-SiC substrate. A two-step emitter structure was used, the first layer being a lightly doped n-type AlGaIn to keep the base-emitter capacitance low, and then a second layer of higher doped n+ GaN film for contact purposes. We used cold Al contact on the backside and cold Cr/Ni contact on the emitter, which was also used as a mask to reactive ion etch the GaN/AlGaIn regions using BCl_3 . Figure 4 shows the I-V characteristics of the heterostructure n/p junction diode at temperatures ranging from 20°C to 300°C . As expected, the forward current increases with temperature, accompanied by a reduction in the knee voltage. The series resistance appears to be high.

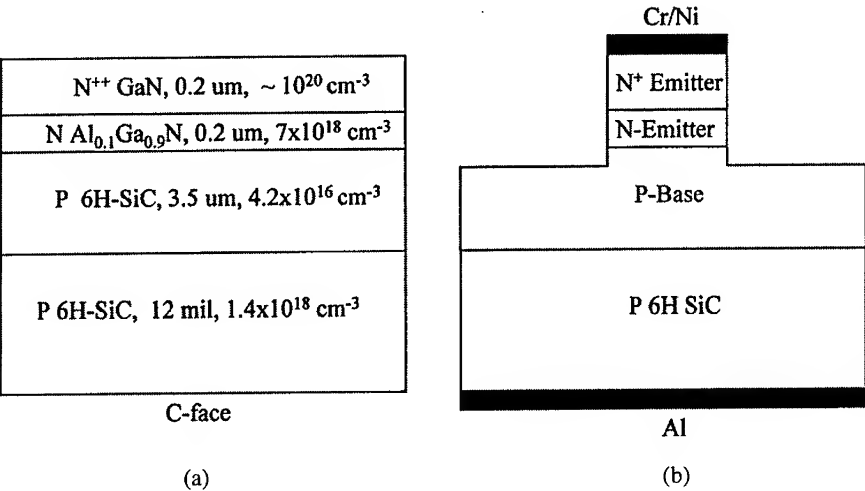


Figure 3: AlGaIn/SiC heterostructure N/P junction diode layer structure (Fig. 3a) and cross-section of the processed diode (Fig. 3b).

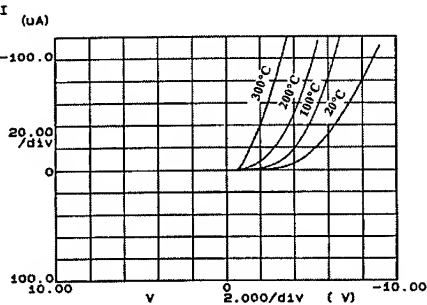


Figure 4: $I (\mu\text{A})$ - V (Volts) characteristics of the junction diode shown in Figure 3 at $20, 100, 200$, and 300°C .

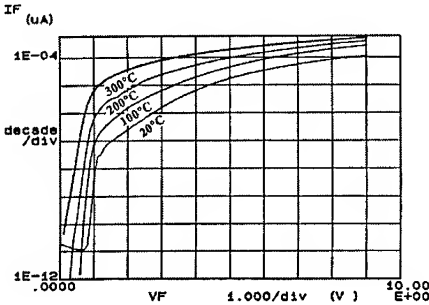


Figure 5: Forward I-V characteristics of the junction diode shown in Figure 3. Logarithm of the forward current (I_F) has been plotted as a function of forward voltage (V_F) at $20, 100, 200$, and 300°C .

This is attributed to insufficient ionization of the Al dopant in the p-SiC substrate. Figure 5 shows the forward I-V characteristics on a log current scale. The linear portion of the plots corresponds to the expected exponential I-V characteristics with a non-ideality factor of 1.4. The non-ideality factor is approximately constant from room temperature to 300°C. Again, the series resistance of the substrate is extremely high, reducing somewhat at higher temperatures because of further activation of the Al dopant in the substrate at those temperatures. Reverse leakage current as a function of reverse bias is shown in Figure 6. Reverse leakage current is less than 100 pA at 5 V reverse bias at room temperature. It increases to 0.5 nA at 200°C and to 2.5 nA at 300°C. Such low reverse currents are indicative of a junction with very low defect density.

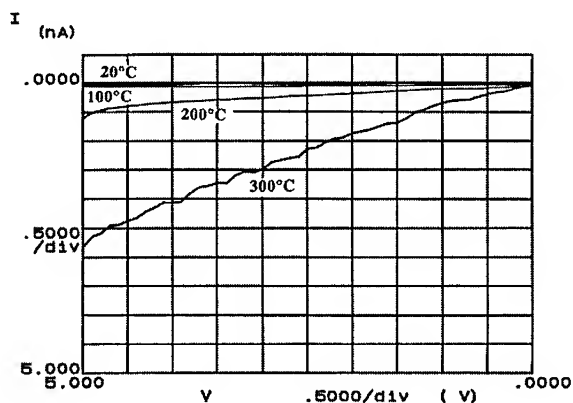


Figure 6: Reverse I-V characteristics of the junction diode shown in Figure 3. The plot shows the reverse current (I) in nanoamperes, as a function of reverse voltage (V) at four different temperatures.

CONCLUSIONS

In conclusion, we have used ECR plasma-assisted MBE to grow undoped GaN and AlGa_xN, as well as n-doped GaN, that are comparable in structural and morphological quality to those reported by other researchers using MBE on 6H-SiC substrates. Doping levels up to $4 \times 10^{20} \text{ cm}^{-3}$ were achieved using silicon, and a calibration curve correlating silicon effusion cell temperature to dopant level in the GaN was established for the first time in MBE films. Comparison of electrical results with SIMS results showed that between 40 and 50% of the incorporated silicon was activated. Unintentionally doped Al_xGa_{1-x}N films ($x \approx 0.1$) were found to be smooth and crack-free, with a carrier concentration of $7.0 \times 10^{18} \text{ cm}^{-3}$. A junction diode fabricated with n-Al_{0.1}Ga_{0.9}N and p-SiC exhibited excellent I-V characteristics with very low leakage current.

ACKNOWLEDGEMENTS

The authors wish to thank W. D. Eagleson and N. J. Doyle for technical assistance. The SIMS measurements were performed by J. W. Erickson of Charles Evans and Associates. One of the authors (S. Sinharoy) thanks Profs. R. F. Davis, T. D. Moustakas, and R. Beresford for helpful discussions in the initial phase of this work.

REFERENCES

1. S. Nakamura, T. Mukai, and M. Senoh, *J. Appl. Phys.* 76, 8189 (1994).
2. R. J. Molnar, R. Singh, and T. D. Moustakas, *Appl. Phys. Lett.* 66, 268 (1995).
3. M. A. L. Johnson, S. Fujita, W. H. Rowland, Jr., K. A. Bowers, W. C. Hughes, Y. W. He, N. A. El Masry, J. W. Cook, Jr., J. F. Schetzina, J. Ren, and J. A. Edmond, to be published in *J. Vac. Sci. Technol. B*.
4. J. M. van Hove, G. Carpenter, E. Nelson, A. Wowchak, and P. P. Chow, to be published in *J. Vac. Sci. Technol. B*.
5. M. A. Khan, J. N. Kuznia, A. R. Bhattarai, and D. T. Olson, *Appl. Phys. Lett.* 62, 1786 (1993).
6. S. C. Binari, L. B. Rowland, W. Kruppa, G. Kelner, K. Doverspike, and D. K. Gaskill, *Electronics Lett.* 30, 1248 (1994).
7. M. A. Khan, M. S. Shur, J. N. Kuznia, Q. Chen, J. Burm, and W. Schaff, *Appl. Phys. Lett.* 66, 1083 (1995).
8. A. Özgür, W. Kim, Z. Fan, A. Botchkarev, A. Salvador, S. N. Mohammad, B. Sverdlov, and H. Morkoç, *Electronics Lett.* 31, 1389 (1995).
9. J. Pankove, S. S. Chang, H. C. Lee, R. J. Molnar, T. D. Moustakas, and B. Van Zeghbroeck, *IEDM-94*, 389 (1994).
10. S. Nakamura, N. Iwasa, M. Senoh, and T. Mukai, *Jpn. J. Appl. Phys.* 31, 1258 (1992).
11. W. C. Hughes, W. H. Rowland, Jr., M. A. L. Johnson, S. Fujita, J. W. Cook, Jr., and J. F. Schetzina, *J. Vac. Sci. Technol. B* 13, 1571 (1995).
12. C. D. Brandt, A. K. Agarwal, G. Augustine, A. A. Burk, R. C. Clarke, R. C. Glass, H. M. Hobgood, J. P. McHugh, P. G. McMullin, R. R. Siergiej, T. J. Smith, S. Sriram, M. C. Driver, and R. H. Hopkins, "Compound Semiconductors 1994", *Proc. 21st. Int. Symp. Compound Semiconductors*, edited by H. Goronkin and U. Mishra (IOP Conf. Series v. 141, IOP Publishing, Bristol, 1995).
13. Z. Sitar, M. J. Paisley, B. Yan, J. Ruan, W. J. Choyke, and R. F. Davis, *J. Vac. Sci. Technol. B* 8 (2), 316 (1990).
14. S. Sinharoy, G. Augustine, L. B. Rowland, A. K. Agarwal, R. L. Messham, M. C. Driver, and R. H. Hopkins, *J. Vac. Sci. Technol. A* (in press).
15. M. E. Lin, B. Sverdlov, G. L. Zhou, and H. Morkoç, *Appl. Phys. Lett.* 62, 3479 (1993).
16. D. J. Smith, D. Chandrasekhar, B. Sverdlov, A. Botchkarev, A. Salvador, and H. Morkoç, *Appl. Phys. Lett.* 67, 1830 (1995).
17. T. W. Weeks, Jr., M. D. Bremser, K. S. Ailey, E. Carlson, W. G. Perry, and R. F. Davis, *Appl. Phys. Lett.*, 67, 401 (1995).
18. N. Koide, H. Kato, M. Sassa, S. Yamasaki, K. Manabe, H. Hashimoto, H. Amano, K. Hiramatsu, and I. Akasaki, *J. Cryst. Growth* 115, 639 (1991).
19. S. Nakamura, T. Mukai, and M. Senoh, *J. Appl. Phys.* 31, 2883 (1992).
20. D. K. Wickenden and W. A. Bryden, in *Silicon Carbide and Related Materials*, edited by M. G. Spencer, R. P. Devaty, J. A. Edmond, M. A. Khan, R. Kaplan, and M. Rahman (Institute of Physics, Bristol), p. 381 (1994).
21. L. B. Rowland, K. Doverspike, and D. K. Gaskill, *Appl. Phys. Lett.* 66, 1495 (1995).
22. A. E. Wickenden, L. B. Rowland, K. Doverspike, D. K. Gaskill, J. A. Freitas, Jr., D. S. Simons, and P. H. Chi, *J. Electron. Mater.* 25, 1547 (1995).

GROWTH OF InGaN FILMS BY MBE AT THE GROWTH TEMPERATURE OF GaN

R. SINGH, T.D. MOUSTAKAS

Molecular Beam Epitaxy Laboratory, Department of Electrical Engineering and Center for Photonics Research, Boston University, Boston MA 02215

ABSTRACT

We report the growth of InGaN alloys over practically the entire composition range at the growth temperature of GaN (700-800 °C) by MBE. We found that when the grown films are thick ($> 0.3 \mu\text{m}$), incorporation of more than about 30% indium results in phase separation of InN, which is consistent with spinodal decomposition. On the other hand we discovered that such phase separation is absent in thin InGaN films ($< 600 \text{\AA}$) grown as GaN/InGaN/GaN heterostructures. In such configurations we were able to incorporate up to 81% In, which is the highest yet reported.

INTRODUCTION

The development of InGaN alloys is important in optical devices operating in the visible and near-UV part of the electromagnetic spectrum [1]. However, there are only limited studies of the GaN-InN quasi-binary system. The difficulty in growing the InGaN alloys in conjunction with AlGaIn alloys which are required for the fabrication of devices is the significantly higher vapor pressure of nitrogen over InGaIn. The first study to address the entire composition was reported by Osamura and coworkers [2]. However, these studies were conducted on polycrystalline films grown at 500 °C on quartz or sapphire substrates. Matsuoka and co-workers reported the growth of InGaIn alloys by low temperature (500 °C) MOCVD [1]. The maximum amount of indium incorporated in these films was 42%. The same study reports the optical gap of the film with the 42% indium concentration to be identical to the bandgap of pure InN, a result which according to the authors is unexplained. Subsequent work by the same group reported the growth of InGaIn alloys at higher substrate temperatures of 800 °C leading to the incorporation of up to 23% indium in these films [3]. Photoluminescence (PL) studies on these films indicate that the PL peak broadens with increasing concentration of indium and also show a broad band of deep level emission. Nakamura investigated the growth of InGaIn alloys ($< 1000 \text{\AA}$) by MOCVD on sapphire substrates coated with thick GaN films in the temperature range of 720-850 °C [4]. Incorporation of up to 33% indium was reported for such films. The growth rate had to be reduced sharply to 5-50 Å/min. to obtain high quality films. Shimizu and co-workers have grown InGaIn alloys using the MOVPE method and they reported alloys with up to 12% indium at a growth temperature of 750 °C [5]. However, these films were found to be decorated with indium droplets. The same group reported that upon growing InGaIn/GaN multilayers, they could incorporate up to 29% indium without droplets. Superlattice structures of $\text{In}_x\text{Ga}_{1-x}\text{N}/\text{In}_y\text{Ga}_{1-y}\text{N}$ were reported by Nakamura and co-workers, who have shown quantum effects in room temperature PL measurements [6].

In this paper we report on the growth and characterization of InGaN alloys grown by the MBE method in the temperature range of 725-800 °C which coincides with the optimum temperature of GaN film growth.

EXPERIMENTAL METHODS

Three series of films were grown by the ECR assisted MBE method. Details of this growth method were reported previously and in the present paper only a brief summary is provided [7,8]. C-plane (0001) sapphire substrates were first subjected to the nitridation process. This leads to a thin atomically smooth AlN layer as revealed by the RHEED pattern. In the second stage these substrates were coated with approximately a 300 Å GaN buffer grown at 550 °C, which was also found to be atomically smooth [8].

The first series of InGaN alloys were grown directly onto a low temperature GaN buffer layer and were approximately 1 µm thick. The growth of the second series of InGaN alloy films was preceded by the growth of a few thousand angstroms of GaN film. The thickness of the InGaN films were between 3000-4000 Å. The third series consists of a double heterostructure with the InGaN film sandwiched between two GaN films. All the films were grown at growth rates between 10-30 Å/min. X-ray diffraction (XRD) measurements were carried out in a four-circle, double crystal X-ray diffractometer with Cu-K α radiation as the excitation source. The radiation was monochromated by a curved graphite crystal. The indium concentration in the films was determined by computing the relative shift of the InGaN Bragg peak with respect to the GaN peak and applying Vegard's law. Photoluminescence measurements were carried out with a 10mW He-Cd laser. A 0.5m grating spectrometer with a holographically blazed grating (1800 grooves/mm) was used to disperse the collected light. Absorption data was obtained from transmission measurements where a tungsten lamp was used as the source.

EXPERIMENTAL RESULTS AND DISCUSSION

Thick InGaN grown on a thin GaN buffer

Fig. 1 shows the XRD data from thick InGaN films grown directly on a 300 Å GaN buffer. The thickness of the InGaN films is 1 µm and the growth rate was determined to be 26 Å/min. for the In_{0.09}Ga_{0.81}N film and 30 Å/min. for the In_{0.21}Ga_{0.79}N. The FWHM of the XRD peak was greater for InGaN films as compared to the GaN film which can be attributed to strain or domain size effects. No attempt was made to incorporate more indium under these conditions of growth.

Fig. 2 shows the optical absorption and the PL spectrum of the In_{0.21}Ga_{0.79}N sample. The energy gap, as determined from the optical absorption data, is 2.65 eV. However, the peak of the photoluminescence spectrum occurs at 2.32 eV which is 330 meV less than the bandgap. The FWHM for the PL is 220 meV. It can be seen from the absorption spectrum that the absorption edge is not sharp but has a tail implying the presence of optically active states present in the bandgap. It is speculated that these deeper states could be due to impurities, although defect related transitions cannot be ruled out.

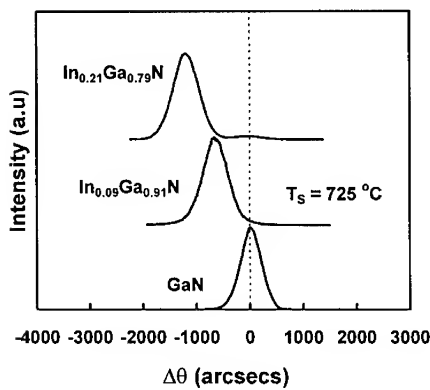


Fig. 1: XRD data for InGaN grown on a thin GaN Buffer

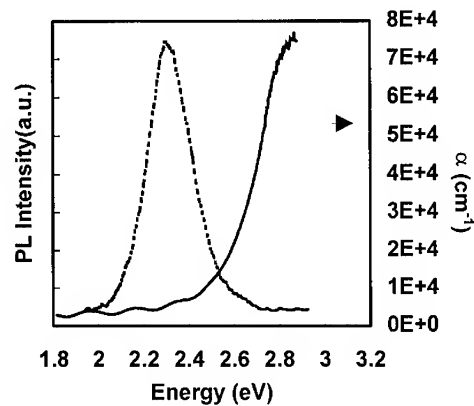


Fig. 2: PL and optical absorption for the InGaN sample with $x=0.21$

Thick InGaN grown on thick GaN Films

Fig. 3 depicts the XRD data for thick (0.5-1.0 μm) InGaN films grown on thick GaN films. The increase in the percentage incorporation of indium in these films is controlled systematically by changing the incident beam flux ratio of In/Ga. All the InGaN films have a mirror-like surface and show no evidence of indium droplets on the surface.

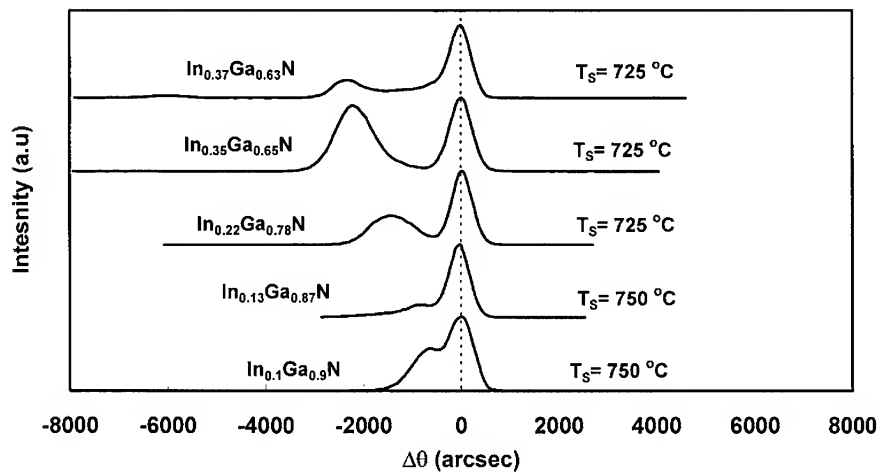


Fig. 3: XRD data for $\text{In}_x\text{Ga}_{1-x}\text{N}$ films grown on thick GaN films.

For $\text{In}_x\text{Ga}_{1-x}\text{N}$ with $x < 0.10$, it is difficult to determine the exact percentage of indium in the films because the Bragg diffraction peaks of InGaN overlap with those for GaN. It was previously mentioned that the XRD analysis of InGaN films on GaN buffer layers shows an increase in the FWHM of the Bragg peak for the InGaN films as compared to the GaN film. Similar results are also observed in the case of InGaN films grown on GaN films as can be seen in Fig. 3.

From the data of Fig. 3, for the sample with the highest indium concentration, there is evidence of a small peak at the diffraction angle which corresponds to approximately pure InN ($\Delta\theta \sim 5980$ arcsec). In fact, upon plotting the same data in a logarithmic scale (see Fig. 4), this InN peak is clearly resolved. In view of this evidence, all the other XRD data was plotted logarithmically. Only the $\text{In}_{0.35}\text{Ga}_{0.65}\text{N}$ and $\text{In}_{0.37}\text{Ga}_{0.63}\text{N}$ show evidence of an InN peak. This is a clear evidence of phase separation which we attribute to spinodal decomposition [9]. Such a phenomenon is expected because of the difference in the lattice parameter of GaN and InN (11% mismatch). Although we are not aware of any calculation of the miscibility gap in the GaN-InN system, the large lattice mismatch should put the growth temperature of these films (700-800 °C) within the miscibility gap [10].

Evidence of phase separation and thus formation of composite films is provided also by the optical absorption measurements. The optical absorption constant for the film with 37% indium is shown in Fig. 5 and is compared with the optical absorption constants of a GaN and a $\text{In}_{0.18}\text{Ga}_{0.82}\text{N}$ film.

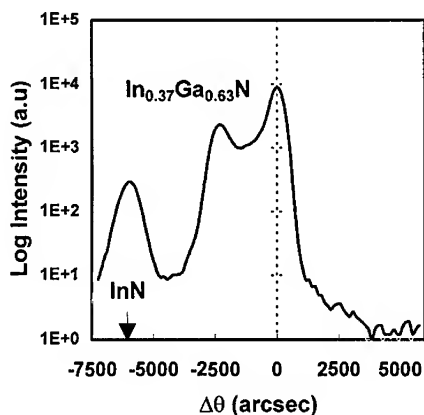


Fig. 4: Logarithmic plot of the XRD data for the $\text{In}_{0.37}\text{Ga}_{0.63}\text{N}$ sample in Fig. 3.

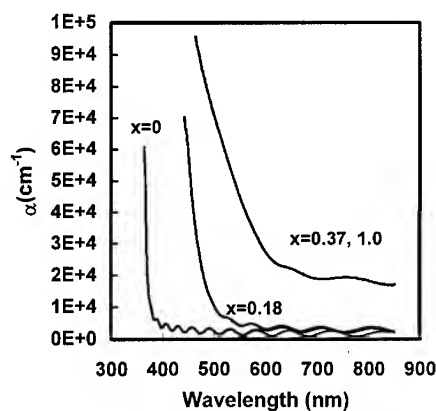


Fig. 5: Optical absorption data for InGaN samples. InGaN sample with $x=0.18$ which shows no phase separation versus an InGaN with $x=0.37, 1.0$ which shows phase separated InN

From this figure, it is apparent that the optical absorption constant of the $\text{In}_{0.35}\text{Ga}_{0.65}\text{N}$ is not as sharp as that of GaN and the InGaN film with smaller indium concentration. A careful inspection of this curve reveals two slopes indicative of a composite material. The determination of an optical gap from these data (at $\alpha = 3 \times 10^4 \text{ cm}^{-1}$) results in a value for the bandgap, $E_g \approx 2.0 \text{ eV}$ (red). We believe that our findings account also for the result of Matsuoka and co-workers who reported that a $\text{In}_{0.42}\text{Ga}_{0.58}\text{N}$ film has an optical bandgap of about 2.0 eV, which is the same as that for pure InN.

GaN / InGaN / GaN Double Heterostructures

Based on the XRD data shown in Fig. 6, this InGaN film has 53% indium with no evidence of phase separated InN. The substrate temperature employed for the growth of the InGaN layer in this structure was 725 °C while that for the GaN layers was 800 °C. These data provide a practical route of how to form InGaN alloys with high indium concentrations. Using the same approach and increasing the In/Ga ratio we were able to make InGaN films with up to 81 % indium in a double heterostructure, which is the highest yet reported by any growth method.

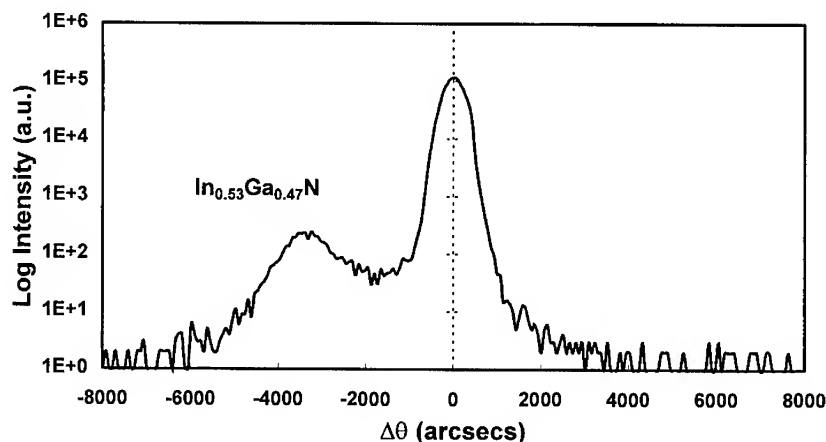


Fig. 6: XRD data from a GaN/ $\text{In}_{0.53}\text{Ga}_{0.47}\text{N}$ /GaN double heterostructure.

CONCLUSIONS

In conclusion, we have grown InGaN alloys by the MBE method at the temperature employed for the growth of GaN films. These studies have shown that up to 30% indium can be easily incorporated in InGaN bulk films ($> 0.3 \mu\text{m}$) grown on predeposited GaN films. Further increase in indium concentration results in phase separation of InN which is attributed to spinodal decomposition [9]. We also discovered that high indium concentrations in InGaN alloys

can be obtained in thin InGa_N layers grown as GaN/InGa_N/GaN double heterostructures. Using such structures, we incorporated up to 81% indium. Such structures are likely to be used for quantum devices operating in the visible part of the electromagnetic spectrum.

ACKNOWLEDGMENTS

The authors are grateful to Prof. K. Ludwig, Dr. G. Morales, Mr. A. Sampath and Mr. D. Korakakis for help and discussions. This work was partly funded by ARPA (Grant No. MDA972-95-3-0008).

REFERENCES

1. T. Matsuoka, T. Sasaki and A. Katsui, *Optoelectron.* **5**, p. 53 (1990)
2. K. Osamura, K. Nakajima and Y. Murakami, *Solid State Commun.* **11**, p. 617 (1972)
3. T. Matsuoka, N. Yoshimoto, T. Sasaki and A. Katsui, *J. Electron. Mater.* **21**, p. 157 (1992)
4. S. Nakamura, *Microelectron.* **25**, p. 651 (1994)
5. M. Shimizu, K. Hiramatsu and N. Sawaki, *J. Cryst. Growth* **145**, p. 209 (1994)
6. S. Nakamura, T. Mukai, M. Senoh, S. Nagahama and N. Iwasa, *J. Appl. Phys.* **74**, p. 3911 (1993)
7. T.D. Moustakas, T. Lei and R.J. Molnar, *Physica B* **185**, p. 36 (1993)
8. T.D. Moustakas and R.J. Molnar, *MRS Review Symp. Proc.* **281**, p. 753 (1993)
9. S. Mahajan, B.V. Dutt, H. Temkin, R.J. Cava and W.A. Bonner, *J. Crystal Growth*, **68**, p. 589 (1984)
10. G.B. Stringfellow, *J. Crystal Growth*, **58**, p. 194 (1982)

P-type Mg-doped GaN grown by molecular beam epitaxy using ammonia as the nitrogen source

Z. YANG, L.K. LI and W.I. WANG

Department of Electrical Engineering, Columbia University
New York, NY 10027

ABSTRACT

The electrical and luminescent properties of Mg-doped GaN films grown by molecular beam epitaxy (MBE) using ammonia as the nitrogen source have been investigated. Due to their different growth environments, the Mg-doped GaN films grown by MBE using ammonia exhibited properties that were different from similar films grown by metal-organic chemical vapor deposition (MOCVD). It has been found that the introduction of positive charges during growth is important in the achievement of p-type Mg-doped GaN grown by MBE using ammonia. With the introduction of a moderate nitrogen plasma, we have achieved p-type Mg-doped GaN films with a hole density of $4 \times 10^{17} \text{ cm}^{-3}$ and a mobility of $15 \text{ cm}^2/\text{V-s}$ at room temperature.

INTRODUCTION

Wide band gap materials such as GaN have been the subject of active research in recent years due to their potential for use in short-wavelength light emitting and high temperature/high power devices. The major obstacle for the use of GaN in device applications was the difficulties in the achievement of p-type conductivity, which is a result of the large ratio of band gap energy to nitrogen vacancy formation enthalpy ($E_g/\Delta H_v=0.8$).¹ The self-compensation of wide-band-gap semiconductors is well-known to be caused by native point defects.^{2,3} J.A. Van Vechten et al.⁴ proposed the use of positive charges in order to compensate the intended shallow p-type dopant (Mg) during growth, thus circumventing the self-compensation of GaN. As a result, p-type GaN can be obtained by activating the dopant from the complexes formed with the positive ions during crystal growth. Once the p-type GaN was achieved,⁵ p-n junction blue light emitting diodes (LED) soon followed.^{5,6,7} In MOCVD, hydrogen atoms compensate the Mg dopant by forming Mg-H complexes during growth, which results in high resistivity and weak photoluminescence (PL) emissions.^{6,7} Post-growth annealing is required to activate the Mg dopant from Mg-H complexes to achieve p-type conductivity and intensify the blue photoluminescence emissions.⁵ The properties of the Mg-doped GaN films grown by MOCVD exhibit a strong dependence on variations in the annealing process.^{6,8}

As a viable alternative to MOCVD, MBE offers ease of control for the growth of multilayer structures, which is essential in high temperature electronics and optoelectronics applications. The growth of GaN by MBE has been intensively investigated in two ways; plasma-assisted MBE which employs N₂ gas through a plasma source,^{9,10} and MBE which directly introduces nitrogen based gas such as NH₃ as the nitrogen source.^{11,12} In plasma-assisted MBE, p-type GaN is easily produced. However, the electrical and optical properties of the GaN films are often adversely affected by energetic ions. MBE employing ammonia as the nitrogen source avoids the ion damages due to the direct reactions between ammonia and gallium on a heated GaN surface. However, due to the different growth environments of MBE and MOCVD which both employ NH₃ as the nitrogen source, p-type GaN grown by MBE could not be achieved using the same method employed in MOCVD. Only recently we have achieved p-type GaN grown by MBE using ammonia for the first time.¹² Unlike the MOCVD growth environment, the amount of hydrogen generated during MBE growth is small due to the direct surface reaction between Ga and ammonia in an ultra-high vacuum. The density of Mg-H complexes is thus much less in the Mg-doped GaN films grown by MBE using ammonia than those grown by MOCVD. However, the low density of Mg-H complexes in GaN films grown by MBE using ammonia as the nitrogen source may not be enough to circumvent the self-compensation of GaN during growth.⁴

Our experiments show that Mg-doped GaN films grown by MBE employing ammonia were highly resistive but exhibited strong PL emissions. Unlike Mg-doped GaN grown by MOCVD, post-growth annealing was unable to reduce the resistivity of the Mg-doped GaN films grown by the MBE method using ammonia as the nitrogen source. In order to circumvent the self-compensation of GaN grown by MBE using ammonia as the nitrogen source, we discovered that the introduction of positive charges by employing an electron cyclotron resonance (ECR) nitrogen plasma during growth results in p-type GaN films. Positive charges could compensate the p-type dopant and raise the Fermi energy thus avoiding the formation of nitrogen vacancies during growth. This new MBE method avoids the problems caused by Mg-H complexes in the Mg-doped GaN films grown by MOCVD. High quality p-type GaN films, grown by this MBE method, have been obtained without post-growth annealing. At room temperature, hole density for these p-type GaN films was $4 \times 10^{17} \text{ cm}^{-3}$ while the mobility was $15 \text{ cm}^2/\text{V-s}$.

EXPERIMENT

The growth was carried out in a MBE system equipped with an ECR plasma source, an ammonia feeding line, and conventional Knudsen cells of Ga, Al and Mg. The applied ECR microwave power was 20 W. The growth rate of GaN was varied between 0.2 $\mu\text{m/hr}$ to 1

$\mu\text{m/hr}$, as calibrated after growth by infrared interference spectra measured from Fourier transform infrared spectroscopy (FTIR). The beam fluxes of ammonia and nitrogen were controlled by mass flow controllers, and the background pressure was kept below 5×10^{-5} torr. A two-step growth process was employed due to the essential role of low temperature buffers in order to achieve device quality epitaxial materials on lattice-mismatched substrates.^{13,14} This two-step growth process consisted of a low substrate temperature (500°C) for AlN buffers and a high growth temperature (750 °C to 800 °C) for subsequent GaN films. ECR nitrogen plasma was used for the buffer layer to circumvent the inefficiency of cracking ammonia at this low temperature (500 °C). During the growth of GaN films, the reflection high energy electron diffraction (RHEED) patterns showed a streaky 1x1 pattern with sharp Kikuchi lines. In addition, RHEED intensity oscillations were observed during the GaN growth indicating that the growth was a layer-by-layer two-dimensional nucleation process. Hall effect measurements were performed by the Van der Pauw method. Photoluminescence (PL) measurements were performed using the 3250Å He-Cd laser line as the excitation source. The unintentionally doped GaN films were n-type with a carrier density of $2 \times 10^{17} \text{cm}^{-3}$ and a mobility of $103 \text{ cm}^2/\text{V-s}$. Without post-growth annealing, p-type Mg-doped GaN with a hole density of $4 \times 10^{17} \text{ cm}^{-3}$ and a mobility of $15 \text{ cm}^2/\text{V-s}$ at room temperature have been achieved by introducing a moderate (0.2 sccm of nitrogen flux) ECR nitrogen plasma during growth.

RESULTS

In order to investigate the growth mechanism of Mg-doped GaN during MBE using ammonia as the nitrogen source, we conducted several experiments on the Mg-doped GaN films. It was found that the electrical and optical properties of the Mg-doped GaN were not affected by post-growth annealing. The Mg-doped GaN films always exhibited high resistivity and strong PL emissions. After annealing the samples at 750 °C for 30 minutes in a high vacuum and in the ambient gas of nitrogen, no obvious changes were observed in the film's resistivity and PL spectra. This behavior is in sharp contrast to the phenomena observed in the post-growth annealed Mg-doped GaN films grown by MOCVD.⁶ The strong PL emission of the Mg doped GaN films indicates that fewer Mg-H complexes exist in Mg-doped GaN grown by MBE using ammonia than by MOCVD. The high resistivity of the Mg-doped GaN film grown by MBE was concluded to be a result of self-compensation of GaN other than Mg-H complexes. In order to circumvent this self-compensation effect of GaN, we deliberately introduced positive charges during the growth by introducing an ECR nitrogen plasma. The mass flow rate of nitrogen gas through the ECR plasma source was kept lower than 0.2 sccm in order to minimize the ion damages. P-type GaN films were achieved without post-growth annealing. The growth conditions were 50 sccm of NH_3 , 0.2 sccm of N_2 with 20W ECR microwave power, and 0.5

$\mu\text{m/hr}$ GaN growth rate. Under these conditions, p-type GaN films were achieved with a hole density of $4 \times 10^{17} \text{ cm}^{-3}$ and a mobility of $15 \text{ cm}^2/\text{V-s}$ at room temperature. No post-growth annealing was necessary. The hole density was found to be proportional to the Mg beam flux.

Although the amount of Mg-H complexes in the Mg-doped GaN films grown by MBE using ammonia are not as large as those grown by MOCVD, a high beam flux ratio of NH_3 over Ga still affects the PL emissions of the films. Hydrogen atoms dissociated from ammonia could conceivably react with Mg to form Mg-H complexes in the film. As shown in Fig. 1, the PL spectra of three samples grown at different conditions were studied. The weak Mg-related blue PL emissions shown in Fig. 1(a) could be due to the Mg-H complexes resulted from the high ammonia flux used. Employing appropriate amounts of ammonia and growth rate, the samples showed strong PL emissions, as shown in Fig. 1(b) and Fig. 1(c), which could possibly due to the much lower density of Mg-H complexes. For the lightly Mg-doped p-type GaN films, the PL spectra were dominated by donor-acceptor recombination (3.27 eV) and two LO-phonon replicas (3.18 eV and 3.09 eV) as shown in Fig. 1(c). The weak 3.46 eV emission in Fig. 1(c) corresponds to an excitonic transition. For the heavily Mg-doped GaN, LO-phonon replicas and excitonic transitions could not be distinguished from the broad strong blue PL emissions.

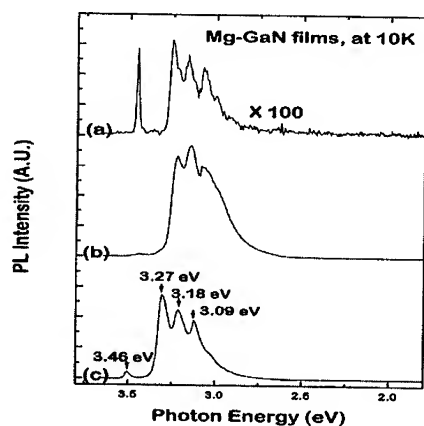


Figure 1. The PL spectra of Mg-doped GaN films grown under different conditions:
 (a) 200 sccm of NH_3 at the growth rate of $0.1 \mu\text{m/hr}$. (high resistive)
 (b) 200 sccm of NH_3 at the growth rate of $0.5 \mu\text{m/hr}$. (high resistive)
 (c) 50 sccm of NH_3 , 0.2 sccm of plasma nitrogen at the growth rate of $0.5 \mu\text{m/hr}$. (p-type)

CONCLUSIONS

In conclusion, we have shown that the properties of Mg-doped GaN films grown by MBE using ammonia as the nitrogen source are different from similar films grown by MOCVD. The employment of positive charges enabled the achievement of p-type Mg-doped GaN film in this MBE growth process. Using ammonia as the predominant nitrogen source with additional ECR nitrogen plasma, high quality p-type Mg-doped GaN films have been obtained without the need for post-growth annealing. The high quality GaN achieved and the high growth rate at which it was obtained indicate that both the growth method and the resulting materials reported here are very promising for future device applications.

This work was supported in part by ARPA.

REFERENCES

1. J.I. Pankove, *Mater. Res. Soc. Symp. Proc.* **97**, 409 (1987).
2. Y. Marfaing, *Prog. Crystal Growth Charact.* **4**, 317 (1981).
3. G. Mandel, *Phys. Rev.* **134**, A1073 (1964)
4. J. A. Van Vechten, J. D. Zook, R. D. Horning, and B. Goldenberg, *Jpn. J. Appl. Phys.* **31**, 3662 (1992).
5. H. Amano, M. Kito, K. Hiramatsu and I. Akasaki, *Jpn. J. Appl. Phys.* **28**, L2112 (1989).
6. S. Nakamura, T. Mukai, M. Senoh and N. Iwasa, *Jpn. J. Appl. Phys.* **31**, (1992) L139.
7. S. Nakamura, M. Senoh, and T. Mukai, *Jpn. J. Appl. Phys.* **30**, L1998 (1991).
8. M. Asif Khan, Q. Chen, R.A. Skogman and J.N. Kuznia, *Appl. Phys. Lett.* **66**, 2046(1995).
9. R. J. Molnar and T. D. Moustakas, *J. Appl. Phys.* **76**, 4587 (1994).
10. A. Ohtan, K. S. Stevens, and R. Beresford, *Appl. Phys. Lett.*, **65**, 61(1994).
11. Y. Yoshida, S. Misawa and S. Gonda, *J. Vac. Sci. Technol.* **B1**, 250(1983).
12. Z. Yang, L.K. Li and W.I. Wang, *Appl. Phys. Lett.*, **67**, 1686(1995).
13. W.I. Wang, *Appl. Phys. Lett.* **44**, 1149 (1984).
14. M. Akiyama, Y. Kwarada, and M. Kaminishi, *Jpn. J. Appl. Phys.* **23**, L843 (1984)

DEFECT MICROSTRUCTURE OF THIN WURTZITE GaN FILMS GROWN BY MBE

B.N. SVERDLOV*, A. BOTCHKAREV*, G.A. MARTIN*, A. SALVADOR*, H. MORKOÇ*,
S.-C.Y. TSEN** AND DAVID J. SMITH**

*Materials Research Laboratory and Coordinated Science Laboratory, University of Illinois, 104
S. Goodwin Ave., Urbana, IL 61801

** Department of Physics and Astronomy and Center for Solid State Science, Arizona State
University, Tempe, AZ 85287

ABSTRACT

Thin films of wurtzite GaN have been grown by molecular beam epitaxy on 6H SiC (basal plane), Si {111} and sapphire (c-plane) substrates with and without various buffer layers. The defect microstructure of the films and the substrate/buffer/GaN interfacial quality have been characterized by cross-sectional transmission electron microscopy. The morphology was dominated by threading defects that originated at the substrate/buffer and/or buffer/film interfaces. Typical defect densities dropped rapidly with distance from the substrate but remained $\sim 10^8$ - $10^9/\text{cm}^2$, depending on the particular substrate, for film thicknesses approaching one micron or more. The best quality films were grown at 770°C on sapphire with AlN buffer layers, and had X-ray rocking curve full-width at half-maximum values of ~ 55 arc-sec.

INTRODUCTION

Thin films of Group III - nitrides have attracted much recent attention because of their potential in many optoelectronic applications [1], particularly for high-temperature and high-power devices [2]. Successful growth of these materials presents several problems, not the least of which is the absence of substrate materials that are both lattice and thermally matched to the nitrides. Another problem is that the quality of the deposited nitride films, whether they are grown by molecular beam epitaxy [3, 4] or metallo-organic chemical vapor deposition [5-7], is highly inferior compared with most other heteroepitaxial semiconductor systems, which probably accounts for the lack of progress in producing long-lived heterostructure devices. Hence, much attention is being given to optimizing growth conditions for higher quality material.

In this comparative study, thin films of wurtzite GaN were grown by molecular beam epitaxy (MBE) on substrates of 6H SiC, Si{111} and sapphire. The overall film quality was quantified using double-crystal rocking curves (DCRC) and transmission electron microscopy (TEM) was used to characterize local variations in defect microstructure and to assess the substrate/buffer/GaN interfacial quality. Special attention was given to substrate surface preparation and to the possible benefits of using buffer layers of InN (Si substrate) and AlN (SiC and sapphire substrates) grown at low temperature.

EXPERIMENTAL DETAILS

The wurtzite GaN films were grown by plasma-enhanced MBE using a Perkin-Elmer 430 system. Details of the system and typical nitride deposition conditions can be found elsewhere [8]. Standard X-ray diffraction double-crystal rocking curves (DCRC) were used to compare the film quality, and transmission electron microscopy was performed in the cross-sectional geometry with a JEM-4000EX high-resolution electron microscope (HREM) operated at 400keV. Prior to

deposition, the chemically cleaned, 6H SiC substrates (basal plane) were subjected to hydrogen plasma treatment *in situ* to ensure oxide removal. All Si {111} substrates were prepared using standard RCA cleaning, with some later preparations also involving treatment with various buffered oxide etches to produce extended flat terraces, and immersion in HF to produce H-terminated surfaces[9]. As the various InN, AlN or GaN buffer layers were being deposited on the substrate, the temperature was usually ramped upward, typically from 550 to 650 or 750°C.

RESULTS

Typical low-magnification and high-magnification electron micrographs of wurtzite GaN thin films grown on substrates of 6H SiC (basal plane), Si {111} and sapphire (c-plane) are shown in figures 1 through 6. For each material, selected area electron diffraction (SAED) patterns confirmed the absence of cubic material and the overall quality of the GaN epitaxial growth.

a) 6H SiC (basal plane)

The morphology of GaN films grown on 6H SiC was invariably dominated by threading defects that originated at the SiC/GaN or AlN-buffer/GaN interfaces, and extended through to the top surface of the GaN film. Examples of these defects are visible in Fig. 1. These faults, which should be labelled as either double positioning boundaries (DPBs) or stacking mismatch boundaries (SMBs) to reflect their origin, are caused by the coalescence of domains that have nucleated on substrate terraces at the same or different levels. It is significant, as shown by the examples arrowed in Fig. 1, that many defects actually terminate within the GaN epilayer. A marked reduction in defect density with distance from the substrate is thus observed, typically ranging from $\sim 10^{10} - 10^{11}/\text{cm}^2$ close to the substrate to perhaps $\sim 10^8 - 10^9/\text{cm}^2$ at a distance of 1 μm away from the substrate. Fig. 2 shows an example of an SMB in a wurtzite GaN film grown directly on an offcut basal plane of 6H SiC (miscut angle of 4°) without any intervening AlN buffer layer. Note the coherent growth of GaN on the terraces of the miscut SiC substrate.

b) Si {111}

The quality of the GaN films initially grown on Si {111} was comparatively poor, which probably reflected the fact that the substrate preparation procedure had not been refined. Later substrates, prepared by buffered oxide etches, were shown by atomic force microscopy (AFM) to have wide, atomically flat terraces, but with surface bumps whose origins are currently unexplained. The corresponding single crystal GaN films were of much improved quality, as also reflected by marked improvements in DCRC full-width at half-maximum values to less than 20 arc-minutes[9]. The low-magnification image in Fig. 3 again shows the presence of the ubiquitous threading defects with a density falling off rapidly with distance away from the substrate. Fig. 4 shows a high-resolution image of the Si {111}/GaN interface from the same sample. Observation at glancing angle along the horizontal lattice fringes reveals lack of continuity of the fringes across the field of view, and small rotations in some places, which are characteristics that are consistent with a slight mosaic disorder.

c) Sapphire (c-plane)

Our latest observations have concentrated on GaN films grown with AlN buffer layers on sapphire substrates that have high smoothness and planarity. As shown in Fig. 5, the threading defects are still prevalent, albeit in reduced densities, despite our various efforts using different buffer layers and changes in deposition conditions. High-resolution imaging reveals, as demonstrated in Fig. 6, that abrupt and coherent interfaces between sapphire and the AlN buffer layer are readily obtained despite the large lattice mismatch between the two materials. Synchrotron X-ray diffraction measurements indicate coherence lengths along the growth direction on the order of several microns for some films [10].



Fig. 1. Cross-sectional transmission electron micrograph of wurtzite GaN film, grown with thin AlN intermediary buffer layer on offcut 6H SiC substrate. Note terminations of threading defects (arrowed).

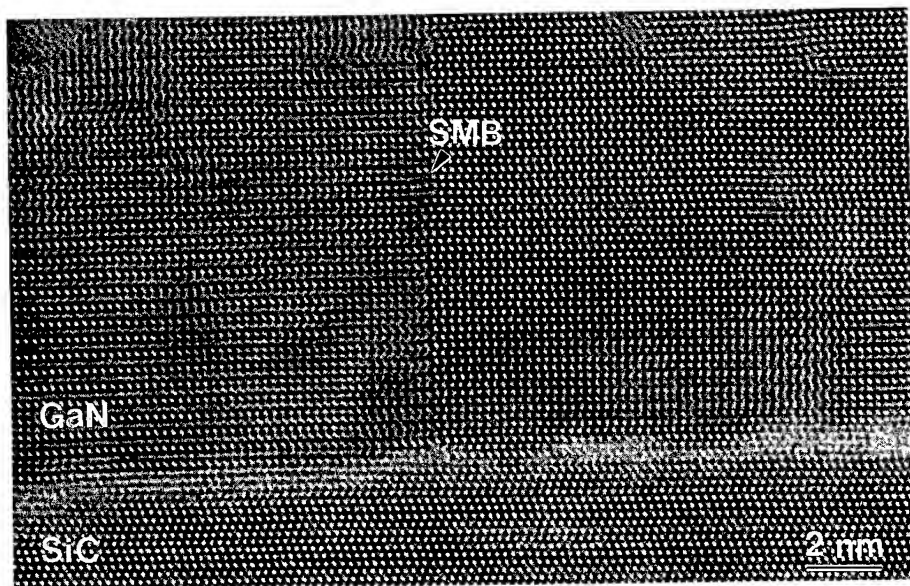


Fig. 2. High-resolution electron micrograph of epitaxial wurtzite GaN grown by plasma-enhanced MBE on offcut 6H SiC (miscut angle of 6°) showing substrate steps and an associated SMB.

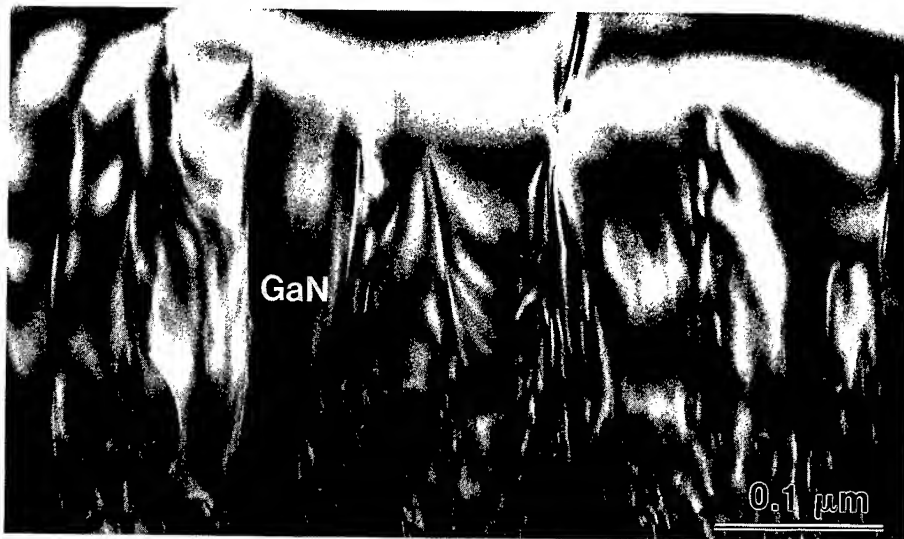


Fig. 3. Cross-sectional transmission electron micrograph of wurtzite GaN film, grown on Si{111} substrate. Note terminations of threading defects within the film.

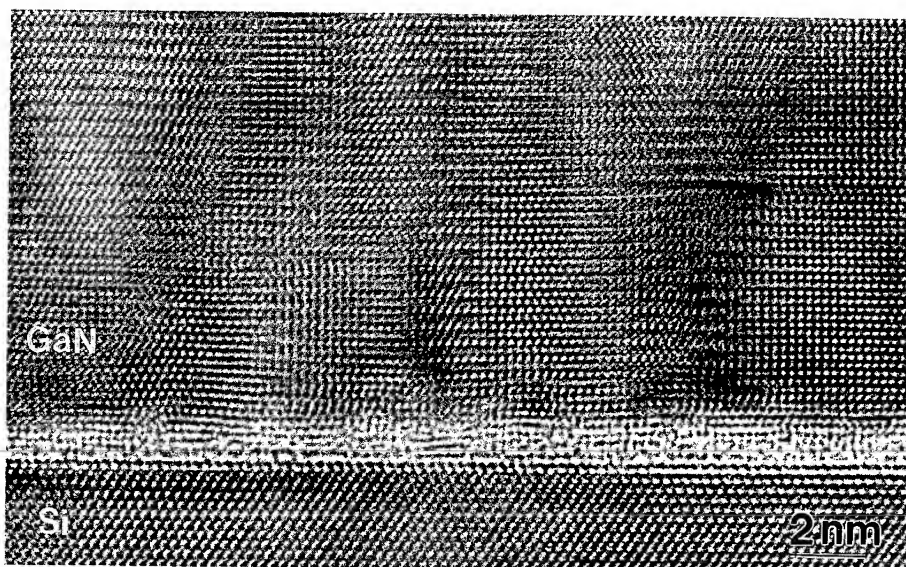


Fig. 4. High-resolution electron micrograph of epitaxial wurtzite GaN grown on chemically cleaned Si{111} substrate. Note lattice fringe terminations and rotations (observe from side of page at glancing angle).



Fig. 5. Cross-sectional transmission electron micrograph of wurtzite GaN film, grown with thin AlN intermediary buffer layer on a sapphire (c-plane) substrate.

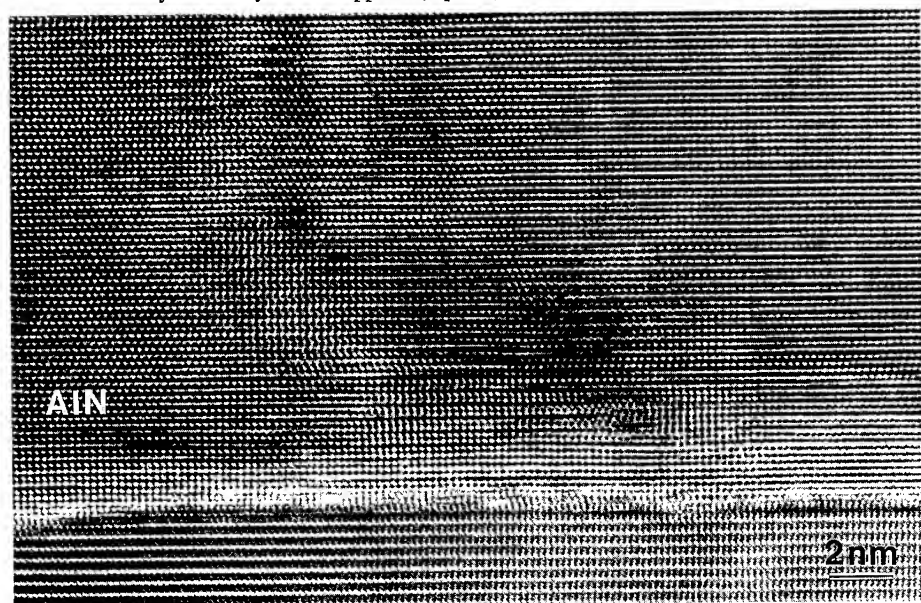


Fig. 6. High-resolution electron micrograph of wurtzite AlN buffer layer grown on sapphire (c-plane). Note abrupt, coherent interface and strain arising from misfit dislocations.

CONCLUSIONS

Our comprehensive TEM observations indicate that, irrespective of the particular substrate/buffer combination, the morphology of thin wurtzite GaN films grown by MBE is dominated by threading defects originating at the substrate/buffer/film interfaces. Although the density of these defects typically drops by two orders of magnitude at a distance of 1 micron from the substrate surface, the observed level of $\sim 10^8/\text{cm}^2$ probably still remains unacceptably high for some device applications. Since the defects originate primarily from the interface region, further work exploring offcut substrates and better substrate cleaning procedures should be pursued. Moreover, since it appears that the SMBs are inherent in the epitaxy of wurtzite GaN on non-wurtzite substrates with surface steps [11], isomorphic substrates such as ZnO or bulk GaN should be investigated as an alternative means for improving crystal quality.

ACKNOWLEDGEMENTS

Electron microscopy was conducted at the Center for High Resolution Electron Microscopy at Arizona State University supported by the National Science Foundation under Grant DMR-93-14326. The work at the University of Illinois was sponsored by the Office of Naval Research under the direction of Max Yoder.

REFERENCES

1. H. Morkoc, S. Strite, G.B. Gao, M.E. Lin, B. Sverdlov and M. Burns, *J. Appl. Phys.* 76, 1363 (1994).
2. R.F. Davis, *Proc. IEEE* 79, 702 (1991).
3. Z. Lilienthal-Weber, H. Sohn, N. Newman and J. Washburn, *J. Vac. Sci. Tech. B* 13, 1578 (1995).
4. D.J. Smith, D. Chandrasekhar, B. Sverdlov, A. Botchkarev, A. Salvador and H. Morkoc, *Appl. Phys. Lett.* 67, 1830 (1995).
5. K.G. Fertitta, A.L. Holmes, J.G. Neff, F.J. Ciuba and R.D. Dupuis, *Appl. Phys. Lett.* 65, 1823 (1994).
6. F.A. Ponce, B.S. Kruser, J.S. Major, W.E. Plano and D.F. Welch, *Appl. Phys. Lett.* 67, 410 (1995).
7. D. Kapolnek, X.H. Wu, B. Heying, S. Keller, B.P. Keller, U.K. Mishra, S.P. DenBaars and J.S. Speck, *Appl. Phys. Lett.* 67, 1541 (1995).
8. S. Strite, J. Ruan, Z.G. Li, N. Manning, A. Salvador, H. Chen, D.J. Smith, W.J. Choyke, and H. Morkoc, *J. Crystal Growth*, 127, 204 (1994).
9. G.A. Martin, B. Sverdlov, A. Botchkarev, H. Morkoc, D.J. Smith, S.-C. Y. Tsen, W.H. Thompson and M.H. Nayfeh, these proceedings.
10. Q. Zhu, A. Botchkarev, W. Kim, O. Aktas, B. Sverdlov, H. Morkoc, S.-C. Y. Tsen and D.J. Smith, *Appl. Phys. Lett.* submitted, Nov. 1995.
11. B.N. Sverdlov, G.A. Martin, H. Morkoc and D.J. Smith, *Appl. Phys. Lett.* 67, 2063 (1995).

Part III

Chemical Vapor Phase Growth Techniques

HIGH-QUALITY III-V NITRIDES GROWN BY METALORGANIC CHEMICAL VAPOR DEPOSITION

R.D. DUPUIS*, A.L. HOLMES*, P.A. GRUDOWSKI*, K.G. FERTITTA*, F.A. PONCE**

*Microelectronics Research Center, The University of Texas at Austin, Austin TX 78712-1100

**Xerox Palo Alto Research Center, 3333 Coyote Hill Road, Palo Alto CA 94304

ABSTRACT

We report the growth of high-quality III-V nitride heteroepitaxial films on (0001) sapphire substrates by low-pressure metalorganic chemical vapor deposition (MOCVD). These films have exhibited narrow X-ray diffraction rocking curves with full-width-at-half-maximum values as low as $\Delta\theta \sim 37$ arc sec. Photoluminescence and transmission electron microscopy analysis further indicate the samples to be of high quality.

INTRODUCTION

The semiconductors in the III-V materials systems have received much attention recently because they are well-suited for a wide range of applications in electronics and optoelectronics. Metalorganic chemical vapor deposition (MOCVD) was first used to deposit III-N single-crystal epitaxial films by Manasevit, et al., who reported the heteroepitaxial growth of GaN and AlN on a variety of insulating oxide substrates, including (0001) Al_2O_3 , in 1971.¹ More recently, Amano, et al., demonstrated the use of an AlN "buffer layer" grown at low-temperature for the MOCVD growth of high-quality GaN films on sapphire substrates.² In addition, Nakamura, et al. have reported the MOCVD growth of GaN on Al_2O_3 substrates using low-temperature GaN buffer layers.³

EXPERIMENTAL RESULTS

We have recently reported the MOCVD growth of high-quality GaN/sapphire heteroepitaxial films with very narrow X-ray rocking curves.⁴ In the present work, we have employed MOCVD to grow heteroepitaxial GaN, $\text{Al}_x\text{Ga}_{1-x}\text{N}$, and $\text{In}_x\text{Ga}_{1-x}\text{N}$ films on (0001) sapphire substrates. The epitaxial layers are grown at a pressure of 60 Torr using adduct-purified triethylgallium (TEGa), trimethylindium (TMIn), trimethylaluminum (TMAI)⁵ and high-purity ammonia (NH_3) as sources and purified H_2 as a carrier gas. The typical precursor molar flow rates for the growth of InAlGaN films are TEGa $\sim 1.3 \times 10^{-5}$ mole min^{-1} , TMAI $\sim 1.2 \times 10^{-5}$ mole min^{-1} , TMIn $\sim 1.5 \times 10^{-5}$ mole min^{-1} , and $\text{NH}_3 \sim 5.3 \times 10^{-2}$ mole min^{-1} , resulting in deposition rates for GaN ~ 0.5 $\mu\text{m/hr}$, as determined by both scanning-electron microscope (SEM) measurements and optical interference-transmission spectra. The heteroepitaxial nitride films are deposited at $\sim 1050^\circ\text{C}$ on thin (~ 25 nm) low-temperature GaN buffer layers grown at $\sim 525^\circ\text{C}$ on (0001)-oriented Al_2O_3 substrates.

The structural quality of the heteroepitaxial nitride films is analyzed using high-resolution X-ray rocking curves or triple-axis X-ray diffractometry employing symmetric (0002) diffraction conditions. For the rocking curve analysis, a Blake Instruments high-resolution five-crystal diffractometer is employed. $\text{Cu K}\alpha$ radiation is used and rocking curves through the (0002) GaN and Al_2O_3 lattice Bragg peaks are made to analyze the quality of the films. The FWHM of the (0002) GaN diffraction peak has been studied as a function of the thickness of the GaN film. The FWHM of the ~ 0.25 μm -thick films are ~ 100 arc sec while thicker films (~ 0.5 - 0.8 μm) have reproducible FWHM values $\Delta\theta \sim 37$ arc sec. Typical (0002) X-ray rocking curves for GaN/sapphire thin films are shown in Figure 1. Note the relatively small FWHM values for these rocking curves and the presence of well-defined Pendellösung fringes.⁶ A plot of FWHM vs. layer thickness for many such thin heteroepitaxial GaN/ Al_2O_3 films is shown in Figure 2.

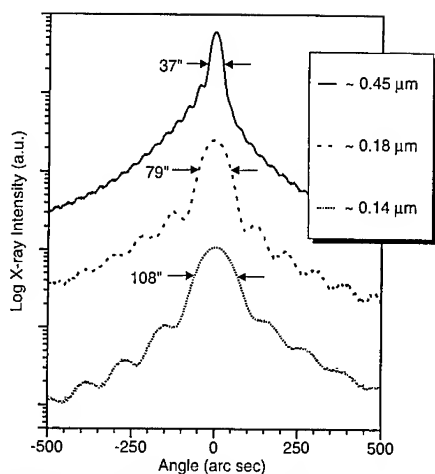


Figure 1: Five-crystal (0002) X-ray rocking curves for various GaN epitaxial layers grown by MOCVD on (0001) Al_2O_3 substrates.

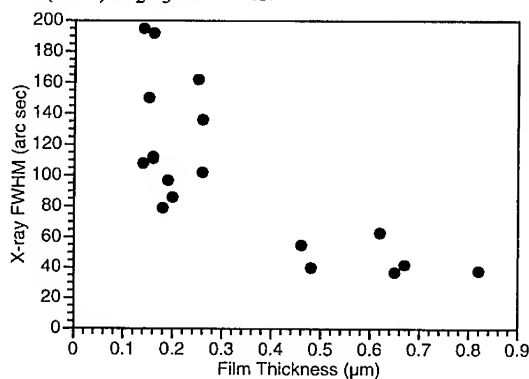


Figure 2: X-ray rocking curve FWHM values of GaN/ Al_2O_3 heteroepitaxial films vs. layer thickness.

The crystalline structure of selected films is also analyzed using high-resolution triple-axis X-ray diffractometry. Shown in Figure 3 are the iso-intensity contours (on a log scale) of the full ω vs. $\omega-2\theta$ scans for one of the GaN/sapphire films. Note the presence of contour lines corresponding to the Pendellösung fringes of Figure 2. These contour fringes are shown more dramatically in the intensity vs. angle form as shown in Figure 4a. The FWHM of this curve is ~ 35 arc-s. The diffracted intensity along the horizontal ($\omega-2\theta$) axis is indicative of the variation of the lattice constant perpendicular to the diffraction planes. Figure 4a shows the distribution of the Bragg diffraction intensity as a function of angle, and the width of the curve is related to the distribution of the (0001) interplanar separations. The extent of the "mosaic tilt" of the GaN film can be related to the diffracted intensity along the vertical (ω) axis, displayed in the intensity plot of

Figure 4b. The narrow FWHM of ~ 11 arc-s for the scan along the ω -axis indicates a low value of mosaicity in the heteroepitaxial GaN layer. The relatively broad ω - 2θ curve compared to the narrower ω curve is consistent with notion that low dislocation densities should be associated with less mosaic structure and that mosaicity plays a strong role in thermal stress relaxation.

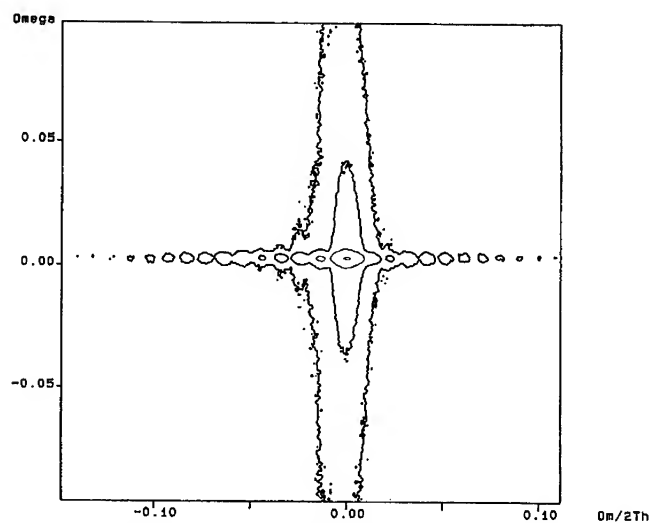


Figure 3: Triple-axis X-ray scan for a GaN/sapphire epitaxial layer grown by MOCVD.

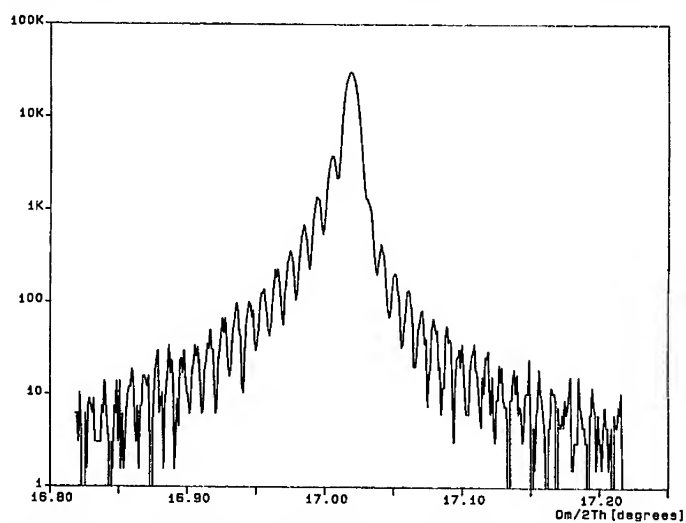


Figure 4a: X-ray intensity along the ω - 2θ axis at the $\omega=0.0$ plane. Note the well-defined Pendellösung fringes and the FWHM value of ~ 35 arc-s.

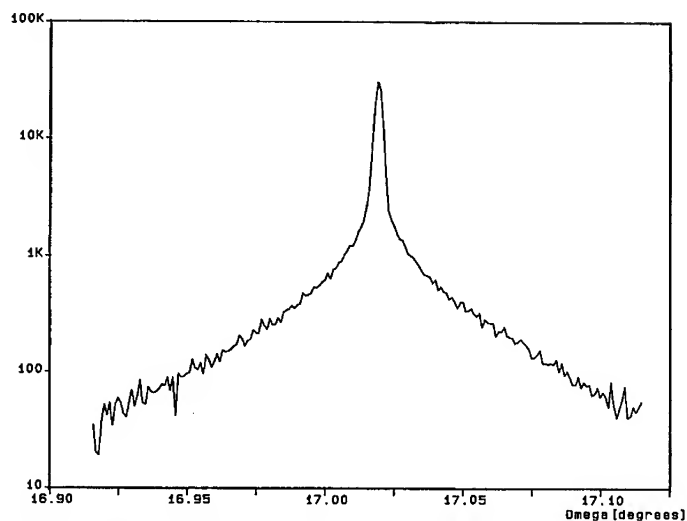


Figure 4b: X-ray intensity along the ω axis at the ω - $2\theta=0.00$ plane; the FWHM ~ 11 arc-s.

Photoluminescence (PL) spectra taken at 300K for the GaN films typically show an intense near-band-edge peak near $\lambda \sim 370$ nm and weak "defect-related" emission at ~ 550 nm. Figure 5 (upper curve) displays the 300K PL spectrum of a ~ 1.2 μm -thick GaN/ Al_2O_3 film. The high integrated intensity of the near-band-edge peak at ~ 367 nm and the high intensity of this peak compared to the deep-level ("yellow") emission at longer wavelengths further indicate the samples to be of good optical quality. The lower curve shows similar PL data obtained from a high-quality "undoped" MOCVD-grown GaN/ Al_2O_3 film (~ 2.0 μm thick)⁷. We note that the "undoped" film has a lower integrated intensity for the band-edge emission and a similar intensity for the "yellow" band luminescence. This indicates that the luminescence efficiency of these "narrow rocking-curve" films is, in principle, quite good. The broad spectral emission near the band edge is indicative of the high "unintentional" doping of the film, probably due to native defects that are acting as shallow donors.

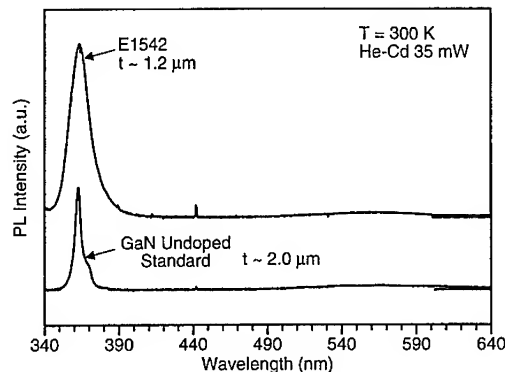


Figure 5: Room-temperature PL for "undoped standard" GaN film (curve a) and an "unintentionally doped n-type" GaN film grown in this study (curve b).

We have also grown alloy films in the InGaN and AlGaIn ternary systems that have narrow X-ray rocking curve FWHM values. These films are grown on GaN buffer layers; the AlGaIn films are grown at $\sim 1050^\circ\text{C}$ and InGaIn films are grown at $\sim 800^\circ\text{C}$. Shown in Figure 6 is the rocking curve for a heterostructure sample consisting of ~ 200 nm of $\text{Al}_{0.45}\text{Ga}_{0.55}\text{N}$ grown on a ~ 200 nm GaN film on (0001) sapphire. Note the presence of Pendellösung fringes and the relatively narrow FWHM values for these layers. No cracking of this film was observed under 500X optical examination. Similar X-ray rocking curve data are shown in Figure 7 for an $\text{In}_{0.55}\text{Ga}_{0.45}\text{N}$ film grown on a thin GaN buffer layer. Note again the relatively narrow rocking curve obtained for this film. In this case, no diffraction due to the GaN buffer layer is shown since this is very weak and is at a much different Bragg angle.

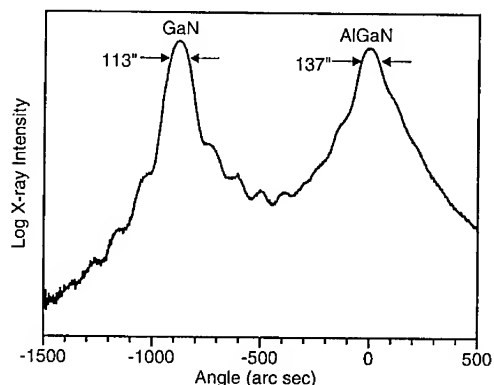


Figure 6: X-ray rocking curve for an AlGaIn/GaN heterostructure grown on (0001) sapphire.

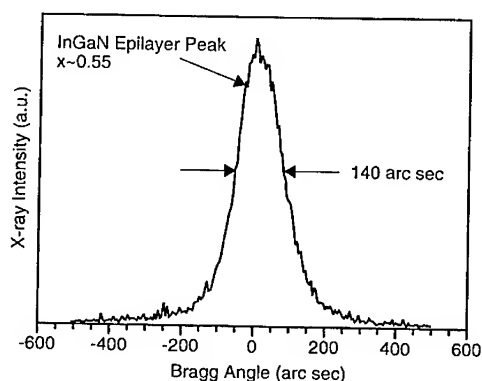


Figure 7: X-ray rocking curve for an InGaIn/GaN heterostructure grown on (0001) sapphire.

High-resolution transmission-electron microscopy (TEM) studies of these heteroepitaxial GaN/ Al_2O_3 films has shown that the interface is very abrupt.⁴ Detailed analysis of lattice images indicates that the spacing of the lattice planes is very constant throughout the film, consistent with the observation of well-defined Pendellösung fringes and the reciprocal-space maps obtained by

triple-axis diffractometry. Lower resolution TEM images show the presence of dislocations and domains with a distribution of various amounts of "twist" in the crystalline orientation. The detailed analysis of this material is under further study.⁸ The density of dislocations is highest near the film—substrate interface. The density of these domains varies throughout the film with densities $\sim 10^{11}$ cm⁻² near the film—substrate interface and $\sim 10^9$ cm⁻² near the top of the GaN film.

CONCLUSIONS

We have grown high-quality GaN heteroepitaxial films on (0001)-oriented Al₂O₃ substrates. Optical transmission, cathodoluminescence, and photoluminescence spectra show the films to have a 300K direct bandgap energy of $E_g \sim 3.4$ eV. Reproducible X-ray diffraction rocking curves having FWHM values of $\Delta\Theta \sim 37$ arc sec have been obtained for heteroepitaxial GaN films having a total thickness ~ 0.5 – 0.8 μm . In addition, triple-axis X-ray diffractometry and TEM characterization confirm the uniformity in lattice parameter for these films. These results represent nearly an order-of-magnitude improvement over typical values reported for significantly thicker GaN layers on Al₂O₃ substrates. Also, we have grown InGaN and AlGaIn films having narrow X-ray rocking curves. We expect that AlGaIn/InGaIn/GaN heterostructures

ACKNOWLEDGMENTS

We thank R.V. Chelakara, C.J. Eiting, J. Emdad, and M.R. Islam for technical assistance. We also thank B.S. Kursor, S.D. Lester, and M.J. Ludowise of Hewlett-Packard Corporation for useful discussions and additional assistance in characterization. This work was partially supported by NSF under grant DMR-93-12947 and by the NSF Science and Technology Center Program under grant CHE-89-20120, the State of Texas Advanced Technology Program, the Army Research Office, and by ARPA under contract MDA972-95-3-0008. Additional support by Ford Motor Company is also gratefully acknowledged. One of us (A.L.H.) acknowledges the support of an Office of Naval Research Graduate Fellowship.

REFERENCES

1. H.M. Manasevit, F.M. Erdman, and W.I. Simpson, *J. Electrochem. Soc.* **118**, 1855 (1971).
2. H. Amano, N. Sawaki, I. Akasaki, and Y. Toyoda, *Appl. Phys. Lett.* **48**, 353 (1986).
3. S. Nakamura, Y. Harada, and M. Seno, *Appl. Phys. Lett.* **58**, 2021 (1991).
4. K.G. Fertitta, A.L. Holmes, F.J. Ciuba, R. D. Dupuis, and F.A. Ponce, *J. Electron. Mat.* **24**, 257 (1995).
5. Metalorganics purchased from Air Products and Chemicals, Allentown, PA, USA and Epichem Ltd., Merseyside, UK.
6. K.G. Fertitta, A.L. Holmes, J.G. Neff, F.J. Ciuba, and R.D. Dupuis, *Appl. Phys. Lett.* **65**, 1923 (1994).
7. This unintentionally doped GaN/sapphire film was grown using MOCVD by other workers and exhibited a more "normal" X-ray rocking curve FWHM ~ 300 – 400 arc-s.
8. R.D. Dupuis and F.A. Ponce, unpublished.

OPTOELECTRONIC AND STRUCTURAL PROPERTIES OF HIGH-QUALITY GaN GROWN BY HYDRIDE VAPOR PHASE EPITAXY

R.J. Molnar, R. Aggarwal, Z.L. Liao, E.R. Brown and I. Melngailis
Massachusetts Institute of Technology, Lincoln Laboratory, Lexington, MA 02173-9108

W. Götz, L.T. Romano and N.M. Johnson
Xerox Palo Alto Research Center, Palo Alto, CA 94304

ABSTRACT

Gallium nitride (GaN) films have been grown by hydride vapor phase epitaxy (HVPE) in a vertical reactor design. We report on GaN growth directly on sapphire using a GaCl surface pretreatment. The electrical properties of these films compare favorably with the highest values reported in the literature for GaN. Specifically, a room temperature Hall mobility as high as 540 cm²/V·s, with a corresponding carrier concentration of 2x10¹⁷ cm⁻³, have been attained. Additionally, the vertical reactor design has assisted in reducing nonuniformities in both film thickness as well as in transport properties due to depletion effects, as compared with horizontal designs. The dislocation density in these films has been determined by plan-view transmission electron microscopy to be ~3x10⁸ cm⁻².

Photoluminescence spectra obtained at 2 K show intense, sharp, near-bandedge emission with minimal deep level emissions. Stimulated emission has been observed in these films, utilizing a nitrogen laser pump source ($\lambda=337.1$ nm) with a threshold pump power of ~0.5 MW/cm². These results suggest that HVPE is viable for the growth of high-quality nitride films, particularly for the subsequent homoepitaxial overgrowth of device structures by other growth methods such as OMVPE and MBE.

INTRODUCTION

Recent progress in high-brightness, efficient nitride-based light emitting diodes (LED's) has strengthened the contention that short-wavelength injection lasers will be possible with improvements in material quality. Typical state-of-the-art material often contains relatively high densities of structural defects (10⁹-10¹⁰ cm⁻²) which do not appear to introduce non-radiative defect centers as in most other III-V semiconductor systems. This has allowed LED's with external quantum efficiencies as high as 9.2 %.¹ It does appear, however, that when these defects are driven under higher current densities, which are required for injection lasers, these devices will degrade, likely through processes mediated by the structural defects. As it is generally agreed that these defects are a direct or indirect result of the lattice mismatch between the nitride epilayer and its foreign substrate, attention has recently focused on developing alternative substrate technologies. Due to the high equilibrium vapor pressure of N₂ over GaN, bulk growth has been carried out at extremely high pressures (~20 kbar) and has produced GaN platelets of limited dimensions (≤ 1 cm). Heteroepitaxial substrate materials with better lattice match to the nitrides, such as ZnO, LiGaO₂ or LiAlO₂, show promise for MBE growth, but their lack of thermal or chemical stability limits their suitability for the CVD growth of nitrides.

In order to generate large areas of thick GaN films, several groups are pursuing hydride vapor phase epitaxy (HVPE) as a quasi-bulk technique.^{2,3} This method has the advantages of high growth rate (typically >10 μ m/h) and low cost. Significant drawbacks associated with this technique are the large background donor concentration usually found in these films,⁴ surface particulates generated by wall deposition and pronounced lateral inhomogeneities due to depletion effects usually observed in films grown in horizontal reactors⁵. This typically limits regions of homogeneous growth to ~1 cm. In order for this technique to become commercially viable, techniques for the growth of high-quality, homogeneous material over large areas (≥ 2 in-diameter) will be necessary. Additionally, the structural and surface quality of the films will have to be such that the quality of epitaxial device overgrowths on these films are superior compared to those grown on available substrate materials.

To understand the mechanisms of nucleation and defect formation and propagation as well as the effect of growth conditions on the properties of GaN grown by HVPE, we have investigated the structural, electrical and optical properties of thick (>10 μ m) GaN films grown in a vertical HVPE reactor. Optimization of growth parameters has resulted in room temperature

mobilities as high as $540 \text{ cm}^2/\text{V}\cdot\text{s}$, and corresponding carrier concentrations of $2 \times 10^{17} \text{ cm}^{-3}$. Dislocation densities of $\sim 3 \times 10^8 \text{ cm}^{-2}$ have also been attained which suggest that such thick layers might provide a useful template for device overgrowth. These films have been successfully utilized as substrates for device epilayers with improved optoelectronic properties.⁶

EXPERIMENTAL

The samples were grown by a vertical HVPE process described previously³ on (0001) 2-in sapphire substrates. The heteronucleation of the GaN layer has proven a critical step in achieving uniform high-quality growth and smooth surface morphology. To enhance the nucleation of the GaN we have utilized both a GaCl pretreatment and a RF-sputtered ZnO buffer-layer technique.^{3,7,8} Here we report on results obtained using a GaCl pretreatment.

For the films investigated in this study, helium carrier gas was used to suppress natural convection effects, although similar results have recently been obtained by using nitrogen as a carrier gas. Additionally, the reactor was constructed to allow the direct injection of HCl gas into the growth stream, downstream from the gallium boat. This free HCl was found to have a beneficial effect on material quality and a moderate reducing effect on growth rate, as observed previously.⁹ The Ga boat temperature was typically held at 900°C and the growth temperature was usually between 1050 and 1100°C . Growth rates were typically $12\text{--}15 \text{ }\mu\text{m/h}$ and growth times are typically 1 h.

The material properties were investigated by a variety of techniques such as transmission electron microscopy (TEM), X-ray diffraction (XRD), atomic force microscopy (AFM), variable temperature Hall effect measurements ($T = 80\text{--}500\text{K}$), 2 K photoluminescence (PL), using a He-Cd laser excitation source, reflection high energy electron diffraction (RHEED) and optical pumping at room temperature and 77 K using a nitrogen laser pump source ($\lambda = 337.1 \text{ nm}$).

RESULTS and DISCUSSION

The films generally are highly transparent and uniform over a 2-in wafer. Usually, the surface structure consists of predominately large ($\sim 50 \text{ }\mu\text{m}$) low angle hillocks ($\sim 2 \text{ }\mu\text{m}$ in height), although some films have been grown with mirror-like surfaces. We believe that further refinements in the growth will afford control over this phenomenon. The hillocks have an RMS roughness of 2 Å, as determined by AFM. This is supported by the streaky RHEED patterns shown in Figure 1. As shown in Figure 1(b), upon heating these films quickly develop a 2X surface reconstruction suggestive that there is a highly ordered surface and minimal oxide removal issues for epitaxial overgrowth.

TEM investigations on these GaN films reveal a 200-nm region at the GaN/sapphire interface which has a high density of stacking faults, as shown in Figure 2. This "auto-buffer" layer is believed to be stress driven and, at a critical thickness, ceases, and growth continues with a comparatively large cell structure. Additionally, cross-sectional TEM images reveal annihilation of dislocations during film growth, resulting in substantially reduced defect densities at the surface of the film, as compared with the initial growth. Studies are currently underway to determine whether this trend continues as the thickness is further increased, thus leading to even lower defect densities. The resulting dislocation density after $12 \text{ }\mu\text{m}$ of growth was $\sim 3 \times 10^8 \text{ cm}^{-2}$, as determined by plan-view TEM. This compares favorably with reported OMVPE GaN films grown both on SiC and sapphire substrates, and suggests that with further optimization even lower defect densities may be possible.

X-ray diffraction studies yield a θ -rocking curve FWHM of 5 arcmin, which is comparable to reports for high-quality OMVPE material. Broadening due to X-ray penetration to the defective layer is expected, considering its penetration depth ($>12 \text{ }\mu\text{m}$), so that the top of the GaN film may have better structural orientation than suggested by this value. As reported by Hiramatsu et al.,¹⁰ for films of these thicknesses, a significant amount of strain resulting from the thermal mismatch between the GaN and sapphire is expected to be relieved through the formation of microcracks. Depending on the growth conditions, these cracks may become visible, although they tend to remain localized at the GaN/sapphire interface.

Temperature-dependent Hall effect measurements reveal the presence of two donor levels at ~ 17 and $\sim 100 \text{ meV}$, as shown in Figure 4. The shallower level is consistent with a Si donor,¹¹ and SIMS analysis is underway to determine whether the Si concentration in these films is

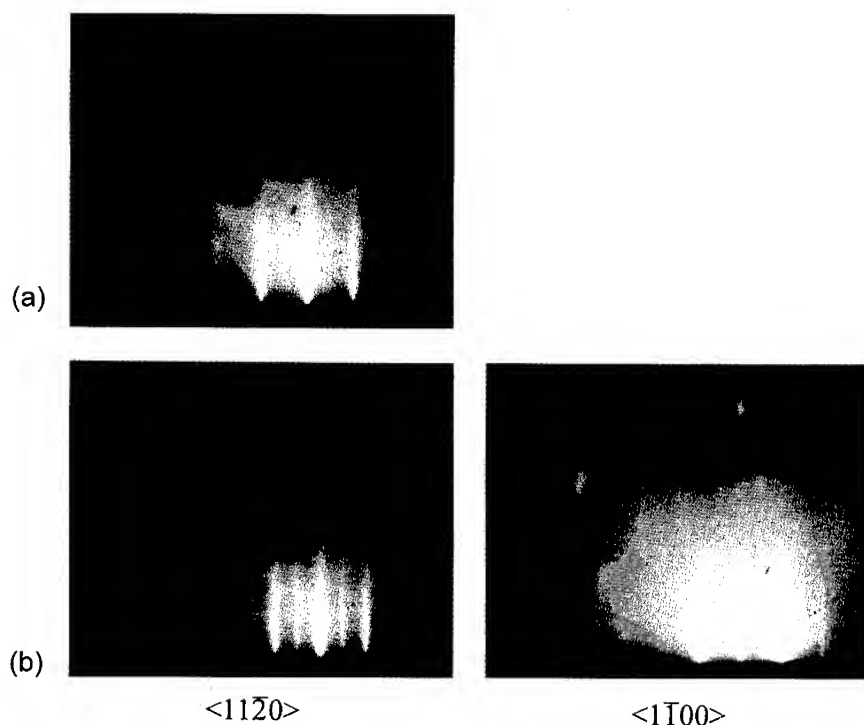


Figure 1 - RHEED patterns along $\langle 11\bar{2}0 \rangle$ and $\langle 1\bar{1}00 \rangle$ directions for HVPE GaN films: (a) as-grown and (b) heated to 750°C.

sufficient to account for these shallow donors. The deeper level is found to vary in a range of 100-200 meV from sample to sample. Also, the concentration of this level appears to be correlated with the thickness of the defective interfacial region. C-V and DLTS measurements performed at high temperature suggest a concentration of these defects near the surface that is far lower than derived from the Hall measurements.¹² Therefore, we speculate that this level may be due to a shunting conduction mechanism through the defective layer which has a high concentration of these deep states ($\sim 10^{20} \text{ cm}^{-3}$). This is supported by the temperature dependence of the mobility at $T > 200 \text{ K}$ which shows a reduction in mobility more rapid than that expected from phonon scattering ($\mu \propto T^{-3/2}$). Further investigations are underway to elucidate this issue. Room-temperature mobilities typically range between 400-540 $\text{cm}^2/\text{V}\cdot\text{s}$ with $n = 1\text{-}2 \times 10^{17} \text{ cm}^{-3}$, and both quantities are highly uniform over the 2-in substrate as shown in Figure 3.

The 2 K PL spectra of these films exhibit intense near-bandedge emission associated with donor-bound excitons (at 3.468 eV, FWHM = 2.42 meV, as shown in the inset of Figure 5). A high-energy shoulder is believed to be due to the free-exciton and is indicative of the high quality of these films. We are not able to detect any yellow emission centered at 2.2 eV, although weak red emissions centered at 2.0 and 1.8 eV are detected in some of the samples. Optically pumping these samples with a nitrogen laser, both at room temperature and 77 K, yields stimulated emission, as shown in Figure 6, with thresholds of 1.8 and 0.7 MW/cm^2 , respectively.

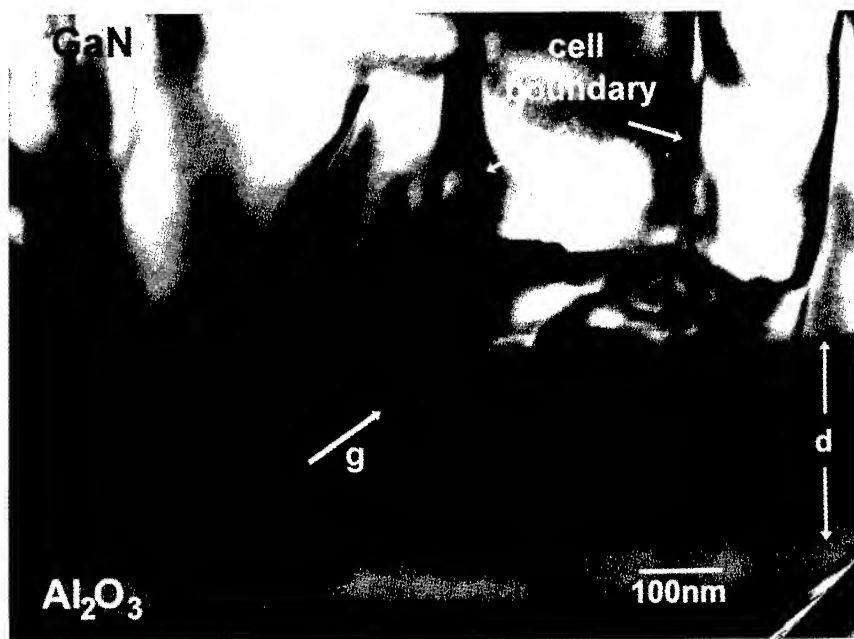


Figure 2 - Cross-sectional TEM image of GaN/sapphire interface for a sample grown using GaCl pretreatment. A thin (~200 nm) defect region with high density of stacking faults can be seen, after which there is an abrupt transition to high-quality growth.

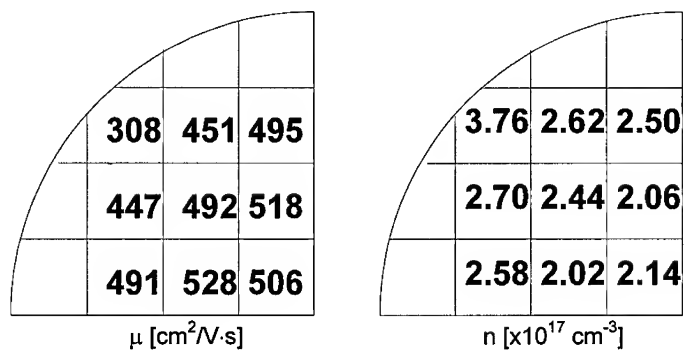


Figure 3 - Wafer map of room temperature transport characteristics over quarter of HVPE-grown GaN film on 2-in (0001) sapphire wafer. Due to the high rotational rate (~38 RPM), the other three quadrants exhibit similar characteristics.

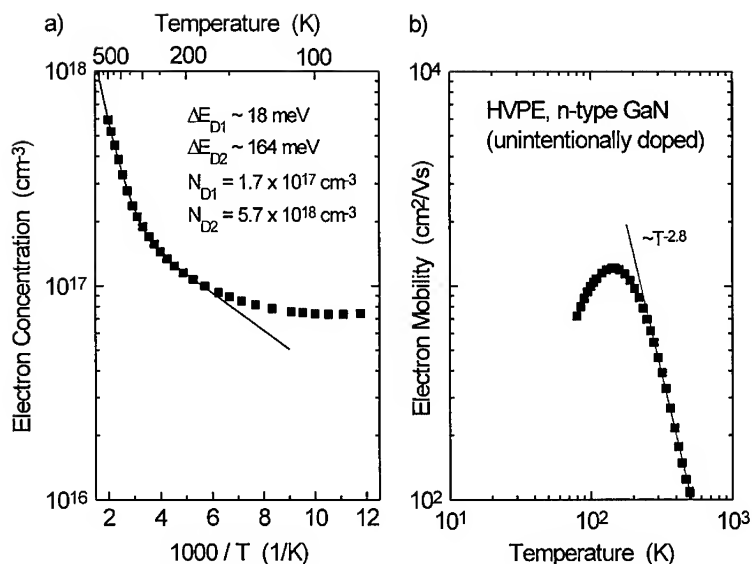


Figure 4 - Temperature dependent Hall effect data for HVPE-grown GaN.

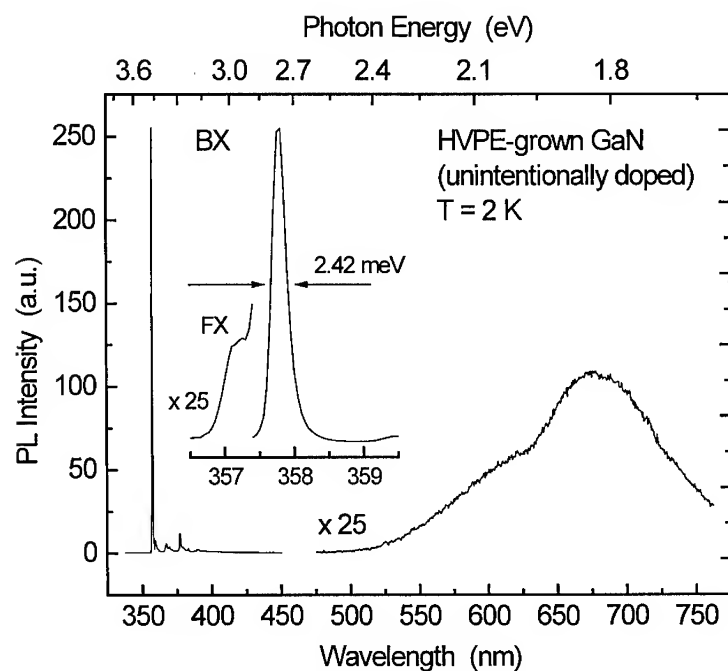


Figure 5 - Normalized 2 K PL spectra of HVPE GaN sample.

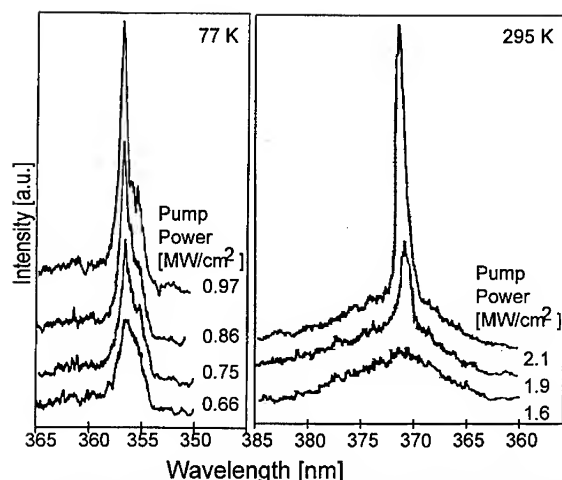


Figure 6 - 77 K and room temperature optical pumping of HVPE-grown GaN.

CONCLUSIONS

High-quality GaN films have been grown by HVPE uniformly over large (2-in diameter) areas. The structural, optoelectronic, and electrical properties compare favorably with OMVPE-grown material. This demonstrates that HVPE is viable for the growth of low-defect GaN thick films. Additionally, its high growth rate and low defect density suggest its employment as a quasi-bulk method for the generation of large area homoepitaxial substrates for nitride-based device overgrowths.

ACKNOWLEDGEMENTS

The authors are grateful to D. Hovey for fine glasswork and useful discussions and to J. Daneu and B.S. Krusor for technical assistance. The work at Lincoln Laboratory is supported by the Department of the Air Force, and the work at Xerox PARC was supported by ARPA (agreement # MDA972-95-3-008). Opinions, interpretations, conclusions, and recommendations are those of the authors and not necessarily endorsed by the United States Air Force.

REFERENCES

- ¹ S. Nakamura, M. Senoh, N. Iwasa and S. Nagahama, *Appl. Phys. Lett.* **67**, 1868 (1995).
- ² T. Detchprohm, K. Hiramatsu, N. Sawaki and I. Akasaki, *J. Cryst. Growth* **145**, 192, (1994).
- ³ R.J. Molnar, K.B. Nichols, P. Maki, E.R. Brown and I. Melngailis, *Mat. Res. Soc. Symp.* **378**, 479 (1995).
- ⁴ W. Seifert, R. Franzheld, E. Butter, H. Sobotta and V. Riede, *Cryst. Res. Technol.* **18**, 383 (1983).
- ⁵ M. Ilegems and H.C. Montgomery, *J. Phys. Chem. Solids* **34**, 885 (1973).
- ⁶ P. Maki, R.J. Molnar, R.L. Aggarwal, Z.L. Liao and I. Melngailis, *this volume*.
- ⁷ K. Naniwae, S. Itoh, H. Amano, K. Itoh, K. Hiramatsu and I. Akasaki, *J. Cryst. Growth* **99**, 381 (1990).
- ⁸ T. Detchprohm, K. Hiramatsu, H. Amano and I. Akasaki, *Appl. Phys. Lett.* **61**, 2688 (1992).
- ⁹ G. Jacob, *Acta Electronica* **21**, 159 (1978).
- ¹⁰ K. Hiramatsu, T. Detchprohm and I. Akasaki, *Jpn. J. Appl. Phys.* **32**, 1528 (1993).
- ¹¹ W. Götz, N.M. Johnson, D.P. Bour, C. Chen, H. Liu, C. Kuo and W. Imler, *to be published in Mat. Res. Soc. Symp.* **395**.
- ¹² W. Götz, L.T. Romano, B.S. Krusor, N.M. Johnson, R.J. Molnar, *Appl. Phys. Lett.*, (submitted).

Growth and Doping of $\text{Al}_x\text{Ga}_{1-x}\text{N}$ Deposited Directly on $\alpha(6\text{H})\text{-SiC}(0001)$ Substrates Via Organometallic Vapor Phase Epitaxy

M.D. Bremser, W.G. Perry, N.V. Edwards, T. Zheleva, N. Parikh*, D.E. Aspnes**, R.F. Davis

Department of Materials Science and Engineering, North Carolina State University, Box 7907
Raleigh, NC 27695-7907

*Department of Physics and Astronomy, University of North Carolina at Chapel Hill, Chapel Hill, NC.

**Department of Physics, North Carolina State University, Raleigh, NC.

ABSTRACT

Monocrystalline $\text{Al}_x\text{Ga}_{1-x}\text{N}(0001)$ ($0.05 \leq x \leq 0.70$) thin films, void of oriented domain structures and associated low-angle grain boundaries, have been grown at high temperatures via OMVPE *directly on* vicinal and on-axis $\alpha(6\text{H})\text{-SiC}(0001)$ wafers using TEG, TEA and ammonia in a cold-wall, vertical, pancake-style reactor. The surface morphologies were smooth and the densities and distributions of dislocations were comparable to that observed in $\text{GaN}(0001)$ films grown on high temperature AlN buffer layers. Double-crystal XRC measurements showed a FWHM value as low as 186 arc sec for the (0002) reflection. Spectra obtained via CL showed strong near band-edge emissions with FWHM values as low as 31 meV. The compositions of the $\text{Al}_x\text{Ga}_{1-x}\text{N}$ films were determined using EDX, AES and RBS and compared to the values of the bandgap as measured by spectral ellipsometry and CL emissions. A negative bowing parameter was found. Controlled n-type, Si-doping of $\text{Al}_x\text{Ga}_{1-x}\text{N}$ for $x \leq 0.4$ has been achieved with net carrier concentrations ranging from $\approx 2 \times 10^{17} \text{ cm}^{-3}$ to $2 \times 10^{19} \text{ cm}^{-3}$. Acceptor doping with Mg for $x < 0.13$ was also successful.

INTRODUCTION

The numerous potential semiconductor applications of the wide bandgap III- Nitrides has prompted significant research regarding their growth and development. GaN (wurtzite structure), the most studied in this group, has a bandgap of $\approx 3.4 \text{ eV}$ and forms continuous solid solutions with both AlN (6.2 eV) and InN (1.9 eV). As such, materials with engineered bandgaps are feasible for optoelectronic devices tunable in wavelength from the visible to the deep UV. The relatively strong atomic bonding of these materials also points to their potential for high-power and high-temperature microelectronic devices.

Single crystal wafers of GaN are not commercially available. Sapphire(0001) is the most commonly used substrate, although its lattice parameter and coefficients of thermal expansion are significantly different from that of any III-Nitride. The heteroepitaxial nucleation and growth of monocrystalline films of GaN on any substrate and AlN on sapphire are difficult at elevated ($>900^\circ\text{C}$) temperatures. Therefore, at present, for successful organometallic vapor phase epitaxy (OMVPE) of GaN films on sapphire the use of the initial deposition of an amorphous or polycrystalline buffer layer of $\text{AlN}^{1,2}$ or $\text{GaN}^{3,4}$ at low-temperatures ($450^\circ\text{--}600^\circ\text{C}$) is necessary to achieve both nucleation and relatively uniform coverage of the substrate surface. Subsequent deposition at higher temperatures and concomitant grain orientation competition has resulted in films of GaN(0001) and various nitrides alloys of improved quality and surface morphology relative to that achieved by growth directly on this substrate.

By contrast, we have observed that AlN and $\text{Al}_x\text{Ga}_{1-x}\text{N}$ alloys containing even low ($x \geq 0.05$) concentrations of AlN deposited on 6H-SiC(0001) substrates at high ($\geq 1000^\circ\text{C}$) temperatures undergo two-dimensional nucleation and growth with resulting uniform surface coverage. In our research, the use of a 1000 Å, monocrystalline, high-temperature (1100°C) AlN buffer has resulted in GaN films void of oriented domain structures and associated low-angle grain boundaries.^{5,6} Monocrystalline films of $\text{Al}_x\text{Ga}_{1-x}\text{N}$ ($0.05 \leq x \leq 0.70$) of the same quality have also been achieved *directly on* 6H-SiC(0001) wafers at 1100°C . The presence of AlN in the

films, the enhanced surface mobility of the adatoms at high temperatures and the reduced mismatch in lattice parameters between $\text{Al}_x\text{Ga}_{1-x}\text{N}(0001)$ and $6\text{H-SiC}(0001)$ ($a/a_0 \approx 1\text{-}3\%$) relative to that between $\text{Al}_x\text{Ga}_{1-x}\text{N}$ and sapphire ($11\text{-}13\%$)² have promoted the growth of these films.⁷ The following is the first known published report of the deposition of undoped and doped high quality $\text{Al}_x\text{Ga}_{1-x}\text{N}$ alloys without the use of a buffer layer.

EXPERIMENTAL PROCEDURES

As-received vicinal $6\text{H-SiC}(0001)$ wafers⁸ oriented $3^\circ\text{-}4^\circ$ off-axis toward $\langle 11\bar{2}0 \rangle$ were cut into 7.1 mm squares. These pieces were degreased in sequential ultrasonic baths of trichloroethylene, acetone and methanol and rinsed in deionized water. The SiC substrates were then dipped into a 10% HF solution for 10 minutes to remove the thermally grown oxide layer and blown dry with N_2 before being loaded onto the SiC-coated graphite susceptor contained in a cold-wall, vertical, pancake-style, OMVPE deposition system. The system was evacuated to less than 3×10^{-5} Torr prior to initiating growth. The continuously rotating susceptor was RF inductively heated to the $\text{Al}_x\text{Ga}_{1-x}\text{N}$ deposition temperature of 1100°C (optically measured on the susceptor) in 3 SLM of flowing H_2 diluent. Hydrogen was also used as the carrier gas for the various metalorganic precursors. Deposition of $\text{Al}_x\text{Ga}_{1-x}\text{N}$ was initiated by flowing various ratios of triethylaluminum (TEA) and triethylgallium (TEG) in combination with ammonia (NH_3). The NH_3 and total metalorganic precursor flow rates were 1.5 SLM and $32.8\text{ }\mu\text{mol/min}$, respectively. The system pressure was 45 Torr. Silicon doped n-type $\text{Al}_x\text{Ga}_{1-x}\text{N}$ samples were achieved via the addition of SiH_4 (12.4 ppm in a balance of N_2) at flow rates between 0.05 nmol/min and 15 nmol/min . Magnesium doped p-type $\text{Al}_x\text{Ga}_{1-x}\text{N}$ samples were achieved via the addition of Cp_2Mg at flow rates between 200 nmol/min and 400 nmol/min .

The structural, microstructural, optical and electrical characteristics of the epitaxial $\text{Al}_x\text{Ga}_{1-x}\text{N}$ thin films were analyzed using several techniques. Scanning electron microscopy (SEM) was performed using a JEOL 6400FE operating at 5 kV which was equipped with an Oxford Light Element Energy Dispersive X-ray (EDX) Microanalyzer. Conventional and high resolution transmission electron microscopy (TEM) was conducted using a Topcon EM-002B microscope operating at 200 kV . Double-crystal x-ray rocking curve (DCXRC) measurements were made on a Philips MR3 thin films diffractometer. The catholuminescence (CL) properties of the $\text{Al}_x\text{Ga}_{1-x}\text{N}$ films were determined at 4.2 K using a Kimball Physics EMG-14 electron gun as the excitation source. Spectral ellipsometry (SE) was performed using a rotating analyzer ellipsometer with a xenon arc lamp ($1.5\text{ eV} - 5.75\text{ eV}$). Capacitance-Voltage (CV) measurements were conducted using a MDC Model CSM/2-VF6 equipped with a mercury probe. Auger electron spectroscopy (AES) was performed using a Perkin-Elmer Model 660 equipped with Zalar rotation. Rutherford backscattering analysis was performed using 1.9 MeV He^+ ions with the detector at an angle of 165° .

RESULTS AND DISCUSSION

Previous research in our laboratories has shown that thin films of GaN deposited directly on $6\text{H-SiC}(0001)$ substrates at high and low temperatures had columnar-like grains, faceted surfaces and high net carrier concentrations ($n_D - n_A > 1 \times 10^{19}\text{ cm}^{-3}$).⁹ In contrast, in the present research monocrystalline thin films of $\text{Al}_x\text{Ga}_{1-x}\text{N}$ ($x \leq 0.05$) have been deposited directly on the same type of SiC substrates *without the use of a buffer layer* with no misorientation or low-angle grain boundaries, as determined by selected area diffraction (SAD) and microstructural analysis via TEM. The stacking fault density was also very low. These results are apparent in the representative cross-sectional TEM micrograph shown in Figure 1a. Inserts in the micrograph show SAD patterns from the top layer of $\text{Al}_{0.13}\text{Ga}_{0.87}\text{N}$ and the film/substrate interface. Overlapping spots from the $6\text{H-SiC}(0001)$ substrate are seen in the latter pattern. The dislocation density of these films at the interface appears to similar to GaN films deposited on a high temperature (HT) buffer layer.^{5,6} The dislocation density of the $\text{Al}_x\text{Ga}_{1-x}\text{N}$ film decreases rapidly as a function of thickness, as shown in Figure 1a, and only threading dislocations which result

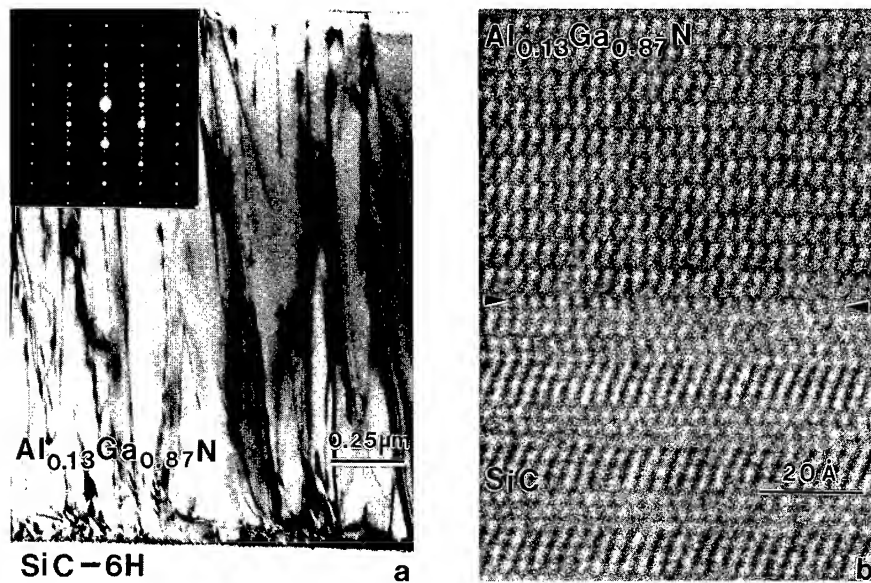


Figure 1. a) Cross-sectional TEM micrograph of a 1.8 μm AlGaIn(0001) film deposited at 1100°C and 45 Torr via OMVPE directly on a vicinal 6H-SiC(0001) substrate. The inset shows the selected area diffraction. b) High resolution TEM of the AlGaIn/SiC interface

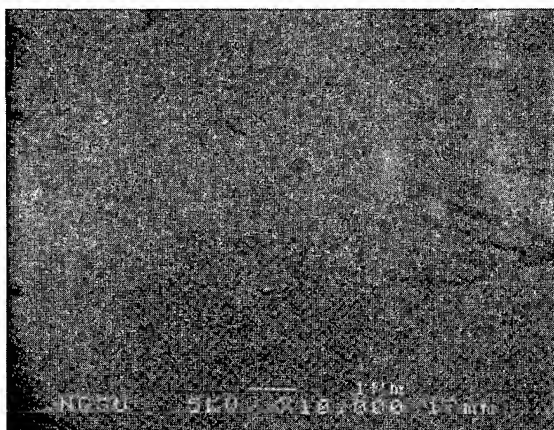


Figure 2. Representative SEM micrograph of the surface of an AlGaIn(0001) film similar to that shown in Figure 1.

from misfit dislocations at the interface persist through the film. High resolution TEM of the AlGa_xN/SiC interface is shown in Figure 1b.

The surfaces of the Al_xGa_{1-x}N films exhibited a slightly mottled appearance, as shown in Figure 2, probably as a result of the step and terrace features on the growth surface of the vicinal 6H-SiC(0001) substrates. Random pinholes, caused by incomplete coalescence of the two dimensional islands which occurred as an intermediate growth stage between the initial nucleation and the final layer-by-layer growth stage representative of the majority of the film, were also observed. For Al_xGa_{1-x}N compositions for $x > 0.5$, a significant number of pinholes appeared on the surface. Based on previous work with GaN, the pinhole density can be decreased with increasing growth temperature due to the enhanced surface mobility of the adatoms at higher temperatures.^{5,6} The higher growth rate of films grown on off-axis material is due to the increased density of steps on the substrate and film. DCXRC measurements taken on the 1.8 μm Al_{0.13}Ga_{0.87}N film shown in Figure 1 revealed the FWHM of the (0002) reflection to be 186 arc sec. For a 0.9 μm film of the same composition, the FWHM value of the same reflection was 315 arc sec. The reduction in FWHM values is consistent with the decrease in alloy concentration.

The low-temperature (4.2K) CL spectra of the undoped Al_xGa_{1-x}N films for various compositions ($0.05 \leq x \leq 0.70$) revealed an intense near band-edge emission which has been attributed to an exciton bound to a neutral donor (I_2 -line emission)^{10,11}. Broadening of this emission is attributed to both exciton scattering in the alloys as well as small variations in alloy composition in the film. The lowest FWHM value observed for the Al_xGa_{1-x}N alloys was 31 meV. Strong defect peaks, previously ascribed to donor-acceptor pair recombination,¹² were observed at midgap energies. The broad peak centered at 545 nm (2.2 eV) for GaN, commonly associated¹³ with deep-levels (DL) in the bandgap, was also observed; however, these emissions shifted sublinearly with changing composition. The nature of this behavior is under investigation.

The compositions of seven films grown under different conditions were determined using EDX, AES and RBS. Standards of AlN and GaN grown in the same reactor under similar conditions were used for the EDX and AES analyses. After carefully consideration of the errors (± 3 at.%) involved with each technique, compositions were assigned to each film. The data from EDX and AES measurements showed excellent agreement. The RBS data did not agree as well with the other two techniques due to small compositional variations through the thickness of the film. Simulation of the composition determined by RBS was conducted only on the surface composition. Analysis via EDX revealed that the Al_xGa_{1-x}N grown on the on-axis SiC substrates tended to be slightly more Al rich than those grown off-axis SiC. It is thought that the presence of steps on the growth surface favors the adhesion of the gallium adatoms. In all cases except one, this difference was less than 2 atomic percent. Under the most aluminum rich growth conditions, the difference was 6-8 atomic percent. This difference was revealed by all three techniques. At this time, the reason for this large difference is unclear.

In Figures 3 and 4, these compositions are compared with their respective CL emission peaks and bandgap as determined by SE. Using a parabolic model, the following relationships describe the bandgap (Eq.(1)) and CL (I_2 -line emission) (Eq.(2)) as a function aluminum mole fraction for $0 \leq x \leq 0.70$.

$$E_g(x) = 3.40 + 1.35x + 1.01x^2 \quad (1)$$

$$E_{I_2}(x) = 3.47 + 1.07x + 0.96x^2 \quad (2)$$

Clearly, both measurements show a negative deviation from a linear fit. This is in agreement with earlier research by other investigators.^{10,11}

Undoped, high quality Al_{0.05}Ga_{0.95}N films grown directly on vicinal 6H-SiC(0001) exhibited residual, n-type background carrier concentrations of $\leq 1 \times 10^{18} \text{cm}^{-3}$. The carrier concentration rapidly decreased with increasing Al content and was $< 1 \times 10^{16} \text{cm}^{-3}$ for Al_{0.35}Ga_{0.65}N, as determined by CV measurements. This origin of this residual carrier concentration is under investigation, since concentrations of $< 1 \times 10^{15} \text{cm}^{-3}$ have been measured for GaN films grown on AlN buffer layers in the same reactor. However, the controlled introduction of SiH₄ allowed the reproducible achievement of donor carrier concentrations within the range of $2 \times 10^{17} \text{cm}^{-3}$ to $2 \times 10^{19} \text{cm}^{-3}$ in films with $x \leq 0.4$. The growth of p-type

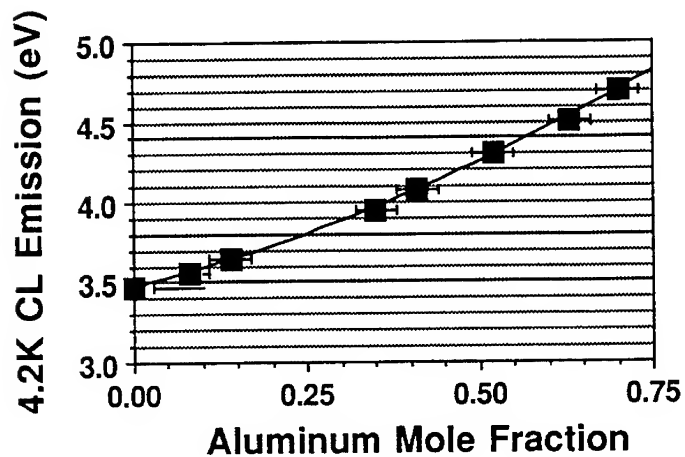


Figure 3. Low-temperature (4.2K) CL emissions of $Al_xGa_{1-x}N$ films as a function of aluminum mole fraction.

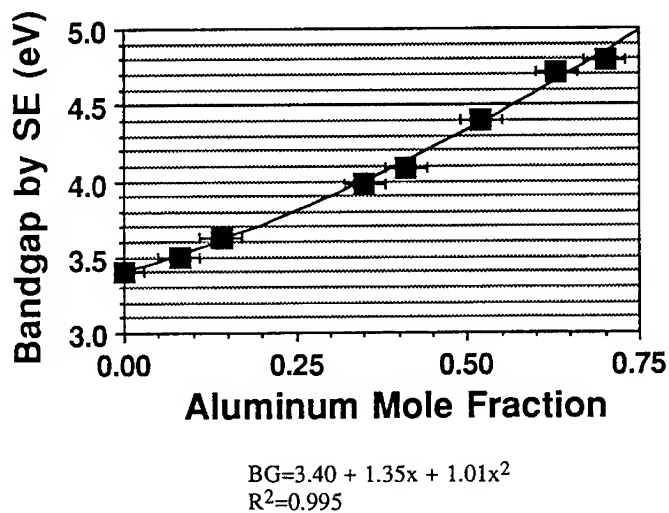


Figure 4. Bandgaps measured by spectral ellipsometry of $Al_xGa_{1-x}N$ films as a function of aluminum mole fraction.

$\text{Al}_x\text{Ga}_{1-x}\text{N}$ films for $x \leq 0.13$ via the introduction of Mg has been successful. All attempts to similarly dope films with $x > 0.13$ have been unsuccessful.

CONCLUSIONS

$\text{Al}_x\text{Ga}_{1-x}\text{N}(0001)$ ($0.05 \leq x \leq 0.70$) thin films void of low-angle grain boundaries and resultant domain microstructures have been grown via OMVPE directly on vicinal and on-axis $\alpha(6\text{H})\text{-SiC}(0001)$ substrates. A significant reduction in dislocation density with increasing thicknesses was observed via TEM. Low-temperature CL spectra of the films showed intense near band-edge emissions. For a $1.8\text{ }\mu\text{m}$ $\text{Al}_x\text{Ga}_{1-x}\text{N}$ film ($x=0.13$), DCXRC measurements revealed a FWHM value of 186 arc sec for the $\text{GaN}(0002)$ reflection. The composition of the $\text{Al}_x\text{Ga}_{1-x}\text{N}$ films was determined using EDX, AES and RBS and compared to the values of the bandgap measured by spectral ellipsometry and CL emissions. A negative bowing parameter was found. Controlled n-type Si-doping of $\text{Al}_x\text{Ga}_{1-x}\text{N}$ has been achieved for net carrier concentrations ranging from $\approx 2 \times 10^{17}\text{ cm}^{-3}$ to $\approx 2 \times 10^{19}\text{ cm}^{-3}$ for $x \leq 0.4$. The p-type doping with Mg of $\text{Al}_x\text{Ga}_{1-x}\text{N}$ for $x < 0.13$ has also been successful.

ACKNOWLEDGMENTS

The authors express their appreciation to Cree Research, Inc. of Durham, North Carolina for providing the SiC wafers and C-V measurements and Dr. A.D. Batchelor and Dr. K. Hiramatsu for their assistance. This research was supported by the Office of Naval Research on Contracts N00014-92-J-1720 and N00014-92-J-1477 and monitored by Mr. Max Yoder.

REFERENCES

1. M.A. Khan, J.N. Kuznia, D.T. Olson and R. Kaplan, *J. Appl. Phys.*, **73**, 3108 (1993).
2. H. Amano, I. Akasaki, K. Hiramatsu, N. Koide and N. Sawaki, *Thin Solid Films*, **163**, 415 (1988).
3. J.N. Kuznia, M.A. Khan, D.T. Olson, R. Kaplan and J. Freitas, *J. Appl. Phys.*, **73**, 4700 (1993).
4. S. Nakamura, *Jpn. J. Appl. Phys.*, **30**, L1705 (1991).
5. T.W. Weeks, Jr., M.D. Bremser, K.S. Ailey, E.P. Carlson, W.G. Perry, R.F. Davis, *Appl. Phys. Lett.*, **67**, 401 (1995).
6. T.W. Weeks, Jr., M.D. Bremser, K.S. Ailey, W.G. Perry, E.P. Carlson, E.L. Piner, N.A. El-Masry, R.F. Davis, *J. Mat. Res.* to be published.
7. R.F. Davis, T.W. Weeks, Jr., M.D. Bremser, K.S. Ailey, W.G. Perry, Z. Sitar, C. Wang and K. Linthicum, *Topical Workshop on III-V Nitrides*, Nagoya, Japan, September 21-23 (1995).
8. Cree Research, Inc., 2810 Meridian Parkway, Suite 176, Durham, NC 27713.
9. T.W. Weeks, Jr., D.W. Kum, E. Carlson, W.G. Perry, K.S. Ailey and R.F. Davis, *Second International High Temperature Electronics Conference*, Charlotte, NC, June 5-10 (1994).
10. M.R.H. Khan, Y. Koide, H. Itoh, N. Sawaki, I. Akasaki, *Solid State Commun.* **60**, 753, (1986).
11. B.V. Baranov, V.B. Gutan, U. Zhumakulev, *Sov. Phys.-Semicond.*, **16**, 819, (1982).
12. R. Dingle and M. Ilegems, *Solid State Commun.*, **9**, 175 (1971).
13. W. Götz, N.M. Johnson, R.A. Street, H. Amano and I. Akasaki, *Appl. Phys. Lett.* **66**, 1340 (1995).

MOVPE GROWTH OF HIGH ELECTRON MOBILITY AlGa_xN/GaN HETEROSTRUCTURES

J.M. Redwing*, J.S. Flynn*, M.A. Tischler*, W. Mitchel** and A. Saxler**

*Advanced Technology Materials, Inc., 7 Commerce Dr., Danbury, CT 06810

**Electronic and Optical Materials Branch, Wright-Patterson AFB, OH

ABSTRACT

We have fabricated Al_xGa_{1-x}N/GaN heterostructures with high two-dimensional electron gas (2DEG) mobilities and high sheet carrier densities by metalorganic vapor phase epitaxy (MOVPE). The 2DEG sheet density and mobility exhibit a compositional dependence on the Al fraction of the electron donor layer. The highest mobility (5750 cm²/Vs at 16K) was measured in a sample with x=0.15 that had a sheet carrier density of 8.5x10¹² cm⁻². The undoped Al_xGa_{1-x}N layers have low background carrier concentrations and can be intentionally doped n-type using SiH₄. The effect of intentional n-type doping of the Al_xGa_{1-x}N donor layer on the electrical properties of the 2DEG was studied in structures that included an undoped Al_xGa_{1-x}N spacer layer of varying thickness. Higher 2DEG mobilities were obtained when a 100Å thick undoped layer was included in the structure due to spatial separation of the 2DEG from ionized impurities in the doped Al_xGa_{1-x}N. These initial results demonstrate that the electrical properties of Al_xGa_{1-x}N/GaN heterostructures can be controlled by intentional doping and appropriate layer design.

INTRODUCTION

GaN and its alloys with AlN are currently under investigation as candidate materials for electronic devices operating at elevated temperatures. The high saturated drift velocity of electrons in GaN, combined with the large conduction band discontinuities and high mobilities achievable in Al_xGa_{1-x}N/GaN heterostructures offers the potential of improved performance for GaN-based devices in high power microwave applications [1]. Prior work in this area has confirmed the existence of a two-dimensional electron gas (2DEG) at the Al_xGa_{1-x}N/GaN heterointerface [2], and Al_xGa_{1-x}N/GaN high electron mobility transistors (HEMTs) with high transconductances and promising dc and microwave operating characteristics have recently been demonstrated [3-5].

Further advances in the performance of GaN-based HEMTs are expected to occur with improvements in material quality. However, to date, there has been relatively little work on characterizing the electrical properties of undoped and intentionally doped Al_xGa_{1-x}N/GaN heterojunctions. Initial Al_xGa_{1-x}N/GaN heterostructures exhibited low 2DEG mobilities [6]. Possible reasons for this include high background carrier concentrations causing parallel conduction in unintentionally doped n-type GaN and Al_xGa_{1-x}N layers and poor quality heterointerfaces. Increased 2DEG mobilities, in the range of 5000 cm²/Vs at 150K, have recently been reported in heterostructures grown by metalorganic vapor phase epitaxy (MOVPE) [7]. The higher mobilities were attributed to improved Al_xGa_{1-x}N made possible by the use of trimethylamine-alane as the Al precursor rather than the more conventional trimethyl- or triethylaluminum sources.

We have fabricated $\text{Al}_x\text{Ga}_{1-x}\text{N}/\text{GaN}$ heterojunctions on (0001) sapphire substrates with high electron mobilities ($5750 \text{ cm}^2/\text{Vs}$ at 16K) and sheet carrier densities ($8.5 \times 10^{12} \text{ cm}^{-2}$) using trimethylgallium and trimethylaluminum. To the best of our knowledge, these are the highest sheet densities and mobilities reported for $\text{Al}_x\text{Ga}_{1-x}\text{N}/\text{GaN}$ heterostructures grown on sapphire substrates. The $\text{Al}_x\text{Ga}_{1-x}\text{N}$ layers have low background carrier concentrations and can be intentionally doped n-type using SiH_4 . In this paper we describe the characteristics of heterostructures fabricated with n-type $(\text{Al,Ga})\text{N}:\text{Si}$ donor layers and undoped $(\text{Al,Ga})\text{N}$ spacer layers and present results on the effect of spacer layer thickness on the electrical properties of the heterojunction.

EXPERIMENTAL METHODS

The III-V nitride layers were grown by low pressure MOVPE on c-plane (0001) sapphire substrates. Trimethylaluminum (TMAI), trimethylgallium (TMGa) and NH_3 were used as precursors, with H_2 as the carrier gas. Prior to growth, the substrates were degreased and etched in hot $\text{H}_3\text{PO}_4:\text{H}_2\text{SO}_4$ and loaded into the reactor. A thin (150Å) AlN buffer layer was initially grown on the substrate at 550°C . The temperature was then increased to 1100°C for film growth. GaN layers with a nominal thickness of $3 \mu\text{m}$ were grown directly on the AlN buffer, followed by growth of the $\text{Al}_x\text{Ga}_{1-x}\text{N}$ donor layer.

In the initial study, a single undoped $\text{Al}_x\text{Ga}_{1-x}\text{N}$ electron donor layer was used, as shown in Figure 1(a), with a composition, x , that varied from 0.05 to 0.25. Samples were also grown with an undoped $\text{Al}_{0.15}\text{Ga}_{0.85}\text{N}$ spacer and an intentionally doped $\text{Al}_{0.15}\text{Ga}_{0.85}\text{N}$ ($n=5 \times 10^{17} \text{ cm}^{-3}$) donor layer, as shown in Figure 1(b). SiH_4 (1 ppm in H_2) was used as the intentional n-type dopant source.

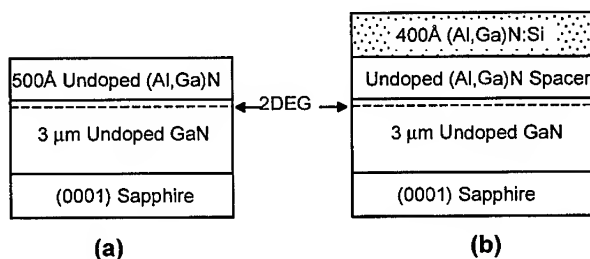


Figure 1. $\text{Al}_x\text{Ga}_{1-x}\text{N}/\text{GaN}$ heterostructures using (a) an undoped donor layer and (b) an n-type ($5 \times 10^{17} \text{ cm}^{-3}$) donor layer with an undoped spacer layer.

X-ray rocking curves (ω -scans) were performed using a double crystal diffractometer with a wide open incident beam and detector slit. A mercury probe was used to measure the capacitance-voltage (C-V) characteristics of the heterojunctions. Hall samples were fabricated using evaporated Al as an ohmic contact and Hall measurements were carried out on the samples over the temperature range from 16K to 300K.

RESULTS AND DISCUSSION

The first series of experiments investigated the electrical properties of undoped (Al,Ga)N/GaN heterojunctions. The basic structure of the layers is shown in Figure 1(a). Three Al compositions were used; $x=0.05$, 0.15 and 0.25 . Cracking of the $\text{Al}_x\text{Ga}_{1-x}\text{N}$ cap layers was not observed, indicating that 500\AA is below the critical thickness for crack formation in $\text{Al}_x\text{Ga}_{1-x}\text{N}$ ($x \leq 0.25$) on GaN. The heterojunctions were characterized using x-ray diffraction, C-V, and Hall measurements. Figure 2 shows the double-crystal x-ray rocking curve of the $\text{Al}_{0.15}\text{Ga}_{0.85}\text{N}/\text{GaN}$ heterostructure. The (0002) $\text{Al}_{0.15}\text{Ga}_{0.85}\text{N}$ peak appears as a shoulder on the right side of the (0002) GaN reflection. The full-width-at-half-maximum (FWHM) of the peak is 316 arcsecs. C-V measurements indicate that the majority of carriers are located near the $\text{Al}_{0.15}\text{Ga}_{0.85}\text{N}/\text{GaN}$ interface, as shown in Figure 3.

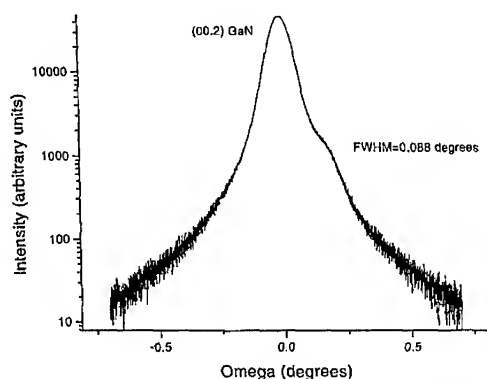


Figure 2. Double crystal x-ray rocking curve (ω -scan) of 500\AA $\text{Al}_{0.15}\text{Ga}_{0.85}\text{N} / 3\text{ }\mu\text{m}$ GaN heterostructure.

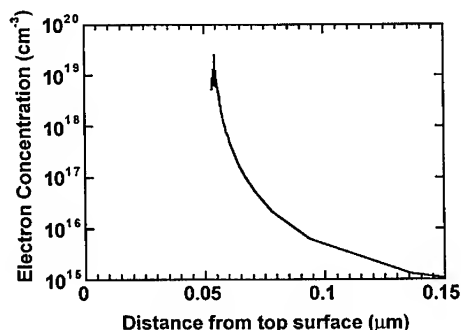


Figure 3. Electron concentration vs. depth as determined by C-V measurement of 500\AA $\text{Al}_{0.15}\text{Ga}_{0.85}\text{N} / 3\text{ }\mu\text{m}$ GaN showing that the majority of carriers are confined to the heterointerface.

The electron mobilities and sheet carrier densities as a function of $\text{Al}_x\text{Ga}_{1-x}\text{N}$ cap layer composition, x , and temperature are plotted in Figure 4. In all of the samples, the mobility and sheet density are independent of temperature below approximately 100K, which is consistent with the existence of a 2DEG at the heterointerface. The sheet density increases with Al fraction from $3 \times 10^{12} \text{ cm}^{-2}$ for $x=0.05$ to $1 \times 10^{13} \text{ cm}^{-2}$ for $x=0.25$. The background carrier concentration of unintentionally n-type doped $\text{Al}_x\text{Ga}_{1-x}\text{N}$ decreases with increasing x [8], and we have measured an increase in the resistivity of our undoped $\text{Al}_x\text{Ga}_{1-x}\text{N}$ layers with increasing Al composition. As a result, we attribute the increase in sheet density to increased carrier confinement in the higher band-gap energy $\text{Al}_x\text{Ga}_{1-x}\text{N}$ layer rather than an increase in unintentional doping.

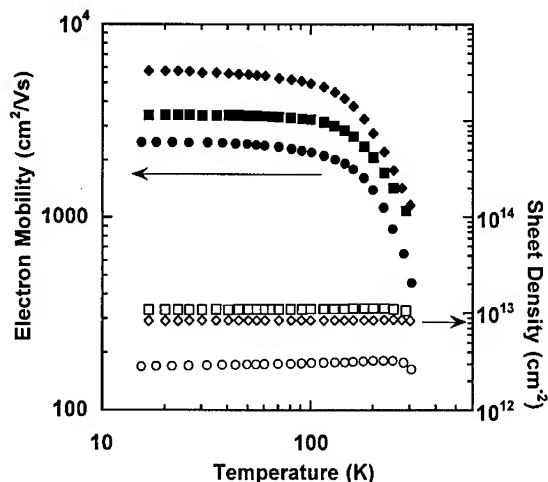


Figure 4. Electron mobility and sheet density as a function of temperature for $\text{Al}_x\text{Ga}_{1-x}\text{N}/\text{GaN}$ heterostructures grown with $x=0.05$ (circles), $x=0.15$ (diamonds) and $x=0.25$ (squares).

The 2DEG mobility also exhibits a compositional dependence, as shown in Figure 4. The $x=0.05$ sample, which had the lowest sheet density also has the lowest mobility. The highest mobility, $5750 \text{ cm}^2/\text{Vs}$, was measured in the intermediate Al fraction ($x=0.15$) sample. Khan *et al* [2] reported a similar dependence of 2DEG mobility on Al fraction and attributed the increased 2DEG scattering at low Al fractions to penetration of the electron wavefunction into the $\text{Al}_x\text{Ga}_{1-x}\text{N}$ layer due to a small conduction band off-set. The 2DEG mobility decreases as the Al fraction is raised to $x=0.25$. Several factors may be responsible for increased scattering at higher Al compositions including a higher sheet carrier density, increased strain resulting from a larger lattice mismatch between $\text{Al}_x\text{Ga}_{1-x}\text{N}$ and GaN, a decrease in structural quality or an increase in impurity incorporation at or near the heterointerface. Further studies are needed to understand the impact of each of these factors on the electrical properties of heterostructures. The 2DEG results obtained to date, however, indicate that $x=0.10$ to $x=0.15$ is the optimum Al composition range for high mobility $\text{Al}_x\text{Ga}_{1-x}\text{N}/\text{GaN}$ 2DEG structures.

GaAs-based HEMTs typically utilize an intentionally doped donor layer and an undoped spacer layer to achieve high 2DEG mobilities with high sheet carrier densities. The role of the undoped spacer layer is to spatially separate the 2DEG from ionized impurities in the doped layer. Our undoped $\text{Al}_x\text{Ga}_{1-x}\text{N}$ layers have a low background carrier concentration ($<10^{17} \text{ cm}^{-3}$) making it possible to controllably dope the layers n-type with Si.

A series of Si doped $\text{Al}_x\text{Ga}_{1-x}\text{N}$ layers were grown in which the Al composition, x , was varied from 0.0 to 0.33. A constant growth rate ($0.03 \mu\text{m}/\text{min}$) and $\text{SiH}_4/\text{Group III}$ ratio (4.0×10^{-5}) were used. The resistivity and electron concentration of the layers, determined by Hall measurements, are shown in Figure 5. The resistivity increases exponentially with x , similar to the results of Zhang *et al* [8]. The electron concentration decreases slightly with increasing x for $x < 0.25$. The resistivity of the $\text{Al}_{0.33}\text{Ga}_{0.67}\text{N}:\text{Si}$ sample was too high to obtain an accurate measurement of the carrier concentration.

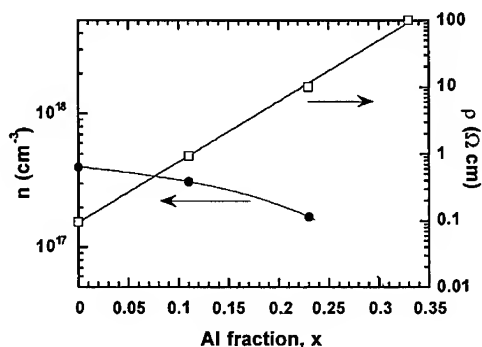


Figure 5. Room temperature resistivity and electron concentration of Si doped $\text{Al}_x\text{Ga}_{1-x}\text{N}$ as a function of Al fraction, x .

The intentional n-type doping capability was used to fabricate 2DEG structures that consist of an intentionally doped n-type $\text{Al}_{0.15}\text{Ga}_{0.85}\text{N}$ layer ($n=5 \times 10^{17} \text{ cm}^{-3}$) and an undoped $\text{Al}_{0.15}\text{Ga}_{0.85}\text{N}$ spacer layer, as shown schematically in Figure 1(b). The thickness of the doped layer was kept constant at 400 \AA and the spacer layer thickness was varied from 0 to 300 \AA .

The effect of spacer layer thickness on sheet density and 2DEG mobility measured at 300K and 77K are shown in Table 1. The use of a 100 \AA undoped spacer layer results in a significant increase in 2DEG mobility and a slight reduction in sheet density compared to the sample that was grown without a spacer. The mobility drops, however, with a further increase in spacer layer thickness to 300 \AA , possibly due to incomplete depletion of the $\text{Al}_x\text{Ga}_{1-x}\text{N}$ layers. A comprehensive carrier transport study is needed to characterize the effects of intentional cap doping and spacer thickness for $\text{Al}_x\text{Ga}_{1-x}\text{N}/\text{GaN}$ heterostructures for comparison to these initial experimental results.

TABLE 1. Sheet carrier density (n) and mobility (μ) of 2DEG $\text{Al}_{0.15}\text{Ga}_{0.85}\text{N}/\text{GaN}$ heterostructures as a function of undoped $\text{Al}_{0.15}\text{Ga}_{0.85}\text{N}$ spacer thickness.

Spacer Thickness (\AA)	n (300K) (10^{12} cm^{-2})	μ (300K) (cm^2/Vs)	n (77K) (10^{12} cm^{-2})	μ (77K) (cm^2/Vs)
0	8.6	1150	8.5	3880
100	7.8	1300	7.5	5200
300	7.6	1100	7.5	3380

CONCLUSIONS

We have fabricated $\text{Al}_x\text{Ga}_{1-x}\text{N}/\text{GaN}$ heterostructures with high 2DEG mobilities and high sheet carrier densities by MOVPE on sapphire substrates. The 2DEG sheet density and mobility exhibit a compositional dependence on the Al fraction of the electron donor layer. The highest mobility ($5750 \text{ cm}^2/\text{Vs}$ at 16K) was measured in a sample with $x=0.15$ that had a sheet carrier density of $8.5 \times 10^{12} \text{ cm}^{-2}$. To the best of our knowledge, these are the highest mobilities and sheet densities reported for $\text{Al}_x\text{Ga}_{1-x}\text{N}/\text{GaN}$ heterostructures grown on sapphire substrates. The effect of intentional n-type doping of the $\text{Al}_x\text{Ga}_{1-x}\text{N}$ layer on the electrical properties of the 2DEG was studied in structures that included an undoped $\text{Al}_x\text{Ga}_{1-x}\text{N}$ spacer layer of varying thickness. Higher 2DEG mobilities were obtained when a 100Å thick undoped layer was included in the structure due to spatial separation of the 2DEG from ionized impurities in the doped $\text{Al}_x\text{Ga}_{1-x}\text{N}$ cap. These initial results demonstrate that the electrical properties of $\text{Al}_x\text{Ga}_{1-x}\text{N}/\text{GaN}$ heterostructures can be controlled by intentional doping and appropriate layer design.

ACKNOWLEDGEMENTS

ATMI would like to acknowledge the partial support of the U.S. Army BMDO under contract no. DASG60-93-C-0143.

REFERENCES

1. M.S. Shur, A. Khan, B. Gelmont, R.J. Trew and M.W. Shin, Inst. Phys. Conf. Ser. **141**, p. 419 (1995).
2. M.A. Khan, J.N. Kuznia, J.M. Van Hove, N. Pan and J. Carter, Appl. Phys. Lett. **60**, p. 3027 (1992).
3. M. A. Khan, A. Bhattarai, J.N. Kuznia and D.T. Olson, Appl. Phys. Lett. **63**, p. 1214 (1993).
4. M. A. Khan, J.N. Kuznia, D.T. Olson, W.J. Schaff, J.W. Burm and M.S. Shur, Appl. Phys. Lett. **65**, p. 1121 (1994).
5. S.C. Binari, L. B. Rowland, G. Kelner, W. Kurppa, H.B. Dietrich, K. Doverspike and D.K. Gaskill, Inst. Phys. Conf. Ser. **141**, p. 459 (1995).
6. M.A. Khan, J.M. Van Hove, J.N. Kuznia and D.T. Olson, Appl. Phys. Lett. **58**, p. 2408 (1991).
7. M. A. Khan, Q. Chen, C.J. Sun, M. Shur and B. Gelmont, Appl. Phys. Lett. **67**, p. 1429 (1995).
8. X. Zhang, P. Kung, A. Saxler, D. Walker, T.C. Wang and M. Razeghi, Appl. Phys. Lett. **67**, p. 1745 (1995).

GROWTH KINETICS AND STRUCTURAL QUALITY IN GaN EPITAXY BY LOW PRESSURE MOVPE

O.BRIOT, J.P. ALEXIS, B.GIL and R.L.AULOMBARD

GES-CNRS

CC074, Université Montpellier II, Place E.Bataillon, 34095 MONTPELLIER Cedex 5, FRANCE

ABSTRACT

GaN epilayers have been grown using low pressure MOVPE (76 Torr) onto (0001) sapphire substrates. Triethylgallium (TEGa) and Ammonia (NH_3) were used as precursors. The growth rate has been determined versus growth parameters. The growth rate versus NH_3 flow displays a rather unusual behavior, in particular at low growth temperature (buffer layer), where the growth rate decreases strongly when the NH_3 flow increases. A growth mechanism involving a competitive adsorption step onto the surface is proposed, and results in a strong dependence of the growth rate on the V/III ratio.

The structural quality of the layers has been assessed by X-ray diffraction versus the growth parameters, and will be reported here. A substrate nitridation step, prior to buffer layer deposition has been introduced in our growth process. The effect of substrate nitridation on the structural and optical properties of the epilayers is studied and we propose an optimized pre-treatment for the MOVPE growth of GaN onto (0001) sapphire substrates.

INTRODUCTION

Gallium nitride (GaN) is a promising material for optoelectronic applications, as it has been brilliantly demonstrated by the realization of candela-class blue, blue-green and green light emitting diodes [1]. Moreover, in addition to optoelectronic devices, field effect transistors and photodetectors have been successfully demonstrated by several groups. Although nice devices have been achieved, many fundamental aspects of the growth of these materials are still unclear and request further investigations. For example, the MOCVD growth of GaN, based on the so-called « double step process » introduced by Amano et al.[2], leads to high quality material, but the process parameters must range in very narrow « windows ». The understanding of the growth mechanisms is a major concern in order to be able to predict the very influence of each growth parameter and the relationship between them. In this paper, we have studied the influence of process parameters on the growth kinetics. This gives insights on the growth mechanism, which is found to be quite different from more classical MOCVD processes.

EXPERIMENT

The GaN layers studied here have been grown by low pressure MOVPE (76 Torr) in an ASM OMR 12 MOCVD equipment. The precursors were triethylgallium (TEGa) and ammonia (NH_3). The substrates were (0001) sapphire, with both sides polished to enable transmission experiments. Different growth temperatures, in the range 950 - 1040°C have been used. The influence of the V/III molar ratio was studied by keeping the molar flow rate of TEGa constant (65 sccm @ 20°C) and changing the NH_3 flow rate in the range 300 - 4000 sccm. The sapphire substrate was cleaned with organic solvents and etched using a H_3PO_4 : 3 H_2SO_4 hot solution. A substrate nitridation step

was realized by heating the sapphire substrate at 1070°C under a NH₃ flow. The influence of the NH₃ flow is reported hereafter.

The sample thicknesses were determined very precisely from room temperature transmission experiments, in the range 350 - 700 nm. The interference fringes were fitted using the optical indexes reported by Lin et al.[3] to determine the thicknesses.

The quality of the samples was determined from 300K and 2K photoluminescence and reflectivity experiments and with X-ray diffraction, concerning the structural properties.

RESULTS AND DISCUSSION

First, the buffer layer growth rate was determined versus V/III molar ratio. Actually, the V/III ratio was changed by keeping the TEGa flow constant and increasing the NH₃ flow rate. Moreover, in order to be able to measure the thicknesses of the buffer layers deposited at 550°C, we have grown «thick» buffer layers and assumed that the growth rate was constant, even for thin layers. This approach is the same which is used in MOCVD for the growth of quantum wells and usually gives

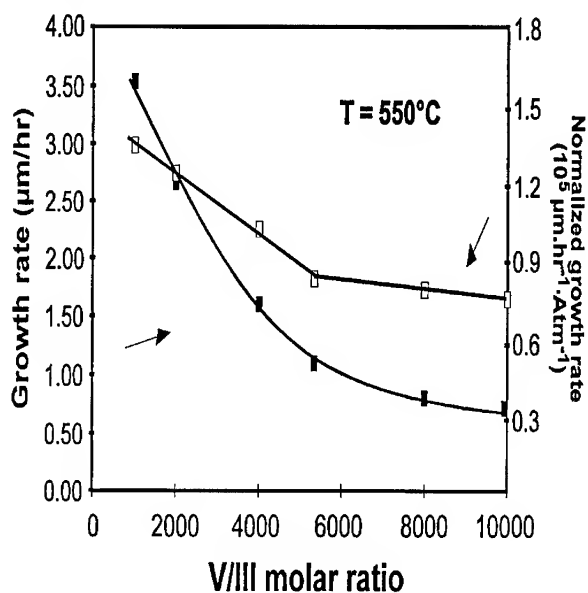


Figure 1 : GaN buffer layer growth rate ($T_g = 550^\circ\text{C}$) and growth rate normalized to the TEGa partial pressure

excellent results.

The growth rate of the buffer layer versus V/III molar ratio is depicted in figure 1. An outstanding result is that *the growth rate decreases with increasing V/III ratio, i.e. with increasing NH₃ flow rate*. Usually, one would expect the growth rate to remain almost constant, if the growth is to be driven by the gas phase diffusion of the group III element.

Before invoking a complicated growth mechanism, we have to rule out possible artifacts: first, premature gas phase reaction may occur, which would consume the TEGa and lower the growth rate. In this case, involatile by-products should be produced which would deposit onto the reactor quartzware. We have not observed the formation of such by-products in our equipment. Second, since the V/III ratio is very large, the NH₃ gas flow is large and increasing it may lead to a dilution effect, by lowering the TEGa partial pressure, thus lowering the growth rate.

In figure 1, we plotted the normalized growth rate, i.e. the growth rate divided by the TEGa partial pressure, in order to get rid of dilution effects. One can see that the growth rate is still decreasing with increasing ammonia flow.

Before attempting to develop a model to explain this behavior, we present, in figure 2, the growth rate of the GaN layer (at a growth temperature of 980°C). At this temperature, the growth rate increases (almost linearly) with increasing V/III molar ratio (NH₃ flow), then decreases (roughly as $P_{\text{NH}_3}^{-1}$). The transition between the two regimes is observed for a V/III ratio of 5000.

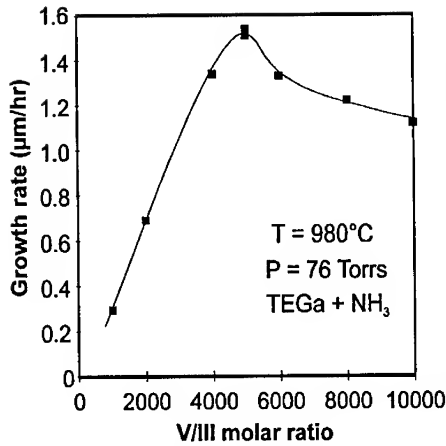


Figure 2: GaN layer growth rate versus V/III molar ratio (fixed by changing the NH₃ flow rate and keeping TEGa constant). Here, the solid line is only a guide to the eye.

The decrease in the growth rate may be explained in terms of *competitive adsorption*, or *site blocking*, if we assume that NH₃ will impinge on the Ga sites on the surface. It is now largely believed that NH₃ is adsorbed, then decomposed onto the layer surface (see for instance the discussion in [4]). Thus, we will make the hypothesis that :

- i) NH₃ is strongly adsorbed on the surface (the area covered by NH₃ is much larger than the surface covered by Ga)
- ii) NH₃ is also adsorbed on Ga sites.

We now describe the reaction as a bimolecular reaction between Ga and NH₃ onto the surface at related sites. The growth rate may be written [5].

$$G = \alpha \cdot P_{Ga} \cdot P_{NH_3} \cdot N_{s2} \quad (1)$$

where N_{s2} is the areal density of bimolecular reaction sites and P_{Ga} and P_{NH_3} are the reactants partial pressures. By assuming that adsorbed NH₃ is mainly covering the surface and also impinge on the Ga sites, the growth rate may be rewritten [5] :

$$G = \gamma \cdot P_{Ga} \cdot P_{NH_3} \cdot (N_0 - N_{NH_3}^{ad})^2 \quad (2)$$

where N_0 is the total areal density of adsorption sites, and $N_{NH_3}^{ad}$ is the areal density of adsorbed NH₃. The assumption made is that the reaction is not site specific, which is quite correct at low temperature, where an amorphous or polycrystalline layer is grown. At higher growth temperature, where a monocrystal is grown, this model will not describe correctly the situation. However this represent a first step towards an understanding of the growth mechanisms and work is in hand to improve the model. A steady state between the absorption and desorption of NH₃ is reached at a given temperature, and is described by an adsorption isotherm :

$$N_{NH_3}^{ad} = K(T) \cdot P_{NH_3} \cdot (N_0 - N_{NH_3}^{ad}) \quad (3)$$

$K(T)$ describe the balance between the adsorption and desorption processes. It may be written as :

$$K(T) = K_0 e^{-\frac{E_a}{kT}} \quad (4)$$

E_a is an activation energy which is a phenomenological parameter. It describes the fact that desorption of species from the surface is thermally activated and should have a negative value to account for a decrease of the adsorption with increasing temperature. By combining equation (2) and (3), the growth rate may be expressed as :

$$G = \gamma P_{Ga} P_{NH_3} \frac{N_0^2}{(1 + K(T) P_{NH_3})^2} \quad (5)$$

a) Low temperature growth (buffer layer)

Due to the low temperature, the thermal desorption rate is low, hence the adsorption of NH_3 on surfaces is high : $K(T).P_{\text{NH}_3} \gg 1$, whatever the P_{NH_3} values. From equation (5), the growth rate will change as $P_{\text{NH}_3}^{-1}$, which corresponds to the experimental observation.

b) High temperature growth

The thermal desorption of NH_3 is important, $K(T)$ is less. If P_{NH_3} is low, $K(T).P_{\text{NH}_3} \ll 1$: the growth rate will change linearly with P_{NH_3} . At high values of P_{NH_3} , we have again $K(T).P_{\text{NH}_3} \gg 1$ and the growth rate decreases as $P_{\text{NH}_3}^{-1}$. There is an intermediate regime connecting both situations.

This also corresponds to the observed situation.

In Figure 3, we have fitted our experimental data with equation (5). A very good agreement is obtained at low growth temperature (buffer layer growth). At higher temperature, the overall behavior of the growth rate is qualitatively well described, but a quantitative agreement is not

achieved. However, the ratio between the $K(T)$ values at 550°C and 980°C yields an activation energy value $E_a = -0.72$ eV, which is in the expected range. As mentioned previously, this simple model still has to be improved to describe properly the growth of monocrystals.

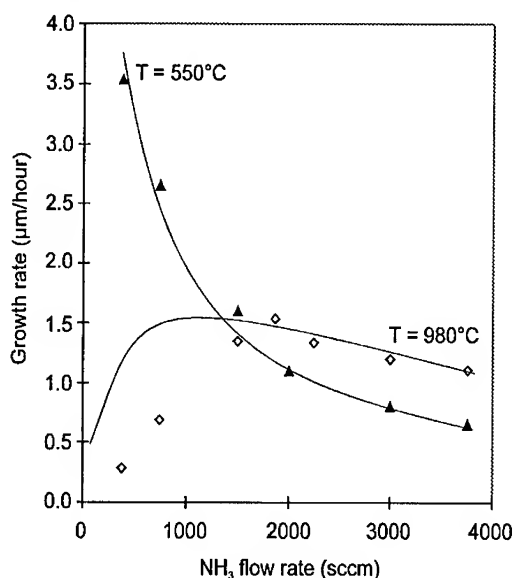
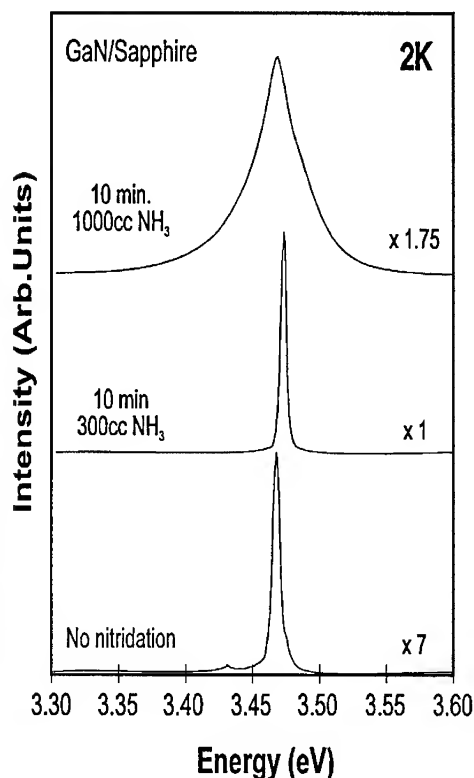


Figure 3: Fit of the experimental data using equation (5) at both 550°C (buffer layer) and 980°C (GaN layer).

In a second part of this work, we have studied the influence of the substrate nitridation. Prior to growth, the sapphire substrate is heated at high temperature (around 1100°C). This heat treatment may be performed under H_2 or under a NH_3 ambient. In the case of the introduction of NH_3 , it may be expected that a « nitridation » is performed which could have a significant impact on the buffer layer nucleation, and thus on the overall layer quality. In order to assess precisely the influence of the nitridation step, we have grown a set of GaN epitaxial layers in the same conditions, except for the nitridation step. One substrate was only heated under H_2 at

1070°C, while the other were submitted to a flow of 300 and 1000 sccm of NH_3 for 10 minutes. The layer quality was then assessed by photoluminescence at low temperature, and the results are displayed in figure 4. The photoluminescence intensity is highly improved by a moderated

nitridation (300 sccm, 10 min.), but the photoluminescence peak broadens if the NH_3 flow is too large.



Finally, we present in figure 5 a structural characterization of a sample grown with an optimized substrate nitridation step. This spectra represents the GaN (0004) X-Ray diffraction. The equipment used is a simple diffractometer, not a double crystal one. As a consequence two copper X-Ray emissions are present: $\text{K}\alpha_1$ and $\text{K}\alpha_2$, giving rise to two diffraction peaks.

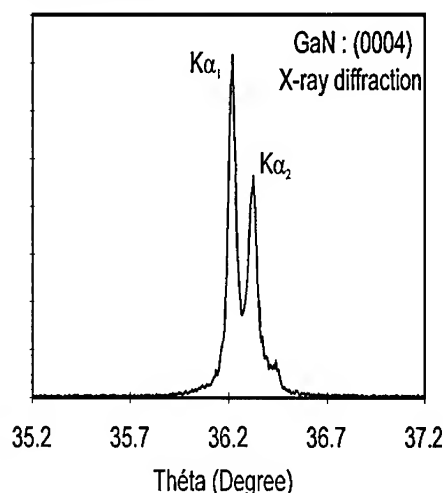


Figure 4: Influence of the substrate nitridation on the 2K photoluminescence of the GaN epilayers.

Figure 5: GaN (0004) X-Ray diffraction peak for a layer grown with an optimized nitridation step.

One can notice that the full width at half-maximum is about 160 arcseconds. In fact, this value corresponds to the apparatus limit, as is evidenced by the fact that the same width is measured on the (0002) diffraction peak. The layer full width at half maximum may be less. This clearly demonstrates that the structural quality of our layers is excellent, and we conclude that a substrate nitridation step is essential to the realization of good quality GaN in MOVPE.

CONCLUSION

We have studied the growth rate of GaN at both low (550°C) and high (980°C) growth temperature versus NH_3 flow rate. We found that the growth rate of the buffer layer (at 550°C) decreases with increasing NH_3 flow. A competitive adsorption process on the surface has to be invoked to explain this behavior. We developed a simple model which describes well the growth of GaN at low temperatures and gives a qualitative explanation of the growth rate at higher

temperature. We have studied the influence of the substrate nitridation and found that such treatment enhance the quality of the GaN epilayers. In our case, an optimum was found for a nitridation performed at 1070°C during 10 minutes, with a NH₃ flow of 300 sccm.

ACKNOWLEDGMENT

This work has been realized in the context of a financial support from THOMSON-CSF-LCR

REFERENCES

- [1] S.Nakamura, T.Mukai and M.Senoh, Appl.Phys.Lett.64,13 (1994) 1687
- [2] H.Amano, N.Sawaki, I.Akasaki and Y.Toyoda Appl.Phys.Lett.48, 5 (1986) 353
- [3] M.E.Lin, B.N.Sverdlov, S.Strite, H.Morkoç and A.E.Drakin,
Electron.Lett.29, 20 (1993) 1759
- [4] T.Sasaki and T.Matsuoka, J.Appl.Phys.77, 1 (1995) 192
- [5] K.J.Laidler, *Chemical Kinetics* (McGraw Hill, New York 1950) p 156

Low-Temperature Growth of High Quality $\text{In}_x\text{Ga}_{1-x}\text{N}$ by Atomic Layer Epitaxy

K.S. Boutros, J.C. Roberts, F.G. McIntosh, E.L. Piner*, N.A. El-Masry*, and S.M. Bedair
Electrical and Computer Engineering Department, *Material Science and Engineering Department
North Carolina State University, Raleigh, NC 27606

ABSTRACT

We report on the low temperature epitaxial growth of $\text{In}_x\text{Ga}_{1-x}\text{N}$ with $0 \leq x \leq 0.27$ by Atomic Layer Epitaxy (ALE). GaN and InGaN single crystal films have been grown by ALE in the temperature range between 600 and 700 °C using the rotating substrate approach. Films were deposited on sapphire substrates using TMG, EdMIn, and NH_3 as precursors. Up to 27% indium content has been achieved in the InGaN films. The FWHM of the (0002) InGaN peak by double crystal X-ray diffraction of these films was as small as 5 minutes. Room-temperature photoluminescence (PL) from these films was dominated by band edge emission between 365 nm and 446 nm. AlGaIn/InGaIn double heterostructures were grown in a hybrid reactor, in which the AlGaIn barrier layers were grown by MOCVD and the InGaIn active layer by ALE. The structures showed good crystal quality, and sharp PL emission with peak intensity at 410 nm.

INTRODUCTION

Typical growth temperatures at which high quality III-nitrides materials can be grown are in the range of 900-1050 °C for the MOCVD environment. These high growth temperatures impose significant limitations on the crystalline quality of the epitaxial films due to the high thermal mismatch between them and the underlying substrates. Also, the growth of InGaIn becomes inhibited at these high growth temperatures. Attempts to grow GaIn and InGaIn at low temperatures resulted in poor quality films, with little or no photoluminescence (PL) emission^{1,2}, due to the inherent consequences of low temperature growth such as poor NH_3 cracking efficiency. Furthermore, intense gas phase reactions cause the formation of polymers which affect the quality of epitaxial layers.

The need for a low temperature growth technique, which also overcomes the problems faced during the growth of nitrides has led us to turn to Atomic Layer Epitaxy (ALE) as a potentially suitable technique for this application. The inherent properties of ALE as a low temperature growth technique, and especially the separation of reactant gases during the ALE process, offer a unique approach for solving the problems facing the synthesis of nitride compounds. Low-temperature growth capability is very important for the growth of indium containing nitride compounds, because of the weakness of the indium-nitrogen bond and the high indium vapor pressure over InGaIn. The growth of high quality nitride compounds is accomplished by ALE. Careful optimization of growth parameters has led to good film properties, and has opened the door for the implementation of optoelectronic devices using this material system.

EXPERIMENTAL CONDITIONS

The ALE system used for the growth of nitrides is based on the rotating susceptor approach. This system has been demonstrated to be effective for the low temperature growth of GaIn and InGaIn. Details of these experiments have been described elsewhere^{3,4}. Sapphire

substrates are annealed at 1050 °C in the reactor in a nitrogen atmosphere for 15 minutes, then exposed to ammonia for 1 minute to passivate the surface before the deposition starts. Growth by ALE was carried out in the temperature range between 600 and 700 °C, and at a pressure of 100 torr. A high flow of N₂ was used at the central purge line to isolate the reactive gases and prevent their mixing, which is believed to cause the formation of adducts that impede the growth of high quality material. The growth was initiated by the deposition of a thin AlN layer by ALE at 700 °C, forming nucleation sites for the subsequent GaN growth. The optimum thickness of the AlN buffer layer was found to be between 40 and 100 Å, with the growth rate at ~0.2 Å/cycle. Following the deposition of AlN, growth of GaN or InGaN was carried out in the temperature range 600-700 °C. Typical susceptor rotation speed used during the growth of these layers was between 30 and 60 rpm, and dwell times under both col. III and col. V reactants were between 0.2 and 1 second, in order to maintain the growth rate between 0.1 and 2 Å/ ALE cycle. It should be noted that these growth rates produce sub-monolayers per rotation cycle, and that the ALE experiments have not been optimized to obtain a monolayer-per-cycle control.

RESULTS AND DISCUSSION

Single crystal GaN with specular surface has been achieved by ALE under these conditions. GaN grown between 650 and 700 °C is single crystal, and shows DCXRD line width of approximately 7 minutes. This value is larger than that obtained from the highest quality GaN films grown by conventional MOCVD at 1000 °C⁵. However, the ALE grown GaN has the highest quality for films grown at 700 °C.

The best optical properties of GaN grown by ALE were obtained when the growth temperature was in the range 650-700 °C. Crystals grown at 700 °C have strong band edge (BE) emission with FWHM ~ 150 meV at room temperature, in addition to a deep level emission at 545 nm. The band-edge emission obtained at 365 nm is of comparable intensity to that obtained from films grown by MOCVD in our lab and by others. This indicates that the film properties obtained by MOCVD can be achieved by ALE with a reduction of about 300 °C in the growth temperature. A deep level emission at 545 nm can also be observed in the PL spectrum of the ALE grown GaN. This emission is always present in the PL spectrum, and can be variable in intensity relative to BE emission, depending on growth conditions. A trend was observed relating this yellow emission to the gallium flux during growth. Given that all other parameters are fixed, the relative BE-to-yellow intensity is strongly dependent on the TMG flux during growth. The influence of the gallium flux on the optical properties of the GaN films can be seen in the PL spectra of figure 1. The gallium flux used during growth for these films was 0.5, 1, and 6 sccm for the curves (a), (b), and (c) respectively. The enhancement of the yellow emission with the increase in TMG flux might be related to an increase in carbon incorporation in the film during growth, due to a higher concentration of reaction products. The nature of this yellow emission is still a subject of controversy, but it has been previously reported to be possibly due to carbon incorporation in the film⁶.

InGaN films grown by ALE were transparent and had a specular surface. Single crystal In_xGa_{1-x}N with 0 ≤ x ≤ 0.27 was achieved by ALE in the 600-700 °C temperature range, with a crystal quality comparable to films grown by conventional MOCVD at 800 °C⁷. Films with high indium content had a slightly yellowish color, and those grown with non-optimum conditions developed indium droplets on the surface. The composition of the ALE grown InGaN, and the crystal quality of the films were measured using double-crystal X-ray diffraction (DCXRD). The composition of the InGaN films was calculated from the splitting between the

sapphire and the InGaN diffraction peaks, with the assumption that Vegard's law is valid for this ternary alloy.

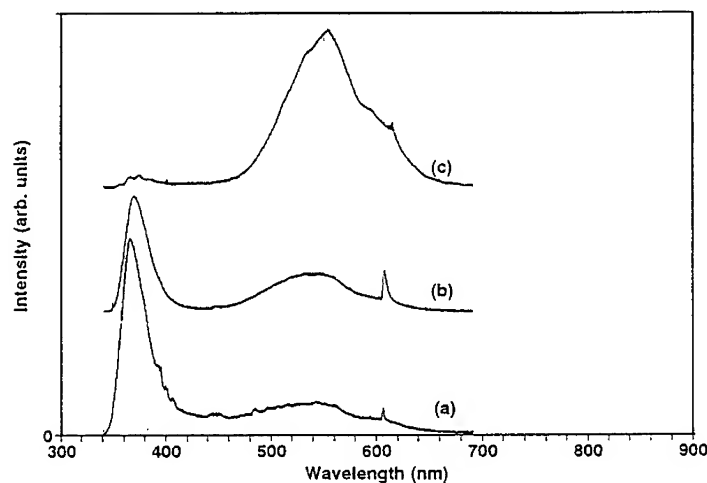


Figure 1. Effect of TMG flux on PL emission of GaN grown by ALE at 700 °C. TMG = 0.5, 1, and 6 sccm for curves (a), (b), and (c) respectively. PL excited with a 30 mW He-Cd laser emitting at 325 nm.

We observed that the reduction of the growth temperature has resulted in a higher incorporation efficiency of indium in the growing InGaN film. This observation has been anticipated from the earlier discussion in regard to the problems facing the growth of InGaN. A further investigation of the effect of growth temperature on the InGaN composition has confirmed that lower growth temperatures are necessary for the growth of InGaN with high indium content. The results of this investigation are plotted in figure 2. The data points plotted in this figure represent experiments which were carried out using the same growth conditions except for the growth temperature. It can be clearly observed that, while maintaining the organometallic fluxes constant, a reduction of 100 °C in the growth temperature has resulted in almost a 3-fold increase of the indium content in the InGaN films.

PL peaks from films grown at the earlier stages of this work were typically broad, single peaks, that shift with the film composition, but were slightly below the bandgap. The increase of both the NH_3 flux and the dwell time under the col. V window caused an improvement in the PL emission. However, the growth temperature had the most significant effect on the PL properties. Figure 3 shows the room-temperature PL from $\text{In}_{0.12}\text{Ga}_{0.88}\text{N}$ films grown at 600, 650 and 675 °C respectively. It can be seen that a continuing improvement occurs in the PL emission with the increase of the growth temperature, and that the peak becomes narrow at the higher temperature.

For the best quality films, room-temperature PL FWHM was ~ 200 meV, and emission peaks were obtained between 365 and 446 nm. Figure 4 shows the room-temperature emission of the highest quality films grown by ALE in the temperature range 600-700 °C, with peaks at 365 nm (for GaN films), 410 nm, and 446 nm corresponding to $\text{In}_x\text{Ga}_{1-x}\text{N}$ (x) value of 0, 0.17, and 0.27 respectively.

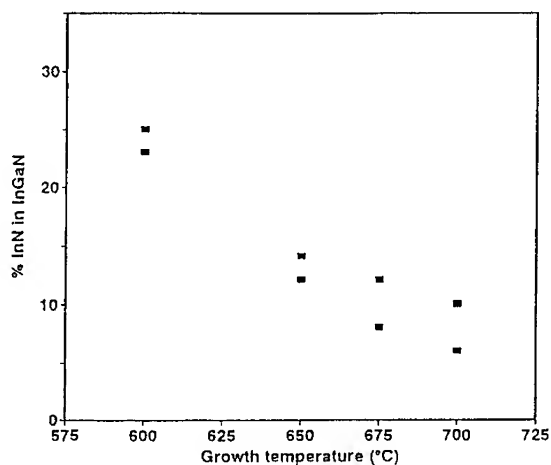


Figure 2. Effect of growth temperature on the indium content of InGaN grown by ALE.

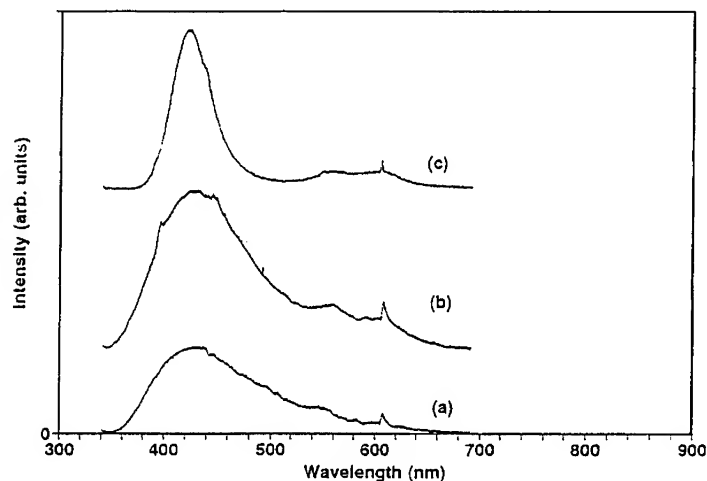


Figure 3. Effect of growth temperature on the PL emission from $\text{In}_{0.12}\text{Ga}_{0.88}\text{N}$ films grown by ALE. Growth temperature is 600, 650, and 675 °C for curves (a), (b), and (c) respectively

Promising preliminary results were obtained for AlGaIn/InGaIn/GaN double heterostructures which were grown with the InGaIn well grown by ALE, and AlGaIn/GaN barrier layers grown by conventional MOCVD. A hybrid operation (ALE/MOCVD) has been implemented in the same reactor via the use of switching manifolds, separating the reactants for the ALE growth, and mixing them at the reaction chamber inlets for MOCVD operation. The growth was started by depositing an AlN buffer layer by ALE as described earlier, followed by the MOCVD growth of the bottom $\text{Al}_{0.2}\text{Ga}_{0.8}\text{N}$ barrier layer at 950 °C. The operation was then

switched back to the ALE mode and a 400 Å thick $\text{In}_{0.07}\text{Ga}_{0.93}\text{N}$ active layer was deposited at 700 °C. While keeping the sample under a continuous flow of ammonia, the temperature was ramped up to 950 °C to grow the GaN cap layer by MOCVD. No intentional doping was attempted during the growth of these layers. The composition of the active layer was assumed from data obtained from X-ray diffraction of bulk InGaN grown with the same growth parameters. Room-temperature PL spectra of these structures show strong emission with a peak at 410 nm as shown in figure 5. A satellite peak at 362 nm can also be observed, which corresponds to emission from the top GaN layer. X-ray diffraction of these films indicates that they are single crystal, with comparable quality to the bulk material grown with the same conditions.

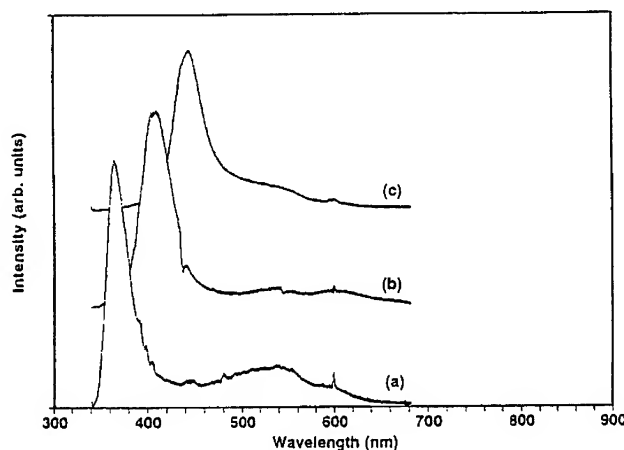


Figure 4. PL spectra for $\text{In}_x\text{Ga}_{1-x}\text{N}$ films with peak emission corresponding to $x = 0, 0.17$, and 0.27 for curves (a), (b), and (c) respectively.

CONCLUSION

The feasibility of low temperature ALE of single crystal GaN and InGaN with high indium content has been demonstrated. Strong band edge emission from GaN grown at 700 °C was obtained. Single crystal $\text{In}_x\text{Ga}_{1-x}\text{N}$ ($0 \leq x \leq 0.27$) was also grown by ALE between 600 and 700 °C. These films showed single crystal XRD peaks with FWHM as small as 5 minutes. The indium concentration in the film, and the optical properties of the films have been shown to strongly depend on the growth temperature. Band edge emission from these films has been achieved with peak emission varying between 365 and 446 nm, and double heterostructures grown with these layers show peak emission at 410 nm, opening the possibility for the fabrication of double heterostructure visible LEDs.

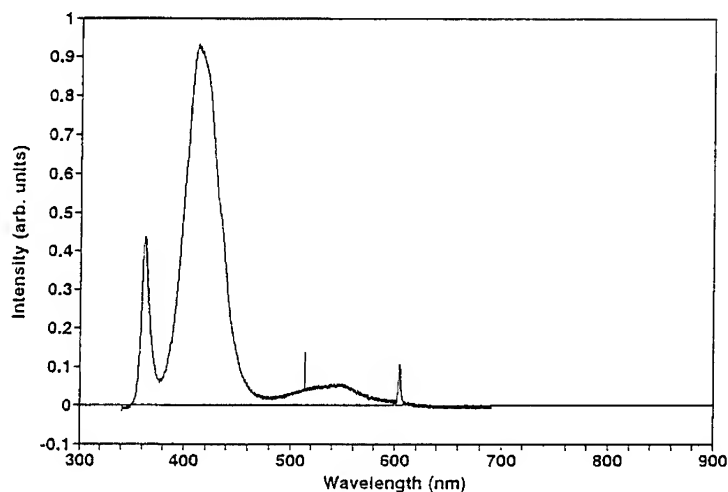


Figure 5. Room-temperature PL spectrum of a AlGaIn/InGaIn/GaN double-heterostructure with the InGaIn well grown by ALE.

ACKNOWLEDGMENT

This work was supported by the Office of Naval Research.

REFERENCES

1. N. Yoshimoto, T. Matsuoka, T. Sasaki, and A. Katsui, *Appl. Phys. Lett.*, **59**, p.2251 (1991).
2. A. Dissanayake, J.Y. Lin, H.X. Jiang, Z.J. Yu, and J.H. Edgar, *Appl. Phys. Lett.*, **65**, p.2317 (1994).
3. N.H. Karam, T. Parados, P. Colter, D. McNulty, W. Rowland, J. Schetzina, N. El-Masry, and S.M. Bedair, *Appl. Phys. Lett.* **67** (1), p.94 (1995).
4. K.S. Boutros, F.G. McIntosh, J.C. Roberts, S.M. Bedair, E.L. Piner, and N.A. El-Masry, *Appl. Phys. Lett.* **67** (13), p.1856 (1995).
5. P. Kung, A. Saxler, X. Zhang, D. Walker, T.C. Wang, I. Ferguson, and M. Razeghi, *Appl. Phys. Lett.* **66** (22), p.2958 (1995).
6. T. Ogino, and M. Aoki, *Jap. Journ. Appl. Phys.*, **19** (12), p.2395 (1980).
7. S. Nakamura, and T. Mukai, *Jap. J. Appl. Phys.* **31**, p.L1457 (1992).

AlGaInN Quaternary Alloys by MOCVD

F.G. MCINTOSH*, E. PINER**, K. BOUTROS*, J.C. ROBERTS*, Y. HE**, M. MOUSSA***, N. EL-MASRY**, S.M. BEDAIR*

*ECE Department, North Carolina State University, Raleigh, North Carolina 27695-7911.

**MSE Department, North Carolina State University, Raleigh, North Carolina 27695-7916.

***Air Defense Academy, Alexandria, Egypt.

ABSTRACT

AlGaInN quaternary alloy based devices can cover the emission wavelength from deep UV to red. This Quaternary alloy also offers lattice matched heterostructures for both optical and microwave devices. We will report on the MOCVD growth of $\text{Al}_x\text{Ga}_{1-x-y}\text{In}_y\text{N}$ ($0 < x < 0.12$), ($0 < y < 0.15$) at 750 °C on sapphire substrates, using TMG, EDMIn, TMAI and NH_3 precursors. Chemical composition, lattice constants and bandgaps of the grown films were determined by EDS, X-ray diffraction and room temperature PL. Data indicates that the lattice constants can also be deduced using Vegard's law, indicating a solid solution of this alloy. PL showed band edge emission, however emission from deep levels was also observed. Optimized growth conditions and heterostructures using this quaternary alloy will be presented.

INTRODUCTION

Current approaches in achieving $\text{In}_x\text{Ga}_{1-x}\text{N}$ based heterostructures rely on the AlGaIn ternary alloys as the high bandgap barrier/confinement layers.^{1,2} The large lattice mismatch between these two ternary alloys will limit either the value of x or the thickness of the InGaIn well. For example, the critical layer thicknesses for the $\text{Al}_{0.1}\text{Ga}_{0.9}\text{N}/\text{InGaIn}$ system with 40% and 60% InN are approximately 20Å and 15Å, respectively. This will limit the applications of InGaIn in the green and yellow regions. Such limitations can be avoided if AlGaIn is replaced by a more versatile $\text{Al}_x\text{Ga}_{1-x-y}\text{In}_y\text{N}$ quaternary compound. As shown in Figure 1, by varying the value of x and y, the bandgap and the lattice constants can each be independently adjusted to achieve AlGaInN/InGaIn lattice matched

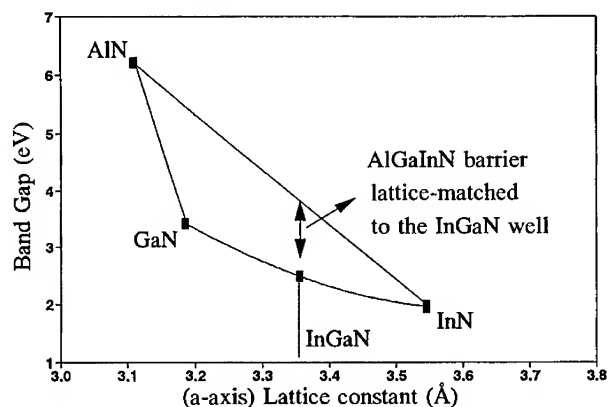


Figure 1: Bandgap versus lattice constants for the AlGaInN quaternary system showing how an InGaIn well can be lattice matched to wider bandgap AlGaInN barrier layers.

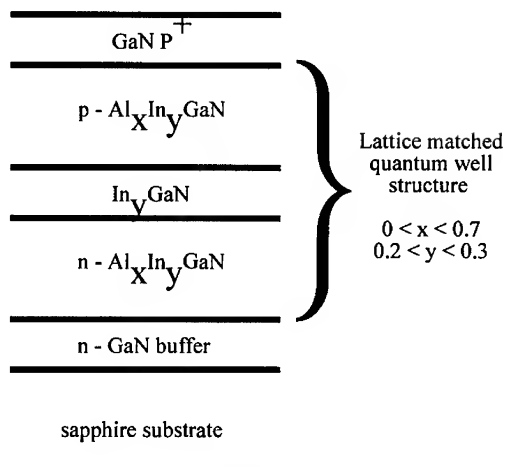


Figure 2: Potential heterostructure design with AlGaInN barrier layers lattice matched to the InGaInN well.

structures. In Figure 2, a potential LED structure with a lattice matched quantum well is shown.

One of the major obstacles in the development of the quaternary is the determination of the optimal growth temperature. Aluminum based compounds generally require higher growth temperatures. Any residual background oxygen impurities in the deposition system or source gases will result in the incorporation of oxygen in the growing films. Therefore, higher temperatures are required in order to desorb these oxides and prevent their incorporation into the epitaxial film. Lower temperatures, however, are required for indium based compounds. Indium compounds have relatively high vapor pressures and the growth temperature must be lowered in order to increase the indium incorporation and to reduce the dissociation of the In-N bond. The growth temperature will therefore govern the limits to which both In and Al can be incorporated into the AlGaInN quaternary alloy.

In this paper we report on the growth of Al_xGa_{1-x-y}In_yN with the composition range (0 < x < 0.2) and (0 < y < 0.15) using a modified MOCVD reactor. We have observed band edge transition of this quaternary alloy by room temperature photoluminescence. These results were achieved by first investigating the MOCVD growth of InGaInN and AlGaInN in the 750-800°C temperature range. This growth temperature seems to be a good compromise for the contradicting requirements for both the aluminum and indium containing compounds. The growth parameters and temperatures used for these ternary alloys were used to determine the favorable conditions for the deposition of high quality AlGaInN.

EXPERIMENT

The reactor design is based on the rotating susceptor and has been previously described.^{3,4} This design allows for three modes of crystal growth: MOCVD, molecular stream epitaxy (MSE), and atomic layer epitaxy (ALE). The organometallics and the ammonia are injected

through separate tubes above one of the windows in the graphite susceptor. This configuration is designed to minimize gas phase reactions between the ammonia and the organometallics prior to reaching the surface of the substrate. For MOCVD, the substrate is positioned directly under this window during the entire growth process.

The growth was conducted at 750 torr on a sapphire substrate. The substrate was first annealed and ammonia passivated at 1050°C. Next an AlN buffer layer was grown by ALE at 700°C, followed by a GaN film grown at 900°C using the MOCVD technique. For the results presented here, the growth temperature was then lowered to the 750-800°C temperature range for the AlGaInN layer deposition. Trimethylaluminum (TMA), trimethylgallium (TMG), ethyldimethylindium (EDMIn) and ammonia were used as precursors. The ammonia flow used was 50,000 : mol/min., and the TMA and EDMIn were varied to control the quaternary composition. Quaternary films with thicknesses of about 0.5 μm were grown and characterized by energy dispersive spectroscopy (EDS), double crystal X-ray diffraction (DCXRD) and room temperature photoluminescence (PL).

RESULTS

The chemical compositions of the AlGaInN quaternary films were obtained by EDS. First EDS was calibrated for In, Al and Ga using standards made from InGaN and AlGaIn ternary films of known compositions determined from DCXRD and using Vegard's law for determination of these ternary compositions. Figure 3 shows the X-ray diffractions pattern of a quaternary film, indicating a lattice constant (c-axis) of 5.185Å. The lattice constants can be also predicted from the following formula:⁵

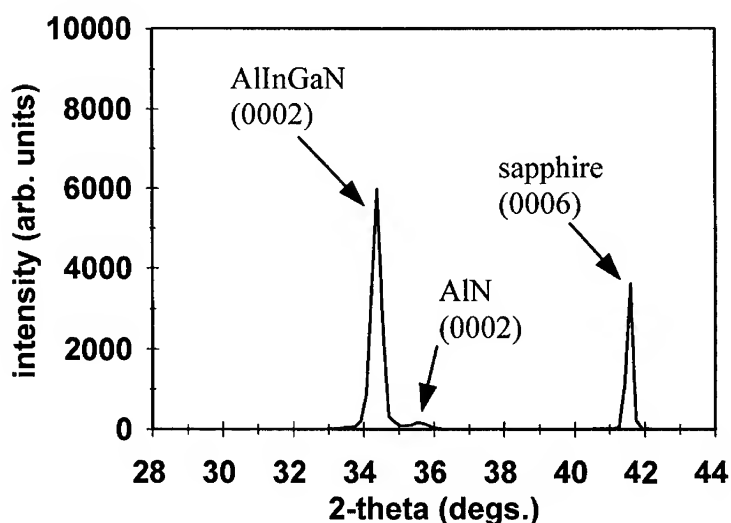


Figure 3: X-ray results for a quaternary film grown by MOCVD at 780°C.

$$a[\text{Al}_x\text{Ga}_{1-x-y}\text{In}_y\text{N}] = x a_{\text{AlN}} + (1 - x - y) a_{\text{GaN}} + y a_{\text{InN}} \quad (1)$$

This above formula is based on the assumption that a solid solution of the binary constituents is present in the quaternary alloy. There is a reasonable agreement between the lattice constants measured from Figure 3 and the value deduced from the above relation using EDS results in obtaining the chemical composition x and y .⁶ Thus at least in the composition range studied, a solid solution does exist between the binary constituents.

The ultimate use of AlGaInN is reducing the lattice mismatch at AlGaInN/InGaN interfaces. Figure 4 shows the DCXRD results of an AlGaInN/InGaN/AlGaInN heterostructure. From this figure it is difficult to resolve the ternary and quaternary peaks due to the fairly close lattice constants. The arrows labeled T and Q in this figure show the lattice constants, determined by X-ray diffraction, of the ternary and quaternary films, respectively, when grown separately, but using the same flows as in this heterostructure. From this figure and the corresponding lattice constants of the ternary and quaternary alloys it can be shown that the lattice mismatch at the InGaN/AlGaInN heterointerface is about 0.3%. The corresponding lattice mismatch of this InGaN film in an AlGaInN/InGaN heterostructure is 1.5%. Figure 5 shows the room temperature photoluminescence for this quaternary film, indicating band edge emission from the active InGaN layer.

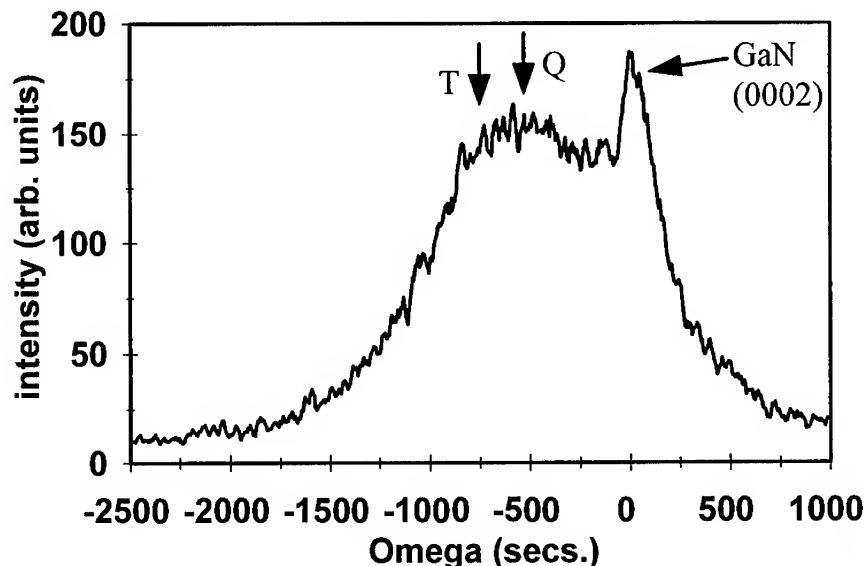


Figure 4: DCXRD results for an AlGaInN/InGaN/AlGaInN heterostructure grown by MOCVD at 780 °C.

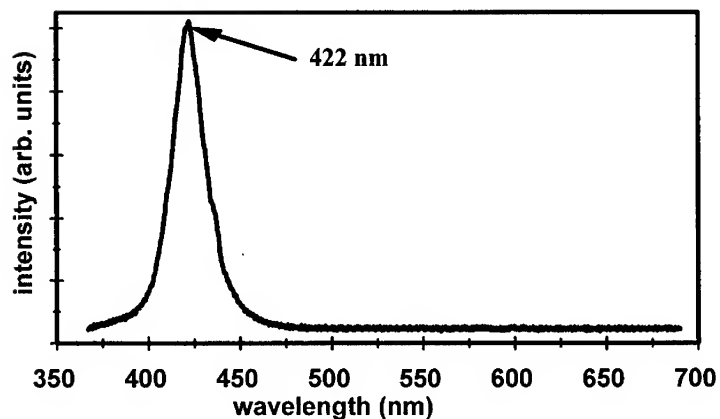


Figure 5: Room Temperature PL for the AlGaInN/InGaN/AlGaInN heterostructure shown in Figure 4.

CONCLUSIONS

In conclusion, $\text{Al}_x\text{Ga}_{1-x-y}\text{In}_y\text{N}$ films were epitaxially grown on GaN by MOCVD in the composition range $0 < x < 0.2$, $0 < y < 0.15$. AlGaInN/InGaN nearly lattice matched heterostructures were grown, allowing the potential for new optoelectronic device structures with the generation of misfit dislocations at critical interfaces.

ACKNOWLEDGEMENTS

This work is supported by ONR, University Research Initiative program.

REFERENCES

1. S. Nakamura, T. Mukai and M. Senoh, Appl. Phys. Lett. **64**, 1687 (1994).
2. S. Nakamura, T. Mukai and M. Senoh, J. Appl. Phys. **76**, 8189 (1994).
3. K.S. Boutros, F.G. McIntosh, J.C. Roberts, S.M. Bedair, E.L. Piner and N.A. El-Masry, Appl. Phys. Lett. **67**, 1797 (1995).
4. N. Karam, T. Parados, W. Rowland, J. Schetzina, N. El-Masry, and S.M. Bedair, Appl. Phys. Lett. **67**, 94 (1995).
5. C.K. Williams, T.H. Glisson, J.R. Hauser, and M.A. Littlejohn, J. Elect. Mat. **7**, 639 (1978).
6. F.G. McIntosh, K.S. Boutros, J.C. Roberts, S.M. Bedair, E.L. Piner and N.A. El-Masry, to be published in Applied Phys. Lett. Jan., 1996.

A STUDY OF THE EFFECT OF GROWTH RATE AND ANNEALING ON GaN BUFFER LAYERS ON SAPPHIRE

J.C. RAMER, K. ZHENG, C.F. KRANENBERG, M. BANAS, AND S.D. HERSEE
University of New Mexico, CHTM, Albuquerque, NM 87131

ABSTRACT

Using atomic force microscopy (AFM) and X-ray diffraction (XRD) we have determined that on [0001] oriented sapphire, the GaN buffer layer shows a degree of crystallinity that is dependent on growth rate. Annealing studies show evolution of the crystallinity and the emergence of a preferred orientation. Also, substrate orientation is found to influence the buffer layer crystallinity. Based on this work and previous results, we propose that the GaN buffer layer growth can be described by the Stranski-Krastanov growth process.

INTRODUCTION

There is now extensive evidence showing that the crystalline characteristics of the low temperature buffer layer control the important crystalline, optical and electrical properties of the main III-N epilayer grown at high temperature [1,2,3,4]. It is therefore essential that we understand how this buffer layer grows and the effect of buffer layer growth parameters. Previous work indicates that the buffer growth temperature [3,4], the buffer thickness [2,3], the buffer growth rate [2,5] and the duration of the ramp to the higher (main) growth temperature [3,6] are critical buffer growth parameters. Furthermore, the three dimensional island nature of the buffer layer is reflected in the main GaN epilayer. XRD measurements on the main GaN epilayers show a large mosaicity, indicating that these are ordered polycrystalline materials [3]. Cross sectional TEM analysis of these structures [7,8,9,10] shows high dislocation densities (typically $> 10^8 \text{ cm}^{-2}$) and strong evidence that these dislocations are clustered at low angle grain boundaries between the polycrystalline domains [9,10].

This paper examines the variation of buffer layer crystallinity with buffer growth parameters and shows that this behavior is consistent with a Stranski-Krastanov (S-K) growth mode [11,12,13], where the buffer layer achieves its lowest free energy by reorganizing from its 2D "as deposited" state to form 3D islands. In practice, the extent of this reorganization is kinetically limited and depends upon the surface mobility of the buffer material. This in turn is controlled by substrate parameters such as polarity, roughness, chemical activity, and MOCVD growth parameters such as temperature, growth rate, and the annealing that occurs during the ramp to the higher temperature growth phase.

EXPERIMENTAL PROCEDURES

The samples analyzed in this study were grown in a horizontal geometry, RF

heated, low pressure MOCVD reactor. The sources used were trimethylgallium (TMGa), high purity ammonia, and UHP hydrogen as a carrier gas. The reactants were introduced into the reaction chamber by a custom radial injection manifold which allows for separate injection of the group III and group V sources. Prior to loading, the substrates were chemically cleaned for 1 minute in a solution of 3:1 HCl:HNO₃, followed by 5 minutes in trichloroethylene, then rinses in acetone and methanol. The substrates were then dried under a nitrogen flow and loaded into the reactor. Prior to growth, the sapphire substrates were heated in H₂ at 1100 °C for 10 minutes.

Experimental conditions for the reactor during the depositions were as follows: pressure 100 Torr, ammonia flow = 3.0 slm, growth temperature = 480 °C, and total gas flow of 4.5 slm. Growth rates from 30 to 440 Å/min were studied for the GaN buffer layers. The layers studied were all nominally 300 Å thick. The annealed samples were ramped up to a reactor temperature of 1025 °C in the same ammonia and hydrogen flow as was present during the buffer deposition.

X-ray diffraction (XRD) measurements were made on the buffer layers using a Philips Materials Research Diffractometer equipped with a 4-bounce germanium (220) monochromator and an open detector. Measurements were made in the rocking mode with the Bragg condition set for the [0002] reflection.

The AFM work was done on a Digital Instruments Nanoscope III Atomic Force Microscope, using an e-beam grown tip with a 200 Å radius. For each sample, the measurements were performed in scanning mode over an area of 0.4 μm x 0.4 μm.

RESULTS

The Effect of Growth Rate on Buffer Layer Characteristics

AFM measurements revealed that the buffer layer consisted of a dense array of growth islands, as observed previously [1,3,6]. All GaN buffer layers showed XRD peaks indicating that they were crystalline, however, the rocking curve peaks were typically very broad (about 1 to 2 degrees). This behavior is typical of polycrystalline material and indicates that there is a large variation in the <0001> direction among the buffer "islands." For buffers grown on c-plane sapphire, the XRD peaks also showed a narrow, higher intensity peak at the center of this broad shoulder (see inset in figure 1). The presence of this higher intensity peak indicates a preferred orientation among the polycrystals.

On both c and a-plane sapphire samples, only c-oriented GaN could be detected; that is, only the (0002) and (0004) diffraction peaks of GaN were observed in the x-ray diffraction spectra.

Figure 1 shows that the integrated (0002) GaN XRD peak intensity for buffers grown on c-plane sapphire varies with the growth rate of the film. At a low deposition rate, the buffer is in crystalline form, while for a higher growth rate, the area under the full XRD peak decreases, indicating that more of the deposited material remains amorphous at the higher growth rate. GaN buffers grown on a-plane

sapphire show no significant variation in crystallinity with the growth rate of the film.

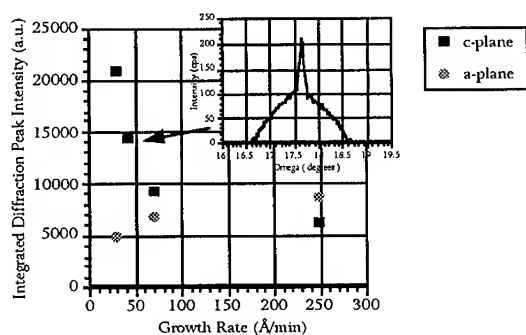
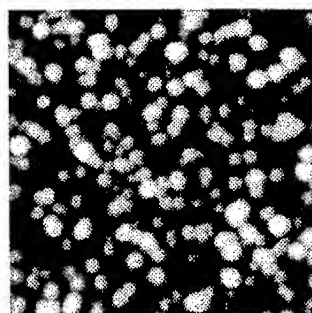
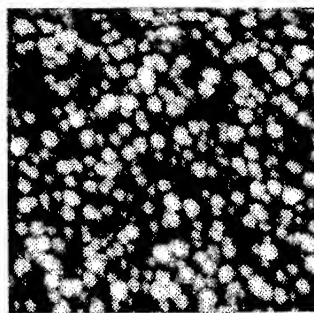


Figure 1: Integrated (0002) GaN diffraction peak intensity vs. growth rate. Inset in the graph is a typical XRD peak of the as deposited GaN buffer layer on c-plane sapphire.

AFM images were also made of the surfaces of the samples in figure 1. The island nature of the buffer layer films is evident in figure 2 (lighter regions of the AFM image correspond to higher surface features) and shows that larger islands grow at lower growth rate. GaN buffer layers deposited on c-plane sapphire showed a decrease in the RMS surface roughness and smaller growth islands with increasing growth rate. The roughness change is expected from the change in island size. Larger islands, with larger spaces in between them, allow the 200 Å AFM probe to sample deeper, which increases the apparent RMS roughness value.



Growth Rate 30 Å/min
RMS roughness = 43 Å



Growth Rate 70 Å/min
RMS roughness = 33 Å

Figure 2: AFM images of GaN buffer layers on c-plane sapphire. The surface area scanned is $0.4\mu\text{m} \times 0.4\mu\text{m}$. In the images, lighter regions correspond to higher surface features.

Thick GaN epilayers were also grown on some GaN buffers grown on c-plane

sapphire under the range of conditions shown in figure 1. Table 1 shows the XRD peak FWHM values for these 5 μm thick epilayers for several buffer growth rates.

Buffer Growth Rate ($\text{\AA}/\text{min}$)	FWHM of epilayer XRD peak (arcsec)
30	180
70	250
90	320

Table 1: FWHM of the GaN epilayer XRD peak for several values of buffer layer growth rate.

The Effect of Annealing Time

The sample is annealed during the ramp between the low temperature buffer growth and the high temperature growth of the main GaN epilayer. This “ramp anneal” also changes the morphology and crystallinity of the buffer as first determined by Wickenden [6]. (Wickenden showed that anneal times greater than 20 minutes led to degradation of morphology and crystalline quality of the GaN buffer layers, so only anneal times up to 30 minutes were studied here.)

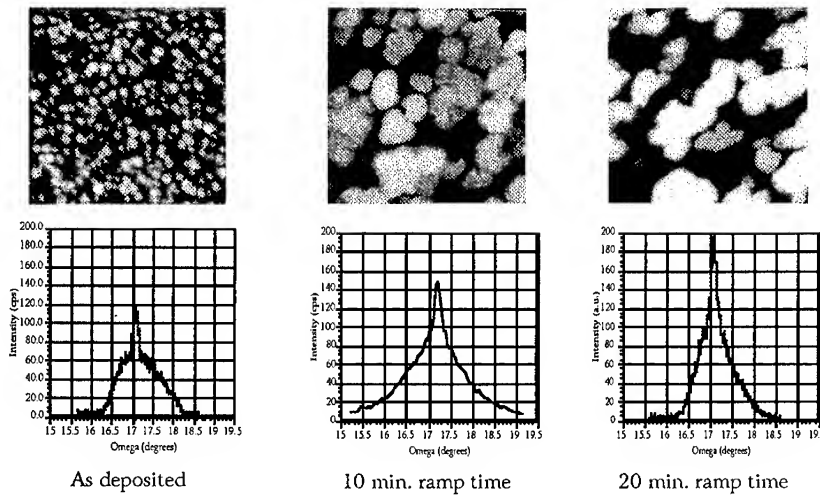


Figure 3: AFM and XRD data for GaN buffer layers on c-plane sapphire for different ramp anneal times. The AFM image area is 0.4 μm x 0.4 μm , with lighter regions corresponding to higher surface features. RMS roughness values for the layers are 33 \AA , 42 \AA , and 84 \AA , respectively.

In order to simulate the temperature change experienced by the buffer layer during conventional 2 step growth of GaN, a series of GaN buffer layer samples were

subjected to different ramp anneal durations. These samples were then removed from the reactor for XRD and AFM characterization.

Figure 3 combines AFM and XRD data for as grown and annealed GaN buffers on c-plane sapphire substrates. The AFM images show an increase in polycrystal island size with increasing anneal time. As explained above, the measured RMS surface roughness also increases with island size. XRD measurements show a narrowing of the broad, lower intensity part of the XRD peak for longer anneals. After an anneal time greater than 10 minutes, a preferred orientation emerges.

DISCUSSION

This paper shows that the degree of crystallinity in GaN buffer layers deposited on c-oriented sapphire at 480 °C varies with growth rate. As the buffer growth rate is increased the buffer XRD peak intensity falls indicating that less of the buffer is polycrystalline and that the rest is presumably amorphous (when AlN buffers are deposited under these conditions no XRD peaks are observed, indicating amorphous material). As the ramp annealing time increases we see an increase in polycrystal island size and XRD measurements show narrowing of the broad, lower intensity part of the XRD peak. This implies that the GaN buffer material is mobile on [0001] plane sapphire and that the larger, on-axis crystallites are growing at the expense of the smaller islands through the process of Ostwald ripening [6,13]. This data reflects the emergence of a preferred orientation among the buffer polycrystals which is then maintained through the growth of the main GaN epilayer.

Interestingly, identical experiments performed on a-plane sapphire show that less of the buffer material is crystalline and that there is no significant dependence on growth rate (figure 1). Also, preliminary ramp-annealing studies show that the buffer material is less mobile on a-plane sapphire and that no preferred polycrystal orientation emerges during annealing.

The buffer-layer growth behavior described here and in previous studies [1-10] has the characteristics of a Stranski-Krastanov growth mode [11-13]. The high mismatch strain between GaN and sapphire drives the buffer material, which is initially deposited uniformly across the wafer, to form 3D polycrystalline islands where the free energy is minimized. At low growth rate (and/or higher temperature) the buffer layer group III species are effectively more mobile on the sapphire surface allowing the growth of polycrystalline islands [13]. At high growth rate (and/or low temperatures) the surface species are less mobile and the buffer material is not able to fully reorganize to achieve minimum free energy. Thus surface kinetics can limit the extent of the S-K reorganization during growth. This kinetic limitation is believed to be responsible for the observed difference in buffer layer behavior on c and a sapphire orientations. Based on polishing studies at UNM, we find that the a-sapphire surface is more reactive than the c-surface, and during growth this means that the buffer group III species will be less mobile on a-plane sapphire. Thus we anticipate the observed result that the buffer layer on a-plane sapphire exhibits a lower crystallinity.

Surface kinetic limitations also explain the amorphous nature of the low temperature AlN buffer layer. The high reactivity of Al species will result in a low surface mobility, and kinetically limit the buffer reorganization during the growth.

Clearly, any growth parameter that affects the surface mobility of the buffer layer material will influence the extent of the S-K reorganization during growth, which in turn controls the buffer layer crystallinity and the eventual crystallinity and properties of the main III-N epilayer.

CONCLUSION

We present evidence that S-K behavior explains the sensitivity of MOCVD growth of GaN on sapphire to substrate orientation, growth rate, growth temperature and ramp annealing duration. Furthermore, we anticipate that any substrate or growth parameter that affects surface mobility will significantly affect the S-K behavior and the final properties of the GaN material. The need for a lattice matched substrate is therefore twofold; A lattice matched substrate will not only reduce the defect density in the III-N material but should also significantly improve control of the MOCVD growth process.

ACKNOWLEDGEMENTS

This work was supported by ARPA.

REFERENCES

1. K. Hiramatsu, S. Itoh, H. Amano, I. Akasaki, N. Kuwano, T. Shiraishi, K. Oki, J. Cryst. Growth, **115**, 628 (1991).
2. S. Nakamura, Jap. J. Appl. Phys., **30**, L1705 (1991).
3. S.D. Hersee, J. Ramer, K. Zheng, C.F. Kranenberg, K. Malloy, M. Banas, and M. Goorsky, J. Electron. Mat., **24**, 1519 (1995).
4. V. Harle, H. Bolay, F. Steuber, B. Kaufmann, G. Reyher, A. Dornen, F. Scholz, paper B2, proc. of EW-OMVPE VI, Gent (Belgium), June (1995).
5. S. Keller, D. Kapolnek, B.P. Keller, B. Heying, Y.-F. Wu, S. Kato, U.K. Mishra, and S.P. DenBaars, paper B7, proc. of EW-OMVPE VI, Gent (Belgium), June (1995).
6. A.E. Wickenden, D.K. Wickenden, and T.J. Kistenmacher, Journal of Applied Physics, **75**, 5367 (1994).
7. R.C. Powell, N.E. Lee, Y.W. Kim and K.E. Greene, J. Appl. Phys., **73**, 189 (1993).
8. S. Chadda, M. Pelczynski, K. Malloy and S.D. Hersee, MRS proc., **326**, 353, (1994).
9. F.A. Ponce, B.S. Krusor, J.S. Major Jr., W.E. Plano and D.F. Welch, Appl. Phys. Lett., **67**, 410 (1995).
10. W. Qian, M. Skowronski, and M. De Graef, K. Doverspike, L.B. Rowland, and D. K. Gaskill, Appl. Phys. Lett., **66**, 1252 (1995).
11. R.W. Vook, Thin Solid Films, **64**, 91 (1979).
12. K-N Tu, J.W. Mayer, L.C. Feldman, Electronic Thin Film Science for Electrical Engineers and Materials Scientists, (Macmillan Publishing Company, 1992), chap. 7
13. M. Ohring, The Materials Science of Thin Films, (Academic Press, Inc., 1992), chapter 5.

THE EFFECT OF A GaN NUCLEATION LAYER ON GaN FILM PROPERTIES GROWN BY METALORGANIC CHEMICAL VAPOR DEPOSITION

W. VAN DER STRICHT, I. MOERMAN, P. DEMEESTER*
J.A CRAWLEY, E.J. THRUSH**
P.G. MIDDLETON, C. TRAGER COWAN, K.P. O'DONNELL***

* University of Gent-IMEC, Department of Information Technology, Gent, Belgium

** Thomas Swan & Co., Ltd., Cambridge, United Kingdom

*** Department of Physics and Applied Physics, Semiconductor Spectroscopy and Devices,
University of Strathclyde, Glasgow, United Kingdom.

ABSTRACT

In this paper GaN films are examined, which are grown on basal plane (0001) sapphire substrates. Growth is performed in a novel type of vertical rotating disk reactor. Results on the effect of a GaN nucleation layer on the properties of the overgrown GaN epilayer are presented. Characterisation includes surface morphology studies, DC X-ray diffraction and optical characterisation. Best film quality so far has a double crystal X-ray half width of 85 arcsec at approximately 1 μm thickness.

INTRODUCTION

With a wide direct bandgap of 3.39 eV and excellent physical properties gallium nitride (GaN) is a very promising material for fabricating blue light emitting devices. A few possible applications are high density optical data storage, full color video-screens and even trafficlights.[1,2] Recently significant progress in epitaxial growth of GaN has already led to commercially available nitride-based high brightness light emitting diodes [3,4]. In spite of this recent success many fundamental problems still remain in the epitaxial growth of GaN and its alloys.

GaN is usually grown heteroepitaxially on sapphire (0001) substrates, which have a lattice mismatch of 13.8 % [5]. When GaN is grown directly on the sapphire however, this results in three-dimensional growth and a film quality which is not suitable for realising devices. Recently experiments have shown that a two-step growth procedure leads to two-dimensional growth and improved film quality [6]. First a thin polymorphic GaN or AlN nucleation layer is grown on the sapphire surface at low temperature (450 to 600 °C). After raising the temperature to between 900 to 1100 °C a GaN layer is deposited. The growth temperature and thickness of this nucleation layer have a great influence on the properties of the overgrown GaN film. The purpose of this paper is to determine optimum growth parameters for GaN films in a novel type of vertical rotating disk reactor.

EXPERIMENT

The GaN films were grown by metalorganic chemical vapour deposition on sapphire (0001) substrates with H₂ and mixed H₂/N₂ carrier gas. Ammonia (NH₃) and trimethylgallium (TMG) were used as source materials. The growth was performed in a vertical rotating disk reactor, manufactured by Thomas Swan & Co. The group III and group V elements are injected separately into the reactor through a water cooled "showerhead" to avoid undesired upstream pre-reactions. A graphite resistance heater, is used to raise the temperature of a graphite susceptor up to 1200 °C. The temperature is measured with an optical pyrometer looking directly at the substrate (fig.1). The rotation speed of the susceptor can be varied between 0 and 1500 rpm. All the deposition was performed under atmospheric pressure (700 Torr).

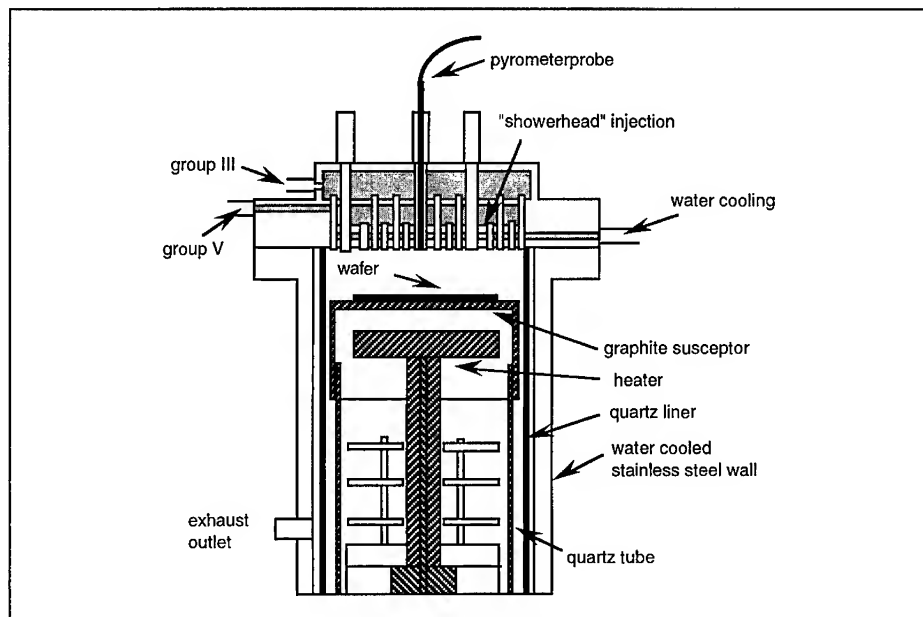


fig. 1 : Novel type of vertical rotating disk reactor

The substrates were degreased in organic solvents (Trichlorethane, Acetone, Isopropyl alcohol) and etched in a hot solution of $\text{H}_2\text{SO}_4:\text{H}_3\text{PO}_4$ (3:1). Before growth the substrates were baked out at epilayer growth temperature in a NH_3 flow. The growth itself is performed as a two step process. In the first step a nucleation layer is grown at a low temperature in between 450 to 550 °C. Then the temperature of the substrate is raised to between 950 to 1100 °C and kept constant for a few minutes. During the annealing the nucleation layer recrystallizes and on this improved nucleation surface the epilayer is deposited. The rotation speed was kept constant at 800 rpm.

Several parameters were varied to optimize the growth proces. GaN films were characterised by X-ray measurements to examine the crystal quality. For this we used a double crystal (DC) diffractometer set-up. We also studied the variation surface morphology under various growth conditions. Optical characterisation was performed by photoluminescence (PL) and cathodoluminescence (CL) measurements. PL samples mounted in a Leybold cryorefrigerator, were excited using loosely focussed light from a 5 mW He-Cd laser operating on the 325 nm line. Monochromatic CL images were obtained at room temperature using a modified Cambrige Instruments scanning electron microscope.

RESULTS

For the growth of smooth layers it is very important to deposit the epilayer on an optimum nucleation layer. We have grown nucleation layers at temperatures between 450 °C and 550 °C. This resulted in various surface hexagonal structures. We found that for nucleation layers deposited at 550 °C the surface was covered with hexagonal pyramids. Decreasing the growth temperature to 500 °C led to a flattening of those pyramids and at 475 °C the surface was completely smooth. The thickness of the nucleation layers was varied between 20 to 100 nm, but it did not have a great influence on the surface morphology. The epilayers were all grown at 1050 °C and under atmospheric pressure.

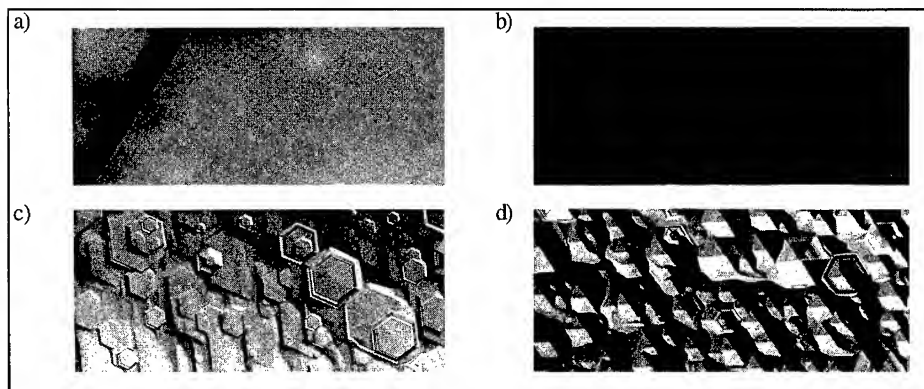


fig.2 : Surface morphology of GaN layers grown on nucleation layers: grown at different temperatures: a) 475 °C, b) 485 °C, c) 500 °C, d) 550 °C

A similar behaviour was observed when the growth temperature of the epilayer was varied. At a low deposition temperature of 950 °C the surface was covered with hexagonal pyramids. Increasing the temperature led to a flattening of the pyramids and thus two dimensional growth. Very high growth temperatures, above 1100 °C, led to a situation where no film was deposited. It seems that the epilayer growth temperature influence is very similar to the behaviour at direct growth of GaN on sapphire.[7,8]

The growth temperature of nucleation layer and epilayer also determine the crystal quality. In double crystal (DC) X-ray diffraction we found rocking curves with a FWHM in the range of 80 to 700 arcsec. Measurements were performed on samples of approximately 1 μm thickness (after one hour growth). From layers with the best morphology (smooth surface) the narrowest DC X-ray rocking curves were obtained. In addition to the growth temperature of the nucleation layer, the thickness of the nucleation layer is also very critical to grow layers with narrow DC X-ray rocking curves. In figure 3(a) the FWHM is shown as a function of growth time. The growth speed of the nucleation layer was approximately 1.8 $\mu\text{m/h}$, so the optimum thickness is approximately 25 nm. The best DC X-ray result was found on a layer grown at 1050 °C on a 25 nm thick nucleation layer, deposited at 475 °C. In figure 3(b) the influence of growth temperature of the epilayer is demonstrated. GaN layers were deposited on the same nucleation layers (growth temperature 500 °C) at different epilayer growth temperatures. Increasing the growth temperature led to narrower DC X-ray rocking curves. It may be relevant to note that the peak intensity decreased at very high growth temperatures due to a lower growth speed.

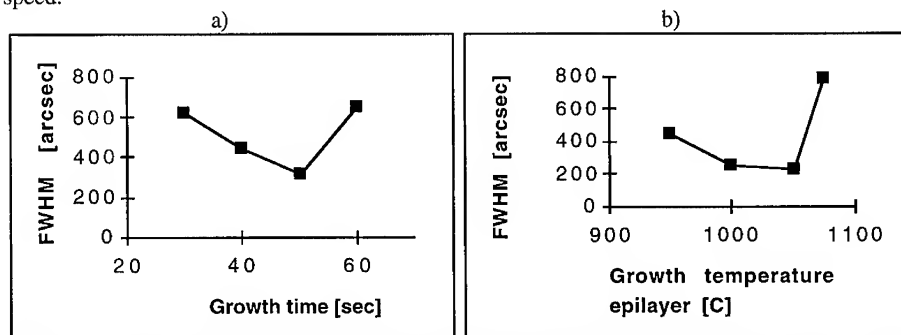


fig. 3 (a : Influence of growth time of nucleation layer on FWHM of DC X-ray rocking curve; (b : Influence of growth temperature of the epilayer on FWHM of DC X-ray rocking curve

Atomic force microscopy (AFM) using a Burleigh SPM instrument reveals substantial differences in the morphology of nucleation layers grown at different temperatures. Layers grown at 550 °C show a large number of shallow "pits" of diameter ranging from several tens to several hundreds of nanometres at the surface of a layer of thickness several microns. In contrast, a layer grown at 500 °C appears to be a continuous mesh of overlapping crystallites.

The photoluminescence technique takes an average over the area of the excitation spot, of order 1 mm x 1 mm in the present case. In general, some non-uniformity may be expected as the excitation spot ranges over a sample. Typical room temperature spectra feature a relatively sharp band edge line near 373 nm, a broad band around 450 nm and a broad band that peaks near 560 nm (the yellow band).

In order to provide a rough assessment of sample quality we introduce two figures of merit. Q1 measures the total fluorescence output for a fixed excitation level. Q2 measures the fraction of the total fluorescence that appears in emission at the band edge. Hence while Q1 gives a measure of the surface condition and radiative efficiency of a sample, Q2 is related to the sample purity. Figure 4 shows the variation of Q1 and Q2 with growth temperature of the nucleation region. Clearly, the optimum values are obtained for buffer layers grown at 475 to 500 °C.

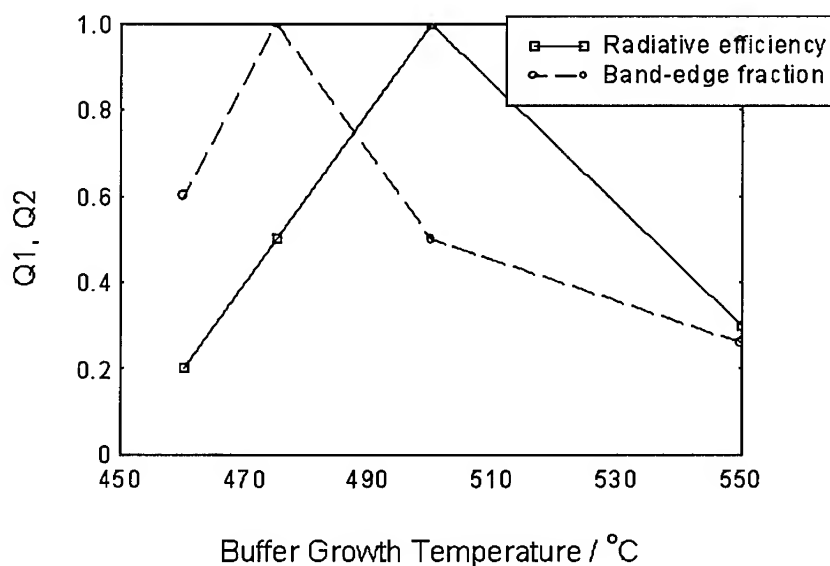


fig. 4 : Effect of nucleation layer growth temperature on PL quality factors.

Upon cooling samples below 50 K, shallow donor-acceptor luminescence bands may emerge near 400 nm. In some samples it appears that the strength of emission in the D-A series reflects the strength of the yellow band, pointing to some commonality in their origin. Figure 5 shows the photoluminescence spectrum of a typical high quality sample at 14 K.

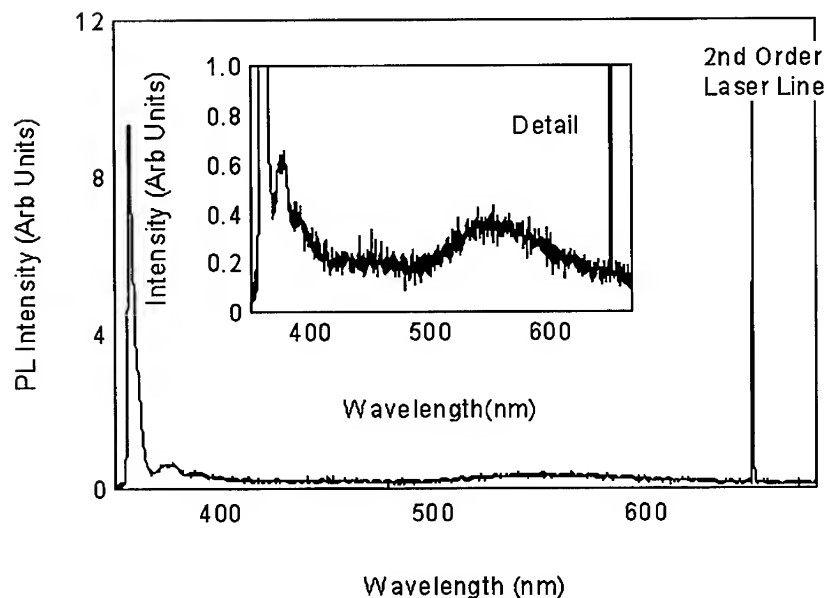


fig 5: Low temperature PL spectrum showing strong band edge luminescence.

Cathodoluminescence imaging provides both morphological and optical information. By inserting a monochromator in the path of the luminescence one obtains information relating to the structural origin of the bands described above. First, we examine an optical microscope image that shows some stacked hexagonal structures (Figure 6). Figures 7 (a) and (b) are cathodoluminescence images that examine the same region of surface in the light of the band edge emission and the yellow band, respectively.

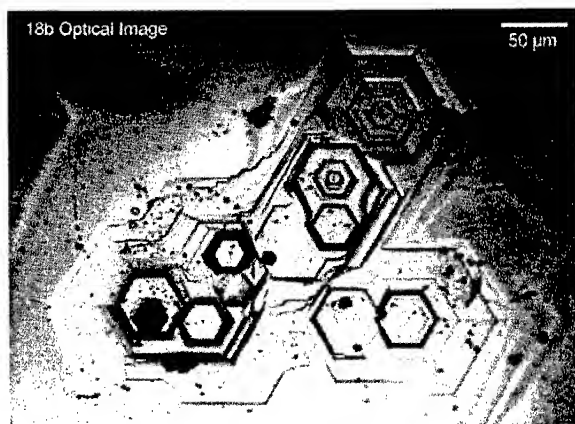


fig 6 : Optical micrograph showing hexagonal crystallites.

The two images are almost complementary: the UV band is stronger in the small hexagons which appear to lie high above the substrate; the yellow band originates almost entirely in low-lying features.

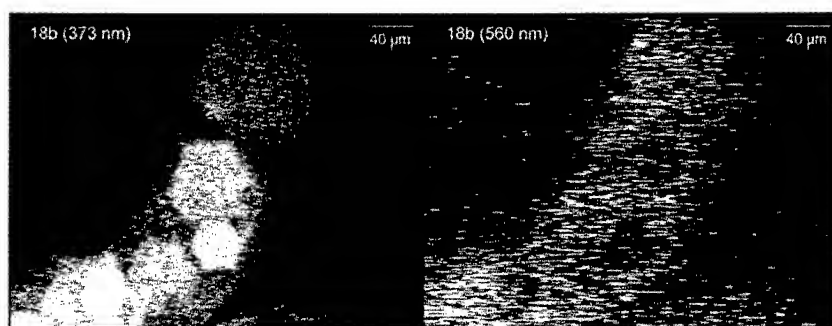


fig 7 : Monochromatic CL images of (a) band-edge emission, (b) yellow emission.

CONCLUSIONS

GaN films grown in a novel type of vertical spinning disk reactor on sapphire (0001) substrates show satisfactory film quality, as judged by X-ray diffraction, optical micrographs and PL characterisation. Cathodoluminescence imaging emphasises the strong structure dependence of inhomogeneities which still exist at the present state of the art.

ACKNOWLEDGMENTS

Wim Van der Stricht thanks the IWT for financial support and An Janssens for carrying out the X-ray measurements in the framework of her graduate thesis. Paul Middleton's studentship is funded by EPSRC.

REFERENCES

- [1] R. Metzger, *Compound Semiconductor*, p. 26-28, July/August 1995.
- [2] S. Nakamura, *Circuits and Devices*, p.19-23, May 1995.
- [3] I. Akasaki, H. Amano, H. Murakami, M. Sassa, H. Kato, K. Manabe, *J. Cryst. Growth* 128, p. 379-383 (1993).
- [4] S. Nakamura, T. Mukai and M. Senoh, *Appl. Phys. Lett.* 64 (13), p.1687-1689 (1994).
- [5] T. Matsuoka, A. Ohki, T. Ohno and Kawaguchi, *J. Cryst. Growth* 138, pp. 727-736 (1994).
- [6] L. Akasaki, H. Amano, Y. Koide, K. Hiramatsu and N. Sawaki, *J. Cryst. Growth* 98, pp. 209- (1989).
- [7] T. Sasaki, *J. Cryst. Growth* 129, pp.81-90 (1993).
- [8] T. Sasaki and T.Matsuoka, *J. Appl. Phys.* 77 (1), pp. 192-200 (1995).

AN ATOMIC FORCE MICROSCOPY STUDY OF THE INITIAL NUCLEATION OF GaN ON SAPPHIRE

M. RICHARDS-BABB*, S. L. BUCZKOWSKI, ZHONGHAI YU, AND T. H. MYERS**

*Chemistry Department, **Physics Department, West Virginia University, Morgantown, WV
26506, thmyers@wvnmvs.wvnet.edu

ABSTRACT

Preliminary results of a study of GaN nucleation and growth by molecular beam epitaxy using a nitrogen rf plasma source are presented. Nucleation layers and 3000 Å thick layers were investigated by atomic force microscopy and x-ray diffraction. Growth under gallium-rich conditions both increased nucleation island size and promoted two-dimensional growth.

INTRODUCTION

The potential applications of blue and ultraviolet optoelectronic devices based on GaN have been recognized for many years [1]. Recent advances in epitaxial GaN growth by metal organic chemical vapor deposition (MOCVD) have lead to commercially available devices from both U.S. (CREE Research, Inc.) and foreign companies (Nichia Chemical Industries). Rapid progress in this direction is also being accomplished by molecular beam epitaxy (MBE) growth using active nitrogen species [2]. The most common substrate for epitaxial growth is sapphire (α -Al₂O₃) due to its availability, low cost and robust nature. GaN layers grown on sapphire, however, typically contain a high density of defects, mainly threading dislocations, due to a large lattice mismatch and thermal expansion coefficient mismatch between the epilayer and the substrate [3,4]. In contrast to growth in other semiconductor systems, these high dislocation densities ($>10^9$ cm⁻²) are reported to persist for up to 4 μ m of growth [3,4]. While some devices are tolerant of such high densities [4], it is desirable to determine growth conditions for improved structural quality.

GaN typically nucleates and grows on sapphire by island formation. The use of low temperature buffer layers (450 - 600 °C) of AlN [5] or GaN [6,7] results in a dramatic improvement in layer morphology and electrical properties. Annealing prior to high temperature growth causes coalescence of the nucleation islands, resulting in low angle grain boundaries which create the observed dislocation arrays [3,4]. This subgrain structure is stable during growth under most conditions. Thus, subsequent crystal quality is strongly dependent on the nucleation layer.

The predominant growth mode is a further factor in dislocation reduction with increasing layer thickness. Two-dimensional growth results in the highest degree of structural perfection in epitaxial layer growth. Typical MBE and MOCVD growth conditions appear to promote three-dimensional growth [8]. This may lead to individual growth of the low angle grains, preventing dislocation recombination and annihilation. A recent study has reported MOCVD growth conditions resulting in two-dimensional step-flow growth [9], with a concomitant reduction in dislocation density to about 2×10^8 cm⁻². This paper presents the initial results of a study to

determine conditions for MBE growth of GaN that result in buffer layers with increased grain size as well as determining the appropriate parameters to promote two-dimensional growth.

EXPERIMENT

The GaN layers for this study were grown at West Virginia University by MBE in a system similar to that described elsewhere [10]. Since we are interested in developing lower temperature growth of GaN by MBE, we have only investigated growth temperatures less than 700°C. A standard MBE source provided the Ga flux. A cryogenically-cooled rf plasma source (Oxford Applied Research CARS-25) operating at 500W was used to produce the active nitrogen flux. The layers were characterized using x-ray diffraction and atomic force microscopy (AFM) (Digital Instruments Nanoscope II).

RESULTS

Several studies [3,4,11] have indicated that the transition between buffer layer and "bulk" film structure occurs in the first 0.4 to 0.5 μm of growth. We grew a series of 3000 Å layers to determine both growth rates and growth modes in this transition region. We were also interested in the transition point between Ga-rich growth and conditions which produced Ga condensation as evidenced by the presence of Ga droplets. Figure 1 illustrates our growth rate for several conditions. Above 2.5×10^{-7} Torr Ga and 600°C, growth is limited by the amount of active nitrogen present as indicated both by the increase in growth rate with temperature at a fixed Ga flux, and by the relatively constant growth rate at a given temperature for increasing Ga flux. The decrease in growth rate between 2.5 and 5.0×10^{-7} Torr Ga at 660°C is apparently related to a change from a three-dimensional to a two-dimensional growth mode, as discussed later.

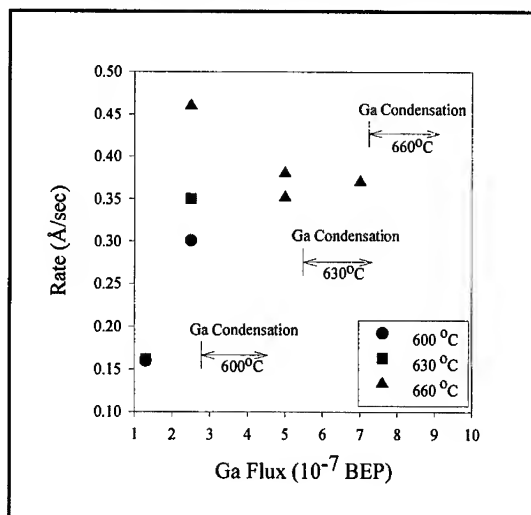


Figure 1. Growth rate of GaN for several temperatures and values of Ga flux.

Early in this study we grew layers using nucleation conditions reported by others [2,5,6,7,12]. We found that exposing the sapphire substrate to an active nitrogen flux resulted in a fine-grained ($<1000\text{\AA}$) island size. Growth of a low temperature nucleation layer at $450\text{ }^{\circ}\text{C}$ followed by an anneal at $660\text{ }^{\circ}\text{C}$ also resulted in a similar small grain size. Thus, we undertook a study of island size distributions in nucleation layers as a function of growth parameters. The nucleation layers were studied using AFM. Figure 2 is a micrograph of one such layer. Distributions were determined by taking ten AFM micrographs at points distributed across the sample surface. The islands were approximated as circular regions of various sizes by visual comparison with a template. A histogram of occurrence frequency vs. diameter was thus obtained. The distributions were adequately represented by poisson statistics, and the mean value was found by a least squares fit to the distribution.

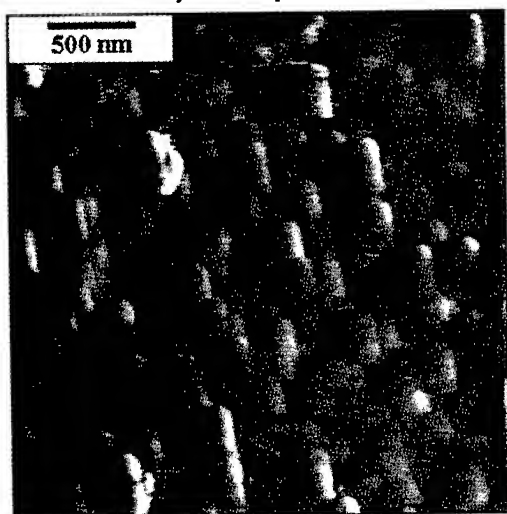


Figure 2. AFM micrograph of a GaN nucleation layer, 100\AA thick, grown at $660\text{ }^{\circ}\text{C}$ under 6 sccm nitrogen flow and 5.0×10^{-7} Torr BEP Ga. The average surface roughness of this layer was about 10 \AA . The mean island diameter was about 3000 \AA .

The nucleation island diameter was found to increase somewhat linearly with temperature over the range investigated. However, in order to obtain this increase, the nucleation had to occur under Ga-rich conditions. Indeed, at a given temperature, the largest island size always occurred near the boundary for Ga condensation. Our results are summarized in Figure 3. For a fixed Ga flux and nitrogen flow rate, we observed a temperature corresponding to a maximum island size. Above this temperature, the nucleation islands became smaller. At a fixed temperature, island size could be increased by increasing the Ga flux, up to the occurrence of Ga condensation. In contrast, increasing the nitrogen flow rate resulted in smaller island size.

Further information was gained by examining layers grown by extending the nucleation growth to 3000 \AA thick. Figure 4(a) is the AFM micrograph of such a layer grown at $660\text{ }^{\circ}\text{C}$. The morphology appeared to consist of well-defined three-dimensional microcrystallites, with an average surface roughness of about 150 nm . These growth parameters appear to promote three-dimensional growth without early coalescence of the islands. Also, up to the 3000 \AA thickness, there was no apparent change in average microcrystallite dimension from the original nucleation island size. X-ray diffraction measurements were consistent with single-crystal, hexagonal GaN for all layers measured. However, the full width at half maximum (FWHM) was fairly large, about 400 arc minutes for the sample depicted in Figure 4(a). Doubling the Ga-flux brought the growth to near-Ga-condensation conditions and gave an increase in island size, as seen in Figure

4(b). More importantly, however, is evidence of two-dimensional growth which was observed for all layers grown above 660 °C for Ga-rich conditions. Coalescence of the islands is occurring and the overall roughness between grains is reduced to about 20 nm. The tops of the islands are fairly flat with well defined sub-nanometer steps corresponding to a few monolayers. We believe this indicates we are near the conditions needed for two-dimensional step-flow growth. The x-ray diffraction FWHM was reduced to about 120 arc minutes for this layer.

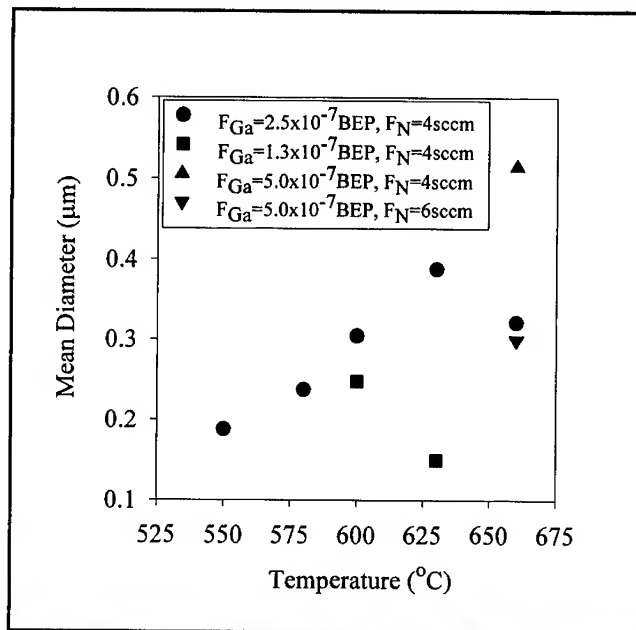


Figure 3 . GaN nucleation island diameter as a function of growth conditions.

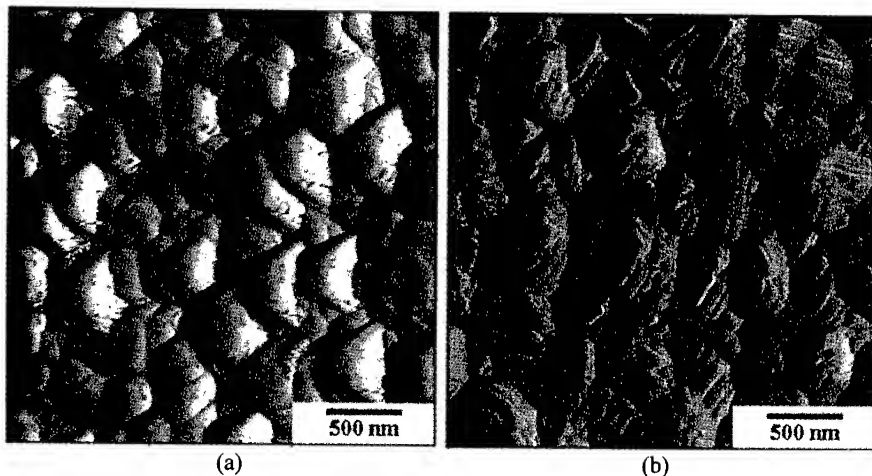


Figure 4 . AFM micrographs of GaN layers, 3000Å thick, grown at 660°C under 4 sccm nitrogen flow and (a) 2.5×10^{-7} Torr BEP Ga (b) 5.0×10^{-7} Torr BEP Ga flux.

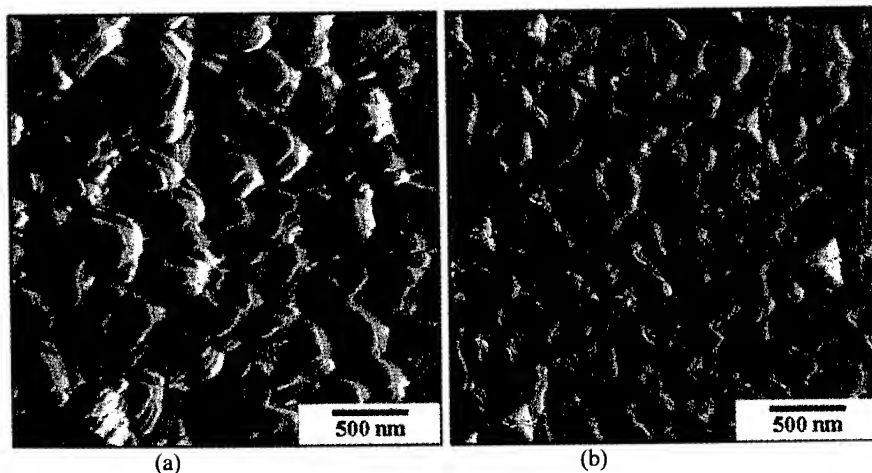


Figure 5. AFM micrographs of GaN layers, 3000 Å thick, grown at 670°C under 6 sccm nitrogen flow and 5.0×10^{-7} Torr BEP Ga flux: (a) without a buffer layer and (b) with a 100 Å thick buffer layer annealed at 670°C for 20 minutes prior to layer growth.

Only layers grown above 660 °C under Ga-rich conditions, where increasing the Ga-flux does not increase the growth rate as shown in Figure 1, exhibit characteristics of two-dimensional growth. All others exhibited a well defined, three-dimensional microcrystallite structure. Figure 5(a) is an AFM micrograph of a layer grown at 670 °C under increased nitrogen flow to move further away from the Ga-condensation point while maintaining Ga-rich conditions. Coalescence is not as evident as for the previous sample, with an average surface roughness of about 30 nm. However, the islands are again flat-topped and steps corresponding to monolayer growth are observed. Figure 5(b) is a 3000 Å layer grown under the same conditions except that growth was interrupted after the first 100 Å of growth. This nucleation layer was then annealed at 670 °C for 20 minutes under nitrogen flux, and growth was resumed. The resulting layer exhibited almost complete coalescence, with an average surface roughness of about 1.5 nm. Sub-nanometer terraces were present on the top of the "flat" regions, again indicating a predominantly two-dimensional growth mode. The x-ray diffraction FWHM obtained for this layer was 51 arc minutes. Further optimization should result in complete coalescence and two-dimensional growth.

CONCLUSIONS

Apparently Ga is the more mobile species under our growth conditions since we obtained larger island sizes and two-dimensional growth only under Ga-rich conditions. Lowering the Ga flux lead to three-dimensional growth with a nucleation layer consisting of smaller island sizes. The nitrogen may only incorporate at available sites near where it initially adsorbs, with little lateral motion before desorbing. The best conditions for growing the nucleation layer appear to be as Ga-rich as possible, near the limit for Ga condensation.

In this study, we have determined conditions for MBE growth of GaN that give large nucleation island size, and promote two-dimensional growth of layers. However, the results presented here are preliminary, as we have not yet performed detailed optical and electrical characterizations. We plan to continue this study by growing thicker layers on annealed buffer layers with the larger island size for further characterization of material properties.

ACKNOWLEDGMENTS

We want to acknowledge the invaluable assistance of T. R. Charlton and D. Buczkowski in the counting of nucleation islands, and E. Hopkins for x-ray diffraction measurements. This work was supported by DoD/ONR Grant N00014-94-1-1149, monitored by M. Yoder.

REFERENCES

1. See, for example, J. Pankove, Mater. Res. Soc. Symp. Proc. **97**, 409 (1987).
2. T. D. Moustakas, T. Lei, and R. J. Molnar, Physica B **185**, 36 (1993).
3. W. Qian, M. Skowronski, M. DeGraef, K. Doverspike, L. B. Rowland, and D. K. Gaskill, Appl. Phys. Lett. **66**, 1252 (1995).
4. S. D. Lester, F. A. Ponce, M. G. Craford, and D. A. Steigerwald, Appl. Phys. Lett. **66**, 1249 (1995).
5. H. Amano, N. Sawaki, I. Asaki, and Y. Toyoda, Appl. Phys. Lett. **48**, 353 (1986).
6. S. Nakamura, Jpn. J. Appl. Phys. **30**, 1705 (1991).
7. J. N. Kuznia, M. Asif Khan, D. T. Olson, R. Kaplan, and J. Freitas, J. Appl. Phys. **73**, 4700 (1993).
8. Z. Sitar, L. L. Smith, and R. F. Davis, J. Cryst. Growth **141**, 11 (1994).
9. D. Kapolnek, X. H. Wu, B. Heying, S. Keller, B. P. Keller, U. K. Mishra, S. P. DenBaars, and J. S. Speck, Appl. Phys. Lett. **67**, 1541 (1995).
10. T. H. Myers, R. W. Yanka, K. A. Harris, A. R. Reisinger, J. Han, S. Hwang, Z. Yang, N. C. Giles, J. W. Cook, Jr., J. F. Schetzina, R. W. Green and S. McDevitt, J. Vac. Sci. Technol. **A7**, 300 (1989).
11. T. W. Weeks, Jr., M. D. Bremser, K. S. Ailey, E. Carlson, W. G. Perry, and R. F. Davis, Appl. Phys. Lett. **67**, 401 (1995).
12. M. E. Lin, B. N. Sverdlov, and H. Morkoç, J. Appl. Phys. **74**, 5038 (1993).

HALIDE VAPOR PHASE EPITAXY OF GALLIUM NITRIDE FILMS ON SAPPHIRE AND SILICON SUBSTRATES

N.R. Perkins[†], M.N. Horton[†], Z.Z. Bandic^{*}, T.C. McGill^{*}, and T.F. Kuech^{†,‡}

[†]University of Wisconsin, Materials Science Program, Madison, WI

^{*}California Institute of Technology, Department of Applied Physics, Pasadena, CA

[‡]University of Wisconsin, Dept. of Chemical Engineering, Madison, WI

ABSTRACT

A major limitation of the current technology for GaN epitaxy is the availability of suitable substrates matched in both lattice constant and thermal expansion coefficient. One alternative for the development of GaN substrates rests in the application of halide vapor phase epitaxy (HVPE) to produce GaN films at high growth rates. In this paper, we describe the growth of thick GaN films via the HVPE technique on (0001) sapphire and (111) Si substrates. At a temperature of 1030°C, films are grown at rates between 70 and 90 $\mu\text{m/hr}$, yielding total thicknesses exceeding 200 μm on sapphire. DCXRD measurements of GaN/sapphire indicate FWHM values less than 220 arcsec on 180 μm thick films. Room temperature PL measurements of GaN/sapphire indicate strong emission at 3.41 eV, with a FWHM value of 65 meV. Moreover, no detectable deep level emission was found in room temperature PL measurement. Under optimized conditions, films are morphologically smooth and optically clear. The GaN morphology appears to be a strong function of the initial nucleation conditions, which in turn are strongly affected by the partial pressure of GaCl. HVPE growth on (111) Si substrates is accomplished using an AlN MOVPE buffer layer.

INTRODUCTION

The nitride family of wide bandgap semiconductors, including GaN and its associated alloys with AlN and InN, have recently gained prominence as proven materials for blue-green light emitting diode devices [1,2,3,4] and as promising candidates for blue-green laser devices. Despite rapid technological progress in the field, a number of basic scientific issues must be resolved to understand the broader applicability of the nitride family of semiconductors in visible light emitting devices. Many of the current materials efforts revolve around problems arising from the use of heteroepitaxial substrates in the growth of GaN-based devices. The most widely used substrate for the growth of nitride-based devices has been (0001) sapphire. However, sapphire suffers from a poor lattice match and substantial coefficient of thermal expansion difference with GaN, leading to the formation of threading defects in the epitaxial layer and fracture of thick layers during cooldown. Existing nitride device structures possess dislocation densities on the order of 10^{10} cm^{-2} , which is an extremely high value by conventional arsenide and phosphide device standards [5]. The relationship between dislocation density and nonradiative recombination in the nitride semiconductors is not fully understood at present, but does not impede the efficient performance of some devices [5]. The GaN/sapphire system also suffers from nucleation problems, which can be ameliorated by the application of a thin low temperature buffer layer of GaN or AlN [6,7]. Alternatively, thick GaN layers produced via the HVPE technique on heteroepitaxial substrates may be used as GaN homoepitaxial substrates [8]. Studies by other researchers suggest that the application of thick GaN films for homoepitaxial

growth of MOVPE GaN films may lead to improved optical and crystalline characteristics as well as improved p-doping behavior on the epitaxial films [9].

EXPERIMENTAL PROCEDURE

All GaN growths were carried out in an atmospheric-pressure clear fused quartz HVPE reactor, equipped with separate annular injection for the reaction gases. The HVPE technique has been discussed by a number of authors [10,11,12,13]. The reactor is heated in a conventional hot wall furnace, with three independent temperature control zones. The first reaction zone was maintained at a temperature of 850°C. MBE-grade 99.9999% Ga metal was loaded in the quartz boat, and high grade HCl gas was reacted with the Ga metal to produce GaCl and hydrogen. The observed extent of reaction for the GaCl reaction was typically in the range of 50-70%, based on measurement of the HCl flow rate and the initial and final Ga metal mass. In the second zone (typically maintained at approximately 1030°C) ammonia was introduced through a separate annular injection line, leading to the formation of GaN on the substrate. Nitrogen carrier gas was used to achieve a total flow rate of 10 slpm (mean gas phase velocity of 21 cm/sec). The ratio of NH_3 to HCl was maintained at 30:1, and the flow rate of HCl was typically 10 sccm. Sapphire substrates of the (0001) orientation are used for the HVPE deposition. The sapphire substrates are degreased, then loaded into the reactor under an atmosphere of flowing nitrogen gas. The growth step is initiated by simultaneous introduction of the HCl and ammonia gases. The samples were slowly withdrawn from the hot zone under an ammonia atmosphere after growth. In cases where an AlN buffer layer is used on Si substrates, the buffer layer has been produced in a conventional inductively-heated horizontal low pressure MOVPE reactor.

RESULTS AND DISCUSSION

Nucleation processes depend, in part, on the partial pressure of the condensing species. The initial nucleation density in the heteroepitaxial GaN system may similarly depend on the partial pressure of the reactant species and growth temperature. The initial nucleation of the GaN film is a determining factor in the subsequent crystalline properties of the GaN. Several experiments are presented investigating this nucleation process.

A. HVPE GaN on sapphire

Experiments have been completed to determine the effect of growth temperature and GaCl partial pressure (at a fixed V/III ratio of 30.0) on the growth rate of the HVPE GaN films. An approximately linear growth rate dependence was observed on the GaCl partial pressure, with a growth rate of approximately 0.5 $\mu\text{m}/\text{min}$ at a GaCl partial pressure of 1×10^{-3} torr. The growth rate of GaN only exhibits a minor dependence on temperature, indicating that the process is probably diffusion controlled.

The double crystal x-ray diffractometry (DCXRD) and photoluminescence results for the GaN films on sapphire indicate a dependence of film quality on temperature (Figures 1a and 1b). An optimum crystallinity is observed between approximately 1030 and 1050°C. Similarly, the FWHM values of the photoluminescence spectra exhibit a rapid decrease after approximately 960°C, indicating improvement in the film optical quality. These experiments show approximate optimum operating parameters for this specific reactor geometry, and are in relatively good agreement with other published results [14].

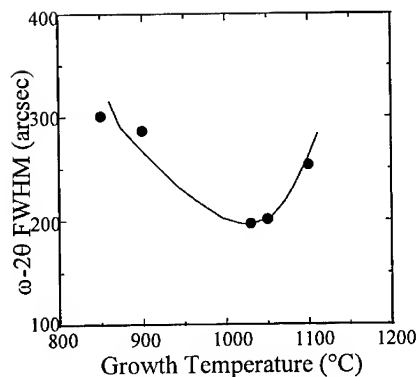


Figure 1a: Dependence of GaN DCXRD FWHM with Growth Temperature (20 μ m film thickness, $T_{gr}=1050^{\circ}\text{C}$)

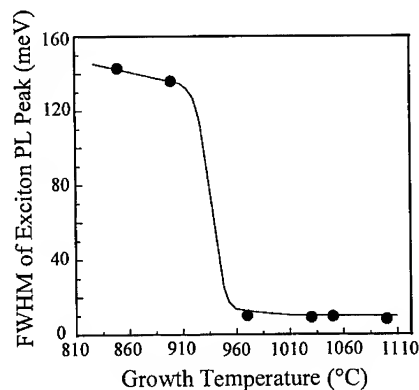


Figure 1b: Dependence of PL Exciton FWHM with Temperature (20 μ m film thickness, $T_{gr}=1050^{\circ}\text{C}$)

The thick HVPE GaN films are nearly specular, with occasional very large hexagonal surface features. At the optimum growth temperatures, product films are nearly transparent, even at thicknesses approaching 200 μ m. Under non optimum growth conditions, occasional pits are noted along the surface. These pits vary in size and distribution. Increasing the partial pressure of the GaCl reactant appears to greatly reduce the density of such surface pits. As expected, the difference in the coefficient of thermal expansion between the sapphire and the GaN film produces great stresses as the films are cooled. Films grown above a thickness of about 20 μ m invariably exhibit cracking in either or both the epilayer and the substrate (see Figure 2). Growth of very thick GaN epilayers results in cracking primarily in the substrate rather than in the epilayer. It may be possible to utilize very thin sapphire substrates, so that the strain is primarily in the substrate, which would further limit cracking in the epilayer.

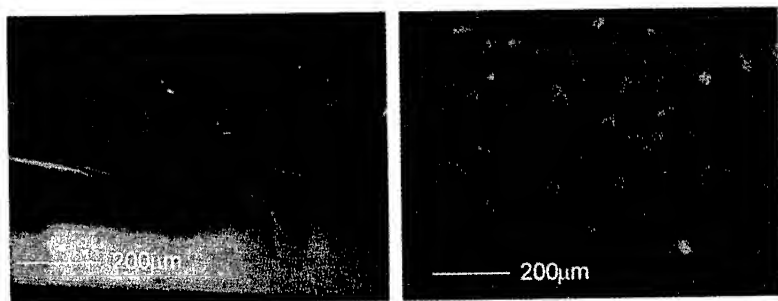


Figure 2: Cross-section and plan Nomarski micrographs of thick GaN on sapphire

The GaN film thickness had a significant effect on the measured film crystallinity. Both ω -rocking curves and ω -2 θ rocking curves were used to characterize the GaN films as a function of thickness (see Figure 3). GaN epitaxial films typically exhibit a small mosaic spread in the epitaxial film [15]. The FWHM obtained through a conventional ω scan is due primarily to the variation in the mosaic spread. Measurement of the FWHM using an ω -2 θ scan leads to broadening attributable to variations in the lattice parameter (i.e., degree of strain) [16]. As shown in Figure 3, the relatively large FWHM value obtained in the ω scan compared to the ω -2 θ scan illustrates the relatively high degree of mosaic misorientation in the epitaxial film compared to the relatively narrow distribution in lattice spacing. From Figure 3, it is apparent that increasing film thickness primarily leads to improvements in film crystallinity by reducing the degree of rotational misorientation in the epitaxial films.

Photoluminescence characterization of a thick HVPE film is shown in Figure 4. These results indicate that the optical quality of the thick GaN HVPE film rivals the best GaN MOVPE films. Moreover, while many reports for HVPE and MOVPE GaN display deep yellow luminescence around 550 nm, it is significant that our HVPE films show an absence of deep luminescence in this region. Additional research is required to understand the mechanisms for the improvements observed in the film optical characteristics.

B. Effect of GaCl Partial Pressure on Film Properties

The morphology of the GaN epilayers was found to be a strong function of the partial pressure of GaCl during the film growth. In general, increased partial pressures of GaCl resulted in improved film morphologies. Very low partial pressures of GaCl frequently led to the formation of discontinuous hexagonal films. As the partial pressure of GaCl increased, the film morphology was observed to improve dramatically, until the resulting film became fairly specular and transparent at a partial pressure of GaCl of about 2.5×10^{-3} torr. The higher pressure of GaCl during the nucleation step is expected to lead to

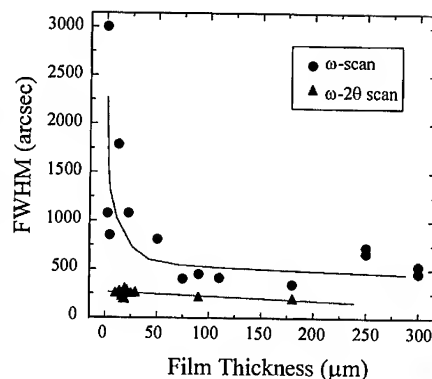


Figure 3: X-ray characterization of GaN films as a function of thickness

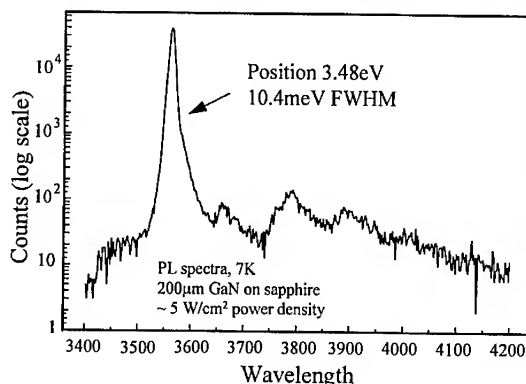


Figure 4: Low temperature PL spectra for GaN/sapphire

an increased nucleation rate on the sapphire, promoting more complete coverage of the sapphire at an earlier thickness.

C. HVPE GaN on Silicon

The growth of GaN on the (111) face of silicon was also examined. Growth of GaN on Si followed by *in-situ* backside etch of the Si substrate is one possible route to the formation of GaN substrates. While promising, this approach appears to be complicated by the formation of intermediate compounds at the growth interface. Growths of HVPE GaN directly on Si have resulted in polycrystalline deposition, probably due to silicon oxides and/or nitrides at the growth interface. Thermodynamic calculations indicate the favorability of forming volatile silicon chloride and nitrides at the free surface of the substrate (see Figure 5). To counter this problem, we have utilized high temperature AlN buffer layers on Si substrates produced via the MOVPE process. Attempts to produce AlN buffer layers at low growth temperatures invariably resulted in specular films that were determined to be polycrystalline by RHEED analysis. However, AlN films deposited at higher temperatures showed good crystallinity by RHEED. This result is similar to the report of Watanabe *et al.* [17]. Meyerson *et al.* have shown that fairly high temperatures may be required to achieve an oxide-free surface on the silicon [18], depending the partial pressures of water present in the growth system. By application of an AlN buffer layer, we were able to deposit smooth GaN films via HVPE. However, the HVPE films still suffered from cracking problems arising from the coefficient of thermal expansion mismatch between the silicon and the GaN film. In addition, any cracks or pinholes in the AlN buffer layer were attacked in the HVPE atmosphere (see Figure 6), producing deposits that were identified by EDS

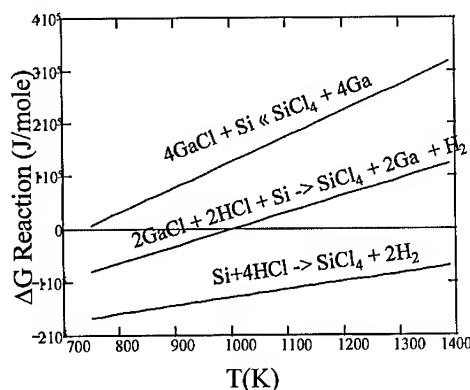


Figure 5: Free energy calculations in the Ga-Si-HCl system

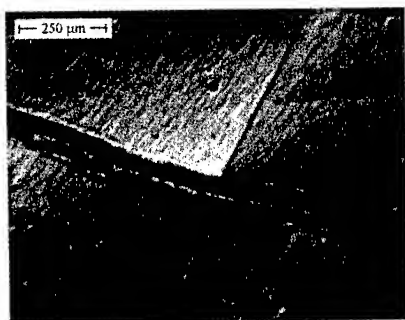


Figure 6: Nomarski micrograph of GaN/AlN/Si structure after HVPE growth

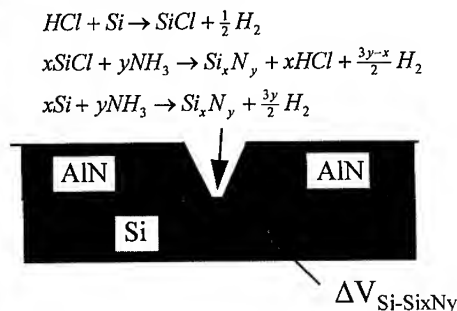


Figure 7: Mechanism for corrosion of AlN/Si substrates at cracks in buffer layer

and Auger analyses as rich in Si and N. A possible mechanism for the formation of these deposits at cracks in the buffer layer involves the attack of silicon by chloride species, forming volatile silicon chlorides which then react with ammonia, forming silicon nitrides. Alternatively, surface diffusion of Si may result in the formation of these compounds. In either case, the volume expansion between the original silicon and the silicon nitride results in delamination of the AlN buffer, resulting in further corrosive attack, as illustrated in Figure 7. This surface morphology, indicative of a multiphase mixture, precluded any detailed characterization. Future efforts will be directed at minimizing these strain-related defects.

CONCLUSIONS

GaN epitaxial films were grown by the HVPE technique on sapphire and silicon substrates. Excellent optical and electrical characteristics are obtained for the films, with DCXRD measurements of GaN/sapphire indicate FWHM values less than 220 arcsec on 180 μm thick films and 7K photoluminescence showing near-band emission at 3.48 eV with a FWHM value of 10.4 meV. Moreover, no detectable deep level emission was found in room temperature PL measurements at low pump power densities. GaN morphology appears to be a strong function of the initial nucleation conditions and the partial pressure of GaCl. HVPE growth on (111) Si substrates is accomplished using an AlN MOVPE buffer layer. The morphology of these films was dominated by nitride formation at cracks and pinholes in the buffer layer.

ACKNOWLEDGMENTS

The authors would like to acknowledge and thank the ARPA URI on Visible Light Emitters and the Naval Research Laboratory for support of various aspects of this work.

REFERENCES

1. H. Amano, M. Kito, K. Hiramatsu, and I. Akasaki, *Jpn. J. Appl. Phys.* **28**, p. L2112-L2114 (1989).
2. S. Nakamura, T. Mukai, and M. Senoh, *Jap. J. Appl. Phys.* **30**, p. L1998-L2001 (1991).
3. S. Nakamura, M. Senoh, and T. Mukai, *Jpn. J. Appl. Phys.* **32**, p. L8-L11 (1993).
4. S. Nakamura, T. Mukai, and M. Senoh, *Appl. Phys. Lett.* **64**, p. 1687-1689 (1994).
5. S.D. Lester, F.A. Ponce, M.G. Craford, and D.A. Steigerwald, *Appl. Phys. Lett.* **66**, p. 1249-1251 (1995).
6. I. Akasaki, H. Amano, Y. Kiode, K. Hiramatsu and N. Sawaki, *J. Crystal Growth* **98**, p. 209-219 (1989).
7. H. Amano, I. Akasaki, K. Hiramatsu, N. Kiode and N. Sawaki, *Thin Solid Films* **163**, p. 415-420 (1988).
8. T. Detchprohm, K. Hiramatsu, N. Sawaki, and I. Akasaki, *J. Crystal Growth* **137**, p. 170-174 (1994).
9. T. Detchprohm, K. Hiramatsu, N. Sawaki, and I. Akasaki, *J. Crystal Growth* **145**, p. 192-196 (1994).
10. H. Maruska and J. Tietjen, *Appl. Phys. Lett.* **15**, p. 327 (1969).
11. T. Detchprohm, K. Hiramatsu, H. Amano, and I. Akasaki, *Appl. Phys. Lett.* **61**, p. 2688-2690 (1992).
12. O. Lagerstedt and B. Monemar, *J. Appl. Phys.* **45**, p. 2266-2272 (1974).
13. J.I. Pankove, J.E. Berkeyheiser, and E.A. Miller, *J. Appl. Phys.* **45**, p. 1280-1286 (1974).
14. K. Naniwae, S. Itoh, H. Amano, K. Itoh, K. Hiramatsu, and I. Akasaki, *J. Crystal Growth* **99**, p. 381-384 (1990).
15. I. Nikitina and V. Dmitriev, (*Inst. Phys. Conf. Ser.* 141, San Diego, CA, 1994), p. 431-436.
16. N. Itoh and K. Okamoto, *J. Appl. Phys.* **63**, p. 1486-1493 (1988).
17. A. Watanabe, T. Takeuchi, K. Hirose, H. Amano, K. Hiramatsu, and I. Akasaki, *J. Crystal Growth* **128**, p. 391-396 (1993).
18. B.S. Meyerson, E. Ganin, D.A. Smith, and T.N. Nguyen, *J. Electrochem. Soc.* **133**, p. 1232-1235 (1986).

AlN FILMS DEPOSITED BY LP-MOCVD ATOMIC LAYER DEPOSITION AT LOWER TEMPERATURES USING DMEAA AND AMMONIA

J.N. KIDDER, JR., J. S. KUO*, T.P. PEARSALL, J.W. ROGERS, JR.*

Department of Materials Science and Eng., University of Washington, Seattle, WA 98195

Department of Chemical Engineering*, University of Washington, Seattle, WA 98195

ABSTRACT

We have investigated the deposition of AlN thin films on Si(100), Al₂O₃(0001), and Al₂O₃(01 $\bar{1}$ 2) substrates at lower temperatures (523-723 K) using a novel aluminum source, dimethylethylamine:alane (DMEAA), with ammonia as a nitrogen source in a low-pressure MOCVD atomic layer growth process. At reactor pressures of 25 and 50 Torr a four-step sequence of reactant flow steps separated by flush steps was cycled. We observed a tendency toward a self-limiting growth rate as the DMEAA step flow time was increased. The deposition uniformity was observed to be dependent on temperature and non-uniform deposition occurred at higher temperatures. The microstructure and crystalline orientation were examined using x-ray diffraction and crystalline AlN films were deposited at temperatures as low as 573 K. Crystallite size decreased with substrate temperature and at 523 K amorphous films were deposited. At T > 650 K preferentially oriented crystalline films were deposited with orientations of Si(100)/AlN(0001), Al₂O₃(0001)/AlN(0001), Al₂O₃(01 $\bar{1}$ 2)/AlN(11 $\bar{2}$ 0).

INTRODUCTION

Conventional processes for depositing epitaxial AlN require high temperatures (>1400K) which are incompatible with many of the other materials processing techniques that are used in fabricating integrated circuits and other devices. When a process is developed for depositing single crystal AlN thin films at temperatures below 800K (527 °C) then it can be more easily integrated with other materials to exploit its exceptional electrical and mechanical properties. Many methods have been used to deposit AlN thin films including conventional chemical vapor deposition (CVD) plasma enhanced CVD, sputtering techniques and reactive molecular beam epitaxy.[1-4] Significant advances towards depositing high quality AlN thin films have been made using metalorganic chemical vapor deposition (MOCVD) techniques.[5, 6] This work investigates the deposition of AlN thin films at temperatures below 800 K by MOCVD using an atomic layer deposition (ALD) technique with ammonia and a specially chosen metalorganic precursor in an near-atmospheric MOCVD reactor.

Aluminum metalorganic precursors to AlN can be categorized into three groups; trialkyl aluminum sources, single source precursors that contain bonded Al-N in the molecule, and alane adduct compounds. Tri-alkyl aluminum sources such as trimethylaluminum (TMAI) and triethylaluminum (TEAI), are the most common metalorganic source gases for depositing Al-containing compound thin films.[7] These compounds have been commercially available for many years and have the advantage of being relatively inexpensive and widely available. A second type of Al source for AlN deposition are single-source precursors, such as amide and azide based compounds, that contain aluminum and nitrogen bonded to each other within the molecule.[8-11]

A third class of Al precursor, and the type that is employed in this research, is the alane adduct compounds. Compounds of alane (AlH₃) adducted to an amine group provide a way to transport alane to the deposition surface.[12] At the heated surface the two molecules easily dissociate and the alane is left on the surface while the amine group is pumped away or exchanged with another reactant molecule such as ammonia.[13] Alane adduct molecules dissociate easily at low temperatures (373 K) and these sources have been used to deposit high quality films at temperatures lower than those required by other precursors.[14, 15] Alane adducts have been successfully used to deposit high purity films of Al, AlAs, Al_xGa_{1-x}As.[15, 18-20] Recently our group and other researchers have reported the deposition of III-V nitride thin films using alane adducts as the aluminum source.[21-23] Dimethylethylamine:alane (DMEAA; (CH₃)₂C₂H₅N:AlH₃) is a liquid alane adduct compound with a relatively high vapor pressure (1.5

Torr (DMEAA) at 20 °C), making it suitable for CVD processes.[16, 17] We recently reported the deposition of AlN thin films using DMEAA and ammonia in an atmospheric MOCVD process.[22]

In a typical ALD process, source gases are alternately introduced to the substrate surface by methods such as switching gas flows in a sequential manner or using a rotating the substrate under the flow of separate gas streams.[5, 24] Under proper conditions adsorption of the reactant species to the surface is self-limiting to a single monolayer per reactant step. Through these self-limiting surface reactions a film can be deposited one atomic layer at a time. Although the growth rates can be inherently low, the nature of the process makes it particularly effective for creating abrupt interfaces and heterostructures and for depositing material of high crystalline quality at lower temperatures.[25, 26]

One cycle of a typical ALE process for depositing a binary compound consists of 4 steps: 1.) a pulse of reactant 1 for A seconds, 2.) a flush of pure carrier gas for B seconds, 3.) a pulse of reactant 2 for C seconds, 4.) a flush of pure carrier gas for D seconds. A process is commonly labeled by the pulse duration and this sequence would then be an A-B-C-D process. In the experiments reported here, DMEAA is employed with ammonia as the nitrogen source. The ALD technique was chosen in order to minimize gas phase reactions between the DMEAA and ammonia and to promote site selective surface reactions which can lead to more ordered growth at lower temperatures.

EXPERIMENTAL

The deposition is carried out in a horizontal laminar flow all-quartz near-atmospheric MOCVD reactor equipped with three-way flush valves. The reactor was operated at 25 - 100 Torr using purified H₂ as a carrier gas. The substrates were placed on a SiC coated susceptor and heated with rf induction. Deposition was done on Si(100), Al₂O₃(0001), Al₂O₃(01 $\bar{1}$ 2) substrates. The substrates were prepared for deposition by a standard degreasing procedure using TCA, acetone, methanol and deionized H₂O. The Si wafers were oxide etched in 10% (by volume) aqueous HF solution and air dried immediately before loading into the reactor. The substrates were heated to 1083 K (810 °C) under a H₂ flow for 10 minutes prior to starting the ALD process. The DMEAA was contained in a stainless steel bubbler and held at 293 K during processing. The bubbler was stored at 280 K to suppress decomposition of the precursor.

In our experiments we have explored deposition at a range of conditions. The total flow through the reactor was 2.4 - 6.0 slm and was held constant during each of the process steps. We used gas velocities of 6 - 50 cm/s, DMEAA partial pressures of 2.9 - 24.6 mTorr and ammonia partial pressures of 1.8 - 15.4 Torr with a constant V/III of 620. The H₂ flow through the bubbler was 0.3 slm and the NH₃ flow into the reactor was 0.3 slm. Details of the reactor system and process were previously described.[22]

RESULTS AND DISCUSSION

One way of examining the kinetics of the film formation mechanism in an ALD process is to observe how the growth rate is affected by the duration of the reactant pulses. A self-limiting process will show a growth rate that reaches a limiting value, independent of the duration of the reactant pulse. The main interest is to find the conditions where the group III precursor reacts in a self-limiting manner; at non-ideal conditions, such as too high a temperature, the group III reactant could pyrolyze to the elemental species, prohibiting self-limiting adsorption and resulting in a growth rate that increases continuously with pulse duration.

Figure 1 shows the per-cycle growth rate versus DMEAA pulse length. The duration of the DMEAA pulse during each cycle was extended from 1 to 8 seconds for deposition runs at temperatures of 613, 673, 723 K. These data are taken from deposition runs done at 50 Torr using X-5-Y-5 ALD process where X,Y = 1 to 8 seconds. From these measurements we observe that extending the pulse from 1 to 4 seconds increases the growth rate by 3 times from approximately 0.1 to 0.3 nm/cycle. However, when the pulse length is extended from 4 to 8 seconds the growth rate only increases from 0.3 to 0.4 nm/cycle. This shows a tendency for the process towards self-limiting growth at approximately 0.4 nm/cycle. The per-cycle growth rate is relatively independent of temperature but was observed to decrease slightly as the temperature increases from 673 to 723

K. The growth rate was calculated from thickness values obtained by ellipsometry measurements. During initial experiments done with smaller substrates (< 20 mm) it was observed that the growth rate was highest at the upstream end of the substrate and that uniformity improved with decreasing reactor pressure. Experiments were done on larger wafers to investigate the growth rate uniformity.

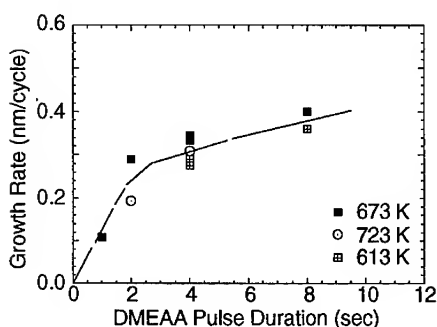


Figure 1 Growth rate vs. Pulse duration

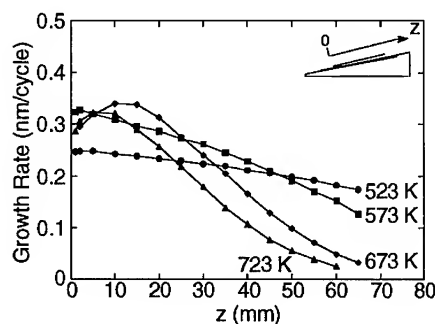


Figure 2 Growth rate vs. Position

Figure 2 shows the per-cycle growth rate versus position on substrate for deposition done on Si(100) substrates at 25 Torr and a gas velocity of 29 cm/s using a 4-5-4-5 ALD process. The position parameter z is along the direction of the gas flow starting at the upstream end of the substrate, as diagrammed in the figure. At higher temperatures of 723 and 673 K the growth rate is highest at the upstream end and decreases rapidly as you move back on the substrate. The maximum growth rate is relatively independent of temperature and is limited to a value slightly above 0.3 nm/cycle. The uniformity improves with decreasing temperature and at 523 K the maximum growth rate, as observed at the upstream edge of the substrate, drops to 2.5 Å/cycle. The non-uniformity can be attributed to a depletion of the reactant concentration in the gas stream with position in the reactor. The growth rate profile at the upstream edge ($z < 10$ mm) originates from complex hydrodynamics where the gas stream first meets the heated substrate. The decrease in the growth rate from 10 mm and 70 mm is due to a depletion in the reactant concentration. The process is mass-transport limited at the higher temperatures where the growth rate is limited by a depletion of the reactant concentration. At 523 K the growth rate profile is more uniform and the maximum growth rate has decreased, indicating a more kinetically limited process.

Using a 4-5-4-5 ALD process crystalline AlN films have been deposited on Si and Al_2O_3 substrates at temperatures as low as 573 K. These crystalline films were observed to be preferentially oriented with respect to the substrate although the microstructure is dependent on the substrate temperature during deposition. Figure 3 shows an x-ray diffraction θ - 2θ scan of an AlN thin film deposited on Si(100) at 673 K and 50 Torr using a 4-5-4-5 ALD process run for 120 minutes. The film is approximately 130 nm thick as measured by ellipsometry. Diffraction peaks from the Si(400) and Si(200) planes are observed. There is also a diffraction peak corresponding to the AlN(0002) at 2θ of 36.0° . No other diffraction peaks from AlN are observed which signifies a planar orientation of AlN(0001)//Si(100).

Figure 4a and 4b show diffraction scans from AlN films deposited on two different orientations of Al_2O_3 . Figure 4a is a θ - 2θ scan of AlN thin film on $\text{Al}_2\text{O}_3(0001)$. Diffraction is observed from the single crystal Al_2O_3 substrate and the AlN(0002) planes as a diffraction peak at 35.9° . This corresponds to a planar orientation of AlN(0001)// $\text{Al}_2\text{O}_3(0001)$. Figure 4b is a θ - 2θ scan of AlN thin film on $\text{Al}_2\text{O}_3(01\bar{1}2)$. Diffraction is observed from the single crystal Al_2O_3 substrate and the AlN(11 $\bar{2}$ 0) planes as a diffraction peak at 59.3° . This corresponds to a planar orientation of AlN(11 $\bar{2}$ 0)// $\text{Al}_2\text{O}_3(01\bar{1}2)$.

In the case of Si(100) no planes of the wurzite AlN lattice match well with this four-fold symmetric surface and energy is minimized by formation of the low energy AlN basal planes parallel to this surface. The lattice mismatch between AlN(0001) and Al₂O₃(0001) has been studied and determined to be 13.3%. Although this match is not very good, hexagonal symmetry of the Al₂O₃(0001) plane results in a preferred orientation of AlN(0001)//Al₂O₃(0001).[6, 27]

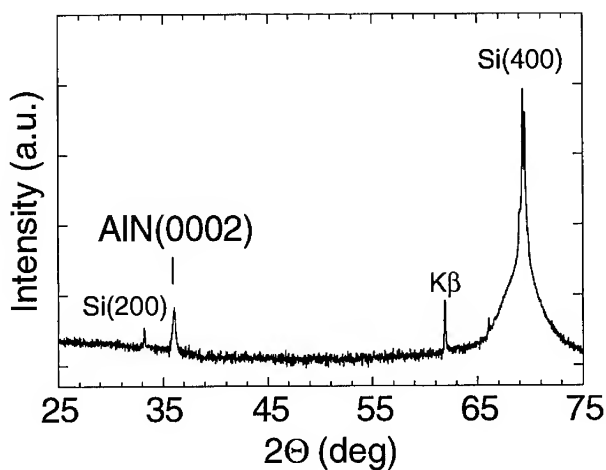


Figure 3 XRD of AlN on Si(100) with preferred orientation of AlN(0001)//Si(100)

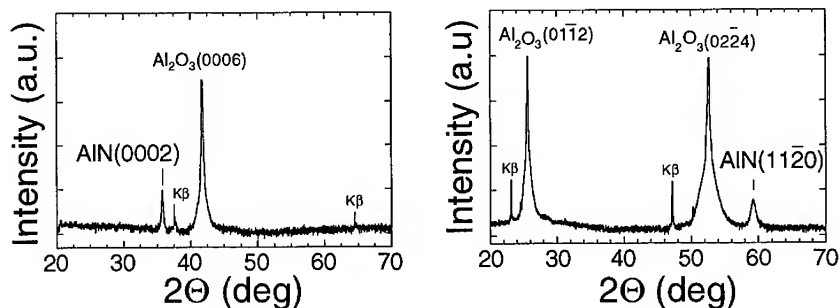


Figure 4a XRD of AlN on Al₂O₃(0001)

Figure 4b XRD of AlN on Al₂O₃(0112)

The preferred orientation of AlN on Al₂O₃(0112) has also been studied. [6, 28, 29] The commonly observed preferred orientation of AlN(1120)//Al₂O₃(0112) is also explained through lattice matching arguments where translation vectors in these two planes are mismatched by 1% and 15.4% in the two orthogonal directions.[29] In summary, our films show preferred planar crystallographic orientations that match those observed in processes done at temperatures above 1100 K.

The microstructure of these films were observed to change with growth temperature. Figure 5 shows x-ray diffraction θ - 2θ scans done on films deposited on Al₂O₃(0001) substrates at five different temperatures. As T decreases the AlN(0002) diffraction peak broadens fairly symmetrically. This broadening is attributed to a reduction in the size of the crystallites in the film.

In this case the size is for the dimension in the direction of the c-axis of the AlN crystal. All of these films are ~120-150 nm thick. The inset shows the FWHM and the crystallite size as calculated using the Scherrer relation is plotted versus T. At T>650 K we deposit films with crystallite sizes in the range of 40-50 nm. As the temperature decreases so does the crystallite size and at 523 K we observe no diffraction intensity, signifying an amorphous microstructure.

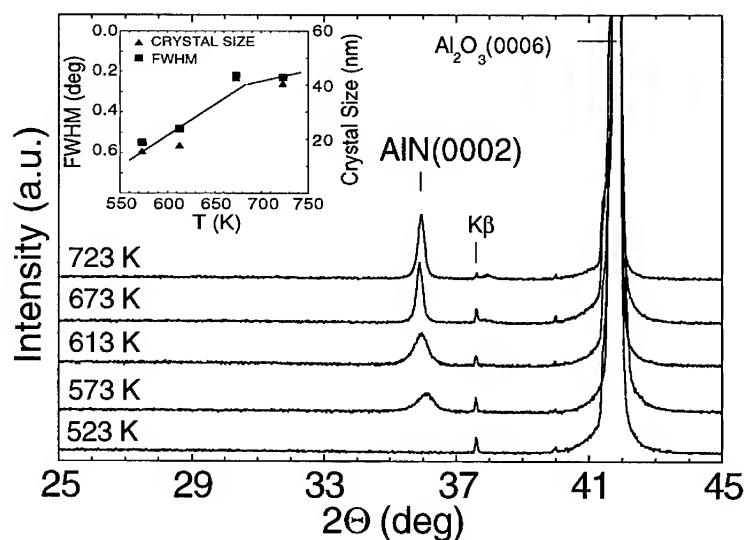


Figure 5 XRD scans of AlN on Al₂O₃(0001) deposited at 5 different temperatures.

We have used atomic force microscopy (AFM) to study the surface morphology. Inspection of the surface by AFM revealed surface features with dimensions of about 40 nm which we interpret as AlN crystallites.

CONCLUSION

In conclusion, DMEAA has been used in an atomic layer deposition process to deposit crystalline AlN thin films at temperatures as low as 573 K (300°C). This process can be used to deposit films with a range of microstructures and orientations. At temperatures above ~650K films are deposited on Si and Al₂O₃ substrates with preferred planar crystallographic orientations of Si(100)//AlN(0001), Al₂O₃(0001)//AlN(0001), Al₂O₃(01 $\bar{1}$ 2)//AlN(11 $\bar{2}$ 0). The strong dependency of the AlN thin film orientation on the substrate orientation demonstrates growth very similar to epitaxy at significantly lower temperatures.

REFERENCES

1. F. Hasegawa, T. Takahashi, K. Kubo and Y. Nannichi, Jpn. J. Appl. Phys. **26**, p. 1555 (1987).
2. F. S. Ohuchi and P. E. Russell, J. Vac. Sci. Tech. A **5**, p. 1630 (1987).
3. T. L. Chu and J. R.W. Kelm, J. Electrochem. Soc. **122**, p. 997 (1975).
4. Z. Sitar, M. J. Paisley, B. Yan, R. F. Davis, J. Ruan and J. W. Choyke, Thin Solid Films **200**, p. 311 (1991).

5. M. A. Khan, J. N. Kuznia, R. A. Skogman, D. T. Olson, M. MacMillan and W. J. Choyke, *Appl. Phys. Lett.* **61**, p. 2539 (1992).
6. H. M. Manasevit, F. M. Erdmann and W. I. Simpson, *J. Electrochem. Soc.* **118**, p. 1864 (1971).
7. G. B. Stringfellow, Organometallic vapor-phase epitaxy: Theory and practice, (Academic Press Inc., San Diego CA, 1989).
8. C. C. Amato, J. B. Hudson and L. V. Interrante, *Mat. Res. Soc. Symp. Proc.* **282**, p. 611 (1993).
9. W. L. Gladfelter, D. C. Boyd, J.-W. Hwang, R. T. Haasch, J. F. Evans, K.-L. Ho and K. Jensen, *Mat. Res. Soc. Symp. Proc.* **131**, p. 447 (1993).
10. L. V. Interrante, W. Lee, M. McConnell, N. Lewis and E. Hall, *J. Electrochem. Soc.* **136**, p. 472 (1989).
11. R. G. Gordon, U. Riaz and D. M. Hoffman, *J. Mater. Res.* **7**, p. 1679 (1992).
12. J. K. Ruff, *Inorg. Synth.* **9**, p. 30 (1967).
13. H. Liu, Ph.D. Thesis, University of Washington (1995).
14. W. L. Gladfelter, D. C. Boyd and K. F. Jensen, *Chem. Mater.* **1**, p. 339 (1989).
15. N. Ohtsuka, T. Ashino, M. Ozeki and K. Nakajima, in Gallium Arsenide and Related Compounds 1992, edited by T. Ikegami, F. Hasagawa and Y. Takeda, (Proceedings of the 19th International Symposium, IOP, Karuizawa, p. 925).
16. J. E. House, *J. of Organomet. Chem.* **263**, p. 267 (1984).
17. D. M. Frigo, G. J. M. v. Eijden, P. J. Reuvers and C. J. Smit, *Chem. Mater.* **6**, p. 190 (1994).
18. C. R. Abernathy, *J. Vac. Sci. Technol. A* **11**, p. 869 (1993).
19. W. S. Hobson, T. D. Harris, C. R. Abernathy and S. J. Pearton, *Appl. Phys. Lett.* **58**, p. 77 (1991).
20. K. Fujii, I. Suemune and M. Yamanishi, *Appl. Phys. Lett.* **62**, p. 1420 (1993).
21. M. A. Khan, D. T. Olson and J. N. Kuznia, *Appl. Phys. Lett.* **65**, p. 64 (1994).
22. J. N. Kidder, J. S. Kuo, A. Ludviksson, T. P. Pearsall, J. W. Rogers, J. M. Grant, L. R. Allen and S. T. Hsu, *J. Vac. Sci. Technol. A* **13**, p. 711 (1995).
23. D. C. Bertolet, H. Lui and J. W. Rogers, Jr., *J. Appl. Phys.* p. (1994).
24. M. A. Tischler and S. M. Bedair, *J. Cryst. Growth* **77**, p. 89 (1986).
25. M. A. Tischler and S. M. Bedair, in Atomic Layer Epitaxy, edited by T. Suntola and M. Simpson (Blackie and Sons, London, 1990) p. 145.
26. J. D. Dapkus, B. Y. Maa, Q. Chen, W. G. Jeong and S. P. DenBaars, *J. Cryst. Growth* **107**, p. 73 (1991).
27. C. J. Sun, P. Kung, A. Saxler, H. Ohsato, K. Haritos and M. Razezghi, *J. Appl. Phys.* **75**, p. 3964 (1994).
28. J. K. Liu, K. M. Lakin and K. L. Wang, *J. Appl. Phys.* **46**, p. 3703 (1975).
29. P. Kung, C. J. Sun, A. Saxler, H. Ohsato and M. Razezghi, *J. Appl. Phys.* **75**, p. 4515 (1994).

A MODELING STUDY OF GaN GROWTH BY MOVPE

S.A. Safvi*, J.M. Redwing**, M.A. Tischler**, T.F. Kuech*

*Department of Chemical Engineering, University of Wisconsin, Madison, WI 53706

**Advanced Technology Materials, Danbury, CT 06810

ABSTRACT

A model for the growth of gallium nitride in a vertical metalorganic vapor phase epitaxy reactor is presented. For a mixture of non-dilute gases, the flow temperature and concentration profiles are predicted. The results show that the growth of GaN epilayers is through an intermediate adduct of TMG and ammonia. Growth rates are predicted based on simple reaction mechanisms and compared with those obtained experimentally. Loss of adduct species due to polymerization leads to lowering in growth rate. An attempt to quantify loss of reacting species is made based on experimentally observed growth rates.

INTRODUCTION

The nitrides of gallium, aluminum, and indium have a great potential for applications in electronics and optoelectronic devices due to wide band gap range and stability at high temperatures. These nitrides have a direct bandgap ranging from 1.9 eV for InN to 6.3 eV for AlN. GaN with its bandgap of 3.4 eV is suitable for making devices operating in blue to ultraviolet range. The bandgap can be engineered by growing ternary alloys of these nitrides. Zhang et al. [1] measured the bandgap of $\text{Al}_x\text{Ga}_{1-x}\text{N}$ using room temperature optical transmission and absorption spectroscopy. By changing the solid composition x , they could obtain a tunable direct bandgap ranging from that of pure GaN to that of pure AlN.

One of the main challenges in the commercial development of GaN based opto-electronic devices has been the optimal design and operation of reactors suitable for growing such materials. Metalorganic Vapor Phase Epitaxy (MOVPE) has emerged as the premier growth technique. A great deal of effort is currently being devoted to the study of the chemical reactions underlying MOVPE of semiconductors [2]. A better understanding of the chemistry during GaN MOVPE can lead to accurate control of film properties, to increased reactor efficiencies, and to the development of new operating procedures for growing custom made films and microstructures. It will also enable the development of predictive models of the process, which can substantially reduce the time and cost associated with reactor scale-up by minimizing the required experimental trial and error.

In typical VPE, there is a dilute concentration of reactants in a carrier gas. For GaN MOVPE, however, there is large concentration of the nitrogen precursor (i.e. ammonia) required to stabilize the growth front. The species conservation equation of ammonia and the carrier gas (hydrogen in this case) has to be solved coupled to the heat, momentum, and continuity equations.

Adduct formation is a notorious problem in the MOVPE of GaN. These adducts polymerize [3] giving a cyclic compound which may lead to severely reduced growth rates. To alleviate this problem, the Group III and Group V flows are not mixed near the inlet but close to the susceptor. This probably provides a shorter time for the reactants to polymerize. Thon and Kuech [4] studied the formation of adduct using trimethylgallium (TMG) and ammonia in a flow-tube system. They found that the adduct formation was instantaneous. The adduct condensed below 120 °C and was

absent from the gas phase. The adduct-species decomposed at slightly higher temperatures than that associated with TMG decomposition.

In this study we will describe a vertical reactor used to grow MOVPE GaN films. The emphasis will be on studying different chemistries that may be feasible. Predicted growth rates are compared to experimentally observed rates to determine the chemistry underlying epitaxial GaN growth.

REACTOR MODEL & EXPERIMENTAL

A schematic of the reactor is shown in Figure 1. TMG in hydrogen carrier gas is supplied in the inner tube while ammonia and hydrogen are supplied in the outer tube. The outer wall of the reactor is water cooled. The graphite susceptor is heated inductively with a RF unit. The ID of the reactor is 85 mm and the OD of the two inlet tubes are 6.4 mm and 25.4 mm respectively. The inner tube is at a distance of 114 mm above the susceptor which is 70 mm in diameter. All runs were performed at a reactor pressure of 100 Torr and a susceptor temperature of 1000 °C. The coolant and the inlet gases were assumed to be at room temperature. The total flowrate was kept constant at 12 slm (2 slm of NH_3 and 10 slm of H_2) and the flowrate of TMG through the inner tube was kept at 0.748 sccm. The films were grown on 2" basal plane sapphire for a period of 1.5 hours. Two extreme cases were studied. In Case I, there was a high hydrogen flowrate of 5 slm through the inner tube. In case II, there was a comparatively low hydrogen flowrate of 0.2 slm in the inner tube. The balance of hydrogen in both cases flowing through the outer tube.

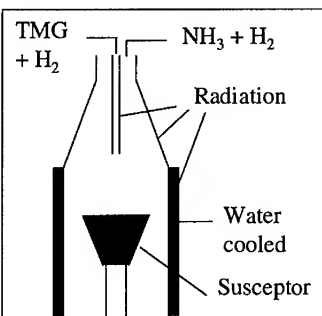


Figure 1: Diagram of the reactor

The flow, temperature, and concentrations are obtained in two dimensions. The properties of the gas mixture are determined at any point using the concentrated species and applying ideal mixing rules.

Cylindrical coordinates have been used in the model and the computational domain extends from 20 cm upstream of the substrate to 40 cm downstream. The fundamental equations of continuity, momentum, and energy balances and species conservation are used to describe the system [5]. With the assumption of no variation in circumferential direction, the flow, temperature, and concentrations are obtained in two dimensions. The properties of the gas mixture are determined at any point using the concentrated species and applying ideal mixing rules.

Physical and Transport Properties of Gaseous Species: Experimental values of thermal conductivity, specific heat, and viscosity of hydrogen [6] and ammonia [7] were fitted to obtain their functions of temperature listed elsewhere [8]. The Lennard Jones parameters obtained from experimental data were used whenever possible. For intermediate species, they were estimated using the method of group contributions [9]. Binary diffusion coefficients of gas phase species were either obtained from literature or estimated from their Lennard-Jones parameters. The thermal diffusion ratio of all the species were estimated using their Lennard-Jones parameters [10]. The values of the binary diffusion coefficient, Lennard-Jones parameters, and thermal diffusion ratios of all gaseous species used in this study are listed elsewhere [8]. The diffusion and thermal diffusion ratio of the dilute species at any point were computed the same way as the gas properties.

Chemistry Model: All the gas-phase reactions considered are listed in Table 1. Reactions G1, G2 and G3 are associated with pyrolysis of TMG [11]. Reaction G4 and G5 describe adduct

formation and adduct conversion to cyclic complex respectively [3]. G6 is the general reaction for thermal decomposition of adduct or the cyclic compound leading to products. For lack of data, the product is taken to be $\text{GaCH}_3\text{:NH}$. Thon and Kuech [4] measured the apparent kinetic parameters for this reaction, but they could not ascertain the exact nature of the species involved. Unity sticking coefficients are assumed for all Ga containing species on the hot substrate. The molar flux of these species at the surface is used to determine growth rates.

Reaction	Reactant \rightarrow Products	k_0 (1/s)	E_a (kcal/mol)	Ref
G1	$\text{Ga}(\text{CH}_3)_3 \rightarrow \text{Ga}(\text{CH}_3)_2 + \text{CH}_3\bullet$	3.5×10^{15}	59.5	11
G2	$\text{Ga}(\text{CH}_3)_2 \rightarrow \text{GaCH}_3 + \text{CH}_3\bullet$	8.7×10^7	35.41	11
G3	$\text{GaCH}_3 \rightarrow \text{Ga} + \text{CH}_3\bullet$	1.0×10^{16}	77.5	11
G4	$\text{Ga}(\text{CH}_3)_3 + \text{NH}_3 \rightarrow \text{Ga}(\text{CH}_3)_2\text{:NH}_2 + \text{CH}_4$	collision limited		4
G5	$3\text{Ga}(\text{CH}_3)_2\text{:NH}_2 \rightarrow [\text{Ga}(\text{CH}_3)_2\text{:NH}_2]_3$	-		3
G6	$\text{Ga}(\text{CH}_3)_2\text{:NH}_2 / [\text{Ga}(\text{CH}_3)_2\text{:NH}_2]_3 \rightarrow \text{Product}$	4×10^{13}	50.5	4

TABLE 1: List of gas phase reactions, their kinetic parameters and literature reference.

Numerical Solution: The system of partial differential equations describing flow, heat transfer, mass transfer, and chemical reactions was solved using the Galerkin finite-element method [13]. A typical mesh consisted of 1100 trapezoidal elements with the mesh being denser near the susceptor where the concentration and temperature gradients are larger. The system of nonlinear algebraic equations obtained after the application of Galerkins technique was solved by using the Newton's method. The system of equations and numerical methodology is presented in detail elsewhere [8]. The computations were performed on a Cray C90 supercomputer.

RESULTS AND DISCUSSION

The pathlines and temperature profiles in the reactor are shown for the two cases. Figure 2(a) shows the pathlines for case I, while Figure 3(a) shows the pathlines for case II. The corresponding temperature profiles are shown in Figure 2(b) and Figure 3(b) respectively. The recirculation patterns are closer to the susceptor for higher inner jet flowrates. High flowrate (12 slm) in the reactor leads to recirculations above the susceptor. These recirculations could lead to trapping of particulate matter, which may subsequently end up on the film, and also lead to transport of material from the wall to the substrate. The recirculations were geometry driven and they existed even at room temperature at the same process flowrates. One way of removing these recirculations is lowering the flowrate which would mean more time for parasitic polymeric reactions. Also, it leads to increase in the temperature upstream of the susceptor leading to premature decomposition of the reactants. Lowering pressure could also decrease the severity of recirculations at the expense of lower growth rates. Besides, it may lead to higher nitrogen desorption from the surface.

The temperature profile for Case II is flat (uniform) above the substrate. For case I, the temperature profiles are compressed near the center of the substrate, because of the high velocity of the inner jet (~ 50 m/s at 100 Torr). Since the recirculation patterns are close to the edge of the substrate, there is an expansion of isotherms. The homogeneous gas phase decomposition may not play a role for deposition at the center of the substrate for Case I, instead the adduct species may decompose mainly on the surface.

The growth of an epitaxial GaN film takes place as a result of gas phase and surface reactions.

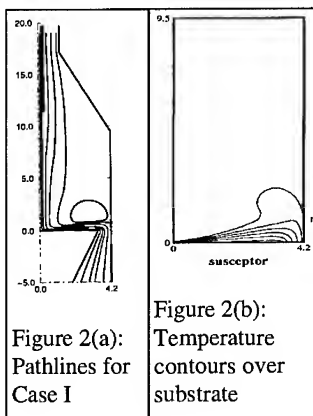


Figure 2(a):
Pathlines for
Case I

Figure 2(b):
Temperature
contours over
substrate

To determine the species that reach to the surface, we tried to determine the amount of TMG that pyrolyzes before it forms an adduct with ammonia. Elimination of species due to surface reactions is not considered. For Case I, Figure 4 shows the product of TMG pyrolysis (i.e. $\text{Ga}(\text{CH}_3)_2$, GaCH_3 , and Ga) along the substrate surface, according to gas-phase reactions G1-G3 when the

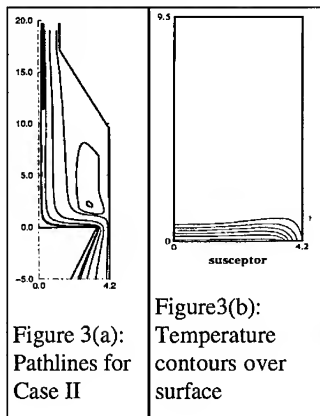


Figure 3(a):
Pathlines for
Case II

Figure 3(b):
Temperature
contours over
surface

adducts reaction G4 is not taken into consideration. If we consider reactions G1-G4, then all TMG forms adducts before pyrolysis can occur even for the case with the higher inner jet velocity (5 slm) and the lower residence time. Figure 4 also shows the resulting adduct concentration along the surface. Negligible amount of TMG, and its pyrolysis products reached the surface. This is expected because of the high amounts of ammonia present in these reactors and points to fact that growth of GaN is due to decomposition of the $(\text{TMG}:\text{NH}_3)$ -based adduct. It is important therefore to understand the decomposition pathways of such species. Even for the case with no consumption due to surface reaction, the adduct concentration decreases radially along the substrate due to dilution from the second inlet stream. Unlike conventional CVD, low conversion of reactants (e.g. lower temperature GaN buffer layer growth) would not guarantee uniform growth across the substrate.

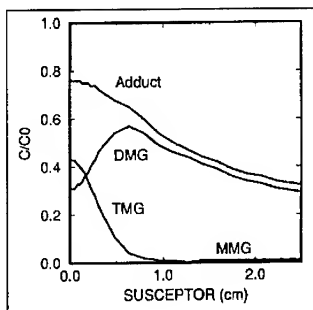


Figure 4: Concentraion profiles along substrate normalized by inlet TMG concentration (C_0). TMG, DMG, MMG profiles obtained for reactions G1-G3. Only adduct profile obtained for reactions G1-G4

The $(\text{TMG}:\text{NH}_3)$ adducts condenses at temperatures below 90°C [4]. Above 120°C and a pressure of 450 Torr, Almond et al. [3,12] have reported the formation of a cyclic compound $[\text{Ga}(\text{CH}_3)_2:\text{NH}_2]_3$, as represented by reaction G5 in Table 1. This cyclic compound is much larger and the thermal diffusion ratio is much higher than that for TMG. We would thus expect the formation of cyclic compound to lower the growth rate. The mechanism by which the cyclic compound affects the growth and quality of the film is not known in detail. To improve our understanding we have compared the following to experimental results: (A) calculated growth rates assuming

adduct does not polymerize (ideal growth), and (B) calculated growth rate assuming all adduct instantaneously forms the cyclic compound, which decomposes similarly to the adduct. Figures 5 and 6 show the predicted growth rate along the susceptor based on these assumptions, for Case I and II respectively. For Case I the thermal gradients close to the surface are large near the center of the substrate (Figure 2(b)). The growth rate from cyclic compound (B) is not only less than the ideal value (A), but also less than the experimental values. If all the adduct does not polymerize

before it reaches the substrate, it would lead to growth rates observed experimentally. Radially along the substrate, the growth rate (B) increases due to two reasons. The thermal gradients decrease and the compound has time to decompose to smaller products which are less sensitive to thermal gradients. After reaching a maximum, the growth rate (B) decreases due to depletion of reactants from consumption and dilution. For case II, the inner jet velocities are lower and the adduct has time to decompose. The predicted growth rate from the cyclic compound (B), is still higher than experimental values for the same process conditions. The experimental

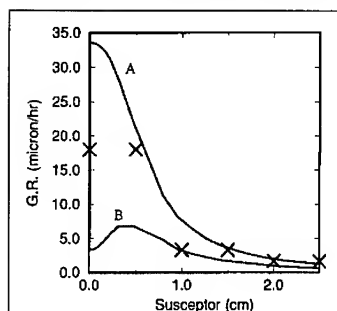


Figure 5: Plot of growth rate along the susceptor for Case I. Curve (A) corresponds to ideal growth, (B) to growth from cyclic compound while (x) are experimental values

observation can be rationalized if either some of the adduct polymerizes to species larger than the cyclic compound, or if the decomposition products of the cyclic compound led to lower growth rate.

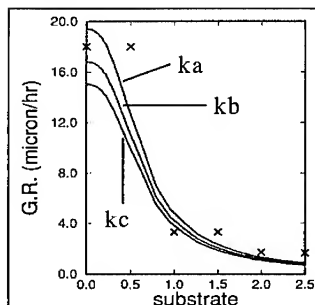


Figure 7: Growth rates along substrate for Case I. k_a , k_b and k_c are 1.0 , 1.5 , and $2 \times 10^{20} \text{ cm}^6 \text{ mol}^{-2} \text{ s}^{-1}$ respectively. (x) are the experimental values.

A numerical model of the vertical MOVPE GaN reactor has been presented. This model predicts the flow patterns, temperature, and concentration distribution in the reactor. We determined that since the precursors form an adduct species before they pyrolyze, the growth rate is determined by the decomposition of adducts and not TMG or NH_3 . Growth rates based on

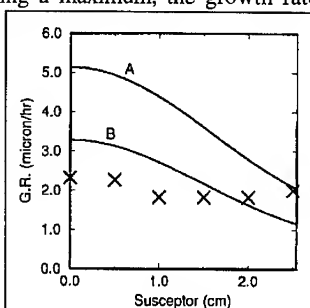


Figure 6: Plot of growth rate along the susceptor for Case II. Curve (A) corresponds to ideal growth, (B) to growth from cyclic compound while (x) are experimental values

On the other end of the spectrum, we have considered the case where cyclic compounds formed would not lead to growth. This is used to quantify the amount of adduct lost to polymerization in the reactor. Previous work (4) indicated that this reaction could be collision rate dependent. The rate parameter would thus be of the form $k = k_0 T^\beta$. To simplify the estimation, we have neglected the temperature dependence. The two competing reactions considered here would be G5 and G6. We have assumed the reaction G5 to be third order. A value of $k = 1.5 \times 10^{20} \text{ cm}^6 \text{ mol}^{-2} \text{ s}^{-1}$ best fit the experimental data for case I and II, respectively. The sensitivity of this value is determined by plotting growth rate along the substrate for $k = 1 \times 10^{20} \text{ cm}^6 \text{ mol}^{-2} \text{ s}^{-1}$ and $k = 2 \times 10^{20} \text{ cm}^6 \text{ mol}^{-2} \text{ s}^{-1}$ for Case I in Figure 7, and $k = 2 \times 10^{17} \text{ cm}^6 \text{ mol}^{-2} \text{ s}^{-1}$ and $k = 3 \times 10^{17} \text{ cm}^6 \text{ mol}^{-2} \text{ s}^{-1}$ for case II in Figure 8.

CONCLUSIONS

these chemistry models indicate that polymerization of the adduct could explain the experimentally observed growth rates and uniformities. An apparent third order kinetic parameter is used to describe the loss of adduct due to parasitic reactions and was obtained from the growth data.

ACKNOWLEDGMENTS

The work was supported by ARPA - URI on Visible Light Emitters. The supercomputing time was provided by DOD. The authors are indebted to A. Thon and N. Perkins at the University of Wisconsin, N. Ingle at the University of Minnesota, and Jeff Flynn at Advanced Technology Materials for many helpful discussions.

REFERENCES

1. X. Zhang, P. Kung, A. Saxler, D. Walker, T.C. Wang, and M. Razeghi, *Appl. Phys. Lett.* **67** (12), 1745 (1995).
2. T.F. Kuech, *Mat. Sci. Rep.* **2**, 1 (1987).
3. M.J. Almond, M.G.B. Drew, C.E. Jenkins, and D.A. Rice, *J. Chem. Soc. Dalton Trans.* (1992) 5-9.
4. Assaf Thon and T.F. Kuech, *AIChE Conference*, 1995
5. R.B. Bird et al., W.E. Stewart and E.N. Lightfoot, *Transport Phenomenon*, Wiley, New York (1960)
6. R.H. Perry & C.H. Chilton, *Chemical Engineer's Handbook*, 5th ed., McGraw-Hill, New York (1977).
7. R.C. Reid, J.M. Prausnitz and T.K. Sherwood, *The Properties of Gases and Liquids*, McGraw-Hill, New York (1977).
8. S.A. Safvi and T.F. Kuech, Manuscript in preperation.
9. T.J. Mountziaris, S. Kalyanasundram and N.K. Ingle, *J. Cryst. Growth*, **131**, 283 (1993).
10. J.O. Hirschfelder C.F. Curtiss and R.B. Bird, *Molecular Theory of gases and Liquids*, Wiley, New York (1967).
11. M.J. Jacko and S.W. Price, *Can. J. Chem.*, **41**, 1560 (1963).
12. M.J. Almond, C.E. Jenkins, and D.A. Rice and K. Hagen, *J. Organomet. Chem.* **439** (1992) 251 - 261.
13. G. Strang & G. Fix, *An Analysis of the Finite Element Method*, Prentice Hall, Englewood Cliffs, NJ (1973).

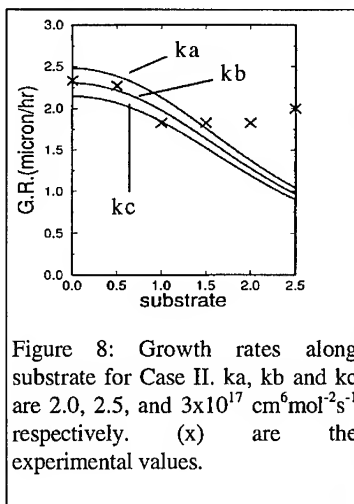


Figure 8: Growth rates along substrate for Case II. k_a , k_b and k_c are 2.0 , 2.5 , and $3 \times 10^{17} \text{ cm}^6 \text{ mol}^{-2} \text{ s}^{-1}$ respectively. (x) are the experimental values.

EFFECT OF CARRIER GAS ON THE SURFACE MORPHOLOGY AND MOSAIC DISPERSION FOR GaN FILMS BY LOW-PRESSURE MOCVD

T. J. KISTENMACHER*, D. K. WICKENDEN*, M. E. HAWLEY**, R. P. LEAVITT***

*Applied Physics Laboratory, The Johns Hopkins University, Laurel, MD 20723

** Los Alamos National Laboratory, Los Alamos, NM 87545

*** U. S. Army Research Laboratory, Adelphi, MD 20783

ABSTRACT

Low-pressure metal-organic chemical vapor deposition (MOCVD) has been used to deposit unnucleated and self-nucleated GaN thin films on (00.1) sapphire substrates. For the self-nucleated films, initial layers were grown at 540°C using trimethylgallium and ammonia as elemental sources and either nitrogen or hydrogen as the carrier gas. Using these same gas phase conditions, overlayers on native (00.1) sapphire substrates or the GaN-nucleated (00.1) sapphire substrates were deposited at 1025°C. The surface morphology and mosaic dispersion of these unnucleated and self-nucleated GaN thin films have been surveyed by a combination of real space images from atomic force microscopy and reciprocal space intensity data from X-ray scattering measurements. As expected, the unnucleated GaN films show a large-grained hexagonal relief, typical of three-dimensional island growth. However, the self-nucleated films are shown to be dense mosaics of highly oriented islands, emblematic of a more two-dimensional growth.

INTRODUCTION

MOCVD has emerged as one of the leading synthetic methods for thin films of GaN [1-7] and its alloys. Generally common to the technique as practiced in various laboratories are: (1) utilization of trimethylgallium as the elemental source for the group IIIA gallium; (2) ammonia as the source for group V nitrogen; (3) deposition temperatures in the range 1000 - 1050°C; and, (4) low temperature [500 - 600°C] nucleation layers, typically comprised of 20 - 50 nm of AlN or GaN (self nucleation).

Of special interest here is that hydrogen has almost universally been selected as the carrier gas used to assist in transport of the gaseous precursors to the heated susceptor. It worthwhile recalling, however, that a variety of carrier gasses were successfully employed in the early CVD growth of unnucleated GaN. For example, Maruska and Tietjen employed hydrogen [8], Ilegems utilized helium [9], and Wickenden and coworkers [10] used nitrogen as the carrier gas.

In this report, the surface morphologies and mosaic dispersion for unnucleated and self-nucleated growth of (00.1) GaN on (00.1) sapphire using nitrogen or hydrogen as carrier gas are contrasted.

EXPERIMENT

Films were prepared on (00.1)-oriented sapphire using trimethylgallium and ammonia as reactants and nitrogen or hydrogen as the carrier gas in a vertical MOCVD reactor operating at 70 torr. Nucleation layers, deposited at 540°C, were optimized for each carrier gas to yield GaN overlayers (grown at 1025°C) suitable for processing into photoconductive devices. The resultant nucleation layer thicknesses

were approximately 20 nm and 50 nm for hydrogen and nitrogen carrier gases, respectively.

The surface morphology of these films was studied by atomic force microscopy (AFM), using a Nanoscope III instrument. Both contact and tapping mode methods were used to obtain the AFM topographs. Contact mode micrographs were acquired employing commercial 100 μm long triangular cantilevers with etched Si_3N_4 tips. Imaging was carried out after the film surfaces were cleaned by dipping each sample in 1M hot HCl for 10 minutes, followed by repeated rinses in ultrapure water and reagent grade methanol, and subsequent drying under a stream of N_2 . Cantilevers used for tapping mode images were 125 μm long diving board type with Si tips. Typical operating parameters for the tapping mode images were 300 kHz drive frequency at 120 mV drive amplitude.

The out-of-plane $[\{00.1\}\text{GaN}/\{00.1\}\text{sapphire}]$ structural coherence was ascertained from conventional $\theta/2\theta$ X-ray diffraction scans collected on a Phillips APD powder diffractometer employing graphite-monochromatized $\text{CuK}\alpha$ radiation. The out-of-plane mosaic spread for these films were measured in reflection from moving-crystal/fixed-counter θ scans (rocking curves), employing a high-precision X-ray spectrometer equipped with a channel-cut, four-bounce germanium monochromator to provide a $\text{CuK}\alpha_1$ beam of high spectral purity and resolution. Additionally, the in-plane $[\{10.0\}\text{GaN}/\{11.0\}\text{sapphire}]$ scattering from these films were examined in transmission using a Buerger precession camera and Zr-filtered $\text{MoK}\alpha$ radiation.

RESULTS AND DISCUSSION

Atomic Force Microscopy: Surface Imaging

Unnucleated Growth. As expected for a three-dimensional island growth mode [8-10], deposition of GaN onto unnucleated (00.1) sapphire yields large hexagonal prisms (Figure 1) with either hydrogen or nitrogen as the carrier gas. In the films grown in hydrogen, Figure 1 (A), these prisms range 50 to 100 μm in diameter, with a mean value clustered about 60-70 μm . Moreover, these prism were typically 1.5 to > 4 μm in

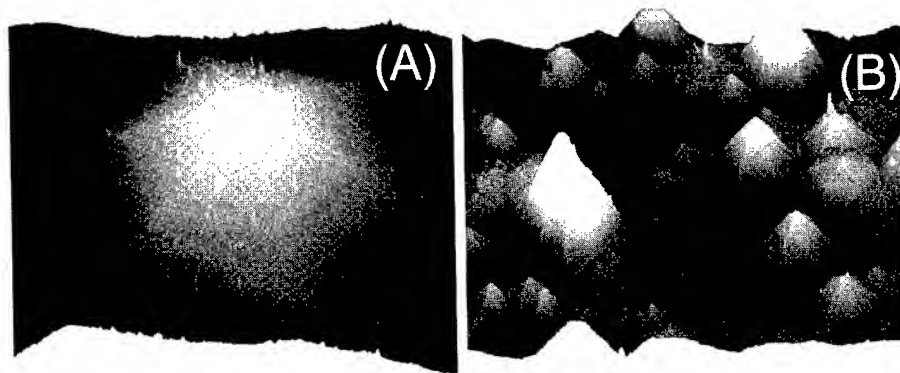


Figure 1. AFM images (100 μm x 100 μm) for unnucleated growth in: (A) hydrogen as the carrier gas and (B) nitrogen as the carrier gas.

height, but many were outside the maximum vertical and horizontal scan limits ($120\text{ }\mu\text{m} \times 4.5\text{ }\mu\text{m}$) of the atomic force microscope. Smaller subunits on prismatic faces appear to be layered (like stacked sand dollars), with an average height of tens of nm high and on average about 400 nm across.

Unnucleated films grown in nitrogen as the carrier gas also exhibit [Figure 1 (B)] large hexagonal prisms, but in this case the prisms are only 10 to 20 μm across the base and 200 to 400 nm high. Even the crystallites that appear flat have a shallow pyramidal top. Here, the smaller subunits are 120 to 145 nm across and are more crystalline in appearance than those for unnucleated growth in hydrogen and the prisms also appear to be less closely packed.

Self-Unnucleated Growth. The pseudo two dimensional growth surfaces of the self-nucleated GaN films [Figure 2 (A) and (B)] are expectedly smooth [1-7, 11] compared

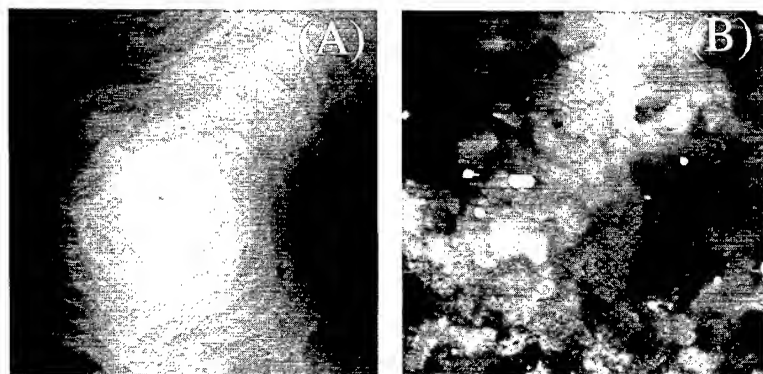


Figure 2. AFM images ($4\text{ }\mu\text{m} \times 4\text{ }\mu\text{m}$) for: (A) self-nucleated growth in hydrogen as the carrier gas; and, (B) self-nucleated growth in nitrogen as the carrier gas.

to those for the island growth of the unnucleated films. These self-nucleated films are, however, still made up of islands 8 to 10 μm across. A few of the islands give the appearance of being as large as 30 μm across, but these are more likely comprised of clusters of smaller islands. The individual islands have terrace steps as small as 0.3 to 0.4 nm high and 150 to 300 nm across depending on the region of the film scanned. In many cases, the tops of the grains appear to end in a spiral; and in other cases some shallow holes are seen to be present. Even though the islands are not well faceted, the terrace edges do have straight edges and the overall appearance of some of the upper half of the islands are suggestive of the same 6-fold symmetry more obviously displayed by the large grains of the unnucleated films.

X-Ray Scattering: Structural Coherence and Mosaic Dispersion

Out-of-plane Coherence and Dispersion. Moderate resolution $\theta/2\theta$ X-ray diffractometer scans through the (00.2)GaN reflection are presented in Figure 3 (A) and (B). The very small difference in the structural coherence across the series of films

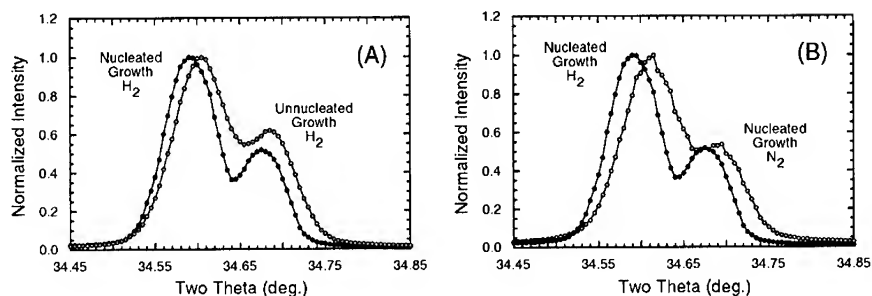


Figure 3. Normalized $\theta/2\theta$ X-ray diffractometer scans for the (00.2)GaN reflection from: (A) un-nucleated and self-nucleated films grown in hydrogen as the carrier gas; and, (B) self-nucleated films grown in hydrogen or nitrogen as the carrier gas.

is well reflected in this Figure. In fact, the range of calculated d-spacing for (00.2)GaN is only from 0.2590 nm (for un-nucleated growth in hydrogen) to 0.2592 nm (for un-nucleated growth in nitrogen). Similarly, the spread in FWHM (full-width at half-maximum) derived from a gaussian fit to the $K\alpha_1$ component is quite small -- from 207 arcsec for nucleated growth in nitrogen to 213 arcsec for either un-nucleated or nucleated growth in hydrogen. Obviously, the out-of-plane structural coherence is markedly unaffected by the nature of the carrier gas.

X-ray rocking curves for the (00.2) GaN reflection are presented in Figure 4(A). These curves very clearly differentiate between films grown in nitrogen and hydrogen. For both un-nucleated and self-nucleated growth in hydrogen, the FWHM for the (00.2)GaN reflection is essentially identical at 0.10° (360 arcsec) and is very similar to that reported for films grown in hydrogen as the carrier gas in a variety of other

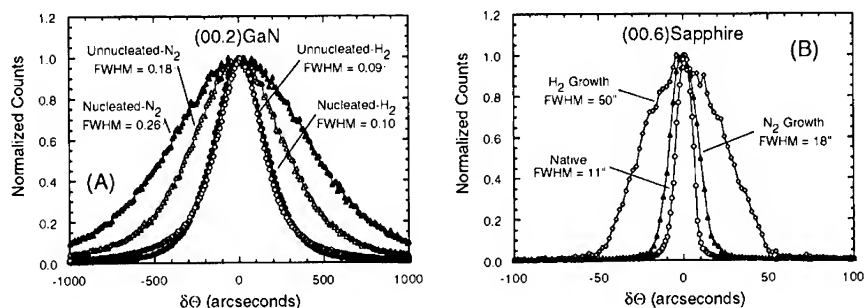


Figure 4. Comparison of X-ray rocking curves (θ scans) for: (A) the (00.2)GaN reflection from nucleated and un-nucleated GaN films grown in hydrogen or nitrogen as the carrier gas; and, (B) the (00.6) reflection from the companion sapphire substrates.

laboratories [12]. In contrast, for growth in nitrogen, FWHM values near 0.2° are found for unnucleated films and even larger values, 0.25 to 0.45° , for self-nucleated films.

Finally, X-ray rocking curves for the (00.6) reflection from the sapphire substrate were also measured and typical scans are shown in Figure 4 (B). The rocking curve for a native (00.1) sapphire substrate shows an expectedly small FWHM of ~ 11 arcseconds, typical of a largely unstrained single-crystal substrate. As is indicated in Figure 4, the inhomogeneous strain and resulting mosaic spread in the (00.1) sapphire substrate has measurably increased along the film growth direction when either nitrogen (~ 18 arcsec) or hydrogen (~ 50 arcsec) is employed as the carrier gas. The larger increase occurs for either nucleated or unnucleated growth in hydrogen.

In-plane Coherence

Variations in the in-plane structural coherence were probed by measuring the X-ray scattering from $\{hh.0\}$ reciprocal lattice vectors for both the thin films and the sapphire substrate by the X-ray precession method. Zero-level precession photographs (Figure 5) of the combined scattering from the $\{hh.0\}$ reciprocal lattice planes of the (00.1) sapphire substrate and the (00.1) heteroepitaxial GaN film reveal a common in-plane epitaxial relationship $[(10.0)\text{GaN} // (11.0)\text{sapphire}]$. There is, moreover, a notable improvement in signal-to-noise ratio for growth in hydrogen, which is largely achieved by a reduction in noise. Several potential processes contribute to the background level, including: fluorescence; extrinsic instrumental scattering; and Bremsstrahlung and diffuse scattering. While it might be expected that fluorescence and the extrinsic incoherent (Compton modified) fraction of the diffuse scattering are largely sample independent, the coherent scattering from various kinds of imperfections (point and line defects, stacking faults, surface roughness, and homogeneous and inhomogeneous stress) is expected to be sample dependent.

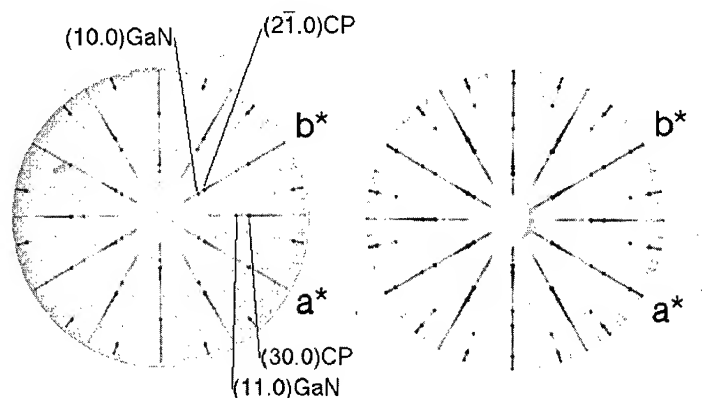


Figure 5. X-Ray precession photographs of the $\{hh.0\}$ reciprocal lattice planes of (00.1)GaN on (00.1)-oriented sapphire (CP) for: (left) self-nucleated growth in a nitrogen and (right) self-nucleated growth in a hydrogen as the carrier gas.

Thus, the reduced background for growth in hydrogen is likely due to a decrease in the density of such imperfections.

In that context, recent transmission electron microscopy studies [13] have begun to appear for growth on a number of substrates using hydrogen as the carrier gas. In parallel, these studies have shown abrupt interfaces, a predominance of (00.1) stacking faults, interfacial misfit dislocations (with densities of order 10^{10} cm^{-2}) and loops, and defect microstructure arising from island nucleation and coalescence. The implications from the present X-ray precession study is that the defect densities could be even greater for growth in nitrogen as the carrier gas.

SUMMARY

Low-pressure MOCVD has been used to deposit unnucleated and self-nucleated epitaxial thin films of GaN on (00.1) sapphire substrates. The island growth mode of the unnucleated GaN films yields a surface morphology composed of large hexagonal grains, with prism diameters ranging from 50 to 100 μm for growth in nitrogen and 10 to 20 μm for growth in nitrogen. In contrast, the pseudo two-dimensional growth of the self-nucleated films give much smoother surface morphologies. These self-nucleated films are, however, still made up of islands 8 to 10 μm across, with minimum steps of 0.4 nm in each case. The structural coherence normal to the film surface is essentially unchanged, but the mosaic dispersion (and apparently the defect density) is measurably larger for growth in nitrogen.

ACKNOWLEDGMENTS

This work was supported in part by the U.S. Department of the Navy under Contract N00039-95-C-00-2.

REFERENCES

1. H. Amano, N. Sawaki, I. Akasaki, and Y. Toyoda, *Appl. Phys. Lett.* **48**, 353 (1986).
2. D. K. Wickenden, T. J. Kistenmacher, W. A. Bryden, J. S. Morgan, and A. Estes Wickenden, *Mat. Res. Soc. Symp. Proc.* **221**, 167 (1991).
3. S. Nakamura, *Jpn. J. Appl. Phys.* **30**, L1705 (1991).
4. M. A. Khan, J. N. Kuznia, J. M. Van Hove, D. T. Olson, S. Krishnankutty, and R. M. Kolbas, *Appl. Phys. Lett.* **58**, 526 (1991).
5. B. Goldenberg, J. D. Zook, and R. J. Ulmer, *Appl. Phys. Lett.* **62**, 381 (1993).
6. W. E. Plano, J. S. Major Jr., D. F. Welch, and J. Speirs, *Electron. Lett.* **30**, 2079 (1994).
7. K. Doverspike, L. B. Rowland, D. K. Gaskill, and J. A. Freitas, Jr., *J. Electron. Mat.* **24**, 269 (1995).
8. H. P. Maruska and J. J. Tietjen, *Appl. Phys. Lett.* **15**, 327 (1969).
9. M. Ilegems, *J. Crystal Growth* **13/14**, 360 (1972).
10. D. K. Wickenden, K. R. Faulkner, R. W. Brander, and B. J. Isherwood, *J. Crystal Growth* **9**, 158 (1971).
11. D. K. Wickenden, C. B. Barger, W. A. Bryden, J. Miragliotta, and T. J. Kistenmacher, *Appl. Phys. Lett.* **65**, 2024 (1994).
12. See, for example, D. Kapolnek, X. H. Xu, B. Heying, S. Keller, B. P. Keller, U. K. Mishra, S. P. DenBaars, and J. S. Speck, *Appl. Phys. Lett.* **67**, 1541 (1995).
13. See, for example, S. D. Lester, F. A. Ponce, M. G. Craford, and D. A. Steigerwald, *Appl. Phys. Lett.* **66**, 1249 (1995).

FACETS FORMATION MECHANISM OF GaN HEXAGONAL PYRAMIDS ON DOT-PATTERNS VIA SELECTIVE MOVPE

Kazumasa Hiramatsu, Shota Kitamura, and Nobuhiko Sawaki
Department of Electronics, Nagoya University
Furo-cho, Chikusa-ku, Nagoya 464-01, Japan
hiramatsu@nuee.nagoya-u.ac.jp

ABSTRACT

Three-dimensional GaN pyramids have been successfully obtained on dot-patterned GaN(0001)/sapphire substrates by using the selective MOVPE technique. The dot-pattern is a hexagon arranged with a 5 μ m width and a 10 μ m spacing. The GaN structure comprises a hexagonal pyramid covered with six {1 $\bar{1}$ 01} pyramidal facets on the side or a frustum of a hexagonal pyramid having a (0001) facet on the top. The facet formation mechanism has been investigated by observing the facet structure with the growth time. The {1 $\bar{1}$ 01} facets are very stable during the growth. The (0001) facet growth is dominant at the initial growth but almost stops at a certain growth time and then the facet structure is maintained. The appearance of the self-limited (0001) facet is attributed to the balance of flux between incoming Ga atoms from the vapor phase to the (0001) surface and outgoing Ga atoms from the (0001) surface to the {1 $\bar{1}$ 01} surface via migration. The longer the diffusion length of the Ga atoms on the (0001) surface is, the more the surface migration is enhanced, resulting in the appearance of the wider (0001) facet on the top.

INTRODUCTION

III-V nitrides including GaN are promising wide bandgap materials for photonic and electronic device applications such as LEDs and LDs in blue and ultraviolet regions and FETs operated at high temperature. Furthermore, fabrication of microstructure of the wide bandgap semiconductors is important to realize high-performance LEDs, LDs, and FETs, as well as wide bandgap quantum wires and dots. Dry-etching technique is usually employed to fabricate microstructure of III-V nitrides, but this technique results in severe damage and contamination of the surface.

Many studies on the selective epitaxial growth have been reported in ordinary III-V compound semiconductors such as GaAs and InP system. [1-6] The selective epitaxial growth enables us to control three-dimensional microstructures such as quantum wires and dots. [3-6] Furthermore, this technique does not cause any damage and contamination of surface in contrast with dry-etching technique.

Recently, the selective epitaxial growth of GaN and AlGaN by metalorganic vapor phase epitaxy (MOVPE) was carried out on linear-patterned GaN (0001) / sapphire substrates and the facet formation mechanism was investigated. [7] However, the selective epitaxial growth on the dot-patterned windows has not been carried out. In this paper, in order to fabricate the three-dimensional microstructure of GaN the selective MOVPE growth is carried out using the dot-patterned GaN / sapphire substrates and the facet structure is investigated in relation to the growth conditions namely, the growth time, the growth temperature and the flow rate of trimethylgallium (TMG). The self-limiting process of the facet is found by observing change in the structure.

EXPERIMENT

The selective epitaxial growth of GaN was performed on a 2 μ m-thick-GaN (0001) thick layer by MOVPE. This GaN layer was grown on a sapphire {on-axis α -Al₂O₃ (1 $\bar{1}\bar{2}$ 0)} substrate using an AlN buffer layer by MOVPE. [8, 9] A 50-60nm thick SiO₂ mask was used for the selective growth of GaN.[7] Patterning of the masks was carried out by conventional photolithography and NH₄HF₂ etching to form dot-patterned windows with hexagons arranged at width of 5 μ m and

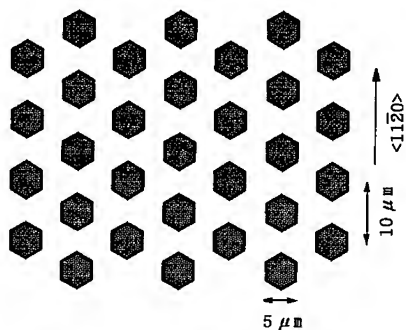


Figure 1. Schematic diagram of the mask with dot-patterns of hexagons arranged at width of $5\mu\text{m}$ and spacing of $10\mu\text{m}$.

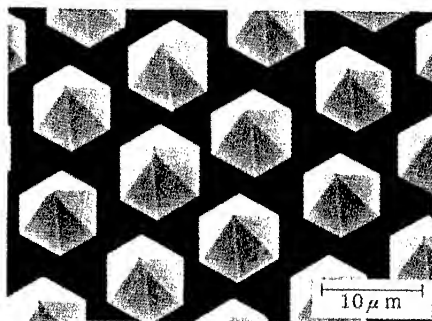
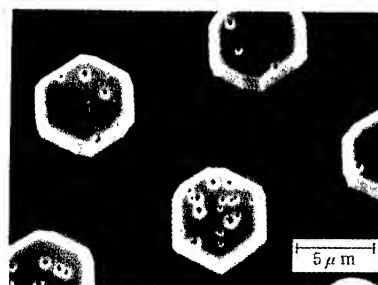


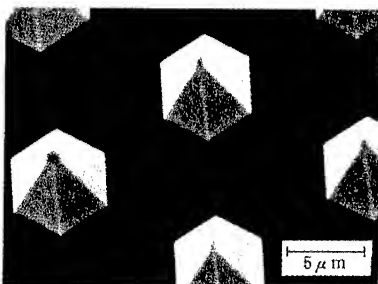
Figure 2. SEM image of the typical GaN facet structure.



(a)



(b)



(c)

Figure 3. SEM images of GaN grown on the dot-patterned windows for different growth times of (a) 2, (b) 5 and (c) 7 min. The growth temperature was $1,025^{\circ}\text{C}$ and the flow rate of TMG was $91.61\mu\text{mol/min}$.

spacing of $10\mu\text{m}$ as shown in Fig. 1. The MOVPE reactor was operated at atmospheric pressure. The source gases were TMG and ammonia (2.0slm) with hydrogen as the carrier gas (2.0slm).

RESULTS

Figure 2 shows the GaN three-dimensional structure grown on the dot-patterned windows. Any GaN deposition is not observed on the SiO_2 mask, indicating the excellent selectivity of GaN growth. The facet structure of GaN is composed of a hexagonal pyramid covered with six $\{1\bar{1}01\}$ facets on the side or a frustum of a hexagonal pyramid having a (0001) facet on the top.

The facet formation mechanism has been investigated by observing change in the facet structure with the growth time. Figures 3 (a), (b), and (c) show SEM images of GaN grown on the dot-patterned windows for different growth times of 2, 5, and 7min. The growth temperature was $1,025^\circ\text{C}$ and the flow rate of TMG was $91.61\mu\text{mol/min}$. Figure 4 and 5 indicate the height and widths (top and bottom) of the facet structure as a function of the growth time. As clearly shown in Fig. 5, the $\{1\bar{1}01\}$ facets does not almost grow and are stable. Figs. 3 and 4 show, however, the (0001) facet growth is dominant at the initial growth stage but almost stops at growth time around 7min and the facet structure is maintained. These results show that the self-limited stable facet structure is obtained after the certain growth time.

Dependence of the facet structure on the growth conditions is summarized in Fig. 6. These samples were grown for enough time longer than the growth time to obtain a self-limited stable facet. The width of the top (0001) facet is shown as a function of the growth temperature for different TMG flow rates. For the same TMG flow rate the width of the (0001) face increases linearly with increasing the growth temperature. The width changes from 0 to $1.6\mu\text{m}$ at the TMG flow rate of $91.61\mu\text{mol/min}$. For the same growth temperature the width of the (0001) facet increases with decreasing the TMG flow rate. The width changes from 0 to $0.7\mu\text{m}$ at the $1,000^\circ\text{C}$. Thus these results indicate that the change in the growth temperature or the TMG flow rate enables us to control the top (0001) facet in the three-dimensional microstructure of GaN.

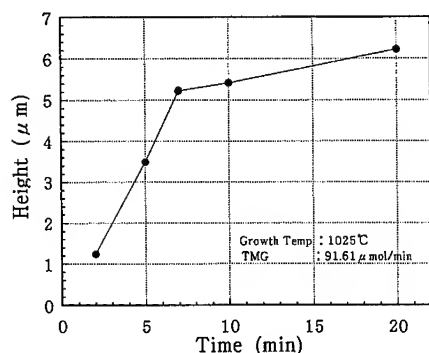


Figure 4. Height of the facet structure as a function of the growth time.

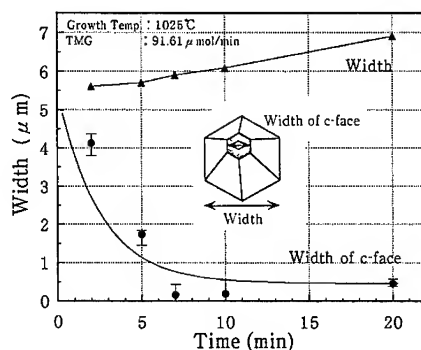


Figure 5. Top and bottom widths of the facet structure as a function of the growth time.

DISCUSSION

We should discuss the formation mechanism of the self-limited (0001) facet in the hexagonal pyramid using the model of Figure 7. This model has been also reported in the GaAs dot-structure.[6] Since supply of the ammonia gas into the growth region is much larger than that of TMG (the V/III ratio is larger than 1,000), the growth process such as vapor phase diffusion and surface diffusion is limited by supply of Ga species. Ga atoms adsorbed on the $\{1\bar{1}01\}$ facet are easily desorbed from the facet because the $\{1\bar{1}01\}$ facet is energetically stable. Ga atoms adsorbed on the (0001) facet migrate at a certain distance around the diffusion length. Once the Ga atom arrives at the $\{1\bar{1}01\}$ facet, it is easily reevaporated from the $\{1\bar{1}01\}$ facet into the vapor phase. During the growth the (0001) facet becomes smaller. If the diffusion length is longer than the width of the (0001) facet, the flux of the outgoing Ga atom from the (0001) facet to the $\{1\bar{1}01\}$ becomes larger. Then, once this flux is balanced with the flux of the incoming Ga atom from the vapor phase to the (0001) facet, the stable and self-limited facet structure is realized. Thus the self-limited facet is attributed to the balance between the incoming and outgoing flux on the (0001) facet.

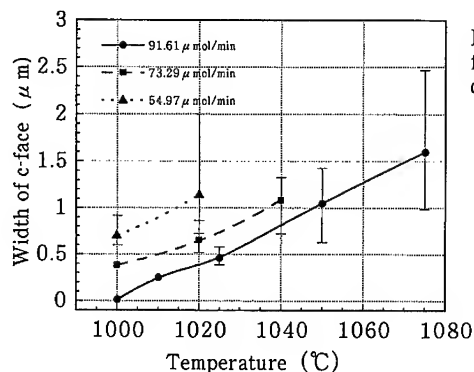


Figure 6. Width of the top (0001) facet as a function of the growth temperature for different TMG flow rates.

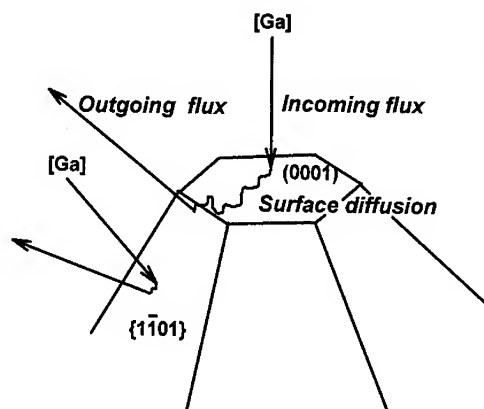


Figure 7. Schematic model indicating the facet formation mechanism.

The diffusion length of the Ga atom on the (0001) facet increases with increasing the temperature. Therefore, the top (0001) facet tends to appear at a high temperature. On the other hand, the increase in the TMG flow rate promotes two-dimensional nucleation on the (0001) facet, which shortens the diffusion length of the Ga atom. Therefore, the top (0001) facet becomes smaller with increasing the TMG flow rate. Thus it is found that the size of the (0001) facet on the GaN hexagonal pyramid is determined by the Ga diffusion length of the order of submicron meters to 2 μm .

CONCLUSIONS

The selective MOVPE growth of wurtzite GaN was carried out on dot-pattern (5 μm in size) GaN (0001) / sapphire substrates using SiO_2 masks. The three-dimensional GaN facet structure was successfully obtained on the dot-pattern, indicating a hexagonal pyramid covered with six $\{1\bar{1}01\}$ facets. A stable and self-limited (0001) facet appeared on the top, depending on growth conditions. The facet formation mechanism was investigated by observing the facet structure with the growth time. The $\{1\bar{1}01\}$ facets were stable. The (0001) facet growth was dominant at the initial growth but almost stops at a certain growth time and then the facet structure was maintained. The appearance of the self-limited (0001) facet is attributed to the balance of flux between incoming Ga species from the vapor phase to the (0001) surface and outgoing Ga atoms from the (0001) surface to the $\{1\bar{1}01\}$ surface via migration. The longer the diffusion length of the Ga atoms on the (0001) surface is, the more the surface migration is enhanced, resulting in the appearance of the wider (0001) facet on the top.

ACKNOWLEDGMENTS

We are grateful to Toyoda Gosei Co. Ltd. for giving substrates. This work was partially supported by Grant-in-Aids for Scientific Research (c), No. 50165205.

REFERENCES

1. K. Imamura, N. Yokoyama, T. Ohnishi, S. Suzuki, K. Nakai, H. Nishi, and A. Shibatomi, *Japan J. Appl. Phys.* **23**, p. L342 (1984).
2. H. Asai, S. Adachi, S. Ando, and K. Oe, *J. Appl. Phys.* **55**, p. 3868 (1984).
3. H. Asai, S. Yamada, and T. Fukui, *Appl. Phys. Lett.* **51**, p. 1518 (1987).
4. T. Fukui, S. Ando, and Y. Fukai, *Appl. Phys. Lett.* **57**, p. 1209 (1990).
5. T. Fukui and S. Ando, *Electron. Lett.* **25**, p. 410 (1989).
6. S. Ando, T. Honda, and N. Kobayashi, *Japan J. Appl. Phys.* **32**, p. L104 (1993).
7. Y. Kato, S. Kitamura, K. Hiramatsu, and N. Sawaki, *J. Crystal Growth* **144**, p. 133 (1994).
8. H. Amano, N. Sawaki, I. Akasaki, and Y. Toyoda, *Appl. Phys. Lett.* **48**, p. 353 (1986).
9. I. Akasaki, H. Amano, Y. Koide, K. Hiramatsu, and N. Sawaki, *J. Crystal Growth*, **98**, p. 209 (1989).

Growth of High Quality InGaN Films by Metalorganic Chemical Vapor Deposition

J. C. Roberts*, F. G. McIntosh*, K. S. Boutros*, S. M. Bedair*, M. Moussa**, E. L. Piner***, Y. He*** and N. A. El-Masry***

* Dept. of ECE, Box 7911, North Carolina State University, Raleigh, N.C. 27695

** Air Defense Academy, Alexandria, Egypt

*** Dept. of MSE, Box 7916, North Carolina State University, Raleigh, N. C. 27695

ABSTRACT

InGaN based optical devices can cover from the violet through orange regions of the visible spectrum. Difficulties in the growth of this alloy, which have impeded its applications, include problems such as the high vapor pressure of In, weak In-N bonds and lack of sufficient nitrogen during growth. We report on the MOCVD growth of $\text{In}_x\text{Ga}_{1-x}\text{N}$ ($0 < x < 0.4$) on sapphire substrates in the 750 - 800 °C temperature range. X-ray diffraction data show full width at half maximum line widths as narrow as 250 arcsec for low values of x , while films with higher InN% exhibit broader line widths. Room temperature photoluminescence spectra exhibit band edge emission, with emission from deep levels increasing with x . Preliminary investigations of AlGaIn/InGaN/AlGaIn double heterostructures have been conducted.

INTRODUCTION

Blue, green, and yellow emission from nitride compounds can rely on impurity transitions in the GaN or $\text{In}_x\text{Ga}_{1-x}\text{N}$ active layers^{1,2,3}. This approach works fairly well in LED's with a low current injection, however band to band transitions and broad emissions are also observed when a high injection level is used, such as might be expected in semiconductor lasers⁴. Rather than moving the emission wavelength through deep impurity levels, the more efficient band edge transition, that necessitates an $\text{In}_x\text{Ga}_{1-x}\text{N}$ ($x > 0.2$) active layer may be a better alternative to achieve light emitting devices that emit from the blue through orange region of the visible spectrum. While there have been many reports on the growth of high quality GaN films by MOCVD in recent years, fewer reports have been published on the growth of high quality $\text{In}_x\text{Ga}_{1-x}\text{N}$, having structural and optical properties that are approaching device quality.

In addition to the usual problems facing MOCVD III-nitride growth such as the lack of suitable substrates, the growth of InGaN alloys by MOCVD can suffer from several other difficulties. These difficulties include: 1) The high equilibrium vapor pressure of nitrogen that is required during growth to prevent the dissociation of the In-N bond. The equilibrium vapor pressure of nitrogen over InN, for example, is several orders of magnitude greater than that of AlN and GaN.⁵ 2) In based compounds suffer from parasitic gas phase reactions between organometallic sources and hydride precursors. It seems that these parasitic reactions are more severe when NH_3 is used relative to the AsH_3 ⁶ and the PH_3 ⁷ cases, especially when In based organometallics (OMs) are used. 3) AlGaIn/InGaN heterostructures can suffer from the fairly high lattice mismatch between these ternary alloys. The quaternary alloy AlInGaIn can offer a lattice matched platform for InGaIn growth, but this quaternary

alloy has barely been studied. 4) High quality interfaces between the InGaN wells and the AlGaN or AlInGaN barrier layers can be difficult to achieve. Poor interfaces can result from poor nucleation (3D vs 2D), lattice mismatch, surface reconstruction, segregation and reaction of In at the interfaces and incompatible growth temperatures. In this paper we report on the growth of $\text{In}_x\text{Ga}_{1-x}\text{N}$ ($0 < x < 0.40$) epitaxial films and AlGaN/InGaN double heterostructures (DHs). These MOCVD grown films were deposited on buffer layers grown by Atomic Layer Epitaxy (ALE) in a specially designed hybrid growth system.

EXPERIMENT

A versatile growth system, capable of operating in several growth modes, has been designed for the growth of III-N compounds. The versatility of the system arises from its unique susceptor design, shown in Figure 1. For this work the system was operated in two growth modes, ALE mode, for the growth of buffer layers, and conventional MOCVD mode, for the growth of the InGaN alloys. Either growth mode could be selected on demand at any time during a growth experiment. For the conventional MOCVD mode (Figure 1), the substrate is kept stationary under a mixed flow of column III and V precursors.

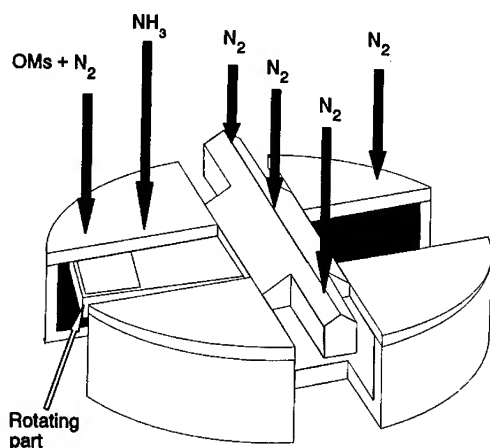


Figure 1. Susceptor design - conventional MOCVD growth mode.

To improve the quality of the deposited films, a novel configuration of quartz tubes minimizes parasitic gas phase mixing of the NH_3 and metalorganic precursors until the gases near the substrate surface. For ALE style growth, the reactants are physically kept separated by injecting them through windows on opposite sides of the stationary susceptor, while the moving part of the susceptor sequentially rotates the substrate under the physically separated gas streams. The exposure time of the substrate to each reactant as well as the time per growth cycle is controlled by the rotational speed

and pause times under the reactant gas stream. This hybrid growth system has been used to grow GaN⁸ and $\text{In}_{0.27}\text{Ga}_{0.73}\text{N}^9$ by ALE at 550 and 650 °C, respectively.

Source gases used were, trimethylgallium (TMG, -10 °C), trimethylaluminum (TMA, +18 °C), ethyldimethylindium (EdMIn, +10 °C) and NH_3 ; N_2 was used as the carrier gas. Basal plane sapphire, cleaved into $\sim 1.5 \text{ cm} \times 1.5 \text{ cm}$ squares, was used as substrate material. After solvent cleaning, substrates were loaded and annealed in N_2 and NH_3 for 15 minutes and 1 minute respectively. ALE growth of AlN/GaN buffer layers¹⁰ was performed at 700 °C, while InGaN films were grown by MOCVD between 750 and 800 °C. The ALE grown buffer layers minimize the formation of threading dislocations in the overlying MOCVD grown nitride films, and offer an effective alternative to the conventional amorphous/recrystallized buffer layer approach¹⁰. The InGaN alloys were typically grown on GaN that was deposited by MOCVD at higher temperatures (900 - 950 °C). MOCVD grown AlGaN cladding layers for DHs were also grown by MOCVD between 900 and 950 °C. In/Ga vapor phase ratios were ≤ 2 for the growth conditions used in this work.

RESULTS

$\text{In}_x\text{Ga}_{1-x}\text{N}$ epitaxial layers have been grown with values of InN up to 40% in the ternary alloy. The full width at half maximum (FWHM) of the double crystal X-ray diffraction (DCXRD) data is broad for high values of x , but is comparable to that of GaN grown at higher temperatures for low values of InN% in the ternary, as shown in Figure 2. Figure 2 shows DCXRD data for an $\text{In}_{0.06}\text{Ga}_{0.94}\text{N}$ alloy grown at 780 °C on GaN. The X-ray line width has a FWHM of ~ 250 arc seconds, the lowest reported to date for InGaN. The X-ray peak of the underlying GaN layer is also relatively sharp.

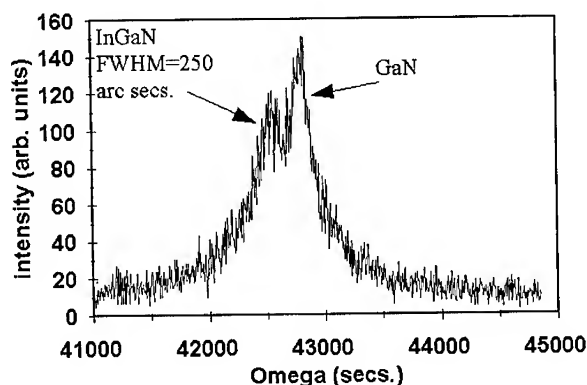


Figure 2. DCXRD data for $\text{In}_{0.06}\text{Ga}_{0.94}\text{N}$ grown by MOCVD at 780 °C on GaN.

Figure 3 shows $\Theta - 2\Theta$ X-ray data for an $\text{In}_{0.40}\text{Ga}_{0.60}\text{N}$ film grown at 750 °C on GaN. The X-ray line width has broadened, due at least in part to the increased lattice

mismatch between the underlying GaN layer and the InGaN alloy. This composition of 40% InN was achieved by MOCVD with a In/Ga gas phase ratio of only ~ 2 , a relatively low ratio as compared to other published results on InGaN having even lower InN%¹¹.

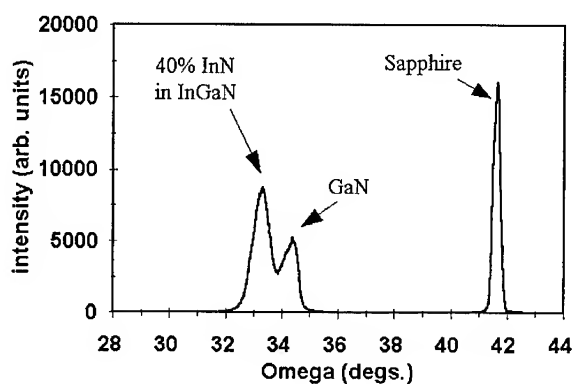


Figure 3. X-ray data for $\text{In}_{0.40}\text{Ga}_{0.60}\text{N}$ grown by MOCVD at 750 °C on GaN.

The optical properties of InGaN films grown in our hybrid MOCVD reactor show intense band edge (BE) emission that is sometimes accompanied by emission from deep levels. Room temperature photoluminescence (PL) data of several $\text{In}_x\text{Ga}_{1-x}\text{N}$ films is presented in Figures 4 and 5.

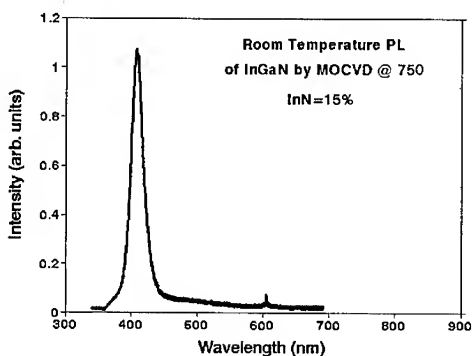


Figure 4. Room temp. PL of $\text{In}_{0.15}\text{Ga}_{0.85}\text{N}$ grown at 750 °C by MOCVD.

Figure 4 shows PL data of an $\text{In}_{0.15}\text{Ga}_{0.85}\text{N}$ alloy that was grown at 750 °C. Strong BE emission near 410 nm, having a FWHM of $\sim 190 \text{ \AA}$ is observed for this film. The peak is fairly sharp and almost free of deep level emission. Room temperature PL data for an $\text{In}_{0.35}\text{Ga}_{0.65}\text{N}$ alloy, also grown at 750 °C, is shown in Figure 5. The PL

spectrum shows BE emission at ~ 470 nm accompanied by a tail which may be attributed to emission from deep levels. This observed PL of Figure 5, with 35% InN, represents one of the highest reported values of x we are aware of. The good to excellent optical properties of these MOCVD grown InGaN alloys, with room temperature PL spectra dominated by BE emission, offer the potential of a basis for light emitting structures.

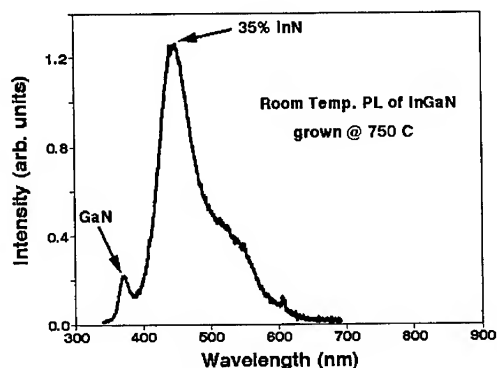


Figure 5. Room temp. PL of $\text{In}_{0.35}\text{Ga}_{0.65}\text{N}$ grown at 750°C by MOCVD.

We have conducted some preliminary investigations into the growth of AlGaIn/InGaIn/AlGaIn DHs by MOCVD. AlGaIn was used as the cladding layer for these structures to offer increased carrier confinement, and was grown with AlN composition between 10 - 30%. Figure 6 shows room temperature PL spectra of $\text{Al}_{0.3}\text{Ga}_{0.7}\text{N}/\text{In}_x\text{Ga}_{1-x}\text{N}/\text{Al}_{0.3}\text{Ga}_{0.7}\text{N}$ DH with $0.1 < x < 0.15$ grown by MOCVD on a GaN buffer layer.

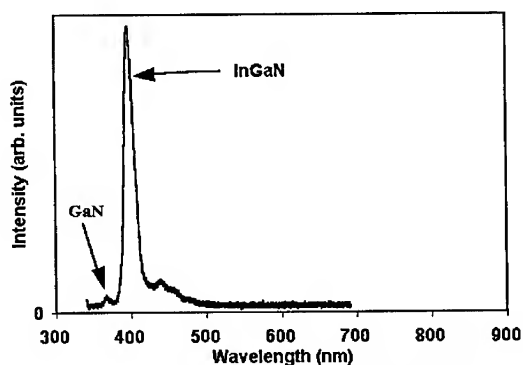


Figure 6. Room temperature PL of a AlGaIn/InGaIn/AlGaIn DH grown by MOCVD on GaN.

The AlGaIn was grown at 900 °C, while the InGaIn film was grown at 780 °C. The PL spectrum, which includes BE emission from the GaIn buffer layer, shows BE emission from the InGaIn active layer with a FWHM of about 15 nm. This value is comparable with that reported by Nichia obtained from their EL studies.

CONCLUSIONS

High quality InGaIn alloys have been grown by MOCVD having an InIn composition as high as 40 %. For low values of x, the $\text{In}_x\text{Ga}_{1-x}\text{In}$ epilayers have a sharp X-ray FWHM, with values as low as 250 arcsec observed, and sharp room temperature PL spectra that are dominated by BE emission. For higher values of x, the X-ray line widths broaden and room temperature PL spectra, while still showing BE emission, also exhibit some emission from deep levels. An AlGaIn/InGaIn/AlGaIn DH has been grown that shows very sharp (FWHM = 15nm) BE emission corresponding to an InIn composition of ~10% in the active layer.

ACKNOWLEDGMENTS

This work is supported by the Office of Naval Research (ONR).

REFERENCES

1. S. Strite and H. Morkoç, J. Vac. Sci. Tech., **B10**, 1237 (1992).
2. M. Asif Khan, S. Krishnankutty, R. A. Skogan, J. N. Kunznia, D. T. Olsen and T. George, Appl. Phys. Lett., **65**, 520 (1994).
3. K. G. Fertitta, A. L. Holmes, J. G. Neff, F. J. Ciuba and R. D. Dupuis, Appl. Phys. Lett., **65**, 1823 (1994).
4. S. D. Lester, F. A. Ponce, M. G. Craford, and D. A. Steigerwald, Appl. Phys. Lett., **66**, 1249 (1995).
5. T. Matsuoka, H. Tanaka, T. Sasaki, and A. Datsui, Inst. Phys. Conf., **106**, 141 (1989).
6. H. Amano, N. Sawaki, I. Akasaki, and Y. Toyada, Appl. Phys. Lett., **48**, 353 (1986).
7. B. McDermott, et. al., Appl. Phys. Lett., **56**, 1172 (1990).
8. N. Karam, T. Parados, W. Rowland, J. Schetzina, N. El-Masry and S. M. Bedair, Appl. Phys. Lett., **67**, 94 (1995).
9. K. S. Boutros, F. G. McIntosh, J. C. Roberts, S. N. Bedair, E. L. Piner and N. A. El-Masry, Appl. Phys. Lett., accepted.
10. E. L. Piner, et. al., presented at MRS 1995 Fall Meeting.
11. S. Nakamura, T. Mukai, Jpn. J. Appl. Phys., **31**, 1457 (1992).

Low Resistivity Aluminum Nitride: Carbon (AlN:C) Films Grown by Metal Organic Chemical Vapor Deposition

K. Wongchotiquil, N. Chen, D. P. Zhang, X. Tang, and M. G. Spencer
Materials Science Research Center of Excellence, School of Engineering, Howard University
Washington, DC 20059

ABSTRACT

Low resistivity single crystal aluminum nitride-carbon (AlN:C) films were grown by metal organic chemical vapor deposition (MOCVD). The growth system used ammonia (NH₃), trimethylaluminum (TMA), hydrogen (H₂), and propane (C₃H₈) precursors. Films produced with high partial pressure of propane during growth exhibited high conductivity. Van der Paw measurements indicated that the resistivity of the as grown films changed dramatically from 10⁸ ohm-cm for unintentionally doped samples to less than .2 ohm-cm for partial pressures of propane greater than 0.5x10⁻³ torr. Reflection electron diffraction (RHEED) measurements performed "in situ" just after film growth indicated that the material is single crystal up to a propane partial pressure of 2.5x10⁻³ torr. P-n junctions of n-type 6H-SiC and p-type AlN:C were fabricated, blue emission (centered at 490nm) was observed from the heterojunction under forward bias.

INTRODUCTION

III/V nitrides have long been viewed as promising materials for semiconductor device applications in the blue and UV wavelengths. The major obstacle stifling nitride progress is the lack of a lattice material substrate. Sapphire is currently the most common substrate employed for CVD nitride growth despite its large thermal and lattice mismatch. The recent availability of commercial 6H-SiC provides an alternative substrate for the growth of III-V nitrides. The lattice mismatch between 6H-SiC and AlN is .97%. Using SiC substrates it is possible to produce high quality epitaxial films of AlN. However, because of the insulating property of AlN, the types of devices fabricated from this materials system is greatly reduced. Highly conducting AlN films would make an important contribution to the development of wide bandgap semiconductor technology. The reported resistivity of AlN films is 10³-10⁵ ohm-cm [1,2,3]. In this work, we present the growth and characterization of AlN:C films with resistivity less than .1 ohm-cm. We believe that the resistivity data presented in this paper is the lowest ever reported for AlN.

EXPERIMENT

AlN layers were grown in a low pressure metal organic chemical vapor deposition (MOCVD) vertical reactor. This reactor has two separated chambers joined by a common load lock. One of the chambers is equipped with a reflection high energy electron diffraction (RHEED) system which allows a quick determination of film crystallinity after growth. The common load lock provides a way of transporting samples between chambers without exposing them to the ambient air. Sapphire substrates were used for most of the experiments. P-n junctions were fabricated on n-type 6H-SiC Lely platelets which are nominally oriented in the (0001) direction. Trimethylaluminum (TMA), ammonia (NH₃) and hydrogen (H₂) were used as precursors. Propane (C₃H₈) was utilized as a independent carbon (C) source. The propane flow rates were 2-8 sccm. The growth temperature and pressure were 1200°C and 10 torr, respectively. The TMA was supplied by passing H₂ through a TMA bubbler which was kept at 35°C. Growth was performed vertical MOCVD system. After growth, surface composition analysis was performed by Auger spectroscopy or secondary ion mass spectroscopy (SIMS). Prior the chemical measurement the surface was sputtered to remove surface carbon. Optical reflection and absorption measurement were made using a computer controlled spectrophotometer. The film thickness was determined by the interference fringes in the optical reflection data, typical sample thickness were about 2000 angstroms. Resistivity, mobility, carrier concentration, and carrier type

were determined by Hall and Van der Paw techniques (In dots were used to form contacts to the Van der Paw pattern). A p-n junction was fabricated from an AlN film grown directly on a n-type 6H-SiC substrate.

RESULTS

Figure 1 shows the electrical and chemical data from as grown films of AlN on sapphire (on which RHEED measurements after growth indicated the films to be crystalline). It can be seen that the conductivity of the AlN:C films changes dramatically from no propane flow to a propane partial pressure of $.5 \times 10^{-3}$ torr. Unintentionally doped films grown on sapphire exhibited a resistivity 10^8 ohm-cm, while films grown at a propane partial pressure of greater than $.5 \times 10^{-3}$ torr had a resistivities less than .2 ohm-cm. The film resistivity continues to drop as the propane flow is increased. Also shown in Fig. 1 is the carbon concentration in the films (obtained from Auger studies) as a function of the partial pressure of propane during growth. The concentration of carbon in the as grown layer is a linear function of the partial pressure of propane during growth and changes from about 4% to 13%.

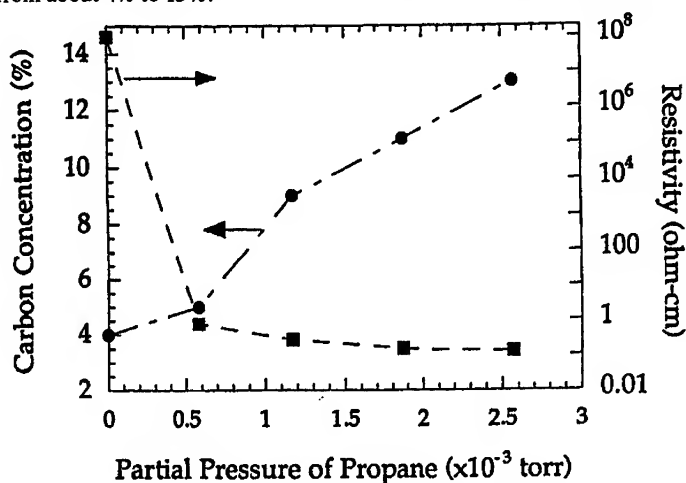


Figure 1. Right axis displays resistivity of as grown AlN films on sapphire as a function of partial pressure of propane during growth. Left axis displays carbon concentration in as grown films of AlN as a function of propane partial pressure during growth. Carbon concentration is determined by Auger measurements on as grown films of AlN on sapphire substrates.

The mobility of the AlN:C films varied from $10\text{--}50\text{ cm}^2\text{V}^{-1}\text{sec}^{-1}$ while the carrier concentration varied from $4 \times 10^{18}\text{ cm}^{-3}$ to $6 \times 10^{17}\text{ cm}^{-3}$. Mobility versus carrier concentration for samples fabricated with carbon doping is shown in Fig 2.

In all the films studied by Auger the dominant impurity was carbon. We believe that the high concentration of carbon in the unintentionally doped films is due to incorporation of carbon from TMA. In Auger studies of the AlN:C films all impurities other than carbon were below the detection limit (about 1-3%). However, in SIMS studies of the AlN:C films high levels of oxygen were detected along with carbon. The concentration of oxygen was about $1 \times 10^{19}\text{ cm}^{-3}$. Oxygen in AlN is thought to be deep donor and as such would provide electrical compensation in the films. The results of the Auger and SIMS studies indicate a large amount of carbon in the crystal is not contributing to the p-type doping (not withstanding the compensation of the oxygen impurities) this carbon must be either on a Al or interstitial site. Several transmission electron micro graphs were taken in order to determine if carbon clusters were present in the film and to check the crystallinity.

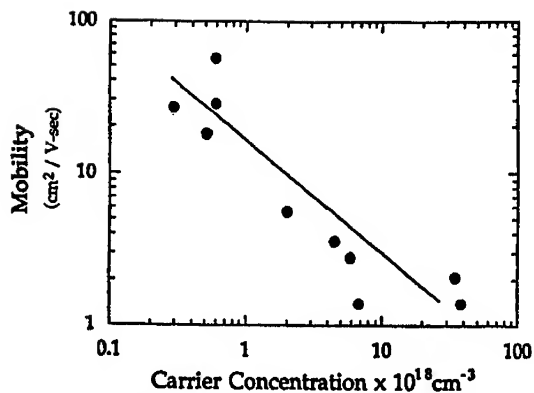


Figure 2 Mobility of AlN:C vs Concentration

Fig 3 shows the interface of one of the AlN:C grown on sapphire. In this micro graph we seen a crystalline interface and no evidence of carbon clusters. Diffraction studies done in the TEM indicated that the epitaxial film had hexagonal symmetry, additionally the 2H stacking sequence can be seen in the TEM micro graph.

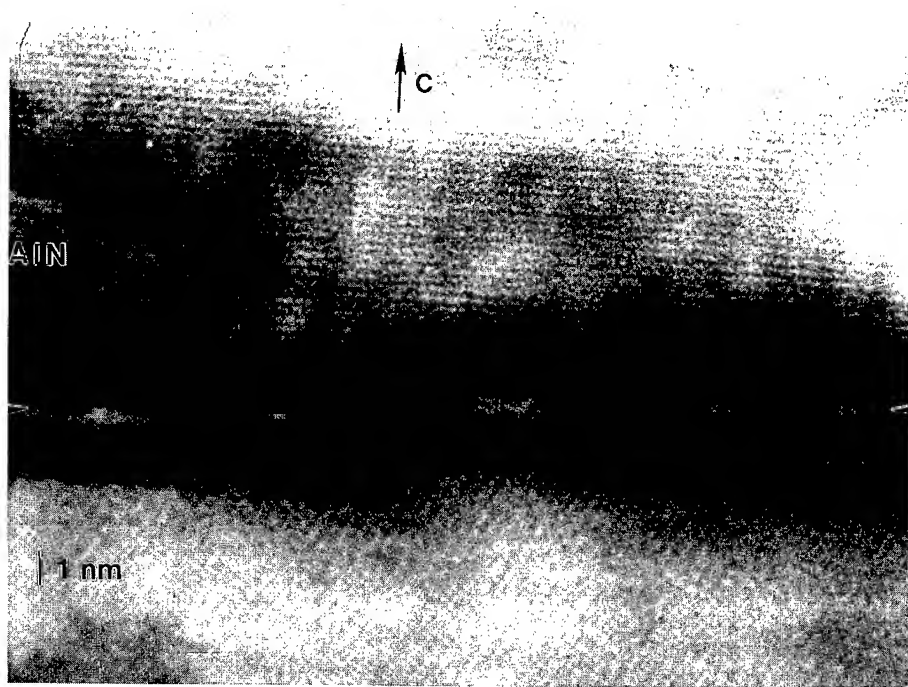


Figure 3. High resolution TEM micro graph of AlN:C Sapphire Interface

In order to confirm the p-type nature of the AlN films, a heterojunction of p-type AlN:C on n-type 6H-SiC was grown. The junctions were isolated by sandblasting and metal contacts were evaporated. I-V measurements indicate that a p-n junction was formed. Blue light emission was observed from the n-SiC indicating hole injection into the SiC. When a two probe experiment was performed on a heterojunction of AlN:C and p-SiC blue emission was not observed.

CONCLUSIONS

In summary, we have grown low resistivity AlN:C by MOCVD. The resistivity of the films is controlled by the flow of propane during growth. The films are single crystal for unintentional carbon flow as well as up to a partial pressure, as high as 2.5×10^{-3} torr. The resistivity of the films is a linear function of the propane flow. From Auger studies it can be determined that a large fraction of the carbon in the material does not contribute to the p-type conductivity of the crystal. TEM micro graphs do not show the presence of a second phase and indicate that the material is crystalline. P-n heterojunctions of SiC and AlN have been fabricated from epitaxial films deposited on 6H-SiC substrates.

ACKNOWLEDGMENTS

The authors acknowledge support from the National Science Foundation under Cooperative Agreement #HRD-9255 378, Contract Monitor Tony Mitchell and the Office of Naval Research under Grant #N00014-94-1-0274, Contract Monitor Max Yoder. The TEM image was taken by Dr. L. Riba. The authors also acknowledge useful discussions with Dr. Clayton W. Bates, Jr. and Dr. Jerry Woodall concerning this work.

REFERENCES

1. T.L. Chu, D.W. Ing, and A.J. Noreika, Solid State Electron, 10, 1023 (1967).
2. W.M. Yim, E.J. Stofko, P.J. Zanzucchi, J.I. Pankove, M. Ettenberk, and S.L. Gilbert, J. Appl. Phys. 44 (1973), 292.
3. R.F. Rutz, Appl. Phys. Lett., 28, 379 (1976).

Part IV

Alloys and Novel Growth Techniques

GaAsN ALLOYS AND GaN/GaAs DOUBLE-HETERO STRUCTURES

Michio SATO

NTT Basic Research Laboratories, Atsugi, Kanagawa 243-01, Japan, sato@will.brl.ntt.jp

ABSTRACT

Ternary alloys; GaAsN ($N < 3\%$) were grown by plasma-assisted metalorganic chemical vapor deposition using triethylgallium, AsH_3 , and plasma-cracked NH_3 or N_2 as the precursors. More N atoms were incorporated into the alloys from N_2 than NH_3 at constant N/As ratios. Both photoluminescence peaks and optical absorption edges were redshifted from GaAs bandgap with increasing the N content, indicating the GaAsN alloys have narrower bandgaps than GaAs.

GaN/GaAs double-hetero structures were grown by exposing GaAs surfaces to N-radical flux to replace surface As atoms by N atoms, and by growing GaAs on the thin GaN layers. When the GaN thickness exceeded one-monolayer, the GaN/GaAs interfaces and the GaAs cap layers deteriorated drastically. The one-monolayer-thick GaN embedded in GaAs attracts electrons and shows intense photoluminescence, whereas the GaN cluster is non-radiative, probably because of the defects caused by the large lattice-mismatch between GaN and GaAs.

INTRODUCTION

Both GaAs and GaN have direct bandgaps: 1.42 eV (infrared) for GaAs and 3.4 eV (ultraviolet) for GaN. It was thought that the GaAsN alloy system might have a direct bandgap between those of GaAs and GaN, which might allow fabrication III-V light emitting devices covering the entire visible spectrum. However, instead of the expected blue shift from GaAs bandgap, $GaAs_{1-x}N_x$ alloys with small N showed a considerable red shift in photoluminescence (PL) and the absorption edge with increasing N concentration.[1] The red shift probably indicates a bandgap bowing of GaAsN that results from the strong electronegativity of N atoms. Calculations of the bandgap of GaAsN have suggested that the bandgap bowing of GaAsN is severe and GaAsN may be semi-metallic in a certain composition range.[2,3] Therefore, one can expect that the GaAsN alloys may be widely applicable in electronic devices using semi-metallic layers as well as in light emitters covering the entire visible spectrum.

Growth of GaAsN alloys by plasma-assisted metalorganic chemical vapor deposition (MOCVD)[1, 4-6], by conventional MOCVD using dimethylhydrazine as the N precursor[7], and by gas-source molecular beam epitaxy (GSMBE)[8] has been reported. So far, the nitrogen concentration in the alloys has been limited to low levels. Furthermore, a strong miscibility gap, caused by the large (more than 20%) lattice mismatch between GaAs and GaN, has been reported.[3] One possible way to increase nitrogen concentration is by growing thin-layer superlattices: $(GaAs)_m(GaN)_n$. This requires GaAs growth on GaN layers and flat interfaces between GaAs and GaN, which has been considered to be difficult. Using a novel method for controlling radical supply precisely, GaAs/GaN/GaAs thin-layer structures have been grown by plasma-assisted MOCVD.[9] This paper reports the growth and the properties of the GaAsN alloys and the GaAs/GaN/GaAs thin-layer structures.

EXPERIMENTAL

Growth Apparatus

The growth apparatus is shown in Fig. 1. A water-cooled stainless-steel chamber is pumped by a combination of a mechanical booster and a rotary vacuum pump. This combination

allowed MOCVD growth at very low pressures of 10~100 Pa. Low pressures are required for plasma operation and efficient supply of reactive species, such as radicals, to a substrate. A downstream-type plasma-cracking cell, irradiated with 2.45 GHz microwaves at a maximum power of 260 W applied through a waveguide with a three-stub tuner, was used to supply N radicals. N-precursors are injected through the cell and cracked in the plasma region. Reactive and electrically neutral N species are carried to the substrate by the gas flow. Because of the very short lifetime of ions in the gas phase, ions created in the plasma cell easily recombine to neutral molecules. Thus, there is less surface damage by ion bombardment. A quadrupole mass spectrometer (QMS), differentially pumped by a turbo-molecular pump (TMP), was installed to monitor the species in the growth chamber. The substrate temperature was monitored by an infrared pyrometer calibrated at the melting point of InSb.

Nitrogen Radical Densities

Since plasma-assisted MOCVD is a new growth technique for growing GaAsN alloys and GaN layers, the growth kinetics should be quantitatively investigated. N-radical densities during MBE, plasma-assisted MOCVD and conventional MOCVD were numerically estimated from the rates of radical recombination and pyrolysis.[10]

There are many kinds of reactive nitrogen species in a plasma. Neutral atomic, ionic, and excited molecular nitrogen were detected by optical diagnostics of the plasma. The molecules and atoms at excited states are easily quenched by releasing their energies through electron transitions with luminescences. The lifetimes of the excited atoms and molecules are so short that their densities are very small outside the plasma where no energies are given. The lifetime of ionic species is also short, especially when the plasma works at high pressures (non-vacuum conditions). Therefore, neutral N atoms at the bottom state are probably the dominant species which act as radicals during growth. The recombination of the atomic N is discussed quantitatively.

The recombination of two radicals is a reaction with no activation energy, therefore, there is little temperature dependence in the recombination rates. The radical recombination needs a third-body to transfer the heat of the reaction. An inert molecule usually acts as the third-body, and a solid surface like a chamber wall can also act as the third-body. When the recombination at the chamber wall can be neglected, the recombination rate is proportional to the square of the radical density and the third-body density. Therefore, the radical lifetime is

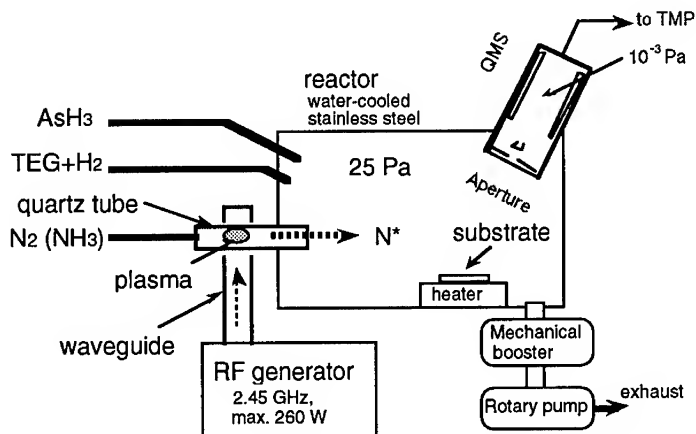


Fig. 1 Plasma-assisted MOCVD apparatus for growing GaAsN alloys and GaAs/GaN/GaAs structures.

very sensitive to the total pressure.

Since plasma is unstable in vacuum where MBE growth is performed, a plasma-cracking cell for supplying radicals into an MBE chamber requires an outlet aperture. Some radicals recombine at the aperture by transferring the heat to the aperture, which decreases the overall cracking yield of the cell. In plasma-assisted MOCVD used in this study, the plasma works at the chamber pressure, and thus, the cracking cell has no outlet aperture. Therefore, higher cracking yield may be expected. The radical densities in the plasma are on the order of $10^{15}\sim 10^{16}$ molecule $\cdot\text{cm}^{-3}$, which is denser than that of a plasma operated at lower pressures. At the pressure of 10~100 Pa, the lifetime of the radicals is $10^{-3}\sim 10^{-1}$ s, which is on the same order as the flight time of the radicals from the cell to the substrate. The estimated lifetime agrees with the lifetime of oxygen radicals at a similar pressure measured by chemical titration.[11,12]

The radical flux is estimated to be 5×10^{17} molecule $\cdot\text{cm}^{-2}\text{s}^{-1}$ under typical conditions, i.e. N_2 flow rate of 100 sccm and chamber pressure of 50 Pa. This value is one order of magnitude higher than that can be achieved by GSMBE, i.e. 2×10^{16} molecule $\cdot\text{cm}^{-2}\text{s}^{-1}$, when N_2 of 1 sccm from several sccm introduced into an MBE chamber is completely dissociated into N radicals and supplied to a surface of 50 cm^2 .

The radical density in the vapor phase during conventional MOCVD can be estimated from the rate equations of the NH_3 pyrolysis and the radical recombinations.[10] The estimated radical densities at the gas temperature of 900~1100°C are on the order of $10^9\sim 10^{10}$ molecule $\cdot\text{cm}^{-3}$, which are not enough for GaN growth. The radical densities must be much smaller at the GaAsN growth temperature of 500°C. The radicals formed in the vapor phase are not the dominant N-source during MOCVD growth. Heterogeneous decomposition of NH_3 at the growing surface is probably the dominant reaction path to create N-atoms for the growth. NH_3 is a polar molecule and is preferentially adsorbed by an electron acceptor. The surface Ga atom is the electron acceptor during growth, therefore, it chemically adsorbs NH_3 , which decomposes to form GaN. During GaAsN growth where As atoms exist, Ga atoms are easily terminated by As atoms and no electron-acceptors are given for NH_3 adsorption. This may be the reason why GaAsN is difficult to grow by conventional MOCVD.

Radical Flux Control

The growth of GaN thin layers requires precise control of N-radical supply. The N-radical supply is started when the N plasma is ignited in the plasma-cracking cell. In conventional plasma-ignition methods, N_2 gas is introduced into the cell and then microwaves at the maximum power are applied to ignite the plasma. A pressure of about 300 Pa, which is too high for stable downstream operation, is needed to ignite the plasma in the cell. It takes about 20 seconds to stabilize the chamber pressure down to the growth conditions. The waveguide tuner should be tuned after the plasma ignition, because the optimal tuning point of the downstream operation is different from the ignition tuning point. This also requires several tens of seconds. Furthermore, the amount of radicals supplied during the plasma-ignition procedure is neither controllable nor reproducible, making short-duration radical-supply impossible.

A novel method to control the radical supply precisely has been proposed.[9] Ar gas is introduced into the cell and Ar plasma is ignited prior to the growth of a GaAs buffer layer. Ar ions are not supplied to the substrate, because of the short lifetime of the ions in the gas phase. No difference between the characteristics of undoped GaAs layers grown with and without Ar plasma was found. When N_2 is introduced into the Ar plasma, N_2 molecules are immediately dissociated by collisions with Ar ions, thus N plasma is ignited without increasing pressure or increasing microwave power. N radicals created in the plasma are supplied to the substrate surface. This method enables the radical supply to be controlled easily and precisely: the N-radical supply is started and stopped simply by opening and closing a valve, and the amount of radicals is controlled by adjusting the flow rate of N_2 gas. The same goal can be attained by using He or Ne instead of Ar.

Growth Conditions

GaAsN alloy layers were grown on (100) oriented semi-insulating GaAs. Triethyl-gallium (TEG) carried by H_2 carrier gas and 100% AsH_3 are used as Ga and As sources, respectively. TEG and AsH_3 are introduced without precracking. Plasma-cracked NH_3 and N_2 were used as the N-precursor. The TEG flux was 0.3 sccm and the growth rate was $0.8 \mu m/h$ at $500^\circ C$. The GaAs substrate was annealed in an AsH_3 flux of 20 sccm at $640^\circ C$ for one minute to remove surface oxide. After cooling to growth temperature under the AsH_3 flux, NH_3 or N_2 was introduced through the plasma cell and the pressure was briefly increased to 300 Pa to ignite the plasma. Pressure was then decreased to the growth pressure of 25 Pa and the growth was started by introducing TEG.

The GaAs/GaN/GaAs thin-layer structures were grown on (100) GaAs substrates. The concept how to make GaN thin layers is shown in Fig. 2. The typical growth temperature was $500^\circ C$, where the desorption of surface As atoms have a lifetime of about 30 seconds.[13] The chamber pressure was typically kept at 30 Pa and some growth was done at 50 Pa. TEG carried by H_2 carrier gas, uncracked AsH_3 , and plasma-cracked N_2 were used as Ga, As, and N sources, respectively. The GaAs substrates were thermally cleaned under AsH_3 fluxes and cooled down to the growth temperature. 250-nm-thick GaAs buffer layers were grown using TEG and AsH_3 whose respective flow rates were 0.3 sccm and 10 sccm. AsH_3 was supplied for an additional second after the buffer-layer growth to establish the As-stabilized surfaces. GaN layers were formed by exposing As-stabilized surfaces of GaAs epitaxial layers to N-radical fluxes. The As atoms were replaced by N atoms, forming GaN thin-layers on GaAs buffer layers. 250-nm-thick GaAs cap layers were grown on the GaN layers. Ar or He plasma was used to control the N-radical supply. The plasma was ignited before the thermal cleaning of the GaAs substrate surfaces.

The structures were characterized by x-ray diffraction (XRD), secondary ion mass spectrometry (SIMS) using N-implanted GaAs as a standard sample, and photoluminescence. Etch-pit density (EPD) measurement using molten KOH and cross-sectional transmission electron microscopy (TEM) were performed for the GaAs/GaN/GaAs structures

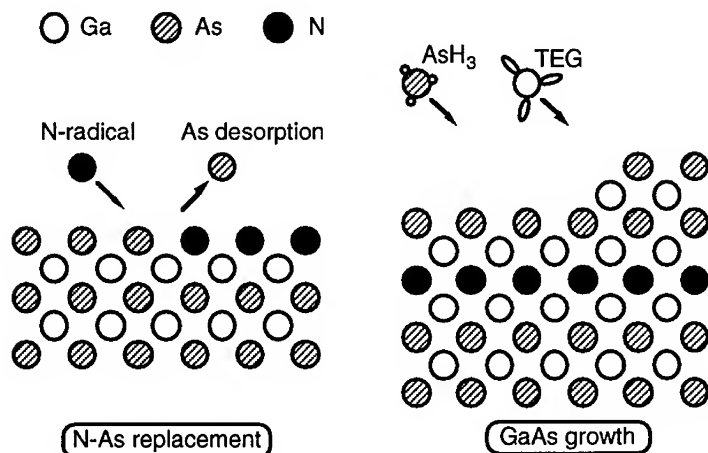


Fig. 2 Schematics of the growth of GaAs/GaN/GaAs structures. GaN layers are created by atomic replacement of As by N.

RESULTS AND DISCUSSIONS

Growth of GaAsN

Several growth runs were performed without plasma cracking of the N precursors. The growth pressure was kept at 25 Pa and the flux of N_2 or NH_3 was 50-100 sccm with H_2 carrier of 100 sccm, TEG of about 0.3 sccm, and AsH_3 of 5-20 sccm. Epitaxial layers with specular surfaces were obtained. The XRD peaks from the epitaxial layers were not separated from the GaAs substrate peak. When uncracked NH_3 was introduced with TEG and AsH_3 , N was detected on the order of 10^{17} cm^{-3} in the grown GaAs layers by SIMS, whose background signal of N was the order of 10^{16} cm^{-3} . However no N was detected when uncracked N_2 was introduced. This indicates that N_2 is more stable than NH_3 and cannot be used as an N source without pre-cracking.

Mass spectroscopic studies of the species in the growth chamber showed that the plasma-cracking cell efficiently decompose NH_3 and N_2 , and that the N radicals effused from the cell can be detected by the QMS. It was also found that the N-radical is active enough to react with stable H_2 carrier gas.[6] This high reactivity may make it possible to grow GaAsN alloys.

GaAsN was grown at 25 Pa and 500°C using TEG, AsH_3 , and plasma-cracked NH_3 or N_2 . Epitaxial layers with specular surfaces were obtained when the AsH_3 flux was above 5 sccm. Almost all samples showed sharp XRD peaks and the clear fringes on both sides of the layer peaks. This indicates that the layers have high crystalline quality and compositional uniformity and that the surfaces and the interfaces between the layers and substrates are very smooth. The N-composition from the lattice constant measured by XRD coincided well with that by SIMS, indicating that N-atoms are substitutionally located at group-V sites of GaAs.

The relationship between N incorporation and AsH_3 flux is shown in Fig. 3. The N content, x , decreases with increasing AsH_3 flux, suggesting competition between N and As for group-V sites. Two N radicals can be formed from each N_2 molecule. However, comparison between experimental data from NH_3 of 100 sccm and N_2 of 50 sccm indicates that more N was incorporated from N_2 than NH_3 . N_2 is thus a better N precursor for growing GaAsN, because of its higher efficiency for nitrogen incorporation as well as its safer characteristics, that is, N_2 is neither corrosive nor toxic.

Thermal cracking of AsH_3 at the growing surface produces reactive As species. The As species and the N radicals compete for group-V sites by creating chemical bonds with Ga atoms. The elementary molecules of As; As_2 and As_4 , can be the As source for GaAs growth. While, as found in the growth trials without plasma cracking, N_2 or NH_3 cannot be the N source, that is, N_2 and/or NH_3 formed at the surface is excluded from the growth reaction. This may be one of the reasons why very high N/As ratio is required for GaAsN growth. Plasma-cracking of NH_3 creates reactive H radicals as well as N radicals. The H radicals probably remove N atoms from the growing surface by creating stable NH_3 molecules, resulting the reduction of N incorporation.

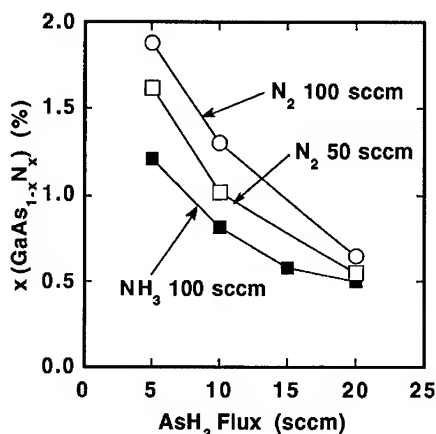


Fig. 3 Relationship between As flux and N incorporation into GaAsN alloys. The x was calculated from the lattice constant measured by x-ray diffraction.

Optical Properties of GaAsN

PL from the GaAsN layers was measured at 77 K using an Ar ion laser as an excitation source and a photomultiplier with an InGaAs cathode as a detector. The PL spectra of 0.4- μm -thick $\text{GaAs}_{1-x}\text{N}_x$ samples with $x=0.32\%$ and $x=1.4\%$ are shown in Fig. 4. The PL emission from the GaAsN sample is shifted to lower energies from GaAs bandgap and no emission in the region of the GaAs band edge is observed. Deep emissions were observed in all PL spectra for GaAsN. The peak of the deep emission was about 0.1 eV lower than the highest energy emission peak for each GaAsN layer. The deep emissions are probably due to defects associated with group-V vacancies, since those samples were grown with a low supply of As. Because the sensitivity of the InGaAs photomultiplier drastically decreases at energies below 1.3 eV, detailed discussion of these deep emissions is difficult.

Figure 5 shows the absorption spectra of the two GaAsN layers whose PL spectra are shown in Fig. 4. With consideration of the Stokes shift in the PL, the PL and the absorption edge in the layer are in excellent agreement. The absorption coefficient of the GaAsN layers above their absorption edge does not show any structure that would be expected if discrete levels in the band gap of a GaAs host are responsible for the absorption. Additionally, the

value of the absorption coefficient of GaAsN is approximately the same as that of GaAs above its absorption edge. These findings indicate that the position of the absorption edge and the highest energy emission peak of the PL represents the bandgap of the GaAsN layer.

The bandgaps of GaAsN layers measured by PL are shown in Fig. 6. The bandgap systematically shifts to lower energies with increasing N content. No difference was observed between the PL results from the layer using the two different N-precursors. When the sensitivity decrease of the photomultiplier is accounted for, the PL from the GaAsN layers was as intense as the PL from a GaAs sample grown with the same apparatus. Results for the GaAsN layers grown by GSMBE[8] are also shown for comparison. The trend of the redshift is very similar. Sakai *et al.* calculated the bandgap of GaAsN alloy[2] and their result is shown by the solid line in Fig. 6 and in Fig. 7 for whole N-concentration range together with the experimental data. Though the experimental data are only available at very small N-contents, the bandgap redshift is well explained by the calculation. If the extrapolation along the calculated curve is possible, the bandgap of GaAsN with more N will be smaller than zero,

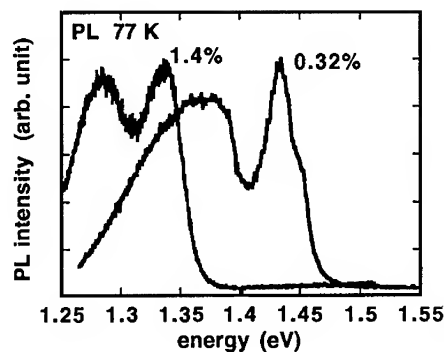


Fig. 4 77 K PL spectra of the GaAsN layers with N=0.32% and 1.4%.

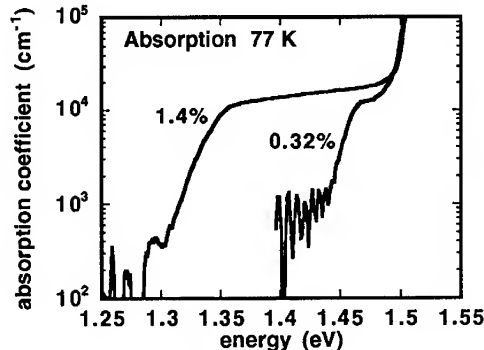


Fig. 5 77 K optical absorption spectra of the GaAsN layers with N=0.32% and 1.4%.

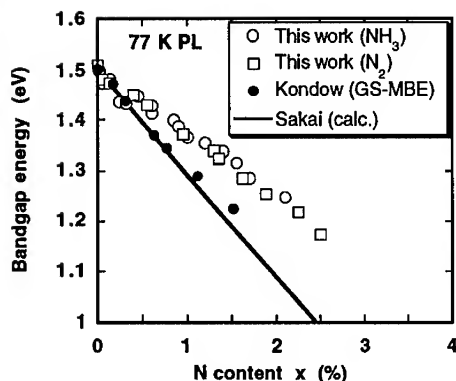


Fig. 6 Bandgap energies of GaAsN.
Data by GSMBE is from ref. [8].

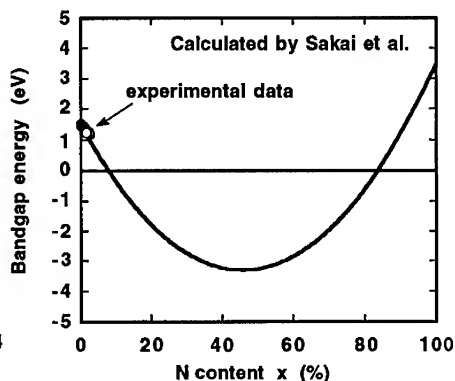


Fig. 7 Calculated bandgap energies from
ref. [2], with the experimental data.

and then the layer will be semi-metallic.

Several applications of GaAsN alloys are proposed and have recently been demonstrated. The GaAsN alloys and similar alloys; GaPN, are lattice-matched to Si substrates at certain N-contents. Therefore, the GaAsN/GaPN system is one of the candidates of the opto-electronic devices on Si substrates. Kondow *et al.* proposed GaAsN/GaPN quantum well (QW) structures for the on-Si device application, and grew GaAsN/GaP QW on GaP substrates by GSMBE for this demonstration.[14] They observed intense PL from the QW on GaP, suggesting that the system is promising. Quarternary alloy; InGaAsN can be lattice matched to GaAs substrates. Since both In and N redshift the GaAs bandgap, InGaAsN can be the material for optical devices for long wavelength applications. Kondow *et al.* introduced some N into the active layer of a GaAs-based InGaAs/AlGaAs laser diode structure, and observed redshift of the lasing spectrum.[15]

Analysis of GaAs/GaN/GaAs Structures

The thicknesses of the GaN layers were measured by integrating the SIMS depth profiles of the samples. Figure 8 shows the SIMS depth profile of the structure whose N-radical exposure time was 10 minutes at the N_2 flow rate of 100 sccm. Secondary ions of 83 amu (GaN) were used for a measure of N depth profiles. The full width at half maximum value is as small as 20 nm, indicating that the grown GaN layer is very thin and that there is no drastic diffusion or segregation of nitrogen during the growth. The profiles were integrated to obtain the total amount of N, and the value is shown in Fig. 9 as a function of the N-radial exposure time. The value for the exposure time of 10

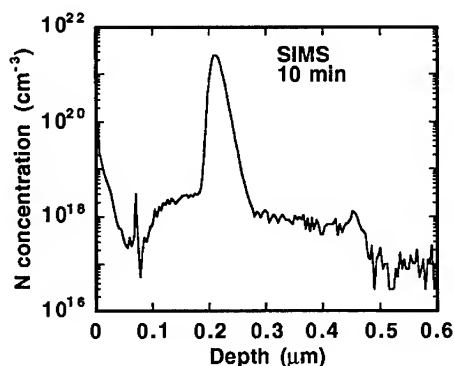


Fig. 8 SIMS depth profile of N concentration
of a GaAs/GaN/GaAs structure.

seconds is almost equal to (or slightly less than) $6.3 \times 10^{14} \text{ cm}^{-2}$, which is the number of the sites in a (100) atomic plane in GaAs, thus indicating that the surface As atoms are easily replaced by the N atoms at 500°C and that one-monolayer (ML)-thick GaN was grown. The N concentration increases with the exposure time, but this increase is not linear, indicating that the replacement of the As atoms in the second or deeper As-plane is slower than those at the surface.[9]

Since the GaN layers in the structures were very thin, no separate peaks from the GaN layers were observed in XRD. When 1-ML-thick GaN was embedded in GaAs, the fringes on both sides of the GaAs diffraction peak were clearly observed, indicating that the GaN/GaAs interface and the surface of the sample were very flat. The structures with more than 1 ML's worth of N showed no fringes, indicating the GaN/GaAs interface and/or the surface of the GaAs cap layer had deteriorated.

The EPDs of the GaAs/GaN/GaAs structures are shown in Fig. 10. When the GaN thickness was 1 ML or less, the EPD was about $1 \times 10^5 \text{ cm}^{-2}$, which was as large as that of a GaAs reference sample grown under the same conditions without exposure to the N-radical flux. The EPD drastically increased with increasing the GaN thickness from 1 ML to 3 MLs, indicating that GaN layers thicker than 1 ML created dislocations in the GaAs cap layers. The EPDs of the structures having two GaN layers separated by 7-ML-thick GaAs are shown by the solid circles in Fig. 10. Though the total N amounts are more than 1 ML worth, the EPDs are as low as 10^5 cm^{-2} , suggesting that GaN/GaAs thin-layer superlattices can be grown when each GaN layer is thinner than 1 ML.[16]

Many dislocations were visible in the GaAs cap layers in the TEM cross sections of the GaAs/GaN/GaAs structures whose GaN thicknesses are 3 and 2 MLs. The lattice image of the GaAs cap layer of the sample having 3-ML-thick GaN was almost invisible in the high-resolution image, suggesting that the GaAs layer was so deteriorated that it became

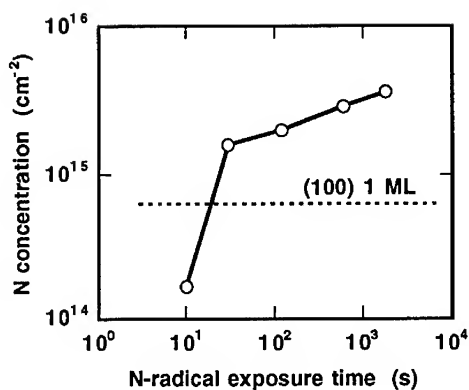


Fig. 9 Total N amounts in the structures by integrating the SIMS profiles. The chamber pressure, the gas fluxes, the microwave power are fixed.

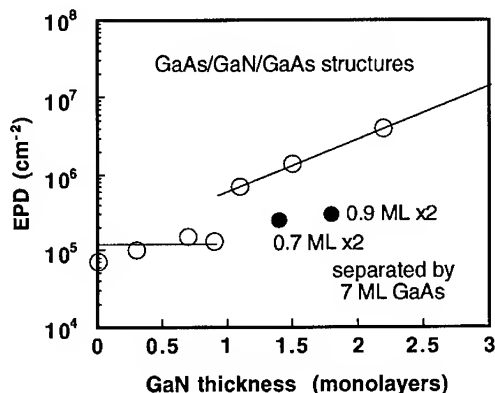


Fig. 10 Etch pit densities of the surfaces of the GaAs/GaN/GaAs structures measured by molten KOH.

poly-crystal or amorphous. No dislocations can be seen in the TEM images of the sample having 1-ML-thick GaN, indicating that 1-ML-thick GaN can be pseudomorphically embedded in GaAs without creating dislocations.[16]

These experimental results indicate that the critical layer thickness of GaN embedded in GaAs is approximately 1 ML. GaN/GaAs thin-layer superlattices can be grown when each GaN layer is thinner than 1 ML.

Optical Properties of GaAs/GaN/GaAs

Low-temperature (10 K) PL was measured using a He-Ne laser (632.8 nm) as an excitation source and a cooled Ge diode as a detector. PL spectra from the structures are shown in Fig. 11 together with the spectrum from GaAs not exposed to N-radicals. Deep emission at 1.43 eV appears as separated peaks in (b), (c) and (e) and as a shoulder peak in (d). The PL intensity of the 1.43-eV peak increases linearly with the excitation intensity, suggesting that the peak represents an excitonic emission like the emission from quantum wells. The PL peak intensities of the 1.49-eV peak (carbon in GaAs) and the 1.43-eV peak drastically decrease at long exposure times. The decrease of the PL intensities also suggests that GaN layers thicker than 1 ML deteriorate the qualities of the GaN/GaAs interfaces and the GaAs cap layers.

The surface As atoms are easily replaced by N atoms and this replacement occurs two-dimensionally, thus forming 1-ML-thick GaN. When the replacement of the surface As-layer is completed, N radicals start to replace As atoms of the second As-layer from the surface. Due to the large lattice-mismatch between GaAs and GaN, the replacement of As atoms situated lower than the second layer cannot be two-dimensional and GaN clusters may be formed. These GaN clusters cannot be pseudomorphic because of the large lattice-mismatch of more than 20% and may be the source of defects causing the rough interface and the low PL intensity from the cap layers. The broad peak at about 1.38 eV in Fig. 11(d) is probably due to GaN clusters whose size is small enough not to create defects.[9]

The origin of the 1.43 eV PL is discussed. Because of the strong electronegativity of N atoms, a GaN layer in GaAs attracts electrons. The 1.43-eV peak is probably due to the excitonic emission from the 1-ML-thick GaN. A simple calculation performed using a finite square well model, which had excellently described the bandgaps and the quantized levels of InAs/GaAs thin-layer structures,[17-19] was used to describe the PL photon energy from the GaAs/GaN/GaAs structures. Conduction- and valence-band discontinuities between GaN and GaAs are 2 eV and -4 eV, respectively.[2] Therefore, a GaN layer embedded in GaAs can be regarded as a deep QW for electrons and a very high barrier for holes. An emission between an electron at the quantized level of the QW and a hole at the valence-band maximum of GaAs may be observed in the PL measurement. The 1-ML-thick GaN is assumed to be 0.225-nm-wide, which is half of the lattice constant of cubic GaN, and 2-eV-deep QW. Since the wave function expands deeply into GaAs, the effective mass in GaAs ($0.0665m_0$, where m_0 denotes free electron mass) was used in the calculation. The strain effects on the bandgap of GaN and on the GaN thickness were ignored in this preliminary calculation. The calculated

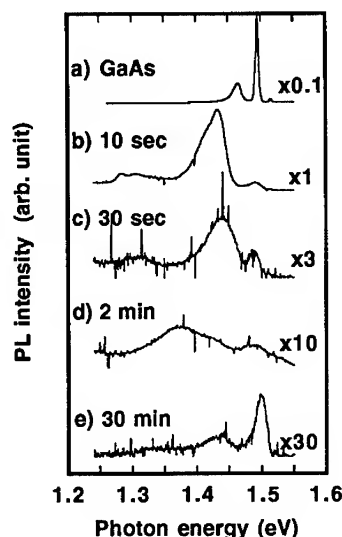


Fig. 11 PL spectra measured at 10 K. a) GaAs reference not exposed to N-radical flux. b-e) GaAs/GaN/GaAs structures. Averaged GaN thicknesses of b), c) and e) are approximately 1 ML, 2 ML and 3 MLs.

quantized level for electrons was 0.08 eV below the conduction-band minimum of GaAs. This agrees with the difference between the GaAs bandgap and the experimental PL photon energy of 1.43 eV.

CONCLUSIONS

Ternary alloys; GaAsN (N<3%) were grown by plasma-assisted MOCVD using TEG, AsH₃, and plasma-cracked NH₃ or N₂ as the precursors. More N atoms were incorporated into the alloys from N₂ than NH₃ at constant N/As ratios, indicating that N₂ is a better N precursor for growing GaAsN, because of its higher efficiency for nitrogen incorporation as well as its safer characteristics, that is, N₂ is neither corrosive nor toxic. Both PL peaks and optical absorption edges were redshifted from GaAs bandgap with increasing the N content, indicating the GaAsN alloys have narrower bandgaps than GaAs.

GaN/GaAs double-hetero structures were grown by exposing GaAs surfaces to N-radical fluxes to replace surface As atoms by N atoms, and by growing GaAs on the thin GaN layers. XRD, EPD measurement, TEM, and PL indicate that the GaN/GaAs interfaces and the GaAs cap layers deteriorated drastically when the GaN thickness exceeded 1 ML that is, the critical layer thickness of GaN embedded in GaAs is approximately 1 ML. The 1-ML-thick GaN embedded in GaAs attracts electrons and shows intense PL, whereas the GaN clusters, which was formed by further As-N replacement than 1 ML, are non-radiative, probably because of the defects caused by the large lattice-mismatch between GaN and GaAs.

ACKNOWLEDGMENTS

The author wishes to thank Dr. Markus Weyers for the GaAsN growth and discussions on the growth mechanisms, Dr. Hiroaki Ando for the absorption measurement and his comments on the optical properties, and Dr. Naoki Kobayashi and Dr. Yoshiji Horikoshi for their continuous encouragement.

REFERENCES

1. M. Weyers, M. Sato and H. Ando, *Jpn. J. Appl. Phys.* **31**, (1992) L853.
2. S. Sakai, Y. Ueta and Y. Terauchi, *Jpn. J. Appl. Phys.* **32**, (1993) 4413.
3. J. Neugebauer and C. G. Van de Walle, *Phys. Rev. B* **51**, (1995) 10568.
4. M. Weyers and M. Sato, *Appl. Phys. Lett.* **62**, (1993) 1396.
5. M. Sato and M. Weyers, *Inst. Phys. Conf. Ser.* **129**, (1993) 555.
6. M. Sato, *J. Cryst. Growth* **145**, (1994) 99.
7. N. Ohkouchi, S. Miyoshi, H. Yaguchi, K. Onabe, Y. Shiraki and R. Ito, 12th Record of Alloy Semiconductor Physics and Electronics Symp., (Izu-Nagaoka, 1993) 337.
8. M. Kondow, K. Uomi, K. Hosomi and T. Mozume, *Jpn. J. Appl. Phys.* **33**, (1994) L1056.
9. M. Sato, *Jpn. J. Appl. Phys.* **34**, (1995) 1080.
10. M. Sato, Abs. of Topical Workshop on III-V Nitrides, (Nagoya, 1995) G-4; to be published in *Solid-State Electronics*.
11. C. H. Chou and J. Phillips, *J. Appl. Phys.* **68**, (1990) 2415.
12. C. H. Chou and J. Phillips, *J. Vac. Sci. Technol.* **A9**, (1991) 2727.
13. N. Kobayashi and Y. Kobayashi, *Jpn. J. Appl. Phys.* **30**, (1991) L1699.
14. M. Kondow, A. Niwa, K. Uomi, S. Watahiki, Y. Yazawa, K. Hosomi and T. Mozume, *Workbook of Int. Conf. on Chemical Beam Epitaxy*, (La Jolla, 1995).
15. M. Kondow, A. Niwa, K. Uomi, S. Watahiki, Y. Yazawa, K. Hosomi and T. Mozume, presented at Topical Workshop on III-V Nitrides, (Nagoya, 1995) G-1.
16. M. Sato, Abs. of Topical Workshop on III-V Nitrides, (Nagoya, 1995) P-32; to be published in *Solid-State Electronics*.
17. M. Sato and Y. Horikoshi, *J. Appl. Phys.* **66**, (1989) 851.
18. M. Sato and Y. Horikoshi, *J. Appl. Phys.* **69**, (1991) 7697.
19. M. Sato and Y. Horikoshi, *Appl. Phys. Lett.* **56**, (1990) 1555.

GaN THREE DIMENSIONAL NANOSTRUCTURES

V. DMITRIEV, K. IRVINE, A. ZUBRILOV*, D. TSVETKOV*, V. NIKOLAEV*, M. JAKOBSON**, D. NELSON**, and A. SITNIKOVA**

Cree Research, Inc., 2810 Meridian Parkway, Durham, NC 27713 USA

* Cree Research EED, 26 Polytechnicheskaya Str., St. Petersburg, 194021 Russia

** A.F. Ioffe Institute, 26 Polytechnicheskaya Str., St. Petersburg, 194021 Russia

ABSTRACT

We report on the growth and characterization of three dimensional nanoscale structures of GaN. GaN dots were grown by metal organic chemical vapor deposition (MOCVD) on 6H-SiC substrates. The actual size of the dots measured by scanning electron microscopy (SEM) and transmission electron microscopy (TEM) ranged from ~20 nm to more than 2 μm . The average dot density ranged from 10^7 to 10^9 cm^{-2} . The single crystal structure of the dots was verified by reflectance high energy electron diffraction (HEED) and TEM. Cathodoluminescence (CL) and photoluminescence (PL) of the dots were studied at various temperatures and excitation levels. The PL and CL edge peak for the GaN dots exhibited a blue shift as compared with edge peak position for continuous GaN layers grown on SiC.

INTRODUCTION

Quantum wires (QW) and quantum dots (QD) are of great interest because of their possible application for low threshold current semiconductor lasers [1], high density optical memory [2], and very large scale integration [3]. There are two main ways to create a semiconductor QW and QD: (1) nanoscale structure fabrication from planar layered structures using lithography and etching, and (2) formation of nanoscale structures in situ during epitaxial growth. The first approach has been used to fabricate GaInAs/GaInAsP/InP and InGaAs/GaAs QD [4,5] and the second was successfully employed for numerous semiconductors including InGaAs and GaAs [6,7]. The optimistic prediction about unique characteristics of quantum size structures was supported by the fabrication of a low threshold current density laser based on GaInP/AlGaInP QW structures [8]. A QD transistor has also been made [9]. No information of experimental QD optoelectronic devices has yet been published.

A³N semiconductors are the subject of intense research due to their potential for short wavelength laser diode fabrication. Stimulated emission has been observed in GaN-based structures under optical pumping [10,11,12,13,14]. Theoretical predictions show that due to specific fundamental parameters of the A³N materials the threshold current density in these structures may be a few times higher than that for GaAs-based laser structures [15,16]. As such, the possibility of threshold current density reduction due to quantum size effects would be very important for A³N laser structures.

One dimensional quantum size structures have been reported for A³N material systems in terms of fabrication and investigation of AlGaN/GaN and AlGaN/InGaN quantum well structures [17,18] and superlattices [19,20]. In this paper we report on the first three dimensional GaN nanostructures.

EXPERIMENT

GaN was grown by MOCVD. 6H-SiC (0001) wafers manufactured by Cree Research, Inc. were used as substrates. The growth was done in such a manner that the GaN formed was not a continuous layer but consisted of separated dots. The dot size was measured by SEM and TEM. Optical properties of the dots were studied at various temperatures and excitation levels. The PL measurements were performed using above band gap radiation provided by a 250 W Hg-lamp (weak excitation) or a 10 kW N₂-laser (strong pulsed excitation). A liquid-helium cryostat was used for PL experiments at 4.2 K. The CL was excited with a 0.05 mA electron beam at an accelerating voltage which was varied from 4 to 15 kV. CL was investigated at 80 K. The PL and CL spectra were measured employing a 0.6 m LOMO MDR-23 monochromator with a photomultiplier detector and corrected for instrumental response.

It was found that depending on growth conditions the dot lateral size in different samples ranged from ~20 nm to more than 2 μm (Fig. 1). The average dot density was controlled in the range from 10^7 to 10^9 cm^{-2} . The HEED and TEM measurements showed that the dots had a single crystal structure (Fig. 2).

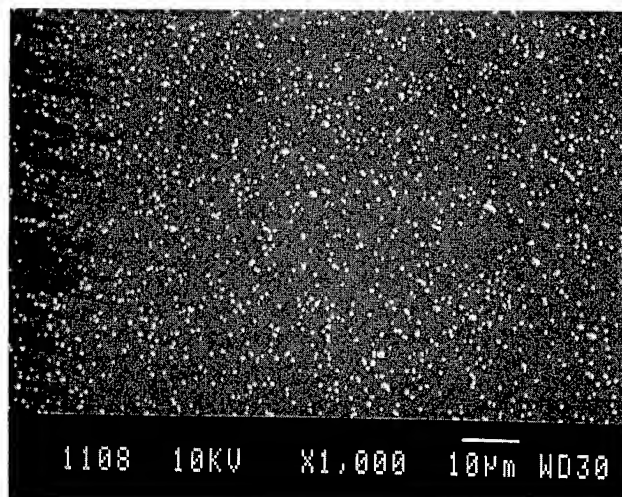


Figure 1. SEM image of the surface of SiC substrate and GaN dots.

Luminescence measurements were performed on a sample with dot sizes ranging from 50 to 250 nm (Fig. 3). The size distribution was measured by TEM. The PL and CL spectra of GaN dots exhibited a blue shift and a broadening of the edge peak as compared with its position and width for continuous GaN layers grown on SiC. The PL spectra for a GaN continuous layer and GaN quantum dots at 4.2 K at high and low excitation levels are shown in Fig. 4.

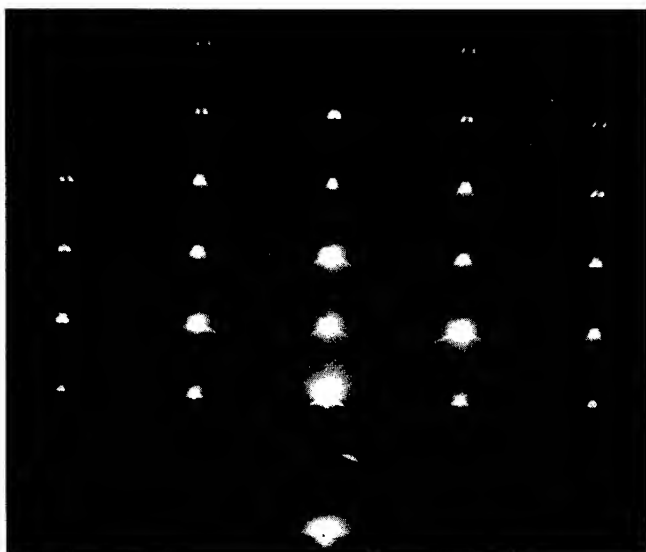


Figure 2. HEED pattern from the sample having GaN dots.

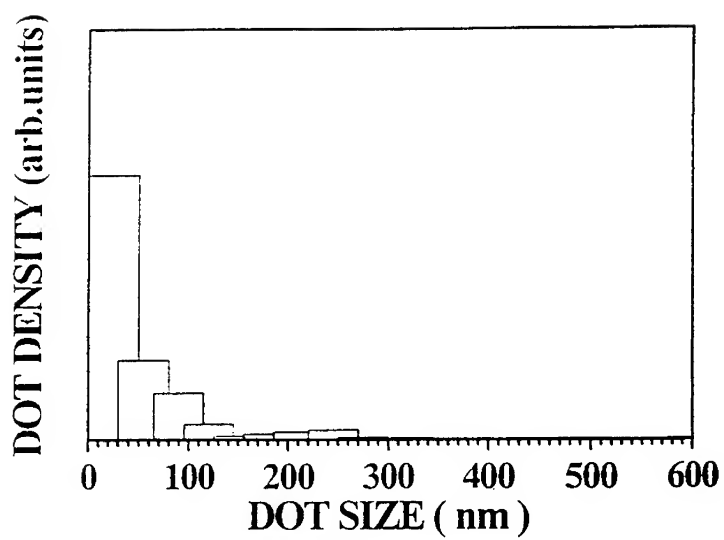


Figure 3. GaN dot density vs. dot size measured by TEM.

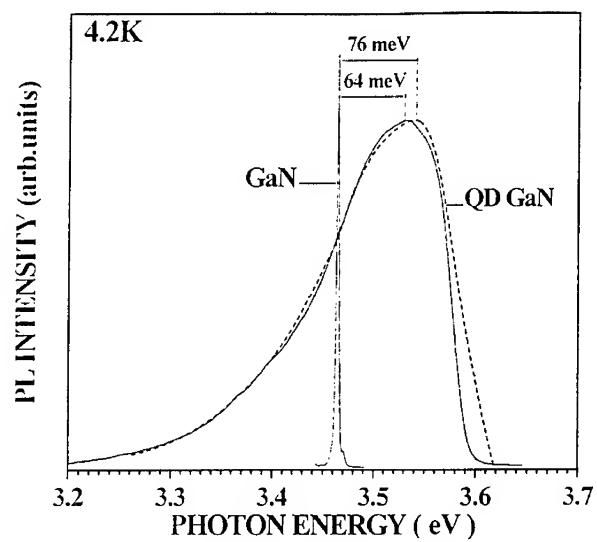


Figure 4. PL spectrum for GaN dots and a continuous GaN layer grown on 6H-SiC wafer: dash line - laser excitation, solid line - hydrogen lamp excitation.

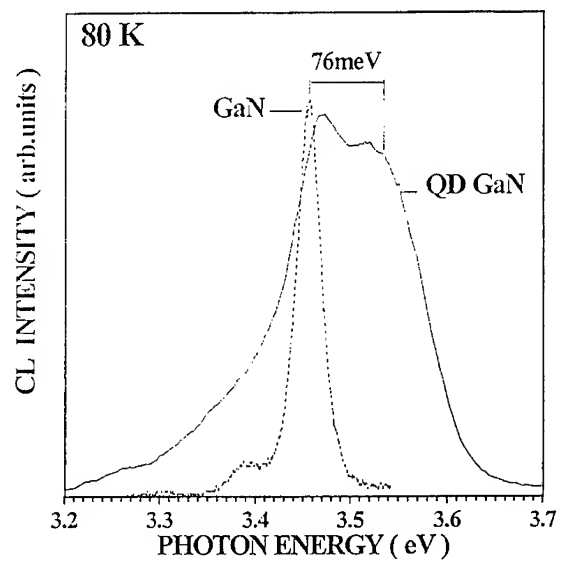


Figure 5. CL spectrum for GaN dots and a continuous GaN layer grown on 6H-SiC .

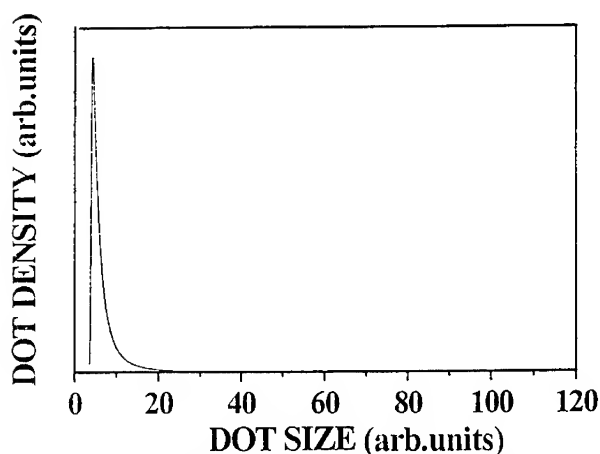


Figure 6. GaN dot density vs. dot size obtained from PL data based on model [21].

Under a weak excitation, the blue shift of the GaN edge peak was ~ 64 meV at 4.2 K (a new peak position was observed at 3.529 eV). The PL line at 3.465 eV (standard peak position for a continuous GaN layer) was not detected. In the case of strong pulsed excitation, the blue PL shift was ~ 76 meV (4.2 K). An edge peak blue shift of ~ 70 meV and peak broadening was also observed for the CL spectra measured at 80 K (Fig. 5).

We believe that the blue shift detected for the edge luminescence peak was due to three dimensional quantum carrier confinement in the GaN dots. Dots with different sizes exhibited different shifts. The wafer surface was covered with dots having different sizes causing the broadening of the luminescence peak. The PL data was used to reconstruct the dot size distribution. Tentative calculations based on a three dimensional quantum confinement model [21] showed that the dot size distribution obtained from the PL spectrum (Fig. 6) is in good agreement with that measured by TEM (compare Fig. 3 and Fig. 6).

SUMMARY

GaN nanoscale dots were fabricated and characterized. The dots were grown on 6H-SiC substrates by MOCVD. Dot size and density ranged from 20 nm to more than $2 \mu\text{m}$ and $10^7 - 10^9 \text{ cm}^{-2}$, respectively. A blue shift of about ~ 70 meV of the edge luminescence has been obtained both in PL and CL spectra from the dots comparing with that from bulk material.

REFERENCES

1. H. Nakayama and Y. Arakawa, in The Proceedings of the 14th Int. Semicond. Laser Conf., September 1994 (Hawaii, 1994) pp. 77-78.
2. S. Muto, *Jpn. J. Appl. Phys.*, **34**, L210 (1995).
3. F. Yamaguchi, K. Kawamura and A. Hubler, *Jpn. J. Appl. Phys.*, **34**, L105 (1995).
4. K. Kudo, Y. Nagashima, M. Tamura, S. Tamura, A. Ubukata, S. Arai, *Jpn. J. Appl. Phys.*, **33**, L1383 (1994).

5. J.D. Reed, Y.-P. Chen, E.S. Tentarelli, W.J. Schaff and L.F. Eastman, *J. Vac. Sci. Technol. B*, **13**, 995 (1995).
6. K. Mukai, N. Ohtsuka, M. Sugawara and S. Yamazaki, *Jpn. J. Appl. Phys.* **33**, L1710 (1994).
7. N. Koguchi, K. Ishige and S. Takahashi, *J. Vac. Sci. Technol. B*, **11**, 787 (1993).
8. J. Yoshida and K. Kishino, *IEEE Photonics Technology Lett.* **7**, 241 (1995).
9. E. Leobandung, L. Guo, Y. Wang, and S.Y. Chou, *Appl. Phys. Lett.* **67**, 938 (1995).
10. H. Amano, T. Asahi, I. Akasaki, *Jap. J. Appl. Phys.* **29**, L209 (1990).
11. M.A. Khan, D.T. Olson, J.M. Van Hove, J.N. Kuznia, *Appl. Phys. Lett.* **58**, 1515 (1991).
12. S. K. Yung, J. Yee, J. Koo, M. Rubin, N. Newman, and J. Ross, *Appl. Phys. Lett.* **64**, 1135 (1994).
13. X.H. Yang, T.J. Schmidt, W. Shan, J.J. Song, and B. Goldenberg, *Appl. Phys. Lett.* **66**, 1 (1995).
14. A.S. Zubrilov, V.I. Nikolaev, D.V. Tsvetkov, V.A. Dmitriev, K.G. Irvine, J.A. Edmond and C.H. Carter, Jr., *Appl. Phys. Lett.* **67**, 533 (1995).
15. W. Fang and S.L. Chuang, *Appl. Phys. Lett.* **67**, 751 (1995).
16. A.T. Meney, and E.P. O'Reilly, *Appl. Phys. Lett.* **67**, 3013 (1995).
17. M.A. Khan, R.A. Skogman, and J.M. Van Hove, *Appl. Phys. Lett.* **56**, 1257 (1990).
18. S. Nakamura in The Abstracts of The Topical Workshop on III-V Nitrides, September 21-23, 1995 (Nagoya, 1995) p. A-2.
19. M.F. Mac Millan, L.L. Clemen, R.P. Devaty, and W.J. Choyke in Technical Digest of Int. Conf. on SiC and Related Materials, Kyoto, 1995, p.233.
20. K. Itoh, T. Kawamoto, H. Amano, K. Hiramatsu, and I. Akasaki, *J. Appl. Phys.* **30**, 1924 (1991).
21. A.I. Ekimov, F. Hache, M.C. Schanne-Klein, D. Ricard, C. Flytzanis, I.A. Kudryavtsev, T.V. Yazeva, A.V. Rodina, A.I.L. Efros, *J. Opt. Soc. Am. B*, **10**, 100 (1993).

SUPERSONIC JET EPITAXY: AN IMPROVED METHOD FOR NITRIDE DEPOSITION

PETER E. NORRIS*, LONG D. ZHU*, H. PAUL MARUSKA*, WILSON HO**, SCOTT USTIN**, L. LAUHON**

*NZ Applied Technologies, Woburn MA 01801

**Department of Physics, Cornell University, Ithaca, NY 14853

ABSTRACT

GaN was grown by supersonic jet epitaxy(SSJE), seeding triethylgallium in helium carrier gas. Activated nitrogen was supplied by a microwave plasma source. Single crystalline GaN films were deposited on the Si-face 6H-SiC and the c-plane sapphire substrates at 600-670°C. A cubic SiC buffer layer was grown on Si(111) at 800°C by SSJE using dichlorosilane, acetylene, and a high quality GaN crystal was grown on this template at 630°C. The materials high quality was proved by hard rectifying characteristics of a diode with an N-GaN/ β -SiC/P-Si(111) structure.

INTRODUCTION

The ideal MOCVD process is governed by surface reactions. In all growth processes, the rate limiting adsorption is often a crucial step and there is a certain value of energy to adsorption for a given surface. Adsorption probability P_{st} , or sticking coefficient, can be expressed as:

$$P_{st} = 1 - e^{-E/E_b} \quad (1)$$

where E_b represents the energy barrier for attachment of an atom at a given surface. In most crystal growth methods, thermal energy allows the reactant molecules to surmount the surface energy barrier to be adsorbed, leading to a need for high growth temperatures. Alternatively, the high kinetic energy, from 0.1eV to several eV, can be imparted to the reactant molecules by supersonic jet expansion. This approach provides a prospect in which one could increase and control the sticking coefficient, reduce the growth temperature and thus increase the growth rate and efficiency, simultaneously avoiding the damage caused by energetic particles ($E > 5E_g$) to the growing crystal film.[1] Figure 1 shows the enhancement of the sticking coefficient of Si from a disilane jet seeded in hydrogen, helium and argon, impinging on a Si substrate, where θ_i is the injection angle.

Compared to the well known epitaxial technologies, such as LPE, VPE, CVD and MBE, supersonic jet epitaxy is a relatively new technology, which utilizes the properties of supersonic free jet expansions. [2,3] When a compressed gas expands freely through a fine orifice, such as a 100 diameter nozzle, the adiabatic expansion reduces the temperature of the expanding gas, creating a molecular beam with a narrow spread in velocity.[4,5] The speed ratio of the mean velocity to the axial velocity spread could be set to a few tens for seeded molecular beams by increasing the pressure ratio across the expansion orifice.[6] The Mach number $M=V/a$, where V is the gas velocity and a is the speed of sound, will reach 1 at the exit of the nozzle when p_i/p_o , (p_i and p_o is the pressure inside and outside of the nozzle, respectively), reaches a critical value given by the relationship

$$G = ((r+1)/2)^{r/(r-1)} \quad (2)$$

Here r is the ratio of the heat capacity at constant pressure to the heat capacity at constant volume of the gas, and G is less than 2.1 for all gases. At this point the pressure at the exit of the nozzle becomes p_i/G , independent of p_o . After leaving the nozzle the gas continues

to expand, gas velocity continues to increase, and M becomes greater than 1. When this occurs, the gas flow becomes a supersonic jet.

The translational energy of this monochromatized supersonic molecular beam can be monitored by controlling the nozzle temperature and gas seeding according to the formula.

$$V_t = (2RT(\sum X_i(r_i/(r_i-1)))/\sum X_i W_i))^{1/2} \quad (3)$$

Here V_t is terminal velocity of the gas, R is the gas constant, T is the nozzle temperature, X_i and W_i is the mole fraction and molecular weight of the component gas in the mixture. It is clear that the terminal energy is proportional to the stagnation temperature inside the nozzle and also inversely proportional to the molar average molecular weight. This means that heating the nozzle could increase the translational energy of the molecules, and gas seeding, e. g., mixing heavy molecules in larger quantity lighter molecules, results in a larger terminal velocity for the heavier molecules[6], resulting in 0.5-5.0 eV kinetic energy.

After expansion, the molecules in the supersonic jet will collide with other background gas molecules in the growth chamber. The collision probability depends on the chamber pressure and gas constituents. The mean free path in nitrogen of 10 mTorr is around 5 mm. To avoid excessive cooling of the beam, the growth chamber pressure should be low so as the mean free path of the molecules is comparable to the distant to the substrate.

The unique characteristics of the supersonic jet arise from the physical processes taking place at the nozzle as the molecules squeeze through the orifice from the high pressure inside the nozzle to the chamber vacuum. When the mean free path inside the nozzle is smaller than the orifice diameter, the expanding molecular beam possesses monochromatic nature and directionality. The monochromatic high energy of the reactant molecules impinging to the growing surface enhances the sticking efficiency, helps to break chemical bonds and promotes surface migration, and makes it possible to reduce the growth temperature and to control the kinetic energy to less than damage threshold of $5x E_g$ of the growing crystal films[1]. The supersonic jet beam also effectively delivers the source molecules to the growing surface so that growth efficiency and rate can be increased. But the ultimate growth rate is limited by the pumping speed required to keep the molecular mean free path large enough for the reactant molecules to reach the substrate without excessive cooling.

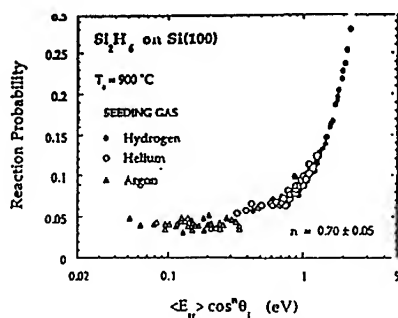


Fig. 1, Reaction probability for Si_2H_6 as a function of translational energy for compositions: 10% Si_2H_6/Ar ; 1% Si_2H_6/He ; 1% Si_2H_6/H_2 .

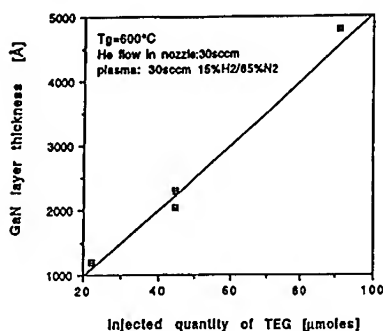


Fig. 2, GaN thickness vs. injected moles of TEG for SSJE.

EXPERIMENT

Supersonic Jet MOCVD System Configuration

The supersonic jet MOCVD System used in this work consists of a small scale stainless steel chamber pumped by a mechanical pump through MKS throttle valve and traps. The gas composition and the residual H₂O vapor and oxygen traces are checked in-situ by an attached UTI Quadrupole gas analyzer. 2.45 GHz, 0-100w microwave power is fed into the microwave cavity, which activates/ ionizes the N₂ as it flows into the reaction chamber through a quartz tube. The plasma cavity surrounding the quartz tube is remote to eliminate damage to the growing crystal film by energetic plasma species. Of course the longer distance exponentially decrease the ionized nitrogen flux density reaching the substrate surface. The reactant metalorganic sources are injected from the gas handling lines to the chamber through a jet nozzle with a 100 μ diameter orifice. The gas handling system, growth temperature and the chamber pressure are under computer control, making it possible to grow designed structures automatically. The susceptor and the resistance heater is made of high purity graphite. Semiconductor grade high purity helium is used as the carrier gas in the supersonic jet flow and the metalorganic sources are seeded in it. The pressure difference Δp across the orifice at the tip of the nozzle is measured to be 1500 Torr when the helium flow rate through the nozzle orifice is 290 sccm.

SSJE Growth of GaN on Sapphire, 6H-SiC, 3C-SiC/Si Substrate

The substrates used in the supersonic jet epitaxial growth experiments are c-plane sapphire from Union Carbide with mis-orientations less than $\pm 0.7^\circ$, Si-face 6H-SiC, and Si(111). The sapphire substrate is degreased in trichloroethylene, acetone, and methanol and etched in H₂SO₄ : H₃PO₄ = 3 : 1 solution at 200°C, then rinsed in deionized water and blown dry with UHP nitrogen. The bulk single crystal Si-face-polished 6H-SiC substrates are first degreased in organic solvents and then oxidized in HCl : H₂O₂ : H₂O = 2 : 1 : 1 solution. Subsequently, the oxides are striped in HF : H₂O = 1 : 3 solution. This process is repeated 5 times to remove the surface damage induced by polishing. Finally, the wafer is rinsed in deionized water and blown dry using nitrogen gas. To grow high quality GaN on Si wafer, a β -SiC buffer layer is epitaxially deposited on Si(111) substrates. The 3C-SiC is grown by supersonic jet epitaxy using dichlorosilane and acetylene at 800°C utilizing atomic layer epitaxy mode. Before the growth of GaN the β -SiC/Si (111) substrate is cleaned with organic solvents, assuming that the SiC surface is damage free.

After loading into the reaction chamber, the bulk 6H-SiC or β -SiC/Si substrates are heated to 600-650°C and thermally annealed for at least one hour. However, in the case of sapphire substrates, N₂ microwave plasma is applied in order to clean and nitride the substrate surface, and the growth was initiated by depositing 300-500Å GaN buffer layer at 520°C and GaN film is grown at 600-650 C. For the 6H-SiC Substrates and β -SiC coated Si (111) substrates, the supersonic jet epitaxy is initiated directly at the growth temperatures. The growth temperatures are 600-670°C. Helium flow rate through the supersonic jet nozzle is 50 sccm, and the microwave power for activation of N₂ is 70W.

The growth rate of the GaN prepared by supersonic jet epitaxy was estimated by correlating the film thickness with the molar amount of TEG injected into the chamber. The relationship is demonstrated in Fig.2. It was found that the maximum growth rate for the supersonic jet epitaxy in our system is not limited by the metalorganic source delivery rate, it is rather determined by the maximum mass transport rate of the activated nitrogen species to the substrate surface. This, in turn, is governed by the maximum microwave power, flow rate of N₂ and most importantly, by the pumping speed of the vacuum system.

For a helium carrier gas flow rate of 50 sccm through the jet nozzle orifice, the pressure drop between the nozzle and chamber was estimated to be 250 Torr. This gives a G value of 250, which is much larger than the G value of He (<2.1) necessary for He to reach the speed of sound. In this case, the local pressure just outside the nozzle orifice should be

about 120 Torr, the gas should continue to expand to reach a Mach number larger than 1. This estimate indicates that in our growth conditions, supersonic jet flow is established and gas velocity at the exit is expected to be $V \sim 1.4 \times 10^5$ cm/s, so that the corresponding kinetic energy of TEG molecule is 1.6 eV. Beside the effect of the kinetic energy on reducing the growth temperature to 600-670°C, it was found that the reactant molecules were delivered more effectively increasing the growth rate and efficiency. Also their transit time is reduced, thereby reducing vapor phase reaction probability, and the expansion cooling should help prevent premature decomposition of TEG.

RESULTS

Gallium Nitride Grown on Si-face 6H-SiC by Supersonic Jet Epitaxy

A 0.6 μ thick GaN film was grown by supersonic jet epitaxy at 670 °C with a growth rate of 17 Å/min. The epitaxial layer was transparent and had mirror-like smooth surface morphology. An X-ray $\Theta - 2\Theta$ scan (Fig.3) indicates that the film is wurtzite structure single crystal with (002) peak at 34.60° and (004) peak at 73.0°. In Figure 3, the peaks at 35.9° and 75.6° are (0006) and (00012) peaks of the 6H-SiC substrate.

GaN Grown on β -SiC Coated Si (111) by Supersonic Jet Epitaxy

The growth of high quality III-nitride epitaxial films on silicon substrates is expected to be an important development from the prospective of monolithic integration of nitride-based electronic and opto-electronic devices with silicon VLSI technology. Although there have been reports of the growth of GaN directly on silicon substrates, we judged that a SiC buffer layer deposited on the silicon wafer would improve the GaN crystallinity because of the chemical proximity of SiC with Silicon and its close lattice matching with GaN. For the first time, supersonic jet epitaxy was used to grow epitaxial films of 3C-SiC on silicon.

The cubic phase silicon carbide buffer layer was grown on silicon(111) substrates utilizing SiH_2Cl_2 and C_2H_2 in the supersonic jet epitaxy system at around 800°C. The β -SiC layer is estimated to be 300-500 Å thick by the interference fringes. The X-ray $\Theta - 2\Theta$ scan curve of the β -SiC/Si(111) template was shown in Fig.4. The only diffraction peak

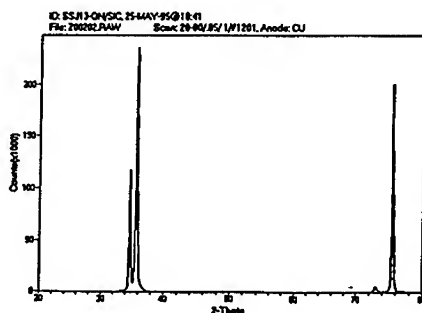


Fig. 3, $\Theta - 2\Theta$ scan of the GaN grown on (0001) Si-face 6H-SiC substrate.

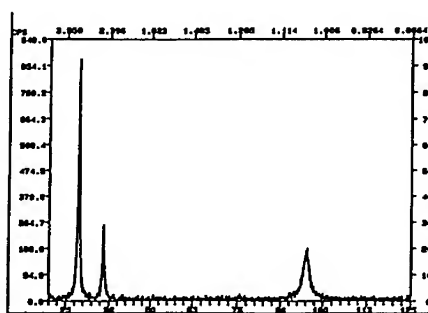


Fig.4, Single crystal β -SiC film grown on Si(111) with (111) peak at 35.6°.

coming from the SiC layer in this scan is at $2\theta=35.6^\circ$, which indicates that the SiC film grown on Si(111) substrate is cubic single crystal with (111) orientation peak. The peak at 35.6° , which is attributed to β -SiC (111) diffraction, is shifted to a larger angle by strain.

A gallium nitride layer was grown on this β -SiC coated Si (111) substrates by supersonic jet MOCVD at 630 C with a growth rate of 0.1 μ /hr. The resulting GaN layer had smooth and shiny surface morphology. The X-ray $\theta - 2\theta$ scan is shown in Fig.5, which demonstrates that, beside the silicon (111) peak at 28.9° , there are only wurtzite structure GaN peaks at $34.8^\circ(002)$ and $73.1^\circ(004)$. This proves that single crystal GaN film can be grown on the cubic SiC coated on a silicon (111) substrate by supersonic jet MOCVD. We attempted to grow GaN directly on Si (100) substrates by SSJE, but resultant films were polycrystal or even amorphous using the same growth conditions.

Effect of V/III Ratio on Electrical Properties of GaN Grown on c- Al_2O_3

To investigate the effect of V/III ratio on GaN electrical properties in the SSJE, the V/III ratio has been systematically changed and Hall measurements were carried out on GaN samples grown on c-plane sapphire substrates. The relationship between the nominal V/III ratios and the product of electron concentration and mobility is given in table 1. The monotonic decrease of the product with the increasing of the nominal V/III ratio is the evidence of change of nitrogen vacancy density with V/III ratio. The rather high conductivity suggests that the TEG delivery by supersonic jet is efficient and the delivery rate of the activated nitrogen is the limiting factor for the GaN films.

Table I, Relative nominal V/III ratio vs product of electron concentration and mobility for the wafers grown by supersonic jet epitaxy.

	relative nominal V/III ratio	$n \times \mu$ ($/\text{cm} \cdot \text{V} \cdot \text{s}$)
ssj-6	1.00	1.7×10^{20}
ssj-8	0.50	4.7×10^{20}
ssj-9	0.33	9.6×10^{20}
ssj-10	1.00	1.8×10^{20}

Preliminary Device Characterization

A preliminary junction diode was prepared and characterized. The starting substrate

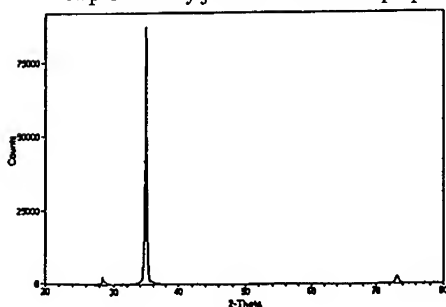


Fig.5, $\theta-2\theta$ scan of GaN grown on 3C-SiC/Si(111) template by SSJE

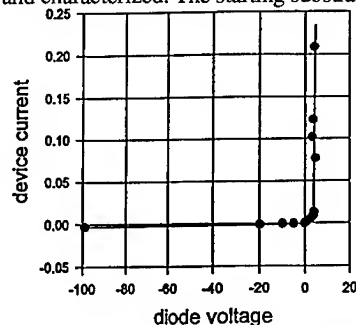


Fig.6, Current-voltage characteristics of N-GaN/3C-SiC/P-Si diode.

was p-type silicon. A buffer layer of 3C-SiC was deposited by supersonic jet epitaxy on the Si wafer, and a GaN layer was subsequently deposited also using the SSJE technology. Square samples of 0.1 cm² area were cleaved from the wafer and Ohmic contacts were made on both sides of the chip using an InHg alloy. The current-voltage characteristics of the diodes were measured. A correction was made for the contact resistance which allowed us to separate the applied voltage into a resistive and a diode junction component. The corrected I-V curve is plotted in Fig. 6. The device shows very hard rectifying behavior, supporting 100 volts of reverse bias without breaking down. This is a p-n junction between p-type Si and n-type GaN mediated by thin n-type β -SiC buffer layer. The good rectifying characteristics suggest that the hetero-junction interface is high quality.

CONCLUSIONS

Supersonic jet epitaxy is an improved growth method of III-nitride wide bandgap semiconductors. A supersonic nozzle with 100 μ diameter hole in a 0.005" thin stainless steel end plate of a 1/4" O.D. stainless steel tubing produced a gas velocity of 1.4×10^5 cm/s when it is expanded from 250 Torr pressure at room temperature. By seeding triethylgallium in helium carrier gas, the metalorganic molecules in the supersonic jet stream attained a kinetic energy of 1.6 eV. The quasi-monochromatic high kinetic energy of the reactant molecules impinging on the substrates effectively reduced the growth temperature of GaN films. Reducing the growth temperature of GaN is expected to be critical for decreasing the density of nitrogen vacancies. Single crystalline GaN films were grown at temperatures of 600-670°C on Si-face 6H-SiC as well as on c-plane sapphire substrates by supersonic jet epitaxy. A high quality wurtzite GaN layer was grown at a temperature as low as 630°C on a cubic silicon carbide coated Si(111) template by SSJE. The 3C-SiC buffer layer on Si(111) wafer was also grown by SSJE using SiH₂Cl₂ and C₂H₂ seeded in He at a growth temperature as low as 800°C. The high quality of the materials grown by the SSJE was demonstrated by the preliminary N-GaN/ β -SiC/P-Si structure diode which exhibited hard rectifying characteristics with more than 100V reverse breakdown voltage.

ACKNOWLEDGMENTS

This work was partially supported by the Office of Naval Research under contract N00014-94-C-0230. We wish particularly to acknowledge the support and encouragement of Dr. Richard Brandt.

REFERENCES

- 1, Max N. Yoder, in Critical Reviews, Vol. CR45, part: Integrated Optics and Optoelectronics, P.105
- 2, J. B. Anderson, "Molecular Beams and Low Density Gas Dynamics" ed. P. Wegener (Dekker, New York, 1974)
- 3, J.B. Anderson, R.P. Andres, and J.B.Fenn, Advan. Chem. Phys., 10, 275(1966)
- 4, J.B. Anderson, R.P. Andres, and J.B.Fenn, in Advances in Atomic and Molecular Physics, Vol. 1, (Academic Press. New York, 1965) P.345
- 5, S.L.Tang, J.D.Beckerle, M.B.Lee, and S.T.Ceyer, J. Chem. Phys., 84, 6488(1986)
- 6, D.R.Miller, in "Atomic and Molecular Beam Methods", Vol.1, ed. G.Scoles, (Oxford University Press. New York, 1988)

NEW BUFFER LAYERS FOR GAN ON SAPPHIRE BY ATOMIC LAYER AND MOLECULAR STREAM EPITAXY

E.L. PINER*, Y.W. HE*, K.S. BOUTROS**, F.G. MCINTOSH**, J.C. ROBERTS**,
S.M. BEDAIR**, N.A. EL-MASRY*

*North Carolina State University, MS&E Department, Raleigh, NC 27695

**North Carolina State University, ECE Department, Raleigh, NC 27695

ABSTRACT

The current approach of depositing a low temperature then annealed AlN or GaN buffer for the growth of GaN on sapphire results in a high dislocation density. These dislocations thread through the GaN layer to the surface. Reducing their density either by growing thicker films or using a strained layer superlattice is ineffective. Two new approaches for AlN/GaN buffer layer growth for GaN on sapphire have been employed: Atomic Layer Epitaxy (ALE) and Molecular Stream Epitaxy (MSE). ALE is distinguished by organo-metallic/ammonia separation while MSE is distinguished by cyclic annealing of the growing film. Both ALE and MSE enhance two dimensional growth of single crystal GaN on sapphire. The structural quality of epitaxial GaN grown on these buffer layers was studied by transmission electron microscopy (TEM) and x-ray diffraction (XRD). The initial result for the ALE buffer shows an improved quality GaN film with lower defect densities. The MSE grown buffer layer closely resembles that of conventionally grown MOCVD buffer layers observed by others, with dislocations threading through the GaN epilayer. The effects of these buffer layers on the structural and optical properties of GaN grown on sapphire will be presented.

INTRODUCTION

Good quality GaN has been grown by conventional MOCVD and ECR-assisted MBE. For GaN/InGaN grown on sapphire using an AlN/GaN buffer, the large lattice mismatch and thermal mismatch between GaN and sapphire is known to enhance three dimensional nucleation that may lead to low angle grain boundaries. The most common buffer layer growth method involves depositing a low temperature AlN or GaN film then anneal at 1000°C or higher to recrystallize before depositing the GaN film.[1-3].

This approach has worked well and several device structures including a blue LED based on the AlGaIn/InGaIn/AlGaIn double heterostructure was produced in Japan based on this buffer layer growth method. However, this method suffers from several problems. First, the electrical properties of the GaN critically depend on the thickness of this buffer layer. Second, the recrystallization of this buffer layer produces low angle grain boundaries that forms a source of dislocation nucleation and propagation to the epilayer surface with a density of $\sim 10^{10} \text{ cm}^{-2}$. And third, these dislocations can be perpendicular to the GaN/buffer layer interface and thread to the growing surface making their reduction by dislocation interaction and annihilation less probable.

In an attempt to reduce the defect density of GaN grown on sapphire we report on two different approaches for the buffer layer growth; Atomic Layer Epitaxy (ALE) and Molecular Stream Epitaxy (MSE). These techniques can enhance two dimensional growth of the buffer layer opposed to the three dimensional growth of the low temperature then annealed AlN buffer. Both techniques were developed by our group in the epitaxial growth of GaAs and their related compounds.[4-7]

In ALE, the substrate rotates between two streams; one containing metalorganics (MO) and the second, NH_3 , as shown in Figure 1a. ALE offers the advantage of reactant gas separation thereby eliminating gas-phase reactions which can hinder high quality material growth. The MSE process is shown in Figure 1b where the substrate rotates crossing one

stream containing both MO and NH_3 thus depositing a few monolayers per rotation. The deposited layer is being annealed during the rest of the cycle and, for example, for a 30 rpm rotational speed growing by MSE, the growth time is 0.2 seconds followed by an annealing time of 1.8 seconds. For conventional MOCVD, the susceptor is stationary and both reactant gases flow over the substrate simultaneously. Typical rotation rates are 30 to 60 rpm. The design of our reactor allows the growth of III-nitride thin films by either conventional MOCVD, MSE, or ALE or any combination of the three.

EXPERIMENT

The nitride films are grown on on-axis (0001) sapphire. Prior to growth, the substrate is cleaned and etched in $\text{H}_2\text{SO}_4:\text{H}_2\text{O}_2$ (1:1) for 45 minutes at 120°C . It is then annealed at 1050°C for 15 minutes inside the reactor and then passivated with ammonia for 1 minute. The layers are grown at temperatures ranging from 550 to 900°C . Column III reactants are TMAI ($+18^\circ\text{C}$), TMGa (-10°C), and EDMIn ($+10^\circ\text{C}$) with flows varying from 3-15, 1-8, and 15-120 sccm, respectively. The column V reactant is NH_3 with flows in the range of 0.5-2 slm. The carrier and purge gases are purified nitrogen. The pressure in the growth chamber can also be varied from less than 100 torr to atmospheric. All samples grown are characterized by double crystal x-ray diffraction (DCXRD) and transmission electron microscopy (TEM) will also be used for interface and microstructural analysis. Photoluminescence (PL) will be used to assess the optical properties.

RESULTS

It is well known that a strained layer superlattice (SLS) can be used to suppress threading dislocations in zinc-blende semiconductor epilayers. However, the threading dislocations in GaN films are mostly perfect edge type that have slip planes of $\{1\bar{1}00\}$ type, which require larger resolved shear stress to initiate glide. Furthermore, since the strain field introduced by the SLS is parallel to the (0001) growth plane, the resolved shear stress on the $\{1\bar{1}00\}$ plane is zero. Therefore, it can be expected that, to suppress or eventually eliminate this type of threading dislocation with a SLS could be difficult. The nature of these threading dislocations suggests that it is important to carefully select the thickness, deposition parameters and growth mode of the buffer layer to minimize or avoid formation of the edge type dislocation in the III-nitride films.

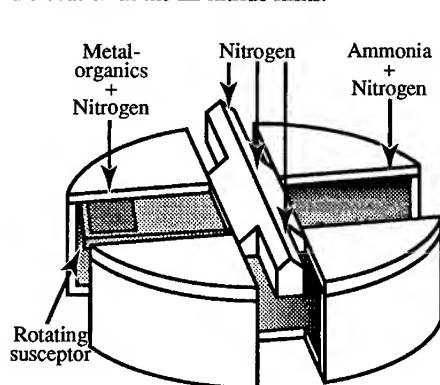


Figure 1a. Schematic drawing of the susceptor and gas flow locations for the ALE growth method.

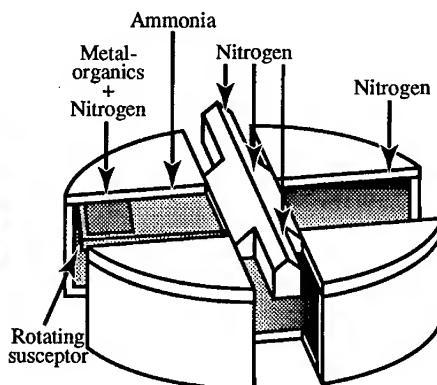


Figure 1b. Schematic drawing of the susceptor and gas flow locations for MSE and MOCVD growth methods.

In this work we have studied the effect of the buffer layers grown by MSE and ALE on the crystalline quality and defect densities of the grown GaN films. The objective is to enhance two dimensional growth of a single crystal buffer layer at lower growth temperatures. Lower growth temperatures reduce the effect of the thermal mismatch between the grown layers and the substrate. The two dimensional growth will enhance the lattice mismatch relief by forming misfit dislocations that are parallel to the interface between the buffer layer and the substrate. We studied the effect of the growth parameters of the buffer layer such as the gas flows, growth temperature and the reactor pressure on the crystalline quality of the grown films.

To compare the effect that the buffer layer has on the GaN film, buffer layers grown by MSE and ALE were observed in cross-sectional TEM (XTEM). For all samples the substrate was (0001) sapphire and the GaN on the buffer was grown by conventional MOCVD at 900°C. The GaN films are single crystalline as determined by x-ray diffraction and selected area diffraction in the TEM.

ALE Grown Buffer Layer

GaN films on ALE grown buffer layers show a significant reduction in the density of threading dislocations; in the low 10^9 range. Figure 2 shows the microstructure of a thin GaN film ($\sim 0.3 \mu\text{m}$) grown at 750°C on a 3.5 nm AlN buffer layer deposited at 700°C and 100 torr by ALE. The quality of this film is reflected in the FWHM of 130 arc seconds obtained by DCXRD and shown in Figure 3. (The absence of the (0002) AlN peak is due to the thinness of the film.) It should be noted that this 130 arcsec FWHM is for a film which is less than the thickness required ($0.4 \mu\text{m}$) for obtaining significant dislocation interaction and reduction. An even lower FWHM would be observed for the same film grown thicker ($1.0 \mu\text{m}$ or greater). PL analysis indicates a sharp GaN band edge peak at 368 nm with no deep level peaks observed.

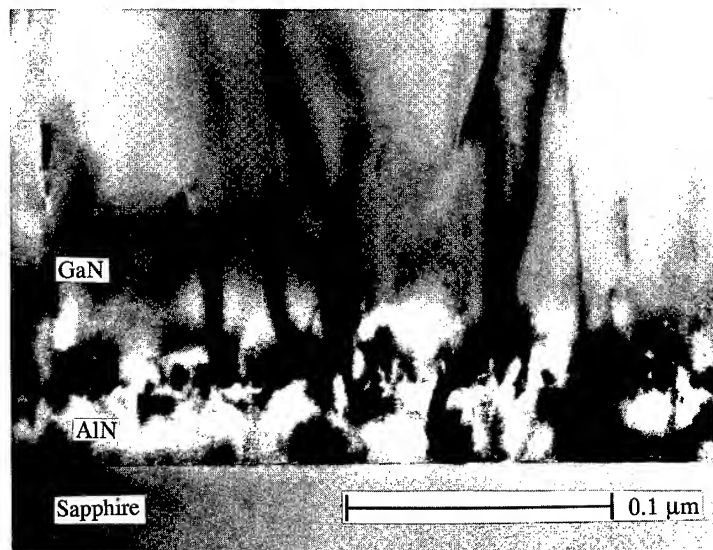


Figure 2. XTEM micrograph of GaN grown on (0001) sapphire at 900°C by MOCVD buffered by an AlN layer grown at 700°C and 100 torr by ALE.

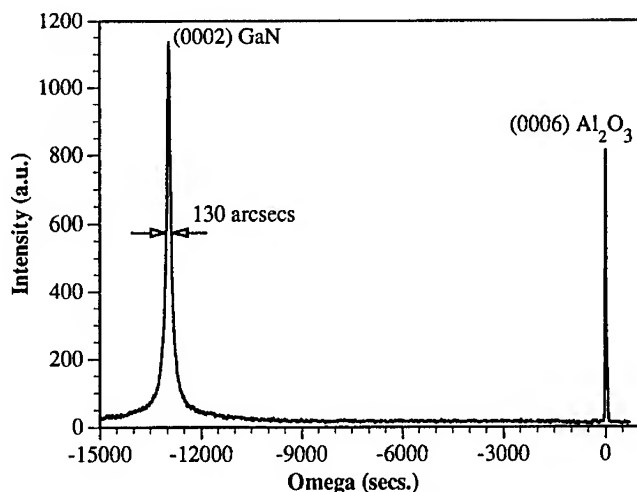


Figure 3. DCXRD of MOCVD GaN epilayer on a 700°C/100 torr ALE AlN buffer with (0001) sapphire as the substrate.

There are several features observed in films grown on ALE buffer layers. First, the layers grow by two dimensional growth modes as single crystals at lower temperatures with thicknesses as small as 2 nm. Second, the lattice mismatch between the buffer layer and the sapphire substrate is mainly relieved by forming misfit dislocations at the buffer/substrate interface. Figure 4 illustrates these interfacial misfit dislocations. These misfit dislocations are in contrast under two beam diffraction conditions where the operating g-vector is a basal plane vector and are not observed under $g = [0002]$. This indicates that these misfit dislocations are perfect dislocations of the $1/3\langle 11\bar{2}0 \rangle$ type. From the diffraction contrast in the figure, these dislocations are parallel to the interface which is the favorable conditions for relieving lattice mismatch in these materials.



Figure 4. XTEM micrograph of MOCVD GaN grown on an ALE AlN buffer all on a sapphire substrate showing strain contrast fringes at the buffer/substrate interface indicating misfit strain relief by the formation of interfacial misfit dislocations.

MSE Grown Buffer Layer

Figure 5 shows a XTEM brightfield micrograph of GaN grown on an AlN buffer layer deposited at 900°C/100 torr by MSE. Threading dislocations of the same order of magnitude seen in conventional buffer layer growth methods are observed as a result of the misfit strain caused by the mismatch between the epilayer and substrate lattices, and low angle grain boundaries. The defect density is highest at the GaN/buffer layer interface and decreases with increasing thickness of the GaN layer as observed by others.[8] The DCXRD FWHM for films grown on these buffer layers are as low as 510 arc seconds as shown in Figure 6. However, this mode of growth has not been fully optimized.



Figure 5. XTEM micrograph of MOCVD GaN on (0001) sapphire buffered by an AlN layer grown at 900°C and 700 torr by MSE.

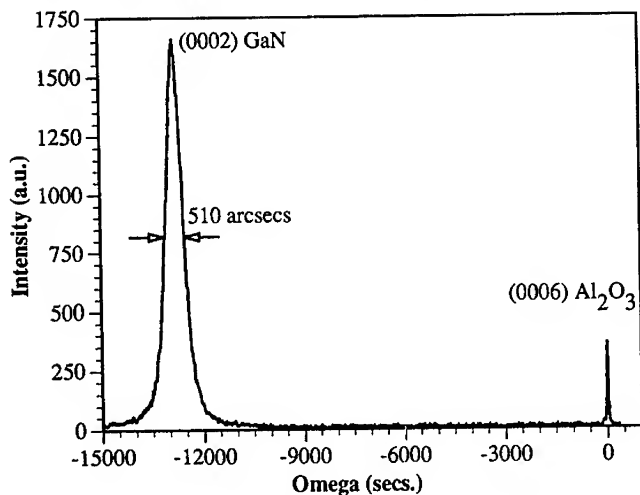


Figure 6. DCXRD of MOCVD GaN/MSE AlN buffer on a (0001) sapphire substrate.

CONCLUSIONS

The results of several studies into the effect the buffer layer has on the quality of GaN films has been presented. The ALE buffer layer growth technique offers a promising alternative to the commonly used low temperature/annealed technique. The MSE buffer layer growth technique has comparable crystal quality to the more commonly used technique. Optimization of the growth conditions help in obtaining good quality buffer layers as well as studying the optimum thickness and its effect on the dislocation density, microstructure, electrical and optical properties of device quality GaN and InGaN films.

ACKNOWLEDGMENTS

This work is supported by the Office of Naval Research under the University Research Initiative.

REFERENCES

1. H. Amano, T. Asahi, and I. Akasaki, *Jpn. J. Appl. Phys.* **29**, L205 (1990).
2. S. Nakamura, Y. Harada, and M. Seno, *Appl. Phys. Lett.* **58**, 2021 (1991).
3. J. N. Kuznia, M. Asif Khan, D.T. Olson, R. Kaplan, and J. Freitas, *J. Appl. Phys.* **73**, 4700 (1993).
4. S. M. Bedair, M. A. Tischler, N. Katsuyama, and N. A. El-Masry, *Appl. Phys. Lett.* **47**, 51 (1985).
5. N. Katsuyama, M. A. Tischler, N. Karam, N. A. El-Masry, and S. M. Bedair, *Appl. Phys. Lett.* **51**, 529 (1987).
6. S. M. Bedair, B. T. McDermott, Y. Ide, M. A. Tischler, and N. A. El-Masry, *J. Cryst. Growth* **93**, 182 (1988).
7. S. M. Bedair, and N. A. El-Masry, *Appl. Surf. Sci.* **82**, 7 (1994).
8. W. Qian, M. Skowronski, M. De Graef, K. Doverspike, L. B. Rowland, and D. K. Gaskill, *Appl. Phys. Lett.* **66**, 1252 (1995).

Low Temperature Epitaxial Growth of AlN & GaN Thin Films by The Method of Ion Beam Assisted Deposition

Ig-Hyeon Kim, Chan-Wook Jeon, Seon-Hyo Kim

Department of Materials Science and Engineering, Pohang University of Science and Technology, San 31, Hyoja-Dong, Pohang 790-784, South Korea

ABSTRACT

The epitaxial layers of AlN and GaN were grown on Si and Sapphire substrate at a relatively low temperature of around 500 °C using the process of reactive ion beam assisted deposition. The optimum ion beam energy for epitaxial growth of AlN and GaN films was found to be about 50 eV. Characterization of the epitaxial layers was carried out by GID (Grazing-Incidence x-ray Diffraction) and high resolution TEM observation. The orientational relations between epitaxial layer and substrate were determined through these analysis. Very thin amorphous layers were observed at the interfaces of both AlN and GaN films grown on Si(111) substrate, whereas the films grown on Sapphire substrate has no amorphous layer. The amorphous layer may act as a buffer layer enabling the growth of the epitaxial layers of AlN and GaN by relaxing the misfit strain in the early growing stage.

INTRODUCTION

Recently epitaxial growth of III-V nitrides with a wide band-gap has been paid much attention for their potential importance on opto-electronic devices operating in the blue-ultraviolet wavelength region. Among these nitrides, wurtzite structured AlN and GaN have outstanding properties, such as an excellent chemical stability at high temperature and high ultrasonic and electron velocity. These properties, combined with their wide band-gap (6.2¹ and 3.4 eV², respectively), make AlN and GaN excellent candidates for high temperature and high power electronic applications. Furthermore, AlN and GaN are reasonably well lattice matched (2.4 % difference)³, which leads to a good hetero-epitaxial structure between the two materials and high performance in band-gap design by forming the nitride alloys. However, the application of these nitride films to opto-electronic devices has been restricted by the difficulties in obtaining high quality hetero-epitaxial films. Various kinds of crystal-growth techniques, substrate types, and orientations have been tried in an effort to grow high quality nitride films, but they usually require a high growth temperature of over 1000°C and yield an unsatisfactory film quality. In recent times, newer Molecular Beam Epitaxy (MBE)^{4,5} techniques assisted by the activated nitrogen sources such as Electron Cyclotron Resonance (ECR) and Kaufman-type ion source, have made a great improvement in film quality, despite the lack of an ideal substrate material that is well lattice and thermally matched to AlN and GaN.

In this work, the AlN and GaN films were grown on Si(111) and Sapphire(0002) substrates using the technique of ion-beam-assisted deposition (IBAD). Low temperature epitaxial growth of these nitride films has been

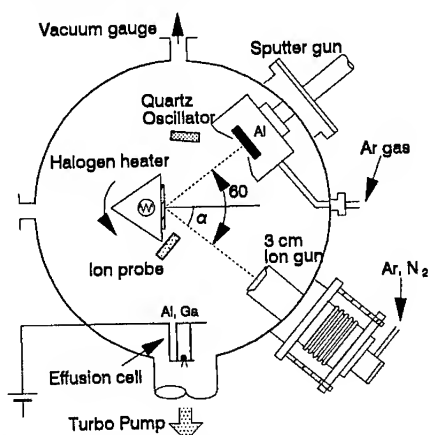


Figure 1. Schematic diagram of IBAD system.

tried by controlling the energy and flux of ion beam. In addition, the interface structure and crystallographical properties of AlN and GaN epitaxial layers grown on Si and sapphire substrates were investigated by XRD (X-Ray Diffraction) and TEM (Transmission Electron Microscopy) analysis.

EXPERIMENTS

Figure 1 shows a schematic diagram of the experimental apparatus. Metal vapor was supplied by magnetron sputtering or thermal evaporation through the lab-made effusion cell. In case of Al, both methods were employed. Ga flux was supplied solely by thermal evaporation due to its low melting point (27°C)⁶. The flux of metal vapor was precisely measured through a quartz oscillator and controlled in a range of 3×10^{14} - 8×10^{14} atoms/cm² · sec. Reactive nitrogen ions were provided by a Kaufman-type ion source with a beam diameter of 3 cm. The beam energy was controlled under the value of 100 eV and the flux of ions varied over the range of 5×10^{14} - 3×10^{15} ions/cm² · sec., which was measured by ball type ion probe. The reaction chamber was evacuated with a turbomolecular pump down to a base pressure of 2×10^{-7} Torr. The operating pressure for thermal evaporation and sputtering were maintained at 2×10^{-4} and 6×10^{-4} Torr, respectively. A substrate was generally pretreated using acetone, deionized water, and alcohol and then pre-sputtered with Ar ions. In case of the Si substrate, the deoxidizing process with 10 % HF solution was included.

The composition and bonding characteristics of films were investigated by X-ray photoelectron spectroscopy and Auger electron spectroscopy. To characterize the epitaxial structure of AlN and GaN films, high resolution TEM and XRD analyses including grazing-incidence X-ray diffraction (GID)^{7,8} were carried out. For the analysis of GID, a rotating anode-type X-ray generator with 10 KW and 4-circle goniometer were used.

RESULTS AND DISCUSSION

The AlN films synthesized by ion-assisted deposition show various crystallographical properties from amorphous to single-crystalline epitaxial structure according to the ion beam conditions and substrate temperatures. The optimum conditions of ion beam energy and arrival ratio of nitrogen to Al atoms for epitaxial growth of AlN were found to be 50 eV and 1.5 (current density of 0.25 mA · cm⁻², deposition rate of 1.2 Å · s⁻¹), respectively. Figure 2 shows high resolution cross-sectional TEM micrograph and (b) diffraction patterns for AlN epitaxial layer grown on Si(111) substrate.

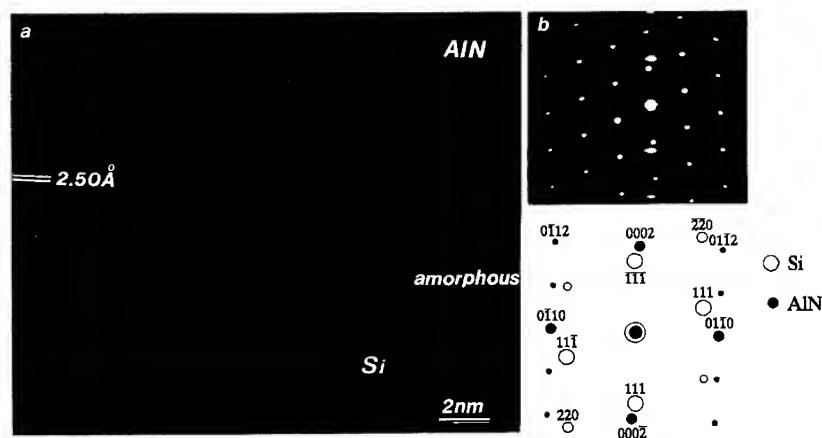


Figure 2. (a) Cross-sectional view high-resolution TEM micrograph and (b) diffraction patterns for AlN epitaxial layer grown on Si(111) substrate.

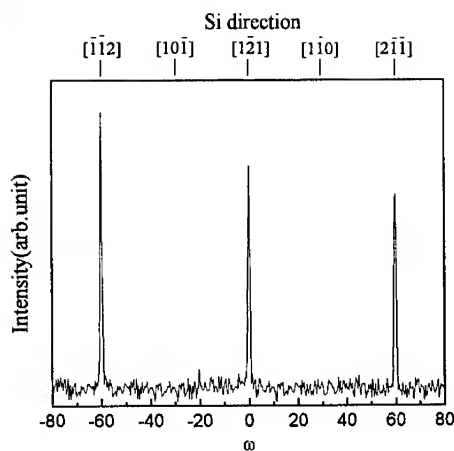


Figure 3. GID ω -scan data for $(10\bar{1}0)$ diffraction of AlN epitaxial layer grown on Si(111) substrate

film growth, the irradiation of the nitrogen ion beam causes surface disordering of silicon, which is known to have a very unstable surface structure, to depth of a few monolayers. The disordered surface of silicon may act as a seed layer for growing an amorphous layer of AlN near the interface. However, the amorphous layer at the interface plays a very important role in growing the epitaxial layer by releasing the misfit strain between Si(111) and AlN(0002) planes. Due to this buffer layer, the AlN film can grow epitaxially avoiding the harm of residual stress, despite the large lattice mismatch of about 23 %.

The selected area diffraction (SAD) pattern (Fig. 2b) obtained from the whole area of film and substrate, shows that the $[2\bar{1}10]$ zone axis of AlN epitaxial layer is well aligned to the direction of the Si $[1\bar{1}0]$ zone axis. This result implies a specific orientational relationship between the epitaxial layer and substrate. Conventional XRD and GID analyses were carried out for quantifying the crystallographical properties of the AlN epitaxial layer. The anisotropy of the epitaxial layer parallel to the surface was investigated by GID ω scan as shown in Fig. 3. The $(10\bar{1}0)$ diffraction peaks of AlN have very narrow width and appear at 60° intervals due to the 6-fold symmetry of the hexagonal structure. This result indicates that the epitaxial layer has a nearly perfect single-crystallinity with extremely low orientational spread in direction parallel to the surface. Moreover, the direction of the diffraction planes perfectly coincide with those of the crystal planes of the Si substrate as noted at the upper side of Fig. 3. From the results of GID and electron diffraction in Fig. 2b, one can easily identify the orientational relationship between AlN epitaxial layer and Si substrate as follows;

$$\text{AlN}(0001) // \text{Si}(111), \text{ and } \text{AlN}[2\bar{1}10] // \text{Si}[\bar{1}10].$$

The existence of this orientational relationship implies that the lattice information of the Si substrate has a direct influence on the growth mechanism of AlN epitaxial layer in spite of the existence of the amorphous interlayer. This interesting phenomenon has been reported in several studies on hetero-epitaxial structure of GaN^{9,10}. However, the transport mechanism of the lattice information through an amorphous interlayer is not clarified yet.

Microstrains of the epitaxial layer at both directions of surface normal and parallel were evaluated by the interplanar spacing of AlN(1010) and (0001) planes obtained from

diffraction patterns of AlN epitaxial layer grown on Si(111) plane at a temperature of 450 °C. As shown in the micrograph, the AlN film has a well-developed epitaxial structure only containing small crystallographical defects such as an anti-phase domain boundary and a very thin amorphous layer of about 30 Å thickness at interface. The measured value of the interplanar spacing of the film is 2.50 Å and in good agreement with the ASTM value of 2.489 Å for (0002) interplanar spacing of bulk AlN crystal. The amorphous layer observed at the interface between AlN epitaxial layer and Si substrate was verified not to be a native silicon oxide through the analysis of AES depth profile at the region of interface. Although the chemistry of this layer is not fully clarified at the moment, most of the amorphous layer might be considered to be composed of aluminium nitride. In an early stage of

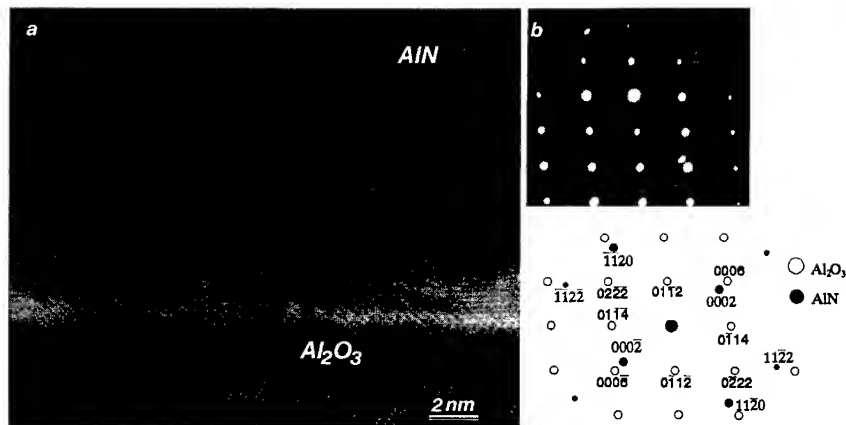


Figure 4. (a) Cross-sectional view high-resolution TEM micrograph and (b) diffraction patterns for AIN epitaxial layer grown on sapphire(0002) substrate.

the results of θ - 2θ scan of GID and conventional XRD. The calculated values of microstrain were found to be $\epsilon_{\perp} = -0.36\%$ and $\epsilon_{\parallel} = +0.12\%$, respectively. This result indicate that extremely low compressive stress remains in the AIN epitaxial layer.

Figure 4 shows a cross-sectional TEM micrograph and diffraction patterns of AIN epitaxial layer on sapphire(0002) plane. In contrast to the case of the Si substrate, the epitaxial layer grown on sapphire has no amorphous interlayer. The orientational relationship between the epitaxial layer and the sapphire substrate obtained from the diffraction patterns and the results of GID ω scan shown in Fig. 5, was found to be as follows:

AIN(0002)// α -Al₂O₃(0002), and AIN[$10\bar{1}0$] // α -Al₂O₃[$2\bar{1}10$]

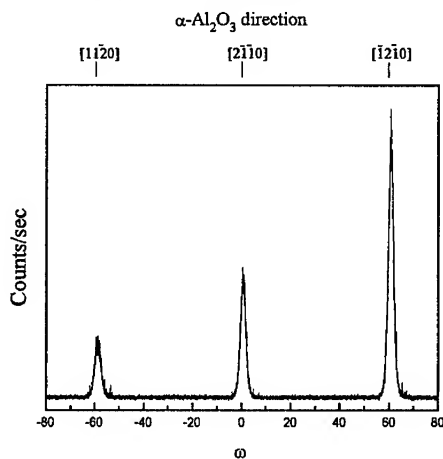


Figure 5. GID ω -scan data for $(10\bar{1}0)$ diffraction of AIN epitaxial layer grown on sapphire(0002) substrate.

However, the diffraction peak in GID ω scan results is broader than the case of the Si substrate. As mentioned above, the line broadening in GID ω scan is directly related to the orientational spread of the epitaxial layer. The degree of orientational spread for AIN epitaxial layer grown on sapphire was found to be about 3° in directions both normal and parallel to the surface, which was much larger than the case of Si substrate as shown in Fig. 3. From the results of GID ω scan, it can be concluded that the quality of epitaxial layer grown on sapphire substrate is slightly inferior to that grown on Si(111). The quality deterioration of epitaxial layer may result from the residual stress employed in the film. The crystallographical parameters of AIN epitaxial layer grown on sapphire measured by X-ray diffraction are listed in Table 1. Microstrains in the epitaxial layer are

Table 1. Crystallographical parameters of AlN epi-layer grown on Al₂O₃(0001)

Diffraction Mode	XRD	GID
Diffraction	AlN(0002)	AlN(1010)
Bragg angle, 2θ	$2\theta_{\perp} = 35.68^{\circ}$	$2\theta_{\parallel} = 33.60^{\circ}$
d - spacing	$d_{\perp} = 2.5163 \text{ \AA}$	$d_{\parallel} = 2.6672 \text{ \AA}$
Lattice strain, ϵ	$\epsilon_{\perp} = +1.07\%$	$\epsilon_{\parallel} = -1.01\%$
rms microstrain, $\langle \epsilon^2 \rangle^{1/2}$	$\langle \epsilon^2 \rangle_{\perp}^{1/2} = 5.39 \times 10^{-3}$	$\langle \epsilon^2 \rangle_{\parallel}^{1/2} = 4.54 \times 10^{-3}$
Orientational spread	$(\Delta\omega)_{\perp} = 3.02^{\circ}$	$(\Delta\omega)_{\parallel} = 2.92^{\circ}$

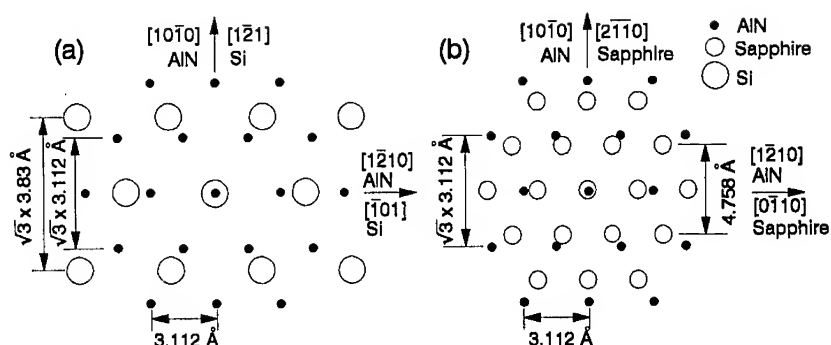


Figure 6. Lattice mismatch and orientational relations (a) between AlN(0002) and Si(111), (b) between AlN(0002) and sapphire(0002).

5-10 times greater than the case of the Si substrate, indicating a significant effect of compressive stress on epitaxial growth of AlN film. Figure 6 shows the schematic lattice configurations of AlN epitaxial layer with respect to the two substrates of Si(111) and sapphire(0002). As a conclusion, the AlN film grown on Si(111) has a well-developed epitaxial structure as a result of the release of the misfit strain by the amorphous interlayer, whereas the film on sapphire(0002) has relatively poor quality in epitaxial structure due to the coherent strain between film and substrate despite smaller lattice mismatch of about 13 % than that between AlN and Si substrate as shown in Fig. 6.

A hexagonal GaN has an identical lattice structure and nearly the same lattice constant as AlN. Due to the extremely small discrepancy in lattice constant between the two materials ($\Delta a_{\text{GaN}} = 3.189 \text{ \AA}$, $\Delta a_{\text{AlN}} = 3.112 \text{ \AA}$), the growing trend of GaN epitaxial layers on Si(111) substrates is very similar to that of AlN as shown in Fig. 7. The optimum ion beam energy for epitaxial growth of GaN film was equal to that of AlN film (50 eV). The optimum arrival ratio, however, was nearly twice greater at the growth temperature of 500 °C. The high resolution TEM micrograph of the epitaxial GaN film also shows a thin amorphous interlayer of about 30 Å thickness at interface and verifies the GaN epitaxial layer to be a very good single crystalline nature. The orientational relation obtained from SAD patterns in Fig. 7, is also equal to that between AlN epitaxial layer and Si(111) substrate, and is as follows:

$$\text{GaN}(0001) // \text{Si}(111) \text{ and } \text{GaN}[2\bar{1}10] // \text{Si}[\bar{1}10] .$$

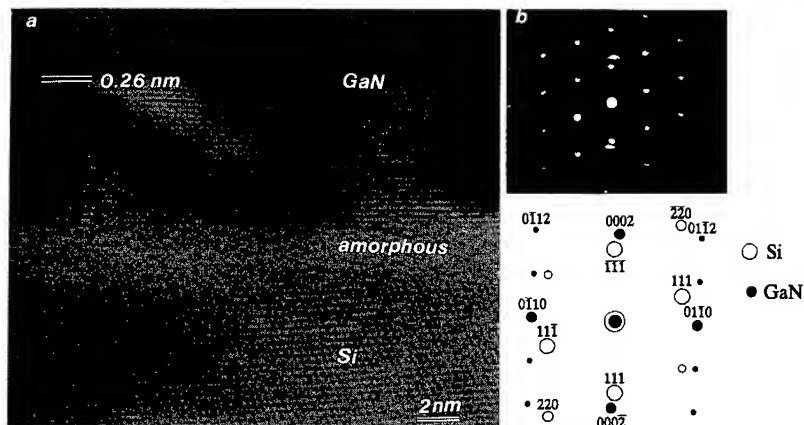


Figure 7. (a) Cross-sectional view high-resolution TEM micrograph and (b) diffraction patterns for GaN epitaxial layer grown on Si(111) substrate.

SUMMARY

Low temperature growth of AlN and GaN epitaxial films on both substrates of Si(111) and sapphire(0002) could be successfully achieved by the process of reactive N_2^+ ion beam assisted deposition at the temperature of around 500 °C. The optimum beam energy of N_2^+ ions was found to be 50 eV for both films of AlN and GaN irrespective of the substrates.

Based on TEM and GID analyses, three types of orientational relations between epitaxial layers and substrates were determined as follows;

AlN(0002)//Si(111), AlN[$2\bar{1}10$]//Si[$1\bar{1}0$],
 AlN(0002)// α -Al₂O₃(0002), AlN[$10\bar{1}0$]// α -Al₂O₃[$2\bar{1}10$], and
 GaN(0002)//Si(111), GaN[$2\bar{1}10$]//Si[$1\bar{1}0$].

In case of the Si(111) substrate, very thin amorphous layers were found at the interfaces for both AlN and GaN films, whereas there was no amorphous layer between AlN film and sapphire substrate. The amorphous layers at interface might act as a buffer layer for epitaxial growth by releasing the misfit strain. Due to the buffer layer the quality of epitaxial layers grown on Si(111) substrate was superior to that grown on sapphire(0002), despite the larger lattice mismatch.

REFERENCE

- ¹W.M.Yim, E.J.Stofko, P.J.Zanzucchi, M. Sttenberg, and S.L.Gilbert, J.Appl.Phys., 44, 292(1973).
- ²H.P.Maruskas and J.J.Tietjen, Appl.Phys.Lett., 15 327(1969).
- ³J.Ross, M.Rubin, and T.K.Gustafson, Mat.Res.Soc.Symp.Proc. Vol. 242, 457(1992).
- ⁴R.C.Powell, N.-E.Lee, Y.-M.Kim, and J.E.Greene, J.Appl.Phys., 73(1), 189(1993).
- ⁵T.Lei, M.Fanciulli, R.J.Molnar, T.D.Moustakas, R.J.Grahan, and J.Scanlon, Appl. Phys.Lett. 59, 944(1991).
- ⁶S.Strite and H.Morkoc, J.Vac.Sci.Technol., B 10(4), 1237(1992).
- ⁷G.Lim, W.Parrish, and C.Ortiz, J.Mat.Res., 2(4), 471(1987).
- ⁸A.Segmüller, J.Vac.Sci.Technol., A9(4), 2477(1991).
- ⁹H.Amono, I.Akasaki, K.Hiramatsu, N.Koide, and N.Sawaki, Thin Solid Films, 163, 415(1986).
- ¹⁰M.J.Paisley, Z.Sitar, J.B.Posthill, and R.F.Davis, J.Vac.Sci.Technol., A7(3), 701(1979).

Single Crystal Wurtzitic Aluminum Nitride Growth on Silicon Using Supersonic Gas Jets

S. A. USTIN, L. LAUHON, K. A. BROWN*, D. Q. HU, and W. HO

Laboratory of Atomic and Solid State Physics and Materials Science Center, Cornell University, Ithaca, New York 14853

*Present address: Applied Materials, 4250 Burton Drive M/S 2441, Santa Clara, CA 95054

ABSTRACT

Highly oriented aluminum nitride (0001) films have been grown on Si(001) and Si(111) substrates at temperatures between 550° C and 775° C with dual supersonic molecular beam sources. Triethylaluminum (TEA;[(C₂H₅)₃Al]) and ammonia (NH₃) were used as precursors. Hydrogen, helium, and nitrogen were used as seeding gases for the precursors, providing a wide range of possible kinetic energies for the supersonic beams due to the disparate masses of the seed gases. Growth rates of AlN were found to depend strongly on the substrate orientation and the kinetic energy of the incident precursor; a significant increase in growth rate is seen when seeding in hydrogen or helium as opposed to nitrogen. Growth rates were 2-3 times greater on Si(001) than on Si(111). Structural characterization of the films was done by reflection high energy electron diffraction (RHEED) and x-ray diffraction (XRD). X-ray rocking curve (XRC) full-width half-maxima (FWHM) were seen as small as 2.5°. Rutherford back scattering (RBS) was used to determine the thickness of the films and their chemical composition. Films were shown to be nitrogen rich, deviating from perfect stoichiometry by 10%-20%. Surface analysis was performed by Auger electron spectroscopy (AES).

INTRODUCTION

Aluminum nitride is a promising candidate for use as a high energy photon emitter and solar-blind photodetector due to its large direct bandgap [1]. It also holds promise as a barrier material in microelectronics applications. The majority of the growth studies, motivated by the photo-coupling applications, have been on sapphire [2]. Using aluminum nitride as a barrier material, however, requires high quality growth on silicon substrates in order to find use in the majority of current microcircuitry technologies. Direct epitaxy of AlN on silicon is complicated by the large lattice mismatch (23%) causing AlN films to have high dislocation densities and broad XRD features. It has been shown that epitaxial hexagonal aluminum nitride can be grown on silicon with orientations of AlN(0001)||Si(001) [3], AlN(0001)||Si(111) [4], AlN(01 $\bar{1}$ 0)||Si(111) [5], and AlN($\bar{1}$ 2 $\bar{1}$ 0)||Si($\bar{1}$ 10) [6]. Studies on the dependence of film quality and growth rate on microscopic molecular dynamics have not been reported.

EXPERIMENTAL PROCEDURE

Growth is performed on both Si(001) and Si(111) substrates. Prior to insertion into vacuum, the substrates are cleaned in a spin-processor. A cleaning cycle consists of degreasing

with ethanol, oxide etching with a 10% HF solution, and an ethanol rinse. Immediately following chemical cleaning, the silicon is inserted into a load-locked turbo pumped sample preparation chamber (base pressure 1×10^{-10} Torr). Further *in vacuo* cleaning is done through 3 cycles of a 1 keV neon sputter followed by a 1000 K anneal. AES is used to confirm surface cleanliness. RHEED patterns taken at room temperature of cleaned Si(111) and Si(001) substrates show clear evidence of 7×7 and 2×1 reconstruction, further confirming the extent of the cleanliness.

Hexagonal AlN films have been grown on silicon substrates using chemical beam epitaxy. The chemical beams were extracted from supersonically expanded free jet sources, giving rise to the name supersonic jet epitaxy (SJE) [7]. The SJE growth region is comprised of two differentially pumped chambers. Deposition takes place in a LN_2 trapped diffusion pumped growth chamber (base pressure 2×10^{-10} Torr). A diffusion pumped expansion chamber (base pressure 1×10^{-8} Torr) contains the four nozzles from which the chemical gas sources supersonically expand. Each nozzle extends into the expansion chamber up to a skimmer mounted between the expansion and growth chambers. The substrate is attached to a pyrolitic boron nitride heating element at the focal point of the four nozzles. Each nozzle is tilted 15° with respect to the surface normal. The flux image cast on the center of the silicon substrate has a 1 cm o.d. Pneumatic valves on each source line allow for growth to proceed in concurrent jet mode or pulsed jet mode (referred to as atomic layer epitaxy or ALE). Each ALE cycle lasts one minute; a cycle is defined as a 25 second exposure of TEA to the surface followed by a 25 second exposure of NH_3 with a 5 second pause between each exposure during which there is no flow. *In situ* RHEED and optical reflectivity characterize the growth. A 20 keV electron beam is incident to the surface at a glancing angle of 2° to produce a RHEED pattern. A He-Ne laser ($\lambda = 632.8$ nm) was used as the optical source to monitor the reflectivity of the surface of the growing AlN. The thickness of the growing film can be determined from the number of oscillations the reflectivity undergoes and the index of refraction of AlN. Elemental composition near the surface was determined by retracting the sample into the preparation chamber for AES analysis. *Ex situ* analysis included XRD, RBS, and ellipsometry.

RESULTS AND DISCUSSION

Crystal Structure

X-ray $\theta - 2\theta$ results indicate that all AlN films grown on Si(001) and Si(111) crystallize in the wurtzite structure with the basal plane parallel to the substrate surface. $\theta - 2\theta$ plots for AlN on Si(001) and Si(111) show single AlN peaks corresponding to AlN(0002). Samples are tilted $\approx 1^\circ$ during $\theta - 2\theta$ scans to reduce huge silicon peaks that may hide AlN peaks (for example the Si(001) peak at 69.1° can hide the AlN(2000) peak at 69.7°). All data reported are taken from scans done with no tilt. Figure 1 shows the XRD data for the highest quality film grown on Si(001). This film was grown in the concurrent jet mode at a temperature of 775°C . The 2θ FWHM for the AlN(0002) peak is 0.25° . The rocking curve is peaked at $\omega = 18^\circ$ and has a FWHM width of 5.3° . Figure 2 shows the highest quality film grown on Si(111). This film was also grown in the concurrent jet mode at a temperature of 700°C . The 2θ FWHM for the AlN(0002) peak is 0.27° and the rocking curve is peaked at $\omega = 18^\circ$ with a FWHM width of 2.5° . Crystal quality, as analyzed by XRD, was found to generally increase with an increase in growth temperature over the range of 550°C to 775°C . Also, significantly narrower XRC widths have been seen for AlN/Si(111) than for AlN/Si(100) grown under similar conditions.

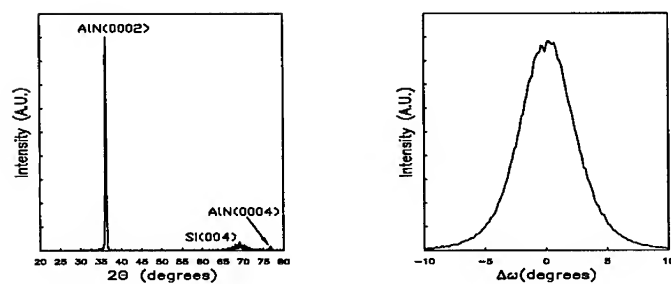


FIG. 1. $\theta - 2\theta$ (left) and rocking curve (right) scans for AlN on Si(001). This 390 nm thick AlN film was grown in the concurrent jet mode at a temperature of 775° C. The 2θ FWHM is 0.25° and the rocking curve width is 5.3°

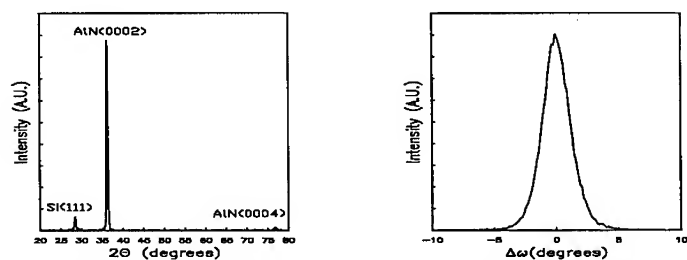


FIG. 2. $\theta - 2\theta$ (left) and rocking curve (right) scans for AlN on Si(111). This 290 nm thick AlN film was grown in the concurrent jet mode at a temperature of 700° C. The 2θ FWHM is 0.27° and the rocking curve width is 2.5°

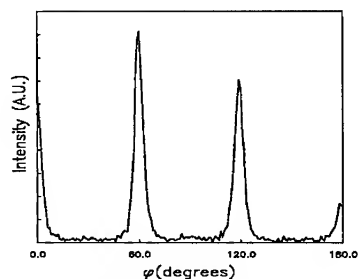


FIG. 3. ϕ -scan performed at the AlN(10 $\bar{1}$ 1) peak of the same wurtzite AlN film as shown in Figure 2.

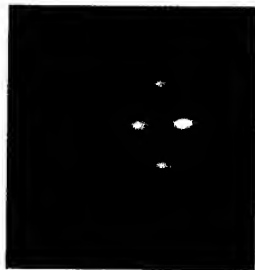


FIG. 4. RHEED pattern of AlN(0002) surface. The RHEED electron beam is oriented along the $[10\bar{1}0]$ AlN azimuth.

An azimuthal scan (ϕ -scan) was used as a check of the crystal quality. The film and diffractometer are oriented to detect the AlN($10\bar{1}1$) 2θ peak. The film is then rotated around its surface normal. The scan should show a peak every 60° , as dictated by the hexagonal symmetry of the basal plane of the AlN. A ϕ -scan for the AlN/Si(111) film that gave the smallest rocking curve width is shown in Figure 3. A peak is clearly seen every 60° as expected for single crystal wurtzite structure. No peaks are seen for the same ϕ -scan on AlN/Si(001) films. It is thus reported that single crystal AlN(0002) has been grown on Si(111) and highly-oriented AlN(0002) has been grown on Si(001). RHEED patterns are seen to be narrow and streaky, giving confirmation that the films are highly-oriented. A typical RHEED pattern is shown in Figure 4.

Growth Rate Dependence on Precursor Kinetic Energy

The major advantage to using supersonic jets as chemical sources is the ease with which and extent to which the molecular kinetic energy of the gases can be altered. Effusion sources are constrained to energies below 1 eV, whereas energies up to 10 eV can be achieved using supersonic sources. This is done through the use of mixed gas seeding techniques. For a binary mixture that has undergone supersonic expansion, the average kinetic energy per molecule within the supersonic jet is given by

$$E_i = W_i R T_o \frac{\bar{F}(\gamma)}{\bar{W}} \quad (1)$$

where

$$\bar{F}(\gamma) = \sum_{i=1,2} X_i \frac{\gamma_i}{\gamma_i - 1} \quad \bar{W} = \sum_{i=1,2} X_i W_i \quad \sum_{i=1,2} X_i = 1$$

and γ is the heat capacity ratio C_p/C_v , W is the molecular weight, R is the gas constant, X is the seeding fraction, and T_o is the nozzle temperature.

Using the approximation $\gamma_1 \approx \gamma_2$ the energy per molecule scales as

$$E_i \propto \frac{W_i}{\bar{W}} \quad (2)$$

Note that this ratio equals 1 for a pure gas source. Thus, in order to increase the kinetic energy of a gas source, the ratio W_i/\bar{W} needs to be made greater than 1. This is accomplished

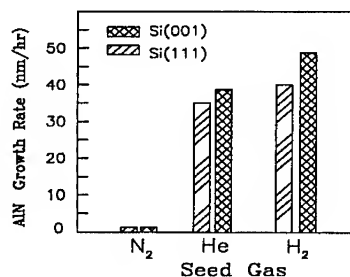


FIG. 5. Growth rate for AlN films on Si(100) and Si(111). Films were grown in the ALE mode on Si(001) and in the concurrent jet mode on Si(111), all at a substrate temperature of 650° C.

by mixing a heavy gas source (TEA or NH₃) in a low concentration with a lighter gas source (H₂, He, or N₂).

Figure 5 shows the variation in growth rate for AlN on Si(001) and Si(111) for different carrier gases. Growth rates are calculated from thickness measurements made from optical reflectivity data and confirmed with RBS and ellipsometry. It is seen that the growth rate increases as we move to lighter carrier gases, corresponding to greater precursor kinetic energies. Growth temperature is kept constant throughout both series. Attempts were made to keep the total flux constant from growth to growth. Precursor fluxes (which varied by no more than 10%) were calculated to be 3.9×10^{13} molecules/cm²/s for TEA and 1.3×10^{17} molecules/cm²/s for NH₃.

The growth rates given correspond to concurrent jet growth on Si(111) and ALE growth on Si(100). It is concluded that the sole source of the increasing growth rates seen is the increase in kinetic energy of the precursors. Growth rates are given for various precursor energies in Table I. The abrupt change in growth rate between N₂ seeded and He seeded precursors suggests that an activation energy exists for the chemical reactions that need to occur for film deposition.

Stoichiometry

RBS was done on all AlN films to determine stoichiometry and thickness. Data analysis indicates that the Al to N ratio in the films grown by SJE is between 1:1.1 and 1:1.25. These ratios are higher than expected for a III-N compound - most growth techniques are found to produce nitrogen deficient films [8]. The excess nitrogen is believed to result from the large flux difference between TEA and NH₃ and the low temperature-low pressure (4×10^{-6} Torr) growth conditions. This result is promising for using SJE to grow high-quality GaN with minimal N vacancies; it is believed that perfect stoichiometry is attainable by changing the relative flux of NH₃ with respect to the organometallic precursor. A better understanding of the microscopic processes controlling growth rate and stoichiometry is desired as precise control of layer thickness and composition is necessary for device fabrication.

AES was performed on all samples immediately following growth and cool-down. Strong aluminum and nitrogen features are seen as is a weak carbon signal. The carbon signal disappears after a 5 minute 1 keV neon sputter, implying that the carbon is a surface contaminant that originates during cool-down. Exposing the AlN film to pure helium during cool-down has shown to reduce the carbon contamination significantly, usually to below AES detection limit.

TABLE I. Growth rates for AlN on Si(001) and Si(111) as a function of precursor energies.

AlN/Si(001) T=650° C ALE mode				
TEA		NH ₃		AlN
E (eV)	seed gas	E (eV)	seed gas	growth rate (nm/hr)
0.37	N ₂	0.060	N ₂	< 2.5
0.37	N ₂	0.205	He	< 2.5
1.85	He	0.060	N ₂	22.5
1.85	He	0.205	He	35.0
5.00	H ₂	0.367	H ₂	40.0

AlN/Si(111) T=650° C Concurrent mode				
TEA		NH ₃		AlN
E (eV)	seed gas	E (eV)	seed gas	growth rate (nm/hr)
0.37	N ₂	0.060	N ₂	< 4.0
1.85	He	0.205	He	38.0
1.85	H ₂	0.367	H ₂	48.0

ACKNOWLEDGEMENTS

Support of this research by the Office of Naval Research Grant No. N00014-93-1-0499 is gratefully acknowledged.

REFERENCES

- [1] S. Strite, M.E. Lin, and H. Morkoç, Thin Solid Films **231**, 197 (1993).
- [2] M.J. Paisley and R.F. Davis, J. Cryst. Growth **127**, 136 (1993).
- [3] L.B. Rowland, R.S. Kern, S. Tanaka, R.F. Davis, J. Mater. Res. **8**, 2310 (1993).
- [4] K. S. Stevens, A. Ohtani, M. Kinniburgh, and R. Beresford, Appl. Phys. Lett. **65**, 321 (1994).
- [5] M. Miyauchi, Y. Ishiwaka, and N. Shinnibata, Jpn. J. Appl. Phys. Lett. **31**, 1714 (1992).
- [6] R.D. Vispute, J. Narayan, H. Wu, and K. Jagannadham, J. Appl. Phys. **77** 4724 (1995).
- [7] K.A. Brown, S.A. Ustin, L. Lauhon, and W Ho, to be published.
- [8] V. Gräfe, W. Niessner, D. Schalch, A. Scharmann, and C. Wiese, Phys. Stat. Sol. A **145**, 527 (1994).

EPITAXIAL GROWTH OF AlN THIN FILMS ON SILICON AND SAPPHIRE BY PULSED LASER DEPOSITION

R.D. Vispute, H. Wu, K. Jagannadham and J. Narayan

Department of Materials Science and Engineering

North Carolina State University, Raleigh, NC 27695-7916.

ABSTRACT

AlN thin films have been grown epitaxially on Si(111) and Al₂O₃(0001) substrates by pulsed laser deposition. These films were characterized by FTIR and UV-Visible, x-ray diffraction, high resolution transmission electron and scanning electron microscopy, and electrical resistivity. The films deposited on silicon and sapphire at 750-800°C and laser energy density of ~ 2 to 3J/cm² are epitaxial with an orientational relationship of AlN[0001]|| Si[111], AlN[2 $\bar{1}$ 10]|| Si[01 $\bar{1}$] and AlN[0001]|| Al₂O₃[0001], AlN[$\bar{1}$ 2 $\bar{1}$ 0]|| Al₂O₃[0 $\bar{1}$ 10] and AlN[10 $\bar{1}$ 0] || Al₂O₃[$\bar{2}$ 110]. The both AlN/Si and AlN/Al₂O₃ interfaces were found to be quite sharp without any indication of interfacial reactions. The absorption edge measured by UV-Visible spectroscopy for the epitaxial AlN film grown on sapphire was sharp and the band gap was found to be 6.1eV. The electrical resistivity of the films was about 5-6x10¹³Ω-cm with a breakdown field of 5x10⁶V/cm. We also found that the films deposited at higher laser energy densities ≥10J/cm² and lower temperatures ≤650°C were nitrogen deficient and containing free metallic aluminum which degrade the microstructural, electrical and optical properties of the AlN films

INTRODUCTION

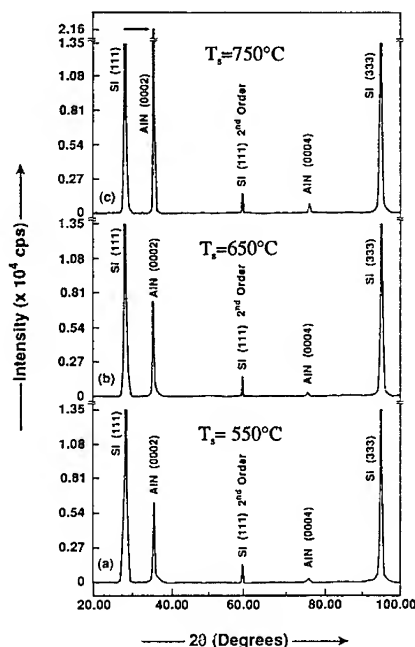
Processing of high-quality metal nitride thin films on silicon is under intense investigation currently, because of desirable optoelectronic, thermal and acoustical properties [1]. Aluminum nitride (AlN), having hexagonal wurtzite structure, lattice constants are $a=3.112\text{\AA}$ and $c=4.982\text{\AA}$, with a band gap of 6.2 eV and high surface acoustic wave (SAW) velocity (6x10⁵cm/s) offers tremendous potential for UV light emitting and SAW devices. Additionally, AlN has high thermal conductivity (320 W/mK), high thermal stability (up to 2200°C), high resistivity (10¹³ohm-cm), high dielectric strength (14KV/mm) and high chemical inertness. Its hardness and thermal coefficient of expansion (2.56x10⁻⁶/K) are comparable to that of silicon. The above properties make AlN an ideal candidate for applications in microelectronics ranging from optoelectronic and high temperature devices to electronics packaging. Various techniques have been reported for the synthesis of AlN films. These include chemical vapor deposition (CVD)[2], metal organic CVD (MOCVD) [3], reactive dc-magnetron sputtering [4], plasma assisted molecular beam epitaxy (MBE) [5], laser chemical vapor deposition [6] and pulsed laser deposition (PLD) [7-9]. High quality epitaxial AlN films have been grown by MOCVD and MBE techniques employing high temperature growth processing in the range of 1050-1250°C. There are only a few reports on the synthesis of high quality epitaxial AlN films on sapphire at relatively low temperatures (300-700°C) that include switched atomic layer epitaxy (SALE) by Khan et al. [10], electron cyclotron resonance plasma assisted CVD by Zhang et al. [11] and reactive sputtering by Okano et al. [12]. Here, we discuss the growth of high quality epitaxial AlN films on Si(111)[13] and sapphire (0001)[14] substrates by PLD at 800°C or lower.

EXPERIMENTAL

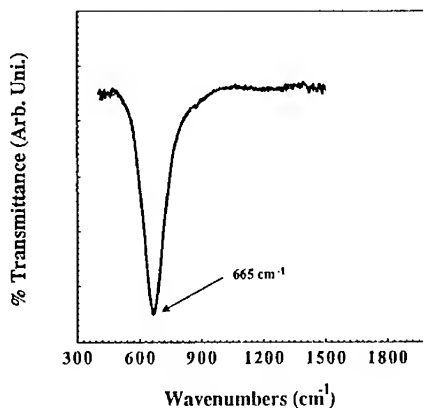
The AlN films were deposited inside a stainless steel vacuum system evacuated by a turbomolecular pump to a base pressure of 1×10^{-7} Torr. Radiation from a KrF excimer laser was used to ablate the AlN target. The stoichiometric hot pressed AlN target was ablated at an energy density (E_D) ranging from 2 to 10 J/cm². Before deposition, the silicon (111) substrates were cleaned to remove the surface oxide layer using 5% HF solution and the sapphire substrates were thermally annealed at 1100°C in O₂ atm. for 12hrs. The films were deposited at different substrate temperatures (T_s) from 25 to 800°C. In order to study the role of nitrogen partial pressure on the quality of the AlN films, the depositions were carried out at nitrogen partial pressure of 5×10^{-4} Torr. In this study, all films were deposited in the range 2000Å to 3000Å. AlN films were characterized by Fourier transform infrared spectroscopy (FTIR), x-ray diffraction, transmission electron microscopy (TEM), scanning electron microscopy (SEM) and electrical resistivity.

RESULTS AND DISCUSSION

AlN Films on Silicon (111)



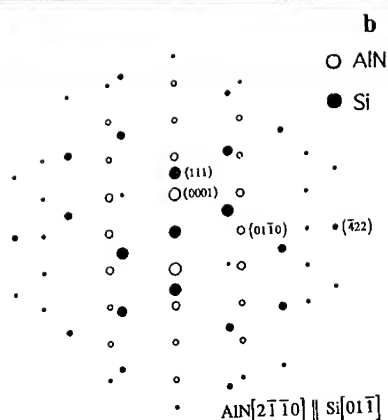
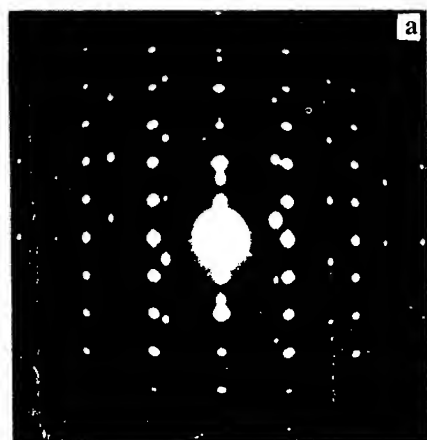
2. XRD patterns of AlN films on Si(111). AlN films were deposited at the base pressure of 3×10^{-7} Torr and the substrate temperatures of (a) 550°C, (b) 650°C, and (c) 750°C.



1. FTIR spectrum of AlN film on Si(111) by PLD.

Fig. 1 shows the FTIR transmittance spectrum of laser deposited AlN film grown on Si(111) at T_s of 750°C. The strong absorption peak at 665 cm⁻¹ is due to the transverse optical phonon modes of AlN[15]. The films deposited at all substrate temperatures had an IR spectrum characteristic of AlN.

Detailed x-ray diffraction measurements (Θ and ω scans) were carried out to study the crystalline properties of the laser deposited AlN films. Fig. 2 shows " Θ -2 Θ " angular scans of the AlN films deposited on Si(111) at three different growth temperatures 550°C [fig.2(a)], 650°C [fig.2(b)] and 750°C [fig.2(c)] and E_D of 3J/cm².



3. SAD pattern of AlN film deposited at 750°C on Si(111), without nitrogen partial pressure, showing epitaxial relationship as $\text{AlN}[2\bar{1}\bar{1}0] \parallel \text{Si}[01\bar{1}]$ and $\text{AlN}[0001] \parallel \text{Si}[111]$, (b) Simulated diffraction pattern of AlN/Si(111).

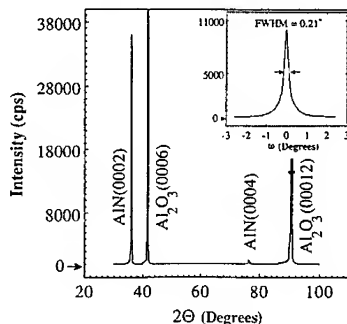
pulse repetition rate of 15Hz, and base pressure of 3×10^{-7} Torr. The diffraction patterns show expected Si(111) family of planes together with AlN (0002) and AlN (0004) reflections. It can also be seen that the integrated intensity of (0002) peak is low for the film deposited at 550°C and increases as a function of T_s . The substantial increase in the integrated intensity of (0002) diffraction line corresponding to the AlN film deposited at 750°C indicates that the AlN basal plane, i.e. (0001) plane is parallel to the (111) plane of the Si substrate. The x-ray rocking curves were obtained for the films deposited at 550, 650 and 750°C. For the film deposited at 550°C, the width of the rocking curve was quite broad indicating poor alignment of the c-axis with the substrate normal. The alignment of the film with respect to the substrate improves steadily with the increase of T_s . The narrowest rocking curve obtained for AlN films grown on Si(111) substrates at 750°C was $\sim 1^\circ$.

Fig. 3(a) shows a selected area diffraction pattern from a cross-sectional specimen deposited at 750°C with base pressure of 3×10^{-7} Torr. The spot diffraction pattern from AlN clearly shows that the film is single crystal. From the simulation (shown in fig.3(b)), the epitaxial nature of AlN on Si(111) is established. In the cross section, $\text{AlN}[2\bar{1}\bar{1}0]$ is aligned with $\text{Si}[01\bar{1}]$ axis. In other two directions, we find that $\text{AlN}[01\bar{1}0] \parallel \text{Si}[\bar{4}22]$ and $\text{AlN}[0001] \parallel \text{Si}[111]$. Similar epitaxial relationship has been reported for AlN films grown by reactive sputtering and chemical vapor deposition on Si(111) substrates [2,4]. The characteristics of AlN film microstructure and the nature of AlN/Si(111) interface were investigated using high-resolution TEM. The AlN/Si(111) interface is quite sharp without any indication of interdiffusion.

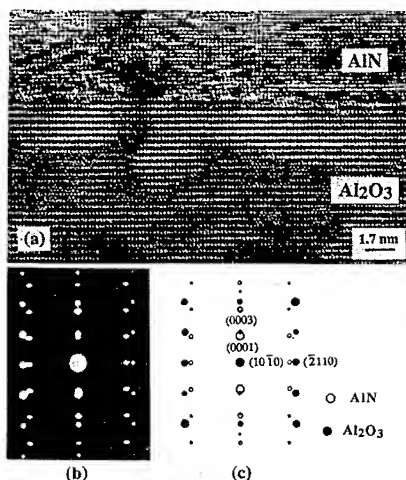
The effect of nitrogen partial pressure during laser deposition on the growth quality of AlN films was also investigated. It was found that the total integrated intensity of AlN(0002) x-ray diffraction peak decreases as a function of nitrogen partial pressure. The intensity of AlN(0002) diffraction peak dropped by factor of 3 while rocking curve broaden from 1.1 to 1.9° for the film deposited at 750°C and nitrogen partial pressure of 5×10^{-4} Torr as compared to the film deposited at base pressure of 3×10^{-7} Torr and the temperature of 750°C.

The effect of E_D on the quality of the AlN film was also investigated. The XRD pattern from a specimen (deposited at E_D of $12\text{J}/\text{cm}^2$ and T_s of 550°C) showed AlN(0001) peak along with small contribution from AlN(1000) and Al(111). The appearance of Al metal is due to the partial decomposition of AlN at higher laser fluence during laser irradiation. The laser treatment of the AlN target causes thermal melting, vaporization and decomposition as well as photochemically induced removal/ablation of materials. At lower laser fluence $\leq 3\text{J}/\text{cm}^2$, however, the single phase AlN was obtained and the decomposition of AlN is minimized.

AlN films on Sapphire (0001)



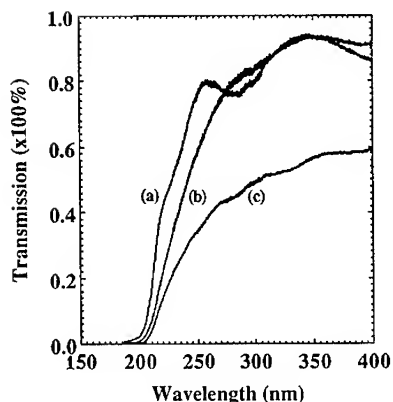
4. XRD pattern of laser deposited AlN film on $\text{Al}_2\text{O}_3(0001)$. The corresponding rocking curve for the AlN(0002) peak is shown in the inset.



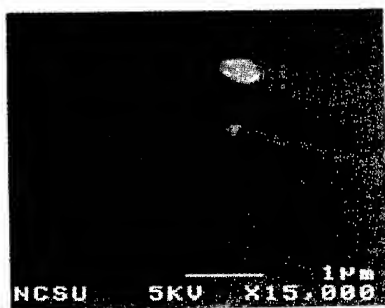
5. (a) High resolution TEM image of AlN/ Al_2O_3 interface along $[0\ 1\ 10]$ zone axis, (b) corresponding SAD pattern, (c) Simulated diffraction pattern of AlN/ $\text{Al}_2\text{O}_3(0001)$.

Fig. 4 shows XRD pattern of the laser deposited AlN film grown on $\text{Al}_2\text{O}_3(0001)$ crystal at E_D of $2\text{J}/\text{cm}^2$, T_s of 800°C and base pressure of 5×10^{-7} Torr. The pattern shows that the AlN film is highly oriented along c-axis normal to the substrate. The rocking curve obtained for AlN film grown at 800°C is shown in the inset of Fig.4. The FWHM of the rocking curve is 0.21° which indicates good alignment of (0001) planes of the AlN with that of substrate ($\Delta\omega_{\text{sapphire}} = 0.095^\circ$).

TEM was used to determine the in-plane epitaxial relationship between AlN film and Al_2O_3 . Two cross-sectional TEM samples with mutually perpendicular zone axes were prepared. Fig. 5(a) shows a high resolution lattice image of AlN/ Al_2O_3 interface along $[0\ 1\ 10]$ zone axis with a corresponding selected area electron diffraction (SAD) pattern (Fig. 5(b)) of AlN film grown at 800°C and E_D of $2\text{J}/\text{cm}^2$. The spot diffraction pattern from AlN clearly shows that the film is single crystal. From the simulated pattern (shown in Fig. 5(c)), the epitaxial nature of the film was established. In the direction of growth, $\text{AlN}[0001] \parallel \text{Al}_2\text{O}_3[0001]$, while the in-plane epitaxial relationships were found to be $\text{AlN}[\bar{1}2\ \bar{1}0] \parallel \text{Al}_2\text{O}_3[0\ \bar{1}\ 10]$ and $\text{AlN}[10\ \bar{1}0] \parallel \text{Al}_2\text{O}_3[\bar{2}\ 110]$. The AlN/ $\text{Al}_2\text{O}_3(0001)$ interface is clean and quite sharp without indication of interdiffusion. The perfect alignment of basal plane of AlN with $\text{Al}_2\text{O}_3(0001)$ is clearly observed at the interface. From TEM micrographs, the number density of dislocations was estimated to be $\sim 10^{10}/\text{cm}^2$. Such dislocation densities in the material have been shown to be low enough to allow optoelectronic device applications [16].



6. UV-Visible spectroscopy of the AlN films on $\text{Al}_2\text{O}_3(0001)$ deposited at T_s of (a) 800°C and (b) 750°C with laser energy density of $2\text{J}/\text{cm}^2$; and (c) 550°C and laser energy density of $12\text{J}/\text{cm}^2$.



7. SEM micrograph of the smooth AlN film grown on $\text{Al}_2\text{O}_3(0001)$ by PLD.

The optical transmission spectra of the AlN films deposited under various processing conditions are shown in Fig.6. The curve (a) corresponds to the spectrum of epitaxial AlN film deposited at T_s of 800°C . The film is highly transparent over the wavelength range of interest and it indicates substantial improvement in terms of transmission, absorption edge and its sharpness over the films deposited at lower T_s and high E_D (curve b and c). The fundamental absorption edge for the epitaxial AlN film was found to be 198 nm which is consistent with the reported value for the high quality films grown on sapphire by and MOCVD [3,10]. From the dependence of absorption coefficient on photon energy, the energy band gap was found to be 6.1 eV . The lower transmission and broad absorption edge of the film deposited at high E_D are attributed to nitrogen deficiency, high density of grain boundaries and aluminum content in the film, all of which introduce defect states in the film.

A typical SEM micrograph (Fig. 7) of a 3500 \AA thick AlN film grown on sapphire by PLD at 800°C , E_D of $2\text{J}/\text{cm}^2$ and base pressure of 5×10^{-7} Torr was extremely smooth with very low density of particulate matter and without formation of hillocks. The AlN films prepared by PLD at E_D of $2\text{--}3\text{J}/\text{cm}^2$ and T_s of room temperature to 800°C were highly insulating with resistivity more than 10^{13} ohm-cm . However, films deposited at higher E_D (i.e. $>10\text{J}/\text{cm}^2$) had resistivities in the range of $7\text{--}25\text{ ohm-cm}$. The low electrical resistivity of these films deposited at higher laser fluence is due to Al rich and nitrogen deficient structures and their composite behavior.

Domain Matching epitaxy (DME)

It is important to note that the lattice parameters of AlN, Si and sapphire differ quite significantly for a lattice matching epitaxy. The lattice misfits [$f_l = 2(b-a)/(a+b)$, where a and b are the lattice parameters (or interplanar distance) of the substrate and the film, respectively] of AlN with Si and sapphire are 22.3% and 13.2% , respectively. These values are quite high for lattice matching epitaxy. The epitaxial growth in these systems is described in terms of domain matching epitaxy [17]. In each domain, " m " lattice parameters (or interplanar distances) in the substrate match with " n " in the epilayer, where, m and n are simple integers. This leads to a residual domain mismatch given by " $f_d = 2(nb-ma)/(nb+ma)$ ". The lattice mismatch strain " f_l " may be large but the

strain associated with the domain given by " f_d " is very small. This decrease in strain is primarily responsible for domain epitaxial growth. In case of AlN epitaxy on Si, 4 interplanar distances of Si(110) closely matches with the 5 interplanar distances of AlN for $\text{AlN}[2\bar{1}\bar{1}0]\parallel\text{Si}[01\bar{1}]$ epitaxial growth, yielding a domain misfit (f_d) of 1.2%. In case of AlN on sapphire (0001), the 30° rotation of film with respect to sapphire in the basal a-b plane gives rise to lattice matching of Al-Al (interatomic distance of 2.74\AA) in sapphire to Al-Al (interatomic distance of 3.11\AA) in AlN with misfit of 13.2%. In this case, domains consisting of 8 Al-Al interatomic distances in AlN are matched with domains of 9 Al-Al interatomic distances in Al_2O_3 . This leads to a residual domain misfit (f_d) of 0.7%.

CONCLUSION

In conclusion, high quality epitaxial AlN films have been grown on silicon (111) and sapphire (0001) substrates by pulsed laser deposition. The quality of the films was found to depend strongly on the laser fluence, substrate temperature, and nitrogen partial pressure during deposition. The XRD, UV-V spectroscopy, electrical resistivity and TEM studies showed that by raising the T_s up to 800°C and lowering of E_D to $2\text{J}/\text{cm}^2$ are effective in improving electrical properties, crystallinity and purity of epitaxial layers. We have also established the following epitaxial relationships as: $\text{AlN}[0001]\parallel\text{Si}[111]$ and $\text{AlN}[2\bar{1}\bar{1}0]\parallel\text{Si}[01\bar{1}]$; $\text{AlN}[0001]\parallel\text{Al}_2\text{O}_3[0001]$, $\text{AlN}[\bar{1}2\bar{1}0]\parallel\text{Al}_2\text{O}_3[0\bar{1}10]$ and $\text{AlN}[10\bar{1}0]\parallel\text{Al}_2\text{O}_3[\bar{2}110]$. The epitaxial AlN films deposited under optimum growth conditions exhibited superior epitaxy, sharp interface between film and sapphire substrate, high resistivity, sharp absorption edge, and smooth surface morphology and these films were found to be consistent with optoelectronic device applications.

ACKNOWLEDGMENT

We acknowledge scientific contributions of Dr. S. Oktyabrsky of our group.

REFERENCES

1. S. Strite, and H. Morkoc, J. Vac. Sci. Technol. B **10**, 1237 (1992).
2. Y. Chubachi, K. Sato, and K. Kojima, Thin Solid Films **122**, 259 (1984).
3. A. Saxler, P. Kung, C.J. Sun, E. Bigan, and M. Razeghi, Appl. Phys. Lett. **64**, 339 (1994).
4. W.J. Meng, J. Heremans, and Y.T. Cheng, Appl. Phys. Lett. **59**, 2097 (1991).
5. K.S. Stevens, A. Ohtani, M. Kinniburgh, and R. Beresford, Appl. Phys. Lett. **65**, 321 (1994).
6. X. Li, and T.L. Tansley, J. Appl. Phys. **68**, 5369 (1990).
7. M.G. Norton, P.G. Kotula, and C.B. Carter, J. Appl. Phys. **70**, 2871 (1991).
8. K. Seki, X.Xu, H. Okabe, J.M. Frye, and J.B. Halpern, Appl. Phys. Lett. **60**, 2234 (1992).
9. P. Bhattacharya, and D.N. Bose, Jpn. J. Appl. Phys. **30**, L1750 (1991).
10. M.A. Khan, J.N. Kuznia, R.A. Skogman, D.T. Olson, M.M. Millan, and W.J. Choyke, Appl. Phys. Lett. **61**, 2539 (1992).
11. W. Zhang, Y. Someno, M. Sasaki, and T. Hirai, J. Cryst. Growth, **130**, 308 (1993).
12. H. Okano, N. Tanaka, Y. Takahashi, T. Tanaka, K. Shibata and S. Nakano, Appl. Phys. Lett. **64**, 166 (1994).
13. R.D. Vispute, J. Narayan, H. Wu and K. Jagannadham, J. Appl. Phys. **77**, 4724 (1995).
14. R.D. Vispute, H. Wu, and J. Narayan, Appl. Phys. Lett. **67**, 1549 (1995).
15. L.E. McNeil, M. Grimsditch and R.H. French, J. Am. Ceram. Soc. **76**, 1132 (1993).
16. K. Dovidenko, S. Oktyabrsky, J. Narayan, and M. Razeghi, Proceeding of Mat. Res. Soc. Vol. **358** (1995) eds. by L. Brus, R.W. Collins, M. Hirose C. C. Tsai and F. Koch, (1994).
17. J. Narayan, P. Tiwari, X. Chen, J. Singh, R. chowdhury, and T. Zheleva, Appl. Phys. Lett. **61**, 1290 (1990); US Patent granted # 5406123 (April 11, 1995).

DEPOSITION OF GALLIUM NITRIDE FILMS USING AMMONIA AND TRIETHYLGALLIUM SEEDED HELIUM BEAMS

J. J. SUMAKERIS*, R. K. CHILUKURI*, R. F. DAVIS **AND H. H. LAMB*

* Chemical Engineering,
North Carolina State University, Raleigh, NC 27695-7905
** Materials Science and Engineering,
North Carolina State University, Raleigh, NC 27695-7907

ABSTRACT

Gallium nitride films have been deposited on Si(100) and Al₂O₃(0001) substrates using triethylgallium and ammonia seeded into highly expanded helium gas streams. A two step deposition process that reproducibly results in continuous crystalline GaN films has been developed. The microstructure and composition of the resultant films were characterized by scanning electron microscopy, reflection high energy electron diffraction and Auger electron spectroscopy and film character was correlated to deposition conditions.

INTRODUCTION

Gallium nitride thin films are of considerable interest in the development of blue light emitting diodes (LEDs) for panchromatic solid state displays. In addition to LEDs, GaN may be used for the fabrication of blue solid state lasers which would facilitate the achievement of greater data density in optical transmissions and optical storage media. Chemical vapor deposition (CVD) is the most popular technique currently employed to grow GaN films [1]. In CVD growth of GaN, activation energy barriers must be overcome in order to grow a film. Typically this energy is supplied by the thermal energy of the substrate. However this method requires very high deposition temperatures that complicate device design and fabrication processes. A reduction in the required deposition temperature is highly desirable. Alternatively, several novel approaches such as plasma discharges [2,3] have been examined as a means of supplementing this thermal energy and assisting in overcoming the activation energy barriers to GaN film deposition via the generation of activated precursors. Unfortunately, plasma processes may damage the substrate or device structures due to ionization effects and ion bombardment.

An interesting alternative method of increasing the reactivity of gaseous reactants is the seeding of highly expanded gas streams. Massive reactant molecules seeded into a highly expanded majority stream of light molecules are swept along at superthermal velocities acquiring a substantial amount of kinetic energy, up to several eV, that can aid in driving surface reactions [4]. In addition, the velocity spread of the seeded molecules is inversely related to the stagnation pressure, permitting the formation of a very monoenergetic molecular beam. With the ability to generate a neutral beam of a well determined, selective energy, various reaction pathways can be studied in detail.

EXPERIMENT

Deposition system

A schematic of the free standing seeded beam deposition reactor used in this research is presented in Figure 1. Base vacuum was achieved using a Varian VHS-6 diffusion pump. During deposition, a CVC 6" diffusion pump backed with a roots blower was also used for increased throughput. The reactor has been configured to operate two seeded beams simultaneously with the ammonia (NH₃) orifice heated to 550°C and the triethylgallium (TEGa) orifice unheated. Research grade He and Ar were each used as carrier gases while high purity NH₃ was further purified using a Nanochem® activated resin bed purifier. The TEGa was delivered using conventional metalorganic bubbler techniques. Samples were mounted onto stainless steel travelers and introduced into the reactor through a load-lock. The travelers were then mounted to a stainless steel housing that was heated by a halogen lamp giving substrate temperatures of up to 650°C. Typical operating conditions are summarized in Table I.

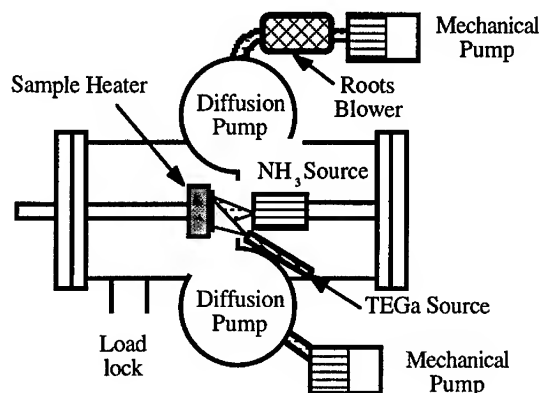


Figure 1. Seeded beam deposition system.

Table I. Typical experimental conditions/ system capabilities.

System parameter	Value
Base vacuum	8×10^{-7} Torr
Pressure during deposition	5×10^{-4} Torr
NH ₃ seeding percentage	5% volume
NH ₃ jet stagnation pressure	800 Torr
NH ₃ /He flow rates during deposition	12/240 sccm
NH ₃ orifice diameter	150 μ m
NH ₃ orifice temperature	550°C
TEGa bubbler temperatures	-10°C
TEGa stagnation pressure	860 Torr
TEGa carrier	40 sccm He
TEGa orifice diameter	20 μ m
TEGa delivery rate	0.034 sccm
NH ₃ :TEGa ratio	354:1
Substrate temperature	600°C

Sample cleaning/ preparation

Al₂O₃ (0001) samples were prepared in a three step cleaning process: 10 minutes in a trichloroethylene containing ultrasonic bath, 15 minutes in an 80°C acid bath containing a 50:50 mixture of H₃PO₄ and H₂SO₄, 5 minutes in 10% HF solution. Si(100) samples were immersed in a 10% HF solution for 5 minutes and subsequently exposed to an ultraviolet light: air oxidation step after which the samples were immersed in a separate 10% HF solution for 5 minutes. Both Al₂O₃(0001) and Si(100) substrates were blown dry with LN₂ boil-off immediately before mounting on travelers and installation into the reactor.

Auger analysis

Auger electron spectroscopy was performed in a 10^{-10} Torr base pressure ultrahigh vacuum analysis system with a Physical Electronics 10-155 cylindrical-Auger Electron optics detector with a coaxial electron gun operated by a Physical Electronics 11-010 electron gun controller. The Auger optics were supported by a Physical Electronics 32-100 electron multiplier module.

Samples were Ar ion sputtered *in-situ* prior to Auger examination. Auger measurements were performed with a primary electron energy of 3 keV and data was collected for 10 ms at each 1 eV scanning step for 15 iterations.

Reflection high energy electron diffraction

Electron diffraction characterization of deposited films was performed with a Physical Electronics electron gun operated at 10 keV by a 20-330 analog HEED gun controller. The electron source was 12" from the sample center and the screen was also 12" from the sample center.

Scanning electron microscopy

A JEOL 6400 field emission scanning electron microscope (SEM) operated with a 5 keV primary beam was used for the SEM images in this report. For the cross sectional images, the samples were cleaved immediately before installation in the SEM.

RESULTS

Single step deposition

A series of experiments was performed to study the effect of the NH_3 :TEGa supply ratio on the properties of resulting films. By varying the TEGa bubbler temperature while holding all flow rates and pressures constant, it was possible to explore this ratio effect without the added complication of gas flow pattern changes. Three samples were prepared and examined via SEM and Auger chemical spectroscopy. The NH_3 :TEGa ratio achieved at each bubbler temperature used is presented in Table II. Figure 2 displays the Auger spectra collected from the three samples. The spectra were normalized to the same Ga_{LMM} peak intensity. A clear trend of decreasing N concentration with decreasing NH_3 :TEGa supply ratio is evident.

Table II. Bubbler temperature and NH_3 :TEGa ratio for deposition studies.

Run Number	Bubbler Temp.	NH_3 :TEGa Ratio
1	0°C	177
2	-8°C	306
3	-10°C	354

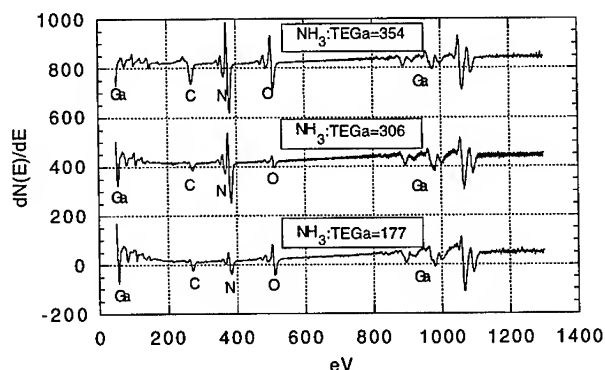


Figure 2. Auger spectra of films deposited at varying NH_3 :TEGa supply ratios.

GaN films deposited on an $\text{Al}_2\text{O}_3(0001)$ substrates under an $\text{NH}_3\text{:TEGa}$ supply ratio of 177 were covered by many spherical particles hypothesized to be balls of Ga surrounded by a skin of GaN, indicating a marked excess of Ga for the available N. A GaN film deposited under an $\text{NH}_3\text{:TEGa}$ supply ratio of 354 is presented in Figure 3. Continuous GaN films were difficult to achieve at high $\text{NH}_3\text{:TEGa}$ ratios and often deposition runs of 2 hours resulted in little deposition. This was attributed to a difficulty in forming stable GaN nuclei at low TEGa flow rates.

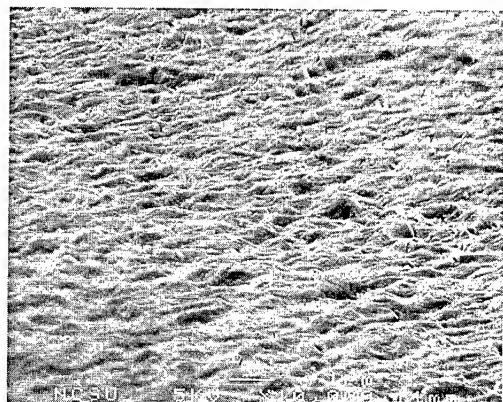


Figure 3. GaN film deposited on $\text{Al}_2\text{O}_3(0001)$ under an $\text{NH}_3\text{:TEGa}$ supply ratio of 354.

An additional deposition run was completed at an $\text{NH}_3\text{:TEGa}$ flow ratio of 617 for one hour. In the SEM image of a resulting sample in Figure 4, the $\text{Al}_2\text{O}_3(0001)$ substrate is still visible beneath the GaN particles. The films deposited under $\text{NH}_3\text{:TEGa}$ ratios of 177 and 617 represent two extremes encountered when deposition is performed with low and high $\text{NH}_3\text{:TEGa}$ ratios, respectively. Although higher $\text{NH}_3\text{:TEGa}$ ratios produce films closer to stoichiometry, the nucleation of GaN under these conditions occurs very slowly. This lead to the development of a two step nucleation→deposition process.

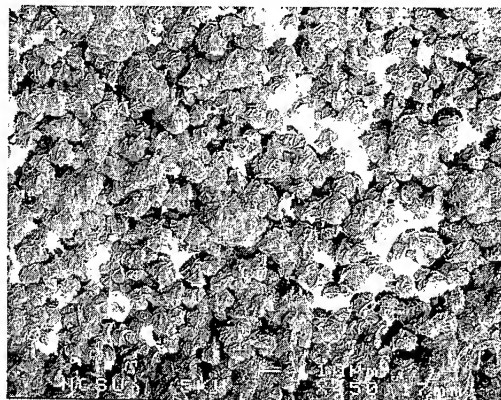


Figure 4. GaN film deposited on $\text{Al}_2\text{O}_3(0001)$ under an $\text{NH}_3\text{:TEGa}$ supply ratio of 617.

Two Step Deposition

A two temperature deposition process was developed to nucleate GaN at lower temperature prior to the deposition of the majority of the GaN film at higher temperature. The surface concentration, n_A , of an adsorbed species is inversely related to temperature as shown in Equation 1[5] where E_a is the bonding energy of species a, τ_0 is a characteristic time factor typically approximated by the lattice vibration time of $\approx 10^{-13}$ seconds and R is the incident flux of species a. This model predicts a higher Ga and N precursor surface concentration at lower temperatures assuming that the precursor sticking coefficients are not strongly temperature dependent in this temperature range. This assumption also gives $n_{\text{Ga precursor}} > n_{\text{N precursor}}$ if $E_{\text{Ga precursor}} > E_{\text{N precursor}}$.

$$n_A = R\tau_0 \exp\left(\frac{E_a}{kT}\right) \quad (1)$$

An optimal two step process was developed where the sample was first heated under the NH_3 seeded beam to 500°C and the TEGa flow was initiated. The sample was held at 500°C for 5 minutes before the temperature was increased to 600°C in 10 minutes. Figure 5 is a cross sectional SEM image of a GaN film deposited on an $\text{Al}_2\text{O}_3(0001)$ substrate under the two step deposition conditions. Slight faceting of the film indicated a degree of preferred orientation in the crystallites. RHEED diffraction patterns for this film are presented in Figure 6 and are consistent with a polycrystalline film exhibiting a large degree of preferred crystallographic orientation.

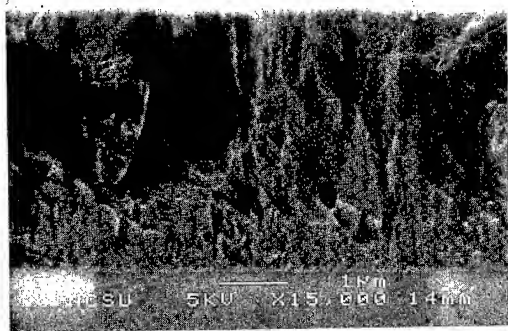


Figure 5. GaN film deposited on $\text{Al}_2\text{O}_3(0001)$ substrate via two step process.

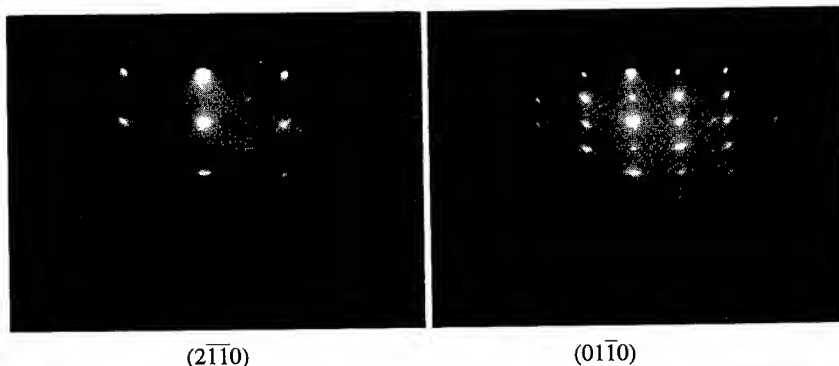


Figure 6. RHEED diffraction patterns from GaN film deposited on Al_2O_3 substrate.

Seeding in Ar free jets

A series of experiments was performed to determine if the seeding of NH_3 and TEGa in He actually enhances film deposition. It is expected that the seeding effect is most important for the N-source as TEGa reacts readily at low temperatures. The seeding effect would be negated if a carrier gas that is heavier than NH_3 such as Ar were employed. Therefore, Ar was used as a carrier gas in this series and the orifices were enlarged to permit operation at very close to the same pressures and flow rates as employed for deposition using He. An Auger spectrum typical of samples processed using Ar is presented in Figure 7. Note that even after extensive Ar sputtering, a very large O_{KLL} peak is still apparent along with a marked excess of Ga. This indicates that seeding NH_3 in Ar is far less effective than seeding in He for supplying reactive N to the growing film.

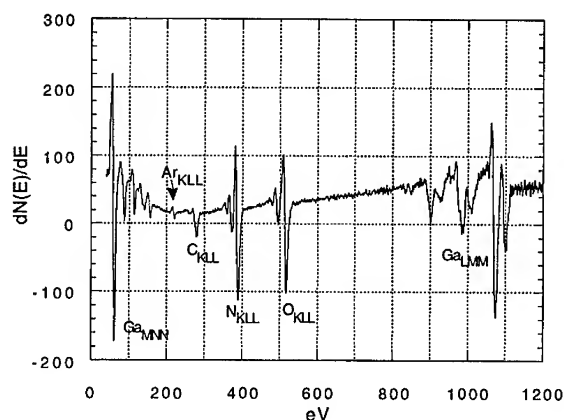


Figure 7. Auger spectrum of GaN film deposited using Ar as a carrier.

CONCLUSIONS

Ammonia and trimethylgallium seeded helium beams have been used to deposit GaN films on $\text{Al}_2\text{O}_3(0001)$ substrates at low temperatures. A two step deposition process has been developed to nucleate and grow the films. An improvement in stoichiometry and crystallinity is observed when seeding into helium as compared to argon gas. This result is consistent with the activation of NH_3 by the seeding effect.

ACKNOWLEDGMENTS

This work is supported by the Office of Naval Research under contract #N00014-95-1-0122

REFERENCES

1. S. Nakamura, Jpn. J. Appl. Phys. 30, L1708.
2. Z. Sitar, M. J. Paisley, B. Yan and R. F. Davis, Thin Solid Films 200, 311 (1991).
3. W. J. Meng, J. Heremans and Y. T. Cheng, Inst. Phys. Conf. Ser. 137, 409 (1993).
4. J. R. Engstrom, D. A. Hansen, M. J. Furjanic and L. Q. Xia, J. Chem. Phys. 99, 4051 (1993).
5. G. E. McGuire, Semiconductor Materials and Process Technology Handbook, Noyes Publications (1988).

ALTERNATIVE ROUTES TO THE MOVPE GROWTH OF GaN AND AlN

V. ROBERTS*, J. S. ROBERTS, A. C. JONES** and S. RUSHWORTH

*University of Sheffield, Department of Electronic and Electrical Engineering, Sheffield, S1 3JD
United Kingdom.

**Epichem Limited, Power Road, Wirral, Merseyside, L62 3QF, United Kingdom.

ABSTRACT

Alternative precursors to group-III nitrides have been studied based on two schemes: 1) The reaction Me_3M ($\text{M}=\text{Al}, \text{Ga}$) with t-BuNH_2 and 2) the decomposition of NH_3 based adducts. Polycrystalline growth of AlN has been demonstrated by both routes. Decomposition of the adduct $\text{Me}_3\text{Al}:\text{NH}_3$ has been used to prepare epitaxial AlN on (0001) sapphire with an X-ray FWHM (full width at half maximum) of 16 arcmin at a growth temperature of 1050°C. Similar growth using analogous gallium precursors always resulted in gallium droplets. We have attributed this difference in chemical reactivities to the lower electronegativity of gallium compounds, thus leading to dissociation rather than sequential methane loss to form the nitride.

INTRODUCTION

Conventional MOVPE growth of group III-nitrides involves the co-deposition of metal alkyls with excess ammonia (NH_3). Such growth is characterised by large V/III ratios (eg 2000:1) and although successful is wasteful when compared to other III-V MOVPE processes. In this work we have investigated alternative MOVPE growth, based on both NH_3 adducts and the reaction of t-Butylamine (t-BuNH_2) with trimethylaluminium (Me_3Al) or trimethylgallium (Me_3Ga). Ammonia was absent from the MOVPE reactor and consequently nitrogen loss from the as-grown surface has not been addressed in this programme.

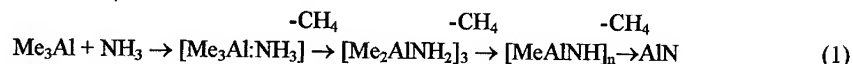
EXPERIMENTAL

The growth studies were performed in a conventional horizontal MOVPE reactor (a modified Cambridge Instruments MR100) with RF substrate heating. This reactor could be operated at both atmospheric pressure (reactor pressure 877 Torr, source pressure 980 Torr) and low pressure (reactor pressure 65 Torr, source pressure 250 Torr). Studies of single source precursors generally required low pressure operation due to the lower vapour pressure of these reagents. All gas lines following the sources were heated to avoid condensation of precursor vapour. Pd/Ag diffused hydrogen was used for both transporting the reagents and reactor carrier gas (8l/min).

Aluminium precursors

The aluminium precursors studied, together with the growth temperature and reactor pressure, summarised in table 1. Two precursor systems were considered; one based on the reaction between trimethylaluminium (Me_3Al) and t-Butylamine (t-BuNH_2), the other, using the single source precursor trimethylaluminium-ammonia adduct ($\text{Me}_3\text{Al}:\text{NH}_3$).

It has been shown that the growth of AlN by MOCVD from the combination Me_3Al and NH_3 arises from an initial formation of the adduct $[\text{Me}_3\text{Al}:\text{NH}_3]$, followed by the sequential elimination of CH_4 thus¹



In this work the initial step of this process is external to the reactor, since the adduct $\text{Me}_3\text{Al}:\text{NH}_3$ has been utilised as a precursor. Any prereactions between Me_3Al and NH_3 , leading to the formation of the adduct, are therefore prevented.

Growth on the Si(100) substrates was expected to be polycrystalline as no attempt was made to remove the silicon native oxide. Epitaxial growth of AlN on c-plane sapphire (Al_2O_3 (0001)) using the single source precursor $\text{Me}_3\text{Al}:\text{NH}_3$ (flow rate = 300 sccm, source temperature = 45 C) was studied over the temperature range 800 C to 1050 C. Prior to deposition on sapphire the substrates were pre-treated in an atmosphere of hydrogen at 1000 C for 10 min.

The high vapour pressure of both Me_3Al (8.67 Torr @ 20 C) and t-Butylamine (288 Torr @ 20 C) allows the reactor to be operated at atmospheric pressure; the single source precursor $\text{Me}_3\text{Al}:\text{NH}_3$ requires low pressure growth due to the lower vapour pressure of this source.

Precursor(s)	Substrate	Growth Temp	Pressure	Comments
$\text{Me}_3\text{Al} + \text{t-BuNH}_2$	Si/SiO ₂	550 C, 950 C	AP	High carbon content and polycrystalline
$\text{Me}_3\text{Al}:\text{NH}_3$	Si/SiO ₂	400 C to 800 C	LP	Growth rate = 33 - 467 nm/hr and polycrystalline
$\text{Me}_3\text{Al}:\text{NH}_3$	$\alpha\text{-Al}_2\text{O}_3$	800 C to 1000 C	LP	Epitaxial growth rate = 250 nm/hr

Table 1 - Precursors studied for the deposition of AlN

Gallium Precursors

The range of precursor reactions investigated include t-BuNH₂/trimethylgallium (Me_3Ga), t-BuNH₂/trimethylgallium-ammonia adduct ($\text{Me}_3\text{Ga}:\text{NH}_3$) as well as several single source precursors based on ammonia adducts with gallium alkyls. These are summarised, together with the growth conditions used, in table 2.

Precursor(s)	Substrate	Growth Temp	Pressure	Comments
$\text{Me}_3\text{Ga} + \text{t-BuNH}_2$	GaAs	700 C	AP	Ga droplets formed
$\text{Me}_3\text{Ga}:\text{NH}_3$ + t-BuNH ₂	$\alpha\text{-Al}_2\text{O}_3$	700 C, 950 C	AP	Ga droplets formed
$\text{Me}_3\text{Ga}:\text{NH}_3$	Si/SiO ₂	200 C, 700 C	AP	Ga droplets formed
$\text{Et}_3\text{Ga}:\text{NH}_3$	$\alpha\text{-Al}_2\text{O}_3$	900 C	LP	Ga droplets formed
$\text{Me}_2\text{GaCl}:\text{NH}_3$	$\alpha\text{-Al}_2\text{O}_3$	700 C	LP	Ga droplets formed

Table 2 - Precursors studied for the deposition of GaN

Film Analysis

Film composition was measured by Auger Electron Spectroscopy (AES) using a Varian Scanning Auger spectrometer. The atomic compositions quoted are from the bulk of the film, free from surface contaminants, and were obtained by combining AES with sequential ion-bombardment until comparable compositions were obtained for consecutive data points.

Layer thickness was determined by ellipsometry combined with a calibrated scanning electron micrograph of cleaved samples; this was used in growth rate calculations. Epitaxial crystalline quality for the AlN/Al₂O₃ samples was determined from the Full Width at Half Maximum (FWHM) of the X-ray rocking curve measured with a double crystal X-ray diffraction system.

RESULTS and DISCUSSION

Aluminium precursors

Polycrystalline films were deposited on Si(100) substrates from the adduct Me₃Al:NH₃ over the temperature range 400 C to 800 C. At temperatures between 600 C and 700 C the AlN growth rate was essentially constant at approximately 460 nm/hr indicating diffusion rate limited growth. Diffusion controlled growth of AlGaAs from methyl-based metalorganics has been observed over a similar temperature range within the same reactor. At higher substrate temperatures (700 C to 800 C) the AlN growth rate decreases, due to an increase in parasitic reactions and/or desorption processes. At lower temperatures (400 C to 600 C) the growth is limited by the decomposition kinetics of the Me₃Al:NH₃ precursor. There was no evidence for the adduct dissociating in preference to the decomposition shown in equation (1).

The growth of AlN from Me₃Al and t-BuNH₂ resulted in high growth rates (typically 1.2 µm/hr) but was discoloured by the inclusion of a large carbon residue; this will be discussed further in the following sections.

The atomic composition of the AlN films grown on Si(100) from Me₃Al:NH₃ was determined by AES and the data are summarised in Table 3.

Film No	Growth Temperature (C)	Film Composition (%)				Al/N Ratio
		Al	N	C	O	
1	400	47.7	46.1	4.8	1.5	1.02
2	500	48.0	47.7	2.7	1.6	1.01
3	600	48.7	40.9	1.6	8.8	1.19
4	700	44.3	45.4	1.4	8.9	0.97
5	800	46.2	49.2	0.6	3.9	0.95

Table 3 AES analysis of AlN grown on Si(100)

The degree of carbon contamination in AlN films grown from Me₃Al:NH₃ (C = 0.6 to 4.8 at %) is higher than that observed in films grown from the related amide precursor (Me₂AlNH₂)₃

(C not detected by AES)². However, much higher carbon concentrations have been observed in AlN grown from the reaction of Me₃Al/t-BuNH₂, both by ourselves in this work (C = 8.0 at %) and by other workers (C = 2.7 to 9.5 at %).³ In addition, growth from t-Bu₃Al/t-BuNH₂ (C = 4.7 to 7.2 at %)⁴ and Me₃Al/Me₃SiN₃ (C = 9.8 to 11.4 at %)⁵ have all resulted in large carbon residues. The relatively low carbon levels in AlN films grown from Me₃Al:NH₃ and (Me₂AlNH₂)₃ can therefore be attributed to the effective removal of (CH₃•) radicals by active hydrogen derived from Al bonded NH₃, NH₂ and NH groups. Carbon contamination derived from Me₃Al:NH₃ shows a general decrease with increasing substrate temperature suggesting (CH₃•) removal is more facile at the higher growth temperature. This is in contrast to the trend usually observed in the growth of Al-containing III-V alloys from methyl-based precursors⁶, in which decomposition of surface methyl radicals generally leads to significant increases in carbon contamination at elevated temperatures.

The residual oxygen levels in AlN deposited from Me₃Al:NH₃ (O = 1.5 to 8.9 at %) are similar to those detected in AlN films grown from (Me₂AlNH₂)₃ (O ~ 5 at %)², and by the reaction Me₃Al/t-BuNH₂ (O = 4.2 to 6 at %)³ and t-Bu₃Al/t-BuNH₂ (O = 1.2 to 10.4 at %)⁴. The strength of the aluminium-oxygen bond hinders the elimination of oxygen from MOVPE grown materials⁷. However, the inclusion of a capping layer can reduce the extent of post-growth oxidation⁴ which occurs over a period of time when AlN is exposed to atmosphere. In order to control post growth oxidation a capping layer of GaAs was added to our structures. However, residual oxygen concentrations were not significantly reduced suggesting the oxygen is associated with the Al precursor, possibly as monomethoxide ((MeO)AlMe₂NH₃) impurity included during reagent synthesis.

Observations with a Normarski microscope showed epitaxial AlN layers grown on Al₂O₃ (0001) from Me₃Al:NH₃ to be almost featureless. However, for 1 micron thick layers several regions with microcracks were noted, particularly near the edge of the 1 inch diameter substrates. X-ray rocking curves were measured for layers grown at growth temperatures from 800 C to 1050 C; the FWHM derived from these curves are summarised in figure 1. This shows that the linewidth is approximately constant (~27 arcmin) over the temperature range 900 C to 1050 C, whilst below 900 C this increases; the narrowest FWHM measured was 16 arcmin, at a growth temperature of 1050 C. The FWHM of these films was found to be constant for layers above 250 nm, below this thickness the FWHM increased to 58 arcmin. We also noted a reduction in the FWHM with precursor use; for example the two values shown in figure 1 for growth at 800 C were separated by 10 growth runs and show a linewidth improvement from 61 arcmin to 30 arcmin. We believe this improvement is due to reduced oxygen contamination of the films as the source container outgases water vapour.

The X-ray FWHM value 16 arcmin is approximately half that of the recent data of Chaudhuri et al⁸ for growth of AlN from Me₃Al and NH₃ at 1250 C and a V/III ratio of 2000:1. However the narrowest FWHM reported to date is 97.2 arcsec⁹, again using Me₃Al and NH₃, a substrate temperature of 1050 C and V/III ratio of 5000:1.

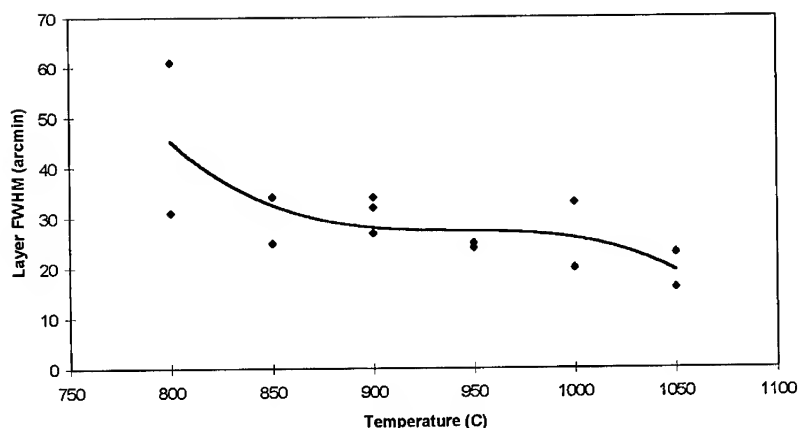


Figure 1 X-ray diffraction rocking curve FWHM of AlN layers grown on c-plane sapphire

Gallium precursors

The growth of GaN from the reaction of Me_3Ga and NH_3 is also expected to proceed via the initial formation of an adduct $[\text{Me}_3\text{Ga}:\text{NH}_3]^{10}$ followed by sequential methane loss (compare with equation 1). However, as shown in table 2, deposition from the adducts $\text{Me}_3\text{Ga}:\text{NH}_3$ and $\text{Et}_3\text{Ga}:\text{NH}_3$ resulted in gallium deposits on the substrate. The R_3Ga compounds ($\text{R}=\text{Me}, \text{Et}$) are weaker electron acceptors than the corresponding R_3Al compounds, thus the associated adducts $[\text{R}_3\text{Ga}:\text{NH}_3]$ are thought to dissociate rather than decompose. Consequently, R_3Ga species are released in the reactor hot zone to form gallium metal through alkyl fission. The inclusion of an overpressure of $-\text{NH}_2$ species in the form of $t\text{-BuNH}_2$ failed to suppress this dissociation. By replacing one of the Me groups in the $\text{Me}_3\text{Ga}:\text{NH}_3$ adduct with a chlorine atom the bond strength of the adduct should be increased. However, as the use of dimethylgalliumchloride-ammonia adduct $[\text{Me}_2\text{GaCl}:\text{NH}_3]$ shows, this precursor also leads to the formation of gallium deposits indicating dissociation of the adduct.

CONCLUSIONS

In this work novel precursors based on adducts of metal alkyls with NH_3 and the combination of $\text{Me}_3\text{Al}(\text{Ga})/t\text{-BuNH}_2$ have been investigated as routes to epitaxial group-III nitrides. We have shown that epitaxial AlN can be grown on sapphire from the single source precursor $\text{Me}_3\text{Al}:\text{NH}_3$. The FWHM of the X-ray rocking curves (as low as 16 arcmin) are comparable with that of recently published data on layers grown by the conventional $(\text{CH}_3)_3\text{Al}$ and NH_3 based process. The lowest carbon contaminated AlN has been noted using $\text{Me}_3\text{Al}:\text{NH}_3$ and may be reduced further by including a modest overpressure of NH_3 . In addition, the inclusion NH_3 should also reduce nitrogen loss from the grown layer. To our knowledge, the deposition of AlN from $\text{Me}_3\text{Al}:\text{NH}_3$ is the only example of III-V epitaxy using a single source precursor. The mechanism is successful because of the inherently large bond strength of Al-N.

The gallium based precursors all resulted in the formation of gallium droplets on the surface of the substrate. This was attributed to the weaker Ga-N bond strength compared to Al-N, thus the reaction intermediates decompose to form gallium metal rather than the nitride.

ACKNOWLEDGEMENTS

The authors would like to acknowledge G. Critchlow, ISST, University of Loughborough, Loughborough, Leicestershire, UK for the Auger analysis. This work is supported by the Engineering and Physical Sciences Research Council.

REFERENCES

- ¹ A C Jones, C R Whithouse and J S Roberts, 'Chemical Approaches to the Metalorganic CVD of Group III Nitrides', *Electronic Materials*, to be published.
- ² Y Takahashi, K Yamashita, S Motojima and K Singiyama, *Surf Sci*, **86**, 1979, pp 238
- ³ A C Jones, J Auld, S A Rushworth, E W Williams, P W Haycock, C C Tang and G W Critchlow, *Adv. Mater.* **6**, 1994, pp 229
- ⁴ A C Jones, J Auld, S A Rushworth, DJ Houlton and G W Critchlow, *J Mater Chem*, **4**, 1994, pp 1591
- ⁵ J Auld, D J Houlton, A C Jones, S A Rushworth and G W Critchlow, *J Mater Chem*, **4**, 1245 (1994).
- ⁶ T F Kuech, E Veuhoff, T S Kuan, V Delane and R Potenski, *J Crystal Growth*, **77**, 257 (1986).
- ⁷ L M Smith, S A Rushworth, A C Jones, J S Roberts, A Chew and D A Sykes, *J Cryst Growth*, **134**, 140 (1993).
- ⁸ J Chaudhuri, R Thokala, J H Edgar and B S Sywe, *J Appl Phy*, **77** (12), 6263 (1995).
- ⁹ A Saxler, P Kung, C J Sun, E Bigan and M Razeghi, *Appl Phy Lett*, **44** (3), 339 (1994).
- ¹⁰ B S Swye, J R Schlup and J H Edgar, *J Chem Mater*, **3**, 737 (1991).

Low Temperature Growth of Oriented Gallium Nitride Using Pulsed Laser Deposition

Robert Leuchtner, W. Brock, Y. Li, and L. Hristakos, Department of Physics,
University of New Hampshire, Durham, NH, 03824

ABSTRACT Oriented GaN has been successfully grown at low substrate temperatures ($\sim 480^\circ\text{C}$) on a- and r-planes of sapphire, using the pulsed laser deposition process. We have examined the effects of several deposition parameters on film growth, including substrate temperature (~ 50 - 500°C), ambient pressure (1×10^{-3} - 10 torr of NH_3), and target material (Ga or GaN). The film deposition rate was typically ~ 3 - $4 \mu\text{m/hr}$. Film characterization was performed using x-ray diffraction (XRD), optical microscopy, x-ray photoelectron spectrometry (XPS), and atomic force microscopy (AFM). In the case of the Ga metal target, a plasma ($\sim 500\text{V}$) between the target and substrate was necessary to promote formation of the GaN phase. The ammonia ambient enhanced the nitrogen content in the films compared to vacuum deposition. In general, the GaN target yielded better quality films (smaller rocking curve widths and smoother film morphology) compared to the Ga metal target. These results suggest that pulsed laser deposition is a promising approach to fabricating high quality films of this potentially important semiconducting material.

INTRODUCTION

Gallium nitride is a III-V semiconductor that holds exciting possibilities for wide bandgap applications such as blue light-emitting diodes and lasers [1]. The growth of device quality gallium nitride is, however, challenging for a variety of reasons. The electronic properties are sensitive to impurities as well as the nitrogen content, and epitaxial film growth is hampered by the paucity of lattice-matched substrates.

Pulsed laser deposition, or PLD, has been very successful for fabricating thin films of many materials [2,3] especially multicomponent oxides, such as high temperature superconductors and ferroelectrics. In PLD, a pulsed laser beam is focused into a vacuum chamber onto a target of the material to be grown, producing a dense and energetic plume of material that is ejected into the gas phase. The plume has both kinetic energy (1 - $>100 \text{ eV}$) [4-6] and potential energy in the form of electronic excitation [7-9]. A reactive background gas is often present at low pressures (< 1 torr) that aids in the deposition process.

The ablated jet of material interacts chemically and physically with the reactive ambient prior to condensation on a substrate located a short distance away from the target. Film growth is straightforward because of stoichiometric transfer of material from the target. Furthermore, the energetic properties of the ablated vapor in PLD can lead to oriented film growth at low temperatures even on poorly matched substrates [10].

The goal of this research was to examine the suitability of the PLD deposition process for the growth of oriented gallium nitride. Since low temperature processing is desirable for electronic device fabrication, it was also our intent to explore a variety of processing variables to optimize epitaxial GaN film growth at relatively low substrate temperatures.

EXPERIMENTAL

A schematic of the experimental set-up used for gallium nitride film

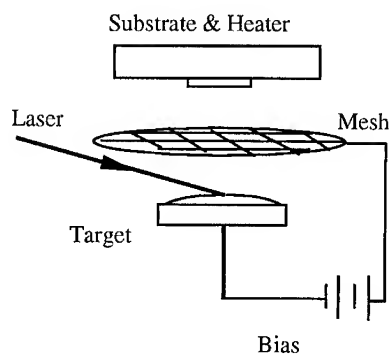


Figure 1. A diagram of the PLD set-up. The laser impinges on the target ($\sim 79^\circ$), producing a vapor plume that deposits on a heated substrate. A plasma was induced between the target and substrate by applying a voltage to an aluminum mesh with a bias supply.

growth is shown in Figure 1. Since this is a novel approach to GaN film fabrication, a detailed description of the deposition process is as follows. The ablation laser was a KrF excimer (248 nm, 30nsec FWHM) that was focused inside a stainless steel vacuum deposition chamber onto the target ($\sim 0.1 \text{ cm}^2$ focal area). Typical pulse energies were 0.13-0.20 J/pulse, yielding a fluence range of 1.3-2.0 J/cm².

The target-substrate distance was $\sim 6 \text{ cm}$ and the base vacuum pressure was $\sim 5 \times 10^{-8}$ torr using a cryopump. The ablation targets were either a GaN pellet or pure Ga metal. The GaN target was pressed from GaN powder (99.0% purity) at 20,000 psi for 5 minutes.

The target was held horizontally in the deposition chamber to accommodate the gallium metal target ($T_m \sim 29^\circ\text{C}$), which normally liquefied upon both handling and laser processing. The metal boule had a nominal diameter of 2.5 cm. The vapor pressure of Ga metal was on the order of 10^{-7} torr at temperatures of $\sim 500^\circ\text{C}$, as estimated from critical vapor pressure data for Ga [11]. The GaN target was rotated (6 rpm) during ablation while the Ga metal target was held stationary. A motivation for trying the Ga metal target was the possibility of greatly reducing the size and density of ejected asperities from a near molten target [12].

Ammonia was used as the background gas (99.9995%) in order to promote nitridation of the gallium vapor using either the GaN or Ga metal target. The reaction of gallium with ammonia to form GaN is a well-known chemical reaction [13], but only occurs appreciably at or above 1000°C . Vapor deposition using other techniques such as CVD [14] with ammonia also seems to require high temperatures. Our approach utilized a low energy plasma above the substrate created both by a physical excitation

from the laser and by externally applying a potential to a wire mesh located between the target and substrate (see Figure 1).

The laser was incident onto the target at an angle of 79° from the target normal. This large incident angle was necessary to accommodate the wire mesh. Applying a potential of +450V to the mesh produced a purple-blue glow that was observed only when the laser fired and then rapidly extinguished until the next laser pulse. The plasma extended from the mesh towards the substrate, implying a high degree of excitation (fragmentation and ionization) of the vapor directly over the substrate.

Although the mismatch is significant ($\sim 14\%$), sapphire substrates were chosen for film growth (both a-, and r-plane). These were $1 \times 1 \text{ cm}^2$ in size, and polished on both sides. No special predeposition conditioning of the substrates was performed. The substrates were attached to the substrate holder via silver paint and were radiatively heated with quartz halogen bulbs. The nominal substrate temperature was monitored by a thermocouple embedded in the holder.

The GaN film growth was explored at several temperatures over the $50\text{--}500^\circ\text{C}$ range and at different ammonia pressures between 0.001 - 10 torr for both target types. Films were typically grown with 10,000 laser shots ($\sim 1 \text{ \AA}/\text{shot}$) for the GaN target and 50,000 shots ($\sim 0.2 \text{ \AA}/\text{shot}$) for the Ga metal target at repetition rates of 10 and 50 Hz, respectively. Film thicknesses were estimated to be $\sim 1 \text{ }\mu\text{m}$. Films were quenched in vacuum and then removed for material characterization using XRD, AFM, and XPS.

RESULTS

Using the Ga metal target, it was found that the gallium vapor did not react appreciably with the ammonia over the $50\text{--}500^\circ\text{C}$ temperature range regardless of the background pressure. The resultant films were typically comprised of metallic gallium. Post deposition annealing in a tube furnace at 800°C for several hours in $\sim 10^5 \text{ Pa}$ of ammonia produced polycrystalline GaN with a mixture of gallium oxides. It was postulated that enhancement of the nitride phase formation would occur by producing a plasma in-situ during film growth. Using the plasma, several films were prepared on sapphire (a- and r-plane) at $\sim 480^\circ\text{C}$. The resultant films were indeed found to be comprised of GaN, as determined by XRD, but had a yellowish tint. It is believed that energetic precursors produced both by ionization and fragmentation of the ammonia molecules and subsequent reaction with the atomic jet of gallium vapor aided the formation of the nitride phase.

Films were grown at two different laser fluences. The laser fluence was also expected to affect the ionic and excited state content of the plume. The XRD patterns of two films prepared using 2.0 and $1.3 \text{ J}/\text{cm}^2$ are shown in Figures 2a and b, respectively. Both films were grown using a +450V plasma in 0.5 torr of NH_3 on sapphire (a-plane) at 480°C . As can be seen in these plots, the films were comprised of $\langle 100 \rangle$ oriented GaN, although

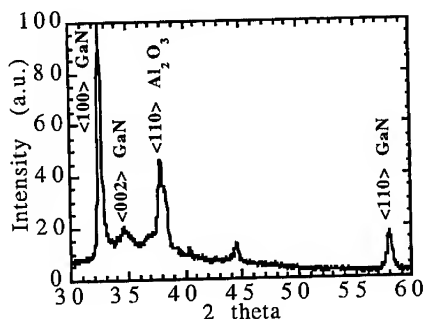


Fig. 2a. XRD plot of a film (with plasma) on sapphire (a-plane) using a Ga metal target, 0.5 torr NH_3 , and 2.0 J/cm^2 .

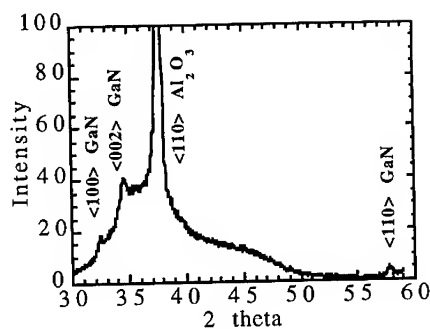


Figure 2b. XRD plot of a film (with plasma) on sapphire (a-plane) using a Ga metal target, 0.5 torr NH_3 and 1.3 J/cm^2 .

some $\langle 110 \rangle$ oriented crystallites were present too. Note that the $\langle 100 \rangle$ peak was very prominent with the higher laser fluence. The $\langle 100 \rangle$ grains were fiber textured (rocking curve FWHM of $\sim 2^\circ$ and $\sim 6\text{--}8^\circ$ for Figures 2a and b, respectively); similar results were obtained on the r-plane of sapphire at 2.0 J/cm^2 : very strong $\langle 100 \rangle$ GaN peak and a weaker $\langle 110 \rangle$ reflection. It is notable that the orientation of the sapphire crystal made little difference in the resultant orientation of the GaN crystallites.

The laser fluence affected the intensity and width of the peaks with the higher laser fluence producing better quality films crystallographically. For example, the broad peak running from $\sim 30\text{--}50^\circ$ in Figure 2b is probably an amorphous reflection, and decreased significantly as the laser fluence increased. The large incident angle precluded the use of even higher laser fluences (limited by the focal spot size), however, the results here imply large laser fluences probably promoted the formation of gas phase precursors needed to form the GaN phase. A higher laser fluence generally produces more ions and excited state species in the ablation plume, and although only speculative at this point, these species are believed to enhance a variety of desirable surface and gas phase processes [7,8].

While the x-ray diffraction analysis showed the presence of the GaN phase, energy dispersive x-ray analysis and XPS measurements of the plasma-enhanced films shown in Figure 2 indicated that they were nitrogen poor ($\sim 30\text{--}35\%$ deficient). Furthermore, using an atomic force and an optical microscope, the surface of the films prepared from the Ga metal target were rough ($\sim 50 \text{ nm rms}$) and contained a large density of droplets that were presumably unreacted gallium metal.

Film growth was then attempted using a fully reacted GaN target. The ablation threshold was lower and the GaN powder was easier to handle than with the Ga metal target. A thorough quantitative chemical analysis of the chemical content of the GaN starting material, however, has not been performed, and its purity is of concern since it will likely affect the resultant electrical properties of the film. In order to compare film growth

using the GaN target with the Ga metal target, similar deposition conditions, including the use of the plasma potential, were examined.

Two XRD patterns of films prepared without (top) and with (bottom) a plasma potential are shown in Figures 3a and b, respectively. Both films showed strong <100> orientation and the rocking curve widths of the <100> peak had a FWHM of $\sim 1^\circ$ and 0.2° for figures 3a and b, respectively. This was about an order of magnitude improvement compared to the films prepared with the pure metal target. Notice also that the plasma had a

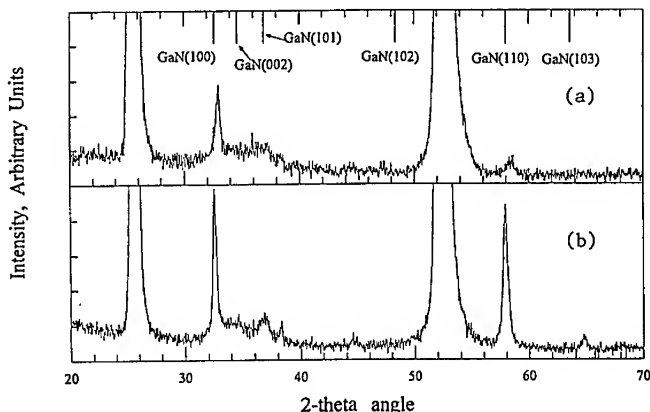


Figure 3. XRD patterns of films processed: (a) without and, (b) with a plasma on a sapphire substrate (r-plane), using a GaN target, 0.5 torr NH_3 , and a fluence of 2.0 J/cm^2 . The reflections at 24.9 and 51.7° are from the substrate.

much less pronounced effect with the GaN target compared to the Ga target, as evidenced by the similarity in the XRD patterns. The presence of the nitrogen atoms (and ions?) from the ablation of the GaN target appears to play an important role in the film growth. The film in Figure 3a still had a slight yellowish tint, while that in 3b was completely clear and transparent to the eye. These films were smoother and had uncharacteristically fewer particulates than the films prepared the gallium metal target.

XPS measurements were also performed on the GaN films produced from the GaN target. For the plasma-enhanced film (see figure 3 for conditions), the Ga $\text{P}_{1/2}$, $3/2$ and the N $2p$ peaks had band edges of 105.6 and 397.6 eV, respectively. It should be noted that the valence band-edge structures were slightly different than the published spectra of Martin et al. [15]. This could be due to the fact that the GaN films were still somewhat nitrogen deficient, even though the plasma promoted nitrogen incorporation. For the plasma-enhanced film, the N/Ga ratio was $\sim 0.47/0.53$, while for the film without the plasma the values were $\sim 0.42/0.58$, respectively. Furthermore, the XPS analysis indicated a significant amount of carbon present ($\sim 15\%$) and was probably an impurity in the target material.

CONCLUSIONS

Oriented gallium nitride films were prepared by pulsed laser deposition. An examination of a several different deposition parameters on film growth was performed, including substrate temperature, ammonia background pressure, ablation target composition, and presence of an externally applied plasma. The kinetic energy of the vapor ejected from the laser ablation process is large ($\sim 1 - >100$ eV), the fragmentation and ionization of the ammonia gas with collisions with the ablated vapor is significant, and the gas phase reaction of these moieties likely leads to energetic precursors that help promote the formation of gallium nitride. Future research will focus upon improving film properties through optimizing deposition conditions, especially the purity of the target material. In addition, we are fabricating epitaxial ZnO with the PLD process and are exploring the potential of these films as lattice-matched substrates for GaN [8]. The results presented herein suggest great promise for the laser deposition approach to GaN film growth.

ACKNOWLEDGMENTS This work was partially supported through the 1995 Discretionary Research Fund program at the University of New Hampshire. The following people are gratefully acknowledged for helpful discussions and for help with data presented herein: J. Krzanowski and T. Gross (Mech. Eng. Dept., UNH) for the XRD and AFM, respectively, and Ursula Gibson (Dept. of Engineering, Dartmouth College, Hanover, NH) for the XPS.

REFERENCES

1. see, e.g., S. Strite and H. Morkoc, *J. Vac. Sci. Technol. B* **10**, 1237 (1992), and the special issue on III-V nitrides in *J. Elect. Mat.* **24** (1995).
2. J. Cheung, H. Sankur, *CRC Crit. Rev. Solid State Mater. Sci.* **15**, 63 (1988).
3. Pulsed Laser Deposition of Thin Films, D. Chrisey and G. Hubler, eds., Wiley, NY, 1994.
4. R.K. Singh and J. Narayan, *Phys. Rev. B* **41**, 8843 (1990).
5. H. Helvajian and R. Welle, *Mat. Res. Soc. Symp. Proc.* **129**, 359 (1989).
6. a. D. Chrisey, J. Horwitz, R.E. Leuchtner, *Thin Solid Films* **206**, 111 (1991); b. R.E. Leuchtner and K. Grabowski, Chap. 24, in ref. [3].
7. R.E. Leuchtner, *Mat. Res. Soc. Symp. Proc.* **354**, 421 (1995).
8. R. Leuchtner, *MRS Symp. B*, "Advanced Laser Processing", Fall 1995.
9. R.P. van Ingen, *J. Appl. Phys.* **79**, 467 (1996), and references therein.
10. Oriented film growth often occurs at temperatures lower than $0.33 T_m$, where T_m is the melting temperature of the bulk material.
11. Handbook of Chemistry and Physics, CRC Press, Boca Raton, FL, 1994.
12. H. Sankur, W.J. Gunning, et al., *J. Appl. Phys.* **65**, 2475 (1989).
13. W. Johnson, J.B. Parsons, and M. Crew, *J. Phys. Chem.* **36**, 2651 (1932).
14. T.A. Kennedy, E.R. Glaser *et al.*, *J. Elect. Mat.* **24**, 219 (1995).
15. G. Martin, S. Strite, A. Botchkarev, et al. *J. Elect. Mat.* **24**, 225 (1995).

Part V
Structural Properties

STRUCTURAL DEFECTS IN HETEROEPITAXIAL AND HOMOEPITAXIAL GaN

ZUZANNA LILIENTAL-WEBER*, S. RUVIMOV*, CH. KISIELOWSKI*, Y. CHEN*,
W. SWIDER, J. WASHBURN*, N. NEWMAN*, A. GASSMANN*, X. LIU*,
L. SCHLOSS*, E.R. WEBER*, I. GRZEGORY**, M. BOCKOWSKI**, J. JUN**,
T. SUSKI**, K. PAKULA**, J. BARANOWSKI**, S. POROWSKI**, H. AMANO*** ,
and I. AKASAKI***

* Materials Science Division, Lawrence Berkeley National Laboratory, Berkeley, CA 94720

**High Pressure Research Center "Unipress" Polish Academy of Sciences, Warsaw, Poland

***Meijo University, Nagoya, Japan

ABSTRACT

The microstructure and characteristic defects of heteroepitaxial GaN films grown on sapphire using molecular beam epitaxy (MBE) and metal-organic-chemical-vapor-deposition (MOCVD) methods and of homoepitaxial GaN grown on bulk substrates are described based on transmission electron microscopy (TEM), x-ray diffraction, and cathodoluminescence (CL) studies. The difference in arrangement of dislocations along grain boundaries and the influence of buffer layers on the quality of epitaxial films is described. The structural quality of GaN epilayers is compared to that of bulk GaN crystals grown from dilute solution of atomic nitrogen in liquid gallium. The full width at half maximum (FWHM) of the x-ray rocking curves for these crystals was in the range of 20-30 arc sec, whereas for the heteroepitaxially grown GaN the FWHM was in the range of 5-20 arc min. Homoepitaxial MBE grown films had FWHMs of about 40 arc sec. The best film quality was obtained for homoepitaxial films grown using MOCVD; these samples were almost free from extended defects. For the bulk GaN crystals a substantial difference in crystal perfection was observed for the opposite sides of the plates shaped normal to the c direction. On one side the surface was almost atomically flat, and the underlying material was free of any extended structural defects, while the other side was rough, with a high density of planar defects. This difference was related to the polarity of the crystal. A large difference in crystal stoichiometry was also observed within different sublayers of the crystals. Based on convergent beam electron diffraction and cathodoluminescence, it is proposed that Ga_N antisite defects are related to the yellow luminescence observed in these crystals.

INTRODUCTION

Gallium nitride has attracted much attention in recent years, due to its wide band gap (3.4 eV) and therefore its possible applications for short-wavelength light-emitting devices [1]. Considerable effort in crystal-growth engineering (MBE, MOCVD) has improved the quality of GaN epitaxial layers to the extent that x-ray rocking curves have improved from a FWHM of 25 arc min to values that are now below 2 arc min [2-5]. Blue-light-emitting diodes could be built based on GaN and GaInN alloys [1]. It has been reported, surprisingly, that, the high emitting efficiency occurred in spite of the high dislocation densities (of the order of 10^{10} cm⁻²) [6]. Further improvement in structural perfection of GaN thin films will depend strongly on the availability of substrate materials having a good lattice match to GaN crystals and a good match in thermal expansion coefficients. Since homoepitaxial growth of GaN is the most natural way to solve this problem, bulk GaN has recently been used as a substrate for thin-film growth [7-8].

In this paper, possible defects in the wurtzite structure will be reviewed; the structural characterization of MBE-grown GaN on sapphire with and without a GaN buffer layer will be

discussed, followed by a discussion of MOCVD-grown GaN on the same substrate with and without an AlN buffer layer. The difference between Si-doped and undoped layers for the later samples will be discussed. For comparison, bulk GaN and homoepitaxial GaN grown by MBE and MOCVD will be described in detail.

GaN-POLYTYPES AND EXTENDED DEFECTS

In general, GaN crystallizes in two polytypes of wurtzite (hexagonal) or zinc-blende (cubic) structure which differ in the stacking sequence of the tetrahedrally bonded Ga-N bilayers. Most epitaxial GaN materials grown on hexagonal substrates (sapphire or SiC) crystallize in the wurtzite structure [9]. Cubic GaN is metastable and can be grown on cubic substrates (e.g. on GaAs) [10]. Both bulk and epitaxial GaN crystals usually contain a high density of structural defects, dislocations, stacking faults (SF), and microtwins.

Crystallography of defects in wurtzite structure GaN is similar to that in hexagonal metals [11] where the close-packed plane is the (0001) basal plane and the close-packed directions are $\langle 11\bar{2}0 \rangle$. The favorable glide system in an ideal closed packed structure ($c/a=1.633$) is $1/3\langle 11\bar{2}0 \rangle$ {0001} with Burgers vector $b=1/3\langle 11\bar{2}0 \rangle$ equal to the shortest lattice vector along a close-packed direction. This is the main slip system observed in GaN, as well. However, other glide planes like the $\{1\bar{1}00\}$ prism plane or $\{1\bar{1}01\}$ although not so favorable in an ideal closed packed structure, are found to be active in GaN. This may explain the limited mobility of threading dislocations lying in those planes in epitaxial GaN. All types of Burgers vectors including $b=1/3\langle 11\bar{2}0 \rangle$, {0001}, and $1/3\langle 11\bar{2}3 \rangle$ typical of perfect dislocations in hexagonal structures have been observed in epitaxial GaN. The strain energy associated with a dislocation is proportional to b^2 and, hence, increases as a^2 , $8/3a^2$ and $11/3a^2$ respectively, in the above sequence of Burgers vectors. The probability of their formation should decrease in the same sequence unless they are formed by dislocation reactions (e.g. $1/3[11\bar{2}0]+[0001]=1/3[11\bar{2}3]$).

SFs are equivalent to local transitions of polytype [12]. In the cubic polytype bonds are rotated 60° with respect to nearest neighbors while in hexagonal GaN the bonds have a mirror symmetry. This leads to difference in symmetry (3C and 2H, respectively), in the atomic environment and, as a result, in physical properties of the cubic and hexagonal polytypes. In the cubic polytype, each GaN bilayer is situated in one of three possible positions assigned as A, B, C with the ideal stacking sequence of ...ABCABC... while in hexagonal GaN a bilayer has only two possible positions, A and B, with the perfect sequence of ...ABABAB... . SFs locally change the bond arrangement and introduce several planes of zinc-blende structure in wurtzite GaN and vice versa. These faults are often terminated by partial dislocations whose Burgers vectors are $b=1/3\langle 1\bar{1}00 \rangle$, $1/2[0001]$ or $1/6\langle \bar{2}203 \rangle$, with strain energy increasing as $1/3a^2$, $2/3a^2$ and a^2 . Analysis of these partial dislocations reveals the nature of the stacking fault.

MBE-GROWN GaN

Two different types of samples grown in home-built MBE chamber were compared. The first was grown with a Kaufman ion source equipped with a tungsten filament for plasma production and a nickel grid for the extraction of ions [13] in order to minimize ion-impact damage and decomposition during film growth. The second was grown using a hollow-anode source to provide activated nitrogen species [14]. The nitrogen source was designed to minimize defect formation from contamination and ion damage. Two samples using these methods of growth are compared. A GaN buffer layer grown at low temperature has been used to grow the first sample, while the second sample was grown without a buffer layer. These two samples differed drastically. The FWHM of the x-ray rocking curve of the first sample grown using the Kaufman source was about 20 arc min, while that of the second sample grown by using the hollow anode source was only 5 arc min. Therefore, it was of interest to compare by TEM the microstructure of these two samples, since it is still not clear which defects in the heteroepitaxial films cause x-ray FWHM broadening, nor is it certain that this nondestructive characterization

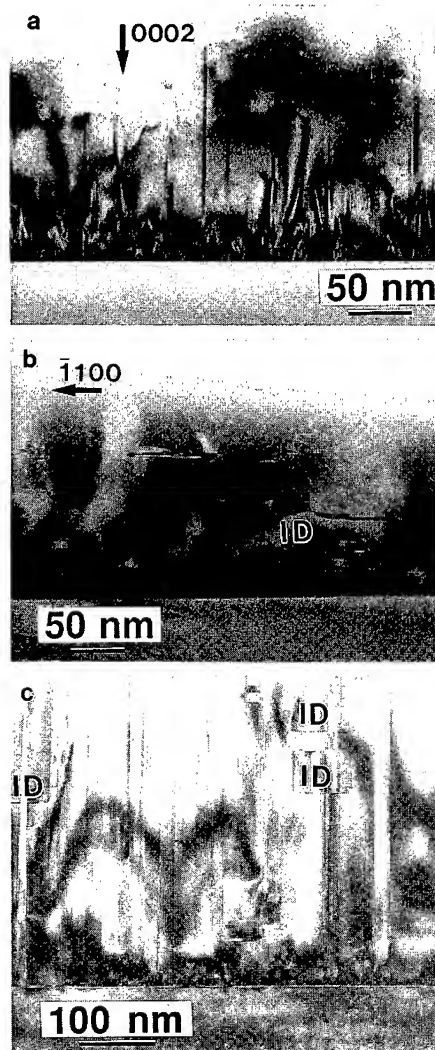


Fig. 1. Cross-section TEM micrographs showing defects in GaN grown by MBE on sapphire: (a) and (b) using a Kaufman source and GaN buffer layer; (a) using [0001] diffraction vector to image defects perpendicular to the growth surface; (b) using $[1\bar{1}00]$ diffraction vector to image defects parallel to the growth surface, (c) using hollow anode source. Note in (c) vertical defects similar as in (a) and inversion domains as in (b).

method provides enough information to qualify material for device fabrication.

TEM studies of both cross-section samples did not show drastic differences (Figs. 1 a, b, c). Both of them had a sharp interface between the sapphire and the GaN layer. Both, misfit and threading dislocations were observed. Two types of planar defects were also visible: one along $(1\bar{1}00)$ GaN planes perpendicular to the growth surface, and the second parallel to the (0001) GaN growth surface. The defects described above are all shown in the micrograph (Figs. 1a, b). When specific diffraction conditions are chosen, only one type of defect is visible. The contrast for the defects perpendicular to the interface disappears for the (0001) diffraction vector. These defects start at the interface and extend through the entire layer thickness as sharp bands (Figs. 1a,c). Their width is of the order of 8-10 nm, and the distance between them is about 20 nm. The apparent width of these defects does not change through the entire layer, except where they interact with other planar defects oriented perpendicularly to them (Fig. 1b). In these places the width of these vertical defects shrinks by one atomic plane. The contrast across the defects differs compared to the surrounding matrix. Based on high resolution micrographs it is not easy to determine the nature of these defects since stacking faults, microtwins, or other special types of grain boundaries formed at surface steps on the substrate/layer interface, or three-dimensional tubes would have similar contrast in cross-sectional micrographs. Only detailed image simulation for each particular defect would bring an answer. Disappearance of contrast for a particular diffraction condition reveals the direction of atomic displacements. Some of these vertical defects could be three-dimensional features that are empty or filled with nonstoichiometric amorphous GaN (very low in N-as suggested by electron energy loss spectroscopy (EELS) studies). It can be seen from plan-view micrographs (Fig. 2a) that stacking faults and microtwins are present in these layers in high densities and they can give the observed contrast in cross-section micrographs. However, there are also many features (pinholes) in plan-view micrographs which appear empty or amorphous that are

distributed randomly in the epilayer (Figs. 2a,b,c). Some of these were located at the intersections of grain boundaries (Fig. 2b). These areas were rather large up to 20 nm having arbitrary shapes. Other amorphous or empty areas were located in the central part of the grains (Figs. 2a,b), very often with a hexagonal faceted shape; their size was in the range of 2 nm. Burgers vector analysis around these empty places located inside the grains showed a central dislocation which had an edge component (Fig. 2c). These defects may be the same type of defects reported earlier [15-16]. However, it was reported that they are formed as empty core screw dislocations. The present results show that the central dislocation also has an edge component. Previous identification was based on atomic force microscopy (AFM) studies [15-16] without TEM Burgers-vector analysis. At this point it is not clear if the defects reported earlier and the ones found in this work are of the same kind. Based on the previous studies [15-16] the "empty core screw dislocations" located at the tops of pyramids which were formed in GaN layers grown by MOCVD. Our defects were found in flat central parts of the grains.

The second type of defect observed in the MBE-grown cross-section samples are parallel to the growth surface (Fig. 1b and marked by arrows Fig. 1c). Their contrast disappears for the diffraction vector parallel to $[10\bar{1}0]$ GaN. These defects were interpreted as either inversion boundaries or stacking faults parallel to the (0001) growth surface, which locally results in fcc stacking order of the crystal. The density of these parallel defects decreases with increasing distance from the substrate.

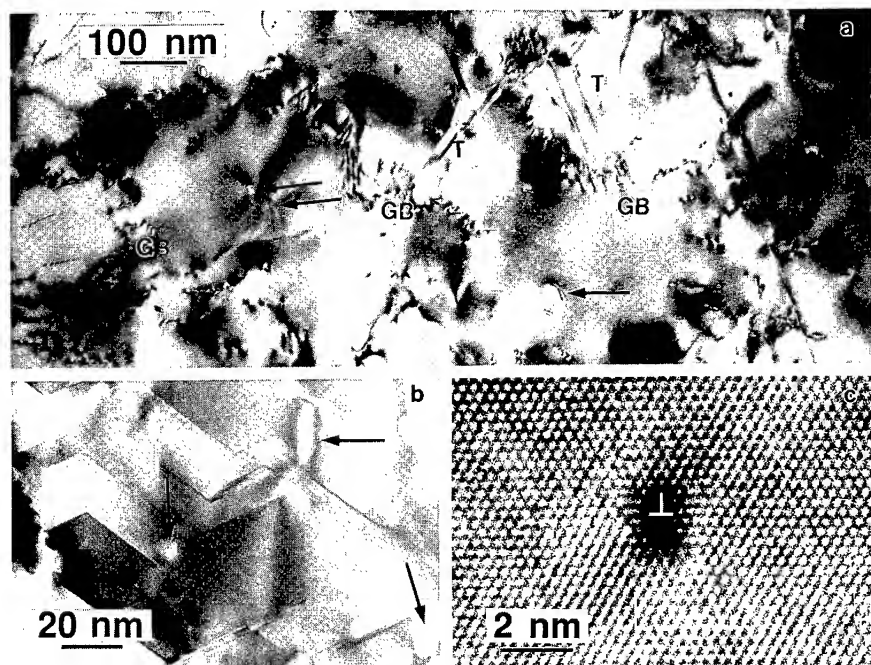


Fig. 2. (a) Plan view micrograph of the layer shown in Figs. 1 a, b. Note small-angle grain boundaries (GB), dislocations and microtwins (T) and open spaces (pinholes) shown by arrows; (b) Plan view micrograph of the layer shown in Figs. 1c. Note twin-like, crystallographically oriented grain boundaries and amorphous looking pinholes similar to these seen in (a); (c) High-resolution image of the small pin-hole with indicated half-plane responsible for the edge-component of the dislocation around which it is formed.

The real difference between these two samples, those grown with the Kaufman source with GaN buffer layer or with the hollow anode source without a buffer layer can be observed in plan-view samples. In the first type of sample, dislocations are mainly arranged on grain boundaries (Fig. 2a), and only a negligible number can be observed within the grain. This sample has a high density of microtwins (see Fig. 2a marked by T) which were seen in cross section as straight vertical lines. The second type of sample has twin-like grain boundaries (Fig. 2b), which can be formed by a simple shift or by 60° rotation plus a shift. These boundaries are arranged crystallographically, with 120° angles between them. The arrangement of dislocations along these boundaries leads to steps along the boundaries. Tilt about an axis in the (0001) plane is not involved between one grain and the surrounding grains; therefore, it is not surprising that the x-ray rocking curve FWHM is much narrower in this sample, compared to the first sample, grown with the Kaufman source.

MOCVD GROWN GaN

A sapphire substrate was used for GaN growth by MOCVD as for the MBE samples. However, in this case (11 $\bar{2}$ 0) Al_2O_3 substrates were used for the growth rather than (0001). Two different samples were studied, one undoped and the other Si-doped. A low-temperature AlN buffer layer was also used to reduce the dislocation density in the GaN layer. X-ray double-crystal diffractometry was used for general characterization of the structural quality of these layers, while TEM techniques were applied for defect investigation. Both plan-view and cross-section specimens were studied by TEM.

Different broadening of the FWHMs (4-7 arc min) of the rocking curves was observed for these two samples, with larger broadening for the undoped compared to the Si-doped sample. Electron diffraction patterns taken from interfacial regions indicated that the GaN grew in the c direction, with the orientation relationship to the Al_2O_3 substrate of (0001)GaN//($11\bar{2}$ 0) Al_2O_3 and [$1\bar{1}$ 00]GaN//[0001] Al_2O_3 . TEM studies of cross-sections of both samples showed a similar defect distribution within the layers. The highest defect density was observed near the interface of the GaN layer and the AlN buffer, but it decreased sharply as the GaN layer thickness reached 0.5 μm . It was interesting to note, that a high density of parallel defects, most probably dislocation loops, was formed in the AlN layer (Fig. 3a). Such defects appeared not to propagate to the sample surface, but they did promote threading dislocation interactions and the formation

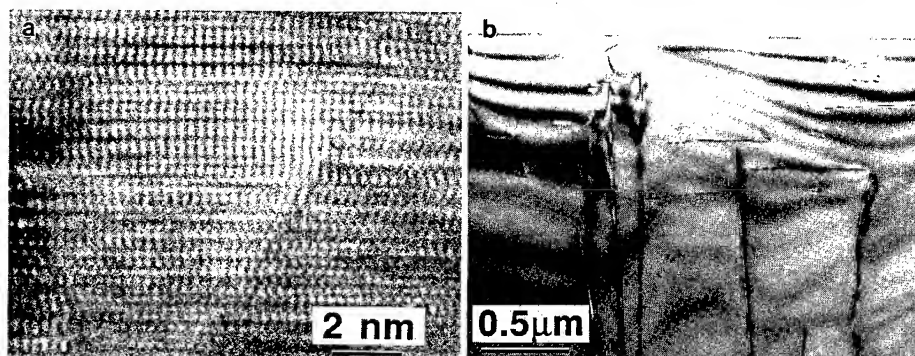


Fig. 3.(a) High resolution image the AlN buffer layer. Note bending of (0001) lattice planes suggesting formation of dislocation loops parallel to the growth surface; (b) TEM micrograph showing cross-section sample of GaN grown by MOCVD close to the sample surface. Note formation of dislocation loops along (0001) basal planes and their interaction with vertical dislocations.

of half-loops near the AlN/GaN interface instead of the straight dislocations, that were observed in the previous samples grown by MBE. Such half loops had mixed Burgers vectors; and, depending on the type of dislocation formed, these half loops remained near the AlN/GaN interface or propagated to the surface. Dislocation loops lying parallel to the sample surface were observed in the upper part of the GaN layer (Fig. 3b). Their appearance in this part of the layer is not understood, however, they were similar to the ones observed in the AlN layer. Whenever threading dislocations interacted with such a loop parallel to the sample surface, they bent and did not simply extend to the surface (Fig. 3b).

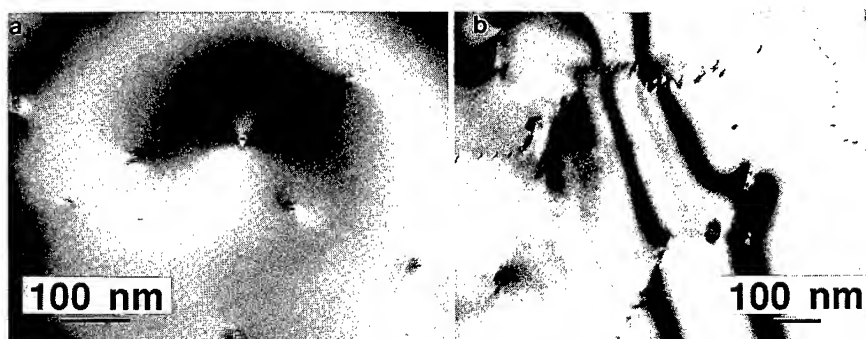


Fig. 4. Plan-view micrographs of the GaN layers grown by MOCVD with AlN buffer layer: (a) with Si doping and (b) without Si doping. Note low-angle grain boundaries formed in (b).

The dislocation density in the layers, estimated from the cross-section samples, was of the same order of magnitude for both samples. However, plan-view images clearly showed the difference in densities of threading dislocations and their distribution for Si-doped and undoped GaN layers. Dislocation densities at the top of the layers were about 5×10^9 and $7 \times 10^8 \text{ cm}^{-2}$ for undoped and Si-doped GaN, respectively. While the dislocations in the Si-doped layer were distributed homogeneously (Fig. 4a), they were arranged in low-angle boundaries in the undoped GaN layer (Fig. 4b). In both cases, threading dislocations near the layer surface were close to the edge orientation. Similarly, as for MBE-grown samples, micro-tubes (pinholes) were observed by AFM and plan-view TEM (Fig. 5). These tubes were associated with dislocations with edge components. Dislocation boundaries in undoped samples divide the layer into grains of 3-5 μm in size; these grains were slightly misoriented with respect each to another. The presence of grains in the undoped GaN layer resulted in a rough surface morphology, in comparison with the rather smooth morphology of the Si-doped layers. In general, misorientation between grains has two components, parallel and perpendicular to the layer surface, depending on the type of

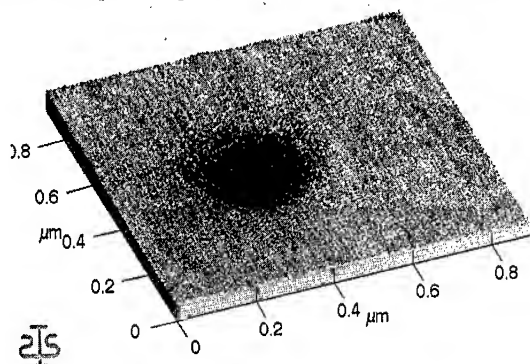


Fig. 5. AFM image of a pinhole formed in MOCVD grown sample.

dislocations at the boundaries. In-plane misorientation is associated with tilt boundaries, while perpendicular misorientation is associated with twist boundaries. A pure twist boundary contains a crossed grid of screw dislocations with Burgers vectors parallel to the dislocation lines. A pure tilt boundary is formed by edge dislocations with Burgers vectors perpendicular to the boundary plane. Dislocations at grain boundaries in our samples were more complex and had both twist and tilt components. The type of dislocation boundaries formed, will influence the broadening of the x-ray rocking curve FWHM.

BULK GaN

The only bulk growth method for GaN crystals reported up to now is growth from a dilute solution of atomic nitrogen in liquid gallium under high nitrogen pressure (up to 20 kbars). Under this pressure GaN crystallizes at temperatures in the range of 1500 to 1800 K, at which the solubility of nitrogen in liquid gallium is about 1% [7-8]. Bulk GaN grown by this technique crystallizes in the form of platelets or rod-shaped crystals. X-ray studies using the (0004) Cu K α reflection from these plate-like crystals show that quality is related to crystal size. The experimental x-ray rocking curve FWHM is about 20-30 arc sec for crystals not larger than 1 mm. For larger crystals (1-3 mm), the rocking curve FWHM is broader, and for crystals from 3 to 10 mm the rocking curve splits [17].

In order to get detailed information on the structural quality of bulk GaN crystals, transmission electron microscopy (TEM) was used. Detailed characterization of this material has been described earlier [18-19]. The small GaN plates of about 1 mm in length were shaped like elongated hexagons and crystallized with the wurtzite structure. The longest axis was along [11 $\bar{2}$ 0]. In all cases the smallest dimension was in the c-axis direction. The ratio of plate length to thickness along the c axis could be as large as 100. This shows that growth in the c axis direction is the slowest. A TEM study of cross-section samples showed that one side of the plate perpendicular to the c axis was almost atomically flat (with fluctuations not larger than 10-15 Å), while the opposite side was rough. In an extreme case, a high density of pyramids was present on the rough side of the plate, with a pyramid height of 100 nm. Planar defects in the form of stacking faults (both low- and high- energy types [11]) were observed close to the rough surface (Fig. 6a). These defects appear to be formed by growth mistakes during crystal growth. They

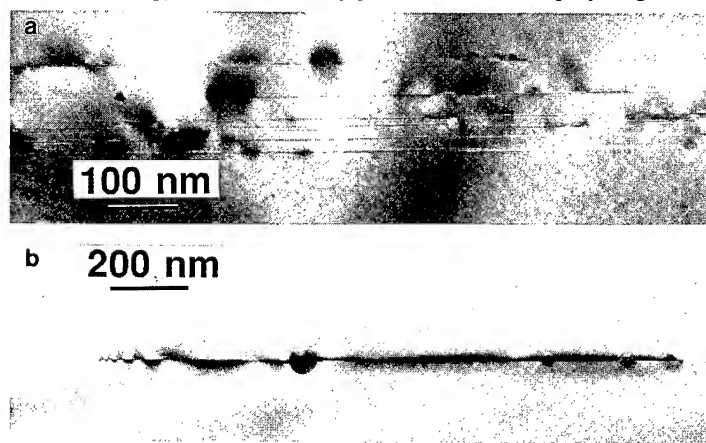


Fig. 6.(a) Stacking faults visible as long lines formed on basal planes and dislocation loops adjacent to them (dark contrast); (b) An example of dislocation loop decorated by Ga precipitates. Note faceting of these precipitates and formation of voids on the side of the precipitate closer to the rough side of the sample perpendicular to c-axis.

were located within 1/10 to 1/4 of the sample thickness nearest to the rough side of the plate. The rougher the sample surface, the more defects were observed. Adjacent to these long individual stacking faults, were dislocation loops separated laterally from each other (Figs. 6 a,b). These loops are additional inserted basal planes parallel to the long stacking faults. The surrounding dislocations acted as a nucleation site for the precipitation of the excess Ga present in this material. These Ga precipitates were faceted (Fig. 6b) and are associated with small voids located closer to the rough side of the crystal [18].

The material near the opposite side of the plates had no extended defects and had an almost atomically flat surface (Fig. 7). This surface would make an ideal substrate for homoepitaxial GaN growth. Such crystals would not need additional polishing. The formation of a rough and flat side of the plate is most likely related to the crystal polarity along the *c* direction (the slowest growth direction). Convergent beam electron diffraction (CBED) was used to determine the arrangement of N and Ga along the *c* direction [20]. It was found that considering the Ga-N pairs along the *c*-axis the Ga atom was closer to the flat surface, while the N atom was closer to the rough surface.

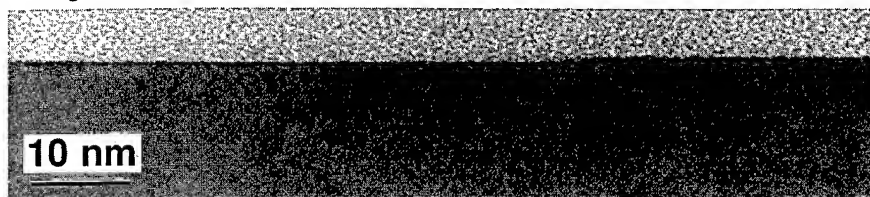


Fig. 7. Cross-section TEM micrograph showing the flat surface and extended defect free GaN sample.

Slightly larger GaN plates showed a weak yellow color upon optical inspection. Cross section samples showed in an optical microscope, that this yellow color was not distributed uniformly, but appeared as small sublayers perpendicular to the *c*-direction, located either in the central part of the crystal or shifted toward the rougher side of the plate. Detailed TEM studies of these yellow areas revealed a high density of dislocation loops parallel to the basal plane, with a diameter of 2-3 nm. They also were decorated by Ga precipitates (Fig. 8). The transparent areas of the crystal, however, were free of extended defects. The formation of these colored sublayers with a different density of planar defects was probably related to variation in crystal stoichiometry as confirmed by CBED studies. The details of these studies are described elsewhere [20]. Based on CBED studies it was concluded that Ga_N antisite defects are present in these bulk samples as a result of the reaction $\text{Ga}_I + \text{V}_N \Rightarrow \text{Ga}_N$, similar to that occurring in GaAs crystals [21]. Theoretical calculations confirmed a high probability for this reaction to occur with a gain of energy of 4 eV [20]. Since these bulk crystals are grown from Ga melt and are strongly n-type [22], supersaturation of Ga_I and V_N is expected to be present in this material. If the precipitation is nucleated the above reaction $\text{Ga}_I + \text{V}_N$ would lead to the formation of V_N(void) + Ga prec.

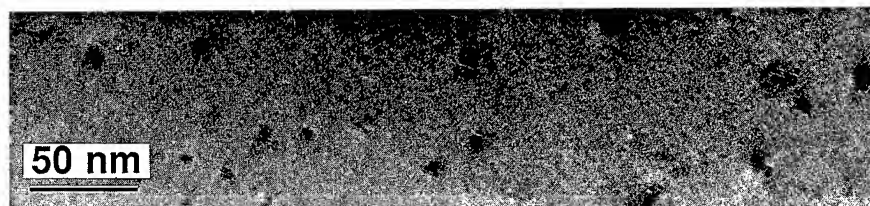


Fig. 8. High density of dislocation loops decorated by Ga precipitates observed in the yellow part of the GaN bulk crystal.

Cathodoluminescence (CL) studies performed on the same crystals showed complementary images obtained using a wavelength of the near-band-edge luminescence and yellow luminescence [19, 20]. Comparing information from TEM (both microstructure and CBED) and CL showed that the yellow luminescence was not only present in defective areas but also can be strong in the perfect parts of the sample [19]. However, the ratio of band-edge luminescence to yellow luminescence depended on the beam position in the sample. There were areas of the sample without any extended defects where the intensity of yellow luminescence was stronger or comparable to band-edge luminescence. Details of these studies will be published elsewhere [20].

MBE GROWN HOMOEPITAXIAL GaN

These GaN layers were grown in a home-built MBE chamber with the hollow anode source used for the heteroepitaxial samples described above. The growth was initiated at 600°C and the substrate temperature was ramped up to 675°C (in ca. 5 minutes). This procedure allowed for a minimal decomposition of the bulk GaN substrate prior to deposition. The films were grown in an 8-hour process, resulting in approximately 0.5- μm -thick layers [23]. The FWHM of the x-ray rocking curve showed 40 arc min, only slightly larger than that obtained from the bulk substrate film. TEM analysis showed dislocations in these layers. A distance of 1-1.5 μm between dislocations allows one to estimate the dislocation density near the surface in the 10^8 - 10^7 cm^{-2} range. This may be compared with 10^{12} - 10^{10} cm^{-2} , typical for heteroepitaxial growth. The homoepitaxial layer exhibits indeed one of the lowest defect densities reported for GaN thin films (Fig. 9 a). However, the dislocation density in the homoepitaxial layer was much higher than in the substrate [17]. In addition, a 50-nm-thick layer with dislocations was found near the interface. The defects found near the interface were attributed to non-optimized surface preparation before the epitaxial growth. As the availability of GaN single crystal substrates in sizes suitable for epitaxial growth was very limited, no specific surface cleaning procedure could be explored in order to avoid degradation of the sample surface. The present results suggest that either the chemical surface cleaning did not remove residual contamination effectively or that during the initial 5 min growth at 600°C, the epilayer was grown with a different stoichiometry than the bulk substrate. Examination of the contrast of TEM micrographs would indeed suggest that the initial layer was grown with different stoichiometry and that three-dimensional growth took place. Coalescence of islands was most likely the source of the threading dislocations. The overgrowth with the main part of the layer at 675°C did not establish a planar surface, but rather an undulated one.

MOCVD-GROWN HOMOEPITAXIAL GaN

Two different samples grown by MOCVD [24] were studied. Prior to growth of the epitaxial GaN layers the bulk GaN substrate was annealed in ammonia at 800°C in order to clean the GaN surface before growth. With the sample still kept in ammonia, the temperature was raised to 1000°C and the trimethylgallium (TMG) valve was opened to start the growth. The sample thickness was in the range of 0.5 μm , similar to the one grown by MBE.

TEM studies in cross section revealed the formation of some inhomogeneities (most probably Ga) at the interface between the bulk substrate and the epilayer, probably formed during substrate annealing (Fig. 9 b). These precipitates were the origin of dislocations, and in some cases stacking faults parallel to the basal plane were formed as well. The distance between the dislocations was on the order of 1-2 μm , leading to a dislocation density in the range of 10^7 - 10^6 cm^{-2} . Since appropriate polarity of the bulk substrate was chosen, and the layer shows an abrupt interface as well as a lack of defects in the substrate below the layer, the substantial dislocation density (comparable to the one obtained by MBE) due to residual impurities, was probably caused by Ga, still present at the interface.

Another sample grown under the same conditions but with a different surface preparation before growth lead to an abrupt interface and a practically defect-free layer. This was the best GaN epilayer grown up to now (Figs. 9 c,d). In the entire layer only one planar defect was observed, located parallel to the basal plane. The interface between the GaN layer and the GaN substrate was atomically flat, and only some minor residual damage (seen in Fig. 9 d with lighter contrast) allowed determination of its location.

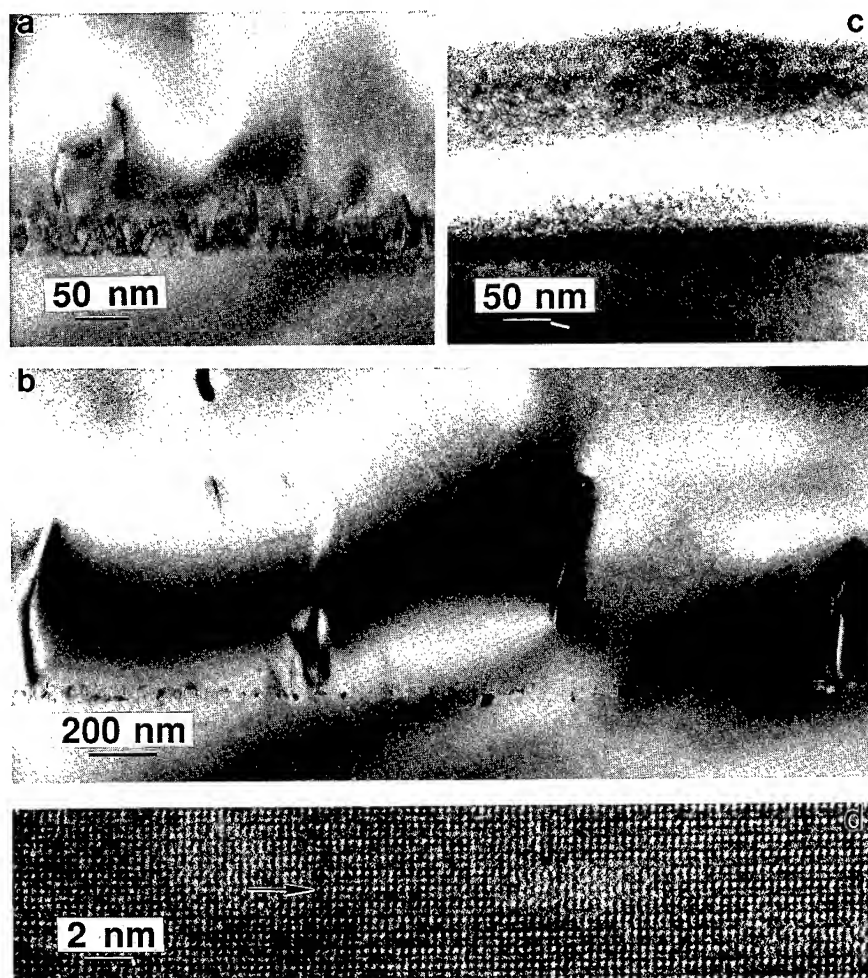


Fig. 9. (a) Cross-section of homoepitaxially grown GaN layers; (a) using MBE-note difference in contrast close to the interface and formation of dislocations; (b) using MOCVD homoepitaxially grown GaN layer-note formation of some inhomogeneities (possibly Ga) at the interface that initiated defect formation; (c) using MOCVD and a special chemical surface cleaning of the bulk GaN substrate before the growth; (d) The interface between the GaN layer and the GaN substrate. Lighter contrast of some residual impurities helped to indicate the location of the interface, since no other defects could be found there.

CONCLUSIONS

In conclusion, it was shown that the best GaN epitaxial layers so far obtained were grown on a bulk GaN substrate. The defects observed in our first grown samples were attributed to the surface preparation before the growth, and when proper procedure was applied almost defect-free layers were obtained using MOCVD growth.

The heteroepitaxial films showed that in spite of different growth techniques (MBE and MOCVD) and different buffer layers, a comparable quality of GaN layers has been observed, but Si-doping in MOCVD-grown layers improves the quality.

Differently shaped tubes (empty or amorphous) are present in both, MBE- and MOCVD-grown GaN. Burgers vector analysis around these empty areas showed a central dislocation had an edge component.

Bulk crystals tend to grow in a plate-like form, with the basal plane parallel to the wide surface. The fastest growth rate was observed along $[11\bar{2}0]$. The two large surfaces (basal planes with slowest growth rate) showed different flatness, which was related to the crystal polarity.

Extended defects present in bulk GaN crystals were primarily stacking faults and dislocation loops, all parallel to the (0001) basal plane. These defects were decorated by Ga precipitates and voids. The presence of these defects suggests the supersaturation of Ga_I and V_N which can lead to the following reactions: $\text{Ga}_I + \text{V}_N \Rightarrow \text{V}_N + \text{Ga prec.}$ or $\text{Ga}_I + \text{V}_N \Rightarrow \text{Ga}_N$. In the areas free of extended defects Ga_N appears to be a dominant defect. The reaction $\text{Ga}_I + \text{V}_N \Rightarrow \text{Ga}_N$ was confirmed by molecular dynamic calculation to be exothermic with an energy gain of 4 eV. This would suggest that Ga_N antisite defects might be related to the yellow luminescence observed in these samples.

ACKNOWLEDGEMENT

This work was supported by the Director, Office of Basic Science, Materials Science Division, U.S. Department of Energy under the Contract No. DE-AC03-76FS00098. N. Newman was supported by the Laboratory Director's Research and Development (LDRD) program of the U.S. Department of Energy under the Contract No. DE-AC03-76FS00098. The use of the facility at the National Center for Electron Microscopy at the Lawrence Berkeley Laboratory is greatly appreciated.

REFERENCES:

1. S. Nakamura, T. Mukai, M. Senoh, Appl. Phys. Lett., **64**, 1687 (1994).
2. M.E. Lin, G. Xue, G.L. Zhou, J.E. Green, and H. Morkoc, Appl. Phys. Lett., **63**, 932 (1993).
3. C. Wang and R.F. Davis, Appl. Phys. Lett. **63**, 990 (1993).
4. N. Newman, J. Ross and M. Rubin, Appl. Phys. Lett. **62**, 1242 (1993).
5. M. Mizuta, S. Fujieta, Y. Matsumoto, and T. Kawamura, Jap. J. Appl. Phys. **25**, L945 (1986).
6. S.D. Lester, F.A. Ponce, M.G. Craford, and D.A. Steigerwald, Appl. Phys. Lett. **66**, 1249 (1995).
7. S. Porowski, I. Grzegory, and J. Jun in "High Pressure Chemical Synthesis" eds. J. Jurczak and B. Baranowski, Elsevier Science Publishers, B.V. (1989) p. 21.

8. S. Porowski and I. Grzegory, in "Properties of Group III Nitrides" ed. James H. Edgar, EMIS Data-reviews Series No. 11 (1994), p. 76.
9. Z. Liliental-Weber, H. Sohn, N. Newman, and J. Washburn, *J. Vac.Sci.Technol. B* **13** (4), 1578 (1995).
10. H. Okumura, *J. Cryst. Growth* **136**, 361 (1994).
11. D. Hull and D.J. Bacon, "Introduction to Dislocations" International Series on Materials Science and technology, vol. 37, Pergamon International Library, Publisher: R. Maxwell, M.C. (1985).
12. X.W. Lin, M. Behar, R. Maltez, W. Swider, Z. Liliental-Weber, and J. Washburn, *Appl. Phys. Lett.*, **67**, 2699 (1995).
13. N. Newman, T.C. Fu, X. Liu, Z. Liliental-Weber, M. Rubin, J.S. Chan, E. Jones, J.T. Ross, I. Tidswell, K.M. Yu, N. Cheung, and E.R. Weber, *Mat. Res. Symp. Proc.* **339**, 483 (1994).
14. E. Jones, N. Newman, A. Gassmann, A. Anders, L. Schloss, X. Liu, J. Chan, Ch. Kisielowski, M. Rubin, E.R. Weber, and N. Cheung-These Proceedings
15. W. Qian, M. Skowronski, K. Doverspike, L.B. Rowland, and D.K. Gaskill, *J. Crystall Growth* **151**, 396 (1995).
16. W. Qian, G.S. Roher, M. Skowronski, K. Doverspike, L.B. Rowland, and D.K. Gaskill, *Appl. Phys. Lett.* **67**, 2284 (1995).
17. M. Leszczynski, T. Suski, P. Perlin, I. Grzegory, M. Bockowski, J. Jun, S. Porowski, and J. Major, *J. Phys. D: Appl. Phys.* **28**, A 149 (1995).
18. Z. Liliental-Weber, C. Kisielowski, Y. Chen and J. Washburn, I. Grzegory, M. Bockowski, J. Jun, and S. Porowski, *Appl. Phys. Lett.*, in press.
19. Z. Liliental-Weber, C. Kisielowski, X. Liu, L. Schloss, J. Washburn, E.R. Weber, I. Grzegory, M. Bockowski, J. Jun, T. Suski, and S. Porowski, *Solid State Electronics*, in press.
20. Z. Liliental-Weber, C. Kisielowski, X. Liu, L. Schloss, J. Washburn, E.R. Weber, I. Grzegory, M. Bockowski, J. Jun, T. Suski, J. Baranowski, S. Porowski, J. Bernholc, and P. Boguslawski-to be published.
21. E.R. Weber, H. Ennen, U. Kaufmann, J. Windscheif, J. Schneider and T. Wosinski, *J. Appl. Phys.* **53**, 6140 (1982).
22. P. Perlin, T. Suski, H. Teisseyre, M. Leszczynski, I. Grzegory, J. Jun, S. Porowski, P. Boguslawski, J. Bernholc, J.C. Chervin, A. Polian, and T.D. Moustakas, *Phys. Rev. Lett.* **75**, 296 (1995).
23. A. Gassmann, T. Suski, Z. Liliental-Weber, N. Newman, H. Helawa, I. Grzegory, M. Bockowski, J. Jun, and S. Porowski, to be published.
24. K. Pakula, A. Wysmolek, K.P. Korona, J.M. Baranowski, R. Stepniewski, I. Grzegory, M. Bockowski, J. Jun, S. Krukowski, M. Wroblewski and S. Porowski, *Proc. of NATO Advanced Research Workshop HEAD 95, Smolenice, Slovakia, (1995)*, in press.

HIGH-PRECISION CHARACTERIZATION OF III-NITRIDE SEMICONDUCTOR ALLOYS WITH SECONDARY ION MASS SPECTROMETRY (SIMS)

J. W. ERICKSON*, Y. GAO*, R. G. WILSON**

*Charles Evans and Associates, 301 Chesapeake Drive, Redwood City, CA 94063

**Hughes Research Lab., 3011 Malibu Canyon Rd., Bldg. 250, M/S RL61, Malibu, CA 90268

ABSTRACT

Samples of representative $\text{Al}_x\text{Ga}_y\text{In}_{1-x-y}\text{N}$ compositions have been studied with secondary ion mass spectrometry (SIMS). First, ionized species of common interest (H, B, C, O, Mg, Si, and Cd) were implanted into the III-nitride samples to provide calibrated standards. Depth profiles and conversion factors for quantification of dopants were then obtained using O_2^+ or Cs^+ bombardment and positive or negative SIMS to measure B^+ and Mg^+ ; H^- , B^- , C^- , O^- , and Si^- ; and CdCs^+ . In addition calibration curves for quantification of stoichiometry were prepared using MCs^+ ions (NCs^+ , AlCs^+ , GaCs^+ , InCs^+) for which the ion yields are relatively independent of the matrix composition; and using atomic, dimer, and trimer ions (Al , Ga , In , Al_2 , Ga_2 , In_2 , Al_3 , Ga_3) which are very sensitive to matrix composition. The empirical calibration curves show small non-linearities. Dopant concentrations can be quantified with great sensitivity (detection limits usually below 1 ppm), accuracy (usually better than 10%), and precision (better than 25%). Matrix stoichiometry can be quantified with an accuracy of about 1-3%.

INTRODUCTION

The III-nitride or AlGaInN material system has recently been the subject of intense research. These wide band-gap semiconductors include the binary compounds AlN, GaN, and InN; the ternaries $\text{Al}_x\text{Ga}_{1-x}\text{N}$, $\text{Al}_x\text{In}_{1-x}\text{N}$, and $\text{Ga}_x\text{In}_{1-x}\text{N}$; and the quaternaries $\text{Al}_x\text{Ga}_y\text{In}_{1-x-y}\text{N}$. The most frequently studied materials are GaN, $\text{Al}_x\text{Ga}_{1-x}\text{N}$, and $\text{Ga}_x\text{In}_{1-x}\text{N}$, in roughly that order and the most popular growth method tends to be metallorganic chemical vapor deposition (MOCVD) on sapphire substrates. Once a new semiconductor can be grown successfully and economically, attention turns to developing new functions and structures. This process has been accelerated for the III-nitrides, due to the commercial momentum of a successful III-V industry accustomed to using diverse compounds such as GaAs, InP, AlGaAs, and AlGaInP.

How can III-nitride crystal growers check whether their samples and heterostructures have the desired dopants and stoichiometry? Secondary ion mass spectrometry (SIMS) is successfully used for this purpose in other III-V materials, with great sensitivity and excellent depth resolution. Unlike electrical measurements, SIMS detects dopants regardless of their site in the semiconductor lattice. Reliable calibration standards have previously been developed for the analogous AlGaInAs [1,2] and AlGaInP [2] systems. The fundamental purpose of this work has been to provide accurate, precise, and reliable quantification of dopant levels and matrix stoichiometries within the AlGaInN alloy system.

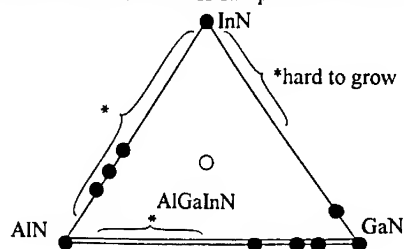
EXPERIMENTAL

Depth profiles were obtained with CAMECA 3f and 4f IMS instruments using 8 keV primary O_2^+ ions with positive SIMS, 5.5 keV primary Cs^+ ions with positive SIMS, or 14.5 keV primary Cs^+ ions with negative SIMS. The primary beam was rastered over a square region 100-125 microns on a side, and the positive or negative secondary ions were collected from a circular

image area 30 microns in diameter, centered in the rastered region. The sputter rates were obtained by measuring the analytical crater depths with a Tencor P10 stylus profilometer.

Samples of GaN, AlN, InN, AlGaInN, GaInN, AlInN, and AlGaInN (Figure 1) were obtained from various sources and the impurity levels in each were estimated using SIMS: ion yield systematics permitted inference of concentrations to within a factor of five based on analogies with quantification in GaAs. The III-nitride samples (except for those of AlGaInN) and a silicon witness sample were then implanted with known doses of ^1H , ^{12}C , ^{16}O , ^{24}Mg , ^{28}Si , and ^{112}Cd . The doses were adjusted to provide implant peaks well above the impurity concentrations, which in several cases were close to 1%. The purpose of the silicon witness sample was to provide an independent means of checking the nominal implant doses against archival data, since SIMS quantification is best understood for silicon (the only NIST standard reference material for SIMS is an implant of B into silicon). The doses in the Si witness sample were checked with SIMS.

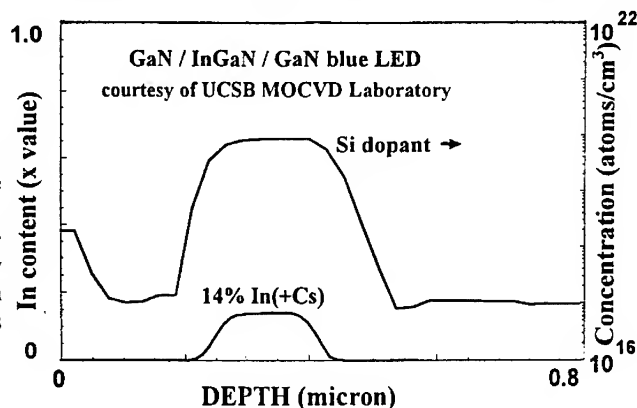
Figure 1. The AlGaInN alloy system, showing the various compositions of the samples used in this work.



RESULTS AND DISCUSSION

The experimental results provide an intriguing picture of how the ion formation mechanisms change with composition in the AlGaInN system. The relative sensitivity factors (RSFs) used in quantification typically are measured with respect to various atomic or molecular matrix ions such as Al^+ , Ga^+ , In^+ , AlIn^+ , NGa^+ , or NIn^+ . Since multiple measurements were made under a range of different instrumental conditions in many cases, relative standard deviations in the RSFs can be estimated. The statistics suggest that calibration with respect to the matrix ion NGa^+ is preferable to the use of Ga^+ in negative SIMS, since the Ga^+ intensity is more sensitive to the instrumental tuning conditions and produces a wider range of RSFs. Similar considerations were used to choose the best matrix ions under the other SIMS analysis conditions. Figure 2 shows how SIMS data can be calibrated with photoluminescence (PL), using a light-emitting diode structure of GaN/InGaN/GaN.

Figure 2. A blue LED GaN/InGaN/GaN structure with high quantum efficiency, grown at the UCSB MOCVD lab. With good crystal quality and a thin active layer, such structures may be precursors to reliable blue laser diodes.



Complications exist for such calibration--the nominal wavelength of the InGa_N layer is not only related to the In content, but also to the dopant concentration. High levels of Zn dopant can shift the wavelength from the 400 nm expected for In_{0.14}Ga_{0.86}N to 440 nm. But, complications aside, SIMS clearly can be calibrated against PL. If the PL results do indeed give the In concentration reliably within 0.1% or so, then the SIMS data is limited chiefly by the measurement precision, which can reach about 0.5%.

The converse relationship is also useful. The SIMS technique plays a role in calibrating the qualitative models used to interpret optical data, since optical methods provide a relatively cheap and non-destructive analytical technique for testing epiwafers and epilayers on production lines.

Figures 3A-C illustrate the trend in ion yields with matrix composition for the implanted elements. (Since RSFs vary considerably between SIMS instruments, the trends are illustrated rather than giving the precise values measured in CAMECA instruments.) These horizontal axes represent chords or cross-sections along the edges of the AlGaInN alloy diagram. Variations in Al content have tended to exert a larger effect on ion yields than variations in Ga or In content, for the AlGaInP and AlGaInAs systems [1,2]. This is attributed to the relative size, electronegativity, and polarizability of the Al cation compared to the Ga and In cations.

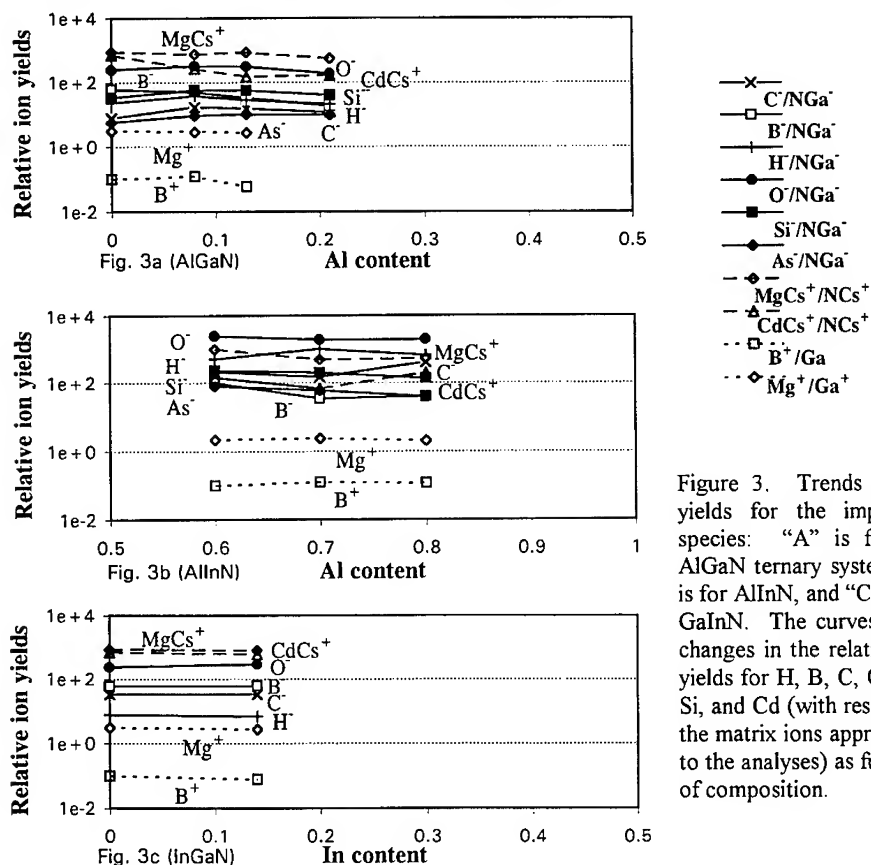


Figure 3. Trends in ion yields for the implanted species: "A" is for the AlGaIn ternary system, "B" is for AlInN, and "C" is for GaInN. The curves show changes in the relative ion yields for H, B, C, O, Mg, Si, and Cd (with respect to the matrix ions appropriate to the analyses) as function of composition.

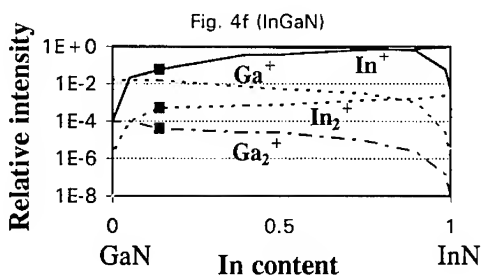
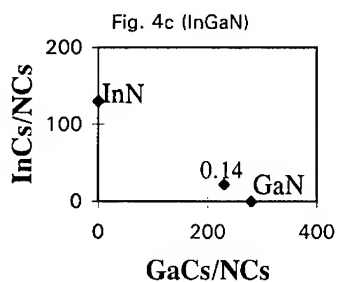
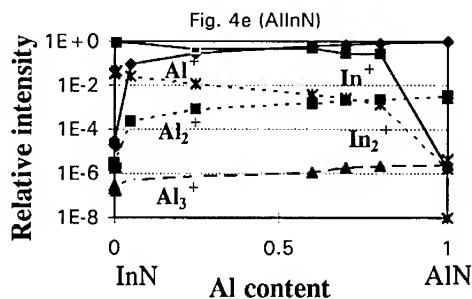
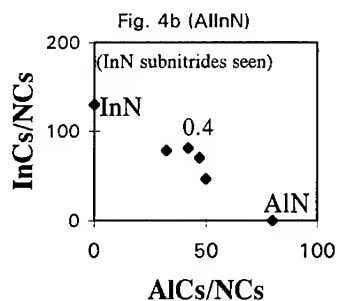
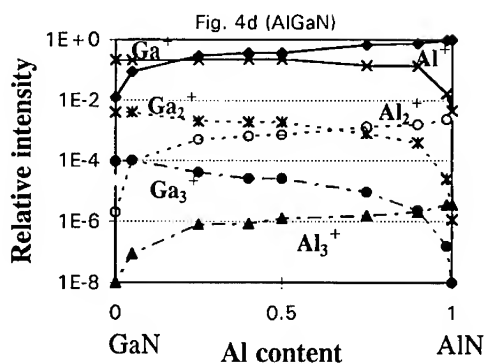
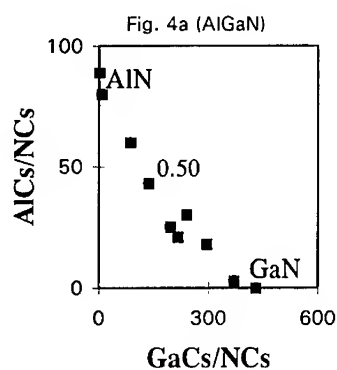


Figure 4. Trends in ion yields are depicted for the matrix ion species. "A" and "D" are for the AlGa_{0.5}N ternary system, "B" and "E" are for AlIn_{0.4}N, while "C" and "F" are for GaIn_{0.14}N. The curves in A, B, and C are for *linear* interpolation of stoichiometry from standards using MC⁺ secondary ions where M is a matrix ion N, Al, Ga, or In. The curves in D, E, and F are for *multivariate* interpolation of stoichiometry from standards using Al⁺, Ga⁺, In⁺; Al₂⁺, Ga₂⁺, In₂⁺; Al₃⁺, and Ga₃⁺ secondary ions.

Figures 4A-C show the trends with changing composition for ion yields of the matrix species AlCs^+ , GaCs^+ , InCs^+ , and NCs^+ . The molecular MCs^+ secondary ions, where M is the matrix element of interest, are often used to determine the stoichiometry of III-V compounds. Secondary MCs^+ ions are formed just outside the sample surface, by combining with neutral M atoms ejected from the sample under cesium bombardment. This formation mechanism reduces matrix-dependent effects on ion yields, which in general are non-linear and somewhat unpredictable variations due to the particular chemical and physical characteristics of a given matrix. Only a moderate matrix effect remains in the ternary III-Vs, due to changes in the character of chemical bonding or local electronic structure with matrix composition.

Figures 4D-F show the trend in ion yields with composition, this time for dimer and trimer ions such as Al_2 , Ga_2 , In_2 , Al_3 , and Ga_3 . The results are quite analogous to data obtained in AlGaAs [4]. Such dimer and trimer ions provide a means for very precise multivariate interpolation of stoichiometry with SIMS.

Three important observations can be made at this point. First, the InN sample may actually be a sub-nitride. The $\text{InCs}^+/\text{NCs}^+$ ratios have been measured in four different InN samples, and vary more than 10-fold: in contrast the NCs^+ intensity is relatively constant in all the GaN , AlN , AlGaIn , and AlInN measured so far. The value measured in the implanted sample used in this work is somewhat high, which suggests that the indium may not have been fully nitrided. Second, some heterogeneity was observed within the AlInN samples both laterally and as a function of depth. Generally the lateral heterogeneity can be attributed to pinhole defects, and the compositional variation with depth amounts to only about 5% on average. Third, neither the AlN nor the InN samples were sufficiently clean to permit useful SIMS measurements, even with very high implant doses achieving peak concentrations of around 1% for H, C, and O.

The use of SIMS in III-nitride crystal growth.

While these trends may seem interesting, what use are they in nitride crystal growth? First, the trends provide the means for producing more accurate SIMS data, which should be of use in for research, development, and production line purposes:

- A. The implant standards permit quantification in corresponding nitride compositions.
- B. The trends within the AlGaInN system provide a basis for accurate inferences, interpolation, and extrapolation to compositions not represented among the standards.
- C. The ion yield systematics of this small set of implanted elements allow one to infer conversion factors for many other elements (with an accuracy of a factor of two). The actual measured isotopic RSFs in GaN were 1.15×10^2 for $\text{MgCs}^+/\text{NCs}^+$, 1.45×10^2 for $\text{CdCs}^+/\text{NCs}^+$; 1.3×10^2 for H^+/NGa^- , 1.7×10^1 for B^+/NGa^- , 4.4×10^1 for C^+/NGa^- , 4.2×10^2 for O^+/NGa^- , 3×10^1 for Si^+/NGa^- , 1.8×10^2 for As^+/NGa^- ; 1×10^4 for B^+/Ga^+ , and 3.3×10^2 for Mg^+/Ga^+ . While the absolute RSFs will vary from instrument to instrument, the trends should persist.

Second, impurity levels can be more accurately measured to evaluate progress in the cleanliness of different growth methods [3]. The routine SIMS detection limits for most species of interest in GaN (for example Li, Be, B, C, Na, Mg, Al, Si, S, Cl, K, Ca, Ti, Fe, Ni, Zn, Cu, Se, Zr, Cd, In, Sn, Sb, and Te) are below 1 ppm during standard depth profiles, while a few others are higher but still below 10 ppm (H, O, Cr, Mn, Mo). In bulk analysis the detection limits can be lowered by another factor of ten, and with further optimization of the analytical conditions most of the detection limits can be lowered somewhat further. While GaN and AlGaIn crystal growth already seems relatively clean, considerable work remains before comparable levels of purity are achieved for AlN , AlInN , and InN [3]. Third, the results can provide some insight into the chemical nature of the III-nitride material itself or the detailed physical structure of epilayers:

- D. Some information about the bond ionicity in the materials is present in the flux of secondary ions. For example, the Al-N and Ga-N bond ionicities appear to differ with consequences for the NCs^- ion yield, based on the non-linearity of the curve in Figure 4A. Moreover, since the corresponding diagram for AlGaAs has a more linear curve, the Al-As and Ga-As bond ionicities in AlGaAs seem more similar [4], than do the Al-N and Ga-N ionicities in AlGa_{0.9}N. Likewise the trend for electropositive B to form more negative ions and electronegative As to form fewer negative ions, with increasing Al content in AlGa_{0.9}N, suggests that the local electronic structure is changing.
- E. Information about local composition is also present in the secondary ion flux. For example if a III-nitride material is heterogeneous, with a nominal composition of $\text{Al}_{0.1}\text{Ga}_{0.9}\text{N}$ but actually made up of separate microscopic regions containing pure AlN and pure GaN, then the intensities of the Al and Ga dimer and trimer ions will be significantly higher than the values seen in Figure 4D-4F.
- F. The dimers and trimers also can be used to study a kind of interfacial defect, in which the interface is atomically abrupt but contains some topographical roughness. This could be of use, for example in checking epilayer flatness in heterostructure laser diodes.

In particular it is worth noting that several InN samples measured had unusually high $\text{InCs}^+/\text{NCs}^+$ ratios (or low NCs^+ intensities), suggesting that these matrices were not fully nitrated. Fourth, SIMS analyses complement many non-destructive optical techniques. Photoluminescence (PL) and x-ray information can be correlated with SIMS results to better understand a particular sample. This is important for the nitrides, since dopant levels alter the PL wavelength and can (by means of strain) alter the lattice constant. Thus fundamental characterization provided by SIMS may help calibrate various other cost-effective, non-destructive methods of monitoring III-nitride quality.

SUMMARY AND CONCLUSIONS

The ion yields of dopant species and matrix elements for the III-nitride or AlGaInN semiconductor system have been characterized with SIMS, making possible more accurate and precise measurements for these compounds. In addition, several minor systematic trends in ion yields have been identified.

ACKNOWLEDGMENTS

We thank Joan Redwing at Advanced Technology Materials Incorporated, Professor S. J. Pearton at the University of Florida, and Professor S. DenBaars at the MOCVD Laboratory of the University of California at Santa Barbara for III-nitride samples.

REFERENCES

1. S. W. Novak and R. G. Wilson, in SIMS VI Proceedings, edited by A. Benninghoven et al, John Wiley & Sons, New York, 1988, p. 303.
2. S. P. Smith, in SIMS IX Proceedings, edited by A. Benninghoven et al, John Wiley & Sons, New York, 1994, p. 227.
3. J. W. Erickson, R. G. Wilson, and J. Redwing, in preparation.
4. J. W. Erickson and S. P. Smith, in preparation.

PHOTOLUMINESCENCE AND SIMS STUDIES OF HYDROGEN PASSIVATION OF Mg-DOPED P-TYPE GALLIUM NITRIDE

*Y. Li^a, Y. Lu^a, H. Shen^b, M. Wraback^b, C.-Y. Hwang^c, M. Schurman^c, W. Mayo^c, T. Salagaj^d,
R. A. Stall^d.

a) ECE Dept., Rutgers University, Piscataway, New Jersey 08855-0909

b) Army Research Laboratory at Fort Monmouth, New Jersey 07703-5601

c) Department of Ceramics, Rutgers University, Piscataway, New Jersey 08855-0909

d) Emcore Corporation, Somerset, New Jersey 08873

* Present address: Emcore Corp., 394 Elizabeth Ave., Somerset, New Jersey 08873

ABSTRACT

The effects of hydrogen passivation in MOCVD grown Mg doped p-type GaN were studied using low temperature (5K) photoluminescence (PL) and secondary-ion-mass spectroscopy (SIMS). GaN films with different Mg doping level were annealed at 700°C in N₂ ambient with different annealing times. The SIMS results indicate that the hydrogen concentration increases with increasing Mg doping level in the as-grown Mg:GaN film. After 20 minutes of annealing, most of the hydrogen escapes from the film. The 3.455 eV PL peak before annealing and the 3.446 eV peak after annealing found in the Mg doped samples were attributed to the exciton bound to the Mg-H complex and to the Mg acceptor, respectively. The shift of the bound exciton peak to higher energy (3.465 eV) in the lightly doped sample is due to an effective n-type compensation associated with an annealing-induced increase in the nitrogen vacancies. In heavily doped Mg:GaN, the decreases in the integrated PL intensity after 700°C annealing may be associated with the hydrogen depassivation of nonradiative recombination centers in the film. The increase of PL intensity in the lightly doped sample after annealing is attributed to the reduction of defects by the annealing process.

INTRODUCTION

Wide bandgap group III nitrides are strong candidates for blue light-emitting diodes (LED) and lasers intended for high density optical storage and display technologies[1]. In order to realize these applications, it is necessary that doping control in both n and p-type materials be achieved. The undoped nitrides usually exhibit n-type conductivity, and it is very difficult to achieve a high level of p-type doping in MOCVD grown GaN. Recently, p-type GaN has been obtained by a low-energy electron beam irradiation (LEEBI) or postgrowth annealing process in Mg doped MOCVD grown GaN[2,3]. The LEEBI and postannealing processes are necessary for the MOCVD grown GaN because hydrogen incorporation in films during the MOCVD growth leads to the formation of an electrically inactive Mg-H complex with the acceptor passivated by hydrogen. The LEEBI and postannealing treatments dissociate Mg-H complexes and electrically activate the magnesium acceptors.

Hydrogen passivation in II-VI and III-V semiconductors has been studied by many techniques[5-8]. It was found that the hydrogen not only passivates shallow donors and acceptors, but also deep-level nonradiative recombination centers in many semiconductors. For example, in Mg doped p-type InP, S. Balasubramanian et al.[6] observed an order of magnitude improvements in PL intensity following hydrogen passivation. This increase of PL intensity was

attributed to the hydrogen passivation of nonradiative recombination centers. In GaP, Weber and Singh[7] reported the observation of hydrogen passivation of nonradiative center as well as the deactivation of donors and acceptors. In addition, there are several reports on the hydrogen passivation of Mg doped GaN[3,9-11]. S. Nakamura et al.[3] observed that the resistivity of Mg doped MOCVD grown GaN film decreases while the room temperature PL intensity increases when the film is thermally annealed in N₂ atmosphere at temperatures above 600°C. In MBE grown GaN samples, M. Brandt et al.[9] studied the effects of hydrogen incorporation on Si donors and Mg acceptors. They observed that the remote-plasma deuteration of Mg doped p-type GaN at 600°C reduces the room temperature hole concentration by a factor of ten, while the deuteration of Si doped n-type GaN under the same conditions will not change the electron concentration. They also studied the heavily Mg doped MBE grown GaN by Raman spectroscopy and IR absorption[10]. Local vibrational modes (LVM) at 2168 and 2219 cm⁻¹ were found in these films and assigned to the Mg-H complexes. Very recently, W. Gotz et al[11] studied the effects of deliberate hydrogenation of GaN grown by MOCVD. The Mg-H complex formation in Mg doped p-type GaN was confirmed by the temperature dependence of the Hall measurements. In this work, we use photoluminescence (PL) correlated with secondary ion mass spectroscopy (SIMS) to study the effects of hydrogen passivation on the spectral positions and relative strengths of radiative transitions in both lightly and heavily Mg-doped GaN grown by MOCVD.

EXPERIMENTAL

The GaN samples used in this work were grown on Al₂O₃ substrates oriented in the [0001] direction by metalorganic chemical vapor deposition (MOCVD) in the EMCORE multi-wafer rotating disk reactor. An initial low-temperature GaN buffer layer of about 200Å thickness was deposited at 530°C before the growth of GaN epilayer at 1040°C. Details of the growth process were reported elsewhere[12]. The resulting GaN epitaxial layer has the wurtzite crystal structure. Three GaN samples, identified as A, B, C were used in this study. Sample A is unintentionally doped GaN, however shows n-type, while B and C are Mg doped with B being lightly doped and C more heavily doped. The epitaxial layer thickness of all samples was about 2 μm. The PL was excited at 5K with a N₂ laser, and was detected with photomultiplier (PMT) and lock-in amplifier electronics. The Mg and H depth profiles were performed on a Physical Electronics 6300 secondary ion mass spectrometer.

RESULTS AND DISCUSSIONS

The typical distribution of H and Mg in the heavily Mg-doped sample C is shown in Fig.1. Magnesium was found to be uniformly distributed through the film at approximately 6x10¹⁹/cm³ while the hydrogen concentration decreased slowly through the film thickness. After annealing for 20 minutes at 700°C in N₂ ambient, the hydrogen concentration dropped from a maximum concentration of 2x10¹⁸/cm³ to a uniform 2.5x10¹⁷/cm³.

All of the as-grown Mg-doped samples were insulators. But after the 700°C anneal, the heavily doped sample C became a p-type with a room temperature hole concentration of 2x10¹⁷/cm³ and mobility was about 10 cm²v⁻¹s⁻¹; however, the sample B which was less heavily doped with Mg concentration of 3x10¹⁹/cm³ still exhibited high resistivity.

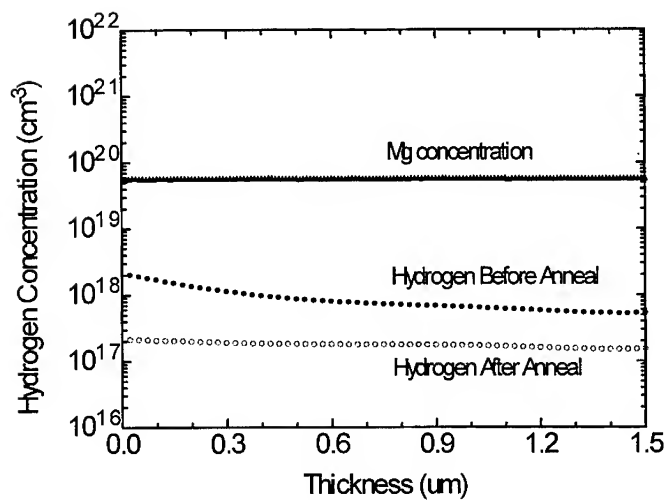


Fig.1. Magnesium and Hydrogen profiles in the heavily doped Mg:GaN. The annealing was performed at 700°C in N₂ ambient for 20 minutes.

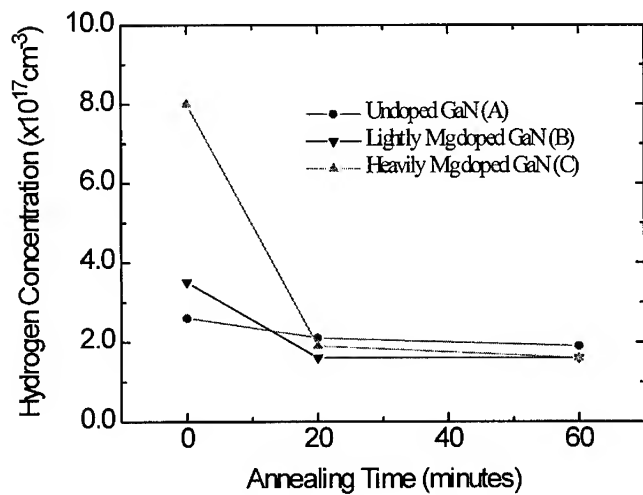


Fig.2. Annealing time dependence of hydrogen concentration in samples A, B, C. The annealing was performed at 700°C in N₂ ambient.

Fig.2 shows the dependence of the maximum hydrogen concentration for the three Mg doping levels as a function of annealing time at 700°C. In the undoped GaN, the hydrogen concentration near the surface is low ($2.5 \times 10^{17}/\text{cm}^3$). As the Mg doping levels increase, the amount of hydrogen incorporated into the film increase. However, for all three samples, a 20 minute anneal is sufficient to remove most of the hydrogen. Even longer anneals (60 minutes) cause the hydrogen concentration to drop below the SIMS detection limit ($\sim 1.5 \times 10^{17} \text{ cm}^{-3}$).

Since the incorporation of hydrogen into the film is linked to the Mg doping level, we believe that Mg-H complexes are being formed. This is consistent with the work reported in [13]. Recently, Neugebauer et al[14] indicated that hydrogen exists in its singly positive charge state (H^+) in p-type GaN and in a negative charge state (H^-) in n-type GaN. The total energy calculation indicates that the diffusion barriers for hydrogen in p-type and n-type GaN are 0.7 eV and 3.4 eV, respectively. Thus, in n-type GaN, the 3.4 eV barrier energy is so high that it is very difficult for hydrogen to incorporate into the film during growth, which is supported by our experimental results of a low hydrogen concentration in unintentionally doped GaN films. However, for p-type film, the barrier energy for H^+ is only 0.7 eV, and it is expected that considerable H^+ diffusion occurs in the film during the film growth or the 700°C annealing.

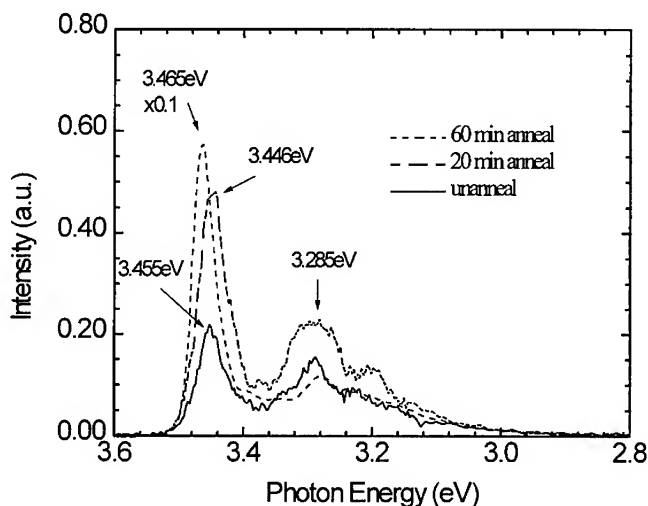


Fig.3. 5K PL spectra of lightly Mg doped GaN (sample B) for 0, 20 and 60 minutes annealing at 700°C in N_2 ambient. The spectra for the 60 minutes annealing was reduced by a factor of 10.

The photoluminescence data were used to characterize the as-grown and annealed samples. Shown in Fig. 3 and 4 are the low temperature (5K) PL spectra for the p-type samples B and C. For both samples, two major peaks were found in the near bandgap region before annealing. The one at 3.285 eV has been identified as the free-to-bound (Mg) transition corresponding to a bounding energy for Mg of 155 meV[15]. The other at 3.455 eV has

previously been attributed to a transition involving exciton bound to Mg [15,16]. After 20 minutes annealing this bonded exciton peak shifts 9 meV to 3.446 eV. We attribute the 3.455 eV

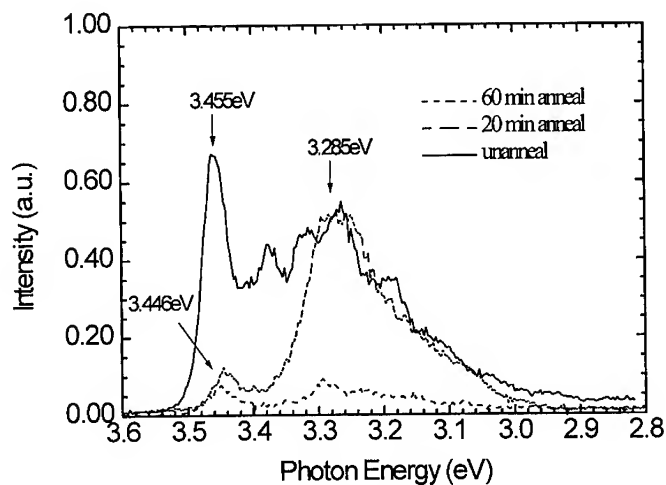


Fig. 4. 5K PL spectra of heavily doped GaN (sample C) for 0, 20 and 60 minutes annealing at 700°C in N₂ ambient.

peak to a transition related to exciton bound to Mg-H complex and the 3.446 eV peak to a transition associated to exciton bound to Mg acceptor. This is supported by the SIMS results which indicate the removal of hydrogen after 20 minutes annealing. After 60 minutes annealing, the excitonic feature in the lightly doped sample shifts to 3.465 eV, while no further shift is observed in the heavily doped sample. This feature has previously been identified as a transition involving an exciton bound to a nitrogen vacancy[16]. Since nitrogen has a high vapor pressure at 700°C, it may diffuse out of the film, resulting in vacancies[3]. Our measurements indicates an effective n-type compensation associated with annealing in lightly doped samples.

The heavily and lightly doped samples possess different dependence of the PL intensity on annealing. For the heavily doped sample, the integrated PL intensity decreases, while for the lightly doped sample, it increases. This behavior suggests that there are significantly more nonradiative recombination centers associated with deep level defects in the heavily doped sample than in its lightly doped counterpart. Removal of hydrogen during annealing activates the nonradiative recombination centers resulting in a decrease of PL intensity in the heavily doped sample. The increase of PL intensity by as much as 40 times in the lightly doped sample implies that the total amount of defect/nonradiative recombination centers in the lightly doped sample is so low that annealing can effectively eliminate them, resulting in an increase in PL intensity.

SUMMARY

In conclusion, low temperature PL and SIMS were used to study hydrogen passivation in Mg doped p-type GaN grown by MOCVD. The SIMS results indicate that the hydrogen incorporation in the Mg:GaN film increases with the increase in Mg doping concentration in the film. Twenty minutes annealing at 700°C in N₂ ambient is sufficient to release the hydrogen from the film. The 3.455 eV PL peak found in the as-grown Mg:GaN samples is attributed to exciton bound to Mg-H complex transition. In the annealed samples, the exciton bound to Mg transition peak was shifted to 3.446 eV and the peak was attributed to the exciton bound to Mg acceptor. Depending on the Mg doping level, the variation of PL intensity due to annealing can be well explained by the hydrogen passivation mechanism or thermal annealing effects. Our experimental results indicate that hydrogen not only passivates the Mg acceptor but also passivates the nonradiative recombination centers.

REFERENCES

1. H. Morkoc, S. Strite, G. B. Gao, M. E. Lin, B. Sverdlov, and M. Burns, *J. Appl. Phys.* **76**, 1363, and references therein.
2. H. Amano, M. Kito, K. Hiramatsu, I. Akasaki, *Jpn. J. Appl. Phys.* **28**, L2112 (1989).
3. S. Nakamura, T. Mukai, M. Senoh, N. Iwasa, *Jpn. J. Appl. Phys.*, **31**, L139 (1992).
4. T. D. Moustakas, R. J. Molnar, *Mater. Res. Soc. Conf. Proc.* **281**, 753 (1993).
5. *Hydrogen in Semiconductors*, edited by J. Pankove and N. Johnson (Academic, San Diego, 1991), and references therein.
6. S. Balasubramanian, K. S. Koteswara Rao, N. Balasubramanian, Vikram, Kumar, *J. Appl. Phys.*, **77**, 5398 (1995).
7. J. Weber, M. Singh, *Mater. Res. Soc. Symp. Proc.* **104**, 325 (1988).
8. S. J. Pearton, J. W. Corbett, T. S. Shi, *Appl. Phys. A* **43**, 153 (1987).
9. M. S. Brandt, N. M. Johnson, R. Molnar, R. Singh, T. Moustakas, *Appl. Phys. Lett.*, **64**, 2264 (1994).
10. M. S. Brandt, J. W. Ager III, W. Gotz, N. M. Johnson, J. S. Harris, Jr. R. J. Molnar, T. D. Moustakas, *Phys. Rev. B* **49**, 14758 (1994).
11. W. Gotz, N. M. Johnson, J. Walker, D. Bour, H. Amano, I. Akasaki, *Appl. Phys. Lett.*, **67**, 2666 (1995).
12. C. Yuan, T. Salagai, R. A. Stall, Y. Li, M. Schurman, C-Y. Hwang, W. E. Mayo, Y. Lu, *J. Electrochem. Soc.*, **142**, L163 (1995).
13. J. Van Vechten, J. Zook, R. D. Horning, B. Goldenberg, *Jpn. J. Appl. Phys.*, **31**, 3663 (1992).
14. J. Neugebauer, C. G. Van de Walle (unpublished).
15. M. Ilegems, R. Dingle, R. A. Logan, *J. Appl. Phys.*, **43**, 3797 (1972).
16. M. Ilegems, R. Dingle, *J. Appl. Phys.*, **44**, 4234 (1973).

XPS MEASUREMENT OF THE SiC/AlN BAND-OFFSET AT THE (0001) INTERFACE

Sean W. King,* Mark C. Benjamin,** Robert J. Nemanich**, Robert F. Davis * and Walter R. L. Lambrecht †

*Department of Materials Science and Engineering, North Carolina State University, Raleigh, NC 27695

**Department of Physics, North Carolina State University, Raleigh, NC 27695

†Department of Physics, Case Western Reserve University, Cleveland, OH 44106

ABSTRACT

X-ray photoelectron spectroscopy is used to determine the band-offset at the SiC/AlN (0001) interface. First, the valence band spectra are determined for bulk materials and analyzed with the help of calculated densities of states. Core levels are then measured across the interface for a thin film of 2H-AlN on 6H-SiC and allow us to extract a band offset of 1.4 ± 0.3 eV. The analysis of the discrepancies between measured peak positions and densities of states obtained within the local density approximation provides information on self-energy corrections in good agreement with independent calculations of the latter.

INTRODUCTION

Silicon carbide wafers are being used increasingly as substrates for the growth of III-V nitride thin films. In particular, SiC is rather closely lattice matched to AlN (0.9 %) which is often used as a buffer layer for GaN growth. The availability of bulk 6H-SiC substrate wafers of high quality is instrumental for this purpose. Since SiC can also be grown on AlN layers on SiC [1], one may also consider the use of SiC as an active quantum well layer in a AlN/SiC/AlN heterostructure device. From both points of view, the band-offset at the SiC/AlN interface is of obvious interest. To date, only two previous values are available: a theoretical value by Lambrecht and Segall [2] which was for the (110) interface between zincblende SiC and AlN; and an experimental value obtained indirectly from measurements of the Fermi level of 2H-AlN grown on 6H-SiC (0001) by Benjamin et al. [3]. The investigations described here provide a more direct experimental determination of the band offset at the basal plane interface between 6H-SiC and wurtzite AlN. The procedure consists of measuring the core levels at the interface between a thin film of AlN (0001) grown on a 6H-SiC(0001) substrate and separately determining the energy of the valence band edges with respect to the core levels for thick films. The calculated densities of states are used to aid in the determination of the valence band edge and allow us to obtain some additional information on the electronic structure of the materials. In particular, we obtain results for the difference in quasi-particle self-energy shifts of the N2s and C2s bands with respect to those of the upper N2p and C2p like valence bands.

EXPERIMENT

A unique and integrated ultra high vacuum (UHV) system consisting of a 36 ft. long UHV transfer line to which several thin film deposition and surface analysis units are connected was employed in this research. The details of this integrated system have been previously described [4]. The as-received, n-type ($N_d \approx 10^{17-18}/\text{cm}^3$), vicinal 6H-SiC(0001)_{Si} substrate wafers containing a one micron thick, n-type ($N_d \approx 10^{16-17}/\text{cm}^3$) 6H-SiC(0001)_{Si} epitaxial layer were sequentially dipped in 10% HF for 5–10 min. to remove the thermally grown 750 Å silicon oxide surface layer, rinsed in 18.4 MΩ de-ionized water, blown dry with N₂, mounted to a molybdenum sample holder, loaded into ultra high vacuum (UHV) and degassed at 250, 500, 700, and 900°C for 30 min. each and annealed in a 10^{-7} – 10^{-6}

Torr flux of silane at 950°C for ~20 min. X-ray photoelectron spectroscopy (XPS) and Auger electron spectroscopy (AES) analyses of the SiC surface revealed that oxygen and non-carbidic carbon had been removed below the detection limits of these instruments. LEED displayed a sharp (1×1) pattern. The SiC bulk core levels and valence band of the SiC were measured via XPS.

Each AlN film was subsequently grown via gas-source molecular beam epitaxy (GSMBE), at 700°C and 10^{-6} Torr total pressure using ULSI (99.9995%) NH_3 and a flux of high purity Al (99.999%) evaporated from a Knudsen cell at 1050°C as sources. The temperature of 700°C was chosen to minimize any reaction between the SiC substrate and the AlN. In order to prevent the formation of Si_3N_4 at the SiC/AlN interface, the SiC wafer was exposed to the Al flux for 5 min. at 700°C prior to the introduction of NH_3 into the system. Very thin films (10–20 Å) were deposited to investigate the AlN/SiC heterojunction/interface. Thicker films (200 Å) were then deposited to measure the bulk AlN core levels and valence band. The films were subsequently transferred within a UHV environment to the chambers containing the XPS, AES and low energy electron diffraction (LEED) units for analyses of the surface chemistry and structure. Analysis via AES and XPS indicated that the films were stoichiometric and contained < 5% ML of surface oxygen. LEED displayed a sharp (1×1) pattern. Further details of the growth and cleaning procedures are described elsewhere [5]. All XPS analysis was performed using the Al anode ($h\nu = 1486.6$ eV) at 20 mA, and 12kV (240W). Due to the inherently poor signal/noise ratio in XPS valence band spectra, 50 or more scans of this region were acquired and summed together. All AES spectra were taken using a beam voltage of 3 keV and an emission current of 1 mA. LEED was performed using rear view optics, a beam voltage of ~100 eV, and an emission current of 1 mA. Calibration of the XPS binding energy scale was performed by measuring the position of the Au $4f_{7/2}$ and shifting the spectrums such that the peak position occurred at 83.98 eV.

THEORY

The densities of states (DOS) used for the analysis of the valence band spectra were calculated using the linear muffin-tin orbital [6] and density functional methods in the local density approximation (LDA)[7]. It is important to realize that strictly speaking the band structures obtained in this theory are not corresponding to the energies for extracting an electron from the material as measured in photoemission. The latter are quasiparticle energies and differ from the LDA Kohn-Sham eigenvalues by a self-energy correction [8]. This is, among other things, responsible for the well-known underestimate of the band gaps by the LDA. While these corrections have been found to be rather insensitive to the structure [9], they are expected to depend on the amount of localization of the states involved. We will show below that these corrections shift the C2s and N2s bands from the LDA calculated positions with respect to the valence band edge. The available calculations of these corrections using the *GW* method (i.e. using the leading term in Hedin's many-body theory [10] with *G* the one-electron Green's function and *W* the screened Coulomb interaction), for SiC [11, 12, 13] and AlN [14] show that they are about constant (but not quite, see below) over the upper valence band but are discontinuous across the ionicity gap. The present comparison between LDA calculated DOS and measured valence band spectra confirms this picture, and can be used to obtain an experimental value for these self-energy corrections.

RESULTS

A comparison of the valence band spectra for 6H-SiC(0001)_{Si} measured from the substrate and the calculated DOS is presented in Fig. 1. The latter is shown unbroadened as obtained from the highly accurate tetrahedron method and with a Gaussian broadening by 0.5 eV. The calculated and measured DOS are aligned to each other in the upper va-

lence band region in a manner described in more detail below. The major atomic orbital character of these peaks is indicated. The reference level in these spectra is based on the Au $4f_{7/2}$ standard and is thus not directly related to any intrinsic materials property of SiC. Thus only relative energy differences are meaningful. The major reason for using the comparison to calculated DOS is that this allows for a more precise determination of the actual valence band edge. First, we note that good agreement is obtained between theoretical and calculated peak positions up to about 10 eV binding energy. The peak intensities of the spectra are influenced by matrix elements and details of the experimental set-up such as collection solid angle and emission angle with respect to the surface normal, not accounted for by the DOS. These intensities also depend slightly on the background subtraction procedure. Here a linear background was used. The recent discovery of the presence of surface states in the SiC band gap may also confuse the direct location of the valence band maximum [15].

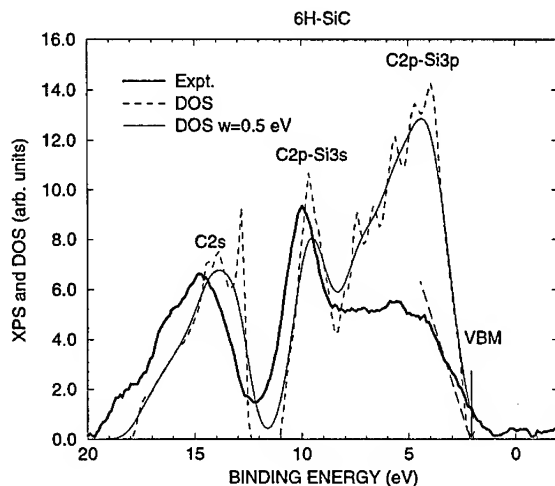


Figure 1: XPS spectra (arbitrary units) and densities of states (in states per unit cell per eV) of 6H SiC.

The major requirement for an accurate band-offset determination is $E_v - E_c$ where E_v is the energy of the valence band maximum (VBM) and E_c is any core-level of SiC. However, the broadening near the valence band edge hinders an unambiguous determination of this edge. In this case, it is preferable to determine experimentally the energy separation of the core levels from the well defined C2p-Si3s peak and take the position of the VBM with respect to that peak from the calculation. If we make use of the calculated *GW* corrections, the alignment can be done even more accurately as explained below.

On closer inspection, we observe that the experimental C2s peak is shifted by about 1.0 eV to lower energy from its theoretical position and the C2p-Si3s peak is shifted by about 0.4 eV. The reason for aligning the spectra in this manner is precisely the self-energy effects mentioned above. Indeed the *GW* calculations by Rohlfing et al. [11] and Backes et al. [12] predict a 0.4 eV shift from the valence band for the X_{3v} eigenvalue in 3C-SiC which in that case is closely associated with the C2p-Si3s peak. Wenzien et al. [13] obtain only 0.2 eV for this shift, so that this must be considered the approximate uncertainty on this alignment procedure. The former calculations reveal that the C2s band self-energy correction is about

1.0 eV larger than that of the valence band maximum while the latter finds this correction to be 1.4–1.6 eV. The present measurement indicates that the former two are in better agreement with experiment. In summary then, we find that the valence-band maximum on the energy scale of Fig. 1 lies at 2.2 ± 0.2 eV. We also see that this agrees well with a simple straight line extrapolation from the half height point of the experimental valence band edge.

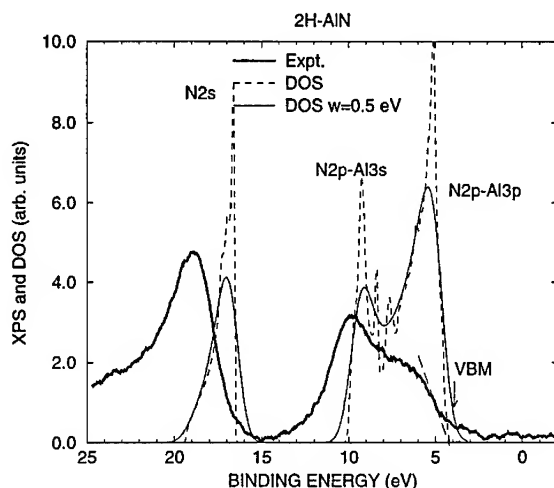


Figure 2: XPS spectra (arbitrary units) and densities of states (in states per unit cell per eV) of 2H-AlN.

Fig. 2 shows a similar analysis for the valence-band spectrum of AlN. In this case, we find that the upper valence band width is only 6 eV wide (in the theoretical DOS). Rubio et al.'s [14] *GW* calculations predict a 2.0 eV shift for the N2s peak and a 0.6 eV shift for the N2p-Al3s like peak. We see that if we align one of these including the above correction, the shift for the other is well reproduced. Due to the insulating nature of AlN, some broadening and shifting of the AlN core levels and valence band spectra may be expected due to charging. No direct evidence of these effects was found. We thus conclude that the AlN was deposited sufficiently thin (200 Å) that the underlying conducting SiC substrate prevented charging. With respect to the same Au $4f_{7/2}$ based reference level, we then find the valence-band maximum of AlN lies at 4.1 eV and is again in good agreement with a direct straight line extrapolation of the edge. The core levels for the bulk and interface system shown in Table I have also been measured on the same energy scale as employed for the studies described above.

These data are then substituted in the expression

$$-\Delta E_v = (E_v^{SiC} - E_c^{SiC})_b - (E_v^{AlN} - E_c^{AlN})_b + (E_c^{SiC} - E_c^{AlN})_i, \quad (1)$$

where the subscripts *b* and *i* indicate bulk and interface respectively. While in the above E_v and E_c are all positive electron binding energies, it is customary to give ΔE_v in terms of the energy levels which are the negative of the binding energies. Hence the minus sign on the left of Eq. 1. Using different core levels and remembering the uncertainties in the alignment of each valence-band spectrum we finally arrive at a value of $\Delta E_v = 1.4 \pm 0.3$ eV.

Table I: Valence-band maxima and core levels measured on the same Au 4f_{7/2} based reference scale

bulk SiC	
Si 2p	101.3
C 1s	283.5
VBM	2.2
bulk AlN	
Al 2p	75.3
N 1s	398.5
VBM	4.1
AlN/SiC heterojunction	
Si 2p	101.5
C 1s	283.6
Al 2p	74.9
N1s	398.2

DISCUSSION

The value obtained for the band-offset is in quite good agreement with the previously calculated offset of 1.5 eV for the (110) zincblende interface [2]. This is perhaps somewhat surprising since the latter is a non-polar interface while here we deal with a polar heterovalent interface. In fact, from simple electron counting rules, one expects that a purely N terminated surface would have an excess of 1/4 electron and thus must reconstruct its surface for example by having one N vacancy every 4 N atoms in order to maintain charge neutrality. In reality one may have a missing dimer every 4 instead of a simple vacancy or any other arrangement which is equivalent in net charge. At present, it is not known on an atomic scale what the interface structure is like, but we may note that if 1/4 of the N are missing at the interface, this is for electron counting purposes equivalent to mixing the nitrogen layer with C (group IV) anions. One expects that this would lower the dipole from that of a non-polar interface [16] by a few 0.1 eV. However, a slightly larger degree of intermixing may completely wipe out this interface dependence. This may indicate indirectly that there are an equal number of Al-C and N-Si bonds at the interface. In the absence of further information on the interface structure, we caution that this interpretation is at present only speculative and will require further study. We also note that while interface specific effects on band-offsets have in the past been predicted theoretically for several semiconductor heterostructures, especially heterovalent ones, these have generally not been observed. This indicates that realistic interfaces have some degree of disorder not accounted for by these theoretical predictions.

The value of 1.4 eV obtained for the SiC/AlN bandoffset is larger than the previously reported experimental value of 0.8 eV [3]. The discrepancies between these two values may be related to the experimental techniques or to the preparation of the SiC/AlN interface. The experiments described in this report employed recently developed surface preparation processes that result in atomically clean and ordered SiC prior to AlN deposition. In contrast, the SiC surface preparation of the prior study would typically exhibit a small amount of oxygen at the interface, ~25–50% ML. In addition the gas source MBE employed in present study results in a higher quality interface as opposed to the ECR technique employed previously. The ECR technique has been shown to result in more damage and an excess of Si-N bonding at the interface [17]. In the study presented in this paper, no oxygen was detected at the SiC/AlN interface. Furthermore, the use of an initial Al flux prior to ammonia exposure avoids the formation of a large amount of Si-N bonding.

These factors can strongly influence the band alignment between two semiconductors. In addition, the initial study also assumed flat bands in the SiC near the interface while upward band bending was noted as a distinct possibility. Since that band-offset value was based on the assumption of alignment of the measured Fermi level of AlN and the bulk n-type doped SiC, it indeed probes the macroscopic band alignment (affected by band bending) rather than the offset in the immediate vicinity of the interface. This differs from the present XPS investigation because of the limited escape depth of the photoelectrons.

CONCLUSION

By combining XPS studies of the valence band spectra with calculated DOS and a careful analysis of the alignment between the two taking into account known self-energy corrections to the LDA band structures, the positions of the valence band maxima of 6H-SiC and 2H-AlN with respect to their core levels has been determined. A subsequent measurement of core levels at the heterojunction between a thin film of 2H-AlN grown on top of 6H-SiC then allowed us to extract a band offset of 1.4 ± 0.3 eV. The latter is in good agreement with the calculated value of the (110) zincblende SiC/AlN which indicates that the expected polar interface specific effects were compensated by some degree of disorder.

The work at CWRU was supported by NSF (DMR-92-22387); the research at NCSU was supported by ONR (N00014-92-J-1477). Appreciation is expressed to Cree Research Inc. for the 6H-SiC wafers used in this study.

REFERENCES

1. L.B. Rowland, R.S. Kern, S. Tanaka, and R.F. Davis, *Appl. Phys. Lett.* **62**, 3333 (1993).
2. W. R. L. Lambrecht and B. Segall, *Phys. Rev. B* **43**, 7070 (1991).
3. M. C. Benjamin, C. Wang, R. F. Davis, and R. J. Nemanich, *Appl. Phys. Lett.* **64**, 3288 (1994).
4. Jacob van der Weide. Ph.D. dissertation, North Carolina State University, 1993.
5. S. W. King, R. J. Nemanich, and R. F. Davis, unpublished.
6. O. K. Andersen, O. Jepsen, M. Šob, in *Electronic Band Structure and its Applications*, ed. M. Yussouf (Springer, Heidelberg 1987), p. 1
7. W. Kohn and L. J. Sham *Phys. Rev.* **140**, A1133 (1965)
8. L. J. Sham and W. Kohn, *Phys. Rev.* **145**, A561 (1966).
9. W. R. L. Lambrecht, B. Segall, M. Yoganathan, W. Suttrop, R. P. Devaty, W. J. Choyke, J. A. Edmond, J. A. Powell, and M. Alouani, *Phys. Rev. B* **50** 10722 (1994).
10. L. Hedin, *Phys. Rev.* **139**, A796 (1965).
11. M. Rohlfing, P. Krüger, J. Pollmann *Phys. Rev. B* **48**, 1791 (1993).
12. W. H. Backes, P. A. Bobbert, W. van Haeringen *Phys. Rev. B* **51** 4950 (1995)
13. B. Wenzien, P. Käckell, F. Bechstedt *Phys. Rev. B* **52**, 10897 (1995)
14. A. Rubio, J. L. Corkill, M. L. Cohen, E. L. Shirley, and S. G. Louie, *Phys. Rev. B* **48**, 11810 (1993).
15. M. C. Benjamin, S. W. King, R. F. Davis, and R. J. Nemanich, unpublished.
16. W. R. L. Lambrecht and B. Segall, *Phys. Rev. B* **41**, 2832 (1990).
17. Z. Sitar, L. L. Smith, and R. F. Davis, *J. Cryst. Growth* **141**, 11 (1994).

A MICROSCOPIC EVALUATION OF THE SURFACE STRUCTURE OF OMVPE DEPOSITED α -GaN EPILAYERS

G. S. ROHRER, J. PAYNE, W. QIAN, M. SKOWRONSKI
Carnegie Mellon University
Department of Materials Science and Engineering
Pittsburgh PA 15213, USA

K. DOVERSPIKE*, L. B. ROWLAND**, AND D. K. GASKILL
Laboratory for Advanced Material Synthesis
Naval Research Laboratory
Washington, DC 20375, USA

*current address: Hewlett-Packard Company, Optoelectronics Division, San Jose, CA 95131.

**current address: Westinghouse Science and Technology Center, Pittsburgh, PA 15235.

ABSTRACT

The surface structure of organometallic vapor phase epitaxy (OMVPE) grown α -GaN films was investigated using optical and scanning force microscopy (SFM). Optical microscopy shows that the surface is decorated with several different types of faceted features that have lateral dimensions of 10 to 75 μm and occur with a density of approximately $10^4/\text{cm}^2$. SFM images show that on the flat regions of the surface, single diatomic layer steps, 2.6 \AA high, are straight, evenly spaced (at 500 to 1500 \AA intervals), and oriented along $\langle 10\bar{1}0 \rangle$ directions. The SFM images also show that the regular step patterns are often interrupted by faceted growth hillocks, 0.8 to 5 μm in diameter and 120 to 400 \AA high, that occur with a density of $10^6/\text{cm}^2$. An open-core screw dislocation with a Burgers vector of 5.2 \AA occurs at the center of each hillock and is a source for spiral steps. Other dislocations are also observed to intersect the flat regions of the surface and create a step, but these have smaller Burgers vectors, do not form spirals, and do not have open cores. Based on these observations, we conclude that thick OMVPE GaN films grow by a combination of the layer-by-layer and spiral growth mechanisms.

INTRODUCTION

Gallium nitride and its related alloys (AlGaN and InGaN) are important wide band-gap semiconductors that have potential applications in both short wavelength optoelectronic and high power/high frequency devices [1]. The most widely accepted technique for the deposition of nitride films and device structures, which was proposed by Amano [2,3] and Akasaki [4], uses sapphire substrates buffered by thin layers of AlN or GaN deposited at low temperature. However, films grown by nominally the same method can have very different microstructures and, accordingly, different properties. For example, the dominant defects in the films considered here are edge dislocations arranged in patterns that define low angle grain boundaries separating almost "dislocation free" grains [5]. The grain structure is columnar and, therefore, largely determined during the nucleation stage of growth. The objective of the work described in this report was to characterize the structure of the film growth surface in order to gain insight into the growth mechanism and its relationship to the through-thickness microstructure.

EXPERIMENTAL

The 2.8 μm thick α -GaN epilayers described here have an (0001) orientation and were grown at 1040 $^{\circ}\text{C}$ on α - Al_2O_3 (0001) substrates in an inductively heated, water cooled, vertical organometallic vapor phase epitaxy (OMVPE) reactor. [6] An AlN buffer layer was first deposited at 450-500 $^{\circ}\text{C}$ using 1.5 $\mu\text{mol}/\text{min}$ triethylaluminum, 2.5 standard liters per minute (SLM) NH_3 , and 3.5 SLM H_2 flows. After annealing in 2.5 SLM NH_3 and 3.5 SLM H_2 for 10 minutes at 1025 $^{\circ}\text{C}$, GaN was grown using 49 $\mu\text{mol}/\text{min}$ trimethylgallium (TMGa), 1.75 SLM NH_3 , and 3.5 SLM H_2 . The resulting growth rate was approximately 2.0 $\mu\text{m}/\text{hr}$. The as-grown films were examined in air with a traditional metallographic microscope and with a Park Scientific Instruments scanning force microscope (SFM). The 5 μm scanner was operated at 2 Hz. All images were acquired in the constant force mode using 3 to 12 nN of contact force.

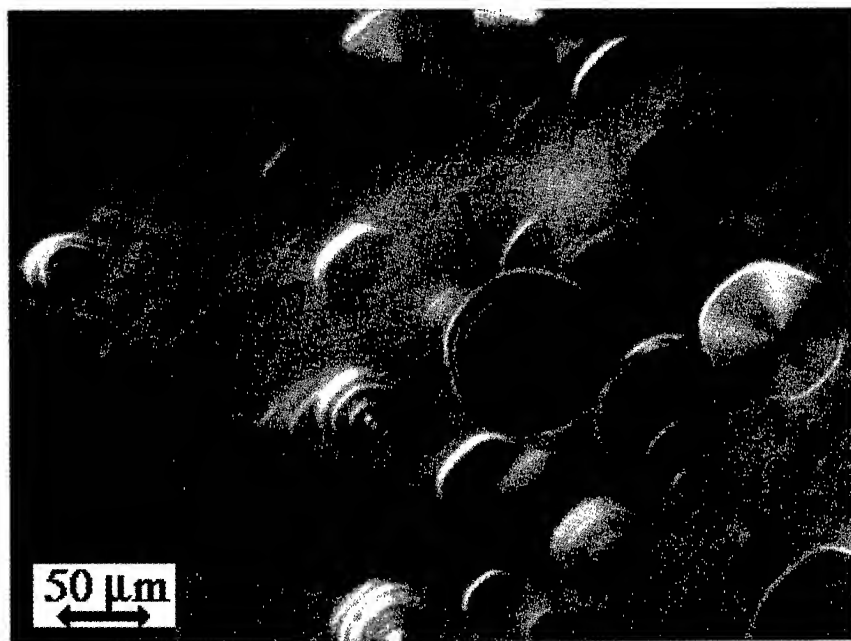


Figure 1. Optical micrograph of the growth surface of an OMVPE grown α -GaN epilayer.

RESULTS

When viewed under an optical microscope, a number of different topographic features were observed on the surface of the GaN epilayer. We classify all of the observed features into one of three groups: flat facets (labeled A and A' in Fig. 1), multifaceted hexagons (labeled B in Fig. 1), and cones (labeled C in Fig. 1). The average size and density of these features was

determined by completely mapping a 2.02 mm x 2.25 mm area of the surface at 100X magnification. In this region, the observed density of flat facets is approximately $1.2 \times 10^4/\text{cm}^2$. The image in Fig. 1 includes both the island-facets (65 to 75 μm in diameter) that are completely bounded by visible steps with prismatic orientations (labeled A in Fig. 1), as well as the more numerous ledge-facets (10 μm and larger) that are only partially bounded by visible steps (labeled A' in Fig. 1). The multifaceted hexagons have lateral dimensions of 30 to 45 μm and a density of $8 \times 10^2/\text{cm}^2$. Most of these features have three concentric hexagonal steps separated by 6 to 8 μm . The density of the cone shaped features is $5 \times 10^2/\text{cm}^2$ and they all are 65 to 75 μm in diameter. Some of the cones appear to come to a point while others have flat tops.

To the optical microscope, the surfaces of the island-facets appear flat. When the facets are imaged with the SFM, however, regular patterns of single layer steps and hexagonally faceted growth hillocks observed on the optically flat surface. The hillocks, such as the ones shown in Fig. 2, are composed of one to five concentric layers and are configured randomly; some of the hillocks have grown on top of each other, while others are separated by distances of more than 20 μm . The smaller hillocks are about 0.8 μm in diameter and 120 \AA high, while the larger ones are more than 5 μm at the base and up to 400 \AA high. Based on the analysis of one large, flat facet, we conclude that the hillock density is $1 \times 10^6/\text{cm}^2$.

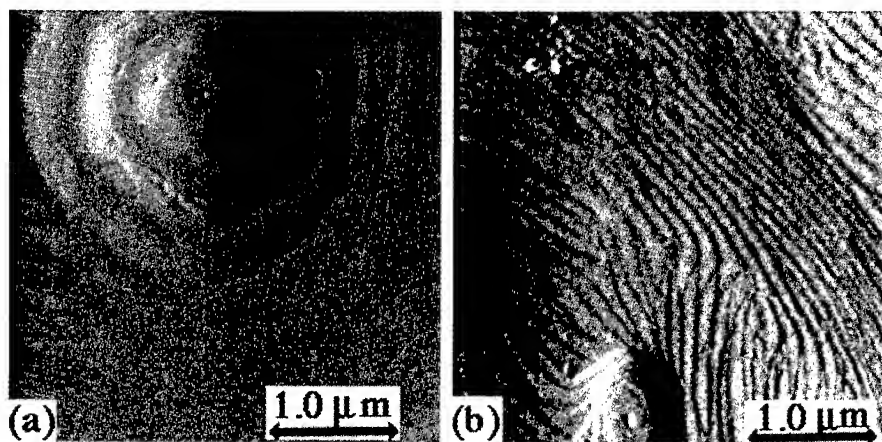


Figure 2. Growth hillocks on the surface of a flat facet on the GaN epilayer. These SFM images were recorded based on the difference between the setpoint deflection and the actual deflection of the probe so that contrast corresponds to changes in the topography. This allows a large dynamic range of height data to be viewed simultaneously. (a) shows one of the larger hillocks and (b) shows a smaller one in the lower portion of the image and single layer steps elsewhere.

Patterns of single layer steps are found between the hillocks. The steps are measured to be $2.8 \pm 0.6 \text{ \AA}$ high. Although there is certainly some error introduced by the presence of the surface contamination layer, this measurement is consistent with the expected dimension of a single diatomic layer of GaN which is one half the length of the c-lattice parameter (2.6 \AA). Far from the hillocks (see the upper right hand corner of Fig. 2b), the steps are straight and spaced at regular intervals of 500 to 1500 \AA . However, in regions near the hillocks, the

direction of step propagation is altered, as illustrated in Fig. 2b. Also, on the left hand side of the hillock, the steps spiral downward and remain evenly spaced. On the right hand side, however, they are bunched. This pattern is typical of all our observations.

We have observed two types of surface/dislocation intersections that we distinguish based on the magnitude of the Burgers vector normal to the surface and the effect that they have on the progress of growing steps. The first type is observed in the relatively flat areas of the surface between the hillocks where single steps are separated by approximately 1000 Å. For example, in the topographic SFM image in Fig. 3a, many surface steps (dark contrast) are clearly visible. Because some of these steps terminate in the middle of a terrace, a Burgers circuit around such a position indicates that a dislocation line must intersect the surface and that the component of the Burgers vector normal to the surface plane is equivalent to one half the length of the c-lattice parameter (2.6 Å). Therefore, the dislocation has at least partial screw character. Two such defects with opposite sign are indicated by arrows in Fig. 3a. By counting such defects in this and similar images, we find that their density varies greatly, but falls in the range $5 \times 10^6/\text{cm}^2$ to $1 \times 10^8/\text{cm}^2$.

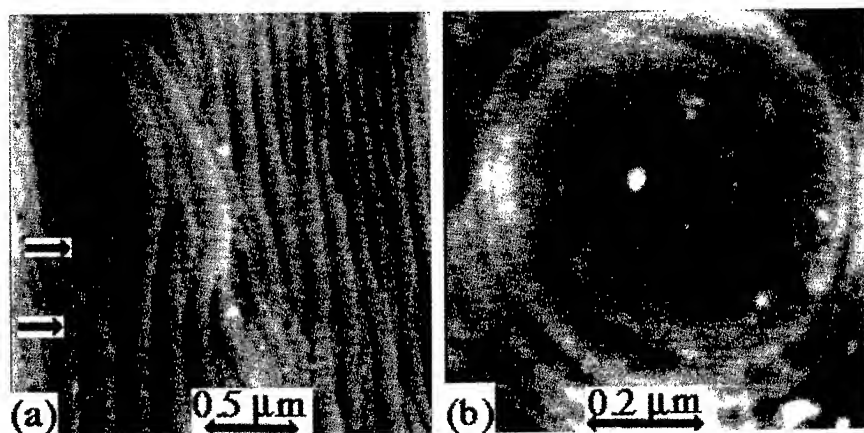


Figure 3. Topographic SFM images showing different types of surface/dislocation intersections. (a) was recorded on a relatively flat region. The vertical lines of contrast correspond to single layer steps. Where the steps end (positions indicated by the arrows), dislocations intersect the surface. (b) was recorded on top of a faceted hillock similar to the ones shown in Fig. 2a. The black spot in the center is the crater formed by the nanopipe that intersects the surface at this point. The spiral steps indicate that there is a screw dislocation at this position.

The second type of surface/dislocation intersection is found at the center of each of the faceted hillocks. SFM images recorded at the tops of these features (see Fig. 3b) illustrate that in the center of each one, there is a hole. Such images also show that a pair of spiral steps, each 3.1 ± 0.8 Å high, originates at this hole. This measurement is consistent with the expected dimension of a single diatomic layer of GaN which is one half the length of the c-lattice parameter (2.6 Å). Thus, the two steps form an additional complete GaN unit cell. The origin of this extra step at the center of the hillock indicates that there is a screw dislocation in the center of the hole with a Burgers vector ($\mathbf{b} = 1/3[0003]$) equal in length to the c lattice parameter (5.2 Å). Numerous hillocks were examined with different probe tips and similar observations were made; each has a hole with an approximately 600 Å radius at the center. In one case, four single steps, each $1/2$ c high, emerged from a single hole with a larger radius

(approximately 925 Å). This corresponds to a "giant" dislocation with Burgers vector $\mathbf{b} = 2/3[0003]$. After spiraling away from the hole on the flat top of the hillock, the steps bunch together and become too close to be individually resolved. Similar features were observed on the flat facets and at the centers of the multifaceted hexagons.

DISCUSSION

The through thickness microstructure of these same films has been studied by transmission electron microscopy (TEM) and described in a previous report [5]. The film microstructure is dominated by submicron grains with relative misorientations of less than 3°. The boundaries between adjacent grains are defined by arrays of edge dislocations, aligned along the [0001] growth direction and with Burgers vectors of $1/3\langle 11\bar{2}0 \rangle$. There is no apparent relationship between this bulk microstructure and the observed surface microstructure. First, the faceted features observed in the optical microscope are all far larger than the observed submicron grain size of the columnar film. Furthermore, when flat areas with micron-scale dimensions were examined in detail with SFM, trains of parallel steps are present which presumably flow uninterrupted over the positions where the edge dislocation arrays that define the low angle boundaries intersect. Therefore, we conclude that the interaction between the steps and the threading edge dislocations is relatively weak and does not affect the progress of growing steps.

On the other hand, the dislocations of screw character that penetrate the surface serve as sources of steps. Those defects with Burgers vectors that are equal to the length of the GaN unit cell can form spirals and add a new layer of crystal to the film on each rotation. Considering the fact that these defects are found at the centers of the hillocks, we assume that these structures are formed by a spiral growth mechanism. The different sizes of these growth mounds suggest that they become active at different times during the growth of the crystal. Those dislocations with smaller Burgers vectors, which occur at the sources of straight steps on the flat regions of the crystal, are unable to create hillocks. Because the Burgers vector parallel to the c-axis is only one half the length of the lattice repeat distance, a stacking fault would be created on every rotation of the spiral. Thus, the other steps must grow over these defects in order for the crystal growth to continue. While steps show some curvature near these defects, they do not appear to act as strong pinning sites.

The voids that appear at the centers of spiral screw dislocations are known as nanopipes. Previously described TEM studies of these films concluded that these pipes penetrate the entire epilayer and occur with a density of 10^5 to $10^7/\text{cm}^2$ [7,8]. The stability of such defects was first demonstrated by Frank [9], who argued that a state of local equilibrium could be achieved by balancing the elastic energy of the dislocation against the surface energy of the facets that bound the pipe. One of the predictions central to Frank's theory is that when the stored elastic energy of the dislocation is sufficiently large, the core will be empty and its radius will be proportional to the square of the Burgers vector. In a qualitative sense, our observations are consistent with these ideas. For example, Frank predicted that the crater formed where the pipe meets the free surface is larger than the pipe itself. TEM observations indicate that nanopipes have radii in the 35-500 Å range, while the surface craters observed in SFM images are larger [8]. Also, the radius (r) of the crater of the super screw dislocation ($b = 10.4$ Å) was larger ($r = 925$ Å) than that of the single dislocation ($b = 5.2$ Å and $r = 600$ Å), as expected. Finally, the dislocations with Burgers vectors smaller than the c-axis repeat distance that were observed on the flat areas of the surface do not have open cores. Since the elastic energy scales as the square of the Burgers vector and these dislocations have Burgers vectors that are $1/2$ the length of those with open cores, they store one quarter of the elastic energy and are proportionally more stable.

We should also note, however, that there are two apparent inconsistencies between our observations and Frank's prediction. First, incorporating two known quantities, the observed Burgers vector ($b = 5.2$ Å) and the smallest observed radius ($r = 35$ Å), into Frank's formula, we extract a ratio of the surface free energy to the shear modulus which is equal to 0.01 Å. For

most materials, however, this ratio is 0.25 \AA . If one assumes that the shear modulus is as high as 400 GPa, the surface energy would be only 40 mJ/m^2 , a physically unlikely value. The second inconsistency is that the radii of the holes should have a discrete distribution of sizes proportional to $(nb)^2$, where n is an integer ≥ 1 . Instead, TEM observations suggest a more random distribution of sizes within the range of 35 to 500 \AA [7].

CONCLUSION

By the time the GaN epilayer is $2.8 \text{ }\mu\text{m}$ thick, growth occurs by both a layer-by-layer and a spiral mechanism. The underlying bulk microstructure of low angle grain boundaries is presumably fixed in the nucleation stage and does not seem to affect the growth of the film in later stages. While the surface has some large topographic features with a density of approximately $10^4/\text{cm}^2$, it also has flat regions that are dominated by single diatomic layer steps. These steps are 2.6 \AA high, straight, evenly spaced (at 500 to 1500 \AA intervals), and oriented along $\langle 10\bar{1}0 \rangle$ directions. These regular patterns are often interrupted by faceted growth hillocks, 0.8 to $5 \text{ }\mu\text{m}$ in diameter and 120 to 400 \AA high, that occur with a density of $10^6/\text{cm}^2$. An open-core screw dislocation with a Burgers vector of 5.2 \AA occurs at the center of each hillock and is a source for spiral steps. Other dislocations are also observed to intersect the flat regions of the surface and create steps, but these have smaller Burgers vectors, do not form spirals, and do not have open cores.

ACKNOWLEDGMENTS

W. Q., J.P., and M. S. acknowledge support under AFOSR Grant No. F29620.94.1.0392 and G.S.R. acknowledges support from the NSF under YIA Grant No. DMR-9458005.

REFERENCES

- [1] H. Morkoç, S. Strite, G. B. Gao, M. F. Lin, B. Sverdlov and M. Burns, *J. Appl. Phys.* **76**, 1363 (1994).
- [2] H. Amano, N. Sawaki, I. Akasaki and Y. Toyoda, *Appl. Phys. Lett.* **48**, 353 (1986).
- [3] H. Amano, I. Akasaki, K. Hiramatsu, Y. Koide, H. Sawaki, *Thin Solid Films* **163**, 415 (1988).
- [4] I. Akasaki, H. Amano, Y. Koide, K. Hiramatsu, H. Sawaki, *J. Crystal Growth* **98**, 209 (1989).
- [5] W. Qian, M. Skowronski, M. D. Graef, K. Doverspike, L. B. Rowland and D. K. Gaskill, *Appl. Phys. Lett.* **66**, 1252 (1995).
- [6] K. Doverspike, L. B. Rowland, D. K. Gaskill, S. C. Binari and J. J.A. Freitas, *J. Electron. Mater.* **24**, 269 (1995).
- [7] W. Qian, M. Skowronski, K. Doverspike, L. B. Rowland and D. K. Gaskill, *J. Crystal Growth* **151**, 396 (1995).
- [8] W. Qian, G. S. Rohrer, M. Skowronski, K. Doverspike, L. B. Rowland, and D. K. Gaskill, *Applied Physics Letters* **67**, 2284 (1995).
- [9] F. C. Frank, *Acta Cryst.* **4**, 497 (1951).

THE MICROSTRUCTURAL STUDY OF ALUMINUM NITRIDE THIN FILMS: EPITAXY ON THE TWO ORIENTATIONS OF SAPPHIRE AND TEXTURING ON Si

K. DOVIDENKO*, S. OKTYABRSKY*, J. NARAYAN*, M. RAZEGHI**

* Department of Materials Science and Engineering, North Carolina State University, Raleigh NC, 27695-7916

** Center for Quantum Devices, Northwestern University, Evanston, Illinois 60208

ABSTRACT

The microstructural study of wide-band gap semiconductor AlN thin films grown on (0001) and (10 $\bar{1}2$) sapphire and (111), (100) Si was carried out using plan-view and cross-sectional high-resolution electron microscopy and x-ray diffraction. The films were grown by MOCVD from TMAI + NH₃ + N₂ gas mixture. Epitaxial relationship for AlN grown on (0001) α -Al₂O₃ was determined to be the following: (0001)_{AlN} || (0001)_{sap} with the 30° in-plane rotation - [01 $\bar{1}0$]_{AlN} || [$\bar{1}2\bar{1}0$]_{sap}. We report also TEM observation of the following epitaxial relationship of the AlN/(10 $\bar{1}2$) α -Al₂O₃ heterostructure: (11 $\bar{2}0$)_{AlN} || (10 $\bar{1}2$)_{sap}; [0001]_{AlN} || [$\bar{1}011$]_{sap} and [$\bar{1}100$]_{AlN} || [$\bar{1}2\bar{1}0$]_{sap}. These epitaxial relationships were determined to be controlled by the bonding of Al and O ions at the interface. The study of interfaces and the defects present in the film was also carried out. Main type of defects were established to be inverted domain boundaries, misfit and threading dislocations - in the films on (0001) sapphire, and stacking faults of high density in the films on (10 $\bar{1}2$) sapphire. The epitaxial AlN films on (0001) sapphire contained dislocation density about 10¹⁰ cm⁻² and exhibited device quality electrical characteristics. The films on both orientations of Si were found to be highly <0001> textured polycrystalline.

INTRODUCTION

Aluminum nitride is a wide - band gap semiconductor (band gap energy $E_g = 6.2$ eV at 300 K). AlN is considered to be a highly attractive material for optoelectronic devices such as lasers and light-emitting diodes operating in the ultraviolet special region. The AlN also has high thermal conductivity (2 W/cm K) and excellent resistance to oxidation. These properties make AlN suitable for coating applications in aggressive environment with extreme thermal, chemical and physical conditions. Many of these important properties are related to the crystal structure of the films, their orientation with the substrate. Epitaxial single crystal films with low defects density (such as dislocations, stacking faults, grain boundaries) are required for possible future device applications. The most prospective substrates for AlN and GaN films growth are considered to be 6H-SiC and, in spite of large lattice mismatch, α -Al₂O₃ (sapphire). The crystal quality of the film is determined by the growth conditions and substrate variables such as temperature, lattice misfit and interfacial chemical free energy [1]. The epitaxial growth of aluminum nitride has been already demonstrated in some papers ([2 - 8], for example). In this paper the details of epitaxial growth of AlN on different substrates as well as microstructural defects, interfaces in the AlN films are discussed.

EXPERIMENT

Aluminum nitride films of 300 nm thickness were grown in a horizontal, atmospheric pressure metalorganic chemical vapor deposition (MOCVD) reactor at a substrate temperature of 1050°C. Films were deposited on sapphire (0001) and (10 $\bar{1}2$) and on Si (111) and (100) substrates. All the films were deposited under similar conditions to investigate crystalline quality as a function of processing and substrate parameters. Details of the MOCVD growth procedure are published elsewhere [2]. Samples for transmission electron microscopy (TEM) were prepared by a conventional planar and cross-sectional sample preparation technique with the Ar⁺ ion-milling at

the final stage. TEM investigations have been carried out using a Topcon 002B electron microscope operated at 200 kV with point-to-point resolution of 0.18 nm.

RESULTS AND DISCUSSION

TEM investigations of the AlN films grown on the two different orientations of sapphire have shown that in both cases the films are epitaxial. Plan-view TEM images and corresponding selected area diffraction patterns (SADPs) for the AlN films on basal and rhombic r-plane of sapphire are shown in Figs. 1 a, b and 2 a, b respectively. Dislocations are visible in the image of AlN film grown on (0001) sapphire (Fig. a), and both dislocations and planar defects of high

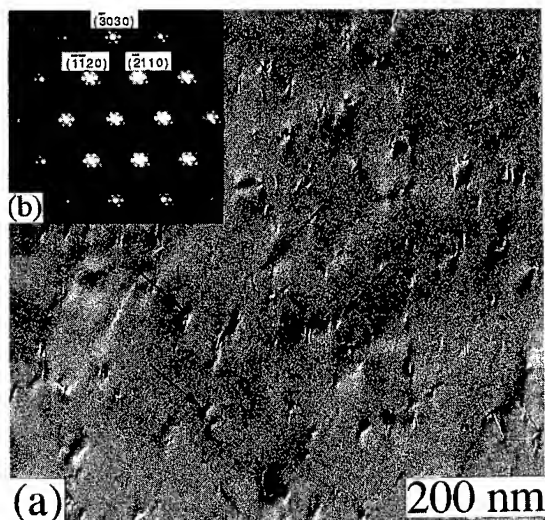


Fig. 1

- a) Plan-view TEM micrograph of AlN thin film grown on (0001) sapphire showing the upper part of the film without the substrate;
- b) [0001] zone axis SADP of overlapping AlN and sapphire regions of the sample.

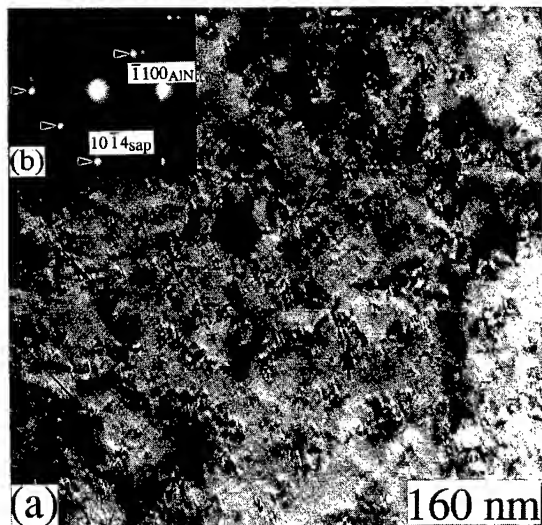


Fig. 2

- a) Plan-view TEM micrograph of AlN thin film grown on $(10\bar{1}2)\alpha\text{-Al}_2\text{O}_3$;
- b) corresponding SADP in $[11\bar{2}0]$ AlN zone (arrows indicate the reflections of sapphire).

concentration present in the film grown on $(10\bar{1}2)$ α - Al_2O_3 (Fig.2 a). Long arrows show the dislocations, short arrows - planar defects. The following epitaxial relationships were obtained from the SADPs: $(0001)\text{AlN} \parallel (0001)_{\text{sap}}$ with the 30° in-plane rotation - $[01\bar{1}0]\text{AlN} \parallel [\bar{1}210]_{\text{sap}}$ - for AlN film grown on the basal plane of AlN; and $(11\bar{2}0)\text{AlN} \parallel (10\bar{1}2)_{\text{sap}}$, with the in-plane relationship $[0001]\text{AlN} \parallel [\bar{1}011]_{\text{sap}}$. Double diffraction spots visible in the SADP in Fig. 1 (b) (obtained from the area of about $0.6\ \mu\text{m}$ in diameter containing both the film and the substrate) arise from the overlapping of the film and the substrates diffraction. The AlN film grown on the (0001) α - Al_2O_3 was found to contain threading dislocations with the Burgers vector $a/3\langle 11\bar{2}0 \rangle$. From the plan-view TEM micrographs, we determined the density of the threading dislocations to be about $10^{10}\ \text{cm}^{-2}$. From the plan-view investigations we concluded that dislocations present in the AlN film grown on $(10\bar{1}2)$ α - Al_2O_3 are always associated with the planar defects and, therefore, are mostly partials. Concentration of these dislocations is at least twice higher than that of threading dislocations in AlN grown on (0001) sapphire plane. The nature of the planar defects in AlN film grown on r-plane of sapphire was studied using HRTEM on the plan-view specimens. Fig. 3 demonstrates the image of the planar defects lying in the basal (0001) plane (normal to the plane of the image) of AlN. The defects appear to be stacking faults. The stacking of closed-packed layers is the following: ABA(CACACAC)BAB where the sequence in brackets corresponds to the area between two stacking faults AC and CB. In this area CACACA is equivalent to the sequence ABABAB in all other parts of crystal, the atomic columns are just shifted to the position C with respect to the rest of the crystal. This is exactly the situation visible in the HRTEM image in Fig. 3: the atomic layers in the area between the two stacking faults are shifted. We have also observed the formation of intrinsic and extrinsic stacking faults in $[11\bar{2}0]$ -oriented AlN due to incorporation of additional layer in the atomic layer sequence or due to the extraction of the atomic layer from the

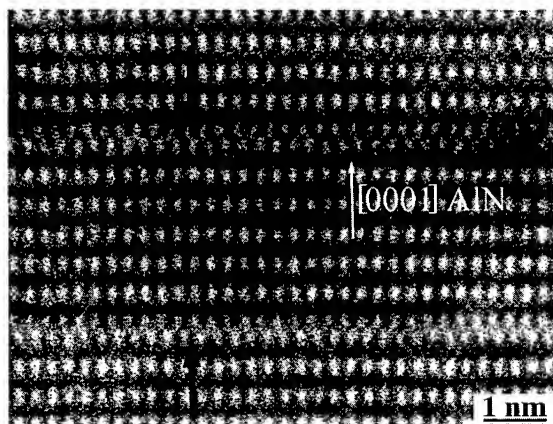


Fig. 3

HRTEM plan-view image of the stacking faults in AlN grown on $(10\bar{1}2)$ α - Al_2O_3 ($[11\bar{2}0]$ zone of AlN, arrows indicate stacking faults).

structure, respectively. Therefore, these stacking faults are terminated by partials with $1/3\langle 1\bar{1}00 \rangle$ or $1/2\langle 0001 \rangle$ Burgers vectors. Detailed analysis and image simulation of these defects will be presented elsewhere [9].

The cross-sectional TEM study was carried out to reveal the structure of AlN/sapphire h- and r-planes interfaces. Dark-field TEM image of AlN/ $(0001)\alpha$ - Al_2O_3 interface taken under $g=10\bar{1}0$ conditions is presented in Fig. 4. Characteristic feature of the AlN films on basal plane of sapphire appeared to be inverted domain boundaries (IDBs) [10, 11]. The HRTEM cross-sectional micrograph of the AlN/ $(0001)\alpha$ - Al_2O_3 interface demonstrating the atomic scale image of the defect we consider to be IDB is presented in Fig. 5 (insert is a corresponding diffraction pattern). Atomic

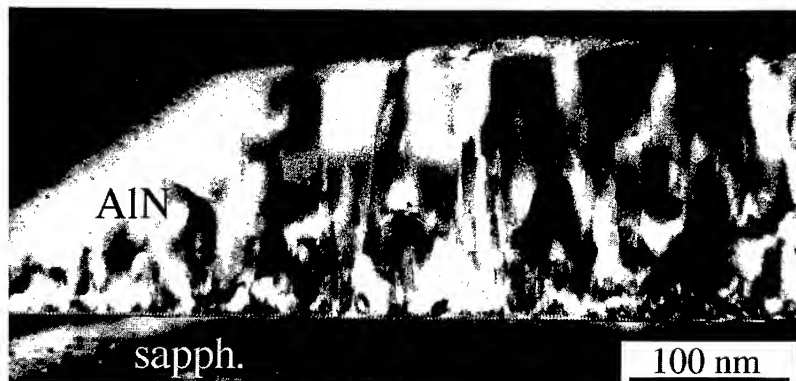


Fig. 4

Dark-field ($g=10\bar{1}0$) cross-sectional TEM image of AlN/(0001) α -Al₂O₃ interface.

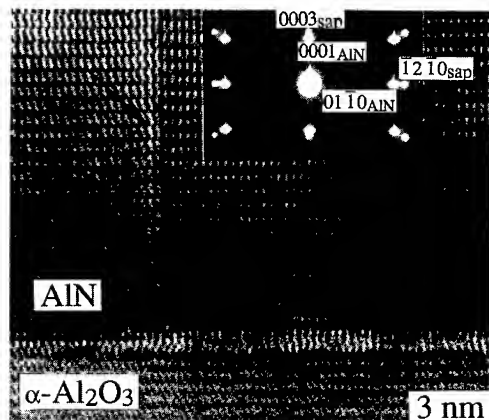


Fig. 5

HRTEM image of AlN/ α -Al₂O₃(0001) cross-section specimen in $[10\bar{1}0]$ zone of sapphire with the superimposed $z=[10\bar{1}0]_{\text{sapp}}$ and $[2\bar{1}\bar{1}0]_{\text{AlN}}$ SAD pattern. Inverted domain boundary is indicated by arrow.

simulation of these defects is now in progress and the results will be published elsewhere [9]. The film/substrate interface (Fig. 5) is sharp and free from any signs of second phase. The average spacing between the misfit dislocations present at the interface (Fig. 4), 2.5 nm, corresponds to a complete relaxation of misfit strain of 12% by the $a/3\langle 11\bar{2}0 \rangle$ misfit dislocations. High-resolution TEM study of the AlN/ r -plane of sapphire interface also proved the absence of any mixed layer.

In considering the growth of AlN on $(10\bar{1}2)$ plane of sapphire we would like to discuss three possible cases of film orientation with respect to the substrate. First, AlN can grow with c -axis perpendicular to the substrate surface, with the $[0001]$ direction of the film perpendicular to the $(10\bar{1}2)$ α -Al₂O₃. This is a kinetically preferred orientation which is found to occur when AlN films are grown on highly mismatched substrates, like Si(100) [3]. In this case, the atomic stacking would be quite poor due to the large lattice mismatch and different type of symmetry of AlN and sapphire in these orientations. Second and third cases arise when the film grows in $[11\bar{2}0]$ orientation because the two possibilities exist: c -axis of AlN aligned either with $[1\bar{2}10]$ direction of sapphire (the lattice mismatch is then 4.3% in the $[0001]$ direction and 5.5% in the

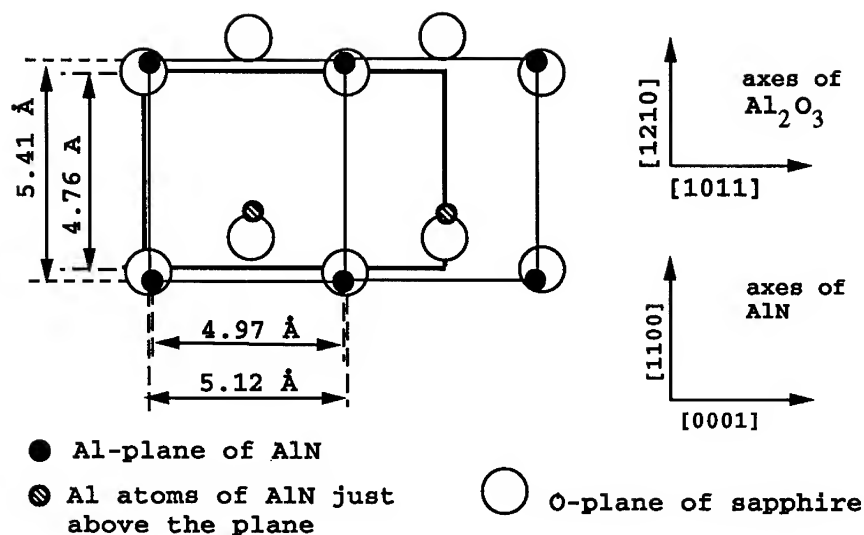


Fig. 6

Schematic representation of epitaxial relationship between the AlN film and the $(10\bar{1}2)$ sapphire substrate: $(11\bar{2}0)_{\text{AlN}} \parallel (10\bar{1}2)_{\text{sap}}$; and $[0001]_{\text{AlN}} \parallel [\bar{1}011]_{\text{sap}}$, $[1\bar{1}00]_{\text{AlN}} \parallel [1\bar{2}10]_{\text{sap}}$.

$[1\bar{1}00]$ AlN direction) or with the normal to the $(10\bar{1}4)$ $\alpha\text{-Al}_2\text{O}_3$ plane, i.e. along $[\bar{1}011]$ direction of sapphire. In our studies we have confirmed the latter epitaxial relationship, where a lattice mismatch of 13.3% between $[1\bar{1}00]$ AlN and $[1\bar{2}10]$ $\alpha\text{-Al}_2\text{O}_3$ and of 2.9% along $[0001]$ AlN is expected. The RHEED (reflection high-energy electron diffraction) results [12] show that this epitaxial relationship does exist for GaN films on sapphire, where the corresponding values of mismatch are 13.8% and 1.1%. Atomic arrangement at the AlN-sapphire interface, as shown in Fig. 6, indicates that the observed epitaxial relationship is favored because it promotes Al-O bonding.

AlN films on both orientations of silicon were found to be polycrystalline c-axis textured. Films on Si (111) were perfectly textured and had preferential in-plane orientation of grains (about 60 nm in size) of $[211]_{\text{Si}} \parallel [10\bar{1}0]_{\text{AlN}}$. The in-plane rotation of $\pm 7^\circ$ about the $[0001]$ axis of AlN was observed in films grown on Si(111). Polycrystalline $[0001]$ - textured films with the average grain size of 20 nm were observed to grow on Si(100) substrates (the grains exhibit random in-plane orientation).

SUMMARY

Epitaxial single crystal AlN films were obtained on hexagonal basal plane (0001) of sapphire and on $(10\bar{1}2)$ $\alpha\text{-Al}_2\text{O}_3$. Crystal quality of AlN film on (0001) sapphire is much higher than on $(10\bar{1}2)$ $\alpha\text{-Al}_2\text{O}_3$. The epitaxial relationships were established for single crystal films on both orientations of sapphire. AlN films on $\alpha\text{-Al}_2\text{O}_3$ (0001) displayed the following epitaxial

relationship: $(0001)_{\text{AlN}} \parallel (0001)_{\text{sap}}$ with in-plane orientation relationship of $[01\bar{1}0]_{\text{AlN}} \parallel [\bar{1}2\bar{1}0]_{\text{sap}}$; AlN films on $(10\bar{1}2) \alpha\text{-Al}_2\text{O}_3$: $(11\bar{2}0)_{\text{AlN}} \parallel (10\bar{1}2)_{\text{sap}}$ with the in-plane alignment of $[0001]_{\text{AlN}} \parallel [\bar{1}011]_{\text{sap}}$. Epitaxial relationship of AlN film grown on sapphire is controlled by the bonding of Al and O ions at the interface. Interfacial structure has been studied for AlN grown on both orientations of sapphire. In both cases the interface was sharp and without the presence of second phase interfacial layers. AlN films on both orientations of Si were determined to be highly (0001) textured. It has been found that epitaxial AlN films on alignments of $\alpha\text{-Al}_2\text{O}_3(0001)$ can be used for advanced semiconductor devices [2], although the threading dislocation density is about 10^{10} cm^{-2} in the specimens.

ACKNOWLEDGMENT

We are pleased to acknowledge useful discussions with and contributions of Dr. R. D. Vispute.

REFERENCES

1. S. Strite and H. Morkoç, *J. Vac. Sci. Technol. B* **10** (4), 1226 (1992).
2. C.J. Sun, P. Kung, A. Saxler, H. Ohsato, K. Haritos, and M. Razeghi, *J. Appl. Phys.* **75** (8) 3964 (1994).
3. K. Dovidenko, S. Oktyabrsky, J. Narayan, and M. Razeghi, "Microcrystalline and Nanocrystalline Semiconductors." *MRS Proc. Vol. 358*, editors: R.W. Collins, C.C. Tsai, M. Hiros, F. Koch, L. Brus, (1995).
4. W. Meng, J. Heremans, and Y. T. Cheng, *Appl. Phys. Lett.* **59** (17), 2097 (1991).
5. Z. Wei, R. Vargas, T. Goto, Y. Someno, T. Hirai, *Appl. Phys. Lett.* **64** (11), 1359 (1994).
6. R. D. Vispute, J. Narayan, H. Wu, and K. Jagannadham, *J. Appl. Phys.* **77**, 4724 (1995).
7. R. Rodriguez-Clemente, B. Aspar, N. Azema, B. Armas, C. Combescure, J. Durand and A. Figueras, *J. of Crystal Growth* **113**, 59 (1993).
8. K. Dovidenko, S. Oktyabrsky, J. Narayan, and M. Razeghi, *J. Appl. Phys.* (in press, Feb. 15, 1996).
9. K. Dovidenko, S. Oktyabrsky, J. Narayan, (to be published).
10. J. Michel, I. Masson, S. Choux, and A. George, *Phys. Stat. Sol. (a)* **146**, 97, (1994).
11. A. D. Westwood and M. R. Notits, *J. Am. Ceram. Soc.* **74** (6), 1226 (1991).
12. J. Hwang, A.V. Kuznetsov, S.S. Lee, H.S. Kim, J.G. Choi, P.J. Chong, *J. Cryst. Growth* **142**, 5, (1994).

UNDERSTANDING THE PYRAMIDAL GROWTH OF GaN

J.-L. Rouviere*, M. Arlery*, A. Bourret*, R. Niebuhr** and K.-H. Bachem**

* CEA/Grenoble Département de Recherche Fondamentale sur la Matière Condensée/SP2M/LS
17 rue des Martyrs - 38054 Grenoble Cedex 9, France

** Fraunhofer-Institut for Applied Solid State Physics Tullast. 72, 79108 Freiburg i.Br.
Germany

ABSTRACT

By a combination of conventional, HREM and CBED TEM experiments we have studied wurtzite GaN layers grown by Metal-Organic Chemical Vapour Deposition (MOCVD) on (0001)Al₂O₃. We experimentally determine the structure of the macroscopic hexagonal pyramids that are visible at the surface of the layers when no optimised buffer is introduced. These pyramids look like hexagonal volcanoes with one hexagonal microscopic chimney (up to 75nm wide) at their core. The crystal inside the chimney is a pure GaN crystal with a polarity opposed to the one of the neighbouring material : the GaN layers grown on (0001)Al₂O₃ are everywhere Ga-terminated except in the chimneys where they are N-terminated. Some of the N-terminated chimneys grow faster and form macroscopic hexagonal pyramids. Chimneys bounded by Inversion Domains Boundaries (IDBs) originate from steps at the surface of the substrate and may be suppressed by an adapted buffer layer.

INTRODUCTION

Thanks to their optoelectronic properties the III-V nitrides (GaN, AlN and InN) have become economically attracting materials. Simple working devices such as diodes are already made and commercialised [1], but the properties of these materials have not yet been studied thoroughly. For instance, growing GaN layers with a low density of defects has not yet been realised.

In this communication, we present new TEM experimental results that highlight the growth mechanism of GaN layers and should give new clues to improve the quality of the material.

It is well known that GaN tends to have a three-dimensional growth with the appearance of macroscopic hexagonal pyramids. These pyramids have long been observed in CdS [2], but to our knowledge, they have never been really understood. Thanks to a combination of TEM techniques we were able to determine the structure of these macroscopic pyramids and were able to understand their growth mechanism.

EXPERIMENT

We investigated GaN layers grown by MOCVD on (0001) Al₂O₃ substrates at temperature varying from 900°C to 1150°C, with or without a buffer layer of AlN or GaN [3]. In this communication, we mainly focus on the TEM results of samples that exhibit macroscopic hexagonal pyramids at their surface (fig. 1a). Such samples were obtained when we tried to optimise the buffer layer. For these samples, the average full width at half maximum (FWHM) for (0004) beam of X-ray rocking curves is about 18 minutes.

Specimens for TEM were prepared using the standard techniques : mechanical polishing and Argon ion milling. Conventional and HREM TEM observations were realised on a JEOL4000EX electron microscope, specially equipped for HREM (Scherzer resolution about 0.17nm). CBED patterns were obtained with a JEOL2010 field emission gun microscope. CBED simulations were made with the EMS software [4].

RESULTS

State of the art GaN multilayers contain a large density of defects, which are mostly dislocations [5]. However, the characteristic of layers containing pyramids is that they contain both linear defects such as dislocations and planar defects (fig.1). Such planar defects have

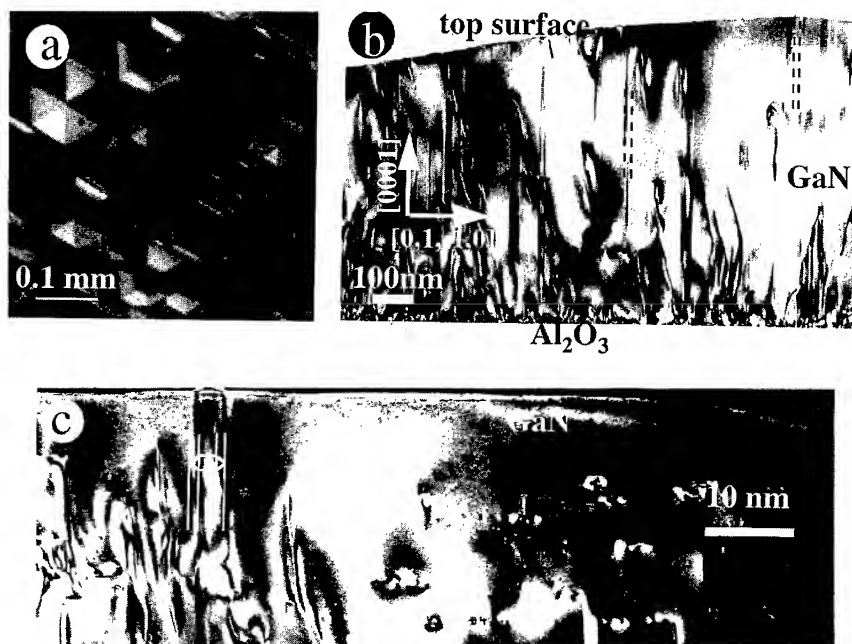


Fig. 1 : a) Image of the surface of a GaN layer ($T_{\text{growth}} = 1150^\circ\text{C}$, GaN buffer layer) made by an optical microscope. Hexagonal pyramids are clearly visible.
 b) Two-beam image of a GaN layer containing the same kind of pyramids ($T_{\text{growth}} = 1000^\circ\text{C}$, no buffer layer) : the layers mainly contains dislocations and b^* -planar defects (the planar defects on the $b^* = \langle 0,1,-1,0 \rangle$ plane form in fact hexagonal chimneys)
 c) Two beam image of the previous sample (viewing direction : $b^* = [0,1,-1,0]$). The top part of the GaN layer is seen. Here we have the chance to cut an hexagonal macroscopic pyramid at its apex. The centre of the macroscopic pyramid contains an hexagonal chimney which has an hexagonal nucleus in top of it.

been commonly reported [6][7]. The most frequent ones are on the c -basal plane and on the $\{0,1,-1,0\}$ planes (denoted b^* -planar defects as the normal of the defect plane is parallel to the basis vector $b^* = [0,1,-1,0]$ of the reciprocal space), but some defects on the $\{2,-1,-1,0\}$ planes (denoted in a similar way, a -planar defects) have also been observed and resolved [6]. As the a -planar defects have been observed only on few samples we refer to reference [6] for a better presentation of these defects. Here, we focus our observations on the b^* -planar defect and its relation to the pyramids.

Observation of these samples in three perpendicular directions (fig. 1c, 2a, 2b) enables to determine that the b^* -planar defects, associated by group of six, form tiny hexagonal chimneys (up to 75 nm in "diameter"). They should be no confusion with nanotubes that people have reported [8] : our chimneys are not empty, but full of GaN material.

The hexagonal form of the chimney appear clearly on HREM images taken along the c -direction (fig. 2a). It can be noticed that the chimney is brighter than the surrounding material. This difference of contrast comes from the preferential etching inside the chimney during TEM specimen preparation : it does not indicate that the chimney is empty. Along the a -direction, only projection of two parallel b^* faces of the hexagonal chimney are seen (fig. 1b, 2b). It can be noticed that the substrate surface (interface $\text{Al}_2\text{O}_3/\text{AlN}$ after growth) contains steps below the

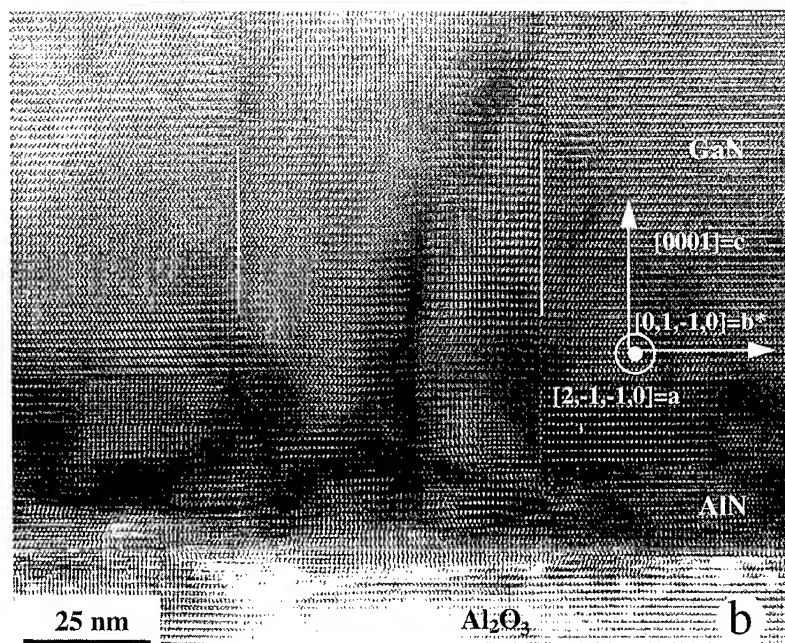
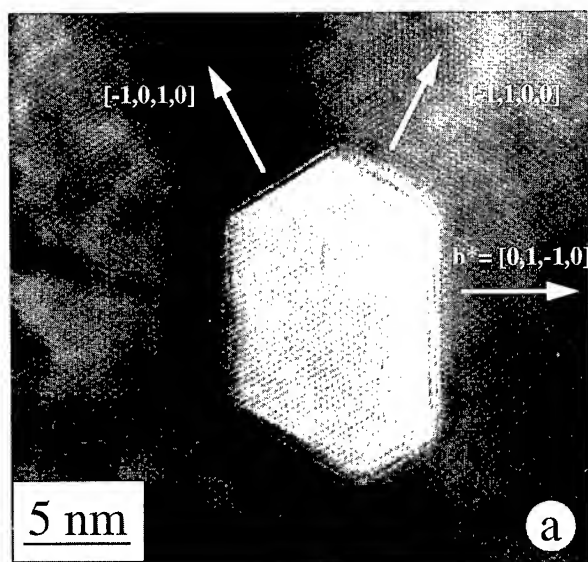


Fig. 2 a) Plan view HREM image of a GaN layer ($T=1000^{\circ}\text{C}$, AlN buffer, viewing direction $c=[0001]$). One tiny hexagonal region that was etched quicker during TEM plan view specimen preparation is shown : this is an non empty hexagonal chimney viewed from above.
 b) HREM image of a cross-section of the same GaN layer seen along the $a=[2,-1,-1,0]$ direction. Along this direction, projections of only two parallel b^* faces of the hexagonal chimney are seen . There is an important step at the substrate surface below the chimney.

chimneys. This is a general observation. Along the $b^*//[0,1,-1,0]$ direction (fig. 1c, 2a), two faces of the chimney are seen inclined. These two inclined faces give a particular contrast in the 2-beam image of fig. 2b. In addition, we cut an hexagonal macroscopic pyramid at its apex : an hexagonal chimney is exactly crossing the apex. In the specific sample of fig. 1c, we also observed a nucleus at the top of all the chimneys. It can be noticed that the top part of the pyramid is rather flat and contains several steps. Statistically, although every pyramid apex is associated with an hexagonal chimney, the inverse is not necessarily true. The hexagonal chimney density could be much larger than the pyramid density, particularly when the pyramid size is large.

Conventional electron diffraction patterns do not reveal any new phases inside the chimneys. No chemical composition difference was detected by EELS between the inside and the outside of the chimneys [9]. In reference [6], the b^* planar defects were tentatively assigned to Inversion Domain Boundaries (IDBs), based on HREM observations. By obtaining Convergent Beam Electron Diffraction (CBED) patterns from inside and outside the chimneys, we are now able to prove that the b^* planar defects are IDBs, implying that the chimney is an Inversion Domain in a GaN matrix (fig. 3). Fig 3a is an experimental CBED pattern taken outside the chimney in a thin area (35nm). For thicknesses around 35nm, the CBED patterns have only coarse details, but one of them is very characteristic as can be seen on the associated simulations : the (0002) spot is brighter than the (0,0,0,-2). We arbitrarily define the positive c direction according to the following convention : the GaN crystal contains Ga-N bonds aligned along the c -axis, the vector starting on Ga and ending on N defines the positive direction of the c -axis (fig. 3ef)]. A careful relationship between TEM electron diffraction and TEM image enables to determine the polarity of the region outside the chimney : the positive c -axis is along the growth direction (fig. 3e). This corresponds to a Ga-terminated surface. The same arguments can be applied inside the chimney (fig. 3bdf). The agreement between the simulated CBED and the

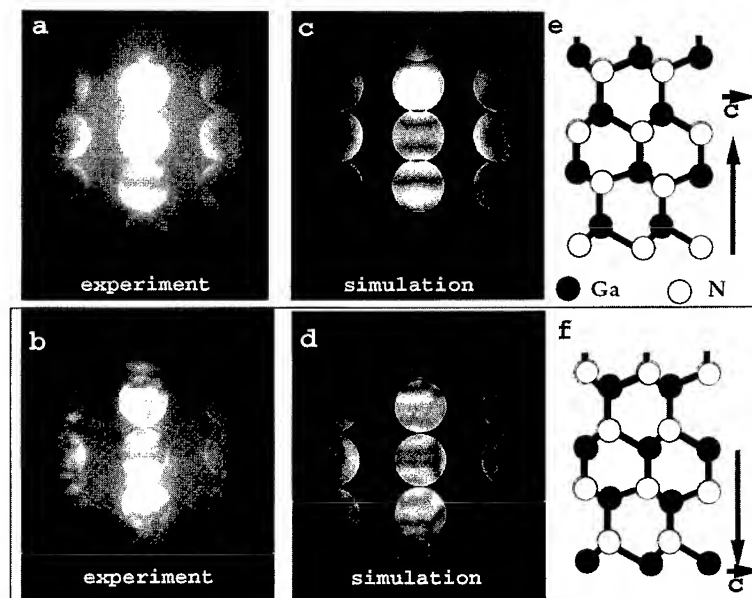


Fig. 3 : Experimental CBED patterns (ab) with their associated simulation (cd) and corresponding crystal structure (ef). Pattern a has been taken outside a chimney (thickness 35nm), whereas pattern b has been taken inside (thickness 70nm). The polarity inside the chimney is opposed to the one outside : chimneys form Inversion Domains in the layer. The chimney is N-terminated (bdf), the outside is Ga-terminated (ace).

experimental data is excellent. The CBED pattern of fig. 3b can only be fitted with a GaN crystal having the positive c-axis in a direction opposed to the growth direction. Therefore the crystal inside a chimney has a N-terminated surface. This result is valid for any hexagonal chimney associated or not to a pyramid apex.

A simple model of the chimney can be constructed without creation of dangling bonds and wrong bonding [9]. Work is in progress to compare this model with HREM images.

CONCLUSIONS

We have now clearly established that :

- (i) at the apex of any macroscopic pyramids (up to 0.1mm wide) there is one tiny hexagonal chimney (up to 75nm in diameter) running from the substrate (or the buffer layer) to the surface
- (ii) the top surfaces of the tiny chimneys (what we call the "inside" top surface of the chimney) are N-terminated while the surface "outside" the chimneys, that is to say most of the surface of the macroscopic pyramids, are Ga-terminated
- (iii) the tiny chimneys are limited by six b*-IDBs
- (iv) the IDBs are nucleated at surface steps.

These results shed some light on the growth process and the pyramid formation. It is a common observation in semiconductor compound epitaxy that the growth velocity is polarity dependant. Depending on the respective velocity of the two species (N or Ga terminated) one would have the three following regimes :

- (i) N-terminated material grows faster : the pyramidal shape is preserved or enhanced during growth
- (ii) N and Ga-terminated materials grow with the same velocity : a flat surface is preserved
- (iii) Ga terminated material grows faster : the chimneys tend to disappear in the surrounding matrix or would form hexagonal holes (may be the nanotubes [8] ?).

We do have observed cases (i) and (ii) after MOCVD growth. The growth velocity itself is controlled by the sticking coefficient of each specie, the surface diffusion and the trapping at steps in the case of a step flow mechanism. A pyramidal shape with N-terminated material in the centre implies a particular mechanism which can be described as follow.

It is well known that N incorporation is difficult during GaN growth [10], because N has a low sticking coefficient or a high evaporation coefficient. Moreover N atoms may diffuse easily on surfaces. Therefore we assume that when pyramidal growth occurs N atoms are preferentially incorporated on N-terminated material (step 2 of fig. 4) and from the chimney they diffuse out (step 3) and are trapped at steps in the surrounding matrix (step 4). It is worth noting that on the so-called N-terminated material, Ga is first incorporated (step 1) and both inside and outside materials have Ga exposed surface. However the new incorporated Ga atoms inside the chimney have 3 dangling bonds instead of one for the Ga atoms outside. As a consequence N atoms are more easily incorporated inside the chimney (step 2). The observations of a tiny nucleus at the top of the chimneys in some cases (fig. 1c) are greatly in favour of our interpretation.

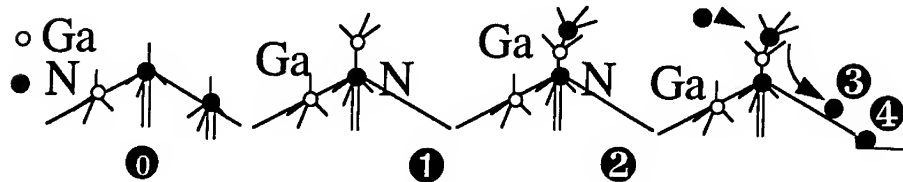


Fig. 4 : Schematic representation of the pyramid growth mechanism.

Step 0 : the surface of the inside of the chimney is N-terminated, outside the chimney the surface is Ga-terminated. Step 1 : a Ga atom is incorporated on the N-terminated surface. Step 2 : a N-atom is incorporated on the Ga atom, inside the chimney, which has 3 dangling bonds. Step 3 : N-atom diffuses out of the chimney. Step 4 : N-atoms are trapped at steps.

Up to now the experimental parameters controlling which regime of growth is active have not been identified. It is clear that such a knowledge will be beneficial, as maintaining always the regime (ii) will preserve a 2D growth. However, it is likely that such a balance is difficult to maintain and would be destroyed by any instability in the experimental parameters. Consequently it is preferable either to avoid the nucleation of N terminated material which seems to be the minority species or to extend it everywhere as it grows faster. Controlling the surface preparation and (or) preparing adequate buffer layer is the way to produce a unipolar layer : this points to further studies on the initial nucleation rate of the different polar species and the exact role of steps.

Independently of the present work , we have established that the same 3D pyramidal growth driven by tiny hexagonal Inversion Domains (the "chimneys", which are full of material) happen in GaN layers grown on Si(111) [11]. We do not see why these type of defects could not be observed in any other kind of substrate like SiC. In any case, the polarity of the GaN layers should be checked carefully.

ACKNOWLEDGEMENTS

Part of this work has been supported by the EU commission under the Brite-Euram II programme (Project BE-7036, BRE2-93-0526). We thank Dr. U. Kaufmann, the coordinator of this European project, and Dr Y. Lu for fruitful discussions. We also thank Dr A. Charai, for his help in obtaining CBED patterns . We should also not forget Dr Stadelmann for his help in simulating CBED patterns.

REFERENCES

1. S. Nakamura, T. Mukai and M. Senoh, Appl. Phys. Lett. **64** 13 (1994)
2. M.H. Christmann, K.A. Jones and K.H. Olsen, J. Appl. Phys. **45**, 4295 (1974)
3. R. Niebuhr, K. Bachem, K. Dombrowski, M. Maier, W. Pletschen and U. Kaufmann submitted to J. Electr. Mat.
4. P.A. Stadelmann, Ultramicroscopy, **21**, 131 (1987).
5. S.D. Lester, F.A. Ponce, M.G. Crawford and D.A. Steigerwald Appl. Phys. Lett. **66**, 1249 (1995)
6. J.-L. Rouviere, M. Arlery, A. Bourret, R. Niebuhr and K. Bachem presented at the 1995 Microscopy of Semiconductor Materials Conference, Oxford, England, 1995 (unpublished)
7. Z. Liliental-Weber, H. Sohn, N. Newman, J. Washburn, J. Vac. Sci. Technol. **B13** (4), 1578 (1995)
8. W. Qian, G.S. Rohrer and M. Showronski presented at the 1995 MRS Fall Meeting, Boston, MA, 1995 (unpublished)
9. J.-L. Rouviere, M. Arlery, A. Bourret, R. Niebuhr and K. Bachem submitted to J. Appl Phys.
10. K. Wang, J. Singh and D. Pavlidis, J. Appl. Phys. **76** (6) 30502 (1994)
11. U. Rossner, J.-L. Rouviere, A. Bourret and A. Barski presented at the 1995 MRS Fall Meeting, Boston, MA, 1995 (unpublished)

ELASTIC CONSTANTS AND RELATED PROPERTIES OF THE GROUP III-NITRIDES

KWISEON KIM, WALTER R. L. LAMBRECHT and B. SEGALL

Department of Physics, Case Western Reserve University, Cleveland, OH 44106-7079

ABSTRACT

The elastic constants of the Group-III nitrides, c-BN, AlN and GaN were calculated from first-principles using the full-potential linear muffin-tin orbital method and local density approximation. The relation between the elastic constants in zincblende and wurtzite is studied by means of a tensor coordinate transformation approach. The latter combined with a correction for the internal displacement of the rotated tetrahedra is found to provide good results for the C_{11}^h , C_{12}^h and C_{44}^h but not for C_{13}^h and C_{33}^h . These two require explicit calculations involving distortions along the c-axis. The calculations also provide information on the transverse optical phonons. By deriving Keating model parameters we show that BN is much stiffer against bond-angle distortions than the other nitrides.

INTRODUCTION

The elastic constants of the Group-III nitrides are of considerable interest for modeling the behavior of thin films of these materials as occurring in heterostructures. Only recently, the latter have been determined by using accurate sound velocity measurements for BN [1], AlN [2, 3] and GaN [4]. In spite of the large number of total energy calculations on these materials, only a few calculations have appeared on the elastic constants. Ruiz et al. [5] calculated the elastic constants of AlN using a Hartree-Fock approach. Rodriguez-Hernandez et al. [6] recently calculated the elastic constants of cubic BN (and BP) using the first-principles pseudopotential plane wave method.

In this paper we present the elastic constants for cubic BN and those for both zincblende and wurtzite GaN and AlN and the relations between them.

COMPUTATIONAL METHOD

The method used for our calculations is the full-potential linear muffin-tin orbital method as described by Methfessel [7]. The underlying framework for the total energy calculations is the local density functional theory [8] and elastic constants are obtained as second derivatives of the total energy curve as a function of suitably chosen strain distortions. We used well converged triple κ muffin-tin orbital basis sets up to d -waves in all three κ values (ddd for short) for zincblende and a fdp basis set for the wurtzite with an additional s orbital included on the large empty spheres. The Brillouin zone summations were carried out with 10 special points for zincblende and 36 for wurtzite. The muffin-tin sphere radii were chosen to be nearly touching and kept fixed during the calculations with distortions so as not to change the volume of the interstitial region. However, for distortions along the c -axis of the wurtzite structure (c/a distortions) we allowed the small empty sphere (centered in between cation and anion in the opposite direction of the bond along the c -axis) to vary in size so as to maintain an accurate interpolation in the local interstitial region.

RELATIONS BETWEEN THE ELASTIC CONSTANTS

For zincblende, we calculate the bulk modulus $B = (C_{11}^c + 2C_{12}^c)/3$ directly by applying a hydrostatic strain, the tetragonal shear modulus $C_s^c \equiv (C_{11}^c - C_{12}^c)/2$ by means of a volume conserving strain along [001], and the trigonal shear modulus C_{44}^c by a volume conserving strain along [111]. For the latter, it is necessary to relax the relative displacement of the anion and cation for each distortion as defined by the Kleinman ζ parameter. The equation

$$C_{44}^c = C_{44}^{c0} - \Omega^{-1} \mu [\omega_{TO}^{T_2} \zeta (a/4)]^2, \quad (1)$$

provides a well-known relation between the elastic constants with and without internal relaxation (indicated by superscript 0), the transverse optical phonon frequency $\omega_{TO}^{T_2}$ and ζ . Here, Ω is the unit-cell volume, a is the cubic lattice constant and μ is the reduced mass. From the above relations, we obtain the complete cubic elasticity tensor and the related quantities mentioned.

Similarly, we derived a relation for the wurtzite structure between the shear elastic constant corresponding to a volume conserving strain along the hexagonal c-axis,

$$C_s^h \equiv C_{33}^h - 2C_{13}^h - (C_{11}^h + C_{12}^h)/2, \quad (2)$$

the A_1 transverse optical phonon frequency $\omega_{TO}^{A_1}$, and a new internal displacement parameter $\xi = du_{min}/d(c/a)$, where $uc = d$ is the bond length along the c-axis:

$$C_s^h = C_s^{h0} - \Omega^{-1} \mu [(3/2) \omega_{TO}^{A_1} \xi c(c/a)]^2. \quad (3)$$

The above elastic constant is essentially obtained in the process of relaxing the total energy $E[\Omega, c/a, u]$ of the wurtzite crystal. For a fixed volume Ω and c/a we first minimize the energy with respect to the u parameter giving $E[\Omega, c/a, u_{min}]$. Then we minimize the latter as a function of c/a providing $E[\Omega, (c/a)_{min}, u_{min}]$ and finally we obtain the global minimum of the latter as a function of volume. From the curvature of the first total energy curve we obtain the A_1 phonon frequency at particular Ω and c/a , from the curvature of the second, we obtain the elastic constant C_s^h at particular volume, and from the final one we obtain the bulk modulus. Finally, we can then obtain the phonon frequency and elastic constants at the equilibrium volume by interpolation to the appropriate volume. We note that although $E[\Omega, c/a, u]$ varies most rapidly as a function of Ω , then as a function of c/a and finally as a function of u , the minimizations are not independent of each other. By varying c at fixed value of a , (i.e with varying volume) on the other hand, we obtain directly the elastic constant C_{33}^h .

For the remaining hexagonal elastic constants, we should in principle consider strains distorting the hexagonal symmetry. Instead we use relations between the elastic constants of zincblende and those of wurtzite obtained by rotating the cubic elasticity tensor to a new set of coordinates with the z-axis along the [111] direction. Since the latter resembles the [0001] axis of wurtzite, the cubic elastic constants tensor viewed as that of a trigonal symmetry system provides a first approximation for that of wurtzite. Martin [13] derived a correction to this simple rotation approach by taking into account the difference in the relative positions of the cations and anions in the tetrahedra in zincblende and wurtzite, which are twinned with respect to each other. The correction term is determined by minimizing the elastic energy with respect to the associated internal strain. This leads to

Table I: Elastic constants and related properties. (Experimental values between parentheses).

	BN	AlN	GaN
	zincblende		
C_{11}^c (GPa)	837 (820 ^a)	304	296
C_{12}^c (GPa)	182 (190 ^a)	152	154
C_{44}^c (GPa)	493 (480 ^a)	199	206
B (GPa)	400	203	201
ζ	0.1	0.6	0.5
$\omega_{TO}^{T_2}$ (cm ⁻¹)	1070 (1060 ^b)	680	580 (556 ^c)
	wurtzite		
C_{11}^h (GPa)	398 (345, ^d 411 ^e)	396 (391 ^f)	
C_{12}^h (GPa)	140 (125, ^d 149 ^e)	144 (143 ^f)	
C_{44}^h (GPa)	96 (118, ^d 125 ^e)	91 (103 ^f)	
C_{13}^h (GPa)	127 (120, ^d 99 ^e)	100 (108 ^f)	
C_{33}^h (GPa)	382 (395, ^d 389 ^e)	392 (399 ^f)	
B (GPa)	218	207	
ξ	0.12	0.11	
$\omega_{TO}^{A_1}$ (cm ⁻¹)	610 (614 ^d)	570 (532 ^g)	

^a Grimsditch et al. et al. [1]

^b Alvarenga et al. [9]

^c Murugkar et al. [10]

^d McNeil et al. [2]

^e Tsubouchi et al. [3]

^f Polian et al. [4]

^g Perlin et al. [11]

the following relation between the elastic constants of wurtzite and zincblende:

$$\begin{pmatrix} C_{11}^h \\ C_{12}^h \\ C_{13}^h \\ C_{33}^h \\ C_{44}^h \\ C_{66}^h \end{pmatrix} = \frac{1}{6} \begin{pmatrix} 3 & 3 & 6 \\ 1 & 5 & -2 \\ 2 & 4 & -4 \\ 2 & 4 & 8 \\ 2 & -2 & 2 \\ 1 & -1 & 4 \end{pmatrix} \begin{pmatrix} C_{11}^c \\ C_{12}^c \\ C_{44}^c \end{pmatrix} - \begin{pmatrix} D/\bar{C}_{44}^h \\ -D/\bar{C}_{44}^h \\ \\ D/\bar{C}_{66}^h \\ D/\bar{C}_{44}^h \end{pmatrix}, \quad (4)$$

where the \bar{C}_{ij}^h are the values obtained without the second term (corresponding to rotation only), $D = (2/9)(C_s^c - C_{44}^c)^2$ and $C_{66}^h = (C_{11}^h - C_{12}^h)/2$.

We will show that that this relation leads to a good agreement with experimental values for AlN and GaN when the correction is taken into account, except for C_{13}^h and C_{33}^h which are in fact, unaffected by this internal strain correction but are affected by non-ideal c/a and its distortions. Our procedure then is to obtain C_{11}^h , C_{12}^h and C_{44}^h from Eq.(4), and C_s^h and C_{33}^h by direct calculations as explained above and finally use the defining Eq.(2) of C_s^h to obtain C_{13}^h . The relation $B^h = C_{33}^h(C_{11}^h + C_{12}^h) - 2(C_{13}^h)^2/2C_s^h$ then provides a check of

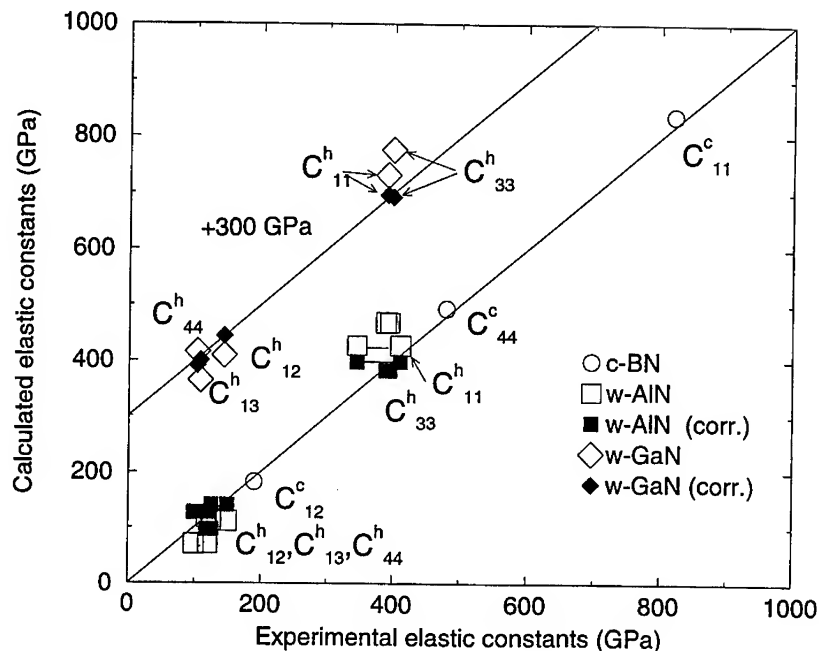


Figure 1: Correlation of calculated elastic constants of c-BN, w-AlN and w-GaN with experimental data (From Refs. [1, 2, 3, 4]). The open symbols represent the values without internal strain correction for C_{11}^h , C_{12}^h and C_{44}^h and without c/a , u relaxation for C_{13}^h and C_{33}^h . For AlN, the two sets of experimental data are joined by horizontal lines. For GaN, the results were shifted up by 300 GPa so as not to overlap with the AlN data.

the direct bulk modulus calculations.

RESULTS

Our results for the elastic constants of c-BN, and zincblende and wurtzite AlN, and GaN and some related properties mentioned above are shown in Table I. Fig. 1 shows a comparison with experimental data and also shows the values obtained in the simple rotation model (without Martin's correction) for C_{11}^h , C_{12}^h and C_{44}^h and the values obtained for C_{13}^h and C_{33}^h from the tensor transformation approach as opposed to the direct calculation. We may see that both Martin's correction and the explicit inclusion of non-ideal c/a improve the agreement with experiment significantly.

Our calculations for c-BN are in good agreement with those of Rodriguez-Hernandez et al. [6] who obtain $C_{11}^c = 844$, $C_{12}^c = 190$ and $C_{44}^c = 483$ GPa. The phonon frequencies are in good agreement with experimental data obtained from Raman scattering and other calculations. See e.g. Gorczyca et al. [12] for other recent calculations and a compilation

of experimental values for GaN and AlN. The elastic constants of c-BN are seen to be much higher than the corresponding ones for the other nitrides and, in fact, are rather close to those of diamond. We recall that the experimental elastic constants of diamond are $C_{11}^c = 1076$, $C_{12}^c = 125$ and $C_{44}^c = 577$ GPa [14] while calculated with the same method as used here [15] the values are respectively 1107, 152 and 534 GPa. The elastic constants of AlN and GaN are rather close to those of SiC which for the cubic form are $C_{11}^c = 420$, $C_{12}^c = 126$ and $C_{44}^c = 287$ GPa [16]. This is not surprising because BN and diamond both contain only elements of the second row of the periodic table while SiC and AlN contain one element of the second and one of the third row. As usual there is only a small difference between Ga and Al in terms of bonding properties. In both cases, (BN, diamond) and (SiC, AlN, GaN), the III-V's appear to have slightly lower C_{11}^c and higher C_{12}^c , which implies a smaller shear modulus C_s^c . Consistent with this, C_{44}^c is also smaller. The bulk moduli of the III-V's are also slightly smaller. We note in passing that for hexagonal SiC, the internal strain corrections of Martin are negligibly small.

From the elastic constants and experimental LO-TO phonon splittings [17], we obtain the force constant parameters of the well-known Keating model [18, 19]. The obtained values are given in Table II. The values of β/α indicate the relative importance of bond-bending stiffness over bond-stretching stiffness. We note that BN has a high value of β/α , a property which is shared with diamond. This is also the reason why ζ is low for this material. The strong resistance against bond-bending in diamond has also been observed in diamond-like amorphous carbon materials with high sp^3 content and may thus also be expected to play a role in amorphous BN.

Table II: Keating model parameters.

	BN	AlN	GaN
α (N/m ²)	139.6	98.0	96.3
β (N/m ²)	57.6	15.0	14.8
β/α	0.41	0.15	0.15

CONCLUSIONS

First-principles calculation results were presented for the elastic constants of the Group-III nitrides, c-BN, wurtzite and zincblende AlN and GaN. The relationship among them is clarified. Good agreement was obtained with recent experimental results for c-BN, w-AlN and w-GaN. We note that the elastic properties of c-BN resemble those of diamond rather than those of the other nitrides, in particular, in its strong resistance to bond-bending and the much higher values of the bulk modulus. The elastic constants of AlN and GaN on the other hand are close to those of SiC. In both cases, the III-V compounds have slightly lower bulk and shear moduli than the corresponding group IV element or compound.

Acknowledgements

We thank Dr. Grimsditch for making available his experimental values for GaN prior to publication and Dr. A. G. Petukhov for helpful discussions. This work was supported by the National Science Foundation under grant No. DMR92-22387. K. Kim was supported by a Korean Government Fellowship.

REFERENCES

1. M. Grimsditch, E. S. Zouboulis and A. Polian J. Appl. Phys. **76** 832 (1994).
2. L. E. McNeil, M. Grimsditch, and R. H. French, J. Am. Ceram. Soc. **76**, 1132 (1993).
3. K. Tsubouchi and N. Mikoshiba, IEEE Trans. Sonics Ultrason. **SU-32**, 634 (1985).
4. A. Polian, M. Grimsditch, and I. Grzegory J. Appl. Phys., to be published.
5. E. Ruiz, S. Alvarez, and P. Alemany, Phys. Rev. B **49**, 7115 (1994).
6. P. Rodriguez-Hernández, M. González-Díaz, and A. Muñoz, Phys. Rev. B **51**, 14705 (1995).
7. M. Methfessel, Phys. Rev. B **38**, 1537 (1988).
8. P. Hohenberg and W. Kohn, Phys. Rev. **136**, B864 (1964); W. Kohn and L. J. Sham, *ibid.* **140**, A1133 (1965).
9. A. D. Alvarenga, M. Grimsditch, and A. Polian, J. Appl. Phys. **72**, 1955 (1992).
10. S. Murugkar, R. Merlin, T. Lei and T. D. Moustakas, Bull. Am. Phys. Soc. **37**, 556 (1992).
11. P. Perlin, C. Jaubertie-Carillon, J. P. Itie, A. San Miguel, I. Grzegory, and A. Polian, Phys. Rev. B **45**, 83 (1992).
12. I. Gorczyca, N. E. Christensen, E. L. Peltzer y Blanca, and C. O. Rodriguez, Phys. Rev. B **51**, 11936 (1995).
13. R. M. Martin, Phys. Rev. B **6**, 4546 (1972).
14. Landolt-Börnstein Numerical Data and Functional Relationships, edited by O. Madelung, New Series, Vol. 22a (Springer, New York, 1987).
15. H. Polatoglou and M. Methfessel, Phys. Rev. B **41**, 5898 (1990).
16. W. R. L. Lambrecht, B. Segall, M. Methfessel, and M. van Schilfgaarde, Phys. Rev. B **44**, 3685 (1991).
17. Properties of Group III Nitrides, edited by J. H. Edgar, Electronic Materials Information Service (EMIS) Datareviews Series (Institution of Electrical Engineers, London 1994).
18. P. N. Keating, Phys. Rev. **145**, 637 (1966).
19. R. M. Martin, Phys. Rev. B **1**, 4005 (1970).

ANALYSIS OF STRAIN IN GaN ON Al₂O₃ AND 6H-SiC: NEAR-BANDEDGE PHENOMENA

N. V. EDWARDS,* M. D. BREMSER,* T. W. WEEKS, Jr,* R. S. KERN,* H. LIU,#† R. A. STALL,# A. E. WICKENDEN,‡ K. DOVERSPIKE,†‡ D. K. GASKILL,‡ J. A. FREITAS, Jr.,§ U. ROSSOW,** R. F. DAVIS,* and D. E. ASPNES**

*Department of Materials Science and Engineering, N. C. State University, Raleigh, NC 27695-7907

#EMCORE Corp., Somerset, NJ 08873

†Presently at Hewlett-Packard, San Jose, CA 95131

‡Naval Research Laboratory, Washington, DC 20375

§Sachs-Freeman Associates, Landover, MD 20785-5396

**Department of Physics, N. C. State University, Raleigh, NC 27695-8202

ABSTRACT

We report the dielectric functions of various GaN samples as measured by spectroscopic ellipsometry. Structure related to the A and B excitons is resolved at room temperature, in principle allowing strain to be assessed. However, the data indicate that dead-layer and dispersion effects are present, preventing a simple interpretation. We discuss various complications including the Edn/dE contribution to dispersion, which is important for laser action. Our data appear to indicate that the spin-orbit splitting of GaN is about 15 meV, somewhat larger than the currently accepted value of about 11 meV.

INTRODUCTION

GaN and related materials are emerging as promising candidates for short-wavelength photonic applications. In contrast to their III-V counterparts, these materials are relatively ionic, crystallizing in the wurtzite structure and hence showing properties more nearly related to II-VI materials such as CdS. Unlike these materials, however, which have seen the successful development of ZnSe substrates, bulk single-crystal nitride material does not yet exist on a commercial scale, making homoepitaxy still unrealized. Strain becomes especially important in these materials and it is almost unavoidable in the thin multilayers required for device applications.

The objective of the present work is to quantify residual strain in GaN films that are grown on Al₂O₃ or 6H-SiC substrates. To do this systematically we have used spectroscopic ellipsometry (SE) to determine the optical response of 28 samples from 3 different sources. The results are complicated, with the overall lineshape being determined by various combinations of dispersion effects of the refractive index, absorption edges related to the dominant A and B thresholds, and the presence of a so-called "dead layer" at the surface, which is a region near the surface where the discrete exciton lines are broadened such that they do not contribute to the observed optical structure. The message is clear: before an unambiguous interpretation of the lineshapes is possible, a detailed understanding of these effects is required.

EXPERIMENT

Data were obtained on a rotating-analyzer ellipsometer. Instrumentation [1] and sample preparation techniques [2] have been described elsewhere. Spectra were taken either from 1.5 to 5.75 eV with a resolution of 17 meV at 3.4 eV or from 3.3 to 3.6 eV with a resolution of 2 meV at 3.4 eV. Since SE spectra are weighted only by the density of states and not by the product of density of states and the thermal occupancy factor, we can readily use the technique to resolve the A and B thresholds at room temperature. Samples were grown on Al₂O₃ and 6H-SiC substrates by organometallic chemical vapor deposition under various conditions [3-5].

RESULTS AND DISCUSSION

Representative broadband and high resolution spectra are shown in Figs. 1 and 2, respectively. The broadband spectrum is qualitatively similar to those obtained by Logothetidis et al. [6]. Our data are presented in pseudodielectric function form, i.e., the complex reflectance ratio

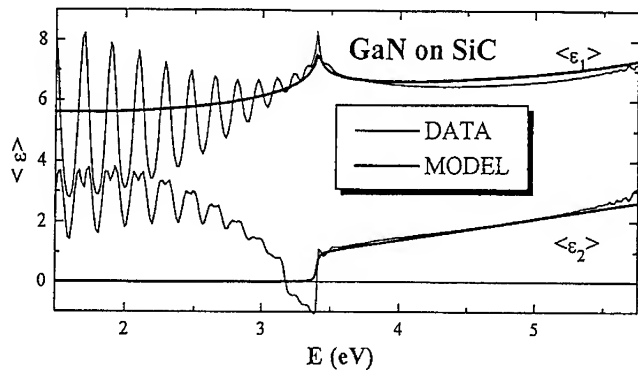


Fig. 1. Pseudodielectric function of a 1.32 μm thick GaN film on a 6H-SiC substrate. These data are approximated by a model calculation where $\langle \epsilon_2 \rangle$ consists of a broadened unit step edge followed by a linear ramp.

Fig. 2. Imaginary part of the pseudodielectric function of GaN layers grown on Al_2O_3 (upper) and 6H-SiC (lower). The spectra were taken with a resolution of 2 meV.

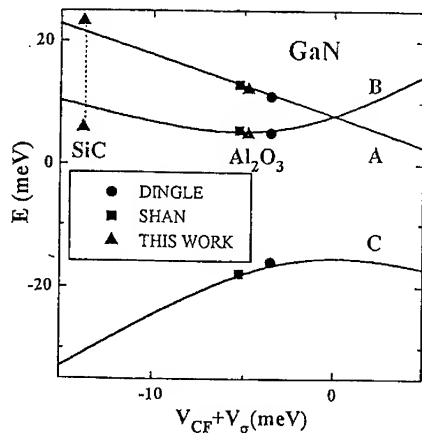
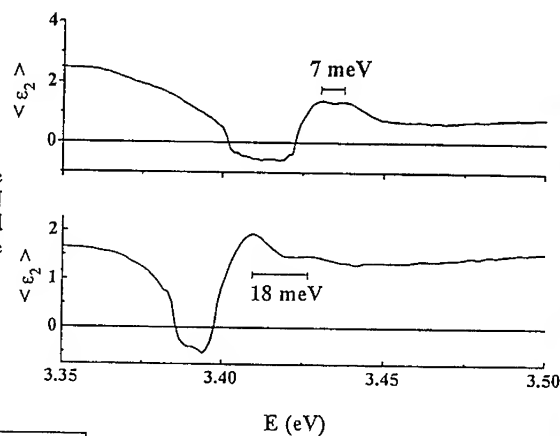


Fig. 3. Calculated variation of the A, B, and C absorption thresholds relative to the top of the valence band as a function of crystal-field and biaxial stress potentials. A spin-orbit splitting of 15.5 meV was used.

ρ that is actually measured by ellipsometry was converted into a pseudo or apparent dielectric function $\langle \epsilon \rangle = \langle \epsilon_1 \rangle + i\langle \epsilon_2 \rangle$ by means of the two-phase (substrate/ambient) model. The spectrum of Fig. 1, which was obtained on a 1.32 micron thick GaN film deposited on 6H-SiC, exhibits characteristic interference oscillations in the region of transparency below the fundamental absorption edge at 3.4 eV, relatively sharp structure in both $\langle \epsilon_1 \rangle$ and $\langle \epsilon_2 \rangle$ at the edge, and a nearly linearly increasing behavior in $\langle \epsilon_2 \rangle$ above the edge. Also shown in Fig. 1 is an approximate analytic representation of the lineshape that will be described below. Figure 2 provides a more detailed view of the variation of $\langle \epsilon_2 \rangle$ with energy in the vicinity of the absorption edge for two samples, a 3.27 μm thick GaN layer grown on Al_2O_3 (upper) and a 1.45 μm thick GaN layer grown on SiC (lower). Here, the fine structure due to the A and B thresholds is evident, with splittings of about 7 and 18 meV, respectively, in the two cases.

We consider first the implications of the A-B splittings shown in Fig. 2. The energy variations of the A, B, and C thresholds can be described in the quasicubic model [7] in terms of 3 parameters: the spin-orbit splitting energy V_{so} , the crystal-field potential V_{cf} , and the rhombohedral strain parameter V_{σ} . The dependence of these threshold energies on these three parameters have been given by Pollak and Cardona [8]. In essence, in the quasicubic model the effect of hexagonal symmetry is described as a deformation of the cube along the [111] direction. Thus for uniform biaxial strain in the plane of the film V_{cf} and V_{σ} are additive, and the results can be expressed in terms of the sum of these two terms. These observations open up the possibility of band structure engineering through the intentional variation of in-plane strain.

Calculated variations of the energies of the A, B, and C thresholds with respect to the top of the unperturbed valence band of the equivalent cubic material are shown as a function of the sum ($V_{\text{cf}} + V_{\sigma}$) in Fig. 3, along with the A-B splitting data of Fig. 2 and the A-B and A-C splitting data of Dingle et al. [9] and Shan et al. [10]. We note that the variation of these bands is completely equivalent to that of the valence bands along [111] as calculated by $k \cdot p$ perturbation theory except for scaling factors. Thus when $E_A = E_B$ the separations $(E_A - E_C) = (E_B - E_C)$ are equal to $(3/2)V_{\text{so}}$, whereas in the limit of large negative ($V_{\text{cf}} + V_{\sigma}$) the A-B splitting ($E_A - E_B$) becomes equal to V_{so} directly. As with the cubic equivalents, the spin-orbit-split band lies below the other two at the crossover point.

The above discussion is appropriate because the value of V_{so} that is consistent with our data and those of Dingle et al. [9] and Shan et al. [10] is 15.5 meV, somewhat larger than the value of 11 meV reported by Dingle et al. but still within their experimental uncertainty. Some ambiguity arises from the fact that V_{so} can be obtained from the energy separations $(E_A - E_B)$ and $(E_A - E_C)$ only by solving a quadratic expression, which necessarily has two roots. In particular, in the absence of an exact knowledge of $V_{\text{cf}} + V_{\sigma}$ the data of the previous workers can be described by choosing V_{so} equal either to 9 or 15.5 meV. The latter value was used to generate Fig. 3. If one has available only material grown on sapphire it is not possible to resolve this ambiguity; indeed, this ambiguity appears not to have been recognized previously. However, if additional data are available, for example for GaN grown on SiC, as is the case here, this uncertainty can be reconciled. Using the fact that $(E_A - E_B)$ must approach V_{so} for large ($V_{\text{cf}} + V_{\sigma}$) it is apparent that our results are consistent with the theoretical calculation only if the larger root, 15.5 meV, is chosen. These larger A-B splittings are observed not only in our own data on 1.4 μm thick GaN films on SiC, which have not yet relaxed via misfit dislocation formation, but also from splittings obtained independently by Schetzina et al. [11] and Redwing et al. [12]. These samples were all apparently under sufficient tension to yield A-B splittings of the order of 16 to 18 meV, inconsistent with the 9 meV root but in agreement with the 15.5 meV root. Further discussion will be given elsewhere.

We now consider the spectrum shown in Fig. 1. There are three points to be made. (1) As indicated by the model calculation, the general character of the data can be represented approximately by an ϵ_2 variation that consists of a broadened unit step function followed by a linear ramp at higher energy. This is an analytic representation for which the Kramers Kronig integral used to generate ϵ_1 can also be evaluated analytically. Note that this expression does not explicitly contain an $n = 1$ exciton contribution, which explains some of the discrepancies between the data and the representation. (2) The interference oscillations in the transparent region of the

spectrum have an energy spacing ΔE that decreases progressively as one approaches the bandedge. (3) The negative value of ϵ_2 seen near the bandedge can be understood in terms of an excitonic dead layer, which is discussed in more detail below.

We consider first points (1) and (2), which are relevant to the spacing of laser modes in a resonant cavity, since these are also defined in terms of 2π increments of the round-trip phase and therefore mimic the spacing of the interference oscillations. The connection is established by the expression for the energy derivative of the round-trip phase:

$$\Delta\theta = \frac{4\pi d}{hc} \left(n + E \frac{dn}{dE} \right) \Delta E, \quad (1)$$

where d is the film thickness, n is the index of refraction, and E is the photon energy. From this expression it is evident from the data of Fig. 1 that the existence of dispersion and a large Edn/dE term means that the mode spacing of a laser with a GaN active region will be unevenly spaced, to the extent that the mode is localized in the GaN material. The model calculation of Fig. 1 shows that this effect is exaggerated in GaN because of the linearly increasing nature of ϵ_2 above threshold, which acts to enhance the absolute value of Edn/dE just below threshold relative to its value above threshold. To illustrate the relative magnitudes of n and Edn/dE we plot both as a function of E in Fig. 4. The derivative term shows a rapid increase as E approaches E_g and becomes much larger than n , which manifests itself in the compression of the interference oscillations mentioned above. This behavior can be quite surprising if the index of refraction is incorrectly evaluated from Eq. (1) with the derivative term neglected, as is often done. This omission is ordinarily of little consequence because the derivative term is typically quite small. However, this is clearly not the case for the nitrides.

We next consider point (3). More generally, many of the 28 lineshapes appeared remarkably similar, even for samples obtained from different sources obtained under different growth conditions. A selection of some of the observed shapes is shown in Fig. 5. Note that approximately 5 samples had lineshapes similar to that labeled as I; 3 were similar to II; 14 were similar to III; and 4 were similar to IV. Two samples were of insufficient quality to obtain any near-bandedge structure at high resolution. While the observed lineshapes departed from the "expected" lineshape for a material with three excitonic band edges, the marked similarities between the shapes prompted further investigation. It was these similarities between ostensibly different samples that suggested the involvement of an excitonic dead layer. This concept was used by previous workers to explain the deformation of reflectance lineshapes in CdS [13].

Comparing spectra shown in Fig. 5, differences include apparent variations in oscillator strength of the A and B structures. We attribute part of this variation to the transfer of oscillator strength that results from band mixing driven by in-plane strain, although the complete variation cannot be explained by this effect. Another contribution can arise from the dead layer, which refers to a region of material adjacent to the surface where the discrete exciton lines are broadened either intrinsically because the center of mass lies too close to the surface for the exciton to exist without serious deformation or extrinsically because of damage to the surface or the presence of a surface electric field. Such surface fields usually result from pinning the surface Fermi level due to surface states. In the former case the thickness of the dead layer is the diameter of the exciton, but in the latter case the thickness varies with surface pinning, bulk doping, and degree of surface damage.

We illustrate the type of behavior that can be expected from dead-layer effects by the set of calculated lineshapes shown in Fig. 6. Here, the model ϵ_2 spectrum of Fig. 1 was supplemented by a broadened Lorentzian at 20 meV below the unit step to represent the $n = 1$ exciton line, and the pseudodielectric function was calculated in the three-phase (substrate/overlayer/ambient) model for a substrate containing the $n = 1$ structure and an overlayer without this structure. It can be seen immediately that with increasing dead layer thickness the apparent relative strengths of the $n = 1$ and edge structures changes and that under proper conditions $\langle \epsilon_2 \rangle$ is driven to negative values, as seen in Fig. 1, and returns to a shape close to the original at 700 Å. The results provide a caveat for the assessment of strain from near-bandedge features as well. While it would be

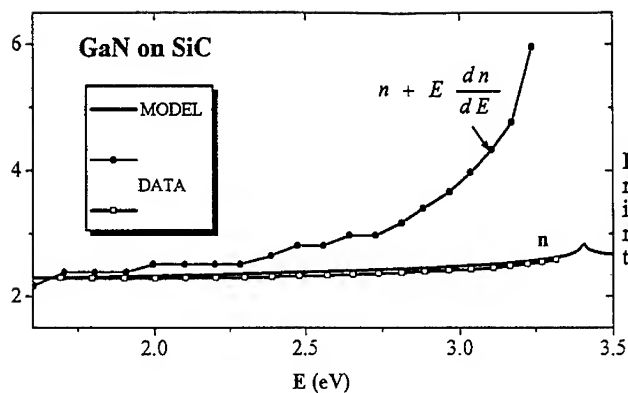


Fig. 4. Dispersion of the refractive index n and n plus its derivative of GaN with respect to energy in the transparent region.

Fig. 5. Representative selection of observed $\langle \epsilon_2 \rangle$ lineshapes of GaN in the vicinity of the fundamental absorption threshold.

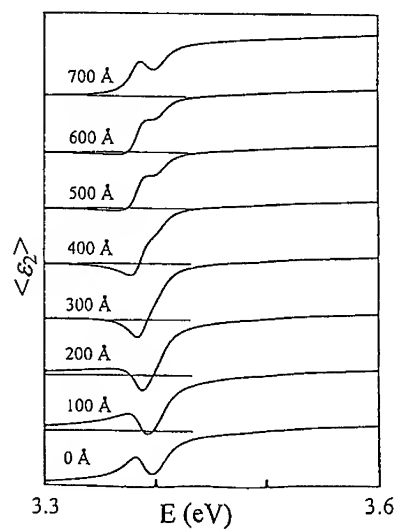
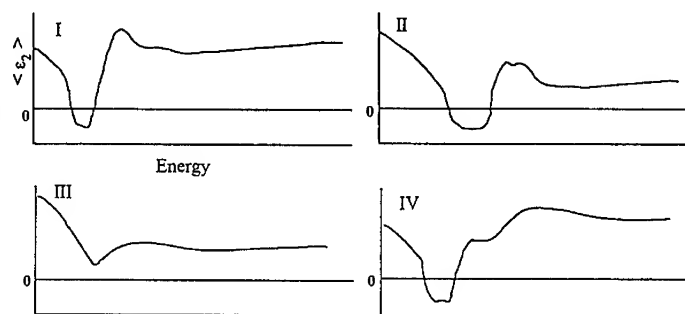


Fig. 6. Model calculation of $\langle \epsilon_2 \rangle$ spectra as a function of increasing dead-layer thickness.

tempting to assign the two features shown in Fig. 6 (for the case of 500 and 600 Å of dead layer) as A and B thresholds, these structures are actually due to the $n = 1$ exciton and continuum threshold of the same edge. Consequently, in any assessment of strain it is clearly important to first obtain an understanding of the lineshapes, and, as indicated by the results shown in Fig. 3, to obtain the C structure as well. Work toward these ends is in progress.

CONCLUSION

A quantitative assessment of strain will require a detailed interpretation of the lineshapes, which are clearly affected by factors in addition to strain, including excitonic dead layers and dispersion effects. In the latter case, the role of n plus its derivative near the bandedge is now well understood, and data showing their dispersion is presented. In the former case, groupings of samples with similar lineshapes are observed and explaining such variations in ostensibly different samples with an excitonic dead layer looks promising.

ACKNOWLEDGMENT

This work was supported by the Office of Naval Research under Contract nos. N00014-92-J-1720, N00014-92-J-1477, N00014-93-0255, N00014-93-G02227, and the Alexander on Humboldt Foundation.

REFERENCES

1. D. E. Aspnes and A. A. Studna, *Appl. Opt.* **14**, 220 (1975).
2. N. V. Edwards, M. D. Bremser, T. W. Weeks, Jr., R. S. Kern, R. F. Davis, and D. E. Aspnes (submitted for publication).
3. T. W. Weeks, Jr., M. D. Bremser, K. S. Ailey, E. Carlson, W. G. Perry, and R. F. Davis, *Appl. Phys. Lett.* **67**, 401 (1995).
4. EMCORE Corporation, Somerset, NJ 08873.
5. L. B. Roland, K. Doverspike, A. Giordana, M. Fatemi, D. K. Gaskill, M. Skowronski, and J. A. Freitas, Jr., *Institute of Physics Conf. Series* 137, ed. by M. G. Spencer, R. P. Devaty, J. A. Edmond, M. Asif Khan, R. Kaplan, and M. Rahman, p. 429 (1994).
6. S. Logothetidis, J. Petalas, M. Cardona, and T. D. Moustakas, *Phys. Rev.* **B50**, 18017 (1994); J. Petalas, S. Logothetidis, S. Bouladakis, M. Alouani, and J. M. Willis, *Phys. Rev.* **B52**, 8082 (1995).
7. J. J. Hopfield, *J. Phys. Chem. Solids* **15**, 97 (1960).
8. F. H. Pollak and M. Cardona, *Phys. Rev.* **172**, 816 (1968).
9. R. Dingle, D. D. Sell, S. E. Stokowski, and M. Ilegems, *Phys. Rev.* **B4**, 1211 (1971).
10. W. Shan, T. J. Schmidt, X. H. Yang, S. J. Hwang, J. J. Song, and B. Goldenberg, *Appl. Phys. Lett.* **66**, 985 (1995).
11. W. C. Hughes, W. H. Rowland, Jr., and M. A. L. Johnson, S. Z. Fujita, J. W. Cook, Jr., J. F. Schetzina, J. Hren, and J. A. Redmond, *J. Vac. Sci. Technol.* **B15**, 1571 (1995).
12. J. M. Redwing, M. A. Tischler, D. A. Loeber, and N. G. Anderson, presented at the 1995 MRS Spring meeting, San Francisco, CA, 1995 (unpublished).
13. J. J. Hopfield and D. G. Thomas, *Phys. Rev.* **132**, 563 (1963); F. Evangelisti, A. Frova, and F. Patella, *Phys. Rev.* **B10**, 4253 (1974).

STRAIN EFFECTS IN GaN ON SAPPHIRE: TOWARDS A QUANTITATIVE COMPREHENSION

O.BRIOT, J.P. ALEXIS, B.GIL and R.L.AULOMBARD

CNRS-GES - Université de Montpellier II, C.C. 074 Place E.Bataillon, 34095 Montpellier Cedex 5 -France

ABSTRACT

We present here a detailed investigation of the optical properties of GaN epilayers grown by low pressure MOVPE on sapphire substrates, using 2K photoluminescence as well as 2K reflectance spectroscopy. A large series of samples has been grown under eclectic conditions (V/III ratio, growth temperature, nitridation steps,...) which allows us to propose the first semi-quantitative investigation of the sample-dependent band gap energies. This dependence of the bandgap is analyzed in terms of i) residual stress, ii) exciton parameters and iii) deformation potential characteristics of the A, B, C excitons. the residual stress cannot be simply explained in terms of the differences between the thermal expansion coefficients of the various compounds, but are strongly correlated to the V/III growth ratio imposed during the growth, and subsequently to the influence of this parameter at the scale of electronic and structural characteristics of the deposited layers.

CRYSTAL GROWTH AND EXPERIMENTS

Spectroscopic data and their analysis were taken from GaN epilayers grown by MOVPE on sapphire. A thin GaN buffer layer was grown at low temperature (~600°C) on the nitridated substrate and recrystallized before to proceed to the high temperature (between 980°C and 1010°C) growth of the GaN epilayers having device-type electronic and structural qualities [1]. The precursors we used are NH₃ and TEGa. Nomarski microscopy technique was used to assess the surface morphology, and electrical characterization was made via room temperature Hall measurements. Details about this has been given in proceedings of preceding conferences [2,3] and in the present volume [4]. Photoluminescence spectra result of sample excitation by the 325 nm of a HeCd laser while reflectivity features were taken using a 100W tungsten wire lamp. All optical information was analyzed behind a THR Jobin Yvon 1.5m focal length equipped with a 1200 grooves/mm grating blazed at 250 nm.

RESULTS AND DISCUSSION

A typical photoluminescence spectrum is given on figure 1 together with three reflectivity features. We note a sample-dependent energy position of both photoluminescence (PL) and reflectance (R) structures. The stokes-shift between PL and R is deduced from a lineshape analysis of the R spectra, made following the method given in [2], and is found to be 5.8 meV within a scattering of 15% in the data. This moderate value is experimental evidence of the dominating extrinsic recombination processes in these samples. A weak residual intrinsic PL is also observed lying on the high energy wing of the PL peak. Selection rules investigations [5] have shown that we deal with a donor bound exciton where according to Pauli's uncertainty principle, the two electrons of the complex form a Γ_1 state and combine with a Γ_9 hole [6].

A careful examination of the reflectance spectra reveals an increase of the A-B and B-C splitting with increasing energy of the A exciton. This universal behavior (it does not depend with growth methods or growth chambers) is evidencing the existence of residual strain fields in the epilayers. Earlier, we have shown from studies of the handful of data available in the literature of the time,

that it could significantly renormalize the valence band parameters of wurtzite GaN[7].

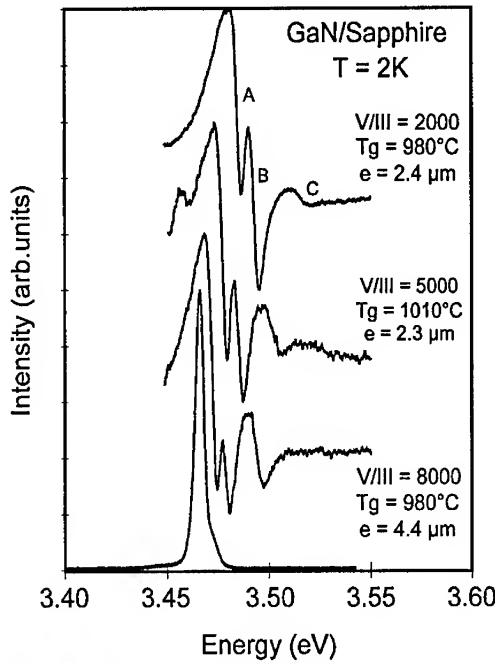


Figure 1 : some typical 2K PL and 2K Reflectance features observed in our samples. The PL spectra corresponds to the sample grown with V/III=8000.

electron. A general result of group theory is to predict that, under any lowering of cubic symmetry the Γ_5 representation splits. A wurtzite (C_{6v}) crystal field results in a discrimination of z-like valence states from x-like and y-like ones. This produces a valence band splitting sketched on figure 2 (left hand part).

In the basis of eigenvectors of the angular momentum \mathbf{l} , we usually write it $\Delta_{\alpha} \mathbf{l}_z^2$. The double group which takes into account the existence of a spin is more adapted than the simple group to describe symmetry properties of electrons. Among the relativistic corrections, we neglect the relativistic correction to the kinetic energy (known to give a smooth deformation of the band structure), and the angular momentum-dependent correction to the potential (the Darwin term). Both of them do not give any splitting which is not the case of the spin-orbit term (H_{so} hereafter), which couples the operators s in spin space with the angular momentum \mathbf{l} in ordinary space. We parametrize H_{so} , prescript it to be invariant under symmetry operations in both spin and ordinary spaces. This gives: $H_{so} = 1/3 \Delta_{so} (\mathbf{l} \cdot \boldsymbol{\sigma})$ and $H_{so} = \Delta_{||} \mathbf{l}_z \boldsymbol{\sigma}_z + \Delta_{\perp} (\mathbf{l}_x \boldsymbol{\sigma}_x + \mathbf{l}_y \boldsymbol{\sigma}_y)$ in cubic and wurtzite symmetry respectively. The resulting effect is dramatic for the valence band and is also sketched in figure 2 (right hand part) where the ordering of the valence sublevels is given for ZnS.

To go further, since the wurtzite deformation potentials are not known, we begin to recall the basic predictions of group theory, to establish the relationships between zinc-blende and wurtzite symmetries in terms of spin-orbit interactions and deformation potential formalism.

From simple arguments based on chemical bonding, and using the language of atomic physics, one can say that, at zone center, the Bloch wave function of the lowest conduction band of the usual semiconductors is essentially built from s atomic functions of the anion whilst p atomic functions of the anion dominate the wave function of valence band.

Transfer of these locutions to the language of group theory requires to include the actual crystal symmetry and to use labels linked to irreducible representation and the crystal point group.

In a cubic (T_d) environment the threefold (Γ_5) and single (Γ_1) irreducible representations account of the symmetries of the spinless valence and conduction

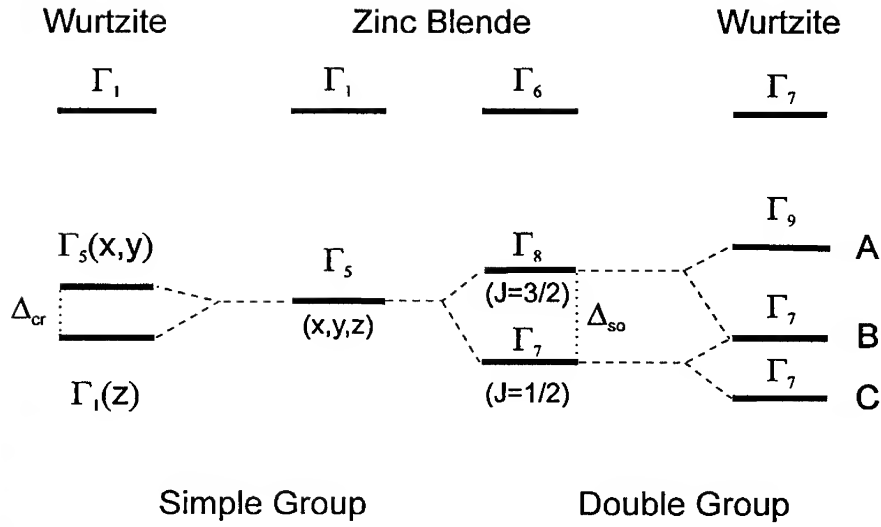


Figure 2: sketch of band structures under zinc-blende and wurtzite symmetries in the context of single group (left) and double group representations (right).

A strain field characterized by a deformation tensor e with components e_{ij} modifies the chemical bonds in the crystal and thus changes its whole band structure. Given a critical point M of the band structure of energy E , its strain-induced evolution δE is, at first order taken proportional to the e_{ij} quantities via quantities v_{ij} . This we write $\delta E = v_{ij}e_{ij}$ using the notations of tensor algebra. It is more realistic to use symmetrized combinations of e_{ij} and symmetrized combinations of the v_{ij} .

Projection of the latter in the basis of irreducible representations gives the deformation potential of interest for point M . As an illustration of this, the evolution of the Γ_7 conduction band of the wurtzite crystal writes $\delta E^c = v_1 e_{\Gamma_1} + v_2 e'_{\Gamma_1}$ where e_{Γ_1} and e'_{Γ_1} represent e_{zz} and $(e_{xx} + e_{yy})$ respectively. Concerning the valence band, six valence deformation potentials are required, which we note a_i :

$$\delta E^v = a_1 e_{\Gamma_1} + a_2 e'_{\Gamma_1} + a_6 e_{\Gamma_6} (l_x^2 - l_y^2) + a_5 (e_{\Gamma_5} \{l_x, l_z\} + e'_{\Gamma_5} \{l_y, l_z\}) + 2a_6 e'_{\Gamma_6} \{l_x, l_y\} + a_3 e_{\Gamma_1} l_z^2 + a_4 e'_{\Gamma_1} l_z^2$$

The strain-induced evolution of the valence band is obtained from diagonalisation of $\delta E^v + H_{so}$ in, for instance the 6x6 basis of the p-electron having been attributed its spin. In our case we assume the residual strain to be biaxial in the growth plane.

To go further we have to consider that the experiment was performed at 2K in the one hand and that the in-plane thermal expansion coefficients of sapphire and GaN are $7.5 \times 10^{-6} K^{-1}$ and $5.6 \times 10^{-6} K^{-1}$ respectively. Thus a straightforward reasoning gives us the sign of the residual stress: it is a biaxial compression.

The fit to the data was made taking into account of the zero-stress value of the GaN band gap E_0 we previously determined from a collection of data taken in the literature and the following parameters :

$$\Delta_{cr} = 10 \pm 0.1 \text{ meV}, \Delta_{//} = 6.2 \pm 0.1 \text{ meV}, \text{ and } \Delta_{\perp} = 5.5 \pm 0.1 \text{ meV} [7] .$$

Furthermore, using

$$C_{11} = 296 \text{ GPa}, C_{33} = 267 \text{ GPa}, C_{12} = 130 \text{ GPa}, C_{13} = 158 \text{ GPa} [8] \\ a_{1,2} = -8.16 \text{ eV}, a_{3,4} = 3.71 \text{ eV} [7]$$

we are able to produce the fit reported on figure 3.

For all samples, the stress was calibrated assuming the PL line to be linear with stress and to have the slope of the A exciton. The experimental values of the localization energy of the exciton to the residual donor results, as said above from a lineshape fitting of the reflectivity spectrum and thus displays a small scattering around 5.8 meV which appears on the figure via slight deviations of the position of the A exciton from the theoretical line.

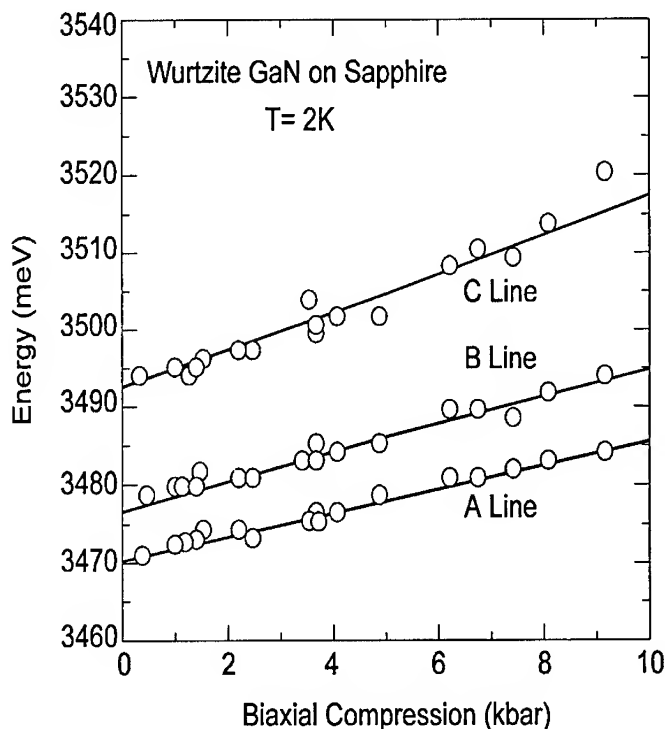


Figure 3: Dependence of the energy of A,B,C excitons with biaxial compression

A plot of the energy of A exciton as a function of the thickness of the epilayers gives the cloudy picture reported on figure 4 (left hand side), as an evidence of the absence of clear correlation. A plot as a function of the V/III ratio is more convenient to evidence correlation as shown on figure 4, (right hand side) for different growth temperatures. Increasing the V/III ratio reduces the incorporation of impurities through several decades, from 10^{20} cm^{-3} for a molar ratio of 1000 down to 10^{16} cm^{-3} for a molar ratio of 8000 when incorporation or residual impurities as well as creating of high density native defects become less efficient.

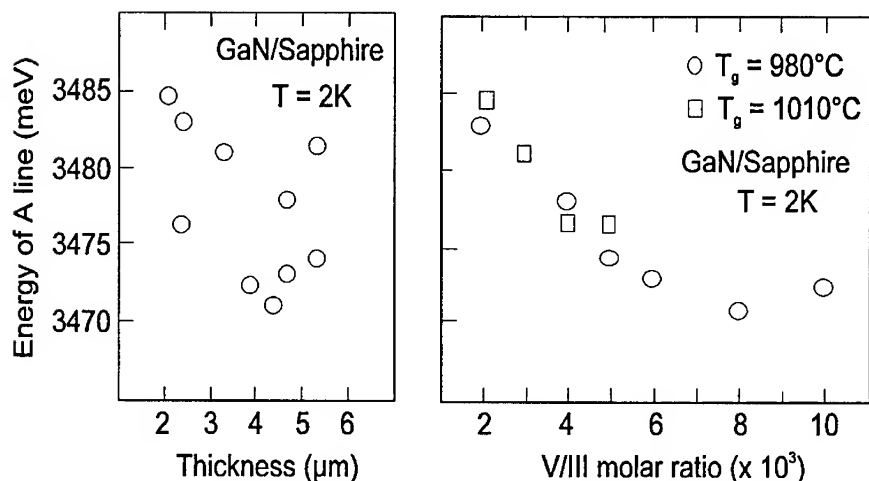


Figure 4: Plot of the energy of A line versus thickness of GaN epilayer (left hand side), and versus the V/III molar ratio for different growth temperatures (right hand side).

CONCLUSION

High resolution spectroscopy measurements were performed on GaN layers grown by MOVPE onto sapphire substrates. This enabled us to evidence details of the valence band structure. In particular we have connected the excitons energies, and the splitting between these levels, to the residual strain in the layers. The nature of this residual strain is not clear at the present stage : it is weakly related to the sample thicknesses, and is rather strongly influenced by the layers growth conditions.

ACKNOWLEDGMENT:

This work was partially made under the auspices of a contract with Thomson CSF-LCR

REFERENCES

- 1- S.Nakamura, T.Mukai and M.Senoh, Appl. Phys. Lett. **64**, 1687, (1994)
- 2- O.Briot, S.Sanchez, B.Gil, and R.L.Aulombard in proceedings of the ICSCRM Kyoto 1995
- 3- O.Briot, J.P.Alexis, S.Sanchez, B.Gil, and R.L.Aulombard in proceedings of the Topical workshop on nitrides TWN'95 Kyoto 1995
- 4- O.Briot, J.P.Alexis, B.Gil, and R.L.Aulombard, this proceedings, paper AAA12.35
- 5- L.Eckey, L.Podlowski, A.Golner, A.Hoffmann, I.Broser, B.K.Meyer, D.Volm, T.Streibl, K.Hiramatsu, T.Detchprohm, H.Amano, I.Akasaki in proceedings of the Topical workshop on nitrides TWN'95 Kyoto 1995
- 6- in this paper, we use the notations of Koster, Dimmock, Wheeler and Statz in "Properties of the thirty-two point groups" MIT Press Cambridge 1963
- 7- B.Gil, O.Briot, and R.L.Aulombard, Phys. Rev.B, (Rapid Com.) **52**, 15 December issue
- 8- Data in Science and Technology - Semiconductors: Group IV Elements and III-V Compounds Edited by O.Madelung Springer Verlag Berlin Heidelberg (1991)

DEFECT STUDIES OF GaN UNDER LARGE HYDROSTATIC PRESSURE

C. WETZEL, S. FISCHER, W. WALUKIEWICZ, J. AGER III, E.E. HALLER,
I. GRZEGORY*, S. POROWSKI*, and T. SUSKI*

Lawrence Berkeley National Laboratory and University of California, Berkeley, CA 94720, USA

*Unipress, Polish Academy of Sciences, Warszawa, Poland

ABSTRACT

GaN plays a key role in the exploration of the properties of group-III nitrides. As grown GaN often shows a high electron concentration, e.g. 10^{19} cm^{-3} , of as yet unidentified origin. Applying large hydrostatic pressure we studied the behavior of these donors and a frequently observed strong luminescence band at 3.42 eV. We find a drop of the electron concentration to $3 \times 10^{17} \text{ cm}^{-3}$ at 27 GPa and derive a binding energy of 126 meV for the neutral singlet donor level at this pressure. Such a pressure behavior of a donor is consistent with the model of strongly localized defects. Within the framework of a bandstructure calculation we predict the neutral level of this donor at $0.40 \pm 0.10 \text{ eV}$ above the conduction band edge at ambient pressure.

INTRODUCTION

The physics of semiconductors currently experiences exciting developments in the group-III nitrides. In many aspects these wide bandgap materials behave differently from the well studied systems. High quality material has become available only recently due to a strong commercial interest in optoelectronic applications [1,2]. One of the key question relates to the nature of defects and impurities. Typically high n-type conduction in the range of $10^{18} - 10^{20} \text{ cm}^{-3}$ [3] is observed posing the question of the responsible donor. No chemical impurity has been found at such high concentrations and intrinsic defects have to be considered. According to theoretical models nitrogen vacancies as well as gallium interstitials act as donors [4-6] but their predicted formation energies are very large in n-type materials making this suggestion controversial [6].

Defects and impurities are most directly observed and studied in their impact on transport and luminescence properties. An important distinction can be made upon the apparent binding energies of the trapped carriers with respect to the band edges. Such a classification, however, is not sufficient in order to separate hydrogenic defect states from strongly localized defects. The first of those are typically treated in a perturbation of the band edge wave functions and extend over many lattice constants. The latter in turn require a description by means of the wave functions of the whole Brillouin zone. This is typically the case for native defects such as vacancies, interstitials, and antisite defects. From the Kronig-Penny-model of the electronic bandgap it becomes obvious that a variation of the bond length in a crystal affects the Eigen energy of the defect state proportional to the extension of its wave function. Therefore hydrogenic defect states mainly follow the band edges whereas strongly localized defects show a much weaker shift. A variation of the bond length can be achieved by either a composition change e.g. in the ternary alloy system AlGaAs or AlGaN, or by application of hydrostatic pressure [7].

EXPERIMENTAL

Small GaN bulk crystals produced by two different growth techniques have been studied. Platelets of bulk GaN at dimensions of typically $150 \times 100 \times 50 \mu\text{m}^3$ have been grown by an unconventional high temperature vapor phase technique [8,9]. From ammonia and elemental gallium thick films of GaN were deposited at 1240°C onto various substrates. At high growth rates of typically $200 \mu\text{m/h}$ a spontaneous nucleation of small crystals can be found in addition. On the other hand crystals at dimensions of approximately $500 \times 300 \times 20 \mu\text{m}^3$ have been grown by high pressure synthesis from molecular nitrogen dissolved in Ga [10]. Crystals from both techniques are optically clear and show no grain boundaries visible to the eye. While the samples from the high pressure synthesis show a brownish color, the vapor phase material studied here appears to be perfectly transparent. The c-axis is normal to the larger dimensions. All samples were nominally undoped and n-type. Hydrostatic pressure was applied by means of a diamond anvil cell using nitrogen as a pressure medium. The pressure was determined using the R_1 ruby fluorescence. Photoluminescence (PL) was excited by the 325 nm line of a HeCd laser in an optical cryostat operating at a temperature of 6 K. The emission was dispersed by a 0.85 m double grating spectrometer and detected by a UV sensitive photomultiplier.

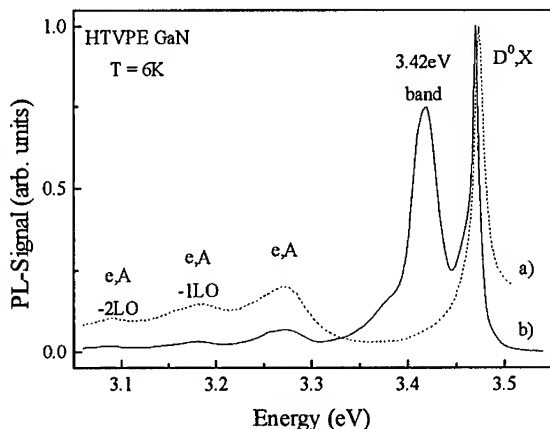


Figure 1: Low temperature PL of GaN. In addition to donor bound exciton and band acceptor transitions (spectrum a) an intense contribution is found at 3.42 eV (spectrum b).

RESULTS

3.42 eV Luminescence Band

Low temperature PL of two different samples of the HTVPE material is presented in Fig. 1. Common features are the donor bound exciton (D^0, X) at 3.472 eV [11] and the set of band-acceptor recombination at 3.27 eV [8] including several phonon replica at lower energies. While no luminescence is observed in the intermediate spectral range for sample a) a strong contribution is found for sample b). The rather broad peak at 3.42 eV has repeatedly been reported in PL studies and was assigned to an oxygen related defect recently [12]. It appears at an optical binding energy of $\sim 80 \text{ meV}$ with respect to the low temperature bandgap of 3.504 eV. This is a very large value when compared to typical binding energies of excitons bound to shallow donors ($\sim 30 \text{ meV}$) or acceptors ($\sim 40 \text{ meV}$). On the other hand this value is too small to be caused by a donor-acceptor pair interaction where the smallest reported optical binding energies are about 260 meV [8]. Such an observation could indicate the participation of a strongly localized defect for which the above energies typically does not apply.

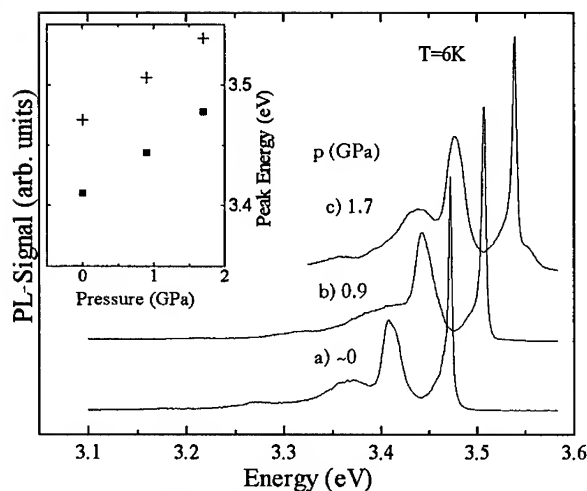


Figure 2: PL in the bandgap region of GaN. For various pressure values the donor bound exciton and the defect related transition shift parallel in energy.

In order to test for such a participation we applied hydrostatic pressure up to 6 GPa. Several spectra are presented in Fig. 2. The shallow bound D^0X -transition is found to shift at the expected rate [13]. However, the same behavior is observed for the questionable transition. We find that up to a pressure of 6 GPa this transition behaves like a hydrogenic state. This includes both, the initial state in the vicinity of the conduction band and the final state of the recombination near the valence band. Although the valence band typically does not shift much, a distinction between a hydrogenic and a strongly localized final state would have become obvious from this experiment.

Free Carrier Concentration

In a second approach we determined the free carrier concentration as a function of hydrostatic pressure. The coupling of the free electron gas to the optical phonons was used to optically determine the carrier concentration contactlessly in a diamond anvil cell. The interaction of optical phonons with the plasmon of the free carriers is well understood. For the case of GaN the correlation between the frequency of the phonon-plasmon coupled mode and the free carrier concentration as determined by Hall experiments has been given experimentally by Barker and Ilegems [3]. They interpreted the position of the characteristic minimum located on the high energy side of the infrared reflection in the range of the reststrahlen band. Recently a similar correlation has been established between the Hall concentration and the position of the phonon-plasmon coupled mode observed in Raman spectroscopy by Kozawa et al. [14]. They used a series of Si doped GaN films. Here we make use of both, infrared reflection and Raman spectroscopy to determine the free carrier concentration in bulk GaN grown by the high pressure synthesis. At ambient pressure a n-type Hall concentration of 10^{19} cm^{-3} is observed. All data are taken at room temperature.

Reflection at various pressures is presented in Fig. 3. At ambient pressure (spectrum a) reflection in the expected region of the reststrahlen band is strong and featureless. Interference fringes arising from the terrace like c-plane surface of the sample can be observed. Due to the strong interaction between the phonons and the electrons the high energy edge of the reststrahlen band is smeared out over a wide range. Up to 2500 cm^{-1} no transmitted light can be measured ($T < 1\%$). After increasing the pressure to 27 GPa the situation has changed dramatically (spectrum c). A distinct minimum can be observed at 925 cm^{-1} . The lower edge of the reststrahlen band is found at 640 cm^{-1} (Al(TO) mode). Apparently the free carrier

concentration has decreased considerably and the A1(LO) phonon which determines the high energy edge of the reststrahlen band is to a great extent uncoupled from the damping effect of the free electrons. For an analysis of this data we take into account the pressure induced shift of all the phonon modes. For the A1(TO) mode we find a shift of about 100 cm^{-1} compared to its reported value at ambient pressure. A very similar pressure shift of the pure LO modes, e.g. the A1(LO), can be expected and is supported by the Raman results (see below). We use these values to describe the dielectric function in the oscillator model including the free carrier contribution in the Drude model. From the minimum in reflection we finally derive a maximum carrier concentration 10^{18} cm^{-3} [15].

After decreasing the pressure to 25 GPa (spectrum b) the A1(TO) phonon edge has shifted to lower wavenumbers and the same shift has to be expected for the bare A1(LO) mode. The minimum in reflection, however, has shifted only very little indicating a small increase in the free carrier concentration.

Complementary information can be obtained from the Raman experiment (Fig. 4. Spectra normalized to the strongest mode and offset for clarity). At ambient pressure (spectrum a) the Raman active modes A1(TO) (529 cm^{-1}) and E2 (565 cm^{-1}) are observed in z(x,-)z backscattering [16]. Again, no indication of the optical A1(LO) mode can be found. Due to the high carrier concentration this mode is strongly damped by the plasmon. At 27 GPa (spectrum d) both, the A1(TO) and the E2 modes have shifted in parallel towards higher energies by about 100 cm^{-1} in this z(x,-)z forward scattering geometry. But in addition now a clear coupled A1(LO) mode can be observed at 825 cm^{-1} . From a modeling of the dielectric function parallel to above interpretation [14] we interpret the position and the linewidth of the observed coupled Raman mode. The position of the mode with respect to its expected value leads to a maximum carrier concentration of $3 \times 10^{17} \text{ cm}^{-3}$. The linewidth in turn directly corresponds to a concentration of $3 \times 10^{17} \text{ cm}^{-3}$ ($\pm 5\%$). The observed asymmetry of the mode is different from the situation observed in Ref. [14]. This can be related to the observation of additional modes at smaller wavenumbers at even higher pressure [17] and needs further investigation. In a conservative treatment, however, we consider a density of $3 \times 10^{17} \text{ cm}^{-3}$. Again decreasing the pressure to 25 GPa results in a mode softening and a broadening of the coupled A1(LO) line. At 20 GPa the coupled mode can not be found as the carrier concentration has increased and the coupled mode is overdamped.

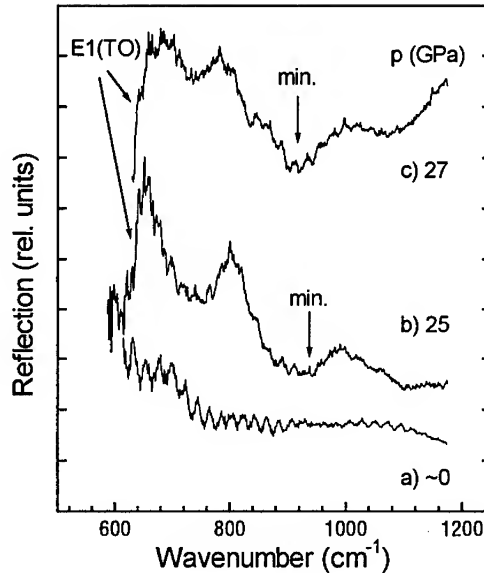


Figure 3: Reflection in the phonon region of a c-plane oriented GaN single bulk crystal. Only at large pressure the reststrahl band extending from the TO to the plasmon-coupled LO mode can be observed after a strong reduction of the free carrier concentration.

RESULTS

From the observed reduction of the free carrier concentration we can determine a mean value of the (thermal) binding energy of the trap that localized almost 10^{19} cm^{-3} carriers at room temperature. Assuming a twofold spin degenerate defect level we find a value of 126 meV at 27 GPa. At ambient pressure this level should be degenerate with the conduction band. Assuming the model of a strongly localized defect the different pressure coefficients have resulted in a crossing of the defect level with the conduction band edge reaching 126 meV below the edge at 27 GPa. The behavior of such a donor state is known to be well approximated by an weighted average over the conduction band edge within the whole Brillouin zone. We find the following contributions Gamma (7.1 %), K (19 %), M (38 %), A (8.7 %), L (19 %), and H (7.9 %) [15]. Applying this weight function to the calculated pressure coefficients of the symmetry points [18] we find a pressure dependence of the defect level

$$\Delta E_{avg}(p) = \sum_{i=c} d_i [E_i(p) - E_i(0)] = 15.4 \text{ meV} \frac{p}{\text{GPa}} - 0.17 \text{ meV} \left(\frac{p}{\text{GPa}} \right)^2. \quad (1)$$

Extrapolation to ambient pressure the neutral defect level should lie at $0.40 \pm 0.10 \text{ eV}$ above the conduction band edge at ambient pressure. Being in resonance with the band the electron would auto ionize to the band edge where it will still feel the attractive interaction of the coulomb tail of the defect it left behind. This results in very interesting effects on the density of states and should strongly affect transport properties.

CONCLUSIONS

The repeatedly observed luminescence band at 3.42 eV shows an optical binding energy that suggests a strongly localized nature of the respective defect. Its pressure behavior, however, reveals the properties of an effective mass defect at pressures up to 6 GPa. The donor responsible for a high free carrier concentration is found to have a deep gap state at 27 GPa and its corresponding level at ambient pressure is predicted at $0.40 \pm 0.10 \text{ eV}$ above the conduction band edge. So far no assumption has been made on the very nature of the strongly localized

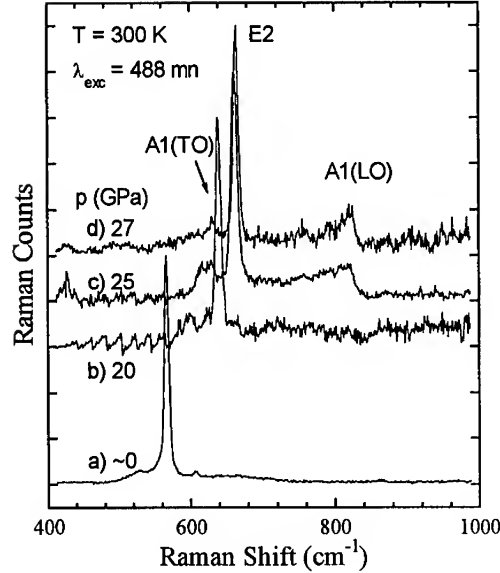


Figure 4: Raman spectroscopy of highly n-type GaN single crystals at various large hydrostatic pressures. The A1(LO) mode does not appear until a pressure of 25 GPa. All modes show a similar shift.

defect. Both, the model of the nitrogen vacancy, as well as the gallium interstitial could be supported by these results. However, considering the calculated formation energies of those candidates under equilibrium conditions, the formation of nitrogen vacancies seems to be more likely.

ACKNOWLEDGMENTS

The authors thank Prof. B.K. Meyer, Prof. J. Schneider, Prof. I. Akasaki, and Prof. P.Y. Yu for valuable discussion. C.W. thanks the Deutsche Forschungsgemeinschaft for a grant. Work partially supported by the Director, Office of Energy Research, Office of Basic Energy Sciences, Materials Science Division of the U.S. Department of Energy under Contract No. DE-AC03-76SF00098.

REFERENCES

1. I. Akasaki, H. Amano, N. Koide, M. Kotaki, K. Manabe, *Physica B* **185**, 428 (1993).
2. S. Nakamura, M. Senoh, and T. Mukai, *Appl. Phys. Lett.* **62**, 2390 (1993).
3. A.S. Barker Jr. and M. Ilegems, *Phys. Rev. B* **7**, 743 (1973).
4. D.W. Jenkins, J.D. Dow, and Min-Hsiung Tsai, *J. of Appl. Phys.* **72**, 4130 (1992).
5. P. Boguslawski, E. Briggs, T.A. White, M.G. Wensell, and J. Bernholc in Diamond, SiC and Nitride Wide-Bandgap Semiconductors, edited by C.H. Carter Jr, G. Gildenblat, S. Nakamura and R.J. Nemanich, (Mat. Res. Soc. Proc. **339**, Pittsburgh, PA 1994) p. 693.
6. J. Neugebauer and C. G. Van de Walle, *Phys. Rev. B* **50**, 8067 (1994).
7. M. Mizuta, M. Tachikawa, H. Kukimoto, and S. Minomura, *Jpn. J. Appl. Phys.* **24**, L143 (1985).
8. S. Fischer, C. Wetzel, E.E. Haller, and B.K. Meyer, *Appl. Phys. Lett.* **67**, 1298 (1995).
9. S. Fischer, C. Wetzel, W.L. Hansen, E. Bourret, and E.E. Haller, unpublished.
10. P. Perlin, I. Gorczyca, N.E. Christensen, I. Grzegory, H. Teisseyre, and T. Suski, *Phys. Rev. B* **45**, 13307 (1992).
11. C. Wetzel, D. Volm, B.K. Meyer, K. Pressel, S. Nilsson, E.N. Mokhov, and P.G. Baranov, *Appl. Phys. Lett.* **65**, 1033 (1994).
12. B.-C. Chung and M. Gershenson, *J. Appl. Phys.* **72**, 651 (1992).
13. C. Wetzel, W. Walukiewicz, E.E. Haller, H. Amano, and I. Akasaki, (Mat. Res. Soc. Proc. **378**, Pittsburgh, PA 1994) p. 509.
14. T. Kozawa, T. Kachi, H. Kano, Y. Taga, M. Hashimoto, N. Koide, and K. Manabe, *J. Appl. Phys.* **75**, 1098 (1994).
15. A detailed analysis will be given in a forthcoming paper: C. Wetzel, W. Walukiewicz, E.E. Haller, J. Ager III, I. Grzegory, S. Porowski, and T. Suski, unpublished.
16. C.A. Arguello, D.L. Rousseau, and S.P.S. Porto, *Phys. Rev.* **181**, 1351 (1969).
17. P. Perlin, C. Jauberthie-Carillon, J.P. Itie, A. San Miguel, I. Grzegory, A. Polian, *Phys. Rev. B*, **45**, 83 (1992).
18. N.E. Christensen and I. Gorczyca, *Phys. Rev. B* **50**, 4397 (1994).

THE PHONON DENSITIES OF STATES OF AlN and ZrN

C.-K. LOONG

Intense Pulsed Neutron Source

Argonne National Laboratory, Argonne, IL 60439, U. S. A.

ABSTRACT

Phonons are thought to play a crucial role in the high thermal conductivity of AlN and ZrN. Using time-of-flight neutron spectroscopy, we have measured the phonon spectra of AlN and ZrN up to 300 meV (2400 cm^{-1}). The one-phonon density of states (DOS) of AlN exhibits relatively sharp bands at about 33, 63, 83 and 91 meV. In addition, distinct multiple-phonon excitations were observed at ~173 and 255 meV. The phonon DOS of ZrN displays similar features with the corresponding phonon energies shifted toward lower energies. The measured DOS of AlN is compared with results of molecular-dynamics simulations.

INTRODUCTION

The unique properties of aluminum nitride have attracted keen attention from materials scientists in recent years. It has a thermal conductivity comparable to most conductive metals (e.g., Al) and much greater than typical ceramics (~5 times of that of alumina). The high electrical resistivity, good dielectric strength, a thermal expansion coefficient closely matching that of silicon, and lack of toxicity (like that associated with BeO) of AlN are ideal for microelectronics applications. [1-3] Furthermore, AlN has high strength (a flexural strength equivalent to alumina), high temperature stability and corrosion resistance. Therefore, hi-tech AlN components can potentially be used under extreme conditions. In metals heat is carried primarily by electrons whereas in nonmetals such as AlN heat is carried primarily by phonons. Therefore, determination of the phonon excitation spectra of AlN and related materials such as ZrN is a fundamental step toward the understanding of the thermophysical behavior of these materials.

Although the crystal structure of aluminum nitride is known for a long time, a finely divided powder of AlN is relatively susceptible to hydrolysis, where AlN and water react to form aluminum hydroxide, ammonia and heat. Only until recently high-purity, and pretreated water-resistant AlN powders become available. Growing large, high-quality AlN single crystals is rather difficult. Although phonons can be investigated using several spectroscopic techniques including Raman and neutron scattering and infrared absorption measurements. Only neutrons can probe phonon modes throughout the Brillouin zone, and the method is relatively insensitive to small amount of impurities. Like other diamond-like materials, the phonon frequencies of AlN is expected to be high ($> 100\text{ meV}$). Perhaps for these reasons a measurement of the full phonon density-of-states (DOS) has not been reported in the literature. In this paper we report the progress in measuring the phonon DOS of AlN and ZrN powders by neutron spectroscopy. The neutron spectra are compared with results of molecular-dynamics (MD) simulations.

EXPERIMENTAL DETAILS

AlN and ZrN fine powders were acquired from Advanced Refractory Technologies, Inc. and Johnson Matthey Alfa Aesar, Inc., respectively. The crystal structures were examined by neutron powder diffraction using the General-Purpose Powder-Diffractometer (GPPD) at the Intense Pulsed Neutron Source (IPNS) of Argonne National Laboratory. A Rietveld structure-refinement analysis confirmed the wurtzite structure (hexagonal, $P6_3mc$) of AlN and the rocksalt structure (cubic, $Fm3m$) of ZrN. In the case of AlN, a few weak extra reflections were

observed, indicating the presence of a small amount ($< 5\%$) of impurities. Fig. 1 displays a part of the observed and fitted powder-diffraction pattern of AlN. Such low level of impurity is not expected to affect the measured phonon DOS of the major phase.

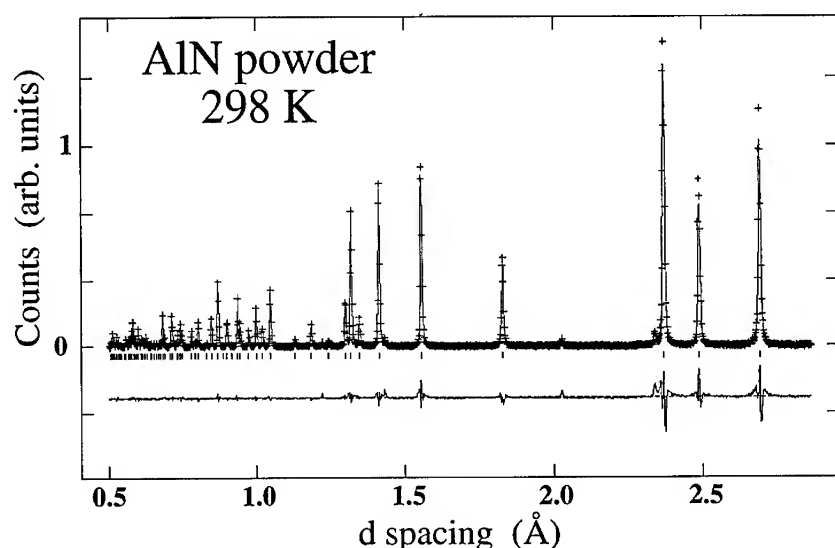


Figure 1. Rietveld profile fit in the 0.8-1.8 Å region of d-spacing for the AlN powder at room temperature. The symbols are the observed, background subtracted intensities. The solid line represents the calculated crystalline intensities. The tick marks indicate the positions of the Bragg reflections. The difference between the observed and calculated intensities is shown at the bottom of the figure.

The inelastic experiments for phonon DOS measurements were carried out using the Low- and High-Resolution Medium-Energy Chopper Spectrometers (LRMECS and HRMECS), also at IPNS. Incident neutron energies (E_0) of 150, 200, 400, and 800 meV were used to study the phonon excitation spectra at 15-300 K over a wide range of energy transfers. The energy resolution ΔE (full width at half-maximum) of HRMECS (LRMECS) varies from $\sim 4\%$ ($\sim 8\%$) of E_0 in the elastic region to $\sim 2\%$ ($\sim 4\%$) near the end of the neutron energy-loss spectrum. Under the incoherent approximation, the low-temperature neutron excitation spectrum of a powder sample averaged over a wide range of detector angles provides a direct measure of the generalized one-phonon density of states (DOS) which differs from the true phonon DOS by the weighting factors $\frac{c\sigma}{m}$ (where c , σ , and m are the concentration, neutron-scattering cross section, and mass, respectively, of the constituent elements). Since the N scattering cross section ($11.5 \times 10^{-24} \text{ cm}^2$) is significantly larger than those of Al ($1.5 \times 10^{-24} \text{ cm}^2$) and Zr ($6.6 \times 10^{-24} \text{ cm}^2$), the observed DOS are weighted more favorably to N.

PHONON DENSITIES OF STATES

Fig. 2 (a) displays the observed neutron-weighted phonon DOS of AlN from a run with an incident energy of 150 meV. This spectrum is dominated by one-phonon excitations which

shows a cut-off energy at about 120 meV. The broad features below 70 meV and the sharp band with two resolved peaks at higher energies reflect the distribution of three groups of optic modes around 32, 63 and 83-91 meV. The upper optic modes show little dispersion throughout the zone, which is typical to the wurtzite structure. The zone-center optic phonons have been investigated with Raman and infrared spectroscopy by many authors [4-10]. Rather significant discrepancies exist among the reported frequencies of the assigned Raman and IR active modes. Qualitatively, the Raman frequency groups around 31-37 meV ($252\text{-}303\text{ cm}^{-1}$), 76-83 meV ($614\text{-}668\text{ cm}^{-1}$), and 110-114 meV ($888\text{-}916\text{ cm}^{-1}$) are in good agreement with the neutron data.

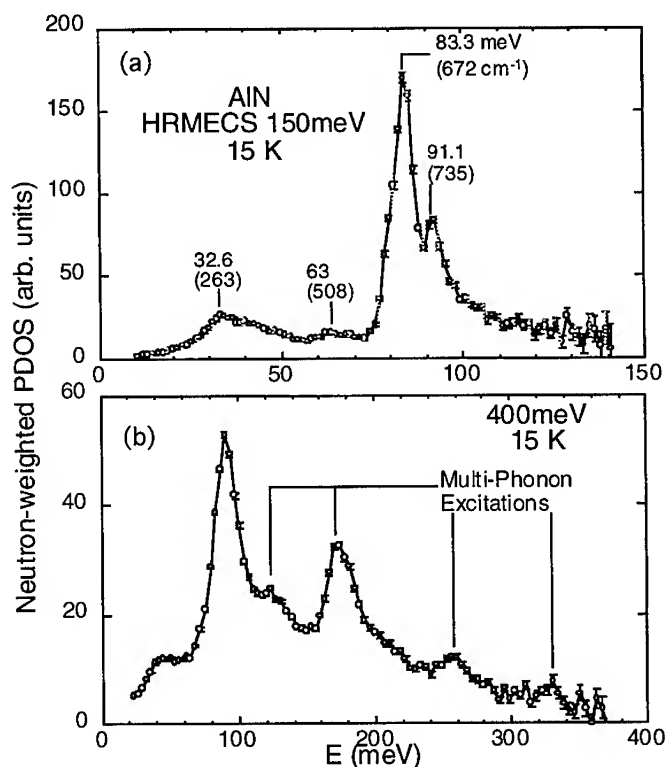


Figure 2. The observed neutron-weighted phonon DOS of AlN at 15 K, obtained from HRMECS runs with an incident energies of 150 meV (a), and 400 meV (b).

Phonon-phonon scattering is one of the mechanisms which affect the conduction of heat in solids. Such process involves excitations and/or de-excitations of multiple phonons. Fig. 2 (b) shows a spectrum taken with an incident energy of 400 meV which contains substantial multi-phonon excitations extending beyond 300 meV.

The phonon DOS of ZrN, as shown in Fig. 3, is somewhat similar to that of AlN, except that the corresponding phonon bands of ZrN shift to lower energies. This is not surprising since Zr has a mass more than three times larger than Al. The spectrum was taken with 200 meV on LRMECS, where the energy resolution was not sufficient to resolve the fine structure of the high-energy bands.

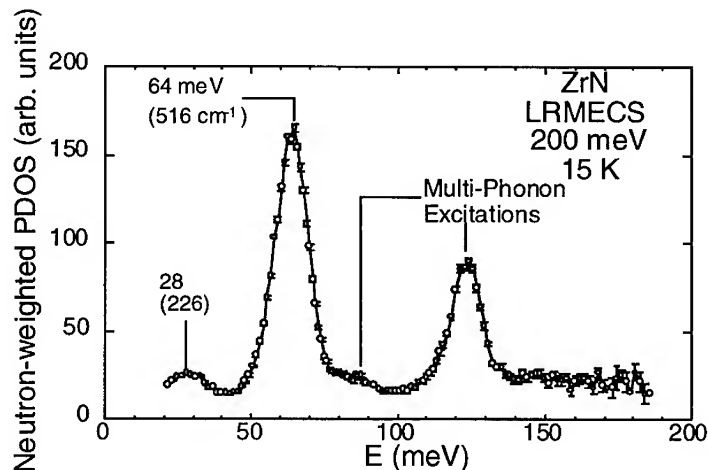


Figure 3. The observed neutron-weighted phonon DOS of ZrN at 15K, obtained from a LRMECS run with an incident energy of 200 meV.

MOLECULAR-DYNAMICS SIMULATIONS

To obtain information about the partial phonon DOS and the true DOS, MD simulations were carried out for AlN using a commercial software package Cerius² from Molecular Simulations Inc. The MD system consisted of a cell with 256 atoms with periodic boundary conditions set up for a isothermal-isobaric (NPT) dynamics ensemble. Since we are interested primarily in the lattice dynamics at low temperatures, only two-body harmonic bond-stretch and three-body angle-bend potentials were employed. After energy minimization, the system was thermalized for 10,000 time steps ($t_s = 1$ fs) at 600 K and then cooled to 300 K and run for 30,000 t_s . The partial DOS from Al and N, the true DOS and the calculated neutron-weighted DOS are shown in Fig. 4. The MD results show that Al and N motions are responsible respectively to the low- and high-energy portions of the DOS. The calculated neutron-weighted DOS bears a fair resemblance to the observed DOS, although the first peak at ~ 23 meV is lower than the observed one (32.6 meV). Such discrepancies indicate the need for refinement of the potential functions used in the MD simulation.

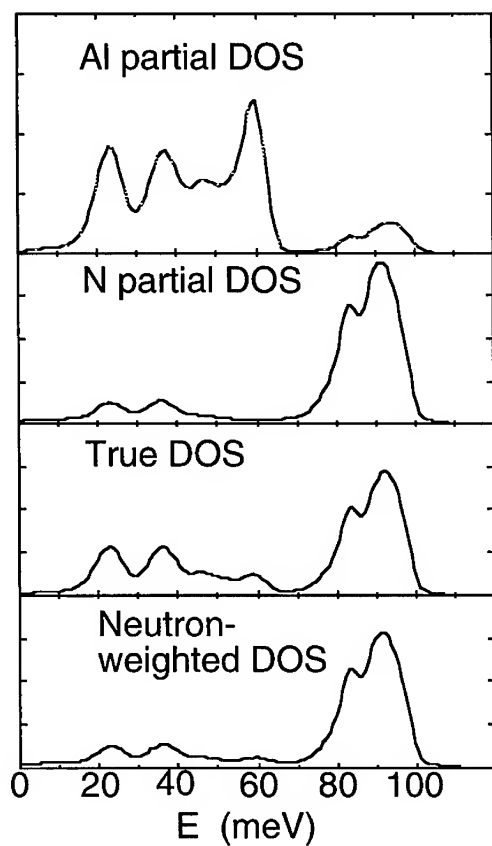


Figure 4. The partial, true, and neutron-weighted phonon DOS of AlN obtained from MD simulations.

We thank F. Trouw for helpful discussion on MD simulations and J. W. Richardson, Jr. and J. Nipko for their assistance in the powder diffraction measurements. The software package for MD simulations made available by Molecular Simulations Inc. is gratefully acknowledged. Work performed at Argonne National Laboratory is supported by the U. S. DOE-BES under Contract No. W-31-109-ENG-38.

REFERENCES

- 1 D. D. Marchant and T. E. Nemecek, in *Advanced Ceramics*, Vol. 26, Ed., M. F. Yan, K. Niwa, H. M. O'Bryan, Jr., and W. S. Young (Am. Ceram. Soc., 1987) p. 19.
- 2 T. Mroz and K. Blakely, in *Materials Engineering* (Advanced Refractory Technologies, Inc., Buffalo, NY) March 1992.
- 3 G. A. Slack, R. A. Tanzilli, R. O. Pohl, and J. W. Vandersande, *J. Phys. Chem. Solids*, **48**, 641 (1987).
- 4 I. Akasaki and M. Hashimoto, *Solid State Commun.* **5**, 851 (1967).
- 5 A. T. Collins, E. C. Lightowers, and P. J. Dean, *Phys. Rev.* **158**, 833 (1967).
- 6 O. Brafman, G. Lengyel, S. S. Mitra, P. J. Gielisse, J. N. Plendl, and L. C. Mansur, *Solid State Commun.* **6**, 523 (1968).
- 7 C. Carlone, K. M. Lakin, and H. R. Shanks, *J. Appl. Phys.* **55**, 4010 (1984).
- 8 K. Hayashi, K. Itoh, N. Sawaki, and I. Akasaki, *Solid State Commun.* **77**, 115 (1991).
- 9 L. McNeil, M. Grimsditch, and R. H. French, *J. Am. Ceram. Soc.* **76**, 1132 (1993).
- 10 P. Perlin, A. Polian, T. Suski, *Phys. Rev. B* **47**, 2874 (1993).

STRUCTURE AND QUASIPARTICLE ENERGIES OF CUBIC, WURTZITE AND HEXAGONAL BN

Giancarlo Cappellini
INFM - Istituto di Fisica, Facoltà di Medicina e Chirurgia, Università di Cagliari,
I-09125 Cagliari, Italy

Vincenzo Fiorentini
INFM - Dipartimento di Scienze Fisiche, Università di Cagliari, I-09124 Cagliari, Italy

Katrin Tenelsen and Friedhelm Bechstedt
IFTÖ, Friedrich-Schiller-Universität, D-07743 Jena, Germany

ABSTRACT

We present local density functional theory (DFT-LDA) studies of the structural properties of boron nitride in the layered hexagonal (h-BN), zincblende (c-BN), and wurtzite (w-BN) structures, performed using a fast implementation of the norm-conserving pseudopotential plane-wave method. Quasiparticle band structures are then calculated for all phases by means of an efficient GW self-energy scheme. To our knowledge, these are the first GW quasiparticle calculations for wurtzite BN including local-field and dynamical screening effects. DFT-LDA band gaps as functions of pressure and uniaxial distortion for h-BN are also discussed.

STRUCTURAL PROPERTIES OF c-, w- AND h-BN

Boron Nitride (BN) has recently become a system of considerable interest for semiconductor industry and material science. The stable phase under normal conditions[1] is layered-hexagonal (graphitic) BN (henceforth h-BN), while at higher pressure and temperature the denser zincblende (c-BN) and wurtzite (w-BN) phases are stable [2, 3]. c-BN has interesting properties such as extreme hardness, high melting point, low dielectric constant, large band gap. h-BN on the other hand has attracted interest in connection with the possibility of synthesizing BN nanotubes [4, 5]. All these properties are of interest for many applications in modern microelectronic devices. An accurate study of structural and electronic properties of these phases seems therefore timely.

The ground state properties of the three structures have been calculated within local density functional theory. The electron wave functions are expanded in plane waves and the electron-ion interaction is treated by fully non-local norm-conserving *ab initio* pseudopotentials. The kinetic energy cutoff for all structures is 150 Rydberg; the exchange-correlation energy of Ceperley and Alder [7] is used, in the parametrization of Perdew and Zunger [8].

Zincblende BN	This work	Furthmüller <i>et al.</i> [10]	Xu and Ching [11]	Exp. [4]
V(Å ³)	5.746	5.718	5.905	5.930
a(Å)	3.582	3.576	3.615	3.615
B(Mbar)	3.52	3.97	3.70	3.69-4.65

Table I: Calculated structural properties of zincblende Boron Nitride (volume per atom, lattice constant and bulk modulus) compared with other theoretical and experimental results.

Wurtzite BN	This work	Furthmüller <i>et al.</i> [10]	Xu and Ching [11]	Exp. [4]
$V(\text{\AA}^3)$	5.716	5.731	5.845	5.97
$a(\text{\AA})$	2.508	2.521	2.536	2.55
u	0.37125			
c/a	1.666	1.652	1.656	1.648
$B(\text{Mbar})$	4.12	4.01	3.90	
$\Delta E(\text{eV/atom})$	0.020	0.020	0.075	

Table II: As in Table I, for wurtzite Boron Nitride. Here the internal bond-length parameter u , the axial lattice parameter and the energy difference ΔE relative to the zincblende structure are also given.

Hexagonal BN	This work	Furthmüller <i>et al.</i> [10]	Xu and Ching [11]	Exp. [4]
$V(\text{\AA}^3)$	8.617	8.613	8.970	9.012
$a(\text{\AA})$	2.477	2.486	2.494	2.50
c/a	2.6068	2.608	2.670	2.664
$B(\text{Mbar})$	2.65	2.61	3.35	
$\Delta E(\text{eV/atom})$	0.078	0.055	-0.35	

Table III: As in Table II for hexagonal Boron Nitride. This phase has no internal parameter.

The k -integration is replaced by a sum over Chadi-Cohen [9] special k -points. The theoretical structural parameters for the three BN phases, and other ground state properties, have been obtained using 3 k -points for the hexagonal and wurtzite structures and 2 for the zincblende one. While structural properties are insensitive to improvements in the k -point sampling, 12 and 10 points (for hexagonal and cubic symmetry respectively) were needed to converge total energy differences between the various phases.

While structural properties are insensitive to improvements in the k -point sampling, 12 and 10 points were needed for the hex and cubic phases respectively, to converge total energy differences between the various phases. In Tables I to III the structural properties of the three structures are reported, and compared with experiments and previous theoretical results. According to the present calculations, the most stable structure is zincblende, in accordance with the accurate recent result of Furthmüller *et al.* [10], but contrary to experiment [4]. This discrepancy may be speculatively ascribed to differences in the volume dependence of the zero point vibration energy of the two lattices; a full calculation of the vibrational spectrum of h-BN, necessary to solve this problem, is planned.

QUASIPARTICLE ENERGIES AND BAND GAPS

An efficient DFT-GW method has been used to determine the quasiparticle spectra of the three phases of BN. It has been originally developed for the calculation of quasiparticle energies of cubic semiconductors [12] and then successfully extended to systems of lower symmetry such as SiC polytypes [13]. Local-field effects in the screening of the material are described within an LDA-like approximation, and dynamical effects are treated by expanding the self-energy operator to linear order in energy. The anisotropy of the inverse dielectric matrix is taken into account. The singularity of the Coulomb potential in the screened-exchange part of the electronic self-energy is treated using auxiliary function of the appropriate symmetry [13].

The self-energy correction of the eigenvalue $E_{n\mathbf{k}}^0$ relative to the Bloch state $|n\mathbf{k}\rangle$ is

Zincblende BN	DFT-LDA	GW(ϵ_1)	GW(ϵ_2)	Suhr <i>et al.</i> [15]	Exp. [4]
$\Gamma_{15}^v - \Gamma_{15}^c$	8.54	11.62	11.46	11.4	14.5
$\Gamma_{15}^v - X_1^c$	4.10	7.01	6.95	6.3	6.0, 6.1, 6.4, 8.0
$\Gamma_{15}^v - L_1^c$	10.26	13.20	13.04	12.4	
TVB Width $\Gamma_1^v - \Gamma_{15}^v$	22.73	25.18	25.10	23.1	22.0
UVB Width $L_1^v - \Gamma_{15}^v$	11.15	11.89	11.86	12.1	15.4, 13.5

Table IV: Calculated excitation energies in eV of zincblende Boron Nitride in comparison with theoretical and existing experimental results. The DFT-LDA values are reported in the first column, in the second and third columns respectively the GW results calculated with $\epsilon^\infty = \epsilon_1 = 4.14$, the theoretical DFT-LDA value after Ref.[14] and the experimental one, namely $\epsilon^\infty = \epsilon_2 = 4.5$ after Ref.[4]. In the fourth column the GW results after Ref.[15] and in the fifth the available experimental data after Ref.[4]. In the fourth and fifth row respectively the total and upper valence-band widths are reported.

calculated according to the equation

$$\Delta_{nk} = E_{nk} - E_{nk}^0 = [\Sigma_{nk}^{\text{COH}} + \Sigma_{nk}^{\text{SEX}} + \Sigma_{nk}^{\text{DYN}}(E^0) - V_{nk}^{XC}]/(1 + \beta_{nk}) \quad (1)$$

The terms appearing in the third member of Eq.1 are the static Coulomb Hole and Screened Exchange terms, the expectation value of the DFT-LDA exchange-correlation potential, and of the two dynamical terms Σ^{DYN} and β (see Refs. [12] and [13] for more details). For hexagonal symmetry, there are two independent components of the static dielectric tensor, which in q-space read

$$\epsilon_{\parallel,\perp}(q, \omega = 0) = 1 + [(\epsilon_{\parallel,\perp}^\infty - 1)^{-1} + q/q_{TF} + q^4/(4\omega_p^2)]^{-1} \quad (2)$$

In Eq.2 the Thomas-Fermi vector q_{TF} and the plasmon frequency ω_p depend on the effective electron densities used to approximately take into account local-field effects in the different contributions to the self-energy corrections. Dynamical screening is accounted for within the single-plasmon pole approximation.

Wurtzite BN	DFT-LDA	GW	Ref.[14]	Ref.[18]
$\Gamma_v - \Gamma_c$	8.11	11.3	8.52	8.89(11.0)
$\Gamma_v - K_c$	4.45	7.38	5.44	5.70(7.8)
$\Gamma_v - M_c$	6.52	9.47	6.67	6.65(8.7)
$\Gamma_v - A_c$	9.61	12.74	9.66	
$\Gamma_v - L_c$	6.31	9.20	6.76	
$\Gamma_v - H_c$	9.31	12.40	9.86	

Table V: Calculated band-gap energies in eV of Wurtzite Boron Nitride with respect to the top of the valence band at Γ . In the first and in the second column are respectively the DFT-LDA and GW data after the present work. Third column: LDA results by Christensen and Gorczyca (Ref.[14]); fourth column: Lambrecht and Segall, Ref.[18], including self-energy corrected data in brackets.

The excitation energies reported in Table IV for the zincblende case are in good agreement with those of Ref.[15]. For the minimum gap our data overestimate that of Suhr *et al.* and the value of 6.38eV calculated without considering local field and dynamical screening effects after Ref.[16]. For w-BN we present the first GW results including local-field and dynamical screening effect. The value of the two components of the dielectric constant are $\epsilon_{\parallel}^\infty = 4.06$ and $\epsilon_{\perp}^\infty = 4.19$ after Ref.[14], corresponding to $\epsilon^\infty = (2\epsilon_{\perp}^\infty + \epsilon_{\parallel}^\infty)/3 = 4.14$.

Hexagonal BN	This work	Ref.[17]	Ref.[11]	Ref.[10]	Ref.[5]
$\Gamma_v - \Gamma_c$	5.96		8.9		5.95
$M_v - M_c$	4.28		4.6	4.5	
$L_v - L_c$	5.42		5.6		
$A_v - A_c$	8.88		10.5		
$H_v - H_c$	4.32	4.3	4.2		
$K_v - K_c$	4.75		4.5		4.64
$H_v - M_c$	3.85	3.9	4.07	4.1	3.9
Total VB Width($\Gamma_1^v - \Gamma_6^v$)	18.39		18.8		16.62

Table VI: Calculated DFT-LDA direct band-gap energies in eV of Hexagonal Boron Nitride. Data after Ref.[17] (FLAPW), Ref.[11] (OLCAO), Ref.[10] and Ref.[5] (pseudopotentials-plane waves).

Hexagonal BN	This work	Blase <i>et al.</i> [5]
$\Gamma_v - \Gamma_c$	8.98	7.53
$M_v - M_c$	6.33	
$L_v - L_c$	7.46	
$A_v - A_c$	11.92	
$H_v - H_c$	6.66	
$K_v - K_c$	7.1	
$H_v - M_c$	6.04	5.4
Total VB Width($\Gamma_1^v - \Gamma_6^v$)	20.52	18.3

Table VII: Calculated direct band-gap energies (eV) of hexagonal Boron Nitride.

The self-energy-corrected data by Lambrecht and Segall [18] (in brackets in Table V) have been obtained by applying a *scissors-operator* [18]. As in the zincblende case, band-gap corrections of the order of 3 eV result for w-BN within our theory. The GW minimum gap corresponds to the transition $\Gamma_v - K_c$, with a 2.93 eV self-energy correction with respect to DFT-LDA.

For h-BN the DFT-LDA transition energies are in Table VI. We found good accordance with previous theoretical results. The minimum gap is indirect and corresponds to the transition $H_v - M_c$. In Fig.1 the principal DFT-LDA band gaps as functions of uniaxial distortion and hydrostatic pressure are reported. While for the hydrostatic case all band gaps increase as a function of pressure, in the case of distortions along the *c*-axis some of the band gaps show almost no variation (*L*, *H*), others increase (*A*, Γ and *K*), and other decrease (*M*) with increasing axial distortion. This behavior may be of interest for the ordering of the DFT-LDA gaps when the system is expanded along the *c*-axis. Using quadratic extrapolation [14], we find the DFT-LDA band gaps $H_v - M_c$ and $H_v - \Gamma_c$ to cross at about $\Delta c/c \simeq 12\%$. This result is in good accordance with the value of 15% obtained by Park *et al.* by FLAPW calculations [19]. This phenomenon may play a crucial role when the material is intercalated: a GW investigation of this band minima inversion is currently underway.

In Table VII we report the GW results for the principal direct gaps and the minimum band gap of h-BN, at the theoretical values of the lattice parameters. The values used for the two components of the static dielectric matrix are the experimental ones after Ref.[4], namely $\epsilon_{||}^\infty = 4.10$ and $\epsilon_{\perp}^\infty = 4.95$ corresponding to $\epsilon^\infty = 4.67$ [4, 14]. This explains the differences between our data and those of Blase *et al.* after Ref.[5] where the value $\epsilon^\infty = 4.9$

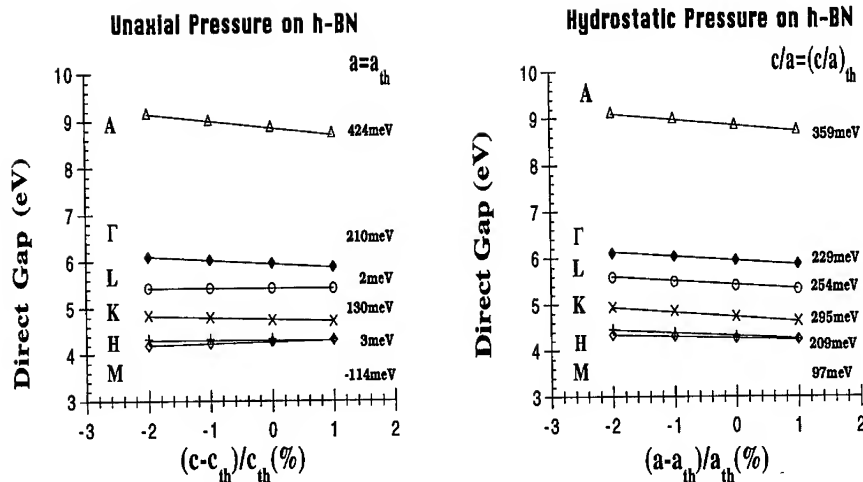


Figure 1: Principal direct band gap of h-BN as a function of applied uniaxial distortion along z-direction (left panel) and hydrostatic pressure (right panel). In the figures the variation rates on the considered lattice parameter range are reported.

has been used. Our results confirm that h-BN is an indirect band-gap material within GW theory, with minimum transition $H_v - M_c$ as found also in Refs.[5, 17]. The corresponding gap is in relatively good accordance with the quoted experimental one ($\simeq 5$ eV). It should be noted that experimental data on BN are of limited precision, since all measurements in the relevant range are affected by extrinsic transitions. Indeed this is a consequence of the difficulty of growing pure single crystals of h-BN [17].

Comparing Tables IV, V, and VII, it appears that the gaps of the three phases are ordered as $E_g^{w-BN} > E_g^{c-BN} > E_g^{h-BN}$, with transitions $\Gamma_v - K_c$, $\Gamma_v - X_c$, $H_v - M_c$ respectively. This ordering is the same within DFT-LDA and GW, and the corresponding self-energy corrections result 2.93 eV, 2.91 eV and 2.19 eV. The relative ordering of c- and w-BN is mainly determined by the DFT-LDA values; the self-energy corrections show only minor differences due to the weak anisotropy of the wurtzite-phase dielectric constants. On the other hand, the gap reduction for h-BN with respect to the denser structures can be nearly totally ascribed to a smaller self-energy correction. This is related to the larger value of the dielectric constant of the graphitic phase. There is an analogy here, apart from the important ionicity contributions in case of BN, with the gap closure occurring upon transition from insulating diamond (d-C) to semimetallic graphite (h-C) [5].

ACKNOWLEDGEMENTS

We thank Roland Stumpf for providing an updated version of his code. G. C. and V. F. thank A. Bosin, G. Bachelet and A. Filippetti for useful discussions. This work has benefited from collaborations within the HCM Network on "Ab-initio calculations of

complex processes in materials" (contract ERBCHRXCT930369): in particular, G.C. acknowledges participation at the Course "Ab initio molecular-dynamics calculations" held at the Fritz-Haber Institut, Berlin, in October 1994.

REFERENCES

1. R. S. Pearse, *Acta Crystallogr.* **5**, 536 (1952).
2. F.P. Bundy and R.H. Wentorf, *J. Chem. Phys.* **38**, 1144 (1963).
3. R.W. Wentzcovitch, M.L. Cohen, and P.K.Lam, *Phys. Rev. B* **36**, 6058 (1987).
4. *Landolt-Börnstein: Numerical Data and Functional Relationships in Science and Technology* edited by K.-H. Hellwege, Group III, Vol. 17a (Springer, New York, 1982).
5. X. Blase, A. Rubio, S.G. Louie, and M.L. Cohen, *Phys. Rev. B* **51**, 6868 (1995).
6. R. Stumpf and M. Scheffler, *Comp. Phys. Comm.* **79**, 447 (1994).
7. D. M. Ceperley and B. J. Alder, *Phys. Rev. Lett.* **45**, 566 (1980).
8. J. P. Perdew and A. Zunger, *Phys. Rev. B* **23**, 5048 (1981).
9. D.J. Chadi and M.L. Cohen, *Phys. Rev. B* **8**, 5747 (1973).
10. J. Furthmüller, J. Hafner and G. Kresse, *Phys. Rev. B* **50**, 15606 (1994).
11. Y. N. Xu and W. Y. Ching, *Phys. Rev. B* **44**, 7787 (1991).
12. F. Bechstedt, R. Del Sole, G. Cappellini, and L. Reining, *Solid State Comm.* **84**, 765 (1992).
13. B. Wenzien, G. Cappellini, and F. Bechstedt, *Phys. Rev. B* **51**, 4397 (1995).
14. N.E. Christensen and I. Gorczyca, *Phys. Rev. B* **50**, 4397 (1994).
15. M.P. Suhr, S.G. Louie, and M.L. Cohen, *Phys. Rev. B* **43**, 9126 (1991).
16. W. R. L. Lambrecht and B. Segall, *Phys. Rev. B* **40**, 9909 (1989).
17. A. Catellani, M. Posternak, A. Baldereschi, and A.J. Freeman, *Phys. Rev. B* **36**, 6105 (1987).
18. W.R.L. Lambrecht and B. Segall, Chap. 4 of *Properties of Group III Nitrides*, ed. J. H. Edgar, EMIS Datareview Series (Institution of Electrical Engineers, 1994).
19. K. T. Park, K. Terakura, and N. Hamada, *J. Phys. C* **20**, 1241 (1987).

SIMULATED THERMAL EFFECTS ON STRUCTURAL AND ELECTRONIC PROPERTIES OF GaN

S. SERRA*, L. MIGLIO*, Vincenzo FIORENTINI**, (*) Istituto Nazionale di Fisica della Materia, Dipartimento di Fisica dell'Universita' di Milano, *via Celoria 16, I-20133 Milano (Italy)*,
(**) Istituto Nazionale di Fisica della Materia, Dipartimento di Scienze Fisiche dell' Universita' di Cagliari, *via Ospedale 72, I-09124 Cagliari, (Italy)*

ABSTRACT

We present preliminary results of tight binding molecular dynamics (TBMD) simulations concerning the thermal effects on the structural and electronic properties of GaN. We derived a semiempirical tight binding (TB) potential which is able to reproduce the band structure and the phase diagram of GaN for zincblende, wurtzite and rock-salt phases. We have found that even at few hundreds K above the experimental melting temperature the local ordering is fairly well conserved, with the fraction of wrong bonds quite low. Defects states appear in the gap at approximately 2.3 eV in agreement to the experimental indication for annealed films.

INTRODUCTION

The Nitrides are III-V compounds characterized by high stability and chemical inertness, with large band gaps, from 1.95 eV to 6.4 eV. For these properties they attracted much attention, since the early eighties, for possible applications in high power and high temperature electronic devices. GaN is the most promising among Nitrides [1,2], in particular for future applications in optoelectronics devices, such as light emitting diodes [3] and UV emitting Lasers [4]. Despite the advances in the growth of GaN films, important problems are still open or have not received much attention. Among the former is the nature of native defects and to the second one belongs the thermal effects on GaN. Any application in electronic devices requires a good understanding of the nature of native defects, and the thermal stability of GaN is an essential question for the high temperature applications and for high power electronic devices. In fact, the thermal generation of defects can compromise the properties of these devices. Then a computational investigation on these subjects would be very important, focusing in particular on the characterization of the thermal disorder induced by an high temperature treatment and the related effects on the gap. We used TBMD which optimally coniugates the needs for a good modelling of the interactions with a relatively low computational cost. Large scale simulations and long period of observation which are out of range for fully *ab-initio* method are instead accessible to TBMD.

THEORY

The TB potential has been determined in the framework of the semiempirical two-center approximation [5]. Within this model the potential is constituted by a sum of two terms: the first one, E_{bs} , give the attractive part and is known as the band structure potential; the second one, E_{rep} , is the repulsive term and phenomenologically accounts for the quantum mechanical repulsion between occupied orbitals.

The band structure contribution is given by the sum of TB eigenvalues up to the Fermi level and parametrically depends on the two center Slater-Koster hopping parameters $h_{ij\alpha\beta}^0$. The latter change, in our case, with the atomic position according to the Harrison-Sawada scaling rules [6], (see eq. (1))

$$h_{ij\alpha\beta}(r_{ij}) = h_{ij\alpha\beta}^0 (v_{ij}) (r_0/r_{ij})^p [1/(\exp((r_{ij}-r_c)/g_c)+1)] \quad (1)$$

Here i,j are the atom indexes and α,β indicate the symmetry of the atomic orbitals. v_{ij} indicates the unit vector of the vector r_{ij} and p, r_c, g_c are disposable parameters of the scaling rules. An sp^3s^* basis set has been chosen: the s^* orbitals represent the shell of d orbitals of gallium atoms. These orbitals give rise to deep and narrow bands, so that they can be considered as a closed shell with s character. We have determined the band structure parameters $h_{ij\alpha\beta}^0, p, r_c$ and g_c by fitting them onto *ab-initio ultrasoft-pseudopotential* bands [7] of rock-salt (rs) and zincblende (zb) along selected high symmetry directions (Γ -X, Γ -L, X-K). The resulting electronic density of states for these phases and wurtzite (wz) are shown in Fig.1.

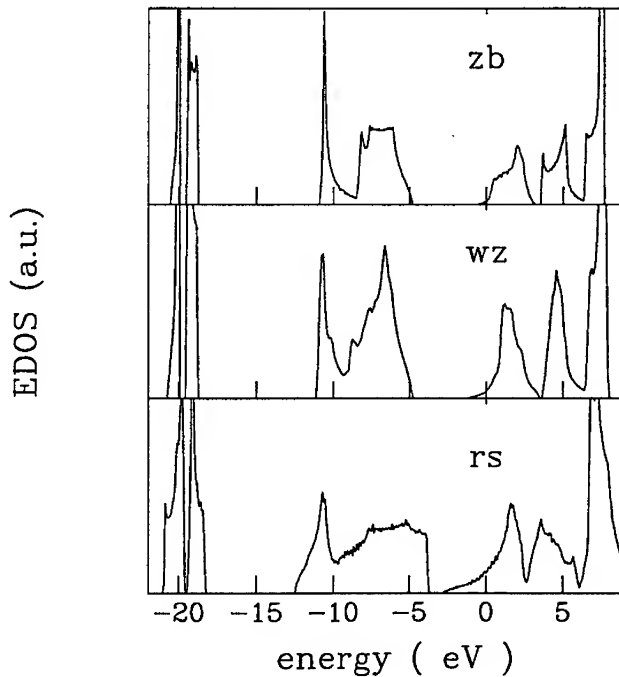


Fig. 1 Electronic density of states (EDOS) of zb-GaN (panel a), wz-GaN (panel b) and rs-GaN (panel c)

The EDOS are in good agreement to the *ab initio* calculations but for the gap which has been fitted to the experimental value of *zb*, since the *ab initio* LDA predictions are known to underestimate it. In particular the rock-salt phase turns out to be semiconducting with a small gap, about 1 eV. This result is generated by the inclusion of the Ga-Ga second nearest neighbour interactions which are also important for the correct prediction on native defects formation energy, as recently shown by Van de Walle *et al* [8]. In fact a TB potential limited to first neighbour interactions, like the one of Jenkins and Dow [9], predicts a metallic character for the rock-salt GaN and displays a limited transferability.

The repulsive potential has been written as a sum of central two-body terms like (2)

$$E_{\text{rep}} = 1/2 \sum_{i,j} \Phi(i,j) (r_0/r_{ij})^q [1/(\exp((r_{ij}-r_c)/g_c)+1)] \quad (2)$$

The parameters $\Phi(i,j)$, q , have been determined from the total energy curves of zincblende and rock-salt phases by fitting the equilibrium volumes, the bulk modula and the cohesion energy difference, while r_c and g_c are the same as in the band structure scaling laws. The long range interactions has been included in the calculations by an Ewald sum concerning the effective charges on each atomic sites. The resulting potential reproduces quite well the *ab initio* total energy diagram of the GaN for all the relevant phases [7,10], as it is shown in Fig. 2.

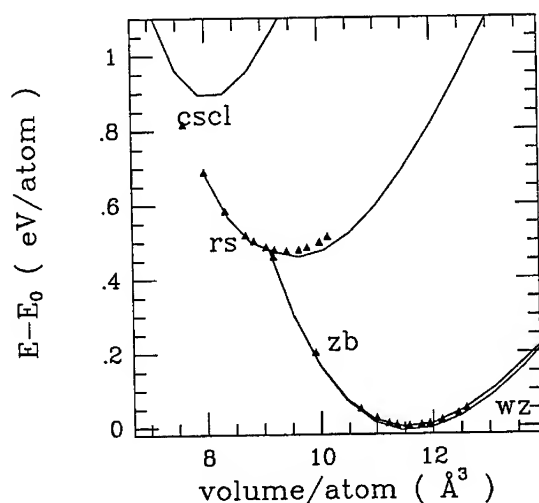


Fig. 2 : Total energy curves vs volume/atom of wz, zb, rs and cesium chloride phases, as referred to the equilibrium energy value E_0 of zb. Triangles represent *ab-initio* data [7]

Additional checks has been done on the formation energy of some native defects: they display a good agreement to the results of Van de Walle *et al.*. We have found a formation energy of 5.9 eV for the N antisite N_{Ga} and 10 eV for the Ga antisite GaN , with a unit cell of 64 atoms in the zincblende structure. Additional calculations on other native defects are still in progress.

RESULTS

We have performed a TBMD simulation within the canonical ensemble, by using the TB potential outline above. In order to attain long simulation times we limited the cubic simulation cell to 64 atoms and the time step was chosen to be 1 fs. This value ensures a good energy conservation (10^{-4} eV/atom). The crystalline sample has been rapidly heated from 300 K up to 4000 K in 2 ps. Then the sample has been held at this temperature for 2 ps. This procedure is commonly used in order to speed up the melting process in the limited time scale allowed by a computer simulation. After that the temperature of the sample has been decreased to 2300 K, slightly above the experimental melting temperature. Finally the sample has been equilibrated at this temperature for 7 ps and observed for a subsequent 1 ps.

The pair correlation function in Fig. 3 (left panel) shows a lack of long range order. Only the first neighbour peak and a smaller second neighbour feature are still detectable.

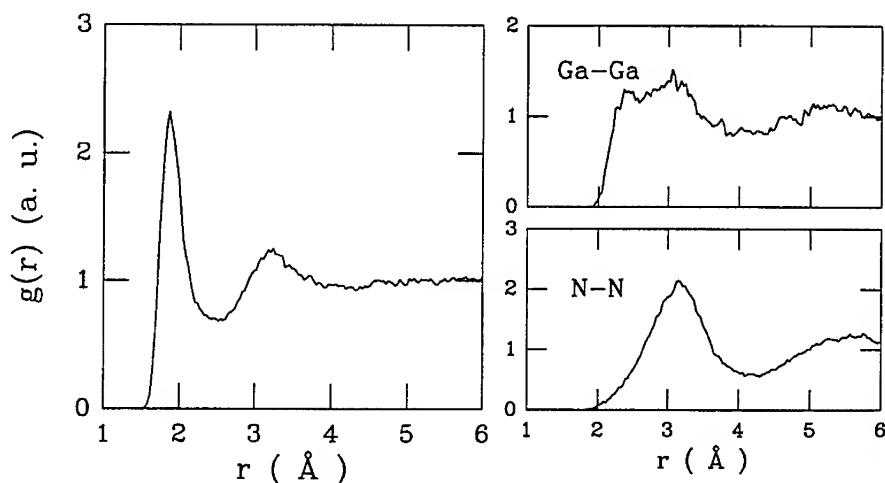


Fig. 3. Left panel : Pair correlation function of the sample at 2300 K.
Right panel : Partial Ga-Ga pair correlation function (top), partial N-N pair correlation function (bottom).

At variance with respect to what should be expected on the basis of a mass criterion it is seen that the Ga atoms are more disordered than N ones. The second neighbour peaks, still present in N-N pair correlation function (top panel), has completely disappeared in the Ga-Ga pair correlation function (bottom panel). The drift of the cations towards a reduced second neighbour distance is quite common in the III-V compounds [11] and it is mainly due to the long range of the Ga p-orbitals. Here, however, the strong repulsion between Ga d orbitals prevents the penetration of the second neighbour cations into the first neighbour anion shell. The conservation of the second neighbour anion shell is probably due to the narrow localization of N orbitals. Moreover, it is well known [12] that the most stable phases for solid N are structures like the α -N₂, which consists of

triple bonded N_2 dimers, on the contrary single-bond networks are highly unstable. Both this mechanisms cooperate in strongly bonding the N atoms to the Ga atoms and inhibit the formation of N-N bonds.

This trend is confirmed by the analysis of the bond angle distribution $g(\theta)$ (see Fig. 4), where the tendency to form Ga-Ga bonds is pointed out by the growth of an additional peak between 50-60° in X-Ga-X $g(\theta)$, a feature which is absent in the X-N-X $g(\theta)$.

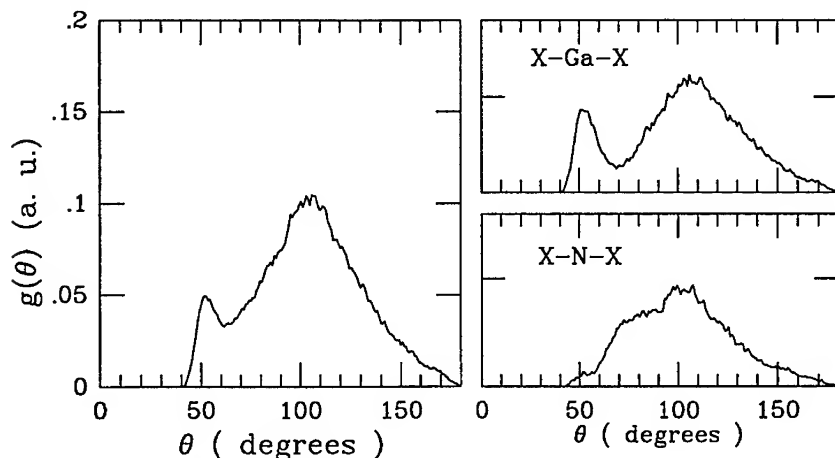


Fig. 4. Left panel : Bond angle correlation function of sample at 2300 K. Right panel : Partial X-Ga-X bond angle correlation function (top), partial X-N-X bond angle correlation function (bottom).

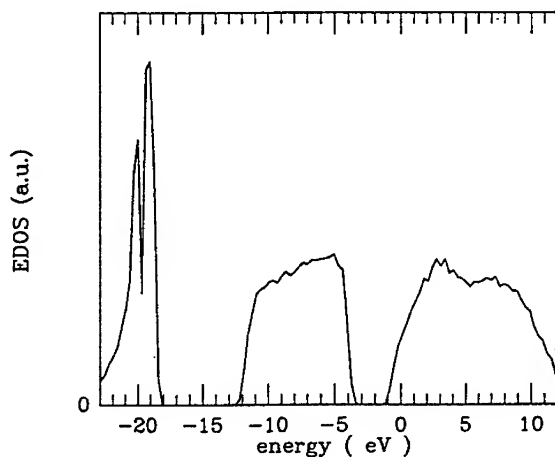


Fig. 5. Electronic density of states (EDOS) for our the sample at 2300 K

In Fig. 5, we report the electronic density of states, for our sample at 2300 K. Still present is a sizable gap (2.3 eV) which is smaller than those of crystalline zincblende (3.5 eV). Despite the fact that no Ga_N defects are present, the gap decrease is due to the appearance of p states above the valence band edge, as is the case for Ga antisites. This feature can be understood as produced by the large overlap between Ga p-orbitals when they come at closer distance. This is consistent with the pair correlation function and bond angle distribution data. Actually our results are in quantitative agreement with the experimental data of Lin *et al.* [13] where the presence of defect states at 2.3 eV is found in photo-luminescence spectra of annealed samples.

Finally the fraction of wrong bonds is very low since the coordination between cations and anions is 3.93 with respect to the total coordination number which is 4.1 for N and 4.5 for Ga.

In conclusion we predict a much more conservative structure for GaN against thermal treatment, with respect to other III-V compounds. We believe that an important contribution to the persisting ordering of anion shells might be given by the strong coulombic interactions, a feature commonly observed in molten salt.

ACKNOWLEDGMENTS

We thank Dr. L. Colombo (Milano) for his useful comments and hints on MD simulations.

REFERENCES

- [1] S.Nakamura, T. Mukai, M.Senoh, J.Appl.Phys. **71**, 5543, (1992)
- [2] T.Lei, M.Fanciulli, R.J.Molnar, T.D.Moustakas, and R.J.Graham, J. Scanlon, Appl. Phys.Lett. **59**, 944, (1991).
- [3] S. Nakamura *et al.*, Appl. Phys. Lett. **64**, 13, (1994)
- [4] R.F.Davis, Proc. IEEE **79**, 703, (1991)
- [5] J.C. Slater, and G.F.Koster, Phys. Rev. **94**, 1498, (1954)
- [6] S.Sawada, Vacuum **1**, 612 (1992)
- [7] V.Fiorentini, M. Methfessel, and M. Scheffler, Phys. Rev. B **47**, 13353 (1993); V.Fiorentini *et al.*, in "The Physics of Semiconductors", D.J. Lockwood ed. (World Scientific, Singapore 1995), p. 137; A.Satta *et al.*, these Proceedings
- [8] J. Neugebauer and C.G. Van de Walle, Phys. Rev B **50**, 8067 (1994)
- [9] D.W. Jenkins and J. D. Dow, Phys. Rev. B **39**, 3317, (1989)
- [10] N.E.Christensen, I. Gorczyca, Phys. Rev. B **50**, 4397, (1994)
- [11] C. Molteni, L. Colombo, L. Miglio, J. Phys.: Condens. Matter **6**, 5255, (1994)
- [12] C.Mailhot, L.H.Yang, A.K.McMahan, Phys. Rev. B **46**, 14419, (1992)
- [13] M.E.Lin, B.N.Sverdlov, M.H.Morkoc, Appl.Phys.Lett. **63**, 3625, (1993)

Part VI
Electronic Properties

SHALLOW AND DEEP LEVEL DEFECTS IN GaN

W. GÖTZ*, N.M. JOHNSON*, D.P. BOUR*, C. CHEN**, H. LIU**, C. KUO**,
W. IMLER**

*Xerox Palo Alto Research Center, Palo Alto, California 94304, USA

**Hewlett Packard Co., San Jose, California 95931, USA

ABSTRACT

Shallow and deep electronic defects in MOCVD-grown GaN were characterized by variable temperature Hall effect measurements, deep level transient spectroscopy (DLTS) and photoemission capacitance transient spectroscopy (O-DLTS). Unintentionally and Si-doped, n-type and Mg-doped, p-type GaN films were studied. Si introduces a shallow donor level into the band gap of GaN at $\sim E_c - 0.02$ eV and was found to be the dominant donor impurity in our unintentionally doped material. Mg is the shallowest acceptor in GaN identified to date with an electronic level at $\sim E_v + 0.2$ eV. With DLTS deep levels were detected in n-type and p-type GaN and with O-DLTS we demonstrate several deep levels with optical threshold energies for electron photoemission in the range between 0.87 and 1.59 eV in n-type GaN.

INTRODUCTION

The III-V nitride semiconductors, GaInAlN, have evolved into the materials of choice for the fabrication of visible light emitting diodes exhibiting external quantum efficiencies of almost 10 %.^{1,2} They are direct, wide bandgap semiconductors that also show great promise for high temperature / high power devices.³ However, despite intensive efforts injection laser diodes have not been achieved to date with III-V nitrides. Low p-type doping efficiency and the presence of deep levels that act as competing recombination centers contribute to the difficulties in achieving threshold carrier densities for lasing in III-V nitride laser diodes. To enable injection laser diodes with III-V nitrides the electronic properties of shallow n- and p-type dopants and of deep level defects need to be understood and controlled.

Little is known about the electronic properties of Si donors and Mg acceptors, which are commonly employed for doping GaN layers n-type⁴ and p-type,⁵ respectively. Also, the nature of the n-type background conductivity observed in most of the epitaxial GaN films is still not fully understood.⁶ Shallow donor and acceptor levels in GaN were mainly characterized by variable temperature Hall effect measurements and activation energies of ~ 27 meV for Si donors⁷ and ~ 150 meV for Mg⁸ are reported in the literature. However, these values were derived from Arrhenius analyses of the measured electron concentration with the assumption of a temperature independent prefactor and, therefore, have a large uncertainty. Mg doping poses an additional problem: as-grown Mg-doped GaN is usually semiinsulating and postgrowth treatments such as low energy electron beam irradiation (LEEBI)⁵, furnace annealing, or rapid thermal annealing (RTA)⁹ are required to activate the Mg dopants.¹⁰⁻¹³

Defects that introduce electronic levels deeper into the bandgap of III-V nitrides have mainly been investigated by photoluminescence spectroscopy (PL).¹⁴⁻¹⁶ PL spectroscopy has the ability to detect deep level related radiative emission processes over the entire spectral range of the band gap of GaN but lacks the information on the position of individual electronic states which participate in electron-hole pair recombination processes. Subject of extensive studies has been the "yellow PL band", which is commonly observed in PL spectra of n-type GaN and related to

deep levels. However, the recombination mechanism and the defects that are responsible for this broad PL signal centered at ~ 2.2 eV are unknown.¹⁷⁻²⁰ Recently, the transition metal impurities Fe, Va, and Cr were identified by the observation of PL lines associated with internal, atomic transitions.²¹

Characterization of deep level defects in GaN by deep level transient spectroscopy (DLTS) has also been demonstrated.²²⁻²⁴ While DLTS is a sensitive spectroscopic tool for the characterization of electronic levels deep in the bandgap of semiconductors, it is of limited use in wide bandgap materials because it utilizes thermal energy for charge emission. Therefore, the accessible range of level energies in the gap is restricted to ~ 1 eV of either band edge, for typical trap parameters and practical measurement conditions. The application of photoemission capacitance transient spectroscopy (O-DLTS), also termed deep level optical spectroscopy, overcomes this limitation by utilizing monochromatic light for carrier emission so that levels in the entire bandgap become accessible for characterization.²⁵

In this study, the electronic properties of shallow dopants were investigated in n-type and p-type MOCVD-grown GaN by variable temperature Hall effect measurements. Undoped, Si-doped and Mg-doped GaN samples were studied. Deep levels in GaN were investigated by DLTS and O-DLTS for Si-doped and Mg-doped samples. For the capacitance transient measurements on the n-type material, Schottky diodes equipped with an Ohmic back contact and low series resistance were designed. The capacitance transient measurements for p-type material were conducted on p-n⁺ junction diodes.

EXPERIMENTAL

The GaN material used in this study was heteroepitaxially grown by MOCVD at $\sim 1050^\circ\text{C}$ on polished (0001)-oriented sapphire crystals. Some of the growth conditions are listed in Table I. The samples were grown in different MOCVD reactors with either GaN or AlN low-temperature buffer layers and at various growth pressures. The n-type GaN films were either unintentionally-doped (sample # 1) or Si-doped (sample # 2 to 7). P-type conductivity was achieved by doping with Mg (sample # 8 and 9). The acceptors were activated by an RTA process. For the Hall-effect measurements, the samples (# 1 to 5, and 8) were cut to $5 \times 5 \text{ mm}^2$ size and metal dots were vacuum evaporated in the four corners to obtain electrical contacts in the Van der Pauw geometry. The contacts were annealed at 230°C for 20 min and were Ohmic over the entire temperature range of the Hall effect measurements. For the fabrication of Schottky diodes (samples # 6 and 7) two layers of intentionally doped GaN were grown. The GaN layer grown directly over the buffer layer was heavily doped with Si. The electron concentration measured at room temperature in the $\sim 1\text{-}2 \mu\text{m}$ thick n⁺ layer was $\sim 2 \times 10^{18} \text{ cm}^{-3}$. A semiconducting layer of n-type GaN was then grown directly on the n⁺ layer. This layer was $\sim 1 \mu\text{m}$ thick in sample # 6 and $\sim 5 \mu\text{m}$ thick in sample # 7. Schottky contacts were fabricated by vacuum evaporating Au onto the n-type GaN layer through a shadow mask. The Ohmic contacts were subsequently applied by evaporating a metal over the laterally exposed n⁺-layer. The metal films were $\sim 150 \text{ nm}$ thick. One-sided, p-n⁺ junction devices were grown to enable capacitance transient measurements for p-type, Mg-doped GaN. The n⁺ layer, deposited directly onto the low-temperature GaN buffer layer was $\sim 5 \mu\text{m}$ thick. On top of the n⁺ layer, a Mg-doped GaN film with a thickness of $\sim 0.56 \mu\text{m}$ was grown. Mesa diodes with a diameter of $\sim 0.5 \text{ mm}$ were fabricated by dry etching and deposition of Ti/Au metal films onto the n⁺ and p-type layers.

The Schottky and pn⁺-diodes were tested by current-voltage and capacitance voltage (C-V) techniques.²² The dopant profile of the n-layer (sample # 6 and 7) or p-layer (sample # 9) derived

Table I: GaN samples investigated in this study. For each sample (column one), the reactor type (column two) and the growth-pressure (column three) are shown. All the GaN samples were grown on sapphire substrates with either a GaN or AlN buffer layer (column four). The samples were unintentionally, Si- or Mg-doped (column five).

sample #	reactor	growth-pressure	buffer layer	doping
1	horizontal	80 Torr	GaN	n-type / unintentionally
2, 3, 4, 5, 6	vertical (EMCORE)	80 Torr	GaN	n-type / Si
7	horizontal	atm. pressure	AlN	n-type / Si
8, 9	vertical	700 Torr	GaN	p-type / Mg

from the analysis of the C-V measurements was found to be uniform in the measured depth range below the surface. The average net ionized donor concentration at room temperature was measured to be $2.2 \times 10^{17} \text{ cm}^{-3}$ for sample # 7 and $1.9 \times 10^{17} \text{ cm}^{-3}$ for sample # 8. For sample # 9, an effective acceptor concentration of $\sim 2 \times 10^{18} \text{ cm}^{-3}$ was determined.

The Hall effect and the DLTS measurement system utilized in this study is described in Ref. 11 and 22, respectively. Hall effect data were taken in the temperature range between 80 K and 500 K and DLTS transients were recorded with 1 K increments over the temperature range from 90 K to 470 K, with the temperature held constant to within ± 0.1 K. The O-DLTS apparatus is described in Ref. 25. During the measurements the samples were situated in a cryostat and the sample temperature was maintained at 150 ± 0.1 K.

UNINTENTIONALLY-DOPED AND Si-DOPED, n-TYPE GaN

Shallow levels in n-type GaN were studied with variable temperature Hall effect measurements. They result in electron concentrations n which were obtained from the experimental Hall constants R_H with $n = r_H/qR_H$ (q = electronic charge); the Hall scattering factor r_H is unknown for GaN, but was assumed to be isotropic, temperature independent and of unity value ($r_H \equiv 1$). A typical data set obtained from unintentionally doped GaN (sample # 1) is presented in Fig. 1. The experimental data are represented by solid squares. To obtain information about the donors which determine the electron freeze-out behavior as demonstrated in Fig. 1a, we performed a least-squares fit of the charge neutrality equation to the experimental data. The charge neutrality equation for n-type, wide band gap semiconductors (intrinsic carriers are neglected) with M independent donors is given by

$$n + N_{\text{comp}} = \sum_{i=1}^M \frac{N_{D_i}}{1 + \frac{g_i n}{N_C} \exp\left(\frac{\Delta E_{D_i}}{kT}\right)}, \quad (1)$$

where the index i refers to the i -th donor; N_{D_i} is its concentration, g_i the degeneracy of its electronic state in the band gap, and ΔE_{D_i} the thermal activation energy of the donor electrons. N_{comp} is the concentration of compensating acceptors and N_C is the conduction band effective density of states; k is the Boltzman constant and T the sample temperature. For the fit shown in

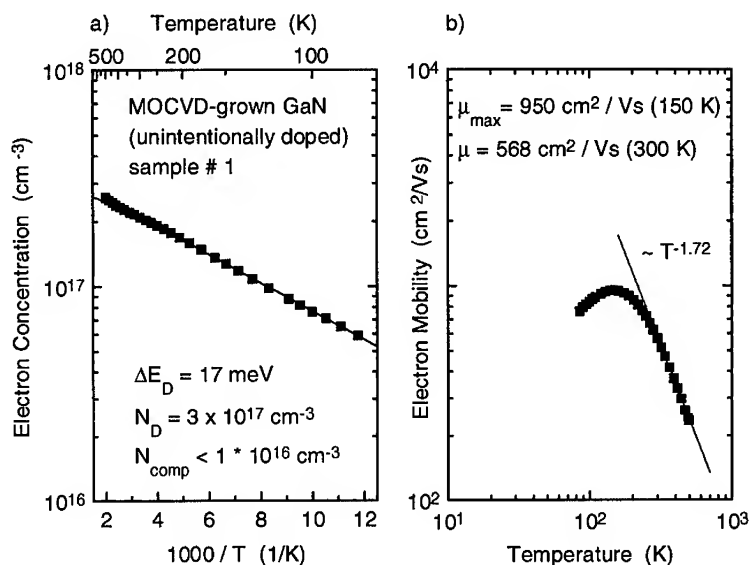


Figure 1. Electron concentration vs reciprocal temperature (a) and Hall mobility vs temperature (b) for unintentionally-doped, n-type GaN. The solid squares refer to the experimental data. The solid line in Fig. 1a results from a least-squares fit which is described in the text. The fit yields parameters for a shallow donor which are defined as follows: ΔE_D is the activation energy for the donor electrons and N_D is the concentration of the donors. N_{comp} is the concentration of compensating acceptors present in the sample. In Fig. 1b, a straight line is fitted to the high energy portion of the mobility data and yields a power dependence of the mobility of $T^{-1.72}$.

Fig. 1a, a single donor and an effective mass for electrons in GaN of $0.2m_0$ (m_0 = mass of a free electron)³ were assumed. The calculated electron concentration as a function of the sample temperature is indicated by the solid straight line. Parameters of the donor level are depicted in Fig. 1a. The room temperature mobility and the peak mobility for sample # 1 is $568 \text{ cm}^2/\text{Vs}$ (300 K) and $950 \text{ cm}^2/\text{Vs}$ (150 K), respectively (Fig. 1b).

Figure 2 shows Hall effect results for Si-doped GaN samples (# 2, 3, 4, 5). The Si doping was achieved by flowing SiH_4 , and the flux was gradually increased from sample # 2 to 5. Consequently, the electron concentrations increased accordingly as determined by Hall effect measurements. For samples # 2, 3, and 4 the experimental Hall effect data were used to obtain information about shallow donors that give rise to the n-type conductivity in Si-doped GaN films by least-squares fits of equation (1). For these fits, two independent donor levels had to be assumed. Defect parameters are summarized in Table II. The temperature dependence of the electron concentration of sample # 4 at temperatures below 250 K indicates defect band conduction leading to a deviation of the fitted curve from the experimental data. For sample # 4 only data above 250 K was used for the fit. The electron concentration of sample # 5 does not vary with the sample temperature indicating a doping level above the degeneracy limit. The charge neutrality condition as given in equation (1) cannot describe the temperature dependence of the electron concentration for a degenerately doped semiconductor and, therefore, no fit was attempted. The room temperature and the peak mobilities of the Si-doped samples depend on the

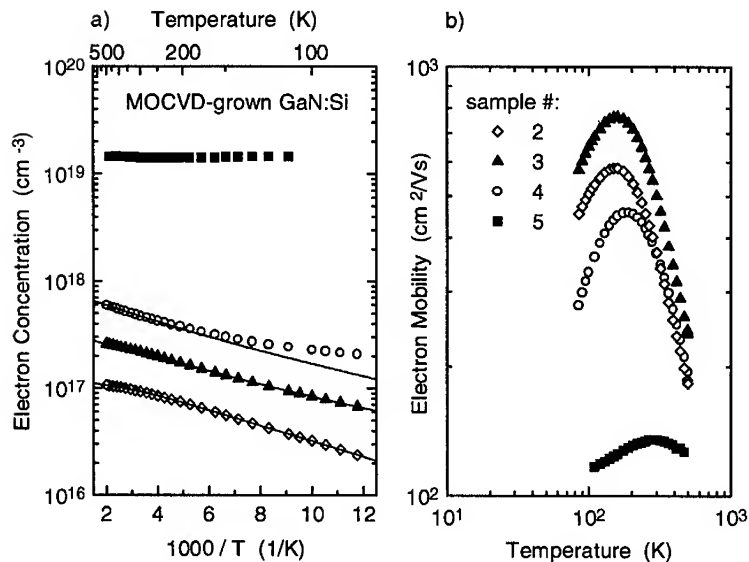


Figure 2. Electron concentration vs reciprocal temperature (a) and Hall mobility vs temperature (b) for Si-doped GaN. The solid squares refer to the experimental data. The solid lines in Fig. 2a result from least-squares fits to the experimental data. The fits yield parameters for shallow donors which are summarized in Table II.

Si content. Sample # 2, which has the lowest Si content has a room temperature (300 K) mobility of $370 \text{ cm}^2 / \text{Vs}$ and a peak mobility of $582 \text{ cm}^2 / \text{Vs}$ at 150 K. The highest mobilities for Si-doped material are measured in sample # 3 with values of $501 \text{ cm}^2 / \text{Vs}$ (300 K) and $764 \text{ cm}^2 / \text{Vs}$ (160 K). In sample # 4 the mobilities are $369 \text{ cm}^2 / \text{Vs}$ and $459 \text{ cm}^2 / \text{Vs}$ (190 K). For sample # 5 the peak mobility is measured at 300 K with $135 \text{ cm}^2 / \text{Vs}$. The temperature dependence of the mobilities at temperatures higher than the peak mobilities is well approximated by a power dependence $\sim T^{-1.5}$ for all Si-doped GaN films shown in Fig. 2b (except sample # 5).

The Hall effect analysis shows that the n-type conductivity in our unintentionally doped material (sample # 1) is due to a shallow donor level with an activation energy of $\sim 17 \text{ meV}$ (Fig. 1a). A donor with a similar activation energy (ΔE_{D1}) is present in samples # 2, 3, and 4, which were intentionally doped with Si (Table II). The concentration of this donor (N_{D1}) increases according to the flow rates of SiH_4 which was increased from sample # 2 to 5. Therefore, it seems reasonable to conclude that the shallow donor level with an activation energy in the range between 12 meV and 17 meV is due to Si incorporation into GaN and that the presence of Si is responsible for the n-type conductivity in our unintentionally doped material. Si substituting for Ga acts as a shallow donor in GaN.⁴ Results from secondary ion mass spectrometry (SIMS) confirm this assumption. First, the concentration of Si increases according to the concentration of the shallowest donor level (Table II, sample # 2 to 4, N_{D1}). Second, the atomic concentration of Si is found to be $\sim 4 \times 10^{17} \text{ cm}^{-3}$ in sample # 1 (Table II). Possible sources for Si incorporation during the growth of undoped GaN are the nitrogen source gas, NH_3 , which may contain residual SiH_4 , or SiO_2 dissolving from the quartz-tube of the MOCVD reactor.

Table II: Parameters for shallow donors as determined from least-squares fits of the charge neutrality equation to the experimental Hall effect data and results from secondary ion mass spectrometry (SIMS) for n-type GaN samples (column one). The parameter set includes donor electron activation energies (ΔE_{D1} , column two and four) and concentration of shallow donors (N_{D1} , column three and five) for two independent donors. Also given is the concentration of compensating acceptors (N_{comp} , column six). SIMS results for the Si content are summarized in column seven.

sample #	Hall effect					SIMS
	ΔE_{D1} (meV)	N_{D1} (cm ⁻³)	ΔE_{D2} (meV)	N_{D2} (cm ⁻³)	N_{comp} (cm ⁻³)	[Si] (cm ⁻³)
1	17	3.1×10^{17}			no	4×10^{17}
2	15	1.1×10^{17}	37	3.9×10^{16}	3.2×10^{16}	2×10^{17}
3	14	2.3×10^{17}	34	6.9×10^{16}	no	5×10^{17}
4	12	7.4×10^{17}	32	6×10^{16}	no	9×10^{17}
5						2×10^{19}

The activation energy for Si donor electrons in GaN was determined previously from Hall effect measurements in Ref. 7 to be ~ 27 meV. However, the authors neglected the temperature dependence of the prefactor in the Arrhenius analysis of the Hall data. It can be shown that the simplified analysis with $n \sim \exp(-\Delta E_D / kT)$ yields a value of $\sim 4 \Delta E_D / 3$.²⁷

The determination of the activation energy of Si donor electrons performed in this study uses an accurate analysis according to the charge neutrality equation (1) and yield activation energies ΔE_{D1} in the range between 12 meV and 17 meV. The decreasing activation energies with increasing donor concentrations observed for samples # 2, 3 and 4 (Table II) can be explained by interaction of the donor wave functions which reduces ionization energies and has also been observed for other semiconductors e.g., Si or Ge.²⁸ However, the unknown Hall scattering factor and its temperature dependence poses an uncertainty in the determination of this value. Results from PL spectroscopy measurements for sample # 1 indicate the position of the optical Si level to be $E_c - (20 \pm 6)$ meV.²⁷ The donor binding energy for a shallow donor can be estimated with a hydrogenic model. With an effective electron mass of $0.2m_0$ (m_0 - mass of a free electron) and a relative dielectric constant of ~ 10 , this analysis yields ~ 27 meV.⁷ However, the parameters for this analysis are not well established and it is too early to conclude whether a negative central cell correction for Si donors applies.

A second donor level with electron activation energies (ΔE_{D2}) between 32 meV and 37 meV is observed in samples # 2, 3, and 4 (Table II). This donor level may be due to oxygen contamination. Oxygen substituting for nitrogen has been suggested to act as a shallow donor and may contribute to the n-type background conductivity in unintentionally-doped GaN.

ACCEPTORS IN Mg-DOPED GaN

In Fig. 3 we show variable temperature Hall effect data for Mg-doped GaN (sample # 8). The hole concentration is given in Fig. 3a and the hole mobility in Fig. 3b. Sample # 8 was annealed at 800°C for 5 min. The freeze-out of the hole concentration is observed over a range of six orders of magnitude. The solid line results from a least-squares fit of equation (1) for a single acceptor. The effective mass for holes was assumed to be equal to m_0 . Parameters of the fit are depicted in

the figure. The hole mobility reaches a maximum value of $\sim 24 \text{ cm}^2 / \text{Vs}$ at 160 K and is $\sim 14 \text{ cm}^2 / \text{Vs}$ at 300 K. The high temperature portion of the mobility data follows a power law of $\sim T^{-1.8}$.

The Hall effect analysis reveals that an acceptor with a hole activation energy of $\sim 170 \text{ meV}$ dominates the p-type conductivity in Mg-doped GaN (Fig. 3a). It is reasonable to assume that the acceptor is identical with Mg atoms substituting for Ga in the GaN lattice. An atomic Mg concentration of $\sim 2 \times 10^{19} \text{ cm}^{-3}$ was measured with SIMS in sample # 8. Therefore, not all of the Mg present in sample # 8 acts as an acceptor ($N_A \sim 7 \times 10^{18}$) after annealing at 800°C . Further activation of sample # 8 at 850°C led to an acceptor concentration of $\sim 1.9 \times 10^{19} \text{ cm}^{-3}$ indicating that, within the uncertainties of the SIMS analysis and the Hall effect measurements, all Mg atoms can be converted into acceptors (Mg_{Ga}). However, in this state impurity band conduction dominates the p-type conductivity at temperatures below 200 K in sample # 8 and limits the usable range of hole concentrations for the determination of the activation energy with our least-squares fit procedure. An activation energy of $\sim 170 \text{ meV}$ is typically observed for Mg-doped, p-type GaN.¹² A hole activation energy of 0.16 eV has been determined for MBE-grown, Mg-doped GaN by Hall effect measurements²⁹ and 0.15 - 0.16 eV were determined from the temperature dependence of donor-acceptor pair recombination of MOCVD-grown, Mg-doped, p-type GaN observed by PL.³⁰ Tanaka and coworkers³¹ used a similar analysis for variable temperature Hall effect data as described in this study and determined a hole activation energy of 157 meV for Mg acceptors in GaN.

Recent analyses of DAP recombinations from PL spectroscopy experiments suggest that the position of the optical Mg acceptor level is $\sim 0.21 \text{ eV}$ above the valence band edge.²⁷

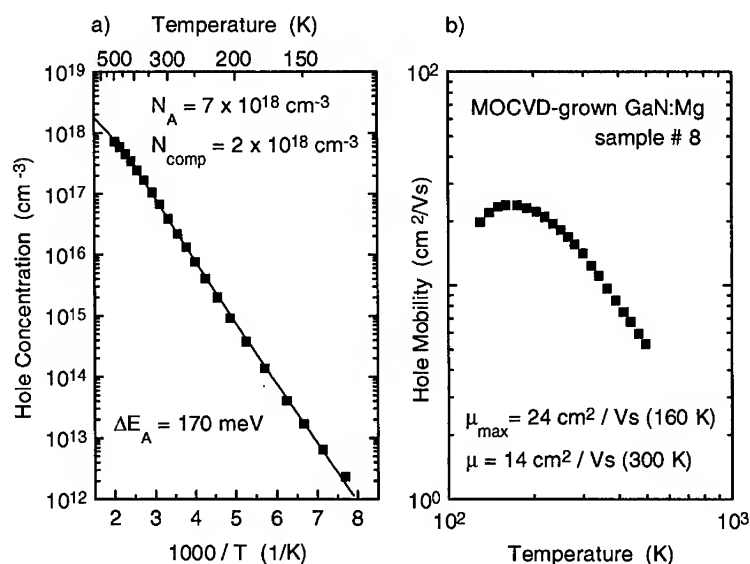


Figure 3. Hole concentration vs reciprocal temperature (a) and hole mobility vs temperature (b) for Mg-doped GaN. The solid squares refer to the experimental data and the solid line in Fig. 3a results from a fit of a model that assumes a single acceptor and with the activation energy ΔE_A (concentration N_A) and donor compensation (N_{comp}).

DEEP LEVELS IN n- AND p-TYPE GaN

Two DLTS spectra for n-type GaN Schottky diodes (# 6 and 7) are presented in Fig. 4. The DLTS signal, $|C(t_1) - C(t_2)|$, for sample # 6 and 7 is displayed for delay times $t_1 / t_2 = 40 \text{ ms} / 160 \text{ ms}$ and $8 \text{ ms} / 32 \text{ ms}$; the emission rates are 11.6 s^{-1} and 57.8 s^{-1} , respectively. The spectrum for sample # 6 reveals three DLTS peaks at 124 K (DLN_1), 284 K (DLN_2), and 445 K (DLN_3), respectively, which arise from electron emission from three electronic deep levels to the conduction band. The peak in the DLTS spectrum of sample # 6 labeled DLN_3 is not completely monitored in the temperature range of our measurement. The spectrum of sample # 7 exhibits two DLTS peaks at 140 K and 304 K which are also labeled DLN_1 and DLN_2 . In the temperature range displayed in Fig. 4 (90 K - 460 K), no other deep level could be detected with the sensitivity of $\sim 1 \text{ fF}$ of our DLTS measurement.

A DLTS spectrum taken for p-type GaN (sample # 9) is shown in Fig. 5. The delay times t_1 and t_2 are 12 ms and 36 ms, respectively; the emission rate is 45.8 s^{-1} . The spectrum reveals three peaks at 230 K (DLP_1), 306 K (DLP_2), and 430 K (DLP_3), which arise from hole emission from three electronic deep levels to the valence band.

The activation energies for electron and hole emission of the deep levels were determined by an Arrhenius analysis of the electron and hole emission time constants.²² The analysis yields activation energies for electron and hole emission into the conduction and valence band, respectively. However, the determination of the activation energy depends on the temperature dependence of the electron and hole capture cross section. In Table III we summarize the activation energies for the observed deep levels in n- and p-type GaN with DLTS. These energies have not been corrected for any temperature dependence ($\sigma_n \propto T^0$). The uncertainty of these values is dominated by the unknown temperature dependence of σ_n . In addition, these values may

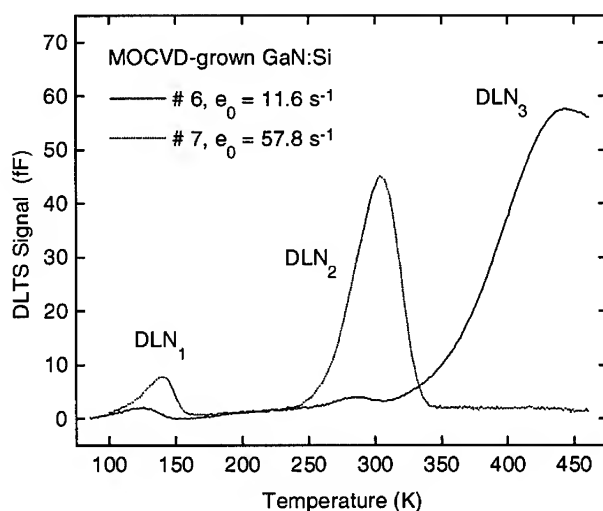


Figure 4. DLTS signal ($C(t_1) - C(t_2)$) vs temperature for Schottky diodes on Si-doped, n-type GaN. The peaks in the spectra result from the emission of electrons from deep levels and are labeled DLN_1 , DLN_2 , and DLN_3 .

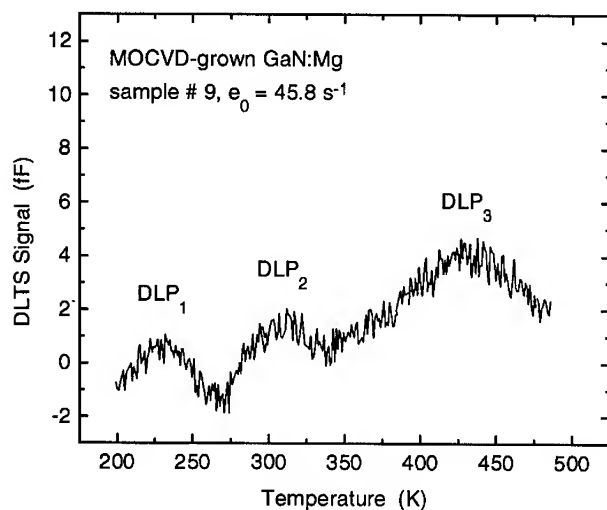


Figure 5. DLTS spectrum for p-type, Mg-doped GaN. The DLTS peaks are due to hole emission from deep levels into the valence band.

be influenced by the Poole-Frenkel effect which significantly lowers the activation energies for electron emission from donor levels or hole emission from acceptor levels in the space charge region of a Schottky or pn-junction diode, respectively.³²

The amplitude of each peak in the DLTS spectra of Fig. 4 and 5 relates to the concentration N_T of the corresponding level.²⁵ The concentration of the deep levels DLN_1 to DLN_3 , and DLP_1 to DLP_3 are also shown in Table III.

The deep levels which are labeled DLN_1 and DLN_2 with activation energies ~ 0.15 eV and ~ 0.45 eV seem to be present in both n-type GaN films. Their origin is unknown and either native defects or common impurities present in source or carrier gases used in MOCVD growth may be responsible. A study, conducted by Lee and coworkers²⁴ investigated the effect on group III-Alkyl-sources on deep levels in GaN grown by MOCVD. Two films one grown with triethylgallium (TEGa) and the other with trimethylgallium (TMGa) as the Ga source were studied. Deep levels with activation energies of ~ 0.14 eV and ~ 0.49 eV were detected in GaN grown with TMGa but none of these levels was observed in the film grown with TEGa. Electronic levels with similar activation energies like DLN_1 and DLN_2 were also reported for GaN material grown by hydride vapor phase epitaxy.²³ The third deep level labeled DLN_3 is observed only in sample # 6. DLN_3 is the dominant defect in sample # 6 but absent in sample # 7. A similar DLTS signal was observed by Lee and coworkers²⁴ but its presence was found to be independent of the metal-organic Ga source. The authors determined an activation energy of 1.63 eV for this level. However, the determination of the activation energies by an Arrhenius analysis for peaks which appear at temperatures above ~ 300 K in the DLTS spectrum is associated with a large uncertainty. Therefore, our level DLN_3 ($\Delta E_T \sim (0.8 \pm 0.3)$ eV) may be identical with the level observed in Ref. 24. The origin of the defect that gives rise to DLN_3 is also unknown.

Table III. Activation energies ΔE_T (row four) and concentrations N_T (row five) as determined with DLTS for the n-type GaN samples # 6 (columns two, four, and six), 7 (columns three and five), and the p-type sample # 9 (columns seven, eight, and nine).

deep level	n-type GaN					p-type GaN		
	DLN ₁		DLN ₂		DLN ₃	DLP ₁	DLP ₂	DLP ₃
sample #	6	7	6	7	6	9	9	
ΔE_T (eV)	0.15	0.16	0.46	0.44	0.8	0.21	0.32	0.47
N_T (10^{13} cm^{-3})	2 ± 1	7 ± 1	6 ± 2	63 ± 10	122 ± 32	39 ± 18	50 ± 35	86 ± 62

Three deep levels were detected with DLTS for the Mg-doped GaN film (DLP₁, DLP₂, and DLP₃). The data presented here represent the first investigation of deep levels with DLTS in p-type, Mg-doped GaN. To resolve the origin of these levels further studies are required.

Deep levels with activation energies for electron or hole emission >1 eV are usually not detectable with DLTS due to practical limitations, for instance, the temperature range of the DLTS measurement. O-DLTS is a sensitive tool to detect deep levels over the entire band gap of wide band gap semiconductors. However, to simplify the interpretation of the O-DLTS results we have limited the energy of the excitation photons to $<E_{\text{gap}} / 2$. With this limitation excitation processes involving minority carriers are excluded. O-DLTS results from sample # 6 and 7 are summarized in Fig. 6. The O-DLTS data are presented as relative steady state capacitances vs

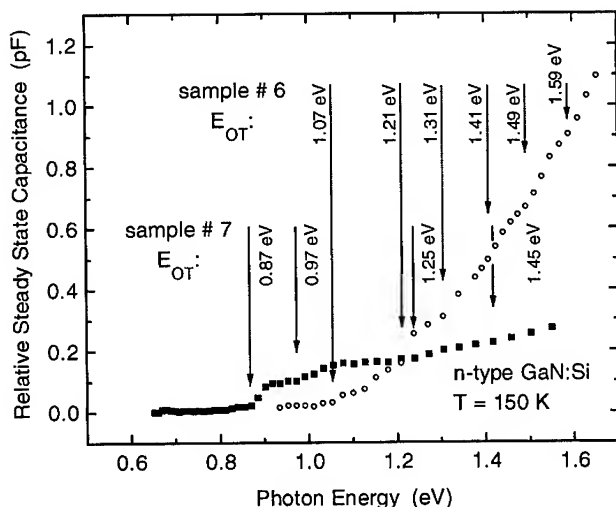


Fig. 6. Dependence of the relative steady state photo capacitance on photon energy for sample A (solid squares) and B (open circles). The spectra display distinct steps marked with arrows and the corresponding optical threshold energy, due to electron photoemission from distinct deep levels.

Table IV. Optical threshold energies (E_{OT}) and concentrations (N_T) of deep levels as characterized in samples A and B with O-DLTS.

sample # 6		sample # 7	
E_{OT} (eV)	N_T (cm ⁻³)	E_{OT} (eV)	N_T (cm ⁻³)
1.07	9.1×10^{14}	0.87	8.9×10^{14}
1.21	1.1×10^{15}	0.97	5.4×10^{14}
1.31	1.3×10^{15}	1.25	6.3×10^{14}
1.41	1.3×10^{15}	1.45	$>4 \times 10^{14}$
1.49	1.7×10^{15}		
1.59	$>1 \times 10^{15}$		

wavelength of the excitation light ($\Delta C_{ss}(h\nu)$). The spectra increase monotonically with $h\nu$ because $\Delta C_{ss}(h\nu)$ is proportional to the sum of charge-change contributions from optically active deep levels that reside within an energy interval that extends up to $h\nu$. Each level introduces a step in the ΔC_{ss} spectrum, near its optical threshold energy E_{OT} . The spectra for sample # 6 and 7 display six and four abrupt increases in slope, respectively, each of which can be associated with a distinct deep level. E_{OT} is defined as the energy position of a peak that appears for each deep level in the derivatives of the ΔC_{ss} spectra.

With each step in the spectra of Fig. 6 is associated a step height, which is proportional to the concentration of the corresponding deep level; saturation was not achieved for the levels with the highest threshold energy for both samples within the chosen ranges for $h\nu$. The uniform densities of deep levels can be estimated from the step heights³³ and are summarized in Table IV.

In both samples energetically closely spaced levels are detected with O-DLTS. In each sample the deep levels appear to have similar concentrations (Table IV). This may be indicative of a common or related origin for the several deep levels. To date, the defects that are associated with these deep levels are unknown. Candidates are transition metal impurities¹⁹ or native defects.³⁴

CONCLUSION

Si is a shallow donor in GaN with an activation energy of ~ 17 meV and is, therefore, well suited as a dopant for the preparation of n-type GaN layers with electron concentrations in the range up to 10^{20} cm⁻³. However, p-type doping with Mg remains problematic for GaN devices. Due to an activation energy of ~ 170 meV, less than ~ 1 % of the acceptor concentration is available as holes in a Mg-doped GaN layer at room temperature even when all the Mg atoms act as acceptors. Still, Mg is the shallowest acceptor known to date, and due to the hole effective mass it seems unlikely that acceptors with smaller activation energies will be available for GaN. Deep levels are present in GaN and may play an important role in defect luminescence bands observed in GaN and may act as parasitic radiative or non-radiative recombination channels in light emitting devices. For the fabrication of laser diodes, removal of deep level defects will be important.

ACKNOWLEDGEMENT

The authors are pleased to thank C.G. Van de Walle and J. Neugebauer for helpful discussions and J. Walker for technical assistance. The work was supported by ARPA, contract # MDA972-95-3-008.

REFERENCES

1. I. Akasaki, H. Amano, N. Koide, M. Kotaki, K. Manabe, *Physica B* **185**, 428, (1993)
2. S. Nakamura, M. Senoh, N. Iwasa, and S. Nagayama, *Jpn. J. Appl. Phys.* **34**, L797 (1995)
3. H. Morkoç, S. Strite, G. B. Gao, M. E. Lin, B. Sverdlov, and M. Burns, *J. Appl. Phys.* **76**, 1363 (1994)
4. S. Nakamura, T. Mukai, and M. Senoh, *Jpn. J. Appl. Phys.* **31**, 195, (1992)
5. H. Amano, M. Kito, K. Hiramatsu, and I. Akasaki, *Jpn. J. Appl. Phys.* **28**, L2112 (1989)
6. M. Asif Khan, D.T. Olson, J.N. Kuznia, W.E. Carlos, and J.A. Freitas Jr., *J. Appl. Phys.* **74**, 5901 (1993)
7. P. Hacke, A. Maekawa, N. Koide, K. Hiramatsu, N. Sawaki, *Jpn. J. Appl. Phys.* **33**, 6443 (1994)
8. R.J. Molnar and T.D. Moustakas, *Bull. Am. Phys. Soc.* **38**, 445 (1993)
9. S. Nakamura, T. Mukai, M. Senoh, and I. Iwasa, *Jpn. J. Appl. Phys.* **31**, L139 (1992)
10. S. Nakamura, N. Iwasa, M. Senoh, and T. Mukai, *Jpn. J. Appl. Phys.* **31**, 1258 (1992)
11. W. Götz, N.M. Johnson, J. Walker, D.P. Bour, H. Amano, and I. Akasaki, *Appl. Phys. Lett.* **67**, 2666 (1995)
12. W. Götz, N.M. Johnson, J. Walker, D.P. Bour, and R.A. Street, to be published
13. M.S. Brandt, J.W. Ager III, W. Götz, N.M. Johnson, J.S. Harris, R.J. Molnar, and T.D. Moustakas, *Phys. Rev. B* **49**, 14758 (1994)
14. M. Illegems, R. Dingle, and R.A. Logan, *J. Appl. Phys.* **43**, 3797 (1972)
15. J.I. Pankove and J.A. Hutchby, *J. Appl. Phys.* **47**, 5387 (1976)
16. B. Monemar and O. Lagerstedt, *J. Appl. Phys.* **50**, 6480 (1979)
17. W. Götz, N.M. Johnson, R.A. Street, H. Amano, I. Akasaki, H. Liu, C. Kuo, and W. Imler, presented at the Topical Workshop on III-V Nitrides, Nagoya, Japan (1995)
18. T. Ogino and M. Aoki, *Jpn. J. Appl. Phys.* **19**, 2395 (1980)
19. T. Suski, P. Perlin, H. Teisseyre, M. Leszcynski, I. Grzegory, J. Jun, M. Bockowski, and S. Porowski, *Appl. Phys. Lett.* **67**, 2188 (1995)
20. E.R. Glaser, T.A. Kennedy, K. Doverspike, L.B. Rowland, D.K. Gaskill, J.A. Freitas, Jr., M. Asif Khan, D.T. Olson, J.N. Kuznia, and D.K. Wickenden, *Phys. Rev. B* **51**, 13326 (1995)
21. J. Baur, U. Kaufmann, M. Kunzer, J. Schneider, H. Amano, I. Akasaki, T. Detchprohm, and K. Hiramatsu, *Appl. Phys. Lett.* **67**, 1140 (1995)
22. W. Götz, N.M. Johnson, H. Amano, and I. Akasaki, *Appl. Phys. Lett.* **65**, 463 (1994)
23. P. Hacke, T. Detchprohm, K. Hiramatsu, and N. Sawaki, *J. Appl. Phys.* **76**, 304 (1994)
24. W.I. Lee, T.C. Huang, J.D. Guo, and M.S. Feng, *Appl. Phys. Lett.* **67**, 1721 (1995)
25. W. Götz, N.M. Johnson, R.A. Street, H. Amano, and I. Akasaki, *Mat. Res. Soc. Symp. Proc.* Vol. **378**, 491 (1995)
26. S. Strite and H. Morkoç, *J. Vac. Sci. Technol. B* **10**, 1237 (1992)
27. W. Götz, L.T. Romano, J. Neugebauer, N.M. Johnson, C. Cheng, H. Liu, to be published
28. T.F. Lee and T.C. McGill, *J. Appl. Phys.* **46**, 373 (1975)
29. R.J. Molnar and T.D. Moustakas, *Bull. Am. Phys. Soc.* **38**, 445 (1993)
30. I. Akasaki, H. Amano, M. Kito, and K. Hiramatsu, *J. Lumin.* **48 & 49**, 666 (1991)
31. T. Tanaka, A. Watanabe, H. Amano, Y. Kobayashi, I. Akasaki, S. Yamazaki, and M. Koike, *Appl. Phys. Lett.* **65**, 593 (1994)
32. N.M. Johnson, *Mater. Res. Soc. Symp. Proc.* **69**, 75 (1986)
33. W. Götz, N.M. Johnson, R.A. Street, H. Amano, and I. Akasaki, *Appl. Phys. Lett.* **66**, 1340, (1995)
34. J. Neugebauer and C.G. Van de Walle, *Phys. Rev. B* **50**, 8067 (1994)

ELECTRONIC AND OPTICAL PROPERTIES OF THE GROUP-III NITRIDES, THEIR HETEROSTRUCTURES AND ALLOYS

Walter R. L. Lambrecht, Kwiseon Kim, Sergey N. Rashkeev and B. Segall
Department of Physics, Case Western Reserve University, Cleveland, Oh 44106-7079

ABSTRACT

Various aspects of the electronic structure of the group III nitrides are discussed. The relation between band structures and optical response in the vacuum ultraviolet is analyzed for zincblende and wurtzite GaN and for wurtzite AlN and compared with available experimental data obtained from reflectivity and spectroscopic ellipsometry. The spin-orbit and crystal field splittings of the valence band edges and their relations to exciton fine structure are discussed including substrate induced biaxial strain effects. The band-offsets between the III-nitrides and some relevant semiconductor substrates obtained within the dielectric midgap energy model are presented and strain effects which may alter these values are discussed. The importance of lattice mismatch in bandgap bowing is exemplified by comparing $\text{Al}_x\text{Ga}_{1-x}\text{N}$ and $\text{In}_x\text{Ga}_{1-x}\text{N}$.

INTRODUCTION

The interest in group-III nitrides for opto-electronic applications is currently experiencing an explosive growth. Still, many of their fundamental materials properties are only poorly known in comparison with other semiconductors. In this paper, we review the current state of understanding of their band structure and related optical properties and discuss some particular aspects in detail.

While many band structure calculations have appeared over the last few years, (See [1] for an overview), the majority of these calculations have focused on obtaining a few of the important total energy properties such as lattice constants, bulk moduli and a general picture of the band structure without providing much discussion of their relation to experimental probes of the band structure. The early band structure work of the 1960's [2] used the semi-empirical pseudopotential method in which UV reflectivity data are used to adjust pseudopotential parameters. While by construction that approach accounts reasonably well for the optical response functions as they were known at the time, it suffers from non-uniqueness in assigning particular interband transitions to observed features in reflectivity. It turns out that the band structures obtained in this manner differ greatly from several recently reported band structure results based on the local density approximation (LDA) [3]. It thus appears necessary to re-examine the relation between the UV optical response and the band structures. The LDA band structure has the disadvantage that strictly speaking it does not provide the quasiparticle excitation energies but merely intermediate results in obtaining the total energy of bonding between electrons and nuclei. Quasiparticle energies are the energies for extracting and electron from or adding an electron to the system as measured by photoemission and inverse photoemission. Fortunately, calculations of the self-energy corrections to the LDA band structure have been carried out for GaN and AlN using the GW¹ approach by a few groups [4, 5]. Furthermore, considerable insights in the magnitude, k-point, specific state and energy dependence of these corrections has accumulated from studies in other semiconductors. From these studies, we know that the main correction to the LDA band structure is an almost constant gap correction for the bands within at least about 5 eV from the gap. Before we can gauge the accuracy of these rather involved GW calculations, however, we need a better understanding of the experimental spectra which means that we need to re-examine the assignment of interband transitions. We [6] (and some other authors [7, 9]) have recently calculated the dielectric response function $\epsilon_2(\omega)$ within the random phase approximation (RPA) from LDA band structures. In addition, we have analyzed in detail how the latter is decomposed into its various interband transition contributions. Here, we briefly present these results for zincblende GaN and wurtzite AlN while for wurtzite GaN this analysis can be found in [6]. We compare our results with experimental reflectivity [6, 8] and spectroscopic ellipsometry data [9, 10, 11]. This is not trivial because optical response (which basically probes two-particle excitations) may involve further many-body corrections beyond the GW approach for

¹GW stands for the first term in a perturbation theoretical expansion for the self-energy introduced by Lars Hedin and Stig Lundqvist in *Solid State Physics*, Vol. 23, p. 1 (1969), with G the one-electron Green's function and W the screened Coulomb interaction.

single particle excitations. Our interpretation of the discrepancies between theory and experiment differs from that of other authors [9, 10, 11]. Further insights are gained by also comparing the occupied states to photoemission data.

While the band structure probes on this large energy (several eV) scale are clearly strongly perturbed by many-body effects, the band structure details near the band edges should not suffer so much from these effects. Of course, excitonic effects are prominent but should not vary greatly with energy. We thus expect that the LDA band structures will account rather well for the excitonic fine structure related to the valence-band splittings near the valence-band maximum. The main issue here is whether the current calculations are sufficiently accurate at meV scale to be useful in the understanding of the strain effects on these splittings. We will show that they are by discussing the spin-orbit splittings and crystal field splitting and their dependence on uniaxial strain in the second part of this paper.

Band offsets at heterostructures among the III-nitrides are expected to depend strongly on interface specific effects because of the polar nature of the interfaces. However, as we shall discuss, we expect these interface and biaxial strain effects to become pertinent only when very high quality interfaces are obtained. Hence, for the time being, a much simpler bulk-like alignment of energy levels seems appropriate. We discuss this issue and provide band offsets between the nitrides and some relevant semiconductor substrates based on the dielectric midgap energy approach [12] and explain how bulk strain corrections can be added to the latter.

Finally, we discuss the band gap bowing in $\text{In}_x\text{Ga}_{1-x}\text{N}$ which has recently become of great interest in view of the important role of this alloy in fine tuning the light emission in the blue-green region in nitride LEDs. By comparing with the results for $\text{Al}_x\text{Ga}_{1-x}\text{N}$ we identify the important role of bond length mismatch. A brief summary of the results concludes this paper.

COMPUTATIONAL METHOD

As discussed in the introduction, the LDA [3] is the basic approximation in our band structure approach. Specifically, we use the Hedin-Lundqvist parametrization [13] of exchange and correlation. For the band structure calculations we use the linear muffin-tin orbital method [14]. The band dispersions of the Ga3d and In4d semi-core levels are included. For the optical calculations we use the standard RPA formulation on which details can be found in [6]. The only difference with the method used in that paper is that we have recently set up an optical properties program using the more efficient tight-binding linear muffin-tin orbital implementation. Also, we have optimized the Brillouin zone (BZ) integrations, which use the tetrahedron method, by including the symmetry rotation operations on the matrix elements while integrating over the entire BZ (instead of only the irreducible wedge) following the approach described by Blöchl et al. [15]. The optical calculations were based on the band structure calculated within the atomic sphere approximation (ASA) and at the experimental lattice constants. We have separately checked the latter with full-potential (FP) [16] calculations which make no shape approximations to the potential or charge density and found that for the eV scale no significant deviations occur. For the calculations of the valence band edge fine structure and its strain dependence, however, where the relevant precision is meV, we found it important to use the FP approach. For the spin-orbit coupling, which mainly derive from the inner part of the atomic spheres, the ASA is adequate and was used.

UV OPTICAL RESPONSE

GaN

Fig. 1 compares our calculated $\epsilon_2(\omega)$ with experimental data for wurtzite (w) and zincblende (z) GaN. The data for wurtzite were obtained from Kramers-Kronig analysis of UV-reflectivity for synchrotron radiation up to 40 eV.[6] The data for zincblende GaN were obtained from spectroscopic ellipsometry also using synchrotron radiation [11]. These provide the largest range of energies presently available. These data agree well with previous ellipsometry studies for both z-GaN and w-GaN by Logothetidis et al. [9, 10] in the lower energy region. The calculated results were in both cases shifted rigidly upwards by ~ 1 eV, which provides a minimum (room temperature) gap of 3.4 eV for w-GaN and 3.1 eV for z-GaN. For w-GaN, the peak positions in theory and experiment agree well over the whole range of energies considered, although there are rather strong deviations in intensity. For z-GaN on the other hand, the upper peaks agree well but the first peak usually identified as the combination of the E_1 and E_2 transitions, is at lower

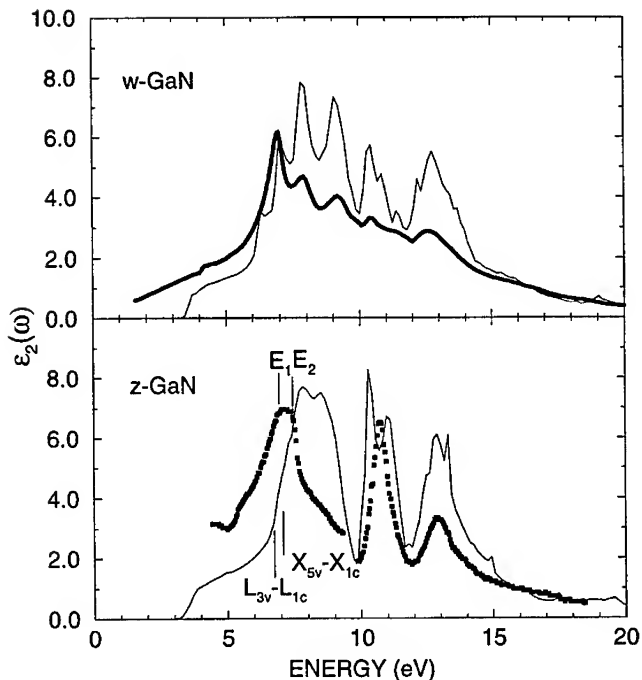


Figure 1: Calculated (thin lines) and experimental (thick lines) $\epsilon_2(\omega)$ for wurtzite [6] and zincblende [11] GaN.

energy than the calculated peak. We note that our theory/experiment alignment differs from that of Petalas et al. [9] and Janowitz et al. [11] who both compare directly with the LDA results without using any gap correction. In that case the lower peak agrees well but the upper peaks are too low and the minimum gap is too low. The latter authors ascribe the discrepancy for the upper peaks tentatively to problems of the calculations for higher energy transitions. However, it is rather difficult to explain why the peak in the 6–8 eV range would come out correctly from the uncorrected LDA calculation if the minimum gap is known to be underestimated by about 1 eV. The GW corrections[4] are found to be approximately constant, in fact slightly increasing, in this energy range rather than decreasing as would be needed to explain the theory-experiment alignment proposed by those authors.

In an attempt to understand the origin of this significant discrepancy, we first examine the nature of the transitions involved. A straightforward decomposition into individual band-to-band transitions (but still integrated over the whole BZ) reveals that the 7–9 eV (theoretical) peak derives mainly from transitions between the top valence band and the lowest conduction band. If the small influence of matrix elements is ignored (which we checked by comparing with a separate calculation with matrix elements assumed to be constant), the peaks should come mainly from the regions of large joint density of states, i.e., regions with nearly parallel bands. Fig. 2 shows the difference between the bands involved as a 2D function within the $\Gamma L X K$ plane. Regions of constant energy difference in this plot correspond to parallel bands. As usual in most semiconductors, there is a region of nearly parallel bands along $\Lambda \equiv \Gamma - L$ near the L -point. The L -point itself is an M_1 saddle point, i.e., the curvature is upward in two directions and downward in one. This 2D singularity or critical line is usually associated with the E_1 transition, or the first peak above the minimum gap. We may note, however, that the $L_{3v} - L_{1c}$ transition itself occurs at 6.79 eV which is below the first main peak in this region. It rather corresponds to a minor change in slope barely detectable on the steeply rising slope. Similarly, there is a somewhat larger

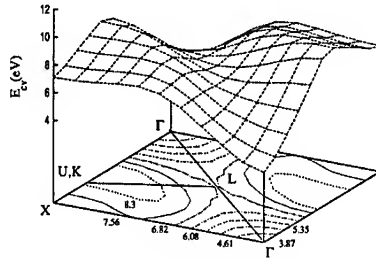


Figure 2: Interband transition energy $E_{c1}(\mathbf{k}) - E_{v1}(\mathbf{k})$ for z-GaN.

flat region along $\Delta \equiv \Gamma - X$ near X which is often associated with E_2 . The $X_{5v} - X_{1c}$ critical point of type M_0 (a minimum) is at 7.09 eV and thus still below the main peak. It is noteworthy that these two critical points are unusually close in energy in GaN. Furthermore we see from Fig. 2 that they form part of a rather extended 2D region in k -space where the band difference is rather slowly varying. This flat region wraps itself around the maximum near the K point and extends from near the $X - K - \Gamma$ axis towards L and back to the $\Gamma - X$ axis. This extended region is responsible for the main first broad peak which has maxima at 7.8 and 8.5 eV in the calculated spectrum. The experimental peak positions labeled E_1 and E_2 are at 7.03 and 7.63 eV. This suggests that strong continuum excitonic effects of the type discussed by del Castillo-Mussot and Sham [17] for Si and Ge may be associated with these critical points. The net effect of these excitonic phenomena is to shift oscillator strength to lower energies. Since a particularly large region of truly parallel bands occurs along Δ near X we speculate that its excitonic strength could be quite pronounced. In fact, del Castillo-Mussot and Sham [17] found that the E_2 transition is reduced in intensity by these many-particle effects and gives rise to an exciton quasi bound state which for Si occurs 0.2 eV below the E_2 edge. Because the high-frequency dielectric constant is considerably lower in GaN, we may expect an even larger excitonic shift. Because the E_1 and E_2 edges in GaN are so close to each other, the E_2 related exciton might fall below the E_1 transition in a region of low spectral intensity and hence be less subject to Fano broadening by interaction with the continuum. These authors also find the E_1 edge to be slightly shifted and increased in intensity. As discussed by Hanke and Sham [18] for diamond and Si, local field effects are also important. From Hanke and Sham's work [18], however, the local-field effect alone without electron-hole attraction tends to shift oscillator strength to higher energies and would thus worsen the agreement with experiment.

What is puzzling is that these phenomena seem to affect z-GaN more strongly than w-GaN. We may note, however, that in w-GaN there is a strong reduction in peak intensity (in experiment compared to theory) with increasing energy. While we have previously argued [6] that this can at least partially be explained by diffuse scattering due to surface roughness and partial misalignment of grains, it could also be a manifestation of the same many-body effects which shift oscillator strength to lower energies. In w-GaN this effect would mainly appear to shift strength from one peak to another. In z-GaN, on the other hand, because of the close proximity of the E_1 and E_2 like transitions, which merge into a single broad band lying above a region of low intensity, the effect has more the appearance of a peak shift. We tentatively suggest that both in z-GaN and in w-GaN excitonic effects may be strong. Clearly, however, more work in this area is desirable.

AlN

Fig. 3 shows our calculated reflectivity for w-AlN compared to the data of Loughin et al. [8]. Again, we shifted the LDA results (by 1.7 eV) so as to adjust the minimum band gap (to 6.3 eV). This apparently provides good agreement for the entire lowest peak below 12 eV. There are some features in the experiment below the 6.3 eV gap which are probably related to defects. Oxygen

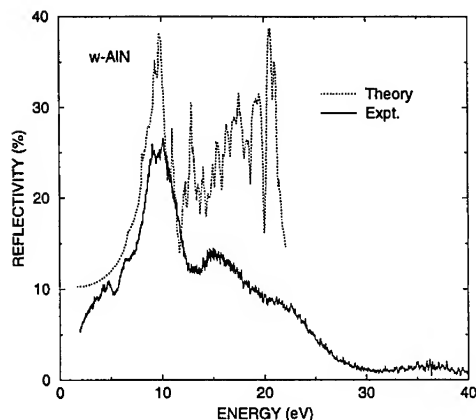


Figure 3: Calculated and measured (from Ref. [8]) UV-reflectivity of w-AlN.

is an important known contaminant in the samples measured by Loughin et al. [8] and may be responsible. Discrepancies in peak position and a strong attenuation of intensity, however, are apparent at higher energies. In particular the second peak in the experiment appears to occur at about 14-15 eV while in the theory it occurs at 12.5 eV. While in this case the shift is towards higher energies, which is a little more expected if self-energy corrections increase with increasing energy separation from the gap, a 1.5-2 eV shift is not expected from Rubio et al.'s [4] GW calculations. Our calculations of the decomposition into band-to-band transitions reveal that the 12.5 eV peak comes mostly from transitions to the 3rd and 4th conduction band in agreement with Christensen and Gorczyca's analysis [7]. The difference in GW corrections for these bands from those at the minimum gap is about 1.2 eV. Further work will be necessary to unravel these discrepancies.

Photoemission

X-ray photoelectron spectroscopy (XPS) of GaN was studied in [19]. There we showed that while the Ga3d states overlap and hybridize with the N2s band in the LDA band structure, the hole left behind when a Ga3d is extracted from the band has a binding energy well below that of the N2s band. This is just another example of the many-body effects which perturb a straightforward comparison of band structures with experimental spectroscopies. We also found that the N2s band undergoes a ~ 1.5 eV downward shift relative to the top of the valence band. This is in good agreement with the predictions of Rubio et al.'s [4] GW calculations.

In InN the same type of effects are expected. We calculated the expected shift of the In4d band from its LDA value to be about 3 eV. In AlN, it is easier to observe the N2s shift because it is not overshadowed by a closeby and strong Ga3d or In4d semicore peaks. Details on the AlN are provided elsewhere in these proceedings [20]. In summary, the comparison of our LDA calculated densities of states with recent photoemission measurements confirms the need for self-energy shifts as predicted by Rubio et al. [4], which are slowly increasing with energy to about 0.5 eV as one goes down into the upper valence band and discontinuously increase to about 1.5 eV-2 eV in the lower N2s band. For the In4d and Ga3d semicore bands these effects are of order of 3-4 eV. Thus, as expected, the corrections become stronger with increasing localization of the orbitals involved.

BAND EDGE STRUCTURE

In this section, we consider the valence-band edge splittings which are revealed by the exciton fine structure. In z-GaN, the modulated reflectivity spectra of Ramirez-Flores et al. [21] reveal the usual E_0 and $E_0 + \Delta_0$ peaks typical of direct gap zincblende semiconductors. The spin-orbit splitting Δ_0 of the valence band Γ_{15} state into a fourfold Γ_8 and doubly degenerate Γ_7 was measured to be 17 ± 1 meV.

For w-GaN, the reflectivity spectra of Dingle et al. [22], Shan et al. [23], Gil et al. [25],

photoluminescence excitation spectra by Monemar [26], and photoluminescence spectra as well as calorimetric absorption and reflection spectroscopy by Eckey et al. [24] show three well separated excitons labeled A, B and C. In the absence of spin-orbit coupling, the hexagonal crystal field splits the zincblende Γ_{15} state into a doublet Γ_6 and a singlet Γ_1 state (not counting spin degeneracy), whose splitting we shall denote by Δ_c . With the inclusion of the spin-orbit coupling, the Γ_6 states splits into a Γ_9 and Γ_7 state, while the Γ_1 becomes a Γ_7 state in the notation of the double group. The two Γ_7 states repel each other and lead to a simple quadratic eigenvalue problem with the result that the $\Gamma_9 - \Gamma_7$ splittings, which correspond to the A-B, A-C splittings, are given by

$$E_{\Gamma_9} - E_{\Gamma_7} = \frac{\Delta_c + \Delta_0}{2} \pm \frac{1}{2} \sqrt{(\Delta_c + \Delta_0)^2 - \frac{8}{3} \Delta_0 \Delta_c}, \quad (1)$$

within the quasi-cubic model of Hopfield[27].

We have separately calculated the spin-orbit splitting parameter Δ_0 of the cubic zincblende structure and the hexagonal crystal field splitting Δ_c and its uniaxial strain dependence, i.e. its dependence on c/a , and then combined them with Eq.(1) to obtain the A-B-C exciton splittings.

Spin-orbit splitting

Table I gives our calculated spin-orbit splitting parameters Δ_0 for zincblende BN, AlN, GaN and InN.

Table I: Spin-orbit splitting Δ_0 (in meV) in zincblende nitrides.

	theory	d as core	experiment
BN	22		
AlN	19		
GaN	19	21	17±1
InN	3	19	

We note that they are very similar in all nitrides except for InN. Within a tight-binding model for the Γ_{15}^u wave function $|\psi_v\rangle$ the spin-orbit splitting has as main contributions:

$$\Delta_0 = (3/2)(|\langle \phi_{N2p} | \psi_v \rangle|^2 \zeta_{N2p} + |\langle \phi_{Xnp} | \psi_v \rangle|^2 \zeta_{Xnp} - |\langle \phi_{X(n-1)d} | \psi_v \rangle|^2 \zeta_{X(n-1)d}) \quad (2)$$

where ζ_{Rnl} are atomic spin-orbit coupling parameters and $|\phi_{Rnl}\rangle$ are the atomic orbitals of quantum numbers nl on atomic site R , with X standing for the cation. Because of the strongly ionic character, the only major contribution for the nitrides (except InN) is from the atomic N2p coupling parameter ζ_p (which is 13.6 meV in the free atom and slightly renormalized by the ionic character in the solid). The contribution from the lower cation d-state (Ga3d and In4d) is negative for reasons explained by Shindo et al. [28] and as first noted empirically by Cardona [29] for the Cu-halides. It is much more significant for InN than for GaN because the In4d ζ_d (385 meV) is almost twice as large as that of Ga3d (206 meV) and because the d-mixing is stronger in InN. Additional evidence of this is that if we neglect the coupling to these d-states by treating them as core states, the GaN value is slightly larger and the InN value becomes similar to that of the other nitrides, as indicated in the second column in Table I. Our result for GaN is in good agreement with the experimental value.

Crystal field splitting and strain

The hexagonal crystal field splitting is similar to that induced by a [111] uniaxial rhombohedral strain in zincblende. Not unexpectedly, this splitting is strongly dependent on the c/a ratio which in turn is closely coupled to the internal structural parameter u , corresponding to a relative displacement of the anion versus the cation sublattice along the c -axis as in the A_1 transverse optical phonon mode[30]. We found that this optical mode deformation potential is quite strong.

Fig. 4 shows the calculated splitting of the Γ_6 and Γ_1 states relative to their weighted average in wurtzite GaN as a function of $\eta = c/a$ (with u relaxed at each point) and u (at the equilibrium c/a) at constant equilibrium volume. The crystal field splitting at the experimental c/a and u parameters is 19 meV, which combined with the 19 meV spin-orbit splitting leads to good agreement with the A-B-C excitonic splittings as can be seen in Table II. The variation

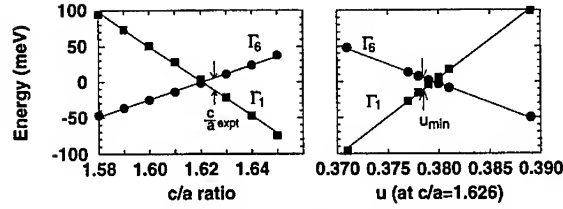


Figure 4: Crystal field splitting as a function of c/a and u in w-GaN.

between the experimental numbers is probably in part due to different strains in the samples. It is presently not entirely clear what the best experimental values are for strain-free material. The experimental determination is further complicated by the occurrence of $n = 2$ excited states of the A exciton near the energy of the C exciton. Our present values were calculated at the experimental c/a and a lattice constants with u determined by energy minimization. We prefer this procedure over using entirely first-principles determined lattice constants because LDA is known to slightly underestimate the lattice constants. The experimental equilibrium value of u , however, is not known sufficiently well and is crucial because of the strong dependence of Δ_c on u .

Table II: Exciton splittings in GaN (in meV).

	A-B	A-C
present	8	30
Ref. [22]	6	27
Ref. [23]	8	32
Ref. [24]	6	22.5
Ref. [25]	7	29

The slopes of the lines in Fig. 4 are closely related to the deformation potentials. In fact, the strain along the c -axis $\epsilon_{||} = (2/3)d \ln \eta$, and within the cubic approximation, we have

$$\begin{aligned} E_{\Gamma_6} &= -(1/2)D_3\epsilon_{||}, \\ E_{\Gamma_1} &= -\Delta_c^0 + D_3\epsilon_{||}, \end{aligned} \quad (3)$$

in terms of the deformation potential D_3 (as defined by Bir and Pikus [31]). Within this cubic approximation, we have $D_3 = \sqrt{3}d$ where d is the deformation potential of zincblende under a rhombohedral distortion along [111]. The value we have calculated for d from z-GaN is -3.75 eV [33]. This predicts a value of -6.5 eV for D_3 , whereas the direct calculation for w-GaN gives -5.7 eV.

Similarly, the slope as a function of u corresponds to the optical deformation potential for the A_1 transverse optical phonon, which we may define by $d(E_{\Gamma_6} - E_{\Gamma_1}) = D^{A_1}d \ln u$. Within the cubic approximation, the latter can be written in terms of the usual transverse optical mode deformation potential of zincblende (in Kane's notation d_{so}), i.e. $D^{A_1} = (3/2)^{3/2}d_{so}/4$. This gives 6.7 eV for D^{A_1} while the direct calculation for wurtzite gives 6.1 eV.

We note that under c/a expansion the A-B-C splittings are expected to increase while under compression they are expected to decrease. For GaN grown on sapphire and relaxed by misfit dislocations at high temperature one expects that upon cooling, the GaN film obtained will be under biaxial compression (because $\alpha(Al_2O_3) > \alpha(GaN)$ with α the thermal expansion coefficient). Using the Poisson ratio for the c -axis $\sigma = -2C_{13}/C_{33}$, one finds that c/a will be under tension or that the A-B-C splitting should be increased compared to the strain free situation. This has indeed been observed by Volm et al.[34] by comparing the exciton splittings in thick (supposedly strain free) films with those in thin films. On SiC, the opposite effect was obtained as expected because $\alpha(SiC) < \alpha(GaN)$. Similar results were also obtained by Monemar et al. [26]. However, if the film were pseudomorphic, i.e. below the critical thickness, and hence without misfit dislocations, one might expect that GaN on SiC would be under biaxial compression, and hence c/a tension, which would again result in an increased splitting of the excitons. This may be the explanation for the opposite data (an increase of the A-B splitting for GaN grown on SiC) reported by Edwards et al. [35] although further investigation of this is required.

Table III: Valence-band effective masses and Kohn-Luttinger parameters for GaN.

wurtzite				
$m_l^{hh} = m_l^{lh}$	m_l^{sh}	m_t^{hh}	m_t^{lh}	m_t^{sh}
2.04	0.18	1.81	0.19	1.88
A_1	A_2	A_3	A_4	A_5
-5.62	-0.53	5.13	-3.39	-2.31
zincblende				
A	B	C		
-5.05	-1.17	-5.85		

From calculations of the band structure in the immediate neighborhood of the valence-band maximum, we can also extract the effective mass parameters. In wurtzite, we must distinguish a longitudinal (along c) and transverse (indicated by subscripts l and t) heavy, light and split-off (indicated by superscript hh , lh , and sh) hole masses whose values are given in Table III. A more complete description of the valence-band manifold is obtained in terms of Kohn-Luttinger-like parameters (also indicated in Table III) as defined in Bir and Pikus for wurtzite [31] and by Luttinger for zincblende [32].

We have also obtained the conduction band masses given in Table IV. They appear to be in good agreement with the value obtained from recent Optically Detected Cyclotron Resonance (ODCR) data [36], the only direct measurement, and with the value obtained from free electron IR absorption [37]. They differ more from the value inferred rather indirectly from the g -value determined by conduction band Electron Spin Resonance (ESR) [38]. The value of Ref. [36] was interpreted as a polaronic mass and a value of 0.20 was deduced from it for the pure band structure mass.

Table IV: Conduction band effective masses in GaN

wurtzite	m_l ($\parallel c$)	0.19
	m_t ($\perp c$)	0.23
zincblende	m_c	0.19
Expt. [36]	ODCR	0.22
Expt. [38]	ESR	0.15
Expt. [37]	IR absorption	0.20

BAND OFFSETS

The band offset can be separated into two contributions

$$\Delta E_v = \Delta E_v^0 + D, \quad (4)$$

where the first one gives the difference in bulk valence band edges as determined with respect to a common reference level such as the average electrostatic potential, and the second one is the interface dipole, which is the difference in the chosen local reference level across the interface. Each of these carry with them a certain degree of arbitrariness because the average electrostatic potential in a periodic bulk solid is not a uniquely defined quantity. Nevertheless, as long as we choose it consistently in the same way on the right and left of the interface, there is no problem. The band offsets between lattice-mismatched systems depend sensitively on the residual strain in the film. As mentioned above, one should distinguish the pseudomorphic situation below the critical thickness where the in-plane lattice constant matches that of the substrate and hence places the film under a biaxial strain, and the situation above the critical thickness where misfit dislocations relieve the strain. In the case of a density of dislocations $\kappa = 1/D$ with D the dislocation spacing and with Burgers vector component in the plane b , the residual in-plane strain is given by $\epsilon_{\perp} = a_f/a_s - 1 - b\kappa$. For a thick enough film, one may assume that the strain is completely relieved by the misfit dislocations ($\epsilon_{\perp} = 0$). In fact, in the case of large mismatch, it is likely that the critical thickness is less than a monolayer and that misfit dislocations are built in from the very start of the growth. The residual strain situation may also depend on experimental growth conditions and post-growth annealing procedures. For a given strain situation, the bulk changes in the band structure which affect ΔE_v^0 can be described by

deformation potentials. In general the strain can be decomposed into a hydrostatic component and a uniaxial strain component. The previous section describes the uniaxial strain effects on the valence band maximum in GaN for the basal plane or c-axis. Similar results for BN, AlN and InN will be published elsewhere [39]. Uniaxial deformation potentials for zincblende for all three symmetry irreducible strain components are given in Ref. [39] allowing one to calculate the strained band structure for any interface orientation. The hydrostatic pressure shift of the valence band maximum is somewhat more difficult to obtain because it itself requires an interface calculation. Below, we discuss a simple model which can provide some estimates of this effect.

For polar interfaces such as the wurtzite basal plane, it is possible that a uniform electric field exists over the thickness of the film, (or a zig-zag field in case of a periodic superlattice), produced by spontaneous polarization and the piezo-electric effect. These fields may complicate the analysis of the band-offsets. Since a uniform electric field over a substantial region of space is energetically costly, we expect that interface structural relaxation will tend to avoid such fields. This problem requires further study.

Table V: Energies (in eV) and absolute deformation potentials of the valence band maxima with respect to the dielectric midgap level in III-nitrides and some related semiconductors.

	AlN	GaN	InN	GaAs	SiC	ZnO
$E_D - E_v$	2.81	2.13	1.42	0.66	1.45	2.23
a_v	1.6	0.8	0.5	-0.5	0.5	0.6

Next, we consider the interface dipole. In principle, it is interface specific. While for the pseudomorphic case, it is feasible to calculate it from first principles using supercell models, it is rather difficult to include explicitly the effects of misfit dislocations. In practice, one usually finds that interface specific effects are washed out by a certain degree of disorder at the interfaces, for example by interdiffusion over a few atomic layers and by specific relaxations of the near interface planes, both of which tend to cancel out the induced dipoles [40, 41]. As discussed in Ref. [42], the screening of interface dipoles can be viewed as being equivalent to the minimization of the total energy of the system for a given long-range dipole potential. Somewhat heuristically, we can extend this concept even to situations where the atoms are displaced or interdiffusing. Because of the efficient screening of any interface specific effects on the dipole, band-offsets to a good approximation can be viewed as differences between bulk quantities. In the Charge Neutrality Point (CNP) model of Flores and Tejedor [43], one assumes that a certain energy level in the middle of the gap (called the CNP) should be aligned across the interface. The idea behind this is that states above this level will lead to an accumulation of negative charge when filled while states below it when empty will tend to produce a positive charge. In a variant of this model, called the Dielectric Midgap Model (DME), [12] this CNP is identified with the average of the highest valence and lowest conduction band over the Brillouin zone. In Table V, we

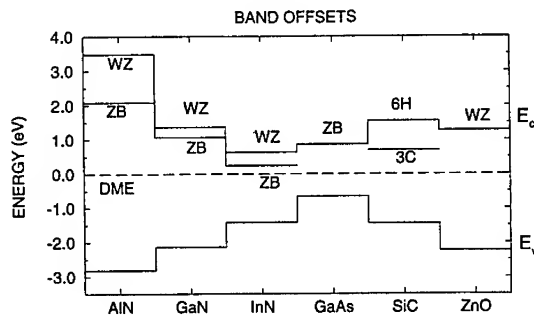


Figure 5: Band offsets within DME model.

provide the energy differences between the valence band maximum and the DME level E_D , calculated for each semiconductor at its own equilibrium lattice constant. Thus, aligning the DME, one only needs to take differences between these values to obtain any desired band offset among the materials listed. This is illustrated in Fig. 5. The valence-band offset for GaN/AlN obtained in this manner (0.68 eV) is in fair agreement with the value obtained from explicit interface calculations for the (110) interface [44], which was 0.85 eV and with XPS results [45]. For the other nitrides, the values of the offsets obtained here deviate somewhat more from the previously given ones [44] because the latter referred to the situation where each solid was considered at the average lattice constant of the two.

The same DME model can be used to obtain the absolute hydrostatic deformation potentials. In fact, if we consider a semiconductor at two different lattice constants, their valence band line-up within this model is again obtained by aligning their E_D level. Thus we merely have to obtain the change in $E_D - E_v$ per fractional change in unit cell volume $d \ln V$, denoted by a_v and given in Table V.

ALLOYS

The band-gap bowing in $\text{Ga}_{1-x}\text{In}_x\text{N}$ was calculated using the LMTO method and various approximations to the alloy problem. Details of this work are given in Ref. [46]. Here we provide only a summary of the main results. The simplest approach we considered is to average the LMTO potential parameters of the constituents according to the composition. In such a model every cation is described as having average characteristics of the Ga and In cations. Local fluctuations in the potential depending on the various possible local environments of a N anion are totally ignored. We find that this seriously underestimates the band-gap bowing parameter b which, in this model is only 0.6 eV. Using instead a cluster expansion approach, we obtain $b = 0.89$ eV if we assume an average lattice constant and $b = 2.57$ eV if we include both volume and bond-length relaxations. The latter is much larger than the experimental value of $b = 1.0$ eV [47]. The discrepancy may be due in part to experimental difficulties such as the partial phase separation of InN and GaN in this system and to the assumption of Vegard's law used in the experimental work in converting lattice constants measured by X-ray diffraction to concentrations. The large value obtained here may explain why emission in the green region appears to have been obtained recently in $\text{Ga}_x\text{In}_{1-x}\text{N}$ quantum wells with smaller In concentrations than previously expected. (See e.g. papers by Nakamura and Moustakas in these proceedings.) In view of the persisting problems in obtaining pure $\text{Ga}_{1-x}\text{In}_x\text{N}$ alloys without inclusions of pure InN, further experimental work appears desirable. Our theoretical work may also require further refinements, e.g., to take into account the interplay between volume and bond-length relaxation and to allow for more elaborate descriptions of the disorder in the system. We can nevertheless safely conclude that the large bond-length mismatch in this alloy system is responsible for the large bowing coefficient. This is in sharp contrast to the $\text{Al}_x\text{Ga}_{1-x}\text{N}$ system where we previously showed that the bandgap bowing is negligible [48].

CONCLUSION

In conclusion, in this paper we have presented new computational results on the UV optical properties of z-GaN from which it appears that continuum excitonic effects may be strong in this system. Our interpretation of the discrepancies with experimental data differs from that of other authors and was based in part on an analysis of the self-energy corrections on the band structure obtained by Rubio et al. [4]. These were found to be in good agreement with photoemission spectroscopy but fail to account for the discrepancies in the optical spectra from LDA calculations, indicating that additional two-particle many-body effects affect the optical transitions. Similar problems also appear to exist for w-AlN . Next, we have presented calculated results for the spin-orbit and crystal field splittings of the valence-band maximum, including strain effects. These results are in good agreement with measurements of the excitonic fine structure. The band-offsets problem was discussed and values based on the DME model were presented which should provide a reasonable starting point for strain relaxed heterojunctions. It was also outlined how specific strain effects could be taken into account if strain is found to be present in the particular film/substrate situation and experimental conditions. The band-gap bowing in $\text{Ga}_{1-x}\text{In}_x\text{N}$ was briefly discussed and found to be much larger than previously anticipated.

Acknowledgements

This work was supported by NSF (DMR-92-22387) and ONR (N00014-94-1-100). We wish to thank Dr. S. Loughin for sending his reflectivity results on AlN in numerical format and Dr. Janowitz for communicating his results prior to publication.

REFERENCES

1. W. R. L. Lambrecht and B. Segall, in *Properties of Group III Nitrides*, edited by J. H. Edgar, Electronic Materials Information Service (EMIS) Datareviews Series (Institution of Electrical Engineers, London 1994), Chapt. 5.
2. S. Bloom, G. Harbeke, E. Meier, and I. B. Ortenburger, *Phys. Stat. Solidi (b)* **66**, 161 (1974).
3. P. Hohenberg and W. Kohn, *Phys. Rev.* **136**, B864 (1964); W. Kohn and L. J. Sham, *ibid.* **140**, A1133 (1965).
4. A. Rubio, J. L. Corkill, M. L. Cohen, E. L. Shirley, and S. G. Louie, *Phys. Rev. B* **48**, 11810 (1993).
5. M. Palummo, L. Reining, R. W. Godby, C. M. Bertoni, and N. Börnsen, *Europhys. Lett.*, **26**, 607 (1994); and in *Proc. 21st Int. Conf. on the Physics of Semiconductors*, Eds. Ping Jiang, Hou-Zhi Zheng (World Scientific Press, Singapore 1993), p. 89.
6. W. R. L. Lambrecht, B. Segall, J. Rife, W. R. Hunter, and D. K. Wickenden, *Phys. Rev. B* **51**, 13516 (1995).
7. N. E. Christensen and I. Gorczyca, *Phys. Rev. B* **50**, 4397 (1994).
8. S. Loughin, R. H. French, W. Y. Ching, Y. N. Xu, and G. A. Slack, *Appl. Phys. Lett.* **63**, 1182 (1993).
9. J. Petalas, S. Logothetidis, S. Boutadakis, M. Alouani, and J. M. Wills, *Phys. Rev. B* **52**, 8082 (1995).
10. S. Logothetidis, J. Petalas, M. Cardona, and T. D. Moustakas, *Phys. Rev. B* **50**, 18017 (1994).
11. C. Janowitz, M. Cardona, R. L. Johnson, T. Cheng, T. Foxon, O. Günther, and G. Jungk, *BESSY Jahresbericht* (1994) p. 230
12. M. Cardona and N. E. Christensen, *Phys. Rev. B* **35**, 6182 (1987).
13. L. Hedin and B. I. Lundqvist, *J. Phys. C* **4**, 2064 (1971).
14. O. K. Andersen, O. Jepsen, and M. Šob, in *Electronic Band Structure and its Applications*, edited by M. Yussouff, (Springer, Heidelberg, 1987), p.1.
15. P. E. Blöchl, O. Jepsen, and O. K. Andersen, *Phys. Rev. B* **49**, 16223 (1994).
16. M. Methfessel, *Phys. Rev. B* **38**, 1537 (1988).
17. M. del Castillo-Mussot and L. J. Sham, *Phys. Rev. B* **31**, 2092 (1985).
18. W. Hanke and L. J. Sham, *Phys. Rev. B* **12**, 4501 (1975); *Phys. Rev. B* **21**, 4656 (1980).
19. W. R. L. Lambrecht, B. Segall, S. Strite, G. Martin, A. Agarwal, H. Morkoç, and A. Rockett, *Phys. Rev. B* **50**, 14155 (1994).
20. S. W. King, M. C. Benjamin, R. J. Nemanich, R. F. Davis, and W. R. L. Lambrecht, in these proceedings.
21. G. Ramírez-Flores, H. Navarro-Contreras, A. Lastras-Martínez, R. C. Powell, and J. E. Greene, *Phys. Rev. B* **50**, 8433 (1994).

22. R. Dingle, D. D. Sell, S. E. Stokowski, and M. Ilegems, *Phys. Rev. B* **4**, 1211 (1971).
23. W. Shan, T. J. Schmidt, X. H. Yang, S. J. Hwang, J. J. Song, and B. Goldenberg, *Appl. Phys. Lett.* **66**, 985 (1995).
24. L. Eckey, L. Podlowski, A. Göldner, A. Hoffmann, I. Broser, B. K. Meyer, D. Volm, T. Streibl, T. Detchprohm, H. Amano, and I. Akasaki, in *Proc. 6th International Conference on Silicon Carbide and Related Materials, held in Kyoto, Sept. 1995*, to be published by (Institute of Physics, London 1995) .
25. B. Gil, O. Briot, and R.-L. Aulombard, *Phys. Rev. B* **52** 91995), to be published.
26. B. A. Monemar, *Phys. Rev. B* **10**, 676, and private communication.
27. J. J. Hopfield, *J. Phys. Chem. Solids* **15**, 97 (1960).
28. K. Shindo, A. Morita, and H. Kamimura, *J. Phys. Soc. Japan.* **20**, 2054 (1965)
29. M. Cardona, *Phys. Rev.* **129**, 69 (1963).
30. K. Kim, W. R. L. Lambrecht, and B. Segall, these proceedings.
31. G. L. Bir and G. E. Pikus, *Symmetry and Strain-Induced Effects in Semiconductors*, (John-Wiley & Sons, New York 1974).
32. J. M. Luttinger, *Phys. Rev.* **102**, 1030 (1956).
33. K. Kim, W. R. L. Lambrecht, and B. Segall, *Phys. Rev. B* **50**, 1502 (1994).
34. D. Volm, K. Oettinger, T. Streibl, D. Kovalev, N. Ben-Chorin, J. Diener, B. k. Meyer, J. Majewski, L. Eckey, A. Hoffmann, H. Amano, I. Akasaki, K. Hiramatsu, and T. Detchprom, to be published.
35. N. V. Edwards, M. D. Bremser, T. W. Weeks, Jr., H. Liu, A. E. Wickenden, K. Doverspike, R. A. Stall, D. K. Gaskill, J. A. Freitas, R. F. Davis, and D. E. Aspnes, these proceedings.
36. M Drechsler, B. K. Meyer, D. M. Hoffmann, D. Detchprohm, H. Amano, and I. Akasaki, *Jpn. J. Appl. Phys.* **34**, L1178 (1995).
37. A. S. Barker, Jr. and M. Ilegems, *Phys. Rev. B* **7**, 743 (1973).
38. M. Fanciulli, T. Lei, and T. D. Moustakas, *Phys. Rev. B* **48**, 15144 (1993).
39. K. Kim, W. R. L. Lambrecht, and B. Segall, *Phys. Rev. B* (1995), submitted.
40. W. R. L. Lambrecht and B. Segall, *Phys. Rev. B* **41**, 2832 (1990).
41. M. S. Hybertsen, *J. Vac. Sci. Technol. B* **8**, 773 (1990).
42. W. R. L. Lambrecht, B. Segall, and O. K. Andersen, *Phys. Rev. B* **41**, 2814 (1990).
43. F. Flores and C. Tejedor, *J. Phys. C* **20**, 145 91987).
44. E. A. Albanesi, W. R. L. Lambrecht, and B. Segall in *Mater. Res. Soc. Symp. Proc. Vol. 339*, p. 607 (1994); *J. Vac. Sci. Technol. B* **12**, 2470 (1994).
45. G. Martin, S. Strite, A. Botchkarev, A. Agarwal, A. Rockett, H. Morkoç, W. R. L. Lambrecht, and B. segall, *Appl. Phys. Lett.* **65**, 610 (1994).
46. W. R. L. Lambrecht, *Proc. Topical Workshop on Nitrides, Nagoya 95*, to be published in *Solid State Electron.* (1995).
47. K. Osamura, S. Naka, and Y. Murakami, *J. Appl. Phys.* **46**, 3432 (1975).
48. E. A. Albanesi, W. R. L. Lambrecht, and B. Segall, *Phys. Rev. B* **48**, 17841 (1993).

CONDUCTIVITY MEASUREMENTS ON GaN GROWN BY OMVPE AND HVPE

M. Ben-Chorin*, J. Diener*, B.K. Meyer*, M. Drechsler*, D. Volm*, H. Amano**, I. Akasaki**, T. Detchprohm*** and K. Hiramatsu***

*Technical University Munich, Department of Physics, 85747 Garching, Germany

**Department of Electrical and Electronic Engineering, Meijo University, 1-501 Shiogamaguchi, Tempaku-ku, Nagoya 468, Japan

***Department of Electronics, School of Engineering, Nagoya University, Furocho, Chikusa-ku, Nagoya 468-01, Japan

ABSTRACT

We report on conductance and cyclotron resonance (CR) experiments on GaN epitaxial films grown by the OMVPE and HVPE techniques. From a precise determination of the electron effective mass the donor binding energy in the effective mass approximation (EMT) is calculated. We obtain 31.7 meV. The transport experiments on the HVPE films show that the conductance is thermally activated with an activation energy of 15 meV in contrast to the OMVPE films which showed temperature independent conductivity for temperatures between 4 and 100 K.

INTRODUCTION

Undoped GaN epitaxial films commonly show n-type conduction[1] with free carrier concentrations at room temperature ranging between 10^{17} and 10^{19} cm⁻³. There is no clear correlation between the free carrier concentrations and the number of residual impurities as found, e.g. by SIMS. Therefore, there is an ongoing discussion whether intrinsic defects, such as nitrogen vacancies or gallium interstitials, are responsible for the autodoping behavior. Recent total energy calculations demonstrated [2,3] that both centers create shallow effective-mass type levels in GaN. Oxygen and silicon might be good candidates for extrinsic shallow donors in GaN when substituting on nitrogen or gallium sites, respectively. However the binding energy determined for the defects causing n-type conduction scatters between 20 and 40 meV [4,5]. A lower limit for extrinsic origin can be given by an effective mass theory calculation, if the electron effective mass is known with high precision. Here we will report on a precise determination of the electron effective mass in GaN with cyclotron resonance.

EXPERIMENTAL

Several GaN films grown by different techniques were investigated. A 400 μ m thick film was grown by hydride vapor phase epitaxial (HVPE) without a buffer layer. The films grown by organometallic vapor phase epitaxy (OMVPE) had a 35 nm AlN buffer layer, whereas the GaN film thickness was 3 μ m. All films were deposited on c-plane sapphire substrates.

For the conductivity measurements four contacts were soldered onto the sample using Ga/In eutecticum. Current-voltage measurements exhibited good ohmic behavior. For the electric measurements the sample temperature was varied between 30 K and 300 K. The luminescence experiments used the 325 nm line of the HeCd laser as excitation. The CR experiments were performed in transmission and with additional optical detection using a CO₂ pumped far-infrared laser. The wavelength was 432 μm . For details see ref.[6]

EXPERIMENTAL RESULTS AND DISCUSSION

The temperature dependence of the conductivity of the HVPE layer is shown in Fig.1. It increases from the lowest temperature measured up to temperatures around 250 K. Above 250 K it decreases again. In the Arrhenius plot this increase turned out to be thermally activated with a single activation energy of 15 ± 1 meV. From independent optical experiments we concluded that the film was n-type conducting with a free carrier concentration of $2.3 \times 10^{17} \text{ cm}^{-3}$ [7].

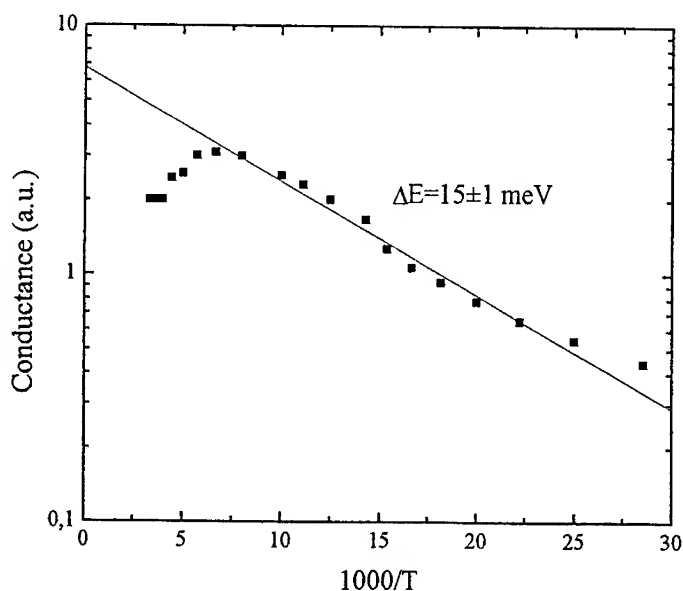


Fig.1: Arrhenius plot of the conductance of a HVPE grown undoped GaN film

The conductivity σ is given by $\sigma = en\tau$ (Drude formalism), where e is the electron charge, n the carrier concentration and τ the relaxation time related to the mobility μ by $\mu = e\tau/m^*$ m^* being the electron effective mass. Since the conduction band density of states as well as the mobility (we assume that ionized impurity scattering is the relevant mechanism at low temperatures) are temperature dependent [8] the activation energy cannot be attributed beyond any doubt to the shallow donor binding energy. The point we want to stress is that

conductance measurements on the OMVPE layer showed a quite different behavior. From 4.2 K up to 100 K basically no change in conductance was found above 100 K it increased linearly with temperature. Both findings remind on metallic conduction. Taking into account the sample structure, the heterointerface between the AlN buffer and the GaN film could be the origin. One could imagine that a two-dimensional electron gas causes the quasi-metallic behavior. We therefore performed transmission cyclotron resonance experiments.

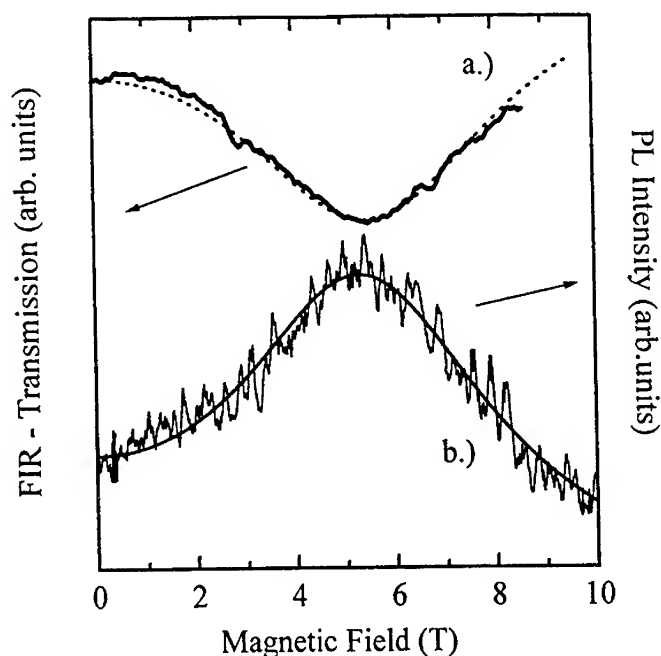


Fig.2: Cyclotron resonance transmission (a) and using optical detection (b) of an OMVPE GaN epitaxial film ($T=6K$)

As shown in Fig.2.a. we observe cyclotron resonance, where the electron effective mass can be calculated from the minimum of the transmission curve. More precise is a fit to line shape as shown in ref. [6] and from which we obtained $m^*=0.22\pm0.005 m_0$ and the scattering time $\tau=10^{-12} s^{-1}$. We rotated the sample with respect to the static magnetic field and observed no change in line position within experimental error. For a two-dimensional electron gas a $\cos\delta$ behavior, where δ is the angle between the sample orientation and the external magnetic field, should be found. We thus conclude that the transport path as monitored by conductance measurements and the transport properties as seen by CR are not the same. Whether the CR is sensitive only to the GaN layer and not to the interfacial region can be answered by performing optically detected CR experiments. Here one monitors the luminescence intensity of a specific defect recombination transition and looks for resonant CR induced changes in luminescence. The luminescence of the OMVPE

sample is shown in Fig.3. At 25 K we clearly resolve free and neutral donor bound exciton recombinations, separated by 6.2 ± 0.2 meV. We use the neutral donor bound exciton line as a monitor in our ODCR experiment. The ODCR signal as a function of magnetic field coincides with the respective minimum of the transmission experiment reported above (Fig. 2b). The mobility was slightly higher, $4000 \text{ cm}^2/\text{Vs}$ compared to $3500 \text{ cm}^2/\text{Vs}$, which can be attributed to the photo-generated carriers neutralizing ionized impurities contributing dominantly to the low temperature mobility. Excitation of the luminescence was well above the band gap of GaN, hence in ODCR we are mainly sensitive to the surface of the layer and not to the interfacial GaN/AlN region. From 5 K up to 25 K the scattering time and hence the mobility did not change. One has to note that the mobility we deduce is the mobility at around 6 T, it not necessarily coincides with Hall mobilities taken at small magnetic fields.

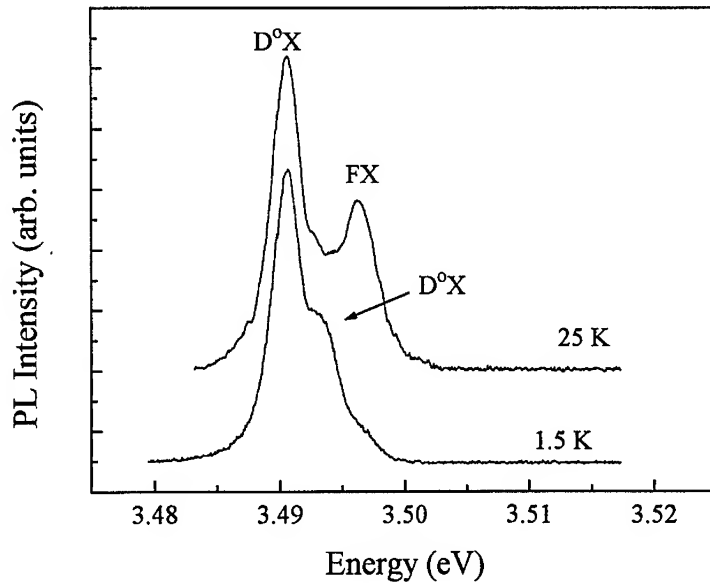


Fig.3: Photoluminescence of an undoped OMVPE GaN film measured at two different temperatures.

With the effective mass determined above we are able to calculate the donor binding energy. It is given by

$$E_D = 13.58 m^*/\epsilon^2 \text{ (eV)}$$

where ϵ is the static dielectric constant. From a fit to the free exciton reflection spectrum a value for ϵ of 9.7 [9] was obtained. Using $m^*=0.22$ and $\epsilon=9.7$ we calculate for $E_D=31.7$ meV. C-V measurements on the same film gave for the free carrier concentration at room temperature $8 \times 10^{16} \text{ cm}^{-3}$. In electrical measurements the activation energy for the uncompensated case should be $E_D/2$, i.e. around 15 meV.

To be conclusive about the residual donor binding energies still more experiments have to be performed. However from our data we want to give a lower limit. From the EMT approach we calculate 31.7 meV. Taking into account chemical shifts we expect the donor binding energy between 31.7 and 38 meV. This is corroborated by a comparison with ZnSe where typically donor binding energies are between 26 and 32 meV depending on the chemical nature of the respective donor. If the influence of the free carrier concentration on the donor binding energy is considered properly for low free carrier concentrations ($<10^{17} \text{ cm}^{-3}$) activation energies from Hall effect should be around 15 meV or more. It is also of importance to consider which residual impurity is dominating with respect to the epitaxial growth method used. OMVPE layers will certainly contain much more Carbon, Hydrogen and molecular species such as C-H as compared to HVPE where the partial pressure in the reactor determines the oxygen content, and growing at higher temperatures compared to OMVPE certainly favors Si incorporation from the quartz reactor walls. However oxygen is considered to be a deep recombination center in III-V semiconductors, at best demonstrated for GaP[11]. Si on gallium sites is a shallow EMT donor in all III-V semiconductors. It moves to the antisite, i.e. on the group V-site, acting as an acceptor at very high doping levels ($>10^{18} \text{ cm}^{-3}$). Our results would certainly favor oxygen and silicon to be the main residual donors in GaN. However, with binding energies around 32 meV, we expect for free carrier concentrations around 10^{17} cm^{-3} at room temperature a complete freeze out at low temperatures. Using Fermi-statistics for uncompensated films with $E_D=32 \text{ meV}$ we calculate the free electron concentrations at 6 K to be 10^4 cm^{-3} or less. This is certainly too low to account for the CR transmission experiments. It is therefore our conclusion that a level shallower than 32 meV contributes to conduction. We have independent evidence for such a shallow level from luminescence experiments (see Fig.3) where a neutral donor bound exciton line 3.7 meV below the free exciton line is seen. It appears independent of the growth technique and we speculate its of intrinsic origin.

CONCLUSIONS

We approach towards an understanding of the residual shallow donor binding energies by performing cyclotron resonance and photoluminescence experiments. An estimate of the shallow donor binding energy results from the effective mass theory approach which gives 31.7 meV. However, there is experimental evidence for a more shallow donor level contributing to the free carrier concentration at low temperatures. It is connected with a neutral donor bound exciton with a localization energy of 3.7 meV.

ACKNOWLEDGEMENT

We thank the DFG for financial support.

REFERENCES

- [1] S. Strite and H. Morkoc, J. Vac. Sci. Technol. B10, 1237 (1992)

-
- [2] J. Neugebauer and C.G. Van de Walle, Phys. Rev.B 50, 8067 (1994)
 - [3] P. Boguslaski, E. Biggs and J. Bernholc, Phys. Rev.B 51, 17255 (1995)
 - [4] R.J. Molnar, T. Lei and T.D. Moustakas, Appl. Phys. Lett. 62, 72 (1993)
 - [5] M. Illegems and H.C. Montgomery, J. Phys. Chem. Solids 34, 885 (1973)
 - [6] M. Drechsler, D.M. Hofmann, B.K. Meyer, T. Detchprohm, A. Amano and I. Akasaki, Jpn. J. Appl. Phys. 34, L1178 (1995)
 - [7] B.K. Meyer, D. Volm, A. Graber, H.C. Alt, T. Detchprohm, H. Amano and I. Akasaki, Solid State Comm. 95, 597 (1995)
 - [8] J.S. Blakemore, Semiconductor Statistics, Pergamon, Oxford 1962
 - [9] A. Hoffmann, private communication
 - [10] H. Amano, private communication
 - [11] B. Monemar and L. Samuelson, Solid State Commun. 26, 165 (1978)

ELECTRONIC STRUCTURES OF WIDE BAND-GAP (AlN)_m(GaN)_n[001] SUPERLATTICES

Z.-J. Tian,^{a,b} M.W.C. Dharma-Wardana,^{a,†} and L.J. Lewis^b

^a*Institute for Microstructural Sciences, National Research Council, Ottawa, Canada K1A 0R6*

^b*Département de physique et Groupe de recherche en physique et technologie des couches minces (GCM), Université de Montréal, Montréal, Canada H3C 3J7*

ABSTRACT

Wide bandgap III-V nitrides, such as GaN and AlN, have become topical in the near-term technology of blue lasers. We report detailed electronic band-structure calculations for (AlN)_m(GaN)_n [001] zinc-blende superlattices (SL), with $m + n \leq 12$, using the all-electron full-potential linear-muffin-tin-orbital method. For $n \geq 3$, the SL are found to have a direct band gap. For $n \leq 2$ and $m \geq 3$, all the band gaps are indirect. In ultrathin SL, $m \leq 3$ and $n \leq 2$, only $(m, n) = (3, 1)$ is found to have an indirect gap. The band offsets are estimated by calculating the core-level shifts of nitrogen atoms in the central planes of the GaN and AlN layers. The calculated densities of states, electron- and hole- effective masses (m^*), etc., as a function of m and n , are reported; a remarkable dependence of m^* on the number of layers is revealed.

INTRODUCTION

The wide-band-gap nitrides have gained attention recently because of their potential in the technology of blue and blue-green lasers [1]. High-quality GaN and AlN layers can now be grown on sapphire and intentionally n- and p-type doped layers and structures can be produced. AlN and GaN usually crystallize in the wurtzite (WR) form, but can also be grown in the zinc-blende (ZB) structure under appropriate conditions [1, 2]. The large band-gap difference between the two materials [$E_g = 6.2$ (5.11) eV for AlN in the WR (ZB) structure, and 3.5 (3.2) eV for GaN], but nearly identical lattice constants, makes it possible to fabricate a class of AlN/GaN alloys and SL with widely tunable wavelengths [3]. The increasing number of theoretical studies of bulk AlN and GaN [4] reflects the growing technological interest. However, very few studies have been performed for the AlN/GaN superlattices (SL).

The electronic structure of short-period AlN/GaN SL in the WR structure has been examined using first-principles methods [5]. Quasiparticle band-structures were calculated in the WR [001] and ZB [111] directions for the 1×1 , 1×2 , and 2×1 configurations [6]. In these studies, the WR SL are found to have direct band gaps, whereas a transition from direct to indirect is found for ZB SL. To our knowledge, there is only one local-density-approximation (LDA) band-structure (BS) calculation of nitride SL in the ZB [001] direction [7]; however, the calculated quantities have not been reported in detail.

In this paper, we study the (AlN)_m(GaN)_n family of ZB SL, with $(m + n) \leq 12$, in the most common growth direction, namely [001]. The electronic properties of pure AlN and GaN crystals are also investigated, as previous studies [4] have not examined in detail the effective masses or energy splittings. Our calculations are carried out within the LDA using the full-potential, linearized-muffin-tin-orbital method (FP-LMTO) [8]. Our purpose is to provide detailed results for the BS, band-gap offsets, and effective masses.

[†]To whom correspondence should be addressed; E-mail: chandre@cm1.phy.nrc.ca

COMPUTATIONAL DETAILS

In this section, we outline the symmetry properties of the SL and give details of our calculations. Because of the inequivalence of the Ga and Al planes along the [001] directions, the point-group symmetry is reduced from $T_d(\bar{4}3m)$ (for the ideal ZB lattice) to $D_{2d}(\bar{4}2m)$; the operations of the latter point group leave the SL invariant under reflections with respect to xy planes or two-fold rotations about the x or y axes, while not changing the z coordinates. For the $(\text{AlN})_m(\text{GaN})_n$ SL in the ideal configuration (i.e., all atoms on the sites of a perfect ZB lattice with unique lattice constant a_0), the Bravais lattice is simple tetragonal when $m+n$ is even and body-centered tetragonal when $m+n$ is odd. The symmetry points associated with various point groups are summarized in Table I.

Unlike the LMTO-ASA (atomic sphere approximation) method [9], which allows the muffin-tin spheres to overlap in order to eliminate the interstitial region, the FP-LMTO method adopted in this study uses non-overlapping spheres and evaluates quantities in the interstitial region explicitly by interpolating from values at the boundaries of the spheres. The method has been applied successfully to various systems, including semiconductors, transition metals, and high-temperature superconductors. It is standard practice in LMTO methods to include a number of empty spheres equal to the number of real atomic spheres [10]. The radii of the muffin-tin and the empty spheres are equal, and fixed to 3% less than the contact distance in the bulk configuration. The angular momentum expansion inside the muffin-tin spheres is truncated at $l_{max} = 4$ for Al, Ga, and N, and $l_{max} = 6$ for empty spheres. Ga 3d electrons are not restricted to their atomic spheres, but are treated as valence states, as they interact strongly with s-type valence electrons.

The lattice constant a_0 of the SL was taken as 8.44 a.u., appropriate to growth on a bulk ZB GaN substrate, calculated within the FP-LMTO scheme. The small ($\sim 3\%$) lattice mismatch with bulk AlN could cause some relaxation of the atoms, but this is not expected to affect the BS significantly [11]. The charge density has been self-consistently determined (variations in total energy of less than 1 mRy) using a mesh of 576 (1000) k points in the first Brillouin zone for $m+n \leq 4$ even (odd). For periods greater than 4, four special k points [12] were used in the self-consistent procedure. For the effective masses, fine dispersion curves in the vicinity of the valence band maximum (VBM) and conduction band minimum (CBM) were calculated using up to 40 k points in a range of width $0.03 \times 2\pi/a_0$ about the extrema; least-squares fits were then used to calculate the masses.

Table I: Symmetry points for the two possible lattice structures of $(\text{AlN})_m(\text{GaN})_n$ [001] SL. a_0 is the lattice constant, and $c/a_0 = (m+n)/\sqrt{2}$. The x and y directions are chosen in the [110] and $\bar{1}\bar{1}0$ directions of the ZB Bravais lattice. The k vectors are in units of π/a_0 .

$m+n$	Even	Odd
Bravais lattice	simple tetragonal	body-centered tetragonal
k	Symm. points	Symm. points
(0,0,0)	Γ	Γ
(1,0,0)	X	
(1,1,0)	M	X
(1,1, a_0/c)	A	
(1,1, $a_0/2c$)		P
(0,0, a_0/c)	Z	Z
(1,0, $a_0/2c$)		N
(1,0, a_0/c)	R	

RESULTS AND DISCUSSION

Table II displays our LDA-results for bulk, zinc-blende, AlN and GaN. Experimental data are in parentheses except for the band gap of AlN, taken from quasiparticle calculations [6]. As is well known, the LDA underestimates the band gaps of semiconductors; the calculated values for AlN and GaN are about 68% of their experimental counterparts. GaN is found to have a direct gap, while it is indirect for AlN. The CBM of AlN is at the X point of the first Brillouin zone of ZB structure.

Spin-orbit interactions are not included in the BS calculations: States at the top of the valence band are contributed mainly by N atoms (see below), and therefore *p*-like (three-fold degenerate). It is known, in the case of III-V semiconductors, that the spin-orbit splitting is quite close to that of atomic valence orbitals. For the *2p* orbitals of atomic nitrogen, the $p_{3/2} - p_{1/2}$ splitting is found in our approach to be about 0.02 eV. We therefore expect the spin-orbit interactions in $(\text{AlN})_m(\text{GaN})_n$ SL to play only a modest role.

The effective masses presented in Table II show significant differences compared to other III-V materials, such as AlAs and GaAs: the conduction-electron masses m_c are about 3 times larger here than in As-based compounds. Our results are comparable to those calculated with the full-potential linearized-augmented-plane-wave (FLAPW) method for AlN and GaN in the WR structure [13]. The dispersion curves along the various symmetry lines are isotropic in the vicinity of the CBM of GaN, whose density of states is mainly *s*-type. However, in AlN, the band curvature near the CBM, at X_{1c} , is anisotropic for different symmetry lines. This is also true for the dispersion of the heavy and light-hole masses near the VBM. All the values given in Table II, therefore, were obtained by averaging over several symmetry directions.

Table II: Calculated electronic properties of bulk AlN and GaN in the ZB structure. Energy levels are measured with respect to the VBM. Numbers in parentheses are experimental data. Energies are in eV, lattice constants a_0 in a.u., and effective masses are in units of the free-electron mass, m_0 .

	a_0	E_g	m_c	m_{hh}	m_{lh}	Γ_{15c}	Γ_{1v}	L_{1c}	L_{3v}	X_{1c}	X_{5v}
AlN	8.16 (8.28)	3.41 (5.11)	0.37	-1.43	-0.29	4.97	-14.99	7.90	-0.49	3.41	-1.82
GaN	8.44 (8.54)	2.18 (3.20)	0.19	-0.84	-0.16	2.18	-16.01	4.94	-1.03	3.49	-2.85

We have calculated the electronic structure of $(\text{AlN})_m(\text{GaN})_n$ SL with $m + n \leq 12$. In Figs. 1(a), (b), and (c), we present typical results for the cases $(m, n) = (1, 1)$, $(2, 2)$, and $(6, 6)$. The gross features of the BS can be drawn from the figures: The lowest bands, located between -15.8 and -11.0 eV, originate mostly from N *2s* and Ga *3d* states. The Ga *3d* states, centered at -13.2 eV, show strong hybridization with the *s* orbitals. Because of this, it is necessary to include the Ga *3d* states as valence states, as mentioned earlier. The broad bands located between -7.0 to 0 eV arise altogether from the *s*, *p*, and *d* orbitals of Al, Ga, and N. However, in the vicinity of the VBM, the states consist exclusively of the N *2p* orbitals. The conduction bands lie above 2.2 eV. In the vicinity of the CBM, states mainly originate from *s*-type functions. We have also calculated the density of states on atomic and empty spheres. The valence charge densities are found to be located mainly within the N-layers (which are perpendicular to the [001] direction), indicating strong charge transfer from the Al and Ga cations to the N anions.

Comparing the BS of the pure nitrides with the SL-BS discussed above, we observe that the degeneracy at the VBM is lifted due to the reduced symmetry of the SL. The valence band maximum at Γ , which is three-fold degenerate in the ZB structure, now splits into a

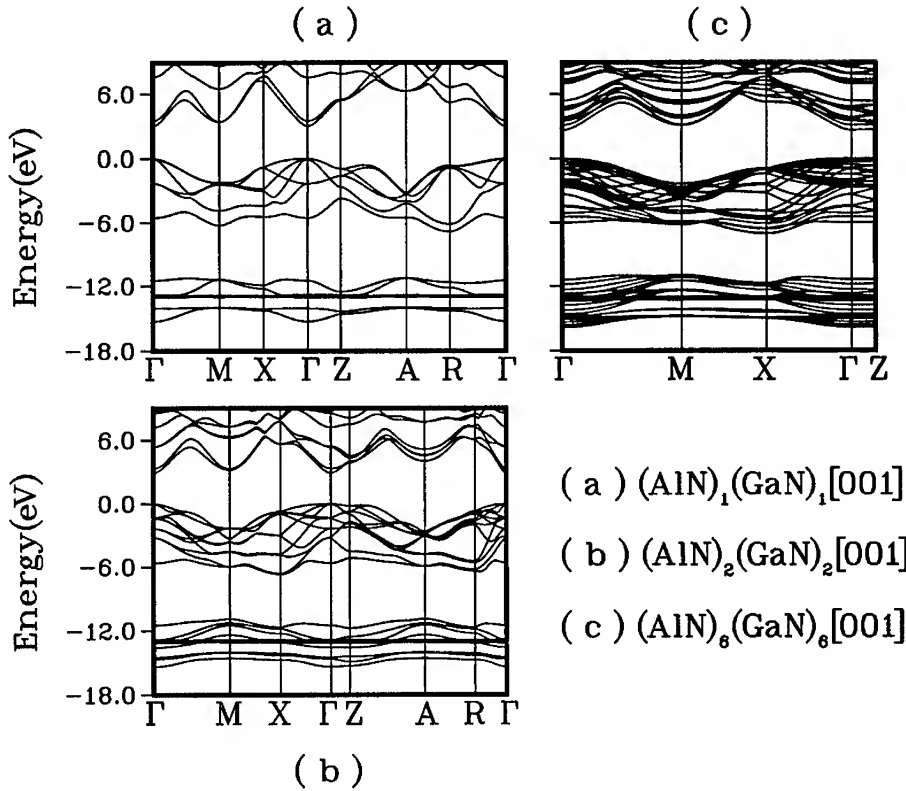


Figure 1: Band structures of the $(\text{AlN})_m(\text{GaN})_n[001]$ ZB SL for $(m,n) =$ (a) - (1,1), (b) - (2,2), and (c) - (6,6).

two-fold-degenerate state at higher energy, and one-fold-degenerate state at lower energy. This "crystal-field splitting" ranges from 0.022 to 0.147 eV for the cases considered here; the values increase with Al content. Also, the largest splitting occurs for a thickness of Ga of $n = 3$.

The energy gap of the $(\text{AlN})_m(\text{GaN})_n$ family shows interesting behaviour as a function of the period $m + n$. For $n > 2$, all band gaps are found to be direct. For $n \leq 2$ and $m > 3$, all the gaps are indirect. The CBM of the indirect gap is located at the M point when $m + n$ is even, and at X when $m + n$ is odd (cf. Table I). In the ultrathin SL, i.e., $m \leq 3$ and $n \leq 2$, all band gaps are found to be direct except for $(m,n) = (3,1)$. Roughly speaking, the band gap decreases with the Ga concentration. In the case of direct-band-gap SL, the CBM is found at the ZB Γ -folded state; it exhibits mainly s -type character and is therefore highly isotropic. This can be seen from the dispersion curves of Fig. 1, as well as from the effective masses, which we discuss next.

The effective masses for our $(\text{AlN})_m(\text{GaN})_n$ SL with $m = 1-6$ are summarized in Table III. In the xy plane ([100] and [110] directions), which is perpendicular to the growth direction ([001]), the conduction electron masses m_c are highly isotropic and remain constant as the SL thickness varies (therefore only results along [110] are given in the table). At the VBM, here the Γ point, there are two degenerate dispersion curves corresponding to the heavy-hole

and light-hole bands. The light-hole effective mass m_{lh} increases as the thickness of the SL increases, while the heavy-hole mass m_{hh} decreases. The subband lying just below the VBM is the crystal-field splitting band; its effective mass m_{spl} changes from negative (hole-like) to positive (electron-like) sign with SL thickness. The conduction-electron mass along the growth direction [001] increases with increasing number of layers. Near the VBM, the two-fold degenerate heavy-hole band rapidly becomes flat (i.e., non dispersive) as the number of layers increases, leading to large effective masses. The effective mass of the crystal-field-splitting subband in the [001] direction is hole-like, small, and depends on layer thickness in a way analogous to the light-hole effective masses in the [100] and [110] directions.

Table III: Effective masses (in units of the free-electron mass, m_0) for various $(\text{AlN})_m(\text{GaN})_m$ SL at the Γ point — crystal-field-splitting-hole (m_{spl}), light-hole (m_{lh}), heavy-hole (m_{hh}), and lowest-conduction-state (m_c) — along the directions parallel ([100] and [110]) and perpendicular ([001]) to the layers.

period (m, n)	[100]			[110]				[001]		
	m_{spl}	m_{lh}	m_{hh}	m_{spl}	m_{lh}	m_{hh}	m_c	m_{spl}	m_{hh}	m_c
(1,1)	-1.19	-0.25	-1.06	-1.07	-0.21	-9.28	0.24	-0.27	-1.14	0.28
(2,2)	-1.12	-0.27	-0.94	-1.09	-0.21	-9.02	0.24	-0.26	-1.38	0.24
(3,3)	-1.51	-0.31	-0.88	-1.48	-0.24	-8.32	0.24	-0.28	-2.33	0.27
(4,4)	-3.45	-0.37	-0.85	-3.16	-0.26	-7.51	0.24	-0.31	-4.93	0.30
(5,5)	5.66	-0.42	-0.85	8.04	-0.29	-6.86	0.24	-0.37	-11.39	0.43
(6,6)	1.78	-0.47	-0.85	1.91	-0.30	-6.43	0.24	-0.45	-23.64	0.69

We have also calculated the AlN/GaN valence-band offsets. In order to do this, we use an approach frequently employed in experiment, namely measuring the core-level shifts of anions which are common to the two semiconductor materials [14]; the offset of the valence band maxima is then taken to be equal to this core-level shift. Here, we consider, as the “common atom”, the nitrogens lying in the central planes of the AlN and GaN layers, and take as the band offset the difference in the self-consistent energies of the 1s core level in the two types of environment. To test the validity of the approach, we have calculated the band offsets for the well-studied $(\text{AlAs})_m(\text{GaAs})_n$ [001] SL in the particular case $m = n$. We find valence-band offsets of 0.50, 0.44, and 0.43 eV for $m = 3, 5$, and 6 respectively; for $m \geq 5$, the sequence rapidly converges to the bulk value of 0.43 eV, in excellent agreement with the experimental value of 0.42 eV [15], and in qualitative agreement with other theoretical calculations, 0.53 eV [16] and 0.37 eV [17].

For the $(\text{AlN})_m(\text{GaN})_m$ [001] system, now, we find valence-band offsets of 0.84, 0.80, 0.73, 0.66 and 0.55 eV for $m = 2-6$. The charge density at the highest VBM is found spatially located in the GaN layers of the SL. It is seen that the convergence with thickness is very slow in comparison to the AlAs/GaAs system. This implies that charge redistribution varies strongly with layer thickness in AlN/GaN. Though we cannot extrapolate these results to the true value of the ‘bulk’ valence-band offset, it is clearly smaller than 0.55 eV; in turn, the conduction-band offset should be greater than 1.36 eV, if we take the experimental bandgaps of AlN and GaN into account. The AlN/GaN SL are of type I superlattice, i.e., the nesting of the GaN band gap at the Γ point occurs entirely within the AlN gaps. The valence-band holes and conduction-band electrons tend to be confined in the GaN layers. Our prediction on the band offset for AlN/GaN SL calls for further calculations and measurements.

CONCLUSIONS

We have used the FP-LMTO method to calculate the band structure of $(\text{AlN})_m(\text{GaN})_n$ -

[001] SL in the zinc-blende structure. We find the band gap to switch from indirect to direct on increasing the thickness of GaN layers. For $n \geq 3$, all SL are found to have a direct band gap. For $n \leq 2$ and $m \geq 3$, all the band gaps are indirect. In ultrathin SL of, i.e., those with $m \leq 3$ and $n \leq 2$, only $(m, n) = (3, 1)$ is found to have an indirect gap. The conduction-electron effective mass in the xy plane is found to be constant, whereas it increases with increasing layer thickness, i.e., along the growth direction. This leads to a remarkable qualitative difference between the m^* in-plane and along the growth direction. Our calculations also indicate that thick-layer AlN/GaN SL are of type I, with a valence-band offset of about 0.55 eV.

Acknowledgments – This work is supported by grants from the Natural Sciences and Engineering Research Council of Canada and the “Fonds pour la formation de chercheurs et l’aide à la recherche” of the Province of Québec to L.J.L. ZJT is grateful to Geof Aers for critical reading the early version of the manuscript.

References

- [1] H. Morkoç, S. Strite, G.B. Gao, M.E. Lin, B. Sverdlov, and M. Burns, *J. Appl. Phys.* **76** 1363 (1994); H. Morkoç and S.N. Mohammad, *Science*, **267** 51 (1995).
- [2] M. Mizuta, S. Fujita, Y. Matsumoto, and T. Kawamura, *Jpn. J. Appl. Phys.* **25** L945 (1986).
- [3] Z. Sitar, M.J. Paisley, B. Yan, R.F. Davis, J. Ruan, and J.W. Choyke, *Thin Solid Films* **200** 311 (1991).
- [4] I. Gorczyca and N.E. Christensen, *Solid State Commun.* **80** 105 (1991); W.L. Lambrecht and B. Segall, *Mat. Rec. Soc. Symp. Proc.* **242** 367 (1992); W.-C. Lu *et al* *J. Phys. Condens. Matter* **5** 875 (1993); P.E. Van Camp, *et al*, *Phys. Rev. B* **44** 9056 (1991); B.J. Min, *et al*, *ibid*, **45** 1159 (1991); Y.-N. Xu and W.Y. Ching, *ibid*, **48** 4335 (1993); A.F. Wright and J.S. Nelson, *ibid*, **50** 2159 (1994); A. Rubio, *et al*, *ibid*, **48** 11810 (1994).
- [5] S.-H. Ke, M.-C. Huang, and R.-Z. Wang, *Solid State Commun.* **89** 105 (1994).
- [6] A. Rubio, J.L. Corkill, and M.L. Cohen, *Phys. Rev. B* **49** 1952 (1994).
- [7] S. Nelson, C.Y. Fong, L.A. Hemstreet, and N. Moll, *Bull. Am. Phys. Soc.* **38** 622 (1993).
- [8] M. Methfessel, *Phys. Rev. B* **38** 1537 (1988); M. Methfessel, C.O. Rodriguez, and O. K. Andersen, *ibid.*, **40** 2009 (1989).
- [9] O.K. Andersen, O. Jepsen, and D. Glötzl, in *Highlights of Condensed-Matter Theory*, eds. F. Bassani, F. Fumi, and M.P. Tosi (North-Holland, Amsterdam, 1985).
- [10] D. Glötzl, B. Segall, and O.K. Andersen, *Solid State Commun.* **36** 403 (1980).
- [11] S.B. Zhang, M.L. Cohen, S.G. Louie, T. Tománek, and M. S. Hyberstsen, *Phys. Rev. B* **41** 10 058 (1990).
- [12] R.A. Evarestov and V.P. Smirnov, *Phys. Stat. Sol. B* **119** 9 (1983).
- [13] M. Suzuki, T. Uenoyama, and A. Yanase, *Phys. Rev. B* **52** 8103 (1995).
- [14] J.R. Waldrop, R.W. Grant, S.P. Kowalczyk, and E. A. Kraut, *J. Vac. Sci. Technol. A* **3** 835 (1985).
- [15] J. Menendez, A. Pinczuk, D. J. Werder, A.C. Gossard, and J. H. English, *Phys. Rev. B* **33** 8863 (1986).
- [16] N.E. Christensen, *Phys. Rev. B* **37** 4528 (1988).
- [17] C.G. Van de Walle and R.M. Martin, *Phys. Rev. B* **35** 8154 (1987).

MONTE CARLO CALCULATION OF HOLE TRANSPORT IN BULK ZINCBLLENDE PHASE OF GaN INCLUDING A PSEUDOPOTENTIAL CALCULATED BAND STRUCTURE

I. H. OGUZMAN*, J. KOLNIK*, K.F. BRENNAN*, R. WANG** AND P. P. RUDEN**

* School of ECE, Georgia Tech, Atlanta, GA 30332, ismail@risc2.mirc.gatech.edu

** Department of EE, University of Minnesota, Minneapolis, MN 55455

ABSTRACT

In this paper, we present ensemble Monte Carlo based calculations of the steady state hole transport properties, i.e. average energy, drift velocity, and band occupancy of zincblende GaN. The Monte Carlo calculation includes the full details of the valence bands and a numerically determined scattering rate derived from an empirical pseudopotential calculation. Calculations are made for electric field strengths up to 1000 kV/cm. It is found that the average hole energies are much lower than the corresponding electron energies at comparable electric field strengths, and that some anisotropy in the drift velocity and average energy appears at the higher fields examined here.

INTRODUCTION

GaN is a very promising semiconductor material for possible use in ultraviolet detection or emission. This is mainly due to its wide and direct energy bandgap which makes the material a potential candidate for optoelectronic devices in the near ultraviolet region of the electromagnetic spectrum. GaN also finds applications in high-power, high-frequency and high-temperature electronics. Although various GaN based devices for such applications have been reported [1-4], there is a scarcity of information about the transport properties of the material.

GaN can be grown in either wurtzite or zincblende phase [5]. Many material properties for the two phases are similar whereas their band structures (Figure 1) are significantly different; the

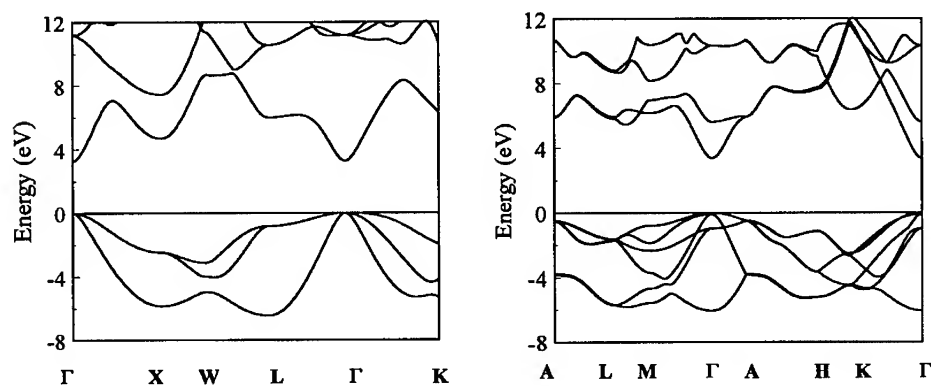


Figure 1. (a) Band structure of zincblende type GaN. (b) Band structure of wurtzite type GaN. Both are calculated using an empirical pseudopotential method.

difference is especially noticeable when one considers the valence bands. In addition to the fact that the number of valence bands within the energy range of interest for transport studies is higher in the wurtzite phase vs. the zincblende phase, extreme band warping creates a non-trivial problem to be solved while modeling the wurtzite type GaN. Although there are several theoretical investigations made to date, to determine the electronic transport properties of bulk GaN [6-9], similar studies are yet to be performed for holes in either possible phase. In addition to complementing the steady-state information already obtained for the electrons [10] such as the drift velocity, average particle energy, etc., it is important to determine the high-energy behavior of holes in GaN. Knowledge of very high energy transport, i.e., the calculation of the impact ionization rates, is particularly useful in assessing the performance of possible ultraviolet avalanche photodetectors.

It is the purpose of this paper to present the first theoretical calculations of the steady-state hole transport properties in the zincblende phase of GaN. Here, it should be noted that the numerous intersections of the valence bands in wurtzite type GaN presents some added complexity in calculating its transport properties. The pseudopotential method labels the bands with respect to their ascending order in energy at each k -point, regardless of the bands' apparent continuity. From a transport viewpoint, this can cause a discrepancy during the free flight of a particle since a particle can be subjected to an abrupt momentum change without the interference of a scattering agent. Even though it is possible to proceed with an improved ordering of the bands beyond what was given by the original pseudopotential calculation, it is a very difficult task to make the new ordering consistent throughout the entire First Brillouin zone of the wurtzite structure. For this reason, we delay the examination of hole transport in wurtzite GaN to a later work where a comparison can then be made between the transport properties of wurtzite and zincblende phases of GaN.

The present calculations are carried out using an ensemble Monte Carlo simulator that includes the full details of the valence bands within the energy range of interest. Results obtained for the steady-state drift velocity, average hole energy and band occupancy under electric field magnitudes up to 1000 kV/cm are presented. In Section II, the details of the Monte Carlo model are described. The simulation results are given and discussed in Section III and conclusions are drawn in Section IV.

MODEL DESCRIPTION

The calculations are performed using an ensemble Monte Carlo simulator which includes the top three bands for the zincblende phase covering all of the valence band states from the band edge up to around -7 eV. The band structure is obtained using an empirical pseudopotential calculation [10] using an expansion over a fixed set of 113 reciprocal lattice vectors. During the course of the simulation, each hole's energy is calculated by making suitable interpolations [11] between mesh points which form a finely spaced, 1419 point, k -space grid spanning the irreducible wedge of the First Brillouin zone.

The Monte Carlo simulator includes all of the relevant phonon scattering rates, i.e., acoustic, nonpolar and polar optical scattering mechanisms, in addition to the ionized impurity scattering. The rates for all these mechanisms are numerically calculated assuming Fermi's Golden Rule by integrating over the actual pseudopotential band structure. The calculated rates are incorporated into the simulator following the technique of Hinckley and Singh [12]. Their approach accounts for the anisotropy and warping of the valence bands by interpolating the scattering rate among the three principal directions. Considering the large size of the basis vector set for the pseudopotential method, the overlap integrals for the transitions are not calculated

directly, instead they are determined through symmetry transformations appropriate for the zincblende crystalline structure [13,14]. The above treatment for the scattering rate calculation holds in the low energy region that is defined to extend up to 0.6 eV. GaN has a relatively high phonon scattering rate at low energies that exceeds 10^{14} s^{-1} , mainly because of the high polar optical scattering rate. This is plausible considering GaN's large longitudinal optical phonon energy (91.75 meV) and high valence band effective masses.

At high energies, the deformation potential scattering is assumed to make the dominant contribution to the total scattering rate. The corresponding rate is calculated through a time-dependent perturbation theory expansion by integrating over the final density of states including collision broadening effects [15]. The deformation potential itself is treated as a constant and the resulting rate is matched to the low energy scattering rates at 0.6 eV. While the inclusion of hole initiated impact ionization rates could provide a better picture of the transport in zincblende type GaN, impact ionization is expected to be insignificant for the field range examined here. As will be seen in the next section, in zincblende type GaN at electric field strengths below 1000 kV/cm, the energy of the holes appears to be too low on average to produce a significant impact ionization rate. For these reasons, we neglect the treatment of impact ionization in this paper. The effects of hole initiated impact ionization in GaN will be addressed in a later work.

RESULTS

The calculated steady-state hole drift velocity along the three major zincblende crystalline axes vs. applied electric field is shown in Figure 2. While the velocities along all three directions are isotropic at low fields, it is seen that holes attain a higher velocity when the field is applied along the [100] direction than the other two directions at higher electric fields. Figure 3 compares the average hole energies vs. electric field and it shows a trend from isotropic properties towards anisotropic ones, as well, as the electric field magnitude is increased. When Figure 2 and Figure 3 are examined together, it is also observed that the holes have very low average energies along with possibly very low mobilities. When compared to the steady-state results obtained for electrons in zincblende type GaN [10], these results become even more striking as the average

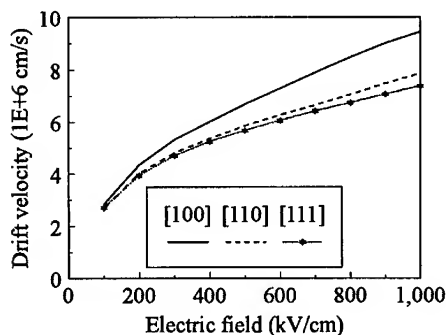


Figure 2. Calculated steady-state hole drift velocity as a function of applied electric field along the three major crystalline axes in zincblende type GaN.

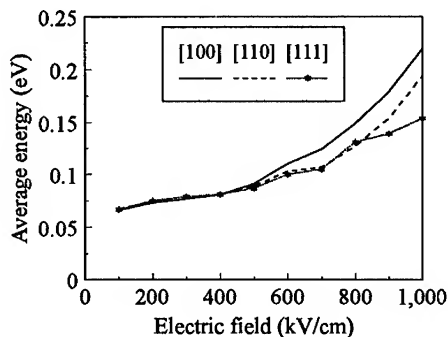


Figure 3. Calculated steady-state average hole energy as a function of applied electric field along the three major crystalline axes in zincblende type GaN.

electron energies are 10 to 20 times higher than average hole energies at similar electric field strengths. Although it is difficult to extrapolate the low field mobilities from the current valence band calculations since the accuracy of the energy interpolation scheme in the current Monte Carlo code becomes relatively poor at energies below 0.05 eV, if the present numerically calculated band structure is retained, some rough estimates can still be made. In that case, the ratio for the theoretically calculated mobilities for the electrons exceeds their hole counterparts by an order of magnitude confirming the comparison made using the average energies.

The somewhat unusually low hole energies calculated here are most likely a result of the very high effective masses, phonon scattering rates, and phonon energies in zincblende GaN. The combination of these three attributes act to restrict the holes to low energies. As can be seen from Figure 1, the first valence band is very much flatter than the corresponding first conduction band. Consequently, the holes will attain a much lower energy on average than the electrons at comparable electric field strength.

Another result of interest is the percentage of band occupancies for the current calculations. The bands are ordered in the present simulation using a simple ordering scheme. The lowest energy points are assigned to the first valence band, here labeled band #1, the next lowest energy points are assigned to band #2, etc., neglecting band crossing effects. Though band crossings can lead to some ambiguity in the identity of each band, in zincblende the number of band crossings, particularly at low energy, is small. Figure 4 very clearly shows that the holes predominantly reside in band #1 along the [100] direction at the field range considered in this work. Approximately, 83 % of all the holes occupy band #1 whereas there is still a sizable population of about 16 % in band #2. Band #3 is very sparsely populated with an occupancy of less than about 1 % at all fields. This is consistent with the valence band density of states obtained using the empirical pseudopotential method as is seen from Figure 5. It should also be noted here

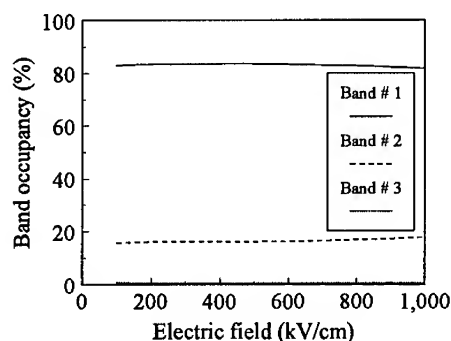


Figure 4. Calculated occupancy for the top valence bands as a function of applied electric field along [100] direction in zincblende type GaN. It is almost identical with the band occupancies along the [110] and [111] directions.

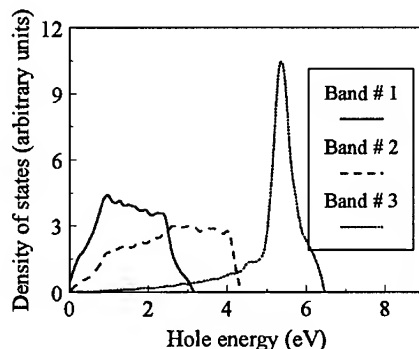


Figure 5. Density of states of the top three valence bands in zincblende type GaN, calculated using the empirical pseudopotential method.

that the band occupancy reported when the electric field is applied along the [100] direction is almost identical with the occupancies as a function of the field along the [110] and [111] directions which signifies an isotropic behavior for this parameter. This indicates that the calculated anisotropy in the carrier energies and velocities does not arise from a difference in band occupancy but might be due to differences in the effective mass or scattering rate along the different directions instead.

CONCLUSIONS

In this paper, the first calculations of the steady-state hole transport properties of zincblende type GaN have been presented. It is found that both the drift velocity and the average energy have an isotropic form at low fields along the three major zincblende crystalline axes whereas at high fields the isotropy disappears. When the electric field is applied along the [100] direction, a higher drift velocity and average energy are calculated. It is also found that the average energy in zincblende GaN is an order of magnitude lower for holes than for electrons. This is consistent with lower carrier mobilities as well. The much lower calculated average energy for holes as compared to electrons is most probably due to the fact that the first valence band is very much flatter than the first conduction band. Consequently, at comparable electric field strength, the holes will attain a significantly lower energy, on average, than the electrons. Another important result is that more than 80% of holes occupy the lowest energy band in the field range considered in this work, with most of the remaining population in the next lowest band. Less than 1% of the hole population is calculated to be in the third lowest energy band at the field strengths considered.

ACKNOWLEDGEMENTS

The authors would like to thank Drs. N. Sano, M. Stobbe, and M. Fischetti for helpful discussions on this work. This work was sponsored in part by the National Science Foundation through a collaborative grant made to Georgia Tech (ECS-9313635) and to the University of Minnesota (ECS-9408479).

REFERENCES

1. M. A. Khan, R. A. Skogman and J. M. Van Hove, *Appl. Phys. Lett.* **56**, 1257 (1990).
2. M. A. Khan, J. N. Kuznia, D. T. Olson, T. George and W. T. Pike, *Appl. Phys. Lett.* **63**, 3470 (1993).
3. M. A. Khan, J. N. Kuznia, D. T. Olson, W. J. Schaff, J. W. Burm and M. S. Shur, *Appl. Phys. Lett.* **65**, 1121 (1994).
4. S. Nakamura, M. Senoh and T. Mukai, *Appl. Phys. Lett.* **62**, 2390 (1993).
5. S. Strite and H. Morkoc, *J. Vac. Sci. Technol. B* **10**, 1237 (1992) and references therein.
6. P. Das and D. K. Ferry, *Solid-State Electron.* **19**, 851 (1976).
7. M. A. Littlejohn, J. R. Hauser and T. H. Glisson, *Appl. Phys. Lett.* **26**, 625 (1975).

8. N. S. Mansour, K. W. Kim and M. A. Littlejohn, *J. Appl. Phys.* **77**, 2834 (1995).
9. B. Gelmont, K. Kim and M. Shur, *J. Appl. Phys.* **74**, 1818 (1993).
10. J. Kolnik, I. H. Oguzman, K. F. Brennan, R. Wang, P. P. Ruden and Y. Wang, *J. Appl. Phys.* **78**, 1033 (1995).
11. M. V. Fischetti and S. E. Laux, *Phys. Rev. B* **38**, 9721 (1988).
12. J. M. Hinckley and J. Singh, *Phys. Rev. B* **41**, 2912 (1990).
13. N. Sano and A. Yoshii, *Phys. Rev. B* **45**, 4171 (1992).
14. M. Stobbe, R. Redmer and W. Schattke, *Phys. Rev. B* **49**, 4494 (1994).
15. Y. C. Chang, D. Z.-Y. Ting, J. Y. Tang and K. Hess, *Appl. Phys. Lett.* **42**, 76 (1983).

EXCITONIC RECOMBINATION PROCESSES IN UNDOPED AND DOPED WURTZITE GaN FILMS DEPOSITED ON SAPPHIRE SUBSTRATES

J.A. FREITAS, Jr.*[#], K. DOVERSPIKE**[#], A.E. WICKENDEN[#]

*Sachs/Freeman Assoc. Inc., Landover MD 20785, Freitas@bloch.nrl.navy.mil

**Hewlett-Packard, San Jose CA 95131

[#]Naval Research Laboratory, Washington DC 20375

ABSTRACT

Excitonic recombination processes in GaN films grown by low pressure metalorganic chemical vapor deposition technique have been studied in the temperature range between 6K to 320K by photoluminescence spectroscopy. Low temperature photoluminescence spectra of high resistivity films show well-resolved spectral features associated with the excitonic interband transitions. A detailed spectral analysis allowed us to estimate the exciton binding energy and the energy gap. Spectral studies of Si-doped GaN films demonstrate that the high energy recombination processes in these films are dominated by excitons bound to neutral Si donors. Comparison between the recombination channels in high resistivity and in Si-doped films indicated that Si has a larger exciton binding energy than the unknown pervasive donor in undoped materials. These results confirm the excellent electronic properties of the undoped and doped films.

INTRODUCTION

The group III-nitrides are well known as a potential material system for the fabrication of opto-electronic devices and/or devices operating under extreme conditions. However, difficulties encountered in the growth of large bulk crystals have limited their practical application. The recent advances in deposition techniques for hetero-epitaxial growth of III-nitrides have resulted in important accomplishments, such as the fabrication of high luminosity blue, blue-green, and green light emitting diodes (LEDs) and high-power field-effect transistors (FETs) for microwave and millimeter wave application [1,2].

Commonly, GaN films deposited by low pressure metalorganic chemical vapor deposition (LP-OMCVD) on sapphire substrates are n-type, with typical carrier concentrations between 5×10^{16} and $5 \times 10^{17} \text{ cm}^{-3}$, and carrier mobilities between 300 and $400 \text{ cm}^2/\text{V-s}$. Recently, we have demonstrated the growth of undoped films with dark resistivity at 300K of about $10^{10} \Omega\text{-cm}$. Disilane was used to dope the material n-type. Typically, films with electron concentrations of around $1 \times 10^{17} \text{ cm}^{-3}$ achieve room temperature mobilities of approximately $600 \text{ cm}^2/\text{V-s}$ [3].

Full realization of the potential applications of the III-V nitrides requires understanding the role of incorporation and activation of unintentional and intentional impurities and structural related defects. Photoluminescence (PL) spectroscopy has proven to be a powerful tool for the detection and identification of impurities and other defects in wide bandgap thin films on the basis of PL spectra attributable to excitons bound to neutral impurities, free carriers recombining with carriers bound at impurities, and donor-acceptor pair (DAP) recombination [4]. In addition, time decay characteristics and excitation power dependence have been used to classify recombination processes on the basis of radiative lifetimes, and impurity ionization energies can be determined from the temperature quenching of the PL bands.

The low temperature photoluminescence (LTPL) spectrum of the high resistivity film shows a dominant peak at 3.4867 eV. The LTPL spectrum of the Si-doped film exhibits an intense peak

at 3.4779 eV which we attribute to the recombination of excitons bound to neutral Si donors. We have performed detailed studies of the excitation power and temperature dependence of the PL spectra to identify the features associated with excitons bound to native neutral donors and free excitons. In addition, we have estimated the binding energy of the exciton to a neutral native donor and to the neutral Si donor.

EXPERIMENT

The growth of undoped and silicon-doped (Si-doped) GaN films were done in an inductively-heated, water cooled, vertical reactor. The source gases, electronic grade ammonia (NH_3) and ultra-high purity trimethylgallium (TMGa), were introduced separately via pressure-controlled manifolds into the top of the reactor, which was held at 57 torr. A nucleation layer was formed at 450 °C onto a sapphire substrate before the film deposition. The film growth was carried out at substrate temperatures between 1000-1080 °C. Under usual growth condition the described reactor yielded a growth rate of 1.1 $\mu\text{m/hr}$ [5].

Si-doping of GaN films were achieved by using Si_2H_6 dilute in either H_2 or in N_2 . In some instances the doped GaN was deposited on a high resistivity 0.5 μm thick unintentionally-doped GaN layer. The doping level was found to be controllable over the range from $1 \times 10^{17} \text{ cm}^{-3}$ to $4 \times 10^{19} \text{ cm}^{-3}$. Comparison between SIMS and room temperature (RT) Hall data suggested a near-unity activation efficiency of Si in the GaN lattice [3]. High frequency FETs have been successfully fabricated on films doped using this procedure [2].

The low temperature PL experiment was carried out with samples placed in a continuous flow liquid helium cryostat and the temperature was kept constant at 6K. The variable temperature measurements were performed in the temperature range between 5K to 320K using a needle valve to control the amount of liquid helium allowed in the sample chamber and the heat generated on resistors placed in the helium diffuser and sample holder. The samples were excited with the 325.0 nm (3.81 eV) line from a He-Cd laser. The laser excitation intensity was controlled with UV transmitting neutral density filters. The radiation emitted by the samples was dispersed and analyzed by a double spectrometer fitted with a 1800 gr/mm grating set and detected with a UV-sensitive GaAs photomultiplier operated in photon counting mode. Different spectrometer band passes were used for diverse spectral ranges. Although the PL spectra presented here are not corrected for instrumental response, we have corrected the spectrometer wavelength calibration near the bandedge emission bands.

RESULTS AND DISCUSSION

We have reported previously the LTPL spectra of nominally undoped GaN films, which commonly have electron concentrations between 5×10^{16} and $5 \times 10^{17} \text{ cm}^{-3}$, and electron mobilities between 250 and 400 $\text{cm}^2/\text{V-s}$ [5,6]. The PL spectra of such films are characterized by a dominant sharp emission line about 3.475 eV and a broad band which peaks around 2.25 eV. The former is assigned to excitons bound to a neutral unknown donor ($\text{D}^0\text{-X}$) and the latter may be associated with structural defects [6-9]. Recently, we were able to grow undoped films with dark RT resistivity of about $10^{10} \Omega\text{-cm}$ [10]. A typical PL spectrum of such high resistivity films (HRF) is represented in figure 1 (top spectrum), combined with the PL spectrum of a Si-doped film, which has an electron concentrations of $1.62 \times 10^{17} \text{ cm}^{-3}$ and room temperature mobility of 560 $\text{cm}^2/\text{V-s}$ (bottom spectrum). Note that the PL spectrum of the HRF has been normalized to the peak intensity of the edge emission of the Si-doped film. Both spectra show the presence of the so called yellow band (2.25 eV). However, the HRF spectrum shows an additional band

around 3.0 eV, which may be associated with an expected partial film compensation. The inset in figure 1 represents the high resolution PL spectra of both films. The edge emission of the HRF has been assigned to free exciton (FE) recombination, in agreement with results reported previously [3,11]. Note the absence of the D⁰-X band, commonly observed in undoped films on the low energy side of the FE, usually red-shifted by 4-5 meV [11]. The high resolution PL spectrum of the Si-doped film exhibits a peak at 3.4779 eV which we attribute to the recombination of excitons bound to neutral Si-donors, since it has been observed only in Si-doped films and not in unintentionally doped films. The energy difference between the emission peaks in the Si-doped and the HRF is about 8.8 meV, suggesting that Si is not the unknown pervasive donor in undoped GaN films. In addition, this spectral analysis may indicate that the binding energy of the Si-impurity is about twice that of the unknown donor [12,13]. Although the nature of the recombination processes associated with the edge emission in both films are not the same and PL is not an adequate technique to quantify relative concentration of competing radiative centers, we can speculate that the FE recombination channel in HRF becomes dominant because of a sizable reduction of the concentration of unknown donors. We would like to point out that if we have an increase in the concentration of compensating centers we should

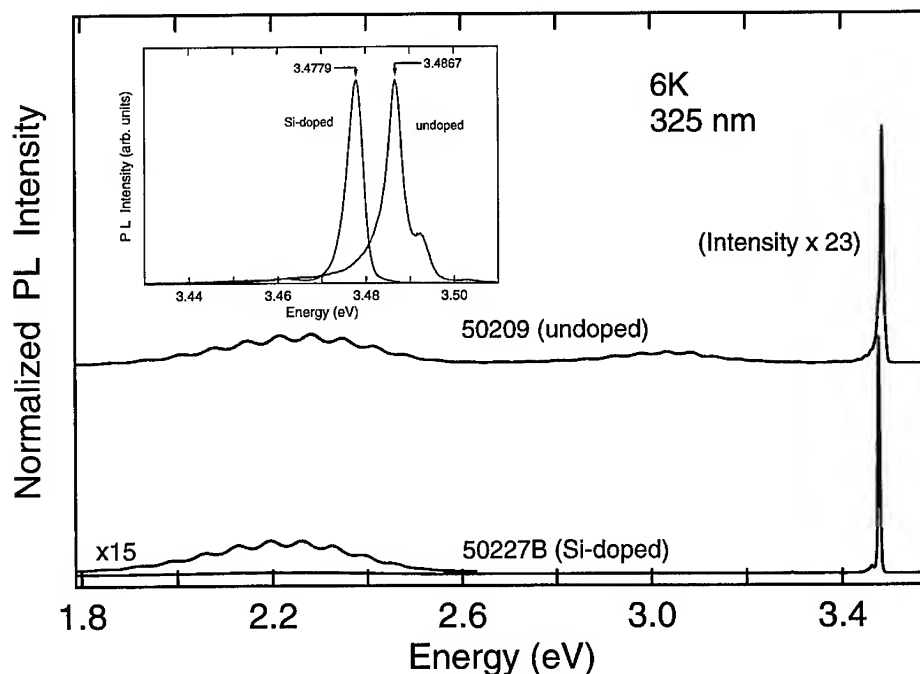


Fig. 1. Photoluminescence spectra of undoped (high resistivity) and Si-doped GaN films. The inset show the high resolution spectra of both films. If the residual level of electrically active impurities is sufficiently low, one may expect that the recombination processes involving free excitons will dominate the near bandedge emission. The peak at 3.4796 eV, observed only in Si-doped samples, is attributed to the recombination of an exciton bound to a neutral Si-donor. The energy difference between the peak at 3.4884 and 3.4796 eV is 8.8 meV, and represents the binding energy of the exciton bound to the neutral Si-donor.

observe a relative increase of the intensity of emission bands associated with recombination processes involving DAP, which is not observed in figure 1 [14].

To obtain more insight on the nature of the recombination processes associated with the edge emission bands in undoped and doped films we have performed measurements of the temperature dependence of the PL intensity. Figure 2 represents the PL spectra of the HRF performed at 6K and 25K. Although we observe a small red-shift in the peak position between the two spectra, the most noticeable spectral change occurs in the relative intensity of the ground state ($n=1$) of the free-exciton A (FE-A) at 3.4867 eV and the ground state of the free-exciton B (FE-B) at 3.4923 eV. The difference in energy between these two peaks (5.6 meV) is the value of the crystal field splitting of the two valance bands. For temperatures above 70K the FE recombination process is dominated by the FE-B. The third peak observed in both spectra is assigned to the first excited state of the FE-A ($n=2$). The separation between the ground and excited states of the FE is about 17.0 meV. Assuming the hydrogenic approximation we estimate a value of 22.7 meV for the binding energy of the FE-A. We would like to point out that most of the differences between the energies reported here and by other research groups can be understood if we take into consideration that the films discussed in the present work have been deposited on a-plane sapphire substrates. A detailed comparison between c-plane and a-plane HRF films will be presented in a forthcoming paper. A study varying the PL excitation intensity has shown that the FE line width increases with increasing excitation level, suggesting that some non-radiative recombination channels are saturating. This observation supports the FE assignment for the bandedge emission and confirms the high quality of the HRF deposited by LP-MOCVD. A recent report by an other group confirms our previously reported observation of FE recombination mechanism being the dominant recombination channel in HRF [3,15].

Figure 3 shows the PL spectra of the Si-doped film measured at 6K and 30K. At lower temperature the recombination process is dominated by excitons bound to neutral Si donors ($\text{Si}^0\text{-X}$). Upon increasing the sample temperature we observed in addition to the expected $\text{Si}^0\text{-X}$ red-shift, the increase of a shoulder on the higher energy side of the $\text{Si}^0\text{-X}$ band. This increasing intensity shoulder is associated with the increase in the population of excitons thermally released

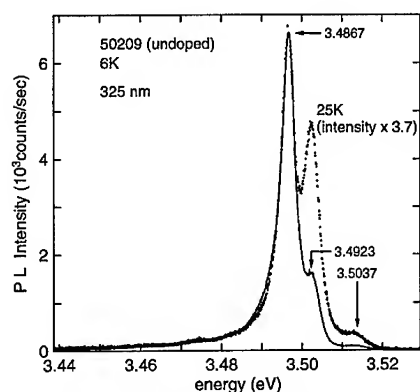


Fig. 2. PL spectra of the high resistivity sample measured at 6K (continuous line) and 25K (dotted line, normalized). The 3.4923 eV line becomes dominant above 70K.

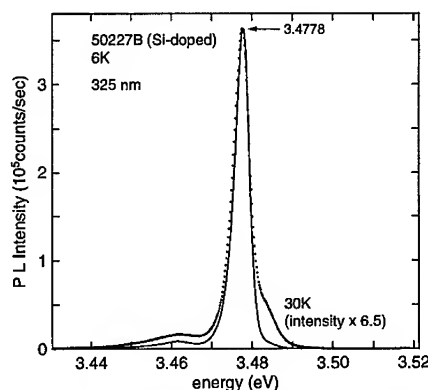
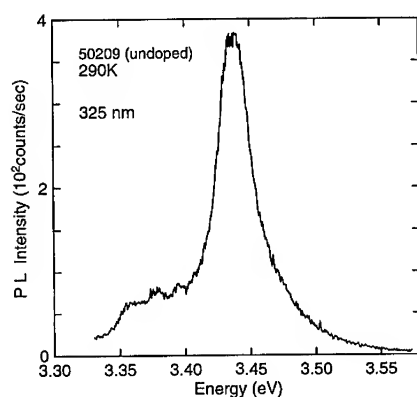


Fig. 3. PL spectra of the Si-doped sample performed at 6K (continuous line) and 30K (dotted line, normalized). Note the increasing relative intensity of the shoulder in the high energy side of the 30K spectrum.

from the neutral Si donor. A detailed study of the temperature dependence of the Si⁰-X band will be presented elsewhere. A PL excitation intensity study of the Si⁰-X has shown no line width variation with increasing excitation power density. This observation confirms the different nature of this bandedge recombination process compared to the bandedge recombination in HRF.

The PL temperature study was carried out from 6K to 320K on HRF, undoped-conducting films, and Si-doped films. At room temperature, as expected, we observed the same PL line shape for all samples. In figure 4 we present the PL spectrum of the HRF measured at 290K. The peak position is at 3.4369 eV and the line width at half maximum is about 33 meV. The features observed on the lower energy side of the FE may be associated with acceptor-impurities. The high energy side of the FE can be fitted with a Maxwell-Boltzman distribution. Presently we are attempting to obtain a complete line shape fitting.



SUMMARY

We have performed photoluminescence measurements in undoped and Si-doped GaN films in the temperature range between 5K to 320K. The bandedge emission spectra of HRF has been assigned to recombination processes associated with free-excitons. We have estimated a value of 22.7 meV for the binding energy of the FE-A. A comparison with PL studies of undoped low-resistivity and p-type doped films suggests that the FE recombination channel becomes dominant due to a reduction in the concentration of native donors. The emission bands observed in Si-doped films are associated with recombination process dominated by excitons bound to neutral Si donors. Spectral analyses of HRF and Si-doped films may indicate that Si is

Fig. 4 Room temperature PL spectrum of the undoped GaN. Similar spectra are observed in Si-doped samples.

not the native donor in undoped films. Since we have often observed 1 to 3 meV shifts in the exciton peak position as a function of location across a 2 inch diameter wafer, the origin of the sample must be taken in consideration before we can draw a final conclusion. Presently we are performing calculation for obtain a complete exciton line shape fitting.

ACKNOWLEDGMENTS

We would like to thank Dr. P.B. Klein for helpful discussions. Work supported in part by the Office of Naval Research

REFERENCES

1. S. Nakamura, to be published in Topical Workshop on III-V Nitrides, edited by K. Onabe, S. Fujishiro and H. Morkoç, Nagoya, Japan, 1995.
2. S.C. Binari, to be published in Topical Workshop on III-V Nitrides, edited by K. Onabe, S. Fujishiro and H. Morkoç, Nagoya, Japan, 1995.
3. A.E. Wickenden, L.B. Rowland, K. Doverspike, D.K. Gaskill, J.A. Freitas, Jr., D.S. Simons, and P.H. Chi, *J. Electron. Mater.*, **24**, p. 1547 (1995).

4. S.G. Bishop and J.A. Freitas, Jr., *J. Cryst. Growth*, **106**, 38 (1990).
5. L.B. Rowland, K. Doverspike, A. Giordana, M. Fatemi, D.K. Gaskill, M. Skowronski, and J.A. Freitas, Jr. in Silicon Carbide and Related Materials, edited by M.G. Spencer, R.P. Devaty, J.A. Edmond, M.A. Khan, R. Kaplan, M. Rahman (*Inst. Phys. Conf. Ser.*, **137**, 1989) p. 429 - 432.
6. M.A. Khan, D.T. Olson, J. N. Kuznia, W.E. Carlos, and J.A. Freitas, Jr., *J. Appl. Phys.*, **74**, 5901 (1993).
7. R. Dingle, D.D. Sell, S.E. Stokowski, M. Ilegems, *Phys. Rev. B*, **58**, 1211 (1971).
8. H.G. Grimmeis and B. Monemar, *J. Appl. Phys.*, **41**, 4054 (1970) .
9. E.R. Glaser, T.A. Kennedy, H.C. Crookham, J.A. Freitas, Jr., M.A. Khan, D.T. Olson, and J.N. Kuznia, *Appl. Phys. Lett.*, **63**, 2673 (1993).
10. K. Doverspike, A.E. Wickenden, S.C. Binari, D.K. Gaskill, J.A. Freitas, Jr., D.S. Simons, and P.H. Chi, to be published in Topical Workshop on III-V Nitrides, edited by K. Onabe, S. Fujishiro and H. Morkoç, Nagoya, Japan, 1995.
11. W. Shan, T.J. Schmidt, X.H. Yang, S.J. Hwang, J.J. Song, and B. Goldenberg, *Appl. Phys. Lett.*, **66**, 985 (1995).
12. J. A. Freitas, Jr., S.G. Bishop, P.E.R. Nordquist, and M.L. Gipe, *Appl. Phys. Lett.*, **52**, 1695 (1988).
13. J.R. Haynes, *Phys. Rev. Lett.*, **4**, 361 (1960).
14. J.A. Freitas, Jr., and M.A. Khan in Diamond, SiC and Nitride Wide Bandgap Semiconductors, edited by C.H. Carter, Jr., G. Gildenblat, S. Nakamura, and R.J. Nemanich (*Mater. Res. Proc.* **339**, Pittsburgh, PA 1994), p. 547-552.
15. M. Smith, G.D. Chen, J.Z. Li, J.Y. Lin, H.X. Jiang, A. Salvador, W.K. Kim, O. Aktas, A. Botchkarev, and H. Morkoç, *Appl. Phys. Lett.*, **67**, 3387 (1995).

IDENTIFICATION OF TRANSITION METALS IN GaN

K. PRESSEL*, R. Heitz**, L. ECKEY**, I. LOA**, P. THURIAN**, A. HOFFMANN**,
B.K. MEYER***, S. FISCHER****, C. Wetzel****, E.E. Haller****

*Institut für Halbleiterphysik, P.O. Box 409, 15204 Frankfurt(Oder), Germany

**Inst. für Festkörperphysik, Techn. Univ. Berlin, 10623 Berlin, Germany

***Physik-Department E16, Techn. Univ. München, 85748 Garching, Germany

****Lawrence Berkley Laboratory, Univ. of California, Berkley, CA 94720, U.S.A.

ABSTRACT

We present a photoluminescence study of residual transition metal contaminants in hexagonal GaN layers. We observe three no-phonon lines peaking at 1.3 eV, 1.19 eV and 1.047 eV. The no-phonon line at 1.3 eV is caused by the internal electronic transition ${}^4T_1 \rightarrow {}^6A_1$ of Fe^{3+} . The 1.19 eV emission, which was first attributed to Cr^{4+} , is caused by Ti^{2+} . GaN layers intentionally doped with Cr, V, or Ti during growth have been investigated. Only the Ti doped samples show an intense signal of the 1.19 eV emission. The experimental data of the luminescence center at 1.047 eV, which appears as natural contaminant only in GaN layers grown by the sandwich technique, fit best to the ${}^4T_2(F) \rightarrow {}^4A_2(F)$ transition of Co^{2+} . The three no-phonon lines show characteristic phonon sidebands. Most of them correspond to phonon modes observed in Raman spectroscopy.

INTRODUCTION

In recent years the development of an AlGaIn/InGaIn blue green light emitting diode [1] stimulated worldwide the efforts to develop also a GaN based blue green laser. Up to now photoluminescence (PL) measurements on GaN have mainly been performed in the near bandedge region at about 3.4 eV and in the range of the yellow luminescence at around 2.2 eV. Only a few studies have been published hitherto on emissions in the near infrared region (NIR) of GaN [2, 3, 4]. Luminescence centers in the near infrared are caused by internal electronic transitions of 3d elements which are incorporated as natural contaminants during crystal growth. In this paper we focus on three luminescence centers in GaN which show no-phonon (NP) lines peaking at 1.3 eV, 1.19 eV, and 1.047 eV and characteristic phonon replica.

EXPERIMENTAL

The GaN samples were grown by means of high temperature vapor phase epitaxy (HTVPE) [5] or by a modification of the sandwich technique [6]. Both techniques utilize liquid metallic Ga and NH_3 as precursors. The main characteristics are the small distances between the Ga melt and the substrates (≤ 5 mm) and the high growth temperature around 1200°C. Doping of the GaN with transition metals was done by adding the respective transition metal in a ratio of 1:1000 to the Ga melt. The films were deposited either on (0001) 6H-SiC or (0001) sapphire substrate. The PL measurements were performed using a BOMEM DA8.02 Fourier spectrometer. The PL excitation (PLE) measurements were performed with conventional monochromator technique. For all the measurements a Ge-detector was used.

RESIDUAL 3d TRANSITION METALS IN GaN

Figure 1 shows a near infrared PL spectrum of a GaN sample grown by the sandwich technique on 6H-SiC. We observe three NP lines with transition energies at 1.3 eV, 1.19 eV, and 1.047 eV and their corresponding phonon sidebands. In the inset a detailed spectrum of one of the samples in the range of the 1.047 eV emission is depicted. In addition to the 1.047 eV emission, labelled A, further weaker emissions appear which are caused by so far unidentified defects.

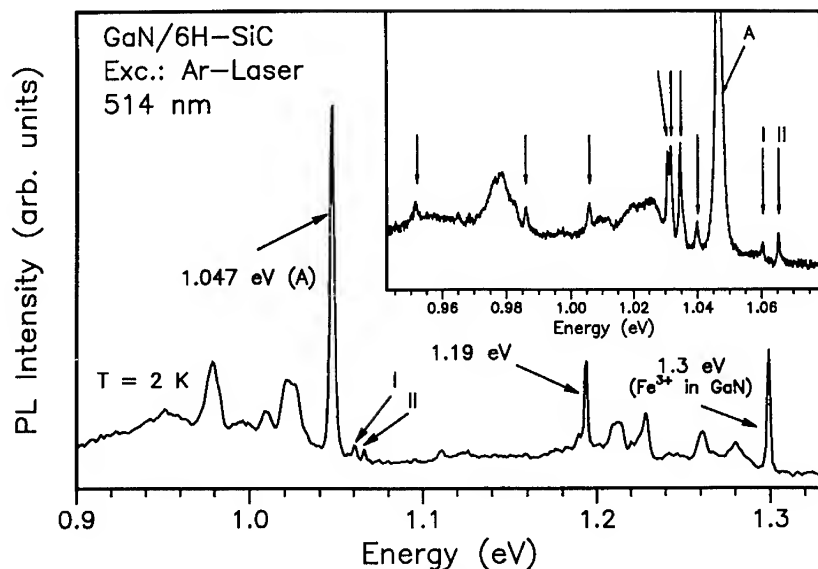


FIG. 1. PL spectrum of GaN/6H-SiC in the near infrared region. Three NP lines peaking at 1.3 eV, 1.19 eV, and 1.047 eV together with GaN related phonon sidebands appear. The inset shows a detailed spectrum of another sample in the range of the 1.047 eV transition. In some of the samples additional luminescence lines indicated by the arrows appear. They are caused by further contaminations and complexes.

The $\text{Fe}^{3+} {}^4\text{T}_1 \rightarrow {}^6\text{A}_1$ in GaN (1.3 eV)

The emission at 1.3 eV was first reported by Maier et al.[2]. Based on EPR-, PL-, and ODMR this emission was assigned to the electronic spin-flip transition between the ${}^4\text{T}_1$ excited state and ${}^6\text{A}_1$ ground state of Fe^{3+} . This attribution has been confirmed using Zeeman spectroscopy showing the typical splitting of the ${}^6\text{A}_1$ ground state [11, 12]. However the excitation mechanism of the Fe^{3+} luminescence is not established yet. Only in some of our samples we can excite the Fe^{3+} emission with the 514 nm green line of the Ar ion laser. Thus, most definitely different defects are involved to excite the Fe^{3+} emission. For instance in some samples the luminescence excitation spectrum of the yellow band at 2.2 eV coincides with the excitation spectrum of Fe^{3+} . Excitation via the substrate has to be considered as well. Therefore the bandoffsets determined from the $\text{Fe}^{3+/2+}$ levels by Baur et al. [4] have to be regarded with care.

In PL and absorption measurements we searched for the internal electronic transition of Fe^{2+} . In nearly all semiconductor hosts the typical four line pattern of the Fe^{2+} transition ${}^5\text{T}_2 \rightarrow {}^5\text{E}$ is resolved. From their PLE measurements Baur et al. assumed that the Fe^{2+} transitions are located at about 0.5 eV [4]. Up to now we were not able to detect any trace of Fe^{2+} in the optical range between 0.2 eV and the visible region. In absorption we studied a n-type 400 μm sample which showed a strong Fe^{3+} emission. Possible explanations are: (a) As already pointed out for Fe^{2+} in ZnO [10], where also the Fe^{2+} emission is not observed, the large vibrational energy of the optical phonons favour nonradiative relaxation. (b) All our samples are n-type. As shown for Fe^{2+} in GaAs and InP the Fe^{2+} emission decreases the higher the n-type character of the samples [7].

The $^1E \rightarrow ^3A_2$ transition of Ti^{2+} in GaN (1.19 eV)

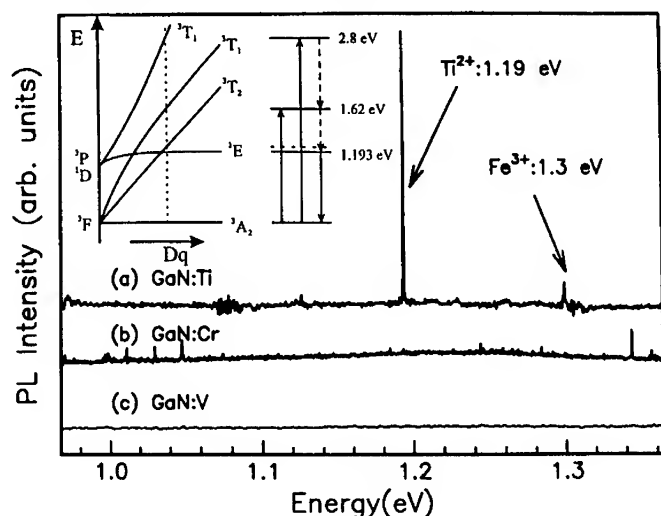


FIG. 2. Near infrared PL spectra of GaN doped with (a) Ti, (b) Cr, and (c) V. Only the Ti doped sample shows the 1.19 eV luminescence center using below and above bandgap excitation. The level scheme explains the observed transitions according to Ref. [12, 13].

The 1.19 eV emission was first reported by Baur et al. in their GaN samples grown on sapphire by VPE or MOVPE [8]. They assigned the luminescence center to Cr^{4+} . But according to our optical investigations the luminescence center is caused by an internal electronic transition between the 1E and 3A_2 levels of Ti^{2+} (see level scheme of Fig. 2).

In contrast to Baur et al. [8] the temperature-dependent PL studies of all our samples both grown by the sandwich technique and grown by MOVPE or HTVPE show no excited state to the 1.19 eV emission. Zeeman measurements show a three-fold splitting of the ground state of the 1.19 eV emission in GaN. Thus the ground state belongs to a $S=1$ system. Details on the excitation and Zeeman measurements are published elsewhere [12, 13]. Thus, the luminescence center has a $3d^2$ electronic configuration. The luminescence center cannot only be excited by above bandgap excitation but also by excitation in the region between 1.5 eV and 1.65 eV. This excitation band is attributed to an absorption into an excited state of our luminescence center. The appearance of the excited state reveals that the defect center is already in its luminescence charge state without illumination in n-type GaN. Possible candidates are Ti^{2+} , V^{3+} , and Cr^{4+} . We observe the 1.19 eV emission also in our samples where the electronic concentration n is higher than 10^{17} cm^{-3} . Because the emission center is already in its luminescence charge state in the dark an attribution to a $3d$ element in a $4+$ charge state is improbable. Thus we attribute the 1.19 eV emission to the $^1E \rightarrow ^3A_2$ transition of Ti^{2+} . This assignment to Ti^{2+} is confirmed by doping experiments where different transition metals were introduced during crystal growth. Fig. 2 shows three spectra of GaN samples which have been intentionally doped with Ti, V, and Cr during HTVPE growth. Only the Ti-doped GaN sample showed the 1.19 eV emission.

The 1.047 eV emission: d^7 configuration

The emission at 1.047 eV occurs only in GaN samples grown by the sandwich technique and no identification has been attempted yet.

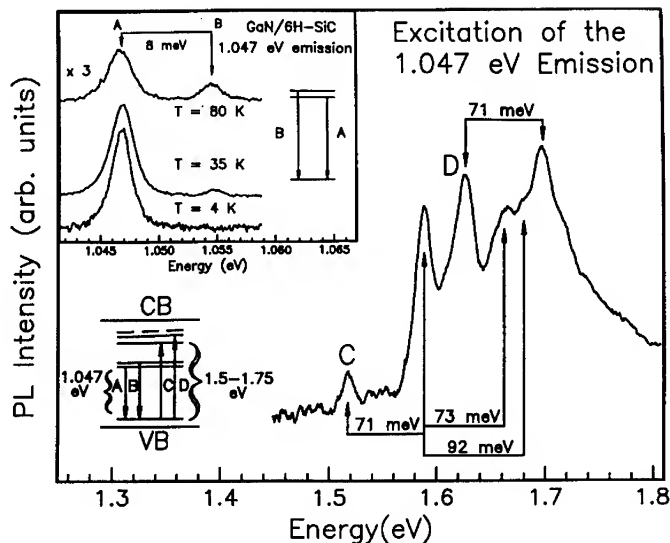


FIG. 3. PL excitation spectrum of the 1.047 eV luminescence center. A set of at least six absorption peaks is detected. The absorptions C and D are caused by NP transitions. The inset shows the appearance of a hot line (B) to the 1.047 eV NP line (A) indicating a splitting of the excited state.

Figure 3 shows an excitation spectrum of the 1.047 eV emission in the optical range between 1.45 and 1.8 eV. Similar to the 1.19 eV emission the 1.047 eV emission can be excited not only by above bandgap excitation but also in the energetic range between 1.5 eV and 1.75 eV. This absorption band consists of a set of at least six sharp peaks. The absorption peaks C and D can be attributed to NP lines. The other peaks coincide with replicas having typical phonon energies of GaN (see also next section)

A charge-transfer transition can most definitely be excluded. As observed for the excitation spectrum of the 1.19 eV emission (Fig. 2) the excitation spectrum of the 1.047 eV emission reveals excitation via an excited state. Therefore the luminescence center is in its luminescence charge state in the dark in n-type material. The inset of Fig. 3 shows three spectra of the 1.047 eV emission detected at different temperatures. With increasing temperature a hot line 8 meV higher in energy appears. Thus we have an at least two-fold split excited state. The scheme in the left part indicates the level scheme derived from the temperature dependent PL measurements and the PLE measurements. We only observe one NP line at 2 K. Thus, the 1.047 eV emission can belong to a 3d transition metal with a d^1 , d^2 , d^5 , or d^7 electronic configuration all having an orbital momentum in the ground state.

For the following reasons the 1.047 eV emission is caused by a transition metal with a d^7 electronic configuration: (a) A d^1 configuration can be excluded because it has no excited state that can explain the higher excited state observed in PLE (Fig. 3) (b) In our n-type samples we exclude Cr^{4+} , Ti^{2+} and V^{3+} are already attributed to other emission centers at 1.19 eV [13] and 0.931 eV [8], respectively. Furthermore, the excitation spectrum of the 1.047 eV emission looks different to the excitation spectrum usually observed for Ti^{2+} or V^{3+} . (c) The ${}^4T_1 \rightarrow {}^6A_1$ spin-flip transition of a $3d^5$ configuration can be excluded because the decay time of less than a few μs is too short.

Therefore the experiments fit to a transition metal with a $3d^7$ electronic configuration. As Fe^+ can be excluded as well, the possible candidates are Ni^{2+} and Co^{2+} . Usually Ni appears as Ni^+ or Ni^{2+} in semiconductors. Therefore the ${}^4T_2 \rightarrow {}^4A_2$ transition Co in its 2+ charge state is the most probable possibility to cause the 1.047 eV emission.

Phonon sidebands compared to Raman phonon modes

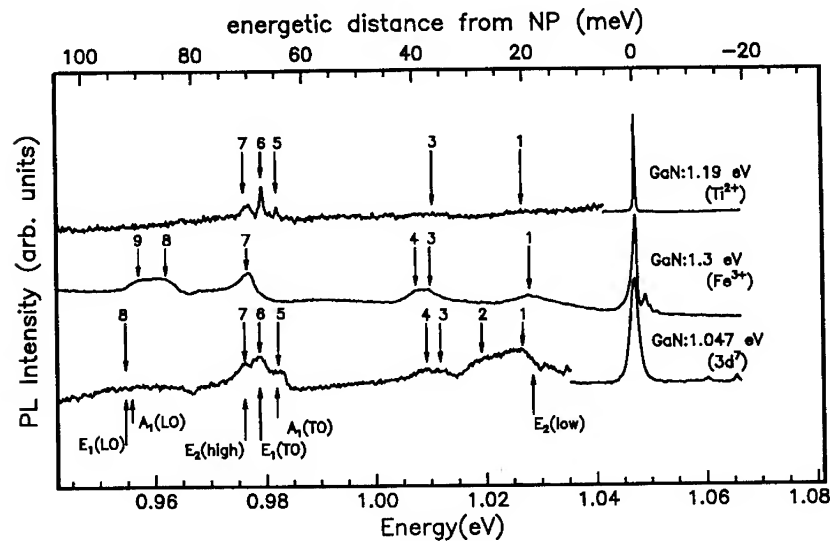


FIG.4 Comparison of the phonon sidebands of the three no-phonon lines caused by residual transition metal contaminants. The emissions are normalized to the 1.047 eV emission. The top scale indicates the distance of the phonon replica from the no-phonon lines. The phonon modes observed from Raman spectroscopy are indicated (see Tab. 1).

Raman modes GaN (Kozawa et al. [14]) cm ⁻¹ /meV	1.047 eV cm ⁻¹ /meV	1.19 eV cm ⁻¹ /meV	1.3 eV (Fe ³⁺ in GaN) cm ⁻¹ /meV
E ₂ (low): 144/17.9	169/21.0 (1) 219.4/27.2 (2) 286.8/35.6 (3) 308.4/38.2 (4)	~ 170/21.1 (1) ~ 295/36.6 (3)	154/19.1 (1) 301/37.3 (3) 316/39.2 (4)
E ₂ (high): 570/70.7	569.4/70.6 (7)	569.0/70.5 (7)	569.3/70.6 (7)
A ₁ (TO): 532/66	527.8/65.4 (5)	524.8/65.1 (5)	
E ₁ (TO): 561/69.6	549.9/68.2 (6)	547/67.8 (6)	
A ₁ (LO): 736/91.2	~		690/85.6 (8)
E ₁ (LO): 745/92.4	750/93.0 (8)		717/88.9 (9)

TAB. 1. Energies of the phonon replica (determined from Fig. 4) of the three NP lines at 1.047 eV (column 2), 1.19 eV (column 3), and 1.3 eV (column 4). The energies of the phonon modes are given in cm⁻¹ (for better comparison with Raman data) and in meV. The numbers in brackets indicate the maxima according to Fig. 4. The phonon modes of hexagonal GaN determined from Raman spectroscopy [14] are summarized in the first column.

In Fig. 4 and Tab.1 the phonon sidebands of the three defect luminescence bands and the phonon modes observed from Raman spectroscopy are compared. The phonon modes observed in the phonon sidebands are close to modes observed from Raman spectroscopy [14].

CONCLUSIONS

In a nutshell, we studied residual transition metal contaminants in GaN samples grown on 6H-SiC and on sapphire substrate. By photoluminescence we observe three no-phonon lines peaking at 1.3 eV, 1.19 eV, and 1.047 eV. Our Zeeman measurements support the attribution of the 1.3 eV emission to the ${}^4T_1 \rightarrow {}^6A_1$ transition of Fe^{3+} . On the basis of Zeeman studies, photoluminescence excitation spectroscopy, and intentional doping experiments, the 1.19 eV emission is attributed to the ${}^1E \rightarrow {}^3A_2$ transition of Ti^{2+} . The 1.047 eV emission is probably caused by an internal electronic transition of a transition metal with a $3d^7$ electronic configuration. Our experimental data at best fit to the ${}^4T_2 \rightarrow {}^4A_1$ of Co^{2+} . The phonon sidebands of the three luminescence centers show resonances close to the phonon modes observed in Raman spectroscopy

ACKNOWLEDGEMENT

The support of the Deutsche Forschungsgemeinschaft DFG is gratefully acknowledged. One of the authors, K. Pressel, is indebted to the *Stifterverband der Deutschen Wissenschaft* for financial support to visit the MRS meeting on *GaN and Related Materials*.

References

- [1] S. Nakamura, T. Mukai, and M. Senoh, *J. Appl. Phys.* **76**, 8189 (1994)
- [2] K. Maier, M. Kunzer, U. Kaufmann, J. Schneider, B. Monemar, I. Akasaki, and H. Amano, in *Material Science Forum 143-147, Defects in Semiconductors 17*, edited by H. Heinrich and W. Jantsch (Trans Tech Publications, Aedermannsdorf, Switzerland, 1994) p. 93
- [3] J. Baur, K. Maier, M. Kunzer, U. Kaufmann, J. Schneider, H. Amano, I. Akasaki, T. Detchprohm, and K. Hiramatsu, *Appl. Phys. Lett.* **64**, 857 (1994)
- [4] J. Baur, K. Maier, M. Kunzer, U. Kaufmann, and J. Schneider, *Appl. Phys. Lett.* **65**, 2211 (1994)
- [5] S. Fischer, C. Wetzel, E. Bourret, W.L. Hansen, and E.E. Haller, presented at the 1995 MRS spring meeting, San Francisco (unpublished)
- [6] C. Wetzel, D. Volm, B.K. Meyer, K. Pressel, S. Nilsson, E.N. Mokhov, and P.G. Baranov, *Appl. Phys. Lett.* **65**, 1033 (1994)
- [7] S.G. Bishop, in *Deep Centers in Semiconductors*, edited by S. Pantelides (Gordon & Breach, New York, 1986), p. 541
- [8] J. Baur, U. Kaufmann, M. Kunzer, J. Schneider, H. Amano, I. Akasaki, T. Detchprohm, and K. Hiramatsu, *Appl. Phys. Lett.* (1995)
- [9] B. Clerjaud, C. Naud, B. Deveaud, B. Lambert, B. PLOT, G. Bremond, C. Benjeddou, G. Guillot, and A. Nouailhat, *J. Appl. Phys.* **58**, 4207 (1985)
- [10] L. Podlowski, R. Heitz, P. Thurian, A. Hoffmann, I. Broser, *J. of Lumin.* **58**, 252 (1994)
- [11] R. Heitz, P. Thurian, I. Loa, L. Eckey, A. Hoffmann, I. Broser, K. Pressel, B.K. Meyer, E.N. Mokhov, accepted for publication in *Appl. Phys. Lett.*
- [12] R. Heitz, P. Thurian, A. Hoffmann, K. Pressel, to be published in *Proc. of the 18th International Conference on Defects in Semiconductors*, Sendai, Japan
- [13] R. Heitz, K. Pressel, P. Thurian, I. Loa, L. Eckey, A. Hoffmann, I. Broser, B.K. Meyer, E.N. Mokhov, accepted for publication in *Phys. Rev. B*
- [14] T. Kozawa, T. Kachi, H. Kano, Y. Taga, M. Hashimoto, N. Koide, and K. Manabe, *J. Appl. Phys.* **75**, 1098 (1994)

MAGNESIUM DOPING OF GaN BY METALORGANIC CHEMICAL VAPOR DEPOSITION

Hongqiang Lu and Ishwara Bhat

ECSE department, Rensselaer Polytechnic Institute, Troy, NY12180, hongql@ecse.rpi.edu

ABSTRACT

P-type GaN films were grown on sapphire substrates in a horizontal metalorganic chemical vapor deposition system using $(C_5H_5)_2Mg$ (Cp_2Mg) as the p-dopant source. It is found that the acceptor concentration in the post-growth annealed GaN samples increases with the Mg flow rate and reaches a peak value of $1 \times 10^{19} \text{ cm}^{-3}$ at Mg flow rate of 0.84 $\mu\text{mol/min}$. The films remain semi-insulating even after annealing when the Mg flow rate is higher than 1.08 $\mu\text{mol/min}$. The effects of annealing temperature and duration on the electrical properties of GaN are also investigated. The results confirm that a 800 °C, 30 minutes post-growth annealing in N_2 ambient is sufficient to activate most of the Mg atoms. In addition, study of rapid thermal annealing of Mg-doped GaN was carried out and the results show that the p-type acceptor concentration obtained is comparable to the results obtained using furnace annealing process. Finally, GaN light emitting diodes (LEDs) are demonstrated using undoped layer as the n-type base layer in a p-on-n structure. The light emission spectra are dominated by the 430 nm peak, accompanied with two relatively weak peaks located at 380nm and 550nm.

INTRODUCTION

Wide band-gap GaN and related III-V nitrides are promising materials for applications in UV and blue light emitting diodes (LEDs) and in high temperature electronics.^{1, 2, 3} For a long time, the main obstacle to the realization of these devices has been the poor material quality, such as the high background n-type carrier concentration and the lack of p-type conductivity. Recently high quality unintentionally doped n-type GaN thin films with low carrier concentration ($< 1 \times 10^{17} \text{ cm}^{-3}$) were obtained by introducing a thin AlN or GaN buffer layer on sapphire.^{4, 5} P-type conductivity was also achieved in GaN material grown both by the metalorganic chemical vapor deposition (MOCVD) and the molecular beam epitaxy (MBE) techniques using Mg as a p-type dopant.^{6, 7} In case of MOCVD grown Mg-doped GaN, a post-growth annealing treatment is required to activate the Mg dopant. This step is believed to dehydrogenate the Mg-H complexes which is formed during the growth.⁸ GaN blue-violet LEDs were soon developed after the achievement of p-type doping.^{7, 9} However, detailed study of properties of the Mg doped GaN material is still needed to increase the p-type doping concentration and to optimize LED efficiency. In this letter, we report the magnesium doping in GaN layer by MOCVD using $(C_5H_5)_2Mg$ (Cp_2Mg) as the dopant source. To optimize the p-type conductivity, we investigate the dependence of acceptor concentration on the dopant source flow rate. Post-growth annealing at different temperature and time are also studied. GaN LEDs based on Mg doped GaN are demonstrated which emit visible light with strongest peak located at 430nm.

EXPERIMENTAL DETAILS

Samples were grown on (0001) sapphire substrates in a horizontal low pressure MOCVD system. High purity trimethylgallium (TMGa), ammonia (NH_3) and Cp_2Mg were used as the precursors for Ga, N and Mg dopant, respectively. Hydrogen (3l/min) was employed as the carrier gas and the reactor pressure was kept at 100 Torr. Before the epitaxy, a GaN buffer layer of $\sim 1000\text{\AA}$ was deposited at 600°C . Wurtzite GaN epilayers were grown at 1050°C with TMGa and NH_3 gas flows kept at $16\text{ }\mu\text{mol/min}$ and 2 l/min for all the runs while the Mg flow rate was varied from $0.48\text{ }\mu\text{mol/min}$ to $1.44\text{ }\mu\text{mol/min}$. After the growth, samples were annealed in N_2 atmosphere at 700 Torr for half an hour. The typical annealing temperature was 800°C unless the study of the influence of annealing temperature on Mg doping efficiency was conducted.

RESULTS AND DISCUSSIONS

Capacitance-Voltage (C-V) measurement using back to back diode structure was performed with the frequency kept at 1 KHz. As-grown samples are always semi-insulating while the concentration difference between the acceptors and the donors ($N_A - N_D$) of the annealed GaN films under typical annealing condition are dependent on the flow rate of Cp_2Mg . (See Fig.1). When the Mg flow (f_{Mg}) is as low as $0.48\text{ }\mu\text{mol/min}$, both C-V and I-V results reveal a n-type behavior with the carrier concentration around 10^{17} cm^{-3} but mobility of only $10\text{ cm}^2/\text{V.s}$ (for undoped GaN films of same carrier concentration, the mobility is as high as $400\text{ cm}^2/\text{V.s}$). By increasing the Mg flow rate to $0.60\text{ }\mu\text{mol/min}$, we could obtain p-type GaN film with ($N_A - N_D$) value of $1.3 \times 10^{17}\text{ cm}^{-3}$. The ($N_A - N_D$) value is very sensitive to the Mg flow beyond this value and soon reaches a peak value of $1 \times 10^{19}\text{ cm}^{-3}$ at f_{Mg} of $0.84\text{ }\mu\text{mol/min}$. The ($N_A - N_D$) begins to fall when the f_{Mg} is over $0.84\text{ }\mu\text{mol/min}$ and eventually the film turns out to be semi-insulating, reflecting a deteriorating crystal quality due to the high Mg incorporation. The sample surface is no longer smooth but shows lots of hexagonal hillocks and platelets.

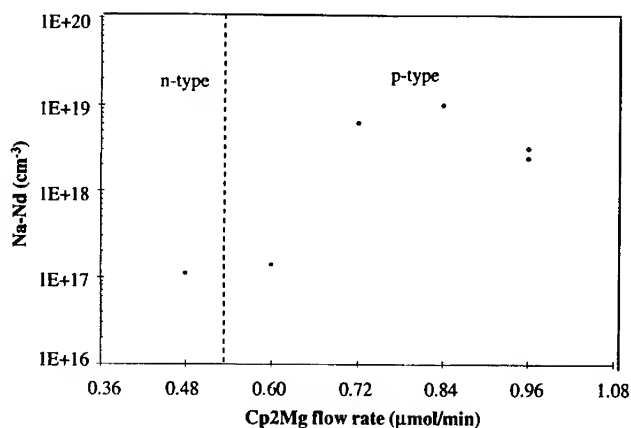


Fig.1 The ($N_A - N_D$) concentration of Mg doped GaN films as a function of Cp_2Mg flow rate

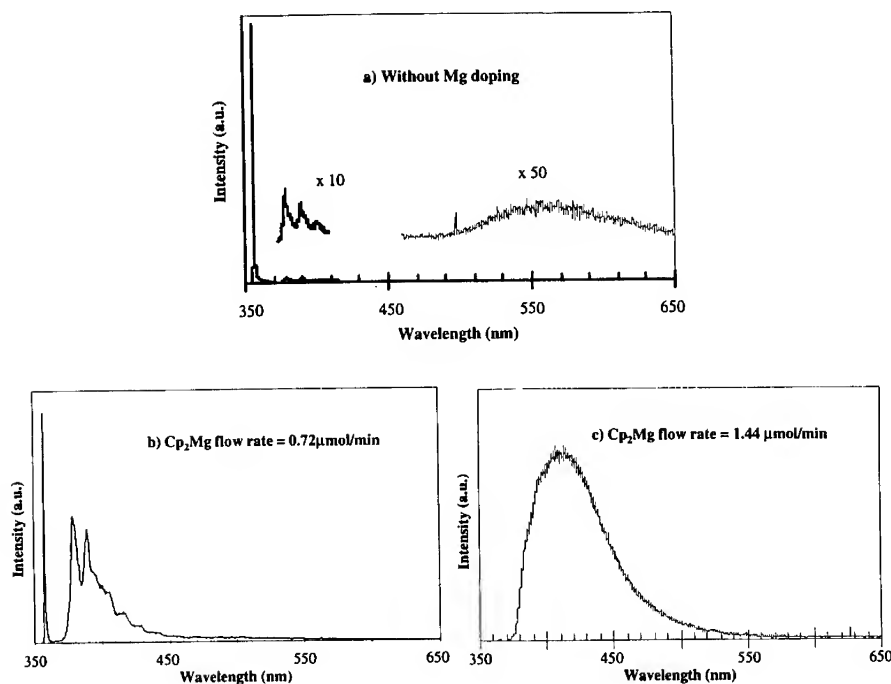


Fig.2 Low temperature (10K) photoluminescence spectra of Mg doped GaN films with different Mg incorporation level: a) without Mg doping; b) Mg flow rate = 0.72 $\mu\text{mol/min}$; c) Mg flow rate = 1.44 $\mu\text{mol/min}$.

Fig.2 exhibits the low temperature (10K) photoluminescence (PL) spectra of annealed GaN samples at different Mg incorporation level. For undoped GaN samples, the PL spectrum is dominated by the near-band-edge emission at 355.8 nm (3.485 eV), while the donor-acceptor pair (D-A) emission at 379.2 nm (3.27 eV) and the deep level (DL) emission around 560 nm (2.2 eV) are very weak. When the Mg is introduced into GaN films, the near-band-edge peak shifts to 357.3 nm (3.47 eV) which corresponds to acceptor-bond exciton emission peak. This peak first increases at low flow of Mg and then decreases at higher Mg flow. The dominant 357.3 nm peak in the spectra is soon replaced by the D-A peak at 379.2 nm (3.27 eV) whose intensity shows an increasing trend with Mg concentration. As long as the Mg flow rate is less than 1 $\mu\text{mol/min}$, the DL emission peak does not appear in the spectra, implying that an appropriate amount of Mg can suppress the deep level in the GaN MOCVD epi-films. However if the Mg flow rate is too high during the growth, only one broad peak can be obtained in the whole spectrum, which is located around 420 nm (2.95 eV). Referring to its semi-insulating property at this high Mg flow range, this peak is probably resulted from the Mg-H complex related deep levels.

The effect of post-annealing temperature on the conductivity of Mg doped samples was then investigated. If the annealing temperature is too low, the Mg-H bond can not be broken,

therefore the films remain semi-insulating; On the other hand, if the temperature is too high, the decomposition of GaN may become severe and affect the crystal and electrical quality of GaN layers. To investigate this, an as-grown GaN sample with the Mg flow rate of 0.84 $\mu\text{mol/min}$ during the growth was cut into several pieces and annealed at different temperature. Fig.3 is the plot of the $(N_A - N_d)$ concentration of these GaN samples obtained by C-V measurement as a function of annealing temperature. When annealing temperature is below 500 $^{\circ}\text{C}$, the films remain semi-insulating. The concentration increases with annealing temperature from 600 $^{\circ}\text{C}$ until 800 $^{\circ}\text{C}$. Above 800 $^{\circ}\text{C}$, the concentration saturates but no deterioration of GaN films due to high temperature annealing was detected within our range of studies. This result illustrates that 800 $^{\circ}\text{C}$ annealing temperature is sufficient to activate almost all the Mg atoms. At the same time it also reveals that GaN is thermally stable around 800 $^{\circ}\text{C}$ in the N_2 ambient.

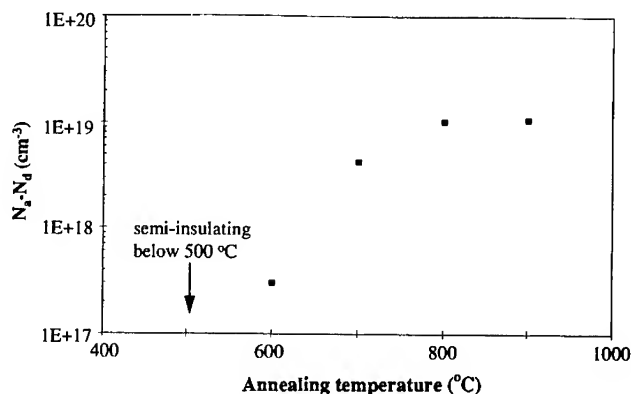


Fig.3 The $(N_A - N_d)$ value in Mg doped GaN samples as a function of annealing temperature

Besides the post-annealing temperature, the annealing duration is also an important parameter in deciding the Mg doping efficiency. In our experiments, Mg-doped GaN films were annealed at 800 $^{\circ}\text{C}$ for 0.5 hour, 1 hour and 1.5 hours, respectively. However no significant differences were observed by PL and C-V measurements, which implies that for 2.5 μm thick GaN 30 minutes annealing in N_2 is enough to fully activate the Mg atoms. Depth profiling using step-etching the film is still necessary to confirm this result since C-V measurement probes only the top few tenths of microns.

Recently rapid thermal annealing (RTA) was also employed to activate the Mg-doped GaN films.¹⁰ Here, we compare the effects of furnace annealing technique with that of RTA on the Mg-doped GaN films. The results are included in Table.1. The samples studied was grown with the Mg flow rate of 0.96 $\mu\text{mol/min}$ and the thickness of the layer is 2.3 μm . After normal annealing (annealed at 800 $^{\circ}\text{C}$ for 0.5 hour in N_2 atmosphere), this sample shows a typical $N_A - N_d$ concentration of $5 \times 10^{18} \text{ cm}^{-3}$. For RTA treatment, if the annealing temperature is higher than 1050 $^{\circ}\text{C}$, the GaN film decomposes, resulting in a bad morphology and degraded quality. A p-type conductivity is observed from the Mg doped GaN sample when RTA temperature is reduced to below 1050 $^{\circ}\text{C}$. The concentration of activated Mg acceptors in these RTA treated samples is comparable to that of GaN annealed by the normal furnace annealing technique. Results shown in Table.1 demonstrate that RTA can be a quick and more efficient means to obtain p-type GaN films compared to the furnace annealing technique.

Table.1 Comparison of Mg dopant concentration between RTA treated GaN and furnace annealed GaN, all the samples were annealed in nitrogen atmosphere.

	RTA treatment			Normal Annealing
	1	2	3	
Annealing condition	1050C, 1minute	1000C, 1minute	900C, 3 minutes	800C, half an hour
(Na-Nd) (cm-3)	3.60E+18	5.90E+18	4.10E+18	5.00E+18

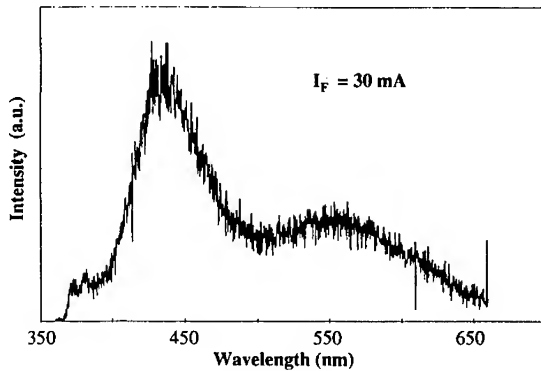


Fig.4 LED emission spectrum at forward current injection of 30 mA

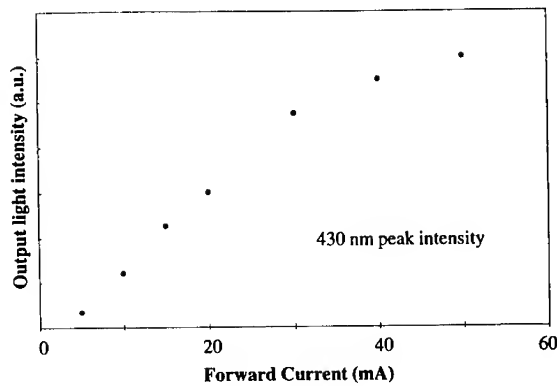


Fig.5 The dependence of LED emission intensity on the forward current level

Finally, GaN p-n homojunction light emitting diodes (LEDs) were demonstrated. A 0.7 μm Mg doped layer with acceptor concentration around $5 \times 10^{18} \text{ cm}^{-3}$ was grown on a 2.0 μm n-type GaN base layer. The base layer carrier concentration is estimated at $1 \times 10^{17} \text{ cm}^{-3}$ from the previous experiments. The sample was then annealed at 800 $^{\circ}\text{C}$ for half an hour as before. Mesa diode structure was fabricated using ion milling. Ti/Au was used for ohmic contact to n-type layer and Cr/Au dots with the diameter of 250 μm were deposited on the p-layer to form

the p-layer contact. The emission spectra under forward biased condition is presented in Fig. 4. There are three peaks observed in these spectra: 380 nm peak at high current; 430 nm peak and a broad peak at 550 nm. The 430 nm peak is the most strong one among the three and probably originates from the carrier recombination between the donor level to the deeper Mg acceptor site.¹¹ The intensity of 430 nm peak increases linearly with the current at low current injection level until 30mA, then gradually saturates (see fig.5). This saturation is probably caused by the finite number of sites available at the donor and acceptor levels. The 380nm peak is weak in our measurements. It is associated with the carrier recombination from the conduction band edge to the Mg-acceptor site close to the valence band edge. It does not appear in the spectra until 30mA where the 430 nm peak begins to saturate. This phenomenon may be interpreted by different densities of these two types of luminescence centers and their relative radiative recombination efficiencies.

CONCLUSIONS

In summary, We have achieved p-type GaN by introducing Mg into the GaN layer during the growth by MOCVD technique. Study of the effect of Mg incorporation rate reveals that the concentration of N_A-N_D as a function of Mg flow rate has a peak at $f_{Mg} = 0.84 \mu\text{mol/min}$. It is demonstrated that post-growth annealing of GaN at 800 °C for 30 minutes in nitrogen ambient is sufficient to activate most of the Mg dopants. RTA is also employed to activate Mg atoms and the results are comparable to that of furnace anneal technique. In addition, GaN LEDs are fabricated using p-type layer as the active layer which give out visible light with the strongest peak located at around 430 nm.

ACKNOWLEDGMENTS

This work was partially supported by Philips Laboratories, Briarcliff Manor and Texas Instruments. We also thank Dr. Nasser Karam and his staff of Spire Corporation for carrying out the device fabrication.

REFERENCES

- [1] H. Morkoc, S. Strite, G. B. Gao, M. E. Lin, B. Sverdlov, and M. Barnes, *J. Appl. Phys.*, **76**, 1363(1994)
- [2] S. Strite, and H. Morkoc, *J. Vac. Sci. Technol. B*, **10**, 1237(1992)
- [3] F. Davis, *Proc. IEEE* **79**, 702(1991)
- [4] I. Akasaki, H. Amano, Y. Koide, K. Hiramatsu, and N. Sawaki, *J. Crystal Growth* **98**, 209(1989)
- [5] S. Nakamura, *Jpn. J. Appl. Phys.* **30**, L1705(1991)
- [6] I. Akasaki, H. Amano, M. Kito, and K. Hiramatsu, *J. Lumin.* **48/49**, 666(1991); H. Amano, M. Kito, K. Hiramatsu, and I. Akasaki, *Inst. Phys. Conf. Ser.* **106**, 725(1990)
- [7] R. J. Molnar, T. Lei, and T. D. Moustakas, *Proc. Mater. Res. Soc. Symp.* **281**, 753(1993)
- [8] S. Nakamura, N. Iwasa, M. Seno, and T. Mukai, *Jpn. J. Appl. Phys.* **31**, 1258(1992)
- [9] S. Nakamura, M. Senoh, and T. Mukai, *Jpn. J. Appl. Phys.* **30**, L1708(1991)
- [10] M. Asif Khan, Q. Chen, R. A. Skogman, and J. N. Kuznia, *Appl. Phys. Lett.* **66**, 2046 (1995)
- [11] B. Goldenberg, J. D. Zook, and R. J. Ulmer, *Appl. Phys. Lett.* **62**, 381(1993)

HYDROGEN, ACCEPTORS, AND H-ACCEPTOR COMPLEXES IN GaN

Andrea Bosin and Vincenzo Fiorentini

INFN-Dipartimento di Scienze Fisiche, Università di Cagliari, I-09124 Cagliari, Italy

David Vanderbilt

Department of Physics and Astronomy, Rutgers University, Piscataway, NJ, USA

ABSTRACT

We present ab-initio calculations on energetics and geometries of atomic hydrogen, of several candidate acceptors, and of H-acceptor complexes in wurtzite GaN. For the H-Mg complex in Mg-doped GaN, we calculate the vibrational frequencies of H. Hydrogen is found to be a negative-U center. H-acceptor complex formation is always exothermic. Substitutional Be has a low formation energy and a shallow impurity level, which makes it a good candidate for *p*-doping in MBE growth. C_N appears not to be shallow. Atomic hydrogen incorporation in undoped GaN is disfavored in an H_2 atmosphere; it becomes favorable in *p* and *n*-type conditions in atomic H environments.

INTRODUCTION

Despite recent achievements, *p*-type doping of GaN is difficult to implement [1], and it is a topic of high current interest. The choice of acceptors alternative to Mg is as yet an unsolved problem. Concurrently, the behavior of hydrogen in semiconductors [1], and in GaN in particular [2], has raised much interest in recent years. Acceptor passivation, e.g., is often attributed to hydrogen [1].

We studied several acceptor species X ($X=C, Ca, Mg, Zn, Be$), H atoms, and H- X complexes in zincblende and wurtzite GaN. Here we present a partial preliminary overview of these studies. H has been examined in several high-symmetry sites: in all cases, the most favorable sites are found to be either the anion-antibonding (AB_V) or bond-center (BC) ones for both cation and anion impurity substitutions, as well as for no substitution. An exception is negatively-charged H (H^-), which sits in the cation-antibonding (AB_{III}) site. In the BC configuration, H sits at the center of the bond between anion and cation, while in the AB_V it sits behind the anion site at a distance close to half bond length; the AB_{III} is behind the cation at about the same distance as in AB_V . In the case of wurtzite, all the above sites have two non-equivalent orientations (axial and planar).

Our results are summarized as follows. H is a negative-U center. The effective Hubbard's U is site-dependent, and ranges from about 0 to -1.2 eV. In *undoped* GaN, incorporation of H should not take place in atomic form in an H_2 atmosphere, but becomes possible under *p* or *n*-type conditions in an atomic-H-rich environment. The acceptor with the lowest formation energy is Be, which also exhibits a shallow thermal impurity level ($E^{0/-} \sim 0.1$ eV). Mg is relatively shallow ($E^{0/-} \sim 0.2$ eV), while C is deeper ($E^{0/-} \sim 0.4$ eV). The use of Be seems a practicable way to improve doping efficiency in GaN. The formation of neutral H^+/X^- complexes is found to be exothermic. Again, the antibonding and bond center sites compete as equilibrium geometries. Acceptor efficiency will be low due to H passivation, but the concurrent incorporation of hydrogen *and* acceptors will be much more favorable than that of H alone. In the case of the H-Mg complex, we calculate the vibrational frequencies of H. None of our frequencies are in even rough agreement with experiment [3]: this discrepancy suggests that the observed frequencies are not due to H-Mg vibrational modes, and other possibilities should be investigated.

In the following text and Tables, all energies are expressed in eV, and distances in atomic units. All formation energies listed include relaxation contributions.

METHOD

Ab-initio calculations have been performed within local density functional theory [4]. A plane-wave basis at constant energy cutoff of 25 Ry, ab-initio ultrasoft pseudopotentials (USPP) [5], and the Monkhorst-Pack [6] (222) special-point mesh for Brillouin zone integration are used. USPP ensure high transferability and require a much lower cutoff than conventional norm-conserving potentials; this is of importance in our case, since the Ga 3d electrons are treated explicitly [7]. Also, localized valence states such as those of Be, N, and Zn, and semicore states as in Ca and Mg, have been easily treated. A conjugate-gradient total-energy minimization has been employed in most cases; for part of the calculations, we used a parallelized iterative diagonalization codes [8].

Hellmann-Feynman forces and a modified Broyden minimization method are used to perform structural optimization for acceptors, hydrogen, and their complexes. For acceptors, we started from the ideal substitutional sites (C on N, and Be, Zn, Ca, and Mg on Ga) in wurtzite supercells of up to 32 atoms. Hydrogen has been studied at some selected sites (BC, AB_V, AB_{III}, and a few others found to be immaterial). For some cases, H vibrational frequencies are calculated: slight displacements are imposed to the H atom along appropriate directions, while the rest of the lattice is kept frozen; fourth-order polynomials are fitted to the total-energy vs. displacement curves, and the harmonic force constants and vibrational frequencies are extracted from second-order terms. Formation energies E_f of substitutional defects $X_{\text{Ga,N}}$ are calculated as

$$E_f = E_{\text{tot}}(X_{\text{Ga,N}}) - E_{\text{tot}}(\text{GaN}) - \mu_X + \mu_{\text{Ga,N}} + Q\mu_e, \quad (1)$$

where $E_{\text{tot}}(X_{\text{Ga,N}})$ and $E_{\text{tot}}(\text{GaN})$ are the total energy of the doped GaN supercell and that of the defect-free GaN supercell, and Q is the charge state (the number of electrons transferred from the defect to a reservoir of electron chemical potential μ_e). μ_X and $\mu_{\text{Ga,N}}$ are the chemical potentials of the acceptor and of the substituted (Ga or N) atoms. For H, the same definition holds, except that Ga and N μ 's drop out; μ_H is either the total energy of the free spin-polarized atom, or half that of the H_2 molecule.

As impurity chemical potentials we use the total energies of metallic bulk phases (Ga bulk and the free N_2 molecule for the host atoms). This amounts to assume Ga-rich and N-rich conditions for Ga and N substitutions respectively. Note that the limiting values of chemical potentials might be determined by different solid phases, e.g. compounds with host atoms. Also, the Fermi level μ_e (chosen here to be a free parameter) is constrained by neutrality conditions [9]. More refined calculations including these ingredients, in particular the explicit determination of solubility limits, will be presented elsewhere.

The formation energy differences of charged defects to their neutral state are given by the energy change $\bar{\epsilon}$ upon addition of an electron to the defect at frozen lattice, minus the Franck-Condon shift E_{FC} (total energy difference for the charged defect in the equilibrium geometry of the neutral state and in its own equilibrium geometry). $\bar{\epsilon}$ is obtained using Slater transition-state concept and Janak's theorem [4] as (e.g. for a positively charged center)

$$\bar{\epsilon} = (\epsilon_0 + \epsilon_+)/2, \quad (2)$$

the ϵ 's being the highest occupied LDA eigenvalues for the $Q=0$ and $Q=+1$ center. This is also the value of Hubbard's U at frozen lattice for the given site (see Refs. [10] for

details). The shallow levels we deal with here (and therefore the energy differences) suffer from uncertainties of order ~ 0.1 eV.

H IN CLEAN GaN

Atomic hydrogen in GaN has been examined in a number of sites in C_{3v} symmetry. The results below should thus be comparable to the zincblende calculations of Ref. [2]. This might not be the whole story, however, as a -plane (C_3 symmetry) sites are not equivalent (see data for the H-Mg complex below). Further analysis will be presented elsewhere. In GaN, matters are considerably complicated by the presence of different competing geometries: the stable one for H^+ is the AB_V site, for H^- the AB_{III} , and for H^0 the BC site. In Table I we report the formation energies at $\mu_e = 0$, referred to the free spin-polarized

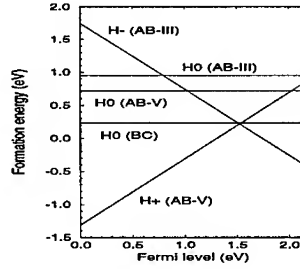


Figure 1: Formation energy of H in GaN referred to free spin-polarized H atom. Add 2.31 eV to energies to refer to (half) free H_2 molecule. Fermi level window starts at valence band top, ends at theoretical gap (2.11 eV).

hydrogen atom. To refer them to the H_2 molecule in free space, one should add the theoretical binding energy, 2.31 eV/atom (zero-point motion included) to the given energies. Also listed are the calculated values of $\bar{\epsilon}$ and the Franck-Condon shifts.

process	E_f	ΔE_f	$\bar{\epsilon}$	E_{FC}
$H_{free} \rightarrow H_{BC}^0$	0.232	—	—	—
$H_{free} \rightarrow H_V^0$	0.718	—	—	—
$H_V^0 \rightarrow H_V^+$	—	-2.029	-1.985	0.044
$H_{free} \rightarrow H_{III}^0$	0.951	—	—	—
$H_{III}^0 \rightarrow H_{III}^-$	—	0.796	1.605	0.809

Table I: Formation energy E_f of substitutional H with respect to defect-free GaN and free H atom, formation energy difference to relevant charge state, electron transfer energy $\bar{\epsilon}$ (Eq. 2), and Franck-Condon shift. Note that formation energy differences equal by definition thermal ionization levels.

The negative U behavior is evident. From the calculated energy levels and Franck-Condon shifts, the thermal ionization energies of H_{III}^- and H_V^+ are found to be $E^{0/-} \simeq 0.80$ eV and $E^{+/0} \simeq 2.03$ eV respectively. The difference of the latter quantities [10] is the effective Hubbard correlation, $U_{eff} \simeq -1.2$ eV. This value is about 1 eV smaller than the -2.4 eV reported in Ref. [2]: this difference matches that of the theoretical gaps in the two calculations, which determines the calculated donor level position.

It is important to note, however, that due to differences in the neutral states of H at the sites involved, the result is not as clearcut as when it is referred to a single site. The

H donor level at site AB_V is above the H acceptor level at site AB_{III}, so that the center captures two electrons simultaneously; however this also requires H to migrate to another site. If we refer all energies to site AB_V, then $U_{\text{eff}} \sim -1.0$ eV. A further complication is that in C_{3v} symmetry the lowest energy site for neutral H is in fact the BC one, at 0.5 eV below the AB_V: as seen in Fig. 1, U_{eff} drops to about zero (-0.02 eV) in this case.

Overall our results are at some variance with those of Ref.[2], especially for H⁰ and the formation energies. More differences may arise from full account of all inequivalent sites.

ACCEPTORS

In Table II we summarize the results for substitutional $X_{\text{Ga,N}}$ impurities in wurtzite GaN, with atomic relaxation limited to C_{3v} symmetry. Be_{Ga} has a very low formation energy (with metallic h-Be as a solubility-limiting phase): at typical GaN growth temperatures the concentration would reach of order 10^{19} - $10^{20}/\text{cm}^3$. The relatively shallow impurity level would then enable carrier concentrations in the 10^{17} 's to be reached at room temperature. Be seems therefore an excellent candidate for *p*-doping; in view of processing problems, it would probably be especially useful in MBE. On the other hand, the high formation energy and relatively deep level of C do not support its intentional use as *p*-type dopant. Mg is somewhat halfway between the former two; a simple-minded estimate based on the data in Table II indicates however that only concentrations as low as $10^{15}/\text{cm}^3$ will be achieved in typical growth conditions. A H-mediated mechanism such as suggested in Ref. [2] may be needed to explain the succesful use of Mg as dopant.

acceptor	limit	thermal $\epsilon(0/-)$	E_{FC}	E_f	E_r	Δd_a	Δd_c
Be _{Ga} (32)	h-Be	0.09	0.04	0.45	0.43	- 5.7	- 9.2
C _N (32)	d-C	0.40	0.18	4.38	0.03	+ 0.5	- 0.8
Mg _{Ga} (32)	h-Mg	0.20	0.05	1.30	0.19	+ 3.2	+ 3.2
Ca _{Ga} (16)	atoms	—	—	2.93	1.99	+ 9.7	+ 17.6
Zn _{Ga} (16)	atoms	—	—	3.32	0.02	+ 0.8	+ 0.2

Table II: Impurities in wurtzite GaN. Energies in eV and distances in a.u. Solubility limiting compounds, thermal impurity levels, Franck-Condon shifts (add to thermal levels to obtain optical ionization energies), relaxed formation energy E_f (see below), relaxation contribution E_r , acceptor geometries (supercell dimension is indicated in parentheses). Δd_a : change in distance to neighbors in the *a*-plane; Δd_c : change in distance to neighbor along *c* axis (both given in percentage of the ideal bond length of 3.70 au). For Be, C, and Mg, formation energies are referred to the indicated compounds, Ga bulk, and N₂; for Zn and Ca, atomic energies are used for all the species involved.

Neugebauer and van de Walle [2] have suggested recently a mechanism of self-compensation driven by N vacancy formation in *p*-type conditions. While certainly relevant for Mg, this mechanism may be less important for Be. Incorporation driven by H-acceptor complex formation may also play a role, as suggested in Ref. [2]. Finally, a competing state of Be could be the donor interstitial, not considered here and to be discussed elsewhere.

Only a slight displacement from the ideal geometry occurs for C_N and Zn_{Ga}, while for other acceptors the relaxation is more sizeable. Be causes a trigonally distorted inward relaxation, while Ca produces an outward relaxation, with a strong trigonal distortion. Mg exhibits a mild quasi-breathing relaxation. Comparison of results for 16- and 32-atom supercells indicates that energies and geometries are well converged with supercell size. Note that the formation energies for Zn and Ca are not significant to incorporation because of the chosen chemical potentials. Estimates may be obtained using the experimental cohesive

energies of the relevant phases. More results will be reported elsewhere.

THE H-Mg COMPLEX, AND OTHER H-ACCEPTOR COMPLEXES

The formation energy of the H-X complex can be referred to that of the substitutional defect plus free H, to evidence the stability of the complex against that of the uncompensated acceptor:

$$E_f = E_{\text{tot}}(\text{H} - \text{X}_{\text{Ga,N}}) - E_{\text{tot}}(\text{X}_{\text{Ga,N}}) - \mu_{\text{H}}. \quad (3)$$

H-Mg complexes have been studied in some detail since experimental data [3] are available for this system. The results are summarized in Table III. Formation/relaxation energies

H site	struc.	symm.	E_f (eV)	E_r (eV)	Δd_a	Δd_c	$\Delta d_{\text{H-N}}$	mode (cm^{-1})
AB _v	w	C_s	0.00	1.09	-	-	+6.5	2939
BC	w	C_{3v}	0.32	6.48	-4.7	+40.8	+3.8	3611
AB _v	w	C_{3v}	0.47	1.13	-2.1	+5.5	+5.9	3069
BC	w	C_s	0.62	6.00	-	-	+2.2	3917

Table III: H-Mg complex formation energy E_f (add $E_f^{\text{AB}_v} = -3.45$ eV to obtain absolute formation energies referred to Mg:GaN and free H), relaxation energy E_r , distances of nearest neighbors from Mg in wurtzite; for C_{3v} symmetry Δd_a gives percentage change in Mg distance to neighbors in the a -plane, Δd_c that along c axis, $\Delta d_{\text{H-N}}$ change in distance from H to N (ideal=1.85 a.u). Vibrational modes of H are along c axis for C_{3v} symmetry, along acceptor-neighbor bond in a -plane for C_s .

and geometries in wurtzite are calculated in C_{3v} and C_s symmetries. We find, unexpectedly, that the most stable site for H is AB_v in the a -plane (C_s symmetry), whose formation energy is -3.45 eV referred to Mg:GaN and free H. This energy is chosen as zero in Table III. We also computed H vibrational frequencies for the various geometries: as turns out from the Table, none of the resulting frequencies is in agreement with experiment. Since the typical error on calculated frequencies is below 1%, this discrepancy suggests that the observed vibrational frequencies may not be due to H-Mg local vibrational modes, and other possibilities should be investigated (as suggested also in Ref.[3]).

H-X _{Ga,N}	H site	E_f (eV)	E_r (eV)	Δd_a	Δd_c	$d_{\text{H-A}}$
H-Be _{Ga}	BC	-4.10	4.20	-11.9	+41.9	+4.8
H-Be _{Ga}	AB _v	-2.99	1.01	-8.9	+16.5	+8.1
H-C _N	BC	-2.84	8.79	-0.5	+49.7	+11.9
H-C _N	AB _v	-2.93	0.60	+1.6	+0.8	+13.0
H-Ca _{Ga}	BC	-2.42	9.50	+5.4	+44.9	+2.2
H-Ca _{Ga}	AB _v	-3.55	3.04	+10.8	+10.0	+4.3
H-Zn _{Ga}	BC	-3.50	6.19	+3.0	+43.2	+5.4
H-Zn _{Ga}	AB _v	-2.97	0.84	+0.8	+9.5	+8.1

Table IV: H-acceptor complex formation energy E_f (relaxed) with respect to doped GaN and free H atom, relaxation contribution E_r . Δd_a : distance change to neighbors in a -plane; Δd_c : distance change to neighbor along c axis; $d_{\text{H-A}}$: distance from H to the anion. All are given in percentage of ideal distances ($d_a = d_c = 3.70$ au, $d_{\text{H-A}} = 1.85$ au.)

Formation and relaxation energies E_f and E_r , and equilibrium geometries for other H-acceptor complexes in the GaN wurtzite structure (16-atom supercell) are shown in Table IV. Again, we considered the C_{3v} BC and AB_v sites. For all complexes, formation is

exothermic. Thus, not unexpectedly, acceptors will suffer from hydrogen passivation. The relaxation is large for the BC site and much less dramatic for the AB site, around which more free space is available.

A tendency common to all the complexes is a competition between BC and AB_v sites. α -plane, C_3 symmetry sites remain to be investigated, and the equilibrium geometries energy order may change, as the indicated by the case of H-Mg. A generally valid simple picture of the behavior of H in a solid is that it likes to sit as much as possible in regions of high electronic density. In Si and GaAs, the bond center is the preferred site. However, in ionic compounds such as GaN, the charge cloud surrounding the anion extends appreciably also on the backside of the anion itself: while for the bond center site to be competitive in energy, a large relaxation energy is required, in the AB_v antibonding site only minor relaxations are needed, and the charge density is still very high. This makes the AB_v competitive, also in view of the small interatomic distances and stiff bonds of GaN.

ACKNOWLEDGEMENTS

Thanks are due to K. Stokbro, R. Valente, and S. Baroni for the parallel iterative diagonalization code. Work supported in part by the European Community through Contract BRE2-CT93-0526, by CINECA Bologna through Supercomputing Grant 93-1-102-9, and by CRS4 Cagliari within the collaborative framework with University of Cagliari.

REFERENCES

1. S. Strite, in *Properties of Group III Nitrides*, J. H. Edgar ed., EMIS Datareview Series (Institution of Electrical Engineers, 1994); S. Estreicher, Mater. Sci. Engin. R14, 319 (1995).
2. J. Neugebauer and C. G. van de Walle, these Proceedings; Phys. Rev. Lett. 75, 4452 (1995); private communication.
3. M. S. Brandt *et al.*, Phys. Rev. B 49, 14758 (1994).
4. R. Dreizler and E. K. U. Gross, *Density functional theory* (Springer, Berlin 1990). Exchange-correlation energy by D. M. Ceperley and B. J. Alder, Phys. Rev. Lett. 45, 566 (1980), parametrized by J. P. Perdew and A. Zunger, Phys. Rev. B 23, 5048 (1981).
5. D. Vanderbilt, Phys. Rev. B 41, 7892 (1990).
6. H. J. Monkhorst and J. D. Pack, Phys. Rev. B 13, 5188 (1976).
7. V. Fiorentini *et al.*, Phys. Rev. B 47, 13353 (1993); V. Fiorentini *et al.*, in *The Physics of Semiconductors*, D. J. Lockwood ed., (World Scientific, Singapore 1995), p.137.
8. R. Valente and S. Baroni, to be published.
9. C. G. van de Walle *et al.*, Phys. Rev. B 47, 9425 (1993).
10. U. Scherz and M. Scheffler, in *Semiconductors and Semimetals*, vol. 38, E. R. Weber ed. (Academic Press, New York 1993), p. 1; L. Pavesi and P. Giannozzi, Phys. Rev. B 46, 4621 (1992).

ELECTRONIC STRUCTURE OF A NITROGEN VACANCY IN CUBIC GALLIUM NITRIDE

V.A. Gubanov*, A.F. Wright**, J.S. Nelson**, C.Y. Fong*** and B. M. Klein***,
*Physics Department, San Jose State University, San Jose, CA, vgubanov@isc.sjsu.edu
**Sandia National Laboratories, Albuquerque, NM,
***Department of Physics, University of California, Davis, CA

ABSTRACT

A nitrogen vacancy in zinc-blende structure gallium nitride (c-GaN) is investigated by the plane-wave pseudopotential (PWPP) and tight binding-linear combination of muffin tin orbitals (TB-LMTO) methods using 32- and 64- atom supercells. The relaxation of the nearest Ga atom to the vacancy site is found to be inward by 0.069 a.u., with a relaxation energy of 0.04 eV/N-atom vacancy. The shell-projected, total and partial densities of states and the charge density maps are obtained to provide detailed information on energy and spatial localization of the N vacancy states.

INTRODUCTION

Recent successful demonstrations of UV and blue light emitting devices [1,2], based on group-III nitrides, have shown that these materials, especially gallium nitride (GaN), are well suited for a wide range of applications in electronics and optoelectronics. However, many questions on the nature of GaN's unique physical properties are still open, one of the most widely discussed being the origin of the high *n*-type conductivity of undoped GaN crystals. The native defects leading to the *n*-type conductivity are believed to be nitrogen vacancies [3] in both the hexagonal wurzite (w-GaN) and cubic (c-GaN) phases. The latter one is considered especially advantageous in optoelectronic applications [4].

In this paper, we investigate the electronic structure of a nitrogen vacancy in c-GaN using the plane-wave pseudopotential (PWPP) [5] and tight binding-linear combination of muffin tin orbitals (TB-LMTO) [6] methods.

MODELS AND RESULTS FOR IDEAL c-GaN

In order to use the PWPP and TB-LMTO methods for studying different aspects of vacancy properties, we first test the methods for the case of stoichiometric c-GaN. Both methods are based on the local density approximation (LDA), and we have used the Ceperley-Alder [7] and Hedin-Lundqvist form [8] of the exchange-correlation potential in the PWPP and TB-LMTO methods, respectively. The crystal lattice parameter, *a*, which is 4.49Å found in epitaxially grown c-GaN [9] has been used in our calculations. The atomic sphere radii in the TB-LMTO method were 2.383 and 1.907Å for Ga and N atoms, respectively. Two empty spheres per unit cell, placed at the standard positions, were also used in the TB-LMTO calculations. A new feature in the PWPP method is the use of a 'soft' gallium pseudopotential. The energy cutoff for the plane-wave expansion is 160Ry. The band structure obtained is practically indistinguishable from our previous results [10]. In both methods, Ga 3d states have been treated as valence states.

The band structures of c-GaN calculated by the two methods are in excellent agreement for the valence and lower portion of the conduction bands [11]. The differences occur only in the high energy region of the conduction bands. The valence bands split into two parts separated by a gap. From the partial density of states (not shown), the upper part of the valence bands consists predominantly of N2p states hybridized with Ga4p states. The hybridization of N2p and Ga4s states occurs near the

bottom of this upper part. In agreement with previously studies [10], the Ga3d states are significantly mixed with the N2s states and make significant contributions to the cohesive energy of the crystal. Both the Ga4s and N2p states contribute to the formation of the states near the conduction band edge.

The calculations were based on the LDA. Neither the self-interaction correction nor the quasi-particle approach to improve the gap were used. The calculated direct energy gaps are 1.82 and 1.92 eV for the PWPP and TB-LMTO calculations, respectively. The experimental value of the gap is 3.2 eV. The lattice constants determined by the minimization of the total energy are 4.46 and 4.50 Å and the bulk moduli are 202 and 212 Mbar for the PWPP and TB-LMTO methods, respectively. The bulk modulus estimated from experiments is 195-245 Mbar.

A NITROGEN VACANCY IN c-GaN: STRUCTURAL RELAXATION

The lattice relaxation around a N vacancy site in c-GaN was investigated by the PWPP method. To model an isolated N vacancy, we began by removing one nitrogen atom from an ideal 32-atom supercell of GaN with the symmorphic space group having the point group T_d . The initial geometry was then relaxed maintaining the symmetry group and calculating self-consistent forces acting on all the atoms in a unit cell. The relaxation energy was found to be 0.04 eV/N-atom vacancy, which is slightly more than 0.03 eV/N-atom vacancy found in Ref. 12.

The relaxation of the nearest neighbor Ga atoms appears to be small. These atoms relax inward by 0.069 a.u., while the next nearest neighbor N atoms are displaced inward by only 0.015 a.u.. The third and fourth shell atoms hardly move at all.

Decomposition of the wave functions at the Γ point in the Brillouin zone into angular momentum components at the vacancy site and various nearby atoms show that a single doubly occupied state with *s*-character localized on the vacancy has its energy at 0.086 Ry (1.17 eV) below the valence band maximum. A triplet state with *p*-character was found to be localized at the vacancy site with energy 0.060 Ry (0.82 eV) above the conduction band minimum. These results are in qualitative agreement with previous density-functional studies of nitrogen vacancy in c- and w-GaN [13].

In order to further investigate the origin of nitrogen vacancy states and their localization, we carried out calculations using the well developed TB-LMTO method.

ELECTRONIC STATES OF A N VACANCY: TB-LMTO CALCULATIONS

The nitrogen vacancy is surrounded by four Ga neighbors, and each of them is coordinated with three N neighbors. Each Ga atom shares 3 electrons ($4s^2 4p^1$) with its nearest neighbors and leaves a total of 3 ($4 \times 3/4$) "dangling" unpaired electrons in the vicinity of the vacancy. These three electrons tend to form bound states with the Ga ions: a doubly occupied (with spin degeneracy) *s*-like state and one partially occupied *p*-like state at a higher energy. The details of the energies and the spatial charge distributions for these two states depend on the full response of the crystal to the formation of the vacancy. We have modeled this response in the TB-LMTO method with a supercell approach. A primitive cubic supercell of 64 atoms (with the central N atom replaced by the vacancy atomic sphere of the same radius as the N atom and 64 empty spheres, i.e. the 128-site supercell) was used in the calculations. The 1s, 2p and 3d vacancy basis functions were included into the basis set and each shell of the atoms around the vacancy was allowed to adjust their charge distributions to the creation of the vacancy. The extent of the spatial delocalization of the vacancy states can then be examined from the local density of states (DOS) of each shell of atoms. The characteristics of the vacancy states and the corresponding energy spectrum can be easily studied from the partial DOS for the vacancy "pseudoatom". Because a small

relaxation of the Ga atoms around the vacancy has been found (see above discussions), the TB-LMTO calculations have been carried out for the unrelaxed crystal.

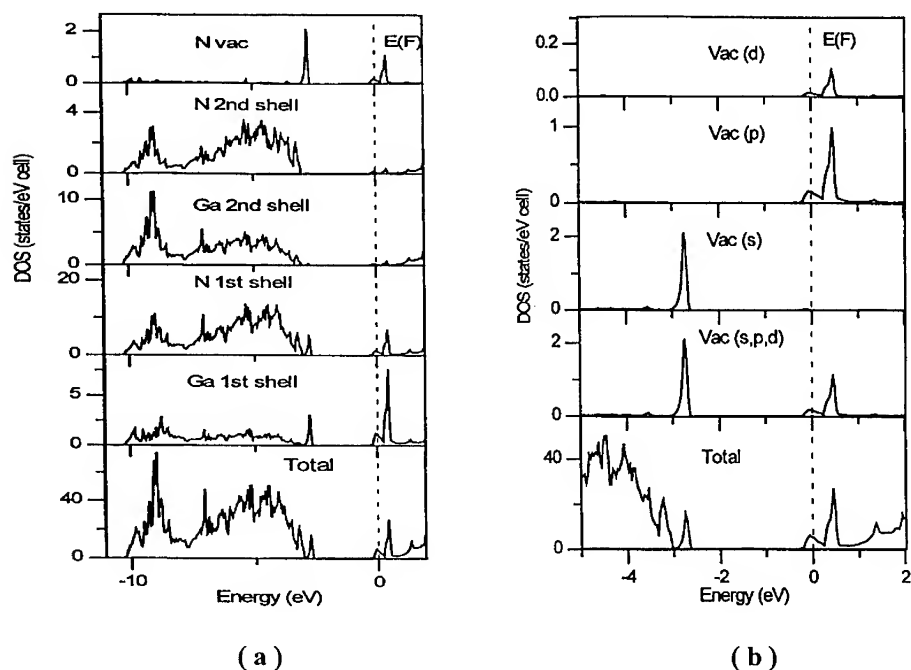


Fig. 1. Shell-projected local densities of states for a N vacancy in c-GaN for: (a) N vacancy site and the neighboring four coordinated spheres; (b) the partial s, p, and d density states for the N vacancy.

Fig.1 presents the total and shell-projected DOS for the atoms up to 4-th neighboring shell. The creation of a nitrogen vacancy results in two distinct structures - "vacancy levels". The lower energy structure has a narrow width (0.34 eV) and is completely occupied. The peak position of this structure is at 0.17 eV below the top of the valence band. There is some quantitative disagreement with the results obtained from PWPP method which gives the position of the s-like states at 1.17 eV below the valence band edge. The higher energy structure is partially occupied and overlaps with the bands near the conduction band edge. The Fermi energy, $E(F)$, is located at the weaker peak of the structure, which is 0.35 eV above the conduction band minimum. The DOS at the Fermi energy is 76.8 states/Ry-cell. The total width of this vacancy structure is 0.78 eV. Qualitatively, the two structures of the "vacancy levels" agree with the results of PWPP method.

As is seen from the shell-projected DOS (Fig. 1a), both vacancy levels originate from states of the 1st shell Ga and the 1st shell N atoms (the structure located at the top of the valence bands). The contributions from the 2nd shell Ga and N atoms decrease drastically. Therefore, both vacancy levels are essentially spread over the two first coordination spheres of atoms around the vacancy. The compositions of the "vacancy levels" can be seen from the partial DOS given in Fig. 1b. The lower energy structure is

related to the *s*-like states of the 1st shell Ga atoms and the hybridization of the states with the rest of the valence bands is small. The higher energy structure is predominantly *p*-like mixed with about 10% *d*-like states. Since the 1st shell of N atoms makes a significant contributions to the vacancy DOS, this indicates that the N vacancy in c-GaN does not induce a sharp localized state, but is due to hybridization of states associated with the two nearest shells of atoms. Both defect DOS structures have a sizable energy dispersion. The higher energy structure is noticeably split, with the energy separation between the two peaks being about 0.45 eV.

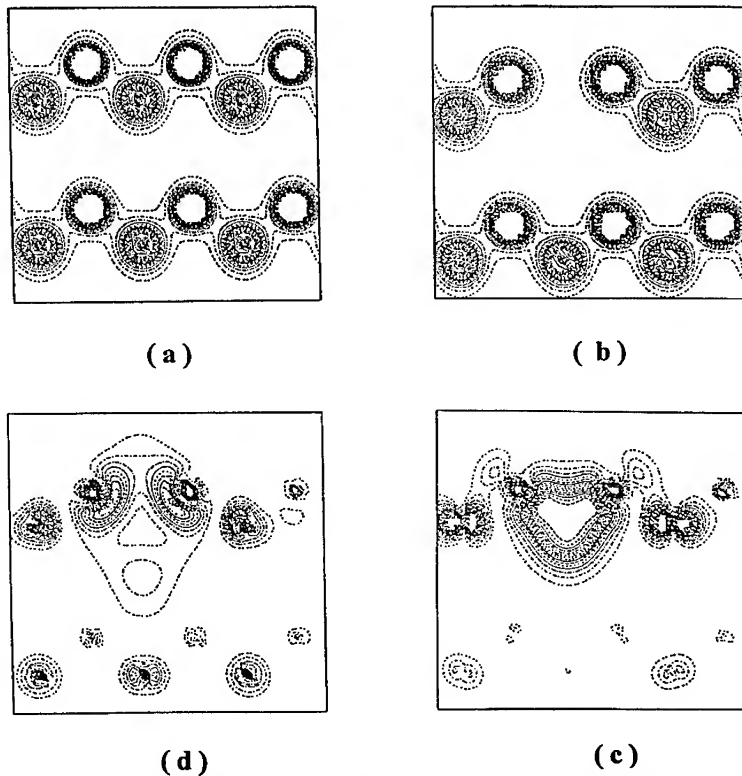


Fig.2. Charge density maps in the (110) plane for a c-GaN crystal with a N vacancy: (a) the total charge density map for ideal c-GaN crystal; (b) the total charge density map for the crystal with N vacancy; (c) the charge density map for s-type vacancy state at the valence band edge; (d) the charge density map for p-type vacancy state at the conduction band edge.

Vacancy states formed by the states of two nearest neighboring shells of Ga and N atoms are not completely localized in space as in the simple picture of a well-localized state. The spatial extensions of both vacancy levels can be seen by calculating the charge density maps. In Fig. 2, we present the maps of the total charge density for ideal

c-GaN and a crystal with a N vacancy. All the charge distributions are given in the (110) plane. Strong ionic character of the bonding between the Ga and the N atoms can be seen from the charge density plots. In the Ga atomic spheres, the charge appears to be depleted by ~ 1.2 electrons (e). The N vacancy does not accumulate a significant electronic charge, and is not a trap for electrons (Fig. 2b). The charge in the vacancy atomic sphere is only 0.62 e (0.49 e from the s -like and 0.13 e from the p -like states). Fig. 2c shows the strong spatial localization of the s -like vacancy states and the dominant origin from the dangling bond type p -like states of the nearest Ga atoms and the states of 1st shell N atoms. The charge densities of the higher energy p -like vacancy states (Fig. 2d) illustrate the formation of Ga-Ga metallic bonding-type states and the distribution extending to the vacancy site. The contribution of the p -like states centered at the 1st shell N atoms is clearly illustrated. These vacancy states can participate in the formation of conduction band states of nitrogen deficient crystals, and may be responsible for the observed n -type conductivity of the undoped GaN samples.

From the above results, it is conceivable that nitrogen vacancies can induce strong and narrow subbands at the valence band edge and at the bottom of conduction bands. The calculated energy position of the p -like states in the conduction band is in a good agreement with the recent photoluminescence, optical absorption, and Raman scattering experiments [14,15]. The measured energy of the vacancy levels at ambient pressure is found to be 0.4eV above the conduction band edge, and 0.13eV below the edge at 27GPa (the data is for w-GaN).

In order to interpret the experimental data, the model of treating a N vacancy as a simple donor-like atom producing zero width levels in the energy spectrum is widely used. It seems that the model is excessively oversimplified. Our calculations show that a N vacancy induced states, especially the p -like states, are delocalized and extend at least to two neighboring shells of atoms. Furthermore, the energies of these states exhibit significant dispersion and cannot be characterized as having zero width.

CONCLUSIONS

The electronic structure calculations of a N vacancy in c-GaN were carried out with PWPP and TB-LMTO methods. The PWPP calculations indicate that the relaxation of the nearest Ga atoms is inward but is very small. Both results show that the vacancy states split into two bands with one located near the valence band edge with a width of 0.3 eV and a strong s -character, and the other is situated near the minimum of the conduction band and has a width of 0.78 eV. These latter states have strong p -like character. The calculated charge densities and the shell-projected DOS show that the s -like vacancy states are localized around the 1st shell coordination spheres of the vacancy. The p -like vacancy states form metallic bond between the nearest Ga atoms and extend their charge distribution to the vacancy site. Furthermore, the 1st shell N atoms contribute significantly to these states. These states may explain the n -type conductivity shown in undoped GaN samples.

ACKNOWLEDGMENTS A grant from the San-Diego Supercomputer Center is gratefully acknowledged. A. F. Wright, J. S. Nelson, and C. Y. Fong acknowledge support by the US Department of Energy under contract # DE-AC04-95AL85000.

REFERENCES

- [1] I. Akasaki, H. Amano, N. Koide, M. Kotaki, and K. Manabe, *Physica B*, **185**, p.428 (1993).
- [2] S. Nakamura, T. Mukai, and M. Senoh, *Appl. Phys. Lett.*, **64**, p.1687 (1994).

- [3] H. P. Maruska and J. J. Tietjen, Appl. Phys. Lett., **15**, p.327 (1969).
- [4] M. Nagahara, S. Miyoshi, H. Yaguchi, K. Onabe, Y. Shiraki, and R. Ito, J. Crystal Growth, **145**, p.1971 (1994).
- [5] A. F. Wright and J. S. Nelson, Phys. Rev. **B50**, p. 2159 (1994).
- [6] M. van Schilfgaarde, T. A. Paxton, O. Jepsen, and O. K. Anderson, TB-LMTO program-Version 44, Max Plank Institute for Solid State Physics, 1994.
- [7] D. M. Ceperley and B. J. Alder, Phys. Rev. Lett., **45**, p.556 (1980); J. P. Perdew and A. Zunger, Phys. Rev. **B23**, p.5048 (1981).
- [8] K. Hedin and B. I. Lundqvist, J. Phys. C, **4**, p.2064 (1971).
- [9] T. Leim, T. D. Moustakas, R. J. Graham, Y. He, and S. Berkowitz, J. Appl. Phys., **71**, p.4933 (1992).
- [10] A. F. Wright and J. S. Nelson, in Physics and Simulation of Optoelectronic Devices III, eds. M. Osinski, and W. W. Chow (The international Society for Optical Engineering, 2399, Bellingham, WA, 1995), p.498.
- [11] V. A. Gubanov, A. F. Wright, J. S. Nelson, C. Y. Fong, and Barry M. Klein, (to be published).
- [12] J. Neugebauer and C. G. van de Walle, in Diamond, SiC and Nitride Wide-Bandgap Semiconductor, eds. C. H. Carter Jr., G. Gildenblat, S. Nakamura, J. Nemanich, (MRS Symposia Proceedings, **339**, Pittsburgh, Pennsylvania, 1995), p.687.
- [13] P. Perlin, T. Suski, H. Teisseyre, M. Leszczynski, I. Grzegory, J. Jun, S. Porowski, P. Boguslawski, J. Berholc, J. C. Chervin, A. Polian, and T. D. Moustakas, Phys. Rev. Lett., **75**, 296 (1995).
- [14] C. Wetzel, W. Walukiewicz, E. E. Haller, J. W. Ager, A. Chen, S. Fisher, P. Y. Yu, R. Jeanloz, I. Grzegory, S. Porowski, T. Suski, H. Amano, and I. Akasaki, proc. 18th Int. Conf. on Defects in Semiconductors, July 24-28, Sendai, Japan, 1995.
- [15] W. R. Lambrecht, B. Segal, J. Rife, W. R. Hunter, and D. K. Wickenden, Phys. Rev. **B51**, 13516 (1995).

STRUCTURAL AND ELECTRONIC PROPERTIES OF AlN, GaN AND InN, AND BAND OFFSETS AT AlN/GaN (10 $\bar{1}$ 0) AND (0001) INTERFACES

A. Satta, Vincenzo Fiorentini, Andrea Bosin, and F. Meloni

INFM-Dipartimento di Scienze Fisiche, Università di Cagliari, I-09124 Cagliari, Italy

David Vanderbilt

Department of Physics and Astronomy, Rutgers University, Piscataway, NJ, USA

ABSTRACT

Ab initio local-density-functional calculations are presented for bulk AlN, GaN, and InN in the wurtzite, zincblende, and rocksalt structures. Structural transition pressures and deformation potentials of electronic gaps are investigated. In addition, we study the band offset at the polar (0001) and non-polar (10 $\bar{1}$ 0) AlN/GaN interfaces. Within AlN-on-GaN epitaxial conditions, we obtain valence-band offset values close to 0.7 eV for both interfaces. From the macroscopic field appearing along the growth direction of the polar interface (tentatively attributed to AlN macroscopic polarization), an estimate of the macroscopic dielectric constant of GaN is extracted. All calculations employed conjugate-gradient total-energy minimizations, ultrasoft pseudopotentials, and plane waves at 25 Ryd cutoff.

INTRODUCTION

Recently III-V nitrides have attracted considerable interest as materials for use in blue-violet optoelectronics and high-power device electronics [1]. An accurate study of the electronic and structural properties of these materials, in equilibrium and under external perturbations, is therefore timely. Also, given the fairly close lattice match of these materials, and the range of fundamental gap energies they encompass, a field of applications that comes naturally to mind is that of nitride heterojunctions and quantum-confinement heterostructures. The basic physical parameter for any application in such a field is the valence band offset at the interface of the two relevant materials. Theory has given abundant proof of being capable of reproducing or predicting interface band offsets in a number of technologically relevant situations [2]. A theoretical prediction of band offsets is therefore expected to provide useful and reliable information to experiments and device modeling.

Here we present a study of the structural and electronic properties, and of their dependence on hydrostatic pressure, for the III-V nitrides AlN, GaN, and InN in the zincblende, wurtzite, and rocksalt phases (BN is the subject of a separate study [3]). Thereafter, we report preliminary estimates of the valence band offsets at polar and non-polar AlN/GaN interfaces.

Our calculations employ a recently developed conjugate-gradient total energy minimization scheme [4], ultrasoft pseudopotentials [5] for the ion-electron interaction, a plane-wave basis, and the local density approximation to density functional theory for the electron-electron interaction [6]. It has been amply demonstrated in previous work [7] that the explicit treatment of the semicore *d* electrons of Ga as valence states is necessary to obtain reliable structural properties for GaN. In the present work we treat as valence states the semicore *d* states for both Ga and In. This is accomplished using ultrasoft potentials, which also allow for an easier treatment of the localized *p* states of N. This approach has allowed to treat large GaN systems, such as impurities and H-impurity complexes [8]. The potentials for Ga, Al, and N were generated from a non-relativistic atomic calculation, while

for In a Koelling-Harmon scalar-relativistic equation was used [4]. Spin-orbit interaction is neglected throughout.

AlN, GaN, AND InN: BULK PROPERTIES

The bulk properties of the rocksalt, zincblende, and wurtzite phases of AlN, GaN, and InN are listed in Table I. For the cubic phases the structural parameters were obtained from a Murnaghan fit of the total energy vs. volume. For wurtzite, the total energy was calculated for a grid of values of a and c , assuming an ideal internal parameter u , and the theoretical values a_{th} and c_{th} were extracted by polynomial interpolation. At a_{th} and c_{th} , atomic positions were relaxed to obtain the internal parameter u_{th} . The bulk modulus was obtained changing the cell volume at c_{th} and u_{th} . Cohesive energies are referred to spin-polarized free-atom energies. k -space integrals were approximated by sums over the Chadi-Cohen 10-point and 12-point meshes for the cubic and wurtzite phases respectively.

GaN	phase	a (bohr)	B (Mbar)	B'	c/a	u	$E_{coh}/pair$ (eV)	P_t (KBar)
3d	wurtzite	6.04	2.13	4.50	1.634	0.375	-10.547	521
	zincblende	8.54	2.00	4.15			-10.536	454
	rocksalt	8.01	2.48	4.68			-9.735	
no-3d	zincblende	8.07	2.58	4.1			-14.08	265
	rocksalt	7.49	3.30	4.3			-13.48	
exp	wurtzite	6.03	2.0		1.628		-9	~ 500

AlN	phase	a (bohr)	B (Mbar)	B'	c/a	u	$E_{coh}/pair$ (eV)	P_t (KBar)
	wurtzite	5.814	2.071	3.82	1.619	0.380	-18.032	132.07
	zincblende	8.20	2.04	4.06			-17.990	104.50
	rocksalt	7.59	2.55	3.90			-17.799	
exp	wurtzite	5.88	2.079	6.3	1.6004			140

InN	phase	a (bohr)	B (Mbar)	B'	c/a	u	$E_{coh}/pair$ (eV)	P_t (KBar)
	wurtzite	6.66	1.49	4.12	1.627	0.377	-8.799	122.9
	zincblende	9.40	1.49	4.41			-8.779	
	rocksalt	8.78	1.95	4.48			-8.376	
exp	wurtzite	6.70	1.26	12.7	1.609			121
	zincblende	9.41						

Table I: Structure, cohesive energy, and transition pressures to rocksalt for GaN, AlN, and InN. Results labeled "no-3d" for GaN were obtained without Ga 3d states in the valence.

The results are in good agreement with experiment for the structural parameters as well as for the transition pressures to rocksalt. An interesting prediction is that wurtzite AlN and InN have have appreciably non-ideal structures, while GaN has an ideal u and quasi-ideal axial ratio. These deviations from the ideal wurtzite structure suggest that AlN may exhibit a large macroscopic polarization; as will be suggested below, this may influence interface properties. A calculation of the macroscopic polarization of AlN is underway.

In Table II we report the gap values and deformation potentials for the principal gaps of AlN and GaN. The deformation potentials are defined as $D = \partial E_g / \partial \ln V$. The valence band top is a Γ_1 singlet state (reminiscent of the p_z state), with a Γ_6 doublet ($p_x - p_y$) slightly below it. As was to be expected, the Γ_1 state is quite sensitive to variation in the axial parameters. The gaps obviously suffer from the well known DFT gap problem: however,

deformation potentials (which are in satisfactory agreement with previous studies [9]) are expected to be given reliably by the LDA [10].

	AlN		GaN	
	D	E_g	D	E_g
wurtzite				
$\Gamma_v - \Gamma_c$	-8.97	4.56	-7.27	2.13
$\Gamma_v - A_c$	-8.70	5.16	-6.60	2.87
$\Gamma_v - M_c$	-1.31	5.66	-0.74	5.54
$\Gamma_v - L_c$	-1.95	5.82	-2.64	5.41
zincblende				
$\Gamma_v - \Gamma_c$	-9.04	4.50	-7.09	2.00
$\Gamma_v - L_c$	-9.06	7.45	-7.23	4.78
$\Gamma_v - X_c$	-0.65	3.27	-0.24	3.17
rocksalt				
$\Gamma_v - \Gamma_c$	-14.61	6.04	-12.19	2.81
$\Gamma_v - L_c$	-6.52	6.28	-5.66	5.15
$\Gamma_v - X_c$	-7.49	5.14	-7.04	1.12

Table II: Calculated deformation potentials D (eV) and gap values E_g (eV) for AlN and GaN.

We do not present data for InN in table II, because the minimum gap turns out to be negative in zincblende. This is due to relativistic effects at the In site on the In- s -like bottom conduction state, on top of the DFT gap error. While controllable at a specific volume, this error affects the reliability of deformation potentials.

AlN/GaN INTERFACE BAND OFFSETS

A fundamental ingredient for any application of semiconductor heterojunctions are band discontinuities at interfaces. While a number of III-V-based heterojunctions have been investigated both experimentally and theoretically, the same is not true for nitride interfaces. This field is now exploding, driven by the potential of these heterostructure systems as blue-to-violet light emitters and detectors.

We performed calculations on abrupt interfaces of AlN and GaN in the wurtzite structure, for two different orientations: the non polar (10 $\bar{1}$ 0) and the polar (0001). (The latter orientation is arguably the most important, as recent findings indicate that GaN will grow on e.g. AlN (10 $\bar{1}$ 0) in such a way as to eventually expose the (0001) face.) We extract band offsets from *ab initio* calculations using the macroscopic average concept. As pointed out by Baldereschi *et al.* [2], the valence band offset (VBO) may be split in two separate contributions as

$$\text{VBO} = \Delta E_v + \Delta V. \quad (1)$$

The first term is the difference between the valence band edges of the two bulk materials, each referred to the average electrostatic potential of the pertaining bulk. The second term, the potential line-up, is defined as the drop in average electrostatic potential across the heterojunction. (Of course, this splitting of the offset is arbitrary, and the two contributions have no meaning *per se*. For instance, with an all-electron method, one calculates the offset via alignment of core levels. Remarkably, it is generally the case that the offset is independent of the technique used.)

While the band term ΔE_v is extracted from bulk calculations (at the same lattice parameters used for the two materials in the interface calculations), the evaluation of ΔV

requires a supercell treatment of real heterojunctions. The self-consistent charge density of the interface supercell is averaged over planes orthogonal to the growth direction, and then filtered with a square-wave weighting function with appropriate periodicity. The resulting *macroscopic average* of the supercell charge density produces the sought-after electrostatic potential via the 1-D Poisson equation [2]. The potential drop is extracted graphically or, equivalently, as

$$\Delta V = 4\pi e^2 \int z \bar{n}_0(z) dz. \quad (2)$$

Here n_0 is the *total* charge density: since our heterojunctions are effectively heterovalent due to the presence of the d electrons on the GaN side, it is convenient to use the macroscopic average of the total density, whereby the electron density is neutralized by an array of ionic charges. All calculations adopt the same representation of ionic charges. For the non-polar orientation we used a 4+4-layers 16-atom cell, and supercells of up to 20 atoms (10+10 layers) for the polar one. The supercell sizes are more than sufficient to obtain bulk-like behavior at the center of the GaN and AlN interfaced regions. Monkhorst-Pack (222) special-point meshes were used in the k-space summation.

Orientation	Valence offset (eV)
(10 $\bar{1}$ 0)	0.77
(0001)	0.68

Table III: Interface valence band offsets (eV) for the GaN/AlN polar (0001) and non-polar (10 $\bar{1}$ 0) orientations. See text for discussion.

The resulting estimates of the valence offsets are summarized in Table III. It must be emphasized that these values should be taken as preliminary, as discussed below. We note however that they are in reasonable agreement with the results of a LMTO calculation by Albanesi *et al.* on the zincblende (110) GaN/AlN interface (0.8 eV), with the empirical estimate by Baur *et al.* based on the Langer-Heinrich rule (0.5 ± 0.1 eV), and with XPS measurements of Martin *et al.* for the polar interface (0.8 ± 0.3 eV) [12]. Our results confirm the possibility of achieving *conduction* confinement potentials as large as 2 eV in GaN/AlN-based quantum well.

Let us discuss in more detail the approximations involved in calculating the offsets just reported. Here we have neglected the appreciable mismatch of the two materials, and have assumed the configurations discussed below. This approximation is clearly a major one: work in progress to account for strain effects will be reported elsewhere. For the (10 $\bar{1}$ 0) non-polar orientation, the lattice parameters of GaN have been imposed throughout the cell. This amounts to AlN epitaxial on GaN, with neglect of elastic effects along the growth directions and of internal parameter changes. Removal of this approximation is not expected to induce major changes in the offset, since the c axis length is constrained by the epitaxial relation to GaN. In this cell there is no macroscopic electric field, as expected from the fact that all planes are neutral.

For the (0001) orientation, the two interfaces are inequivalent. The interface planes are conventionally placed at the center of an Al-N axial bond, and of a Ga-N axial bond respectively. Again, we used a cell with GaN lattice parameters throughout, except AlN u_{th} on the AlN side. A macroscopic electric field appears within the bulk regions, as depicted in Fig. 1. It is important to note, however, that the field is superimposed onto a dipole-related potential offset, which is very close to that of the non-polar interface. In this geometry, the offset values at the two inequivalent interfaces are found to be essentially the same.

This macroscopic field signals a net charge accumulation at one interface with respect to the other. Integrating the macroscopically-averaged total charge density in the interface region, one finds an excess charge of 0.3 electrons accumulated at the Al-N axial-bond interface (right side in Fig.1), accompanied by an equal and opposite deficit at the other interface. Interestingly, despite the fact that in this orientation all atomic planes carry a net charge, relaxation at the interface *does not affect the field at all*. (Relaxation changes the (0001) interface offset appreciably, but this is not necessarily meaningful because of the highly strained geometry of AlN in the interface cell.)

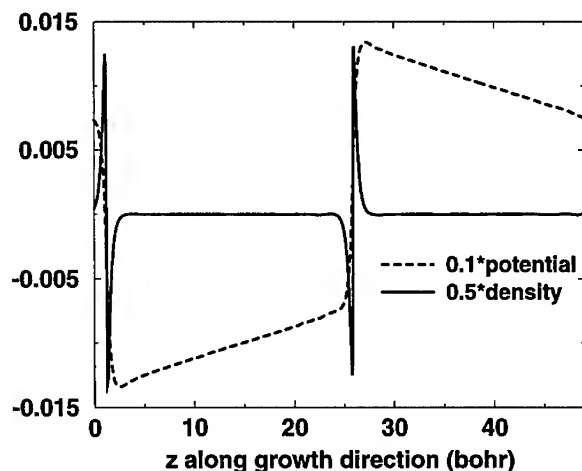


Figure 1: Macroscopic average of the density, and electrostatic potential at the GaN-AlN (0001) interface. Potential (Ryd) and density (bohr^{-3}) have been downscaled by factors of 10 and 2 respectively.

The macroscopic field in the polar interface is therefore related to polarization. As mentioned above, AlN may have a spontaneous macroscopic polarization. GaN has a quasi-ideal structure, so that its (symmetry-permitted) polarization should be smaller than that of AlN). Thus the AlN portion of the cell may be viewed as a piece of polarized matter embedded into an inert matrix (in the spirit of Ref. [14], where a similar device was used to evaluate the polarization of BeO). The interface charge accumulation would then result from the spontaneous macroscopic polarization of AlN.

However, this can not be concluded from just the present calculation, since the strained internal geometry imposed on AlN changes the polarization (i.e. the field) in the AlN region via piezoelectricity. Piezoelectric response, which is the only source of polarization in a *zincblende* interface, may be split in general into electronic (clamped-ions) and ionic (internal-parameter-related) contributions [13]. These have comparable magnitude and opposite signs in many systems (e.g. ZnO, BeO and ZnS [13], and many III-V's), and tend to cancel out. Should complete cancellation occur, any residual field in a *wurtzite* must be due to spontaneous polarization. However, at the present stage, the relative magnitudes of these contributions remain to be determined, and no conclusive statement can be made. In particular, the structure of the AlN cell half must be optimized before attempting further

refinements. We are currently working in this direction.

An interesting spin-off of our results concerns the dielectric constant of GaN. Since the field is constant within the GaN half of the supercell, we can safely picture that region as a capacitor filled with GaN. Then the high-frequency macroscopic dielectric constant of GaN can be estimated trivially from our calculated data. The field and the interface charge are obtained directly from the interface calculation; the distance between the “capacitor plates” is chosen to be the distance between the peaks of the macroscopic-average primitive

$$N(x) = \int_0^x \bar{n}_0(z) dz.$$

Of course, $N(d) = 0$ when d is the supercell length. The resulting estimate for the dielectric constant is $\epsilon_{\text{GaN}}^\infty = 5.2$, which is by all means a reasonable value in comparison to known experiments. Obviously this estimate only contains electronic contributions. For AlN the same procedure would be inaccurate, as the AlN half-cell is geometrically quite different from real AlN.

A. S. and V. F. acknowledge useful discussions and support from Sandro Massidda (Cagliari). This work was supported in part by the European Community through Contract BRE2-CT93-0526, and by CINECA Bologna through Supercomputing Grant 93-1-102-9.

REFERENCES

1. R. F. Davis, *Proceedings IEEE* **79**, 702 (1991).
2. See e.g. A. Baldereschi, S. Baroni, and R. Resta, *Phys. Rev. Lett.* **61**, 734 (1988); M. Peressi *et al.*, *Phys. Rev. B* **48**, 12047 (1993).
3. G. Cappellini *et al.*, these Proceedings; and to be published.
4. R. D. King-Smith and D. Vanderbilt, *Phys. Rev. B* **49**, 5828 (1994).
5. D. Vanderbilt, *Phys. Rev. B* **41**, 7892 (1990).
6. R. Dreizler and E. K. U. Gross, *Density functional theory* (Springer, Berlin, 1990). Exchange-correlation energy by D. M. Ceperley and B. J. Alder, *Phys. Rev. Lett.* **45**, 566 (1980) as parametrized by J. P. Perdew and A. Zunger, *Phys. Rev. B* **23**, 5048 (1981).
7. V. Fiorentini, M. Methfessel, and M. Scheffler, *Phys. Rev. B* **47**, 13353 (1993); V. Fiorentini *et al.*, in *The Physics of Semiconductors*, D. J. Lockwood ed., (World Scientific, Singapore 1995), p.137. See also S.-H. Wei and A. Zunger, *Phys. Rev. B* **37**, 8958 (1988) (on II-VI materials).
8. A. Bosin *et al.*, these Proceedings, and to be published.
9. I. Gorczyca and N. Christensen, *Phys. Rev. B* **50**, 4397 (1994).
10. V. Fiorentini, *Phys. Rev. B* **46**, 2086 (1992).
11. V. Fiorentini, to be published.
12. W. L. Lambrecht *et al.*, *J. Vac. Sci. Technol. B* **12**, 2470 (1994); J. Baur *et al.*, *Appl. Phys. Lett.* **65**, 2211 (1994); G. Martin *et al.*, *ibid.*, 610.
13. A. Dal Corso, M. Posternak, R. Resta, and A. Baldereschi, *Phys. Rev. B* **50**, 10715 (1994).
14. M. Posternak, A. Baldereschi, A. Catellani, and R. Resta, *Phys. Rev. Lett.* **64**, 1777 (1990).

THE ROLE OF IMPURITIES IN LP-MOCVD GROWN GALLIUM NITRIDE

C.Y. HWANG*, Y. LI*, M. J. SCHURMAN*, W. E. MAYO*, Y. LU* and R. A. STALL**

*Rutgers University, Piscataway, NJ 08855

**EMCORE Corp., Somerset, NJ 08873

ABSTRACT

We have investigated the relationship of the Hall electron mobility to the background carrier concentration in low pressure MOCVD grown GaN. The highest electron mobility ($400 \text{ cm}^2/\text{V}\cdot\text{s}$) of the unintentionally doped GaN was obtained at a carrier concentration of $1 \times 10^{17} \text{ cm}^{-3}$ and samples with carrier concentrations lower than this exhibited lower mobilities. SIMS analysis shows C and O concentrations in the range of $2\text{--}3 \times 10^{16} \text{ cm}^{-3}$ and H in the $2\text{--}3 \times 10^{17} \text{ cm}^{-3}$ range. Structural defects, stoichiometry and impurities in the GaN films grown under different conditions are investigated to understand their relationship to the electron Hall mobilities. In particular, different growth temperatures and pressures were used to grow undoped GaN and modify the background doping effect of the impurities.

INTRODUCTION

Most III-V compound semiconductors like GaAs and InP have high electron or hole mobility when the impurity or carrier concentration is low¹. In such materials, the mobility decreases gradually as the impurity concentration increases. For GaN films grown by MOCVD, however, the highest mobility tends to occur at an intermediate carrier concentration and the mobility decreases as the background carrier concentration drops below this value. We have investigated this unusual behavior of the electron mobility by several approaches. First, because the defect density in GaN films is much higher than in Si or other III-V materials, we must examine the potential role of the defect density. Then, we examined the film stoichiometry and impurity levels to pinpoint the origin of the unusual carrier concentration/mobility behavior.

EXPERIMENTAL

Samples were grown by MOCVD with TMG and NH_3 as the precursors as described in a previous publication². Several characterization techniques were used to find the correlation between residual stress, stoichiometry, impurities and the electron Hall mobility. Strain was measured by both X-ray $\theta\text{--}2\theta$ scans and rocking curves for samples with different mobilities. We also performed RBS and AES analysis on samples with different values of mobility and carrier concentration to determine their Ga to N ratio. Finally, to monitor the impurity levels in the films, we performed concentration depth profiles using SIMS analysis on several samples. Based upon our use of the MOCVD method with a rotating sample holder, the most likely impurities in the film are H, C and O from the source gases and Fe, Cr, Ni and Mo from the reactor itself.

RESULTS

A. Dislocation Density of the Films

Structural imperfections in the GaN films are one possible explanation for the low electron mobility of the film. To investigate this possibility, several samples with different electron mobilities were chosen for cross-sectional and plane-view TEM. From the cross-sectional TEM samples, one can compare the crystal structure of the epilayer/buffer layer/substrate interfaces. When the growth conditions, i.e. growth temperature and thickness of the buffer layer are the same, the structure of the epilayer varies little. Also, by measuring the dislocation density from plane view TEM micrographs, we found that the dislocation density is not strongly related to the mobility. For example, we found one sample with high dislocation density ($2.8 \times 10^9/\text{cm}^2$) but higher mobility than a second sample with only half the dislocation density. This is supported by published work³ where a commercial sample had a dislocation density of the order of $1 \times 10^{10}/\text{cm}^2$ but still had high mobility. This suggests that sources, other than the dislocation density, are responsible for the decrease of the mobility.

B. Stoichiometry of the Films

RBS and AES analysis were performed on six samples with different values of mobility and carrier concentration to measure the N to Ga ratio. Due to the low atomic weight of nitrogen and large difference of atomic weight between Ga and N, it is not easy to measure the amount of N with high precision. But, based upon test standards and computer simulations, we are confident that the N/Ga ratio is very close to the desired value of 1.0 in all samples.

The film thickness of the grown films is about 2 μm . The GaN sample has some carbon contamination on the surface as measured by AES. But after sputtering off a few hundred angstroms, both the carbon and oxygen content are dramatically reduced. Also, the N/Ga atomic ratio was measured by AES and was found to be close to 0.99 through most of the films.

Both the RBS and AES measurements indicate that the stoichiometry of the films was very close to 1. Due to the limited sensitivity of the techniques, the nitrogen vacancy concentration can not be determined because it is probably at the impurity level.

C. Impurities in the Films

Effect of Growth Temperature

Growth temperature is an important issue in GaN growth. Because NH_3 is used as the nitrogen source, the growth temperature must be high enough to pyrolyze ammonia. Films grown below 900°C have a yellowish color and poor electrical properties. This is due to the fact that at these lower temperatures ammonia does not decompose completely. Thus, the nitrogen concentration in the film is low and the hydrogen concentration is not high enough to remove the methyl group from the TMG molecules. Evidence for this is seen in the SIMS analysis of a sample as shown in Fig. 1. In the middle of a growth run, the temperature of the film was increased from 1000°C to 1030°C . As one can see, the carbon concentration decreases from $5 \times 10^{17}/\text{cm}^3$ to $1 \times 10^{17}/\text{cm}^3$ as the temperature increased, which is consistent with a more complete reaction of the feed gases.

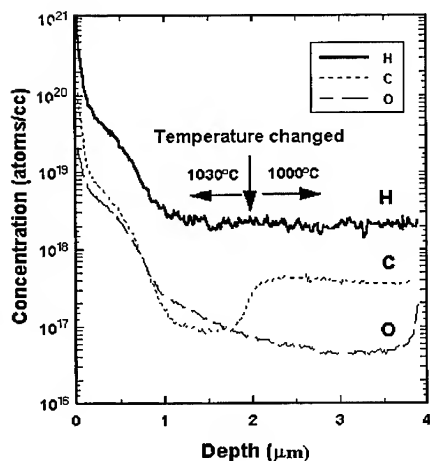


Figure 1 SIMS depth profile of a film grown via an interrupted deposition during which the temperature was abruptly changed.

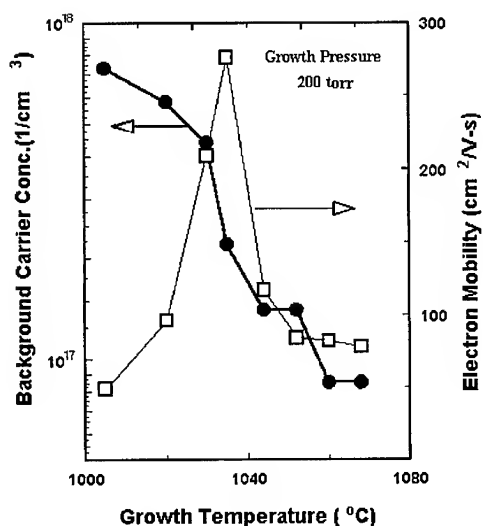


Figure 2 Background carrier concentration and electron mobility of GaN films grown at different growth temperatures.

Figure 2 shows the effect of growth temperature on the background carrier concentration and electron mobility. As expected, the background carrier concentration decreases as growth temperature increases, which is probably due to more complete decomposition of the NH_3 . Also, the higher temperature will result in a higher nitrogen partial pressure above the substrate and cause more nitrogen to be incorporated into the film. When we examine the effect of the growth temperature on the mobility, however, we find that the film grown at an intermediate temperature (1035°C) exhibits the best mobility.

The Effect of Growth Pressure

The major impurities determined by SIMS analysis are H, C and O. Films grown at higher pressures exhibit lower impurity concentrations than films grown at lower pressures at the same growth temperature. An example of a SIMS depth profile is shown in Fig. 3 for a sample grown at 1030°C and 200 torr. The C concentration is at a level of $2\text{-}3 \times 10^{16} \text{ cm}^{-3}$ and H is in the $2\text{-}3 \times 10^{17} \text{ cm}^{-3}$ range. The O concentration in GaN is $2 \times 10^{16} \text{ cm}^{-3}$ through most of the film but jumps to $1 \times 10^{18} \text{ cm}^{-3}$ near the surface. Surprisingly, the transition metals like Fe, Cr, Ni and Mo are all below the detection limit which is estimated to be $1 \times 10^{16} \text{ cm}^{-3}$ for our testing conditions. The C, O and H concentrations for a film grown at 1030°C and 50 torr are 7×10^{16} - 1×10^{17} , $5\text{-}8 \times 10^{16}$ and $2\text{-}3 \times 10^{17} \text{ cm}^{-3}$ respectively. When the growth pressure increases, the C and O concentrations tend to decrease. For example, the O and C concentrations are about 3-4 times higher for films grown at 50 torr than the ones grown at 200 torr.

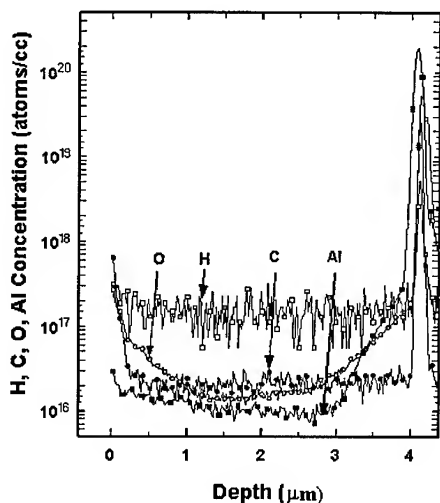


Figure 3 SIMS depth profile of H, C, O, and Al in a GaN film grown at 1030°C and 200 torr.

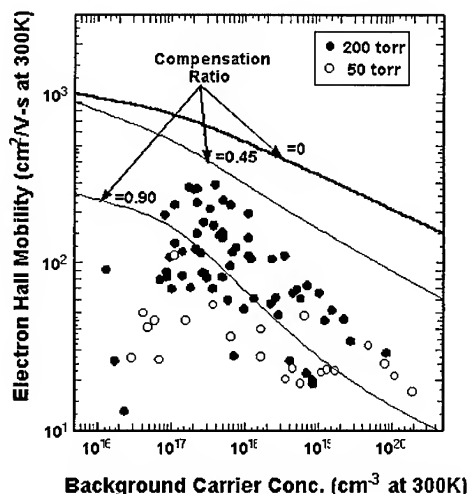


Figure 4 Electron Hall mobility at room temperature versus background carrier concentration for GaN films grown at 50 and 200 torr.

The electron Hall mobility versus background carrier concentration for samples grown at two different pressures is shown in Fig. 4. The growth condition for each sample is different but generally all have smooth surfaces and good crystal quality (FWHM = 5-8 arc min measured by x-ray rocking curves). Note from Fig. 4 that the mobility decreases as the carrier concentration drops below 10^{17} cm^{-3} and peaks when the concentration is $2 \times 10^{17} \text{ cm}^{-3}$. A simulation by Chin et al.⁴ shows that the curve of the electron Hall mobility versus background carrier concentration of GaN should be very similar to GaAs. They also calculated the curves for different compensation ratios. For comparison, these calculated curves are also plotted in Fig 4. Compared to the theoretical calculation, our films show strong compensation behavior with the compensation ratio between 0.45 to 1.0. The data for films grown at 200 torr show higher mobility than films grown at 50 torr at the same background carrier concentration level. The highest mobilities for films grown at 200 torr were obtained at carrier concentration of $2 \times 10^{17} \text{ cm}^{-3}$. However, those samples with background carrier concentration lower than $2 \times 10^{17} \text{ cm}^{-3}$ exhibit lower mobility.

DISCUSSION

As described previously, the mobility decreases as the background carrier concentration drops below $2 \times 10^{17} \text{ cm}^{-3}$. This electrical behavior is not typical for semiconductors. Most III-V compound semiconductors like GaAs and InP have high electron or hole mobility when the impurity or carrier concentration is low and the mobility decreases gradually when the impurity concentration is above 10^{16} cm^{-3} . The reason for this behavior is that the ionized impurities result in carrier scattering that significantly affects the

mobility. This is true for crystals like GaAs whose background carrier concentration is as low as $1.5 \times 10^6 / \text{cm}^3$ at room temperature.

Because of the high nitrogen vapor pressure at high temperature, it is difficult to grow intrinsic material. The as-grown GaN always shows unintentionally doped n-type behavior due to nitrogen deficiency. We feel that this may be attributed to nitrogen vacancies that act as donors in GaN. Therefore, if we accept the nitrogen vacancies as impurities, a similar mobility-carrier concentration relation as the one described above for GaAs should occur in GaN. As one can see in Fig. 4, although the compensation ratio is high, our samples show very similar mobility-carrier concentration behavior as Chin predicted. Only in the range of low background carrier concentration ($> 1 \times 10^{17} \text{cm}^{-3}$) do the mobilities drop dramatically. We suspect that these impurities are the cause of the compensation. Carbon is thought to be the main species that lowers the electron mobility. Pearton et al⁵ showed that C in GaN acts as an acceptor when C is in the nitrogen vacancy site. Although it is not a good p-type dopant, C can be a good compensation center. In this case, the C introduced by TMG during growth may affect the electrical property of the film if the C concentration is high enough. The Hall mobilities of the film grown at 50 torr generally show lower mobilities. This is probably due to a higher impurity level which causes a high compensation ratio.

When the nitrogen vacancy concentration ($[V_N]$) is much higher than the carbon concentration ($[C]$), the GaN film can be treated as an n-type semiconductor whose mobility decreases as $[V_N]$ increases. As $[V_N]$ decreases below $2 \times 10^{17} \text{cm}^{-3}$, $[C]$ is close to $[V_N]$ and the film becomes highly resistive. In this case the compensation ratio can be very high. Thus, the mobility drops dramatically and this would explain the experimentally observed drop at low background carrier concentrations.

SUMMARY

In summary, the unusual behavior of electron Hall mobility has been investigated. Stoichiometric analysis by AES and RBS indicate that the Ga:N is close to 1 and both oxygen and carbon are below the detection limit (< 1 atomic %). Structural defects such as dislocations in the range of 10^8 to $10^{10} / \text{cm}^2$ do not appear to affect the electrical properties judging from the insensitivity of the electron mobility to the dislocation density. SIMS analysis showed H, O, and C impurities at the level of 2×10^{17} , 2×10^{16} and $2 \times 10^{16} \text{cm}^{-3}$ respectively, for films grown at 1030°C and 200 torr. Impurities, especially carbon, are thought to be the source of compensation centers which reduce the electron mobility. Our experiments have shown that the carbon incorporation rate increases with decreasing growth temperature and decreasing growth pressure.

ACKNOWLEDGMENTS

We are indebted to BMDO/IST for support of this work under contract N00014-93-C-0269 and to Mr. Max Yoder for support of our efforts.

REFERENCES

1. T. J. Russell, C. L. Wilson and M. Gaitan, IEEE Trans. Electron Dev. **ED-30**, 1662 (1983).
2. C. Y. Hwang, M. J. Schurman, W. E. Mayo, and R. A. Stall, J. Vac. Sci. Technol. **A13**, 672 (1995).
3. S. D. Lester, F. A. Ponce, M. G. Craford and D. A. Steigerwald, Appl. Phys. Lett. **66**, 1249 (1995).
4. V. W. L. Chin, J. Appl. Phys. **75**, 7365 (1994).
5. J. D. MacKenzie, C. R. Abernathy and S. J. Pearton, presented at the 1995 MRS Spring Meeting, San Francisco, CA, 1995 (unpublished).

Optical Properties of Mg-GaN, GaN/AlGaN SCH structures, and GaN on ZnO Substrates

H. Morkoç*, W. Kim, Ö. Aktas, A. Salvador, and A. Botchkarev, University of Illinois, Coordinated Science Laboratory and Materials Research Laboratory, 104 South Goodwin Avenue, Urbana, IL 61801

D. C. Reynolds, and D. C. Look, University Research Center, Wright State University, Dayton Ohio 45435

M. Smith, G. D. Chen, J. Y. Lin, and H. X. Jiang, Department of Physics, Kansas State University, Manhattan, Kansas 66506-2601

T.J. Schmidt, X.H. Yang, W. Shan, and J.J. Song, Dept. of Physics, Oklahoma State University, Stillwater, OK 74078-0444

B. Goldenberg, Honeywell Technology Center, 4B75, 1201 State Highway 55 Plymouth MN 55441-4799

C. W. Litton and K. Evans, Electronic Research Directorate, WL/ELR, Building 620 Wright Patterson AFB, OH 45433

Abstract

GaN films and GaN/AlGaN heterostructures have been grown by MBE. GaN films doped with varying levels of Mg indicate effective mass acceptor at low doping concentrations, as determined from strong photoluminescence emission at about 380 nm. As the Mg concentration is increased the photoluminescence emission line red shifts considerably, indicating the formation of Mg-related or induced complexes whose lifetimes are relatively short. GaN/AlGaN separate confinement heterostructures grown on sapphire show strong near ultraviolet stimulated emission at room temperature in a side-pumping configuration. The pumping threshold for stimulated emission at room temperature was found to be $\sim 90 \text{ kW/cm}^2$. Initial GaN films grown on ZnO substrates show the A exciton in low temperature photoluminescence. ZnO is being considered for nitride growth because of its stacking order and close lattice match.

* On sabbatical leave at Wright Laboratory on a University Resident Research Program funded by AFOSR.

Introduction

Unlike Si and GaAs technologies, devices based on group-III nitrides are capable of operating at high temperatures and hostile environments as well as emitters and detectors for wavelengths shorter than green^{1,2,3,4}. Most notable of the group-III nitrides are AlN, GaN, InN and their alloys, which are all wide bandgap semiconductors. They crystallize in both wurtzite and zincblende polytypes, the former being the more stable phase. Wurtzitic GaN, AlN and InN have direct room temperature bandgaps of 3.4, 6.2, and 1.9 eV, respectively. The group-III nitrides thus formed span a continuous range of direct bandgap energies throughout much of the visible spectrum well into the ultraviolet wavelengths. This is one of the reasons fueling the recent interest in GaN, AlN, InN, and their tertiary alloys for short wavelength optoelectronic device applications. These optoelectronic devices, especially emitters such as the light emitting diodes (LEDs) and lasers, can be active in the yellow, green, blue, and ultraviolet (uv) wavelengths.⁵ LEDs have expanded remarkably not only in terms of the range of wavelengths of emission available, but also brightness^{6,7,8}. These LEDs have proved to be reliable and have applications, for example, in displays, lighting, indicator lights, advertisement, traffic signs and traffic signals, possibly light sources for accelerated photosynthesis, and medicine for diagnosis and treatment^{9,10,11,12,13,14,15}. As for coherent sources, they are crucial for high density optical read and write technologies. Because the diffraction limited optical storage density increases roughly quadratically as the probe laser wavelength is reduced, nitride based coherent sources at wavelengths down to uv are attracting a good deal of attention.

Many of the difficulties besetting nitrides have recently been overcome or are about to be overcome. Despite disappointing results early on, p-type conductivity has been achieved for GaN, AlN, and some of their alloys. On the metal contact front, specific contact resistivities have steadily dropped to below $10^{-7} \Omega\text{cm}^{-2}$. While the recent developments in GaN and related compounds have been truly breathtaking, further progress in this material system hinges on the reduction of defects which is closely tied to substrates. Ultimately, substrates with close lattice match and stacking order match to GaN or InGaN, most likely native substrates, may be necessary to achieve the potential performance. In this article we will discuss our recent effort in the growth and characterization of GaN and GaN/AlGaIn heterostructures.

Experimental

The structures were grown by Reactive MBE. The chamber pressure was kept at 2.5×10^{-5} Torr during film growth, and the substrate temperature was varied between 610 and 820 °C, which was monitored by a pyrometer focused on the surface of the growing film. Sapphire substrates were degreased with organic solvents, and etched in a hot solution of H_2SO_4 and H_3PO_4 ($\text{H}_2\text{SO}_4 : \text{H}_3\text{PO}_4 = 3 : 1$) for about 20 mins. They were then rinsed with deionized (DI) water and dried by blowing filtered nitrogen. Nitridation was performed by exposing sapphire substrates to a nitrogen flux for 5-15 mins. at 800 °C. Prior to the GaN growth, about 650 Å of AlN was grown on sapphire at a growth temperature of 800 °C. Note that this growth is decidedly different from that with the low temperature buffer layers employed in the MOCVD process.

Separate Confinement Heterostructures

The GaN/AlGaIn separate confinement heterostructure has a 600 Å thick AlN layer, directly grown on sapphire, followed by a GaN buffer layer, an AlGaIn cladding layer, a low mole fraction AlGaIn waveguide layer, a 70 Å thick GaN quantum well which is capped by a low mole fraction AlGaIn waveguide and an AlGaIn cladding layer. The quantum well was doped with Si to a level of $5 \times 10^{17} \text{ cm}^{-3}$. Samples having a size of $3 \times 1 \text{ mm}^2$ were cut and mounted on a sapphire heat sink, which were then attached to copper sample holders for optical pumping experiments.¹⁶ Under low-excitation, the room temperature spectra exhibit a relatively weak and broad emission feature with the peak position around 365 nm, and the emission intensity linearly increases with the excitation power density. As the excitation power density increases, a sharp narrow emission feature appears on the higher energy side of the spontaneous emission peak. The position of the maximum of this newly emerged emission feature is at ~361.5 nm. Its emission intensity increases super linearly with the excitation power. This new emission structure becomes the dominant feature as the pumping power density is further increased. Spectral narrowing, super linear increase in intensity with the excitation power density, as well as the complete suppression of the broad emission background, are characteristics of stimulated emission.

The onset of the steep rise of the emission intensity marks the threshold for stimulated emission. The pumping threshold for stimulated emission was determined to be ~90 kW/cm² for our GaN/AlGaIn SCH sample. The measured threshold value is approximately one order of magnitude less than our previously reported value for the GaN bulk-like films grown by metalorganic chemical vapor deposition.¹⁷ Generally, the threshold value can be affected by parameters which are dependent on the pumping source and quality of the sample and the facets. The specimens were just small pieces simply cut off from the large GaN/AlGaIn SCH wafer with no attempt to finesse the cut surfaces. Difficulties of forming high quality facets in sapphire are well known. This provides the basis for our optimism that the pumping power threshold for stimulated emission lasing in GaN can be lowered substantially with improved facets, possibly brought about by employing other substrates such as ZnO and spinel which are much more amenable to cleaved facet formation.

Mg Doped GaN

As in any wide bandgap semiconductor, p type doping in GaN and related materials is rather complex. In GaN for example, while the effective mass like acceptor is about 200 meV from the valence band, Mg doped GaN exhibits emission at centers which are about 0.5 eV above valence band when the Mg concentration exceeds a certain level. In optical spectra, two broad emission bands of about 290 (dominant for $T < 150$ K) and 550 meV (dominant for $T > 150$ K) below the band gap appear. Typical continuous-wave (CW) PL spectrum of p-type GaN layers at 10 K is dominated by a band at about 3.21 eV which nearly disappears for $T > 150$ K. As the temperature is increased above 150 K, a weak emission band at ~ 2.95 eV appears. Moreover, the peak position of the lower energy emission red shifts considerably as the Mg doping level is increased. At room temperature, the peak position of this lower energy emission band can be varied from 430 to about 700 nm.

In order to explore the physical origin of the observed emission lines, their dynamical behaviors have been studied.¹⁸ At low temperatures, PL decay is non exponential, but can be approximated by two exponential decay. The typical lifetime of the fast component which contributes 90 percent of the PL signal is about 0.6 ns, and the slow component is about 5.0 ns. In the temperature region $T < 150$ K where the 3.21 eV emission band dominates, the recombination lifetime decreases progressively from 0.6 to 0.3 ns as temperature increases from 10 to 140 K. This behavior can be accounted for by an increased nonradiative recombination rate at higher temperatures, caused by the nonradiative carrier transfer to the lower energy recombination channels. This is consistent with the observation of the thermal quenching of the 3.21 eV emission line and the subsequent increase in the emission intensity of the lower energy band at 2.95 eV with temperature.

In the higher temperature region ($T > 150$ K) where the lower energy emission band (~ 2.95 eV at $T < 150$ K) dominates, the fast decay component contributes nearly 95 percent of the PL signal and consequently the decay kinetics of PL are nearly single exponential. The temperature dependence of the recombination lifetime of the lower energy emission band indicates an increase with temperature reaching 0.3 at room temperature. This is due to the carrier transfer from the 3.21 eV recombination channel as discussed above.

The observed sub nanosecond PL recombination lifetimes suggest that the band- edge emissions in Mg-doped p-GaN result predominantly from the conduction band-to-impurity recombination, involving substitutional shallow Mg acceptors at low temperatures ($T < 150$ K) and Mg related deep level centers at high temperatures ($T > 150$ K). In such a context, the quenching of the 3.21 eV emission line is due to either thermal ionization of shallow neutral Mg acceptors or hole transfer from the shallow to the deep impurities as temperature increases.

GaN on ZnO

Lattice and thermal expansion mismatch between nitride films and the most frequently used substrates (SiC, sapphire) are often cited as one of the major causes of the observed extended and point defects. Inversion domain boundaries (IDB) and double positioning boundaries (DPB), have been identified as defects spreading into the bulk GaN layers^{19,20,21}, the former, being well known in III-V on Si (100) epitaxy,²² arise from an inversion transformation of a binary compound. If special care were taken to initiate growth with only one species, such as As, then IDB's would not form. However substrates invariably contain steps, and with single-species initiation the lattice inverts across each single step on Si (100) and produces an IDB. One solution for avoiding IDB's on Si (100), is by making double-stepped substrates. In the case of DPB's there is an equal probability of nucleating two different FCC stacking sequences (ABC and ACB), a topic treated recently by Sverdlov et al.²³ who also suggested that ZnO would be a better substrate to GaN and related materials because of its stacking match to nitrides under discussion.

Attempts have already been made to take advantage of the relatively small lattice mismatch between ZnO and GaN in that there have been several preliminary reports of GaN growth on ZnO and InGaN on ZnO with crystalline quality of InGaN to be superior when grown on the well matched ZnO substrate²⁴. ZnO substrates also would allow for the growth of lattice matched or coherently strained heterostructures for optoelectronic and electronic devices²⁵. In this paper we report on the optical emission and reflection properties of GaN grown on vicinal c plane ZnO substrates.

We have utilized ZnO substrates prepared by Litton industries by the hydrothermal method. The GaN layers were then grown at substrate temperatures of about 650 °C with a growth rate of 1 µm/hour. The optical transitions from the sample were studied by photoluminescence (PL) and optical reflection. The PL was excited with a He-Cd laser. The reflection source was a Xenon lamp. The reflection was measured at approximately 15° off normal incidence. The details of the measurement apparatus can be found elsewhere²⁶.

The PL spectra for the GaN samples show that the ground state exciton transition associated with the A band appears dominant. The exciton associated with the B-band is not seen in emission; however, it can be seen in reflection. In this experiment we did classical reflection; however, it is off normal incidence by approximately 15° as noted before. The minimum in the A reflection peak is shifted to the higher energy from the A emission peaks by approximately 7 meV. Although the work is its embryonic stage and high quality substrates are lacking, clean luminescence emission with only the A exciton present is very exciting. The observed energies of A and B excitons, the latter in reflection only, provide us with necessary information to deduce the sign and extent of strain in the film. Following a procedure employed previously^{27,28}, we calculate at T=4 K, the strain induced energy shift, ΔE , for GaN/ZnO is -3.8 meV while that for GaN/(6H SiC) is -6.7 meV, and for GaN/(a - Al₂O₃) is +9.3 meV. This should yield a difference of 13 meV in GaN grown on Sapphire and ZnO in the band gap energy. This compares with the observed 8 meV. This discrepancy may be due to several factors including the strain variation from sample to sample grown on sapphire substrates. What is certain is that more research is necessary before conclusive remarks can be made.

Conclusions

We have briefly described stimulated emission in GaN/AlGaIn separate confinement heterostructures, discussed the nature of Mg related transitions in lightly and heavily doped GaN, and preliminary growth experiments on ZnO substrates. Investigation of Mg doped GaN show an optical shallow level at 290 meV above the valence band for lightly doped samples. When the Mg concentration is increased past about 10¹⁹ cm⁻³ level, Mg-related complexes form deeper in the band, the width of which depends on concentration, form and dominate the high temperature luminescence. The transition to this complex is presently used in some commercial LEDs for producing blue light.

Acknowledgments.

The research at the university of Illinois is funded by grants from ONR, AFOSR and BMDO. We thank Mr. M. Yoder and Drs. G. L. Witt, K. Wu and J. Johnson for their interest and support. H. M. acknowledges Dr. G. McCoy at Wright Laboratory for his support.

References:

1. See, for example, See *Transactions of the First International High Temperature Electronics Conference*, June 10-20, Albuquerque, New Mexico, U.S.A., 1991.
2. H. Morkoç, S. Strite, G.B. Gao, M.E. Lin, B. Sverdlov, and M. Burns, *J. Appl. Phys. Rev.* **76**, 1363-1398 (1994). S. Strite and H. Morkoç, "GaN, AlN and InN: A Review," *J. Vac. Sci. & Technol B*, Vol. 10(4), pp. 1237-1266, 1992.
3. See, for example, D. Zook, and B. Goldenberg, in *Proceedings of International Conference on Silicon Carbide and Related Materials*, Nov. 1-3, 1993, Washington, DC, U.S.A., Eds. M.G.

- Spencer, R.P. Davaty, J.A. Edmond, M.A. Khan, R. Kaplan, and M. Rahman, *Institute of Physics Conference Series*, Number 137, 1994.
4. M.E. Lin, S. Strite, and H. Morkoç, in *The Encyclopedia of Advanced Materials*, Eds. D. Bloor, M.C. Fleming, R.I. Brook, S. Mahajan, Senior Ed. R.W. Cahn, pp. 79-86, Pergamon Press, 1994.
 5. S. Nakamura, M. Senoh, N. Isawa, and S. Nagahama, *Jpn. J. Appl. Phys.* **34**, Part 2, No. 10B, Oct 15 (1995) issue (in press); (c) S. Nakamura, M. Senoh, N. Isawa, and S. Nagahama, *Jpn. J. Appl. Phys.* **34**, Part 2, No. 7A, L795 (1995); (d) S. Nakamura, M. Senoh, N. Isawa, and S. Nagahama, *Jpn. J. Appl. Phys.* **34**, Part 2, No. 7A, L797 (1995).
 6. I. Akasaki and H. Amano, *Mater. Res. Soc. Fall Meeting*, Boston, MA, U.S.A., 1991.
 7. S. Nakamura, Technical Digest of the IEEE Electron Devices Meeting, pp. 567-570, Dec. 11-14, 1994, San Fransisco, CA, U.S.A.
 8. D.B. Eason, Z. Yu, W.C. Hughes, W.H. Roland, C. Boney, J.W. Cook, Jr., J.F. Schetzina, G. Cantwell, and W.C. Harsh, *Appl. Phys. Lett.* **65**, 115 (1995).
 9. M.E. Hoemecke, R.J. Bula, T.W. Tibbits, *HortScience* **27**, 427 (1992).
 10. K. Werner, *IEEE Spectrum* **31**, 30 (1994).
 11. M. G. Crawford, *IEEE Circuits & Devices Mag.* **8**, 24 (1992).
 12. R. Engelmann, *IEEE LEOS News Lett.* **8**, 6 (1994).
 13. H. Morkoç and S.N. Mohammad, *Science* **267**, 51 (1995).
 14. R. Engelmann, 3rd Progress Report to DOE Contract No. DE-AC01-89-CE23821, 17 June, 1994.
 15. See, for example, (a) S. Nakamura, *Research Concerning InGaN High-Brightness Blue LEDs* (published in Japanese), Corporate Report, 1994; (b) S. Nakamura, M. Senoh, N. Isawa, and S. Nagahama, *Jpn. J. Appl. Phys.* **34**, Part 2, No. 10B, Oct 15 (1995) issue (in press); (c) S. Nakamura, M. Senoh, N. Isawa, and S. Nagahama, *Jpn. J. Appl. Phys.* **34**, Part 2, No. 7A, L795 (1995); (d) S. Nakamura, M. Senoh, N. Isawa, and S. Nagahama, *Jpn. J. Appl. Phys.* **34**, Part 2, No. 7A, L797 (1995).
 16. T. J. Schmidt, X. H. Yang, W. Shan, J. J. Song, A. Salvador, W. Kim, Ö. Aktas, A. Botchkarev, and H. Morkoç, *Appl. Phys. Letts.* pending.
 17. X.H. Yang, T. Schmidt, W. Shan, J.J. Song, and B. Goldenberg, *Appl. Phys. Lett.* **66**, 1(1995).
 18. M. Smith, G. D. Chen, J. Y. Lin, H. X. Jiang, A. Salvador, W. Kim, Ö. Aktas, A. Botchkarev, H. Morkoç, and B. Goldenberg, *Appl. Phys. Letts.* pending.
 19. Z. Sitar, M. J. Paisley, B. Yan, R. F. Davis, *Mat. Res. Soc. Symp. Proc.* **162**, 537 (1990).
 20. S. N. Basu, T. Lei, T. D. Moustakas, *J. Mat. Res.* **9**, 2370 (1994).
 21. D. Smith, D. Chandrasekhar, B. N. Sverdlov, A. E. Botchkarev, and H. Morkoç, 2nd Workshop on GaN and Related Compounds in St. Louis, October 1994 (unpublished); *Appl. Phys. Lett.*, in press.
 22. S. Iyer, H. Morkoç, H. Zabel, and N. Otsuka, *Comments Cond. Mat. Phys* **15**, 1 (1989).
 23. G. M. Martin, S. V. Sverdlov and D. J. Smith, *Appl. Phys. Letts.* October 2, 1995.
 24. S. N. Mohammad and H. Morkoç, *Progress in Quantum Electronics*, in press.
 25. S. N. Mohammad, A. Salvador, and H. Morkoç, *Proc. IEEE* in press, October 1995.
 26. D. C. Reynolds and D. C. Look, W. Kim, Ö. Aktas, A. Botchkarev, A. Salvador, H. Morkoç, and D. N. Talwar, *Appl. Phys. Lett.* pending.
 27. A. Salvador, G. Liu, W. Kim, Ö. Aktas, A. Botchkarev and H. Morkoç, *Appl. Phys. Lett.* pending.
 28. H. Amano, K. Hiramatsu and I. Akasaki, *Jpn. J. Appl. Phys.* **27**, L1384 (1988).

Part VII
Optical Properties

GROWTH AND OPTICAL PROPERTIES OF GaN GROWN BY MBE ON NOVEL LATTICE-MATCHED OXIDE SUBSTRATES

J.F.H. NICHOLLS, H. GALLAGHER, B. HENDERSON, C. TRAGER-COWAN,
P.G. MIDDLETON and K.P. O'DONNELL*
T.S.CHENG and C.T. FOXON**
B.H.T. CHAI***

* Department of Physics, University of Strathclyde, Glasgow, UK.

** Department of Physics, University of Nottingham, Nottingham, UK.

*** Centre for Optics Research, University of Central Florida, Orlando, FL, USA.

ABSTRACT

In this paper we demonstrate the feasibility of growing III-N semiconductors on novel lattice-matched oxide substrates. Although the growth parameters are not yet optimal, acceptable GaN layers have been grown.

INTRODUCTION

The recent successes of III-N compound semiconductor light emitting diodes [1] point to the future use of these materials in displays, optical data storage, reprographics, underwater communications and so on. Their direct optical bandgaps span the UV-orange spectral region. They are mechanically robust, with high melting temperatures and good resistance to chemical attack. These materials offer several advantages over their main competitors, such as II-VI compounds and silicon carbide, in that they offer longer device lifetimes, higher efficiencies and higher powers. As yet, however, no laser diode based upon III-N semiconductors has yet been demonstrated, although this situation is ripe for change.

Among the problems which stand in the way of the realisation of a laser diode we may identify:

- (1) The very high density of structural imperfections, that may be described either as dislocations [2] or grain boundaries [3],
- (2) The relative difficulty of p-doping, ascribed to acceptor passivation,
- (3) The presence of an uncontrolled deep centre, that contributes to a strong yellow luminescence band in competition with the bandedge emission [4].

All of these problems relate, to a greater or lesser extent, to the lattice mismatch that exists in all cases between the III-N epilayer or heterostructure and the underlying substrate. The purpose of this contribution is to advocate the use of some novel oxide substrates for the epitaxial growth of GaN and its III-N alloys. Table 1 compares the structural properties of several III-N compounds with those of the substrates that may be used for III-N epitaxy. It is clear that the lithium salts offer much better lattice matching than any of the conventional substrates. In addition, they have comparable coefficients of

thermal expansion. This is necessary to preserve lattice matching at the high growth temperatures used for widegap III-V materials.

Crystal	Band Gap (eV)	a-axis (nm)	Mismatch %	Thermal (10^{-6} /K)
AlN	6.20	0.3112	-2.10	4.2
GaN	4.20	0.3180	-	5.6
InN	1.95	0.32530	2.30	---
LiAlO ₂	6.20	0.3134	-1.45	7.5
LiGaO ₂	4.20	0.3186	+0.19	7
Li ₂ GeO ₃	5.35	0.3203	-0.16	---
Al ₂ O ₃	8.70	0.3476	9.30	7.5
ZnO	5.60	0.3252	2.26	2.9
6H-SiC	3.70	0.3080	3.14	---

Table 1: structural properties of III-N compounds and substrates.

In terms of crystal structure, lithium aluminate (LiAlO₂) is tetragonal, while the gallate and germanate are orthorhombic. These compounds all feature purely tetrahedral bonding, so that they may be said to be "structure-matched" as well as lattice-matched to both the wurtzite and cubic forms of the III-N semiconductors. In addition, they are all widegap materials with high transparency in the ultraviolet spectral region. Finally, the germanate is particularly interesting for laser applications because of its strong cleavage normal to the direction of growth (c-axis).

SAMPLE GROWTH

The melting points of the aluminate, gallate and germanate are 1275 °C, 1600 °C and 1700 °C, respectively. At the Optical Materials Centre in the University of Strathclyde, Li₂GeO₃ and LiGaO₂ were grown by the Czochralski technique using an induction heated furnace. The crystals were grown in a nitrogen atmosphere from a melt contained in an iridium crucible. Seed material was obtained by spontaneously nucleating a stoichiometric melt. The crystal growth furnace employs power/crystal weight feedback to control the

growth rate. The optimum growth conditions for both the germanate and gallate was found to be a translation rate of 1-2 mm per hour and a rotation rate of 20-30 rpm.

GaN layers were deposited on the gallate substrate at the University of Nottingham. The gallate substrate was degreased using standard solvents and rinsed in DI water. It was etched in a solution of (1:1) sulphuric + phosphoric acid mixture for 5-10mins at 80 degrees before insertion into the MBE system. The dedicated MBE system, featuring a nitrogen RF activated plasma source adapted for III-N growth, has been described elsewhere [5]. The substrate was thermally heated to the growth temperature of 630 degree C and nitrided for 30mins. The surface was continuously monitored throughout the growth using in-situ Reflection High Energy Electron Diffraction (RHEED).

SAMPLE CHARACTERISATION

The good crystal match between substrate and epilayer is shown by the powder diffraction spectrum reproduced in Figure 1.

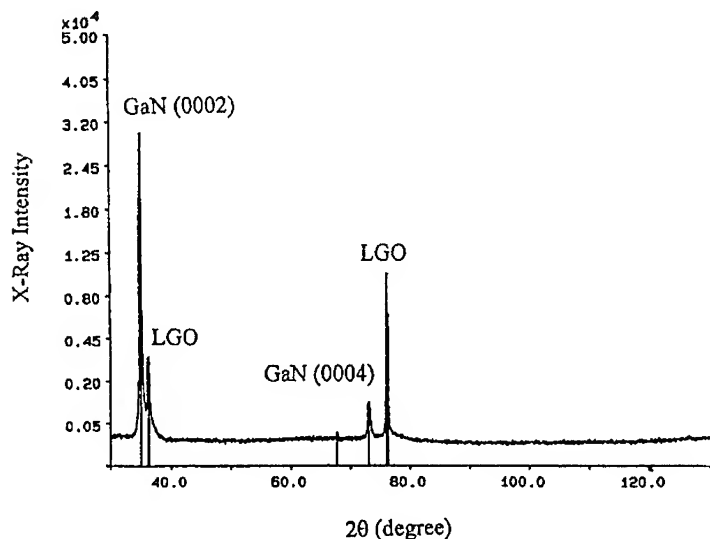


fig 1 Powder diffraction spectrum of GaN grown on LiGaO₂

Figure 2 compares a typical photoluminescence (PL) spectrum obtained from a layer grown on gallate at room temperature with one obtained from a layer grown on a sapphire substrate under comparable conditions. There are several features to note. The bandedge features appear broad and structured in the sample grown on gallate; the yellow band is

however much weaker; a new band appears near 490 nm. The origin of these features is still under investigation.

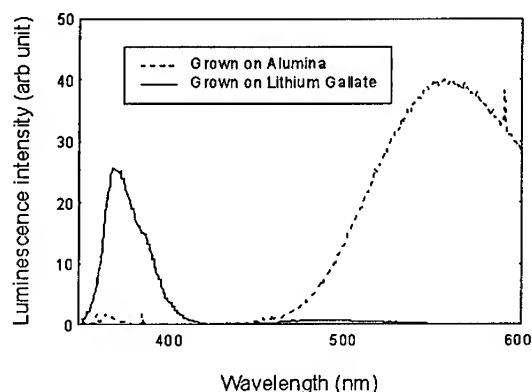


fig 2: Comparing PL spectra of GaN layers grown on different substrates.

Cathodoluminescence (CL) spectroscopy of a typical layer reveals a similar spectrum to PL, showing a strong band-edge feature and a weaker deep band. By monitoring the luminescence intensity as the electron beam is rastered over the sample surface, a cathodoluminescence image is formed. Figure 3 shows such an image obtained using light centred at 380 nm with a pass band of 5 nm. The lack of discernible structure in this image is actually a good sign: it indicates good homogeneity of the emitting surface and a lack of the distinguishable crystalite formation which is a feature of some GaN growth [3].

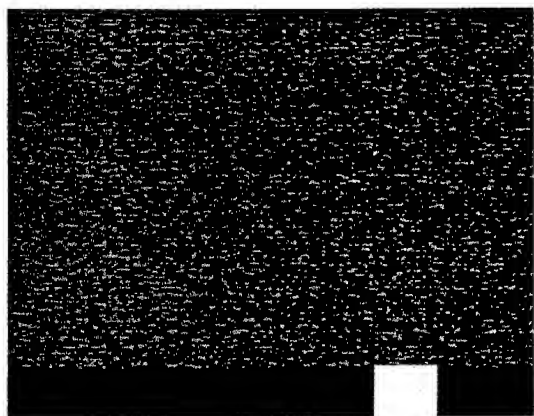


fig. 3: CL image of GaN layer at 380 nm. The light bar represents 40 μm .

SUMMARY

Our preliminary results confirm the feasibility of III-N growth on novel oxide substrates that are both lattice- and structure-matched to the epilayers. Among the benefits that are apparent from this exploratory work, we highlight the suppression of both the microcrystal formation and the impurity-related deep emission.

ACKNOWLEDGMENTS.

This work was partially supported by UK EPSRC grants.

REFERENCES

- [1] S. Nakamura, T. Mukai and M. Senoh, *Appl. Phys. Lett.* **64**, 1687-1689 (1994).
- [2] S.D. Lester, F.A. Ponce, M.G. Craford and D.A. Steigerwald, *Appl. Phys. Lett.* **66**, 1249-1251 (1995).
- [3] C. Trager-Cowan, K.P. O'Donnell, S.E. Hooper and C.T. Foxon, To be published in *Appl. Phys. Lett.* (Jan 15, 1996).
- [4] T.A. Kennedy, E.R. Glaser, J.A. Freitas, W.E. Carlos, M.A. Khan and D.K. Wickenden, *J. Electron. Mat.*, **24**, 219-223 (1995)
- [5] C.T. Foxon, T.S. Cheng, S.V. Novikov, D.E. Lacklison, L.C. Jenkins, D. Johnston, J.W. Orton, S.E. Hooper, N. Baba-Ali, T.L. Tansley and V.V. Tret'yakov, *Journal of Crystal Growth*, **150** (1995) 892-896

ELECTROREFLECTANCE FROM GALLIUM NITRIDE USING SECOND-HARMONIC GENERATION

JOSEPH MIRAGLIOTTA AND DENNIS K. WICKENDEN

The Johns Hopkins University, Applied Physics Laboratory, Johns Hopkins Road, Laurel, MD 20723-6099

ABSTRACT

The optical second-harmonic (SH) response of a reverse biased gallium nitride (GaN) film was investigated for SH photon energies near the fundamental absorption edge. With the application of a DC electric field (~ 100 to 220 kV/cm) along the optical axis of the sample, a strong two-photon resonance was observed in the specular reflected SH signal. This resonance was attributed to electric-field induced SH generation, EFISH, a third-order nonlinear response which arises from an induced polarization that is linearly dependent on the amplitude of the DC field. The EFISH contribution was spectrally localized at the bandedge, demonstrating the potential of SH spectroscopy for analysis of critical points in the band structure of semiconductors.

INTRODUCTION

It has been recognized since the early 1960's that the application of a DC electric field can perturb the linear and nonlinear optical properties of a semiconductor crystal. This principle is the basis of many forms of optical spectroscopy where field-induced variations are generally enhanced near critical point energies in the joint density of states (JDOS) [1]. In linear electroreflectance (ER) spectroscopy, dielectric variations are generally on the order 10^{-3} of the unperturbed function when a DC electric field of 100 to 500 kV/cm is applied to the space-charge region of the semiconductor. Interestingly, Aspnes and co-workers [2,3] have shown that the low-field limit of linear ER can be represented as a third-order nonlinear phenomena which involves the coupling of two DC fields and one optical field with the third-order susceptibility. This mixing process induces a nonlinear electric polarization at the same frequency of the incident optical source which then generates a variation in the linear dielectric function.

A similar DC field-dependent nonlinear phenomena that arises in semiconductors is electric-field induced second-harmonic generation, i.e., EFISH. Unlike the linear ER process, the nonlinear response is a result of the coupling of two optical fields of frequency ω and one DC field so as to generate a second-harmonic (2ω) polarization that is linearly dependent on the applied DC field [4-6]. The EFISH signal has been shown to be enhanced near electronic transitions such as critical point resonances in the JDOS of one-dimensional semiconductor systems [7]. Although EFISH offers the potential for spectroscopic studies of semiconductors, investigations using this 2ω response have been limited to single-wavelength investigations of bulk materials [8-10].

In this paper, we demonstrate that the EFISH response from a n-type GaN film can be resonantly enhanced when the photon energy of the SH field is tuned through the direct fundamental absorption edge (E_0 critical point). The EFISH response was found to be similar to linear ER measurements in that the field-induced signal at 2ω was localized at the E_0 critical point. The magnitude of the EFISH signal exceeded the 2ω contribution from the intrinsic second-order nonlinearity when a field on the order of 10^5 V/cm was applied to the GaN surface. As such, the sharp field-induced SH resonance at the bandedge was easily observed in either differential or absolute intensity measurements.

EXPERIMENTAL PROCEDURE

The GaN sample was grown on sapphire using metal organic chemical vapor deposition [11]. The as-grown single-crystal film was oriented with the (0001) surface parallel to the (0001) surface of the substrate with a 30° azimuthal rotation of the GaN layer with respect to the underlying sapphire substrate as verified by x-ray diffraction.

A DC electric field was applied to the GaN sample by placing the semiconductor film in contact with an HCl aqueous solution. The DC potential difference and field strength in the GaN space-charge region were controlled with a standard potentiostat in a three-electrode quartz cell using a Pt counter electrode and a saturated calomel reference electrode (SCE).

The nanosecond pulse, tunable dye laser source used for the SH measurements has been previously described in the literature [12]. Linearly s-polarized radiation was incident at an angle of 45° to the GaN/electrolyte interface so as to generate a specularly reflected p-polarized SH signal. Typical incident power densities at the GaN surface were kept below 1 MW/cm² so as to minimize sub-bandgap photocarrier generation from possible deep-level traps in the GaN sample. The reflected signal at 2ω was detected with a high-gain photomultiplier tube (PMT) and analyzed with a gated integrator. The SH nature of the signal was verified by demonstrating its quadratic dependence to the incident light intensity.

Linear ER measurements were performed using s-polarized light from a xenon lamp that was transmitted through a monochromator and focused onto the GaN/electrolyte interface at an angle of 45°. The DC electric field in the depletion layer was modulated between the flatband (zero field) and a reverse bias condition by superimposing an AC square-wave voltage (220 Hz) on the DC potential. After detection with a PMT, the AC component of the reflected light was analyzed with a lock-in amplifier and normalized to the zero DC field reflectance.

EXPERIMENTAL RESULTS

Prior to the optical investigations, the DC field characteristics of the n-type GaN film ($N_d \sim 3 \times 10^{17} \text{ cm}^{-3}$) were analyzed with a series of AC capacitance measurements. In these electrical

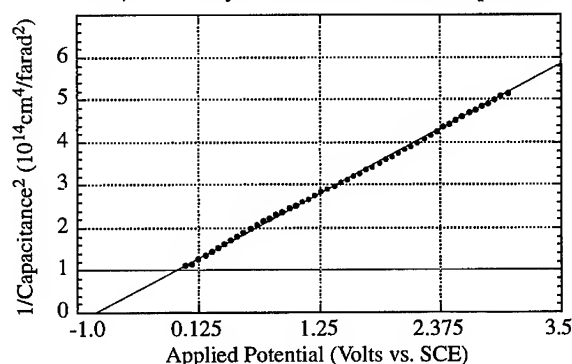


Figure 1. Mott-Schottky plot for a GaN sample in 0.1 M HCl aqueous solution. Solid line is a linear fit to the experimental data (solid circles).

measurements, the AC current response to a 3 kHz, 10 mV r.m.s. AC voltage (superimposed on the DC applied potential) was analyzed with a two-phase lock-in amplifier. The GaN/electrolyte interface was modeled as a simple RC series circuit, where the semiconductor space-charge was considered the dominant capacitance relative to the solution phase [13]. The depletion layer capacitance was de-convoluted from the AC current and plotted in a Mott-Schottky format as shown in Figure 1. The linear behavior is characteristic of a well-behaved depletion layer.

The spectra in Figure 2 show the SH reflected intensity from the GaN/electrolyte interface

for various reverse bias potentials. The flatband spectrum, Figure 2a, exhibited weak dispersion in the SH photon energy range above the bandedge which was consistent with previous measurements of $\chi^{(2)}$ in wurtzite GaN [14]. The SH profile below the bandedge (dashed line) was found to be dependent on film thickness and incident angle due to the phase-velocity

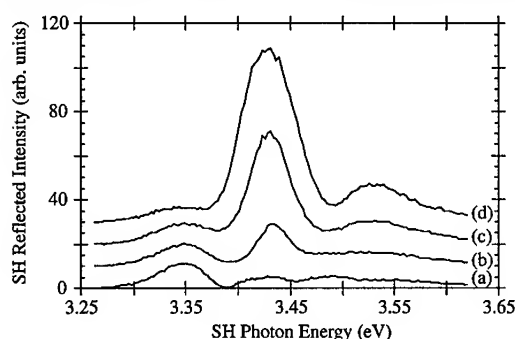


Figure 2. Reflected SH intensity from an electrolyte/GaN interface for a bias of (a) 0.0, (b) 0.1, (c) 0.25, and (d) 0.5V relative to the flatband.

interference between the nonlinear source polarization and the generated SH field. Under reverse bias conditions (Figure 2b-d), a narrow resonance appeared in the SH intensity at a photon energy of 3.43 eV and a linewidth of ~50 meV. A weak secondary feature appeared near 3.53 eV as the applied potential was increased to 0.5V. Both resonant features were observed to increase linearly in amplitude as the surface field was increased from 100 to 225 kV/cm with a slight broadening in the linewidth.

The resonances in the SH spectra were more noticeable when the optical measurements were performed in a differential rather than absolute detection mode. In the differential measurements, the applied bias to the GaN sample was modulated at a repetition rate of 5 Hz so as to vary the surface DC field from the flatband value to DC fields in the range of 100 to 225 kV/cm. Field modulation and laser repetition were synchronized to insure sample illumination during both the flatband and reverse bias conditions. At the end of each potential cycle, the difference between the reverse bias and flatband signals was normalized to the flatband response. Figure 3 shows the SH differential results for three different modulation potentials. In each scan, the differential signal was characterized by two positive peaks that were consistent with the location and linewidth of the EFISH resonance in the Fig. 2 spectra.

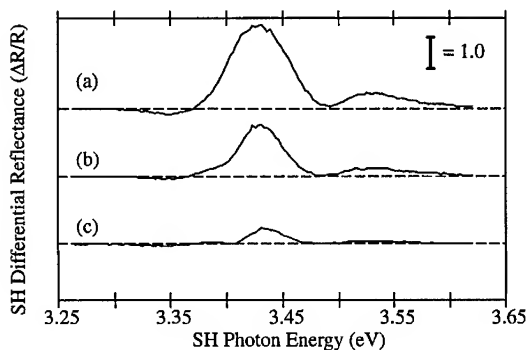


Figure 3. Differential SH reflectance from an electrolyte/GaN interface for a potential modulation of (a) 0.1, (b) 0.25, and (c) 0.5V relative to the flatband.

In addition to the SH measurements, differential linear ER spectra ($\omega_{in} - \omega_{out}$) were recorded near the E_0 critical point for the same range of applied DC fields as used in the SH scans of Figure 3. In Figure 4, the negative peak associated with the E_0 optical resonance exhibited a slight broadening in linewidth and shift to

lower energies as the applied DC field was increased in the GaN depletion layer. Reflectance variations were observed to be on the order of 10^{-2} to 10^{-3} . Typical of linear ER measurements, Franz-Keldysh oscillations (FKO) were observed at photon energies above the bandedge with a period that increased with increasing DC field.

THEORY AND DISCUSSION

In the case of GaN, the 2ω polarization response from an electrified sample is a superposition of the intrinsic second- and DC field-dependent third-order nonlinear contribution. Under electrochemical control, the DC field in the GaN sample was directed along the optical

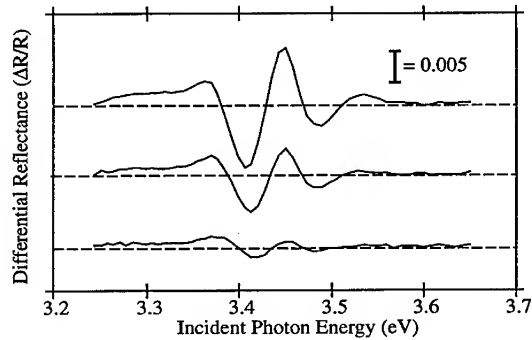


Figure 4. Linear differential reflectance spectra from an electrolyte/GaN interface for a potential modulation of (a) 0.1, (b) 0.25, and (c) 0.5 V relative to the flatband.

axis of the crystal which corresponded to the surface normal of the sample. The x-y plane of the crystal was rotated about the optical axis until the plane of incidence coincided with the x-z-plane of the crystal. With the sample in this orientation, s-polarized incident light (along the y-axis of the crystal) generates a nonlinear polarization along the optical axis (p-polarized) with the following form:

$$P_z^{nl}(z, 2\omega) = \chi_{eff}^{nl}(z) E_y^2(z, \omega) \quad (1a)$$

where the effective nonlinearity $\chi_{eff}^{nl}(z)$ is given by [15]:

$$\chi_{eff}^{nl}(z) = \chi_{zyy}^{(2)}(-2\omega; \omega, \omega) + 3\chi_{zyyz}^{(3)}(-2\omega; \omega, \omega, 0)E_s(z) \quad (1b).$$

In these two expressions, $E_y(z, \omega)$ is the y component of the fundamental field, $E_s(z)$ is the DC field directed along the optical axis, and $\chi^{(2)}$ and $\chi^{(3)}$ are the second- and third-order nonlinear susceptibility tensors, respectively.

The reflected SH intensity from the GaN sample is dependent upon the product of the nonlinear polarization and its conjugate:

$$I_{SH} \rightarrow P_z^{nl}(z, 2\omega)^* P_z^{nl}(z, 2\omega) \quad (2a)$$

$$= |\chi_{zyy}^{(2)}|^2 + |3\chi_{zyyz}^{(3)}E_s(z)|^2 + 6E_s(z) |\chi_{zyyz}^{(3)} \chi_{zyy}^{(2)}| \cos\psi \quad (2b).$$

The effect of the EFISH contribution on the total SH signal will depend on the relative phase difference (ψ) and magnitudes between the second- and third-order susceptibilities as well as the sign of the DC field in the depletion layer. The SH results in Figures 2 and 3 showed that the EFISH term in Eq. (1b) was clearly the dominant 2ω term when DC fields on the order of 100 kV/cm are applied to the GaN sample. However, the spectroscopic nature of the phase difference between the second- and third-order terms has not been examined in earlier investigations. The two SH resonances in Figures 2 and 3 may, in fact, arise from a wavelength dependent phase difference between $\chi^{(2)}$ and $\chi^{(3)}$. Further SH studies are needed to determine the role of the phase difference on the spectral lineshape at critical point transitions.

A comparison of the flatband SH response with the EFISH contribution in Figure 2

shows that the dispersion of $\chi_{zyz}^{(3)}$ is narrower than the corresponding response of $\chi_{zyy}^{(2)}$ in the bandedge region. Previous band structure calculations of $\chi^{(2)}$ for bulk cubic zincblende III-V and II-VI semiconductors near E_0 critical point in the JDOS have shown that the second-order nonlinearity, which is proportional to the product of three dipole-matrix elements, has the following form [16,17]:

$$\chi_{zyy}^{(2)} \propto \frac{\langle \psi_i^y | z | \psi_n^c \rangle \langle \psi_n^c | y | \psi_m^c \rangle \langle \psi_m^c | y | \psi_j^y \rangle}{(\omega_{ni} - 2\omega - i\gamma_{ni})(\omega_{ml} - \omega - i\gamma_{ml})} \quad (3).$$

where ψ_i^y and ψ_j^y are the wavefunctions for the i^{th} and j^{th} valence and conduction band, ω_{ij} is the energy separation and γ_{ij} is the broadening parameter for the i to j transition. The summation in this expression is over the valence band (index l), and the conduction band (indices n and m). As is evident from this expression, the second-order nonlinearity is resonantly enhanced when either ω or 2ω is the frequency difference between two single-particle states (valence or conduction bands). Since the SH experiments on GaN were performed with $2\hbar\omega \sim E_{\text{gap}}$, the 2ω response should exhibit a single resonance in the bandedge region since other interband transitions (E_1 critical point) are at least 4 eV above the fundamental gap. Previous SH transmission measurements of GaN [14] have shown that $\chi^{(2)}$ exhibits weak dispersion near the bandedge region with only a slight increase in amplitude at the bandedge. Therefore, the sharp resonance in the SH response of Figures 2 and 3 is unlikely due to the intrinsic $\chi^{(2)}$ response.

In regards to the third-order susceptibility, a number of recent calculations by Tsang et al. on the EFISH effect in semiconductor quantum-wells have predicted a significant field-induced enhancement in the SH nonlinearity of GaAs/Al_xGaAs_{1-x} structures [19]. In general, $\chi^{(3)}$ is proportional to the product of four dipole-matrix elements and is dominated by "three-state" processes which involve simultaneous interband transitions between the valence and conduction bands [16,18]. In this process, the dipole-matrix elements is proportional to the following expression:

$$\chi_{zyyz}^{(3)} \propto \frac{\langle \psi_i^y | z | \psi_n^c \rangle \langle \psi_n^c | y | \psi_l^v \rangle \langle \psi_l^v | y | \psi_m^c \rangle \langle \psi_m^c | z | \psi_j^y \rangle}{(\omega_{vi} - 2\omega - i\gamma_{vi})(\omega_{nl} - 2\omega - i\gamma_{nl})(\omega_{ml} - \omega - i\gamma_{ml})} \quad (4)$$

when the 2ω photon energy is close to a resonance in the GaN band structure. The parameters in Eq. (4) are similarly defined as for the parameters in Eq. (3). Eq. (3) shows that the 2ω resonance in the EFISH signal is inversely proportional to the square of $(E_{2\omega} - E_{\text{gap}})$ when SH photon energy is near the bandedge ($\omega_{vi} = \omega_{nl} \sim \omega_{\text{gap}}$). A resonant response of this form will exhibit narrower dispersion near the fundamental bandedge relative to the second-order resonance in Eq. (3) provided the resonance has minimal overlap with other critical point transitions. Experimentally, the narrow resonance in Figures 2 and 3 supports the conclusion that the third-order nonlinear response is the dominant contribution to the 2ω signal since the majority of the field-induced SH variations were localized within $\sim \pm 0.1$ eV of the E_0 critical-point.

Finally, a comparison of the differential ER spectra at 2ω and ω (Figures 3 and 4, respectively) show that the field-induced response in the linear and nonlinear cases are spectrally localized at the E_0 critical point energy. The two optical responses exhibit different lineshape profiles, but both techniques are characterized by minimal broadening and position shifts with DC fields in the 100 to 225 kV/cm region. In the 2ω case, the field-induced contribution exceeded the intrinsic second-order response by over 100% with surface DC fields on the order of 10^5 V/cm. Under similar field conditions, ΔR values of $\sim 10^{-3}$ were observed in the linear ER data. Interestingly, linear refractive index variations as determined from the ΔR spectra in

Figure 4 were found to produce variations in the 2ω signal that were 3 to 4 orders of magnitude below the >100 % increase observed in the spectra of Figs. 2 and 3. This confirmed that the narrow resonance in the SH spectra was due to the resonant behavior of $\chi^{(3)}$ and not from the field-induced dielectric variations of the linear ER spectra.

In summary, we have measured the DC field-induced contribution to the SH response near the fundamental bandedge in wurtzite GaN on sapphire. The 2ω signal near E_{gap} was dominated by a third-order nonlinearity, EFISH, when a DC field of ~ 100 kV/cm was applied to the space-charge region of the sample. The sharp resonance (~ 50 meV linewidth) at this critical point suggests that SH spectroscopy may be a useful probe of the electronic band structure of semiconductor materials.

REFERENCES

1. B. O. Seraphin, in *Proceedings of the Seventh International Conference on the Physics of Semiconductors*, edited by M. Hulin (Dunod, Paris, 1964), p. 165.
2. D. E. Aspnes and J. E. Rowe, *Phys. Rev.* **B5**, 4022 (1972).
3. D. E. Aspnes and A. A. Studna, *Phys. Rev.* **B7**, 4605, (1973).
4. C. H. Lee, R. K. Chang, and N. Bloembergen, *Phys. Rev. Lett.* **18**, 167 (1967).
5. B. F. Levine and C. G. Bethea, *J. Chem. Phys.* **65**, 2429 (1976).
6. K. D. Singer and A. F. Garito, *J. Chem. Phys.* **75**, 3572 (1981).
7. H. Kishida, T. Hasegawa, Y. Iwasa, T. Koda, Y. Tokura, H. Tachibana, M. Matsumoto, S. Wada, T. T. Lay, and H. Tashiro, *Phys. Rev.* **B50**, 7786 (1994)).
8. J. Qi, M. S. Yeganeh, I. Koltover, A. G. Yodh, and W. M. Theis, *Phys. Rev. Lett.* **71** (1993).
9. J. M. Lantz and R. M. Corn, *J. Phys. Chem.* **98**, 4899 (1994).
10. O. A. Aktsipetrov, A. A. Fedyanin, V. N. Golovkina, and T. V. Murzina, *Optics Letters* **19**, 1450 (1994).
11. D. K. Wickenden, T. J. Kistenmacher, W. A. Bryden, J. S. Morgan, and A. Estes-Wickenden, *Mat. Res. Soc. Symp. Proc.* **221**, 167 (1991).
12. J. Miragliotta and D. K. Wickenden, *Phys. Rev.* **B50**, 14960, (1994).
13. J. Schefold, *J. Electrochem. Soc.* **139**, 2862 (1992).
14. J. Miragliotta, W. A. Bryden, T. J. Kistenmacher, and D. K. Wickenden, *Mat. Res. Soc. Symp. Proc.* **339**, 465 (1994).
15. R. Boyd, *Nonlinear Optics*, (Academic Press, 1992), Chap. 1.
16. E. Ghahramani, D. J. Moss, and J. E. Sipe, *Phys. Rev.* **B43**, 9700 (1991).
17. E. Ghahramani, D. J. Moss, and J. E. Sipe, *Phys. Rev.* **B43**, 8990 (1991).
18. D. J. Moss, E. Ghahramani, J. Sipe, and H. M. van Driel, *Phys. Rev.* **B41**, 1542 (1990).
19. L. Tsang, S.-L. Chuang, and S. M. Lee, *Phys. Rev.* **B41**, 5942 (1990).

OPTICAL PROPERTIES OF WURTZITE-AND ZINCBLENDE-GaN FILMS GROWN BY RF PLASMA-MBE

F. SEMENDY*, N. BAMBHA*, J.G. KIM**, H. LIU**, AND R.M. PARK**

* Army Research Laboratory, Fort Belvoir, VA 22060, fsemendy@nvl.army.mil

** Department of Material Science and Engineering, University of Florida, FL 32611

ABSTRACT

Both wurtzite-and zincblende-GaN films have been grown on sapphire and MgO substrates, respectively, and examined by photoluminescence and x-ray analysis. GaN films were grown on suitably prepared Al_2O_3 and MgO substrates by molecular beam epitaxy employing a rf plasma discharge, nitrogen free radical source. The wurtzite-and zincblende-GaN films exhibited dominant near band-edge emission, the nature of which will be compared and contrasted for both phases in this paper. X-ray diffraction data for both phases will also be discussed.

INTRODUCTION

GaN and related materials are considered to be excellent materials for applications of optoelectronic devices that operate in the near-UV as well as in the visible regions with appropriate bandgap modifications. GaN and its solid solutions such as AlGaN and InGaN have been used in the development of ultraviolet sensors,¹ blue light emitting diodes², photodetectors³, and heterostructure field-effect transistors⁴ and optical pumping structures⁵. In all cases wurtzitic materials are used for device structures. However, these hexagonal materials are difficult to cleave and hence lasing action in an appropriate structure may be difficult to obtain. Furthermore p-doping in the α -GaN is rather difficult. Zincblende GaN (β -GaN), which is thermodynamically metastable phase of GaN, is thought to be easier to cleave and p-dope.

With the current success in making long lasting blue light emitting devices using GaN, its detailed optical behavior in both α and β phases should be studied under varying conditions. Significant knowledge is available on α -GaN,^{6,7} whereas data on zincblende GaN particularly grown on MgO are scarce^{8,9}. Optical properties of cubic and hexagonal GaN in the regions of the fundamental gaps were studied by J. Petalas *et al*¹ who found that the gap of hexagonal GaN is larger than that of the cubic polytype.

EXPERIMENTAL

Film-growth experiments were carried out in a Varian Gen II MBE system with a base pressure of 10^{-10} Torr range. The substrates used in this work were highly polished Al_2O_3 (0001), and MgO (001) wafers of 1 cm. square. Both types of substrates were degreased in successive rinsing of trichloroethane, acetone, methanol, and isopropyl alcohol. The Al_2O_3 wafers were then etched in hot (160°C) 3:1 H_2SO_4 : H_3PO_4 . The samples were dried by blowing dry nitrogen and mounted on a strain-free MO holder, and then inserted into the vacuum system. The substrates were heated to $\sim 730^\circ\text{C}$ for 30 minutes. Sharp lines (1x1) were observed in the RHEED pattern. Growth temperature was between 650°C to 700°C for both of these substrates. Fig.1 shows the MBE chamber with rf plasma source.

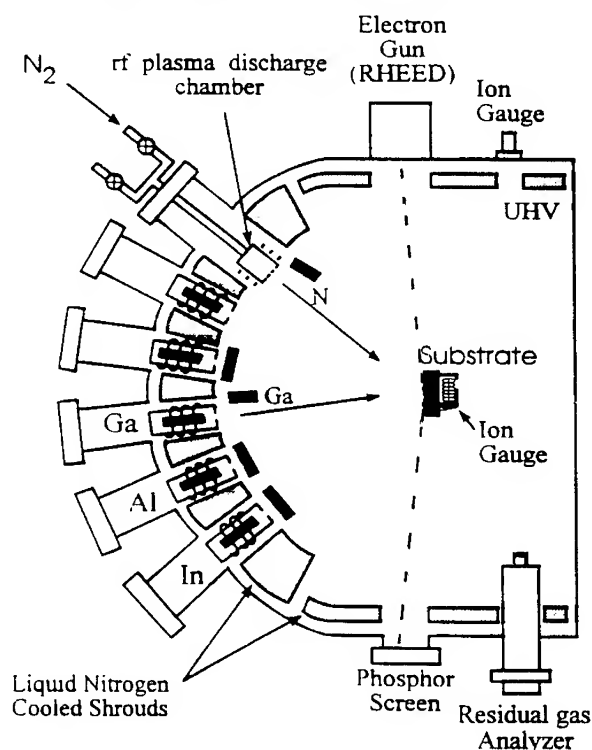


FIG. 1. Schematic of rf plasma MBE system used to grow α -GaN and β -GaN films.

The source of nitrogen in this MBE system is a rf plasma discharge, free-radical source manufactured by Oxford Applied Research (OAR). Active nitrogen plasma was generated by inductively coupling 13.56 MHz rf energy into a small cylindrical pyrolytic boron nitride (PBN) discharge chamber supplied with ultrapure nitrogen gas. The PBN discharge tube is surrounded by a water-cooled rf coil and the N_2 gas is fed into the tube via an entry hole at one end of the tube while a PBN disk with several small holes (0.3mm)

serves as the exit plate and permits a fraction of the active nitrogen species to diffuse out of the discharge chamber towards the substrate inside the MBE growth chamber. In this work, the forward power supplied to the discharge chamber in the source was 320 W for α -GaN and 200W for β -GaN, the reflected power being <2 W as established by an on-board manual tuning network. A Si photodiode which has on-axis line-of-sight vision monitors the integrated intensity of the plasma emission, the measured intensity being dependent on both rf power and N_2 pressure in the chamber. In this work, the Si photodiode output was maintained at a constant value of 350 mV for α -GaN and 150 mV for β -GaN which was obtained by establishing an equilibrium N_2 background pressure in the MBE growth chamber typically around 10^{-5} Torr. The active nitrogen in the chamber was characterized using molecular emission spectroscopy. A previous study had indicated that a significant concentrations of nitrogen atoms in both the ground and excited states was present in the active nitrogen plasma.⁹

As-deposited GaN films were analyzed *in situ* by RHEED and, following deposition, by XRD and room temperature photoluminescence. For the experiment reported, a Philips 5-crystal high resolution x-ray diffractometer was operated in the Ω -2 θ mode, with the detector rotation being twice the sample rotation.

The photoluminescence measurements were performed at room temperature. A 325 nm He-Cd laser with a power of 50 mW and focused beam size of 0.5mm was used as the excitation source for the measurements. The α -GaN and β -GaN films were 2 μ m and 3 μ m thick, respectively.

RESULTS AND DISCUSSION

Films grown on Al_2O_3 (0001), and MgO (001) were single crystals. RHEED and XRD results showed that the films grown on sapphire were wurtzite, grown on MgO was zinc-blende. RHEED patterns obtained during growth were sharp (1x1) for both α -GaN and β -GaN films. The growth rate in both cases was between 0.3 - 0.4 μ m/hr. Figures 2 and figure 3 show the XRD diffraction patterns obtained from α -GaN grown on Al_2O_3 (0001) at $T_g \sim 720$ °C and β -GaN grown on MgO at $T_g \sim 650$ °C respectively. As can be seen from the figure 2, peaks associated with (002) hexagonal GaN and (006) sapphire reflections are evident in the spectrum.

X-ray measurements provided FWHM for the substrate sapphire for α -GaN was about 10 arc seconds for the epi layer, it was close to 7 arc minutes. In figure 3 peaks associated with (002) cubic GaN and (002) MgO reflections are evident. The FWHM for the substrate was about 60 arc seconds whereas for the β -GaN the FWHM was found to about 17 arc minutes.

Figure 4 and 5 illustrate the room temperature PL spectrum of α -GaN grown on Al_2O_3 (0001) and β -GaN grown on MgO (001). In the case of hexagonal GaN as indicated in fig. 4 the dominant peak is at 364 nm (3.41 eV) with an additional small peak at 590 nm. In the case of the cubic GaN, the peak is at 384 nm (3.23 eV) with additional shoulders indicating the nature of the crystal structure. At present there is some dispute as to the magnitude of zincblende GaN bandgap. There are various claims^{5,10} that

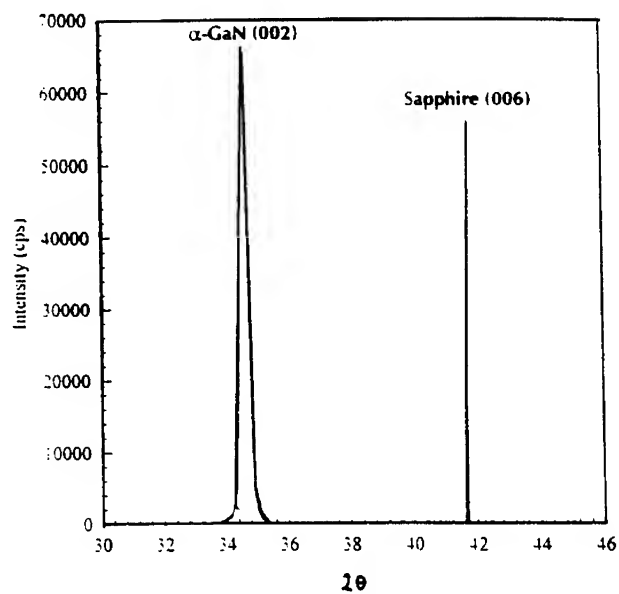


FIG. 2. X-ray diffraction pattern of GaN epilayers on Sapphire (0001)

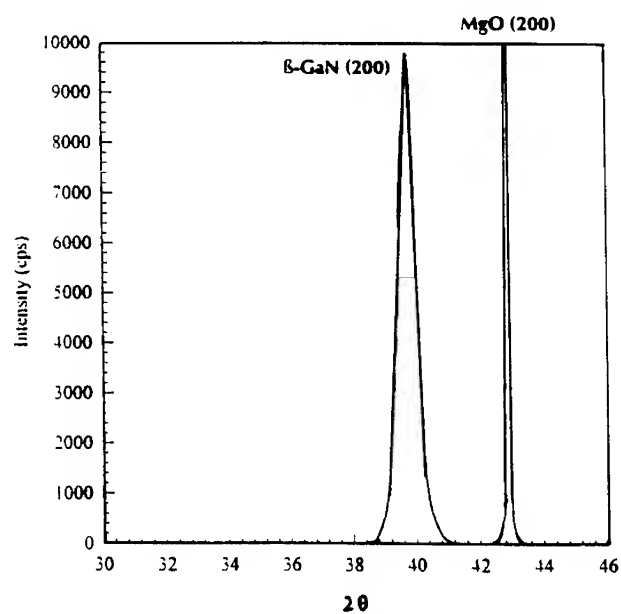


FIG. 3. X-ray diffraction patterns of GaN epilayer on MgO (001)

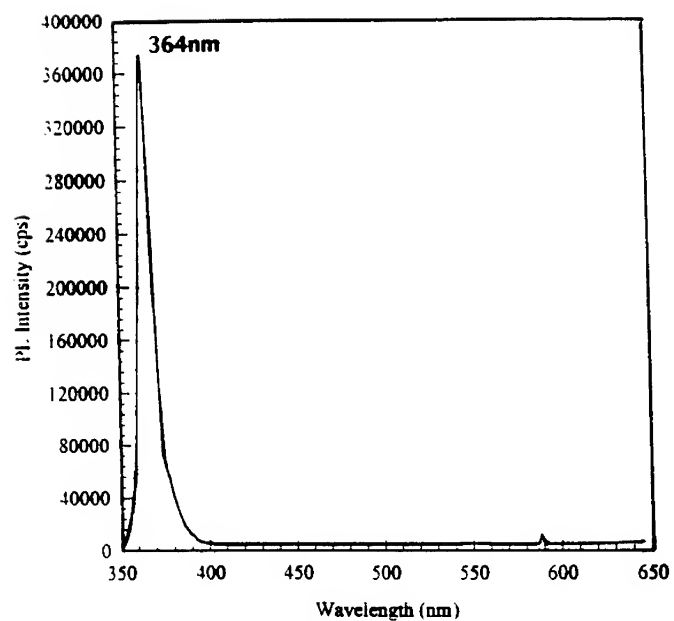


FIG. 4. Photoluminescence (RT) spectrum of hexagonal GaN

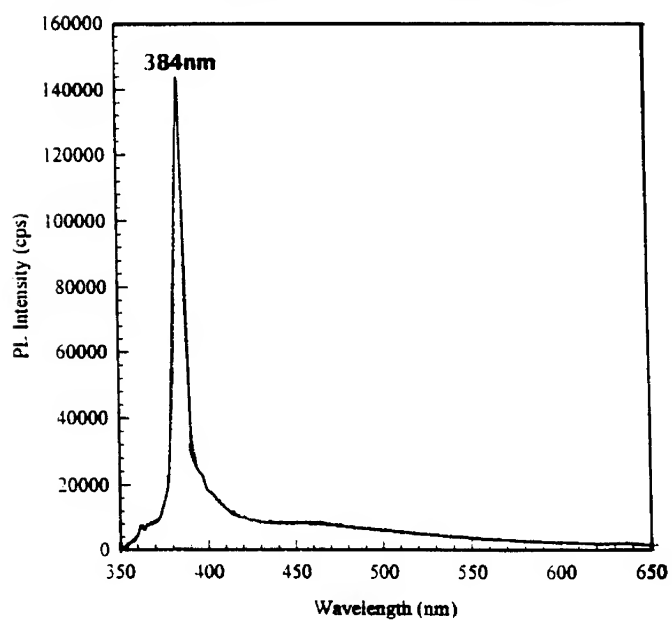


FIG. 5. Photoluminescence (RT) spectrum of cubic GaN

the bandgap of β -GaN is at 3.33 eV at 15K and 3.28 eV at room temperature. Powell *et al*⁷ claim a room temperature bandgap of 3.21 eV based upon optical absorption measurements. Strite *et al*⁸ suggest that the bandgap to be ~ 3.45 eV at room temperature based on cathodoluminescence measurements. They observed weak peaks at higher energies, other than the dominant peak at 3.2 eV. Min *et al*¹⁰ predict the bandgap energy of β -GaN to be direct and $\approx 0.1 - 0.6$ eV less than that of α -GaN, indicating that our results are well within the range. This observed bandgap difference between hexagonal and cubic GaN can be attributed to their conduction band characteristics¹.

CONCLUSIONS

In conclusion, we have shown for the first time that zincblende GaN films can be grown on MgO by MBE using a rf plasma discharge, nitrogen free-radical source with reasonable growth rate. Room temperature PL measurements indicated that the bandgap energy is about 3.23 eV which is smaller than that of hexagonal GaN and in agreement with other results and theoretical predictions. Low temperature PL measurements are planned in order to study both phases in more detail and these results will be reported in a future publication.

REFERENCES

1. J. Petalas, S. Logothetidis, S. Bouladakis, M. Alouani, and J.M.Wills, Phys.Rev, B 52, 8082 (1995)
2. B.Dingle, D.D.Sell, S.E. Stokowski, and M. Ilegems, Phys. Rev, B 4, 1211 (1971)
3. H. Okumura, Y. Yoshida, and T. Okahisa, Appl. Phys. Lett. 64, 2997 (1994)
4. R.C. Powell, N.E. Lee, Y.W. Kim, and J.E. Greene, J. Appl. Phys. 73, 189 (1993)
5. Z. Sitar, M.J. Paisley, J. Ruan, J.W. Choyke, and R. F. Davis, J. Mater. Sci. Lett., 11, 261 (1992)
6. G.R-Flores, H. Navarro-Contreras, A. Lastras-Martinez, R.C. Powell, and J.E. Greene, Phys. Rev B 50, 8433 (1994)
7. R.C. Powell, G.A. Tomasch Y.W. Kim, J.A. Thornton, and J.E. Greene, MRS Symposia Proceedings No. 162, 525, (1990)
8. S. Strite, J. Ruan Z. Li, A. Salvador, H. Chen, D.J. Smith, W.J. Choyke, and H. Morkoc, J. Vac. Sci. Technol. B 9, 1924 (1991)
9. H. Liu, A.C. Frenkel, J. G. Kim, and R. M. Park, J. Appl. Phys. 74, 6124 (1993)
10. B.J. Min, C.T. Chan, and K.M. Ho, Phys. Rev. B 45, 1159 (1992)

Temperature Dependence of the Absorption Band Gap Edge of GaN

M. O. MANASREH and A. K. SHARMA

Phillips Laboratory (PL/VTRP), Kirtland AFB, NM 87117-5776

ABSTRACT

The optical absorption near the fundamental absorption edge in GaN thin films grown on sapphire substrates is studied as a function of temperature. The absorption band edge was determined from either the energy position of the exciton line in samples grown by metalorganic chemical vapor deposition technique, or from the first derivative of the absorption spectra in samples grown by molecular beam epitaxy technique. The band edge energies determined in the temperature range of 13 - 300 K were fitted with Varshni empirical relationship: $E_g(K) = E_g(0) - \alpha T^2/(T + \theta_D)$ and with the expression: $E_g(K) = E_g(0) - \kappa / [\exp(\theta_E/T) - 1]$. It is found that $E_g(0)$, α , θ_D , and θ_E to be sample-dependent, which suggests that defects and dislocations significantly affect the optical band edge in GaN.

INTRODUCTION

There has been an increasing interest in GaN and related materials due to their optoelectronic properties in the visible and ultraviolet spectral regions.^{1,2} Ultraviolet detection is one of the future applications of these wide band gap materials. The band edge absorption is one of the fundamental parameters that one has to address when ultraviolet detector or sensor is fabricated from GaN thin films and other related materials.³ The band edge of GaN has been the subject of several studies.⁴⁻⁹ In this paper, we present results on the temperature dependence of the optical absorption near the band edge of GaN thin films grown by metalorganic chemical vapor deposition (MOCVD) and molecular beam epitaxy (MBE) techniques. The optical absorption spectra of GaN sample grown by MOCVD exhibit an exciton line observed in the entire temperature range of 13 - 300 K. The energies of the band edge were determined either by the exciton line or by the first derivative of the optical absorption spectra. The data were fitted with two different empirical expressions to determine the behavior of the band edge as a function of temperature. It is found that the fitting parameters were sample-dependent, suggesting that the variation of the band edge is influenced by the presence of defects and dislocations.

EXPERIMENT

The GaN layers were nominally undoped and grown by MOCVD and MBE techniques on c-plane, i.e. (0001), oriented sapphire substrates. The optical absorption spectra were recorded, using CARY 05E spectrometer in conjunction with a closed cycle refrigerator. The temperature was controlled between 13 and 300 K to within ± 1 K.

The optical absorption spectra recorded at 13 K for two samples are shown in Fig. 1. Spectra (a) and (b) were taken for two samples grown by MOCVD and MBE, respectively. An exciton sharp line is observed in spectrum (a) at 353.556 nm (3.507 eV). This exciton line was observed in the entire temperature range, but its full width half maximum is increased as the temperature increases. The MBE sample, on the other hand, exhibits a spectrum with a broad exciton line at 356.33 nm (3.479 eV). Spectrum (c) was obtained for a GaN sample grown by sputtering technique and plotted for comparison. The band edge absorption is almost washed out in this sample.

DISCUSSIONS

The band edge absorption of GaN samples is studied as a function of temperature. The result is shown in Fig. 2. It is well known that the band edge of any III-V semiconductor becomes less steep (less abrupt) as the temperature is increased. This phenomena causes a difficulty in

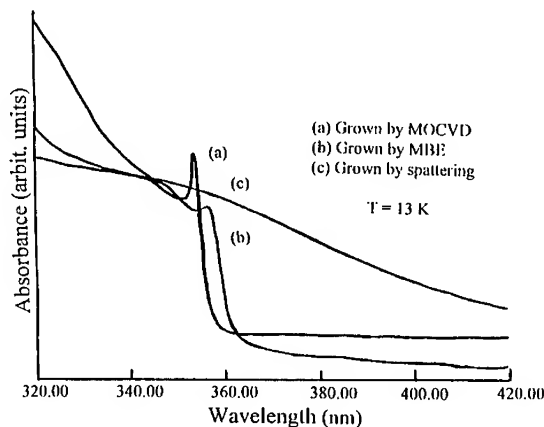


Fig. 1. The absorbance as a function of photon energy at temperature = 13 K. Spectrum (a), (b), and (c) were taken for samples grown by MOCVD, MBE, and sputtering techniques, respectively. The absorption peak in spectrum (a) at 353.556 nm is due to an exciton line in the MOCVD GaN Layer.

determining the band edge as a function of temperature, especially above 50 K where the exciton lines are usually washed out. However, we found, in the present study, that the exciton line in the MOCVD GaN samples is still present, even at room temperature in agreement with Amato *et al.*¹⁰ We defined the band gap of this sample by the exciton peak energy. The result is shown in Fig. 2 as the solid circles. However, since the exciton line is not that sharp in the MBE GaN sample [Fig. 1, spectrum (b)], the band gap of this sample is defined in a different method in order to minimize the error in the band gap energy. This method is based on the calculation of the first derivatives of the spectra recorded as a function of temperature. Two spectra recorded at 13 and 300 K (lower panel) and their derivatives (upper panel) were selected and plotted in Fig. 3. It

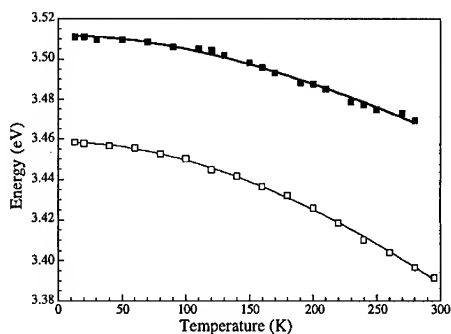


Fig. 2. The band gap energy variation as a function of temperature. Solid circles and squares were taken for MOCVD and MBE samples, respectively. The solid lines are the result of fitting the experimental data using Eq. (1) with $E_g(0)$, α , and θ_D as fitting parameters.

is clear from this figure that the peaks of the first derivatives are well defined at all temperatures. Thus, the band gap energy extracted from the first derivatives exhibits minimum errors. The band gap energy, as determined from the first derivatives of the spectra, is plotted in Fig. 2 as the solid squares. It should be noted that the first derivative reflects the variation of the slope. Thus, the band gap of this sample is smaller than the exciton peak energy. However, the band gap of the MBE GaN samples was always found to be smaller than that of the MOCVD GaN samples.

The experimental data of the band gap energies in Fig. 2 were fitted with the Varshni empirical relationship¹¹

$$E_g(K) = E_g(0) - \alpha T^2 / (T + \theta_D), \quad (1)$$

where $E_g(0)$ is the band gap at 0 K, α is a constant, and θ_D is approximately the 0 K Debye temperature. $E_g(0)$, α , and θ_D were used as fitting parameters. The values of these parameters are given in Table I, and the results of the fitting procedure are shown as solid lines in Fig. 2. The band gap data in Fig. 2 are also fitted using the expression¹²

$$E_g(K) = E_g(0) - \kappa / [\exp(\theta_E/T) - 1], \quad (2)$$

where κ is a constant, θ_E is the Einstein temperature, and $E_g(0)$ is the same as in Eq. (1) and all were used as fitting parameters. The results are also shown in Table I. The fitting curves using Eq. (2) are somewhat similar to those obtained using Eq. (1).

It is clear from Table I that the values of $E_g(0)$, α , κ , θ_D , and θ_E are sample-dependent. The most important parameter here is the band gap energy. It is obvious from Figs. 1 and 2 that the band gap energy of MBE sample (growth temperature $\sim 780^\circ\text{C}$) is smaller than that of the MOCVD sample (growth temperature $\sim 1050^\circ\text{C}$). The growth temperature plays a major role in the introduction of defects, extended defects, and dislocations. Thus, one would expect to see more defects in the MBE samples as compared to the MOCVD samples. On the other hand, the exponential part of the band edge absorption (Urbach band edge¹³) is influenced by the defects and dislocation which, in turns, affect the band edge energy. This premise is supported by: First, the exciton line observed in the MOCVD sample is much sharper than that of the MBE sample as shown in Fig. 1. In addition, this exciton line does not exist in polycrystalline sample grown by

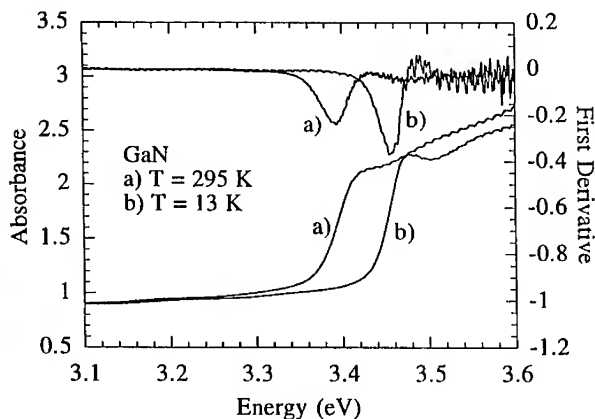


Fig. 3. Optical absorption spectra of the MBE samples taken at (a) 300 K and (b) 13 K and their respective first derivatives. The peaks of the first derivatives were used to estimate the band gap energy.

the sputtering technique. Second, the band edge absorption of the polycrystalline sample grown by the sputtering technique [see spectrum (c) in Fig. 1] is very soft and does not exhibit an exponential behavior similar to that of the other samples.

The other two parameters worth discussing here are Einstein (θ_E) and Debye (θ_D) temperatures. It should be pointed out that θ_D in Eq. (1) is not exactly Debye temperature. It is, however, proportional to, but somewhat less than, the usual specific heat Debye temperature.¹² In addition, it is assumed that $\theta_E \simeq (3/4)\theta_D$. It has been observed that $\theta_E/\theta_D \sim 0.60$ for other

Table I. The results of the fitting parameters using Eqs. (1) and (2) and the data in Fig. 2 for both MOCVD and MBE samples are presented. The results of other work are listed for comparison.

Sample	$E_g(K) = E_g(0) - \alpha T^2/(T + \theta_D)$			$E_g(K) = E_g(0) - \kappa / [\exp(\theta_E/T) - 1]$			
	$E_g(0)$ (eV)	α (10^{-4} eV/K)	θ_D (K)	$E_g(0)$ (eV)	κ (10^{-3} eV)	θ_E (K)	θ_E/θ_D
^(a) MOCVD Sample	3.512	5.66	737.9	3.510	75.5	289.0	~0.39
^(a) MBE Sample	3.458	11.56	1187.4	3.457	119.3	307.9	~0.26
^(b) MOCVD Sample							
$\Gamma_9^v - \Gamma_7^c$	3.486	8.32	835.6	3.484	103.7	292.2	~0.35
$\Gamma_7^v - \Gamma_7^c$	3.494	10.90	1194.6	3.492	112.9	310.6	~0.26
^(c) VPE Sample	3.503	5.08	996				

^(a) Present work (optical absorption).

^(b) Reference 4 (photoreflectance).

^(c) Reference 7 (PLE).

semiconductors (as an example, see references 14 - 16). In case of GaN, this ratio is much smaller than 0.60 as shown in Table I. It was shown that the Debye temperature can be derived as a function of the elastic constants (C11, C12, and C44) for semiconductors.¹⁷ If one assumes that θ_D is somewhat the same as the usual specific heat Debye temperature, then it is tempting to explain the above discrepancy according to the following proposition. The present GaN samples contain defects, extended defects, dislocations, and possibly local (residual) strains, which resulted in different elastic constants for different samples, which leads to different θ_E/θ_D . It is also noted that the present results of θ_E and θ_D extracted from the optical absorption technique are different from those obtained from photoreflectance⁴ and photoluminescence excitation⁷ techniques (see Table I). However, the results of the MOCVD sample in the present work are in good agreement with the results of the $\Gamma_9^v - \Gamma_7^v$ transition reported by Shan *et al.*⁴ and with the results reported for a vapor-phase epitaxy (VPE) sample⁷ as shown in Table I.

CONCLUSION

In conclusion, we presented for the first time the band gap energy of GaN thin films as a function of temperature using the optical absorption technique. A sharp and a broader exciton line was observed in MOCVD and MBE samples, respectively. Einstein (θ_E) and Debye (θ_D) temperatures were extracted by fitting the experimental band gap energy data with two different

empirical expressions. The results indicate that θ_E and θ_D , as well as Urbach band gap, are sample-dependent, suggesting that defects and dislocations significantly affect the band edge absorption in GaN.

REFERENCES

1. See for example S. Nakamura, IEEE Circuits and Devices **11**, 19 (1995).
2. "GaN and Related Materials", edited by S. J. Pearton, to be published.
3. See for example K. S. Stevens, M. Kinniburgh, and R. Beresford, Appl. Phys. Lett. **66**, 3518 (1995).
4. W. Shan, T. J. Schmidt, X. H. Yang, S. J. Hwang, and J. J. Song, Appl. Phys. Lett. **66**, 985 (1995).
5. M. Smith, G. D. Chen, J. Y. Lin, H. X. Jiang, A. Salvador, B. N. Sverdlov, A. Botchkarev, and H. Morkoc, Appl. Phys. Lett. **66**, 3474 (1995).
6. R. Dingle, D. D. Sell, S. E. Stokowski, P. J. Dean, and R. B. Zetterstorm, Phys. Rev. **B 3**, 497 (1971).
7. B. Monemar, Phys. Rev. **B 10**, 676 (1974).
8. C. R. Aita, C. J. G. Kubiak, F. Y. H. Shih, J. Appl. Phys. **66**, 4360 (1989).
9. J. I. Pankove, H. P. Maruska, and J. E. Berkeyheiser, Appl. Phys. Lett. **17**, 197 (1970).
10. H. Amato, N. Watanabe, N. Koide, and I. Akasaki, Jpn. J. Appl. Phys. **32**, L1000 (1993).
11. Y. P. Varshni, Physica **34**, 149 (1967).
12. G. D. Cody in "Semiconductors and Semimetals", vol. 21 B, edited by J. I. Pankove (Academic Press, New York, 1984), chapt. 2, pp. 11-79.
13. F. Urbach, Phys. Rev. **92**, 1324 (1953).
14. C. D. Clark, P. J. dean, and P. V. Harris, Proc. Roy. Soc. **A 277**, 312 (1964).
15. W. Bludeau, A. Onton, and H. J. Heinke, Appl. Phys. **45**, 1846 (1974).
16. P. D. Persans, A. F. Ruppert, S. S. Chan, and G. D. Cody, Solid State Commun. **51**, 203 (1984).
17. An expression of the 0 K Debye temperature was derived as a function of the elastic constants by P. M. Marcus and A. J. Kennedy, Phys. Rev. **114**, 459 (1959) which was then used by E. F. Steigmeier, Appl. Phys. Lett. **3**, 6 (1963) to estimate the Debye temperature for many semiconductors.

NEAR-BANDGAP PHOTOLUMINESCENCE DECAY TIME IN GaN EPITAXIAL LAYERS GROWN ON SAPPHIRE

A. HANGLEITER, J. S. IM, T. FORNER, V. HÄRLE, AND F. SCHOLZ
4. Physikalisches Institut, Universität Stuttgart D-70550 Stuttgart, Germany
E-mail: A.Hangleiter@physik.uni-stuttgart.de

ABSTRACT

Using picosecond time-resolved photoluminescence we have studied the decay time of excess carriers in GaN epitaxial layers over a wide range of temperatures from 4 K up to 400 K. At low temperature, a thermal dissociation of donor-bound excitons is observed. At higher temperatures up to room temperature, the luminescence decay at moderate excitation is governed by trapping of photogenerated electrons in ionized shallow donor levels. Using measured luminescence intensities to determine the quantum efficiency, we obtain the radiative lifetime of free excitons from low temperature up to room temperature. We use these data to determine the radiative recombination coefficient and the interband momentum matrix element.

INTRODUCTION

The group-III nitrides GaN, AlN, and InN have recently attracted much interest due to their potential application for blue light emitters. Among the key quantities influencing the properties of optoelectronic devices is the recombination lifetime of excess charge carriers. Only low temperature results for exciton lifetimes in GaN have been reported up to now [1, 2]. There are no experimental data on the radiative recombination coefficient or on the interband matrix element available to date.

In this paper, we report on our time-resolved study of the luminescence decay time in the near-bandgap region of epitaxial wurtzite GaN layers. From our data, we determine the bound and the free exciton radiative lifetimes as a function of temperature and derive the first reliable values for the radiative recombination coefficient and the interband momentum matrix element.

EXPERIMENTAL DETAILS

Samples

Our GaN samples were grown on 0001-oriented sapphire substrates using low pressure metal-organic vapor phase epitaxy (LP-MOVPE) and employing an AlN buffer layer. The layer thickness was in the range 1 to 3 μm . The samples exhibited X-ray diffraction linewidths of 50 to 80 arcsecs and photoluminescence linewidths of around 2 to 4 meV. The net donor concentration of nominally undoped GaN was less than $1 \cdot 10^{17} \text{cm}^{-3}$.

Measurement Setup

The carrier dynamics were investigated using a picosecond time-resolved photoluminescence setup, where the samples were excited with 5 ps pulses from a cavity-dumped frequency-doubled synchronously mode-locked dye laser. The luminescence was detected with a Hamamatsu R3809-U microchannel-plate photomultiplier and processed using time-correlated single-photon-counting electronics. By employing suitable deconvolution techniques, an overall time resolution of less than 20 ps was reached. The samples were mounted in a variable-temperature cryostat, allowing for a temperature range from 2 K up to 400 K.

EXPERIMENTAL RESULTS

Low temperature: Bound excitons

At low temperature (5 K) our samples exhibit a rather sharp emission with a maximum at 3.488 eV close to the GaN band edge. The intensity of donor-acceptor pair transitions etc. is lower by more than a factor of 10. A close look at highly resolved spectra (Fig. 1) reveals that, depending on temperature, there are at least 3 lines, which are about 6 and 8 meV apart. From the dynamic behavior (see below) and in accordance with the recent literature [2, 3] we interpret these as being due to a shallow-donor-bound exciton (D^0X) and two symmetry-split states of the free exciton (A, B).

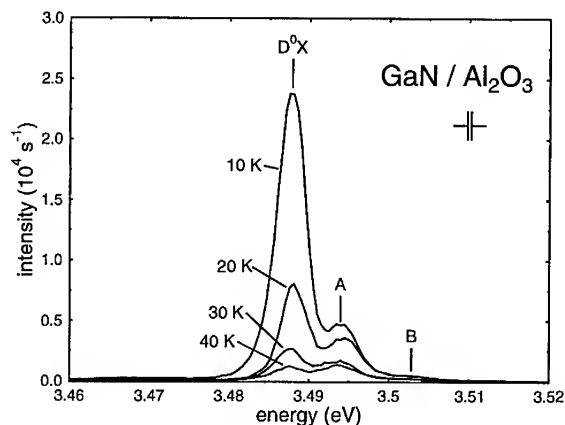


Figure 1: Temperature dependent PL spectra in the excitonic region close to the band gap at low temperature.

The decay times of the emission lines labeled D^0X and A at low temperature are depicted in Fig. 2. Since the decay time of the lower energy line D^0X decreases rapidly between 15 and 30 K our previous interpretation as shallow-donor-bound excitons is confirmed. It is interesting to note that obviously there is no equilibrium between bound and free excitons at these low temperatures, since otherwise their decay times would be identical. Therefore we have to solve the full rate equations including the capture and thermal emission times in order to fit the measured data as shown in Fig. 2. For the fit we have used the spectroscopic binding energy of 6.2 meV as the activation energy. There is some deviation between theory and experiment for the lower branch of the decay times. This is probably due to the fact that experimentally one expects to observe a biexponential decay, which may not have been resolved in our experiments.

As a subtle detail, we observe a slight increase of the bound exciton decay time between 5 and 15 K. This leads us to suspect that there might be a shallow excited state of the bound exciton at about 1 meV above the ground state, which has a considerably lower decay rate.

The absolute values of the bound exciton decay time below 15 K show only little variation between different samples, as expected. On the other hand there are considerable differences for the free exciton decay times, as will be discussed below.

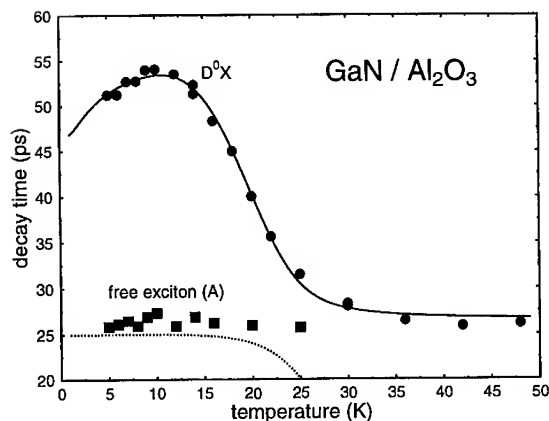


Figure 2: Bound exciton and free exciton luminescence decay times versus temperature. The full line and the dotted line represent a fit using the two solutions of the coupled rate equations.

Towards room temperature: Free excitons and free carriers

At temperatures larger than about 50 K, the bound exciton line vanishes completely. Only the free exciton line remains and dominates the spectrum, with the higher-lying states being increasingly populated at high temperature. An integration of the intensities in the excitonic region of the spectrum yields the temperature dependent intensities as shown in Fig. 3. We find that

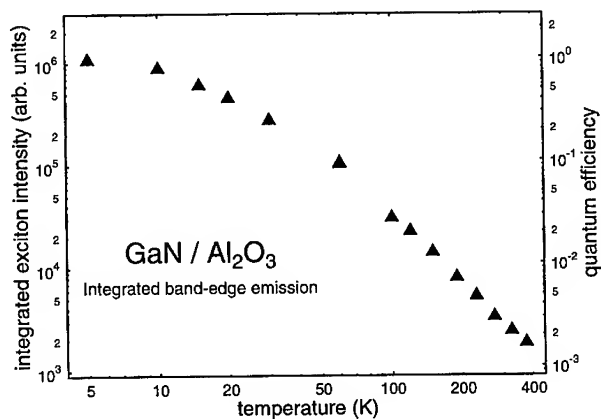


Figure 3: Temperature dependence of the integrated band-edge emission intensity and the radiative quantum efficiency. Here we assume that the quantum efficiency approaches unity at low temperature.

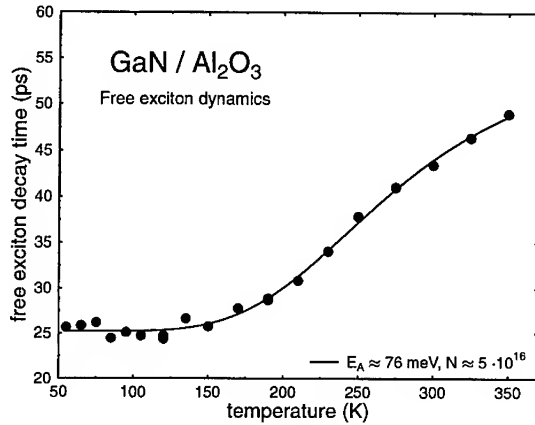


Figure 4: Temperature dependence of the free exciton / free carrier luminescence decay time up to above room temperature. The fit is explained in the text.

between 5 K and 400 K there is a decrease of the overall intensity by about 3 orders of magnitude. If we assume a unity quantum efficiency at low temperature, we find a quantum efficiency of about $3 \cdot 10^{-3}$ at room temperature under our experimental conditions.

Even though the total intensity at elevated temperatures decreases considerably, we were able to measure the decay times after pulsed excitation. Fig. 4 shows the results of these measurements for the temperature range between 50 and 350 K. Initially, at lower temperatures, the decay time remains constant at a level of 25 ps for this particular sample. At higher temperatures there is a slightly sub-linear increase of the decay time reaching about 50 ps at 350 K. Comparing different samples we note that there is some variation of the absolute values of the decay times (between 25 and 40 ps at 50 ... 100 K) but the overall behavior does not change significantly.

Considering the fact that the quantum efficiency of the luminescence is far below unity over the whole temperature range of these measurements, we have to conclude that we are dealing with a nonradiative decay. Since we are working at rather low excitation densities of the order of 10^{16}cm^{-3} we may suspect that trapping of electrons or holes into shallow donor or acceptor levels is responsible for this decay. Based on this assumption we have fitted our data using a rate equation model and found an activation energy of about 76 meV and a trap density of about $5 \cdot 10^{16} \text{cm}^{-3}$.

RADIATIVE LIFETIME

Using our measured data presented above, we are able to derive a quantitative estimate of the radiative lifetime τ_{rad} in our samples. We do this by using the quantum efficiency η determined from the luminescence intensities and the measured nonradiative decay time τ_{nonrad} with the relation

$$\tau_{\text{rad}} = \tau_{\text{nonrad}} \left[\frac{1}{\eta} - 1 \right]. \quad (1)$$

Since our quantum efficiency really gives an upper bound for the real quantum efficiency, this procedure provides us with a lower bound for the radiative lifetime.

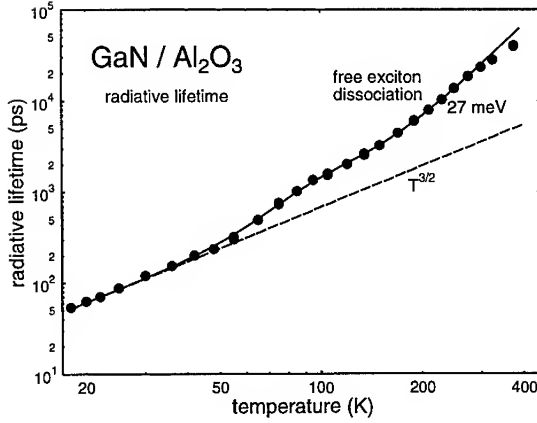


Figure 5: Temperature dependence of the radiative lifetime determined from our data. The dashed line indicates the $T^{3/2}$ dependence expected for free excitons or free carriers in a direct semiconductor. The full line is explained in the text.

The results are shown in Fig. 5. First, we note that for temperatures below 50 K the radiative lifetime follows a $T^{3/2}$ law as expected for either free excitons or free carriers in a direct semiconductor [4]. At higher temperature the radiative lifetime increases more rapidly, but again following a $T^{3/2}$ law between about 100 and 150 K. At even higher temperatures we observe an exponential increase of the radiative lifetime.

In order to explain this behavior, we have to keep in mind that the free excitons present at low temperature are increasingly dissociated into free electrons and holes at higher temperature. In a very simple picture this is governed by a mass-action law

$$\frac{n \cdot p}{x} = 2 \left(\frac{\mu k T}{2\pi \hbar^2} \right)^{3/2} e^{-\frac{E_x}{kT}}, \quad (2)$$

where n, p, x are the densities of electrons, holes, and free excitons, respectively, E_x is the free exciton binding energy, and μ is the reduced effective mass. Since the electron and the hole forming the exciton are strongly localized, the free exciton is expected to have a much smaller radiative lifetime than free carriers at a given carrier density.

In order to fully understand the data in Fig 5, we have to consider the background electron density present due to unintentional doping. Since the shallow donor binding energy is about 35 meV [5], we expect the background electron density to vary strongly in the temperature range between 50 and 150 K.

Taking into account all these considerations [6], we are able to fit our data as shown in Fig 5 with the full line, reaching excellent agreement. From the fit we find a free exciton binding energy of about 27 meV, a shallow donor binding energy of about 37 meV, and a donor concentration of about $9 \cdot 10^{16} \text{cm}^{-3}$. Our free exciton binding energy is in good agreement with the spectroscopic value of 26.1 meV [3].

Based on the same argument we are led to conclude that in the temperature region below 50 K

we observe the intrinsic free exciton radiative lifetime. From the fit we find

$$\tau_x \approx 0.7 \cdot T^{3/2} [ps] \quad (3)$$

as a lower bound for the free exciton radiative lifetime. Using published data for the effective masses ($m_e = 0.22$ [5], $m_{hh} = 0.54$ [3]) and for the dielectric constant ($\epsilon = 8.9$ [7]) we calculate a free exciton Bohr radius of $a_0 = 3.0$ nm. Using the relation

$$B = \frac{1}{\tau_x |\Psi(0)|^2} = \frac{\pi a_0^3}{\tau_x} \quad (4)$$

for the free carrier radiative recombination coefficient B , where Ψ is the free exciton ground state wavefunction, we find an upper bound for B at room temperature.

$$B \approx 2.4 \cdot 10^{-11} \text{ cm}^3/\text{s}. \quad (5)$$

Going one step further we use B to determine the interband momentum matrix element E_p according to

$$E_p = \frac{3m_0 c^3 (M kT)^{3/2}}{2\sqrt{\pi} n e^2 \hbar^2 \nu} \cdot B, \quad (6)$$

where M is the exciton effective mass, and find $E_p \approx 2.2$ eV (as an upper bound).

DISCUSSION

Previously, no data have been available for the free exciton radiative lifetime and for the radiative recombination coefficient, and only theoretical estimates for the interband momentum matrix element have been presented [8, 9]. We note that our value of 2.2 eV is considerably lower than both of these estimates (9.8 eV [8], 24.6 eV [9]).

For the potential use of GaN and related material for semiconductor lasers, this is both good and bad news. The low value of the interband matrix element means that the optical gain at a given carrier density is low on one hand, but that the spontaneous radiative recombination rate is also low on the other hand. Detailed investigations of the consequences of these results for the threshold current of GaN-based lasers are currently in progress.

REFERENCES

1. C. I. Harris, B. Monemar, H. Amano, and I. Akasaki, *Appl. Phys. Lett.* **67**, 840 (1995).
2. W. Shan, X. C. Xie, J. J. Song, and B. Goldenberg, *Appl. Phys. Lett.* **67**, 2512 (1995).
3. C. Merz, M. Kunzer, and U. Kaufmann, to be published.
4. G. Lasher and F. Stern, *Phys. Rev.* **133**, A553 (1964).
5. B. K. Meyer, D. Volm, A. Graber, H. C. Alt, T. Detchprohm, K. Amano, and I. Akasaki, *Solid State Commun.* **95**, 597 (1995).
6. A. Hangleiter, in *Proc. 20th Intern. Conf. on the Physics of Semiconductors*, edited by E. Anastassakis and J. D. Joannopoulos (World Scientific, Singapore, 1990), Vol. 3, p. 2566.
7. K. Matsubara and T. Takagi, *Jpn. J. Appl. Phys.* **22**, 511 (1982).
8. W. Fang and S. L. Chuang, *Appl. Phys. Lett.* **67**, 751 (1995).
9. A. T. Meney and E. P. O'Reilly, *Appl. Phys. Lett.* **67**, 3013 (1995).

PICOSECOND RAMAN STUDIES OF ELECTRON-PHONON INTERACTIONS IN THE WIDE BANDGAP SEMICONDUCTOR GaN

K.T. TSEN*, D.K. FERRY**, A. BOTCHKAREV***, B. SVERDLOV***, A. SALVADOR***, H. MORKOC***

*Department of Physics and Astronomy, Arizona State University, Tempe, AZ 85287

**Department of Electrical Engineering, Arizona State University, Tempe, AZ 85287

***Coordinated Science Laboratory, University of Illinois, Urbana, IL 61801

ABSTRACT

Picosecond Raman spectroscopy has been employed to study electron-phonon interactions in the wide bandgap semiconductor GaN. An ultraviolet picosecond laser with photon energy $\hbar\omega = 4.36\text{ eV}$ was used to excite electron-hole pairs in an undoped bulk GaN. The relaxation of these high energy electrons and holes were used to interrogate electron-phonon interactions. We have found that electrons thermalize toward the bottom of the conduction band by emitting primarily longitudinal optical phonons. Our work demonstrates that the Fröhlich interaction is much stronger than the deformation potential interaction in wurtzite GaN.

INTRODUCTION

Wide bandgap semiconductors such as AlN, SiC and GaN have recently attracted much attention[1]. This is partly due to the need for electronic devices capable of operation at high power levels, at high temperatures, and in severe environments, and partly due to a need for optical materials which operate in the blue and ultraviolet spectral range. Particularly, GaN and AlN form a continuous alloy system whose bandgaps can cover from 3.4 to 6.2 eV. This property makes the applications for many novel optical devices based upon these wide bandgap semiconductors very promising.

Because of advances in crystal growth techniques and the ease of doping with both n-type and p-type impurities, SiC has so far received the greatest attention. On the other hand, GaN may prove to be superior for wide bandgap applications owing to its lower ohmic contact resistances and its larger predicted electron saturation velocity[2].

We note that although much progress has been made in device-oriented applications with these wide bandgap semiconductors, very little information on their dynamical properties has yet been obtained; in particular, the carrier relaxation mechanisms in these wide bandgap semiconductors remain completely unexplored. In this paper, we report results of our picosecond Raman studies of electron-phonon interactions in wurtzite GaN. Our experimental results demonstrate that high energy electrons relax primarily through the emission of longitudinal optical phonons and that the Fröhlich interaction is much stronger than the deformation potential interaction in this wide bandgap semiconductor.

SAMPLE AND EXPERIMENTAL SETUP

The sample used in this work was a wurtzite structure, undoped GaN (with electron density $n \approx 5 \times 10^{16} \text{ cm}^{-3}$) grown by molecular beam epitaxy on a (0001)-oriented sapphire substrate. The z-axis of this wurtzite structure GaN is perpendicular to the sapphire substrate plane. The thickness of the GaN layer was about 2 μm .

Very short ultraviolet laser pulses were generated by the frequency-doubling of a cavity-dumped R6G dye laser which was synchronously pumped by the second harmonic of a cw mode-locked Nd:YAG laser[3]. The ultraviolet laser was chosen to operate at a photon energy of $\hbar\omega = 4.36 \text{ eV}$, at a repetition rate of 10 MHz. The average output power of the ultraviolet laser was about 10 mW. We note that the photons in our laser beam have sufficient energy to directly excite electron-hole pairs with large excess energies ($\approx 1.0 \text{ eV}$). The same ultraviolet laser beam was also used to study the strength of the electron-phonon interaction by monitoring

the non-equilibrium phonon population with Raman scattering. The photoexcited electron-hole pair density was estimated to be $3 \times 10^{16} \text{ cm}^{-3}$ from the fitting of time-integrated luminescence spectrum[4]. Polarized Raman scattering experiments were carried out in a variety of scattering geometries as specified below. The sample was kept in contact with a cold finger tip of a close-cycled refrigerator. The temperature of the sample was estimated to be $T \cong 25 \text{ K}$. The scattered signal was collected and analyzed with a standard Raman setup with a CCD detection system.

EXPERIMENTAL RESULTS AND DISCUSSIONS

Figs. 1(a) and 2(a) show two polarized Stokes Raman spectra of a GaN sample taken at $T=25 \text{ K}$ and in $Z(X,X)\bar{Z}$, $Y(X,X)\bar{Y}$ scattering geometries, respectively; where $X = (100)$, $Y = (010)$ and $Z = (001)$. Similar Raman spectra were reported by Azuhata et al.[5] at $T = 300 \text{ K}$. In Fig. 1(a), the sharp peak around 757 cm^{-1} comes from scattering of light by the E_g phonon mode of sapphire; the shoulder close to 741 cm^{-1} belongs to the $A_1(\text{LO})$ phonon mode; On the other hand, in Fig. 2(a), the sharp peak around 574 cm^{-1} corresponds to the E_2 mode; the peak centered about 538 cm^{-1} represents the $A_1(\text{TO})$ mode; the small structure around 422 cm^{-1} is from the A_{1g} mode of sapphire.

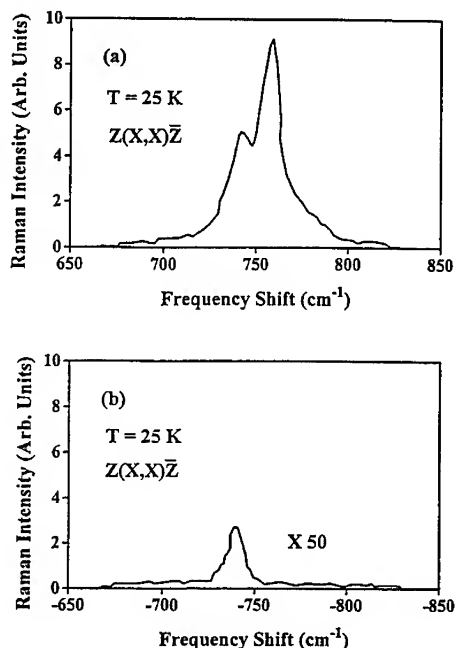


Fig. 1: Polarized Stokes Raman spectrum (a) and anti-Stokes Raman spectrum (b) for a GaN sample taken at $T=25 \text{ K}$, and in the scattering geometry $Z(X,X)\bar{Z}$. For clarity, the anti-Stokes Raman signal has been multiplied by a factor of 50. The appearance of the $A_1(\text{LO})$ mode in the anti-Stokes spectrum is an indication of strong electron-LO phonon interaction in GaN.

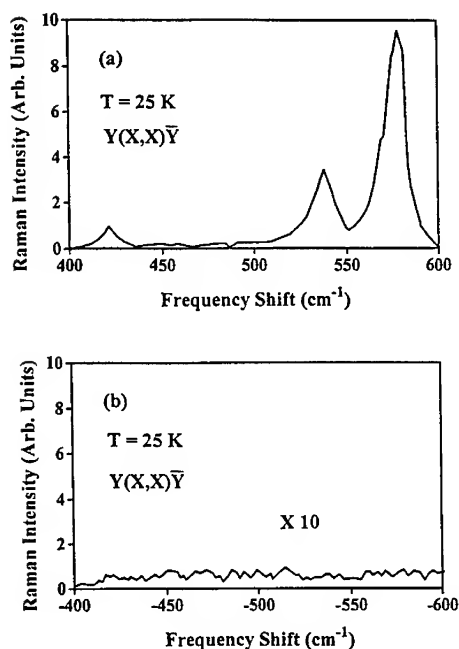


Fig. 2: Polarized Stokes Raman spectrum (a) and anti-Stokes Raman spectrum (b) for a GaN sample taken at $T=25\text{K}$ and in a scattering geometry $Y(X,X)\bar{Y}$. For clarity, the anti-Stokes signal has been multiplied by a factor of 10. The fact that no observable phonon modes in the anti-Stokes Raman spectrum suggests that neither E_2 nor $A_1(\text{TO})$ phonon modes interacts strongly with electrons.

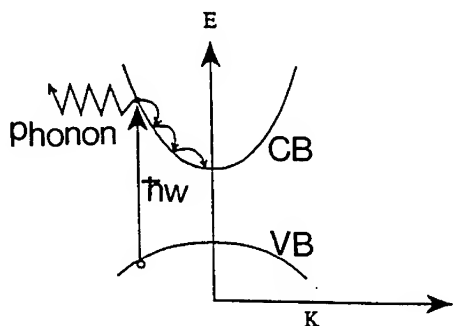


Fig. 3: A diagram showing how the strength of electron-phonon interactions can be probed by picosecond Raman spectroscopy. Here CB, VB represent conduction and valence bands, respectively.

As depicted in Fig. (3), one way[6] to study electron-phonon interactions in semiconductors is to first generate electron-hole pairs with sufficient kinetic energy ($\gg \hbar\omega_{LO}$); the high energy electrons then relax to the bottom of the conduction band by emitting all types of high frequency phonons. By monitoring this thermalization process with Raman spectroscopy at very low temperatures, information such as the relative strength of the interaction of electrons with each type of phonons can be obtained.

The anti-stokes Raman spectra corresponding to Figs. 1(a) and 2(a) were shown in Figs. 1(b), 2(b), respectively. Since at very low temperatures, thermal occupations of phonons are vanishingly small, any Raman signal observed in the anti-stokes Raman spectra must arise from the presence of non-equilibrium phonon modes. With the help of Stokes Raman spectra in Figs. 1(a) and 2(a), we can make the following identification: The broad structure centered around -741 cm^{-1} comes from Raman scattering of light from non-equilibrium $A_1(\text{LO})$ phonon mode. We note that within our experimental accuracy there is no detectable non-equilibrium phonons for either the $A_1(\text{TO})$ mode or the E_2 mode of GaN and for the E_g mode as well as A_{1g} modes of sapphire.

Similar Raman experiments were also carried out in scattering geometries of $A(Z,X)Y$ and $Y(Z,X)\bar{Y}$, where $E_1(\text{LO})$ and $E_1(\text{TO})$ phonon modes could be observed;⁴ here, $A = (\sin\theta, -\cos\theta, 0)$ with $\theta \cong 108^\circ$. These experimental results (which were not shown) indicated that a substantial occupation of non-equilibrium phonons was observed for the $E_1(\text{LO})$ mode but not for the $E_1(\text{TO})$ mode.

Our experimental results therefore show directly that hot electrons thermalize primarily through the emission of polar longitudinal optical phonons in wurtzite structure GaN. Electrons interact with LO phonons through the Fröhlich interaction as well as the deformation potential interaction, and they interact with TO phonons via the deformation potential interaction only. Since only the LO phonon modes are driven out of equilibrium, these experimental results demonstrate that the Fröhlich interaction is much stronger than the deformation potential interaction in this wide bandgap semiconductor.

From the measured Raman spectra we can estimate that the phonon occupation number of the observed non-equilibrium $A_1(\text{LO})$ and $E_1(\text{LO})$ phonons is about $\Delta n \cong 0.018 \pm 0.001$, 0.015 ± 0.001 , respectively. This suggests that electrons interact almost as strongly with $A_1(\text{LO})$ as with $E_1(\text{LO})$ phonon modes in GaN.

Because the laser pulse width in our experiment is $\cong 2\text{ ps}$, if the phonon lifetimes for various phonon modes vary dramatically then it can play a role in the interpretation of the observed phonon populations. However, since the energies of those high frequency phonons are very close to each other (ranging from 550 to 750 cm^{-1}), we expect that their lifetimes should be about the same. Therefore, the increase in the measured phonon populations of the $A_1(\text{LO})$ and $E_1(\text{LO})$ modes must be an indication that the electron-phonon interaction is much stronger for these particular phonon modes. This is expected from the polar nature of GaN, as the Fröhlich interaction is usually the dominant electron-phonon interaction.

CONCLUSIONS

Picosecond Raman spectroscopy has been used to study electron-phonon interactions in the wide bandgap semiconductor GaN. Our experimental results demonstrated that high energy electrons in this wurtzite structure semiconductor relax toward the bottom of the conduction band primarily through the emission of longitudinal optical phonons, and that the Fröhlich interaction is much stronger than the deformation potential interaction.

ACKNOWLEDGEMENTS

This work was supported in part by the National Science Foundation under Grant No. DMR-9301100.

REFERENCES

1. For a review, see H. Morkoc, S. Strite, G.B. Gao, M.E. Lin, B. Sverdlov and M. Burns, J. Appl. Phys. Rev. Vol.76, No. 3,1363 (1994); also, S. Strite and Morkoc, J. Vac. Sci. Tech. B10(4), 1237 (1992).
2. D.K. Ferry, Phys. Rev. B12, 2361 (1975).
3. K.T. Tsen, R.P. Joshi, D.K. Ferry and H. Morkoc, Phys. Rev. B39, 1446 (1989).
4. D.S. Kim and P.Y. Yu, in Light Scattering in Semiconductor Structures and Superlattices, edited by D.J. Lockwood and J.F. Young (Plenum Press, New York, 1991), p. 383.
5. T. Azuhata, T. Sota, K. Suzuki, S. Nakamura, J. of Phys. Condensed Matter 7, L129 (1995).
6. K.T. Tsen, K.R. Wald, T. Ruf, P.Y. Yu and H. Morkoc, Phys. Rev. Lett. 67, 2557 (1991).

FINE STRUCTURE OF THE 3.42 eV EMISSION BAND IN GaN

S. FISCHER*, C. WETZEL, W. WALUKIEWICZ, and E.E. HALLER

Lawrence Berkeley National Laboratory and University of California, Berkeley, CA 94720, USA

ABSTRACT

A luminescence band centered around 3.42 eV is commonly observed in GaN. Its appearance has been tentatively assigned to an oxygen donor level. Stimulated laser activity has also been reported at this energy. We present a study of this band in GaN grown by high temperature vapor phase epitaxy (HTVPE). The high quality of this material, with an excitonic line width as narrow as 3 meV, allows us to distinguish four different peak positions of this luminescence band. They appear at 3.4066, 3.4121, 3.4186, and 3.4238 eV ($T = 6$ K). Within the experimental error the lines exhibit an equidistant spacing of 6 meV. They show a pressure behavior similar to shallow levels described by effective mass theory. We discuss our results in the context of incorporation of oxygen and structural defects in GaN.

INTRODUCTION

The strong commercial interest for the group-III nitrides is primarily based on its application in light emitting devices. A characterization of the materials properties by photoluminescence (PL), however, is not just a natural consequence, but in addition can provide detailed information on the recombination processes involved. So far several characteristic luminescence bands have been described in GaN which can be attributed to one of the following: Transitions between shallow bound carriers in the vicinity of the bandgap, transitions in the blue-violet spectral range involving an acceptor level and a broad band in the yellow part of the visible spectrum of as yet unidentified origin. In addition a strong band centered around 3.42 eV is frequently observed in low temperature PL spectra of GaN [1-8]. Lying energetically between the transitions of shallow bound carriers and acceptor related transitions this band recently attracted considerable interest. Several groups have reported stimulated emission at this photon energy in optically pumped GaN. Laser activity was observed at 3.424 eV (10 K) [9] and 3.43 eV (77 K) [10]. These values coincide with the 3.42 eV band described here. In those reports, however, no explanation could be given on the origin of this transition. In PL studies this transition has been found in GaN powder [2,5,7], single crystal needles [1], as well as in epitaxial films on sapphire (HVPE [4,6], MBE [3] and MOCVD [8]). The reported peak energy vary between 3.41 and 3.435 eV. The appearance of this band could not be correlated to special conditions of the growth processes in these reports.

It has been reported that doping of GaN by incorporation of C [5], Hg or Li [7] in the Ga melt produces or enhances this emission. In a very recent report, however, it was found that both, injection of H_2O during MOCVD growth, or implantation of O can produce this PL band (3.424 eV) [8]. In the same work it was found that implantation of O in HVPE material produced this band at 3.415 or 3.424 eV and it was assigned to a donor to valance band (D^0h) transition involving a 78 meV deep O related donor level. The observed PL features were broad and no fine structure could be resolved most likely due to the high n-type conductivity [8].

In a study of this band by time resolved PL a wide distribution of recombination life times was found. The peak energy ranged between 3.414 and 3.422 eV in these MBE grown samples. From the distribution of the life times found incorporation of several levels in this transition was concluded. But again, no fine structure in standard, time integrated, PL could be found [3].

We present data of various GaN samples resolving up to four different peaks contributing to the 3.42 eV band.

EXPERIMENTAL

Nominal undoped GaN films were grown by High Temperature Vapor Phase Epitaxy (HTVPE). In this unconventional growth technique liquid Ga and NH_3 act as Ga and N sources. No transport gas is necessary. Growth onto various substrates was performed at a temperature of 1200 - 1240°C. GaN was grown either on sapphire (c- and r-plane), 6H-SiC (c-plane) or directly onto the graphite crucible. Highly oriented films at thicknesses up to 20 μm were obtained on the substrates, whereelse growth by nucleation on the graphite resulted in microcrystalline grains (typically 100 μm in diameter). The best crystalline quality was achieved on SiC substrates as shown by x-ray rocking curve measurements. More details are given in Ref. [11].

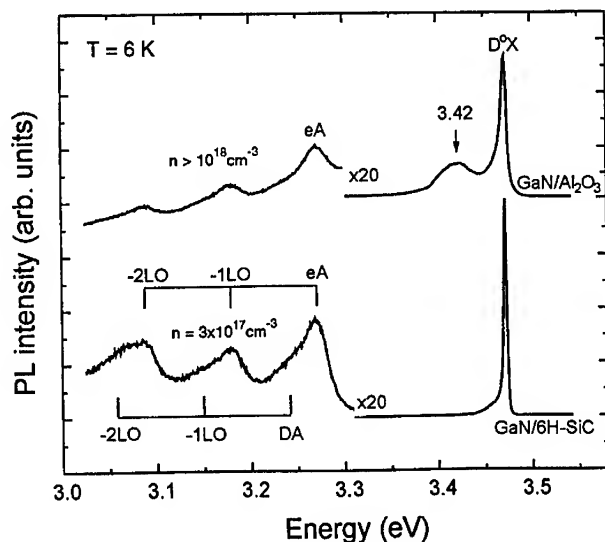


Fig. 1: Representative PL spectra of GaN films grown on sapphire and 6H-SiC. Both are dominated by the donor bound exciton at 3.472 eV. The striking feature is the appearance of a strong 3.42 eV luminescence in the film grown on sapphire.

PL was performed at both low temperature (6 K) and temperature dependent (6 K-300 K). The luminescence was excited with the 325 nm line of a 10 mW HeCd Laser. The emitted light was dispersed by a 0.85 m double monochromator and detected by a UV sensitive photomultiplier using lock-in technique. Additional hydrostatic pressure was applied by means of a Merrill-Bassett type diamond anvil cell. The fluorescence of the R_1 ruby lines at 6 K was used for pressure determination [12].

RESULTS

A typical PL spectrum at 6 K of GaN/6H-SiC and GaN/sapphire films is presented in Fig. 1. For GaN/6H-SiC the PL is dominated by the donor bound exciton (D^0X). At lower energies clearly resolved band-acceptor (eA) and donor-acceptor (DA) transitions between the residual donor and carbon acceptor are present [13]. In this material no contribution can be found in the vicinity of 3.42 eV. The energetic distance between the DA and eA transitions can be used to determine the free carrier concentration by an interpretation of the coulomb shift. The derived concentrations are in the high 10^{16} and low 10^{17} cm^{-3} for the GaN on 6H-SiC films. For GaN/sapphire the PL is also dominated by the D^0X . However, a second prominent emission is the band found at 3.42 eV. At lower energies in the range of the acceptor related transitions, an eA, but no DA transition is observed. This indicates a rather high carrier concentration above $n = 1 \times 10^{18}$ cm^{-3} [13]. The PL of small substrate-free grown crystals is very similar to the spectrum of GaN on sapphire.

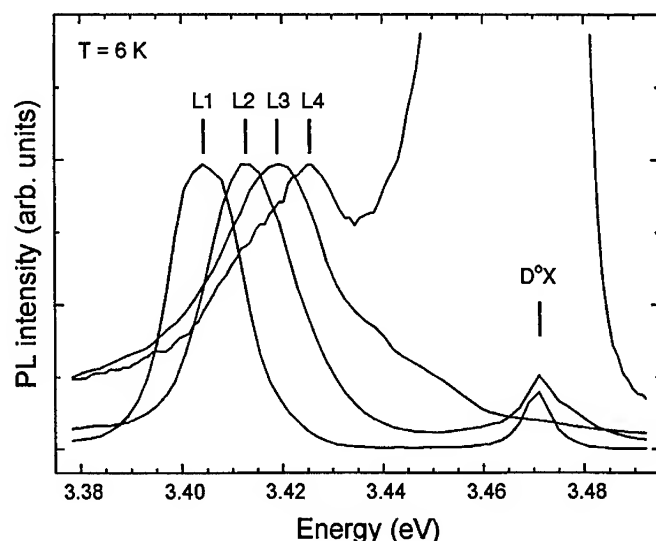


Fig. 2: Normalized PL spectra of different samples showing the four distinct peak positions of the 3.42 eV band. The peaks are named L1, L2, L3, and L4 with peak energies of 3.4066, 3.4121, 3.4186, and 3.4238 eV, respectively. The peak at higher energy is the donor-bound exciton (D^0X).

The peak position of the 3.42 eV band varies within different samples of the HTVPE material. We are able to resolve four distinct peak positions. They appear at 3.4066, 3.4121, 3.4186, and 3.4238 ± 0.002 eV and are named furtheron L1, L2, L3, and L4, respectively (see Fig. 2). For all of those samples we find the identical value of the D°X line at 3.4715 ± 0.0019 eV. This value is very close to the energy observed in bulk material [14]. This indicates that all films are already relaxed and no residual stress is present. This therefore rules out any stress effect that could have let to a splitting of a single transition at 3.42 eV. Therefore we find optical binding energies of 96.4, 90.9, 84.4, and 79.2 meV with respect to the bandgap of GaN (3.503 eV at 6K [15]).

It is seen in Fig. 2 that L1 - L3 appear as the dominant emissions in the PL spectrum. However this behavior is only observed on samples grown on sapphire, where the growth process was stopped before the entire substrate area was covered. In this case the full width at half maximum (FWHM) of the L1 - L3 lines is below 30 meV and as low as 14.1 meV. If the (D°X) is the dominant emission the FWHM of the lines L1 - L4 is above 30 meV and as broad as 60 meV. This gives rise to the assumption that the broad emissions contain contributions of their adjacent lines. Additionally a weak 3.42 eV luminescence is found in GaN films grown on 6H-SiC of lower crystalline quality exhibiting a cracked surface.

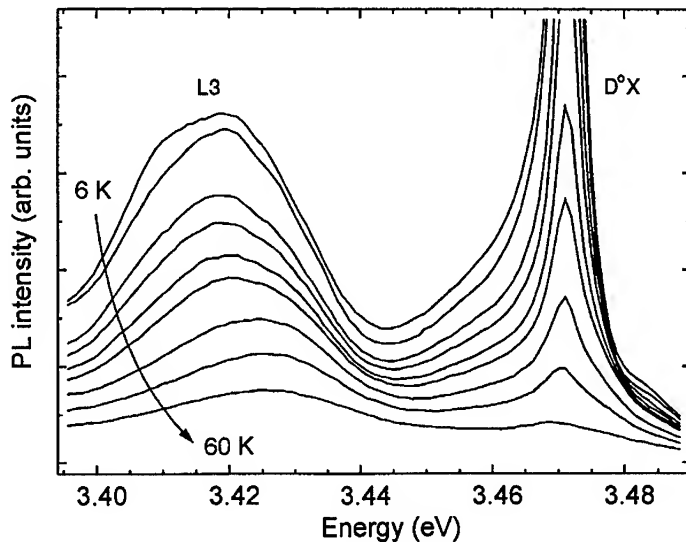


Fig. 3: The luminescence of the L3 line is shown as a function of temperature. From 6 to 40 K L3 shifts to higher energies. Above 40 K it decreases in energy simultaneously to the (D°X). This temperature dependence is typical for a free-to-bound transition.

In order to investigate the origin of these recombinations temperature dependent PL was performed on a sample with a peak emission at L3. From 6 to 40 K L3 shifts to higher energies with a slope of 0.21 meV/K. Above 40 K it shifts to lower energies almost simultaneously with the (D°X), see Fig. 3. Contrary to another report both emissions can be well separated above 80 K

and even resolved at 300 K. From the thermal quenching a activation energy of the L3 line of $E_A = 19 \pm 2$ meV is determined.

Additional hydrostatic pressure up to 1.7 GPa was applied to the small GaN crystals exhibiting the same PL as the GaN films grown on sapphire. The 3.42 eV emission was again on the L3 position. Under increasing hydrostatic pressure L3 shifts towards higher energies parallel to the (D^0X). We find a linear pressure dependence for both, the L3 line and the (D^0X), similar to a recently determined one in an AlGaIn/GaN/sapphire sample for the (D^0X) of the GaN layer [16].

DISCUSSION

We will mainly discuss the L3 level under the assumption that L1, L2, and L4 show a similar behavior.

The shift to higher energies with increasing temperature is typical for a free to bound transition. This shift can be attributed to an increase in the mean velocity of holes in the valence band of a (D^0h) transition. In this case the thermal activation reveals the involved donor. One has to keep in mind that in n-type material the Fermi level lies approximately in the middle between the dominant shallow donor level and the conduction band (CB). Only half of the donor binding energy is therefore necessary to excite electrons from the Fermi level to the CB. This would indicate that a donor level 38 meV below the CB is involved, which is within the experimental error the residual donor in GaN ($ED = 35.5$ meV [17]). The activation energy and the residual donor level depth are significantly lower than the determined level position of 85 meV below the CB. Also the appearance of four different peak positions can not be explained within the simple (D^0h) model.

On the other hand the pressure dependent measurement showed that the level shifts parallel to the bandgap. This is the expected behavior for a hydrogenic level which can be described by effective mass theory. Therefore deep localized levels can be excluded.

In general in GaN films grown on sapphire an one order of magnitude higher carrier concentrations compared to the films grown on 6H-SiC is observed. High resolution transmission electron microscopy reveals that the sapphire substrate is significantly affected at the growth temperature in contrast to 6H-SiC [18]. Thus a release of O from the substrate and a doping of the GaN film is possible. In Ref. [8] injection of H_2O during growth lead to higher carrier concentrations, which was attributed to an additional incorporation of O donors. O is also a candidate for the residual donor in GaN [19], whereas as shown above the residual donor level is much shallower than the L1 - L4 levels.

However the following has to be taken into account. On GaN/SiC samples of lower structural quality a weak 3.42 eV luminescence can be observed. Additionally the microcrystalline GaN exhibit the same PL as GaN on sapphire. In both, the microcrystalline GaN and the films grown on sapphire much more structural defects are observed than in the GaN films grown on 6H-SiC [18]. This seems to be obvious considering the larger lattice mismatch of sapphire compared to 6H-SiC or the random nucleation on the crucible. Therefore one also has to consider structural defects to be responsible for the L1 - L4 lines. This could explain the observations in other publications where the 3.42 eV band vanished in the films of higher structural quality [4,6].

To summarize we have found four distinct peak position of the 3.42 eV band, named L1, L2, L3, and L4, at 3.4066, 3.4121, 3.4186, and 3.4238 eV, respectively. Under hydrostatic pressure the respective levels shift like shallow hydrogenic levels parallel to the bandgap. Temperature dependent PL measurements show a shift towards higher energies as expected for a (D^0h) transition. However the revealed thermal activation energy is much lower than the corresponding energetic position of the respective level.

Besides the believed involvement of a O related donor level in these transitions [8] there is experimental evidence for structural defects playing a major role.

ACKNOWLEDGMENTS

We gratefully acknowledge helpful discussions with B.K. Meyer. This work was partially supported by US DOE under contract DE-AC03-76SF00098. C.W. thanks the Deutsche Forschungsgemeinschaft for a grant.

REFERENCES

* current address: Physik Department E16, Technical University Munich, 85747 Garching, Germany

- [1] T. Matsumoto and M. Aoki, Jap. J. Appl. Phys. **13**, 1804 (1974).
- [2] T. Ogino and M. Aoki, Jap. J. Appl. Phys. **18**, 1049 (1979).
- [3] M. Smith, G.D. Chen, J.Y. Lin, H.X. Jiang, A. Salvador, B.N. Sverdlov, A. Botchkarev, and H. Morkoc, Appl. Phys. Lett. **66**, 3474 (1995).
- [4] R. Dai, S. Fu, J. Xie, G. Fan, G. Hu, H. Schrey, and C. Klingshirn, J. Phys. C **15**, 393 (1982).
- [5] T. Ogino and M. Aoki, Jap. J. Appl. Phys. **19**, 2395 (1980).
- [6] R. Dingle, D.D. Shell, S.E. Stokowski, and M. Ilegems, Phys. Rev. B **4**, 1211 (1971).
- [7] H.G. Grimmeis and B. Monemar, J. Appl. Phys. **41**, 4054 (1970).
- [8] B.-C. Chung and M. Gershenson, J. Appl. Phys. **72**, 651 (1992).
- [9] X.H. Yang, T.J. Schmidt, W. Shan, J.J. Song, and B. Goldenberg, Appl. Phys. Lett. **66**, 1 (1995).
- [10] H. Amano, I. Asashi, M. Kito, and I. Akasaki, J. Luminescence **48&49**, 889 (1991).
- [11] S. Fischer, C. Wetzel, E. Bourret, W.L. Hansen, and E.E. Haller, presented at the 1995 MRS Spring Meeting, San Francisco, CA, 1995 (unpublished).
- [12] H.K. Mao, J. Xu, and P.M. Bell, J. Geophys. Research **91**, 673 (1986).
- [13] S. Fischer, C. Wetzel, E.E. Haller, and B.K. Meyer, Appl. Phys. Lett. **67**, 1298 (1995).
- [14] K. Naniwae, S. Itoh, H. Amano, K. Itoh, K. Hiramatsu, and I. Akasaki, J. Crystal Growth **99**, 381 (1990).
- [15] B. Monemar, Phys. Rev. B **10**, 676 (1974).
- [16] C. Wetzel, W. Walukiewicz, E.E. Haller, H. Amano, and I. Akasaki in Defect and impurity engineered semiconductors and devices, edited by A. Ashok, J. Chevallier, I. Akasaki, and N.M. Johnson (Mater. Res. Soc. Proc. **378**, Pittsburgh, PA, 1995).
- [17] B.K. Meyer, D. Volm, A. Graber, H.C. Alt, T. Detchprohm, H. Amano, and I. Akasaki, Solid State Commun. **95**, 597 (1995).
- [18] Z. Liliental-Weber, private communication.
- [19] W. Seifert, R. Franzheld, E. Butter, H. Sobotta, and V. Riede, Cryst. Res. & Technol. **18**, 383 (1983).

SPATIALLY-RESOLVED PHOTOLUMINESCENCE AND RAMAN STUDY ON THE GaN/SUBSTRATE INTERFACE

H. SIEGLE, P. THURIAN, L. ECKEY, A. HOFFMANN, AND C. THOMSEN

Institut für Festkörperphysik, Technische Universität Berlin, 10623 Berlin, Germany

B. K. MEYER

Technische Universität München, Physik-Department E16, 85747 Garching, Germany

T. DETCHPROHM, K. HIRAMATSU

Nagoya University, Nagoya, Japan

H. AMANO, I. AKASAKI

Meijo University, Nagoya, Japan

ABSTRACT

We performed spatially-resolved photoluminescence and Raman experiments on the substrate interface region of wurtzite GaN layers. We found that the broad "yellow" photoluminescence band is strong only near the interface. Our investigations reveal that both the substrate interface and a region of structural reorientation of the layer near the interface act as source of the photoluminescence. The Raman-scattering experiments show that at least a portion of the GaN layer near the substrate interface is oriented in such a way that the c-axis of the layer is parallel to the substrate interface. At a distance about 30 μm away from the interface the layer reorients by turning the c-axis by 90° into a direction perpendicular to the substrate interface.

INTRODUCTION

The wide-bandgap semiconductor GaN has attracted considerable attention over the last years because of its application as a basic material for optoelectronic devices working in the blue and UV spectral region, such as blue laser diodes [1]. Apart from the near-bandgap excitonic and donor-acceptor-pair luminescence GaN shows an unwanted broad "yellow" photoluminescence band between 2.0 and 2.5 eV at low temperatures [2]. Recently, intensive work has been done to clarify its origin, and some authors connect this luminescence band with the inherent property of GaN to be automatically n-type conductive [3-5]. However, this issue is still controversial.

Similar luminescence bands are also known from several II-VI semiconductors like ZnS [6]. They are often interpreted as a recombination between shallow donors and deep acceptors in which the donors or the acceptors were built by anion or cation vacancies. The creation of such intrinsic vacancies is very probable near surfaces, interfaces or grain boundaries.

In order to clarify whether the broad "yellow" photoluminescence band is an intrinsic property of GaN or caused by defects located near the interface to the substrate, we performed spatially-resolved photoluminescence and Raman measurements on hexagonal GaN samples which were grown on sapphire. We found that the luminescence band is strong only in a region near the interface and hence not an intrinsic property of GaN. Our investigations reveal that the photoluminescence originates from both the substrate interface and a region of structural reorientation near the interface where the c-axis of the GaN layer rotates by 90° from a direction parallel into a direction perpendicular to the substrate interface.

EXPERIMENT

The samples investigated were undoped wurtzite GaN layers grown on [0001] sapphire using hydride vapor phase epitaxy (HVPE) with thicknesses of 220 μm , 230 μm and 400 μm and a free carrier concentration of about $1 \cdot 10^{17} \text{ cm}^{-3}$. The spatially-resolved photoluminescence and Raman experiments were carried out using a Dilor XY800 triple-grating spectrometer with a charge-coupled device (CCD) detector and confocal optics. The sample was excited either parallel (in-plane) or perpendicular (on-plane) to the substrate surface using the 488 nm (2.54 eV) line of an $\text{Ar}^+ \text{-Kr}^+$ mixed-gas laser and the 632.8 nm (1.96 eV) line of an He-Ne Laser. By passing the laser through a microscope objective (x80) the laser beam was focused on a point spot with a diameter of about 1 μm and a power of 2 mW. The scattered light was detected in backscattering geometry which corresponds to an $x(\cdot)\bar{x}$ configuration for in-plane excitation and a $z(\cdot)\bar{z}$ configuration for on-plane excitation (under the assumption, that the z is parallel to the c -axis). The samples were cooled down to 4.2 K using an Oxford microscope cryostat. With this setup we obtained a spatial resolution of about 1 μm and a spectral resolution better than 1 cm^{-1} .

RESULTS

Figure 1 shows a 40 μm long linescan across the GaN-substrate interface where we have taken a spectrum every 1 μm . The region of the substrate is marked by the presence of the A_g sapphire mode at 419 cm^{-1} [7]. The transition to the GaN layer is indicated by the appearance of the $A_1(\text{TO})$ and the E_2 modes at 534 cm^{-1} and 569 cm^{-1} , respectively. A photoluminescence band with an intensity maximum at 2.4 eV appears directly at the interface with the substrate; it is seen as constant in Raman shift background, since it is broad compared to the spectral range observed here. The spatial width of the region from which this photoluminescence occurs is about 3 μm . The GaN region is dominated by the abruptly increasing $A_1(\text{TO})$ mode. At a

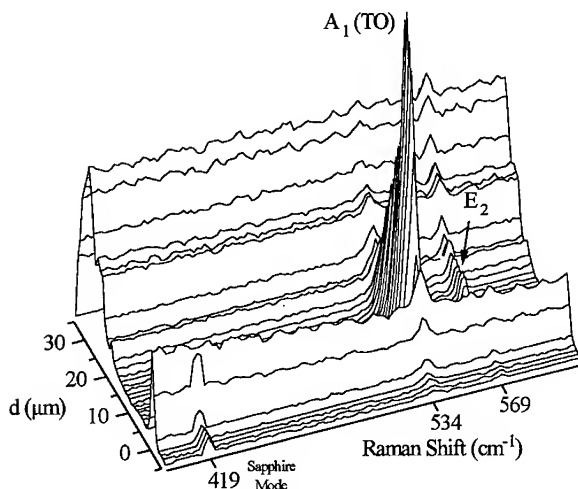


Fig. 1: Linescan across the GaN-substrate interface of a 400 μm thick layer taken at 4.2 K. In order to emphasize the sapphire Raman mode it was multiplied by a factor of 2.

distance d of about $30\text{ }\mu\text{m}$ away from the substrate interface, in a region several μm wide, a second broad photoluminescence band appears peaking at the same spectral position as the first photoluminescence band. Simultaneously with the increasing photoluminescence the intensity of the $A_1(\text{TO})$ Raman signal decreases but the modes continues to be visible.

The spatial continuation of Fig. 1 is shown in Fig. 2 on an expanded spectral and spatial scale. The decrease of the $A_1(\text{TO})$ Raman signal (near $d = 20\text{ }\mu\text{m}$) and the broad photoluminescence band (at $d = 30\text{ }\mu\text{m}$) can be seen. Of particular importance is the change in scattering intensity of the different phonon modes. While both, the E_2 mode and the $A_1(\text{TO})$ mode appear in this region the ratio of their intensity inverts with increasing distance from the substrate interface. We have clarified this in Fig. 3 where we show individual spectra taken at 15, 25 and $50\text{ }\mu\text{m}$. The strong luminescence was subtracted in the middle spectrum of Fig. 3. The change in intensity starts where the second photoluminescence band appears. While near the interface with the substrate ($0 \leq d \leq 20\text{ }\mu\text{m}$) the spectra are dominated by the $A_1(\text{TO})$ mode the intensity of the E_2 mode increases with the appearance of the second photoluminescence band and becomes the most intensive phonon mode ($d > 35\text{ }\mu\text{m}$). The inversion of the relative intensities can be explained by a structural reorientation of the GaN layer. It is interesting to note that the frequencies of both, the $A_1(\text{TO})$

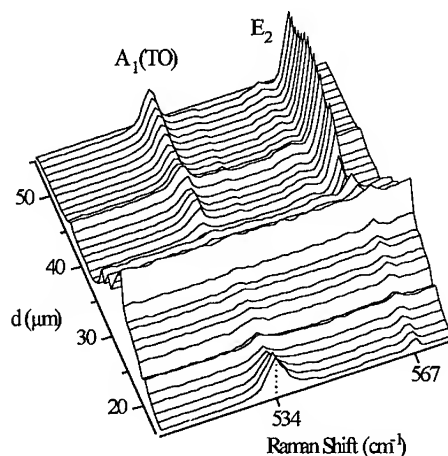


Fig. 2: Spatial continuation of Fig. 1. Linescan across the inner interface caused by a reorientation of the GaN layer taken at 4.2 K. For clarification the spectral scale was enlarged.

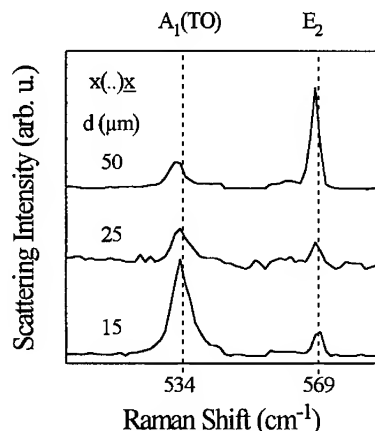


Fig. 3: Raman spectra of the $400\text{ }\mu\text{m}$ thick GaN layer taken at various distances d from the interface with in-plane excitation. The red shift can be explained by strain relaxation.

mode and the E_2 mode decrease by about 2 cm^{-1} for distances larger than $25 \text{ }\mu\text{m}$ (Fig. 3), which is likely to be caused by strain relaxation. This is consistent with the results of Kozawa et al. [8] who observed a decrease of $\sim 1 \text{ cm}^{-1}$ for increasingly relaxed GaN layers.

In Table I the selection rules for first-order Raman scattering of hexagonal material and in-plane excitation are listed [9, 10]. Comparing Table I with the corresponding Raman spectra in Fig. 3 reveals that for the region near the substrate interface ($0 \leq d \leq 20 \text{ }\mu\text{m}$) where the spectra are dominated by the $A_1(\text{TO})$ mode the GaN layer is oriented in such a way that the scattering geometry corresponds to $x(\text{zz})\bar{x}$. For $d > 35 \text{ }\mu\text{m}$ the E_2 mode is the strongest mode and the $A_1(\text{TO})$ is still observable. This combination corresponds to $x(\text{yy})\bar{x}$. Since the incident polarization of the exciting laser remained parallel to the substrate interface and constant throughout the experiment our results show that the c-axis of the GaN layer near the substrate is parallel to the interface and turns by about 90° at a larger distance ($d > 20 \text{ }\mu\text{m}$) from the interface. This becomes more clear when considering Fig. 4 in which a depth profile of room-temperature Raman spectra taken in $z(\text{yy})\bar{z}$ configuration on a $220 \text{ }\mu\text{m}$ layer are plotted. By using the 632.8 nm line of a He-Ne laser no photoluminescence was excited. The confocal optics allows to record Raman spectra at several depths, i. e. distances to the substrate interface. All spectra are

Tab. I: Raman selection rules for backscattering configuration used in this work. The c-axis is parallel to the z direction.

Scattering Configuration	Allowed Modes
$z(\text{yy})\bar{z}$	$A_1(\text{LO}), E_2$
$x(\text{zz})\bar{x}$	$A_1(\text{TO})$
$x(\text{yz})\bar{x}$	$E_1(\text{TO})$
$x(\text{yy})\bar{x}$	$A_1(\text{TO}), E_2$

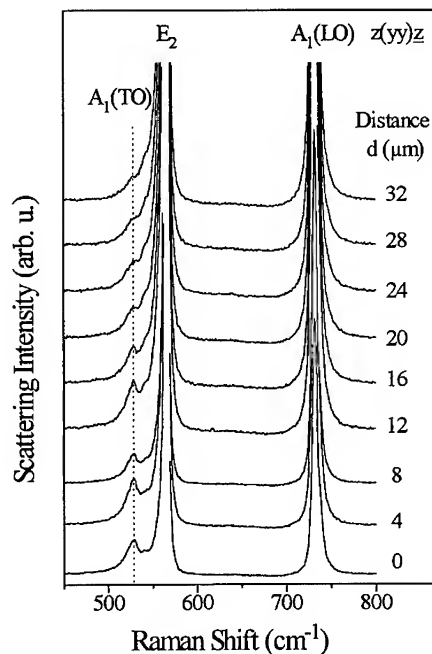


Fig. 4: Depth profile of a $220 \text{ }\mu\text{m}$ thick GaN layer. The Raman spectra are taken at room temperature using the 632.8 nm line of a He-Ne laser.

dominated by the E_2 and the $A_1(\text{LO})$ modes but near the substrate interface the $A_1(\text{TO})$ mode can clearly be seen. The scattering intensity decreases with increasing distance to the interface. According to the selection rules listed in Tab. I the $A_1(\text{TO})$ is only excitable if the c-axis lies perpendicular to the incident wave vector. Hence it follows from both in- and on-plane Raman measurements that at least a portion of the GaN layer near the interface to the substrate is oriented parallel to it. This reorientation yields a further interface which like the substrate interface acts as source of the broad luminescence band.

CONCLUSIONS

We have shown that the origin of the broad photoluminescence band with an intensity maximum at 2.4 eV is not homogeneously distributed in our GaN layers. Instead, we found that the luminescence is strong only near the interface region. A first luminescence band appears directly at the interface with the substrate, a second one appears approximately 30 μm away from the interface in a region which is several μm wide. Simultaneously performed Raman scattering experiments allowed us to analyze layer orientation and strain and revealed that the second band appears where a significant reorientation of the wurtzite GaN c-axis from parallel to perpendicular to the substrate surface occurs. This observation suggests that the 2.0 - 2.5 eV luminescence is not intrinsic to GaN but occurs primarily near structural defects.

ACKNOWLEDGMENTS

This work was in parts supported by the Stifterverband für die Deutsche Wissenschaft.

REFERENCES

- [1] R. F. Davis, *Physica* **185B**, 1 (1993); S. Strite and H. Morkoç, *J. Vac. Sci. Technol.* **B10**, 1237 (1992)
- [2] J. I. Pankove and J. A. Hutchby, *J. Appl. Phys.* **47**, 5387 (1976); T. Ogino and M. Aoki, *Jap. J. Appl. Phys.* **19**, 2395 (1980)
- [3] D. M. Hofmann, D. Kovalev, G. Steude, B. K. Meyer, A. Hoffmann, L. Eckey, T. Detchprom, A. Amano, and I. Akasaki, *Phys. Rev. B*, in print
- [4] E. R. Glaser, T. A. Kennedy, H. C. Crookham, J. A. Freitas jr., M. Asif Khan, D. T. Olson, and J. N. Kuznia, *Appl. Phys. Lett.* **63**, 2673 (1993)
- [5] P. Perlin, T. Suski, H. Teisseyre, M. Leszczynski, I. Grzegory, J. Jun, S. Porowski, P. Boguslawski, J. Bernholc, J. C. Chervin, A. Polian, and T. Moustakas, *Phys. Rev. Lett.* **75**, 296 (1995)
- [6] J. R. James, J. E. Nicholls, B. C. Cavenett, J. J. Davies, D. J. Dunstan, *Solid State Commun.* **17**, 969 (1975)
- [7] For a survey of Raman spectra on sapphire see for example: S. P. S. Porto and R. S. Krishnan, *J. Chem. Phys.* **47**, 1009 (1967)
- [8] T. Kozawa, T. Kachi, H. Kano, H. Nagase, N. Koide, and K. Manabe, *J. Appl. Phys.* **77**, 4389 (1995)
- [9] C. A. Arguello, D. L. Rousseau, and S. P. S. Porto, *Phys. Rev.* **181**, 1351 (1969)
- [10] H. Siegle, L. Eckey, A. Hoffmann, C. Thomsen, B. K. Meyer, D. Schikora, M. Hankeln, K. Lischka, *Solid State Commun.* **96**, 943 (1995)

EXCITATION WAVELENGTH AND SATURATION EFFECTS ON GALLIUM NITRIDE PHOTOLUMINESCENCE

Mike Banas, Guangtian Liu, Jeff Ramer, Kang Zheng, Steve Hersee, Kevin Malloy
Center for High Technology Materials, University of New Mexico, Albuquerque, NM 87131.

Abstract

We report on the excitation wavelength and power dependence of LPMOCVD grown GaN photoluminescence (PL). A mode-locked Ti:Sapphire laser that is doubled to provide a tunable wavelength range of 350-500 nm is used to pump the GaN samples. Special attention has been paid to the "yellow" (~567 nm) luminescence. Different power dependence characteristics of the yellow emission are observed when pumping above and below the bandgap. A measurement of the photoluminescence excitation spectrum of the yellow peak (~567 nm) is also performed and this spectrum shows a peak at room temperature at 3.36 eV (369 nm), an additional broad peak at 77 K and only the broad peak at 7 K. An excitation model is used to explain the behavior of the yellow emission, suggesting the neutral donor serves as a key species for the yellow emission.

Introduction

A broad yellow photoluminescence band centered at about 2.2 eV is frequently observed in GaN crystals. This important parasitic transition may limit the possible optical applications of GaN. Previous work¹⁻⁴ suggested that the yellow emission involves a shallow donor level. We report the photoluminescence excitation (PLE) of the yellow emission which supports the involvement of the shallow donor and provides additional insight into the mechanism of the yellow emission.

Experiment

Thin films of unintentionally doped wurtzite GaN were grown by low pressure metal-organic chemical vapor deposition (LPMOCVD). A-plane [1120] sapphire substrates were used and were solvent-cleaned before growth. Low temperature buffer layers were deposited at temperatures between 480 and 600 °C. The temperature was then ramped to the main growth temperature of 1025 °C and the GaN epilayers were grown at a chamber pressure of 100 Torr. Trimethylgallium and high purity ammonia sources were used with a hydrogen carrier gas. A typical deposition rate was about 2 $\mu\text{m h}^{-1}$, yielding samples with thicknesses of about 4 or 5 μm . Hall measurements indicate n-type conduction, with a mobility of 200-500 $\text{cm}^2\text{V}^{-1}\text{s}^{-1}$ and an electron concentration of 10^{17} cm^{-3} .

The PL excitation source is a Coherent Mira Model 900 Ti:Sapphire laser that is frequency doubled or tripled to give a tunable wavelength range of 233-333 nm and 350-500 nm. The Ti:Sapphire laser has a pulse width of 200 fs and a repetition rate of 76 MHz. A typical average power from the doubler is about 150 mW. This power is focused to an estimated 10 μm spot radius to give a maximum average power density on the order of 10^4 W cm^{-2} and a maximum peak power density on the order of 100 MW cm^{-2} . The PL was collected by a lens and focused onto the entrance slits of an Acton SpectraPro 0.275 m monochromator. A Hamamatsu GaAs photomultiplier (R-636) was used to detect the UV and visible light and a North Coast Ge detector (EO-817) cooled by liquid nitrogen was used to detect the infrared light. The detector outputs were read by a Stanford Research Systems SR850 lock in amplifier. Measurements were made at room temperature as well as liquid nitrogen and liquid helium temperatures.

The excitation wavelength was varied from 350-450 nm. A set of neutral density filters was used to attenuate the incident laser intensity for studying the excitation power dependence of the PL. The yellow emission at 567 nm was measured as a function of incident power at each wavelength step. This data was then used to obtain the PLE spectrum for fixed photon fluxes.

Results and Discussion

Excitation Wavelength Dependence

The PLE spectrum at room temperature for the yellow emission is shown in Figure 1. A PL spectrum is overlaid on this plot to demonstrate that absorption and emission occur at different wavelengths.

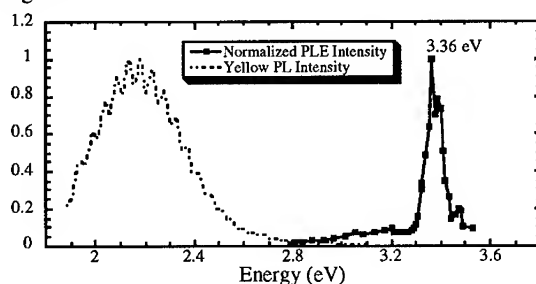


Figure 1: Normalized PLE spectrum with overlaid yellow PL spectrum.

Neither the peak nor the full width at half maximum of the broad yellow emission changes as the excitation wavelength is varied. The PLE spectrum indicates the existence of a narrow band of shallow donors. The plot also shows some as yet unidentified fine structure. The donor absorption mechanism can be represented by $D^+ \rightarrow D^0 + h$, from which it is concluded that the yellow transition begins with a process involving the neutral donor. The model shown in Figure 2 is used to describe the observed transition. It is evident that the radiative yellow transition is only accessible through the shallow donor states since no direct absorption of the yellow is observed. The complimentary infrared transition that has been previously reported⁵ has not been observed in these experiments, and therefore some form of nonradiative relaxation is assumed to occur before yellow emission.

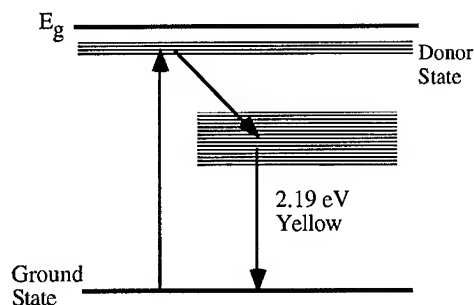


Figure 2: Excitation model of yellow emission.

Power Dependence

The PL intensity was measured as a function of incident power at each wavelength step. Figure 3 illustrates the behavior of the bandedge and the yellow for above gap pumping as the pump power is varied. It is observed that the yellow PL intensity is proportional to F^k where F is the intensity of the pump. The measured value of k is plotted as a function of excitation energy in Figure 4.

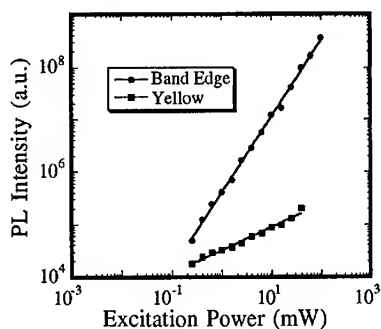


Figure 3. Typical PL power dependences for above gap pumping.

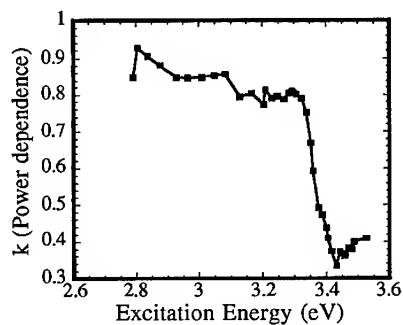


Figure 4: Yellow PL power dependence as a function of excitation energy.

Above gap pumping yields a nearly square root dependence ($k \approx 0.4$) while below gap pumping yields a nearly linear ($k \approx 0.8-0.9$) dependence on input power. We note that the data does not fit well to an F^k dependence in the wavelength region where k changes rapidly. The data outside this region can easily be explained by a three level model in which the conduction band and shallow donor band are treated as one level. Figure 5 shows this model with the labeled transition rates and level occupancies. N_1 represents the total number of midgap states and n_1 represents the number of occupied midgap states.

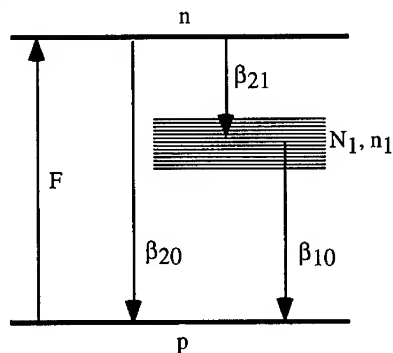


Figure 5: Rate model used to explain yellow emission kinetics.

Two independent rate equations and a charge neutrality equation can be written to analyze this model in the steady state:

$$\frac{dn}{dt} = F - \beta_{20}np - \beta_{21}n(N_1 - n_1) = 0 \quad (1)$$

$$\frac{dn_1}{dt} = \beta_{21}n(N_1 - n_1) - \beta_{10}n_1p = 0 \quad (2)$$

$$n = p + (N_1 - n_1). \quad (3)$$

If the excitation energy is below the bandedge and there is no competition with the bandedge transition ($\beta_{20} = 0$), the yellow emission term ($\beta_{10}n_1p$) becomes proportional to the pump (F). For above gap pumping, the assumption of high level injection ($n=p$) is invoked. Equation (3) implies that all the midgap states are filled which implies with Equation (1) that n and p are both proportional to \sqrt{F} . Thus the yellow emission term ($\beta_{10}n_1p$) also follows a \sqrt{F} dependence.

Temperature Dependence

Figure 6 shows the PLE spectrum as a function of temperature. Notice that the ionized donor absorption shifts to higher energies as the temperature is reduced, as expected for a near band gap donor transition. More significant is the emergence of a broad absorption peak at 3.22 eV. This absorption is consistent with a donor-acceptor-pair transition represented by $D^+A^- \rightarrow D^0A^0$ with an acceptor activation energy of about 0.25 eV. Figure 7 shows the photon flux dependence of this absorption at 77 K. At low incident flux the donor absorption dominates but as the flux is increased the DAP transition emerges and dominates. The temperature and flux dependence is consistent with freeze-out of free carriers on donors at low temperatures and the saturation of the donor absorption. Together, this data suggests the importance of the neutral donor state as key to the yellow luminescence.

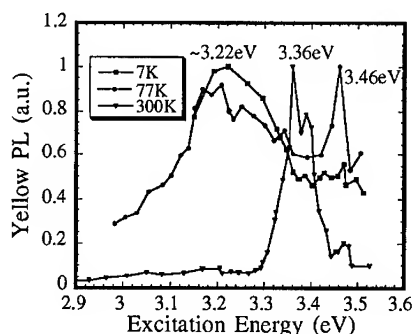


Figure 6. Temperature dependence of PLE Spectrum.

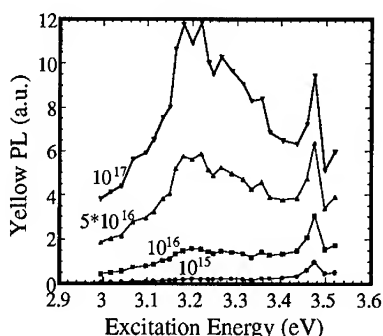


Figure 7. PLE spectrum at 77 K for various pumping photon fluxes (photons s^{-1}).

The power dependence of the yellow at 77K and 7K follow the same trend as at room temperature, i.e. a nearly square root dependence for above gap pumping and a nearly linear dependence for below gap pumping.

Conclusion

Previous investigations have linked the yellow emission with shallow donors. The room temperature PLE spectrum supports this identification with some as yet unidentified

structure occurring on an ionized donor absorption. As temperature is reduced, the reduction in the ionized donor concentration allows DAP absorption to occur. Both of these data suggest the neutral donor is crucial for yellow emission. The absence of a complementary infrared signal indicates that significant lattice relaxation probably occurs. The power dependent measurements indicate competition between bandedge emission and yellow emission for above gap pumping.

References

1. T. Ogino, M. Aoki, Jpn. J. Appl. Phys. **19**, 2395 (1980)
2. T. Suski, P. Perlin, H. Teisseyre, M. Leszczynski, I. Grzegory, J. Jun, M. Bockowski, S. Porowski, and T. Moustakas, Appl. Phys. Lett. **67**, 15 (1995)
3. E. Glaser, T. Kennedy, K. Doverspike, L. Rowland, D. Gaskill, J. Freitas, M. Asif Khan, D. Olson, J. Kuznia, and D. Wickenden, Phys. Rev. B **51**, 19 (1995)
4. S. Kim, I. Herman, J. Tuchman, K. Doverspike, L. Rowland, and D. Gaskill, Appl. Phys. Lett. **67**, 3 (1995).
5. M.W. Leksono, C.H. Oiu, W. Melton, and J.I. Pankove in Infrared Luminescence From MOCVD GaN, edited by C. Carter, G. Goldenblat, S. Nakamura, and R. Nemanich (Mater. Res. Soc. Proc. **339**, Pittsburgh, PA, 1994) pp. 559-564

SELECTIVE DYNAMICAL STUDY OF LUMINESCENCES NEAR THE SURFACE AND THE INTERFACE OF EPITAXIAL GaN

L. ECKEY, A. HOFFMANN, R. HEITZ, I. BROSER, B.K. MEYER*,
T. DETCHPROHM**, K. HIRAMATSU**, H. AMANO***, I. AKASAKI***
Technische Universität Berlin, Hardenberstraße 36, 10623 Berlin, Germany
*Technische Universität München, Germany
**Nagoya University, Nagoya, Japan
***Meijo University, Nagoya, Japan

ABSTRACT

Recombination processes and their dynamics are selectively studied (a) near the interface between a 400µm thick GaN epilayer and its Al₂O₃ substrate and (b) in the structurally relaxed regions near the surface of this sample. Strong radiative excitonic recombination is observed in the relaxed regions. However, the recombination dynamics of free and shallow-bound excitons here are strongly influenced by shallow and deep defects. Near the substrate the presence of dislocations suppresses radiative recombination of free and shallow bound excitons. Deeper emissions appear which we attribute to excitons deeply bound to dislocation-related defects. They exhibit ps-recombination dynamics effected by strong nonradiative contributions.

INTRODUCTION

The now demonstrated use of the InGaAlN alloy system over most of the visible spectrum makes it one of the key materials for future optoelectronic applications. Among the major research issues at this point is the development of a GaN-based blue laser diode. Present light-emitting diodes use an impurity related recombination process [1] and exhibit excellent performance despite a dislocation density as high as 10^9 cm^{-2} [2]. For laser action sufficient gain is expected to rely on an intrinsic recombination process involving free carriers or excitons. Present growth techniques using mismatched substrates cannot prevent the creation of dislocations and defects near the interface nor the incorporation of the intrinsic shallow donor 35 meV below the conduction band edge. It is therefore necessary to assess the influence of impurities and dislocations on the excitonic recombination processes and their dynamics in GaN.

The present paper will show that the dominating recombination processes near the interface between GaN and its lattice-mismatched substrate differ strongly from those far away from the interface, i.e., near the surface of the epilayer. We will show that in structurally perturbed regions such as in the vicinity of the interface, the radiative recombination of free and shallow bound excitons is quenched and deep dislocation excitons appear in the spectrum. A detailed report on the recombination dynamics both near and far away from the interface will be given.

EXPERIMENTAL

To separate the influence of the dislocations having a high density near the substrate interface from the properties of relaxed single-crystalline GaN we used in the main an epitaxial GaN layer of 400µm thickness grown by hydride vapor phase epitaxy without a buffer layer [3]. Using band-to-band excitation from either the epilayer side, or the substrate side we sampled without any overlap either high-quality, relaxed GaN near the surface or strongly perturbed GaN near the interface. Due to the high absorption coefficient above the gap, the estimated depth of excitation within the sample is less than 5 µm. We therefore use the terms 'bulk' and 'interface'

luminescence to distinguish between excitation from either the epilayer or the substrate side. The sapphire substrate is transparent at the energies of excitation and detection and does not influence the spectrum taken from the interface region. For continuous-wave (cw-) measurements a HeCd laser was employed. Time-resolved measurements were performed at various temperatures using a frequency-doubled dye laser synchronously pumped by an actively mode-locked and frequency-doubled Nd:YAG laser. The overall time resolution employing convolution techniques was 15 ps.

RESULTS

'Bulk' and 'Interface' Photoluminescence

Comparative cw low-temperature photoluminescence spectra taken from the 400 μm GaN epilayer are shown in Fig. 1. The spectrum in Fig. 1 (a) was obtained after excitation of the sample on the surface of the epilayer. The donor-bound-exciton line I_2 at 3.4782 eV is most prominent. Emission from the free A-exciton is seen at 3.4800 eV. The localization energy of the exciton at the donor thus amounts to 7.18 meV. High resolution spectra reveal the presence of a weak second donor-bound-exciton line with a localization energy of 3.6 meV. The energy positions of the free exciton and I_2 agree precisely with calorimetric reflection and absorption data taken from the same sample [4] and thus unambiguously determine the low temperature energy positions of the free and bound excitons in relaxed GaN. The linewidth of I_2 amounts to 920 μeV , a value that confirms the high quality of HVPE-grown 'bulk' GaN and its potential for a lattice-matched substrate material. Due to the high intensity of I_2 , the spectrum on its low-energy side has to be multiplied by a factor of 40 in the spectrum of Fig. 1 (a) to make manifest an acceptor bound exciton line I_1 at 3.446 eV. The other emissions are due to phonon-assisted decay of excitons except for the line at 3.26 eV which is of unknown origin. Donor-acceptor-pair recombination can be excluded because of missing characteristic phonon replica.

The spectrum obtained after excitation of the epilayer through the sapphire substrate at the same excitation density (Fig. 1 (b)) differs very much from that just described. No free and shallow-bound-exciton

luminescences are observed here. Instead we see a complex structure of lines between 3.37 eV and 3.31 eV which at higher excitation densities reveals even more lines down to 3.29 eV, see Fig. 4. These lines were already observed in hexagonal epilayers on SiC [5], and also cubic samples on GaAs [6, 7], all grown without buffer layer. The fact that they were observed in samples on various lattice-mismatched substrates indicates that they are an inherent property of structurally disturbed GaN. We see that here the free and shallow bound excitons decay entirely

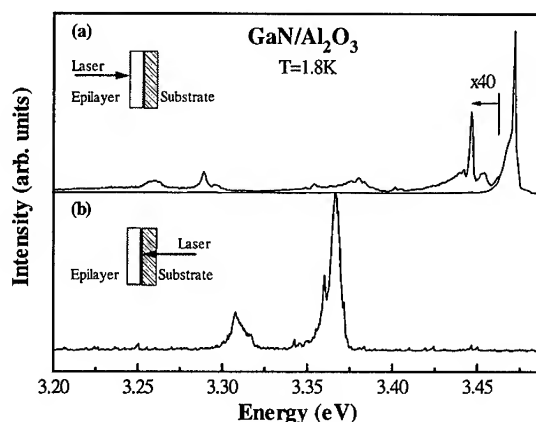


Fig. 1: Low temperature cw-photoluminescence spectra of a 400 μm epitaxial GaN/Al₂O₃ layer. (a) 'bulk' luminescence excited from the epilayer side, (b) 'interface' luminescence excited through the substrate.

nonradiatively. We attribute the observed 'interface' emissions to the annihilation of excitons deeply bound to defect centers connected with dislocations. The excitonic character of these lines will become clear below. Dislocation excitons are well known in other materials like CdS [8, 9]. Beside these dislocation excitons a broad emission band at 2.4 eV is also observed [10].

Summarizing the results of the cw-spectra, we see that far away from the substrate HVPE GaN exhibits strong radiative recombination at low temperatures due to free and shallow bound excitons. On the other side, in the presence of defects and dislocations near the substrate, the decay of free and shallow bound excitons is completely nonradiative. The excitation energy is transferred to deep levels associated with defects and dislocations localized near the interface, giving rise to emissions between 3.37 eV and 3.31 eV.

In the following section the dynamics of the energy relaxation of free and shallow bound excitons and of the deeply bound dislocation excitons will be investigated.

Recombination Dynamics in 'bulk' GaN: Free and Shallow bound Excitons

In the previous section we showed that free and donor-bound excitons contribute to strong radiative recombination in high-quality GaN at low temperatures. To get a better picture of the influence of nonradiative processes it is necessary to increase the temperature. We observed a rapid decrease of the intensity of the donor-bound exciton with raised temperatures governed by an activation energy of 7 meV. This value agrees very well with the localization energy of the exciton at the shallow donor. The physical process involved is the dissociation of the exciton from the donor caused by the absorption of low-energy acoustical phonons which are present even at relatively low temperatures. We will now show that this process also governs the recombination dynamics of the donor-bound exciton. In Fig. 2 (a) luminescence transients of the shallow-donor-bound-exciton line after band-to-band excitation are shown for different values of the lattice temperature. 'Bumps' in the very fast transients are caused by the response of our detection system to ps-signals and do not have any physical meaning. No rise process can be resolved in any transient from which we have to conclude that the lifetime of the free exciton is shorter than our time resolution of 15 ps at low temperatures. The lifetime of the donor-bound exciton of 70 ps at 8 K is seen to decrease continuously with increasing temperature, corresponding well to the expected increased dissociation rate as was also reported by Chen et al. [11]. How does

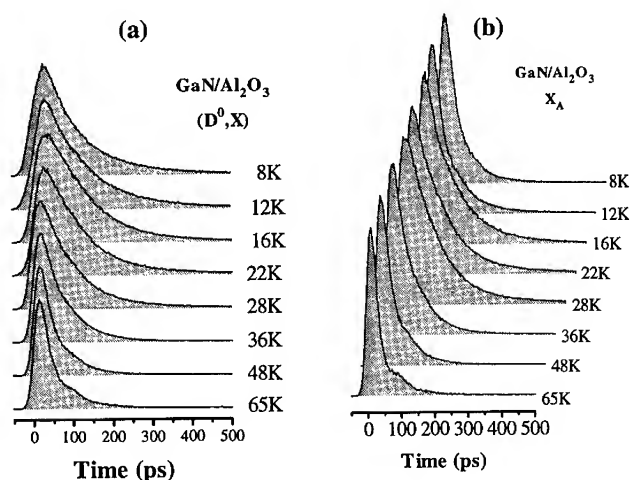


Fig. 2: Luminescence transients (a) from the donor-bound exciton (D^0, X), (b) from the free A-exciton X_A , taken at different lattice temperatures after excitation from the epilayer side ('bulk' luminescence).

this increased dissociation affect the transients of the free exciton? The answer is given in Fig. 2 (b). At low temperatures the decay is fast as expected from the lack of a rise process in the bound-exciton transients. As soon as the donor-bound exciton decay becomes faster with increasing temperature, the luminescence transient of the free exciton slows down. Above 28 K the free exciton decay becomes again faster.

To prove that the dissociation of the bound-exciton from the donor is responsible for this temperature dependence of the free-exciton transient, we evaluated a three-level model with temperature-dependent transition probabilities, Fig. 3 (a). Corresponding to our experimental excitation conditions we assume the system to be in the free-exciton state initially. Here we neglect the comparatively short exciton formation time. We also assume that the only temperature-dependent process is the thermally activated dissociation of the bound exciton from the donor, given by the characteristic time constant τ_{23} , cf. Fig. 3 (a). Its temperature dependence is set as

$$\tau_{23} = \tau_{23}^{\infty} \cdot \exp(\Delta E / kT) \quad (1)$$

ΔE denotes the localization energy of the exciton at the shallow donor, k Boltzmann's constant and T the lattice temperature. The decay rate of the free exciton is assumed to be independent of the lattice temperature. The solution from the two coupled rate equations was used to model luminescence transients by convolution with the response of our detection system to the laser pulse, see Fig. 3 (b). The effects observed in the experiment are nicely reproduced by the calculated transients even though a perfect fit has not been achieved. We ascribe the difference between the measured and calculated transients to the effect of the second donor-bound exciton with 3.6 meV localization energy. However, the parameters used in the calculation of the transients, which give the closest resemblance to the observed temperature behaviour, are shown in Fig. 3 (b) and serve as a reasonable estimate of the actual transition times. We see that not

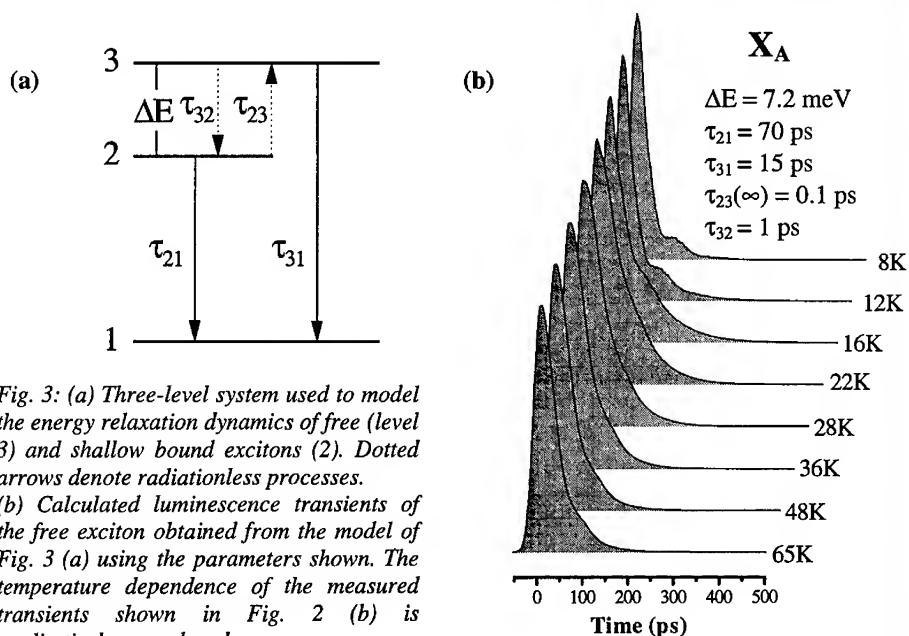


Fig. 3: (a) Three-level system used to model the energy relaxation dynamics of free (level 3) and shallow bound excitons (2). Dotted arrows denote radiationless processes. (b) Calculated luminescence transients of the free exciton obtained from the model of Fig. 3 (a) using the parameters shown. The temperature dependence of the measured transients shown in Fig. 2 (b) is qualitatively reproduced.

only the decay time τ_{31} describing the annihilation of the exciton is short in comparison with free exciton lifetimes in other high-quality materials such as CdS, but also that there is a strong influence of the shallow donors which capture free excitons at low temperatures within 1ps.

To summarize of the results on free and shallow bound excitons in structurally relaxed regions of GaN, through an analysis of the temperature dependence of the luminescence transients we obtained an estimate of the time constants governing the energy relaxation in this energy range. We observe a fast luminescence decay of the free exciton which is additionally accelerated at low temperatures by the capture at the shallow donor. Further nonradiative relaxation processes have to be taken into consideration to account for the short exciton decay time τ_{31} of less than 15ps. The observation of transition metals in this sample which are known to act as 'luminescence killers' is a likely explanation [12].

Recombination Dynamics near the Substrate Interface: Deeply Bound Excitons

We performed a comparative study of the recombination dynamics of emissions between 3.29 eV and 3.37 eV in various samples grown by HVPE or MOCVD. We find that the results agree with our previously reported measurements on GaN/SiC [5], showing again that these emissions are a general feature of disturbed GaN. The time constants vary only slightly between different samples. As an example, the results obtained from a thinner GaN/SiC epilayer is summarized in Fig. 4, which also gives a spectrum using pulsed excitation. Lines are marked L_1 to L_8 with increasing energy. As also observed by Hong et al. [7] the shoulder at 3.360 eV observed in Fig. 1 (b) develops into a well resolved line L_7 given higher excitation densities. Also, additional lines L_1 and L_2 at 3.28 and 3.29 eV are detected at higher excitation densities. The luminescence decay in the whole range is fast with time constants in the ps-range. It can be fitted using one or two exponential decays. The spectral analysis of the decay shows that transients with two time constants are always caused by the spectral overlap of different

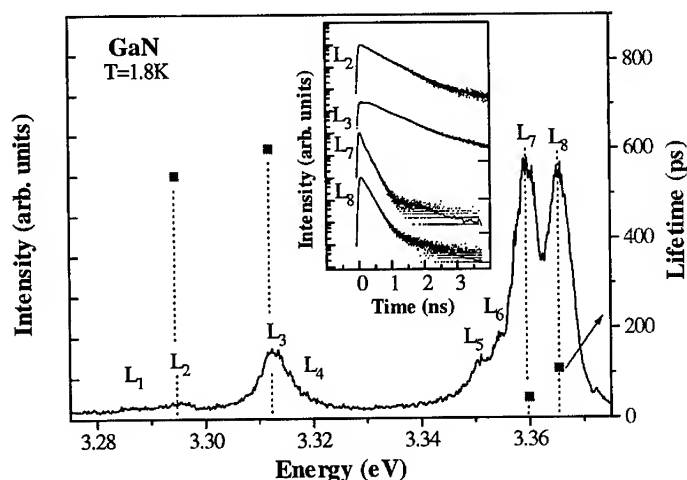


Fig. 4: Luminescence spectrum of deeply bound excitons in GaN at higher excitation densities effected by ps-laser pulses. The filled squares denote the decay constant (right scale) at the respective energy positions. In the inset the pertaining luminescence transients are shown. Here dotted curves stand for the experiment while full lines represent two-exponential fits.

luminescences. Thus, the decay of each luminescence is essentially monoexponential. On the basis of this result, donor-acceptor-pair recombination as suggested by some groups [7, 13] for the 3.311 eV line can be excluded as interpretation of this luminescence. Due to the energy position close to the band gap and the monoexponential luminescence decay we attribute the lines observed to excitonic recombination at dislocations. The decay constants in the ps range are unusually fast for a localization energy of more than 100meV and suggest strong nonradiative contributions to the recombination process. Electron-phonon coupling and Auger processes probably add to the short lifetimes observed.

CONCLUSIONS

In conclusion, we compared recombination processes and their dynamics in single-crystalline GaN near the surface of a thick epilayer with those of structurally disturbed GaN near the interface to the lattice mismatched substrate. We observe strong, radiative excitonic recombination due to free and shallow bound excitons near the surface. However, the decay of the free exciton is fast due to the impact of deep impurities. It slows down at temperatures between 20 K and 40 K where thermally activated dissociation of shallow bound excitons contributes to the free-exciton population. Near the substrate the presence of dislocations suppresses the radiative decay of free and shallow bound excitons. Instead, we observe characteristic emissions between 3.31 and 3.37 eV whose decay is fast and monoexponential strongly suggesting that they are caused by dislocation excitons.

ACKNOWLEDGMENTS

The authors in Berlin and München gratefully acknowledge financial support by the Deutsche Forschungsgemeinschaft.

REFERENCES

- [1] I. Akasaki and H. Amano, *Mat. Res. Soc. Symp. Proc.* Vol. 242 (1992), 383-393
- [2] M. Osinski, D. L. Barton, J. Zeller, P. Chiu, B. S. Phillips, N. Berg, C. J. Helms, *Proc. Int. Conf. SiC and Related Materials*, Kyoto, Japan, 1995, to be published
- [3] K. Naniwae, S. Itoh, H. Amano, K. Hiramatsu, I. Akasaki, *J. Cryst. Growth* **99**, 381 (1990)
- [4] L. Eckey, L. Podlowski, A. Göldner, A. Hoffmann, I. Broser, B. K. Meyer, D. Volm, T. Streibl, T. Detchprohm, K. Hiramatsu, H. Amano, I. Akasaki, *Proc. Int. Conf. SiC and Related Materials*, Kyoto, Japan, 1995, to be published
- [5] L. Eckey, J.-Ch. Holst, P. Maxim, R. Heitz, A. Hoffmann, I. Broser, B. K. Meyer, C. Wetzel, E. N. Mokhov, P. G. Baranov, in press, *Appl. Phys. Lett.* (1996)
- [6] H. Siegle, L. Eckey, A. Hoffmann, C. Thomsen, B. K. Meyer, D. Schickora, M. Hankeln, K. Lischka, *Solid State Commun.* **96** (1995), 943
- [7] C. H. Hong, D. Pavlidis, S. W. Brown, S. C. Rand, *J. Appl. Phys.* **77** (1995), 1705
- [8] J. Gutowski, A. Hoffmann, *Materials Science Forum* **38-41** (1989), 1391-1396
- [9] A. Hoffmann, J. Christen, J. Gutowski, *Advanced Materials for Optics and Electronics* **1** (1992), 25
- [10] H. Siegle, P. Thurian, L. Eckey, A. Hoffmann, C. Thomsen, B. K. Meyer, T. Detchprohm, K. Hiramatsu, H. Amano, I. Akasaki, this volume
- [11] G. D. Chen, M. Smith, J. Y. Lin, H. X. Jiang, M. Asif Kahn, C. J. Sun, *Appl. Phys. Lett.* **67** (1995), 1653.
- [12] R. Heitz, A. Hoffmann, and I. Broser, *Phys. Rev B* **49**, 14307 (1994)
- [13] R. Dai, S. Fu, J. Xie, G. Fan, G. Hu, H. Schrey, C. Klingshirn, *J. Phys. C: Solid State Phys.* **15** (1982), 393

PHOTOLUMINESCENCE RELATED TO THE 2-DIMENSIONAL ELECTRON GAS IN MODULATION DOPED GAN/ALGAN STRUCTURES

J.P. BERGMAN*, T. LUNDSTRÖM*, B. MONEMAR*, H. AMANO** AND I. AKASAKI**

* Department of Physics and Measurement Technology, Linköping University, S - 58183 Linköping, Sweden. ped@ifm.liu.se.

** Department of Electrical and Electronic Engineering, Meijo University, Nagoya, Japan

ABSTRACT

We report low temperature photoluminescence (PL) spectra related to a two-dimensional electron gas confined at a GaN/AlGaN heterointerface. The recombination between electrons confined in the bottom of the interface potential and photoexcited holes causes a broad PL emission about 50 meV below the bulk GaN exciton emission. A second emission, attributed to the recombination of electrons in the first excited level at the interface, is also observed close to the excitonic band gap in GaN. The data agrees with a self consistent calculation of the energy levels and the electron concentration at the interface. Similar PL data from a modulation doped AlGaN/GaN quantum well exhibit three PL emissions related to the 2D electron gas.

INTRODUCTION

Modulation doping, i.e. doping of the barrier layer at a heterointerface, causes a redistribution of electrical charge across the interface. In the case of n-type doping of the barrier layer, the region in the barrier close to the interface will be depleted and the corresponding electrons accumulated in a triangular shape potential in the active layer close to the interface [1]. The electrons accumulated in the potential form a two-dimensional electron gas (2DEG). These electrons normally have a very high mobility, since the carriers are separated from dopants in the barrier layer. This fact is frequently used for device applications, such as the high electron mobility transistor. The properties, electrical and optical, related to the 2DEG electrons have previously been extensively studied by several groups, mainly in the GaAs/AlGaAs [2-6] but also in the InGaAs/InP [7] material system. Single and double heterostructures, involving different nitride compounds, are also expected to be used for optoelectronic devices. The understanding of the recombination processes related to the modulation doped heterointerface and quantum wells is thus of vital importance.

EXPERIMENTAL DETAILS

The samples used in this study were grown by Metal Organic Vapour Phase Epitaxy (MOVPE) on optical grade polished sapphire substrates. An initial AlN buffer layer was introduced to accommodate the lattice mismatch with the substrate. For the single heterostructure sample this was followed by an intentionally undoped GaN layer and a 0.16 µm thick Si doped Al_{0.3}Ga_{0.7}N barrier, see Fig. 1a. For the quantum well sample two additional AlGaN layers as well as a GaN buffer layer was added, see Fig 1b.

PL and time-resolved PL measurements were performed, in the temperature range from 2 K to room temperature, using pico second pulsed excitation from a frequency doubled mode locked dye laser. For

spectral measurements the emitted PL was detected with a cooled CCD camera, while the time resolved measurements were performed with a syncroscan streak camera with a time resolution of about 20 ps. For longer time decays we used a time correlated photon counting system with a time resolution of about 150 ps.

EXPERIMENTAL RESULTS AND DISCUSSION

The 2DEG in the single heterojunction sample is formed in the GaN layer at the interface to the modulation doped AlGa_N barrier. The electron concentration in the 2DEG is about 10^{13} cm^{-2} , as measured by electrical measurements as shown in Fig. 2. The electron concentration is almost independent of temperature. The mobility shows, on the other hand, a strong temperature dependence reaching about $4000 \text{ cm}^2/\text{Vs}$ at 77 K. This value of the mobility is larger than for bulk GaN, where the highest reported value at 77 K is $3000 \text{ cm}^2/\text{Vs}$ [9].

The time-integrated PL spectra of a modulation doped single heterostructure GaN/AlGa_N sample are shown in Fig. 3 for different temperatures. The spectra are dominated by exciton emissions typical for bulk GaN, originating from the flat band region of the GaN epitaxial layer. At low temperatures the donor bound exciton (DBE) is dominating with a recombination energy at 3.488 eV. At higher temperatures the DBE is thermally quenched and the recombination of free excitons (FE), at 3.493 eV, is instead dominating. These values are 19 meV higher than values for unstrained bulk GaN. Similar energy shifts, due to the residual stress of the epilayer, have previously been observed in heteroepitaxial GaN layers [10]. The broad emission about 50 meV below the exciton emission is attributed to recombination involving electrons from the 2DEG at the GaN/AlGa_N heterointerface and photoexcited holes in the GaN layer.

The recombination related to the 2DEG is known to be strongly dependent on the band bending, caused by the equilibrium carrier concentration and the photoexcited carriers [3-6]. A strong blue shift with increasing excitation intensity

a)		b)	
AlGa _N : Si	0.16	AlGa _N : Si	0.1
GaN		AlGa _N	0.003
AlN	0.05	GaN	0.01
Sapphire	[μm]	AlGa _N	2
		GaN	1
		AlGa _N	0.07
		AlN	0.05
		Sapphire	[μm]

Figure 1. Schematic description of the two different modulation doped structures. a) shows the modulation doped single hetero interface, while b) shows the modulation doped quantum well sample. The 2DEG is, in both samples, formed in the shaded GaN layer.

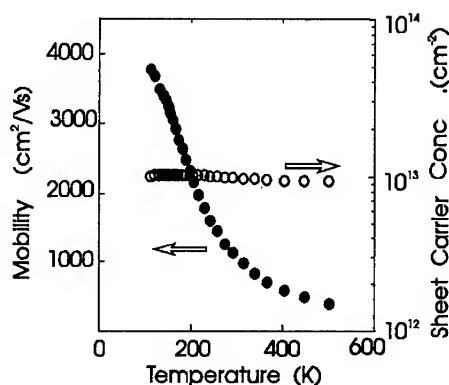


Figure 2. Mobility and sheet carrier concentration as a function of temperature in the modulation doped GaN/AlGa_N heterostructure.

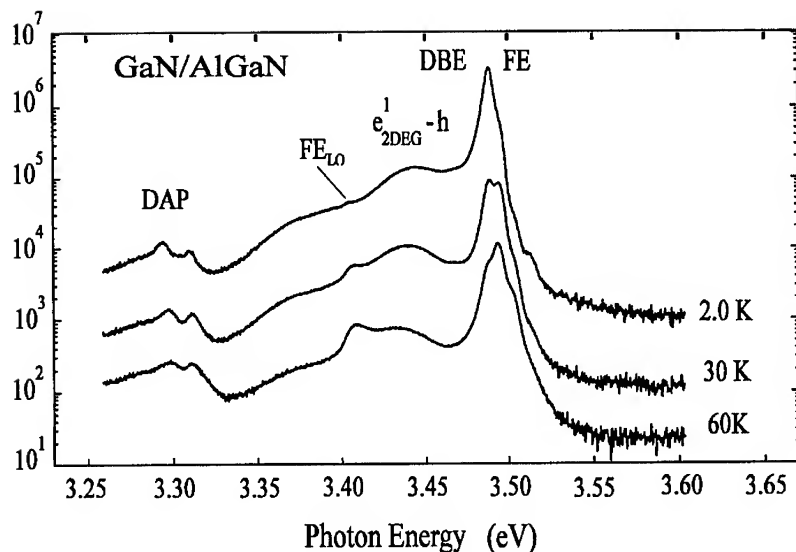


Figure 3. Photoluminescence spectrum of a modulation doped GaN/AlGaIn sample. The spectrum is at low temperatures dominated by BE and FE emissions typical for bulk GaN, originating from the flat band region of the active layer. The broad emission about 50 meV below the exciton emission is attributed to recombination involving electrons from the 2DEG at the GaN/AlGaIn heterointerface.

has previously been observed in GaAs/AlGaAs structures, but is not observed in the time integrated spectra of the GaN/AlGaIn structure. However, spectral measurements at increasing time delays after the pulsed excitation show a weak red shift of the broad emission. The conditions during a time delayed spectral measurements are similar, but not identical, to measurements varying the excitation intensity, since the concentration of photo excited carriers decreases with time after the excitation pulse due to carrier recombination. Spectral curves at different time delays are shown in Figure 4.

In this figure we also observe a red shift of the emission in the exciton range. We believe that this component, observed at longer time delays, is related to electrons in the first excited state of the 2DEG. This emission is spectrally overlapping with the bulk DBE emission, and can not be distinguished from this exciton emission in a time-integrated spectrum, as in Fig. 3.

The time decay of all observed emissions is quite similar, with a dominating fast component with a decay time of 150 ps and a slower component with a decay time of several ns. The decay of the emissions related to the 2DEG should be directly determined by the lifetime of the photo-excited holes, since the electrons in the 2DEG are always present at a high equilibrium concentration. The lifetime of the holes is determined by the dominating excitonic recombination, present in the flat band region. The observed 2DEG related emission will consequently have the same initial decay as the bulk exciton recombination. When the exciton recombination disappears, due to a limited number of photoexcited electrons in the flat band region, the recombination of remaining photoexcited holes and electrons in the 2DEG will dominate the spectrum, as observed in fig. 3. The decay of the holes will now be determined by

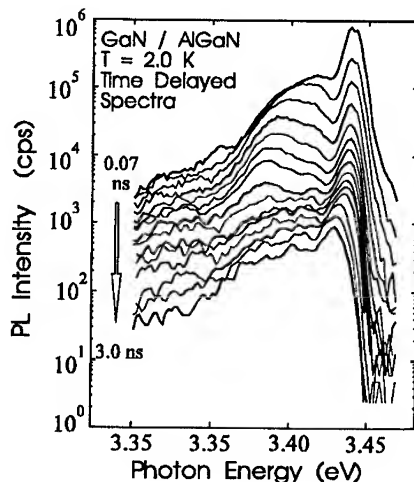


Figure 4. Time resolved spectra, at 2 K, of the band gap region of the modulation doped GaN/AlGaN heterointerface. The time delay between each spectrum is not

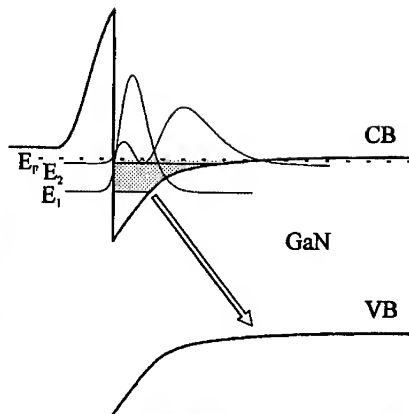


Figure 5. The band potential at the GaN/AlGaN heterointerface. The energy levels are obtained from a self-consistent calculation. Two electron levels are obtained with energies of 139 meV and 223 meV above the notch potential. Also shown are the electron probability function for the two occupied levels.

this much slower recombination, which corresponds to the slower component observed in the decay measurements.

The identification of these emission bands is supported by the results from a self-consistent calculation of the energy band potential and energy levels at the heterointerface, as schematically shown in fig. 5. In the calculation we have used an electron mass of $0.2m_e$ [11], a conduction band offset of 0.666 eV, obtained from the linear interpolation of the GaN [12] and AlN [13] band gaps with $x=0.3$ and 80% of the energy offset in the conduction band [14]. The Fermi level in the AlGa_N was assumed to be determined by shallow donors with $E_D = 25$ meV. The concentration of the electrons in the 2DEG is dependent on the doping concentration in the AlGa_N layer. The experimentally measured electron concentration of $1 \times 10^{13} \text{ cm}^{-2}$ was obtained with a doping concentration of $2.0 \times 10^{19} \text{ cm}^{-3}$. The position of the donor levels in $\text{Al}_x\text{Ga}_{1-x}\text{N}$ is to our knowledge not determined, but model calculations shows that the result is relatively independent on the shallow donor energy position, as long as we require a certain electron concentration at the interface. An increase of the donor binding energy to 100 meV, requires an increase of the doping concentration to $2.2 \times 10^{19} \text{ cm}^{-3}$ in order to obtain the same electron concentration, while the electron energy levels are almost unaffected. Under this condition two energy levels are occupied in the 2DEG, with energies 139 and 223 meV above the bottom of the potential notch, while the Fermi level is 242 meV above the potential notch. Recombination between electrons in the 2DEG and photo excited holes in the flat band region of the valence band would result in recombination energies 24 and 107 meV below the bandgap. This is in reasonable agreement with the energies of the observed emissions, in Fig. 3-4.

The higher PL intensity of the emission related to the excited electron state in the 2DEG, as compared to the emission related to the ground state, can be understood from the overlap of the hole and electron wavefunctions. The electron wavefunctions, probability functions, are shown in fig. 5. The photo excited holes are located close to the flat band region, due to the band

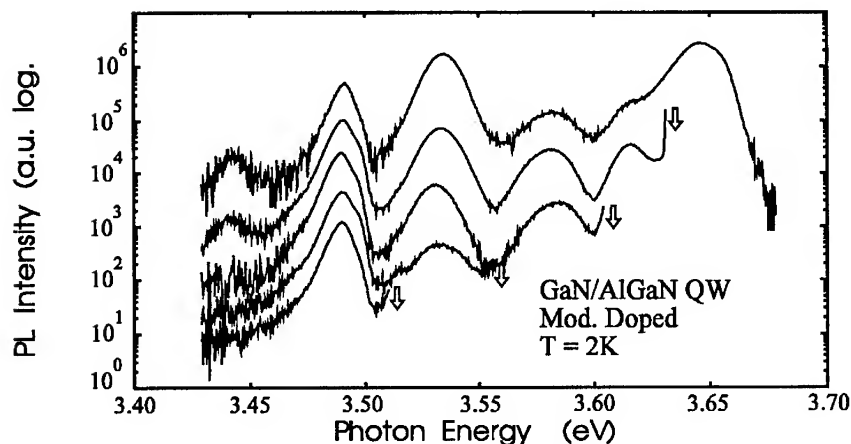


Figure 6. PL spectra from the modulation doped QW. The top spectrum is obtained with excitation above the AlGaIn barrier, while the lower spectra are measured with selective excitation as indicated by the arrow in each case.

bending of the valence band. The electron ground state is strongly localised to the notch region, while the first excited electron state penetrates further into the flat band region. This gives a higher recombination probability, and hence a stronger PL intensity for the emission involving the excited electron state.

We have also studied the emission from a single side modulation doped GaN/AlGaIn structure, as described in Fig. 1. This sample has an electron concentration of $3.0 \times 10^{12} \text{ cm}^{-3}$ and a mobility of $850 \text{ cm}^2/\text{Vs}$ at 300K, and we assume that a 2DEG is formed in the QW. PL spectra from the modulation doped QW are shown in Fig. 6. The upper spectrum shows the emission with excitation above the AlGaIn barrier, while the lower spectra shows the emission with the excitation at different energy position below the barrier bandgap, as indicated by the arrows. The high energy emission peaking at 3.64 eV is attributed the exciton recombination in the AlGaIn barrier while the lowest emission at 3.48 eV originates from the GaN buffer layer. Between these two peaks we observe three well defined peaks which we attribute to recombination processes in the QW. The spectra obtained with different excitation energies show that these peaks do not originate from the barrier.

The origin of the three middle peaks are not yet fully understood. Since the structure is modulation doped only on one side of the quantum well, we expect a significant electric field across the GaN well, giving a similar potential as for the heterostructure sample shown in Fig. 5. In addition we have quantum effects giving rise to several electron and hole subbands. This is however difficult to calculate and we can not at the moment determine how many electron or hole subbands that are expected to be populated. An important but yet unsolved problem is the energy levels and dispersion of the top valence band for the 2D case in GaN.

Possible explanation for the observed emissions include three electron sublevels populated in the notch potential or two electron sublevels together with higher states in the valence band.

CONCLUSIONS

We have observed low temperature photoluminescence related to a two-dimensional electron gas confined at a GaN/AlGa_N heterointerface. The energy position and the recombination kinetic of the emission can be explained assuming a recombination between electrons confined in the bottom of the interface potential and photoexcited holes. This is supported by a self consistent calculation of the band potential, which gives confined energy levels in agreement with the experimental results.

We have also observed similar PL data from an asymmetric modulation doped AlGa_N/GaN quantum well. The spectrum exhibits three PL emissions, which we attribute to recombinations with electrons in the 2D electron gas in the QW. A definite assignment of the origin of the three peaks has not been possible, due to the complex and partly unknown energy splittings in the QW. Further studies of the emission from the modulation doped QW is necessary, and in progress.

ACKNOWLEDGEMENT

The work at Meijo University was supported by the Ministry of Education, Science and Culture of Japan (Contract #'s 06452114, 07650025 and 07505012), Research Foundation for Electrotechnology of Chubu, Nissan Science Foundation and Iketani Science and Technology Foundation.

REFERENCES

1. G. Bastard 1992 Wave Mechanics Applied to Semiconductor Heterostructures (Paris: Les Editions de Physique).
2. R. Dingle, H.L. Stormer, A.C. Gossard, and W. Wiegmann, Appl. Phys. Lett. 33 665-667 (1978)
3. Y.R. Yuan, M.A.A. Pudensi, C.A. Vawter, and J.L. Merz, J. Appl. Phys. 58, 397-403 (1985).
4. I.V. Kukushkin, K.V. Klitzing, and K. Ploog, Phys. Rev. B. 37, 8509-8512, (1988).
5. Q.X. Zhao, J.P. Bergman, P.O. Holtz, B. Monemar, C. Hallin, M. Sundaram, J.L. Merz, and A.C. Gossard, Semicond. Sci. Technol. 5, 884-889 (1990).
6. J.P. Bergman, Q.X. Zhao, P.O. Holtz, B. Monemar, M. Sundaram, J.L. Merz, and A.C. Gossard, Phys. Rev. B. 43, 4771-4776 (1991).
7. Q.X. Zhao, P.O. Holtz, B. Monemar, T. Lundström, J. Wallin, and G. Landgren, Phys. Rev. B. 48 1189-1194 (1993).
8. M.A. Kahn, J.M. van Hove, J.N. Kuznia, and D.T. Olson, Appl. Phys. Lett. 58, 2408-2410 (1991).
9. S. Nakamura, T. Mukai, and M. Senoh, J. Appl. Phys. 71, 5543-5549 (1992).
10. W. Shan, T.J. Schmidt, X.H. Yang, S.J. Hwang, J.J. Song, and B. Goldenberg, Appl. Phys. Lett. 66, 985-987 (1995).
11. A.S. Barker, and M. Illegems, Phys. Rev. B. 7, 743 (1973).
12. B. Monemar, Phys. Rev. B. 10, 676 (1974).
13. P.B. Perry, and R.F. Rutz, Appl. Phys. Lett. 33, 319 (1978).
14. J. Baur, K. Meier, M. Kunzer, U. Kaufmann, and Schneider, Appl. Phys. Lett. 65, 2211 (1994).

DIELECTRIC FUNCTIONS OF WURTZITE AND ZINCBLLENDE STRUCTURE GaN

R. Wang*, P.P. Ruden*, J. Kolnik**, I. Oguzman**, and K.F. Brennan**

*Dept. of EE, Univ. of Minnesota, Minneapolis, MN 55455, rpwang@ee.umn.edu

**School of ECE, Georgia Tech., Atlanta, GA 30332

ABSTRACT

We present calculated longitudinal frequency and wavevector dependent dielectric functions of zincblende and wurtzite structure GaN using band energies and wavefunctions generated in the framework of the empirical pseudopotential method. We discuss the anisotropy of the static dielectric function and find that our results are in satisfactory agreement with experimental data for $|\vec{q}| \rightarrow 0$.

INTRODUCTION

GaN in both wurtzite and zincblende modifications has considerable potential as a novel semiconductor material for short wavelength optoelectronic and high temperature electronic devices. Its most attractive property for many applications is its large direct bandgap (3.4 eV and 3.3 eV at 300K for wurtzite and zincblende phases, respectively)[1]. Together with the similar direct bandgap materials InN and AlN and their alloys with GaN, the range of direct gaps of III-N materials extends from 1.9 eV (InN) to 6.2 eV (AlN), which may lead to the fabrication of light emitting diodes, lasers, and photodetectors over the full visible spectrum and into the ultraviolet range. Considerable effort also is directed towards the realization of electronic devices capable of high temperature operation. Theoretical research on GaN transport[2] has pointed out a number of properties that are different for the two crystal modifications (wurtzite and zincblende) that have been grown successfully as epitaxial layers. Current work on high field transport properties, e.g. impact ionization, and on impurity states requires a quantitative understanding of the electronic screening, i.e. of the frequency and wavevector dependent dielectric function, $\epsilon(\vec{q}, \omega)$. In this paper we will discuss results for $\epsilon(\vec{q}, \omega)$ for both crystalline modifications of GaN.

THEORY

Outline of method

The screening function associated with electronic interband transitions in crystals was formulated by Ehrenreich and Cohen[3] in the mean-field approximation. The frequency and wavevector dependent dielectric function can be expressed as

$$\epsilon(\vec{q}, \omega) = 1 + \frac{2e^2}{\pi^2 q^2} \lim_{\alpha \rightarrow 0} \sum_{\Delta \vec{k}, c, v} \frac{(\Delta k)^3 |\langle \vec{k}, c | \vec{k} + \vec{q}, v \rangle|^2 [E_c(\vec{k}) - E_v(\vec{k} + \vec{q})]}{[E_c(\vec{k}) - E_v(\vec{k} + \vec{q})]^2 - [\hbar\omega + i\alpha]^2} \quad (1)$$

Where c and v represent the indices of empty conduction and occupied valence bands, respectively, and $(\Delta k)^3$ is a reciprocal space volume associated with each mesh element in the first Brillouin zone. The sum is over all mesh elements. In this work the band energies $E_c(\vec{k})$ and $E_v(\vec{k})$ were determined in the framework of the empirical pseudopotential method[4],

and the overlap integrals, $\langle \vec{k}, c | \vec{k} + \vec{q}, v \rangle$, were evaluated using pseudowavefunctions. The pseudopotential form factors for GaN were empirically determined from experimental data for several critical point bandgaps and the conduction band effective masses[5][1]. Following this procedure, the pseudopotential bandstructure calculation for zincblende GaN yielded results in satisfactory agreement with the published experimental data and with first-principles calculations[6]. For wurtzite structure GaN, however, we had difficulty in fitting all experimental parameters simultaneously. The best fit was achieved by choosing pseudopotential form factors that yielded a bandstructure with all critical point bandgaps larger than the experimental values by approximately 1 eV. This discrepancy was then corrected by shifting all conduction bands rigidly down by 1 eV. Fig. 1(a) displays the bandstructure for zincblende GaN, and Fig. 1(b) shows the corrected bandstructure for wurtzite GaN. In all calculations the spin-orbit interaction was neglected.

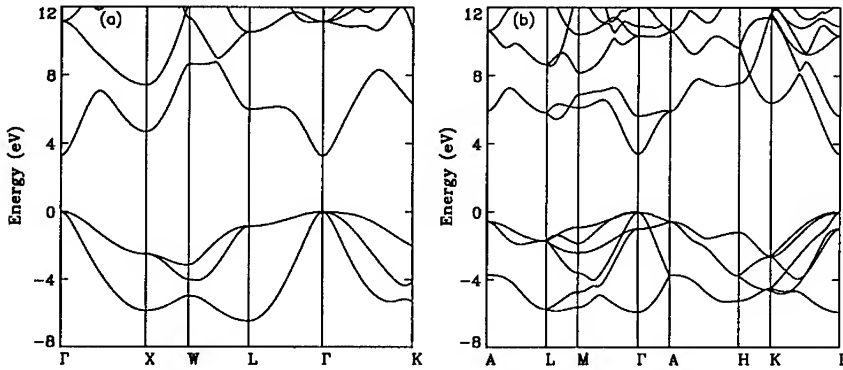


Figure 1: (a). Bandstructure of zincblende GaN with a direct gap of 3.3 eV. (b). Bandstructure of wurtzite GaN with a direct gap of 3.4 eV. Both are produced by the empirical pseudopotential method.

Numerical evaluation of equation (1) is straightforward for non-vanishing \vec{q} . We used a $\vec{k} \cdot \vec{p}$ expansion of the overlap integral to obtain the long wavelength limit:

$$\lim_{\vec{q} \rightarrow 0} \epsilon(\vec{q}, \omega) = 1 + \frac{2e^2 \hbar^2}{\pi^2 m^2} \sum_{\Delta \vec{k}, c, v} \frac{|\hat{q} \cdot \vec{p}_{cv}|^2 (\Delta k)^3}{[E_c(\vec{k}) - E_v(\vec{k})] \{ [E_c(\vec{k}) - E_v(\vec{k})]^2 - [\hbar\omega + i\alpha]^2 \}} \quad (2)$$

where \hat{q} is the unit vector in the direction of \vec{q} , and the overlap integral has been replaced by the matrix element $\vec{p}_{cv} = \langle \vec{k}, c | \vec{P} | \vec{k}, v \rangle$, where \vec{P} is the momentum operator.

The static dielectric function $\epsilon(\vec{q})$ was directly calculated from equation (1). However, for $\hbar\omega > E_g$ the denominator will be zero at certain \vec{k} points, and equation (1) becomes singular. Therefore we first calculated the imaginary part of the dielectric function $\epsilon_2(\vec{q}, \omega)$ and then used the Kramers-Kronig relation to calculate the real part $\epsilon_1(\vec{q}, \omega)$.

From equation (1) the expression of $\epsilon_2(\vec{q}, \omega)$ has the form

$$\epsilon_2(\vec{q}, \omega) = \frac{e^2}{\pi q^2} \sum_{\Delta \vec{k}, c, v} |\langle \vec{k}, c | \vec{k} + \vec{q}, v \rangle|^2 (\Delta k)^3 \delta(E_c(\vec{k}) - E_v(\vec{k} + \vec{q}) - \hbar\omega) \quad (3)$$

To evaluate $\epsilon_2(\vec{q}, \omega)$, we replaced the delta function by a Gaussian function. Using the Kramers-Kronig relation, we obtained immediately the real part of the dielectric function $\epsilon_1(\vec{q}, \omega)$. We will discuss the Brillouin zone discretization schemes and the bands included for zincblende structure and wurtzite structure GaN separately.

Zincblende GaN

For the zincblende structure we set up a mesh which divides the first Brillouin zone into small cubes[7]. The coordinates of the centers of the cubes are given by $\frac{1}{16}(2n_x + 1, 2n_y + 1, 2n_z + 1)$ in units of $2\pi/a$, where n_x , n_y , and n_z are integers from -8 to +7 and a is the lattice constant. Hence, the first Brillouin zone is divided into 2432 parts.

In the calculation of the dielectric functions, four valence bands and the lowest 11 conduction bands were used. The contribution from higher conduction band states is negligible because of the small overlap integrals and the big energy differences. From equation (2) we obtained the "optical" dielectric constant $\epsilon(\vec{q} \rightarrow 0, \omega = 0) \equiv \epsilon_\infty = 5.16$. Evaluating equation (3) with a denser mesh (each cube is further divided into 27 smaller cubes), we obtained a reasonably smooth dielectric function.

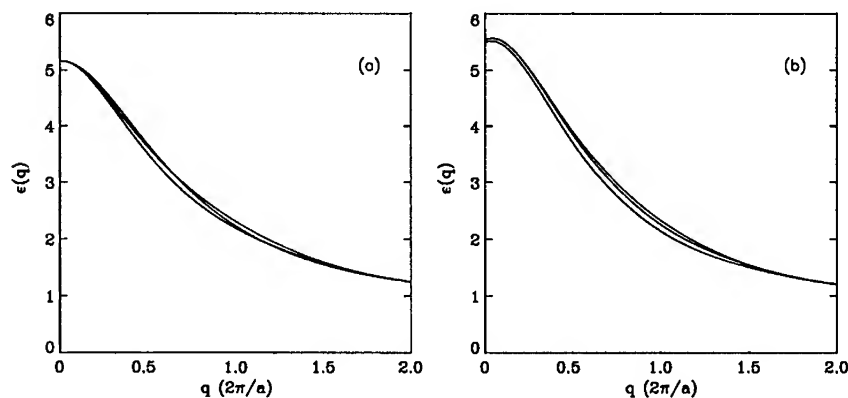


Figure 2: (a) Static dielectric functions for \vec{q} along the (100), (110) and (111) directions in zincblende GaN; (b) and along (100), (010) and (001) directions in wurtzite GaN.

Wurtzite GaN

For wurtzite GaN we chose a coordinate system in which the direct primitive lattice vectors are defined as $\vec{a}_1 = (\frac{\sqrt{3}}{2}a, -\frac{1}{2}, 0)$, $\vec{a}_2 = (\frac{\sqrt{3}}{2}a, \frac{1}{2}, 0)$, $\vec{a}_3 = (0, 0, c)$, where a and c are the lattice constants; the corresponding reciprocal lattice vectors are $\vec{b}_1 = 2\pi(\frac{1}{\sqrt{3}a}, -\frac{1}{a}, 0)$, $\vec{b}_2 = 2\pi(\frac{1}{\sqrt{3}a}, \frac{1}{a}, 0)$, and $\vec{b}_3 = 2\pi(0, 0, \frac{1}{c})$, respectively. In this coordinate system we defined three unit vectors: $\vec{v}_1 = (\frac{\sqrt{3}}{2}, \frac{1}{2}, 0)$, $\vec{v}_2 = (\frac{\sqrt{3}}{2}, \frac{1}{2}, 0)$, and $\vec{v}_3 = (0, 0, 1)$. The mesh points in the Brillouin zone were defined by $\vec{k} = C_1(l\vec{v}_1 + m\vec{v}_2) + C_2n\vec{v}_3$, where l , m , and n are integers, $C_1 = \frac{8\pi}{3N_1a}$ and $C_2 = \frac{2\pi}{N_2c}$. For the results presented here we used $N_1 = 18$ and $N_2 = 12$, and the Brillouin zone was, hence, divided into 3024 parts.

The calculations for wurtzite GaN included 8 valence and the lowest 12 conduction bands; the higher conduction bands contribute negligibly and were ignored. With these approximations we obtained “optical” dielectric constants of 5.49 in the c-direction and 5.54 in perpendicular directions. For $\omega \neq 0$, each mesh element was further divided into 7 parts.

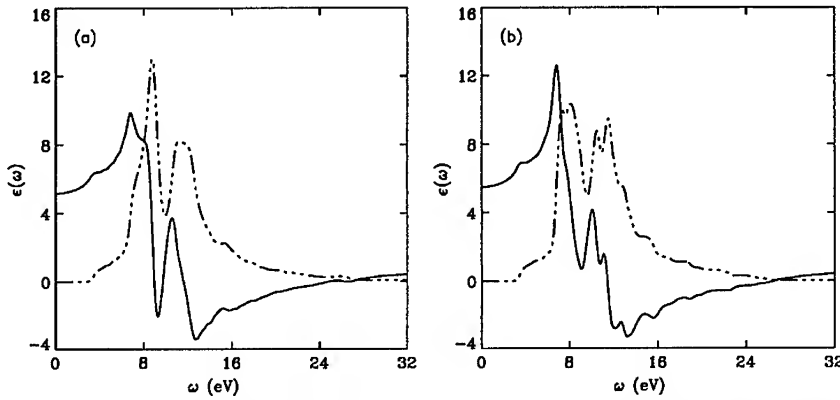


Figure 3: The real and imaginary parts of the optical dielectric functions. (a) Zincblende GaN; (b) Wurtzite GaN. The solid lines show the real and the dash-dotted lines the imaginary parts.

RESULTS

Fig. 2(a) displays the static dielectric function of zincblende GaN along (100), (110) and (111) directions; Fig. 2(b) shows those of wurtzite GaN along (100), (010), and (001) directions. In both cases, the three curves converge to the same values for very small and large wavevectors, but noticeable anisotropy occurs for intermediate \vec{q} . For wurtzite GaN a small anisotropy persists even at $\vec{q} = 0$.

Fig. 3(a) shows $\epsilon_2(\vec{q} \rightarrow 0, \omega)$ and the corresponding $\epsilon_1(\vec{q} \rightarrow 0, \omega)$ for zincblende GaN in the (111) direction, and Fig. 3(b) shows those of wurtzite GaN along the (001) direction (here we again used the $\vec{k} \cdot \vec{p}$ expansion).

Figs. 4(a) and (b) depict $\epsilon_1(\vec{q}, \omega)$ and $\epsilon_2(\vec{q}, \omega)$ of zincblende GaN with \vec{q} in the (111) direction. Each curve corresponds to a different, fixed \vec{q} value. To show the anisotropy more clearly, we plot in Figs. 5(a) and (b), respectively, the differences of the $\epsilon_1(\vec{q}, \omega)$ and $\epsilon_2(\vec{q}, \omega)$ between (100) and (111) directions. Comparable differences are also observed between (100) and (110) directions, and between (111) and (110) directions, indicating that the anisotropy is more significant at non-zero frequency than in the static case shown in Fig. 2.

CONCLUSIONS

Comparing our results with other calculations, we found that our “optical” dielectric constant values lie between those of LMTO calculations within the atomic sphere approximation[8] and those based on LDA pseudopotential calculations with local-field corrections[9]. The former yield 4.78 for zincblende GaN, and 4.71 for wurtzite GaN, while the latter give

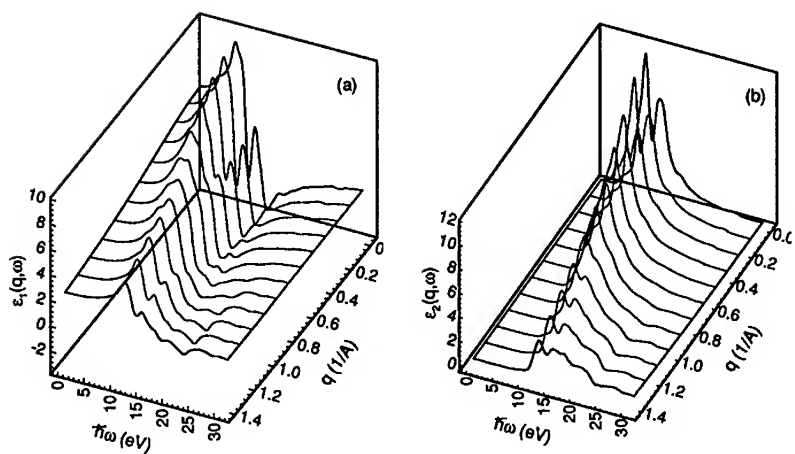


Figure 4: (a) Real part of the dielectric function of zincblende GaN with \vec{q} changing in the (111) direction; (b) The corresponding imaginary dielectric function.

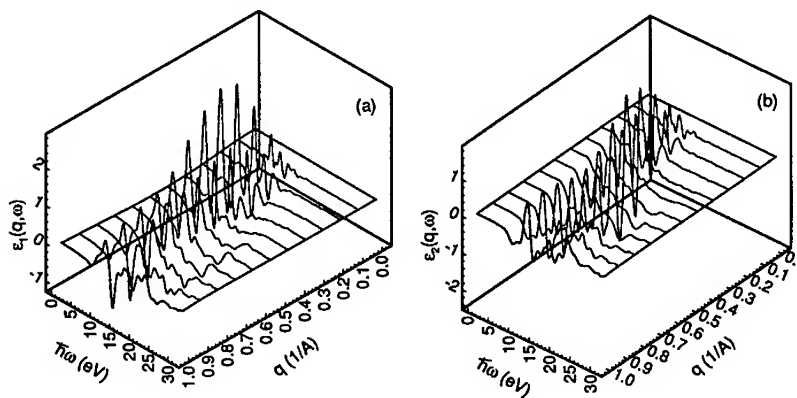


Figure 5: Difference of dielectric functions of zincblende GaN between (111) and (100) directions. (a). Difference in real part; (b). Difference in imaginary part.

5.74 for zincblende GaN and 5.54 for wurtzite GaN (the experimental value of ϵ_∞ for wurtzite GaN is 5.35 ± 0.20).

In comparing to experimental data, we found our result of $\epsilon_2(\vec{q} \rightarrow 0, \omega)$ to be quantitatively different from the measurements of Logothetidis, et. al [5]. As shown in Fig. 3(b), we found that our optical dielectric function in the c-direction peaks at 7 and 8 eV, which is very close to the experimental values. However, our peaks are much higher. For zincblende GaN, as shown in 3(a), our result reveals a dominant (E_2) peak located at 8.6 eV, which is associated with transitions near $\frac{\pi}{2a}(3, 1, 1)$. The experimental data appears to suggest that this peak occurs close to 7.6 eV and that it is considerably weaker. It may be speculated that residual strain in epitaxial layers could lead to significant shifts of some resonance peaks relative to the unstrained material. We also noticed that the experimentally measured dielectric function at frequencies close to the bandgap is systematically larger than our result. The second peak, positioned at 11.5 eV, is approximately 1 eV below an experimentally observed feature[6].

In summary, we calculated the dielectric functions for zincblende structure and wurtzite structure GaN based on a mean field formula; band energies and wavefunctions were produced by empirical pseudopotential calculations. Our results for the "optical" dielectric constant, ϵ_∞ , agree quantitatively with experimental values.

ACKNOWLEDGMENTS

One of us (RW) thanks Drs. James Chelikowsky and Barry Schaudt for helpful discussions and suggestions. We acknowledge the Minnesota Supercomputer Institute (MSI) for technical support. This work was supported in part by NSF under contract ECS-9408479.

REFERENCES

1. S. Strite and H. Morkoc, J. Vac. Sci. Technol., **B10**, p.1237, (1992) and references therein.
2. J. Kolnik, I. H. Oguzman, K. F. Brennan, R. Wang, P. P. Ruden and Y. Wang, J. Appl. Phys., **78**, p.1033, (1995).
3. H. Ehrenreich and M. H. Cohen, Phys. Rev., **115**, p.786, (1959).
4. M. L. Cohen and T. K. Bergstresser, Phys. Rev., **141**, p.789, (1966).
5. S. Logothetidis, J. Petalas, M. Cardona and T. D. Moustakas, Phys. Rev., **B50**, p.18017, (1994).
6. W. R. L. Lambrecht, B. Segall, J. Rife, W. R. Hunter and D. K. Wickenden, Phys. Rev., **B51**, p.13516, (1995); K. Kim, W. R. L. Lambrecht and B. Segall, Phys. Rev., **B50**, p.1502 (1994); and W. R. L. Lambrecht (private communication).
7. J. P. Walter and M. L. Cohen, Phys. Rev., **B5**, p.3101, (1972).
8. N. E. Christensen and I. Gorczyca, Phys. Rev., **B50**, p.4397, (1994).
9. J. Chen, Z. H. Levine and J. W. Wilkins, Appl. Phys. Lett., **66**, p.1129, (1995).

EXCITON LUMINESCENCE OF SINGLE-CRYSTAL GaN

J.R. MÜLLHÄUSER, O. BRANDT, H. YANG, K.H. PLOOG

Paul-Drude-Institut für Festkörperelektronik, Hausvogteiplatz 5-7, 10117-Berlin, Germany,
jochen@pdi.wias-berlin.de

ABSTRACT

Detailed photoluminescence (PL) studies of high-quality MBE-grown single-crystal cubic and hexagonal GaN are presented. We identify free and bound exciton recombination. By means of a line-shape analysis, we quantitatively analyze our spectra, which were taken as a function of temperature ($T = 4 - 300$ K) and excitation density ($P_{\text{ex}} = 0.3 - 200$ W/cm²). We show the dominant recombination channel at 300 K to be free-excitonic in nature with an internal small-signal quantum efficiency of $6 \cdot 10^{-3}$ for both cubic and hexagonal material. Based on a three-level model, activation energies for exciton dissociation are evaluated. Radiative ($\tau_{\text{rad}} \approx 2$ ns) and nonradiative lifetimes ($\tau_e \approx 1$ μ s, $\tau_h \approx 20$ ps) are determined, where in the latter case, electron and hole trapping are considered separately. Furthermore, we show that the dominant nonradiative recombination center, being a hole trap, saturates at $P_{\text{ex}} \geq 20$ W/cm².

INTRODUCTION

GaN has become subject of intensive research, since it is not only a promising candidate for optical devices in the near-UV spectral range, but also for high-power and high-frequency electronic applications. Triggered by a realization of a blue LED in 1994, many groups have started working on group-III nitrides grown on sapphire with the objective to develop a blue laser diode. However, fundamental problems regarding, e.g., crystal quality, cleavability and p-type doping are still to be solved.

Even though a sound understanding of the dominant recombination channels at room temperature in general and the intrinsic luminescence in particular are of crucial importance for the design of such a laser diode, little is known about these processes. In this work, we fill this gap for both phases not only by investigations on exciton recombination, band-band recombination and carrier trapping, but also by determination of the figures of merit for device operation, which are the quantum efficiency and the (non)radiative lifetimes.

We mainly focus on the two radiative transitions at $FX_C = 3.27$ eV and $FX_H = 3.47$ eV ($T = 4$ K). Cathodoluminescence (CL) studies were used to assign these to cubic and hexagonal GaN [1], respectively. By a careful analysis of the temperature dependence of the photoluminescence, we show that FX_C and FX_H follow the band-gap of cubic [2] and hexagonal GaN [3], respectively, being shifted to lower energies by the estimated free-exciton binding energy $R_X \approx 28$ meV [3].

Having identified FX_C and FX_H to arise from free-exciton recombination, we determine their quantum efficiency and investigate the room-temperature behavior of the band-gap luminescence (BGL), which consists of the band-band and free-exciton transitions. We model the dependence of the BGL intensity on P_{ex} and extract the (non)radiative lifetimes. The values obtained are not only consistent with time-resolved PL studies [4], but also with the phenomenon of defect saturation, which we observe to occur for the sample investigated.

EXPERIMENT: Sample and Photoluminescence Apparatus

All the measurements were performed on one sample grown in a custom-made MBE system equipped with a DC glow-discharge N_2 plasma source.

A $1.5\text{ }\mu\text{m}$ thick single-phase cubic GaN film was grown on a (100) GaAs substrate. On top of this film, cubic and hexagonal microcrystals with diameters of $\approx 3\text{ }\mu\text{m}$ were grown by a vapor-liquid-solid like epitaxial process under Ga-rich conditions [5]. The crystals, being extremely pure and hence defining an optical standard, dominate the sample's luminescence. Therefore, this sample structure was chosen for our investigations. The structural and morphological properties of the sample were verified by means of *in situ* RHEED, XRD, TEM and SEM, while CL was used to selectively analyze the crystals and the film [1].

The PL measurements were carried out in a standard apparatus using the 325 nm line of a HeCd laser for carrier injection. Neutral density filters were employed to vary the excitation power which was measured in front of the sample by a calibrated joulemeter. The luminescence signal was detected by a photomultiplier after having been analyzed in a grazing-incidence spectrometer (600 lines/mm). The sample itself was kept in an evacuated continuous flow cryostat with $T = 3.8\text{--}300\text{ K}$.

RESULTS AND DISCUSSION

Photoluminescence: Temperature Dependence

In order to identify the band-gap luminescence and to study the behavior of defect-mediated radiative recombination, temperature dependent photoluminescence measurements were performed with T ranging from 4 to 300 K. As already mentioned above, we are mainly interested in the two emission lines with $FX_C = 3.27\text{ eV}$ and $FX_H = 3.47\text{ eV}$ at 4 K.

Cathodoluminescence studies [1] reveal that these lines originate from cubic and hexagonal material, respectively. FX_C does not only appear upon excitation of cubic crystals but can also be found in the cubic film underneath the crystals. In this case, the linewidth of the FX_C transition is larger due to the inferior crystal quality of the film as compared to the cubic crystals. FX_H can only be detected in hexagonal crystals and not in the film.

Having three different emission sources on one sample, namely, two kinds of crystals and the cubic film, the PL spectra will generally be rather complex in nature. To cope with the resulting problems of quantitative interpretation, a line-shape analysis program has been developed. We distinguish between 1.) Band-Band (*BB*), 2.) Free Exciton (*FX*), 3.) Bound Exciton (*BX*) and 4.) Defect-Mediated Recombination [6, 7]. This enables us to obtain good fits for all the spectra, where the average deviation from the data points is of the order of the noise level. In Fig. 1–4, examples of such a spectral decomposition are displayed.

Apart from the FX_C and FX_H lines, which will be shown to arise from the recombination of free excitons, the bound exciton of the cubic phase *BX* can be seen. Furthermore, a broad band higher in energy than FX_C is found, which we tentatively assign to the band-band transition (*BB*) of the cubic phase, since its position agrees with the reported value [2] and because it has the theoretically predicted lineshape [7].

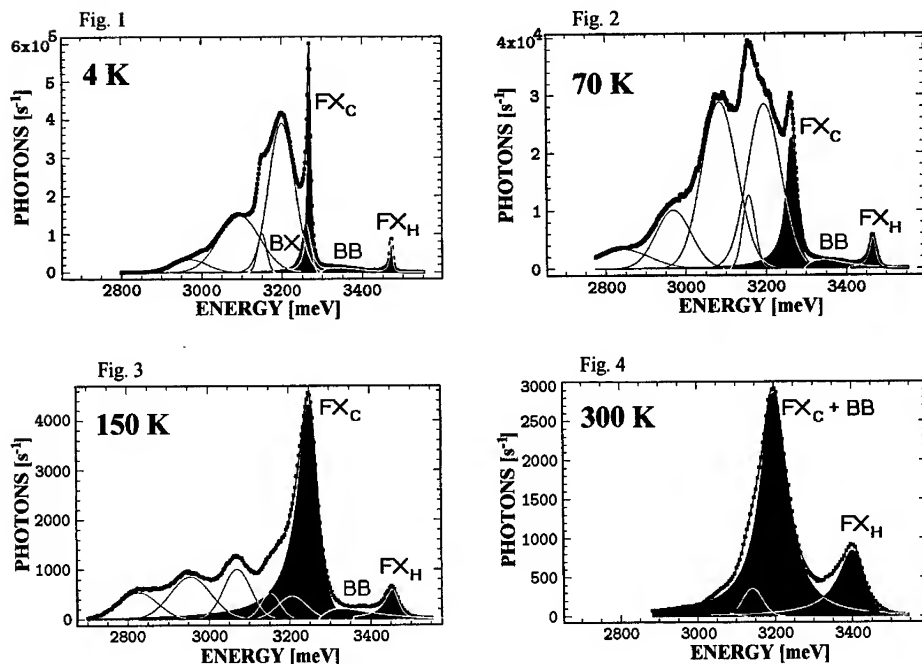


FIG. 1-4: PL spectra with line-shape analysis at various temperatures. The symbols are the measured data whereas the solid lines show the least squares fits and their individual contributions.

BX can be observed only for $T \leq 50$ K. The binding energy of the bound exciton has been estimated to ≈ 5 meV [1]. All the other peaks are related to defects and prevail for $10 \leq T \leq 70$ K. At higher temperatures, however, the FX_C and FX_H transitions are getting stronger and finally dominate the PL at 300 K.

In FIG. 5a, the energy positions of FX_C and FX_H are compared to the band gaps (dashed lines) of cubic [2] and hexagonal GaN [3]. The solid lines are fits to

$$E_G(T) = E_G(0) - S \langle \hbar\omega \rangle \coth \left(\frac{\langle \hbar\omega \rangle}{2kT} - 1 \right), \quad (1)$$

where $\langle \hbar\omega \rangle$ stands for an average phonon energy and S is the Huang-Rhys-Factor [8]. The data for the cubic phase are shifted by an average of 27 ± 3 meV to lower energies, while those for the hexagonal phase are shifted by 30 ± 3 meV. Taking into account that the predicted free-exciton binding energy is $R_X \approx 28$ meV, this provides strong evidence for the interpretation of these peaks as free exciton transitions. The observed position of BB , which can be resolved at low temperatures to within 1%, agrees with the reported values. Furthermore, FX_C and FX_H have the same exciton-like line-shape and their intensity versus excitation density behaves intrinsically, i.e. linearly for $P_{ex} \geq 20$ W/cm², as will be shown below. We thus identify these transitions as arising from free-exciton recombination.

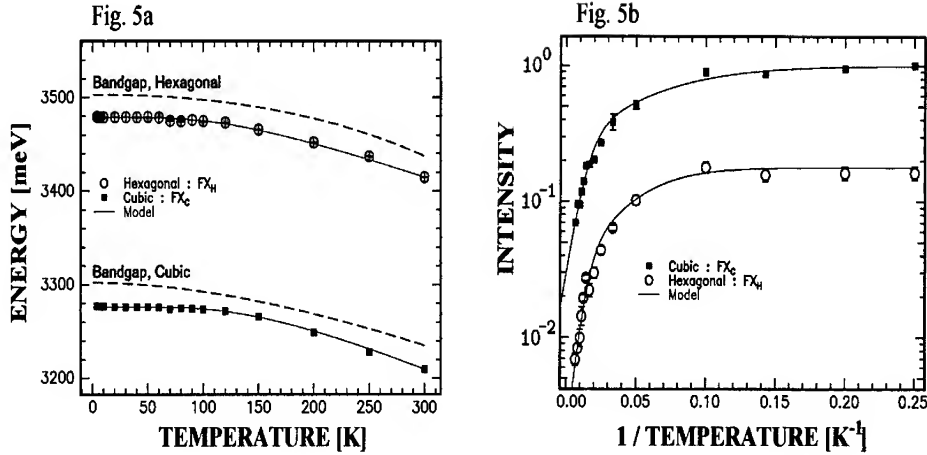


FIG. 5a: Free-exciton energies (symbols) and band-gaps (dashed lines) as functions of temperature. The solid lines are fits to Eq.(1).

FIG. 5b: Intensity of exciton luminescence (symbols) against T^{-1} at small signal excitation ($P_{\text{ex}} = 2 \text{ W/cm}^2$) with fits (solid lines) based on Eq. (2).

In FIG. 5b, the intensity I of the free-exciton luminescence is plotted versus T^{-1} . The data were taken under small signal excitation conditions ($P_{\text{ex}} = 2 \text{ W/cm}^2$). The lines represent a fit based on a 3-level exciton model [9] with two activation energies $E_{1,2}$:

$$I(T) = \frac{I_0}{1 + C_1 \exp(-E_1/kT) + C_2 \exp(-E_2/kT)}. \quad (2)$$

We obtain $E_1^C = 13.4 \text{ meV}$, $E_2^C = 2.1 \text{ meV}$ for cubic and $E_1^H = 18.5 \text{ meV}$, $E_2^H = 3.5 \text{ meV}$ for hexagonal GaN. E_1 is compatible with the thermal exciton dissociation, which is known to occur at kinetic energies of $3/4 \cdot R_X$. This process is predominantly responsible for the quenching of the free-exciton recombination with increasing temperature. E_2 , being considerably lower than R_X , is still under discussion. We suppose E_2 to be due to local potential fluctuations which can create quasi-bound excitons. The total decrease in intensity of the exciton luminescence from 4 K to 300 K is $\eta = I(300)/I(4) \approx 10^{-2}$ for both cubic and hexagonal GaN. Under the assumption that the quantum efficiency of free exciton recombination is unity at 4 K, this factor η represents the room temperature small signal quantum efficiency. By comparison with FIG. 6b, we see that η is close to the quantum efficiencies extracted from intensity dependent measurements at 300 K and low excitation densities for both phases.

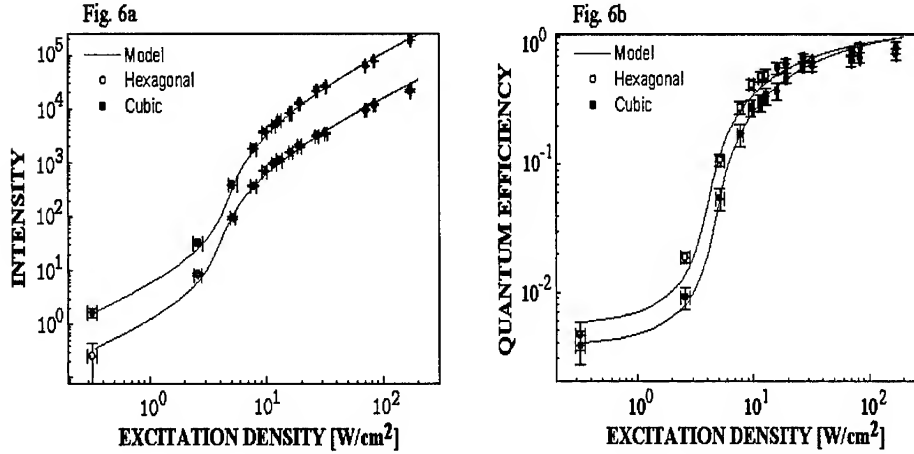


FIG. 6a,b: Intensity and quantum efficiency of the near band-edge luminescence against excitation density (symbols) compared to model calculations (solid lines).

Photoluminescence: Excitation-Density Dependence

To obtain the (non)radiative lifetimes and quantum efficiencies, PL spectra were taken at 300 K as a function of excitation density P_{ex} . In FIG. 6a, the intensity of the band-gap luminescence is depicted against P_{ex} .

At $P_{ex} < 10$ W/cm², the intensity varies nonlinearly due to the existence of non-radiative recombination centers. At $P_{ex} \approx 10$ W/cm², we observe a strong increase in intensity. For $P_{ex} > 20$ W/cm², the band-gap luminescence behaves intrinsically, i.e. increases linearly with increasing excitation density.

Based on a modified version of a rate equation model developed in [10], which takes into account radiative band-band recombination, free-exciton recombination, electron and hole capture and exciton formation and dissociation, we are able to extract the intrinsic radiative lifetime τ_{rad} and the nonradiative lifetimes τ_e , τ_h for electron and hole capture:

TAB. 1: (Non)Radiative lifetimes at 300 K

	Cubic	Hexagonal
τ_{rad}	2 ns	2 ns
τ_h	10 ps	40 ps
τ_e	0.7 μ s	3 μ s

It has to be pointed out that absolute values can only be obtained upon calculation of the radiative recombination coefficient B and the absorption coefficient α . The above results, which have to be taken as order-of-magnitude estimate are however consistent with the lifetimes which have been determined directly by time-resolved PL measurements [4]. They

reveal that the dominant nonradiative recombination center acts as a hole trap. Moreover, the data show that this trap saturates at modest excitation densities because of $\tau_e \gg \tau_h$. In FIG. 6b, the quantum efficiency as function of excitation density can be seen. It approaches unity at $P_{ex} \approx 100 \text{ W/cm}^2$ for both cubic and hexagonal GaN, while under very low excitation conditions, quantum efficiencies of $\approx 6 \cdot 10^{-3}$ are obtained.

CONCLUSIONS

In this work, we have shown that, for both phases of GaN, the dominant radiative recombination channel at room temperature is free-excitonic in nature while the dominant nonradiative recombination center acts as a hole trap which can be saturated under modest excitation conditions. This explains the well-known fact that the luminescence of state of the art GaN is very intense despite its high defect density.

ACKNOWLEDGMENTS

We gratefully acknowledge U. Jahn, R. Klann and J. Menniger for their supporting optical measurements and for many valuable discussions.

REFERENCES

- [1] J. Menniger, U. Jahn, O. Brandt, H. Yang, K.H. Ploog, Phys. Rev. B, to be published (15.01.96)
- [2] G. Ramírez-Flores, H. Navarro-Contreras, A. Lastras-Martínez, Phys. Rev. B **50**, 8433 (1994)
- [3] B. Monemar, Phys. Rev. B **10**, 676 (1974)
- [4] O. Brandt, R. Klann, J.R. Müllhäuser, H. Yang, K.H. Ploog, unpublished
- [5] O. Brandt, H. Yang, B. Jenichen, Y. Suzuki, L. Däweritz, K.H. Ploog, Phys. Rev. B **52**, R2253 (1995)
- [6] H.B. Bebb, E.W. Williams in *Semiconductors and Semimetals Vol. 8*, edited by R.K. Willardson, A.C. Beer (Academic Press, New York and London 1972), pp. 227-317
- [7] M. Shinada, S. Sugano, J. Phys. Soc. Jap. **21**, 1936 (1966)
- [8] K.P. O'Donnell, X. Chen, Appl. Phys. Lett. **58**, 2924 (1991)
- [9] D. Bimberg, M. Sondergeld, E. Grobe, Phys. Rev. B **4**, 3451 (1971)
- [10] O. Brandt, K. Kanamoto, M. Gotoda, T. Isu, N. Tsukada, Phys. Rev. B **51**, 7029 (1995)

TRANSITION METAL LUMINESCENCE IN AlN CRYSTALS

K. PRESSEL*, R. HEITZ**, S. NILSSON*, P. THURIAN**, A. HOFFMANN**, B.K. MEYER***

*Institut für Halbleiterphysik, P.O.Box 409, 15204 Frankfurt(Oder), Germany

**Institut für Festkörperphysik, TU-Berlin, 10623 Berlin, Germany

***Physik-Department E16, TU-München, 85748 Garching, Germany

ABSTRACT

We study deep defects in AlN crystals in the near infrared by photoluminescence and compare the observed emissions with those in GaN. By below bandgap excitation with an Ar ion laser three no-phonon lines at 1.043 eV, 0.943 eV, and 0.797 eV were detected, which are caused by different residual transition metal contaminants. The weak emission at 1.043 eV and the intensive emission at 0.797 eV show AlN related phonon sidebands, whereas the emission at 0.943 eV has practically no phonon sideband. No hot lines could be detected for the emissions at 0.943 and 0.797 eV in temperature dependent measurements. We discuss possible identifications of the luminescence centers and the similarity between GaN and AlN in view of transition metals.

INTRODUCTION

With the tremendous increase of interest for GaN to develop not only a blue light emitting diode (LED) but also a blue laser, the interest in the nitrides increased in general. With the three nitride based semiconductors InN, GaN, and AlN the bandgap can be varied between 1.9 eV (bandgap of InN) and 6.3 eV (bandgap of AlN). Thus, not only the blue-green LED is possible [1], but also optical devices in the ultra-violet region. Up to now only a few photoluminescence (PL) studies of AlN have been done because no conventional ion lasers are available to excite electrons with 6.3 eV from the valence band to the conduction band. Deep defects like transition metals are believed to be omnipresent defects in the nitride compounds. However no quantitative information is available, yet. One method to gain information about deep traps also at low doping concentrations can be PL. For GaN various luminescence centers, which are caused by transition metals, were detected in the near infrared region (NIR) and could partly be identified [2-7]. Recently Baur et al. [4] reported two emission centers in AlN which have no-phonon (NP) lines at 1.201 eV and 1.297 eV. On the basis of a comparison of their results with two emissions at 1.19 eV and 1.3 eV in GaN they attributed the 1.201 eV luminescence center to Cr^{4+} and the 1.297 eV luminescence center to Fe^{3+} . Although we believe that the two emissions in GaN and AlN have the same origin, we attribute the 1.19 eV center in GaN [7] and therefore also the 1.201 eV center in AlN to the ${}^1\text{E} \rightarrow {}^3\text{A}_2$ internal electronic transition of Ti^{2+} and not to Cr^{4+} . In this paper we focus on further luminescence centers in AlN that could be detected in various crystals by below bandgap excitation with an Ar ion laser.

EXPERIMENTAL

The samples were partly grown by mixing Al and N at very high temperatures (1900°C). Small AlN crystalline needles were obtained with a typical length of 3 mm and a diameter of about 100 µm. For comparison we also investigated AlN powder and AlN layers grown by metal organic vapor phase epitaxy. Preliminary intentional doping experiments of GaN and AlN crystals by indiffusion of Fe at temperatures between 700 and 900°C in vacuum were unsuccessful to stimulate the Fe^{3+} luminescence signal at 1.3 eV in GaN and 1.297 eV in AlN.

The PL measurements were performed using either conventional monochromator technique or a BOMEM DA8.02 Fourier spectrometer. The excitation was performed with an Ar ion laser, which had a possible UV option. For all measurements a Germanium detector

was used.

EXPERIMENTAL RESULTS AND DISCUSSION

Figure 1 shows a PL spectrum of an AlN needle in the NIR. We observe one weak NP line at 1.043 eV and two intense NP lines peaking at 0.943 eV and 0.797 eV by below bandgap excitation with the 514 nm green line of the Ar ion laser. Only the 0.943 eV luminescence center could be detected under UV excitation, the other two emissions could not be detected by the UV light (360 nm) of the Ar laser.

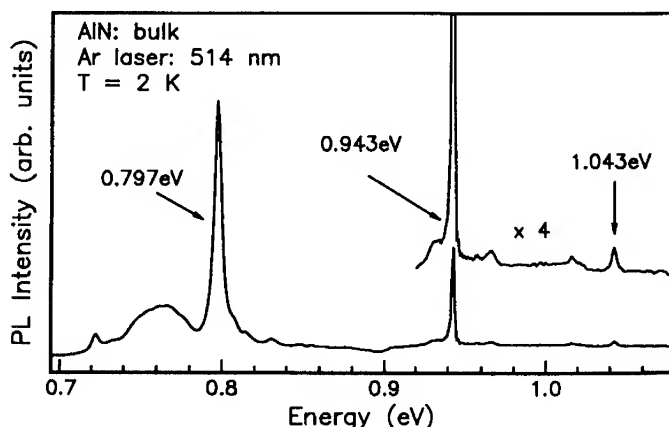


FIG. 1 NIR PL spectrum of an AlN crystalline needle excited with below bandgap excitation of the 514 nm green line of an Ar ion laser. Besides a weak NP line at 1.043 eV we observe two strong emissions peaking at 0.943 eV and 0.797 eV.

The 1.043 eV emission

Figure 2 (a) shows a more detailed spectrum of the weak 1.043 eV emission. The linewidth is about 2 meV. The defect center shows coupling to phonon modes close to modes observed for AlN in Raman spectroscopy [8]. The peaks in the phonon sideband at 86.3 meV, and 112.8 meV ($E_1(\text{LO})$) coincide with the modes observed in Raman spectroscopy on the AlN needles. The mode at 77.9 meV is a little lower in energy than the corresponding Raman mode. Thus, this mode is caused by a local mode of the defect. A part of the peak, which is attributed to the phonon at 112.8 meV, belongs to a shoulder of the 0.943 eV emission (see next section).

The 1.043 eV luminescence is still visible with about the same intensity at 80 K. We only observe a small shift of about 0.2 meV to lower energy, which is typical for internal electronic transitions of 3d elements [9]. As already pointed out in the introduction internal electronic transitions of the same transition metal ion in GaN and AlN seem to have nearly equal energies. On the basis of this argument the 1.043 eV emission in AlN is caused by the luminescence center responsible for the 1.047 eV emission in GaN[10, 11], which is depicted in the upper spectrum of Fig. 2. This emission is attributed to the $^4T_2 \rightarrow ^4A_2$ transition of a 3d element with a $3d^7$ electronic configuration. Co^{2+} and Ni^{3+} are discussed as luminescence centers [10, 11].

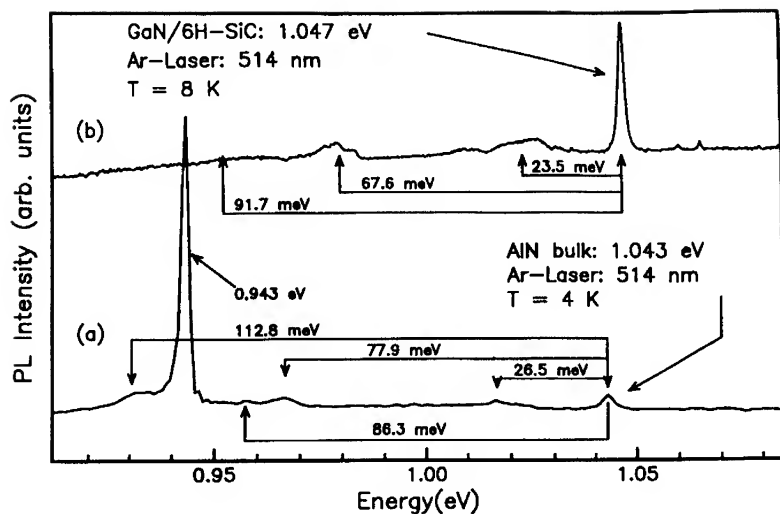


Fig. 2. (a) PL spectrum of the 1.043 eV emission in AlN together with the corresponding phonon sideband. The energy values belong to phonon energies and localized vibrational modes. (b) A comparison spectrum of the 1.047 eV luminescence in GaN together with the GaN related phonon sideband.

The 0.943 eV emission

The emission at 0.943 eV is close to an emission at 0.931 eV in GaN reported by Baur et al. [4]. They observed in temperature dependent PL spectra a hot line 1.6 meV higher in energy. This was their basis to attribute the 0.931 eV emission to an internal electronic transition of V^{3+} .

Figure 3 shows the 0.943 eV emission for three different samples. The inset compares two spectra recorded at different sample temperatures.

With rising temperature we observe no hot line (also at higher energies not shown here). The energy shift towards lower energy between the 2 K and the 85 K spectrum is about 0.2 meV. In some samples the emission showed a shoulder, labelled A, on the low energy side. A similar observation can be made for the 1.19 eV emission in GaN. Possibly this is caused by internal strain or rather a disturbance in the neighborhood of the luminescence center.

The linewidth of this emission is between 0.5 and 0.6 meV depending on the sample. For rising temperatures up to 85 K the linewidth only slightly increases from 0.5 meV to 0.7 meV.

Phonon sidebands could practically not be resolved for this emission. By chance the weak emission at 0.832 eV, labelled a (compare also Fig. 4), is 112.8 meV from the 0.943 eV NP line in this sample. But the emission at 0.832 eV belongs most definitely to a fine structure of the 0.797 eV luminescence center and not to the coupling of a phonon mode of AlN. The experimental behavior of this emission is very similar to that of the 1.19 eV emission in GaN and may also be caused by the $^1E \rightarrow ^3A_2$ transition of a $3d^2$ configuration (possibly V^{3+} or Cr^{4+}). Maybe in AlN the 1E excited state is energetically below the 3T_2 excited state, similar to Ti^{2+} in GaN [7]. Zeeman measurements have to be performed to identify this emission center. The linewidth of 0.5 meV in the best samples is sufficient to allow these studies.

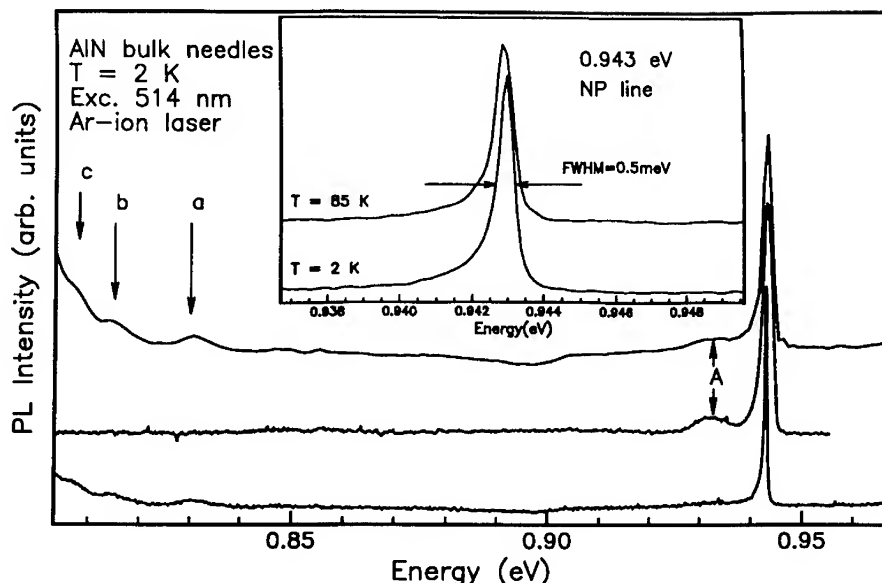


Fig. 3. PL spectra in the energy range of the 0.943 NP line. Spectra with and without the low energy shoulder labelled A are shown. In the inset two spectra detected at 2 K and 85 K are depicted. The linewidth of the peak is 0.5 meV.

The 0.797 eV emission

In general the strongest luminescence in our samples is the emission at 0.797 eV. Figure 4 gives a detailed spectrum in the range of this emission. Besides the strong NP line at 0.797 eV we resolve four weak satellite peaks in the range of the 0.797 eV emission at 0.832 eV (a), 0.815 eV (b), 0.811 eV (c), and 0.777 eV (e). The whole set of lines is indicated by the rake with five arrows.

The linewidth of the main peak at 0.797 eV is 4 meV in our samples. As shown in the inset of Fig. 4 no hot lines could be resolved up to 85 K. Similar to the 0.943 eV emission also the strong 0.797 eV emission shows nearly no increase in linewidth and only the small shift of about 0.2 meV to lower energy.

On the low energy side of the 0.797 eV emission a broad shoulder appears. The maximum of this shoulder is close to the $E_2(\text{low})$ (30.7 meV) phonon mode, which is observed in Raman measurements. 76 meV lower in energy a further set of peaks appears. The spacing of the two main peaks at 0.722 eV (d') and 0.782 (c') agrees excellently with the $A_1(\text{TO})$ (76.1 meV) mode, which can be observed in Raman measurements.

In general the spectrum of the 0.797 eV luminescence center looks similar to the well-studied 0.84 eV emission of Cr in GaAs [12]. This luminescence center is attributed to an internal electronic transition of Cr^{2+} on a Ga substitutional lattice site. The tetrahedral environment of the Cr center is disturbed by a defect atom on one of the four As nearest neighbor sites. The 0.797 eV luminescence center may be caused by a similar defect. A $^5\text{T}_2$ ground state is a good possibility for this emission. Thus possible candidates are Mn^{3+} , Cr^{2+} , and V^{+} .

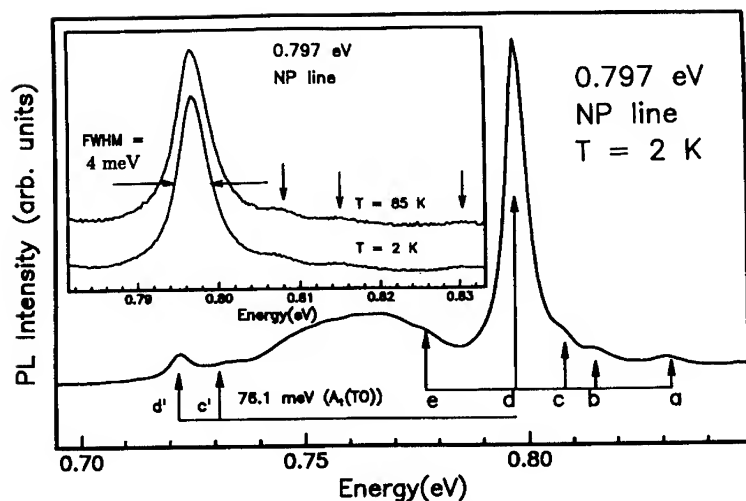


Fig. 4. PL spectrum of the 0.797 eV emission. In addition to the main no-phonon line we observe further weak satellite peaks indicated by the rake. The inset compares two spectra of the 0.797 eV emission detected at 2 K and 85 K.

To the 0.797 eV emission in AlN we also observed an emission with the main peak at 0.77 eV in GaN samples grown by the sandwich technique. This luminescence in GaN is shown in the upper part of Fig. 5. The shape looks similar to the 0.797 eV emission, but it is broader and therefore possible fine structures can not be resolved.

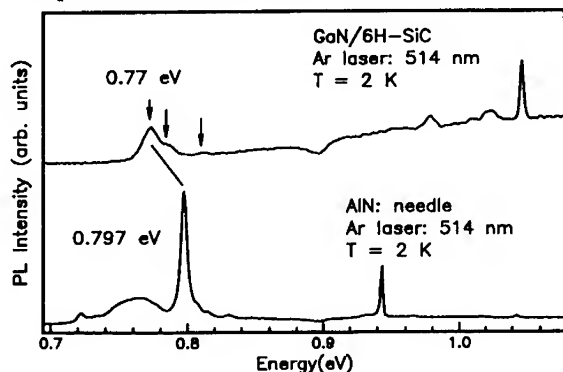


FIG. 5. PL spectra of AlN and GaN in the optical range of between 0.7 eV and 1.4 eV. The emission at 0.797 eV seems to have a counterpart in GaN at 0.77 eV.

CONCLUSIONS

By photoluminescence we studied residual transition metals in AlN. We observe three luminescence centers at 1.043 eV, 0.943 eV, and 0.797 eV. As already pointed out by Baur et al. [4] it seems possible to transfer the identifications of internal electronic transitions in GaN also to AlN. In Tab. I transition metal emissions in AlN and GaN are summarized.

AlN Energy (eV)	GaN Energy (eV)	possible identification in GaN
1.297 [2,3]	1.30 [2,3,5]	$\text{Fe}^{3+} (^4\text{T}_1 \rightarrow ^6\text{A}_1)$
1.201 [4]	1.193 [7]	$\text{Ti}^{2+} (^1\text{E} \rightarrow ^3\text{A}_2)$
1.043 this work	1.047 [11], this work	$3d^7 (\text{Co}^{2+}, \text{Ni}^{3+})$
0.943 this work	0.931 [4]	V^{3+}
0.797 this work	0.77 this work	transition metal complex

TABLE I. Comparison of transition metal emissions in AlN and GaN. The possible identifications obtained for GaN also seem to fit in AlN.

On the basis of a comparison with GaN the 1.043 eV center in AlN is caused by the same contaminant as the 1.047 eV emission in GaN. An exception to these nearly equivalent transition metal energies is the 0.943 eV emission in AlN. In contrast to the 0.931 eV emission in GaN the 0.943 eV emission in AlN shows no hot line. In general the intense 0.943 eV no-phonon line shows similar properties as the 1.19 eV emission in GaN. Thus it might also be attributed to a $^1\text{E} \rightarrow ^3\text{A}_2$ transition. Possibly for V^{3+} in AlN the ^1E excited state shifts below the $^3\text{T}_2$ state as observed for Ti^{2+} in GaN [7]. The 0.797 eV no-phonon line has at least 4 weak satellite peaks. The whole spectra looks like the 0.84 eV luminescence of Cr in GaAs. Probably a similar transition metal complex is responsible for this emission. Zeeman measurements are now essential to identify these defects.

Reasons for the appearance of the internal electronic transitions at about the same energies in GaN and AlN are the same neighborhood of nitrogen atoms (N has a much larger electronegativity than P and As), the almost equal covalent bonding, the similar lattice constant, and the large bandgap.

ACKNOWLEDGEMENT

The authors are indebted to J. Pasternak for the supply with AlN samples. We gratefully acknowledge the financial support of the *Stifterverband der Deutschen Wissenschaft*.

References

- [1] S. Nakamura, T. Mukai, and M. Senoh, J. of Appl. Phys. **76**, 8189 (1994)
- [2] J. Baur, K. Maier, M. Kunzer, U. Kaufmann, J. Schneider, H. Amano, I. Akasaki, T. Detchprohm, and K. Hiramatsu, Appl. Phys. Lett. **64**, 857 (1994)
- [3] J. Baur, K. Maier, M. Kunzer, U. Kaufmann, and J. Schneider, Appl. Phys. Lett. **65**, 2211 (1994)
- [4] J. Baur, U. Kaufmann, M. Kunzer, J. Schneider, H. Amano, I. Akasaki, T. Detchprohm, and K. Hiramatsu, Appl. Phys. Lett. **67**, 1140 (1995)
- [5] R. Heitz, P. Thurian, I. Loa, L. Eckey, A. Hoffmann, I. Broser, K. Pressel, B.K. Meyer, E.N. Mokhov, Appl. Phys. Lett. **67**, 2822 (1995)
- [6] R. Heitz, P. Thurian, I. Loa, L. Eckey, A. Hoffmann, I. Broser, K. Pressel, B.K. Meyer, and E.N. Mokhov, presented at the 18th International Conference on Defects in Semiconductors, Sendai, Japan (unpublished)
- [7] R. Heitz, K. Pressel, P. Thurian, I. Loa, L. Eckey, A. Hoffmann, I. Broser, B.K. Meyer, E.N. Mokhov, accepted for publication in Phys. Rev. B
- [8] L.E. Mc Neil, M. Grinsditt, R.H. French, J. Am. Ceram. Soc. **76**, 1132 (1993)
- [9] B. DiBartholo, Optical Interactions in Solids (John Wiley & Sons, New York, 1968)
- [10] K. Pressel, R. Heitz, L. Eckey, I. Loa, P. Thurian, A. Hoffmann, B.K. Meyer, S. Fischer, the same conference
- [11] K. Pressel, S. Nilsson, R. Heitz, A. Hoffmann, B.K. Meyer, accepted for publication in Journal of Appl. Phys.
- [12] Ch. Uihlein and L. Eaves, Phys. Rev. B **26**, 4473 (1982)

2.2 eV LUMINESCENCE IN GaN

D. M. Hofmann, D. Kovalev, G. Steude, D. Volm, B. K. Meyer, C. Xavier*, T. Monteiro*, E. Pereira*, E. N. Mokov**, H. Amano***, and I. Akasaki***

Physik Department E 16, Technische Universität München, D-85747 Garching, Germany

* Departamento de Física, Universidade de Aveiro, Portugal

** Ioffe Physico-Technical Institute, St. Petersburg, Russia

*** Department of Electrical and Electronic Engineering, Meiji University, 1-501 Shiogamaguchi, Tempaku-ku, Nagoya 468, Japan

ABSTRACT

The yellow Luminescence in GaN centered at 2.2 eV has been studied in various epitaxial layers grown by MOVPE on sapphire and by the sandwich sublimation methode on 6H-SiC substrates. The photoluminescence and optically detected magnetic resonance results can be consistently explained by a recombination model involving shallow donors and deep donors.

INTRODUCTION

The near bandgap-luminescence efficiency of semiconductors is severely influenced by the presence of deep level defects in the bandgap. Therefore it is of importance to study the properties of these defects and, if possible, to identify their chemical nature which might help to avoid their presence in furture crystal growth experiments.

For GaN its was realized quite early that a deep broad photoluminescence (PL) band located with its peak maximum at 2.2 eV is omnipresent [1]. In a photoluminescence (PL) investigation on doped GaN microcrystals and needle like crystals it was shown that the properties of this PL band (i.e. the temperature dependence of its intensity and halfwidth as well as PL-excitation) can be described by a recombination model of randomly distributed shallow donors and deep acceptors - a model originally developed by Thomas and Hopfield [2]. In addition, from doping experiments evidence was obtained that carbon might be involved in the deep acceptor structure.

In contrast in an optically detected magnetic resonance (ODMR) investigation on GaN epitaxial layers grown under various growth conditions the observed signals were attributed to shallow donors and deep donors, likely to be caused by an intrinsic defect [3]. The recombination mechanism for the 2.2 eV PL was explained by a recombination from a deep intrinsic double donor to a singly positively charged shallow acceptor.

We have investigated the yellow luminesence in epitaxial GaN layers by PL, time resolved-PL, PL-excitation spectroscopy and ODMR. The results can be consistently explained by a recombination model involving shallow donors and deep donors.

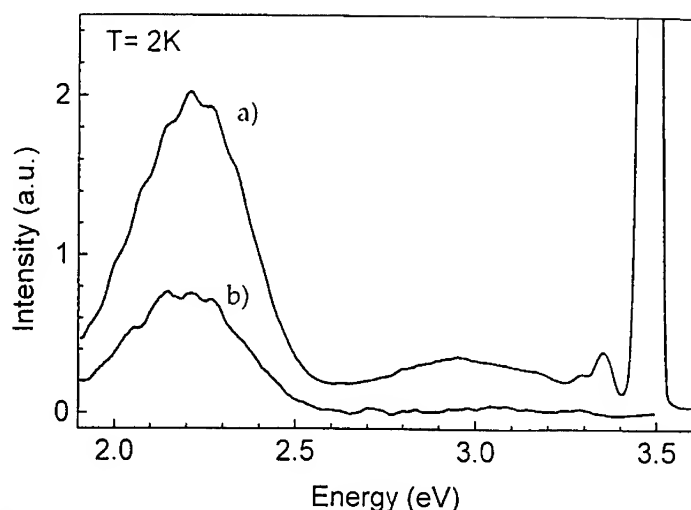


Figure 1: a) Low temperature photoluminescence spectrum of GaN/sapphire
b) excitation spectrum of the optically detected magnetic resonance signals

RESULTS AND DISCUSSION

Two type of samples were used for the experiments: undoped GaN epitaxial layers grown by MOVPE on sapphire substrates and GaN epitaxial layers grown by the sandwich sublimation method on 6H-SiC substrates. The layer thicknesses of the MOVPE samples were about 3 μm . To improve the crystalline quality of the layers a 35 nm AlN buffer was grown at low temperatures. The n-type carrier concentrations of the layers as determined by C/V measurements are below 10^{17}cm^{-3} at room temperature.

A typical steady state low temperature PL spectrum of a GaN sample is shown in Fig. 1a). Near band gap the strong excitonic recombination of the donor bound excitons (D^0X) is detected. In the 3.4 eV - 2.6 eV range the donor acceptor pair recombination of the so called "violet band" occurs. At lower energies the 2.2 eV ("yellow") luminescence is visible. These spectral features are very similar for the MOVPE and sandwich sublimation grown samples. Especially the energy position and spectral shape of the yellow PL band presented here is also very similar to the C doped GaN samples used by Ogino and Aoki [1], and to that observed by Glaser et al [3].

Measuring the temperature dependence of the 2.2 eV PL intensity in the range from 2 K to 300 K we find an activation energy of 15 ± 2 meV [4]. For an uncompensated semiconductor the binding energy of the involved defect is expected to be twice this value. It corresponds approximately to the shallow donor binding energy of 35 meV.

The ODMR signals observed on the yellow band at 2 K are shown in Fig. 2. The position of the resonance at higher magnetic field is slightly dependent on the orientation of the crystal in the static magnetic field. Its g-value is $g = 1.95 \pm 0.01$ which is very close to the

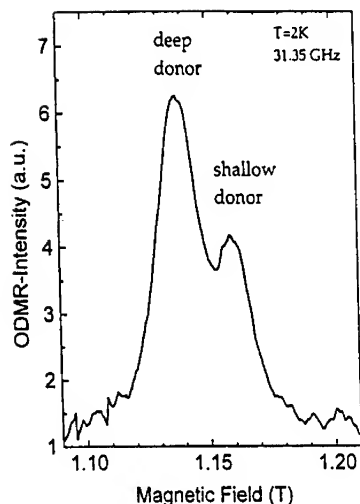


Figure 2:
Optically detected magnetic resonance spectrum
of the 2.2 eV luminescence in GaN

value of the effective mass donors known from EPR experiments [5]. The resonance position of the signal at lower field corresponds to the deep donor resonance (labeled A1) reported by Glaser et al [3]. It should be noted that the halfwidth of the donor resonance is very sample dependent in some samples it was as high as 40 mT which prevents the resolution of the deep donor signal. Such broadening can be explained by higher donor concentrations causing additional exchange interaction [6]. Both signals enhance the PL intensity which is usually taken as evidence that the defects are directly involved in the radiative recombination [7]. The ODMR excitation spectrum, i.e. keeping the resonance conditions fixed and scanning the PL detection wavelength (Fig. 1b) shows that the signal intensity follows the lineshape of the 2.2 eV band. It is known that the 2.2 eV PL can be excited not only above bandgap but down to 2.6 eV [1]. Independent of above or below bandgap excitation we observed both the shallow and the deep donor ODMR, which gives further evidence that both defects are directly involved in the recombination.

The two discussed recombination models for the yellow emission in GaN are shown in Fig.3. Model A is the shallow donor to deep acceptor model which is favoured by Ogino and Aoki [1]. Model B was developed by Glaser and coworkers [3]. Here the yellow emission originates from a recombination between a deep double donor and a shallow acceptor. The electron transfer from the shallow donor to deep state is assumed to occur via a spin dependent nonradiative transfer process. Initially the shallow and deep donor are singly occupied, and thus observable by ODMR. the yellow luminescence occurs between the neutrally charged (doubly occupied) deep donor and the effective mass acceptor.

Our investigations support Model A, except that a deep donor is involved instead of a deep acceptor. To associate the A1 resonance with a deep acceptor would be in conflict with the

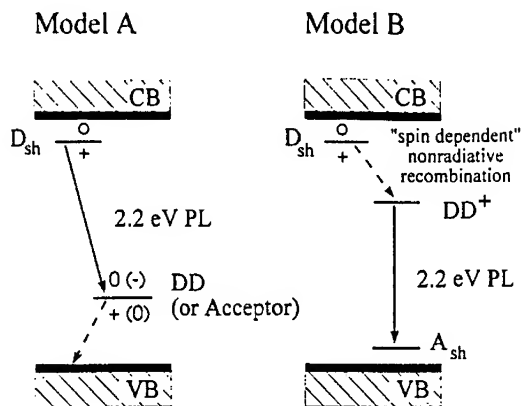


Figure 3: The two recombination models under discussion for the 2.2 eV luminescence in GaN

observed g -values ($g_{\parallel}=1.989$, $g_{\perp}=1.992$) which are smaller than the free electron value ($g_e=2.0023$). In first order perturbation theory the deviation of the g -value is given by $g \sim \lambda/\Delta E$ [6], λ is the spin orbit interaction constant. Thus electron centers (negative λ) should show g -values smaller than the free electron value and hole centers should have a positive g -shift. Exceptions from this rule are known. For example arsenic antisite defects in GaAs which are double donors have a g -value of 2.04 [8]. However, the negative g -shift is a strong argument for the observation of a donor type defect.

Model A is further supported by our time resolved PL experiments, for a recombination between a shallow donor with an extended wavefunction and a deep defect which is localized in real space one expects to observe a broad lifetime distribution, whereas for a recombination between two localized defects (deep donor and an acceptor) a single lifetime or only a narrow distribution is expected [2]. A broad lifetime distribution is observed for the 2.2 eV PL in GaN grown on sapphire [4]. Thus our experiments strongly support model B.

The time resolved PL experiments on the GaN grown on 6H SiC show a peculiarity. In addition to the lifetime distribution observed in the GaN/sapphire samples a distinctly slower (> 5 msec.) component is observed (see fig. 4). The measurements indicate that its peak maximum position is at about 2.1 eV with a similar halfwidth as the 2.2 eV band. Although the defects responsible for this slow luminescence are not identified a relation to the substrate seems to be likely. The presence of the 2.2 eV band in almost all type of GaN, independent of the growth technique and the substrate used make it likely that the defects are of intrinsic origin. The ODMR results give strong evidence that the deep defects are donor-type. To

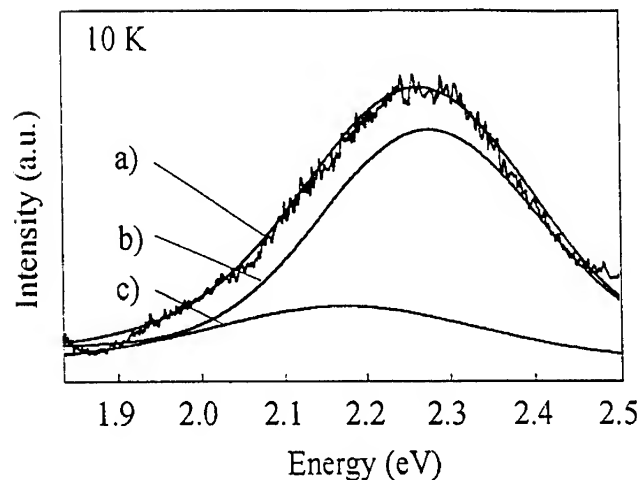


Figure 4: a) Photoluminescence spectrum of the GaN on 6H SiC sample grown by the sandwich sublimation method and, based on the results of time resolved spectroscopy, a deconvolution of the spectrum into two recombinations: b) the shallow Donor to deep donor recombination and c) the component showing an extremely long lifetime (> 5 msec.)

obtain more specific information possibly optically detected electron nuclear double resonance experiments or ODMR experiments with enhanced resolution (using higher microwave frequencies) may be helpful.

CONCLUSIONS

The 2.2 eV luminescence band in GaN has been studied by photoluminescence and optically detected magnetic resonance spectroscopy. The results can be consistently explained in a shallow donor to deep donor recombination model. The GaN samples grown on 6H:SiC substrates show superimposed on the 2.2 eV band a slow recombination with a maximum at 2.1 eV. Its origin is likely to be related to the use of this special substrate material, whereas the omnipresent 2.2 eV band is likely to be caused by intrinsic defects.

REFERENCES

- [1] T. Ogino and M. Aoki, Jpn. J. Appl. Phys. **19**, 2395 (1980)
- [2] D. G. Thomas, J.J. Hopfield, W. M. Augustyniak, Phys. Rev. **140**, A202 (1965)

-
- [3] E. R. Glaser, T. A. Kennedy, K. Doverspike, L. B. Rowland, D. K. Gaskill, J. A. Freitas jr., M. Asif Khan, D. T. Olson, J. N. Kuznia, and D. K. Wickenden, *Phys. Rev. B* **51**, 13326 (1995).
 - [4] D. M. Hofmann, D. Kovalev, G. Sreude, B. K. Meyer, A. Hoffmann L. Eckey, *Phys. Rev. B*, in press
 - [5] W. E. Carlos, J. A. Freitas, M. Asif Kahn, D. T. Olson, and Kuznia, *Phys. Rev. B* **48**, 17878 (1993)
 - [6] G. E. Pake and T. L. Estle, *The Physical Principles of Electron Paramagnetic Resonance* (Benjamin, Reading, MA, 1973)
 - [7] J. J. Davies, *J. Crystal Growth* **72**, 317 (1985)
 - [8] E.R. Weber, H. Ennen, U. Kaufmann, J. Windscheif, J. Schneider and T. Wosinski, *J. Appl. Phys.* **53**, 6140 (1982)

GROWTH OF GAN WITHOUT YELLOW LUMINESCENCE

X. ZHANG, P. KUNG, D. WALKER, A. SAXLER AND M. RAZEGHI

Center for Quantum Devices, Department of Electrical Engineering and Computer Sciences,
Northwestern University, Evanston, IL 60208

ABSTRACT

We report the growth and photoluminescence characterization of GaN grown on different substrates and under different growth conditions using metalorganic chemical vapor deposition. The deep-level yellow luminescence centered at around 2.2eV is attributed to native defect, most possibly the gallium vacancy. The yellow luminescence can be substantially reduced By growing GaN under Ga-rich condition or doping GaN with Ge or Mg.

INTRODUCTION

The realization of high brightness blue, green and yellow light emitting diodes from InGaN, GaN and AlGaIn [1] has stimulated tremendous scientific interest in these large bandgap (1.9eV to 6.2eV) III-Nitride semiconductors. It is expected that these devices can bring a revolution to high-density optical storage, full-color displays and huge energy savings. Besides that, these materials are ideal candidates for efficient, highly selective (and thus solar-blind) UV-photodetectors, which can find numerous applications such as astronomical physics, undersea detection , space-to-space communication, surveillance and recognition of spacecraft [2].

III-Nitride semiconductors are usually grown on basal plane sapphire substrate by metalorganic chemical vapor deposition (MOCVD) or molecular beam epitaxy (MBE). At the early stage, these materials normally occurred as a naturally heavily doped n-type semiconductors and it was impossible to obtain device quality p-type layers. With the introduction of the AlN [3] or GaN [4] buffer layer, the layer quality has been dramatically improved, n-type background carrier concentration has been reduced to around 10^{16}cm^{-3} and p-type doping has been successfully achieved. However, it is widely recognized that even in high quality III-Nitride layers, the dislocation density is very high (10^{10}cm^{-2}) and there exist high-density deep levels and other defects which limit the performance of the devices [5].

One of the very popular phenomena associated with the deep-level is the so-called yellow luminescence (YL). It is a broad luminescence band centered around 2.2 -2.3eV and exists virtually in all samples from different laboratories and growth methods. Intensive studies have been carried out experimentally and theoretically to investigate the origin and mechanism of this emission. Ogino and Aoki [6] did the most complete study and proposed a band model. In their model, the YL is attributed to an emission between a shallow donor level to a deep-level originating from a complex consisting of a gallium vacancy and an impurity. In their case, they suggested the impurity is carbon, but Pankove [7] showed that ion implantation can also introduce such a deep level. The impurity related deep-level is also supported by the argument of Singh *et.al.*[8]. Recently, using the results from optically detected magnetic resonance and low temperature photoluminescence, Glaser *et.al.* [9] proposed another model to explain the yellow luminescence. In their scheme, the YL is the radiative recombination of electrons between a deep double donor of A_1 character (with a depth of about 0.8eV) and an acceptor state of the effective-mass character. But Suski *et.al.*[10] showed that this model cannot explain the pressure-dependent behavior of the YL. The origin of the YL has also been studied theoretically by calculations of defects states in GaN. These state-of-art calculations [11,12,13] showed that

native defects are the natural candidates for the origin of the electronic levels participating in the YL. Contrary to conventional beliefs, Neugebauer and Van de Walle showed that in n-type GaN, the gallium vacancy is the most energetically favorable native defect [13].

The above studies show important characteristics of the YL. However, a correlation between the growth conditions and the YL would be more helpful to relate these results with each other. In our previous studies [14,15,16], we noticed that the YL becomes barely detectable for Si- or Mg-doped GaN. For undoped samples, GaN grown on SiC substrates shows the weakest YL. In this paper, we report a systematical photoluminescence study of GaN samples grown under different growth conditions. With the correlation between photoluminescence and growth conditions, the results shown here strongly suggest that: (i) the gallium vacancy and related complexes are responsible for the YL emission; (ii) These defects are generated due to the large lattice and thermal mismatch between epilayer and substrates. The closer to the epilayer-substrate interface, the higher the density of defects.

EXPERIMENTS

The growth conditions are the same as those we have reported [14,15,16]. Briefly, all epitaxial layers were grown by MOCVD. Trimethylgallium, trimethylaluminum, ammonia, germane and bis-cyclopentadienylmagnesium were used as starting materials for Ga, Al, N, Ge and Mg elements, respectively. The carrier gas was H₂. The effect of lattice mismatch was studied by using two different substrates: sapphire (00.1) and 6H-SiC (00.1). These substrates were always put side by side on a 4.5"-diameter SiC-coated graphite susceptor. The susceptor is rotated by gas-foil rotation technology and heated by a RF-coil. Thus excellent uniformity can be achieved across the susceptor. For other studies, only sapphire (00.1) was used as the substrate. A thin AlN buffer layer was deposited before the GaN layer with a thickness of 0.5 μ m to 4 μ m.

Photoluminescence spectra were measured with a He-Cd laser as the excitation source (25nm, \approx 5mW), a grating monochromator and a standard synchronous detection setup. The power density on the sample is approximately 50W/cm² after focusing. At this power density, we measured that the dependence of the integrated peak intensities of YL and bandedge emission are both linear. All photoluminescence experiments reported in this paper are carried out at room temperature.

Two series of experiments were performed to study the correlation between the growth conditions and YL. One is the doping of GaN with Ge and Mg; the other is the growth of GaN with different TMGa flow.

RESULTS AND DISCUSSION

The photoluminescence of undoped GaN, Ge-doped GaN and Mg-doped GaN are shown in Fig. 1 (a), (b) and (c) respectively. Clearly shown is the absence of YL emission from both GaN:Ge and GaN:Mg on (00.1) Al₂O₃. Such emission was not observed from doped layers on other substrates either. Ge (group IV) acts as a donor and Mg (group II) as an acceptor in GaN by substituting to Ga (group III) sites. In this instance, the removal of the deep-level YL in Ge-doped or Mg-doped GaN strongly suggests that the YL is closely related to the Ga-vacancies because Ge or Mg atoms would fill the Ga vacancies for a successful doping. Complementary evidence can be found in the results reported by Nakamura *et al.* [18]. They showed that the YL was eliminated when GaN was doped with Mg and activated by LEEBI or thermal annealing treatments.

Figure 2 shows the photoluminescence spectra of undoped GaN which were grown on (00.1) Al_2O_3 with TMGa flow rates of 1.25 and 2.5 sccm respectively. All other parameters were kept the same for these two growths. Deep-level YL can be observed from GaN grown with a lower TMGa flow rate while it was absent from the samples with higher TMGa flow rate. Since fewer Ga vacancies are expected in the case of a higher TMGa flow rate, these experiments again strongly suggest that the YL result from Ga vacancies or its related complexes.

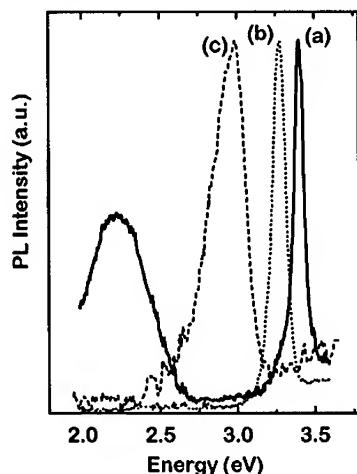


FIG. 1. photoluminescence (300K) of (a) undoped GaN, (b) GaN:Ge, (c) GaN:Mg. Yellow luminescence is undetectable from doped GaN.

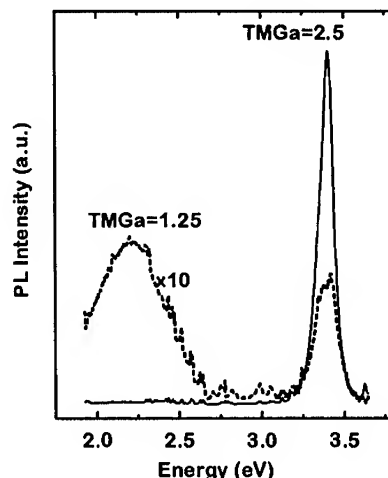


FIG. 2. Photoluminescence (300K) of undoped GaN grown with different TMGa flows. Yellow luminescence are substantially reduced with more TMGa flow.

During our experiments, it was found out that the YL of GaN on 6H-SiC substrates is always much lower than that of GaN on basal plane sapphire. Figure 3 shows the room temperature PL of GaN grown on these two different substrates. The same scale is used for the two curves. It can be clearly seen that the YL of GaN/6H-SiC is barely detectable.

Between basal plane 6H-SiC and sapphire, the former is expected to provide lower density of defects since it has closer lattice and thermal match with GaN crystals. Wetzel *et al.* [17] have also shown that no YL was detectable from high quality GaN grown on 6H-SiC. Generally it is observed that the defect density is as high as 10^{10} cm^{-2} near the interface of GaN and basal plane sapphire substrate. It is very possible that these defects are responsible for the YL emission.

Figure 4 (a) and (b) are two other interesting results which show the effect of defects on YL. Two PL spectra were obtained by front-side (Fig.4(a)) and back-side excitation (Fig.4(b)) of the same sample, which is GaN on basal plane sapphire and is $0.7 \mu\text{m}$ thick. Clearly shown is the stronger YL and weaker bandedge emission using the backside excitation scheme. Because of the high absorption coefficient of GaN at the laser wavelength ($> 2 \times 10^5 \text{ cm}^{-1}$ for 325nm) [14] and the transparency of sapphire in the UV and visible range, the PL emission is mostly from the top layer or interface layer within a depth of approximately $0.1 \mu\text{m}$ in the case of front-side or backside excitation respectively. The above results strongly suggest that the YL is from the

defects close to the GaN/sapphire interface. These defects are introduced by the large lattice and thermal mismatch.

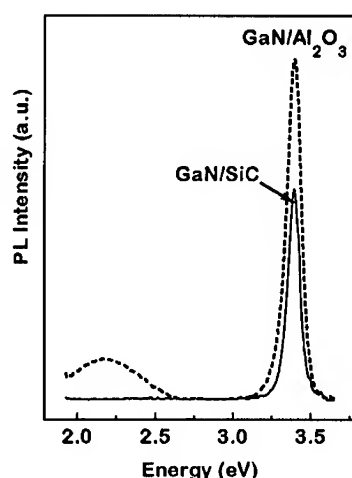


FIG. 3. photoluminescence (300K) of (a) undoped GaN grown on 6H-SiC and Al₂O₃ substrates.

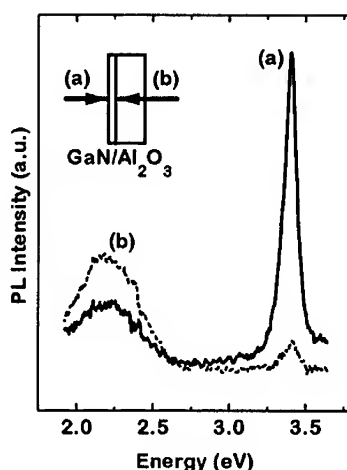


FIG. 4. Photoluminescence (300K) of undoped GaN with (a) front-side excitation, (b) back-side excitation.

CONCLUSIONS

Correlation between growth conditions (by MOCVD) and the deep-level yellow luminescence (YL) of GaN centered around 2.2eV has been found. The YL was usually observed from GaN grown on basal plane sapphire while it was not detected from GaN on basal plane 6H-SiC, which possesses smaller lattice and thermal mismatch. It was also found that YL is more intense at the epilayer/substrate interface. The YL can be eliminated in two ways: (i) grow GaN under Ga-rich conditions; (ii) dope GaN with Ge or Mg. Since Ga-rich ambient favors the reduction of gallium vacancies and both Ge and Mg substitute Ga-sites, it is strongly suggested that YL be related to Ga-vacancies and its complexes, which may be introduced by the big lattice mismatch.

ACKNOWLEDGMENTS

The authors would like to acknowledge Max Yoder and Yoon-Soo Park at the Office of Naval Research, John Fan at Kopin Corporation, Gail Brown and Bill Mitchel at the US Air Force Wright Laboratory, and Dean Jerry Cohen for their permanent support and encouragement. This work is funded by the Office of Naval Research through Grant No. N00014-93-1-0235. The technical support from AIXTRON Inc. is also acknowledged.

REFERENCES

- [1] S. Nakamura, M. Senoh, N. Isawa and S. Nagahama, *Jpn. J. Appl. Phys.* **34**, L797 (1995).
- [2] M. P. Ulmer, M. Razeghi and E. Bigan, *SPIE Proceedings*, Vol. **2397**, San Jose, CA, 1995, p.210
- [3] H. Amano, N. Sawaki, I. Akasaki and Y. Toyoda, *Appl. Phys. Lett.* **48**, 353 (1986).
- [4] S. Nakamura, *Jpn. J. Appl. Phys.* **30**, L1705 (1991).
- [5] S. D. Lester, F. A. Ponce, M. G. Crawford and D. A. Steigerwald, *Appl. Phys. Lett.* **66**, 1249(1995).
- [6] T. Ogino and M. Aoki, *Jpn. J. Appl. Phys.* **19**, 2395 (1980)
- [7] J. I. Pankove and J. A. Hutchby, *J. Appl. Phys.* **47**, 5387 (1976)
- [8] R. Singh, R. J. Molnar, M. S. Ünlü and T. D. Moustakas, *Appl. Phys. Lett.* **64**, 336 (1994)
- [9] E. R. Glaser, T. A. Kennedy, K. Doverspike, L. B. Rowland, D. K. Gaskill, J. A. Freitas, Jr., M. A. Khan, D. T. Olson and J. N. Kuznia, *Phys. Rev.* **B51**, 13326 (1995).
- [10] T. Suski, P. Perlin, H. Teisseyre, M. Leszczynski, I. Grzegory, J. Jun, M. Bockowski, S. Porowski and T. D. Moustakas, *Appl. Phys. Lett.* **67**, 2188 (1995)
- [11] D. W. Jenkins, J. D. Dow and M.-H. Tsai, *J. Appl. Phys.* **72**, 4130 (1992).
- [12] P. Boguslawski, E. Briggs, T. A. White, M. G. Wensell and J. Bernholc, in Diamond, SiC and Nitride Wide-bandgap Semiconductors, edited by C. H. Carters, Jr., G. Gildenblat, S. Nakamura and R. J. Nemanich, *MRS Symposia Proceedings*, No. **339** (Material Research Society, Pittsburgh, 1994), p. 693.
- [13] J. Neugebauer and C. G. Van de Walle, *Phys. Rev.* **B50**, 8067 (1994)
- [14] X. Zhang, P. Kung, A. Saxler and M. Razeghi, Invited talk in *Physics of Semiconducting Compounds*, Jaszowiec, Poland, May 29 - June 2, 1995.
- [15] X. Zhang, P. Kung, A. Saxler, D. Walker, T. C. Wang and M. Razeghi, *Appl. Phys. Lett.* **67**, 1745 (1995).
- [16] X. Zhang, P. Kung, D. Walker, J. Piotrowski, A. Rogalski, A. Saxler and M. Razeghi, *Appl. Phys. Lett.* **67**, 2028 (1995)
- [17] C. Wetzel, D. Wolm, B. K. Meyer, K. Pressel, S. Nilsson, E. N. Mokhov and P. G. Baranov, *Appl. Phys. Lett.* **65**, 1033 (1994).
- [18] S. Nakamura, T. Mukai, M. Senoh and I. Iwasa, *Jpn. J. Appl. Phys.* **31**, L139 (1992)

Part VIII
Point Defects

LIGHT GENERATING CARRIER RECOMBINATION AND IMPURITIES IN WURTZITE GaN/Al₂O₃ GROWN BY MOCVD

U. KAUFMANN, M. KUNZER AND C. MERZ, I. AKASAKI* AND H. AMANO*

Fraunhofer-Institute for Applied Solid State Physics, Tullastrasse 72, D-79108 Freiburg, Germany

*Department of Electrical Engineering, Meijo University, Nagoya 468, Japan

ABSTRACT

We have studied by photoluminescence (PL) and optically detected magnetic resonance (ODMR) undoped, n-doped and p-doped thin wurtzite GaN layers grown by metal-organic chemical vapor deposition on sapphire substrates. From the PL data for free excitons an accurate value of the free A-type exciton binding energy and a more accurate estimate for the hole effective mass is deduced. The localization energies of the Mg and the Zn neutral acceptor bound excitons are found to be in good agreement with Haynes' rule. A sharp emission line, assigned to free electron recombination at a 116 meV shallow acceptor, together with three additional weak zero-phonon-lines (ZPLs), assigned to distant donor-acceptor (DA) pairs, are reported for the first time. The chemical nature of this acceptor and that of three residual donors, inferred from the DA pair ZPLs, is discussed. The effects of strain in thin GaN layers on a dissimilar substrate like sapphire are emphasized with respect to the energetic position of narrow PL lines. The ODMR data obtained for undoped, Mg-doped and Zn-doped GaN layers provide insight into the recombination mechanisms responsible for the broad yellow (2.25 eV), the violet (3.15 eV) and the blue (2.8 eV) PL bands, respectively. The ODMR results for Mg and Zn also show that these acceptors do *not* behave effective mass like and indicate that the acceptor hole is mainly localized in the nearest neighbor shell surrounding the acceptor core.

INTRODUCTION

Samples of gallium nitride, GaN, were synthesized already in 1959 and the highest energy optical emission from this material was found to be peaked near 3.44 eV at 90 K [1]. Twelve years later when crystals grown by hydride vapor phase epitaxy [2] were available it was established that wurtzite GaN is a direct band gap semiconductor with $E_g = 3.50$ eV at low temperatures in thick (≥ 100 μm) quasi-bulk layers [3]. Thus, the potential of GaN for short wavelength optoelectronic emitters was obvious at an early time but the failure to achieve p-type conductivity during the early seventies delayed this development for decades. During the late eighties GaN layers with high crystalline quality and good surface morphology were prepared by metal-organic vapor phase epitaxy [4]. The real breakthrough was achieved in 1989 with the discovery that p-type conductivity can be enforced in Mg doped GaN [5]. Since then the progress in the technology of GaN based p-n junction light emitting diodes (LEDs) was breath taking. Blue [6,7,8], green [9], and even yellow [10] high-brightness LEDs based on GaN and its alloys with In and Al have been realized and are or will soon be available commercially.

In view of the above technological successes it is surprising that the light generating carrier recombination processes in GaN as well as the residual impurities involved in most cases are still poorly understood. An important point that renders comparisons of optical spectra, in particular luminescence data, from different GaN samples more difficult is the following. Normally in a given semiconductor a particular recombination process gives rise to a recombination line at a fixed photon energy which is sample independent as long as effects due to confinement or pseudomorphic strains do not play a role. This is no longer the case for GaN layers grown on a dissimilar substrate like sapphire. Here the large mismatch in thermal expansion coefficients of the substrate and the layer can induce large strains in the layer which depend on

layer thickness in the range 1 to 100 μm [11]. The associated hydrostatic strain component modifies the band gap energy E_g , as compared to stress relaxed thick quasi-bulk ($> 100 \mu\text{m}$) layers, and consequently the energetic position of all luminescence recombination lines tied to the band gap. An increase in E_g of 25 meV in 1 μm thick layers can occur. As a result, the energetic positions of e.g. exciton lines reported in the literature scatter significantly. Therefore, it is often impossible to judge from the position of an exciton line alone whether a free or a bound exciton is involved. Similar problems exist for other, relatively narrow recombination lines, and reliable assignments of such lines are possible only by studying their temperature dependence.

In this article we present photoluminescence (PL) examples for some of the fundamental recombination processes expected in a high band gap semiconductor like GaN, namely free and bound exciton-, free to bound (FB)-, and distant donor-acceptor (DA) pair recombination. We emphasize the role of strain on the energetic positions of the recombination lines. In addition recent results for donors and acceptors obtained by magnetic resonance are presented and their implications on the nature of several recombination bands of practical interest are discussed.

EXPERIMENTAL DETAILS

Six different wurtzite GaN films were studied all of which were grown by metal-organic chemical vapor deposition (MOCVD) on a-plane (11 $\bar{2}$,0) sapphire substrate above a 50 nm AlN buffer-layer [4,7]. Sample A4 is undoped with a thickness of about 10 μm . Layer A1 is also undoped but has a thickness of 1 μm only. Layer A5 is Mg doped in the low 10^{19} cm^{-3} range. It is p-conducting and has a thickness of about 3 μm . The p-type Mg doped film A3 has the same thickness but the Mg concentration is near 10^{20} cm^{-3} . Layers A7 and A8 are doped with Si ($n \approx 10^{18} \text{ cm}^{-3}$) and Zn (concentration about 10^{18} cm^{-3}), respectively. The doped layers of the latter two samples have a thickness of 1 μm and were grown on top of a 1 μm thick undoped GaN layer. Thus the total GaN thicknesses of samples A1, A3, A5, A7 and A8 are comparable (1-3 μm).

Photoluminescence was excited with the 325 nm line of a He-Cd laser or with the 337 and 350 nm lines of a Kr⁺ laser. Power densities usually were less than 50 mW/mm². The luminescent light was collected normal to the excitation beam, dispersed by a 0.85 m double monochromator and detected by a cooled GaAs photomultiplier. Polarization effects have not been studied. The absolute accuracy of the wavelength calibration was 0.08 nm which converts into an energy accuracy of 0.8 meV near the band edge of GaN. The samples were mounted in a variable temperature (1.8 - 300 K) cryostat and either immersed in liquid helium or kept in cold flowing helium gas.

Optically detected magnetic resonance (ODMR) spectra were taken with a K-band setup (about 21 GHz) built around a 4 T superconducting magnet. Luminescence was excited with the 351 nm line of an

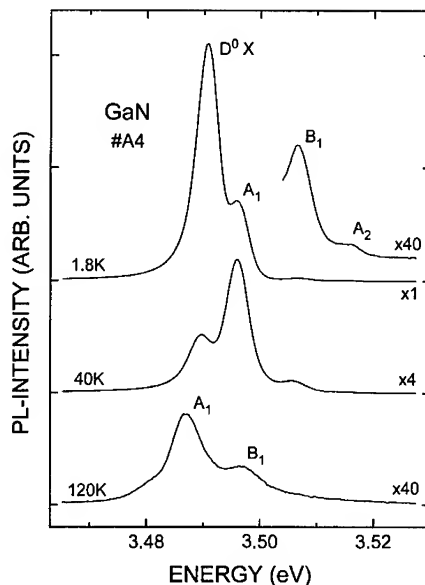


Fig. 1 Free and bound exciton PL lines and their evolution with temperature as observed from the 10 μm thick nominally undoped, n-type GaN MOCVD layer A4.

Ar⁺ laser. The emitted light was detected with a cooled Si diode. The ODMR signals were measured as microwave induced changes in luminescence intensity using synchronous detection with microwave chopping frequencies in the range 30 to 1000 Hz.

FREE AND BOUND EXCITONS

The best near band gap excitonic PL spectra were obtained from the 10 μm thick undoped layer A4. As can be seen from Fig. 1, the line labelled D⁰X dominates the spectrum at 1.8 K. Three additional lines labelled A₁, B₁ and A₂ appear at higher energies. In accordance with the interpretation of early PL and reflection measurements [3] on quasi-bulk samples and recent PL data from thin layers [12], the lines D⁰X, A₁, and B₁ have been assigned to the neutral donor bound exciton, the n=1 state of the free A exciton series, and the n=1 state of the free B exciton series, respectively. Several arguments are in conflict with the assumption that line A₂ is related to the C exciton of wurtzite GaN. We have therefore attributed this line to the n=2 state of the A exciton series [13]. The same conclusion has been independently reached by another group [14]. Upon warming up from 1.8 K, the D⁰X line in Fig. 1, as expected, continuously shifts to lower energies reflecting the shrinkage of the band gap with increasing temperature. On the other hand, the positions of the free exciton lines are independent of temperature up to about 30 K. Free excitons gain kinetic energy with increasing temperature and therefore can show exciton polariton dispersion effects. We have suggested that such effects for the free exciton lines just compensate the decrease in band gap up to 30 K.

The temperature dependence of the line intensities in Fig. 1 suggests the following picture. At elevated temperatures, see the 40 K trace, the neutral donor bound excitons are thermally released from the donors and "feed" the free A₁ exciton line. At even higher temperature, see the 120 K trace, where D⁰X is just still visible as the shoulder at 3.48 eV, A excitons partially dissociate. The free holes thus generated are thermally excited into the B valence band where they can form B excitons. This mechanism provides a natural explanation for the increase of the B₁ intensity relative to A₁ with increasing temperature. From the data in Fig. 1 accurate values of the A exciton localization energy $E_{\text{loc}}(\text{D}^0\text{X})$ at neutral shallow donors and the free A exciton binding energy E_x^b have been determined. They are given by $E_{\text{loc}}(\text{D}^0\text{X}) = (5.9 \pm 0.5)$ meV at 2 K and $E_x^b = (26.1 \pm 0.7)$ meV. With the latter value and the energetic position of the A₁ line one finds that the band gap energy of the 10 μm thick layer A4 is given by $E_g = (3.522 \pm 0.002)$ eV. Thus E_g is 22 meV larger than in thick quasi-bulk GaN layers [3]. As mentioned in the introduction it has been argued [13] that this increase in E_g results from the hydrostatic stress component which thin GaN layers experience when grown on sapphire with an AlN nucleation layer.

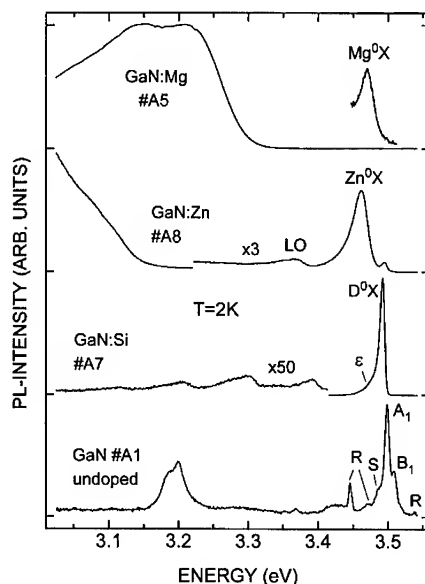


Fig. 2 Near band gap PL spectra at 2K of four MOCVD GaN layers with thicknesses in the range 1 to 3 μm .

In the previous literature the effective hole mass of the uppermost Γ_9 (C_{6v}) valence band in wurtzite GaN scatters between 0.4 and 1 in units of the free electron mass m_0 . With the above precision value of E_x^b , the spectroscopically determined effective mass (EM) shallow donor binding energy $E_D = 35.5$ meV [15] and the effective electron mass $m_e = 0.20 m_0$ [16] from cyclotron resonance studies, a more accurate hole mass can be deduced. The band hole mass inferred in this way is $m_h \approx 0.54 m_0$ [13].

Since the band gap of GaN can vary with layer thickness, a systematic study of free and bound excitons by PL requires a set of undoped and doped samples all of which have similar layer thicknesses and which are grown on the same type of substrate with the same type of buffer layer. This is the case for the 1 to 3 μm thick layers A1, A5, A7 and A8 used in the present work. Their near band gap PL spectra are shown in Fig. 2. The undoped sample A1 again reveals the free exciton lines A_1 and B_1 , and with better resolution also line A_2 but no D^0X line. The lines labelled R are phonon Raman replicas of the laser excitation line and arise either from the GaN layer or the sapphire substrate. The low energy shoulder S of line A_1 is separated by ≈ 11 meV from the A_1 peak. Its origin is uncertain, see the following section, as well as that of the structure near 3.2 eV.

The dominant recombination line in the Si doped layer A7 is the D^0X line. A weak shoulder ϵ occurs 20 meV lower in energy (≈ 53 meV below E_g) which will be discussed in the next section. The D^0X and the A_1 line in samples A7 and A1 respectively, occur about 2.5 meV higher in energy than the corresponding lines of sample A4 in Fig. 1. This shows that the band gap of the samples in Fig. 2 is 2.5 meV higher than that of sample A4, i.e. $E_g = (3.525 \pm 0.002)$ eV at 2K.

The lines labelled Mg^0X and Zn^0X in the acceptor doped samples A5 and A8 have been assigned to excitons bound to the neutral Mg acceptor and to the neutral Zn acceptor, respectively [13]. The localization energies of these A^0X acceptor bound excitons are given by the separation of the bound exciton lines

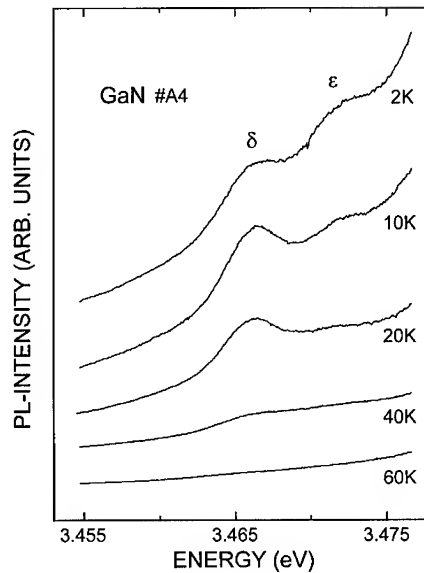


Fig. 3 Temperature dependence of the two weak PL lines δ and ϵ superimposed on the low energy tail of the D^0X line in Fig. 1.

Tab.1 Energetic positions (eV) at 2 K of free and bound exciton lines in thick quasi-bulk and thin GaN layers on a a-plane sapphire with AlN buffer. The line positions marked with an asterisk have been obtained from reflection measurements.

Ref.	t(μm)	A^0X	D^0X	A_1	B_1	C_1	A_2	E_g^A
3	≥ 100	3.455	3.467	3.474*	3.480*	3.501*		3.500 ± 0.010
this work	1-3	Zn 3.465 Mg 3.480	3.493	3.499	3.509		3.518	3.525 ± 0.002
difference		0.025	0.026	0.025	0.029			0.025

from the free exciton A_1 line. We find $E_{loc}(Mg^0X) = (19 \pm 4)$ meV and $E_{loc}(Zn^0X) = (34 \pm 4)$ meV. These values correlate surprisingly well with the acceptor ionization energies of Mg ($E_A \approx 200$ meV) and Zn ($E_A \approx 340$ meV), i.e. with Haynes' rule, the proportionality factor being very close to 0.1.

The localization energy of the neutral donor bound exciton, as mentioned before, is $E_{loc}(D^0X) = 5.9$ meV. In the following section we provide evidence for two shallow donors with binding energies around 55 meV. If they gave the dominant contribution to the D^0X line one would infer that $E_{loc}(D^0X)$ is close to 10 percent of the donor binding energy, as for the acceptor case discussed before.

The free and bound exciton line positions from Fig. 2 are collected in Tab. 1, and compared to the data from thick quasi-bulk samples. It is evident that, whenever a comparison is possible, the lines of the 1 to 3 μm thick layers occur about 25 meV higher in energy as a result of the hydrostatic stress component in these thin layers grown on a-plane sapphire with an AlN buffer. The mismatch in the substrate-layer thermal expansion coefficients also induces a dilative axial stress along the growth direction which is parallel to the wurtzite GaN c-axis in the present case [17]. This axial stress modifies the intrinsic axial field of bulk wurtzite GaN. This has consequences for the valence band splitting and therefore the splittings between the free exciton lines in thin layers are not necessarily the same as those in quasi-bulk samples. A comparison of the $A_1 - B_1$ separations in Tab. 1 provides an indication for this effect.

FREE TO BOUND AND DISTANT DONOR-ACCEPTOR PAIR RECOMBINATION

In sample A4, see Fig. 3, two weak lines labelled δ and ϵ appear on the low energy slope of the D^0X line. At 2 K they are separated from E_g by ≈ 56 meV and ≈ 52 meV, respectively. At present their origin is uncertain. However, as will be shown later, there is independent evidence for two residual donors in sample A4 with binding energies near $E_D^a \approx 57$ meV and $E_D^b \approx 54$ meV, both being deeper than the $E_D^c = 35.5$ meV shallow EM donor [15,16]. Lines δ and ϵ occur close to the energetic positions expected for the recombination of free holes with these two deeper donors when neutral (D^0h recombination). Fig. 3 shows that line δ increases in intensity upon warming up from 2 K to about 20 K but loses intensity above that temperature. This dependence would be consistent with a D^0h recombination process provided that free holes can be thermally generated at temperatures as low as 10 K. A conceivable hole source are excitons bound to the ionized 35.5 meV EM donor, D^+X . They are expected to exist in GaN ($m_e/m_h = 0.37$) [13] but close to the stability limit ($m_e/m_h \approx 0.43$) above which D^+X dissociates into D^0X and a free hole [18]. In this m_e/m_h range D^+X can equally well be viewed as D^0 weakly binding (~ 1 meV) a hole. Obviously, this hole is bound only at the lowest temperatures (< 5 K) and becomes ionized at elevated temperatures thus "feeding" D^0h recombination processes. If present in sample A4, the D^+X recombination line is expected near 3.485 eV where it is likely masked by the low energy slope of the D^0X line, see Fig. 1.

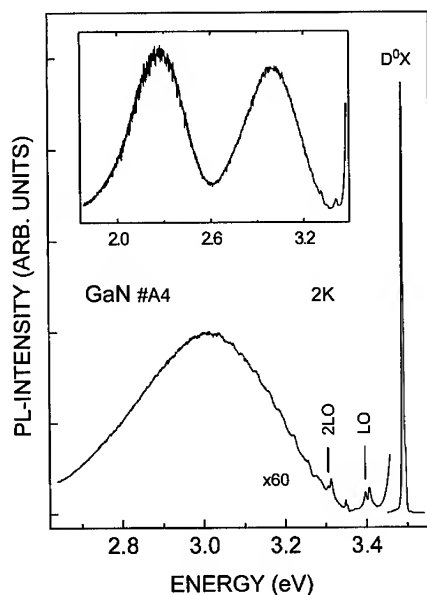


Fig. 4 Overall near band gap PL spectrum of layer A4 at 2K. The inset in addition to the broad 3.0eV vibronic band reveals the deep 2.25eV yellow emission band.

Let us now consider a clearcut example for free to bound recombination. Fig. 4 shows the PL spectrum of sample A4 on a wider energy scale. The by far dominating D^0X signal is followed by LO (E_i) and 2LO (E_i) phonon replicas 93 and 184 meV lower in energy. In addition there is a new broad recombination band peaked near 3.0 eV showing partially resolved structure on its high energy wing. As the inset of Fig. 4 shows another broad PL band peaks near 2.25 eV which corresponds to the notorious yellow luminescence band of GaN.

The key to the understanding of the broad 3.0 eV band are several weak but sharp zero-phonon-lines (ZPLs) between 3.34 and 3.41 eV in Fig. 4. These are shown in more detail in Fig. 5 together with their temperature dependence in the range 2 K to 90 K and are labelled α , β , γ and FB. We note first, that *all* partially resolved structures on the high energy wing of the 3.0 eV band can be explained as LO replicas of these four lines, the first series of replicas being correspondingly labelled in Fig. 5. The FB line occurs 116 meV below E_g and with increasing temperature displays the classical shape expected for free carrier recombination with a neutral acceptor or donor [19]. Note also, that the overall, *absolute* intensity of this line *increases* with rising temperature. Originally, the FB line was thought to be related to the recombination of free holes with a 116 meV deep donor [13]. However, there are strong arguments against such a model and in favor of the opposite case, namely the recombination of free electrons with a 116 meV deep acceptor. First, in the temperature range 10 to 60 K, shallow donors rather than shallow acceptors become ionized in GaN and thermally generated electrons rather than holes contribute to the increase in FB intensity when the temperature is raised. Secondly, the FB to FB-LO intensity ratio indicates a strong vibronic (electron - phonon) coupling which also clearly favors an A^0e recombination model. We therefore associate line FB with free electron recombination at a residual 116 meV shallow acceptor. This is the shallowest acceptor reported for GaN to date.

In contrast to line FB, the weak lines α , β and γ fade out with increasing temperature similar as the broad 3.0 eV band. They are therefore interpreted as the ZPLs which, together with line FB, give rise to the broad vibronic 3.0 eV band. The next point to note is the separation of line γ from line FB which amounts to ≈ 34 meV. This value matches the shallow EM donor ionization energy, 35.5 meV [15, 16], within experimental error. Thus, the data in Fig. 4 and 5 suggest the following model. Line γ is the ZPL of *distant* (≥ 200 Å) DA pairs with nearly negligible Coulomb interaction, involving the 116 meV acceptor and the 35.5 meV EM donor. Obviously, the donors in these pairs will "feed" the FB recombination line when the temperature is raised. Lines α and β are separated from line FB by ≈ 57 meV and ≈ 54 meV, respectively. They behave very similar to line γ except that they disappear somewhat less rapidly when the temperature is raised. In accordance with the tentative interpretation of lines δ and ϵ in Fig. 3 we therefore postulate two deeper residual donors with ionization energies $E_D^\alpha \approx 57$ meV and $E_D^\beta \approx 54$ meV and attribute lines α and β to the ZPLs of distant DA pairs involving these donors and the

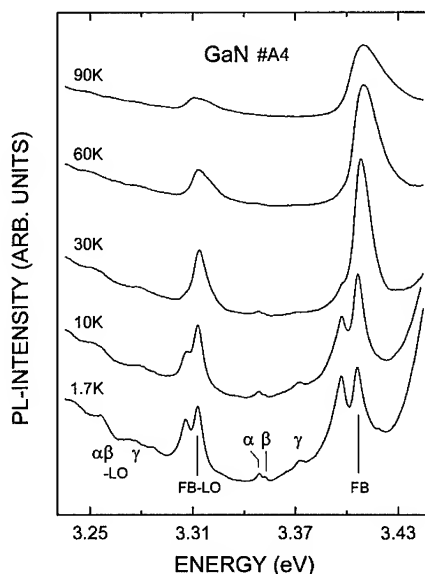


Fig. 5 Temperature dependence of the weak but sharp PL structures near the high energy threshold of the broad 3.0 eV band in Fig. 4. The lines without a label are the LO and 2LO replicas of the D^0X line.

116 meV acceptor. Taken together, the broad 3.0 eV band in Fig. 4 is interpreted as the vibronic sideband of the distant DA pair ZPLs α , β and γ with additional higher order LO replicas of the FB line superimposed on its high energy wing. The vibronic coupling evidently is strong, the Franck-Condon shift and the width of the broad band being comparable, about 370 meV.

Nothing definite is presently known about the chemical nature of the 116 meV acceptor and the donors involved in the 3.0 eV pair band. A very likely acceptor candidate in the present MOCVD layers is carbon, C_N . It has been reported recently that carbon can be incorporated in MOCVD GaN in high concentrations [20] and it is known that carbon doping of molecular beam epitaxy grown GaN produces p-type material [21]. However, Si_N or even an intrinsic defect like the Ga vacancy [22-25] cannot be excluded at present. Once the nature of the 116 meV acceptor is known it must be tested whether it is a *practical* p-type dopant since the Mg acceptor, conventionally used for this purpose, is considerably deeper ($E_A \approx 200$ meV). One of the donors involved in the 3.0 eV pair band is likely silicon, Si_{Ga} . Other candidates are germanium, Ge_{Ga} , group VI impurities on the nitrogen site, and the nitrogen vacancy, V_N [22-26].

So far an exciton bound to the 116 meV acceptor has not been identified. Applying Haynes' rule with the proportionality factor from the previous section one expects this exciton line ≈ 12 meV below the free exciton A_1 line. If present in sample A4, Fig. 1, it would be masked by the low energy slope of D^0X . However, the shoulder S in sample A1, Fig. 2, occurs at the position expected. Further studies are required to ascertain the possible acceptor bound exciton character of shoulder S.

The deeper acceptors Mg and Zn are known to give rise also to broad PL bands in the violet and blue spectral range in deliberately doped GaN. Portions of these bands are seen in the two upper traces of Fig. 2. In the following section we will present and discuss evidence from optically detected magnetic resonance that, at low temperatures, also these bands result from DA pair recombination, but now involving pairs with closer separations of their members. So far neither ZPLs of these broad bands nor free to bound recombination lines of these acceptors have been reported so that precision values for the acceptor ionization energies of Mg and Zn are not yet available. Nevertheless, the hypothetical ZPLs of the broad Mg and the broad Zn band occur roughly at 3.30 and 3.15 eV, respectively, compare Fig. 2. These values are in agreement with the binding energies usually quoted for Mg ($E_A = 200 \pm 30$ meV) and Zn ($E_A = 340 \pm 30$ meV). Therefore, there is no need to invoke a different, deeper Mg acceptor level (0.5 eV) as proposed by another group [27] to account for the peak position of the broad Mg band. Its shift to lower energies with increasing Mg concentration presumably results from the broadening of the 200 meV Mg acceptor level for very high Mg doping levels ($>10^{19} \text{ cm}^{-3}$). It appears likely that the DA pair band with a ZPL near 3.26 eV [28], frequently observed in nominally undoped and lightly Mg doped layers, is also related to the Mg acceptor but now involves DA pairs with a larger separation of their members.

There is early evidence [29] that the 2.25 eV yellow luminescence band, practically always observed from GaN, compare the inset of Fig. 4, is carbon related. Recent studies of MOCVD GaN layers support this view [20]. It has been suggested that this band also has DA pair character involving a shallow donor and a deep carbon related acceptor [29]. However, in view of the likely nature of the 116 meV acceptor and the ODMR data to be discussed in the next section the alternative model involving DA recombination between a deep donor (≈ 0.7 eV) and the shallow carbon acceptor must be considered seriously.

Apart from the PL recombination bands discussed, the samples studied in this work reveal sharply structured PL bands in the near infrared spectral range due to residual 3d-transition metal impurities like iron [30]. They result from carrier capture at these deep impurities and subsequent internal 3d-3d deexcitation.

MAGNETIC RESONANCE OF DONORS AND ACCEPTORS

Optically detected magnetic resonance (ODMR) is particularly suited to study defects and impurities in thin GaN layers and to elucidate the recombination mechanisms giving rise to specific luminescence bands.

At 2 K the undoped sample A4 reveals two weak, nearly isotropic ODMR signals which have been labelled D and X [31, 32]. Their g-factors are $g_{\parallel} \approx 1.950$, $g_{\perp} \approx 1.947$ ($\Delta H \approx 6$ mT) and $g = 1.995 \pm .005$ ($\Delta H \approx 15$ mT), respectively. They are observed on the yellow 2.25 eV band in the inset of Fig. 4. These observations parallel the findings of other authors for similar MOCVD layers who labelled these two resonances as EM and DD, respectively [27]. There is virtually no doubt [27, 31, 33] that the D signal corresponds to the resonance of shallow donors. The origin of signal X is less well established but is thought to correspond to a deep donor [27].

The spectral dependencies of the above donor resonance and the resonance X reflect the position and shape of the yellow band [27]. This indicates that its pumping-recombination cycle involves both defects. At present it is not clear whether the residual 116 meV acceptor in sample A4 also participates in this recombination process. If this were the case, this would be consistent with the deep donor to shallow acceptor pair recombination model recently suggested for the yellow band [27]. In this connection it appears important to clarify the donor properties of residual oxygen in GaN, having GaP:O in mind.

All Mg doped layers investigated by us [31, 32] and other authors [27] exclusively reveal an ODMR signal ($\Delta H \approx 20$ mT) with a characteristic axial g-factor anisotropy, see the line labelled Mg in Fig. 6. The largest anisotropy is observed in the least heavily doped sample A5 for which $g_{\parallel} = 2.084$ and $g_{\perp} = 1.990$. Since this resonance is Mg specific it has been tentatively assigned to the Mg acceptor [31]. The problem with this assignment is the explanation of the g-factors to which we return later. When ODMR is detected on the broad Mg related PL band, compare the uppermost trace in Fig. 2, one observes the shallow donor resonance D in addition to the Mg signal, see Fig. 6. The recently reported spectral dependencies for these two signals [27] provide strong support for the DA pair character of the broad Mg PL band at low temperatures. However, as already alluded to in the previous section, we suggest that the normal $E_A \approx 200$ meV Mg acceptor level is involved rather than a deeper (0.5 eV) perturbed Mg related acceptor.

An ODMR spectrum similar to that of the Mg doped layers is observed from the Zn doped layer A8, see Fig. 7, when detected on the broad blue Zn emission peaked near 2.8 eV. Apart from the shallow donor D a weakly anisotropic line with $g_{\parallel} \approx 1.997$, $g_{\perp} = 1.992$ and $\Delta H \approx 7$ mT appears. This line is Zn specific as comparative studies of a Zn doped vapor phase epitaxial layer have shown [32]. Closer inspection of the H||c spectrum in Fig. 7 reveals a low field shoulder of the Zn line which moves towards the main line when the magnetic field is rotated towards H \perp c. Whether or not the shoulder and the main line belong together is presently not clear, thus preventing a proper g-factor analysis. However, it is obvious that both g_{\parallel} and g_{\perp} are close to the free spin value (2.002) as for the Mg acceptor resonance. The fact that the Zn resonance

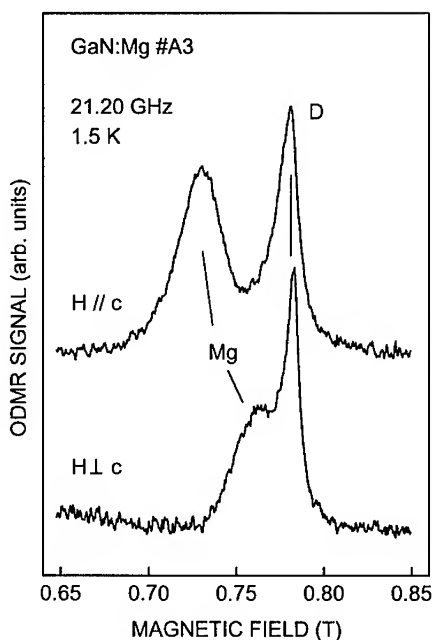


Fig. 6 ODMR spectra of a Mg-doped MOCVD GaN layer for two orientations of the magnetic field. The spectrum has been detected on the broad Mg PL band centered near 3.15 eV in Fig. 2.

together with the shallow donor resonance D are observed on the broad blue Zn emission band provides support for the DA character also of this band at low temperatures.

Both g_{\parallel} and g_{\perp} of the Mg and the Zn acceptor resonance are close to 2 and for Mg the g -factor anisotropy is definitely such that $g_{\parallel} > g_{\perp}$. It is known that quasi-bulk GaN shows the normal wurtzite valence band ordering, the uppermost band transforming as Γ_9 (C_{6v}) [3]. In this case the resonance of an EM acceptor consists of a single, highly anisotropic line with $2 \leq g_{\parallel} \leq 4$ and $g_{\perp} = 0$ [34]. It appears unlikely that the strain induced axial field in thin layers reverses the sign of the intrinsic wurtzite axial field splitting. Nevertheless, we have considered this hypothetical case where the topmost valence band would transform as Γ_7 (C_{6v}). Now, EM acceptor g -values g_{\parallel} and g_{\perp} near 2 are possible for axial field splittings large compared with the spin-orbit splitting. However, the g -factor anisotropy predicted ($g_{\parallel} < g_{\perp}$) is opposite to that observed for the Mg resonance. We therefore conclude that the Mg acceptor resonance in GaN does not show EM behavior.

The hole bound to the negatively charged core of a typical EM acceptor in a covalent semiconductor like GaAs ($E_A \approx 30$ meV) has a Bohr radius of 20 Å and is distributed over hundreds of lattice sites. When an acceptor level becomes deeper and deeper the hole radius shrinks and, in the extreme case, for a cation substitutional acceptor, the hole finally can be trapped at a single nearest-neighbor (nn) anion ligand. Now the hole binding energy amounts to about 1 eV. There are well documented examples for such a behavior in those II_B-VI compounds having strongly ionic character similar as GaN. Of particular relevance in the present context are the Li [35] and the Na [36] acceptor in ZnO. Their resonance properties are those of a hole in the p-shell of a nn oxygen ligand, and the spectrum consists of several lines since the hole can be trapped at either of the four nn ligands with $2 \approx g_{\parallel} < g_{\perp} \approx 2$. A less extreme case, where the hole binding energy is about 0.7 eV, is the chlorine A-center in ZnS, a Zn vacancy paired with a nn Cl donor [37]. At 2 K this acceptor traps the hole at a single nn S ligand of the vacancy. However, at temperatures above ≈ 70 K an averaged spectrum appears (9 GHz) showing that the hole now is equally shared among the three nn S ligands of the vacancy in the A-center. The essential point to note is that the g -factor anisotropy of the high temperature resonance spectrum ($2 \approx g_{\parallel} > g_{\perp} \approx 2$) is reversed compared to that of the 2 K spectrum ($2 \approx g_{\parallel} < g_{\perp} \approx g_x \approx g_y \approx 2$). A similar situation is encountered for the ≈ 300 meV deep boron acceptor in cubic SiC, B_{Si} , where below 40 K the hole is trapped at a single nn carbon ligand while at higher temperatures it is shared among the four C ligands [38]. Since the Mg acceptor in GaN is even shallower it is reasonable to associate the single Mg line in Fig. 6 at 2 K with a hole distributed mainly over the four nn N ligands surrounding the Mg^- core. The g -factor anisotropy then expected is that observed in the high temperature spectrum of the Cl A-center in ZnS which is consistent with that of Mg in GaN. Taken together, the resonance behavior of Mg is not that of an EM acceptor but indicates that the hole is mainly localized at the four nn N ligands.

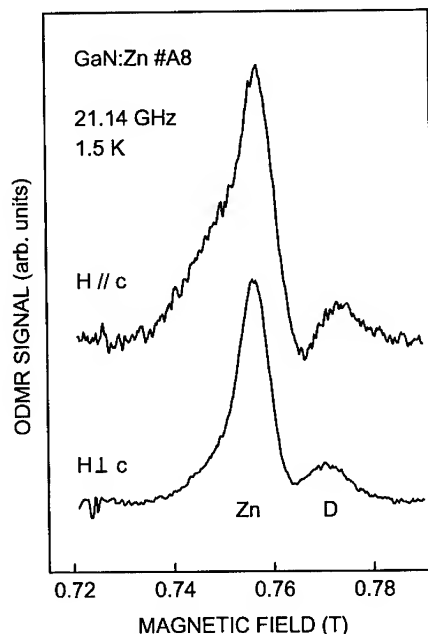


Fig. 7 ODMR spectrum of a Zn-doped MOCVD GaN layer detected on the broad 2.8 eV Zn PL band the high energy wing of which is seen in Fig. 2

This experimental finding also appears reasonable in the light of EM theory. When the Bohr radius r_B of the 116 meV acceptor from the previous section is calculated with the EM relation $r_B = \hbar (2m_h E_A)^{-1/2}$ using $m_h = 0.54$ [13] one obtains $r_B \approx 7.5 \text{ \AA}$. Therefore, an r_B value of the order of the GaN nn distance for the almost twice as deep Mg acceptor makes sense, but EM theory no longer applies.

SUMMARY

We have presented PL results for MOCVD GaN layers which provide examples for the fundamental carrier recombination processes in a high band gap semiconductor. A precision value for the free A exciton binding energy and a more accurate hole effective mass has been derived. The localization energies of the neutral acceptor bound excitons were found to be in line with Haynes' rule. A new 116 meV shallow acceptor has been identified, presumably C_N . The nature of the broad PL bands induced by the deeper acceptors Mg and Zn are discussed in the light of ODMR results. The ODMR data also indicate that Zn but also Mg do *not* behave EM like in GaN.

ACKNOWLEDGEMENTS

We thank E. R. Glaser, T. A. Kennedy (NRL, Washington, D.C.) and B. Meyer (TU Munich) for communicating results prior to publication. Thanks are also due to V. Fiorentini (Univ. Cagliari), J. Baur, J. Schneider and J. Wagner (IAF, Freiburg) for useful discussions. This work has been supported by the EU Commission under the BRITE EURAM Programme and the German Ministry BMBF, the HOSO Bunka Foundation and the Japanese Ministry of Education and Culture.

REFERENCES

1. H.G. Grimmeiss and H. Koelmans, *Z. Naturforschung* **14a**, 264 (1959)
2. H.P. Maruska and J.J. Tietjen, *Appl. Phys. Lett.* **15**, 327 (1969)
3. R. Dingle, D.D. Sell, S.E. Stokowski and M. Ilegems, *Phys. Rev. B* **4**, 1211 (1971)
4. H. Amano, N. Sawaki and I. Akasaki, *Appl. Phys. Lett.* **48**, 353 (1986)
5. H. Amano, M. Kito, K. Hiramatsu and I. Akasaki, *Japanese J. Appl. Phys.* **28**, L 2112 (1989)
6. I. Akasaki and H. Amano, *Inst. Phys. Conf. Ser.* **129**, 851 (1993)
7. I. Akasaki and H. Amano, *J. Electrochem. Soc.* **141**, 2266 (1994)
8. S. Nakamura, T. Mukai and M. Senoh, *Appl. Phys. Lett.* **64**, 1687 (1994)
9. S. Nakamura, T. Mukai and M. Senoh, *J. Appl. Phys.* **76**, 8189 (1994)
10. S. Nakamura, M. Senoh, N. Iwasa and S. Nagahama, *Japanese J. Appl. Phys.* **34**, L 797 (1995)
11. T. Detchprohm, K. Hiramatsu, K. Itoh and I. Akasaki, *Japanese J. Appl. Phys.* **31**, L 1454 (1992)
12. W. Shan, T. J. Schmidt, X. H. Yang, S. J. Hwang and J. J. Song, *Appl. Phys. Lett.* **66**, 985 (1995)
13. C. Merz, M. Kunzer and U. Kaufmann, submitted to *Phys. Rev. B*
14. L. Eeckey, L. Podlowski, A. Göldner, A. Hoffmann, I. Broser, B. K. Meyer, D. Volm, T. Streibl, T. Detchprohm, H. Amano, I. Akasaki, *Int. Conf. "Silicon Carbide and Related Materials"*, Kyoto (Japan), Sept. 18-21, 1995, in press
15. B. K. Meyer, D. Volm, A. Graber, H. C. Alt, T. Detchprohm, H. Amano and I. Akasaki, *Solid State Commun.* **95**, 597 (1995)
16. H. C. Alt, B. K. Meyer, D. Volm, A. Graber, M. Drechsler, D. M. Hofmann, T. Detchprohm, H. Amano and I. Akasaki, *Int. Conf. "Defects in Semiconductors"*, Sendai (Japan), July 23-28, 1995, in pre

17. Strictly speaking, the decomposition of the in plane biaxial stress also contains an orthorhombic component. However, the major effect on the positions of sharp PL lines is due to the hydrostatic and the tensile axial stress components.
18. T. Skettrup, M. Suffczynski and W. Gorzkowski, *Phys. Rev B* **4**, 512 (1971)
19. D. M. Eagles, *J. Phys. Chem. Solids* **16**, 76 (1960)
20. R. Niebuhr, K. Bachem, K. Dombrowski, M. Maier, W. Pletschen, and U. Kaufmann, *J. Electronic Mat.* **24**, 1531 (1995)
21. C. R. Abernathy, J. D. MacKenzie and S. J. Pearton, *Appl. Phys. Lett.* **66**, 1969 (1995)
22. J. Neugebauer and C. G. Van de Walle, *Phys. Rev. B* **50**, 8067 (1994)
23. J. Neugebauer and C. G. Van de Walle, 22nd Int. Conf. "The Physics of Semiconductors", Vancouver, Canada 15. - 19. 8. 1994, Ed. D. J. Lockwood (World Scientific Publishing, Singapore, 1995) Vol 3 pp 2327
24. P. Boguslawski, E. Briggs and J. Bernholc, see Ref. 22, pp 2331
25. P. Boguslawski, E. Briggs and J. Bernholc, *Phys. Rev. B* **51**, 17255 (1995)
26. P. Perlin, T. Suski, H. Teisseyre, M. Leszczynski, I. Grzegory, J. Jun, S. Porowski, P. Boguslawski, J. Bernholc, J. C. Chervin, A. Polian, and T. D. Moustakas, *Phys. Rev. Lett.* **75**, 296 (1995)
27. E. R. Glaser, T. A. Kennedy, K. Doverspike, L. B. Rowland, D. K. Gaskill, J. A. Freitas, Jr. M. Asif Khan, D. T. Olson, J. N. Kuznia and D. K. Wickenden, *Phys. Rev. B* **51**, 13326 (1995)
28. R. Dingle and M. Ilegems, *Solid State Commun.* **9**, 175 (1971)
29. T. Ogino and M. Aoki, *Japanese J. Appl. Phys.* **19**, 2395 (1980)
30. J. Baur, U. Kaufmann, H. Kunzer, J. Schneider, H. Amano, I. Akasaki, T. Detchprohm and K. Hiramoto, *Appl. Phys. Lett.* **67**, 1140 (1995)
31. M. Kunzer, U. Kaufmann, K. Maier, J. Schneider, N. Herres, I. Akasaki and H. Amano, *Mat. Sc. Forum* **143-147**, 87 (1994)
32. M. Kunzer, PhD Thesis, University of Freiburg, 1995
33. W. E. Carlos, J. A. Freitas, Jr., M. Asif Khan, D. T. Olson and J. N. Kuznia, *Phys. Rev. B* **48**, 17878 (1993)
34. Le Si Dang, K. M. Lee, G. D. Watkins and W. J. Choyke, *Phys. Rev. Lett.* **45**, 390 (1980)
35. O. F. Schirmer, *J. Phys. Chem. Solids* **29**, 1407 (1968)
36. D. Zwingel and F. Gärtner, *Solid State Commun.* **14**, 45 (1974)
37. J. Schneider, W. C. Holton and T. L. Estle, *Phys. Lett.* **5**, 312 (1963)
38. V. Bratus, N. Baran, V. Maksimenko, T. Petrenko, V. Romanenko, *Mat. Sc. Forum* **143-147**, 81 (1994)

THEORY OF POINT DEFECTS AND COMPLEXES IN GaN

Jörg Neugebauer and Chris G. Van de Walle

Xerox Palo Alto Research Center, 3333 Coyote Hill Road, Palo Alto, California 94304

ABSTRACT

We have studied the electronic and energetic properties of native defects, impurities and complexes in GaN applying state-of-the-art first-principles calculations. An analysis of the numerical results gives direct insight into defect concentrations and impurity solubility with respect to growth parameters (temperature, chemical potentials) and into the mechanisms limiting the doping levels in GaN. We show how compensation and passivation by native defects or impurities, solubility issues, and incorporation of dopants on other sites influence the acceptor doping levels. The role of hydrogen in enhancing the *p*-type doping is explained in detail. We also discuss the mechanisms responsible for the experimentally observed limitation of the free-carrier concentration in *p*-type GaN.

INTRODUCTION

During the past few years interest in GaN-based devices has grown rapidly, stimulated by the accomplishment of bright, highly-efficient green/blue light-emitting diodes [1]. However, despite the progress in devices, doping problems remain an important issue. Current doping levels are sufficient for producing light-emitting diodes, but the lack of high *p*-type doping levels may be a major obstacle in achieving III-V nitride laser diodes. Native defects are often invoked to explain the shortcomings in doping.

With the advent of increasingly fast computers and methodical improvements, first-principles calculations have evolved into a powerful tool to study various properties of defects and impurities in semiconductors. With the capability to calculate accurate total energies and electronic structure, it became possible to investigate the character and the position of defect levels, the atomic structure of the defect, as well as the energy to create the defect. More recently, formalisms have been developed to use the total energy of the defect to calculate defect concentrations, under the assumption of thermodynamic equilibrium [2, 3]. The same formalism can also be extended to the calculation of impurity solubilities [4, 5].

In the present paper we will give an overview about theoretical results for native defects and impurities in GaN. We will mainly focus on the problem of acceptor doping limits in GaN, particularly for Mg, which is presently the acceptor of choice to obtain *p*-type conductivity. However, hole concentrations are still lower than desired. We therefore discuss various mechanisms which may limit the hole concentration: compensation by native defects and impurities, solubility limits, and incorporation of the Mg acceptor on other sites. The role of hydrogen, in particular its ability to enhance the *p*-type doping, is discussed in detail.

FORMALISM

The equilibrium concentration c of an impurity or defect at temperature T is determined by its formation energy, E^f :

$$c = N_{\text{sites}} g \exp^{S/k_B} \exp^{-E^f/k_B T} \quad (1)$$

where N_{sites} is the number of sites the defect can be built in. g is a degeneracy factor representing the number of possible configurations in which a defect can be formed on the same site. k_B is the Boltzmann constant and S the vibrational entropy. The vibrational entropy is, at the present stage of our work, not explicitly included, which would be computationally very demanding. Entropy contributions cancel to some extent [6], and are small enough not to affect any qualitative conclusions. The effect of entropy can be included in an approximate way; experimental and theoretical results show that the entropy S is typically in the range between 0 (no entropy contributions) and $10 k_B$ (where k_B is the Boltzmann constant) [7].

The formation energy depends on various parameters. For example, the formation energy of a Mg acceptor is determined by the relative abundance of Mg, Ga, and N atoms. In a thermodynamic context these abundances are described by the chemical potentials μ_{Mg} , μ_{Ga} , and μ_{N} . If the Mg acceptor is charged, the formation energy depends further on the Fermi level (E_F), which acts as a reservoir for electrons. Forming a substitutional Mg acceptor requires the removal of one Ga atom and the addition of one Mg atom; the formation energy is therefore:

$$E^f(\text{GaN:Mg}_{\text{Ga}}^q) = E_{\text{tot}}(\text{GaN:Mg}_{\text{Ga}}^q) - \mu_{\text{Mg}} + \mu_{\text{Ga}} + qE_F \quad (2)$$

where $E_{\text{tot}}(\text{GaN:Mg}_{\text{Ga}}^q)$ is the total energy derived from a calculation for substitutional Mg, and q is the charge state of the Mg acceptor. Similar expressions apply to the hydrogen impurity, and to the various native defects. For calculating the total energies we have performed first-principles calculations based on density-functional theory (DFT) using a supercell approach with 32 atoms per cell, a plane-wave basis set with 60 Ry cutoff and soft Troullier-Martins pseudopotentials [8]. Details of the method and convergence checks can be found elsewhere [9, 10, 11].

NATIVE DEFECTS

We have calculated the position of the defect levels and the formation energies for all native defects in GaN: vacancies (V_{Ga} , V_{N}), antisites (Ga_{N} , N_{Ga}), and interstitials (Ga_i , N_i). All relevant charge states were taken into account. The positions of the defect levels corresponding to the neutral charge state are shown in Fig. 1. From these results we can immediately classify the defects into donors, acceptors and amphoteric defects: V_{N} and Ga_i are donors, V_{Ga} is an acceptor, and N_i and both antisites are amphoteric.

We find that antisites and interstitials have high formation energies, and are therefore very unlikely to occur in any significant concentration [11]. The vacancies, however, have lower formation energies. Under conditions of thermodynamic equilibrium, low formation energies are required for the defect to occur in high concentration. In particular, the nitrogen vacancy (a single donor) has a low formation energy under p -type and semiinsulating conditions, and the Ga vacancy (a triple acceptor) gets a low formation energy under n -type conditions. Thus, based on the assumption of thermodynamic equilibrium, the dominant

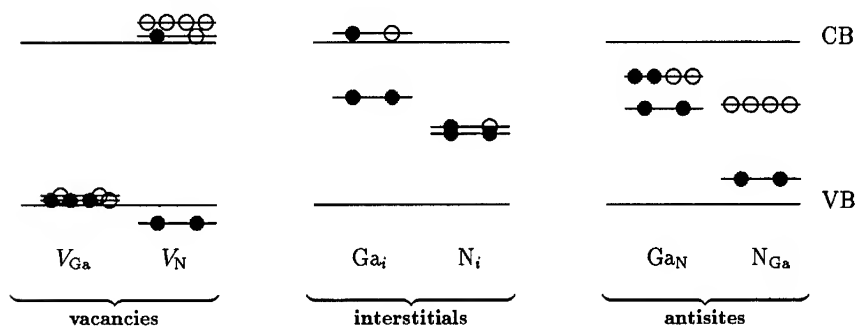


Figure 1: Schematic representation of the defect levels in GaN. The occupations are shown for the neutral charge state; filled circles indicate electrons, open circles indicate holes.

native defects are the vacancies: in *p*-type GaN the N vacancy, in *n*-type GaN the Ga vacancy.

Based on Eq. (1) the defect concentration as a function of temperature can be calculated. The results are shown in Fig. 2, where we have assumed Ga-rich conditions (which appear to be common in experimental growth conditions). For this calculation undoped GaN is assumed; no impurities are included. It is important to note that the defect concentrations are not independent from each other: they are coupled via the condition of charge neutrality. The total charge associated with electrons in the conduction band, holes in the valence band, and charges on the defects must be zero [7].

Figure 2 shows that for all growth temperatures the N vacancy is the defect with the highest concentration in undoped GaN. The concentration of Ga vacancies is orders of magnitude smaller, and the other native defects occur only in insignificant concentrations. Generally, the defect concentration increases with increasing temperature. However, even at growth temperatures as high as 1300 K [typical for metalorganic vapor deposition (MOCVD)] the N vacancy concentration is orders of magnitude too small to explain the high unintentional carrier concentrations of $10^{18} \dots 10^{20} \text{ cm}^{-3}$ found in "autodoped" GaN samples.

We have proposed two alternative explanations for the high unintentional carrier concentration. First, we stress that our conclusions about N vacancies applies to *isolated point defects*. A vacancy-related defect or extended defect may be involved, if it acts as a donor. Second, we propose unintentional incorporation of donor impurities. In particular, we find Si and O to have a high solubility in GaN; our calculations also show that C can be excluded as a possible donor [12]. Recent progress has enabled the growth of GaN with low unintentional carrier concentrations ($10^{16} \dots 10^{17} \text{ cm}^{-3}$), and even semiinsulating GaN has been reported.

ATOMIC AND MOLECULAR HYDROGEN IN GaN

Hydrogen is a common impurity in many semiconductors, and well known for its ability

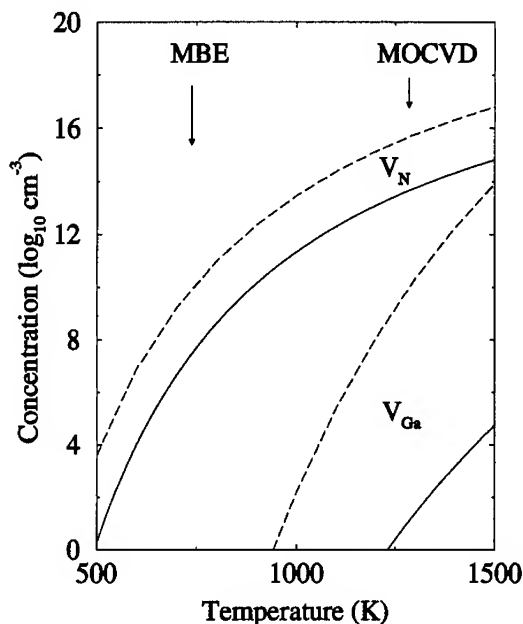


Figure 2: Equilibrium concentration of native defects in undoped GaN versus growth temperature. Ga-rich conditions are assumed. Lower (solid line; $S = 1k_B$) and upper limit (dashed line; $S = 10k_B$) are shown.

to terminate dangling bonds, passivate or compensate both shallow and deep defects, and to induce extended defects [13]. In modern high-temperature growth techniques such as MOCVD and HVPE (hydride vapor phase epitaxy), which are used to grow high-quality epitaxial GaN, hydrogen is highly abundant. There is also strong experimental evidence that hydrogen is involved in the passivation of acceptors in GaN [14].

We have recently investigated energetics and migration behavior of monatomic H and H molecules in GaN. The main results regarding the energetics of interstitial H in GaN are summarized in Fig. 3, which displays the formation energy for the different charge states of H (H^+ , H^0 , H^-) as a function of the Fermi level. For this plot, we assumed that the H chemical potential μ_H is fixed at the energy of a free H atom, as a reference. In p -type GaN, H^+ has the lowest formation energy, indicating that H acts as a donor. For n -type GaN, H^- has the lowest formation energy: H acts as an acceptor. From these results we can conclude that: (i) H is not a dopant but (ii) it may compensate both acceptors and donors.

From Fig. 3 we further derive that the solubility of p -type GaN is considerably higher under p -type conditions than under n -type conditions. We also found that the migration barrier for diffusion of H^+ is low, while the barrier of diffusion of H^- is high [15]. Our theoretical predictions were very recently confirmed by experimental observations of Götz and Johnson [16] on plasma hydrogenation of MOCVD-grown GaN: H is readily incorporated in p -type GaN, consistent with a high diffusivity and solubility, whereas no detectable levels

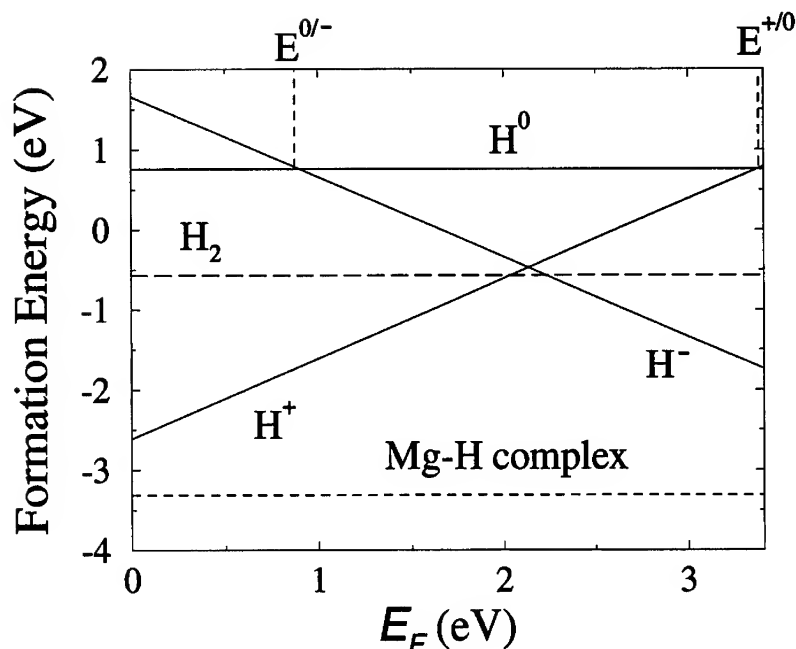


Figure 3: Formation energy as a function of the Fermi level for H^+ , H^0 and H^- (solid lines), for a hydrogen molecule (dashed line), and for a magnesium-hydrogen complex (long-dashed line). The formation energy is referenced to the energy of a free H atom.

of H were found in *n*-type GaN, consistent with a low diffusivity as well as lower solubility.

The fact that the neutral charge state is never stable is characteristic for a “negative- U ” system. The value of U is given by the difference between the $+/0$ and $0/-$ transition levels: $U = E^{0/-} - E^{+/0} \approx -2.4$ eV. A negative- U behavior appears to be common for H in semiconductors; it was also found for H in Si and GaAs. However, the value found here for GaN is unusually large, and, to the best of our knowledge, larger than any predicted or measured value for any defect in any semiconductor.

We have also studied hydrogen molecules in GaN. The formation energy and atomic geometry were calculated for several symmetric as well as asymmetric configurations. The formation energies for all the calculated structures are nearly degenerate; the value for the energetically most stable configuration is included in Fig. 3. We have also investigated the H_2^* geometry, proposed by Chang and Chadi [17], where one H is located at the bond-center site and the other at either the N or Ga antibonding site. Our calculations show that these configurations are energetically even less favorable than those where the H atoms may form a H-H bond. As shown in Fig. 3, H_2 is unstable with respect to dissociation into monatomic H. The formation energy of ≈ -0.6 eV is much higher than that of H_2 in vacuum (-2.4 eV). Both properties, the unfavorably high formation energy and the low stability of the H_2 molecule are distinctly different from the behavior of H in Si and GaAs.

DOPING LIMITS OF Mg-DOPED GaN

Magnesium is the most commonly used acceptor in GaN; it has an ionization energy of ≈ 0.16 eV [18] and can be incorporated in concentrations up to $\approx 10^{20}$ cm $^{-3}$. However, the relatively deep character of the Mg acceptor level implies that only a tiny fraction of the Mg acceptors will be ionized, explaining why the maximum achievable hole concentration is much smaller than the Mg concentration. Several procedures are conceivable to overcome this problem: (i) use of acceptors with a lower ionization energy and (ii) an increase of the acceptor concentration. In the past, several other acceptor impurities were studied, but Mg was found to be the most shallow acceptor [19]. However, even if an acceptor with a smaller binding energy exists, the question is whether it can be incorporated in sufficiently high concentrations.

We will therefore discuss in detail what the doping-limiting mechanisms are for Mg in GaN. The conclusions we draw can be applied also to other acceptors. The doping level can be limited by three mechanisms: (i) solubility issues, (ii) compensation or passivation by native defects and impurities, and (iii) incorporation of the dopant on sites where it no longer acts as an acceptor. In the following discussion we will show that these mechanisms cannot be treated independently, but the achievable hole concentration depends on a combination of these effects.

Solubility

The formation energy to create a Mg_{Ga} acceptor can be separated into two independent processes: (i) the removal of a Ga atom (creation of a Ga vacancy) and (ii) the chemisorption of a Mg atom on this site. For both processes the energy depends on the specific growth conditions which are characterized by the chemical potentials. The removed Ga atom has to be brought to a reservoir for Ga atoms where it has the energy μ_{Ga} . If this energy is high (Ga-rich environment) the formation energy will be high as well. The same argumentation can be applied to the incorporation of Mg; the formation energy depends thus on two external parameters (μ_{Ga} , μ_{Mg}). An upper limit for the Mg chemical potential is the formation of bulk Mg. Our calculations show that an even more stable configuration is Mg_3N_2 , having a large cohesive energy of 4.8 eV. The chemical potentials then have to obey the relation:

$$2\mu_{\text{Mg}} + 3\mu_{\text{Ga}} = \mu_{\text{Mg}_3\text{N}_2} \quad (3)$$

The formation of Mg_3N_2 is thus an *upper limit* for the solubility of Mg in GaN, giving at the same time a *lower limit* for the Mg_{Ga} formation energy.

The formation of Mg_3N_2 or Mg precipitates may be suppressed by working far away from thermodynamic equilibrium, i.e., at low temperatures. This may work for MBE (molecular beam epitaxy) growth (where low temperatures are characteristic), however, we expect that the temperatures in MOCVD and related growth methods ($T > 1000\text{K}$) are high enough to realize thermodynamic equilibrium.

Compensation by native defects

The incorporation of acceptors dramatically changes the position of the Fermi level causing strong changes in the formation energies of native defects and impurities. Defects that are very high in energy under semiinsulating or *n*-type conditions (and thus occur

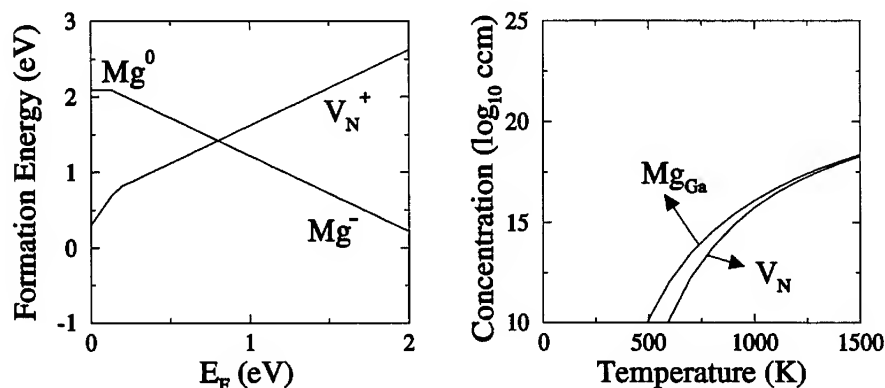


Figure 4: Formation energy vs. Fermi level for the Mg_{Ga} acceptor and the native defects. The corresponding equilibrium concentrations are given in (b). Ga-rich conditions are assumed.

only in small concentrations) may now become energetically favorable. In *p*-type GaN, as discussed in the Section about native defects, the N vacancy (a donor) is the defect with the lowest formation energy. Figure 4(a) shows the calculated formation energies for the native defects and the Mg_{Ga} acceptor under Ga-rich conditions. For the calculation of the Mg_{Ga} formation energy the limited solubility of Mg in GaN [Eq. 3] was taken into account, which gives a lower limit for the formation energy. The position of the kink in the Mg formation energy at ≈ 0.2 eV gives the position of the acceptor level, close to the experimental value (0.16 eV) [18].

Using the calculated formation energies, and taking into account that the Fermi energy is not a free parameter but fixed by the condition of charge neutrality, the equilibrium defect concentration [Eq. 1] for each defect can be calculated as function of temperature [3]. The results, displayed in Fig. 4(b), show that the Mg concentration, as expected, increases with the growth temperature. The only native defect which occurs in relevant concentrations is the N vacancy. At temperatures exceeding 1000 K the Mg acceptors become increasingly compensated by the N vacancies. Compensation by native defects is therefore *potentially* a major concern for high-temperature growth techniques. Growth at low temperatures as characteristic for MBE may suffer less from this problem since non-equilibrium conditions probably apply. This may explain why *p*-type GaN without post-growth treatment was successful in MBE [20, 21].

Role of hydrogen in achieving *p*-type doping in GaN

Until recently, efforts to dope GaN *p*-type led to highly-resistive material. It was not until 1989 that Amano *et al.* made a major breakthrough when they observed that initially compensated Mg-doped GaN can be activated by low-energy electron beam irradiation (LEEBI) [22]. Nakamura later showed that the Mg activation can be achieved equally well by thermal annealing at 700°C under N_2 ambient [14]. Nakamura further observed that the process was reversible, with *p*-type GaN reverting to semiinsulating when annealed in a NH_3

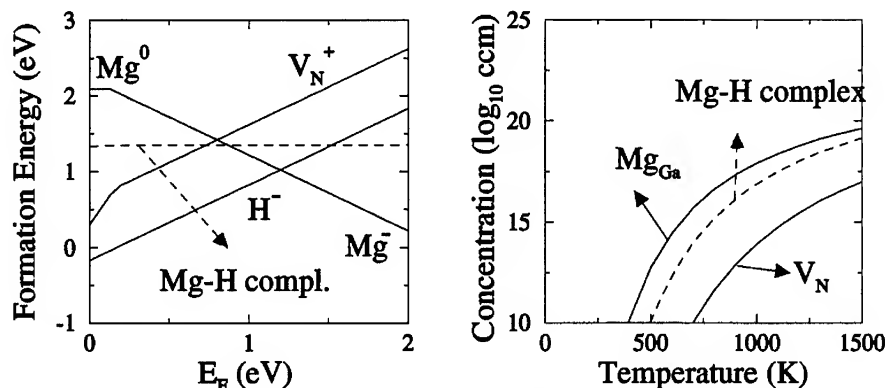


Figure 5: Formation energy vs. Fermi level for the Mg_{Ga} acceptor and the neutral Mg-H complex. Also included are the native defects and interstitial H. The corresponding equilibrium concentrations are given in (b) as a function of the growth temperature. H rich conditions are assumed.

ambient [14], revealing the crucial role played by hydrogen. Based on these observations, Van Vechten *et al.* [23] proposed a model describing acceptor passivation by H in which Mg-H defect complexes are converted to active Mg acceptor impurities by LEEBI. This model highlights the important role of H, but leaves various issues unanswered, such as why activation can be achieved also by thermal annealing, the lack of H incorporation in *n*-type GaN, and the success of *p*-type doping without post-growth treatments in MBE.

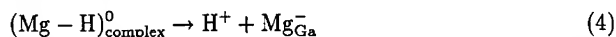
We will now combine our results about native defects, interstitial hydrogen and Mg acceptors to address these questions. Figure 5(a) displays the formation energies as a function of the Fermi level. In addition, the formation energy of the neutral Mg-H complex is included, which will be discussed later in detail. Figure 5(a) shows that for all Fermi energies H is energetically more favorable than the dominant native defect, the N vacancy. From the calculated formation energies the equilibrium concentrations for all defects can be calculated. The results, displayed in Fig. 5(b), reveal a remarkably different behavior compared to the H-free limit (Fig. 4): the Mg concentration is *increased* and the N vacancy concentration is *decreased*. Both effects are beneficial for doping. We further find that the Mg and H concentrations are virtually identical indicating that H completely compensates the Mg acceptors. At the growth temperature, the concentration of Mg-H complexes is orders of magnitude smaller than isolated (but compensated) Mg_{Ga} . Our finding of virtually complete compensation of the Mg acceptors is consistent with the experimental observations: the only cases where *p*-type GaN has been achieved without any post-growth treatment involved MBE growth where H is absent. MOCVD-grown Mg doped GaN (where H is highly abundant) is compensated and highly resistive.

Let us now describe the beneficial role of H on the Mg incorporation in GaN in a more qualitative way. In Fig. 5(a) the Fermi level can be roughly estimated to be near the crossing point between the acceptor and the dominant donor species. At this point their formation energies, and hence their concentrations, are equal, ensuring charge neutrality. This approximation works well if the Fermi level is far enough from the valence-band edge;

free carriers can then be neglected. If only native defects are present (H-free case), the N vacancy is the dominant defect, and the crossing occurs at about ≈ 0.8 eV. If H is present, the crossing point and thus the Fermi energy shifts to higher energies, resulting in a *decrease* of the acceptor (Mg) formation energy and an *increase* of the donor (N vacancy) energy. Consequently, a lowered defect concentration and an increased acceptor concentration is achieved.

In order to study the interaction between Mg and H in more detail we have calculated the complete total-energy surface for a H atom around a Mg_{Ga} acceptor [15]. We find that Mg and H form a neutral complex with an atomic structure very different from the well established acceptor-hydrogen complexes in other semiconductors (where a bond center (BC) configuration is preferred): The H prefers the (antibonding) AB site of one of the N neighbors around the Mg atom.

Our calculated binding energy for the neutral Mg-H complex with respect to its dissociation



is $E_b \approx 0.7$ eV [15], the positive binding energy indicating that the formation of Mg-H complexes is energetically favorable. If the formation of Mg-H complexes is energetically favorable, why then is the concentration of isolated Mg and H atoms larger than the concentration of complexes [see Fig. 5(b)]? The reason is the large difference in the configurational entropy between a point defect and a complex. As pointed out above, the condition of charge neutrality ensures that the formation energies of the acceptor (Mg) and the dominant donor (H) are almost equal; let us call this energy $E_{\text{defect}} = E_f^{\text{Mg}} = E_f^{\text{H}}$. The complex formation energy is then given by $E_{\text{compl}} = 2E_{\text{defect}} - E_b$. The prefactor in the equilibrium concentration [Eq. (1)] depends on the number of possible configurations, which is for a point defect the number of either Ga or N atoms (N_{sites}). For the Mg-H complex it is the number of Ga sites (the location of the Mg atom) times the degeneracy factor g indicating the number of possible orientations of the Mg-H complex, which is four; indeed, the H atom can bond to each of the four N atoms surrounding the Mg atom. The concentrations for the defect and the complex are then given by:

$$c_{\text{defect}} = N_{\text{sites}} \exp(-E_{\text{defect}}/k_B T) \quad (5)$$

$$c_{\text{complex}} = N_{\text{sites}} g \exp(-E_{\text{compl}}/k_B T) \quad (6)$$

If we neglect the degeneracy factor the ratio between complex concentration and the concentration of the isolated defects depends solely on the difference in formation energy: for $E_{\text{compl}} < E_{\text{defect}}$ (which is equivalent to $E_{\text{defect}} < E_b$) the complex formation dominates, otherwise dissociation is predominant. Thus, complex formation is the dominant mechanism (and controls the achievable concentration of the dopants) only if the energy gain due to complex formation is larger than the energy necessary to create either one of the constituents.

For the specific choice of chemical potentials made here, the complex binding energy is not large enough to prevent dissociation of the Mg-H complex during growth. However, the Mg and H will form pairs when the sample is cooled to room temperature, consistent with experimental observations [16]. The beneficial character of H incorporation is thus not due to complex formation, but simply due to compensation. Complexes are formed only after growth and do not affect the achievable acceptor concentration.

In order to activate the Mg, post-growth treatments are necessary. The first step in the activation process is the dissociation of the Mg-H complex. Our calculated dissociation

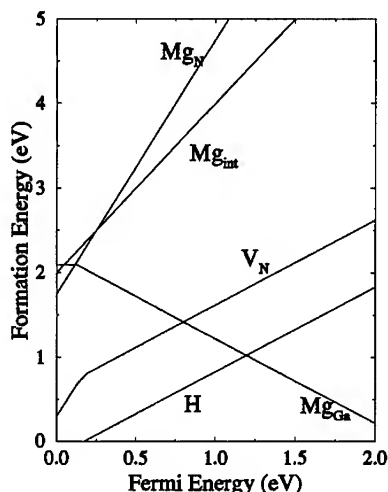


Figure 6: Formation energy as a function of the Fermi level for Mg in different configurations (Mg_{Ga} , Mg_i , Mg_N). Also included are the native defects and interstitial H.

barrier is ≈ 1.5 eV, which should be considered a lower limit: only a jump to a nearest neighbor site has been considered in this calculation, and the attractive electrostatic interaction between the negative Mg acceptor and the positive H atom may slightly increase this value. This barrier is low enough to be overcome at modest annealing temperatures (around 300°C). Experimental results show, however, that activation has to be carried out at much higher temperatures ($> 600^\circ\text{C}$) [14]. The reason is that dissociation alone is insufficient; in order to prevent the H from compensating the Mg acceptor it has to be either removed (to the surface or into the substrate) or neutralized (e.g., at an extended defect). This phenomenon is well known from studies of complex dissociation in Si; activation can be achieved at much lower temperatures if an electric field is applied which sweeps the H out of the region [24].

Incorporation of Mg on other sites

Another mechanism, that may limit the hole concentration, is self-compensation of the Mg acceptors: instead of being incorporated on the Ga substitutional site the Mg may be built in on other sites where it is electrically inactive or even becomes a donor. As possible configurations we have investigated the N substitutional site (Mg_N) and several interstitial configurations.

The calculated formation energies are displayed in Fig. 6. The positive slope in the formation energy indicates that Mg in both configurations acts as a donor: Mg_i as a double donor, Mg_N as a triple donor. Whereas the behavior of Mg_i is expected, the donor character for Mg_N is not as obvious: at first sight Mg should act as a triple acceptor. The replacement of the “small” N atom ($r_{cov} = 0.75 \text{ \AA}$) with a “large” Mg atom ($r_{cov} = 1.36 \text{ \AA}$) results in a large increase of the nearest neighbor bond length (by 24%!), giving rise to substantial changes in the positions of the defect levels. The large strain around the Mg atom further explains the high formation energy, rendering this site energetically unfavorable.

Figure 6 shows that the formation energies of Mg_i and Mg_N become comparable with Mg_Ga only under extreme p -type conditions. We further find that the N vacancy or hydrogen (if present), are the dominant donors: their formation energies are lower for *all* Fermi energies. We therefore conclude that Mg will always prefer the Ga substitutional site: incorporation on other sites can be ruled out. For other possible acceptors (particularly elements with a small ionic radius), the situation may be different.

CONCLUSIONS

Based on first-principles calculations we have studied several mechanisms which may limit the hole concentration in Mg-doped GaN. Two mechanisms are found to be important: (i) the formation of Mg_3N_2 precipitates (solubility limit) and (ii) the compensation by native defects. Incorporation of the Mg atoms on the N site or in an interstitial configuration was found to be negligible. Combining our numerical results about native defects, interstitial H and the Mg impurity we could identify why H incorporation increases the acceptor concentration and simultaneously reduces compensation by native defects. An analysis of these results reveals that this mechanism should also work for other *acceptors* in GaN. However, it is by no means general: it does not work for donor impurities in GaN and may fail for other wide-band-gap semiconductors.

ACKNOWLEDGMENTS

This work was supported in part by ARPA. One of the authors (J.N.) acknowledges financial support by the DAAD (German Academic Exchange Service).

References

- [1] S. Nakamura, T. Mukai, and M. Senoh, Appl. Phys. Lett. **64**, 1687 (1994).
- [2] S. B. Zhang and J. E. Northrup, Phys. Rev. Lett. **67**, 2339 (1991).
- [3] D. B. Laks, C. G. Van de Walle, G. F. Neumark, and S. T. Pantelides, Phys. Rev. Lett. **66**, 648 (1991).
- [4] J. E. Northrup and S. B. Zhang, Phys. Rev. B **47**, 6791 (1993).
- [5] C. G. Van de Walle, D. B. Laks, G. F. Neumark, and S. T. Pantelides, Phys. Rev. B **47**, 9425 (1993).
- [6] G.-X. Qian, R. M. Martin, and D. J. Chadi, Phys. Rev. B **38**, 7649 (1992).
- [7] D. B. Laks, C. G. Van de Walle, G. F. Neumark, P. E. Blöchl, and S. T. Pantelides, Phys. Rev. B **45**, 10965 (1992).
- [8] N. Troullier and J. L. Martins, Phys. Rev. B **43**, 1993 (1991).
- [9] J. Bormet, J. Neugebauer, and M. Scheffler, Phys. Rev. B **49**, 17242 (1994).
- [10] R. Stumpf and M. Scheffler, Comp. Phys. Commun. **79**, 447 (1994).

- [11] J. Neugebauer and C. G. Van de Walle, Phys. Rev. B **50**, 8067 (1994).
- [12] J. Neugebauer and C. G. Van de Walle, in *The Physics of Semiconductors*, edited by D. J. Lockwood (Materials Research Society, World Scientific, Singapore, 1994), Vol. 3.
- [13] *Hydrogen in Semiconductors*, edited by J. I. Pankove and N. M. Johnson (Academic Press, Boston, 1991).
- [14] S. Nakamura, N. Iwasa, M. Senoh, and T. Mukai, Jpn. J. Appl. Phys. **31**, 1258 (1992).
- [15] J. Neugebauer and C. G. Van de Walle, phys. Rev. Lett. in press.
- [16] W. Götz, N. Johnson, J. Walker, and D. P. Bour, accepted for publication in Appl. Phys. Lett.
- [17] K. J. Chang and D. J. Chadi, Phys. Rev. B **42**, 2426 (1990).
- [18] I. Akasaki, H. Amano, M. Kito, and K. Hiramatsu, J. Lumin. **48&49**, 666 (1991).
- [19] S. Strite and H. Morkoc, J. Vac. Sci. Technol. **10**, 1237 (1992).
- [20] R. J. Molnar, T. Lei, and T. D. Moustakas, Proc. Mater. Res. Soc. Symp. **281**, 753 (1993).
- [21] M. E. Lin, C. Xue, G. L. Zhou, J. E. Greene, and H. Morkoc, Appl. Phys. Lett. **63**, 932 (1993).
- [22] H. Amano, M. Kito, K. Hiramatsu, and I. Akasaki, Jpn. J. Appl. Phys. **28**, L2112 (1989).
- [23] J. A. Van Vechten, J. D. Zook, R. D. Hornig, and B. Goldenberg, Jpn. J. Appl. Phys. **31**, 3662 (1992).
- [24] T. Zundel and J. Weber, Phys. Rev. B **39**, 13549 (1989).

SPIN-DEPENDENT TRANSPORT IN GaN LIGHT EMITTING DIODES

M. S. BRANDT, N. M. REINACHER, O. AMBACHER, and M. STUTZMANN
Walter Schottky Institut, Technische Universität München, Am Coulombwall,
D85748 Garching, Germany, mbrandt@physik.tu-muenchen.de

ABSTRACT

Electrically detected magnetic resonance (EDMR) is used to study recombination processes in two types of gallium nitride light emitting diodes: in $m/i/n/n^+$ and InGaN/AlGaN double-heterostructure devices. In the MIS-diodes, two resonances at $g=1.96$ and 2.00 , corresponding to the effective mass donor and a deep defect are observed at room temperature. At low temperatures, an acceptor-related resonance at $g=2.06$ is visible as well. After current degradation, the spectra are dominated by the defect resonance, indicating that the creation of this defect is responsible for the decreased electroluminescence efficiency. In the double-heterostructure devices, EDMR can only be observed below 60 K showing the $g=2.00$ defect resonance. The same defect resonance is also observed in conventional electron spin resonance experiments under illumination (light-induced ESR).

INTRODUCTION

Various electronic devices such as high brightness light emitting diodes and field effect transistors have recently been developed on the basis of GaN. To further improve the performance of these devices, detailed information on electrically active defect states will be important. A notable problem where defect studies will become important is the difficulty to achieve stimulated emission from the group III-nitrides: The extremely short lifetime of the luminescence requires enormous excitation densities to achieve the necessary occupation inversion. The short lifetime is most probably due to an unidentified deep defect leading to an efficient nonradiative recombination path quenching the radiative transition. The large bandgap of the material makes the simple extension of existing techniques for the electrical characterisation of defects in other semiconductors difficult. As an example, the thermal excitation used in conventional deep level transient spectroscopy (DLTS) has to be replaced by optical excitation, which has indeed led to the observation of several deep states [1]. Here, we will show that both donor and acceptor levels as well as deep defects can be detected via electronic transport measurements in GaN diodes with the help of electrically detected magnetic resonance (EDMR).

We will briefly discuss why magnetic resonance can influence electronic transport processes such as recombination. Imagine that an electron encounters a paramagnetic defect state (ie. a singly occupied defect) on its path through the sample. Both have a spin of $S=1/2$. The possible recombination step would in this case be the capture of the electron by the defect leading to a doubly occupied defect. The Pauli principle only allows this final state to be an $S=0$ singlet state. However, the spins of the two initial states can form both a singlet or a triplet ($S=1$). Since angular momentum is conserved in a non-radiative recombination, only the initial electron/defect states

forming a spin singlet will be able to recombine, the transition of the triplet is forbidden. However, flipping the spin of either the electron or the defect with the help of electron spin resonance (ESR) transform the triplet into a singlet state. This increases the total recombination rate. Although the induced resonant changes of the total current through the device are small (typically of the order of 10^{-6} at room temperature), they can easily be measured with the help of lock-in techniques. We then obtain the resonance signature of both states involved in the recombination which, in principle, allows us to form a detailed model of the transport processes present in the material or device.

Electron spin resonance (ESR) provides detailed information on the microscopic structure of paramagnetic states in semiconductors. In GaN, several groups have studied the ESR signature of the residual donor at low temperatures [2,3]. However, due to the low sensitivity of this method, comparatively thick samples have to be studied. Optically detected magnetic resonance (ODMR) uses similar selection rules for the resonant detection of paramagnetic states involved in recombination processes as EDMR. Indeed, this method has been applied successfully to GaN, and additional resonances, assigned to a deep defect and the Mg acceptor-state, have been reported [4,5]. However, this type of measurements is usually performed at very low temperatures and is therefore not necessarily suitable for device investigations.

The non-equilibrium carriers, whose recombination is studied with the help of EDMR, can either be created by light (leading to resonant changes of the photoconductivity) or by injection (eg. in diode structures). In both crystalline and amorphous silicon, for example, electrical detection of magnetic resonance has been used successfully to understand carrier recombination and degradation processes in pn-junctions, MOSFETs and solar cells [6,7]. Until now, the extension of this technique to compound semiconductors is very limited, probably due to the extremely short relaxation times caused by the strong spin-orbit coupling [8]. However, we have previously shown that a defect resonance in undoped GaN films can be detected with spin-dependent photoconductivity even at room temperature [9], with a g-factor of $g=2.00$ and a full-width at half-maximum linewidth of $\Delta H_{1/2}=120\text{G}$. The magnitude of the resonant change, normalized to the dc conductivity, was found to be $\Delta I/I=10^{-6}$ at a microwave frequency of 9 GHz and 200 mW microwave power.

For the present study on GaN devices, two different light emitting diodes have been investigated: MIS-type structures which are only made from GaN and InGaN/AlGaIn heterostructures. While the second type of LED exhibits the highly efficient blue electroluminescence which has led to the recent excitement and therefore is of current interest, the former LED is potentially easier to analyse with respect to the EDMR resonances observed since ODMR measurements on pure GaN have led to the necessary assignments. In addition, it is well known that these diodes exhibit a pronounced degradation which could be addressed using this method.

m/i/n/n⁺-DIODES

Commercial m/i/n/n⁺-GaN LEDs were obtained from LEDtronics, CA. The structure of the LED as reported by Koide et al. is as follows [10]: sapphire substrate, AlN buffer (50 nm thickness, 400°C growth temperature), n⁺-GaN (Si concentration of $1.5 \times 10^{18} \text{ cm}^{-3}$, 2 μm , 1150°C), undoped GaN (1.5 μm), i-GaN (Zn-doped, 100 nm,

900°C). Aluminum is used as contact material both to the n^+ - and the i -layer. The diode was placed inside the TE₁₀₂ cavity of a Bruker X-band ESR spectrometer, with the symmetry axis of the diode housing perpendicular to the magnetic field H_0 . The diode could be cooled down to liquid helium temperatures. However, since the diode was not removed from its epoxy housing and the EDMR measurements were performed under strong forward bias, the actual temperature will be above the temperature given by the thermocouple in the cryostat. EDMR measurements were performed under constant voltage conditions. With the help of a small resistor between the voltage source and the diode the current changes under ESR resonance conditions were detected with a lock-in amplifier. Typical modulation frequencies of the microwave power were in the 10kHz range. The nonresonant microwave conductivity, which is appearing as a background when using microwave modulation, has been removed from the spectra below.

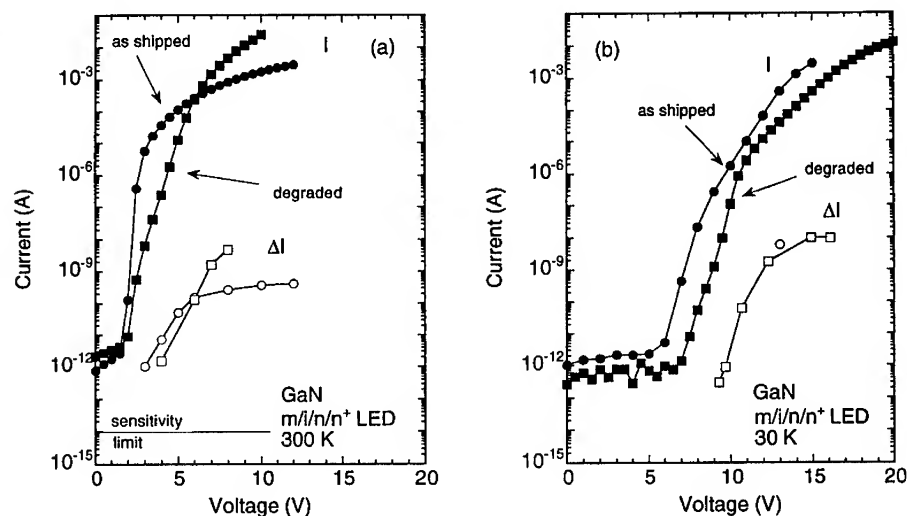


Fig.1: Room temperature and 30 K I-V-characteristics (labeled I) of the GaN m/i/n/n⁺-diodes studied. The circles correspond to the as shipped diode, the squares show the characteristic after a low temperature current degradation. The open symbols give the size of the peak current change, ΔI , under ESR resonance conditions.

Figure 1 (a) shows the room temperature I-V-characteristics of the diode as shipped. At a forward bias of about 2 V, the ideality factor is best (ie. smallest) with a value slightly above 2. Electroluminescence with a peak wavelength of 485 nm is observed for forward biases above 4 V. The corresponding room temperature EDMR resonance spectrum is shown in the top of Fig. 2. An asymmetric resonance line is found with a g-factor of $g=1.96$ and a shoulder at higher g-factors. The size of the resonant change, ΔI , is included in Fig. 1 (open symbols). The relative change under

resonance conditions is $\Delta I/I = 3 \times 10^{-7}$. The sign of the change is difficult to determine due to the large non-resonant background. However, in other diodes studied with EDMR so far a resonant increase of the current was observed, which we also assume in GaN. Below 3 V forward bias, the size of the spin-dependent current was below the measurement limit of 10 fA. Both under reverse bias and when monitoring the open circuit voltage, the spin-dependent signal also was below this detection limit.

The diode was subsequently cooled down to 30 K. The corresponding change in the forward bias I-V-characteristic is shown in Fig. 1 (b). The low temperature EDMR spectrum is considerably changed with respect to the room temperature spectrum as can be seen in Fig. 2. The resonance is shifted to lower magnetic fields and is dominated by two resonances, with $g=2.00$ and $g=2.06$. Again, a shoulder can be found, corresponding to the g -factor of $g=1.96$. The relative change of the current under resonance, $\Delta I/I = 2 \times 10^{-5}$, is significantly larger than at room temperature.

Under high forward bias ($>15V$), the light emitting diode degraded considerably at 30 K. This can be seen by the change in the I-V-characteristics. The resonance lineshape observed in EDMR also changed as shown in Fig. 2, the spectrum is now dominated by the $g=2.00$ resonance.

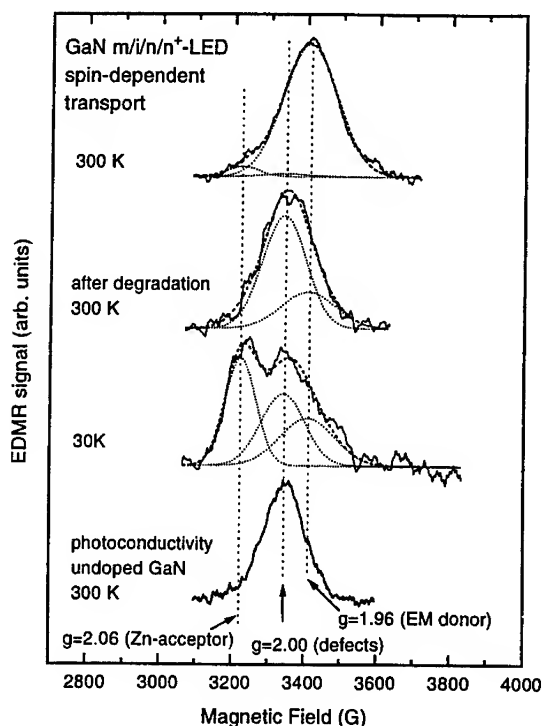


Fig. 2: Electrically detected magnetic resonance spectra of the MIS GaN diode at 300 K and 30 K. The spectra have been decomposed into three resonances, with g -factors of 1.96, 2.00 and 2.06, as shown by the dotted lines and discussed in the text. The EDMR spectrum observed in the photoconductivity of undoped GaN films is included.

	$g \parallel c$	$g \perp c$	Ref.	EDMR (this work)	$\Delta H_1/2$ (this work)
donor	1.943-1.948 1.951	1.940-1.951 1.948	[4] [5]	1.96	150G (RT)
defect X	1.983	1.936	[4]		
narrow defect		1.99	[14]		
deep donor	1.989	1.992	[5]	2.00 2.01 ($g \perp c$)	120G (RT) 150G (4K)
defect Y	2.000	1.95	[4]		
acceptor (Mg)	2.08	1.992	[4]		
acceptor (Zn)	1.997	1.992 2.00	[11] [14]	2.06	85G (30K)

Table I: g-factor of donor and acceptor related resonances as well as defect resonances observed in ODMR, compared to the EDMR resonances found here.

To identify the different resonances observed in the EDMR spectra, we have fitted the spectra with a superposition of three resonances, taking into account the assignments obtained from previous ODMR measurements (Tab. I). The width $\Delta H_1/2$ of the $g=2.00$ resonance is assumed to be 120 G as observed in the EDMR of the photoconductivity (bottom spectrum of Fig. 2). The width of the donor related resonance is known to be strongly temperature dependent due to lifetime broadening. Fitting the spectra provided an estimated width of 150 G at room temperature. For the Zn acceptor, we find $g=2.06$ and $\Delta H_1/2=85$ G at 30 K. The observed similarity between the Zn- (measured here) and Mg-acceptors (ODMR) is at variance with recent ODMR measurements on Zn-doped GaN [17], an issue which remains to be resolved. Taking into account the reduced g-factor resolution due to the X-band spectrometer used, however, an overall good agreement is found. No anisotropy could be detected with the LED examined in the present work.

A detailed analysis of the recombination processes involved in EDMR is somewhat more difficult than the corresponding analysis in ODMR, since the ability to lock onto specific processes via the detection of their characteristic PL emission is not possible. However, some conclusion can already be drawn from the schematic band diagram of the GaN diode under forward bias as shown in Fig. 3. In principle, three different transport steps are expected to be spin-dependent in the GaN LED: the hopping between EM donors both in the n^+ - and n-layers, the recombination between donor and deep defect states, probably near the n/i-interface and the recombination between the acceptor and defect states near the m/i-interface. As seen from the resonance spectrum in Fig. 2, the donor-band hopping is dominant in the as-shipped diode at room temperature, with a very small ($\Delta I/I \approx 10^{-8}$) contribution due to defect-acceptor recombination. This situation inverts at low temperatures: Now the defect-acceptor recombination dominates the spectrum, with a small contribution due to donor-band hopping. The reduction in the latter might be linked to changes in the Fermi-level position in the n-layer. Finally, after degradation, the deep defect resonance

dominates, which suggests that recombination of electrons and/or holes via defect becomes the dominant spin-dependent process.

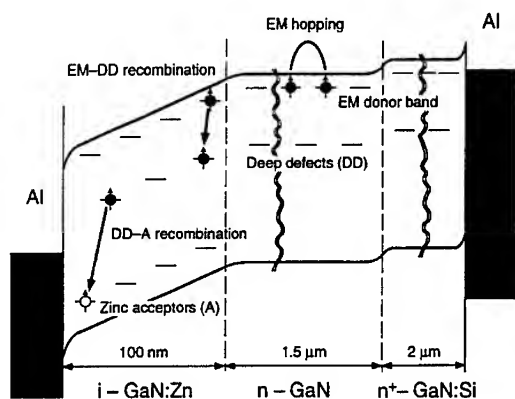


Fig. 3: Schematic band diagram under forward bias of the MIS GaN diode studied. The arrows indicate the possible spin-dependent transport processes.

Independent of the exact origin of the spin-dependent transport steps, the EDMR results can be used to identify the microscopic process responsible for degradation. Time dependent processes including degradation have already been reported in GaN metal-insulator-semiconductor structures, including the changes in the I-V-characteristics shown in Fig. 1 [12]. It was already then speculated that the decreased luminescence efficiency could be due to a deep, nonradiative recombination center. Our EDMR results show that indeed the recombination via defects is strongly enhanced after degradation, directly linking this defect to the detrimental changes in the device properties.

DOUBLE-HETEROSTRUCTURE LED

From the point of view of device applications, the study of transport and recombination in the new high-brightness LEDs is certainly much more interesting. We have therefore studied EDMR on the first generation of commercial Nichia InGaN/AlGaIn double-heterostructure LEDs (NLPB 500) [13]. Similar to Fig. 1, the I-V-characteristic of the diode at room temperature and at 4K is shown in Fig. 4. At room temperature, no resonant EDMR signal could be observed. However, at 4K, the EDMR signal shown in Fig. 5 was found, with a resonant change of about $\Delta I/I = 5 \times 10^{-4}$, which slightly increases over the forward bias range of 4.5 to 6V where the low-temperature EDMR signal could be observed.

Due to a very large microwave conductivity shown by the diodes, microwave power modulation could not be used for the lock-in detection of the EDMR signal as in the case of the other diodes. Instead, magnetic field modulation was used resulting in a resonance line shape which is the first derivative compared to the absorption-type lineshape of Fig. 2. In the Nichia diodes, we observe only the defect resonance at

$g=2.01$. Carlos and coworkers have found, using EDMR at 2K, an additional narrow resonance at $g=1.99$. In our measurements at 4K and above, this additional resonance could not be detected with the same relative intensity with respect to the broad $g=2.01$ defect resonance as reported by these authors [14]. The measurements indicate that at low temperatures a recombination current via deep defects contributes to the transport processes in the heterostructure LEDs in a similar way as in the degraded MIS LEDs. The exact position inside the diode structure where this recombination occurs might be determined by a very careful analysis of the g -factor observed, since it should be dependent on the composition of the alloy carrying the defect. However, no systematic study of the ESR on InGaN or AlGaIn alloys exists which could be used for such an comparative analysis.

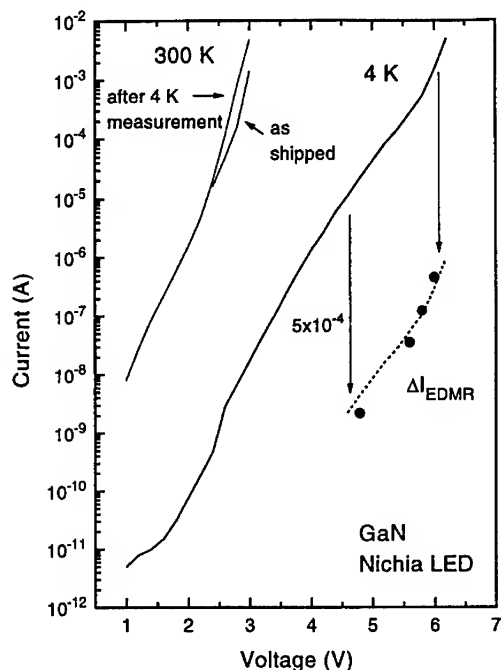


Fig. 4: Room-temperature and 4K I-V characteristics of the blue Nichia LED. The full circles show the size of the resonant current change at 4K.

In passing, we would also like to point out that, although on a much smaller scale, the heterojunction LEDs also show changes in the I-V-characteristics after EDMR measurements at low temperatures, as shown in the top of Fig. 4. Although of more academic interest due to the low temperatures necessary, it would nevertheless be important to understand the microscopic mechanism of this apparent degradation in more detail.

We finish the section on EDMR with some brief remarks concerning more the experimental technique, namely the microwave power and temperature dependence of the EDMR signal intensity. In the case of an inhomogeneously broadened line, the microwave power dependence is expected to follow a square-root law [15]. This is indeed found for the EDMR of the Nichia diodes.

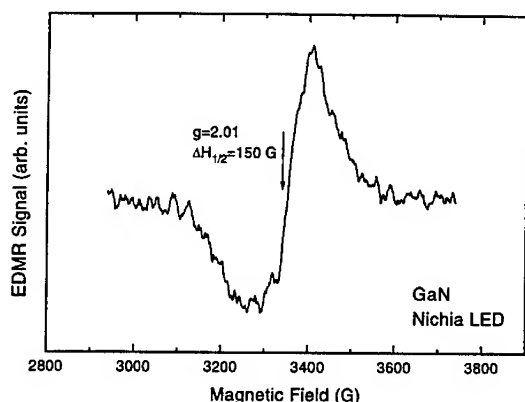


Fig. 5: EDMR spectrum of the Nichia LED at 4 K. Note that magnetic field modulation was used to obtain this spectrum, resulting in a lineshape which is the first derivative of the lines shown in Fig.2.

Turning to the temperature dependence of the EDMR signal intensity two different models have to be discussed [16,17]. In fact, it is very difficult to separate the pure temperature dependence of the EDMR from the large changes in the non-resonant diode characteristic. As a first attempt to overcome this problem, we have studied the temperature dependence of the EDMR at a fixed current of 0.2mA, therefore adjusting the bias voltage when changing the temperature. This results in a rather weak temperature dependence of $T^{-0.65}$, which would point to spin-pair formation as the underlying process causing the spin-dependence [16]. An additional argument is the fact that the resonant current change of $\Delta I/I = 3 \times 10^{-5}$ at room temperature in the degraded MIS diodes is also above the maximum value predicted by Lepine's spin-polarization model. The temperature dependence of $\Delta I/I$ in the as-shipped MIS diodes, in contrast, would be in accordance with the spin-polarisation model, which predicts $\Delta I/I = (g\mu_B H_0 / k_B T)^2$. Since however the resonant recombination channel changed drastically as seen from the resonance spectra, such a comparison cannot be drawn. The mechanism leading to the spin-dependence should better be studied by performing EDMR measurements at different magnetic fields. Although some aspects concerning the application of EDMR to GaN LEDs still have to be understood more thoroughly, the results shown above clearly indicate that EDMR can provide valuable information on the physics of GaN but can also be of interest for applications.

LIGHT-INDUCED ELECTRON SPIN RESONANCE

The exact microscopic structure of the deep defect at $g=2.00$ is still under investigation. The study of this resonance is further made complicated by the fact that it has not yet been observed with standard ESR techniques which would provide a direct measure of the defect concentration. Instead, the defect resonance has been detected

with the help of either ODMR or EDMR which, due to the indirect detection of the resonance do not provide quantitative information. In addition, the energy position of the correlated defect state within the bandgap has only indirectly been inferred and is still subject to discussion. To detect the resonance in ESR, the defect state has to be paramagnetic, i.e. the Fermi level must be at about the same position as the defect level. However, due to the native background doping the Fermi level is generally near the conduction band and the deep defect therefore doubly occupied and not accessible to standard ESR. This can be overcome by illuminating the sample which leads to the excitation of electrons from the deep defect states and provides singly-occupied, paramagnetic defects. This technique is called light-induced electron spin resonance (LESR).

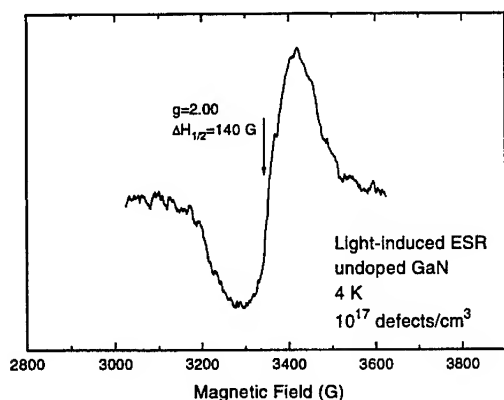


Fig. 6: Light-induced electron spin resonance of a thick undoped GaN film.

Figure 6 shows the LESR signal of a thick undoped GaN film grown by MOCVD, which has a particularly strong yellow luminescence band at 2.2 eV, under illumination with white light. It should be noted that the sapphire substrate shows background signals which, in some cases, are also photosensitive and care has to be taken to properly subtract these resonances from the spectrum. However, the well-known GaN $g=2.00$ defect resonance is found again in LESR, with a half-width of about 140 G. Measurements using monochromatic light for excitation, which could identify the energetic position of the defect level with respect to the conduction band, are currently under way.

The identification of the microscopic defect structure based on a g -factor alone is difficult. A more detailed understanding would be possible if, e.g., hyperfine-split lines caused by nuclear spins in the vicinity of the electronic defect are observed. Since this has not yet been achieved in GaN, comparisons with ESR results on similar materials might provide valuable information. Indeed, an ESR resonance at $g=1.997$ is observed for group VI-donors in GaP. For both S and Te, the resonance line is much narrower as observed in GaN. However, substitutional oxygen on the phosphorous lattice site, which acts as a deep donor, was found to show both a g -factor and a line width which is extremely similar to the defect resonance observed in GaN [18]. Oxygen on the nitrogen lattice site in GaN would have the identical local configuration, namely four

Ga nearest neighbors, and might show the same ESR resonance. Indeed, the effects of oxygen impurities on GaN are currently under investigation as can be seen from these proceedings. More detailed studies on the dependence of the LESR signal on the oxygen concentration as well as theoretical studies on the electronic levels induced by oxygen will be necessary to resolve this issue.

SUMMARY

In conclusion, we have shown that electrically detected magnetic resonance can be used to study recombination processes in GaN even at room temperature and in commercial devices. Donor and acceptor related resonances as well as deep defects have been observed. In addition, the observation of the relative intensity changes for the different resonances allows further understanding of device relevant processes such as degradation due to deep defects.

The support of Deutsche Forschungsgemeinschaft is gratefully acknowledged. The authors thank Ted Moustakas for discussions.

REFERENCES

1. W. Götz, N. M. Johnson, R. A. Street, H. Amano, I. Akasaki, *Appl. Phys. Lett.* **66**, 1340 (1995)
2. M. Fanciulli, T. Lei, T. D. Moustakas, *Phys. Rev. B* **48**, 15144 (1993)
3. W. E. Carlos, J. A. Freitas, M. Asif Khan, D. T. Olson, J. N. Kuznia, *Phys. Rev. B* **48**, 17878 (1993)
4. M. Kunzer, U. Kaufmann, K. Maier, J. Schneider, N. Herres, I. Akasaki, H. Amano, *Mat. Sci. Forum* **143-147**, 87 (1994)
5. W. R. Glaser, T. A. Kennedy, K. Doverspike, L. B. Rowland, D. K. Gaskill, J. A. Freitas, M. Asif Kahn, D. T. Olson, J. N. Kuznia, D. K. Wickenden, *Phys. Rev. B* **51**, 13326 (1995)
6. I. Solomon, *Solid State Commun.* **20**, 215 (1976)
7. see e.g. K. Lips, W. Fuhs, *J. Appl. Phys.* **74**, 3993 (1993)
8. N. M. Reinacher, M. S. Brandt, M. Stutzmann, B. K. Meyer, *Verhandlungen der Deutschen Physikalischen Gesellschaft (VI)* **30**, 1282 (1995)
9. M. S. Brandt, *International Workshop on Wide-Bandgap Nitrides*, St. Louis, USA (1994)
10. N. Koide, H. Kato, M. Sassa, S. Yamasaki, K. Manabe, M. Hashimoto, H. Amano, K. Hiramatsu, I. Akasaki, *J. Crystal Growth* **115**, 639 (1991)
11. U. Kaufmann, these proceedings
12. T. Yanagisawa, *Electronics Letters* **22**, 846 (1986)
13. S. Nakamura, T. Mukai, M. Senoh, *Appl. Phys. Lett.* **64**, 1687 (1994)
14. W. E. Carlos, E. R. Glaser, T. A. Kennedy, S. Nakamura, *Appl. Phys. Lett.* **67**, 2376 (1995)
15. C. F. O. Graeff, M. Stutzmann, M. S. Brandt, *Phys. Rev. B* **49**, 11028 (1994)
16. D. Kaplan, I. Solomon, N. F. Mott, *J. Phys. (Paris)* **39**, L51 (1978)
17. D. J. Lepine, *Phys. Rev. B* **6**, 436 (1972)
18. S. Toyotomi, K. Morigaki, *J. Phys. Soc. Jpn* **29**, 800 (1970)

DETECTION OF MAGNETIC RESONANCE ON SHALLOW DONOR - SHALLOW ACCEPTOR AND DEEP (2.2 eV) RECOMBINATION FROM GaN FILMS GROWN ON 6H-SiC

E.R. GLASER*, T.A. KENNEDY*, S.W. BROWN*, J.A. FREITAS Jr.**, W.G. PERRY***, M.D. BREMSER***, T.W. WEEKS***, and R.F. DAVIS***

*Naval Research Laboratory, Washington, D.C. 20375-5347

**Sachs Freeman Associates, Landover, Maryland, 20785

***Department of Materials Science and Engineering, North Carolina State University, Box 7907, Raleigh, North Carolina 27695-7907

ABSTRACT

Photoluminescence (PL) and optically-detected magnetic resonance (ODMR) experiments have been performed on undoped GaN epitaxial layers grown on 6H-SiC substrates. The defects observed in these films are compared with those found from previous ODMR studies of undoped GaN layers grown on sapphire substrates. Strong, sharp donor-bound exciton bands at 3.46 - 3.47 eV and weak, broad emission bands at 2.2 eV were observed from several 0.7 and 2.6 μm -thick films. In addition, fairly strong shallow donor - shallow acceptor (SD-SA) recombination with a zero-phonon-line at 3.27 eV was found for GaN layers less than 1 μm -thick. The first observation of magnetic resonance on this SD-SA recombination from undoped GaN is reported in this work. Two magnetic resonance features attributed to effective-mass (EM) and deep-donor (DD) states were detected on the 2.2 eV emission bands from all the GaN/6H-SiC films. These resonances were observed previously on similar emission from undoped GaN layers grown on sapphire substrates. The same EM donor resonance, though much weaker, was also found on the SD-SA recombination. However, a resonance associated with shallow acceptor states was not observed on this emission. The weakness of the donor resonance arises from the weak spin-dependence of the recombination mechanism involving spin-thermalized shallow acceptors. The absence of an EM acceptor is due to the broadening of the resonance through the spreading of the acceptor g-values by random strains in these films.

INTRODUCTION

There has been much activity lately by several groups to study and, if possible, to identify intrinsic defects in undoped epitaxial layers of GaN grown by either organo-metallic chemical vapor deposition (OMCVD) or molecular beam epitaxy (MBE). In addition, there has been some work to obtain more detailed information on the participation of these defects in the recombination processes observed from these GaN films. Both shallow, effective-mass like and deep states of donor or acceptor character have been revealed from a variety of techniques. The origin of these states in undoped GaN, either due to residual impurities or non-stoichiometric defects such as vacancies, anti-sites, or interstitials, is a subject of much discussion. Much of this work has focused on GaN films grown on sapphire (Al_2O_3) substrates, typically with the use of AlN buffer layers. Since the in-plane lattice constant mismatch is $\sim 1\%$ between AlN and 6H-SiC as compared to the $\sim 13\%$ difference between AlN and sapphire, the expected lower degree of strain in the GaN layers grown on 6H-SiC should lead to improved film quality. Recently, it has been reported that GaN films grown with the use of high-temperature AlN buffer layers on 6H-SiC substrates has resulted in a significant reduction of the dislocation density in these films after the first micron of growth [1].

We have previously reported PL and ODMR experiments performed on both undoped and Mg-doped GaN films grown on (0001)-oriented sapphire (Al_2O_3) substrates. Both shallow and deep states were revealed by magnetic resonance obtained by detection on the 2.2 eV broad emission band from undoped GaN layers [2-4] and on emission from heavily Mg-doped GaN films [3,4]. Preliminary results obtained for undoped GaN layers grown on 6H-SiC substrates were presented recently [4].

In this work we discuss in more detail the results of PL and ODMR studies of undoped wurtzite GaN layers grown by OMCVD on 6H-SiC. One of the goals of this work is to compare the

magnetic resonance obtained from GaN films grown on 6H-SiC with the results obtained from layers grown on sapphire substrates. In addition, it was found from this work that the PL observed from these films was found to be quite dependent on the layer thickness. In particular, a rather strong shallow donor - shallow acceptor band was observed from films less than 1 μm -thick (in addition to a stronger donor-bound excitonic peak near the band-gap energy and a relatively weak 2.2 eV emission band also observed from these thin films and for layers greater than 2 μm). The first observation of magnetic resonance on this SD - SA recombination from undoped GaN is reported in this work. Thus, the thin GaN layers grown on 6H-SiC provided the opportunity to contrast the magnetic resonance detected on the 2.2 eV deep emission band with that found on shallow donor - shallow acceptor recombination from the same film. In addition, the ODMR studies of the SD-SA recombination allowed us to learn more about the character of the effective-mass (EM) acceptors in GaN epitaxial layers in the presence of random strain fields derived from growth of these films on lattice-mismatched substrates.

EXPERIMENTAL BACKGROUND

The PL and ODMR experiments reported in this work were performed on undoped GaN films grown on 6H-SiC substrates by OMCVD at 950 $^{\circ}\text{C}$. The epitaxial layers were of wurtzite crystal structure. The films were grown with the use of high-temperature (~ 1100 $^{\circ}\text{C}$) AlN nucleation layers which have shown to improve the film quality of GaN grown on 6H-SiC substrates [1]. Further details of the growth procedure are described elsewhere [1]. This paper focuses on the results obtained for two GaN samples (referred to as No. 1 and No. 2) which are representative of the PL and ODMR found from several 0.7 and 2.6 μm -thick films. The film thickness of sample No. 1 is 0.7 μm while No. 2 is 2.6 μm thick. Room-temperature Hall-effect measurements reveal that both layers No. 1 and No. 2 are n-type with carrier concentrations equal to $1.2 \times 10^{17} \text{ cm}^{-3}$ and $1.4 \times 10^{17} \text{ cm}^{-3}$, respectively.

The PL from the GaN layers was excited with radiation provided by the 325.0 nm line of a HeCd laser. The emission from 1.7 - 3.5 eV was analyzed by a 0.85-m double-grating spectrometer and detected by a UV-enhanced GaAs photomultiplier tube.

The ODMR was detected synchronously as a change in the total intensity of PL which was coherent with the on-off amplitude modulation (700 Hz - 10 kHz) of 50 mW of microwave power. The GaN layers were studied in both K-band (24 GHz) and Q-band (35 GHz) spectrometers. For the ODMR, the PL was generated by 351.1 nm radiation from an Ar^{+} -ion laser with power densities between 5 and 500 mW/cm^2 . The emission was detected by a room-temperature, UV-enhanced Si photodiode. Visible cut-off filters were placed in front of the detector to isolate and separately study the emission bands observed from these films.

RESULTS AND DISCUSSION

Photoluminescence

The photoluminescence obtained at 6 K from the two representative GaN/6H-SiC films reported in this work is shown in Fig. 1. Several recombination processes are revealed.

The dominant emission observed from both samples No. 1 ($t=0.7 \mu\text{m}$) and No. 2 ($t=2.6 \mu\text{m}$) are sharp peaks (FWHM $\sim 4 - 6 \text{ meV}$) at 3.46 - 3.47 eV (labeled D^0X in Fig. 1). This band has been assigned to excitons bound to neutral donors and is considered a PL signature of high quality, n-type GaN [5].

The next highest-energy PL emission observed from these samples is characterized by a zero-phonon-line (ZPL) at 3.27 eV and a series of well-resolved LO phonon replicas at lower energies ($E_{\text{LO}}=92 \text{ meV}$). This emission has been assigned previously to shallow donor - shallow acceptor (SD-SA) recombination with a donor binding energy of $\sim 35 - 40 \text{ meV}$ and an acceptor binding energy of $\sim 200 \text{ meV}$ [6]. As seen in Fig. 1, it was found that the amplitude of the SD-SA recombination relative to the amplitude of the D^0X peak was a much larger fraction for the GaN films less than 1 μm -thick compared to the ratio found for the GaN layers greater than 2 μm -thick. This indicates that these thin films are more highly compensated by residual shallow acceptors closer to the film/buffer layer interface (i.e. within a micron) compared to the degree of

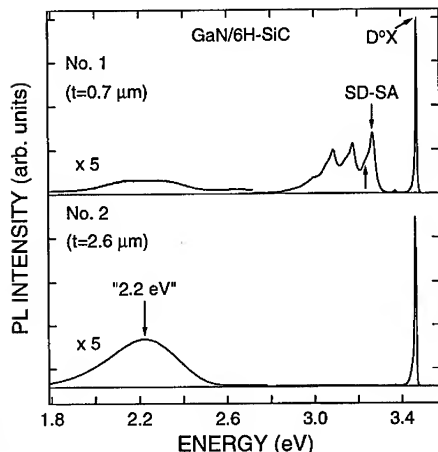


Fig. 1. PL spectra obtained under similar conditions from two undoped GaN/6H-SiC layers at 6 K.

compensation that exists in the top $\sim 0.5 \mu\text{m}$ layer of the thick films [7] (note that the penetration depth of the laser excitation, 325.0 and 351.1 nm, employed in the PL and ODMR studies is $\sim 0.5 - 1 \mu\text{m}$). It has also been found that GaN films grown on 6H-SiC substrates at $\sim 100^\circ\text{C}$ higher temperature than that employed for samples No. 1 and No. 2 exhibited PL that had the same dependence on film thickness as shown for these samples. We note that the 3.27 eV band can be observed, though weakly, from sample No. 2 and similar thick, undoped GaN/6H-SiC films at low excitation power densities.

Additional structure (unlabeled arrow in Fig. 1) is also found in this near-bandedge spectral region on the low-energy side of the 3.27 eV peak at approximately 3.24 eV and with associated GaN-like LO phonon replicas found on the low-energy shoulders of the LO phonon sidebands associated with the 3.27 eV SD-SA band. This additional PL band was first reported by Dingle and Ilegems [6] from PL studies of 250 μm -thick epitaxial layers of

GaN grown from the vapor phase on (0001)-oriented sapphire substrates. It was suggested by these workers that this emission is associated with a second SD-SA recombination system.

The dislocated nature of the GaN layers near the film/buffer layer interface may be the reason why the shallow donor - shallow acceptor recombination is so much stronger in the thin films ($t < 1 \mu\text{m}$) compared to what is observed from the 2.5 μm layers. The dislocation density within the first 0.5 μm of the GaN films grown using the high-temperature AlN buffer layers ($t = 100 \text{ nm}$) was found to be $\sim 1 \times 10^9 \text{ cm}^{-2}$, as determined from plan-view transmission electron microscopy [1]. Most noteworthy, the dislocation density was found to decrease rapidly (by \sim two orders of magnitude) with increasing film thickness. Thus, it is possible that the dislocations may be very efficient at trapping residual donors and acceptors leading to higher compensation near the film/buffer layer interface. However, it is also plausible that the strong SD-SA recombination observed from the $t = 0.7 \mu\text{m}$ GaN film arises from the tendency of point defects such as donors and acceptors to pile-up near interfaces.

The lowest energy band observed from these samples is a broad emission of Gaussian shape with peak energy near 2.2 eV (the so-called "yellow" emission band). The 2.2 eV band was found to be weaker than the SD-SA recombination for the thin GaN films and stronger than the 3.27 eV emission for the thick layers. The 2.2 eV band has been commonly observed to some degree of strength from all of the undoped GaN layers grown on sapphire substrates by OMCVD or MBE studied by our group [3,4] and from PL studies reported in the literature by numerous workers. The origin of this band is still under discussion. Ogino and Aoki assigned this recombination to donor-acceptor pairs involving shallow donors and deep acceptors [8]. One group has interpreted the results of their PL/hydrostatic pressure experiments to support this recombination model [9]. We have proposed that both capture and recombination processes involving EM donors, EM acceptors, and deep donors are needed to fully describe the origin of this band [3,4]. This model is supported by recent photoemission capacitance transient spectroscopy experiments which have revealed evidence for a series of deep-level states located $\sim 0.9 - 1.5 \text{ eV}$ below the conduction band edge [10]. It should be noted that there has been no definitive report to date of the chemical identification of the deep defect state that participates in the 2.2 eV emission band.

Optically-Detected Magnetic Resonance Found on the 2.2 eV Band

The ODMR spectra obtained at 24 GHz on the 2.2 eV emission bands from samples No. 1 and No. 2 with $B \perp c$ are shown in Fig. 2. Three resonances are revealed in these spectra. As discussed below, two of the features derive from the GaN epitaxial layers while the third line is attributed to the underlying 6H-SiC substrate.

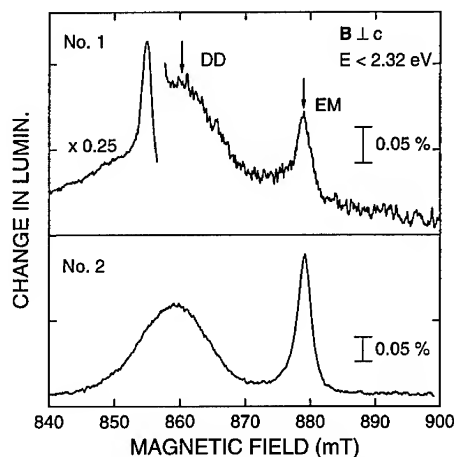


Fig. 2. ODMR spectra found at 24 GHz on emission less than 2.32 eV from a 0.7 μm -thick GaN layer (sample No. 1) and a 2.6 μm -thick GaN film (sample No. 2) with $B \perp c$. The feature observed from sample No. 1 at 855 mT is due to residual N donors detected on weak emission from the underlying 6H-SiC substrate.

tion light incident on the substrate side of sample No. 1 and from the non-observation of the N donor signal on emission less than 2.32 eV from the 2.6 μm -thick GaN films (bottom spectrum in Fig. 2).

Optically-Detected Magnetic Resonance Found on the Shallow Donor - Shallow Acceptor Recombination

The ODMR spectrum obtained at 35 GHz on the shallow donor - shallow acceptor recombination (ZPL @ 3.27 eV) from sample No. 1 with $B \parallel c$ is shown in Fig. 3. A single ODMR feature (labeled EM) is found on this emission. The amplitude of the ODMR signal is quite small ($\Delta I/I \sim 0.015\%$). Also, the g-tensor of this feature is identical to that found for the ODMR resonance labeled EM detected on the 2.2 eV emission band from this sample (see Fig. 2). Thus, this line is also assigned to electrons bound at EM-donors.

No additional resonances were detected on the SD-SA recombination in this study from wider magnetic field scans with $B \parallel c$ or for any field orientation. In particular, an ODMR feature associated with shallow acceptors, as might be expected, was not observed on this emission.

Previous studies have clearly demonstrated for particular GaN films that the four-fold degeneracy of the $J = 3/2$ upper valence band is removed due to the wurtzite structure crystal field. In particular, recent PL and reflectance studies [12] of high-quality 4.2 μm -thick GaN epitaxial layers have confirmed the results of reflectance studies [5] of 100 μm -thick GaN films reported nearly 25 years ago that the $J_z = \pm 3/2$ (heavy hole) ground-state valence band is split

The ODMR feature labeled EM is a sharp resonance (FWHM ~ 3 mT) with $g_{\parallel} = 1.9515 \pm 0.0002$ and $g_{\perp} = 1.9485 \pm 0.0002$, where \parallel refers to the c-axis. The line labeled DD is a broader resonance (FWHM ~ 13 mT) with $g_{\parallel} = 1.989 \pm 0.001$ and $g_{\perp} = 1.992 \pm 0.001$. This feature was much better resolved for sample No. 1 from studies in the 35 GHz spectrometer due to the increased spread in resonance field positions of the three peaks. We note that the same two resonances have been found on the 2.2 eV broad emission bands from undoped GaN films grown by several laboratories on sapphire substrates [2-4]. As discussed previously, the resonances have been assigned to effective-mass (EM) and deep donor (DD) states, respectively, in these undoped GaN epitaxial layers.

The feature observed from sample No. 1 at 855 mT is due to residual N donors ($g=2.005$) found on deep emission from the underlying 6H-SiC substrate [11]. The substrate emission is produced by the penetration of the 351.1 nm excitation light through the thin GaN film and, perhaps in part, by the GaN band-edge excitonic emission since this energy is larger than the 6H-SiC bandgap (~ 3.1 eV). This was confirmed from ODMR studies performed with the 351.1 nm excita-

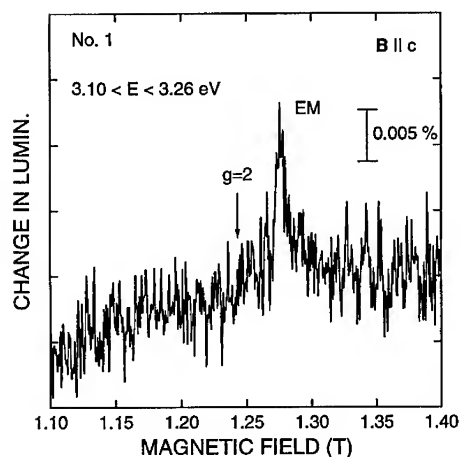


Fig. 3. ODMR spectrum obtained at 35 GHz on shallow donor - shallow acceptor recombination from GaN film No. 1 with $B \parallel c$.

No. 1 is of similar thickness, these ODMR results provide evidence that the energy splittings of the $J_z = \pm 3/2$ and $\pm 1/2$ valence bands caused by the random strain fields that arise in this thin GaN layer are comparable ($\sim 6 - 8$ meV) to the splitting of the heavy and light hole valence bands produced by the wurtzite structure crystal field. Thus, the shallow acceptor states in this film are not all associated with the $J_z = \pm 3/2$ ground-state valence band as would be expected for a perfect wurtzite crystal. This has two important consequences which can account for the ODMR observations on this emission noted above. First, the shallow acceptors participating in the SD-SA recombination from this layer will be spin-thermalized. Based on the observations and analyses of ODMR found on SD-SA recombination from Zn-doped InP [16], the weakness of the GaN EM donor resonance on the 3.27 eV band is attributed to the weak spin-dependence of this recombination mechanism involving spin-thermalized shallow acceptors. Second, the EM acceptor resonance will broaden beyond observability through the spreading of the acceptor g -values [17].

CONCLUSIONS and FUTURE WORK

Photoluminescence and optically-detected magnetic resonance experiments have been performed on undoped GaN layers grown on 6H-SiC substrates by OMCVD with the use of high-temperature AlN buffer layers. PL and ODMR results were obtained for 0.7 and 2.6 μm -thick films. The defects observed in these films are compared with those found from previous ODMR studies of undoped GaN layers grown on sapphire substrates. In addition, the first observation of magnetic resonance on shallow donor - shallow acceptor recombination from undoped GaN is reported in this work.

Several conclusions are drawn from this work. First, the correlation of the intensity of the SD-SA recombination with the film thickness as revealed by the PL studies indicates that the layers are more highly compensated near the film/buffer layer interface. Second, the ODMR found on the 2.2 eV emission band from GaN films grown on 6H-SiC substrates is the same as that detected on this band from GaN layers grown on sapphire substrates. Third, the influence of the random strain fields in these films is revealed by the weakness of the shallow donor signal and the non-observation of an EM acceptor resonance as found from the magnetic resonance studies of the SD-SA recombination.

These PL and ODMR results suggest some issues that still need to be addressed and some interesting future work. First, in addition to the unknown chemical identity of the residual

above the $J_z = \pm 1/2$ (light hole) valence band by $\sim 6 - 8$ meV. The expected g -tensor for shallow hole states associated with the $J_z = \pm 3/2$ ($\pm 1/2$) valence band is $g_{\parallel} \sim 4$ (2), $g_{\perp} = 0$ (4) [Ref. 13]. Such highly anisotropic g -tensors have been observed from ODMR studies on emission involving shallow acceptors from bulk 6H-SiC [14] and from bulk CdS [15], semiconductors with similar hexagonal crystal structure, valence band parameters, and shallow acceptor binding energies.

Both the weakness of the effective-mass donor signal and the non-observation of an EM acceptor resonance on the SD-SA emission from sample No. 1 are attributed to the influence of the random strain fields in this film. As noted above, the dislocation density was found to be $\sim 1 \times 10^9 \text{ cm}^{-2}$ for 0.5 μm GaN films grown on 6H-SiC using the high-temperature AlN buffer layers [1]. This dislocation density is still lower than that typically found for films of comparable thickness grown on sapphire substrates. Since sample

donors, the identity of the residual acceptors in these films is also not well-established. One candidate for the residual shallow acceptors is C as suggested by recent workers [18]. There has been evidence from doping studies that C can behave as a shallow acceptor in GaN [19]. Second, this work provides evidence that an observation of residual shallow acceptors in GaN films via magnetic resonance is quite difficult in the presence of large dislocation densities. A better chance to observe magnetic resonance of shallow acceptors (associated with a unique valence band edge) on SD-SA recombination should occur for GaN films with much lower dislocation densities, such as recently found for thick ($t > 1.5 \mu\text{m}$) GaN films grown using high-temperature AlN buffer layers on 6H-SiC substrates [1]. The SD - SA recombination observed from such films investigated in this study was too weak to study via ODMR. This opportunity may arise, also, from the growth of GaN homoepitaxial films.

ACKNOWLEDGMENTS

S.W. Brown acknowledges support from a NRC-NRL Cooperative Research Associateship. Also, this work was supported in part by the Office of Naval Research.

REFERENCES

1. T.W. Weeks Jr., M.D. Bremser, K.S. Ailey, E. Carlson, W.G. Perry, and R.F. Davis, *Appl. Phys. Lett.* **67**, 401 (1995).
2. E.R. Glaser, T.A. Kennedy, H.C. Crookham, J.A. Freitas, Jr., M. Asif Khan, D.T. Olson, and J.N. Kuznia, *Appl. Phys. Lett.* **63**, 2673 (1993).
3. E.R. Glaser, T.A. Kennedy, K. Doverspike, L.B. Rowland, D.K. Gaskill, J.A. Freitas Jr., M. Asif Khan, D.T. Olson, and J.N. Kuznia, *Phys. Rev. B* **51**, 13326 (1995).
4. E.R. Glaser, in *Proceedings of the 18th International Conference on Defects in Semiconductors*, to be published.
5. R. Dingle, D.D. Sell, S.E. Stokowski, and M. Ilegems, *Phys. Rev. B* **4**, 1211 (1971).
6. R. Dingle and M. Ilegems, *Solid State Commun.* **9**, 175 (1971).
7. W.E. Carlos, J.A. Freitas, Jr., M. Asif Khan, D.T. Olson, and J.N. Kuznia, *Phys. Rev. B* **48**, 17878 (1993).
8. T. Ogino and M. Aoki, *Jpn. J. Appl. Phys.* **19**, 2395 (1980).
9. T. Suski, P. Perlin, H. Teisseyre, M. Leszczynski, I. Grzegory, J. Jun, M. Bockowski, S. Porowski, and T.D. Moustakas, *Appl. Phys. Lett.* **67**, 2188 (1995), and references therein.
10. W. Götz, N.M. Johnson, R.A. Street, H. Amano, and I. Akasaki, *Appl. Phys. Lett.* **66**, 1340 (1995).
11. N.G. Romanov, V.V. Vetrov, and P.G. Baranov, *Sov. Phys. Semicond.* **20**, 96 (1986).
12. W. Shan, T.J. Schmidt, X.H. Yang, S.J. Hwang, J.J. Song, and B. Goldenberg, *Appl. Phys. Lett.* **66**, 985 (1995).
13. G.E. Pake and T.L. Estle, *The Physical Principles of Electron Paramagnetic Resonance* (Benjamin, Reading, MA, 1973).
14. Le Si Dang, K.M. Lee, G.D. Watkins, and W.J. Choyke, *Phys. Rev. Lett.* **45**, 390 (1980).
15. J.L. Patel, J.E. Nicholls, and J.J. Davies, *J. Phys. C* **14**, 1339 (1981).
16. I. Viohl, W.D. Ohlsen, and P.C. Taylor, *Phys. Rev. B* **44**, 7975 (1991).
17. See, e.g., F. Mehran, T.N. Morgan, R.S. Title, and S.E. Blum, *J. Mag. Res.* **6**, 620 (1972).
18. S. Fischer, C. Wetzel, E.E. Haller, and B.K. Meyer, *Appl. Phys. Lett.* **67**, 1298 (1995).
19. C.R. Abernathy, J.D. MacKenzie, S.J. Pearton, and W.S. Hobson, *Appl. Phys. Lett.* **66**, 1969 (1995).

MAGNETIC RESONANCE STUDIES OF RECOMBINATION PROCESSES IN GaN-BASED LIGHT EMITTING DIODES

W.E. Carlos*, E.R. Glaser*, T.A. Kennedy* and S. Nakamura**

*Naval Research Laboratory, Washington, D.C.

**Nichia Chemical Industries, Ltd., 491 Oka, Kaminaka, Anan, Tokushima 774, Japan.

ABSTRACT

Magnetic resonance techniques are used to study the recombination processes in GaN-based light emitting diodes (LEDs). Electrically-detected magnetic resonance (EDMR) and electroluminescence-detected magnetic resonance (ELDMR) results on InGaN/AlGaIn double heterostructures are presented for blue and green LEDs. In either technique our signals are dominated by a broad feature that we ascribe to a deep Zn-related acceptor. Our ELDMR measurements show that this is associated with the blue or green emission. Our EDMR measurements resolve a second center that is tentatively identified as a deep donor trap.

INTRODUCTION

Recent advances in the growth and processing of GaN-based materials¹ have made possible devices such as efficient blue and green light emitting diodes (LEDs).^{2,3} These devices have impressive external quantum efficiencies (~1-10%) in spite of high dislocation densities that would quench the luminescence from LEDs based on other semiconductors. Recently, we have applied electroluminescence detection of magnetic resonance (ELDMR) and electrical detection of magnetic resonance (EDMR) to double heterostructure blue LEDs in an effort to understand the radiative recombination processes in GaN-based materials and devices.⁴ In this work we compare the green LEDs, which have a higher InN mole fraction in the optically-active region, with the blue diodes. These resonance techniques have many advantages over conventional electron spin resonance (ESR), including greatly enhanced sensitivity and selective detection of centers that are important to recombination processes. Previously, both techniques have been applied to polymer-based⁵ and amorphous Si-based LEDs.⁶ EDMR has long been applied to Si devices⁷ and has recently been employed as a probe of compound semiconductors.^{4,8} ESR and ODMR (optically detected magnetic resonance in which changes in photoluminescence are monitored) have been applied to doped and undoped wurtzite GaN thin films.^{9,10,11,12} The observed resonances include an effective mass (EM) donor, a deep double donor and a deep Mg-related acceptor state (in Mg-doped films).

Devices used in this work are double heterostructure AlGaIn/InGaIn LEDs whose structure and manufacture have been discussed in detail in previous publications.² These devices, based on wurtzite-phase material grown on sapphire, rely on donor-acceptor pair recombination for their intense emission. The bottom contact is made through a relatively thick (~4 μm) layer of n^+ GaN. The active device, grown on this GaN layer, is a 50 nm layer of InGaIn co-doped with Si and Zn sandwiched between n and p -type layers of $\text{Al}_{0.15}\text{Ga}_{0.85}\text{N}$ that, in addition to serving as sources of electrons and holes, respectively, help to confine the carriers in the InGaIn layer. Zinc is used as the acceptor in the InGaIn

because it forms deeper levels in GaN than Mg, thereby shifting the luminescence to somewhat lower energies and minimizing the In mole fraction (and the accompanying strain) in the active layer. Two variations of the device were studied, differing only in the InN mole fraction in the active InGaN layer comprised either of $\text{In}_{0.06}\text{Ga}_{0.94}\text{N}$ (referred to as blue diodes) or $\text{In}_{0.23}\text{Ga}_{0.77}\text{N}$ (referred to as green diodes). The c-axis of the thin-film LED was always perpendicular to the magnetic field and light was extracted using a quartz light pipe and detected by a UV-enhanced Si photodiode. Electroluminescence (EL) spectra were measured using a 0.22 m double grating spectrometer. The magnetic resonance apparatus is based on a Varian E9 ESR X-band (9.25 GHz.) spectrometer and a p-i-n modulator for microwave power modulation. Samples were cooled to approximately 2 K using a liquid helium flow cryostat and biased with a constant current. ELDMR signals were detected as changes in the EL in-phase with the microwave power modulation and EDMR signals were obtained by detecting the AC voltage across the sample in-phase with magnetic field modulation.

LOW TEMPERATURE ELECTROLUMINESCENCE

The intense room temperature blue and green EL from these devices has attracted considerable interest recently. Our magnetic resonance measurements require cryogenic temperatures and relatively low biases; therefore, an examination of the low temperature, low current EL is important in interpreting our results. EL spectra taken at $T=2$ K for typical blue and green diodes are shown in Fig. 1. Our low temperature EL spectra both show two distinct peaks. To analyze the two peak structures further we have fit each spectrum to a pair of gaussian lines. We believe the peaks at ~ 2.7 eV (blue LEDs) and ~ 2.4 eV (green LEDs) are due to a deep donor to Zn-acceptor recombination.⁴ In both diodes there is a second line at ~ 2.9 eV that, other than differences in relative intensity, is essentially the same for the two diodes, as illustrated in the inset to Fig. 1. We also note that the relative intensity of this line increases with increasing bias for both diodes. While it could be argued that this band in the green diodes is due a near bandedge emission (energy gap of $\text{In}_{0.23}\text{Ga}_{0.77}\text{N} \approx 3.00$ eV), this would require a separate explanation for the existence such a band at the same energy in the blue diode and the lack of a similar band, presumably shifted down in energy, in the green diode. Since this EL line is independent of In fraction, we suggest that this line is due to a transition outside the InGaN layer, most probably in one of the AlGaIn layers.

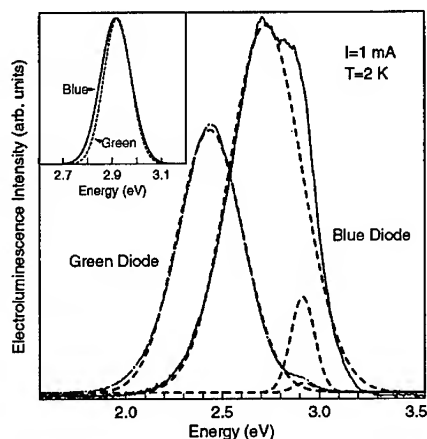


Figure 1 The electroluminescence spectra of blue and green LEDs. The dashed lines are the results of fitting each spectrum to two gaussians. In the inset the fits to the feature at ~ 2.9 eV are compared.

ELECTROLUMINESCENCE DETECTED MAGNETIC RESONANCE

Results of ELDMR measurements for the two diodes are shown in Fig. 2. The signals represent much smaller changes ($\sim 0.001\%$) in the luminescence level than were typically observed in ODMR measured by monitoring the photoluminescence ($\sim 0.1\%$) from thin films of GaN. To establish that the magnetic resonance signal was due to small changes in the blue or green EL rather than larger fractional changes in a weak deep emission we inserted bandpass filters, peaked at 465 nm for the blue diode and 520 nm for the green diode in front of the detector. The same resonance with the same relative intensity is observed with the appropriate filter inserted as with no filter, associating this resonance with the blue and green EL bands in the different LEDs. The bandwidths of the filters are large enough to prevent us from definitively ruling out any involvement of the weak blue EL at 2.9

eV in the ELDMR signal. However, the intensities of the ELDMR signals are comparable for the blue and green diodes, while the relative intensity of the 2.9 eV band is much weaker in the green diode, suggesting that this band is not involved in the ELDMR. For this orientation ($B_{\perp}c$ -axis) the resonance has a Landé g value of 2.00 and a full width at half maximum of ~ 18 mT, both of which are very similar to the resonance assigned to a deep Mg-related acceptor in GaN:Mg films. The resonance is not due to a shallow EM-like acceptor state since for this orientation one expects¹³ $g \sim 0$ rather than ~ 2 as we observe. The two donor states observed in GaN films both have g values less than 2 and InN alloying should decrease the energy gaps and increase the spin-orbit splittings, thus increasing the shift of the g value from the free electron value of 2.0023. Based on the similarities with the Mg resonance and its role in the blue or green EL, we assign the observed resonance to a deep Zn-related acceptor state in the InGaN layer.

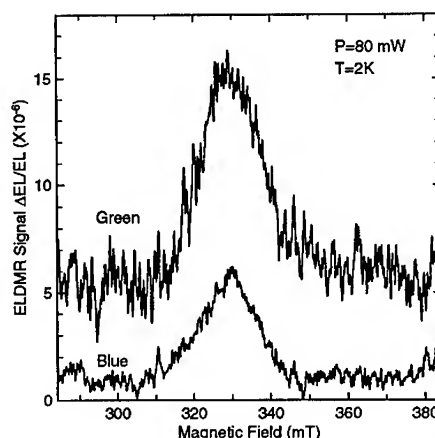


Figure 2 The ELDMR signals for blue and green diodes. The higher amplitude and lower signal to noise ratio for the green diode is a result of lower EL intensity.

ELECTRICALLY DETECTED MAGNETIC RESONANCE

EDMR signals were obtained by monitoring the effects of changes in the recombination rate and hence, the recombination current in the LEDs. As mentioned previously, the sample is biased at a constant current and the ac voltage in-phase with the magnetic field modulation is detected. The voltage across the sample includes several parasitic voltages, e.g., those due to high resistance contacts and to the layer resistances. While these become more significant at low temperatures, they are generally not related to electron-hole recombination and should not contribute to the magnetic resonance signal. We believe that the observed signals are due to changes in the recombination rate in the InGaN/AlGaIn hetero-junction region. Examples of the EDMR spectra

are shown in Fig. 3. The spectra consist of a sharp feature superimposed on a dominant broad line. For this orientation ($\mathbf{B} \perp c$ -axis) the broad resonance has a Landé g value of ~ 2.00 and a full width at half maximum of ~ 22 mT and we, therefore, associate this resonance with a deep Zn-related acceptor level observed in ELDMR. The narrow line has a g value of 1.990 ± 0.005 (blue diodes) and 1.997 ± 0.005 (green diodes). It is not certain whether the small difference in g value for the two diodes is significant. However, either value is in good agreement with that of the deep donor observed in ODMR, although the linewidths are only about half as large. Based on the g value agreement and the difference in linewidth, we assign this resonance to a similar but not identical deep donor to that observed by ODMR in GaN thin films. In Fig. 3 we marked the expected positions of an EM donor at $g \approx 1.94$ (InGaN in blue diodes), $g \approx 1.91$ (InGaN in green diodes) or $g \approx 1.97$ (AlGaIn layer), based on our observations in GaN films and accounting for InN or AlN alloying. Note that we do not observe this resonance in either diode.

The peak positions of the two resonances observed in EDMR are only ~ 2 mT apart and the sharp line represents only $\sim 10\%$ of the total intensity. Given the relative strengths of the two lines, their widths and their separation, it is reasonable that the narrow line is only resolved because of the derivative lineshape. A numerical integration of the EDMR signal gives a lineshape very similar to the ELDMR signal with no obvious second line.¹⁴

The intensity of the resonance signal depends on the bias conditions, i.e., on the rate at which electrons and holes are injected into the active region. The relationship between the EDMR signal intensity and the applied bias voltage for the two diodes is illustrated in Fig. 4. The signal intensity is $\delta V(dI/dV)/I$ scaled to account for the field modulation amplitude.¹⁵ The two diodes give

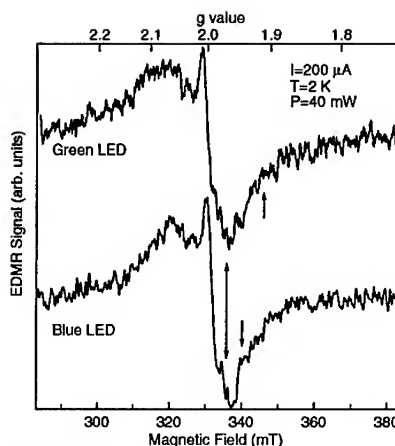


Figure 3 The EDMR spectra for the two diodes. The single headed arrows indicate expected positions for an effective mass donor resonance in the InGaIn layers, while the double headed arrow indicates the expected position for such a resonance in an AlGaIn layer.

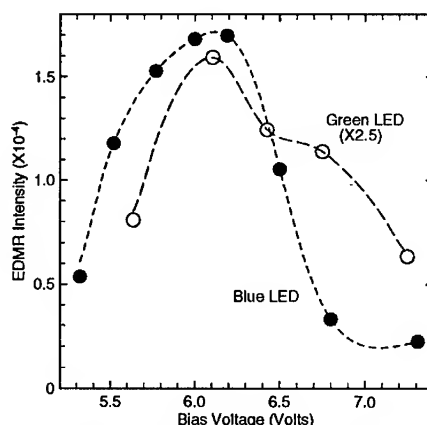


Figure 4 The intensities of the EDMR as a function of bias for the blue and green LEDs. The dashed lines are intended as aids to the eye.

a maximum EDMR signal at very similar bias voltages. The currents at this voltage are significantly different ($\sim 100 \mu\text{A}$ for the blue LED vs. $\sim 500 \mu\text{A}$ for the green LED). This may be because of the higher leakage current due to strain-induced lattice defects in the InGaN layer of the green LED. As noted above, the bias voltage contains parasitic voltages that add to voltage across the active region. However, these are expected to be similar for the two diodes. The ELDMR intensity of the blue LED has a similar functional form to that of the EDMR and the magnitudes are reasonably close.⁴ The EL signal from the green diode is more dependent on the magnetic field at that causes a significant background signal in the ELDMR, particularly at low bias currents. This makes extraction of a reliable intensity difficult.

SUMMARY

In summary we have detected magnetic resonance effects in both the electroluminescence and the electrical characteristics of GaN-based double heterostructure LEDs. These techniques can be powerful probes of the recombination mechanisms in semiconductor devices, as is demonstrated by our observation of a Zn-related acceptor and a deep donor in both diodes. The fact that these two resonances are so similar, i.e., insensitive to In mole fraction, in the two diodes is consistent with our association of them with deep levels. Clearly much work still needs to be done to understand the radiative and nonradiative recombination processes in GaN-based materials and devices fully.

REFERENCES

1. H. Amano, N. Sawaki, I. Akasaki and Y. Toyoda, *Appl. Phys. Lett.* **48**, 353 (1986); H. Amano, M. Kitoh, K. Hiramatsu and I. Akasaki, *J. Electrochem. Soc.* **137**, 1639 (1990); S. Nakamura, M. Senoh and T. Mukai, *Jpn. J. Appl. Phys.* **30**, L1708 (1991).
2. Shuji Nakamura, Takashi Mukai and Masayuki Senoh, *Appl. Phys. Lett.* **64**, 1687 (1994); *J. Appl. Phys.* **76**, 8189 (1994).
3. Shuji Nakamura, Masayuki Senoh, Naruhito Iwasa and Shin-ichi Nagahama, *Appl. Phys. Lett.* **67**, 1868 (1995); *Jpn. J. Appl. Phys.* **34**, L797 (1995).
4. W.E. Carlos, E.R. Glaser, T.A. Kennedy and S. Nakamura, *Appl. Phys. Lett.* **67**, 2376 (1995); *Proceedings of 1995 International Conference on Defects in Semiconductors*, to be published.
5. L.S. Swanson, J. Shinar, A.R. Brown, D.D.C. Bradley, R.H. Friend, P.L. Burn, A. Kraft and A.B. Holmes, *Phys. Rev. B* **46**, 15072 (1992).
6. K.P. Homewood, B.C. Cavenett, I.G. Austin, T.M. Searle, W.E. Spear and P.G. Lecomber *J. Phys. C* **17**, L103 (1984).
7. D.J. Lépine, *Phys. Rev. B* **6**, 436 (1972); I. Solomon, *Solid State Commun.* **20**, 215 (1976); F.C. Rong, G.J. Gerardi, W.R. Buchwald, E.H. Poindexter, M.T. Umlor, D.J. Keeble and W.L. Warren, *Appl. Phys. Lett.* **60**, 610 (1992); B. Stich, S. Greulich-Weber and J.-M. Spaeth, *J. Appl. Phys.* **77**, 1546 (1995).
8. N.M. Reinacher, M.S. Brandt and M. Stutzmann, *Proceedings of 1995 International Conference on Defects in Semiconductors*, to be published.
9. W.E. Carlos, J.A. Freitas, Jr., M. Asif Khan, D.T. Olson and J.N. Kuznia, *Phys. Rev. B* **48**, 17878 (1993).

10. E.R. Glaser, T.A. Kennedy, K. Doverspike, L.B. Rowland, D.K. Gaskill, J.A. Freitas, Jr., M. Asif Khan, D.T. Olson, J.N. Kuznia, and D.K. Wickenden, *Phys. Rev. B* **51**, 13326 (1995).
11. M. Kunzer, U. Kaufmann, K. Maier, J. Schneider, N. Herres, I. Akasaki, and H. Amano, *Mat. Sci. Forum* **143-147**, 87 (1994); K. Maier, M. Kunzer, U. Kaufmann, J. Schneider, B. Monemar, I. Akasaki and H. Amano, *Mat. Sci. Forum* **143-147**, 93 (1994).
12. D.H. Hoffmann, D. Kovalev, G. Steude, B.K. Meyer, A. Hoffmann, L. Eckey, R. Heitz, T. Detchprom, H. Amano and I Akasaki, *Phys. Rev. B*, to be published.
13. Le Si Dang, K.M. Lee, G.D. Watkins and W.J. Choyke, *Phys. Rev. Lett.* **45**, 390 (1980).
14. W.E. Carlos, E.R. Glaser, T.A. Kennedy and S. Nakamura, *J. Electronic Mat.*, to be published.
15. See, for example, G.V.H. Wilson, *J. Appl. Phys.* **41**, 98 (1963) for an analysis of the relative amplitudes of the harmonics of an absorption signal detected with magnetic field modulation.

ON COMPENSATION AND IMPURITIES IN STATE-OF-THE-ART GaN EPILAYERS GROWN ON SAPPHIRE

A.E. WICKENDEN*, D.K. GASKILL*, D.D. KOLESKE*, K. DOVERSPIKE**, D.S. SIMONS† and P.H. CHI†

* Naval Research Laboratory, Laboratory for Advanced Material Synthesis, Washington, D.C. 20375

** Currently at Hewlett-Packard, San Jose, CA 95131

† National Institute of Standards and Technology, Gaithersburg, MD 20899

ABSTRACT

A comparison between 300 K electron transport data for state-of-the-art wurtzite GaN grown on sapphire substrates and corresponding theoretical calculations shows a large difference, with experimental mobility less than the predicted mobility for a given carrier concentration. The comparison seems to imply that GaN films are greatly compensated, but the discrepancy may also be due to the poorly known values of the materials parameters used in the calculations. In this work, recent analysis of transport and SIMS measurements on silicon-doped GaN films are shown to imply that the compensation, N_A/N_D , is less than 0.3. In addition, the determination of an activation energy of 34 meV in a GaN film doped to a level of $6 \times 10^{16} \text{ cm}^{-3}$ suggests either that a second, native donor exists in the doped films at a level of between $6 \times 10^{16} \text{ cm}^{-3}$ and $1 \times 10^{17} \text{ cm}^{-3}$, or that the activation energy of Si in GaN is dependent on the concentration, being influenced by impurity banding or some other physical effect. GaN films grown without silicon doping are highly resistive.

INTRODUCTION

Significant advances have recently been reported on the performance of devices based on the III-N material system for both opto-electronic as well as high power and high temperature electronic applications. For the fabrication of high frequency field effect transistors (FET's), thin, high mobility active layers, typically grown on highly resistive buffer layers, are required. Optimal device performance is dependent upon optimization of the transport properties in the active layer, hence a comparison of active layer transport properties to thick film state-of-the-art GaN properties is desired. Previously, we have reported the growth of high mobility silicon-doped FET structures on highly resistive GaN buffer layers¹. In the present work the properties of lightly Si-doped and unintentionally doped thick ($\sim 3 \mu\text{m}$) GaN layers are investigated as a preliminary step toward achieving the stated objective.

EXPERIMENT

An inductively heated, water-cooled, vertical organometallic vapor phase epitaxy reactor operated at 57 torr (7,600 Pa) was used for the growth of the GaN films as previously described in the literature². The films discussed in this paper were grown on a-plane (11 $\bar{2}$ 0) sapphire substrates. An AlN nucleation layer of approximately 20 nm thickness was deposited at 450 °C, using triethylaluminum and ammonia (NH₃) as the source reagents. The GaN films were grown using trimethylgallium (TMG) and NH₃ at a growth temperature of 1040 °C. Disilane, in a concentration of 8 ppm in H₂, was used as the dopant source. Variable temperature Hall measurements were performed using the van der Pauw technique with a cloverleaf geometry and indium contacts at a magnetic field of 0.2 T. The current-voltage characteristics of highly resistive GaN films were determined by a 2-point surface probe. In these highly resistive films, surface breakdown voltages in excess of 1200 V were typical, using a probe spacing of approximately 3 mm.

High-mass-resolution secondary ion mass spectroscopy (SIMS) was performed in an ion microscope operating with a Cs^+ beam, as previously described³. Pieces of a representative highly resistive, unintentionally doped GaN film were implanted at room temperature with 200 keV ^{29}Si ions, to a dose of $5 \times 10^{14} \text{ cm}^{-2}$. The reference standard was profiled by SIMS using the same conditions as the GaN films being investigated to generate the relative sensitivity factor of Si in the GaN matrix. The depth scale of the SIMS profiles was established by measuring the crater depths with a stylus profilometer.

RESULTS AND DISCUSSION

A sequence of Si-doped GaN films was grown, varying the $[\text{Si}_2\text{H}_6]/[\text{TMG}]$ ratio over the range 1.4×10^{-6} to 6.0×10^{-6} . The relationship of the 300 K Hall electron concentration to the disilane dopant flow is illustrated in Figure 1, and is seen to be linear. A film grown with no disilane flow was determined to be highly resistive. The ability to controllably dope the GaN films demonstrated here validates their potential for FET applications.

Variable temperature Hall measurements were performed on three of the Si-doped GaN films of this series. The Hall electron concentration and mobility are plotted as functions of temperature in Figure 2. The data was analyzed using a single, monovalent donor model of density N_D , ionization energy E_D and degeneracy $= 1/2$, in the Boltzman approximation for a non-degenerate semiconductor:

$$N = \frac{2 N_D (1 - K)}{\left(1 + \frac{K N_D}{x}\right) + \left[\left(1 + \frac{K N_D}{x}\right)^2 + \frac{4 N_D (1 - K)}{x}\right]^{1/2}} \quad (1)$$

where $K = N_A/N_D$ is the compensation ratio, and $x = 1/2 (N_C \exp(-E_D/kT))$, where N_C is the density of states at the conduction band edge⁴. We assumed a Hall scattering factor, $r_H = 1.1$, for all temperatures⁵. Fits to the data were constrained to values for an electron effective mass $0.18 m_e \leq m^* \leq 0.22 m_e$, a donor energy value $14 \text{ meV} \leq E_D \leq 40 \text{ meV}$, and a compensation ratio $0 \leq K \leq 1$. In the case of the higher doped samples, as seen in Figure 2b, the data showed significant parallel-conduction-type behavior at low temperatures. The single-donor model does not apply for values of $1000/T$ greater than $10\text{-}20 \text{ K}^{-1}$ in samples where curvature of the data due to parallel conduction is seen.

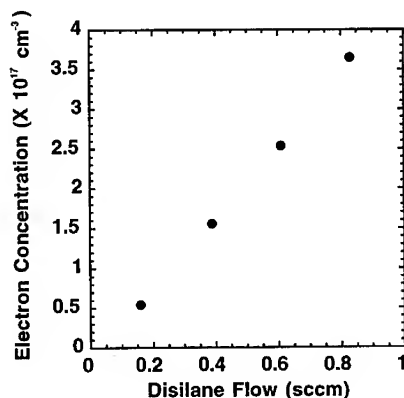


Figure 1. Relationship of 300K Hall electron concentration to disilane dopant flow.

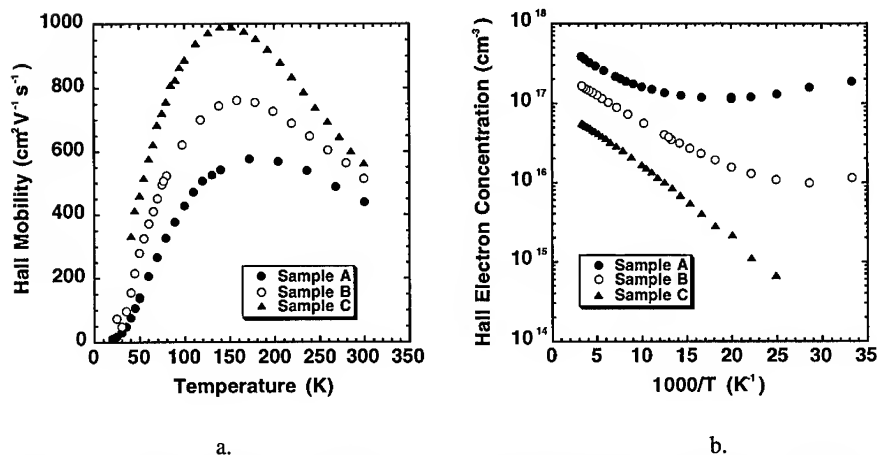


Figure 2. a.) Hall mobility vs temperature and b.) Hall electron concentration vs $1000/T$ for the samples listed in Table I.

The results of the curve fitting analysis, using $K = 0$ and $m^* = 0.22 m_e$ (Samples A and B) or $0.18 m_e$ (Sample C), as well as the measured 300 K Hall electron concentration and SIMS silicon concentration, are given in Table I for the three samples. In the highest doped Sample A, a fit to data up to $1000/T = 10 \text{ K}^{-1}$ yielded a derived value of N_D in excellent agreement with the silicon concentration of $8 \times 10^{17} \text{ cm}^{-3}$ seen in SIMS analysis of a sample grown under identical conditions and with identical 300 K Hall transport properties. The fit for the mid-doped Sample B was made to data up to $1000/T = 20 \text{ K}^{-1}$, and the derived N_D value is in close agreement with the silicon concentration measured by SIMS for a sample with the same silicon doping level but slightly higher V/III ratio during film growth. The fit for the lowest-doped Sample C was made to data up to $1000/T = 25 \text{ K}^{-1}$. SIMS analysis was not performed on this sample.

The ionization energy for the moderately doped Sample B, taken from the fit described above, agrees well with the expected energy of $26 \pm 1 \text{ meV}$ value previously reported⁶, and is in close agreement with the value of 28 meV reported by Hacke and co-workers⁷, as well as the value of 29 meV recently determined by Wang and co-workers in infrared absorption experiments on Si doped GaN films⁸. The highest doped film, Sample A, exhibits a smaller value of ionization energy, which may be explained by the effects of impurity banding. For Sample C, the film with the lowest Si concentration, an ionization energy of 34 meV was derived from fitting the Hall data, as shown in Figure 3. This energy level has previously been identified as being associated with a native donor in GaN films^{6, 9, 10}, and is of particular interest here since the films grown in this study without the introduction of Si exhibited highly resistive, semi-insulating type behavior.

In the case of each of the samples listed in Table I, the best fit to the data using the monovalent, single donor model occurred for $K = 0$. In the case of Sample A, an accurate fit to the data may not be possible due to the significant curvature in the data for $1000/T > 10 \text{ K}^{-1}$.

Table I. Results of Hall, SIMS and theoretical analysis of Si-doped films.

	Si_2H_6 flow	N300K Hall	E_D (calc)	N_D (calc)	SIMS Si Conc.
A	0.88 sccm	$3.8 \times 10^{17} \text{ cm}^{-3}$	19.8 meV	$7.9 \times 10^{17} \text{ cm}^{-3}$	$8 \times 10^{17} \text{ cm}^{-3}$
B	0.44 sccm	$1.6 \times 10^{17} \text{ cm}^{-3}$	26.5 meV	$3.1 \times 10^{17} \text{ cm}^{-3}$	$4 \times 10^{17} \text{ cm}^{-3}$
C	0.21 sccm	$5.4 \times 10^{16} \text{ cm}^{-3}$	36.0 meV	$9.4 \times 10^{16} \text{ cm}^{-3}$	N/A

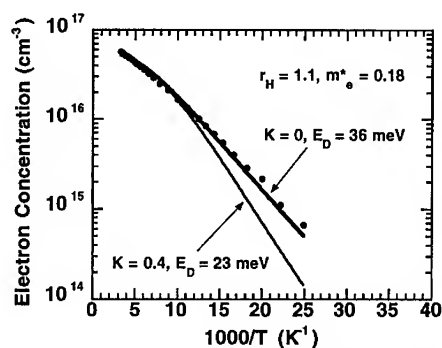


Figure 3. Data fit to low-doped Sample C, varying $K = N_A/N_D$ between 0 and 0.4.

Reliable fits to the data are achieved for data with substantially larger values of $1000/T$, in the range of 20-30 K^{-1} . The data from Sample B is a better candidate for analysis. Setting $K = 0.3$ while keeping $E_D = 26.5$ meV resulted in a very poor fit. The best attempt at fitting the data with this compensation resulted in $N_D = 4.4 \times 10^{17} \text{ cm}^{-3}$ and $E_D = 14.6$ meV. This derived value of N_D agrees with the SIMS concentration data within error limits. Attempts to fit the data with different values of E_D were worse, and m^* was varied in the range of 0.18 to 0.24 with no improvement. At best, a compensation ratio, $0 < K < 0.3$ may be deduced for this film, with $14.6 \text{ meV} < E_D < 26.5 \text{ meV}$. Enough data appears to be present for an adequate curve fit to Sample C. The best fit for this film occurs for $K = 0$ and $E_D = 36$ meV. Attempts to fit the data with larger values of K resulted in very poor fits to the data which could not be explained by the curvature at low temperatures. Figure 3 illustrates the fit to this set of data for two sets of conditions, $K = 0$ with $E_D = 36$ meV and $K = 0.4$ with $E_D = 23$ meV (the best fit for the $K = 0.4$ case). Further attempts at decreasing K to 0.25 and 0.1 showed improvements in the curve fit at high temperatures, but deviated from the data for $1000/T > 12 \text{ K}^{-1}$. Fitting attempts with $K = 0$ and $E_D = 26.5$ meV were very poor. Thus, the model implies that this sample is not strongly compensated, with a probable compensation ratio $K < 0.1$.

Figure 4 illustrates the relationship between the Si concentrations measured by SIMS and calculated values of N_D assuming $K = 0$ for Si-doped GaN films. Data from the samples in

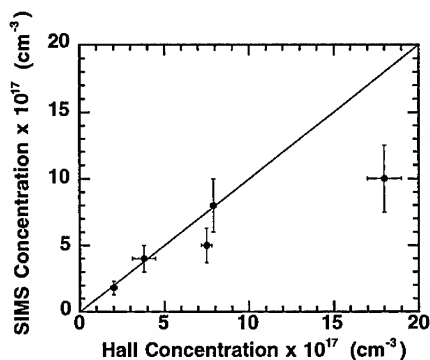


Figure 4. Relative agreement between N_D value derived from model and SIMS data.

Table I, as well as higher doped films from a previous study³, are plotted. For the highest doped film, the fit to the data was made assuming $E_D = 0$, as an approximation for a degenerately doped film. Consistency of the model with the empirical data is evident for the samples with low concentrations of Si. The implication of the validity of the model in this doping range is that compensation is low. Divergence of the data occurs for the more highly doped GaN films. Even using conservative estimates of error, the model predictions are in excess of measured Si concentrations. An additional source of electrons is implied which should be included in the analysis.

CONCLUSIONS

We have shown, based on analysis of variable temperature Hall measurements using a single-donor model, that the compensation in our Si-doped GaN films lies in the range $0 < N_A/N_D < 0.3$. This assertion is supported by the variable temperature Hall data from the lightly-doped Sample C, which exhibits no curvature of the data at electron concentrations of less than $1 \times 10^{15} \text{ cm}^{-3}$.

The data for the series of Si-doped GaN films presented in this study may suggest that a second, native donor exists in the doped films at a concentration between $6 \times 10^{16} \text{ cm}^{-3}$ and $1 \times 10^{17} \text{ cm}^{-3}$. Alternatively, the data may suggest that the activation energy of Si in GaN is dependent on the Si concentration, being influenced by impurity banding to and perhaps below a concentration of $6 \times 10^{16} \text{ cm}^{-3}$, or by the formation of point defects upon varying the Fermi level in the GaN films, as suggested by Boguslawski and co-workers¹¹. Initial analysis of the data using a two-donor model results in poorer fits to the data than using the single donor model. Additionally, the linear fit between the measured electron concentration and dopant flow, shown in Figure 1, would not be expected if two donors were present. Further studies are in progress to determine the nature of the variation of the Si activation energy in lightly-doped GaN films.

ACKNOWLEDGEMENTS

Helpful discussions with and preliminary curve fitting to a 2-donor model by Dr. W.J. Moore are gratefully acknowledged, as are electrical measurements of highly resistive GaN films by Mr. S.C. Binari.

REFERENCES

1. K. Doverspike, A.E. Wickenden, S.C. Binari, D.K. Gaskill and J.A. Freitas, Jr., to be published in *Topical Workshop on III-V Nitrides*, edited by K. Onabe, S. Fujishiro and H. Morkoc, Nagoya, Japan, 1995.
2. L.B. Rowland, K. Doverspike, A. Giordana, M. Fatemi, D.K. Gaskill, M. Skowronski and J.A. Freitas, Jr., *Silicon Carbide and Related Materials*, ed. M.G. Spencer, R.P. Devaty, J.A. Edmond, M.A. Khan, R. Kaplan and M. Rahman (Bristol: Institute of Physics, 1994), p. 429.
3. A.E. Wickenden, L.B. Rowland, K. Doverspike, J.A. Freitas, Jr., D.S. Simons and P.H. Chi, *J. Elect. Mat.*, **24** (11), 1547 (1995).
4. *Semiconductor Statistics*, J.S. Blakemore (Pergamon Press, New York, 1962).
5. This value of the Hall scattering factor is an average of the calculation in D.L. Rode, *Phys. Stat. Solidi B*, **55**, 687 (1973).
6. D.K. Gaskill, A.E. Wickenden, K. Doverspike, B. Tadayon and L.B. Rowland, *J. Elect. Mat.* **24** (11), 1525 (1995).
7. P. Hacke, A. Maekawa, N. Koide, K. Hiramatsu and N. Sawaki, *Jpn. J. Appl. Phys.* **33**(Part. 1, No. 12A), 6443-6447 (1994).
8. Y.J. Wang, R. Kaplan, H.K. Ng, K. Doverspike, D.K. Gaskill, T. Ikeda, I. Akasaki and H. Amano, presented at the Fall MRS Meeting, Boston, MA, 1995.
9. S. Nakamura, *Jpn. J. Appl. Phys.* **30**, L1705 (1991).
10. B.K. Meyer, D. Volm, A. Graber, H.C. Alt, T. Detchprohm, A. Amano and I. Akasaki, *Sol. St. Com.* **95**(9), 597 (1995).
11. P. Boguslawski, E.L. Briggs and J. Bernholc, *Phys. Rev. B*, **51**(23), 17255 (1995).

ROLE OF C, O AND H IN III-V NITRIDES

⁽¹⁾C. R. Abernathy, ⁽¹⁾S. J. Pearton, ⁽¹⁾J. D. MacKenzie, ⁽¹⁾J. W. Lee, ⁽¹⁾C. B. Vartuli
⁽²⁾R. G. Wilson, ⁽³⁾R. J. Shul, ⁽³⁾J. C. Zolper, and ⁽⁴⁾J. M. Zavada,

⁽¹⁾University of Florida, Gainesville FL 32611

⁽²⁾Hughes Research Laboratories, Malibu, CA 90265,

⁽³⁾Sandia National Laboratories, Albuquerque NM 87185; and

⁽⁴⁾U. S. Army Research Laboratory, RTP, NC 27709

ABSTRACT

The light ion impurities C, O and H have been implanted or diffused into GaN and related compounds and their effect on the electrical properties of these materials measured by Hall, C-V and SIMS as a function of annealing temperatures from 300-1100°C. While C in as-grown GaN appears to create an acceptor under MOMBE conditions, implanted C shows no measurable activity. Similarly, implanted O does not show any shallow donor activity after annealing at $\leq 700^\circ\text{C}$, but can create high resistivity regions ($10^6 \Omega/\square$) in GaN, AlInN and InGaN for device isolation when annealed at 500-700°C. Finally, hydrogen is found to passivate shallow donor and acceptor states in GaN, InN, InAlN and InGaN, with dissociation of the neutral complexes at $>450^\circ\text{C}$. The liberated hydrogen does not leave the nitride films until much higher annealing temperatures ($>800^\circ\text{C}$). Typical reactivation energies are $\sim 2.0\text{eV}$ for impurity-hydrogen complexes.

INTRODUCTION

The most common impurities in GaN are probably C, O and H from the growth precursors $[(\text{C}_2\text{H}_5)_3\text{Ga}$ and $\text{NH}_3]$ and the ambient. Past work has shown that C has a deep acceptor level in the gap and is an ineffective dopant,⁽¹⁾ although recent theoretical studies suggest it may have utility.⁽²⁾ There has been one report of p-type GaN grown by Metal Organic Molecular Beam Epitaxy (MOMBE) in which the hole density increased with CCl_4 flow, but a completing parasitic etching reaction by the chlorine reduced the growth rate severely and a maximum hole concentration of $\sim 3 \times 10^{17} \text{cm}^{-3}$ was achieved.⁽³⁾

Oxygen has been ascribed by some workers to be responsible for at least part of the residual n-type doping in most GaN,⁽⁴⁾ although others suggest this is due to nitrogen vacancies.⁽⁵⁾ Hydrogen is of course important for its role in passivating the electrical activity of Mg acceptors in GaN grown by Metal Organic Chemical Vapor Deposition. Both e-beam irradiation or simple thermal annealing are found to restore the electrical activity of the Mg by dissociating the neutral Mg-H complexes.⁽⁷⁾ We have also recently found that forward bias injection of minority carriers in hydrogenated GaN p-n junctions can reactivate the Mg acceptors, a phenomenon that has also been observed for passivated B in Si and S donors in GaAs.

In this paper we report on some experiments in which C, O or H have been introduced into GaN and related materials by implantation or diffusion and the effects on the electrical properties of the material measured.

EXPERIMENTAL

The nitrides employed in this work were prepared in a Varian Gas Source Gen II system fitted with a Wavemat MPDR 610 ECR plasma source.⁽⁸⁾ The nitrogen beam was generated using 200W forward power and nitrogen flows of 1-20 sccm. All layers grown on Al_2O_3 contain an initial 500Å low temperature AlN buffer grown at 425°C using 1 sccm N_2 flow. Triethylgallium III (TEG) was used as the Ga source, trimethylamine alane (TMAA) and dimethylamine alane (DMEAA) were used as the Al sources, and trimethylindium (TMI) and triethylindium (TEI) were employed as In sources.

Some samples were implanted with C^+ or O^+ ions at typical energies of 100keV and doses of 10^{14} - 10^{15}cm^{-2} followed by annealing up to 1100°C under a flowing N_2 ambient in an RTA system. Hydrogen was introduced by exposing the samples to either a ^1H or ^2H ECR discharge for 30 mins at 250-400°C. Carrier densities and mobilities were obtained from van der Pauw geometry Hall measurements using alloyed HgIn contacts and impurity profiles obtained from Secondary Ion Mass Spectrometry (SIMS) measurements performed at Charles Evans and Associates.

RESULTS AND DISCUSSION

(a) Carbon

We find that $\text{In}_x\text{Ga}_{1-x}\text{N}$ and $\text{In}_x\text{Al}_{1-x}\text{N}$ alloys grown by MOMBE are strongly n-type for $x \geq 0.15$ (InGaN) and $x \geq 0.3$ (InAlN), with steadily decreasing conductivity as the In concentration is decreased. High electron concentrations have also been reported for InN grown by other methods,⁽⁹⁾ and are usually ascribed to the presence of N vacancies, although this seems less likely in light of trends observed in InN grown using various III/V ratios.⁽¹⁰⁾ Furthermore, ion channeling and AES do not indicate nitrogen deficiency in these films.

Another possible explanation for the electrical behavior is the presence of unintentionally incorporated carbon. Though carbon has been shown capable of producing p-type GaN, the hole concentrations obtained have been limited to low $\sim 10^{17}\text{cm}^{-3}$ even though carbon levels are measured to be 10^{20}cm^{-3} or higher. It has been found in other III-V materials that the maximum hole concentration which can be obtained using carbon is related to the difference in bond strength between the group III-carbon case and group V-carbon sites. In the case of InP, the carbon actually sits on the group III site and acts as a donor resulting in n-type material. Based on this simple model, it is expected that carbon will be a donor in InN and high In concentration alloys (see Figure 1). Thus at least some of the conduction observed in these ternary films may be due to carbon. Further, as the composition is reduced in In, the tendency for carbon to act as an acceptor rather than a donor increases, thus possibly explaining the reduction in electron concentration observed with increasing Ga or Al concentration. Clearly more work is needed in this area in order for the role of carbon to be fully understood.

We also implanted C into GaN and annealed at temperatures up to 1100°C, but did not obtain p-type conductivity. Based on the results to date we find that C probably displays amphoteric behavior in the nitrides, with acceptor formation under some conditions (MOMBE-grown GaN) and possible donor action in other cases (implantation in GaN; growth of In-containing alloys).

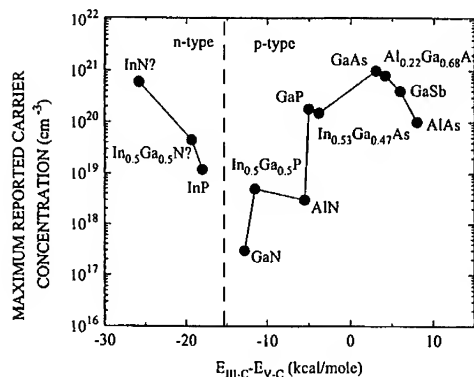


Figure 1. Maximum reported carrier concentration for materials with various group III-carbon and group V-carbon bond strengths as a function of the difference between the two bonds.⁽¹⁴⁾

(b) Oxygen

Oxygen implantation into initially doped GaN produces damage-related compensation which is thermally stable to $\leq 750^{\circ}C$, and indicates that oxygen does not have a deep acceptor or donor state with high concentration in this material. InGaN which is initially n-type shows less effective implant isolation characteristics, with a maximum of a 100 fold increase⁽¹¹⁾ in sheet resistance independent of ion species after a $500^{\circ}C$ anneal.

As seen in Figure 2, InAlN, in contrast to InGaN, can be highly compensated with N- or O-implantation with over a three order-of-magnitude increase in sheet resistance after a 600 to $700^{\circ}C$ anneal while F-implantation produces only one order-of-magnitude increase in sheet resistance. The compensating level in InAlN is also high in the bandgap with the deepest level estimated at 580meV below the conduction band edge in high dose N-isolated material, however it is sufficiently deep to achieve highly compensated material. The enhanced compensation for N- and O-implantation in InAlN may result from a reduction in N-vacancies for N-implantation or the formation of an O-Al complex for O-implantation. An O-Al complex is thought to also be responsible for thermally stable implant isolation in O-implanted AlGaAs.⁽¹²⁾

When O is implanted into GaN and annealed at $1100^{\circ}C$, Zolper has demonstrated it creates n-type doping with an ionization level of $\sim 29meV$ and poor activation efficiency ($\leq 4\%$).⁽¹³⁾ The diffusivity was $\leq 2.7 \times 10^{-13} cm^2/sec$ at $1125^{\circ}C$.

(c) Hydrogen

By analogy with the models for neutral hydrogen-dopant complexes in other III-V semiconductors, Figure 3 shows schematic representations of the likely configurations in GaN. For donor dopants, the H occupies an antibonding position either attached to the dopant in the case of group IV donors or attached to the Ga neighbor in the case of a group IV donor.

For acceptor dopants, the H is at a bond-centered position, bonded predominantly either to the acceptor or a N neighbor, respectively, depending on whether the acceptor is from column IV or II of the Periodic Table.

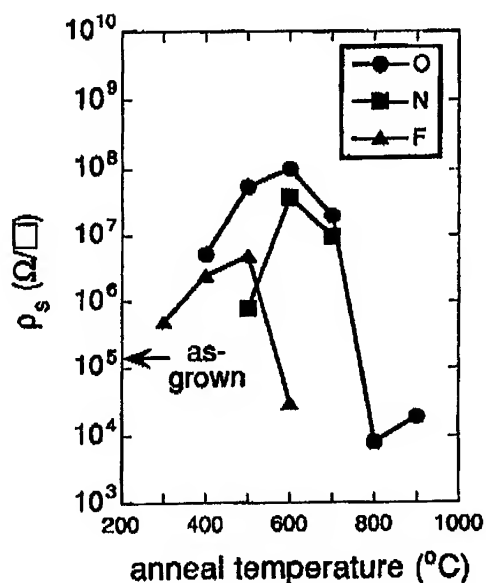


Figure 2. Sheet resistance versus anneal temperature for autodoped $\text{In}_{0.75}\text{Al}_{0.25}\text{N}$ implanted with O, N or F with an average ion concentration = $5 \times 10^{18} \text{ cm}^{-3}$.

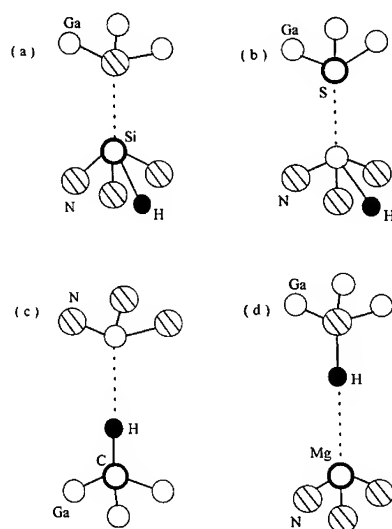


Figure 3. Schematic representation of hydrogen-dopant complexes in GaN.

The native donors in InGaN and InAlN are also passivated by association with atomic hydrogen. Figure 4 shows the fraction of passivated donors remaining in both alloys as a function of post-hydrogenation annealing temperature. Both samples displayed a decrease in carrier concentration of approximately an order of magnitude after H plasma exposure. On subsequent annealing the passivated donors begin to reactivate around 500°C. The reactivation was fit to the relation

$$N_0/N = 1 - \exp[-\nu \exp(E_d/kT)] \quad (1)$$

where N_0/N is the fraction of passivated centers reactivated by annealing at temperature T for time t , ν is the attempt frequency (assumed to be 10^{14} s^{-1}) and E_d is the activation energy for reactivation. The recovery of the donor activity occurred over a broader temperature range than generally observed for passivated dopants and was consistent with the presence of a Gaussian distribution of activation energies. We obtained values for E_d around 2.4 eV with a FWHM of $\sim 0.3 \text{ eV}$. The hydrogen does not leave the crystal at these temperatures, but probably associates with other hydrogen atoms to form molecules and larger clusters. At much higher temperatures ($> 800^\circ\text{C}$) these clusters are evolved from the sample.

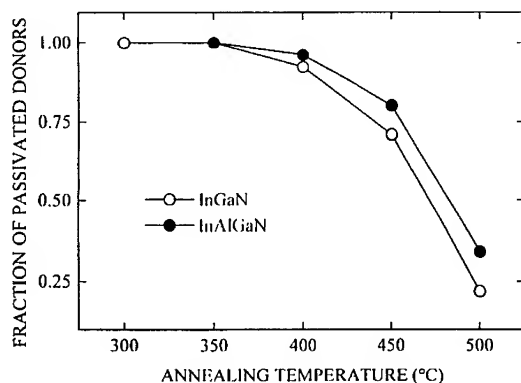


Figure 4. Fraction of passivated donors remaining in InAlN or InGaN after deuteration at 250°C and subsequent annealing at different temperatures.

ACKNOWLEDGMENTS

The work at UF is supported in part by AASERT grant through USARO, an NSF grant through DMR (94-21109) and an ONR/ARPA URI (N00014-92-J-1895). The work at HRL is partially supported by ARO and that at Sandia is supported by DOE contract No. DE-AC04-94AL85000. The UF authors greatly appreciate the help of the Microfabritech staff.

REFERENCES

1. J. I. Pankove and J. A. Hutchby, *J. Appl. Phys.* **47** 5387 (1976).
2. S. Strite, *Jap. J. Appl. Phys.* **33** 1699 (1994).
3. C. R. Abernathy, J. D. MacKenzie, S. J. Pearton and W. S. Hobson, *Appl. Phys. Lett.* **66** 1969 (1995).
4. B. C. Chung and M. Gershenzon, *J. Appl. Phys.* **72** 651 (1992).
5. R. J. Molnar, K. B. Nichols, P. Maki, E. R. Brown and I. Melngailis, *Mat. Res. Soc. Symp. Proc.* Vol. **378** 479 (1995).
6. H. Amano, M. Kito, K. Hiramatsu and I. Akasaki, *Jap. J. Appl. Phys.* **28** L2112 (1989).
7. S. Nakamura, N. Iwasa, M. Senoh and T. Mukai, *Jap. J. Appl. Phys.* **31** 1258 (1992).
8. C. R. Abernathy, J. D. MacKenzie, R. J. Shul, A. Howard and J. S. Williams, *Proc. Electrochem. Soc.* **95-211** (1995).
9. T. L. Tansley and C. P. Foley, *Electron. Lett.* **20** 1066 (1984).
10. C. R. Abernathy, P. Wisk, F. Ren and S. J. Pearton, *J. Vac. Sci. Technol.* **B11** 179 (1993).
11. J. C. Zolper, S. J. Pearton, C. R. Abernathy and C. B. Vartuli, *Appl. Phys. Lett.* **66** 3042 (1995).
12. J. C. Zolper, A. G. Baca and S. A. Chalmers, *Appl. Phys. Lett.* **62** 2536 (1993).
13. J. C. Zolper et al. (to be published).
14. C. R. Abernathy, *Mat. Sci. Eng. Rep.* **14** (5) 204 (1995).

INFRARED ABSORPTION AND ELECTRON SPIN RESONANCE STUDIES OF
NANOCRYSTALLINE CUBIC BORON NITRIDE/AMORPHOUS HYDROGENATED
BORON NITRIDE MIXED PHASE THIN FILMS

SHU-HAN LIN, IAN M. BROWN and BERNARD J. FELDMAN

Departments of Physics and Chemistry and the Center for Molecular
Electronics, University of Missouri, St. Louis, MO. 63121,
C4840@silvaxa.ums1.edu

ABSTRACT

Both infrared absorption (IR) and electron spin resonance (ESR) spectroscopies have been used to investigate the complicated structure of nanocrystalline cubic boron nitride/amorphous hydrogenated boron nitride thin films. The ESR spectra from this material consist of a component with a four-line hyperfine structure and/or a component with a ten-line hyperfine structure superimposed upon a broad central line. The hyperfine structures are associated with defect centers located in the nanocrystalline phase, whereas the broad line is attributed to dangling bonds in the amorphous phase. The IR spectra consist of three lines around 1400 cm^{-1} : the lines at 1263 and 1505 cm^{-1} originate in a boron-poor amorphous hydrogenated boron nitride region; the line at 1371 cm^{-1} , in a boron-rich amorphous hydrogenated boron nitride region. These results, together with previously reported electron diffraction spectra, suggest the following picture: small (2.5 nm) nanocrystallites of cubic boron nitride (about 5% of the material) are imbedded in a mixed amorphous phase. The amorphous region can be approximated by a mixture of boron-rich and boron-poor amorphous hydrogenated boron nitride.

INTRODUCTION

Boron nitride thin films have a number of attractive properties, such as an extremely large bandgap, hardness, low conductivity, chemical inertness, and good adhesion to substrate materials. They have found technological applications as insulating layers in optical devices and high temperature electronics. Thin films of boron nitride have been grown by a variety of growth techniques -- sputtering, evaporation, ion plating and plasma assisted chemical vapor deposition (CVD) [1]. The growth of polycrystalline cubic and hexagonal boron nitride by CVD usually requires very high substrate temperatures (900 C) [2], but amorphous boron nitride can be grown by rf plasma assisted CVD at low substrate temperatures (250 C) [3,4].

We have followed up on this low substrate temperature work and recently reported chemical composition, electron diffraction, optical absorption, infrared absorption and electron spin resonance results [5-7]. From the electron diffraction results, the thin films grown at a substrate temperature of 250 C were a 5% mixture of cubic boron nitride nanocrystals (2.5 nm average size) interspersed in an amorphous medium [5]. From the chemical composition results, our films contain approximately 49 at. % boron, 28 at. %

nitrogen and 23 at. % hydrogen. From the optical absorption results, the optical bandgap increases from 4.0 to 5.6 eV as the substrate temperature increases from 60 C to 250 C. From the infrared absorption results, the dominant absorption feature around 1400 cm^{-1} consists of three separate lines, two associated with small bandgap amorphous hydrogenated boron nitride and one with large bandgap amorphous hydrogenated boron [6]. The ESR results consist of a broad spectrum, associated with dangling bonds in the amorphous regions, superimposed on two less intense spectra showing hyperfine structures. The latter are associated with defects in the cubic boron nitride nanocrystals [7]. In this paper, we extend our measurements to samples grown at various substrate temperatures to learn how the structure of our films changes with substrate temperature.

EXPERIMENT

The boron nitride thin films were grown in a capacitively coupled rf plasma reactor with a feedstock of diborane (B_2H_6), ammonia (NH_3) and hydrogen (H_2). The growth parameters are: diborane partial pressure of 4.0 mT; ammonia partial pressure of 40 mT; hydrogen partial pressure of 356 mT; rf power of 23 W; self-bias voltage of 430 V; and the films were grown on silicon or aluminum foil substrates mounted on an anode heated between 60 C and 300 C. The films grown on silicon substrates were inserted into a Perkin Elmer Model 1610 FTIR spectrophotometer for infrared absorption measurements. The films grown on aluminum substrates were immersed in dilute hydrochloric acid until the aluminum was dissolved. The remaining film was washed, dried and placed in a 5mm OD sample tube which was inserted into the dual mode microwave cavity of a Varian E-12 ESR spectrometer. The signal averaging, spectral subtractions and integrations were accomplished with software obtained from Scientific Software, Bloomington, Illinois. Both the first and second derivative spectra of the ESR absorptions were always recorded. For the best resolution together with reasonable sensitivity, it was preferable to use first derivative spectra for the four-line and broad central line features, and the second derivative spectra for the ten-line features.

RESULTS

The infrared absorption spectrum of boron nitride thin films grown at a substrate temperature of 150 C is shown in Figure 1 as the open circles. This spectrum is fitted to a sum of three Lorentzian lines with peaks at 1263, 1371, and 1505 cm^{-1} (solid line in Figure 1). This fitting procedure was performed on four other infrared spectra of samples grown at various substrate temperatures ranging from 60 C to 300 C. As a function of increasing substrate temperature, the integrated intensity of the 1371 cm^{-1} line increases until it totally dominates at substrate temperatures at or above 250 C, whereas the integrated intensity of the 1263 and 1505 cm^{-1} lines decrease until at or above 250 C, they have a negligible contribution [6]. The transverse optical mode of cubic boron nitride is a very sharp line at 1070 cm^{-1} , but it is unobserved in any of our spectra.

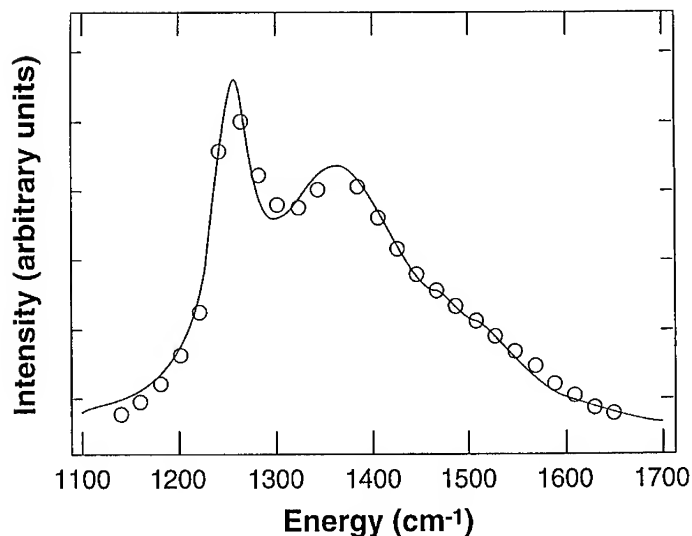


Figure 1. The infrared absorption spectrum of our boron nitride thin film grown at a substrate temperature of 150 C. The open circles are the measured data and the solid line, the fit of the data to a sum of three Lorentzian lines centered at 1263 cm^{-1} , 1371 cm^{-1} , and 1505 cm^{-1} .

The first and second derivative ESR spectra of our boron nitride thin films grown at 120 C and 250 C substrate temperatures are shown in Figures 2 and 3. Three spectra were observed from our boron nitride samples; a sharp four-line spectrum, a sharp ten-line spectrum and a broad single-line spectrum, all centered at $g = 2.0028$. The broad single-line feature in Figures 2 and 3 has a peak-to-peak width of 1.2 mT and a spin count of $1.6 \pm 0.2 \times 10^{19}$ spins/gram. Both Figures 2 and 3 exhibit weak four-line and ten-line features; however, these are much more pronounced in the spectrum of the sample grown at 250 C.

DISCUSSION

We have attempted to identify the three infrared absorption lines in our spectra. It is useful to compare our thin films to amorphous hydrogenated boron thin films, where the infrared spectra consist of a single line at 1362 cm^{-1} and the optical bandgaps range from 5.1 to 5.6 eV as the substrate temperature varies from 60 to 250 C [6]. Our boron nitride thin films grown at 250 C also have an optical bandgap of 5.6 eV, are boron-rich from the chemical composition analysis, and only have the 1371 cm^{-1} line present in the infrared absorption spectra. Hence, we associate the 1371 cm^{-1} line with a large bandgap, boron-rich amorphous hydrogenated boron

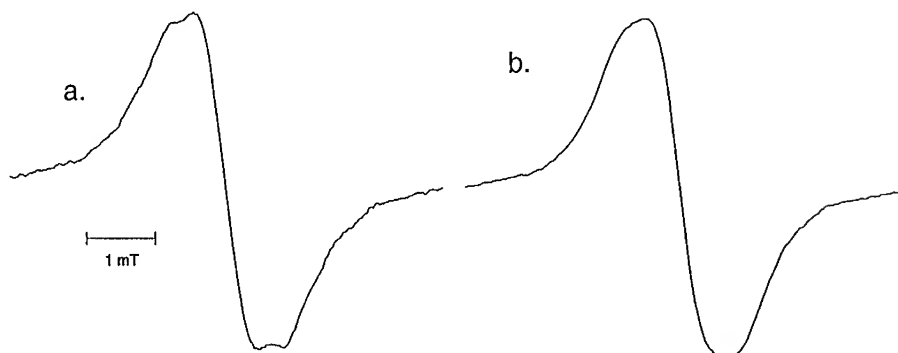


Figure 2. The first derivative ESR spectra of our boron nitride films grown at substrate temperatures of (a) 250 C and (b) 120 C.

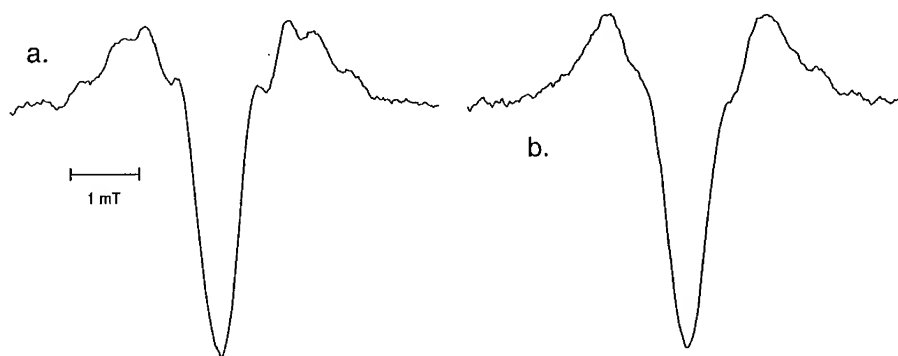


Figure 3. The second derivative ESR spectra of our boron nitride films grown at substrate temperatures of (a) 250 C and (b) 120 C.

nitride (a-B:N:H) phase. In contrast, the low substrate temperature material has a smaller optical bandgap of 4.1 eV and significant amplitudes of the 1271 and 1505 cm^{-1} lines in the infrared spectra. We therefore associate the 1271 and 1505 cm^{-1} lines with small bandgap, boron-poor a-B:N:H. Finally, previous workers in boron-rich materials provide convincing evidence that infrared absorption lines around 1400 cm^{-1} are due to modes from boron containing clusters--most likely, icosahedral structures [8].

In contrast, previous workers in CVD boron nitride have concluded that the infrared lines around 1400 cm^{-1} are due to the presence of hexagonal boron nitride [2-4]. This identification is suggested by the fact that single crystal hexagonal boron nitride has

a transverse optic infrared active mode at 1367 cm^{-1} and a Raman active mode at 1370 cm^{-1} [9]. The truth may lie somewhere between these two interpretations, given that the composition of the material -- 49 at. % boron, 28 at. % nitrogen, and 23 at. % hydrogen -- is almost half-way between boron nitride and amorphous hydrogenated boron. However, because boron icosahedra are so tightly bound, they have very large oscillator strengths so that they dominate the infrared absorption spectra [10]. The 1070 cm^{-1} line of cubic boron nitride is also undetected, presumably because of the low nanocrystallite concentration and the much smaller oscillator strength of this mode in comparison to that of the boron clusters.

Hyperfine structures are easily seen in the first and second derivative ESR spectra, because their linewidths (0.7 mT) are smaller than that of the central line (1.2 mT). Since the splittings observed in the four-line and ten-line features were attributed to hyperfine interactions with ^{11}B nuclei, these hyperfine structures were assigned to a one-boron paramagnetic defect center and a three-boron paramagnetic defect center, respectively [7]. Both centers are located in the cubic boron nitride nanocrystalline phase. The central single-line spectrum was associated with dangling bonds present in the amorphous phase [7]. The linewidth of this central line in a-B:N:H is larger than the linewidths of the hyperfine components because of the random site-to-site variations in bond angles and bond lengths due to the heterogeneous environments present in an amorphous matrix.

The preparation of partially deuterated samples by using deuterium gas instead of hydrogen gas in the feedstock resulted in a marked narrowing of the central spectrum and no effect on the linewidths of the four-line and ten-line spectra [7]. This result indicates that the hydrogen resides only in the amorphous regions and not in the nanocrystalline regions. Furthermore, it is evidence that the central spectrum can be associated with dangling bonds located in the amorphous regions.

The relative intensities of the three features depend upon the exact conditions present at the substrate during film growth. For example, as is shown in Figure 3, the intensity of the ten-line feature increases when the substrate temperature is increased from 120 C to 250 C. On the other hand, the linewidth, lineshape and value of the double integral of the central line (i.e. the spin concentration in the amorphous phase) is within experimental error, independent of substrate temperature. These results suggest that increasing the substrate temperatures from 120 to 250 C increases the concentration of cubic boron nitride nanocrystals. This conclusion is consistent with previous reports that mainly polycrystalline boron nitride material forms at high substrate temperatures (900 C) whereas amorphous boron nitride material is formed at lower temperatures (250 C) [2-4]. Furthermore, the lack of any dependence of the spin concentration on the substrate temperature suggests that the dangling bonds are located primarily in the boron-rich a-B:N:H phase.

CONCLUSIONS

The structure of our nanocrystalline cubic boron nitride/amorphous hydrogenated boron nitride mixed phase thin films is compli-

cated. However, the infrared absorption and ESR spectra are useful tools to deconvolute that structure and monitor its components as a function of substrate temperature. In particular, infrared absorption spectra indicate that there are two amorphous phases, a boron-rich phase associated with the 1371 cm^{-1} line and a boron-poor phase associated with the 1263 cm^{-1} and 1505 cm^{-1} lines. As a function of increasing substrate temperature, the boron-poor phase decreases and the boron-rich phase increases until it totally dominates at substrate temperatures at or above 250 C . The ESR spectra are sensitive to the concentration of cubic boron nitride nanocrystals. The nanocrystal concentration increases as a function of increasing substrate temperature.

REFERENCES

1. S. P. S. Arya and A. D'Amico, *Thin Solid State Films* **157**, 267 (1988) and references therein.
2. T. Ichiki and T. Yoshida, *Appl. Phys. Lett.* **64**, 851 (1994).
3. H. Miyamoto, M. Hirose and Y. Osaka, *Jap. J. Appl. Phys.* **22**, L216 (1983).
4. T. H. Yuzuriha and D. W. Hess, *Thin Solid Films* **140**, 199 (1986).
5. S.-H. Lin and B. J. Feldman in Microcrystalline and Nanocrystalline Semiconductors, edited by R. W. Collins, C. C. Tsai, M. Hirose, F. Koch and L. Brus (Mater. Res. Soc. Proc. 358, Pittsburgh, PA 1995), p. 817-822.
6. S.-H. Lin and B. J. Feldman, *Solid State Commun.* **96**, 29 (1995).
7. S.-H. Lin, I. M. Brown and B. J. Feldman, *Solid State Commun.* **96**, 421 (1995).
8. H. Stein, T. Aselage and D. Emin in Boron-Rich Solids, (AIP Conference Proc. 231, New York, NY, 1991) p. 322.
9. R. Geich, C. H. Perry and G. Rupprecht, *Phys. Rev.* **146**, 543 (1966).
10. S.-H. Lin, D. Li and B. J. Feldman in Mechanical Behavior of Diamond and Other Forms of Carbon, (Mater. Res. Soc. Proc. 383, Pittsburgh, PA 1995), in press.

MAGNETO-OPTIC STUDIES OF GaN FILMS AND GaN/AlGa_N HETEROSTRUCTURES

Y.J. WANG*, H.K. NG†, R. KAPLAN***, K. DOVERSPIKE***, D.K. GASKILL**, T. IKEDO‡, H. AMANO‡ and I. AKASAKI‡

* National High Magnetic Field Laboratory, Florida State University, Tallahassee, FL 32306

† Department of Physics, Center for Materials Research and Technology, Florida State University, Tallahassee, FL 32306-3016

** Naval Research Laboratory, Washington DC 20375

‡ Department of Electrical and Electronic Engineering, Meijo University, I-501, Shiogamaguchi, Tempaku-Kuku, Nagoya 468, Japan

ABSTRACT

Magneto-studies have been carried out for several MOCVD grown GaN thin films and GaN/AlGa_N heterostructures at magnetic fields up to 30 T and at temperatures between 4.2 K to 100 K. Electron cyclotron resonance was observed in two heterostructures with high mobilities ($\mu > 2000 \text{ cm}^2/\text{V}\cdot\text{s}$), the effective mass obtained from the cyclotron resonance measurement is $0.23 \pm 0.01 m_0$, where m_0 is the mass of free electron. For Si-doped thin film GaN there was no sign of electron cyclotron resonance even when samples were heated up to 100 K. However, a 1s to 2p⁺ absorption line was observed for Si-doped GaN samples. A binding energy of 29 meV and low frequency dielectric constant of 10.4 is obtained.

INTRODUCTION

GaN belongs to group-III nitride semiconductor where the large energy gap is expected to play a significant technological role such as the blue light emitting diode, and in electric power generation [1]. Until recently, sample quality has prevented direct measurement of the effective mass via cyclotron resonance since this technique requires $\omega\tau > 1$ where τ is the scattering time. We present here cyclotron resonance (CR) measurements on free electrons on the 2 dimensional electron gas (2DEG) on GaN/Al_xGa_{1-x}N heterojunction, and on impurity transition on Si-doped GaN films using high magnetic fields.

Recently, Meyer [2] *et al.* and Alt [3] *et al.* have reported effective mass of $m^* = 0.236 \pm 0.005 m_0$ where m_0 is the free electron mass using transmission experiment on unknown residual donors on GaN. Our measurements employ Fourier transform spectroscopy and high magnetic field to probe the cyclotron resonance absorption in GaN/Al_xGa_{1-x}N heterostructures, and the 1s to 2p⁺ absorption of Si donor in GaN films.

EXPERIMENT AND RESULTS

The magneto-optical experiments were performed at the National High Magnetic Field Laboratory in Tallahassee, Florida. A Bruker 113v interferometer with focusing parabolic mirrors was used to direct the infrared radiation down a light pipe to the sample [4]. Static magnetic fields up to 30 T were obtained and the temperature range is from 2 K to 100 K. After passing through the sample the infrared radiation is picked up using a composite Si bolometer. Both the Si-doped GaN films and the GaN/AlGa_N heterostructures were grown by metalorganic vapor phase epitaxy on a 0.5 mm thick sapphire substrate with a AlN buffer layer that is about 350 Å thick. The Si donor films are about 2 μm thick. In the case of the heterostructure samples, the

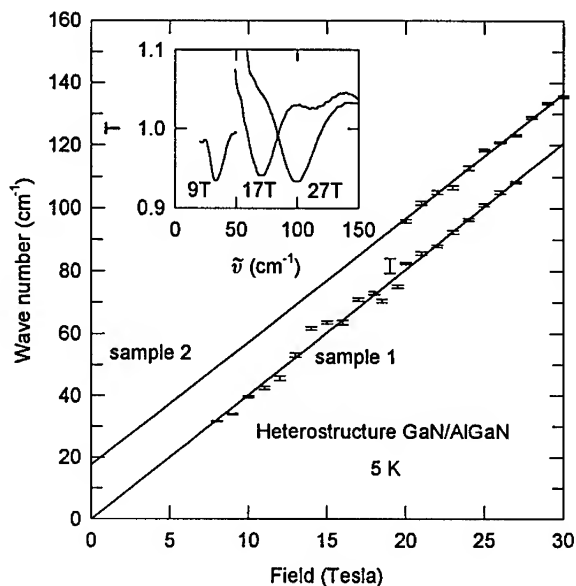


Figure 1. Field dependence of the cyclotron resonance. Inset shows representative resonance absorption for sample 1.

GaN is 3 μm thick that is capped off with a 500 \AA thick AlGa N layer.

Figure 1 shows the cyclotron resonance position versus field for spectra at 4.2 K for 2 heterostructure GaN/Al $_x$ Ga $_{1-x}$ N samples. The sample labelled as sample 1 has $x = 0.12$ while that of sample 2 has $x = 0.23$. The inset in Fig. 1 illustrates some typical cyclotron resonance absorption for the sample 1. While the absorption can be clearly observed for fields as low as 4 T for sample 1, in sample 2 the absorption is only visible above 20 T. The points on Fig. 1 were obtained by applying the Marquardt-Levenberg algorithm with a Lorentian model to the absorption spectra to give the resonance frequency and the absorption half-width. From the fit, sample 1 gives an absorption half-width of 7 cm^{-1} from which the mobility and scattering time is estimated to be 6000 $\text{cm}^2/\text{V}\cdot\text{s}$ and 2×10^{-13} s respectively. The corresponding values for the second sample are about 3 times smaller.

A linear regression fit applied to both set of measurements yields a common slope within experimental errors from which the electron effective mass for the 2DEG is $m^* = 0.23 \pm 0.01 m_0$. This value agrees with the 3DEG value of 0.22 m_0 on GaN films, where the measured mass is associated with the polaron mass[3]. The slope also indicates that there is no evidence of non-parabolicity in the band.

Further investigations have been carried out to prove that the observed resonance are indeed the CR of 2DEG. Figure 2a shows the temperature dependence of sample 1 at 27 T. It is clear that no appreciable change in absorption can be seen even for temperatures as high as 70 K. The

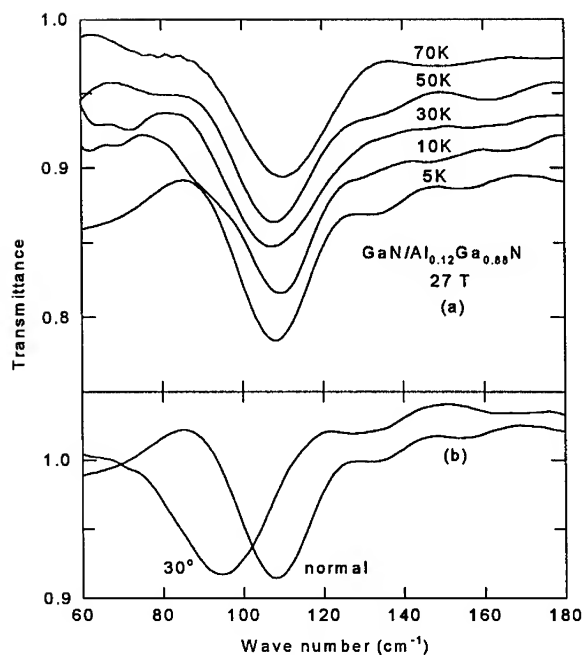


Figure 2. (a) Insensitivity of absorption line to increased temperature. (b) Shift in absorption line when the sample is tilted 30°.

same result is seen in the second sample. That the absorption is from the 2DEG can be seen by orienting the normal of the sample at an angle, θ , to the magnetic field. In Fig. 2b we show that the absorption minimum is shifted down precisely by a factor of $\cos \theta$ when $\theta = 30^\circ$ as one would expect.

The intercept for sample 1 is at the origin as expected. However, for sample 2 the intercept is shifted up by 18 cm^{-1} . One possible reason for the upward shift may be due to structural defects as a result of increased Al concentration. These defects would explain the shorter scattering time for sample 2. The decreased mobilities and scattering times with increasing Al is in line with transport measurements at 16 K for similar heterostructures [5]. Structural defects at the heterojunction can be modelled using a set harmonic oscillator potentials with different characteristic frequencies, ω_c . The potentials confine the electrons and result in an upward shift in the cyclotron frequencies as given by [6]

$$\omega = \frac{1}{2}[\omega_c + (\omega_c^2 + 4\omega_o^2)^{1/2}]. \quad (1)$$

Fig. 1 suggests a level crossing at about 70 cm^{-1} corresponding to a magnetic field of 17 T. A possible candidate for level crossing may be due to the reduced screening when one of the Landau levels is completely filled. However, calculations of the filling factor, ν , yields $\nu = 5$ at

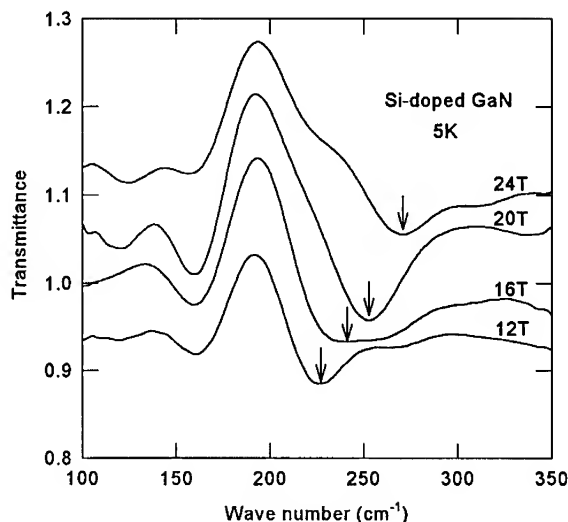


Figure 3. Absorption in Si-doped GaN film with Si concentration of $1.7 \times 10^{17} \text{ cm}^{-2}$. Arrows indicate absorption minimum.

at 17 T for a 2DEG density of 10^{12} cm^{-2} , the level crossing was not observed at fields corresponding to neighboring integer values of ν . Also, it is unlikely to be due to electron-phonon coupling since there is no phonon band at this frequency range for GaN. The third possibility of the level crossing may involve coupling to sub-band transition. But, the 10 % observed absorption strength of the resonance line (inset Fig. 1) corresponds to a 2DEG density of 10^{12} cm^{-2} . An estimation based upon triangular potential approximation requires the 2DEG electron concentration $N_s = 4 \times 10^{10} \text{ cm}^{-2}$ for the lowest sub-band excitation occurring at 70 cm^{-1} [7]. Thus, it is unclear at this point as to the origin of the level crossing.

We next look at the donor excitation of Si-doped GaN. The spectra shown in Figure 3 is for a sample with Si concentration of about $1.6 \times 10^{17} \text{ cm}^{-3}$ and a mobility of about $559 \text{ cm}^2/\text{V}\cdot\text{s}$ at 300 K. The absorption minimum (indicated by arrows) increases linearly with increasing field and can be clearly identified for fields greater than 12 T. A second sample of higher Si concentration of $5.7 \times 10^{17} \text{ cm}^{-3}$ and lower mobility of $339 \text{ cm}^2/\text{V}\cdot\text{s}$ also shows absorption minimum that increases with magnetic field. However, the half-width is much broader compared to the 45 cm^{-1} seen in the first sample, indicating higher scattering rate. This line width is much larger than the 2 cm^{-1} line width of undoped sample reported in Ref. 2. On samples with semi-insulating characteristics no absorption could be seen.

A plot of the absorption minimum with field yields a straight line (Figure 4) with the same slope as the case for the heterostructure GaN/AlGaIn. The zero field intercept is at 175 cm^{-1} (21.7 meV). Since Si is a donor in GaN, it is reasonable to use a hydrogenic model, in which the

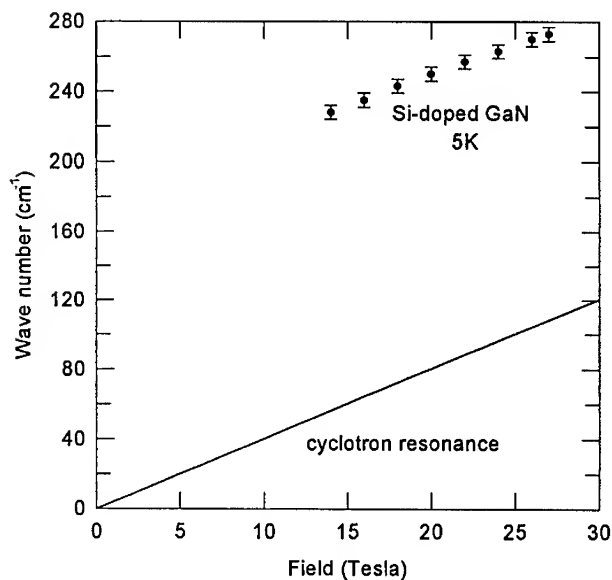


Figure 4. Si donor in GaN film transition minimum versus field. Solid line is the cyclotron resonance as obtained from Fig. 1.

energy levels are given by

$$E = 13.6 m^* / (\epsilon_0 n)^2 \text{ eV} \quad (2)$$

where ϵ_0 is the static dielectric constant and n are integers. Assuming the donor is hydrogenic, then the $1s$ to $2p+$ transition energy is $3/4$ of the donor binding energy, which is thus determined to be 29 meV.

Another quantity not well known is the low frequency dielectric constant, ϵ_0 . Previous calculations use $\epsilon_0 = 9.0$ to give a binding energy of 38.6 meV [8,9]. A much earlier optical measurement in 1970 suggests that $\epsilon_0 = 12.0$ for which the binding energy is 22 meV [10]. From our measurements the low frequency dielectric constant was calculated to be 10.4 using Eq. 2. It seems that the present result of ϵ_0 is an appropriate estimation since the Zeeman splitting is well described by the hydrogenic model.

In summary, the effective mass of 2DEG in GaN/Al_xGa_{1-x}N heterojunctions is $m^* = 0.23 \pm 0.01 m_0$, with scattering times that increases with Al concentration. There is as yet unexplained level crossing at 70 cm⁻¹. On Si-doped GaN, the binding energy for the Si donor is 29 meV and low frequency dielectric constant is 10.4.

ACKNOWLEDGEMENTS

This work is supported in part by the National Science Foundation through the National High Magnetic Field Laboratory, and the State of Florida through the Center for Materials Research and Technology. The work at Meijo University was partly supported by the Ministry of Education, Science, Sports and Culture of Japan (contract numbers 06452114, 07505012 and 07650025), Research Foundation for Electrotechnology of Chubu, Nissan Science Foundation, Iketani Science and Technology Foundation, Hosono Bunka Foundation and Daiko Foundation.

REFERENCES

- ° SFA, Landover, Maryland, 20785
- * Present Address: Hewlett Packard Co., San Jose, CA 95131
- 1. S. Strite and H. Markoc, J. Vac. Sci. Technol. B **10**, p1237 (1992).
- 2. B. K. Meyer, D. Volm, A. Graber, H. C. Alt, T. Detchprohm, A. Amano, and I. Akasaki, Sol. St. Comm. **95**, 597 (1995).
- 3. H. C. Alt, B. K. Meyer, D. Volm, A. Graber, M. Drechsler, D. M. Hoffman, T. Detchprohm, A. Amano, and I. Akasaki, Proc. 18th Internatl. Conf. on Defects in Semicond., Sendai, (1995), to be published.
- 4. H. K. Ng and Yong-Jie Wang, to be published in the *Proceedings of the Physical Phenomena at High Magnetic Field II*, Science World Press, Singapore.
- 5. J. M. Redwing, M.A. Tishchler, S. Choi, W. Mitchel, and A. Saxler, Res. Soc. Symp. GAN and Related Materials, Fall 1995, to be published.
- 6. H. J. Mikesta and H. Schmidt, Z. Phys. B **20**, 43 (1975).
- 7. F. Thiele, U. Merkt, J. P. Kotthaus, G. Lommer, F. Malcher, U. Rossler, and G. Weimann, Sol. St. Comm. **62**, 841 (1987).
- 8. H. Morkoc, S. Strite, G. B. Gao, M. E. Lin, B. Sverdlov, and M. Burns, J. Appl. Phys. **76**, 1363 (1994).
- 9. J. A. Miragliotta in *Properties of Group III Nitrides*, EMIS Data Reviews No. 7, J. H. Edgar, ed., INSPEC (1994), p. 190
- 10. D. D. Manchon, Jr., A. S. Barker, Jr., P. J. Dean, and R. B. Zetterstrom, Sol. St. Comm. **8**, 1227 (1970).

DEEP STATES IN GaN STUDIED BY THERMALLY STIMULATED CURRENT SPECTROSCOPY

Z.C.HUANG*, J.C. CHEN** AND D.B. MOTT***

* Hughes STX Corporation, 7701 Greenbelt Road, Suite 400, Greenbelt, MD 20770

** Department of Computer Science and Electrical Engineering, University of Maryland
Baltimore County, Baltimore, MD 21228

*** Goddard Space Flight Center, Code 718.1, NASA, Greenbelt, MD 20771

ABSTRACT

Deep levels in insulating GaN grown by metalorganic chemical vapor deposition have been studied using thermally stimulated current (TSC) and photocurrent (PC) spectroscopies. Five main traps were observed by TSC measurement in the as-grown undoped GaN in the range of 0-0.75 eV below the conduction band edge or above the valence band edge. Their activation energies were 0.11, 0.24, 0.36, 0.53 and 0.62 eV, respectively. PC measurements showed three deep levels located within the bandgap at 1.32, 1.70 and 2.36 eV, respectively. Furnace annealing was carried out on GaN for identifying all the observed deep levels. We have found that the 0.24, 0.36 and 0.53 eV traps were eliminated by annealing at 1000°C under N₂ for six hours, whereas the 0.62 eV trap density increased after annealing. The three deep levels detected by the PC measurement were not affected by annealing. The 1.70 eV trap, which is located at the midgap, does not seem to compensate with narrow donors. We attribute the 0.11 eV trap to surface states, and the 0.62 eV trap to nitrogen vacancies.

INTRODUCTION

Gallium nitride has been considered to be one of the most promising materials for the development of high responsivity and solar blind ultraviolet (UV) detectors due to its wide bandgap (3.4 eV). This allows instruments utilizing GaN UV detector arrays to operate in an environment with significant visible radiation without expensive visible blocking filters and extensive stray light baffling. One of the central problems in GaN UV detectors is the slow response to the UV radiation. Khan et al.¹ reported that the response time for their metal-semiconductor-metal (M-S-M) GaN detectors was about 1ms. We have found that the M-S-M detectors made from insulating GaN epilayers grown by different groups (Cree Research Inc., Applied Physics Lab. of John Hopkins University, and Naval Research Lab. etc.) have a response time ranging from 0.25 to 10ms. It is suggested that the high density of defects in GaN was the cause for the slow response. These defects are mainly stacking faults and dislocations in the materials grown by metalorganic chemical vapor deposition (MOCVD). Lester et al.² and Qian et al.³ reported that the dislocation density in GaN was as high as 10⁹-10¹⁰ cm⁻². According to Kurtin et al.⁴, GaN is an ionic material, in which the electronic properties are fundamentally different from those of more covalent materials such as Si, GaAs, or InP. In view of the electrical properties of the defects in undoped insulating GaN, almost no results have been reported to date. Its insulating nature and its low carrier mobilities make it difficult to carry out conventional electrical measurements^{5,6}. In this paper, we studied the deep levels in undoped GaN by thermally stimulated current (TSC) and photocurrent (PC) spectroscopies. Micron size M-S-M structures were fabricated on GaN wafers for a better

current collection. We observed at least five deep traps in GaN by TSC measurements, and three deep levels by PC measurement. Furnace annealing was employed to investigate the origin of these levels.

EXPERIMENT

The GaN samples studied in this paper were provided by the Applied Physics Lab. of John Hopkins University. An 1.5- μm -thick GaN layer was grown on (0001) sapphire by MOCVD at 1100°C. Because of the insulating nature of the GaN (resistivity $> 10^8 \Omega\cdot\text{cm}$), we have found that the TSC current was below 10^{-13} A at 300K under an applied bias of 20V if two contacts were made 2 mm apart. Therefore it is very difficult to determine TSC peaks based on such a small current. Hence the two electrodes made for TSC and PC measurements should be close enough so that they can collect current efficiently. For this purpose, we have made M-S-M photoconductors with 1 μm finger size and spacing, as shown in Fig.1, by a conventional lift-off technique. The ohmic contacts were made by evaporating 300Å Al followed by 1200Å Au, and annealing at 450°C for 5 mins. After fabrication, the patterned wafer was sliced into 5x5 mm² pieces, and packaged for measurements. The TSC measurement was carried out using a Keithley 617 Electrometer and a 9620-1 Temperature Controller interfaced with a computer. The temperature scan was from 40 to 360K with a constant heating rate of 0.35K/s. Illumination was performed at 30K for 2 mins by broad-band light from a Xenon lamp. For PC measurements, a monochromator with a 1200/mm line density grating was used for different wavelength light beams ranging from 200 to 1100nm. Furnace annealing was done at 1000°C for six hours under N₂ environment without proximity capping. Prior to the contact fabrication, the annealed wafer was dipped into 40% NaOH solution for 5 mins. to remove any possible surface damage.

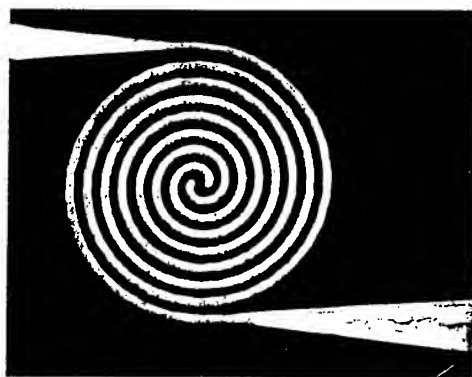


Fig.1. M-S-M structure on GaN with 1 μm width and spacing.

RESULTS AND DISCUSSIONS

Figure 2 shows the TSC spectra for as-grown insulating GaN. The data were taken under an applied bias of 20V. The dark current shown in Fig.2 was taken under the same condition but without illumination at low temperature. Five traps, T1, T2, T3, T4 and T5, were

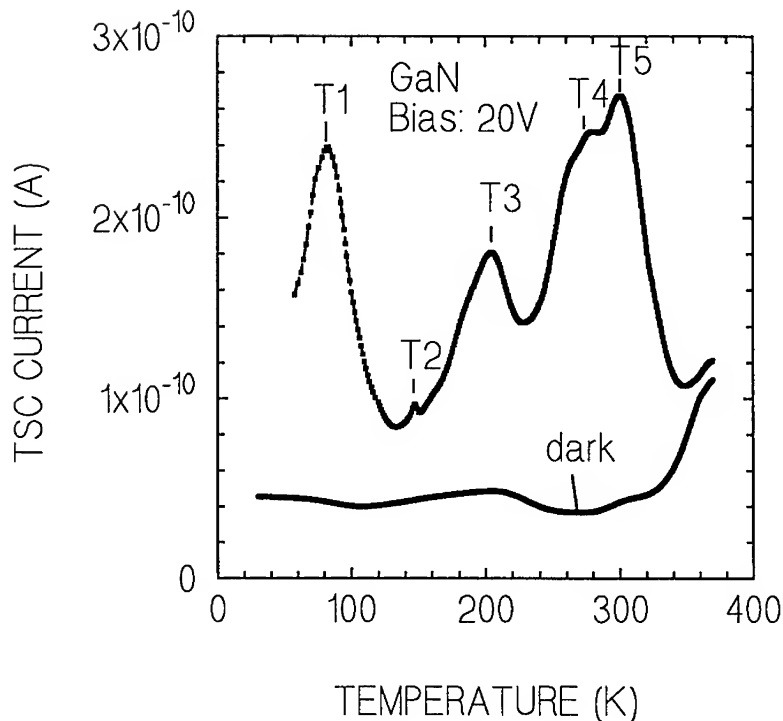


Fig.2. The TSC spectra for insulating GaN with and without illumination at low temperature.

observed in a temperature range of 40-360K with activation energies of 0.11, 0.24, 0.36, 0.53 and 0.62 eV, respectively, as obtained from an approximation⁶: $E_a = kT_m \ln(T_m^4/\beta)$, where k is the Boltzman constant, T_m is the peak temperature and β is heating rate(0.35K/s). The high temperature range was limited by our measurement system. We have noticed that the 0.11 eV trap T1 has higher density during the first temperature scan, but it disappeared after the second run, and never appeared in the following consecutive runs. This phenomenon was observed only in some GaN samples, not all of them. It may be related to surface states or adsorbates, caused by moisture or oxidation. The 0.62 eV trap T5 has the highest density among all the observed traps. The dark current measurement showed that this trap dominates the conduction band conduction in the high temperature range (>300K). We have found that T5 is the only trap left in GaN after furnace annealing, whereas other traps, T2, T3 and T4 disappeared (Fig.3). In Fig.3, the dark current has increased, meaning that the GaN layer becomes more conductive after annealing. The net peak height of trap T5 increased about four times as much as that in as-grown materials, indicating an increased trap density after annealing. Here the net peak height is the difference between the measured TSC peak and the dark current. We suggest that the trap T5 is related to nitrogen vacancies (V_N), because the out-diffusion of nitrogen tends to happen during thermal annealing, which creates more nitrogen vacancies in the material. Our 0.53 eV trap T4 is very close to the 0.49 eV trap observed by Gotz et al.⁷ and Huang et al.⁸ in their Si-

doped and undoped GaN, respectively. This trap becomes dominant in Si-doped and Si-ion implanted⁹ GaN layers, and is probably related to Si_N substitutionals. We are not clear, at this moment, about the origins of traps T2 and T3. However, they seem to be less important than the trap T5, which we found is responsible for the slow response in GaN UV detectors⁹.

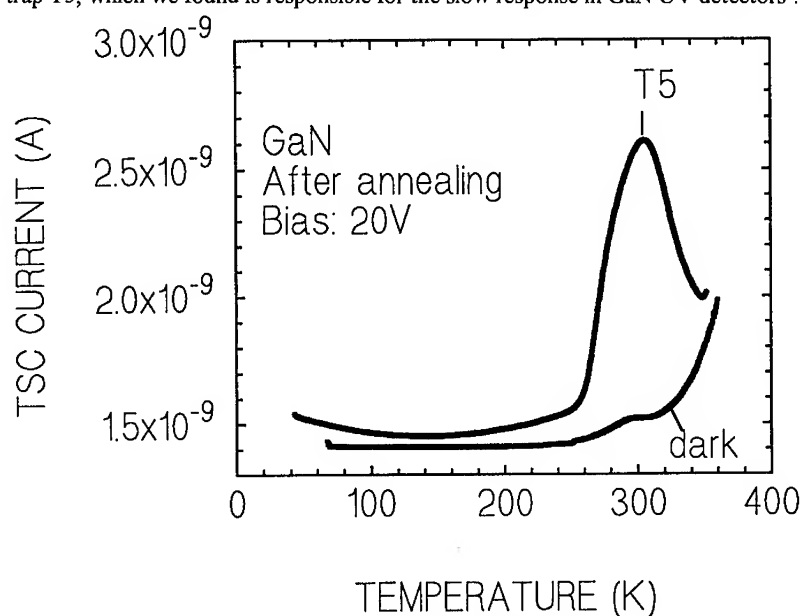


Fig.3. The TSC spectra for GaN after annealing.

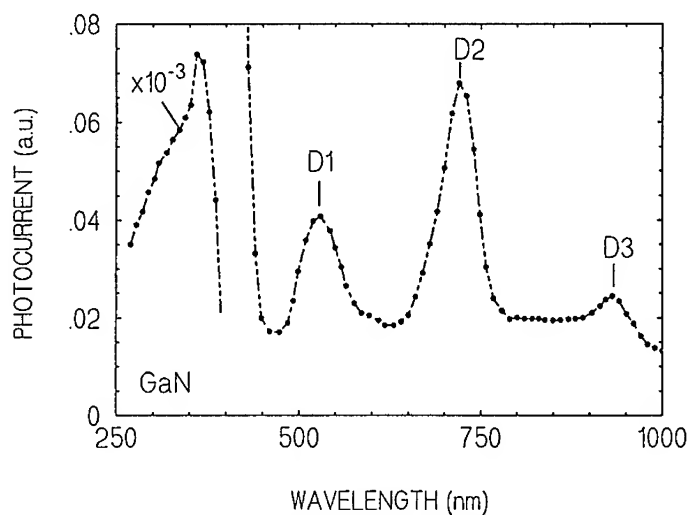


Fig.4. Photocurrent spectrum for GaN photoconductor at room temperature.

Due to our system limit, the TSC measurement can only detect deep levels in the range of 0-0.75 eV below the conduction band edge or above the valence band edge. In order to measure deeper levels, we have carried out the photocurrent measurement, which was performed at the room temperature under an applied bias of 20V. Figure 4 shows the PC spectrum for insulating GaN taken from M-S-M photoconductors. In Fig.4, the photocurrent was normalized by a calibrated light source. Besides the bandgap excitation at about 3.41 eV, three other deep levels, D1, D2 and D3, were observed in this material. Their energy levels converted from wavelengths are 2.36, 1.70 and 1.32 eV, respectively. We did not observe much difference in the curve shape and the relative peak height of these three levels before and after annealing. However, it is interesting to examine the deep level at 1.70 eV. This level, similar to EL2 in semi-insulating GaAs, is located at the midgap, and has the highest concentration compared to the other two levels. In undoped liquid-encapsulated Czochralski-grown GaAs, the semi-insulating property is due to the compensation of shallow acceptor carbon by midgap donor EL2¹⁰. This property can be changed by the so-called "EL2 out-diffusion"¹¹ after annealing, because many lattice vacancies are created near the surface due to the loss of lattice atoms, and hence the surface acceptor concentration increases. This brings us to question whether D2 in GaN plays a similar role as EL2 does in GaAs. It is commonly reported that some of the MOCVD-grown undoped GaN exhibited high n-type carrier concentrations (10^{17} - 10^{18} cm⁻³), which are generally attributed to nitrogen vacancies^{12,13}. As mentioned above, if annealing indeed increases the concentration of nitrogen vacancies, the insulating property of GaN should have changed after annealing, which is consistent with our results based on the fact that our GaN becomes more conductive after annealing. However, there is no evidence to show that an increase of V_N causes a decrease of trap D2, i.e., the D2 out-diffusion. This suggests that the 1.70 eV level is not compensated with V_N . The nature of such a level may be different from EL2 in GaAs. A study to clarify this issue is now underway.

CONCLUSIONS

In conclusion, we have studied deep levels in insulating GaN grown by MOCVD using thermally stimulated current and photocurrent spectroscopies. Five main traps, with activation energies of 0.11, 0.24, 0.36, 0.53 and 0.62 eV, were observed by TSC measurements in the as-grown undoped GaN. PC measurements showed three deep levels located within the bandgap at 1.32, 1.70 and 2.36 eV, respectively. We have found that the 0.24, 0.36 and 0.53 eV traps can be eliminated by annealing at 1000°C for six hours, whereas the 0.62 eV trap density increased after annealing. The presence of three deep levels observed by PC measurements was not affected by annealing. We attribute the 0.11 eV trap to surface adsorbates, and the 0.62 eV trap to nitrogen vacancies.

ACKNOWLEDGMENTS

This work was supported by NASA through contract number NAS5-32350. One of the authors (JCC) acknowledges the support from Army Research Office (Dr. J. Zavada and the AASERT program). The authors would like to thank Dr. Dennis Wickenden for the GaN material preparation.

REFERENCES

1. M.A.Khan, J.N. Kuznia, D.T.Olson, J.M. Van Hove, M.Blasingame and L.F.Reitz. Appl. Phys. Lett., **60**, 2917 (1992)
2. S.D. Lester, F.A. Ponce, M.G. Craford and D.A. Steigerwald, Appl. Phys. Lett., **66**, 1249 (1995)
3. W. Qian, M. Skowronski, M. De Graef, K. Doverspike, L.B. Rowland and D. K. Gaskill, Appl. Phys. Lett., **66**, 1252 (1995)
4. S. Kurtin, T.C. McGill, and C.A. Mead, Phys. Rev. Lett., **22**, 1433 (1969)
5. K. Xie, Z.C. Huang, C.R. Wie, J. Electron. Mater., **20**, 553 (1991)
6. Z.C. Huang, K. Xie and C.R. Wie, Rev. Sci. Instrum., **62**, 1951 (1991)
7. W. Gotz, N.M. Johnson, H.Amano and I. Akasaki, Appl. Phys. Lett., **65**, 463 (1994)
8. W.I. Lee, T.C. Huang, J.D. Guo and W.S. Feng, Appl. Phys. Lett., **67**, 1721 (1995)
9. Z.C. Huang, J.C. Chen and Brent D. Mott, to be submitted.
10. G.M. Martin, J.P. Farges, G. Jacob, and J. P. Hallais, J. Appl. Phys., **51**, 2840 (1980)
11. L.B. Ta, H.M. Hobgood, A. Rohatgi, and R.N. Thomas, J. Appl. Phys., **53**, 5771 (1982)
12. S. Strite and H. Morkoc, J. Voc. Sci. Technol. **B10**, 1237 (1992)
13. H. Morkoc, S. Strite, G.B. Gao, M.E. Lin, B. Sverdla and M. Burns, J. Appl. Phys., **76**, 1363 (1994)

EXCITON LIFETIMES IN GAN

J.P. BERGMAN*, C. HARRIS*, B. MONEMAR*, H. AMANO** AND I. AKASAKI**

*Department of Physics and Measurement Technology, Linköping University,
S - 58183 Linköping, Sweden

**Department of Electrical and Electronic Engineering, Meijo University,
Nagoya 468, Japan

ABSTRACT.

We have performed time resolved photoluminescence measurements of the exciton recombination in different GaN samples at low temperatures. In epitaxial layers the decay time of the free exciton is typically faster than 100 ps. This is due to a dominating non-radiative recombination process. In thick bulk samples we have resolved and measured the decay time of the free exciton with a value of about 200 ps. We believe that this value is close to the radiative lifetime for free excitons in GaN. We have also shown that excitation transfer occurs between free and bound exciton states. We have furthermore measured the decay of the donor and acceptor bound excitons, and obtained values of the decay time of 250 ps and 1200 ps, respectively.

INTRODUCTION

GaN and nitride based compounds have in recent years attracted a great interest. This is due to the potential for nitrides as excellent materials for devices, mainly in optoelectronic applications. The radiative lifetimes, and the influence of Coulomb correlation on such lifetimes as well as on gain spectra are very important parameters for future laser applications, in a conventional laser structure. A long radiative lifetime will make it more easy to obtain the carrier concentration needed for a specific gain. On the other hand, a long radiative lifetime increases the possibility for a dominating non-radiative recombination, as compared to the radiative recombination.

Optical time resolved spectroscopy of bulk material can provide important information on the radiative lifetimes. At low temperatures the photoluminescence (PL) spectrum in bulk semiconductors is typically completely dominated by the recombination of bound excitons (BE). The BE's, both the donor BE (DBE) and the acceptor BE (ABE) are thermally quenched at about 50 K due to the relatively low exciton binding energy. At higher temperatures the emission is typically dominated by the recombination of free excitons (FE).

So far only scattered studies of time resolved measurements have been published [1-3]. These results are also somewhat contradictory mainly dependent on the large difference in sample quality used for the studies. In this work we have mainly studied three different samples. Sample A is an epitaxial double heterostructure, with a GaN layer surrounded by AlN and AlGaN barriers. This sample shows a PL spectrum typical for epitaxial GaN layers, where the emission at low temperatures is dominated by the recombination of DBE's. The second sample, Sample B, is also an epitaxial layer but with lower substitutional defect concentration, so that the emission is dominated by the recombination of FE's. The third sample, sample C, is a thick (500 μm) bulk crystal grown by vapour phase epitaxy. This sample is of higher optical quality with narrow emission lines.

We have studied these three samples with optical time resolved spectroscopy, and the exciton dynamics is discussed based on the different behaviour in the different samples.

EXPERIMENTAL DETAILS

Samples A and B were grown by Metal Organic Vapour Phase Epitaxy (MOVPE) on optical grade polished sapphire substrates, with an initial AlN buffer to accommodate the lattice mismatch with the substrate. Sample A consisted of a nominally undoped GaN layer and a likewise undoped AlGaIn barrier. For the second sample (B) the buffer was followed by a 3 μm thick intentionally undoped GaN layer and a top InGaIn layer. The third sample (C) is a 500 μm thick quasi bulk sample grown by hydride vapour phase epitaxy (VPE) as described previously [4].

PL and time resolved PL measurements were performed in a combined bath and flow cryostat, where the temperature could be varied in the range between 2 K to room temperature. A mode locked Ar⁺-laser synchronously pumping a dye laser, using the DCM dye, was used as excitation source. This produced 10 pico-second pulses in the red spectral region, which were frequency doubled with a LiIO₃ crystal to obtain pulsed excitation in the region of the bandgap of GaN. For spectral measurements the emitted PL was detected with a cooled CCD camera, while the time resolved measurements were performed with a syncroscan streak camera with a time resolution of about 20 ps.

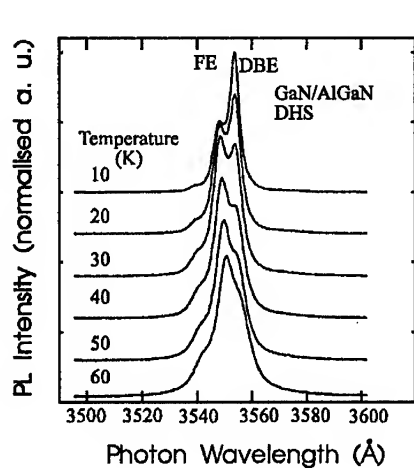


Figure 1. PL spectrum from a GaN epitaxial layer (sample A). The spectrum is at low temperatures dominated by the recombination of the DBE. This is thermally quenched at about 40K, after which the FE recombination dominates the spectrum.

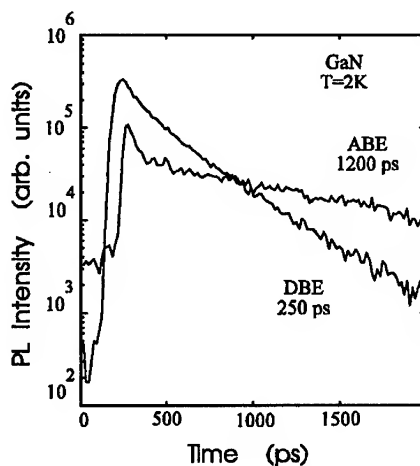


Figure 2. Measured decay curves for the DBE and the ABE in epitaxial GaN.

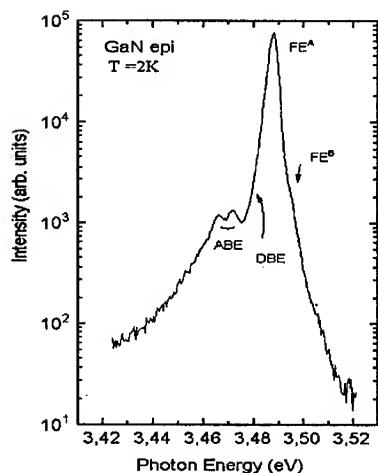


Figure 3. PL spectrum from a high quality epitaxial layer (sample B), where the FE recombination dominates the emission.

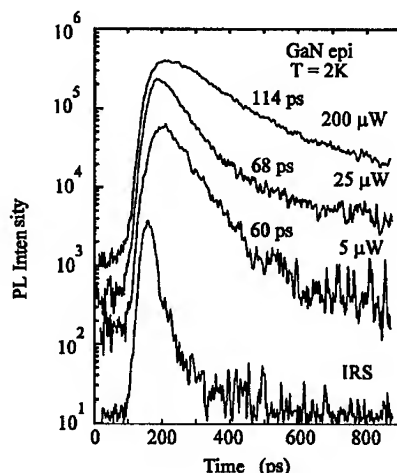


Figure 4. Decay curves of the FE recombination from sample B.

EXPERIMENTAL RESULTS AND DISCUSSION

The PL spectrum from sample A is shown in Fig. 1. The spectrum is at low temperatures dominated by the recombination of donor bound excitons, with a shoulder at the high energy side corresponding to the recombination of FE's. At increasing temperature the intensity of the DBE is quenched due to the relatively small binding energy of the DBE. At the same time, the intensity of the FE recombination increases giving an almost constant total PL emission intensity. This increase demonstrates the strong interaction between the FE and the DBE, where an important recombination mechanism for the FE is the capture to a donor thus creating a DBE. The decay time of the FE in this sample is relatively fast, below 100 ps. The decay time for the DBE is longer, about 260 ps, as shown in Fig. 2. Also shown in Fig. 2 is the measured decay at low temperature for the ABE, which is weakly observed in some samples.

The PL spectrum for the epitaxial layer B is shown in Fig. 3. The emission is dominated by the FE recombination at 3.488 meV. Weak shoulders on the high energy side of the main peaks indicate the presence of the two higher exciton states. The lowest two different states, labelled A and B, are due to the corresponding splitting of the valence band. On the low energy side additional weaker peaks corresponding to the recombination of the DBE and the ABE are observed. The time decay of the dominating FE recombination is shown in Fig. 4, for different excitation intensities. At low excitation intensity the observed decay time is relatively fast, of the order 60 ps. This is comparable to previously published decay times of the FE. With increasing excitation intensity we observe an increase of the observed decay time. This is interpreted as a partial saturation of non-radiative recombination channels. The observed decay time at low excitation intensity should then be dominated by this non-radiative recombination. By increasing the intensity we saturate the centers responsible for the non-radiative recombination and the observed decay time increases and should eventually approach the true radiative recombination rate. The decay time at highest available excitation intensity is about 114 ps. Since we can not further increase the excitation intensity, we can not determine whether this decay time is the

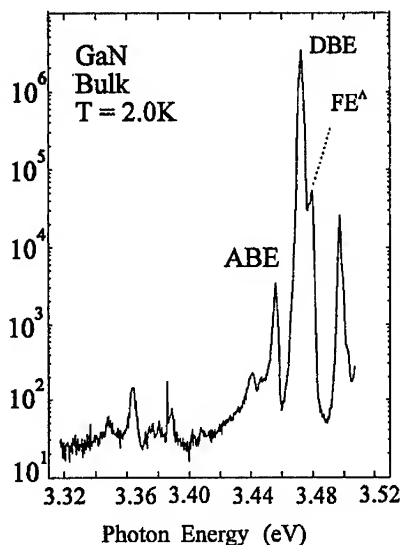


Figure 5. PL spectrum from the high quality bulk GaN sample (C).

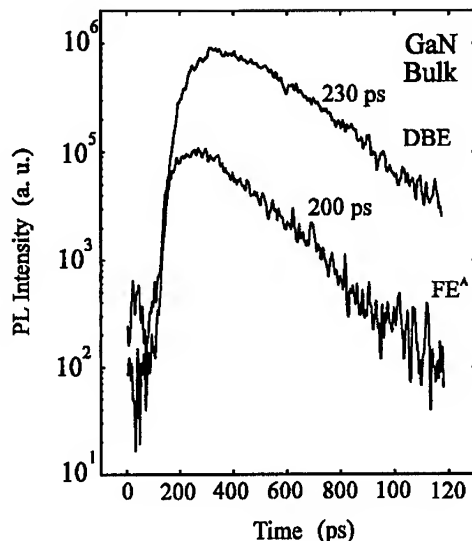


Figure 6. Decay curves at 2K of the DBE and the FE emissions in GaN

radiative lifetime or whether it is still dominated by non-radiative recombination processes. The decay time of the FE shows only a very weak temperature dependence at these low temperatures. It increases slightly up to 10K and is at higher temperatures rapidly decreasing. There are several possible non-radiative recombination channels. One important non-radiative recombination processes for the FE is the capture of the exciton to defects, donors or acceptors. This process is non-radiative in the sense that it reduces the FE population without emitting a photon at the corresponding FE energy. However, the recombination of the DBE and ABE are mainly radiative so this capture process is not a non-radiative process for the photoexcited carriers. The emission intensity related to the DBE and the ABE is however very low in this sample and we believe that the concentration of these substitutional defects are too low to be the dominating recombination channel. The observed decay time at low excitation intensities is also comparable to the value obtained in other samples which shows a much higher emission from the bound excitons. The most probable non-radiative recombination is instead dislocations which are known to exist in high concentration, due the stress induced by the lattice mismatch in heteroepitaxial samples.

The spectra at 2.0 K, using pulsed excitation, from the bulk sample (C) is shown in Figure 5. The sample has sharper emission lines, as compared to the previous sample, with a FWHM less than 2.0 meV. The different exciton emissions can clearly be resolved at 3.471 eV (DBE), and 3.479 eV (FE^A), respectively. The origin of the emission at 3.497 eV is yet unknown. Several emissions such as excited states of the FE^A and FE^B or band to band recombinations are possible at this energy region. The ABE at 3.455 eV [1] is also present, but relatively weak, in this sample. Under certain excitation conditions, i.e. with the excitation energy below the bandgap, it

is possible to resolve another BE at 3.468 eV [1] as a weak shoulder on the low energy side of the DBE, as can be seen in Fig. 5.

The decay curve of the DBE and FE^A exciton emissions are shown in Figure 6. The FE^A exciton has a fast rise time with an almost exponential decay with a decay time of 200 ps. The spectrally dominating DBE emission has a longer decay time of more than 230 ps. The rise time is however also longer and similar to the decay time of the FE^A emission. It is reasonable to assume that transfer processes occur between the free and bound state. This means that the population of DBE's is formed by capture of free excitons. The observed value for the DBE decay time obtained with above bandgap excitation could then be determined by the population lifetime of the FE. By assuming a complete feeding from the FE^A state and deconvoluting the observed decay curve for the DBE, we obtain a decay time of 190 ps for FE^A at 2.0 K.

The values for the decay time in this third sample is somewhat longer than previously reported for thin GaN layers [6]. In general, it is difficult, especially for the FE recombination, to determine whether the observed decay time is the true radiative recombination time or influenced by non-radiative processes. The longest measured decay time for the FE's should be the value closest to the radiative decay time. The presence of other and additional processes can only reduce the observed decay time. The most probable non-radiative recombination process for the FE in bulk material is the capture of the FE to defects.

In this sample we have not observed any intensity dependence of the measured decay time, which as a comparison to previous samples, indicates that the recombination at low temperatures in sample C is dominated by radiative recombinations.

We have also measured the temperature dependence of the FE emission, as seen in Fig. 7. The observed increase of the measured decay time is a strong indication that the observed recombination is close to the true radiative recombination time. For the radiative recombination of a FE we do expect an increase in decay time due to a thermal redistribution of the excitons. This reduces the relative number of excitons with small momentum, which are the only excitons involved in the radiative recombination. The observed increase of the FE decaytime is only present up to about 20 K. At higher temperatures we observe a decrease of the decay time, believed to be due to the onset of a non-radiative recombination process.

The decay time values for the FE's in the GaN sample C is still very fast as compared to other materials. In GaAs a longest free exciton decay time of 3.3 ns at 2K has been observed [7]. An increase of the recombination probability is expected for GaN as compared to GaAs, mainly due to the increase in photon energy. The exciton decay time is roughly proportional to the recombination photon energy, the exciton absorption coefficient and the refractive index

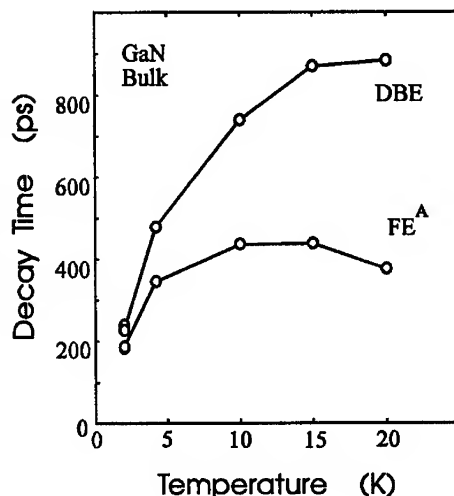


Figure 7. Temperature dependence of the decay time for the DBE and the FE, in the bulk sample (C). The observed increase is expected for a dominating radiative recombination.

according to $(\hbar\omega^2 \eta^2 \alpha_{ex})^{-1}$. This gives a reduction of the decay time with a factor of 20 as compared to GaAs. The so estimated value of 200 ps is in reasonable agreement with our experimental results. A more exact calculation of the FE decay time in GaN requires knowledge of several additional material parameters, such as effective masses and spin-orbit splittings, which are not yet accurately determined for GaN.

ACKNOWLEDGEMENT

The work at Meijo University was supported by the Ministry of Education, Science and Culture of Japan (Contract #'s 06452114 and 07650025), Research Foundation for Electrotechnology of Chubu, Nissan Science Foundation and Iketani Science and Technology Foundation.

REFERENCES

- 1 R. Dingle, D.D. Sell, S.E. Stokowski, and M. Heegans, Phys. Rev. B4, 1211 (1971).
- 2 P. Bergman, Gao Ying, B. Monemar, and P.O. Holtz, J. Appl. Phys. 61, 45989, (1987).
- 3 M. Smith, G.D. Chen, J.Y. Lin, H.X. Jiang, A. Salvador, B.N. Sverdlov, A. Botchkarev, and H. Morkoc, Appl. Phys. Lett. 66, 3474 (1995).
- 4 T. Detchprohm, H. Amano, K. Hiramatsu, and I. Akasaki, Appl. Phys. Lett. 61, 2688 (1992).
- 5 B. Monemar, Phys. Rev. B10, 676 (1974).
- 6 C.I. Harris, B. Monemar, H. Amano, and I. Akasaki, Appl. Phys. Lett. 67, 8061 (1995).
- 7 G.W.'t Hooft, W.A.J. van der Poel, L.W. Molenkamp, and C.T. Foxon, Phys. Rev. B. 35, 8281 (1987).

Part IX

**Hydrogen, Etching and Other Materials
Processes**

DRY ETCHING OF III-V NITRIDES

S. J. Pearton⁽¹⁾, R. J. Shul⁽²⁾, G. F. McLane⁽³⁾ and C. Constantine⁽⁴⁾

⁽¹⁾University of Florida, Gainesville, FL 32611 USA

⁽²⁾Sandia National Laboratories, Albuquerque NM 87185 USA

⁽³⁾Army Research Laboratory, Ft. Monmouth NJ 07703 USA

⁽⁴⁾Plasma Therm IP, St. Petersburg FL 33716 USA

ABSTRACT

The chemical inertness and high bond strengths of the III-V nitrides lead to slower plasma etching rates than for more conventional III-V semiconductors under the same conditions. High ion density conditions ($>3 \times 10^{11} \text{ cm}^{-3}$) such as those obtained in ECR or magnetron reactors produce etch rates up to an order of magnitude higher than for RIE, where the ion densities are in the 10^9 cm^{-3} range. We have developed smooth anisotropic dry etches for GaN, InN, AlN and their alloys based on $\text{Cl}_2/\text{CH}_4/\text{H}_2/\text{Ar}$, BCl_3/Ar , Cl_2/H_2 , Cl_2/SF_6 , HBr/H_2 and HI/H_2 plasma chemistries achieving etch rates up to $\sim 4,000 \text{ \AA}/\text{min}$ at moderate dc bias voltages ($\leq 150 \text{ V}$). Ion-induced damage in the nitrides appears to be less apparent than in other III-V's. One of the key remaining issues is the achievement of high selectivities for removal of one layer from another.

INTRODUCTION

Applications for the wide bandgap nitrides include emitters in the blue/green/UV sections of the spectrum, solar-blind UV detectors and transistors capable of operation up to $\sim 500^\circ\text{C}$.⁽¹⁾ Much of the recent progress in these technologies has occurred on the materials side,⁽²⁻⁵⁾ with improvements in epitaxial growth quality, higher n- and particularly p-type doping levels and lower impurity concentrations. A significant road-block to realization of a continuous wave, electrically-pumped diode laser is the fact that most GaN and related alloys are grown on c- Al_2O_3 substrates with hexagonal symmetry. Therefore, cleavage to form laser facets is not feasible, at least with any practical yield. There is interest in dry etched laser facets for the nitrides and this will require achievement of smooth, highly anisotropic sidewalls in GaN-based epitaxial layers. A particularly relevant feature of forming laser mirrors or mesas by dry etching is that the sidewall usually has vertical striations that result from transfer of roughness on the mask edge into the semiconductors. The other requirement is that the GaN etch rates be reasonably fast (at least more than a few thousand angstroms per minute) since the total etch depth is going to be $\geq 4 \mu\text{m}$.

Table 1 shows a compilation of published dry etch rates for GaN.⁽⁶⁻¹⁶⁾ The conclusions from this data are fairly clear, namely

(i) etch rates under high ion density conditions (Electron Cyclotron Resonance, ECR, or magnetron-enhanced reactive ion etching, MIE) are much higher than for conventional RIE.

(ii) Halogen-based plasma chemistries produce much higher rates than for CH_4/H_2 , regardless of the etching technique.

(iii) the highest etch rates are $\leq 4,000 \text{ \AA}/\text{min}$, which is slower by a factor of 3-5 than conventional III-V's like GaAs under the same conditions.

In this paper we contrast some of the results obtained with Cl_2/H_2 , HBr/H_2 and HI/H_2 ECR etching of the binary nitrides in terms of rates, surface morphology and quality of the resultant sidewall. Under optimized conditions, the quality of this sidewall again appears to be determined by the initial mask material.

EXPERIMENTAL

The nitride layers were grown on Al_2O_3 or GaAs substrates by Metal Organic Molecular beam Epitaxy.⁽¹⁷⁻¹⁹⁾ The materials are defective single-crystal with a high density of threading dislocations and stacking faults ($\sim 10^{10} \text{ cm}^{-2}$). They were patterned with SiN_x masks and etched in several SLR 770 Plasma-Therm systems with rf biased, He-backside cooled sample chucks and ECR plasma sources.

RESULTS AND DISCUSSION

In general etch rates increased with rf power (or ion energy) or microwave power (ion current) and decreased with increasing pressure in $\text{Cl}_2/\text{CH}_4/\text{H}_2/\text{Ar}$ plasma chemistries, while there was little dependence on temperature. In Figure 1, we observe a general increase in etch rate as the microwave power and therefore the ion density is increased. This trend agrees with decreasing etch rates which were observed at higher pressures and lower ion densities. The etch rate for GaN and AlN increases moderately (less than a factor of 2) as the microwave power is increased from 125 to 850W, whereas the InN etch rate increases monotonically from 1040 to 3670 Å/min. Following exposure to the plasma, within experimental error, there is no change in the stoichiometry of the GaN surface for either 30 or 170°C etching and some residual atomic Cl is present. Similar results were observed for the InN and AlN samples.

Table I. Plasma chemistries for dry etching of GaN

Plasma	Technique	GaN etch rate (Å/min)	dc bias	Ref.
Cl_2/H_2	ECR	1,100	-150	10, 11
Cl_2/SF_6	ECR	900	-150	11
$\text{CH}_4/\text{H}_2/\text{Ar}$	ECR	400	-250	10
$\text{Cl}_2/\text{CH}_4/\text{H}_2/\text{Ar}$	ECR	3,100	-125	12
$\text{Cl}_2/\text{H}_2/\text{Ar}$	ECR	2,200	-100	13
CCl_2F_2	ECR	400	-250	14
BCl_3	RIE	500	-230	15
BCl_3	MIE	3,500	-75	16
$\text{SiCl}_4(\text{Ar}, \text{SiF}_4)$	RIE	500	-400	17
$\text{HBr}(\text{H}_2/\text{Ar})$	RIE	600	-400	18
HI/H_2	ECR	1,100	-150	19
HBr/H_2	ECR	900	-150	19
Ar	ion milling	250	-400	20
Cl_2/Ar	CAIBE	2,000	-600	13

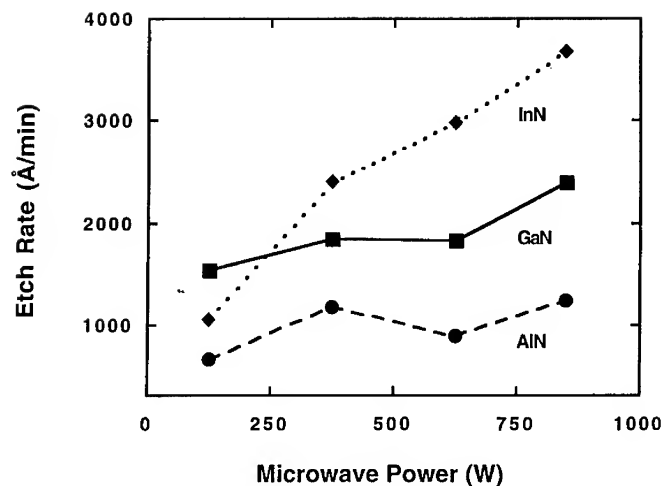


Figure 1. Etch rates of GaN, InN and AlN as a function of microwave power for an ECR generated $\text{Cl}_2/\text{H}_2/\text{CH}_4/\text{Ar}$ plasma.

SEM micrographs of mesas formed in GaN by ECR etching in a $10\text{HI}/10\text{H}_2$, -150V , 1000W (microwave) discharge are shown in Figure 2. The SiN_x mask has been removed. The etched field has similar morphology to that of the initial (masked) area on top of the mesa. The anisotropy is reasonably good ($\sim 75^\circ$ sidewall angle). The striations present originate from similar roughness on the edge of the SiN_x mask, which in turn is transferred from the original photoresist that was used to pattern the SiN_x . This illustrates one of the key problems in trying to form an etched laser facet. The striations lead to scattering and loss of light either propagating down a laser stripe or incident on a facet.

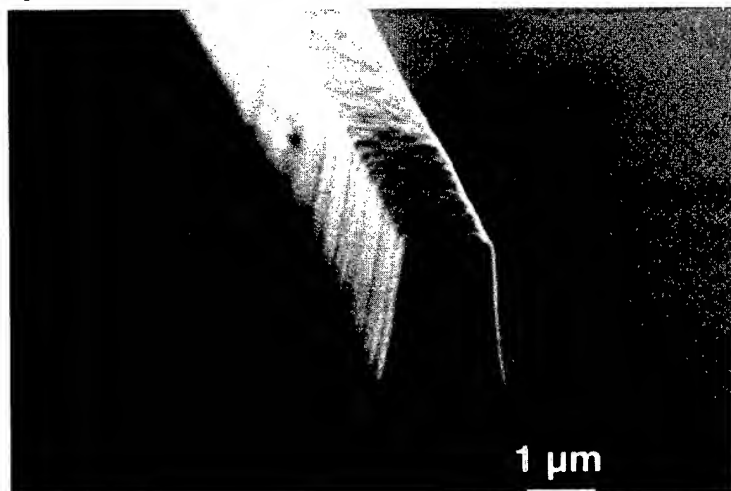


Figure 2. SEM micrographs of feature etched into GaN with HI/H_2 .

The fastest etch rates were obtained with $\text{Cl}_2/\text{CH}_4/\text{H}_2/\text{Ar}$ ECR discharges. Figure 3 shows both GaN etch rate and root mean square (RMS) surface roughness measured by AFM, as a function of rf power in $10\text{Cl}_2/3\text{CH}_4/15\text{H}_2/10\text{Ar}$ discharges at a pressure of 1mTorr and a microwave power of 850W. Note that the etch rate increases in a linear fashion, suggesting that the sputter-assisted desorption of the etch products is the limiting step. The GaN surface roughness remains fairly similar to that of the as-grown material until ~150W, and worsens rapidly thereafter. However it is still possible to achieve a rate of $\sim 2,500\text{\AA}/\text{min}$ with excellent morphology. The onset of surface roughening corresponds to an increasing Ga-to-N ratio measured by Auger Electron Spectroscopy as N is preferentially lost by sputtering at high ion energies. The $\text{Cl}_2/\text{CH}_4/\text{H}_2/\text{Ar}$ plasma chemistry produces etch rates of $\geq 1\mu\text{m}/\text{min}$ for InP, GaAs and other more common III-V materials for these same conditions, emphasizing the difficulty in achieving very high rates for the nitrides.

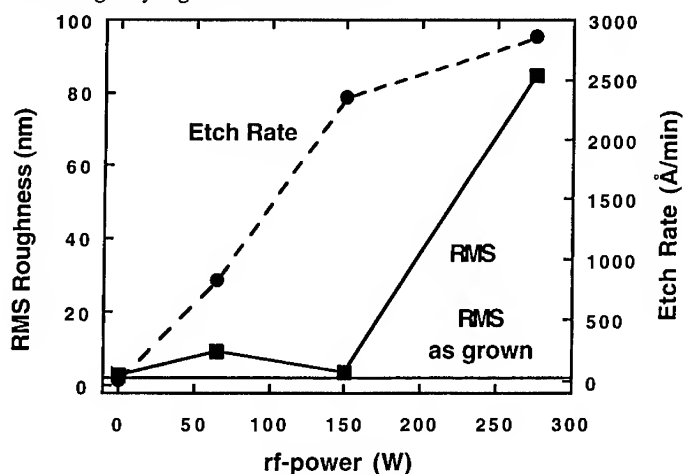


Figure 3. GaN surface roughness and etch rate as a function of rf power in ECR $\text{Cl}_2/\text{CH}_4/\text{H}_2/\text{Ar}$ discharges.

Figure 4 (top) shows SEM micrographs of features produced in nitride structures with $10\text{HBr}/10\text{H}_2$, 1000W (microwave) discharges. The structure is an $\text{AlN}/\text{GaN}/\text{AlN}$ multilayer, which clearly demonstrates the differential undercut between the two materials in HBr/H_2 discharges. By contrast, use of a HI/H_2 plasma chemistry under the same conditions produces relatively uniform mesas (Figure 4, bottom). Note that the etched surface morphology even after removing $\sim 3.5\mu\text{m}$ is still good, and there is little differential etching between the foot of the mesa and areas out on the field. This is a benefit of the low process pressures employed under ECR conditions, which minimize such effects.

The sidewall roughness is also considerably worse under high dc bias conditions (Figure 5, left) due to mask erosion, whereas it is much smoother at dc biases $\leq 125\text{V}$ (right of figure)

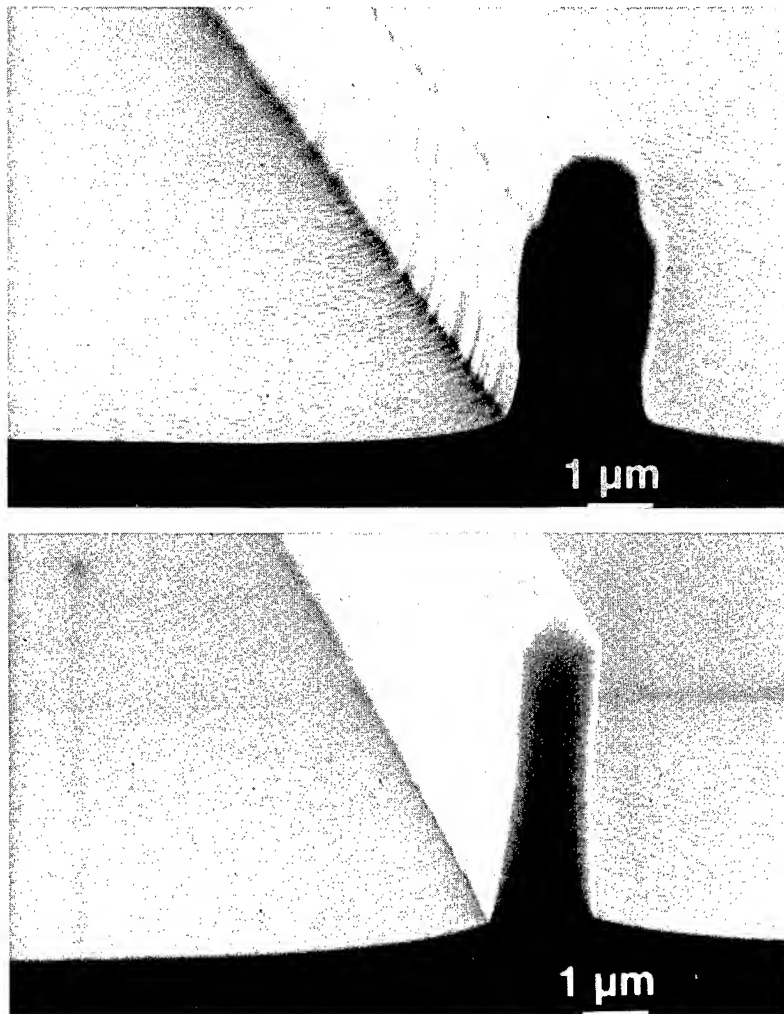


Figure 4. SEM micrographs of features etched into AlN/GaN/AlN structure using HBr/H₂ or HI/H₂ (bottom).

CONCLUSIONS AND SUMMARY

The same basic plasma chemistries that are used for conventional III-V materials also work for GaN, AlN and InN. The resulting etch rates are typically 3-4 times slower than for GaAs, InP and so on. High ion densities conditions such as those found in ECR or MIE systems produce significantly faster rates than reactive ion etching. Sidewall corrugations on dry etched photonic device structures are usually present, and will require careful control of the masking material quality and its integrity during the etching processes.

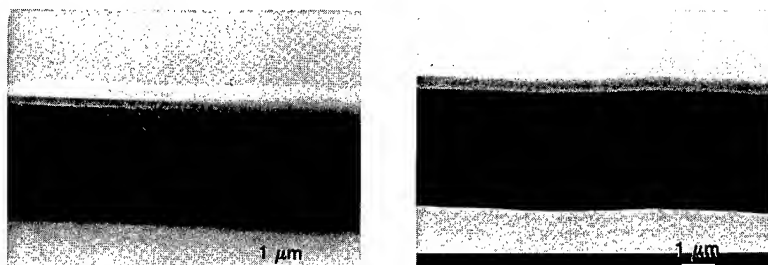


Figure 5. SEM of laser structure sidewall using (left) high dc bias or (right) low dc bias.

ACKNOWLEDGMENTS

The authors at UF is partially supported by a DOD University Research Initiative administered through AFOSR (Project 3484RS). The work at SNL is supported by DOE under contract no. DE-AC04-94AL85000. The work at UF is performed in the Microfabritech facility.

REFERENCES

1. see for example, Properties of Group III Nitrides, ed. J. H. Edgar, INSPEC Datareview (IEEE, London UK, 1994).
2. I. Akasaki, H. Amano, M. Kito and K. Hiramatsu, *J. Lumin.* **48/49** 666 (1991).
3. T. Matsuoka, *J. Cryst. Growth* **124** 433 (1992).
4. C. R. Abernathy, S. J. Pearton, F. Ren, P. Wisk, *J. Vac. Sci. Technol. B* **11** 179 (1993).
5. S. Nakamura, T. Mukai and M. Senoh, *Jap. J. Appl. Phys.* **32** L169 (1993).
6. S. J. Pearton, C. R. Abernathy and F. Ren, *Appl. Phys. Lett.* **64** 2294 (1994).
7. S. J. Pearton, C. R. Abernathy and F. Ren, *Appl. Phys. Lett.* **64** 3643 (1994).
8. R. J. Shul, A. J. Howard, S. J. Pearton, C. R. Abernathy, C. B. Vartuli, P. A. Barnes and M. J. Bozack, *J. Vac. Sci. Technol. B* **13** 2016 (1995).
9. R. J. Shul, S. P. Kilcoyne, M. H. Crawford, J. E. Parmeter, C. B. Vartuli, C. R. Abernathy and S. J. Pearton, *Appl. Phys. Lett.* **66** 1761 (1995).
10. S. J. Pearton, C. R. Abernathy, F. Ren, J. R. Lothian, P. Wisk, A. Katz and C. Constantine, *Semicond. Sci. Technol.* **8** 310 (1993).
11. M. E. Lin, Z. F. Fan, Z. Ma, L. H. Allen and H. Morkoc, *Appl. Phys. Lett.* **64** 887 (1994).
12. G. F. McLane, L. Casas, S. J. Pearton and C. R. Abernathy, *Appl. Phys. Lett.* **66** 3328 (1995).
13. I. Adesida, A. Mahajan, E. Andideh, M. A. Khan, D. T. Olsen and J. N. Kuznia, *Appl. Phys. Lett.* **63** 2777 (1993).
14. A. T. Ping, I. Adesida, M. A. Khan and J. N. Kuznia, *Electron. Lett.* **30** 1895 (1994).
15. S. J. Pearton, C. R. Abernathy and C. B. Vartuli, *Electron. Lett.* **30** 1985 (1994).
16. S. J. Pearton, C. R. Abernathy, F. Ren and J. R. Lothian, *J. Appl. Phys.* **76** 1210 (1994).
17. C. R. Abernathy, *J. Vac. Sci. Technol. A* **11** 869 (1993).
18. C. R. Abernathy, J. D. MacKenzie, S. J. Pearton, S. Bharatan and K. S. Jones, *J. Vac. Sci. Technol. A* **13** 2104 (1995).
19. C. R. Abernathy, J. D. MacKenzie, S. J. Pearton and W. S. Hobson, *Appl. Phys. Lett.* **66** 1969 (1995).

HYDROGEN IN GaN

N. M. JOHNSON, W. GÖTZ, J. NEUGEBAUER, AND C. G. VAN DE WALLE
Xerox Palo Alto Research Center, Palo Alto, California 94304, USA

ABSTRACT

Hydrogen is implicated in the low doping efficiency of acceptors (e.g., Mg) in MOCVD-grown GaN by the following observations: the well-established role of hydrogen in the same phenomenon in other semiconductors; re-passivation of thermally activated Mg in GaN upon exposure to NH_3 or H at temperatures $> 400^\circ\text{C}$; correlation between Mg and H concentrations; and computational studies on the diffusivities of charged H in GaN and on the configuration and stability of the Mg-H complex in GaN. Strong experimental evidence for the Mg-H complex comes from variable-temperature Hall effect measurements which reveal that after hydrogenation of activated GaN:Mg the hole mobility increases as the hole concentration decreases, which is consistent with removal of ionized scattering centers and not with the introduction of separate compensating defects. However, experimental evidence is also accumulating to suggest that the Mg activation process involves the generation or transformation of electrically active defects.

INTRODUCTION

Epitaxial layers of GaN grown by MOCVD require a deliberate post-growth processing step to activate the shallow acceptor dopant, which is commonly Mg. Demonstrated activation techniques are low energy electron beam irradiation (LEEBI) [1] and furnace annealing [2]. The involvement of hydrogen in the low acceptor doping efficiency of MOCVD-grown GaN is implicated by many observations and theoretical considerations, which are summarized in this review.

Acceptor-Hydrogen Complexes

It is now well established by both theory and experiments that hydrogen forms stable complexes with shallow acceptor dopants in a host of elemental and compound semiconductors [3]. For boron acceptors in silicon, the complex is energetically most stable with the hydrogen situated at a bond-center site between the substitutional boron and an adjacent silicon [4]. Similarly, for the zinc acceptor in GaAs the hydrogen resides in a bond-center position between the zinc (on a Ga site) and an adjacent As atom [5]. In both cases the electrical consequence of the complex is neutralization of the dopant impurity so that the acceptor energy level is removed from the bandgap and, therefore, the material becomes more electrically resistive.

Another important common feature of such complexes is that they are only moderately stable. The thermal dissociation energies for B-H in silicon [6] and Zn-H in GaAs [7,8] are both ~ 1.3 eV. The dissociation energy is approximately equal to the sum of the binding energy of the complex and the activation energy for diffusion of the (charged) hydrogen [9]. The most reliable values for dissociation energies have been

obtained from experiments designed to isolate the dissociation kinetics from the total phenomenon of dopant activation which includes dissociation, recombination, and hydrogen migration. With the "depletion-layer" technique the dopant-hydrogen complexes are situated in the space-charge layer of a reverse-biased diode so that recombination is suppressed due to field-driven sweep-out of the dissociated charged hydrogen [10]. Such experiments have not yet been reported for Mg-doped GaN.

Sources of Hydrogen

The MOCVD growth technique is inherently rich in sources of hydrogen that can be incorporated into the growing film. The group III gaseous precursors for the AlGaInN system are metalorganic compounds (e.g., TMGa) that can produce hydrocarbon radicals (e.g., CH_3) and stable hydrocarbons (e.g., CH_4) as products of the growth reactions. The currently most widely used precursor for nitrogen is NH_3 . The precursors for dopant impurities are typically obtained from either metalorganics (e.g., Cp_2Mg and DEZn) or hydrides (e.g., SiH_4). Finally, the carrier gas is typically molecular hydrogen, although its stability renders H_2 the least serious source of hydrogen incorporation.

Hydrogen incorporation during MOCVD-growth of Mg-doped GaN has been demonstrated with secondary ion mass spectrometry (SIMS). In particular, it has been shown that the hydrogen concentration increases linearly with the Mg concentration [11]. It has also been reported with SIMS data that the hydrogen concentration decreases after furnace anneals which activate the Mg acceptors [11,12]. The furnace anneal is typically performed in the temperature range from 700°C to 850°C for times of 5 to 60 min and in an ambient of flowing N_2 .

High acceptor doping efficiencies have been achieved in Mg-doped GaN layers without post-growth treatment by MBE [13]. Chemically active nitrogen was obtained from N_2 with an ECR plasma source, and none of the other precursors deliberately contained hydrogen. The high doping efficiency may reflect the absence of hydrogen in the growth process, although there are other fundamental differences between MOCVD and MBE (e.g., approximation to thermal equilibrium).

EXPERIMENTAL RESULTS

Hydrogen Diffusion

Hydrogen diffusion into GaN depends strongly on the conductivity type of the material as well as on diffusion conditions (e.g., temperature and time). This is illustrated in Fig. 1 with depth profiles of deuterium in MOCVD-grown GaN [14]. The p-type conductivity was obtained from Mg-doped, furnace-activated GaN samples with a hole concentration at room temperature of $8 \times 10^{17} \text{ cm}^{-3}$. The n-type GaN was Si doped to a concentration of $2 \times 10^{17} \text{ cm}^{-3}$. The deuterations were performed in a remote microwave plasma system [15], and the hydrogen isotope was detectable with high sensitivity by SIMS. For the p-type material, depth profiles are shown after deuteration at 400°C and 600°C. The amount of deuterium that has diffused into the p-type GaN at 600°C is substantial and available to play a role in acceptor passivation [2,14,16], as further discussed below. In dramatic contrast, no deuterium is detectable in the n-type material after deuteration at temperatures from 200°C to 600°C, and there is no change

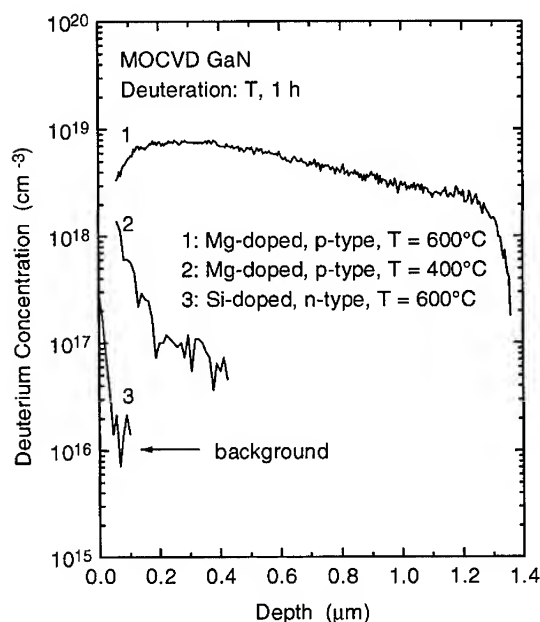


Fig. 1. Depth distributions of deuterium in specimens of GaN with either p-type or n-type conductivity after deuteration at different temperatures.

in the electronic properties after these deuteration. Computational studies to be reviewed below provide a fundamental understanding of these results.

H-neutralized Mg

Strong experimental evidence for the existence of the Mg-H complex has been obtained from variable-temperature Hall effect measurements [14]. Results are presented in Fig. 2 for p-type, Mg-doped GaN before and after deuteration at 600°C. (The p-type material and deuteration conditions were the same as for Fig.1.) The material was furnace activated prior to the experiment. In Fig. 2(a) the hole concentration is observed to be thermally activated above 250 K and dominated by impurity band conduction at lower temperatures. The solid lines in Fig. 2(a) were calculated from the charge neutrality condition by assuming that the Mg introduces a single acceptor level with an activation energy of 170 meV and allowing for uniform donor compensation [17]. The analysis yields an effective acceptor concentration of $8 \times 10^{19} \text{ cm}^{-3}$ after the post-growth furnace anneal, which agrees within experimental uncertainty ($\sim 50\%$) with the total Mg concentration as determined from SIMS. After deuteration the hole concentration has significantly decreased, as reported in a

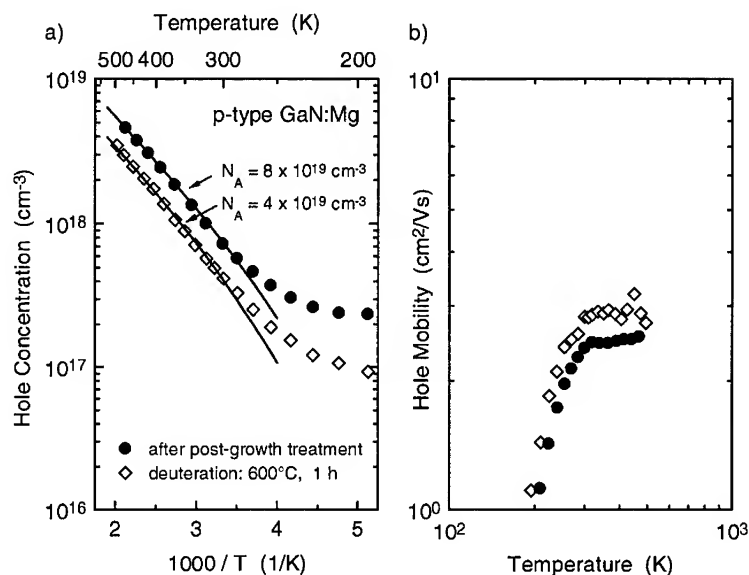


Fig. 2. Variable-temperature Hall effect data for p-type, Mg-doped GaN before and after deuteration at 600°C : (a) hole concentration and (b) hole mobility.

previous study [16], which indicates a reduction in the effective acceptor concentration. This response to hydrogenation could be the consequence of either the introduction of separate compensating defects or the formation of acceptor-hydrogen complexes.

Examination of the Hall mobility for holes before and after the 600°C deuteration provides a means to distinguish between the two possible passivation processes. As shown in Fig. 2(b), the hole mobility increases after deuteration. This is consistent with removal of ionized acceptor scattering centers and not with the introduction of separate compensating defects.

Defects

The process of thermally activating Mg acceptors in GaN appears to be accompanied by the generation or transformation of deep level defects. This is illustrated in Fig. 3 [18] with photoluminescence (PL) spectra from a single specimen of the material first as-grown and then after sequential anneals at 500°C , 700°C , and 775°C ; the spectrum after a 600°C anneal is identical to that for the 500°C anneal. The spectrum for the as-grown material is dominated by a broad luminescence band in the blue region of the visible spectrum. The band contains a zero phonon line, labeled L1, and LO phonon replicas. This band "red-shifts" (within the blue region) by $\sim 0.25 \text{ eV}$ after anneals at $\geq 500^\circ\text{C}$, with the new zero phonon line labeled L2. After annealing at 775°C a weak broad (blue) band appears centered at 435 nm .

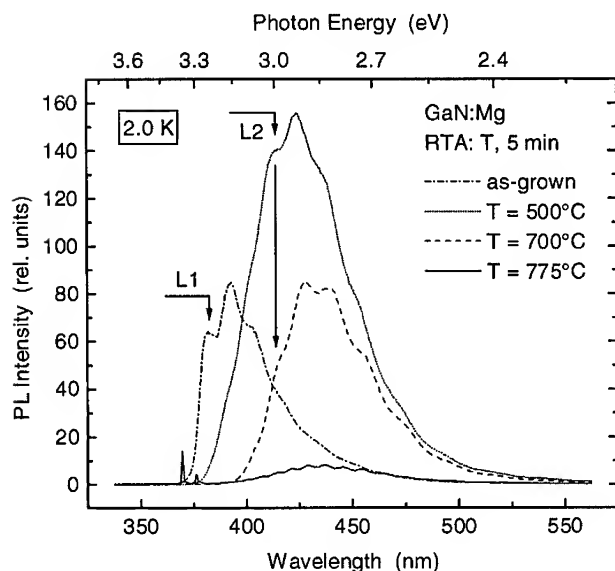


Fig. 3. Photoluminescence (PL) spectra for Mg-doped ($\sim 6 \times 10^{19} \text{ cm}^{-3}$) GaN as-grown and after annealing at incremental temperatures. The sample was annealed in a rapid thermal anneal (RTA) system at the specified temperatures T for 5 min in flowing N_2 , and the PL measurement utilized a HeCd laser (325 nm) for photogeneration of electron-hole pairs with the specimen at 2 K.

In addition to the red-shifted blue band, a set of sharp lines appears near the bandedge after the 775°C anneal. These lines are observed only when Mg is present in the material, and their intensities are attenuated by hydrogenation at 600°C, which also reduces the hole concentration. These observations suggest a correlation between the near-bandedge PL lines and activated Mg. However, the microscopic nature of this connection remains to be determined.

THEORY

Detailed information has recently become available from computational studies on the electronic structure, energetics, and migration of hydrogen and hydrogen complexes in GaN [19,20]. These studies utilized first-principles total-energy calculations based on density-functional theory and *ab-initio* pseudopotentials. They were performed for cubic GaN in order to take advantage of its higher symmetry as compared to the wurtzite structure; the results are considered valid for hydrogen in either the zincblende and wurtzite structure. Highlights of these studies are summarized below for later comparison with experimental results.

Monatomic Hydrogen

The total energy calculations for monatomic interstitial hydrogen in GaN have identified stable sites, migration paths, and diffusion barriers for all three charge states (i.e., H^+ , H^0 , H^-). Total energies were calculated by fixing the H atom at different positions and allowing all other atoms to relax. The energetically most stable site for H^+ was found to be the nitrogen antibonding site (AB_N), as depicted in Fig. 4(a). This preference for the AB_N site is in striking contrast to the behavior of H^+ in Si and GaAs, where the bond-center position is the most stable site. This difference reflects the more ionic character of GaN as compared to GaAs. The H^+ prefers sites with high negative charge density for maximum screening. Unlike GaAs, in GaN there is no local maximum at the bond center, rather the charge density monotonically increases from the Ga towards the much more electronegative N, which results in a nearly spherically symmetric charge density around the N. While this feature alone favors all positions around the N atom, the BC site is unfavorable due to the addition of strain energy involved in relaxing the Ga and N atoms outwards. The migration barrier for H^+ was found to be 0.7 eV, which is sufficiently small to ensure high mobility even near room temperature.

The energetically most stable position for H^- was found to be the Ga antibonding site (T_d^{Ga}), as depicted in Fig. 4(b). The H^- is strongly confined at the T_d^{Ga} site, with a large migration barrier of ~3.4 eV. Therefore, H^- is expected to have a very limited mobility in GaN.

The formation energies of the different charge states of monatomic hydrogen in GaN were calculated as a function of the Fermi energy [19,20]. For Fermi energies

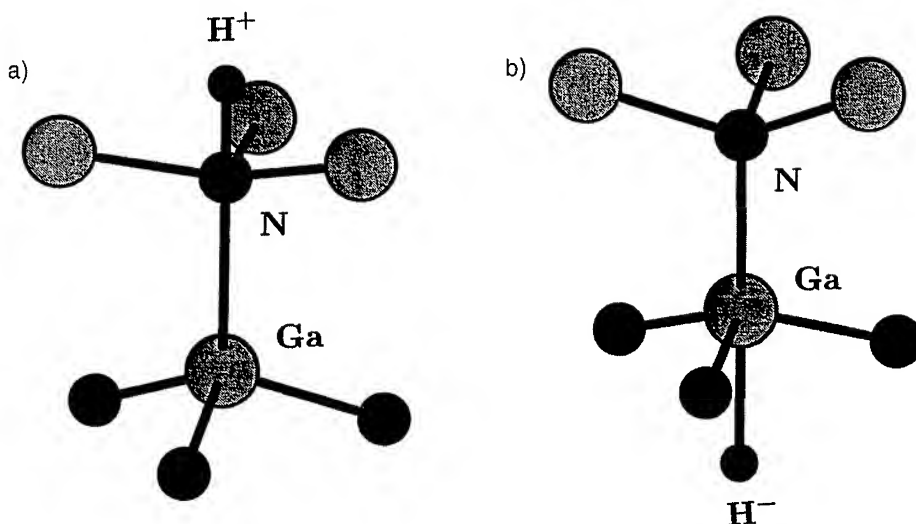


Fig. 4. Stick-and-ball illustrations of the most stable configurations for isolated interstitial hydrogen in GaN from total energy calculations: (a) H^+ and (b) H^- .

within ~ 2.1 eV of the valence band, H^+ is the energetically most stable charge state. Thus, H^+ is expected to be the predominant charge state in p-type GaN. For Fermi energies higher than ~ 2.1 eV, H^- is the most stable species, so that H^- predominates in n-type GaN. The H^0 is never the predominant stable charge state. This reveals that hydrogen in GaN has a negative effective correlation energy (commonly designated "negative U "), with a calculated value of -2.4 eV. This is the largest negative U yet calculated or measured for hydrogen in a semiconductor. For example, for H in silicon, $U \approx -0.4$ eV [21]. The formation energies also indicate that the solubility is high for H^+ in (p-type) and low for H^- in (n-type) GaN.

Mg-H Complex

The calculations also provide strong support for the formation of the Mg-H complex in GaN and reveal a novel atomic structure which is qualitatively different from the well-established configuration for the acceptor-hydrogen complex in other semiconductors [19,20]. As illustrated in Fig. 5, the hydrogen prefers the AB site of one of the N neighbors. The Mg-H complex contains a N-H bond with a calculated H stretch mode frequency of 3360 cm^{-1} , which is very close to that of H in NH_3 (3444 cm^{-1}). An estimate

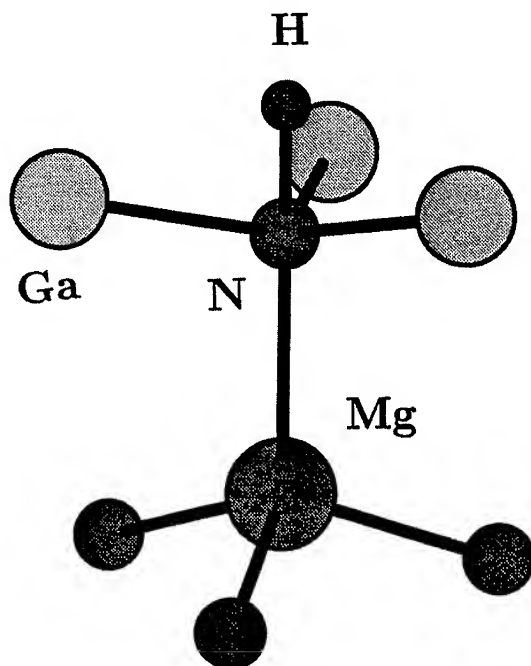


Fig. 5. Stick-and-ball model for the Mg-H complex in GaN from total energy calculations.

of 1.5 eV was obtained for the dissociation energy of the Mg-H complex. This estimate specifically applies to a jump from the AB_N site to a neighboring N atom which is a second-nearest neighbor to the Mg atom. This is only the first step in the dissociation reaction after which the Mg atom is still compensated by the H^+ atom. Therefore, this calculated dissociation energy may represent only a lower limit to the actual value, for which there is as yet no experimental determination.

DISCUSSION AND CONCLUSIONS

It has been proposed that hydrogen incorporation during growth of GaN is actually beneficial for the practical realization of p-type conductivity [22,23]. When acceptors are intentionally incorporated in the growing material it is energetically favorable for compensating donors to form in wide bandgap semiconductors under thermal equilibrium. In the absence of donor impurities and if formation energies permit, donor-like native defects will be generated to provide the compensation. Such defects can be highly stable. Since their concentration is determined by thermal equilibrium, high-temperature post-growth annealing cannot remove the compensating native defects. Alternatively, incorporation of hydrogen donors (H^+) during growth suppresses the formation of compensating native defects. In Mg-doped GaN, compensation can be enabled by the presence of monatomic hydrogen donors during growth. These complexes can subsequently be dissociated at moderate temperatures (e.g., [18]) and the hydrogen removed or rendered electrically inactive (perhaps at internal surfaces such as grain boundaries or at extended defects such as dislocations) to achieve p-type conductivity.

Comparison of electrical and PL data for the thermal activation of Mg acceptors raises questions regarding the connection between the defect luminescence and dopant activation. There is no evidence that the set of PL lines containing L1 (Fig.3) is directly due to the Mg or that the red-shift after annealing at $\geq 500^\circ\text{C}$ is directly related to the acceptor activation of Mg. For example, the red-shift is substantially complete after a 500°C anneal, while the amount of electrical activation at this temperature is negligible [14]. The complex pattern of defect generation and removal revealed by PL strongly indicates that acceptor activation involves more than simply the dissociation of Mg-H complexes, although this process is implicated.

Convergence of theory and experiment on the existence and nature of the Mg-H complex has yet to be achieved. In particular, the microscopic model for the complex (Fig. 5 and [19]) yields an estimate of 3360 cm^{-1} for the vibrational frequency of the H stretch mode, which is close to that for H in NH_3 . This disagrees with reported experimental values for local modes (2168 and 2219 cm^{-1}) detected in MBE-grown, Mg-doped, H-contaminated GaN by vibrational mode spectroscopy [24]; while it was suggested that these modes may arise from two nonequivalent Mg-H configurations in the wurtzite structure, it was also suggested as an alternative assignment that the experimentally observed modes might arise from a hydrogen-decorated native defect such as a nitrogen vacancy with one or more Ga atoms passivated by hydrogen.

Experimental information on the properties of hydrogen in GaN substantially lags theory. The list of physical parameters yet to be experimentally determined for a quantitative description of hydrogen in GaN includes such basic information as the

diffusivities and solubilities for H^+ and H^- , donor and acceptor transition energies, and acceptor-hydrogen dissociation energies.

ACKNOWLEDGMENT

The authors are pleased to thank D. P. Bour for helpful discussions and J. Walker for technical support. One of the authors (JN) was partially supported by DAAP. The work was supported by ARPA under agreement # MDA972-95-3-0008.

REFERENCES

1. H. Amano, M. Kito, K. Hiramatsu, and I. Akasaki, Jpn. J. Appl. Phys. **28**, L2112 (1989).
2. S. Nakamura, T. Mukai, M. Senoh, and I. Iwasa, Jpn. J. Appl. Phys. **31**, L139 (1992).
3. Hydrogen in Semiconductors, eds. J. I. Pankove and N. M. Johnson, Semiconductors and Semimetals Vol. 34 (Academic Press, San Diego, 1991).
4. G. G. Deleo and W. B. Fowler, in Hydrogen in Semiconductors, eds. J. I. Pankove and N. M. Johnson, Semiconductors and Semimetals Vol. 34 (Academic Press, San Diego, 1991), ch. 14.
5. J. Chevallier, B. Clerjaud, and B. Pajod, in Hydrogen in Semiconductors, eds. J. I. Pankove and N. M. Johnson, Semiconductors and Semimetals Vol. 34 (Academic Press, San Diego, 1991), ch. 13.
6. T. Zundel and J. Weber, Phys. Rev. B **39** 13549 (1990).
7. A. W. R. Leitch, Th. Prescha, and M. Stutzmann, Appl. Surf. Sci. **50**, 390 (1991).
8. S. J. Pearton, C. R. Abernathy, and J. Lopata, Appl. Phys. Lett. **59**, 3571 (1991).
9. C. Herring and N. M. Johnson, in Hydrogen in Semiconductors, eds. J. I. Pankove and N. M. Johnson, Semiconductors and Semimetals Vol. 34 (Academic Press, San Diego, 1991), ch. 10.
10. N. M. Johnson, Mat. Res. Soc. Symp. Proc. **262**, 369 (1992).
11. Y. Ohba and A. Hatano, Jpn. J. Appl. Phys. **33**, L1367 (1994).
12. C. Yuan, T. Salagaj, A. Gurary, P. Zawadzki, C. S. Chern, W. Kroll, R. A. Stall, Y. Li, M. Schurman, C.-Y. Hwang, W. E. Mayo, Y. Lu, S. J. Pearton, S. Krishnankutty, and R. M. Kolbas, J. Electrochem. Soc. **142**, L163 (1995).
13. T. D. Moustakas, T. Lei, and R. J. Molnar, Mat. Res. Soc. Symp. Proc. **281**, 753 (1993).
14. W. Götz, N.M. Johnson, R.A. Street, H. Amano, and I. Akasaki, Appl. Phys. Lett. **66**, 1340 (1995).
15. N. M. Johnson, in Hydrogen in Semiconductors, eds. J. I. Pankove and N. M. Johnson, Semiconductors and Semimetals Vol. 34 (Academic Press, San Diego, 1991), ch.7.
16. M. S. Brandt, N. M. Johnson, R. J. Molnar, R. Singh, and T. D. Moustakas, Appl. Phys. Lett. **64**, 2264 (1994).
17. W. Götz, this proceedings.
18. W. Götz, N.M. Johnson, J. Walker, D. P. Bour, and R. A. Street, Appl. Phys. Lett., in press.

19. J. Neugebauer and C. G. Van de Walle, Phys. Rev. Lett., in press.
20. J. Neugebauer and C. G. Van de Walle, this proceedings.
21. N. M. Johnson, C. Herring, and C. G. Van de Walle, Phys. Rev. Lett. **73**, 130 (1994).
22. J. S. Van Vechten, J. D. Zook, R. D. Hornig, and B. Goldenberg, Jpn. J. Appl. Phys. **31**, 3662 (1992).
23. J. Neugebauer and C. G. Van de Walle, Appl. Phys. Lett., in press.
24. M. S. Brandt, J. W. Ager III, W. Götz, N. M. Johnson, J. S. Harris Jr., R. J. Molnar, R. Singh, and T. D. Moustakas, Phys. Rev. B **49**, 14758 (1994).

Theoretical Study of Electron Initiated Impact Ionization Rate in Bulk GaN using a Wave Vector Dependent Numerical Transition Rate Formulation

J. Kolnik, I. H. Oguzman, K. F. Brennan, R. Wang*, P.P. Ruden*

School of ECE, Georgia Tech, Atlanta, GA 30332, kolnik@celdec1.mirc.gatech.edu

*Department of Electrical Engineering, University of Minnesota, Minneapolis, MN 55455

ABSTRACT

In this paper, we present ensemble Monte Carlo based calculations of electron initiated impact ionization in bulk zincblende GaN using a wavevector dependent formulation of the interband impact ionization transition rate. These are the first reported estimates, either theoretical or experimental, of the impact ionization rates in GaN. The transition rate is determined from Fermi's golden rule for a two-body screened Coulomb interaction using a numerically determined dielectric function as well as by numerically integrating over all of the possible final states. The Monte Carlo simulator includes the full details of the first four conduction bands derived from an empirical pseudopotential calculation as well as all of the relevant phonon scattering mechanisms. It is found that the ionization rate has a relatively "soft" threshold.

INTRODUCTION

The large gap III-V nitride materials have been the subject of increased interest in recent years, because of their potential usage in high temperature electronics, blue electroluminescent devices and ultraviolet detectors and emitters. In addition, their radiation hardness makes them attractive for space applications. Among the varieties of III-V nitride materials, gallium nitride with its direct bandgap of approximately 3.4 eV in the hexagonal (wurtzite) phase and slightly lower bandgap in the cubic (zincblende) phase, plays an important role as a potential candidate in all of these applications. There have been many investigations on both phases of GaN reported recently, involving both experimental as well as theoretical work [1,2]. However, the latter deals mostly with the band structure calculations; few theoretical investigations of transport properties of GaN have been reported to date [3-7].

Recently we presented the results of Monte Carlo based calculations of low field electronic transport properties in both wurtzite and zincblende GaN using a realistic band structure obtained by the empirical pseudopotential method [8]. These calculations were restricted to the range for which impact ionization events do not typically occur. However, the performance of many devices depends in part upon impact ionization, such as avalanche photodiodes, APDs. In order to evaluate the potential performance of APD photodetectors for ultraviolet detection, information about the high field transport physics including impact ionization is required. In this paper, we extend our previous investigations to the case of high field electronic transport in bulk zincblende GaN. We present results of calculations of the electron interband impact ionization transition rate based on Fermi's golden rule. Results from ensemble Monte Carlo simulations, namely the electron initiated impact ionization transition rate, quantum yield and electron energy distribution functions are reported too.

MODEL DESCRIPTION

The details of our Monte Carlo simulator have been reported previously [8], therefore only its salient features are reviewed here. The total electron initiated impact ionization rate, quantum yield and electron energy distribution are determined using an ensemble Monte Carlo simulation, which includes the full details of the first four conduction bands of zincblende GaN. The calculation of the electronic band structure was performed within the framework of the empirical pseudopotential method using an expansion over a closed, fixed set of 113 G vectors, which produces a reasonably accurate band structure over the entire Brillouin zone. The energy eigenvalues, their gradients with respect to the \mathbf{k} -vector, and their second derivatives are calculated at regularly spaced points within a \mathbf{k} -space mesh and are used to calculate the electron energy during its free flight [9]. The band structure used in the calculations is shown in Fig. 1.

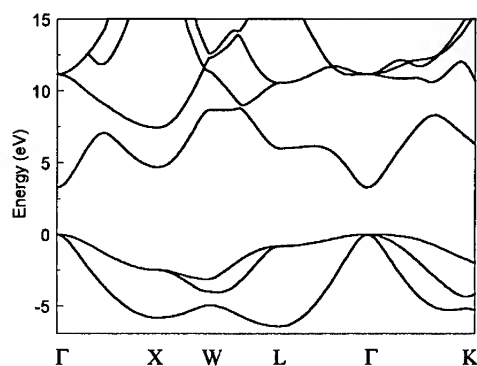


Fig.1 Bandstructure of zincblende GaN

The electron-phonon scattering mechanisms included in the simulation are polar optical, acoustic and intervalley scatterings. The rates are determined for each of these mechanisms at low energies. Polar optical scattering is included only within the central valley. The parameters used in our calculations have been reported previously [8]. At higher electron energies, deformation potential scattering is assumed to be the dominant scattering mechanism. In this regime the scattering rate has been obtained by integrating over the pseudopotential calculated final density of states including collision broadening [10]. The deformation potential is assumed to be constant and the high energy scattering rate is matched to the low energy scattering rate at a selected energy. Another scattering mechanism included in the simulator is ionized impurity scattering, calculated using the approach of Ruch and Fawcett [11]. Their approach takes into account the effect of nonparabolicity, Bloch states and a screened Coulomb potential.

In addition to the above mentioned scattering mechanisms, impact ionization has to be incorporated in the simulations in the high field regime as well. The \mathbf{k} -vector dependent

impact ionization transition rate has been calculated using Fermi's golden rule, which applies as

$$W_{ii}(n_1, \mathbf{k}_1) = \frac{2\pi}{\hbar} \frac{V^2}{(2\pi)^6} \sum_{n_1, n_2, n_2'} \int \int d^3 \mathbf{k}_1' d^3 \mathbf{k}_2' |M|^2 \delta(E_f - E_i) \quad (1)$$

where \mathbf{k}_1, n_1 are the wave vector and band index of the initiating electron, respectively, $\mathbf{k}_2, n_2, \mathbf{k}_1', n_1', \mathbf{k}_2', n_2'$ are the wave vectors and band indices of the particles after the impact ionization event (a hole and two electrons, respectively). V is the crystal volume, E_f and E_i represent the final and initial energies of the particles. M stands for the matrix element of the interaction and can be expressed in terms of the direct M_D and exchange M_E elements as

$$|M|^2 = 2|M_D|^2 + 2|M_E|^2 - (M_D^* M_E + M_D M_E^*). \quad (2)$$

The matrix element is calculated based on the plane-wave expansion of the wave functions using the approach described in [12]. The energy values and the wave functions have been calculated and stored at the 916 \mathbf{k} -points in the irreducible wedge of the Brillouin zone, corresponding to the mesh size of $0.05 \times \frac{2\pi}{a}$, where a is the lattice constant. To obtain the wave functions at the points outside the irreducible wedge, symmetry properties of the zincblende structure have been utilized [12,13]. For the numerical evaluation of Eq. (1), the delta function has been replaced by a rectangle with a height of $1/\delta E$ and width δE , with δE equal to 0.2 eV. The integration is performed using the Monte Carlo method, the four lowest conduction bands and all four valence bands are taken into account for the final states. The dielectric function is evaluated numerically from the pseudopotential calculation [14] and is included in the impact ionization transition rate formulation. To evaluate the energy dependent rate, an additional integration over the initial particles states

$$W(E) = \frac{\sum_{n_1} \int d^3 \mathbf{k}_1 \delta(E(n_1, \mathbf{k}_1) - E) W_{ii}(n_1, \mathbf{k}_1)}{\sum_{n_1} \int d^3 \mathbf{k}_1 \delta(E(n_1, \mathbf{k}_1) - E)} \quad (3)$$

is performed. The calculated impact ionization transition rate is plotted as a function of energy in Figure 2a.

RESULTS

The energy dependent ionization transition rate is incorporated into the ensemble Monte Carlo simulation to calculate the total electron initiated ionization rate as a function of inverse applied electric field. The results are shown in Figure 2b. As can be seen from Figure 2b, the ionization rate is calculated to be relatively low, between $10^{+1} - 10^{+2} \text{ cm}^{-1}$ at an electric field of 1.0 MV/cm. More appreciable ionization occurs as the field increases up to 3.0 MV/cm, the limiting field used in this analysis. The calculated rate at 1.0 MV/cm has a great amount of uncertainty due to the lack of sufficient ionization statistics. A statistically valid sampling including an accounting of the standard deviation will be given

in a later work. The statistical reliability is far better at the higher electric fields analyzed here. However, it should be noted that the Monte Carlo model itself becomes questionable at these high electric field strengths. It is possible that at high electric fields, the band structure exhibits Stark effects, and the neglect of the intra-collisional field effect and the basic assumption of semi-classical transport physics become suspect. Nevertheless, the calculations given here provide a first attempt at ascertaining the magnitude of the ionization rate in GaN.

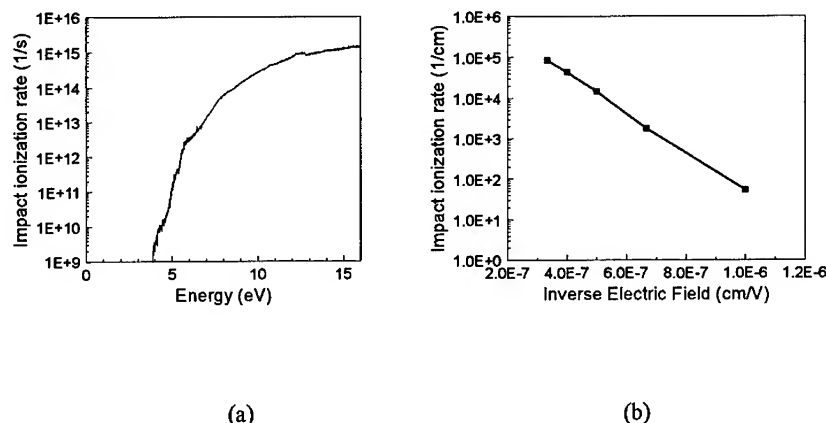


Figure 2: (a) Electron initiated impact ionization transition rate in zincblende GaN.
(b) Impact ionization rate in zincblende GaN vs. inverse electric field.

The Monte Carlo model was also used to evaluate both the quantum yield and the distribution functions. The quantum yield is defined as the average number of impact ionization events caused by a high energy injected electron until its kinetic energy relaxes below the ionization threshold through scattering and/or ionization events. The quantum yield is particularly useful since it provides a means of assessing the relative hardness or softness of the ionization threshold. The calculated quantum yield in zincblende GaN is plotted as a function of injection energy in Figure 3a. As can be seen from Fig. 3a, the slope of the quantum yield is relatively low implying that the threshold is quite "soft"; carriers survive to energies substantially above the energy bandgap before suffering an impact ionization event. Notice that 100% ionization probability does not occur until the carriers reach nearly 10 eV, almost three times the direct energy bandgap. Further information about the nature of the threshold can be gleaned from examination of the distribution functions. The number density distribution function, defined as the product of the density of states, $g(E)$, and the energy distribution function, $f(E)$, is plotted for two different electric fields, 1.0 and 3.0 MV/cm respectively, in Figure 3b. Inspection of Figure 3b shows that a significant high energy tail appears in the distribution particularly at 3 MV/cm. Notice that the population of electrons persists to well above 9 eV, in good agreement with the quantum yield data discussed above.

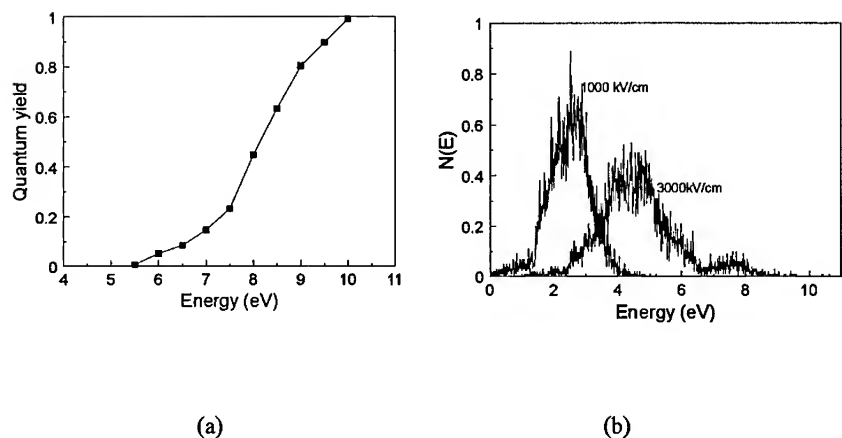


Figure 3: (a) Quantum yield as a function of electron energy.
(b) The electron number density function at 1000 kV/cm and 3000 kV/cm.

CONCLUSIONS

In this paper, the first determination of the electron initiated interband impact ionization rate in bulk zincblende GaN has been presented. From the calculations it is found that little appreciable ionization occurs at electric fields below 1.0 MV/cm. From the calculated quantum yield and distribution functions, it appears that the ionization process is quite "soft", implying that the electrons survive to energies substantially above the direct energy bandgap before suffering an impact ionization event. Though the present analysis omits the Stark effect, the intra-collisional field effect and a full quantum mechanical treatment of the ionization transition rate which all may be important at the field strengths and carrier energies examined, the results give a rough first estimate of the impact ionization rate in GaN.

ACKNOWLEDGEMENTS

The authors would like to thank Drs. N. Sano, M. Stobbe and Y. Wang for helpful discussion. This work was sponsored in part by the National Science Foundation through a collaborative contract made to Georgia Tech (ECS-9313635) and the University of Minnesota (ECS-9408479).

REFERENCES

1. S. Strite and H. Morkoc, J. Vac. Sci. Technol., **B 10**, 1237 (1992) and references therein.

2. Diamond, Silicon Carbide and Nitride Wide-Bandgap Semiconductors, Edited by C.H. Carter, Jr., G. Goldenblat, S. Nakamura, and R.J. Nemanich, MRS Symposia Proceedings No. 339 (Materials Research Society, Pittsburgh, 1994).
3. P. Das and D.K. Ferry, *Solid State Electron.* **19**, 851 (1976).
4. M.A. Littlejohn, J.R. Hauser, and T.H. Glisson, *Appl. Phys. Lett.* **26**, 625 (1976).
5. B. Gelmont, K. Kim, and M. Shur, *J. Appl. Phys.* **74**, 1818 (1993).
6. N.S. Mansour, K.W. Kim, and M.A. Littlejohn, *J. Appl. Phys.* **77**, 2834 (1995).
7. R.P. Joshi, A.N. Dharamsi, and J. McAdoo, *Appl. Phys. Lett.* **64**, 3611 (1994).
8. J. Kolnik, I.H. Oguzman, K.F. Brennan, R. Wang, P.P. Ruden, and Y. Wang, *J. Appl. Phys.* **78**, 1033 (1995).
9. M. V. Fischetti and S.E. Laux, *Phys. Rev. B*, **38**, 9721 (1988).
10. Y.C. Chang, D.Z.-Y. Ting, J.Y. Tang, and K. Hess, *Appl. Phys. Lett.* **42**, 76 (1983).
11. J.G. Ruch and W. Fawcett, *J. Appl. Phys.* **41**, 3843 (1970).
12. N. Sano, A. Yoshii, *Phys. Rev. B* **45**, 4171 (1992).
13. M. Stobbe, R. Redmer, W. Schattke, *Phys. Rev. B* **49**, 4494 (1994).
14. R. Wang, P. P. Ruden, J. Kolnik, I. Oguzman, and K. F. Brennan, these proceedings.

EX SITU AND IN SITU METHODS FOR OXIDE AND CARBON REMOVAL FROM AlN AND GaN SURFACES

Sean W. King, Laura L. Smith, John P. Barnak, *Ja-Hum Ku, *Jim A. Christman, *Mark C. Benjamin, Michael D. Bremser, *Robert J. Nemanich, and Robert F. Davis
Department of Materials Science and Engineering, and *Department of Physics
North Carolina State University, Raleigh, NC 27695.

ABSTRACT

Exposure to numerous acids and bases and UV/O₃ oxidation were used to determine the best ex situ cleaning techniques for the (0001) surfaces of AlN and GaN. HF and HCl were the most effective in removing the oxide from AlN and GaN, respectively. However, AES and XPS revealed the surfaces to be terminated with F and Cl which inhibited re-oxidation prior to loading into vacuum. TPD showed that temperatures of 650 and 850°C are necessary to thermally desorb the Cl and F, respectively. UV/O₃ oxidation in air was not effective in removing hydrocarbons from either surface but was effective for oxide growth. In situ remote hydrogen plasma exposure at 450°C removed halogens and hydrocarbons remaining after ex situ cleaning of both AlN and GaN surfaces; however, oxide free surfaces could not be achieved. Thermal desorption of hydrocarbons from GaN in UHV was achieved at 650°C. Complete thermal desorption of the surface oxide in UHV was only achieved at temperatures > 800°C where some GaN decomposition occurred. Annealing GaN in NH₃ at 700°C reduced the surface oxide without loss of surface stoichiometry.

INTRODUCTION

Surface cleaning and preparation is an absolutely critical first step in all semiconductor processing [1]. Improper removal of surface contamination and oxides prior to Si homoepitaxy has been shown to result in an increase in the density of line and planar defects in epitaxial films from $<10^4/\text{cm}^2$ to $>10^{10}/\text{cm}^2$ [2-4] and an associated drop in device yield [2]. Improper removal of surface oxides prior to metal contact deposition has been demonstrated to result in higher contact resistances, changes in Schottky barrier heights, and lack of parameter uniformity [5,6]. Surface preparation/cleaning can passivate the surface dangling bonds which control the existence and density of surface/interface states in metal contacts and metal-insulator-semiconductor devices [7,8]. In the latter, a large density of interface states can produce changes in threshold voltage and must be controlled to ensure uniformity in device operation. Drift in the MIS parameters has also been linked to the presence of alkali ions at the interface which can, in part, be controlled by surface cleaning prior to insulator deposition [9]. Lastly, the existence of either positive or negative electron affinities in diamond [10] have been shown to be significantly dependent on surface preparation. The control of the surface electron affinity may be important for the development of cold cathodes from AlN and AlGaIn alloys.

To the authors' knowledge there has been no systematic investigation and comparison of surface preparation and cleaning techniques for III-V Nitride surfaces. Thus the objectives of this ongoing study have been to investigate the applicability of both ex situ and in situ cleaning techniques found useful in semiconductor technologies based on Si and GaAs. The removal of adventitious carbon and oxygen were of paramount importance; however, the elimination of other contaminants including Na and residual species associated with the cleaning processes were also addressed. The information gained in these studies will then be used to tailor and refine selected cleaning techniques specifically to the III-V nitrides.

EXPERIMENTAL

The surfaces of a variety of AlN and GaN samples were investigated. The AlN samples were derived from (1) films epitaxially grown either on 6H-SiC (0001)_{Si} by organometallic vapor phase epitaxy (OMVPE) [11] or gas source-molecular beam epitaxy (GSMBE) [12] or (2) deposited via reactive ion sputtering on Si (111) and (3) hotpressed polycrystalline AlN wafers. The GaN surfaces investigated were those of GaN films either epitaxially deposited directly on 6H-

SiC(0001) or on epitaxial AlN buffer layers previously grown on 6H-SiC (0001) by OMVPE [11] and GSMBE [12], respectively.

The in situ cleaning and the surface analyses of the samples subjected to ex situ and in situ cleaning were conducted in a unique ultra-high vacuum (UHV) system consisting of a 36 ft. long UHV transfer line to which were connected several surface analysis and thin film deposition units. The details of each unit and the transfer line have been described elsewhere [10]. CMOS grade acids and bases were used for the ex situ wet cleaning processes. After wet chemical cleans, samples were briefly rinsed in 18.4 M Ω de-ionized water, blown dry with N₂, mounted to a molybdenum sample holder and loaded into the transfer line load lock. After evacuation for \approx 20 min., the samples were placed in the transfer line for immediate analysis by x-ray photoelectron spectroscopy (XPS) and Auger electron spectroscopy (AES). For the ultra-violet/ozone (UV/O₃) oxidation studies, a specially designed box was used which incorporated a Hg lamp in a design described in ref. [13]. In situ methods consisted of exposure to a H plasma or annealing in UHV or fluxes of NH₃, Al, or Ga. After in situ cleaning in either the GSMBE or the H plasma system, samples were immediately (< 5 min.) transferred for analysis by AES, low energy electron diffraction (LEED), and XPS. XPS analysis was performed using both the Al (h ν =1486.6 eV) and Mg (h ν =1253.6 eV) anodes at 20 mA and 10kV. AES spectra were obtained using a beam voltage of 3 keV and an emission current of 1 mA. LEED was performed using rear view optics, a beam voltage of approximately 100 eV, and an emission current of 1 mA. Calibration of the XPS binding energy scale was performed by measuring the position of the Au 4f^{7/2} and shifting the spectrums such that the peak position occurred at 83.98 eV. All sample temperatures quoted here were measured using an optical pyrometer and an emissivity of 0.5.

RESULTS

Ex situ and In situ cleaning of AlN

Figure 1(a) shows an AES spectrum of the surface of an as-received OMVPE AlN sample which is oxidized due to the strong affinity of Al for O₂. Additional oxidation via UV/O₃ was investigated initially as a possible ex situ method for C removal from the nitride surfaces. Both AES and XPS were used to examine an OMVPE AlN film which had been cleaned in trichloroethylene, acetone, and methanol for 5 min. in each solvent and then exposed to UV/O₃ for 10 min. at room temperature. As shown in Fig. 1(b), the combination of solvent cleaning and UV/O₃ exposure reduced the surface C from the AlN surface by 50%. Longer UV/O₃ exposures (30 min. - 1 hr.) with or without a solvent pre-clean did not further decrease the surface C. However, Fig. 1(b) does show that the AlN surface was further oxidized by the UV/O₃ exposure which indicates that O₃ was being generated by the Hg UV lamp.

As AlN is reasonably chemically inert, oxidation of an AlN surface in a typical laboratory ambient does not proceed rapidly. Therefore, UV/O₃ exposure was used to repeatedly grow a thin oxide on an AlN surface to assess the efficacy of wet chemical removal of this oxide. Various acids, bases, and acid/base mixtures such as HCl, HF, HNO₃, H₂SO₄, H₃PO₄, H₂O₂, NH₃OH, NaOH, acetic, 1:1:7 H₂O:H₂O₂:H₂SO₄, AND RCA SC1 & SC2 were investigated as possible etchants. The 1:1 HCl:DI and NH₃OH:H₂O₂ solutions reduced the surface oxide, however, HF based solutions produced surfaces with the lowest oxygen levels in both AES and XPS. Fig. 1c shows an AES spectrum taken from an AlN surface exposed to UV/O₃ for 20 min. and then dipped in 10:1 buffered HF (7:1 NH₄F:HF) for 3 min. A dramatic reduction in the amount of oxygen was achieved. A change in the Al KLL line shape from that typical of aluminum oxide to that of aluminum nitride is also observed (compare Figures 1(b) and 1(c)) [14]. Figure 1(c) also shows the presence of a small concentration of F. Relative to XPS, AES is particularly insensitive to detecting the presence of fluorine. Therefore, XPS was employed to further investigate AlN surfaces cleaned using HF based solutions. For this purpose, a thin (\approx 200Å) AlN film was intentionally grown on 6H-SiC (0001) by GSMBE such that the electrons tunneling from the conducting SiC substrate into the insulating AlN film would be sufficient to prevent charging effects in the XPS spectra. Figure 2(a) shows an XPS spectrum of the F1s region from a GSMBE AlN film after dipping in 10:1 buffered HF (BHF) for 10 min. A very broad peak is detected which can be deconvoluted using a Gaussian-Lorentzian distribution into two peaks having peak positions of 688.5 and 686.8 eV.

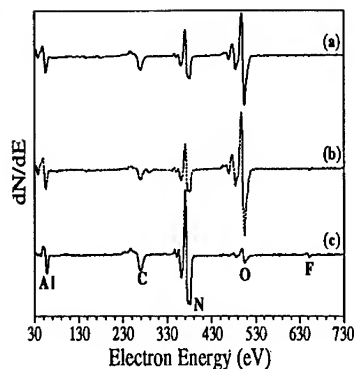


Figure 1. AES spectra of OMVPE AlN: (a) As received, (b) Solvent clean and 20 min. UV/O₃ exposure, and (c) 3 min. in 10:1 buffered HF (BHF).

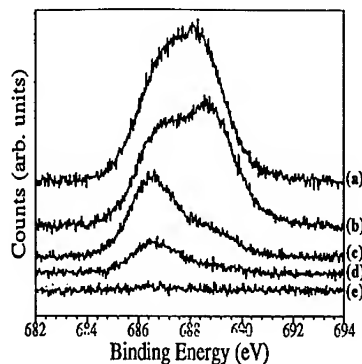


Figure 2. XPS of F 1s from 200Å AlN film on (0001) 6H-SiC after: (a) dipping in 10:1 BHF, and annealing for 15 min. each at: (b) 400°C, (c) 600°C, (d) 800°C, and (e) 950°C.

The chemistry of F on AlN was further investigated using AES, XPS, and temperature programmed desorption (TPD). Fig. 2(b) shows that after annealing an HF dipped AlN surface at 400°C for 15 min., the two F peaks become more distinguishable and positioned at 688.7 and 686.7 eV. Annealing at 600°C resulted in a reduction in the high binding energy peak, as shown in Fig. 2(c); this peak was further reduced after annealing at 800°C. Complete elimination of the low binding energy peak at 686.5 eV was not achieved until 950°C for 15 min. (Fig. 2e). In a separate study (data not shown) [12], TPD was performed on an AlN film sputtered on Si (111) which had been subsequently dipped in 10:1 BHF. A large TPD peak was detected for desorption of m/e 19 and 20 (F and HF) at approximately 400°C while a small peak for m/e 38 (F₂) was detected at 500°C. A general increase in m/e 19 and 20 occurred after 600°C and continued until 1000°C after which annealing was stopped.

As complete thermal desorption of fluorine from AlN occurred only at elevated temperatures, the lower temperature process of remote H plasma cleaning was investigated for this purpose and for the removal of other contaminants. The details regarding the RF plasma system and its operation are described elsewhere [15]. Atomic H has been previously shown to be extremely efficient for the removal of halogens from Si (001) surfaces [15,16]. Figure 3 shows an XPS spectrum of the F 1s region taken from a polycrystalline AlN wafer before and after exposure to a remote H plasma. Figure 3(a) shows the presence of a large quantity of F on the AlN surface after dipping in 10:1 BHF. This result demonstrates that HF is also useful for removing surface oxides from AlN ceramics. Fig. 3(b) reveals that almost complete removal of fluorine is achieved after exposure of the AlN wafer to a 15 mTorr 20W remote H plasma at 450°C for 5 min. This technique was also efficient for removal of C from AlN surfaces, as shown by the AES spectrums in Fig. 4(a) and 4(b). However, it was not found efficient for removing oxygen from AlN surfaces. Annealing AlN grown via OMVPE and GSMBE in UHV in fluxes of Al, Ga, and NH₃ was investigated, but none of these processes was found particularly affective in further removing oxygen from the AlN surface. Exposure to silane at high temperatures (1000°C) was the only in situ clean found capable of appreciably removing oxygen from an AlN surface [12]. Unfortunately, the loss of oxygen produced by the silane exposure was at the expense of some formation of Si-N bonding at the surface.

Ex situ and In situ Cleaning of GaN

Figure 5(a) shows an AES spectrum from an as-received GaN film grown via GSMBE. As this sample was kept on a laminar flow bench for the period of time that it was removed from

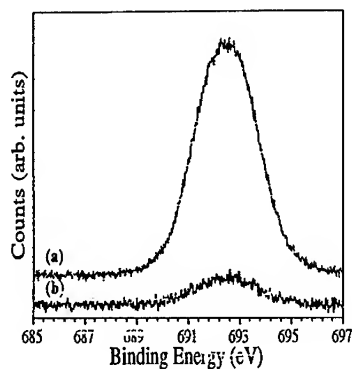


Figure 3. XPS of F 1s from polycrystalline AlN wafer cleaned in 10:1 BHF (a) before and (b) after remote H plasma at 450°C (15 mTorr, 20W). Note F 1s shifted due to sample charging.

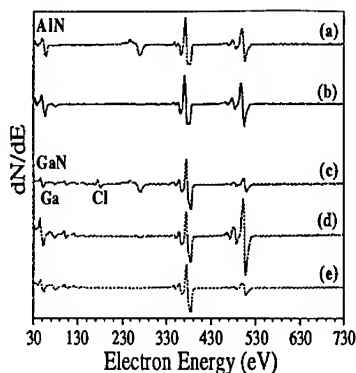


Figure 4. AES spectra of OMVPE AlN after: (a) UV/O₃ and 10:1 BHF dip (b) remote H plasma at 450°C. OMVPE GaN after: (c) UV/O₃ and HCl:DI, (d) remote H plasma at 100°C, and (e) H plasma at 450°C.

vacuum (1 day), the level of C contamination was quite small. To investigate the ability of UV/O₃ to remove carbon from GaN surfaces, the GaN film was exposed to UV/O₃ for 10-20 min. and investigated with AES. Figure 5(b) shows that this exposure resulted in additional oxidation of the GaN surface without significantly affecting the level of C contamination. On the contrary, the C level actually increased, probably as a result of the increased handling of the sample during unmounting and remounting for the UV/O₃ treatment. Examination of the UV/O₃ treated GaN surfaces with LEED did not detect any diffraction patterns, indicating that the O₃ generated oxide is amorphous.

The combination of UV/O₃ oxidation and exposure to the same acids and bases investigated above for oxide removal from AlN was used to determine the best chemical method for removing oxides from GaN surfaces. In this case, 1:1 HCl:DI, NH₃OH:H₂O₂, and 10% HF mixtures, were very effective for oxide removal. The HCl:DI etch produced surfaces with the lowest oxide levels. The surfaces exhibited (1x1) LEED diffraction patterns after cleaning. However, these surfaces contained Cl, as shown in Fig. 5c.

In a separate study [17], the thermal desorption of Cl and the removal of contaminants from HCl-cleaned GaN surfaces were examined. The concentration of the former was decreased below the detection limit of AES by annealing at 600°C or greater. Annealing at > 800°C resulted in decomposition of the GaN films, as detected by monitoring the evolution of m/e 28 and 69 with a residual gas analyzer (RGA). Further investigation of GaN oxide (native or produced via UV/O₃ processing) removal via annealing in fluxes of Ga and NH₃ were also conducted. Both procedures resulted in a reduction in the amount of surface oxides (see Fig. 6a-f), but annealing in NH₃ produced the most stoichiometric surface with the lowest levels of oxygen. However, oxygen could not be removed below the detection limit ($\approx 0.1\%$) of our AES system.

The use of a remote hydrogen plasma for cleaning GaN was also investigated. Figure 4 (c) shows an AES spectrum from a HCl:DI cleaned OMVPE GaN film before plasma exposure. Exposure to a 15 mTorr, 20W remote H plasma for 5 min. at 100°C resulted in the complete removal of Cl and surface C within the detection limit of AES. However, the level of oxygen was found to increase dramatically, due to the low temperature plasma exposure (Fig. 4d). A second exposure of the same sample to a H plasma at 450°C for 10 min. resulted in a reduction of the oxygen level to that prior to the first H plasma exposure. Higher sample temperatures during plasma processing were investigated, but further reduction of the surface oxygen levels was not realized.

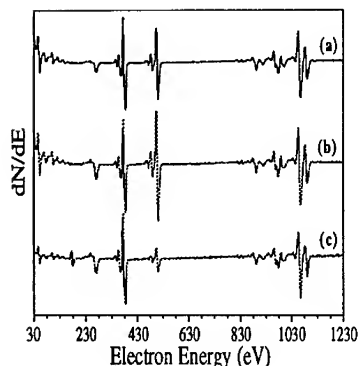


Figure 5. AES spectra from GSMBE GaN after: (a) 1 day in air, (b) UV/O₃ oxidation, and (c) 5 min. etch in HCl:DI.

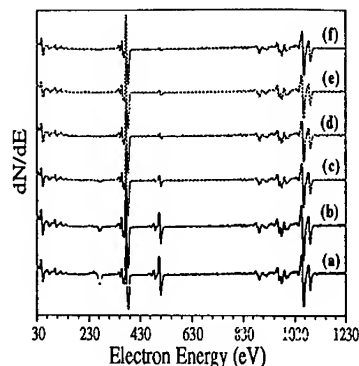


Figure 6. AES spectra of GSMBE GaN (a) exposed to UV/O₃, and after annealing in: (b) UHV at 650°C, 20 min., (c) NH₃ at 650°C, 20 min., (d) Ga at 650°C, 40 min., (e) NH₃ at 720°C, 20 min., and (f) NH₃ at 800°C, 25 min.

DISCUSSION

Ex situ wet chemical cleaning of GaN and AlN surfaces with HCl- and HF-based solutions produced surfaces with the lowest levels of oxygen but with significant concentrations of Cl and F, respectively. The authors hypothesize that the halogens tie up dangling bonds at the nitride surface and inhibit re-oxidation. As such, the presence of significant amounts of Cl on GaN and F on AlN is not unexpected given their respective metal-halogen bond strengths (Ga-Cl=481 and Al-F=664 kJ/mol [18]). The increased halogen content on the III-V nitrides relative to other III-V materials may be related to the larger ionic component to bonding in the former. The rather high temperature stability of fluorine on AlN also parallels with the thermal stability of AlF₃ (T_m=1300°C) [18].

In the AlN-F TPD experiments, two F 1s XPS peaks were detected at \approx 688.7 and 686.6 eV which disappeared after annealing at 600 and 950°C. The lower binding energy F 1s peak is attributed to fluorine directly bonded to aluminum, as the value of 686.6 eV directly corresponds with the value of 686.3 eV reported for AlF₃·H₂O [19]. As binding energies of atomic core levels tend to be higher in molecules, the authors propose that the higher binding energy F 1s peak is due to physisorbed HF, NF_x, or CF_x. This would correlate with the lower desorption temperature observed for the higher binding energy peak.

Halogen removal from silicon surfaces using atomic H has been shown to be via an Ely-Rideal mechanism [16]. In this mechanism, atomic H is able to extract halogens from silicon without being thermally accommodated at the surface. The H atom can accomplish this due to the 220 kJ/mol (relative to $\frac{1}{2}$ H₂(g)) of excess potential energy residing in the H atom. In the case of GaN and AlN, a detailed study has not yet been made to ascertain whether Ely-Rideal is operable in halogen extraction from these surfaces. However in Fig. 3, it was shown that a small amount of F was still present on the AlN surface after H plasma exposure at 450°C. Given the large flux of atomic H (10^{16} /cm²s [15]) produced in the plasma, complete removal of F from AlN would be expected if Ely-Rideal were operable.

It was shown in Fig. 6 that annealing GaN in NH₃ at 800°C reduced the surface oxide while maintaining a stoichiometric surface and prohibiting decomposition of the GaN film. This is analogous to other III-V compounds where it has been found necessary to anneal in a flux of the group V component during oxide desorption. However, it should be noted that removal of oxygen below the AES detection limit was not achieved when annealing in NH₃. This could be related to problems particular to the use of ammonia. Water is a notorious contaminant in ammonia the detection of which is non-trivial. Ammonia also displaces H₂O from stainless steel chamber walls

and tubing which increases the background concentration of the latter in a system during cleaning [20]. For these reasons, it may be difficult to completely remove oxygen from GaN via annealing in ammonia. However, the small levels of oxygen detected in AES may also be due to electron beam induced oxidation of GaN during the AES analysis. This effect has been documented for II-VI compounds such as ZnSe [21]. Currently, investigations are underway to determine the source of the small amounts of detected oxygen.

CONCLUSIONS

Of the numerous acids and bases examined, HF and HCl solutions were the best for removal of oxides from AlN and GaN, respectively. However, significant amounts of F and Cl were detected using AES and XPS on these surfaces after dipping in HF and HCl, respectively. It is hypothesized that these halogens tie up dangling bonds at these nitride surfaces hindering re-oxidation of the surface. Fluorine was very thermally stable requiring temperatures of $> 850^{\circ}\text{C}$ for desorption. Remote H plasma exposure was effective for removing halogens and hydrocarbons from both AlN and GaN surfaces at temperatures of 450°C , but was not particularly efficient for oxide removal. Annealing GaN in NH_3 at $700\text{--}800^{\circ}\text{C}$ produced clean as well as stoichiometric GaN surfaces.

ACKNOWLEDGEMENTS

The work described herein was supported by the ONR under contract N00014-91-J-1416. Appreciation is expressed to Cree Research, Inc. for the 6H-SiC wafers.

REFERENCES

1. W. Kern, J. Electrochem. Soc., **137** 1887 (1990).
2. G.R. Srinivasan and B.S. Meyerson, J. Electrochem. Soc., **134** 1518 (1987).
3. B. Meyerson, E. Ganin, D. Smith, and T. Nguyen, J. Electrochem. Soc., **133** 1232 (1986).
4. J.H. McFee, R.G. Swartz, V.D. Archer, S.N. Finegan, and L.C. Feldman, J. Electrochem. Soc., **130** 3083 (1989).
5. F. Ren, A.B. Emerson, S.J. Pearton, T.R. Fullowan, and J.M. Brown, Appl. Phys. Lett., **58** 1030 (1991).
6. M. Kodama, Electronics Letters, **30** (1) 89 (1994).
7. A. Zangwill, Physics at Surfaces, (Cambridge Univ. Press, New York, 1988) pp. 221-231.
8. E.H. Rhoderick, and R.H. Williams, Metal-Semiconductor Contacts, 2nd ed. (Oxford University Press, New York, 1988), pp. 5-17.
9. E. Yon, W.H. Ko, and A.B. Kuper, IEEE Trans. Electron Devices, **13** 276 (1966).
10. J. van der Weide and R.J. Nemanich, Appl. Phys. Lett. **62** 1878 (1993).
11. T.W. Weeks, Jr., M.D. Bremser, K.S. Ailey, E. Carlson, W.G. Perry, and R.F. Davis, Appl. Phys. Lett. **67** 401 (1995).
12. S.W. King, R.J. Nemanich, and R.F. Davis, to be published.
13. J.A. McClintock, R.A. Wilson, N.E. Byer, J. Vac. Sci. Technol., **20** 241 (1982).
14. H.H. Madden and D.W. Goodman, Surface Science, **150** 39 (1985).
15. J.P. Barnak, S.W. King, J.S. Montgomery, Ja-Hum Ku, and R.J. Nemanich in Ultraclean Semiconductor Processing Technology and Surface Chemical Cleaning and Passivation, M. Liehr, M. Heyns, M. Hirose, and H. Parks eds., (Mater. Res. Soc. Proc. **386**, Pittsburgh, PA, 1995) pp. 357-362.
16. C.C. Cheng, S.R. Lucas, H. Gutleben, W.J. Choyke, and J.T. Yates Jr., J. Am. Chem. Soc., **114** 1249 (1992).
17. L.L. Smith, S.W. King, R.J. Nemanich, and R.F. Davis, submitted??????????????.
18. D.R. Lide, CRC Handbook of Chemistry and Physics, 71st ed, (CRC Press, New York 1991) p. 4-41, 9-87.
19. V.I. Nefedov, Y.A. Buslaev, Y.V. Kokunov, Zh. Neorg. Khim., **19** 1166 (1974).
20. Dr. J.T. Yates Jr., University of Pittsburgh (private communication).
21. J.L. Melendez and C.R. Helms, J. Electrochem. Soc., **141** 1973 (1994).

THE EFFECT OF HYDROGEN-BASED, HIGH DENSITY PLASMA ETCHING ON THE ELECTRONIC PROPERTIES OF GALLIUM NITRIDE

C.R. EDDY, JR.*, B. MOLNAR**

*Naval Research Laboratory, Code 6671, 4555 Overlook Ave. SW, Washington, DC 20375-5345, eddy@ccfsun.nrl.navy.mil

**Naval Research Laboratory, Code 6856, 4555 Overlook Ave. SW, Washington, DC 20375

ABSTRACT

Development of devices based on the wide gap semiconductor gallium nitride (GaN) requires the realization of reliable, high fidelity, low damage pattern transfer processes. In this work, GaN thin films grown by OMVPE have been subjected to both chlorine- and methane/hydrogen-based etch chemistries in an electron cyclotron resonance microwave plasma reactive ion etching system. Both n-type and semi-insulating thin films have been utilized to examine the effect of these etch processes on the electronic properties of the materials. The methane/hydrogen-based etch system ($\text{CH}_4/\text{H}_2/\text{Ar}$) induced considerable changes in the electrical properties of both n-type and semi-insulating films, causing the former to become more insulating and the latter to become conducting. In both cases, the original electrical properties were recoverable after a short, high temperature anneal. In the chlorine-based etching system (Cl_2), no changes in the electrical properties were observed and etch rates five times greater than in the methane/hydrogen-based system were achieved. Proposed mechanisms responsible for the observed behavior will be discussed. These results show that pattern transfer processes based in chlorine etch chemistries are more suitable for the generation of high performance GaN devices.

INTRODUCTION

The wide band-gap, compound semiconductor gallium nitride (GaN) continues to increase in importance for the development of high temperature electronic and blue/green optoelectronic device structures. Consistent with this trend, the ability to pattern GaN using dry etching techniques has been an area of increasing research[1-7]. As with most semiconductor processing techniques, the objective is to achieve the desired result (here, the delineation of small areas of semiconducting thin film) with minimal modification to the properties of the material, namely, the electronic properties. In dry etch processing, the electronic properties of the remaining thin film structures can be affected in several ways: 1) the direct ion bombardment of the surface can cause structural defects to form near the surface of the semiconductor, 2) reactive specie from the plasma can penetrate into the remaining structure and alter the electronic properties through passivation of carriers, and 3) the creation of recombination centers at the surface as a result of unpassivated semiconductor bonds. Carrier passivation, particularly when hydrogen is present in the process, has been shown to be a significant problem for III-V materials[8]. Several studies have shown that at elevated temperatures, hydrogen exposure can result in significant passivation of carriers in GaN to depths of up to a micrometer[9,10]. Previous works have examined GaN etching in high density discharges using chlorine- [1-3,5,7], methane/hydrogen-based [1-4], and mixtures of these chemistries[6]. These works have shown that both discharges are effective in performing anisotropic pattern transfer on GaN even down to nanometer-scale feature sizes, but none of these works evaluate the effect of the etch process on the properties of the remaining structures.

In this work, we report on the effects of electron cyclotron resonance microwave plasma reactive ion etching (ECR-RIE) in both $\text{CH}_4/\text{H}_2/\text{Ar}$ and Cl_2 chemistries on the electronic properties of n-type and semi-insulating gallium nitride layers. In both materials, modifications to the electronic properties are observed. The effects of post-etch rapid thermal anneals on the electronic properties are also presented and preliminary explanations are offered for the observed behaviors.

EXPERIMENT

Two types of GaN thin films were used in this study and both were grown between 1 and 3 μm thick onto sapphire substrates by organometallic vapor phase epitaxy. The first set of films were undoped, n-type GaN films with carrier concentrations between 10^{17} and 10^{18} cm^{-3} and carrier mobilities between 150 and 300 $\text{cm}^2/\text{V}\cdot\text{s}$. These mobility values indicate that the films are highly compensated[11]. The second set were highly resistive or semi-insulating GaN thin films. For the n-type films Van der Pauw type Hall measurements were used for evaluation of electronic properties during processing steps. For semi-insulating films, simple I-V characteristics were used to determine the general resistivity of the films. For these measurements ohmic contacts of tungsten/10% titanium were used. These 1500 \AA thick contacts also served as lithographic masks for etch processing to aid in determination of the change in layer thickness by profilometry.

The etching techniques applied to the GaN thin films were predominantly performed in an ECR-RIE system described previously[12]. In these processes, the total pressure was held at 1mTorr while total flows of 12.8 sccm, 9.6 sccm, 6.8 sccm and 9.0 sccm were used for $\text{CH}_4/\text{H}_2/\text{Ar}$ (2.8/6.8/3.2 flow fractions), CH_4/H_2 (2.8/6.8), H_2 and Cl_2 chemistries, respectively. Microwave powers of 400W and 200W were used for hydrogen-containing and chlorine-based chemistries, respectively. The capacitively coupled, rf-induced dc bias level of the substrate platen was typically -300 V ($1.6 \text{ W}/\text{cm}^2$) for methane/hydrogen-based etch chemistries and -250V ($1.4 \text{ W}/\text{cm}^2$) for the chlorine etch chemistry. The substrates were placed 32 cm downstream of the position of the electron cyclotron resonance condition, defined by the on-axis location of the 875 G magnetic field intensity contour. A fewer number of etching experiments were performed in a traditional parallel plate reactive ion etching apparatus using BCl_3 chemistry and in wet chemical etching using hot phosphoric acid. The etching rates of both GaN and the W/Ti ohmic contact material for the various dry etch chemistries are presented in Table I.

TABLE I. GaN and W/10%Ti etch rates in various plasma chemistries.

Plasma Chemistry	GaN etching rate ($\text{\AA}/\text{min}$)	W/Ti etching rate ($\text{\AA}/\text{min}$)
$\text{CH}_4/\text{H}_2/\text{Ar}$	140	14
CH_4/H_2	90	1-5
H_2	30	1-5
BCl_3 (RIE)	80	10
Cl_2	500	100-200

Rapid thermal annealing experiments were performed to evaluate the response of electrical parameters to annealing treatments. In these experiments, the wafer is placed face down on a Si wafer with the GaN surface in contact with the smooth Si surface. Annealing was performed in flowing N_2 gas. The sample was first annealed at 400 $^\circ\text{C}$ for 30 sec and then a room temperature

Hall measurement was performed. Using the Hall data, the sheet electron concentration, n_s , was calculated using a Hall factor, β , equal to one. The annealing was continued by 100 °C increments, each of 30 sec duration. After each anneal the electrical parameters were determined.

RESULTS

When GaN is subjected to an etch involving hydrogen-containing gas mixtures (either methane/hydrogen/argon, methane/hydrogen, or hydrogen alone) the electronic properties of the remaining film are severely altered. In all of the above etch chemistries, the films resistivity is increased to levels significantly above those expected based on the reduction in film thickness alone. Meanwhile, the mobility is substantially reduced. For example, when a 3 μm thick GaN sample is exposed to the $\text{CH}_4/\text{H}_2/\text{Ar}$ etching environment for 1 hour, approximately 8000 Å of film is removed. With this removal, the expected increase in resistivity is about 40% over the original value of the film and the mobility is expected to be largely unaffected as a result of the reduction in film thickness. However, when the films properties are measured after exposure, the resistivity is seen to increase by 120% and the mobility is decreased by 50%.

In sharp contrast, if 3 μm thick GaN films are exposed to either an 8 minute ECR Cl_2 plasma (under nearly identical conditions) or a BCl_3 parallel plate RIE plasma for 35 minutes only small changes in the resistivity and mobility values are observed. These changes are consistent with the thickness variation before and after the etching. It should also be noted that wet chemical etching in hot phosphoric acid causes no change in the resistivity or mobility values.

The observed changes to the electronic properties of GaN thin films etched in H_2 -containing plasmas can be summarized as follows: 1) the measured sheet resistivity is significantly greater than the calculated sheet resistivity, 2) the measured mobility is less than the calculated mobility and 3) the measured sheet carrier concentration is greater than the expected sheet carrier concentration. All of these observations can be satisfied if the near surface layer doping level ($n = N_d - N_a$) is increased. In principle, the creation of hydrogen complexes by passivating acceptors or the formation of hydrogen-related donor levels could explain our observations. Acceptors forming neutral complexes with hydrogen, would decrease the ionized acceptor concentration N_a^- . Therefore, the free carrier concentration, $n = (N_d^+ - N_a^-)$, would increase. Simultaneously, with the decreased concentration of ionized acceptors, the mobility would decrease. Likewise, increasing the ionized donor concentration would increase the free carrier concentration and decrease the mobility. These results are consistent with the known results of hydrogen interaction with III-V semiconductors[10,13].

It is well known that the dopants in the dopant-hydrogen complexes can be reactivated by annealing. Therefore, the annealing behavior of the as-grown and plasma etched GaN thin films has also been investigated. As grown GaN layers subjected to 30 sec anneals from 400 °C to 900 °C did not display any changes in their sheet resistivity or Hall mobility values. However, when the annealing process was applied to GaN films previously subjected to hydrogen-containing plasma etches, a continuous decrease in the sheet resistivity and a continuous increase in the mobility values was observed. The calculated sheet carrier concentrations are also decreased. Table II presents the measured sheet resistivity and mobility values, and the calculated n_s values for the GaN films before and after the annealing process. We have found that after 30 sec annealing at approximately 800 °C, the n_s and the mobility values agree with those of the pre-etched films for samples exposed to H_2 , or CH_4/H_2 or $\text{CH}_4/\text{H}_2/\text{Ar}$ plasmas. The recovery of the layers electrical properties is consistent with the breaking of the hydrogen-complex bond. Therefore, it should lead to the original sheet carrier concentration and

the mobility values. However, for the samples exposed to Cl_2 or BCl_3 plasma environments, similar anneals did not change n_s or the mobility. Without hydrogen in the plasma there should be no change in n_s or the mobility values during anneals.

TABLE II. Effect of post-etch anneal on electronic properties of GaN thin films.

Sample, Step#	RIE plasma time (hr)	Anneal Temperature ($^{\circ}\text{C}$)	Anneal Time (sec)	Sheet Resistivity (Ω/sq , $\times 10^3$)	Mobility ($\text{cm}^2/\text{V}\cdot\text{s}$)	n_s (cm^{-2} , $\times 10^{13}$)
A,0				2.6	190	1.3
A,1	$\text{CH}_4/\text{H}_2/\text{Ar}, 0.5$			6.2	45	2.2
A,2		500	30	3.6	95	1.8
A,3		600	30	3.0	125	1.7
A,4		700	30	2.7	160	1.4
A,5		800	30	2.3	210	1.3
A,6		800	30	2.3	216	1.3
B,0				1.6	170	2.3
B,1	$\text{BCl}_3, 0.6$			1.7	165	2.1
B,2		700	30	2.1	160	1.9
C,0				0.197	120	26
C,1	$\text{Cl}_2, 0.05$			0.203	123	25
C,3		700	30	0.203	115	27

The effect of hydrogen-containing plasma etching on high resistivity or semi-insulating GaN thin films was also examined. This experiment looked at the current-voltage (I-V) trace between any two of the four Van der Pauw Hall measurement contacts before and after various plasma treatments. The as-grown material demonstrated a flat line I-V characteristic indicative of a highly resistive sample. This material was then exposed to either $\text{CH}_4/\text{H}_2/\text{Ar}$ or Cl_2 plasmas under conditions similar to those discussed above. After exposure to the hydrogen-containing plasma, the I-V trace is linear with a positive slope indicative of a resistance of $\sim 10^3 \Omega$. On the other hand, exposure to Cl_2 plasmas resulted in no change of the I-V characteristic. If the altered sample, which was previously exposed to the hydrogen-containing plasma, was subsequently exposed to the chlorine plasma, the original high resistivity was restored after 2000 Å of GaN removal. Thus, it appears that the effected depth of the hydrogen is $\leq 2000 \text{ Å}$.

CONCLUSIONS

It has been shown that plasma etching in hydrogen containing plasmas (either $\text{CH}_4/\text{H}_2/\text{Ar}$, CH_4/H_2 , or H_2) results in an increase in the n-type GaN layer sheet resistivity and decreases the mobility. Wet chemical etching in hot phosphoric acid or dry etching in a high density Cl_2 discharge or a parallel plate RIE, BCl_3 discharge did not introduce changes in the layer electrical properties. The hydrogen-containing plasma etch's influence on electronic properties can be removed by subsequent annealing at 800°C . The creation of hydrogen complexes $\{\text{HN}_a\}^0$ by passivating acceptors or by the formation of hydrogen related donors $\{\text{H-N}_d^+\}^+$ could explain the effects observed due to hydrogen plasma exposure by increasing the sheet carrier concentration,

$n=[N_d^+-N_a^-]$. It has also been shown that exposure of high resistivity or semi-insulating GaN to hydrogen-containing plasmas results in increased conductivity of the top $\leq 2000\text{\AA}$ of the remaining GaN layer. In general, these results show that pattern transfer processes based in chlorine etch chemistries are more suitable for the generation of high performance GaN devices.

ACKNOWLEDGMENTS

The authors wish to acknowledge Steve Binari of NRL for performance of the parallel plate RIE work and useful discussions, and Kathy Doverspike and Kurt Gaskill for the growth of the GaN films used in this study. The authors also wish to acknowledge the financial support of the Office of Naval Research.

REFERENCES

1. S.J. Pearton, C.R. Abernathy, F. Ren, J.R. Lothian, P.W. Wisk and A. Katz, *J. Vac. Sci. Technol. A* **11**, p. 1772 (1993).
2. S.J. Pearton, C.R. Abernathy and F. Ren, *Appl. Phys. Lett.* **64**, p. 2294 (1994).
3. S.J. Pearton, C.R. Abernathy, F. Ren, J.R. Lothian, P.W. Wisk, A. Katz and C. Constantine, *Semicond. Sci. Technol.* **8**, p. 310 (1993).
4. S.J. Pearton, F. Ren, C.R. Abernathy and J.R. Lothian, *Semicond. Sci. Technol* **9**, p. 338 (1994).
5. G.F. McLane, L. Casas, S.J. Pearton and C.R. Abernathy, *Appl. Phys. Lett.* **66**, p. 3328 (1995).
6. R.J. Shul, A.J. Howard, S.J. Pearton, C.R. Abernathy, C.B. Vartuli and P.A. Barnes in Proceedings of the Symposium on Wide Bandgap Semiconductors and Devices (SOTAPCS XXIII), edited by F. Ren, D.N. Buckley, S.J. Pearton, P. Van Daele, G.C. Chi, T. Kamijoh and F. Schuermeyer (The Electrochemical Society, Inc., Pennington, NJ 1995), p. 217-230.
7. W. Pletshen, R. Niebuhr and K.H. Bachem, *ibid.*, p. 241-246.
8. S.J. Pearton, *Inter. J. Modern Phys. B* **8**, p. 1247 (1994).
9. J. M. Zavada, R.G. Wilson, C.R. Abernathy and S.J. Pearton, *Appl. Phys. Lett.* **64**, p. 2724 (1994).
10. M.S. Brandt, N.M. Johnson, R.J. Monlar, R. Singh and T.D. Moustakas, *Appl. Phys. Lett.* **64**, p. 2264 (1994).
11. C.L. Chin, T.L. Tansley and T. Osotchan, *J. Appl. Phys.* **75**, p. 7365 (1994).
12. C.R. Eddy, Jr., E.A. Dobisz, J.R. Meyer and C.A. Hoffman, *J. Vac. Sci. Technol. A* **11**, p. 1763 (1993).
13. R. Madar, G. Jacob, J. Hallais and R. Fruchart, *J. Cryst. Growth* **31**, p. 197 (1975).

PLASMA CHEMISTRY DEPENDENT ECR ETCHING OF GaN

*R. J. Shul, *C. I. H. Ashby, *D. J. Rieger, *A. J. Howard, **S. J. Pearton, **C. R. Abernathy,
C. B. Vartuli, *P. A. Barnes, and ***P. Davis

*Sandia National Laboratories, Albuquerque, NM 87185-0603

**University of Florida, Gainesville, FL 32611

***Auburn University, Auburn, AL 36849

ABSTRACT

Electron cyclotron resonance (ECR) etching of GaN in $\text{Cl}_2/\text{H}_2/\text{Ar}$, $\text{Cl}_2/\text{SF}_6/\text{Ar}$, $\text{BCl}_3/\text{H}_2/\text{Ar}$ and $\text{BCl}_3/\text{SF}_6/\text{Ar}$ plasmas is reported as a function of percent H_2 and SF_6 . GaN etch rates were found to be 2 to 3 times greater in $\text{Cl}_2/\text{H}_2/\text{Ar}$ discharges than in $\text{BCl}_3/\text{H}_2/\text{Ar}$ discharges independent of the H_2 concentration. In both discharges, the etch rates decreased as the H_2 concentration increased above 10%. When SF_6 was substituted for H_2 , the GaN etch rates in BCl_3 -based plasmas were greater than those for the Cl_2 -based discharges as the SF_6 concentration increased. GaN etch rates were greater in $\text{Cl}_2/\text{H}_2/\text{Ar}$ discharges as compared to $\text{Cl}_2/\text{SF}_6/\text{Ar}$ discharges whereas the opposite trend was observed for BCl_3 -based discharges. Variations in surface morphology and near-surface stoichiometry due to plasma chemistries were also investigated using atomic force microscopy and Auger spectroscopy, respectively.

INTRODUCTION

Wide band-gap group-III nitrides continue to attract interest as blue and ultraviolet emitters and detectors, high temperature electronics, and passivation layers¹⁻⁵. Recent advances in the growth of GaN films have resulted in device demonstrations of GaN light emitting diodes (LEDs)^{6,7} and metal semiconducting field effect transistors (MESFETs)^{5,8}. Although progress has also been reported in dry patterning these materials, rapid development of material growth and advanced device structures including lasers and heterojunction bipolar transistors (HBTs) has increased the need for anisotropic, smooth, high-rate etching. A variety of plasma etch chemistries have been reported in a reactive ion etch (RIE) system using chlorine^{10,11} and bromine¹² based plasma chemistries. Etch rates for GaN up to approximately 650 Å/min have been reported at dc biases of -400 V. Significantly higher etch rates have been reported in electron cyclotron resonance (ECR) etch systems where the plasma is confined by a magnetic field to provide a high density plasma at low pressure and low ion energies. Most ECR etching of GaN has been performed using Cl_2/H_2 -based plasmas.¹³⁻¹⁵ Highly anisotropic GaN etching was obtained at dc-biases ranging from -150 to -250 V with etch rates exceeding 2800 Å/min.

In this paper, we report ECR etching of GaN as a function of plasma chemistry using $\text{Cl}_2/\text{H}_2/\text{Ar}$, $\text{Cl}_2/\text{SF}_6/\text{Ar}$, $\text{BCl}_3/\text{H}_2/\text{Ar}$, and $\text{BCl}_3/\text{SF}_6/\text{Ar}$ plasmas. These discharge chemistries are expected to etch GaN due to the high volatility of the Ga-chlorides and the formation of volatile NH_x or NF_x etch products with the addition of H_2 or SF_6 to the plasma.

EXPERIMENT

The GaN films were grown using Metal Organic Molecular Beam Epitaxy (MO-MBE) on GaAs substrates in an Intevac Gen II system described previously.¹⁶ The group-III source was triethylgallium and the atomic nitrogen was derived from an ECR Wavemat source operating at 200 W forward power. The layers were single crystal with a high density of stacking faults and microtwins and were resistive as-grown.

The GaN samples were patterned using a photoresist mask. The ECR plasma reactor used in this study was a load-locked Plasma-Therm SLR 770 etch system with an ECR source operating at 2.45 GHz. Energetic ion bombardment was provided by superimposing an rf-bias (13.56 MHz) on the sample. Samples were mounted using vacuum grease on an anodized Al carrier that was clamped to the cathode and cooled with He gas. Etch gases were introduced through an annular ring into the chamber just below the quartz window. To minimize field divergence and to optimize plasma uniformity and ion density across the chamber, an external secondary collimating magnet was located on the same plane as the sample and a series of external permanent rare-earth magnets were located between the microwave cavity and the sample. ECR etch parameters held constant in this study were: 30°C electrode temperature, 1 mTorr total pressure, 30 sccm total gas flow, 5 sccm of Ar, 850 W of applied microwave power, and 150 W rf-power with a corresponding dc-bias of -150 ± 10 V.

Etch rates were calculated from the depth of etched features measured with a Dektak stylus profilometer after removing the photoresist mask. Samples etched in the ECR were approximately 1 cm² and depth measurements were taken at a minimum of three positions. Error bars for the etch rates were $\pm 10\%$ across the sample. Limited sample supply precluded multiple runs at each condition. The gas phase chemistry of the plasma was studied using a quadrupole mass spectrometer (QMS). Surface morphology, anisotropy, and sidewall undercutting were evaluated with a scanning electron microscope (SEM). The root-mean-square (rms) surface roughness was quantified using a Digital Instruments Dimension 3000 atomic force microscope (AFM) system operating in tapping mode with Si tips. Auger electron spectroscopy (AES) was used to investigate the near-surface stoichiometry of GaN before etch and after exposure to several plasma conditions.

RESULTS AND DISCUSSIONS

The etch rate for GaN is plotted in Figure 1 as a function of percent hydrogen concentration for the Cl₂/H₂/Ar and BCl₃/H₂/Ar plasma discharges. The GaN etch rates were consistently greater

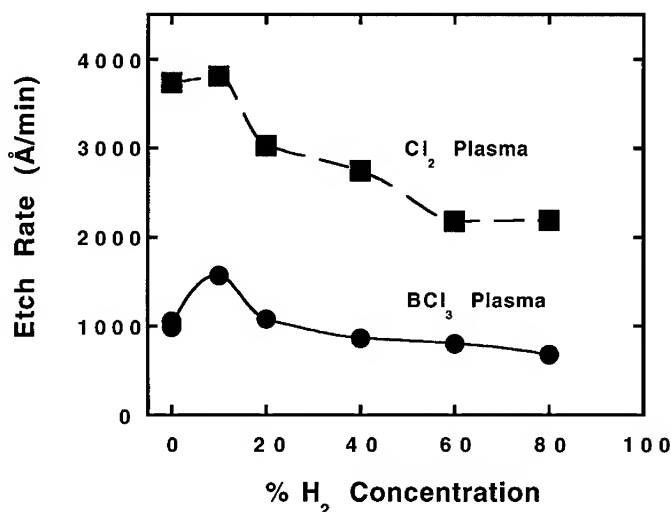


Figure 1. GaN etch rates as a function of %H₂ concentration for Cl₂/H₂/Ar and BCl₃/H₂/Ar plasmas.

in the Cl_2 -based plasma as compared to BCl_3 by a factor of 2 to 3 due to the higher concentration of active Cl species. The trends were similar for both plasmas as the H_2 concentration was increased, however, the increase in etch rate at 10% H_2 was much more significant in the BCl_3 -plasma. The increase in etch rate observed at 10% H_2 concentration in BCl_3 correlated with an increase in the reactive Cl concentration indicated by $m/e = 35$ peak intensity. In the Cl_2 -based plasma, the GaN etch rate and Cl concentration remained relatively constant at 10% H_2 . As the H_2 concentration was increased further, the Cl concentration decreased and the HCl concentration increased as the GaN etch rates decreased in both plasmas, presumably due to the consumption of reactive Cl by hydrogen.

In Figure 2, GaN etch rates are shown for the $\text{Cl}_2/\text{SF}_6/\text{Ar}$ and $\text{BCl}_3/\text{SF}_6/\text{Ar}$ plasmas. With the substitution of SF_6 for H_2 in the Cl_2 -based plasma, the GaN etch rate was typically a factor of 2 lower. As the concentration of SF_6 was increased the etch rate decreased up to 30% SF_6 followed by a slight increase at 40%. As the % SF_6 was increased from 0 to 20, the Cl concentration ($m/e = 35$) decreased but remained significant; GaN etching at 20% SF_6 might be expected based on the Cl concentration alone. However, formation of SCl ($m/e = 67$) was observed at 20% SF_6 . Consumption of the reactive Cl by S may be responsible for the reduced GaN etch rate. At 30 and 40% SF_6 , the Cl concentration was greatly reduced and low GaN etch rates result. The opposite trend was observed for BCl_3 , where the GaN etch rates were significantly greater when SF_6 was substituted for H_2 . The GaN etch rate increased up to 30% SF_6 and then decreased sharply at 40% SF_6 . The Cl concentration ($m/e = 35$) also increased as the SF_6 increased to 30% and then decreased at 40%. As with the Cl_2 -based plasma, there appeared to be a competitive reaction of sulfur with chlorine as the SCl concentration increased above 30% SF_6 . Under most etch conditions, the trend of the Cl concentration correlated with the trends observed for the GaN etch rate. However, a higher concentration of Cl was observed at 40% SF_6 than 0% SF_6 while the GaN etch rate was greater at 0% SF_6 . Studies are planned to elucidate the chemistry involved.

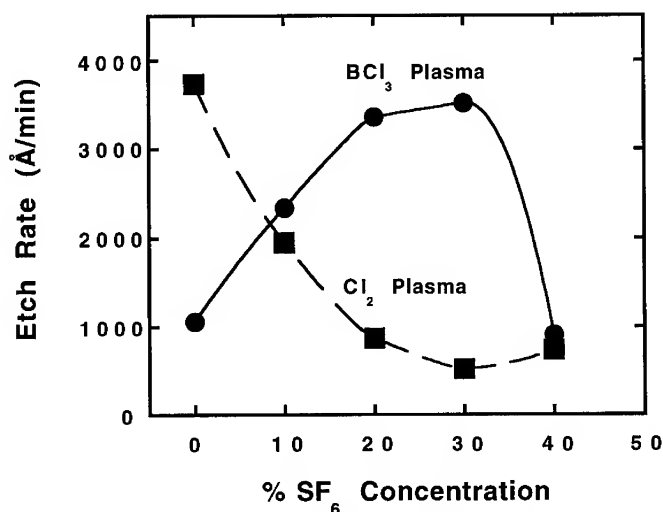


Figure 2. GaN etch rates as a function of % SF_6 concentration for $\text{Cl}_2/\text{SF}_6/\text{Ar}$ and $\text{BCl}_3/\text{SF}_6/\text{Ar}$ plasmas.

The root-mean-square (rms) roughness of the etched surfaces were quantified using AFM. In Figure 3 the rms roughness is plotted as a function of % H_2 for the Cl_2 -based and BCl_3 -based

plasmas. The rms roughness for the as-grown GaN was 6.4 ± 0.5 nm. The rms roughness for GaN etched in $\text{Cl}_2/\text{H}_2/\text{Ar}$ increased as the $\%\text{H}_2$ increased from 0 to 10 and then decreased as the H_2 concentration was increased further. The roughest surface was observed at 10% H_2 where the etch rate was greatest. In the $\text{BCl}_3/\text{H}_2/\text{Ar}$ plasma the rms roughness increased slightly as the $\%\text{H}_2$ increased, but remained relatively smooth. Pattern transfer into GaN was very smooth in $\text{Cl}_2/\text{SF}_6/\text{Ar}$ and $\text{BCl}_3/\text{SF}_6/\text{Ar}$ discharges with rms roughness ranging from 7.5 to 3.6 nm.

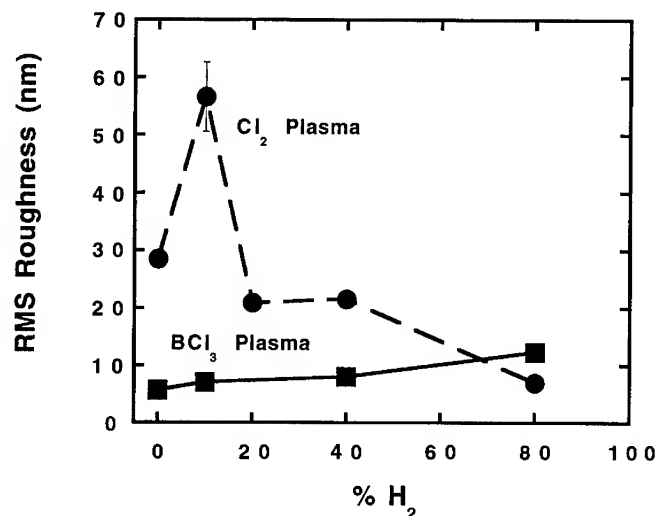


Figure 3. GaN rms roughness as a function of $\%\text{H}_2$ concentration for $\text{Cl}_2/\text{H}_2/\text{Ar}$ and $\text{BCl}_3/\text{H}_2/\text{Ar}$ plasmas. The rms roughness for the as-grown GaN is 6.4 ± 0.5 nm.

The etch profiles showed a strong dependence on the discharge chemistry (Figure 4). The etched surface was quite rough (Figure 4a) in the Cl_2/Ar plasma possibly due to preferential removal of the GaCl_x etch products. The foot observed at the edge of the etched feature may be attributed to mask-edge erosion due to the aggressive attack of photoresist by reactive Cl. As the H_2 concentration was increased to 20% the etch became smooth and very anisotropic (Figure 4b).

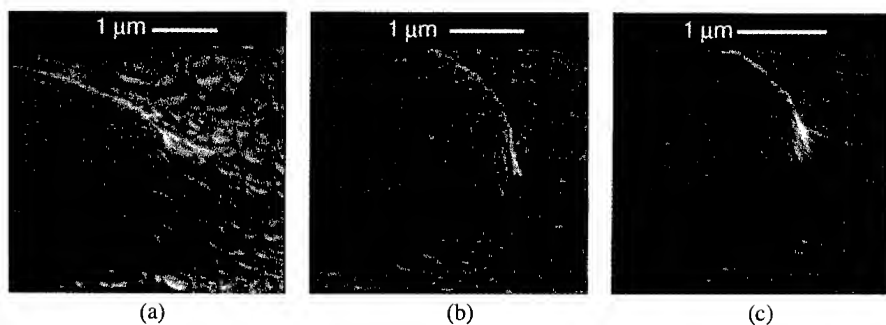


Figure 4. SEM micrographs of GaN samples ECR etched in (a) Cl_2/Ar plasma, (b) 20% H_2 $\text{Cl}_2/\text{H}_2/\text{Ar}$ plasma, and (c) 60% H_2 $\text{Cl}_2/\text{H}_2/\text{Ar}$ plasma. The photoresist mask has been removed.

However, the SEM micrograph showed a lower density of surface roughness near the etched feature than AFM images scanned in open $10 \times 10 \mu\text{m}$ areas. This may be attributed to a proximity effect of the etch where redeposition is worse in the open areas. It may also explain the smooth etch observed in Figure 4b where the rms roughness measured in the field was approximately 21 nm. At 60% H_2 , the etch remained smooth and anisotropic with a slight foot at the base of the feature (Figure 4c). The GaN etch profiles in Cl_2/SF_6 plasmas were anisotropic with relatively smooth sidewalls and etched surfaces. Etching GaN in BCl_3/H_2 or BCl_3/SF_6 resulted in anisotropic profiles with etched surface morphologies similar to the as-grown samples. The anisotropic profiles may have been improved in the BCl_3 -based plasmas due to the higher physical component of the etch mechanism as compared to Cl_2 -based plasmas.

Auger spectra for GaN samples etched under several different plasma conditions were taken to determine the near-surface stoichiometry. Prior to exposure of the GaN to the plasma, the Auger spectrum for the as-grown GaN showed a Ga:N ratio of 1.5 with normal amounts of adventitious carbon and native oxide on the GaN surface. The Auger spectra showed virtually no Ga or N for GaN samples exposed to the Cl_2/Ar plasma or the 80% H_2 $\text{Cl}_2/\text{H}_2/\text{Ar}$ plasma. This is not understood since the GaN was grown on GaAs and showed a minimum of 2500 Å of GaN remaining after etch. Since the Auger spectra were near-surface and did not include any depth profiling, redeposition during etch may have prevented the observation of the Ga and N peaks. Further surface analysis is underway. For GaN samples etched in $\text{Cl}_2/\text{SF}_6/\text{Ar}$, the Ga:N ratio increased as the SF_6 concentration increased implying that the N is effectively removed as NF_x . In the BCl_3/Ar plasma the Ga:N ratio increased from 1.5 for the as-grown sample to 1.9 following exposure to the plasma. This may be attributed to the preferential removal of the lighter N atoms due to the strong physical component of the etch mechanism in BCl_3 plasmas. As the H_2 or SF_6 concentration was increased in the BCl_3/Ar plasma, the Ga:N ratio increased to 6.3 for 80% H_2 and 4.2 for 40% SF_6 . Within experimental error, these trends imply that the GaN film is being depleted of N perhaps due to preferential chemical etching of the N atoms with the addition of H_2 or SF_6 to either Cl_2 - or BCl_3 -based plasmas.

CONCLUSIONS

In summary, ECR etching of GaN is reported as a function plasma chemistry. GaN etch rates were greatest in Cl_2/Ar and $\text{Cl}_2/\text{H}_2/\text{Ar}$ at 10% H_2 . Etch rates were a factor of 2 to 3 times higher in Cl_2/H_2 plasmas than BCl_3/H_2 plasmas due to higher concentrations of reactive Cl. As the hydrogen concentration was increased above 10%, the GaN etch rate decreased in both plasmas possibly due to consumption of the reactive Cl by hydrogen. When SF_6 was substituted for H_2 , the GaN etch rates were greater in the BCl_3 -based plasma. The GaN etch rate increased as SF_6 was added to the BCl_3/Ar plasma up to 30% and then dropped sharply at 40% SF_6 . This trend correlated qualitatively with the concentration of reactive Cl. In general, GaN etch rates increased as the concentration of reactive Cl increased. Surface morphologies were evaluated and quantified using AFM. Very smooth pattern transfer was obtained for a wide range of plasma chemistries; however, the etched surface morphology was rougher in Cl_2/Ar and $\text{Cl}_2/\text{H}_2/\text{Ar}$ plasmas at low H_2 concentrations. Etch profiles were more anisotropic with the addition of H_2 or SF_6 to Cl_2 . The etch profiles were typically more anisotropic with BCl_3 -based plasmas due to the physical nature of the etch while the etch rates were slower due to less reactive Cl present in the plasma. Using Auger spectroscopy, we have observed a general trend where the Ga:N ratio increased as the concentration of H_2 or SF_6 increased implying a substantial chemical etch mechanism to remove N atoms from the GaN film.

ACKNOWLEDGMENTS

The authors would like to thank P. L. Glarborg, A. T. Ongstad, and L. Griego for their technical support. This work was performed at Sandia National Laboratories supported by the U.S. Department of Energy under contract # DE-AC04-94AL85000.

REFERENCES

1. S. Nakamura, T. Mukai, M. Senoh, and N. Iwasu, *Jpn. J. Appl. Phys.* **31**, L139 (1992).
2. J. S. Foresi and T. D. Moustakas, *Appl. Phys. Lett.* **62**, 2859 (1993).
3. S. Nakamura, T. Mukai, and M. Senoh, *Appl. Phys. Lett.*, **64**, 1687 (1994).
4. S. J. Pearton, C. R. Abernathy, P. Wisk, W. S. Hobson, and F. Ren, *Appl. Phys. Lett.* **63**, 1143 (1993).
5. S. C. Binari, L. B. Rowland, W. Kruppa, G. Kelner, K. Doverspike, and D. K. Gaskill, *Electron. Lett.* **30**, 1248 (1994).
6. S. Nakamura, M. Senoh, and T. Mukai, *Jpn. J. Appl. Phys.* **30**, L1708 (1991).
7. I. Akasaki, H. Amano, M. Kito, and K. Hiramatsu, *J. Lumin.* **48/49**, 666 (1991).
8. S. Nakamura, M. Senoh, and T. Mukai, *Appl. Phys. Lett.* **62**, 2390 (1993).
9. M. A. Khan, J. N. Kuznia, A. R. Bhattarai, and D. T. Olson, *Appl. Phys. Lett.* **62**, 1248 (1993).
10. I. Adesida, A. Mahajan, E. Andideh, M. A. Khan, D. T. Olsen, and J. N. Kuznia, *Appl. Phys. Lett.* **63**, 2777 (1993).
11. M. E. Lin, Z. F. Fan, Z. Ma, L. H. Allen, and H. Morkoç, *Appl. Phys. Lett.* **64**, 887 (1994).
12. A. T. Ping, I. Adesida, M. Asif Khan, and J. N. Kuznia, *Electron. Lett.* **30**, 1895 (1994).
13. S. J. Pearton, C. R. Abernathy, and F. Ren, *Appl. Phys. Lett.* **64**, 2294 (1994).
14. R. J. Shul, S. P. Kilcoyne, M. Hagerott Crawford, J. E. Parmeter, C. B. Vartuli, C. R. Abernathy, and S. J. Pearton, *Appl. Phys. Lett.* **66**, 1761 (1995).
15. R. J. Shul, A. J. Howard, S. J. Pearton, C. R. Abernathy, C. B. Vartuli, P. A. Barnes, and M. J. Bozack, *J. Vac. Sci. Technol. B*, **13**, 2016 (1995).
16. C. R. Abernathy, *J. Vac. Sci. Technol. A* **11**, 869 (1993).

REACTIVE ION ETCHING OF AlN, AlGa_N, AND GaN USING BCl₃

W. C. HUGHES, W. H. ROWLAND, JR., M. A. L. JOHNSON, J. W. COOK, JR., and
J. F. SCHETZINA
Department of Physics, North Carolina State University, Raleigh, NC 27695-8202

ABSTRACT

The III-V nitrides are promising materials for use in UV-blue-green optoelectronics, high-temperature electronics, and negative-electron-affinity (NEA) electron emitter applications. In order to realize this potential, it is important to develop an etching technology for device fabrication. The stability of the III-V nitrides to harsh chemical environments makes most wet etching extremely difficult, so that dry etching alternatives are desirable. Recent experiments have shown that BCl₃-based chemistries are effective for reactive ion etching of GaN and that KOH-based solutions may preferentially etch AlN from GaN. This paper reports on the use of BCl₃ for etching AlN and AlGa_N in addition to GaN and the creation of structures such as mesas and lines. It also examines the potential use of potassium Hydroxide (KOH) as a wet etchant of the nitrides. AlN, AlGa_N, and GaN films grown by either metal-organic chemical vapor deposition (MOCVD) or molecular beam epitaxy (MBE) were patterned with Ni in 250 μm x 250 μm squares and 5 μm wide lines to create mesas and lines for typical light emitting diode (LED) or laser diode applications. Reactive ion etching was performed in a commercial reactor using BCl₃ pressures ranging from 5 to 30 mTorr. Gas flow rates of 5 to 50 sccm and RF powers of 50 to 150 W were employed. High nitride etch rates of up to 730 $\text{\AA}/\text{min}$. were observed but lower etch rates were needed to avoid etching of the Ni mask. Smooth mesa surfaces and sidewalls were observed in scanning electron micrographs of the etched nitride structures. Mesas as small as 5 μm x 5 μm were patterned and made in this way. Lines were also made in a similar manner as narrow as 5 μm on GaN/AlN epilayers. Subsequent wet etching of these lines showed that KOH-based solutions such as AZ400K developer attack not only AlN but also GaN depending upon the quality of the film. Possibilities for using this wet etch as a defect etchant or selective etch of nitrides on SiC are discussed.

INTRODUCTION

The pursuit of short wavelength light-emitting devices based on wide band-gap semiconductors has been one of the most active areas of research in semiconductor physics over the past decade. After the initial successes of MBE-grown ZnSe-based II-VI semiconductor devices, GaN based materials have emerged at the forefront with Nichia Chemical developing commercial blue and green LEDs utilizing MOCVD-grown GaN and InGa_N structures [1].

The commercial introduction of LEDs from III-V nitrides have led many researchers to consider new electronic and opto-electronic devices for which III-V nitrides may be well suited. In addition to their wide band-gaps, these materials also are quite chemically stable, allowing their use in other applications where resistance to harsh environments, high temperatures, or radiation is needed. There is also the possibility of using the negative electron affinity of AlN in the development of electron emitters.

For many, if not all these applications it is necessary to pattern the nitride films into mesa, line, or tip structures. Unfortunately, the same characteristics that make these materials desirable in harsh environments make them difficult to pattern. The chemical stability has limited the use of wet etchants for standard etching of structures. Recently

published results have shown that potassium hydroxide (KOH) solutions may be useful in selectively removing AlN from InGaN layers [2]. In addition, much recent research has been dedicated to finding appropriate dry-etching formulas.

The most common dry-etch chemistries that have been studied for III-V nitride processing include chlorine or fluorine-containing gases. Some of these have used chlorocarbon or fluorocarbon compounds which are somewhat undesirable because of environmental concerns [3]. Other authors have reported results using other chlorine-containing gases such as HCl or BCl₃ to etch GaN [4,5], AlN, and InN [6]. At North Carolina State (NCSU), we have attempted to optimize the etching of GaN and related III-V nitride materials using reactive ion etching (RIE) with BCl₃ to determine if these processes may be used to produce useful devices from MBE-grown films. BCl₃ provides the active chlorine necessary for etching the Ga and Al-containing compounds while breaking down into components that can be easily removed from the reactor exhaust. In addition, using BCl₃ avoids the risk of hydrogen contamination. We have also studied wet chemical etching with KOH solutions to compare the advantages and disadvantages of the wet-etch and the dry-etch techniques.

EXPERIMENTAL DETAILS

Our experiments were performed on III-V nitride epilayers grown either by MOCVD at Cree Research, Inc. or by MBE at NCSU. The MOCVD-grown layers were grown on 6H-SiC. These high quality films exhibited double-crystal X-ray rocking curve peaks as narrow as 85 arcsec. MOCVD-grown GaN films were also used as homoepitaxial substrates for the MBE growth. The MBE growth was performed in a commercial reactor with an RF plasma source for nitrogen activation. The details of MBE film growth have previously been published [7].

The dry-etching experiments were done using a Plasma-Therm Batch-Top RIE system. This commercial reactor uses a parallel plate geometry with a RF power generator that could supply up to 500 W over a cathode area of 180 cm². The system was pumped by a corrosive duty turbo molecular pump to pressures on the order of 10 mTorr with BCl₃ gas flow rates of up to 50 sccm.

Squares of 250 μm, 100 μm, and 5 μm and lines ranging from 80 μm to 5 μm wide were patterned with Ni on the samples using standard lithographic techniques. After etching, the nitride surfaces were examined using a SEM to determine etch quality. Etch rates were determined by measuring the heights of the mesas or stripes using a Dektak profilometer both before and after removing the Ni masks. The change in step height after stripping the Ni mask was used to determine the selectivity between the etching of the nitride over the etching of the Ni.

RESULTS AND DISCUSSION

Dry-Etch Rates of AlGa_{0.95}N Epilayers

MOCVD-grown Al_{0.05}Ga_{0.95}N samples with Ni squares and stripes were etched at powers ranging from 50 to 150 W. Other masking materials such as Al or photoresist were also tested, but were found to etch too quickly for selective etching of the nitride.

It was found that the etch rate increased with increasing power up to 730 Å/min. for films etched at 10 mTorr with gas flow rates of 50 sccm (Fig. 1). This increase came at the cost of decreased selectivity. For these particular parameters, the Ni was removed at a rate almost one fourth as large as the AlGa_{0.95}N itself. This means that to create structures over 1 μm high, more than 2500 Å of Ni would be needed. This is not only time-consuming, but also introduces the possibility of contamination as the mask is

sputtered. Furthermore, the surface quality was somewhat degraded at these higher etch rates. The etch rates also increased with decreasing pressure. As has been observed previously by other authors while etching of AlN, InN, and GaN, the etch rate had very little variation with changes in the gas flow rate between 5 sccm and 30 sccm [8,9]. It was concluded that the best surfaces and etch rates ($\approx 333 \text{ \AA/min.}$) came when the etches were done at 100W, 20 sccm, and 10 mTorr. The etch rates observed here were slightly higher than those reported by Lin, et al. [4] It is likely that this is due to the Al content of the film.

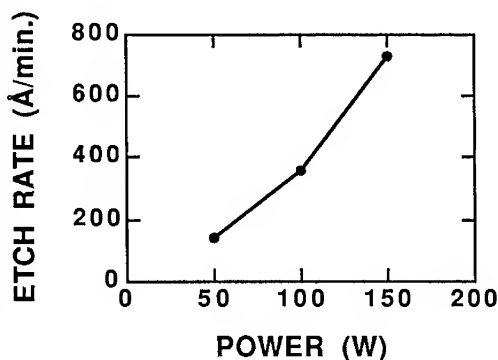


Fig. 1 - Etch rate vs. power from $\text{Al}_{0.05}\text{Ga}_{0.95}\text{N}$ films reactive ion etched at 10 mTorr and 50 sccm of BCl_3 .

Dry-Etching of Mesa Structures

After demonstrating that reactive ion etching with BCl_3 is a viable technique for patterning AlGaN films, we tested this technique for making mesas and lines in AlN, GaN, and AlGaN-containing structures. In particular, we were concerned with isolating mesas for the development of LEDs. These mesas would be useful either current isolation through the active region of a light emitting device and for diode structures that require front-side contacts to both the p-type and n-type layers.

Double heterostructures consisting of $\text{Al}_{0.10}\text{Ga}_{0.90}\text{N}$ between GaN layers were patterned and etched using the methods described above into $250 \mu\text{m} \times 250 \mu\text{m}$ squares. The etch was timed to expose the active region of the heterostructure and allow a contact to be made to the n-type GaN layer. In this way, the diode could be tested without interference from the heterojunction between the SiC underlayer and the MOCVD-grown n-GaN. Scanning electron micrographs of the etched structure show sharp side walls with a clean, exposed n-GaN surface around them (Fig. 2). Tests of diodes made in this way showed diode characteristics with some blue light emission.

Even smaller mesa features can be created if the Ni is deposited in $100 \mu\text{m}$ or even $5 \mu\text{m}$ squares. Test patterns with these small squares were made on undoped GaN layers to determine the feasibility of

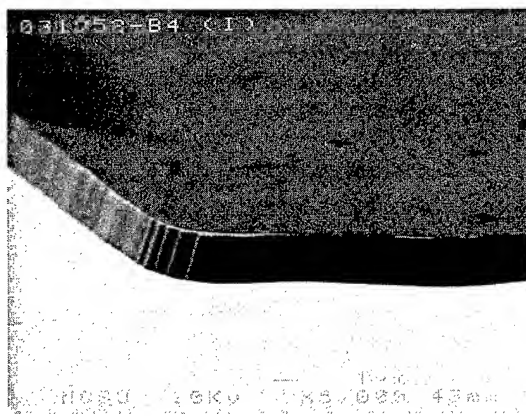


Fig. 2 - SEM photograph of $250 \mu\text{m}$ square mesa from a double heterostructure light emitting diode.

etching structures below 10 μm on a side. Fig. 3 shows an SEM photograph of one of these 5 μm x 5 μm mesas after etching 1 μm deep. Again, smooth sidewalls and surface morphology can be seen though some sloping of the sidewalls was observed. This is believed to be caused by the sputtering of the Ni mask from the edges inward.

Dry and Wet Etching of Line Structures

In order to make diode lasers, features on the scale of the 5 μm squares mentioned above must be created. Test samples were made with 1 μm of GaN on 2 μm of AlN grown on top of the MOCVD GaN buffer layer. The layers were etched to a depth of 4 μm to expose all of the MBE grown layers and part of the MOCVD-grown substrate. An SEM photograph of the end of one of these lines shows the difference in contrast between the layers; the dark layer which is the AlN sandwiched between the two GaN layers with the remaining Ni mask on top (Fig. 4). With the proper structure for optical confinement, this etching technique could be used to make stripes which could then be cleaved into laser diodes.

Recent results at the University of Florida have shown that AlN can be wet chemically etched in KOH-containing solutions [2]. It was shown that the AlN was preferentially etched by AZ400K developer. To test this, we exposed the reactive ion etched line structures to AZ400K at 85°C. Gas bubbles were evolved at the surface of the sample while soaking in this solution. After 60 min., the sample was removed and examined by scanning electron microscopy (Fig. 5). A side view of one of the lines on the same sample shown in Fig. 4 shows that the GaN and AlN layers grown by MBE have been undercut from beneath the Ni mask. In addition,

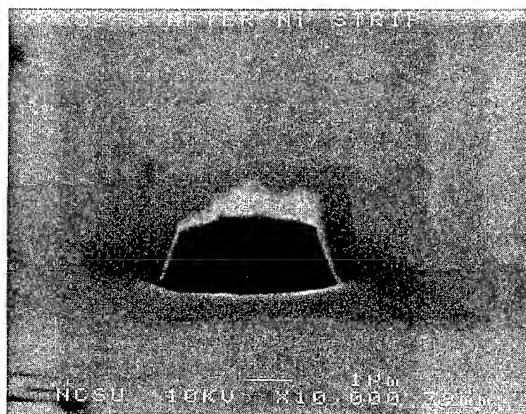


Fig. 3. - SEM photograph of 5 μm square mesa test structure.

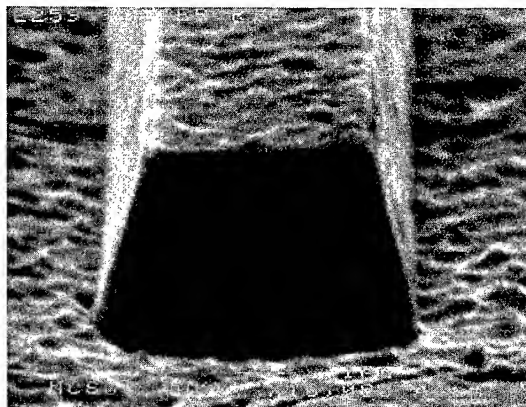


Fig. 4. - SEM photograph the end of a 5 μm wide line etched in a GaN/AlN/GaN film. The dark layer on top is the remaining Ni mask.

regions of the MOCVD-grown GaN substrate have also been etched down to the SiC underneath. Similar results were seen when the samples were etched in 1% KOH:H₂O solutions. It appears from these results that the KOH-based solutions are not selective etches for the AlN over the GaN. Rather, since the MOCVD-grown GaN substrate for these particular samples was of better quality than the GaN/AlN epilayers, it seems that the etch is heavily influenced by the quality of the film. This can be seen most dramatically in the etching that did occur on the substrates, where only large cracks at 60° angles were formed. Further, the etch did selectively remove the nitride from the SiC beneath.

A micrograph taken of a wider line structure after KOH exposure for only 15 min. dramatically illustrates the defect-sensitive nature of this etch (Fig. 6). Here, large hexagonal pits have been formed where previously none could be found. These pits are presumed to arise from the long, hollow pipes which form around screw dislocations in a number of hexagonal crystals such as SiC, ZnO, and GaN [10]. It should be noticed that the etch rate lower dislocation density films is dramatically lower, so that while this wet-chemical treatment may not be adequate for producing device structures, it may have some use in determine defect density and overall film quality.

CONCLUSIONS

We have shown that BCl₃-based reactive ion etching is a viable technology for processing III-V nitride semiconductor devices. Etch rates greater than 700 Å/min. have been achieved, though rates below 400 Å/min. are better suited for patterning since the Ni mask is more stable.

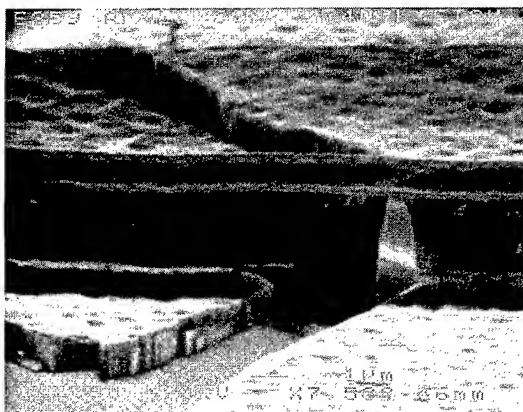


Fig. 5 - Side view of a 5 μm wide line etched in a GaN/AlN film after 60 min. exposure to 85° C AZ400K developer. Note that this is the same line shown in Fig. 4 at a different orientation.

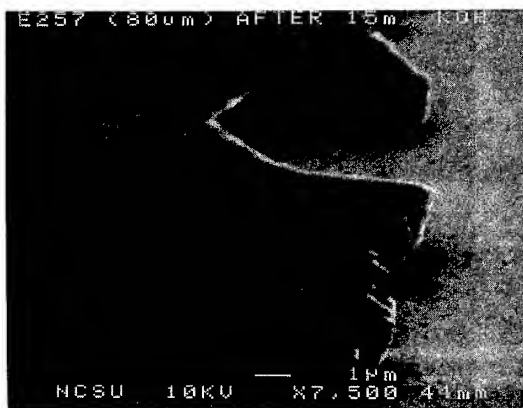


Fig. 6 - Side view of an 80 μm wide line etched in a GaN/AlN film after 60 min. exposure to 1% KOH at 85°C.

Mesas as small as $5\text{ }\mu\text{m} \times 5\text{ }\mu\text{m}$ have been etched in GaN, AlN, and AlGaIn-containing films. These have been used to create light emitting diodes which emit in the blue region of the spectrum. The same etch procedures were used to make $5\text{ }\mu\text{m}$ wide lines which could be used for the production of laser diodes.

The use of KOH as a wet etchant of AlN was also examined and not found to etch selectively the AlN, but defective material rather than less defective. This etch did not attack higher quality GaN or SiC. The hydroxide etch also revealed the presence of micropipe defects associated with screw dislocations. These had not been visible by SEM before exposure to the KOH. It is possible that this treatment may be useful in determining the defect density and overall quality of nitride films.

ACKNOWLEDGMENTS

This work was supported by ARPA/ARO grant DAAH04-94-G-0255 and by Cree Research, Inc. internal funds. The authors wish to thank J. Ren for assistance in growing the MBE films used in this work, and Cree Research, Inc. for supplying the MOCVD-grown films used.

REFERENCES

1. Shuji Nakamura, Masayuki Senoh, Naruhito Iwasa, and Shin-ichi Nagahama, Jpn. J. Appl. Phys. **34**, L797 (1995).
2. J. R. Mileham, S. J. Pearton, C. R. Abernathy, J. D. MacKenzie, R. J. Shul, and S. P. Kilcoyne, Appl. Phys. Lett. **67**, 1119 (1995).
3. Heon Lee, David B. Oberman, and James S. Harris, Jr., Appl. Phys. Lett. **67**, 1754 (1995).
4. M. E. Lin, Z. F. Fan, Z. Ma, L. H. Allen, and H. Morkoç, Appl. Phys. Lett. **64**, 887 (1994).
5. A. T. Ping, I. Adesida, M. Asif Khan, Appl. Phys. Lett. **67**, 1250 (1995).
6. G. F. McLane, L. Casas, R. T. Lareau, D. W. Eckhart, C. B. Vartuli, S. J. Pearton, and C. R. Abernathy, J. Vac. Sci. Technol. A **13**, 724 (1995).
7. W. C. Hughes, W. H. Rowland, Jr., M. A. L. Johnson, Shizuo Fujita, J. W. Cook, Jr., J. F. Schetzina, J. Ren, and J. A. Edmond, J. Vac. Sci. Technol. B **13**, 1571 (1995).
8. G. F. McLane, L. Casas, S. J. Pearton, C. R. Abernathy, Appl. Phys. Lett. **66**, 3328 (1995).
9. G. F. McLane, L. Casas, R. T. Lareau, D. W. Eckhart, C. B. Vartuli, S. J. Pearton, and C. R. Abernathy, J. Vac. Sci. Technol. A **13**, 724 (1995).
10. W. Qian, M. Skowronski, K. Doverspike, L. B. Rowland, and D. K. Gaskill, J. Cryst. Growth **151**, 396 (1995).

Electron cyclotron resonance etching characteristics of GaN in plasmas with and without hydrogen

L. ZHANG, J. RAMER, J. BROWN, K. ZHENG, L. F. LESTER, S. D. HERSEE
Center for High Technology Materials, University of New Mexico, Albuquerque, NM 87131

ABSTRACT

Electron cyclotron resonance (ECR) plasma etching characteristics of gallium nitride (GaN) are investigated using low pressure (4-10 mTorr) SiCl_4/Ar and $\text{Cl}_2/\text{H}_2/\text{Ar}$ ECR discharges. The purpose of this effort is to develop a dry etching process for making laser mirrors on GaN and to examine dry etching processes of GaN that do not require hydrogen, which is known to cause carrier compensation in GaN. The etch rate is found to increase near-linearly with increasing DC bias, and a minimum DC bias of 100V is required to initiate etching in SiCl_4/Ar . We have also found that the material quality significantly affects the etch rate. The latter decreases with x-ray rocking curve half-width and increases with defect density. A reasonable etch rate of 660Å/min and good surface morphologies obtained in SiCl_4/Ar ECR etching make this process suitable for gate recess of an FET. An etch rate of 5270Å/min has been achieved in $\text{Cl}_2/\text{H}_2/\text{Ar}$ plasmas. This is the highest reported etch rate of GaN so far. The smooth and vertical etch sidewalls (etch to mask selectivity of 16 is obtained) make this process promising for dry-etched laser mirrors on GaN.

INTRODUCTION

GaN has attracted considerable interest for making visible and near UV light emitting diodes (LEDs) and semiconductor lasers because of its large direct band gap energy (3.39 eV at room temperature). Its excellent chemical stability, high thermal conductivity, and high melting temperature also make it suitable for high temperature electronic and photonic device applications. Commercially available blue LEDs based on InGaN/AlGaN double heterostructures have been successfully fabricated by Nichia Chemical Company and Cree Research [1], and high responsivity photodetectors operating at UV wavelength have also been reported [2]. In the past few years, significant progress has been made in obtaining reproducible high quality GaN epilayers [3,4], but considerable work is required in the area of process development. Etching studies are especially needed because GaN is chemically inert in all acids and bases at room temperature. This circumstance leaves dry etching as the only practical way for reliable pattern definition of GaN.

Various systems have been used to dry-etch GaN, including reactive ion etching (RIE), electron cyclotron resonance (ECR) plasma etching, chemically assisted ion beam etching (CAIBE), and magnetron reactive ion etching (MIE). To date, the highest etch rates of GaN are 3500Å/min in BCl_3 MIE [5], 2340Å/min in $\text{Cl}_2/\text{H}_2/\text{CH}_4/\text{Ar}$ ECR plasma at 170°C [6], 2100Å/min in Cl_2/Ar CAIBE [7], and 1800Å/min in HCl/Ar CAIBE at 300°C [8]. Typically, CAIBE tends to cause more damage to the material than ECR etching because of higher ion energy, and the uniformity of MIE plasma is unsatisfactory. Compared to conventional RIE, ECR plasma etching has the advantage of providing higher ion density ($\geq 5 \times 10^{11} \text{ cm}^{-3}$) at lower pressures. These conditions yield high etch rates with large etch anisotropy. With a separately controlled RF power source that controls the ion energy independently of the ion density, ECR obtains a high ion density plasma with a relatively low ion energy that minimizes the ion induced damage to the material.

The addition of hydrogen to plasmas containing chlorine has resulted in some of the highest etch rates of GaN by enhancing the removal of N as NH_x [6,8]. Achieving high etch rates of GaN is very important for the fabrication of etched laser mirrors. Since GaN grown on sapphire does not have the same orientation as the substrate, cleaved mirrors cannot be expected. Thus, to make diode lasers other than vertical cavity surface emitting lasers (VCSELs), a process for dry-etched mirrors has to be developed.

Hydrogen incorporated into semiconductors, however, passivates both donor and acceptor shallow levels causing lower free carrier concentrations [9,10]. For III-V semiconductor power-

FET processing, hydrogen compensation during the gate recess would be very undesirable because this step is critical in determining a transistor's performance. Nakamura has shown that N_2 -ambient thermal annealing can eliminate donor/acceptor-hydrogen complexes in GaN at an optimum temperature of 700°C and restore conductivity. Our own studies of Ti/Al contacts to undoped GaN grown by metal organic chemical vapor deposition (MOCVD) indicate that the optimum anneal temperature for driving out the hydrogen and maximizing the conductivity is about 800°C. Nakamura has shown, however, that the annealing process causes dissociation of GaN at the surface [11]. This dissociation can have a variety of deleterious effects on device characteristics and processes, e.g., it can cause lower surface carrier concentration which would make low resistance ohmic contacts more difficult to fabricate. In the gate-drain region of FETs, surface dissociation can increase the leakage current and lower the breakdown voltage due to the increased defect density at the surface.

The first part of this work investigates a dry-etch process that potentially leaves less damage than CAIBE, is more uniform than MIE, and does not incorporate hydrogen. Based on this reasoning and our prior experience with the dry etching of GaAs [12], ECR plasma etching of GaN using $SiCl_4/Ar$ was selected. This type of process is best suited for gate recess of an FET and surface preparation prior to ohmic contact metalization. The influence of the DC self-bias, the fraction of $SiCl_4$ in the plasma, the pressure, and the material quality on the etch rate are investigated for hydrogen-free etching. The second section describes an ECR process using Cl_2 , H_2 , and Ar that is designed for maximum etch rate and selectivity. This recipe is best suited for laser mirror fabrication since hydrogen compensation is of less concern.

EXPERIMENT

The GaN samples used in this work were grown by MOCVD on c-plane [0001] or a-plane [11 $\bar{2}$ 0] oriented sapphire substrates [4]. Trimethylgallium and high purity ammonia were used as Ga and N sources. A thin GaN buffer layer was deposited on the sapphire substrate at a temperature of approximately 480°C. The main GaN epilayer was grown at 1025°C with pressure of 100 Torr. A typical growth rate was 2 μm /hour. The surface of the samples were smooth and the thickness of the layers ranged from 3 μm to 6 μm . AZ4330 photoresist was used for the mask in the $SiCl_4/Ar$ plasmas, and a more durable mask, Ni, was employed in the $Cl_2/H_2/Ar$ mixture. Etch rates were obtained from stylus profilometry after removing the mask. Wet chemical etching experiments have been conducted on these samples and no detectable etching was observed in room temperature buffered HF, HF, 90°C NaOH, or 80°C KOH.

Dry etching of GaN samples is performed in a Plasma Quest 877-U ECR system with an Astex S-700i microwave generator (2.45 GHz). DC bias is induced by an independently controlled RF power source (13.56 MHz). For etching in the $SiCl_4/Ar$ plasmas, the microwave input power is fixed at 300W. Fig. 1 shows the etching rate of GaN in an 8 sccm $SiCl_4$ /15 sccm Ar discharge as a function of DC bias at a fixed pressure of 10 mTorr. Under these conditions, a minimum DC bias of 100V is required to initiate the etching. This voltage is relatively high compared to the biases needed to etch GaAs in ECR $SiCl_4/Ar$ plasmas. (We have found that GaN etches approximately 50 times slower than GaAs for the same plasma conditions using $SiCl_4/Ar$.) Unlike GaAs, GaN does not spontaneously etch in chlorine-

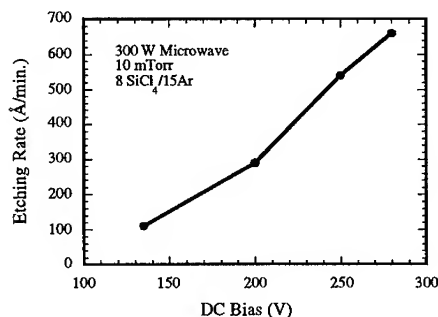


Figure 1: Etch rates of GaN as a function of the DC self-bias voltage. The etch parameters are 300 W microwave power, 8 sccm $SiCl_4$ /15 sccm Ar flow rate, and 10 mTorr pressure. A minimum DC bias of 100 V to initiate etching can be obtained by extrapolating to zero etch rate.

containing gases at temperatures below at least 200 °C and, thus, highly energetic ions are needed to break the strong chemical bond of GaN [7]. The etching is enhanced by a factor of 4 between 150 and 280V, and an etching rate of 660 Å/min is obtained at 280V DC bias.

Fig. 2 shows the etch rates as a function of the fraction of SiCl₄ in the SiCl₄/Ar plasma at a constant Argon flow rate of 15 sccm. As expected, enhanced rates are obtained as the fraction of active chemical etching species (SiCl₄) is increased, but at SiCl₄ fractions greater than 0.5, the etched surface becomes rougher. We presume from this observation that Ar ensures a smooth etched surface by efficiently removing the reaction products. A maximum rate of 960 Å/min is achieved in a pure SiCl₄ plasma. This rate is the highest reported for SiCl₄-based etching of GaN. Keeping the microwave input power and the DC-bias constant, the etch rate increases by a factor of 2 when the processing pressure is increased from 4 to 10 mTorr. In comparison to RIE of GaN in SiCl₄/Ar discharges [13], which shows a 150V threshold DC bias and no dependence of etching rates on pressure or SiCl₄/Ar ratios, enhanced chemical etching and a lower threshold DC bias are achieved in our experiment. For the same DC bias, much higher etching rates are obtained using the ECR process developed in this work. This result is attributed to the higher ionization efficiency in ECR systems.

Variation in the etch rate is observed as a function of material quality. One way to assess the material quality is by the FWHM of the X-ray diffraction rocking curve. Generally, the better the crystalline quality, the smaller the rocking curve half-width. As shown in Fig. 3, the etch rate decreases by 30% for GaN with a half-width of 260 arc-sec compared to a 650 arc-sec sample. Fig. 4 shows the significant difference in etching rates and pit densities for two different wafers labeled sample A and B. The two samples were etched at the same time with conditions of 300W microwave power, 15 SiCl₄/15 Ar gas flow rates, -180V DC-bias voltage, and 4 mTorr etching pressure. Sample A shows a pit density of 2x10⁸ cm⁻² and sample B has a smooth surface with no evidence of pitting. The etch rates are 450 Å/min and 310 Å/min for samples A and B, respectively. These two samples have similar rocking curve half-widths of 260 and 300 arc-sec, but we can infer from the etch surfaces that they have different defect densities or defect types. The growth rate of the unpitted sample B is 1 μm/hour, and 2.5 μm/hour for sample A. This result suggests that lower growth rates gives better material quality, i.e. lower defect density. Sample B showed a smooth etched surface, indicating that Ga and N were removed at near-equal rates in

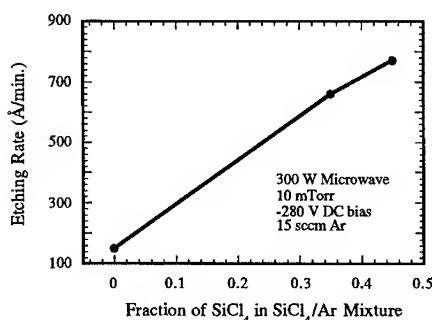


Figure 2: Etch rates of GaN as a function of the fraction of SiCl₄ in the SiCl₄/Ar plasma. The etch parameters are 300 W microwave power, 10 mTorr pressure, -280 V DC bias, and 15 sccm Ar flow rate.

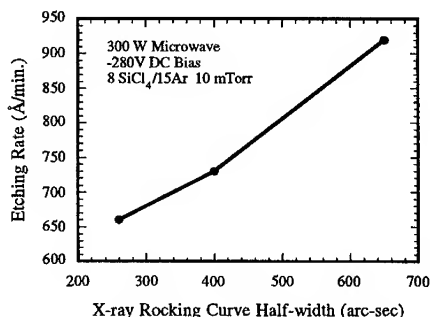


Figure 3: Etch rates of GaN as a function of the measured X-ray rocking curve half-width. The etch parameters are 300 W microwave power, 8 sccm SiCl₄/15 sccm Ar flow rate, -280 V DC bias, and 10 mTorr pressure.

15SiCl₄/15Ar ECR discharges. The etching is anisotropic and the slight overcut on the etched profiles is attributed to the mask erosion due to physical sputtering.

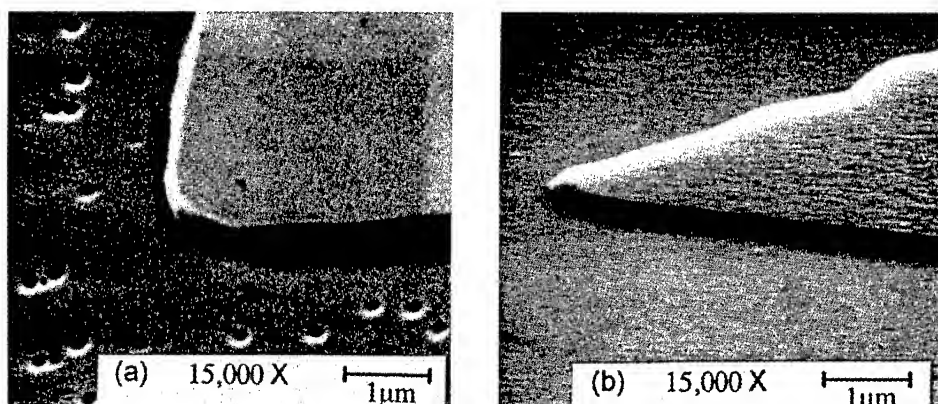


Figure 4: SEM micrographs of GaN samples A and B exhibit a significant difference in their etched surface morphologies. The conditions are 300 W microwave power, 15 sccm SiCl₄/15 sccm Ar flow rate, -185 V DC bias, and 4 mTorr pressure. The etch rates are 450 Å/min and 310 Å/min for samples A and B, respectively.

In [8], Ping and Adesida demonstrate vertical etched facets in GaN at a very high process temperature. Our approach for obtaining high temperature etching is to rely on self-heating of the sample in a Cl₂/H₂/Ar plasma. Accordingly, the wafer is placed on the chuck with no provisions made for heating sinking. The etch conditions are 700 W microwave power, 300 W RF power, 10 sccm, 15 sccm, and 9 sccm of Cl₂, H₂, and Ar, respectively, -120 V DC bias, and 4 mTorr chamber pressure. Ni is used as the etch mask, and an etch rate of 5270 Å/min is achieved. This rate is the highest yet reported for GaN, which is we attribute predominantly to self-heating of the sample during the etching. Fig. 5 shows the sidewall profile of a sample etched to a total depth of 2.6 μm. The bottom 1.5 μm of the facet is vertical, while the upper 1.1 μm has an angle that is slightly less than vertical due to the recession of the Ni mask. A maximum GaN to Ni etch selectivity of 16 is obtained, which make this process suitable for laser mirror fabrication in GaN.

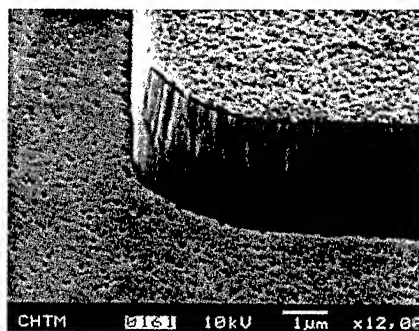


Figure 5: SEM micrograph of the sidewall profile of a GaN sample etched in Cl₂/H₂/Ar ECR plasma. The conditions are 700 W microwave power, 10Cl₂/15H₂/9Ar, 300 W RF power, -120 V DC bias, and 4 mTorr chamber pressure. The etch rate is 5270 Å/min. The GaN to Ni mask etch selectivity is 16. The bottom 1.5 μm smooth and vertical facet which corresponds to the first few minutes etching is large enough to provide sufficient feedback for lasing.

CONCLUSIONS

The ECR etching characteristics of GaN in SiCl_4/Ar have been investigated. The influence of DC self-bias, the fraction of SiCl_4 in the plasma, and the material quality on the etch rate have been presented. A reasonable etch rate of $660 \text{ \AA}/\text{min}$ for a hydrogen-free plasma has been obtained with smooth etched surfaces and an anisotropic profile. This process is appropriate for device process steps such as gate recess of an FET and surface preparation prior to ohmic contact metalization. An etch rate as high as $5270 \text{ \AA}/\text{min}$ and a GaN to Ni mask selectivity of 16 have been achieved with $\text{Cl}_2/\text{H}_2/\text{Ar}$ ECR plasma etching. Vertical and smooth facets with a depth of $1.5 \text{ }\mu\text{m}$ have been demonstrated. This process makes etched facet laser diodes feasible for III-N heterostructures.

ACKNOWLEDGMENTS

This work was supported by the ARPA Optoelectronic Materials Center under grant # MDA 972-94-1-0003, the National Science Foundation under a Career grant # ECS-9501785, and Sandia National Laboratories under the SURP program. The authors thank J. Cecchi and G. Melden for helpful discussions related to ECR etching.

REFERENCES

1. S. Nakamura, T. Mukai, and M. Senoh, Appl. Phys. Lett. **64**, 1678 (1994).
2. M. Asif Khan, J. N. Kuznia, D. T. Olson, J. M. Van Hove, M. Blasingame and L. F. Reitz Appl. Phys. Lett. **60**, 2917 (1992).
3. S. Nakamura, Jpn. J. Appl. Phys. **30**, L1620 (1991).
4. S. D. Hersee, J. Ramer, K. Zheng, C. Kranenberg, K. Malloy, M. Banas, and M. Goorsky, to be published in J. of Electronics Materials, November 1995.
5. G. F. McLane, L. Casas, S. J. Pearton, and C. R. Abernathy, Appl. Phys. Lett. **66**, 3328 (1995).
6. R. J. Shul, S. P. Kilcoyne, M. Hagerott Crawford, J. E. Parmeter, C. B. Vartuli, C. R. Abernathy, and S. J. Pearton, Appl. Phys. Lett. **66**, 1761 (1995).
7. I. Adesida, A. T. Ping, C. Youtsey, T. Dow, M. Asif Khan, D. T. Olson, and J. N. Kuznia, Appl. Phys. Lett. **65**, 889 (1994).
8. A. T. Ping, I. Adesida, M. A. Khan, Appl. Phys. Lett. **67**, 1250 (1995).
9. S. J. Pearton, C. R. Abernathy, C. B. Vartuli, J. D. Mackenzie, R. J. Shul, R. G. Wilson, and J. M. Zavada, Electron. Lett. **31**, 836 (1995).
10. J. A. Van Vechten, J. D. Zook, R. D. Horning and B. Goldenberg, Jpn. J. Appl. Phys. **31**, 3662 (1992).
11. S. Nakamura, N. Iwasa, M. Senoh, and T. Mukai, Jpn. J. Appl. Phys. **31**, L1258 (1992).
12. L. F. Lester, W. J. Schaff, S. D. Offsey, and L. F. Eastman, IEEE Photon. Technol. Lett., **3**, 403 (1991).
13. I. Adesida, A. Mahajan, E. Andideh, M. Asif Khan, D. T. Olson, and J. N. Kuznia, Appl. Phys. Lett. **63**, 2777 (1993).

Effects of Reactive Ion Etching on the Electrical Properties of n-GaN Surfaces

A. T. Ping*, A. C. Schmitz*, M. Asif Khan**, and I. Adesida*

* Center for Compound Semiconductor Microelectronics and Department of Electrical and Computer Engineering, University of Illinois at Urbana-Champaign, Urbana, IL 61801

** APA Optics, Inc., Blaine, MN 55449

ABSTRACT

Dry etch damage on n-GaN has been investigated using Pd Schottky diodes fabricated on surfaces etched by conventional reactive ion etching with SiCl_4 plasma. The Schottky barrier height and ideality factor were investigated as a function of the plasma self-bias voltage. Current-voltage measurements revealed severe degradation of both the forward and reverse characteristics for plasma self-bias voltages in excess of -150 V.

INTRODUCTION

Dry etching has become an important avenue for reliable pattern definition in the III-V nitrides due to their resistance to wet chemical etchant solutions. Several reports have been published over the last few years on various dry etching techniques: conventional reactive ion etching (RIE) [1], electron cyclotron resonance (ECR) RIE [2], magnetron RIE [3], and chemically assisted ion beam etching (CAIBE) [4, 5]. These reports characterize various aspects of each technique from etch rates, etch profiles, to etch-induced stoichiometric surface changes. However, not much is known about the damages created in the nitrides as a result of dry etching. Pearton et al. [6] have investigated the change in sheet resistance of InN, InGaN, and InAlN layers exposed to Ar plasmas under both ECR-RIE and RIE conditions. It was found that InGaN was the most resistant to damage. To date, no work has been reported on the Schottky barrier properties of etched surfaces. Knowledge of etch-induced damages are important in the fabrication of devices, especially for recessed-gate field effect transistors.

In this paper, we investigate the electrical characteristics of reactive ion etched surfaces of n-type GaN using Pd Schottky diodes. Reactive ion etching was performed in a SiCl_4 plasma. The forward and reverse characteristics were investigated using current-voltage (I-V) measurements as a function of the plasma self-bias voltage. The Schottky barrier height and ideality factor were also investigated as a function of the plasma voltage.

EXPERIMENT

The GaN used for this study was epitaxially grown by metal-organic chemical vapor deposition (MOCVD) on (0001) sapphire substrates. The epitaxial layer was 4 μm

thick. The electron carrier concentration was $1 \times 10^{17} \text{ cm}^{-3}$. The room temperature mobility was $\sim 300 \text{ V/cm-s}$. The Schottky diode structure consisted of an array of $300 \mu\text{m}$ openings in a large-field ohmic contact patterned over the GaN surface. The ohmic contact consisted of a Ti/Al bilayer and was annealed using rapid thermal annealing (RTA). Prior to etching, the exposed surface was cleaned in dilute HCl. The exposed GaN was then etched in a Plasma Technology RIE system equipped with a nitrogen-purged load-lock. The system uses a 17 cm diameter cathode which is covered by a 1/2 cm thick quartz plate. The anode and cathode are spaced 5 cm apart. Both are water cooled to maintain a temperature during processing of 20°C . The cathode was rf-driven at 13.56 MHz for plasma excitation. A turbomolecular pump is used to evacuate the 30 cm diameter chamber to a base pressure of 5×10^{-6} Torr. A mechanical pump, though, was used during etching to remove the process gases. An array of $250 \mu\text{m}$ dots for the Schottky contacts was then patterned at the center of ohmic contact openings using AZ5214 photoresist. The exposed GaN surface was cleaned in a plasma asher. The samples were then dipped in dilute HCl, rinsed in deionized water, blown dry with nitrogen, and immediately loaded into the evaporator. The chamber was pumped to a base pressure of 6×10^{-7} Torr prior to metal deposition. Palladium metal was used for the Schottky contacts [7]. The Pd thickness was 100 nm. The Schottky characteristics were then measured using a four-point probe technique with an HP4142 analyzer.

RESULTS AND DISCUSSION

Figure 1 shows the forward I-V characteristics of samples etched under plasma self-bias voltages from -100 to -350 V. This corresponds to a RF power plasma density

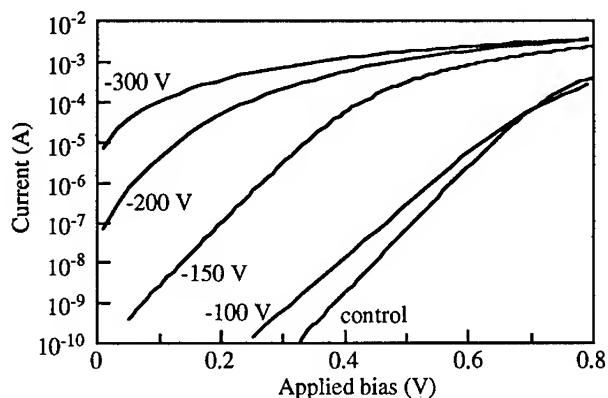


Fig. 1. Forward characteristics of Pd Schottky diodes unetched and etched using RIE/SiCl₄ at various plasma self-bias voltages. Etching was conducted at 25 mT and 10 sccm SiCl₄ flow rate for 2 min.

from 0.2 to 0.75 W/cm² in our system. Etching parameters consisted of a chamber pressure of 25 mT, a SiCl₄ flow rate of 10 sccm, and an etch time of 2 min. From the figure, we observed severe degradation for plasma self-bias in excess of -150 V.

Figure 2 shows the reverse saturation leakage current as a function of the plasma self-bias voltage. The lower and upper curves were measured at an applied bias of -5 and -10 V, respectively. We observe severe degradation of the leakage current for plasma self-bias voltages in excess -150 V, similarly as with the forward characteristics.

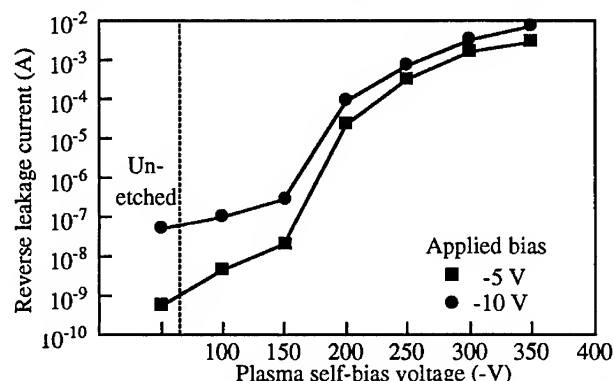


Fig. 2. Reverse saturation leakage current of Pd Schottky diodes plotted as a function of plasma self-bias voltage.

The barrier height and ideality of the Schottky contacts were determined using the thermionic emission theory. Using a linear curve fit of the forward log I vs V curve of Fig. 1, the Schottky barrier heights and the ideality factors can be determined from the y-intercept and slope, respectively. The barrier heights were determined using a theoretical value for the Richardson constant where the electron effective mass was assumed to be 0.22m₀ [8]. Figure 3 shows the Pd Schottky barrier height plotted as a function of the plasma self-bias voltage. Etching conditions consisted of a chamber pressure of 25 mT and a SiCl₄ flow rate of 10 sccm. Etch times were conducted for 2 min for all samples. The barrier height was found to degrade rapidly with plasma voltage. The barrier height was observed to be reduced by a factor of two after etching at -250 V. The barrier height could not be measured for plasma voltages in excess of -250 V because of the severe degradation of the forward characteristics. The ideality factor of the contacts as a function of the plasma self-bias voltage are plotted in Fig. 4. Ideality factor was found to increase rapidly from the control/unetched sample of 1.06 to 1.18 after etching at -250 V. The increase in the ideality factor and lowering of the barrier height both indicate that significant traps are being created at the surface [9].

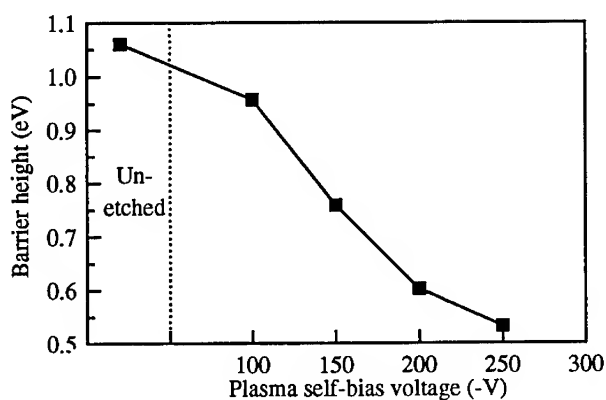


Fig. 3. Pd Schottky barrier height plotted as a function of plasma self-bias voltage. Etching was conducted at 25 mT and 10 sccm SiCl_4 flow rate for 2 min.

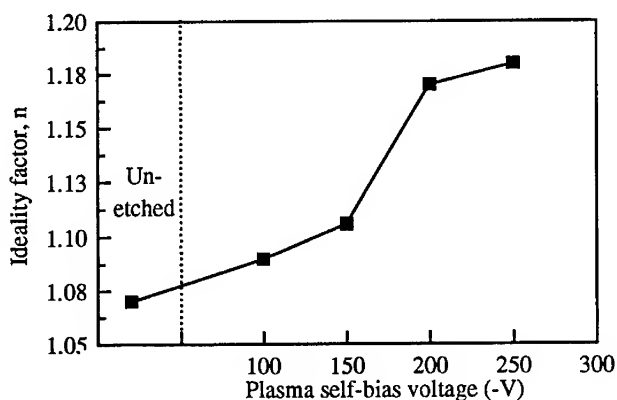


Fig. 4. Pd Schottky ideality factor plotted as a function of plasma self-bias voltage. Etching was conducted at 25 mT and 10 sccm SiCl_4 flow rate for 2 min.

SUMMARY

Reactive ion etching-induced damage on n-type GaN using SiCl_4 plasma has been investigated with Pd Schottky diodes. The forward and reverse I-V characteristics were found to be significantly degraded for plasma self-bias voltages in excess of -150 V. The barrier height was found to rapidly decrease with plasma voltage. The ideality factor was observed to increase and indicates significant states are being created at the surface. Issues of how to anneal out the induced-damages are currently being addressed.

ACKNOWLEDGMENTS

The material work at APA Optics was supported under Air Force Office of Scientific Research under Contract No. F46920-93-C-0059 and the work at the University of Illinois was supported under NSF Grant ECS 95-21671.

REFERENCES

- [1] I. Adesida, A. Mahajan, E. Andideh, M. Asif Khan, D. T. Olson, and J. N. Kuznia, *Appl. Phys. Lett.* **63**, p. 2777 (1993).
- [2] S. J. Pearton, C. R. Abernathy, F. Ren, J. R. Lothian, P.W. Wisk, and A. Katz, *J. Vac. Sci. Technol. A*, **11**, p. 1772 (1993).
- [3] G. F. McLane, L. Casas, R. T. Lareau, D. W. Eckart, C. B. Vartuli, S. J. Pearton, and C. R. Abernathy, *J. Vac. Sci. Technol. A*, **13**, p. 724 (1995).
- [4] I. Adesida, A. T. Ping, C. Youtsey, T. Dow, M. Asif Khan, D. T. Olson, and J. N. Kuznia, *Appl. Phys. Lett.* **65**, p. 889 (1994).
- [5] A. T. Ping, C. Youtsey, I. Adesida, M. Asif Khan, J. N. Kuznia, *J. Electron. Mat.*, **24**, p. 229 (1995).
- [6] S. J. Pearton, J. W. Lee, J. D. MacKenzie, C. R. Abernathy, and R. J. Shul, *Appl. Phys. Lett.*, **67**, p. 2329 (1995).
- [7] A. T. Ping, A. C. Schmitz, M. Asif Khan, and I. Adesida, submitted to *Electronic Letters*.
- [8] S. Strite and H. Morkoç, *J. Vac. Sci. Technol. B*, **10**, p. 1237 (1992).
- [9] S. W. Pang, G. A. Lincoln, R. W. McClelland, P. D. DeGraff, M. W. Geis, and W. J. Piacentini, *J. Vac. Sci. Technol. B*, **1**, p. 1334 (1983).

Part X
Surfaces and Metal Contacts

(NEGATIVE) ELECTRON AFFINITY OF AlN AND AlGaN ALLOYS

R.J. Nemanich, M.C. Benjamin, S.P. Bozeman, M.D. Bremser, S.W. King, B.L. Ward,
R.F. Davis, B. Chen, Z. Zhang, and J. Bernholc
Department of Physics and Department of Materials Science and Engineering,
North Carolina State University, Raleigh, NC 27695-8202

ABSTRACT

The electron affinity of a semiconductor defines the relationship of the vacuum level and the semiconductor band structure. It is dependent on the atomic orbitals of the material and the surface termination. We report experimental and theoretical results that support the presence of a negative electron affinity on AlN and the Al rich AlGaN alloys. The GaN surface is found to exhibit a (positive) electron affinity of 3.3eV. The experimental measurements employ UV-photoemission spectroscopy on in situ gas-source MBE samples and on CVD samples. Theoretical results indicate that the (negative) electron affinity of AlN depends sensitively on the surface reconstruction and adatom termination. The experimental dependence of the electron affinity on alloy concentration is presented. The results indicate that AlGaN alloys with band gap similar or greater than that of diamond will exhibit a negative electron affinity. Field emission results are reported, and the characteristics are similar to those obtained from a diamond film. Issues related to cold cathode electronic devices based on NEA surfaces are noted.

INTRODUCTION

Wide bandgap semiconductors have the potential of exhibiting a negative electron affinity (NEA). These materials could be key elements of cold cathode electron emitters which could be used in applications that include flat panel displays, high frequency amplifiers, and vacuum microelectronics. The surface conditions have been shown to be of critical importance in obtaining a negative electron affinity on diamond surfaces.[1,2,3,4] In this paper, angle resolved UV-photoemission spectroscopy (ARUPS) is used to explore this effect on AlN,[5] GaN and AlGaN alloy surfaces. The value of UV photoemission in characterizing electron emission is that the technique emphasizes effects of the emission process. To fully characterize electron emission properties it is necessary to also employ additional measurements such as field emission, and secondary electron emission. The measurements are interpreted with the help of theoretical calculations. Measurements of field emission from AlN on 6H-SiC are presented to demonstrate the device potential of the materials.

The electron affinity of a semiconductor is defined as the energy required to remove an electron from the conduction band minimum to a distance macroscopically far from the semiconductor (i.e. away from image charge effects.). At the surface this energy can be shown schematically as the difference between the vacuum level and the conduction band minimum. The electron affinity is not, in general, dependent on the Fermi level of the semiconductor. Thus while doping can change the Fermi level in the semiconductor and the work function will change accordingly, the electron affinity is unaffected by these changes. An alternative view is that the electron affinity is a measure of the heterojunction band offset between the vacuum and a semiconductor of interest. For most semiconductors, the conduction band minimum is below the vacuum level and electrons in the conduction band are bound to the semiconductor by an energy equal to the electron affinity. In some cases, surface conditions can be obtained in which the conduction band minimum is above the vacuum level. In that case, the first conduction electron

would not be bound to the sample but could escape with a kinetic energy equal to the difference in energy of the conduction band minimum and the vacuum level. This situation is termed a negative electron affinity. (Note that the electron is still bound to the vicinity of the sample by coulomb forces.)

The electron affinity or work function of a material is usually ascribed to two aspects of the material: (1) the origin of the atomic levels, and (2) the surface dipole due to the surface termination.[6] These effects are shown schematically in Fig. 1. The atomic levels are more or less intrinsic to a material and cannot be changed. This is not the case for the surface dipole. The surface dipole can be substantially affected by surface reconstructions and surface adsorbates. Recent results on diamond have indicated a positive electron affinity of $\sim 0.5\text{eV}$ for clean or oxygen terminated surfaces and a NEA of approximately 1.5eV for hydrogen terminated surfaces.[7,8] These changes are directly attributed to changes of the surface dipole. Because of the large effect of the surface dipole, it is essentially impossible to determine if a material is "intrinsically NEA." Thus the surface termination is critical in describing the electron affinity (or NEA) properties of a material.

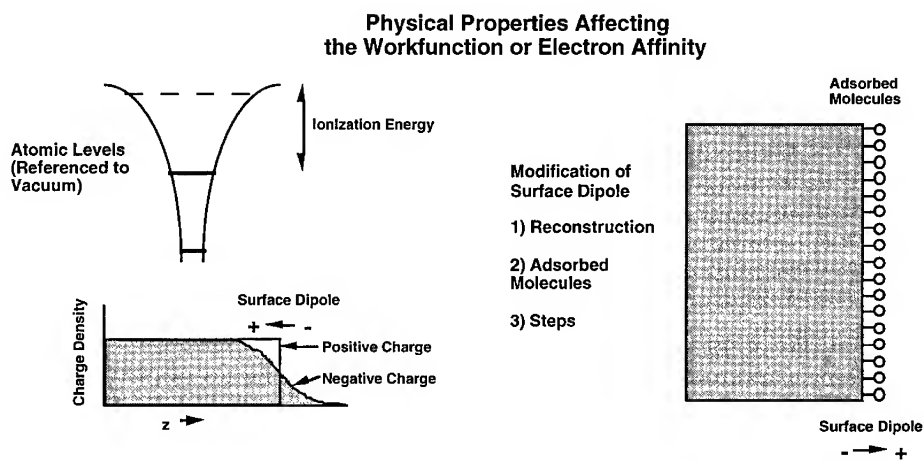


Fig. 1 A representation of the effects which contribute to the work function (or electron affinity) of any material. While the atomic levels are an intrinsic property of the material, changes in the surface bonding can substantially affect the work function or electron affinity.

One method to explore aspects of the electron affinity of a semiconductor is UV-photoemission.[1,2] For a material with a positive electron affinity the value can be directly deduced from the measurements (see below). Furthermore, the UV-photoemission can be used to indicate the presence of a NEA. The changes in the spectra due to a NEA are indicated in Fig. 2.[3] The electrons from the valence band are excited into the conduction band. In transiting towards the surface, electron scattering occurs and a large number of secondary electrons accumulate at the conduction band minimum. For materials with a positive electron affinity these electrons cannot escape, while for a NEA the electrons can be emitted directly and will be observed with a low kinetic energy. Thus the two effects which signify a NEA are an extension of the spectral range to lower energy and the appearance of a sharp peak at low kinetic energy. This

feature will appear at the largest (negative) binding energy in typical presentations of UPS spectra.

In addition to the sharp feature that is often evident in the spectra of a NEA semiconductor, the width of the photoemission spectrum (W) can be related to the electron affinity (χ). The spectral width is obtained from a linear extrapolation of the emission onset edge to zero intensity at both the low kinetic energy cutoff and at the high kinetic energy end (reflecting the valence band maximum). From Fig. 2, it is evident that we can write the following relations:

$$\begin{aligned}\chi &= h\nu - E_g - W && \text{for a positive electron affinity, and} \\ 0 &= h\nu - E_g - W && \text{for a negative electron affinity}\end{aligned}$$

where E_g is the bandgap and $h\nu$ is the excitation energy. We stress that the photoemission measurements cannot be used to determine the energy position of the electron affinity for the NEA surface. Careful measurements of the width of the spectra are helpful in distinguishing whether the effect is direct emission of the electrons from conduction band states or whether excitons are involved in the emission process. The effects of excitons have recently been reported by Bandis and Pate.[9]

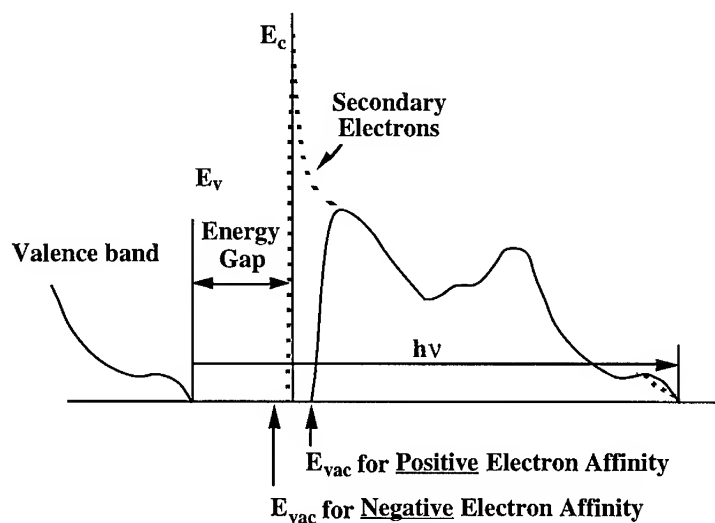


Fig. 2 A schematic of how NEA affects the photoemission spectra. For a NEA surface the spectrum is broadened to lower kinetic energy, and a peak due to quasi thermalized electrons is detected at the lowest kinetic energy (highest negative binding energy).

In addition to measurement of the electron affinity, UV photoemission can be used to determine the position of the surface Fermi level. The Fermi level of the sample will be the same as that of the metal sample holder, and the Fermi level of the metal can easily be determined. The energy difference of the valence band maximum and the metal Fermi level then gives the position of the surface Fermi level of the semiconductor. The position of the surface Fermi level will be critical in determining the band bending near the surface.

THEORETICAL RESULTS

Previous theoretical studies of the electron affinity of wide bandgap semiconductors have focused on non-polar surfaces, namely diamond.[7,8,10] The study of polar surfaces is substantially more complicated, and special techniques were developed to deal with charge transfer effects inherent at such surfaces.

The theoretical technique is based on ab initio molecular dynamics (Car-Parrinello method [11]). A plane wave basis was employed, and soft core, norm conserving pseudopotentials were used to describe the ions. The supercells consisted of 10-12 layers of AlN with 4-16 atoms in each layer. For most calculations, a 12Å vacuum region separated the surfaces. One side of each slab was terminated by hydrogen atoms to reduce charge transfer caused by the finite width of the slab.

A surface created by truncating the bulk always has dangling bonds. To achieve a more stable state, the partially filled dangling bonds must be eliminated - a process which involves the formation of new bonds that inevitably increases the strain between the surface and the subsurface layers. The balance between the lowering of the energy due to the elimination of the dangling bonds and the induced strain determines the nature of the surface reconstruction. In the calculations, reconstruction patterns were chosen based on either experimental observations or physical intuition. In the case of a polar surface, the difference of the work functions between two different sides of the slab causes a non-physical dipole field in the ideal bulk-cleaved slab. The work functions of two different sides of the slab are not independent. This problem is aggravated when dealing with a polar surface, since the electrons will move to the side which has the higher work function in order to lower the total energy. In a real physical system, the effect of the surface from one side is screened within the distance of a few lattice constants. This is not true in a thin slab which is only 10-12 layers thick. To reduce this "screening" problem in these calculations, one side of the slab was terminated with hydrogen atoms. The charge transfer caused by the infinite slab width was then reduced to less than 0.02 electrons per surface atom. The other problem is the periodic boundary conditions that result in a slope of the electrostatic potential in the vacuum region when the slab consists of two non-equivalent surfaces. To solve this problem, we employed a compensating field deep inside of the vacuum region, which cancels out the effect caused by the periodic boundary conditions. The details of this technique will be discussed elsewhere.[12]

The electron affinity of a semiconductor can be related to the bulk average potential through the following:

$$\chi = D - (E_c - V_{bulk})$$

where D is defined as the surface dipole potential that determines the relative energies of the bulk electron states and the vacuum level and $(E_c - V_{bulk})$ is the position of the conduction band minimum relative to the bulk-averaged electrostatic potential. The surface dipole potential was obtained in these calculations from the difference of the electrostatic potential across the surface. The electron affinities of different surface configurations of AlN are listed in Table I, where prior results for diamond (111) surface are also listed.

Table I. The Calculated results of electron affinities [in eV] for different surface configurations.

Surface Specie	Bare Surface	H-terminated (1x1)	Vacancy (2x2)
Diamond (111)	positive	-1.5	N.A.
Al - AlN	+0.85	+1.60	-0.70
N - AlN	+0.30	+0.05	+1.40

The results exhibit trends for changes between clean and chemisorbed surfaces. Once chemisorption occurs, the adsorbates saturate the dangling bonds by bonding with the surface atoms. The bonding causes a charge transfer between the adsorbates and the surface atoms, and an additional dipole field occurs. The strength and direction of the additional dipole field determines the change of the electron affinity.

In general the electronegativity can be used as a good indicator of the sign of the surface dipole. For an adsorbate with a lower electronegativity than the surface atoms, when the adsorbate atoms attach to the surface atoms, the bond charge will tend to get closer to the surface atom, which results in an additional dipole field pointing outwards with respect to the surface. This field will reduce the surface barrier or lower the electron affinity of a semiconductor. An opposite charge transfer would result in an additional dipole directed towards the surface, which would increase the electron affinity.

In AlN, Al has a lower electronegativity than H, while the opposite is true for N. Thus hydrogen adsorbed on the Al-terminated surface is expected to result in an increased electron affinity, and this is reflected in the full calculations. Moreover, from their electronegativities, it is expected that both Al- and N-terminated AlN surfaces with chemisorbed Li or Be should exhibit reduced or negative electron affinities.

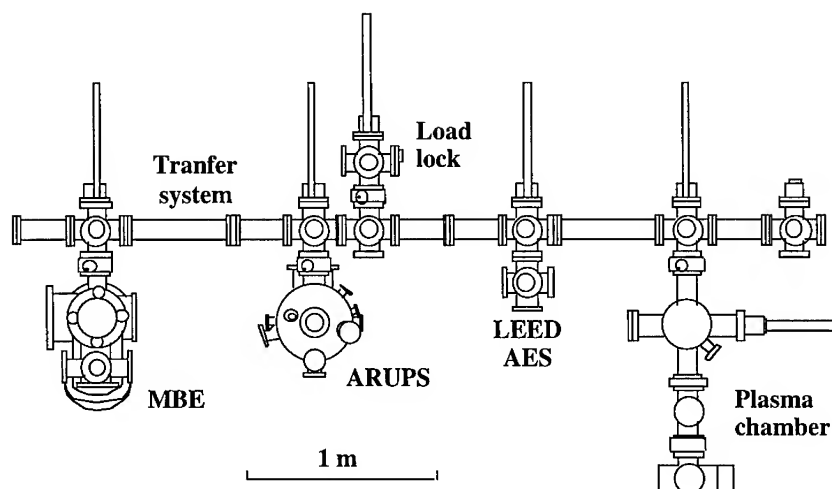


Fig. 3. A schematic of a portion of the integrated surface processing and characterization system used in the studies described here.

EXPERIMENTAL

The experiments described in this summary paper were carried out in an integrated UHV system with surface preparation, film growth and surface characterization capabilities. The system consists of eight chambers interconnected by a linear sample transfer mechanism. The overall length of the sample transfer chamber is ~35ft. A portion of the system is shown schematically in Fig. 3. This figure shows the positions of the UV photoemission system, the plasma surface processing system, the LEED/Auger systems, and the MBE chamber. In the experiments

described here, the UV-photoemission measurements were made with HeI (21.21eV) radiation and the electrons were analyzed with a VSW HAC50 50mm mean radius hemispherical electron analyzer. The spectra were collected at normal emission with a collection angle of $\sim 2^\circ$. The sample was biased with ~ 1 to 3V so that the low energy electrons can overcome the work function of the analyzer. While higher sample bias can be employed, the low bias used here is to minimize spectral distortions that occur due to changes in the effective collection angle for the higher sample bias.

To avoid charging and to obtain high quality epitaxy, the AlGa_N films were grown on (0001) 6H-SiC substrates. The substrates were supplied by Cree Research, Inc. [1] The SiC wafers were n-type with doping concentrations of 10^{16} to $10^{18}/\text{cm}^3$. The AlGa_N alloy samples were grown by CVD (OMVPE) in a remote location and transported in ambient to the analysis system. Clean, as-grown surfaces of AlN and GaN were prepared in the integrated UHV transfer system (described above) by gas source molecular beam epitaxy (GSMBE), and transferred directly to the UPS system. The Al concentration of the alloy samples was estimated from respective cathodoluminescence measurements.

Field emission measurements were obtained within a separate high vacuum chamber (pressure $< 10^{-5}$ Torr). During the experiment, samples were placed beneath a 2 mm diameter movable platinum anode with a flat tip. The anode was controlled by a stepper motor such that one step yielded a translation of 0.44 μm . The current-voltage (I-V) measurements were taken at several distances ranging from 2 to 20 μm and for bias voltages in the range of 0 to 1100 volts. The relative travel of the probe was determined by the number of steps and the step size established by the translation stage. The I-V curves were measured at intervals as the probe approached the sample and the absolute distance was calculated when the probe tip touched the sample. Using this procedure, the measurements were made before the probe tip touched the sample. In both the field emission and UV-photoemission, the techniques probed a similar sample area of 2-3 mm in diameter. While the field emission properties of the samples may not be uniform, this nonuniformity is expected to be on a microscopic scale so that the probe area averages over the variation in emission sites.

UV-PHOTOEMISSION RESULTS

The UV photoemission spectra of AlN, GaN and the two alloy samples are shown in Fig. 4. [20,21] Samples were biased with 2-3 V to overcome the work function of the analyzer, and all spectra were shifted to be aligned at the valence band maximum. The spectra were scaled such that the strongest emission was the same for all curves.

The first aspect to be noted is that the spectra of the Al rich alloy and AlN exhibit sharp strong features at the largest (negative) binding energy, which corresponds to the lowest kinetic energy. These features are often indicative of a negative electron affinity. As noted in the introduction, the feature is attributed to emission from electrons quasi-thermalized to the conduction band minimum. The emission from the Al_{0.13}Ga_{0.87}N sample is significantly weaker, and the GaN emission does not show the sharp peak at all.

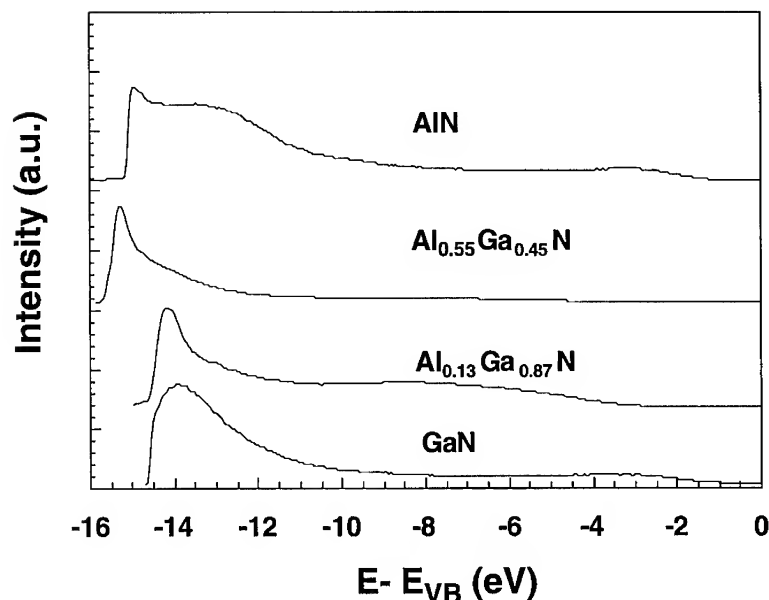


Figure 4. The UV photoemission spectra of $\text{Al}_x\text{Ga}_{1-x}\text{N}$ films grown on 6H-SiC. The spectra were excited with 21.21 eV HeI radiation. Samples were biased at -3V such that the low energy electrons could overcome the work function of the analyzer. All spectra are aligned at the valence band maximum, and the energy scale references this energy as 0.

A second indication of the change in electron affinity with alloy concentration is the extension of the $\text{Al}_x\text{Ga}_{1-x}\text{N}$ spectra to lower energy as x is decreased. A more precise description of the relation of the NEA is obtained from the spectral width. To determine the energy position of the valence band maximum, each spectrum was magnified, and the intensity was extrapolated to 0 emission. The spectral widths obtained from the $\text{Al}_x\text{Ga}_{1-x}\text{N}$ samples were 14.5, 14.5, 15.5, and 15 eV for $x=0, 0.13, 0.55$, and 1.0 , respectively. To apply the relations noted above, the bandgap of each sample must also be known. The reported values of the AlN and GaN bandgaps are 6.2 and 3.4 eV respectively. The band gap of the alloy samples was determined from the respective cathodoluminescence measurement. Using the relations described above, the AlN satisfies the relations for a NEA, while the $\text{Al}_{0.55}\text{Ga}_{0.25}\text{N}$ surface exhibits a low but positive electron affinity. The GaN and $\text{Al}_{0.13}\text{Ga}_{0.87}\text{N}$ surfaces, do not satisfy the relations for a NEA. We can, however, determine the value of the electron affinity of these materials and find that $\chi = 3.3$ eV and 2.9 eV for $x = 0$ and 0.13 respectively.

Another aspect that is evident from the photoemission spectra is the position of the surface Fermi level relative to the valence band maximum. It was found that E_F ranges from 2 to 3.5 eV above the valence band maximum for each sample. For the GaN and $\text{Al}_{0.13}\text{Ga}_{0.87}\text{N}$ surfaces, these values position E_F in the upper part of the gap while for the Al rich samples, the values indicate that the surface Fermi level is pinned near midgap. The surface Fermi level position and the bandgap of the alloys are indicated in Fig. 5. The pinning at midgap may be an indication of surface states or increased impurity incorporation. In particular, the strong affinity of Al with oxygen may result in increased oxygen incorporation at the surface or in the bulk of these films.

The deduced electron affinities versus alloy concentration are shown in Figure 5. Again we note that the photoemission measurements cannot be used to determine the position of the vacuum level for a NEA surface. Therefore, the electron affinity of the AlN is indicated at $\chi = 0$ with an arrow to larger negative values. The results suggest that the electron affinity depends on the alloy concentration. It should be noted that we have made no effort to control the surface termination for these samples. Previous results for diamond indicate that the observation of a NEA may be critically dependent on the surface termination. This may not be the case with the nitrides. Future studies should explore whether the electron affinity of AlGaN materials is also affected by different surface preparations.

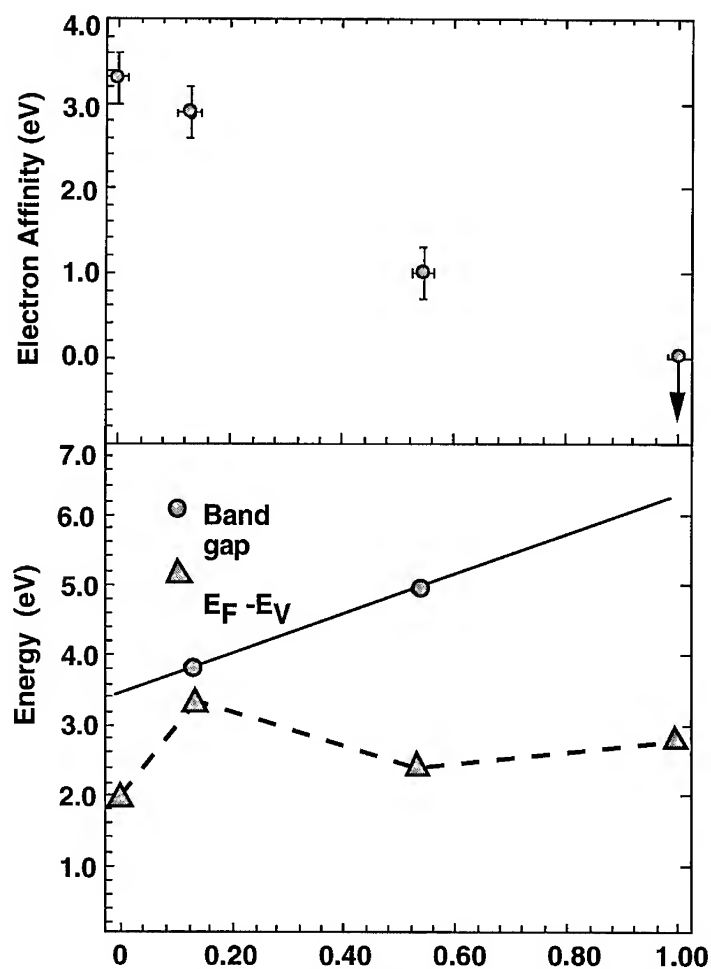


Fig. 5. The dependence of the electron affinity (upper panel), bandgap (filled circles) and surface Fermi level position (triangles) for the AlGaN alloys. The electron affinity and surface Fermi level are obtained from the UPS spectra of Fig. 4.

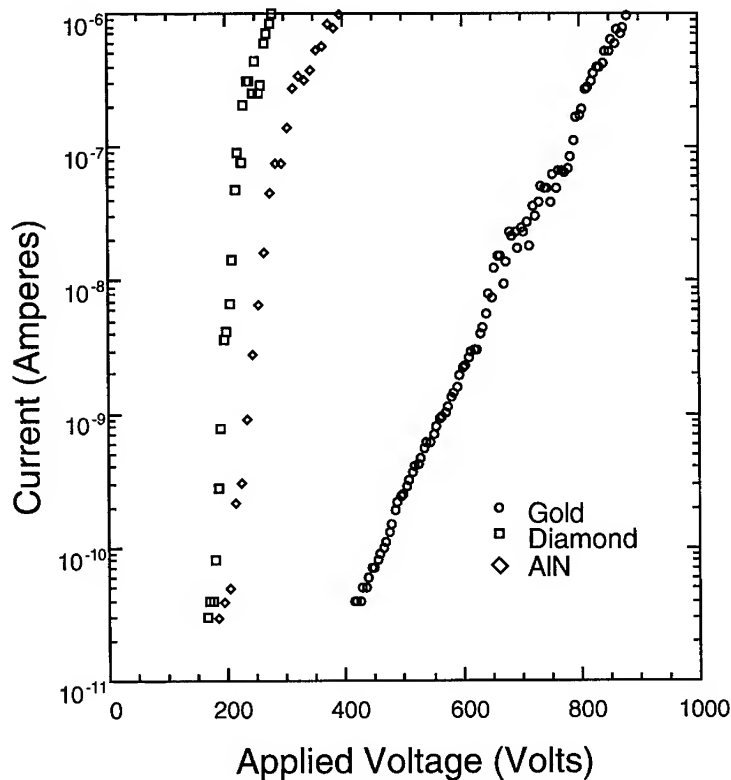


Fig 6. The field emission I-V measurements obtained from AlN (10nm) on 6H-SiC compared to that from a polished p-type diamond film (50 μ m) and a sputtered gold film. The (Pt) anode to film surface distance of the AlN, diamond and Au measurements were 7.2 ± 1.3 , 6.2 ± 0.9 , and 6.5 ± 1.5 μ m respectively.

ELECTRON EMISSION FROM A NEGATIVE ELECTRON AFFINITY SURFACE

The major device related goal of these studies is the development of a cold cathode electron emitter. Three steps can be considered in understanding the emission process: (1) electron supply to the semiconductor, (2) transport from the supply electrode to the surface, and (3) the emission into vacuum. The photoemission and theoretical sections above have focused mostly on the last of these processes. In contrast, field emission involves all three process.

The field emission I/V curves for a thin (10nm) AlN sample is compared to that of p-type diamond and a sputtered gold film in Fig. 6. All measurements were obtained at similar distances so that the electric field dependence near the surface is essentially the same for all three samples. The diamond sample was a 50 μ m thick p-type film deposited on Si and polished such that the RMS roughness from AFM measurements was ~ 1 nm. While we did not measure the flatness of the AlN and the Au films, we expect a similar surface roughness. Compared to the emission from gold, the AlN and diamond show a significant reduction in the field to obtain similar electron

emission currents. It is interesting to note that both semiconductors exhibited emission currents of 1nA at a field of 31V/ μ m.

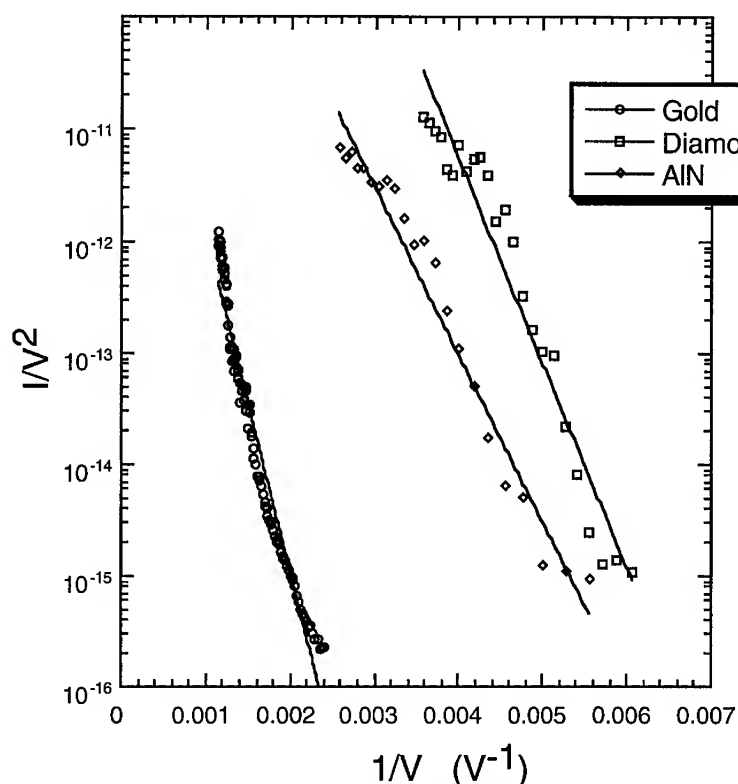


Fig. 7. A Fowler-Nordheim plot of the current voltage data shown in Fig. 6. The straight lines show regions in which the emission exhibits F-N characteristics.

All three samples exhibit Fowler Nordheim type dependence in the I-V measurements. The F-N plots for the samples are shown in Fig. 7. The F-N characteristics suggest the presence of a barrier to emission. For metals this is simply the surface barrier due to the work function. There is still considerable discussion on the mechanism of electron emission from p-type diamond films.[13,14,15] We note that the work function from these films is slightly less than 5eV which is similar to the value for most metals. In contrast, the photoemission results indicate that the Fermi level of the AlN is near the center of the 6.3eV band gap. This would imply a ~3eV work function. The band alignment for the AlN on n-type SiC has previously been discussed,[5] and new results are reported in this conference.[16] It was suggested that the AlN-6H-SiC band offset at the conduction band is no larger than 2.7 eV. Thus it is probable that the F-N field emission characteristics from the AlN is limited by electron injection from the SiC into the AlN.

There have been many studies of field emission from point emitters (i.e. Spindt tips). The sharp point emitters result in a field enhancement at the tip and a possible reduction in the work function due to the steps on the surface. The I-V characteristics from a field emitter follow the

Fowler-Nordheim expression. In contrast, the I-V dependence of an ideal NEA based emitter should exhibit emission at any negative bias. At low fields the current would be limited by the space charge in the vacuum around the emitter (following Child-Langmuir dependence) and at higher fields the current would be limited by the resistance of the semiconductor and the contact. The energy distribution of the emitted electrons from a NEA cathode should be very narrow ($\sim kT$), and the current should exhibit a noise component related to the resistance of the semiconductor and contact. This is in contrast to either thermal emitters (i.e. hot cathodes) or field emitters that exhibit fluctuations based on the statistics of the highest energy part of the electron distribution.

An electron emitter based on a negative electron affinity material would have several unique advantages over pointed field emitters. These would include low turn on voltage, high current density, low sputter erosion, and low noise. In addition, the field emitter requires a significant field established through a potential between the tip and a nearby grid layer. In contrast, a true NEA device would be controlled by a small field established by the grid to modulate the anode to cathode field. Notice that for an ideal NEA structure the grid potential would actually range from 0 to a small negative value. Then, when the grid is at the cathode potential, the potential established at the anode would control the emission. A small negative grid potential would then be used to limit or modulate the electron emission.

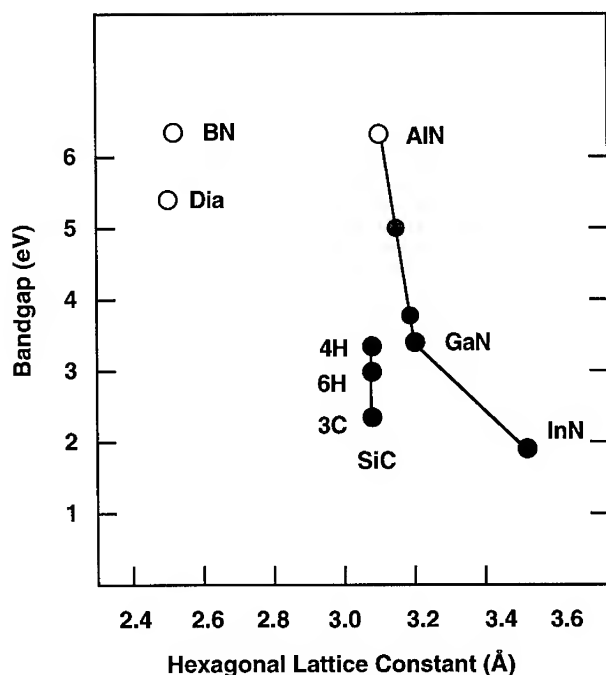


Fig. 8. The bandgap vs. hexagonal lattice constant for a group of wide bandgap semiconductors. For the cubic materials, the lattice constant is the unit cell in the (111) plane. The open circles represent materials that have been shown to exhibit a negative electron affinity, while the gray circle represents the low electron affinity GaAlN alloy studied here.

CONCLUDING REMARKS

The experimental and theoretical results presented here demonstrate that a negative electron affinity surface can be obtained for nitride and other wide bandgap semiconductors. Fig. 8. summarizes the hexagonal lattice constant and bandgap dependence for the nitride and carbon related materials. We also show on this figure the materials that have been shown to exhibit a NEA. In addition to the measurements described here, recent results have demonstrated that BN exhibits a negative electron affinity.[17] It is interesting to note that all materials from this group which have a bandgap larger than that of diamond exhibit an negative electron affinity. The results of the alloy data presented here are also consistent with this value.

For the development of cold cathodes, the electron supply may be as critical as the emission properties. The potential of obtaining n-type nitrides with a NEA offers the real possibility of a high current cold cathode emitter. It is possible that structures based on this material could produce space charge limited currents.

Studies of nitride surfaces are still at a very early stage. While there have been reports of different surface reconstructions, there is still considerable uncertainty as to the stable structure of the surfaces and the dependence on stoichiometry. The theoretical and experimental results presented here suggest further studies of well characterized surfaces.

Acknowledgment We acknowledge helpful discussions with Peter Baumann. This work was supported in part by the Office of Naval Research.

REFERENCES

1. F.J. Himpsel, J.A. Knapp, J.A. van Vechten, and D.E. Eastman, Phys. Rev. B20, 624 (1979).
2. B.B. Pate, Surf. Sci. 165, 83 (1986).
3. van der Weide, J., and R. J. Nemanich, Appl. Phys. Lett. 62, 1878 (1993).
4. P.K. Baumann and R.J. Nemanich, J. Diamond Rel. Mat. 4, 802 (1995).
5. M.C. Benjamin, C. Wang, R.F. Davis, R.J. Nemanich, Appl. Phys. Lett. 64, 3288 (1994).
6. Zangwill, A (1988), Physics at Surface, (Cambridge).
7. J. van der Weide, Z. Zhang, P.K. Baumann, M.G. Wensell, J. Bernholc and R.J. Nemanich, Phys. Rev. B 50, 5803 (1994).
8. Z. Zhang, M.C. Wensell, and J. Bernholc, Phys. Rev. B51, 5291 (1995).
9. C. Bandis and B.B. Pate, Phys. Rev. Lett. 74, 777(1995).
10. W. Pickett, Phys. Rev. Lett. 73, 1664 (1994).
11. R. Car and M. Parrinello, Phys. Rev. Lett. 55, 2471 (1985).
12. Z. Zhang, B. Chen, and J. Bernholc, to be published.
13. C. Wang, A. Garcia, D.C. Ingram, M. Lake, and M.E. Kordes, Electron. Lett. 27, 1459 (1991).
14. N.S. Xu, R.V. Latham and Y. Tzeng, Electron. Lett. 29, 1596 (1993).
15. Z.- Huang, P.H. Cutler, N.M. Miskovsky and T.E. Sullivan, Appl. Phys. Lett. 65, 2562 (1994).
16. S.W. King, M.C. Benjamin, R.J. Nemanich, R.F. Davis, W.R.L. Lambrecht, (this volume).
17. M. J. Powers, M. C. Benjamin, L. M. Porter, R. J. Nemanich, R. F. Davis, J. J. Cuomo, G. L. Doll and Stephen J. Harris. Appl. Phys. Lett., (in press).

NEGATIVE DIFFERENTIAL RESISTIVITY IN GaN METAL-SEMICONDUCTOR-METAL PHOTOCONDUCTORS

Z.C.HUANG*, J.C. CHEN**, YUODOU ZHENG * AND D.B. MOTT **

* Hughes STX Corporation, 7701 Greenbelt Road, Suit 400, Greenbelt, MD 20770

** Department of Electrical Engineering, University of Maryland Baltimore County, Baltimore, MD 21228

* Department of Physics, Nanjing University, Nanjing 210008, China

** Goddard Space Flight Center, Code 718.1, NASA, Greenbelt, MD 20771

ABSTRACT

We have observed a negative differential resistivity (NDR) in metal-semiconductor-metal (M-S-M) photoconductor made from unintentionally doped GaN grown by metalorganic chemical vapor deposition. The threshold field for the onset of NDR was found to be independent of the spacing of M-S-M fingers, and was measured to be 1.91×10^5 V/cm for GaN with an n-type carrier concentration of 10^{14} cm⁻³. We believe that the observed NDR is due to transferred electron effect in GaN. The threshold field value is very close to the value obtained from the theoretical simulation. This observation, to the best of our knowledge, is the first experimental evidence of transferred-electron effects in GaN, which is important in understanding GaN energy band structure and in the application of Gunn-effect devices using GaN materials.

INTRODUCTION

GaN has received extensive interest in recent years due to its successful application in blue light emitting diodes (LEDs)¹ and its great potential in high power and high temperature electronic devices. It is also predicted that GaN can be used for high frequency devices such as transferred electron devices (TED) due to its large longitudinal optical phonon energy and large energy separation between the central valley (Γ) of the conduction band and the next-lowest-energy minimum^{2,3}. In 1975, Littlejohn et al.⁴ first predicted a negative differential resistivity (NDR) in GaN under high electric field. Recently, Gelmont et al.⁵ showed through an ensemble Monte Carlo simulation that intervalley electron transfer plays a dominant role in GaN in high electric fields leading to a strongly inverted electron distribution and to a large negative differential resistance. The mechanism responsible for the NDR is a field-induced transfer of conduction-band electrons from a low-energy, high-mobility valley to high-energy, low-mobility satellite valleys. The NDR is important for microwave device applications. However, no direct evidence of NDR phenomena has been reported so far in GaN materials or related devices. The direct measurement of the velocity of electrons as a function of the electric field is usually difficult in semiconductors due to oscillations in high conductivity materials and nonuniformity of electric field in low conductivity materials, and becomes even more difficult in GaN due to its large energy band gap which requires a large threshold field. In this letter, we report the first observation of the negative differential resistance in GaN material through a metal-semiconductor-metal (M-S-M) system. The threshold field was found to be 1.91×10^5 V/cm in GaN with a background concentration of 10^{14} cm⁻³.

EXPERIMENT

The GaN material used in this letter was grown on (0001) sapphire by metalorganic chemical vapor deposition. It is unintentionally doped and has a carrier concentration of 10^{14} cm^{-3} at room temperature as obtained from capacitance-voltage measurement. The M-S-M finger-type patterns, shown in Fig.1, were fabricated using a lift-off technique. The fingers are $1.5 \mu\text{m}$ wide and $50 \mu\text{m}$ long and the spacing between the fingers are $1.5 \mu\text{m}$, $3.0 \mu\text{m}$ and $4.5 \mu\text{m}$. This M-S-M structure was originally fabricated as a photodetector. But in this study, an ohmic contact is needed rather than a Schottky contact. We made contacts by evaporating Au/Al on the GaN front surface, and alloying at 450°C for 5 min. The contact showed a fairly good ohmic behavior. Current-voltage (I-V) measurements were performed at room temperature in dark conditions using a Keithley 617 Electrometer, which is controlled by a computer.

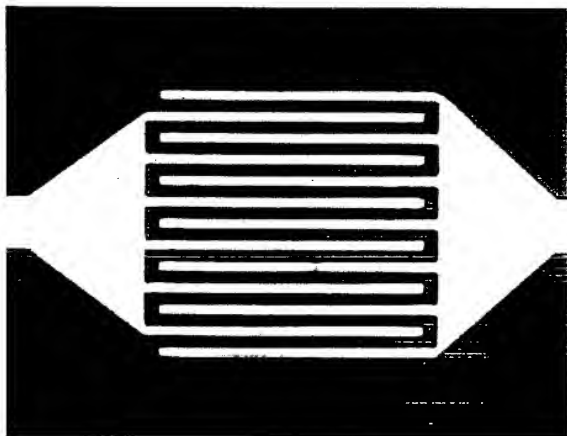


Fig.1. Metal-semiconductor-metal structure. Finger width= $1.5 \mu\text{m}$, spacing= $1.5 \mu\text{m}$

RESULTS

Figure 2 shows the current of our M-S-M ($3 \mu\text{m}$ spacing) as a function of electric field measured at room temperature. We consider the electric field to be uniform in the space between fingers, and hence the current-electric field (I-E) curves are directly converted from I-V curves. Figure 2 clearly shows a negative differential resistivity in the high electric field region when the electric field is beyond the threshold point of $1.91 \times 10^5 \text{ V/cm}$. There are two most likely causes which are responsible for the observed NDR phenomenon. One is field enhanced trapping⁶, which is a thermal effect in the high electric field region due to the accumulation of heat between fingers. Another possible cause is the transfer of electrons from the central valley to higher energy valleys, which is the so-called transferred-electron effect (TEE)⁷.

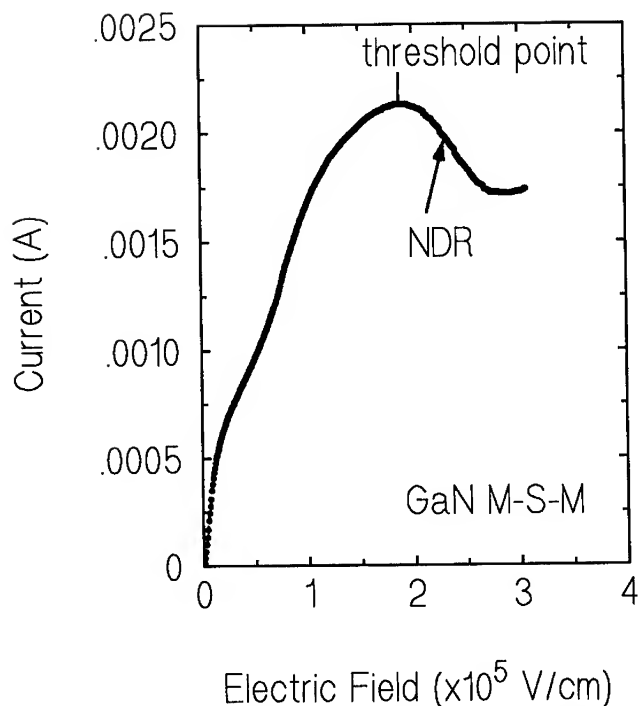


Fig. 2. I-E curve at room temperature for the GaN M-S-M system.

If there is a negatively-charged impurity center in a semiconductor, the capture of an electron is strongly influenced by the presence of the potential barrier arising from the Coulomb repulsion. The heated electrons tend to have increased probability of tunneling through the barrier, and so have an increased capture rate. The resultant fall in electron density would cause bulk negative differential resistivity. However, we have found that the I-E curve was repeatable, and the curve shape did not change after several consecutive runs. This indicates that the thermal effect is unlikely to be the cause of NDR in our case because the capture of electrons would tend to saturate after several voltage scans, which would change the shape of I-E curves. We also measured the I-E characteristics for M-S-Ms with different spacing, and found that M-S-Ms with different spacing show almost the same threshold electric field, as shown in Fig. 3, suggesting that the onset of NDR is uniquely determined by the electric field. Therefore we believe that the observed NDR in Fig. 2 is due to the transferred-electron effect in our case.

It should be pointed out that not every GaN sample could show the NDR phenomenon. We tried very low resistivity materials and semi-insulating materials, and only observed NDR in the sample with a background concentration of 10^{14} cm^{-3} . For the low-resistivity material, the carrier mobility in central valley could be small, and not able to show this effect. On the other hand, in semi-insulating materials the threshold field could be very high, beyond the limit of our measurement.

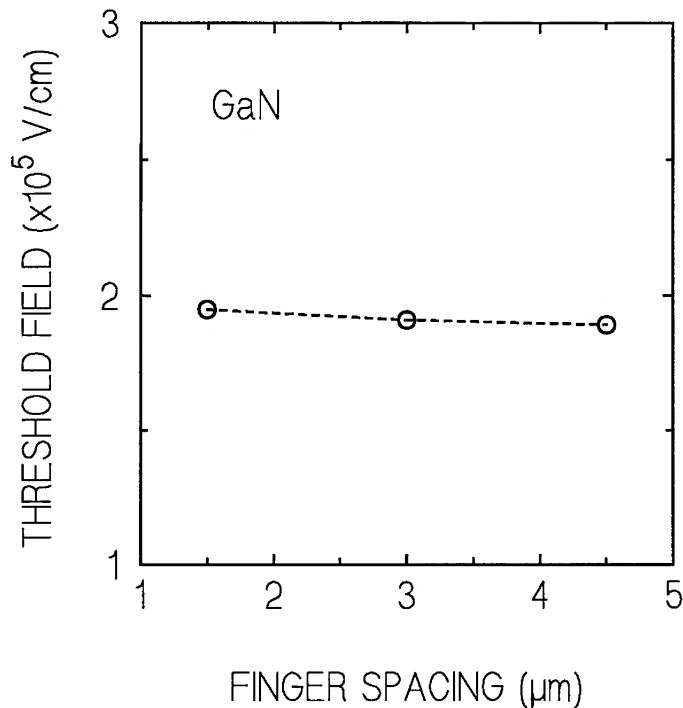


Fig.3. Threshold electric field vs the finger spacing of M-S-M system.

The measured threshold electric field ($1.91 \times 10^5 \text{ V/cm}$) in GaN is much higher than those in other III-V semiconductors, such as GaAs ($3 \times 10^3 \text{ V/cm}$) and InP ($1.1 \times 10^4 \text{ V/cm}$). This is reasonable because GaN is a high-band-gap material and the separation between the central valley and the next-lowest-minimum is much higher⁸ ($>1.5 \text{ eV}$) compared to GaAs and InP. Our value is very close to the values obtained from a Monte Carlo simulation by Littlejohn et al.⁴ and Gelmont et al.⁵.

Finally it should be stressed that the observation of TEE effects in GaN is important in understanding its energy band structure, and makes it possible for the application of Gunn-effect devices as predicted.

CONCLUSIONS

In conclusion, we have observed, for the first time, the transferred-electron effect in GaN through a metal-semiconductor-metal system. The threshold electric field was found to be $1.91 \times 10^5 \text{ V/cm}$, which is consistent with the theoretical simulation. This observation confirms that the GaN material can be used for Gunn-effect devices for microwave applications.

ACKNOWLEDGMENTS

This work was supported by NASA through contract number NAS5-32350. One of the authors (JCC) acknowledges the support of the AASERT program from Army Research Office. Authors would like to thank Naval Research Laboratory for the GaN material preparation.

REFERENCES

1. S.Nakamura, T. Mukai and M. Seno, Jpn. J. Appl. Phys., **30**, L1998 (1991).
2. S. Bloom, Phys. Chem. Solids, **32**, 2027 (1971).
3. D. Jones and A.H. Lettington, Solid State Commun., **11**, 701 (1972).
4. M.A. Littlejohn, J.R. Hauser and T.H. Glisson, Appl. Phys. Lett., **26**, 625 (1975).
5. B. Gelmont, K. Kim and M. Shur, J. Appl. Phys., **74**, 1818 (1993).
6. B.K. Ridley and R.G.Pratt, Phys. Lett., **4**, 300 (1963).
7. B.K. Ridley and T.B. Watkins, Proc. Phys. Soc. Lond. **78**, 293 (1961).
8. S. Bloom, G. Harbeke, E. Meier and I. B. Ortenburger, Phys. Status Solidi, **B66**, 161 (1974).

Properties of Zn Implanted GaN

S. STRITE ^{*(a)}, P. W. EPPERLEIN ^{*(b)}, A. DOMMANN ^{**}, A. ROCKETT ^{***}, R. F. BROOM ^{****}

^{*}IBM Research Division, Zurich Research Laboratory, CH-8803 Rüschlikon, Switzerland

^(a)srt@zurich.ibm.com, ^(b)pep@zurich.ibm.com

^{**}Neu-Technikum Buchs, CH-9471 Buchs, Switzerland, dommann@ntb.ch

^{***}Materials Research Laboratory, University of Illinois at Urbana/Champaign, Urbana, IL 61801, rockett@ux1.cso.uiuc.edu

^{****}Department of Materials Science and Metallurgy, Cambridge University, Cambridge CB2 3QZ United Kingdom, rfb12@cus.cam.ac.uk

ABSTRACT

We report the optical and structural properties of ion implanted GaN:Zn. Post-implant annealing up to 1100 °C was performed under flowing N₂ in both a tube furnace and a rapid thermal annealing (RTA) system, with and without SiN_x encapsulation layers. The implantation damage is quantified by transmission electron microscopy (TEM). Secondary ion mass spectroscopy (SIMS) detects significant rearrangement of implanted Zn only at the highest temperatures and doses investigated. Strain reduction, observed in GaN:Zn annealed at or above 975 °C by high-resolution x-ray diffractometry (HRXRD), indicates successful damage removal. The optical activation of annealed GaN:Zn is measured by photoluminescence (PL). The room temperature (RT) Zn acceptor transition at ~430 nm is consistently observed in annealed GaN:Zn, but at low efficiency. We conclude that residual implantation damage and/or N loss during annealing limits the optical quality of implanted GaN:Zn.

INTRODUCTION

Ion implantation is widely used in semiconductor device technology to locally alter the electrical properties of materials, e.g. for doping or isolation. Less attention has been paid to ion implantation as a method for introducing optically active impurities. GaN LEDs can luminesce in any of the visible colors dependent on the dopant introduced [1]. If it is possible to realize good optical quality implanted GaN, LEDs would benefit from dopants incompatible with epitaxial growth processes. It would also be possible to fabricate monolithic multicolor LED arrays [2].

Two groups in the 1970's reported PL in ion implanted GaN. Pankove and Hutchby [3] implanted 35 different elements into GaN, reporting on GaN:Zn in detail [4]. Metcalfe et al. [5] investigated As and P doping. Each find that post-implantation annealing activates the dopants, but no estimates of the absolute PL efficiency are given.

Our work evaluates ion implanted, annealed GaN:Zn for optical device applications.

EXPERIMENT

Our starting material was 1.5 µm GaN/sapphire MOVPE grown epilayers [6] having a background electron concentration of ~10¹⁶ cm⁻³ which exhibit strong bandedge and negligible midgap PL. Zn⁺ ions were implanted up to 200 keV and Zn⁺⁺ ions for 400 keV. Implanted samples were annealed (800 - 1100 °C) under flowing N₂ in a tube furnace (sample pairs face to face) or RTA, some with chemical vapor deposited SiN_x encapsulation layers deposited after

implantation, to inhibit N loss. GaN:Zn maintains its specular surface after 1 hr furnace anneals up to 1025 °C. At higher temperatures, unencapsulated samples decomposed leaving a liquid Ga surface. SiN_x (10 - 50 nm) encapsulation permits annealing up to our experimental limit (1100 °C) without Ga droplet formation. However, above 900 °C, the SiN_x encapsulation blisters badly, suggesting that significant N loss is occurring.

A Cameca IMS 5f SIMS instrument rastered 8 keV O₂⁺ or 17 keV Cs⁺ primary ions over (250 μm)² to sputter flat bottomed craters. GaN:Zn structural data was recorded with a 4-circle Philips MPD 1880 HRXRD tool equipped with a Ge (220) monochromator (+--+ arrangement). For PL, the signal excited by a 15 mW HeCd ultraviolet laser was dispersed in a SPEX 1404 double-grating spectrometer and detected by a cooled photomultiplier and photon counting electronics.

RESULTS

TEM

A TEM cross section (Fig. 1) of GaN:Zn (200 keV, $5 \times 10^{15} \text{ cm}^{-2}$) illustrates the implantation damage. Images of lower doses (200 keV, $5 \times 10^{13} \text{ cm}^{-2}$) are qualitatively similar, but the damage is less pronounced. Typical GaN/sapphire dislocations propagate vertically from the heterointerface. Within ~260 nm of the surface heavy implant damage causes the dislocations to be no longer resolvable. Contrast variations between the next ~100 nm and undamaged material nearer the substrate suggests scattering from additional point defects.

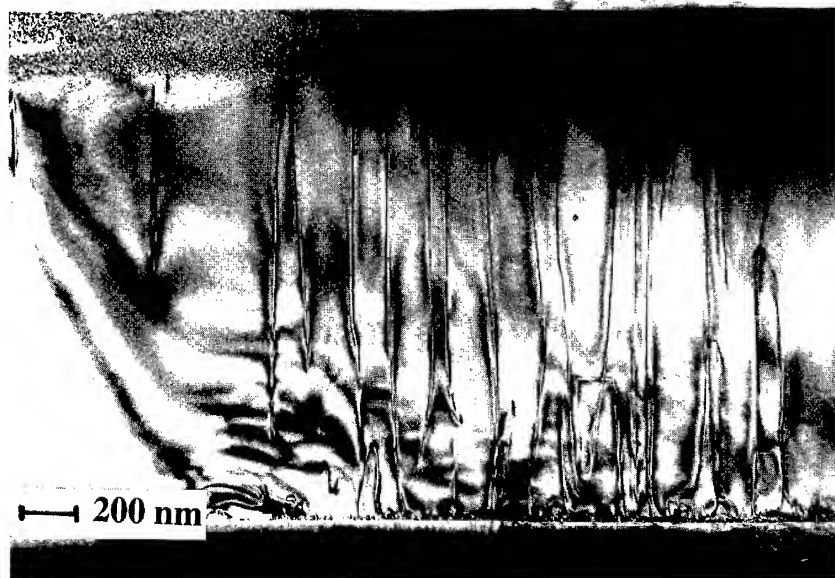


Figure 1. Bright field TEM image of Zn implanted GaN (200 keV, $5 \times 10^{15} \text{ cm}^{-2}$).

SIMS

SIMS Zn depth profiles (Fig. 2) for ion energies of 100 keV (10^{14} cm^{-2}), 200 and 400 keV ($5 \times 10^{13} \text{ cm}^{-2}$) are plotted. The profiles are slightly asymmetric, falling off more slowly into the substrate. Zn concentration maxima occur at 66 nm, 134 nm, and 189 nm penetration with full width half maxima (FWHM) of 132, 177, and 185 nm for ion energies of 100, 200 and 400 keV, respectively. Comparing the SIMS and TEM data, the heavily damaged uppermost layer seen in Fig. 1 extends roughly to the Zn concentration half maximum on the substrate side of the peak.

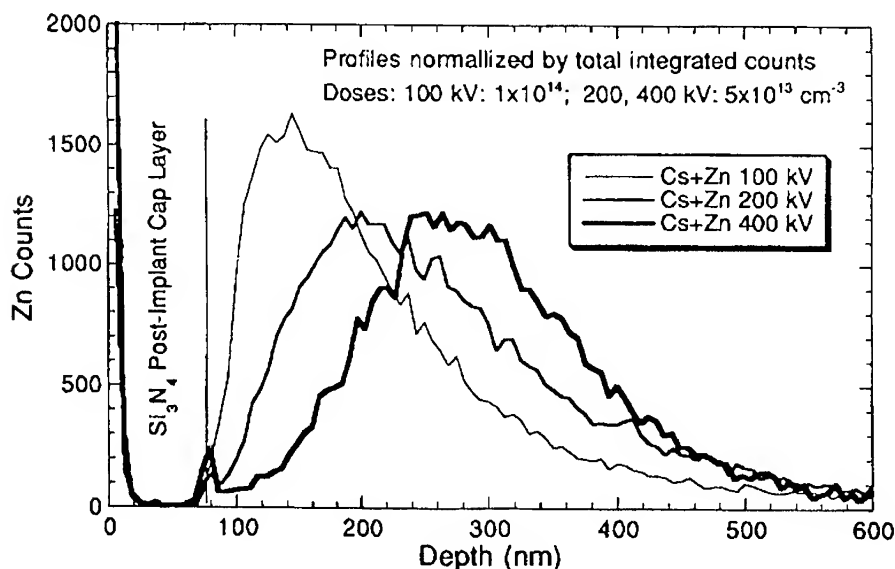


Figure 2. SIMS profiles of GaN:Zn as a function of Zn ion energy.

Zn diffusion in annealed samples (200 keV, $8 \times 10^{12} - 5 \times 10^{15} \text{ cm}^{-2}$) was also studied with SIMS. We concentrated on higher annealing temperatures than those previously reported [7,8]. Slight Zn diffusion is observed in RTA (1100 °C, 10 min) samples only at doses above $2 \times 10^{14} \text{ cm}^{-2}$. At $2.5 \times 10^{15} \text{ cm}^{-2}$, significant redistribution of the Zn into a two peaked profile is observed in some cases.

HRXRD

Figure 3 contrasts two pairs of HRXRD GaN (00.4) rocking curves from furnace annealed and unannealed GaN:Zn implanted at 200 keV, 10^{13} cm^{-2} and 35 keV, 10^{15} cm^{-2} . Higher doses result in greater strain as seen from the broader FWHM of the 35 keV curves, despite their lower implantation energy. Strain relaxation is seen only in GaN:Zn furnace annealed for 1 hour at 975 °C or above in the 35 keV sample. HRXRD is not highly sensitive to implant damage and annealing in the lower dose sample.

The inset of Fig. 3 compares the rocking curves of annealed (200 keV, $2 \times 10^{13} \text{ cm}^{-2}$) GaN:Zn. No relaxation is observed after 15 min RTA at 900 °C. At 1100 °C, no further

improvement results from a 1 hr furnace anneal compared to 10 min RTA. These observations suggest that temperature plays a larger role than the duration of the anneal.

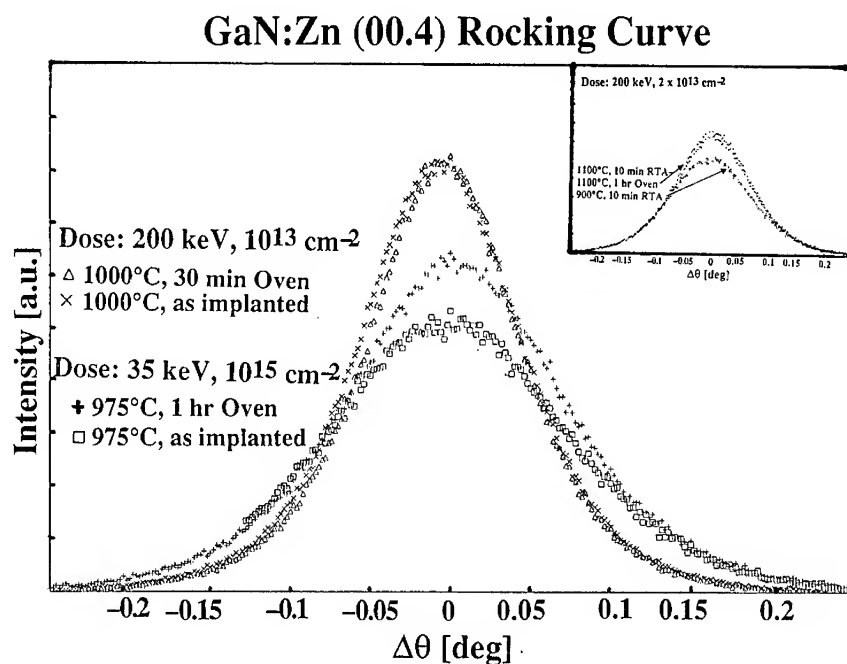


Figure 3. High-resolution x-ray diffraction rocking curves of the (00.4) GaN Bragg peak. Higher doses produce greater damage, even at lower implant energy. Strain relaxation is observed for anneals 975 °C or above. Inset: Annealing at 1100 °C for 10 min or 1 hr produce identical results while a 10 min anneal at 900 °C has no effect on the rocking curve.

PL

A characteristic RT Zn acceptor transition at ~430 nm is observed in a wide variety of samples (35 - 400 keV, 10^{12} - 10^{15} cm^{-2}) annealed at or above 900 °C. In addition, all annealed GaN:Zn exhibits the oft seen yellow defect luminescence suspected to derive from N vacancies [9]. We take the ratio of blue Zn to defect luminescence maxima as a figure of merit. Our best results (Fig. 4) are obtained by RTA (1100 °C, 10 min, SiN_x cap) on a 200 keV, $8 \times 10^{12} \text{ cm}^{-2}$ sample, which yields roughly four times the maximum count rate at 430 nm versus midgap. We varied several parameters to observe their effect on this ratio. The blue PL is enhanced by a factor of 16 with respect to the yellow when the RTA temperature (10 min) is increased from 900 to 1100 °C. Enhancements of roughly a factor of two are realized by lengthening the RTA time from 1 to 5 min, or reducing the implanted dose from 5×10^{14} to $8 \times 10^{12} \text{ cm}^{-2}$. We observed no enhancement when the substrate temperature is raised to 600 °C during the ion implantation.

At 77 K (inset), the Zn signal in this sample is greatly enhanced both with respect to the defect level and in absolute intensity. Compared to epitaxially doped GaN:Zn, the RT blue PL intensity of the best implanted material is 1-2 orders of magnitude weaker. At 77 K, the implanted Zn signal is still about a factor of 10 weaker than the epitaxial GaN:Zn transition. Thus, we are only partially successful in activating implanted Zn with our annealing conditions. Furthermore, the RT blue PL of implanted samples is more severely reduced with respect to the 77 K signal than in epitaxial GaN:Zn. This observation indicates that annealing induced and residual implantation defects are contributing to the quenching of RT Zn luminescence.

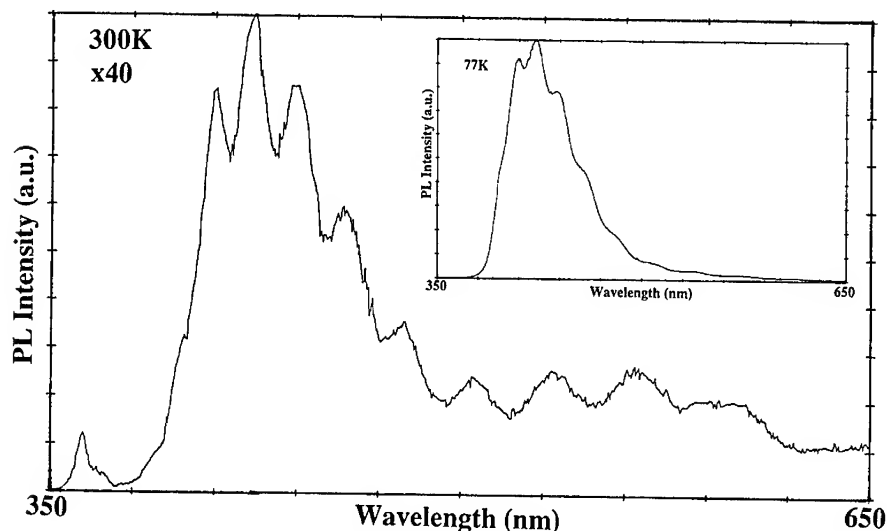


Figure 4. Room temperature and 77 K (inset) photoluminescence from a RTA (10 min, 1100 °C) Zn implanted GaN sample (200 keV, $8 \times 10^{12} \text{ cm}^{-2}$). The low temperature PL is roughly a factor of 40 more intense.

CONCLUSION

We find that annealing removes much of the implantation damage from GaN and optically activates implanted Zn impurities. However, N loss during annealing and/or residual implant damage severely limit the RT PL efficiency of GaN:Zn. Higher annealing temperatures may succeed in obtaining high optical quality ion implanted GaN:Zn if an improved encapsulation layer can be identified.

ACKNOWLEDGEMENT

We acknowledge the assistance of P. Baumgartner, H.-J. Brändle of NTB and W. Heuberger of IBM, and discussions with H. P. Meier of IBM. A. Rockett acknowledges the support of the U.S. Dept. of Energy (DOE) under contract DEFG02-91-ER45439 and the use of the UIUC DOE supported Center for Microanalysis of Materials.

REFERENCES

1. S. Strite and H. Morkoç, J. Vac. Soc. Technol. B **10**, 1237 (1992).
2. V. A. Dmitriev, Ya. V. Morozenko, I. V. Popov, A. V. Suvorov, A. L. Syrkin and V. E. Chelnokov, Sov. Tech. Phys. Lett. **12**, 221 (1986).
3. J. I. Pankove and J. A. Hutchby, Appl. Phys. Lett. **24**, 281 (1974).
4. J. I. Pankove and J. A. Hutchby, J. Appl. Phys. **47**, 5387 (1976).
5. R. D. Metcalfe, D. Wickenden and W. C. Clark, J. Luminescence **16**, 405 (1978).
6. Cree Research, Durham, NC.
7. R. G. Wilson, S. J. Pearton, C. R. Abernathy and J. M. Zavada, Appl. Phys. Lett. **66**, 2238 (1995).
8. R. G. Wilson, C. B. Vartuli, C. R. Abernathy, S. J. Pearton and J. M. Zavada, Solid-State Electronics **7**, 1329 (1995).
9. S. Strite in Properties of the III-V Nitrides. EMIS Datareview Series #11, edited by J. E. Edgar (The Institution of Electrical Engineers, London 1994) p. 255-275.

ION IMPLANTATION DOPING AND HIGH TEMPERATURE ANNEALING OF GaN

J. C. ZOLPER,^a M. HAGEROTT CRAWFORD,^a A. J. HOWARD,^{a,c} S. J. PEARTON,^b C. R. ABERNATHY,^b C. B. VARTULI,^b C. YUAN,^c R. A. STALL,^c J. RAMER^d, S. D. HERSEE,^d and R. G. WILSON^e

^aSandia National Laboratories, Albuquerque, NM 87185-0603, ^bUniversity of Florida, Department of Materials Science and Engineering, Gainesville, FL 32611, ^cEmcore Corp., Somerset, NJ 08873, ^dUniversity of New Mexico, Albuquerque, NM 87131, ^eHughes Research Laboratory, Malibu CA 90265

ABSTRACT

The III-V nitride-containing semiconductors InN, GaN, and AlN and their ternary alloys are the focus of extensive research for application to visible light emitters and as the basis for high temperature electronics. Recent advances in ion implantation doping of GaN and studies of the effect of rapid thermal annealing up to 1100 °C are making new device structures possible. Both p- and n-type implantation doping of GaN has been achieved using Mg co-implanted with P for p-type and Si-implantation for n-type. Electrical activation was achieved by rapid thermal anneals in excess of 1000 °C. Atomic force microscopy studies of the surface of GaN after a series of anneals from 750 to 1100 °C shows that the surface morphology gets smoother following anneals in Ar or N₂. The photoluminescence of the annealed samples also shows enhanced bandedge emission for both annealing ambients. For the deep level emission near 2.2 eV, the sample annealed in N₂ shows slightly reduced emission while the sample annealed in Ar shows increased emission. These annealing results suggest a combination of defect interactions occur during the high temperature processing.

INTRODUCTION

The III-V nitride-containing semiconductors InN, GaN, and AlN and their ternary alloys are attracting renewed interest for application to visible light emitters^{1,2} and as the basis for high temperature electronics.³⁻⁵ Their attractive material properties include bandgaps ranging from 1.9 eV (InN) to 6.2 eV (AlN), an energy gap ($E_g(\text{GaN}) = 3.39 \text{ eV}$) close to the short wavelength region of the visible spectrum, high breakdown fields, high saturation drift velocities and relatively high carrier mobilities.⁶

There have been limited reports of the implantation properties of the III-V nitrides.⁷ Early work by Pankove⁸ focused on the optical properties of GaN implanted with an array of elements while Khan investigated the implantation of Be or N in GaN⁹ and AlGa¹⁰ to improve Schottky barrier characteristics. Recently there have been reports on the implant isolation properties of III-Nitride materials^{11, 12, 13} but there has been only one report of the achievement of implantation doping of GaN.¹⁴ In this work we report in more detail on the properties of implantation doping in GaN. Specifically, Hall data for the sheet carrier concentration versus annealing temperature is reported. Variable temperature Hall data is reported and used to estimate the ionization energy levels for implanted Mg and Si in GaN.

In addition, secondary ion mass spectroscopy (SIMS) data is presented for as-implanted and annealed samples to study the redistribution properties of implanted Mg and Si in GaN. Furthermore, since an implant activation anneal in excess of 1000 °C is required to achieve electrical activation, data for the effect of such an anneal on the morphology and luminescence properties of GaN is presented. Results are also given for ohmic contact formation to Si-implanted GaN.

EXPERIMENTAL

The GaN layers used in the implant doping experiments were 1.5 to 2.0 μm thick grown on c-plane sapphire substrates by metalorganic chemical vapor deposition (MOCVD) in a multiwafer rotating disk reactor at 1040 °C with a ~ 20 nm GaN buffer layer grown at 530 °C.¹⁵ The GaN layers were unintentionally doped, with background n-type carrier concentrations $\leq 5 \times 10^{16} \text{ cm}^{-3}$. The as-grown layers had featureless surfaces and were transparent with a strong bandedge luminescence at 3.484 eV at 14 K. The GaN layers used in the annealing experiments were also grown by MOCVD but in a RF-heated, horizontal geometry reactor consisting of a double walled deposition chamber, a rectangular-section flow-liner, and an uncoated graphite susceptor angled for optimum uniformity.¹⁶ This GaN

was grown on solvent cleaned, a-plane $[11\bar{2}0]$ oriented, sapphire substrates. The growth sequence involved a thin GaN buffer at 480 °C followed by a $\sim 5 \mu\text{m}$ GaN layer at 1025 °C with a 2 $\mu\text{m/hr}$ growth rate. The as-grown GaN is colorless, has a specular morphology, shows a typical n-type background doping in the $6 \times 10^{16} \text{ cm}^{-3}$ to $3 \times 10^{17} \text{ cm}^{-3}$ range, a mobility between 200 and 600 $\text{cm}^2/\text{V-s}$, and an x-ray rocking curve FWHM of approximately 200 arc seconds.

For implantation doping, the samples were implanted with either ^{28}Si ($5 \times 10^{14} \text{ cm}^{-2}$, 200 keV), ^{24}Mg ($5 \times 10^{14} \text{ cm}^{-2}$, 180 keV), or $^{24}\text{Mg}+^{31}\text{P}$ ($5 \times 10^{14} \text{ cm}^{-2}$, 180/250 keV). The samples were annealed from 700 to 1100 °C for 10 s in a SiC coated graphite susceptor in flowing N_2 . Electrical characterization was performed by van der Pauw Hall measurements using alloyed (350 °C, 10 s) HgIn contacts at the corners of each sample.

For the annealing experiment, the anneals were done in a similar fashion as above except for 15 s and in one of three ambients: 4% H_2 :96% N_2 , Ar, or N_2 . The samples surface morphology were characterized by atomic force microscopy (AFM) with a Digital Instruments Dimension 3000 AFM operating in the tapping mode with a silicon tip by taking $10 \mu\text{m} \times 10 \mu\text{m}$ images at three points on each sample. Each image was then analyzed for the RMS surface roughness. The as-grown material and the Ar and N_2 1100 °C annealed samples were also characterized by photoluminescence using a 10 mW HeCd laser (325 nm) excitation source with the spectra taken at 15 K.

RESULTS AND DISCUSSION

Figure 1(a,b) shows the sheet electron and hole concentration versus activation annealing temperature for Si, Mg, Mg+P, or unimplanted GaN. For Si-implantation (Fig. 1a) electrical activation first occurs after a 1050 °C anneal with a ~ 16 fold increase in sheet electron concentration which increases by a additional factor of 5 after a 1100 °C anneal. Co-implantation of P with Mg was found to be necessary to achieve p-type material after a 1050 °C anneal as evident in Fig. 1b. In contrast, the Mg-only sample remains n-type and shows little difference from the unimplanted sample. The effect of the P co-implantation may be explained by a reduction of N-vacancies or an increase in Ga-vacancies leading to a higher probability of Mg occupying a Ga-site. Co-implantation of P has also been shown to be effective in enhancing activation and reducing diffusion for p-type implantation in

GaAs.^{17,18,19} Figure 2a,b shows an Arrhenius plot of the sheet electron concentration and the resistance/temperature product for Si-implanted GaN after a 1100 °C anneal. Both Arrhenius plots for Si are included in Fig. 2, since there is some discussion regarding the possibility of two-band conduction in GaN and its potential effect on the extracted ionization energy for n-type conduction.²⁰ By fitting the data of Fig. 2, ionization levels for Si-implanted GaN of 61 or 29 meV are estimated. These values are in the range reported for epitaxial Si-doped GaN.²¹ Figure 2c shows the Arrhenius plot for the sheet hole concentration for Mg+P implanted GaN annealed at 1100 °C from which an ionization of 171 meV is estimated. This also is consistent with the literature values for Mg-doped GaN.²

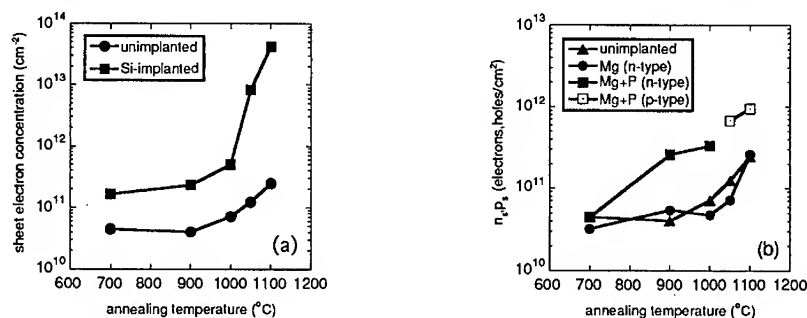


FIG 1. Sheet carrier concentration versus annealing temperature for unimplanted and a) Si-implanted or b) Mg and Mg+P implanted GaN.

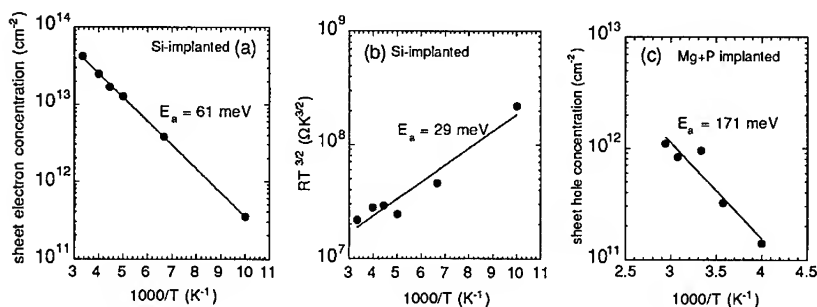


FIG 2. Arrhenius plots of a) the sheet electron concentration and b) the resistance/temperature product for Si-implanted and c) the sheet hole concentration for Mg-implanted GaN annealed at 1100 °C.

When applying ion implantation doping to device structures, knowledge of impurity redistribution during the activation anneal process is needed. Figure 3a,b shows the SIMS profiles for Mg and Si implanted GaN either as implanted or after a 15 s, 1050 or 1150 °C anneal. For Mg, the annealed samples show a slight shift towards the surface that is estimated to be 50 nm near the profile peak. Based on a 50 nm diffusion length, an upper limit on the diffusivity of Mg in GaN at 1150 °C of 6.75×10^{-13} cm²/s is estimated. Profiles for Mg co-implanted with P gave similar results. For Si (Fig 3b) no measurable redistribution has occurred after a 1050 °C anneal. Using a conservative estimate of the depth resolution of the SIMS measurement of 20 nm, an upper limit of 2.7×10^{-13} cm²/s is estimated for the diffusivity of Si in GaN at 1050 °C.

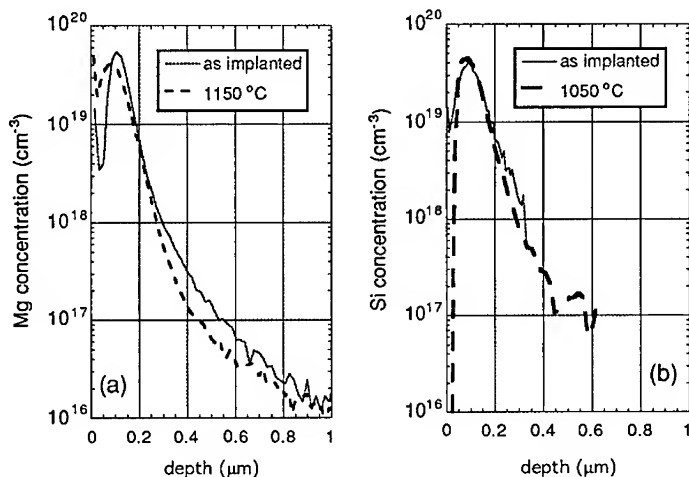


FIG 3: SIMS plots for a) Mg-implanted (5×10^{14} , 100/140 keV) or b) Si-implanted (5×10^{14} , 100 keV) GaN either as implanted or annealed at the temperature listed in the legend.

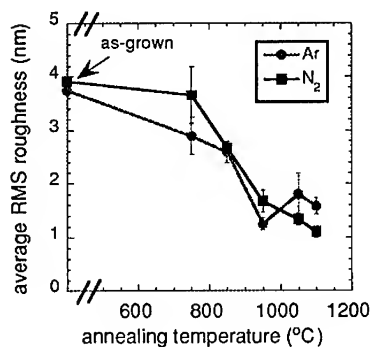


FIG 4: Average RMS roughness of GaN versus annealing temperature for anneals in Ar or N₂.

Turning to the effect of high temperature anneals on the surface morphology of GaN films, Fig. 4 shows the evolution of the root-mean-square (RMS) surface roughness versus annealing temperature for samples annealed in Ar or N₂. The roughness of these samples decreases with increasing annealing temperature. Figure 5 shows three dimensional AFM images of the as-grown and 1100 °C, N₂ annealed samples. The annealed sample is seen to be smoother with less fine structure.²² Samples annealed in forming gas (4%H₂:96%N₂) were also studied and showed visual evidence of decomposition via Ga-droplet or Ga-puddle formation on the surface. Therefore, a valid assessment of the surface roughness of these samples could not be made due to the Ga-rich regions and thus data for forming gas annealed samples are not included in Fig. 4.

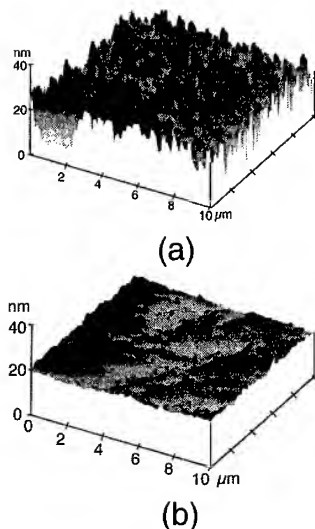


FIG 5: Three dimensional AFM images of GaN a) as-grown and b) after a 15 s, 1100 °C anneal in N₂.

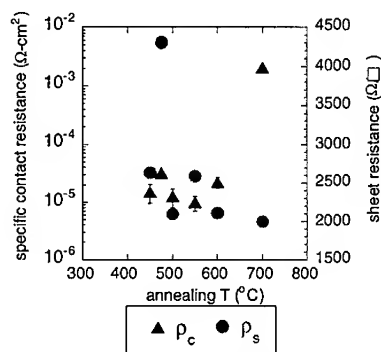


FIG 6. Specific contact resistance of Ti/Al and sheet resistance versus contact annealing temperature for Si-implanted GaN (5×10^{14} , 40 keV, 7.5×10^{14} , 100 keV) annealed at 1150 °C for 15 s.

To further understand the effect of high temperature annealing on GaN, photoluminescence measurements were performed on as-grown and annealed samples.²² Samples annealed at 1100 °C in Ar or N₂ demonstrated stronger bandedge emission (2x for Ar, 4x for N₂) than the as-grown sample. This suggests that non-radiative defect levels are being removed by the annealing process. The annealed samples also showed more intensity modulation of the Fabry-Perot interference fringes associated with the deep level emission. We attribute the enhanced interference to the smoother surfaces of the annealed samples as seen from the AFM data of Figs. 4 and 5. Finally, both annealed samples have higher ratios of the bandedge to deep level emission than the as-grown sample. Improvements in this ratio are often taken to correspond to improved material quality. Further structural and chemical analysis is required to fully understand the mechanisms responsible for the material improvements resulting from the high temperature anneals. In particular, since studies on other compound semiconductors have shown that changes in photoluminescence properties resulting from thermal treatments often depend on the condition of the starting material, more work is needed to correlate the luminescence improvements with the characteristics of the as-grown material.

Finally, we have done preliminary work on ohmic contact formation to n-type implantation doped GaN. Figure 6 shows the specific contact resistance and sheet resistance of Si-implanted GaN contacted with Ti/Al (20 nm/200 nm) metallization versus the contact annealing temperature. A minimum specific contact resistance of $1 \times 10^{-5} \Omega\text{-cm}^2$ was realized after a 550 °C anneal which is in the range typically reported for contacts to n-type GaN. Further optimization of the implant and anneal to reduce the sheet resistance of the implanted region will improve this contact resistance.

CONCLUSION

Ion implantation is expected to play an enabling role in the realization of many high performance devices in the III-Nitrides as it has in other mature semiconductor material systems. To this end, we have reported on the realization of n- and p-type doping of GaN by

implantation of Si and Mg+P, respectively. The high temperature anneal required for implant activation was also shown to cause minimal redistribution of Si and Mg.

Acknowledgments: The portion of this work performed at Sandia National Laboratories was supported by the U.S. Department of Energy under contract # DE-AC04-94AL85000. The work at the University of Florida is partially supported by a National Science Foundation grant (DMR-9421109) and a University Research Initiative grant from ONR (N00014-92-5-1895). The work at EMCORE was supported by BMDO-IST managed by M. Yoder at ONR. The SIMS work was performed at Hughes and was supported by ARO (Dr. J. M. Zavada). Work at Un. of New Mexico was supported by ARPA. The technical support of J. Escobedo at Sandia with implantation and annealing and the support of the MicroFabritech facility at UF is greatly appreciated.

References

- ¹ S. Nakamura, T. Mukai, and M. Senoh, *Appl. Phys. Lett.*, **64**, 1687 (1994).
- ² I. Akasaki, H. Amano, M. Kito, and K. Hiramatsu, *J. Lumin.* **48/49**, 666 (1991).
- ³ S. C. Binari, L. B. Rowland, W. Kruppa, G. Kelner, K. Doverspike, and D. K. Gaskill, *Electronics Lett.*, **30**, 1248 (1994).
- ⁴ M. A. Kahn, J. N. Kuznia, D. T. Olsen, W. J. Schaff, J. W. Burm, and M. S. Shur, *Appl. Phys. Lett.*, **65**, 1121 (1994).
- ⁵ T. P. Chow and R. Tyagi, *IEEE Trans. Electron. Dev.*, **41**, 1481 (1994).
- ⁶ S. Strite and H. Morkoç, *J. Vac. Sci. Technol. B* **10**, 1237 (1992).
- ⁷ J. C. Zolper, M. Hagerott Crawford, S. J. Pearton, C. R. Abernathy, C. B. Vartuli, C. Yuan, and R. A. Stall, *J. Elec. Mat.* in press.
- ⁸ J. I. Pankove and J. A. Hutchby, *J. Appl. Phys.*, **47**, 5387 (1976).
- ⁹ M. A. Khan, R. A. Skogman, R. G. Schule, and M. Gershenson, *Appl. Phys. Lett.*, **42**, 430 (1983).
- ¹⁰ M. A. Khan, R. A. Skogman, R. G. Schule, and M. Gershenson, *Appl. Phys. Lett.*, **43**, 492 (1983).
- ¹¹ S. J. Pearton, C. R. Abernathy, P. W. Wisk, W. S. Hobson, and F. Ren, *Appl. Phys. Lett.*, **63**, 1143 (1993).
- ¹² J. C. Zolper, S. J. Pearton, C. R. Abernathy, and C. B. Vartuli, *Appl. Phys. Lett.* **66**, 3042 (1995).
- ¹³ C. B. Vartuli, S. J. Pearton, C. R. Abernathy, J. D. MacKenzie, and J. C. Zolper, submitted to *J. Vac. Science and Technology*.
- ¹⁴ S. J. Pearton, C. B. Vartuli, J. C. Zolper, C. Yuan, and R. A. Stall, *Appl. Phys. Lett.* **67**, 1435 (1995).
- ¹⁵ C. Yuan, T. Salagaj, A. Gurary, P. Zawadzki, C. S. Chern, W. Kroll, R. A. Stall, Y. Li, M. Schurman, C.-Y. Hwang, W. E. Mayo, Y. Lu, S. J. Pearton, S. Krishnakutty, and R. M. Kolbas, *J. Electrochem. Soc.* **142**, L163 (1995).
- ¹⁶ S. D. Hersee, J. Ramer, K. Zheng, C. Kranenberg, K. Malloy, M. Banas, and M. Goorsky, *J. Elec. Mat.* **24**, 1519 (1995).
- ¹⁷ K. K. Patel and B. J. Sealy, *Appl. Phys. Lett.* **48** 1467 (1986).
- ¹⁸ M. E. Sherwin, J. C. Zolper, A. G. Baca, T. J. Drummond, R. J. Shul, A. J. Howard, D. J. Rieger, R. P. Schneider, and J. F. Klem, *J. Elec. Mater.* **15**, 809 (1994).
- ¹⁹ J. C. Zolper, A. G. Baca, M. E. Sherwin, and R. J. Shul, *Elec. Letts.* **31**, 923 (1995).
- ²⁰ R. J. Molnar, T. Lei, and T. D. Moustakas, *Appl. Phys. Lett.* **62** 72 (1993).
- ²¹ J. G. Kim, A. C. Frenkel, H. Liu, and R. M. Park, *Appl. Phys. Lett.* **65**, 91 (1994).
- ²² J. C. Zolper, M. Hagerott Crawford, A. J. Howard, J. Ramer, and S. D. Hersee, *Appl. Phys. Lett.*, to be published, January 8 1996.

ION DAMAGE AND ANNEALING OF EPITAXIAL GALLIUM NITRIDE AND COMPARISON WITH GaAs/AlGaAs MATERIALS

H.H. Tan*, J.S. Williams*, C. Yuan** and S.J. Pearton***

* Department of Electronic Materials Engineering, RSPSE, Australian National University, Canberra, 0200, Australia

** Emcore Corp., Somerset, N.J. 08873, USA (deceased)

*** Department of Materials Science and Engineering, University of Florida, Gainesville, Fl. 32611, USA

ABSTRACT

Ion damage build up has been measured by ion channeling in good quality epitaxial GaN films on sapphire. GaN is found to be remarkably resistant to ion damage, with extremely efficient dynamic defect annihilation occurring at liquid nitrogen temperature during ion implantation. When disorder does accumulate at doses around 10^{16} cm^{-2} of 90 keV Si ions, the surface appears to be a strong sink for damage build up and possibly the nucleation of amorphous layers. Once ion disorder has been produced in GaN, it is extremely difficult to remove by annealing. GaN exhibits disordering and annealing behaviour which is somewhat similar to that in high Al-content AlGaAs.

INTRODUCTION

III-V nitrides and GaN in particular are generating considerable interest for sources of blue-green light, high temperature electronics and as passivating films [1-7]. Successful doping of selected areas of such layers by ion implantation (particularly for p-type doping) would be potentially advantageous for device fabrication [8] but the removal of implantation damage must be achieved. Indeed, there have been no studies to date on ion damage production and its removal in GaN. In this paper, we report on Si ion damage production (and preliminary annealing) in high quality epitaxial GaN films on sapphire and compare the results with ion damage in AlGaAs layers of various Al contents [9].

EXPERIMENTAL

Layers of high quality GaN were grown epitaxially on sapphire by MOCVD at Emcore Corp. Ion channeling was used to assess the crystalline perfection of the layers. In all cases the minimum yield (χ_{\min}) was measured to be $\leq 4\%$ for GaN films of the order of or greater than $1 \mu\text{m}$ in thickness. This is close to what would be expected from perfect epitaxial GaN films [10] and confirms the very high quality of the epitaxial layers.

These layers were implanted with 90 keV Si ions to various doses in the range $4 \times 10^{13} \text{ cm}^{-2}$ to $2.4 \times 10^{16} \text{ cm}^{-2}$ at liquid nitrogen (LN) temperature. Similar implants were carried out into AlGaAs of various Al compositions [9] for comparison. Ion channeling, using 2 MeV He^+ ions, was used to monitor the ion damage build up in these samples with increasing ion dose. Annealing was carried out in flowing Ar in a tube furnace for 10 mins at 800°C to study the removal of disorder in such cases. Cross sectional transmission electron microscopy (XTEM) was used to study the microstructure of selected samples but details of such results will be given elsewhere.

RESULTS AND DISCUSSION

Fig.1 shows ion channeling spectra (at glancing angle geometry to improve near-surface depth resolution) illustrating the build up of damage in GaN as a function of 90 keV Si ion dose at LN temperature. Note that the unimplanted spectrum indicates a very high quality single crystal GaN layer with a χ_{\min} of $\sim 3.5\%$. The implantation results indicate that the GaN is

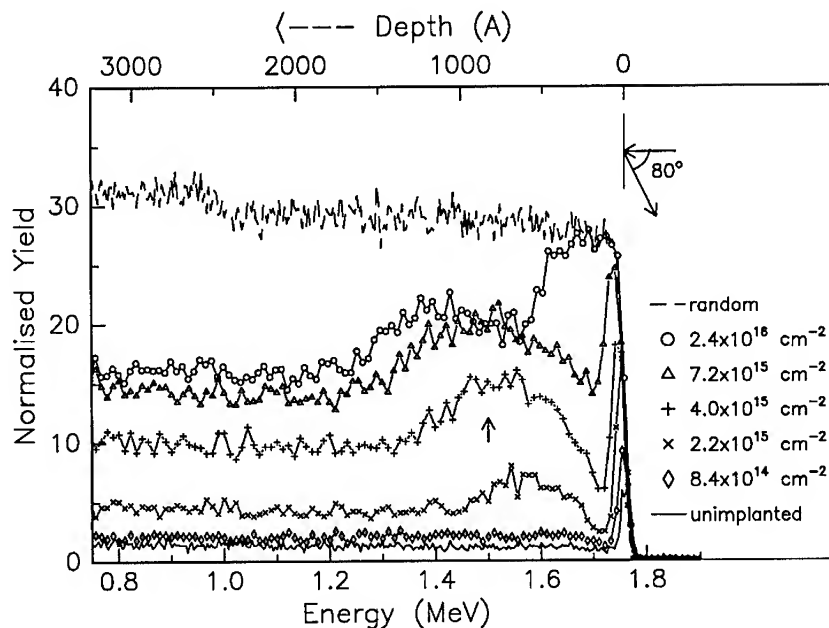


Fig.1 2MeV He⁺ ion channeling spectra illustrating the build up of 90 keV Si disorder (LN temperature) in epitaxial GaN on sapphire.

remarkably resistant to ion damage even at LN temperatures. A dose of $8.4 \times 10^{14} \text{ cm}^{-2}$ produces less than a twofold increase in both χ_{\min} and the surface peak area, whereas an order of magnitude lower dose into GaAs [9] would have produced a continuous amorphous layer extending to a depth of about 1200 Å. This suggests that dynamic annealing involving annihilation of implant-induced defects is extremely efficient. Indeed, by a dose of $7.2 \times 10^{15} \text{ cm}^{-2}$, the ion channeling spectrum still has not reached the random level (complete disordering) even though every lattice atom at the peak of the damage distribution ($\sim 900 \text{ Å}$) has been displaced more than 100 times. It is interesting that the damage (when it does accumulate) builds up both at the ion range (arrowed) and at the surface. By a dose of $7.2 \times 10^{15} \text{ cm}^{-2}$ there is little evidence for amorphous material as obtained from TEM. However, when the surface peak reaches the random level the damage extends back into the bulk from the surface at higher doses (e.g. $2.4 \times 10^{16} \text{ cm}^{-2}$). The surface appears to be a strong sink for defects and the results suggest that the surface may eventually be a nucleation site for growth of the amorphous phase, although this has not been confirmed as yet by TEM.

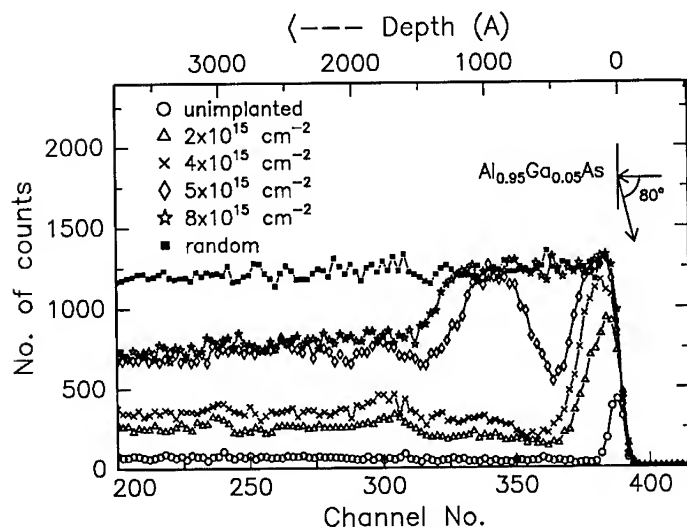


Fig.2 2 MeV He⁺ ion channeling spectra illustrating the build up of 90 keV Si disorder (LN temperature) in Al_{0.95}Ga_{0.05}As on GaAs. Note that a GaAs cap layer of $\leq 100\text{\AA}$ is present on the sample.

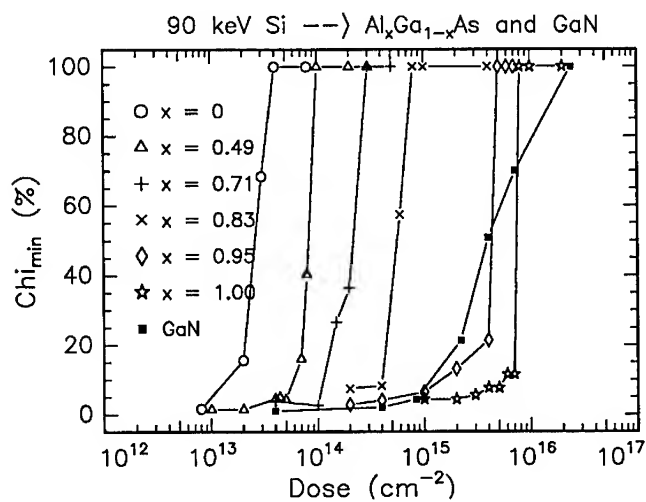


Fig.3 Disorder (χ_{\min}) from ion channeling as a function of Si dose (90 keV, LN) for AlGaAs of various composition compared with GaN.

The strong dynamic annealing in GaN and the extreme difficulty in producing an amorphous phase by ion bombardment of this material are features somewhat similar to AlGaAs material of high Al content. We illustrate this comparison in Figs.2 and 3. Fig.2 shows channeling spectra illustrating damage build up (90 keV Si ions) at LN temperature in $\text{Al}_{0.95}\text{Ga}_{0.05}\text{As}$. In this latter material a dose of $5 \times 10^{15} \text{ cm}^{-2}$ is required [9] to generate a buried amorphous layer (centred around 1000 Å). Note that a strong surface peak also results in this case but it is attributed to a GaAs cap layer of $\leq 100 \text{ Å}$ thickness which was necessary to stop the AlGaAs layer from oxidation. In comparison with AlGaAs, GaN appears to be even more difficult to amorphise. This is further illustrated in Fig.3 where the χ_{min} (from ion channeling) is plotted as a function dose for AlGaAs layers of different composition and also for GaN. In high Al-content AlGaAs it has been shown previously [9,11] that amorphization is preferentially nucleated at high doses on either crystalline defects (dense loop concentrations) close to the Si ion end of range or at surfaces and interfaces. In GaN, the surface appears to be the preferred site for the accumulation of gross damage (amorphization).

In Fig.4 we illustrate typical annealing results by a set of ion channeling spectra. Annealing at 800 °C for 10 min only results in a small change in the damage level as measured by channeling. Again, this result is very similar to AlGaAs where crystalline defects (loops, etc.) are extremely difficult to remove by annealing [9] and also amorphous layers are found to crystallize into very defective layers containing a high density of twins, low angle boundaries and other defects. Preliminary TEM on our GaN layers indicates similarly defective material after annealing. Thus, it is clearly desirable to select implantation conditions (low doses and presumably elevated temperatures) for GaN to limit implantation damage so that the complications of poor annealing behaviour are minimised.

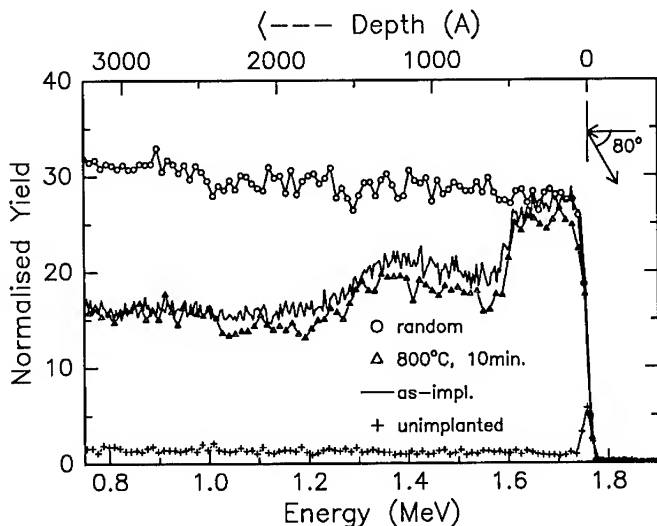


Fig.4 2 MeV He^+ ion channeling spectra illustrating the annealing behaviour (800 °C, 10 min) for a $2.4 \times 10^{16} \text{ cm}^{-2}$ Si implant of GaN at LN.

In summary, we have shown that GaN is remarkably resistant to implantation damage even at LN temperature. The surface appears to be a favourable sink for defect accumulation at high implantation doses and may be a nucleation site for the amorphous phase. When ion disorder forms in GaN, it is extremely difficult to remove by an annealing step.

REFERENCES

1. I. Akasaki, M. Amano, M. Kito and K. Hiramatsu, *J. Lumin.* **48/49**, 666 (1991).
2. R.F. Davis, *Proc. IEEE* **79**, 702 (1991).
3. S. Nakamura, N. Iwasa, M. Sendi and T. Mukai, *Jpn. J. Appl. Phys.* **31**, 1258 (1992).
4. M.E. Lin, B. Sverdlov, S. Strite, H. Morkoc and A.E. Drakin, *Electron. Lett.* **29**, 1759 (1993).
5. T. Matsulka, T. Susaki and A. Katsui, *Optoelectron. Device Technol.* **5**, 53 (1990).
6. E.R. Glaser, T.A. Kennedy, H. Crookham, J.A. Freitas, M.A. Khan, D. T. Olsen and J.N. Kuznia, *Appl. Phys. Lett.* **63**, 2673 (1993).
7. S.J. Pearton, C.R. Abernathy, P. Wisk, W.S. Hobson and F. Ren, *Appl. Phys. Lett.* **63**, 1143 (1993).
8. R.G. Wilson, S.J. Pearton, C.R. Abernathy and J.M. Zavada, *Appl. Phys. Lett.* **66**, 2240 (1995).
9. H.H. Tan, C. Jagadish, J.S. Williams, J. Zou, D.J.H. Cockayne and A. Sikorski, *J. Appl. Phys.* **77**, 87 (1995).
10. *Ion Beams for Materials Analysis*, edited by J.R. Bird and J.S. Williams (Academic, Sydney, 1989) Chap.6.
11. H.H. Tan, C. Jagadish, J.S. Williams, J. Zou and D.J.H. Cockayne, *J. Appl. Phys.* (in press).

ANNEALING STUDY OF ION IMPLANTED MOCVD AND MBE GROWN GaN

E. SILKOWSKI*, Y. K. YEO*, R. L. HENGHOLD*, M. A. KHAN**, T. LEI***,
K. EVANS***, and C. CERNY***

*Air Force Institute of Technology, Wright-Patterson AFB, OH 45433

**APA Optics, Blaine, MN 55449

***Wright Laboratory, Wright-Patterson AFB, OH 45433

ABSTRACT

MOCVD and MBE grown GaN were implanted with Ar, Mg, Si, Be, C, and O, and annealed in a conventional oven under flowing NH_3 or N_2 gas. Absorption measurements confirmed that implantation damage was annealed out after 90 minutes at a temperature of 1000 °C. Surface damage caused by NH_3 annealing was evident in absorption and photoluminescence measurements for annealing temperatures of over 1000 °C. Although most of the implants showed no unique luminescence peaks, systematic changes in the relative intensities of the exciton, donor-acceptor pair, and yellow peaks were noted. The Mg implanted samples showed evidence of the acceptor bound exciton line at 3.44 eV, and a unique peak at 3.3 eV possibly due to a Mg free-to-bound transition.

INTRODUCTION

Several luminescence studies of ion implanted GaN have appeared in the literature [1-3]. Pankove and Hutchby [1] observed unique luminescence peaks associated with Mg at 3.2 eV, As at 2.58 eV, and Be at 2.16 eV, and these peaks were quite broad in nature. Metcalfe, Wickenden, and Clark [2] found a similar broad peak at 2.58 eV after As implantation. Chung and Gershenzon [3] identified an oxygen related peak at 3.424 eV. In all of these studies, the annealing conditions were not reported in detail, nor were variations in annealing conditions reported. Furthermore, high peak dopant concentrations above $5 \times 10^{19} \text{ cm}^{-3}$ [3] or shallow implanted depths of a few hundred Å were used [1,2]. The present study addressed a wide variety of annealing conditions including annealing method, annealing temperature, and annealing gas environment for samples implanted with peak concentrations of $\sim 10^{18}$ to $3 \times 10^{19} \text{ cm}^{-3}$ and peak ranges of $>2000 \text{ Å}$, so the implanted peak would be well below the surface.

EXPERIMENT

GaN was grown on sapphire by low-pressure MOCVD [4] or gas-source MBE [5]. Samples were implanted with the parameters given in Table I. Annealing was performed in a conventional tube furnace at temperatures ranging from 600 to 1100 °C under an atmosphere of flowing NH_3 or N_2 . Several unimplanted samples were annealed under conditions identical to the conditions used for the implanted samples in order to observe any effects purely due to annealing of the undoped GaN. Rapid thermal annealing (RTA) was also performed under vacuum at temperatures about 1000 °C for 90 sec.

Photoluminescence (PL) was performed at 2 K using a frequency-doubled argon ion laser operating at 257.2 nm, 3/4-meter spectrometer, and C31034 PMT tube. Room temperature absorption measurements were carried out using a Perkin-Elmer Lambda 19 UV/VIS spectrophotometer.

Table I. Implanted ion species including the implantation energy and dose. The peak range and peak concentration were calculated using the PROFILE Code [6].

Species	Energy (keV)	Dose (cm ⁻²)	Range (Å)	Peak Conc. (cm ⁻³)
Ar	390	5×10 ¹⁴	2211	2.6×10 ¹⁹
Mg	300	2.2×10 ¹⁴ , 8.2×10 ¹⁴	3035	7.4×10 ¹⁸ , 2.7×10 ¹⁹
Si	390	5×10 ¹⁴	3339	1.6×10 ¹⁹
Be	200	5×10 ¹³	4270	1.5×10 ¹⁸
C	390	1×10 ¹⁴	4990	3.1×10 ¹⁸
O	390	1×10 ¹⁴	4203	3.3×10 ¹⁸

RESULTS AND DISCUSSION

Low temperature PL of unimplanted GaN annealed in NH₃ and N₂ revealed significant changes in luminescence due to annealing. The NH₃ annealed samples showed a distinct increase in donor-acceptor pair (D-A) emissions as annealing temperature was increased as shown in Figure 1. However, all of the annealed samples showed a factor of 2 to 3 drop in exciton intensity compared to their unannealed counterparts. The yellow peak intensity also dropped by a factor of 2 for the highest anneal temperatures. Samples annealed in N₂ at the same temperature and for the same annealing time show only a decrease in overall luminescence by a factor of about 2. No increase in the D-A peak intensity was found for N₂ annealing. Absorption measurements of the bandedge show almost no change in slope with annealing for 90 minutes at temperatures ranging from 600 to 1050 °C.

Argon is an inert element, and was therefore implanted into GaN to study the damage created by implantation and its subsequent annealing. In contrast to earlier reports [1,2], the Ar implanted samples did not show any unique PL peaks. In all Ar implanted and annealed samples, the D-A band dominated the spectrum. The PL peaks in the NH₃ annealed sample were better resolved than the N₂ case. However, the absorption edge showed identical damage recovery for both N₂ and NH₃ annealing. Near the bandedge, the absorption data revealed an exponential tail of states. The length of which could be characterized by an energy E₀, which is given by

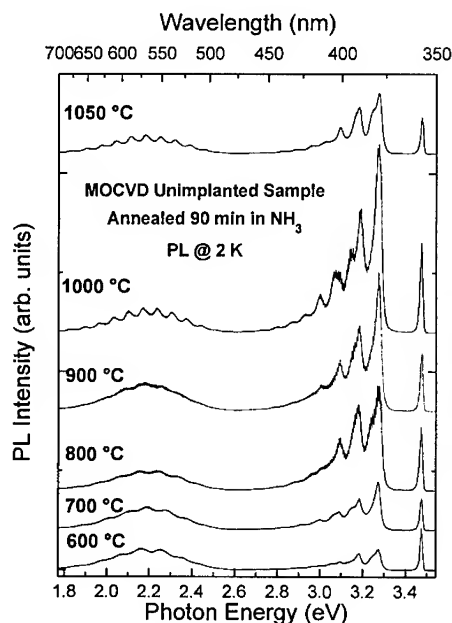


Figure 1. Photoluminescence of as-grown, MOCVD GaN samples annealed in NH₃ for 90 min at temperatures of 600 to 1050 °C.

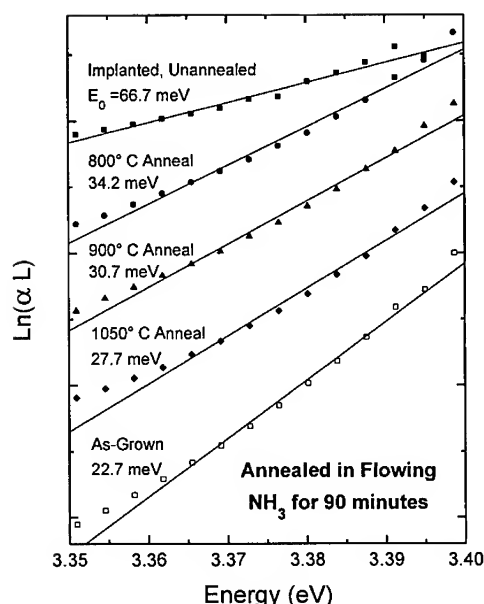


Figure 2. Recovery of the room temperature absorption edge of Ar-implanted MOCVD grown GaN with increasing annealing temperature.

implantation, but after implantation a strong shoulder appeared. The shoulder appeared at 3.44 eV, which was approximately the energetic location expected for the Mg acceptor-bound exciton [8]. Also, a new peak appeared just above the energetic location of the D-A band as shown in Figure 3. This peak was found at 3.30 eV making it too deep to be an LO phonon replica of either exciton peak. The energetic location and the presence of the Mg acceptor-bound exciton line suggests the origin of this peak as a Mg-related free-to-bound transition or a closer pair dominant D-A transition.

MBE grown GaN was also implanted with Mg and annealed in N_2 at temperatures of 700, 800, and 900 °C. A peak at 3.43 eV was observed for these samples as well as blue emissions peaking near 2.8 eV as shown in Figure 4. Prior to implantation, this sample had low temperature cathodoluminescence peaks at 3.448 eV and 3.402 eV. However, implantation induced broadening could have resulted in the overlap of the original two peaks into one structure at 3.43 eV.

The other implanted species resulted in no unique PL peaks, and only shifts in the relative intensities of the exciton, D-A, or yellow bands as shown in Figure 5. Some general observations can be made however. Silicon implanted GaN always showed strong D-A emissions with the exciton and yellow bands usually being quenched. This result is similar to the PL reported for GaN:Si grown by MOCVD [9]. Carbon implants always resulted in a strong yellow band; however, some oxygen implants also gave the same result. This result is not inconsistent with the results suggesting that carbon is linked to the yellow band [10]. The oxygen implanted samples did not show a peak at 3.424 eV as observed by Chung and

$1/E_0 = d(\ln\alpha)/d(h\nu)$ [7]. Here α is the absorption coefficient, and $h\nu$ is the incident photon energy. The room temperature absorption edge of the Ar-implanted MOCVD GaN is shown in Figure 2. The longest tail was observed in the as-implanted material, and a steady decrease in E_0 was observed as annealing temperature was increased. The 1050 °C anneal showed significantly increased absorption at longer wavelengths compared to lower anneal temperatures. Identically prepared samples annealed in N_2 gave values of $E_0 = 34.7$ meV for the 800 °C anneal and 29.4 meV for the 1000 °C anneal which compare very closely with the values for the NH_3 anneals.

Magnesium implanted samples either showed strong D-A peaks at 3.27 eV with several 90 meV LO phonon replicas or a set of peaks near the bandedge. The sample annealed in NH_3 at 1000 °C for 90 minutes exhibited the donor-bound exciton at ~3.47 eV as was observed in the GaN prior to

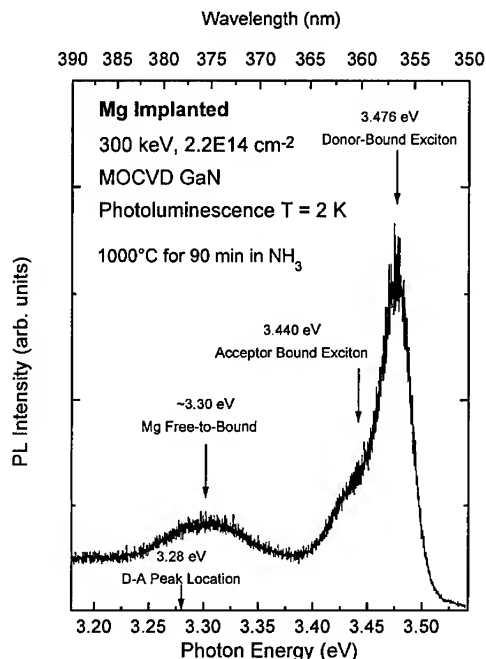


Figure 3. Photoluminescence of Mg-implanted MOCVD grown GaN annealed at 1000 °C for 90 min in NH_3 .

absorption edge. This demonstrates that recrystallization of the heavy lattice damage due to implantation is recovered substantially at annealing temperatures of 800 °C, and almost fully at 1000 °C. The fact that NH_3 annealing results in a substantial increase in D-A emissions and N_2 annealing does not can be related to the surface decomposition of GaN at elevated temperatures. Especially at an anneal temperature of 1050 °C, serious surface degradation becomes evident in the NH_3 anneals but not in the N_2 anneals. The likely mechanism of decomposition is $\text{GaN} \rightarrow \text{Ga} + \frac{1}{2}\text{N}_2$, which proceeds more quickly in an NH_3 atmosphere. The D-A emissions are therefore related to the formation of N vacancies, V_N , near the GaN surface.

The D-A peak was also present in the photoluminescence of many NH_3 annealed, implanted samples. The luminescence intensity of other peaks observed from the implanted and annealed samples was always of lower intensity than the corresponding peaks before implantation. Furthermore, N_2 annealed samples always resulted in a drop in luminescence intensity. From this, it can be concluded that implantation damage and the effects of annealing certainly result in an increase in non-radiative recombination. This problem must be addressed before fabricating optoelectronic devices reliably using the ion implantation technique.

Implantation did not result in any unique, deep PL peaks as reported by other researchers [1,2], nor were any unique implantation related peaks observed after high temperature annealing. Since redistribution of implanted ions is not considered significant during annealing [11], it is likely that the implanted doses are below the threshold for observation of such deep level luminescence bands. It is also possible that surface effects may have been necessary for the formation of such deep bands, which would not be evident here due to the depth of the implants.

Gershenzon [3]. However, the oxygen peak concentration necessary to observe this peak was $\sim 10^{20} \text{ cm}^{-3}$, which was well above the concentration used in this study. Samples implanted with beryllium and annealed in either NH_3 or N_2 showed nearly complete recovery of the original PL spectrum as anneal temperature was increased. Furthermore, an Arrhenius plot of the natural log of the exciton peak intensity against $1/kT_\text{A}$, where T_A is the anneal temperature, results in an activation energy of 880 meV. The yellow peak did not show significant enhancement in contrast to a previous report on Be implanted GaN [1].

After RTA at a temperature of about 1000 °C, the samples still showed discoloration due to implantation. Also, annealing did not show complete recovery of the absorption bandedge, and no photoluminescence could be detected. Therefore, temperatures higher than 1000 °C must be required for RTA.

Both NH_3 and N_2 annealing showed nearly identical recovery of the GaN

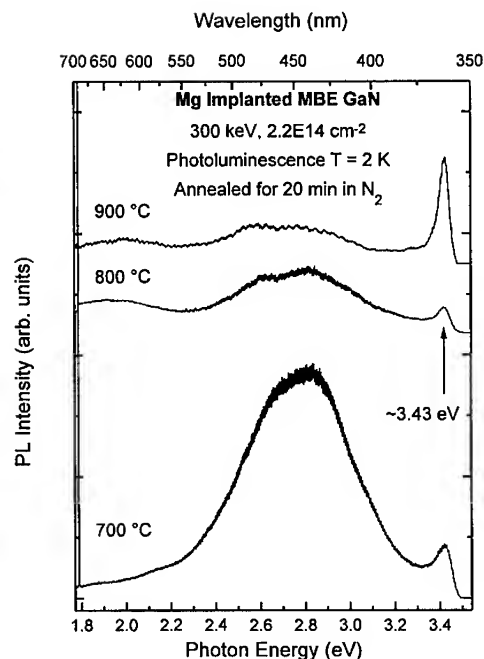


Figure 4. Photoluminescence of Mg implanted MBE grown GaN annealed at 700 to 900 °C for 90 min in N₂.

CONCLUSIONS

At a given annealing temperature and time duration, both N₂ and NH₃ annealing resulted in similar recovery of the sharp GaN absorption edge. An anneal temperature of 1000 °C for 90 min was found sufficient for a nearly full recovery. However, visible surface degradation was observed with NH₃ annealing at temperatures over 1000 °C, whereas N₂ annealing showed almost no surface degradation. Furthermore, low temperature PL showed a substantial increase in D-A luminescence with increasing annealing temperature in NH₃ anneals but not in N₂ anneals. The D-A has been attributed to V_N which are formed when GaN decomposes. RTA at similar temperatures for 90 sec was insufficient to anneal out implantation damage.

Since annealing resulted in a recovery of the absorption edge and a measurable PL signal, the levels formed by the implanted ions must be either non-radiative or be related to the centers responsible for the D-A and yellow peaks found in as-grown material. The only exception was Mg implantation, which showed two unique PL peaks. These peaks only appeared in the 1000 °C anneal, whereas the 900 °C anneal showed significant D-A emissions. Just the opposite would have been expected if these peaks were due to annealing in NH₃, since NH₃ annealing has been shown to increase the D-A band. Further work is necessary to more closely examine the activation taking place from the 900 to 1000 °C anneals.

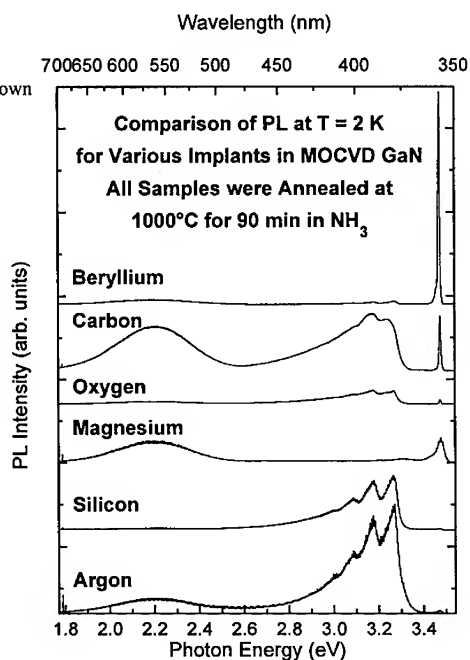


Figure 5. Photoluminescence of Be, C, O, Mg, Si, and Ar-implanted MOCVD grown GaN.

Of the several species implanted, only Mg resulted in unique PL peaks. The Mg acceptor bound exciton line near 3.440 eV was observed as well as a previously unreported line at 3.43 eV, which may be a free-to-bound transition to a Mg level lying about 200 meV above the valence band or a closer pair dominant D-A transition. The other implants may be associated with PL peaks already present in the as-grown material such as the D-A and yellow bands.

ACKNOWLEDGMENTS

This work was partially supported by AFOSR. Author Ting Lei was supported by the National Research Council. The authors would like to thank John Hoelscher who performed some of the implantations.

REFERENCES

1. J. I. Pankove and J. A. Hutchby, *J. Appl. Phys.* **47**, 5387 (1976).
2. R. D. Metcalfe, D. Wickenden, and W. C. Clark, *J. Lum.* **16**, 405 (1978).
3. B-C. Chung and M. Gershenson, *J. Appl. Phys.* **72**, 651 (1992).
4. M. A. Khan, J. N. Kuznia, J. M. Van Hove, D. T. Olson, S. Krishnakutty, and R. M. Kolbas, *Appl. Phys. Lett.* **58**, 526 (1991).
5. T. Lei, C. Jones, K. Evans, E. Silkowski, Y. K. Yeo, R. L. Hengehold, presented at the 1995 MRS Spring Meeting, San Francisco, CA, 1995 (unpublished).
6. PROFILE Code Version 2.1, Implant Sciences Corp, Danvers, MA 1988.
7. J. I. Pankove, *Phys. Rev.* **140**, A2059 (1965).
8. M. Ilegems and R. Dingle, *J. Appl. Phys.* **44**, 4234 (1973).
9. S. Nakamura, T. Mukai, and M. Senoh, *Jpn. J. Appl. Phys.* **31**, 2883 (1992).
10. T. Ogino and M. Aoki, *Jpn. J. Appl. Phys.* **19**, 2395 (1980).
11. R. G. Wilson, S. J. Pearton, C. R. Abernathy, and J. M. Zavada, *Appl. Phys. Lett.* **66**, 2238 (1995).

INTERFACIAL REACTIONS BETWEEN METAL THIN FILMS AND p-GaN

J.T. TREXLER*, S.J. MILLER*, P.H. HOLLOWAY*, M.A. KHAN**

*Department of Materials Science and Engineering, University of Florida, Gainesville, FL 32611-6400, **APA Optics Inc., 2950 NE 84th Lane, Blaine, MN 55449.

ABSTRACT

The reactions between Au, Au/Ni and Au/C/Ni thin films on p-GaN have been studied using current-voltage (I-V) measurements, Auger electron spectroscopy (AES) and secondary ion mass spectrometry (SIMS). The metallization schemes consisted of $\approx 2000\text{\AA}$ sputtered Au, 1000\AA Au/ 500\AA Ni, and 1000\AA Au/ 100\AA C/ 500\AA Ni electron beam evaporated. The Au/Ni metallization scheme is of particular interest since it is the basis for the most commonly used ohmic p-type contacts for blue GaN LED's. Au does not decompose the GaN matrix, while Ni has been shown to react with GaN above a temperature of 400°C for times longer than 5 minutes. Upon decomposition of the GaN by Ni, incorporation of C at the metal/GaN interface occurred. It is believed that a regrowth of GaN occurred, with the surface region being doped with C. Attempts at increasing this doping concentration by introducing an interfacial C layer were not successful.

INTRODUCTION

The group III-nitrides, in particular GaN, are promising materials for semiconductor device applications in the blue and ultra-violet (UV) wavelength region, particularly in the field of optical emission and data storage. GaN tends to auto-dope n-type with the native defect believed to be nitrogen vacancies.^{1,3} This tendency to intrinsically dope n-type has presented difficulties in the generation of p-type conductivity in the material. This obstacle has been overcome through the use of a high temperature anneal in N_2 following the growth of the GaN,^{4,5} or a low-energy electron beam irradiation (LEEBI) treatment.⁵⁻⁷ With the ability to reproducibly grow both n- and p-type GaN, LED's have been demonstrated by various groups.^{7,8} For n-type material, low resistance contacts have been reported using Ti/Al,⁹ while the problem of producing a low resistance contact to p-type material still exists.

For the formation of low resistance ohmic contacts the dominant carrier transport mechanism should be tunneling through the potential barrier present at the metal/semiconductor interface. The tunneling probability can be increased by lowering the potential barrier through the use of a high work function metal, and/or by increasing the carrier concentration in the semiconductor. The Fermi level in GaN is reported to be unpinned, so a low resistance ohmic contact should be possible by choosing a metal with a work function approximately equal to the sum of the semiconductor band gap and its electron affinity. GaN, with a band gap of $\approx 3.4\text{ eV}$ and an electron affinity of $\chi = 2.7\text{ eV}$, would require a metal with a work function of $\approx 6.1\text{ eV}$ for alignment of the energy levels. This is a problem because metal work functions are never much larger than 5 eV .¹⁰ Since selection of the proper work function is unlikely to lead to ohmic contacts to p-GaN, methods to increase the carrier concentration need to be investigated. By increasing the carrier concentration in the near-surface region of the semiconductor, the depletion width in the semiconductor would be decreased. With this decreased depletion width, the amount of carrier transport would be greater from a higher tunneling probability, resulting in low resistance ohmic contacts. Early research on contacts used thin films of Au,^{8,11,12} while the commercially available LED's reported by Nakamura *et al.*^{12,13} used a Au/Ni contact scheme.

However, there have been no reports in the literature of the conduction processes that occur in these Au/Ni contacts on p-GaN. This research has investigated the interfacial reactions that occur between the Au/Ni contact and p-GaN when a nearly ohmic contact was achieved.

EXPERIMENT

Contacts were deposited on MOCVD grown p-GaN doped with Mg with carrier concentrations of 5×10^{16} and $2 \times 10^{17} \text{ cm}^{-3}$. The GaN was cleaned with acetone, methanol, and de-ionized water for 5 minutes each before deposition. Three metallization schemes, Au, Au/Ni, and Au/C/Ni were investigated. In all cases, dot contacts (diameter=0.8 mm) were patterned during deposition using a stainless steel shadow mask. Pure Au contacts 2000Å thick were DC magnetron sputter deposited using a 2 inch diameter US Gun. The sputtering atmosphere was 25 mTorr argon with a power of 40 W. The 1000Å Au/500Å Ni and 1000Å Au/100Å C/500Å Ni contacts were both deposited using an Airco Temescal electron beam evaporator, with a base pressure of $\approx 6 \times 10^{-7}$ Torr for each element. All samples were heat treated at 200°C, 400°C, and 600°C in an Applied Test Systems conventional tube furnace under a flowing forming gas (90% N_2 , 10% H_2) ambient for 5, 15 and 30 minutes. Following each heat treatment, I-V data were measured over a range of -5V to +5V using a Tektronix 577 Curve Tracer with a 177 Standard Test Fixture. Compound formation and elemental concentrations at the surface and metal/p-GaN interface were evaluated using a Phi 660 Scanning Auger Microprobe and a Phi 6600 secondary ion mass spectrometer to perform surface analysis and depth profiles. The AES data was collected at an accelerating voltage of 5 keV with a beam diameter of $\sim 1 \mu\text{m}$, and the SIMS analysis used 3 and 5 keV Cs^+ beam with a current of 30 nA and a raster size of $300 \times 300 \mu\text{m}^2$.

RESULTS

The optimum heat treatment conditions and thermal stability of the different metallizations schemes were determined using I-V measurements between two front surface dot contacts, initially representing back-to-back reverse-biased rectifying contacts, as discussed below. Au with $\phi_m = 5.1 \text{ eV}$ was not expected to make an ohmic contact due to the large offset present. For the sputtered Au contacts, the I-V curves were rectifying as-deposited and remained rectifying upon all heat treatments (Figure 1). There was a reduced offset at 400°C for 5 minutes, but the offset increased again upon heat treating at 600°C for 5 minutes as shown in Figure 1. AES depth

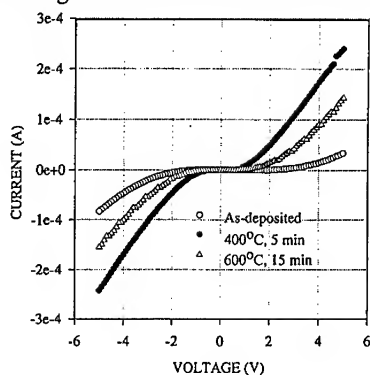


Fig. 1 I-V data for Au/p-GaN.

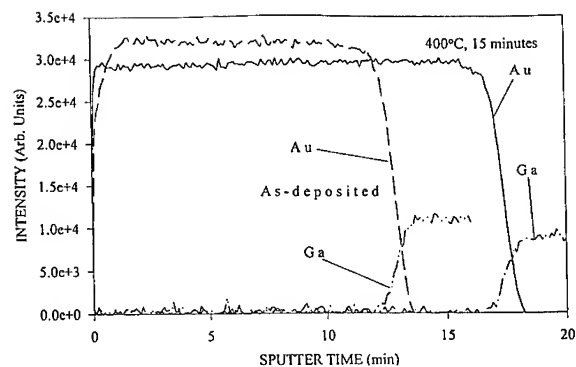


Fig. 2 AES plots for Au/p-GaN as-deposited and after 400°C, 5 min. heat treatment.

profiles were employed to determine if any interfacial reactions were occurring between the Au and GaN. In Figure 2, data from an as-deposited sample and one annealed at 400°C for 15 minutes are compared. It can be seen that Au does not decompose the GaN matrix in either case, since the slope of the Au signal at the Au/GaN interface did not change upon heat treatment.

Since a good ohmic contact was not obtained with Au, introduction of a metal that would interact with the GaN was investigated. A 500Å interfacial Ni layer was deposited onto the clean GaN surface for this purpose. Bermudez *et al.*¹⁴ have shown that Ni films on GaN will decompose the GaN film upon heat treatment. I-V results were again rectifying as-deposited and remained so at 200°C for up to 30 minutes (Figure 3). When the temperature was increased to 400°C for 5 minutes, the I-V curve became nearly linear with a slight offset. Once again, annealing to 600°C caused degradation of the contacts (Figure 3). AES and SIMS depth profiles of the heat treated sample were used to determine the cause of the changes in electrical behavior. In Figure 4 an AES depth profile is shown from the Au/Ni/p-GaN sample annealed at 600°C for

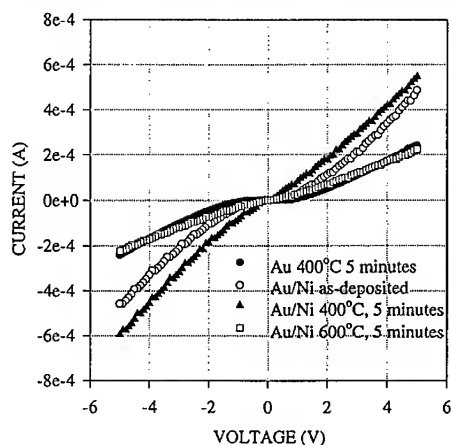


Fig. 3 I-V data for Au/Ni/p-GaN.

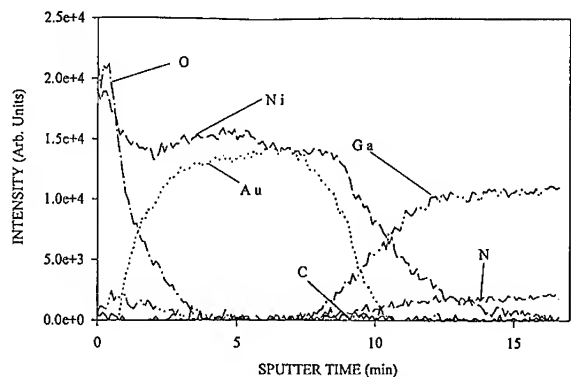


Fig. 4 AES of Au/Ni/p-GaN, heat treated 600°C, 15 min.

15 minutes. In this figure, it can be seen that Ni has diffused both towards the surface and also into the GaN. The Ni profile into the GaN and the increased Ga signal at the surface indicates that Ni caused dissociation of GaN and out-diffusion of Ga to the surface. Presumably N is incorporated into a Ni-N solid solution. Decomposition of the GaN surface leads to increased doping of the near surface region. Doping could result from formation of Ga vacancies acting as p-type dopant sites analogous to the well known nature of N vacancies to act as dopant sites.¹⁵ It is further believed that upon the formation of Ga vacancies, C located at the interface may be incorporated into the GaN where it has been shown to act as a p-type dopant.¹⁶ Along with the movement of the Ni layer into the GaN, Ni also is shown to diffuse through the Au film towards the surface of the contact. There is a strong driving force for the formation of a Au-Ni solid solution which we believe provides a driving force for regrowth of GaN from the Ga and N in solution in Ni. We postulate that this regrown GaN layer has been doped with C in the near-surface region, leading to a p^+ layer which will lower the depletion width. This will lead to a

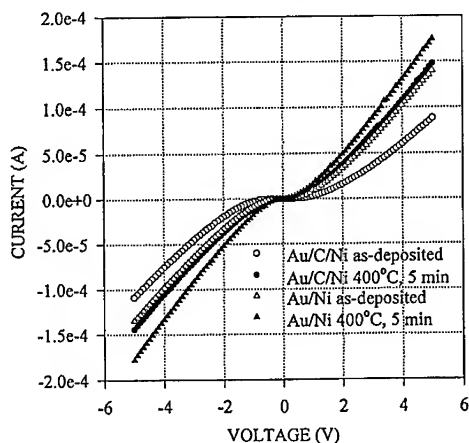


Fig. 5 I-V data for Au/C/Ni and Au/Ni on p-GaN.

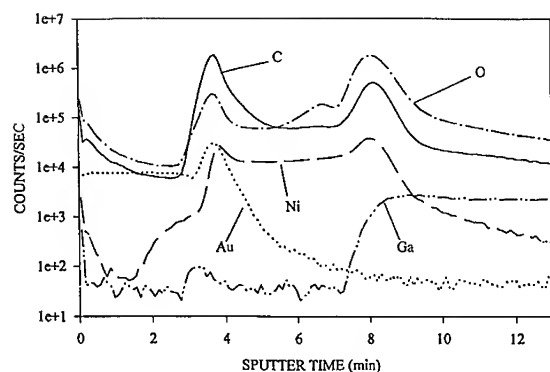


Fig. 6A SIMS for Au/C/Ni/p-GaN as-deposited.

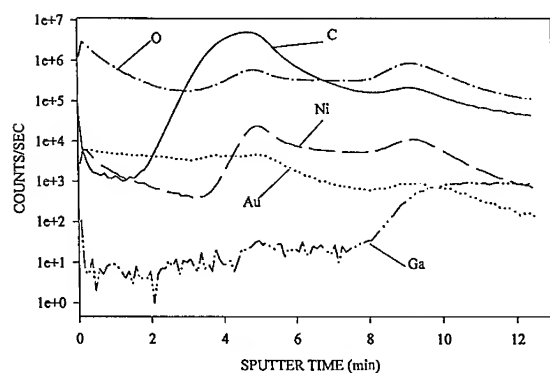


Fig. 6B SIMS for Au/C/Ni/p-GaN heat treated at 400°C, 15 min.

higher probability of tunneling, reducing the resistance of the contacts. Evidence of C at the metal/GaN interface has also been detected using SIMS.

Since the improved ohmic character of the contacts is postulated to result from C doping from adventitious contamination, we attempted to incorporate an even higher concentration of C at this interface through deposition of a 100Å C layer between the Ni and Au. I-V data showed the as-deposited contacts were rectifying, and the rectifying nature remained even upon heat treatments to 400°C for 30 minutes. The offset voltage was reduced by heat treatment, but it remained larger than for Au-Ni contacts. Figure 5 shows I-V data from Au/C/Ni and Au/Ni contacts on samples from the same GaN wafer. The electrical behavior of the Au/C/Ni contacts is more rectifying than for Au/Ni. SIMS results (Figure 6A) showed abrupt interfaces between all layers for as-deposited samples, with an increased C signal at the metal/GaN interface. Upon heating to 400°C for 30 minutes (Figure 6B) the interfaces broadened. As in the Au/Ni contacts,

there is an increased C signal at the metal/GaN interface and evidence of Ni diffusion throughout the Au contact to form the Au-Ni solid solution and force regrowth of GaN. Ni also diffused into the p-GaN. However, since the I-V characteristics are less favorable than for Au/Ni contacts, additional C at the Au/Ni interface does not improve the contact. The increased carbon concentration may lead to carbon complexes or amphoteric behavior in GaN, which would lower the carrier concentration of the near-surface region. Formation of carbon complexes may also be increased due to the use of graphitic carbon as the deposition source. A possible solution to this problem is the use of a thinner C layer. However, more research needs to be done to precisely determine the role of C in the ohmic contact mechanism to p-GaN.

CONCLUSIONS

Interfacial reactions between Au, Au/Ni, and Au/C/Ni thin films and p-GaN have been investigated for as-deposited samples and following various heat treatments at $T \leq 600^\circ\text{C}$. Au has been shown to result in a rectifying contact for both as-deposited and heat treated samples, with no diffusion into the GaN matrix. The addition of a 500\AA Ni metallization between the Au and p-GaN led to nearly linear I-V curves after heat treating at 400°C for 5 minutes. This Ni layer decomposed the GaN which provided the opportunity for doping of the surface region of the GaN. It was postulated that C doped the GaN which increased tunneling transport. A regrowth of GaN doped with C was postulated to be driven by formation of a Au-Ni solid solution. Attempts at lower contact resistance with a 100\AA layer of C between the Au and Ni were unsuccessful, possibly due to the formation of carbon complexes.

ACKNOWLEDGEMENT

The authors would like to thank Eric Lambers for help with the AES and Maggie Puga-Lambers for help with the SIMS. This work was supported by ONR/ARPA Grant N00014-92-J-1895.

REFERENCES

- ¹ H.P. Maruska and J.J. Tietjen, *Appl. Phys. Lett.* **15**, 327 (1969).
- ² J. Pankove, *J. of Lumin.* **7**, 114 (1973).
- ³ D.W. Jenkins and J.D. Dow, *Phys. Rev. B* **39**, 3317, (1989).
- ⁴ S. Nakamura, T. Mukai, M. Senoh, and N. Iwasa, *Jpn. J. Appl. Phys.* **31**, L139 (1992).
- ⁵ S. Nakamura, N. Iwasa, M. Senoh, and T. Mukai, *Jpn. J. Appl. Phys.* **31**, 1258 (1992).
- ⁶ M. Inamori, H. Sakai, T. Tanaka, H. Amano, I. Akasaki, *Jpn. J. Appl. Phys.* **34**, 1190 (1995).
- ⁷ H. Amano, M. Kito, K. Hiramatsu, and I. Akasaki, *Jpn. J. Appl. Phys.* **28**, L2112 (1989).
- ⁸ S. Nakamura, T. Mukai, and M. Senoh, *Jpn. J. Appl. Phys.* **30**, L1998 (1991).
- ⁹ M.E. Lin, Z. Ma, F.Y. Huang and H. Morkoc, *Appl. Phys. Lett.* **64**, 2557 (1994).
- ¹⁰ S.M. Sze, *Physics of Semiconductor Devices*, 2nd ed. (John Wiley + Sons Inc. Publishers, New York, 1981) p. 251.
- ¹¹ S. Nakamura, M. Senoh, and T. Mukai, *Jpn. J. Appl. Phys.* **32**, L8 (1993).
- ¹² S. Nakamura, M. Senoh, and T. Mukai, *Appl. Phys. Lett.* **62**, 2390 (1993).
- ¹³ S. Nakamura, T. Mukai, M. Senoh, *Appl. Phys. Lett.* **64**, 2557 (1994).
- ¹⁴ V. M. Bermudez, R. Kaplan, M.A. Khan, and J.N. Kuznia, *Phys. Rev. B.* **48**, 2436 (1993).
- ¹⁵ M.E. Lin, Z. Ma, F.Y. Huang, Z.F. Fan, L.H. Allen, and H. Morkoc, *Appl. Phys. Lett.* **64**, 8 (1994).
- ¹⁶ C.R. Abernathy, J.D. MacKenzie, S.J. Pearton W.S. Hobson, *Appl. Phys. Lett.* **66**, 1969 (1995).

THERMAL STABILITY OF OHMIC CONTACTS TO $n\text{-In}_x\text{Ga}_{1-x}\text{N}$

A. Durbha⁽¹⁾, S. J. Pearton⁽¹⁾, C. R. Abernathy⁽¹⁾, J. W. Lee⁽¹⁾
P. H. Holloway⁽¹⁾ and F. Ren⁽²⁾

⁽¹⁾University of Florida, Gainesville FL 32611

⁽²⁾AT&T Bell Laboratories, Murray Hill NJ 07974

ABSTRACT

The microstructural properties and interdiffusion reactions of Au/Ge/Ni, Ti/Pt/Au, WSi_x and AuBe contacts on GaN and $\text{In}_{0.5}\text{Ga}_{0.5}\text{N}$ have been examined using Scanning Electron Microscopy and Auger Electron Spectroscopy. The WSi_x contacts possess excellent thermal stability and retained good structural properties at annealing temperatures as high as 800°C on GaN. The electrical characteristics of WSi_x contacts on $\text{In}_{0.5}\text{Ga}_{0.5}\text{N}$ had a specific contact resistivity of $1.48 \times 10^{-5} \Omega\text{cm}^2$ and an excellent surface morphology following annealing at 700°C. The increase in contact resistance observed at higher temperatures was attributed to intermixing of metal and semiconductor. In contrast the Ti/Pt/Au and Au/Ge/Ni contacts were stable only to $\leq 500^\circ\text{C}$. AuBe contacts had the poorest thermal stability, with substantial reaction with GaN occurring even at 400°C. The WSi_x contact appears to be an excellent choice for high temperature GaN electronics applications.

INTRODUCTION

Owing to their large band gaps and high dielectric constants, III-V nitrides are very attractive for high temperature electronics and blue and UV optoelectronic device applications. Improved material properties have recently led to a variety of devices being demonstrated.⁽¹⁾ Blue light-emitting devices (LED's)^(2,3) and metal-semiconductor field-effect transistors (MESFET's) have been successfully fabricated.⁽⁴⁾ However, forming low resistance, thermally stable and uniform ohmic contacts to a wide band gap semiconductor, such as GaN with a band gap about 3.4 eV, constitutes a major obstacle to the furtherment of nitride based devices. All these devices provide high efficiency and high reliability only if their contacts are stable and have low resistance ohmic characteristics.

In an earlier attempt to achieve ohmic contacts on GaN epilayers, Foresi et al.⁽⁵⁾ used Al and Au contacts with 575°C anneal cycle. However, the specific contact resistivity of these contacts was relatively poor ($10^{-3} \Omega\text{cm}^2$). Khan et al.⁽³⁾ used Ti/Au to contact n-type GaN and measured a contact resistance of $7.8 \times 10^{-4} \Omega\text{cm}^2$ after annealing at 250°C for 30s. Nakamura et al.⁽²⁾ have used Au (and later Au/Ni and Al) as p and n-type contacts respectively in their LED structures. While the contact resistances were not reported in their LED structures, an operating voltage of 4V and 20mA forward bias is clear evidence that reasonable contact resistances were obtained. Recently Lin et al.⁽⁶⁾ have obtained extremely good ohmic contacts on n-type GaN layers grown on sapphire substrates. Using Ti/Al metallization scheme they were able to obtain specific contact resistivities as low as $8 \times 10^{-6} \Omega\text{cm}^2$ after annealing at 900°C for 30s. Lin et al.⁽⁷⁾ also demonstrated a novel ohmic contact scheme to GaN using an InN/GaN short-period superlattice (SPS) and an InN cap layer. Ohmic contact resistivities as low as $6 \times 10^{-5} \Omega\text{cm}^2$ were achieved even without any post-annealing.

An ohmic contact study of four standard metallization schemes: Ti/Pt/Au, Au/Ge/Ni, WSi_x and AuBe/Au has been undertaken in this work. Also we investigated a novel scheme which had an InGaN layer on top of GaN. The InGaN has a lower bandgap than GaN and should produce lower contact resistance. WSi_x was used for metallization to the InGaN layer. Electrical characterization of the contacts was done using standard transmission line measurements (TLM) and materials characterization including Scanning Electron Microscope (SEM) and Auger electron Spectroscopy (AES).

EXPERIMENTAL

The GaN and $\text{In}_{0.5}\text{Ga}_{0.5}\text{N}$ was grown on GaAs at 800°C using $(\text{CH}_3)_3\text{Ga}$ and an Electron Cyclotron Resonance plasma generated N_2 flux in a Metal Organic Molecular Beam Epitaxy system. The samples predominantly consisted of the cubic phase, with typical x-ray FWHM of 300-500 arc sec. The n-type doping level in the ternary was $\sim 10^{19}\text{cm}^{-3}$, while the GaN was typically $\leq 10^{17}\text{cm}^{-3}$.

Four different metallization schemes common in III-V technology were investigated, i.e. Ti/Pt/Au, Au/Ge/Ni, AuBe and WSi_x . The contact metals were deposited using two techniques, namely, electron beam evaporation and sputtering. The deposition sequences and the layer structures were as follows: (1) Ti-250Å/Au-1000Å; (2) Ge-50Å/Ni-50Å/Au-Ge-268Å-132Å/Au-1100Å; (3) AuBe-200Å/Au-1000Å and (4) WSi_x -1000Å. Also WSi_x contacts having thickness of 1000Å was deposited on an $\text{In}_{0.5}\text{Ga}_{0.5}\text{N}$ sample. The above three metallizations were performed using electron beam evaporation in a Temescal system. Prior to loading in a UHV system the wafers were rinsed in a solution of $\text{H}_2\text{O}:\text{NH}_4\text{OH} = 20:1$ for 1 minute to remove the native oxide from the GaN samples in order to ensure uniform contact properties upon subsequent deposition and alloying. After a pump down to a pressure of about 2×10^{-7} Torr and in-situ Ar^+ ion beam sputtering for oxide removal the metallization schemes were evaporated with an electron gun.

The WSi_x ($x \sim 0.45$) contact was deposited using the sputtering technique. Prior to loading the samples in the deposition chamber a 1 minute rinse in a $\text{H}_2\text{O}:\text{NH}_4\text{OH}$ (20:1) solution was done after which the contacts were deposited by sputtering with an Ar discharge at a bias voltage of 90-100V. The contact metal was deposited onto square openings ($100 \times 100\mu\text{m}^2$) linearly spaced (with intervals of 2 to $16\mu\text{m}$) in a photoresist layer. Subsequently, InGaN mesas were etched to give the required one-dimensional current flow. After the metallizations were performed the samples were each split into pieces and thermally annealed at a temperatures range from 400 - 900°C for 30s in a N_2 ambient using rapid thermal annealing technique (AG Heatpulse 410 System).

RESULTS AND DISCUSSION

The Au/Ge/Ni sample was annealed at temperatures of 400°C , 500°C , 600°C and 700°C . The Au/Ge/Ni sample heat treated at 600°C showed signs of degrading (Figure 1). The surface is no longer smooth and as the sample annealing temperature is increased further to 700°C the SEM micrograph at a magnification of 10,000 reveals many shallow small pits.

The Ti/Pt/Au samples were heat treated at temperatures of 500°C , 700°C , 800°C and 900°C for 30s.

The sample that was annealed at 500°C showed signs of degradation and at 700°C the surface becomes more degraded. The formation of little islands seem to be more apparent and the size and density of

these islands increase at 800°C. The maximum temperature for annealing these contacts would be around 450-500°C which is approximately about the temperature used for obtaining low temperature Ti/Pt/Au contacts on GaAs samples.⁽⁸⁾

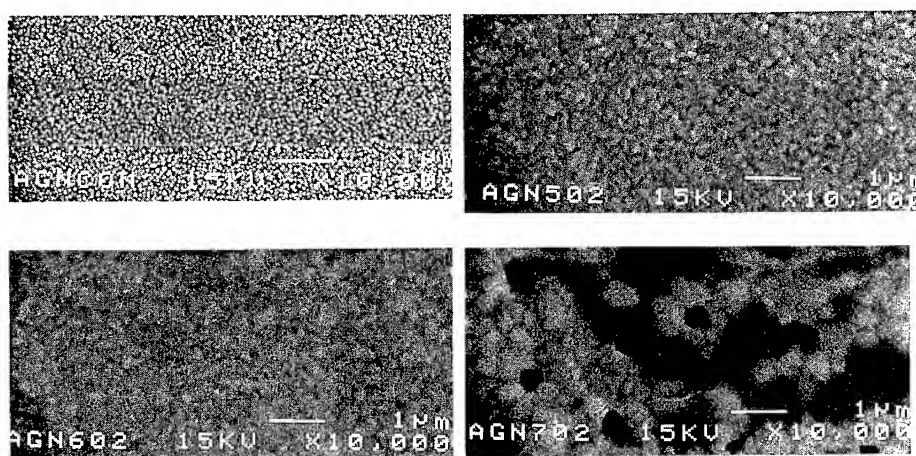


Figure 1. Surface morphology of Au/Ge/Ni/GaN contacts (magnification x10,000); (top left) as-deposited, (top right) annealed at 500°C, (bottom left) annealed at 600°C and (bottom right) annealed at 700°C.

The WSi_x contacts on GaN samples were heat treated at temperatures of 400°C, 700°C, 800°C and 900°C for 30s. The SEM studies performed on these samples revealed that the as-deposited sample exhibited a very smooth surface and that there was no change in the surface morphology of samples annealed at temperatures of 400°C and 700°C. The surface morphology of the samples annealed at 900°C showed only a small amount of surface roughness. The maximum annealing temperature to obtain good surface morphology WSi_x contacts on InGaN samples would therefore be in the range 700-800°C.

The AuBe samples were annealed at temperatures of 400°C, 500°C, 600°C and 700°C for 30s. The as-deposited AuBe sample was characterized by a smooth surface through the sample annealed at 400°C already showed amount of roughness. It was clearly evident from the micrograph of the sample annealed at 700°C that the sample surface was badly degraded.

The Auger depth profile of as-deposited Au/Ge/Ni contacts on GaN indicated a slight interdiffusion between Au and Ni and extensive interdiffusion between Ni and Ge. The penetration of Au into the GaN was insignificant. The suggestion of interdiffusion of Ni and Ge agrees with results of Au/Ge/Ni contacts on GaAs samples.⁽⁸⁾

The Auger depth profile of the as-deposited Ti/Pt/Au sample seen in Figure 2 did not show much interdiffusion between the metals compared to the Au/Ge/Ni as-deposited sample. In comparison to the as-deposited sample the sample that was heat treated at 600°C showed extensive interdiffusion between Ti and Pt (Figure 2). There appears to be more Ga outdiffusion into the metal layers in the heat treated sample compared to the as deposited sample. The depth profiles of the as-deposited and annealed samples of WSi_x shown in Figure

3a and 3b indicated that the 900°C annealed sample showed more intermixing of the metal and GaN at the interface compared to the as-deposited sample.

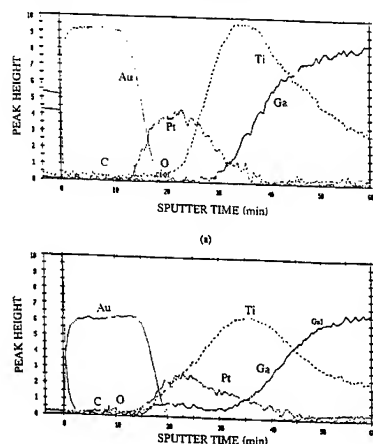


Figure 2. AES depth profiles of TiPtAu contacts on GaN (a) as-deposited and (b) after annealing at 700°C for 30secs.

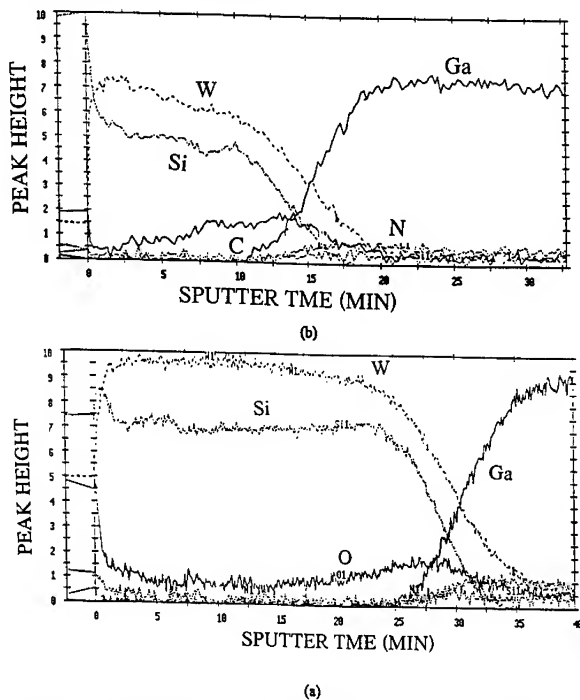


Figure 3. AES depth profiles of WSi_x contacts on GaN (a) as-deposited and (b) after annealing at 900°C for 30 secs.

The contact and sheet resistance of the contact can be derived from a plot of measured resistance versus gap spacing. The method of least square fit was used to get a linear fit to the experimental data which typically yielded correlation coefficient of 0.9972 or better.

The specific contact resistivity (ρ_c) is calculated from a measurement of the effective contact resistance (R_c), the contact width (W) and the transfer length (L_T):

$$\rho_c = R_c W L_T \quad (1)$$

The specific contact resistance dropped from 5.95×10^{-5} on the as-deposited sample to 3.92×10^{-5} after annealing at 400°C . The contact resistance reached a minimum value of 1.48×10^{-5} after annealing at 700°C (Figure 4) The trends are similar to those of WSi_x on InGaAs .⁽⁹⁾

It has been noted that the Ti/Au contacts on GaN ⁽⁶⁾ have large contact resistance even after thermal annealing. The Ti/Au contacts generally suffer from the problem of spiking into the underlying semiconductor upon annealing.⁽¹⁰⁾ To mitigate this problem, Pt which is a very good diffusion barrier has been used between Ti and Au to prevent Au spiking. In our work a similar kind of observation was made. The AES studies of the as-deposited sample did not show intermixing of metals and the SEM studies confirmed these results since the sample surface appeared to be smooth. From the AES studies of the sample annealed at 600°C it was realized that Au does not interact with Ga which confirms that the Pt barrier has prevented the Au spiking into the underlying GaN . This solid phase reaction between Ti and GaN forming TiN can help the contact operate through a tunneling mode. From the AES depth profile it can be seen that for the sample annealed at 600°C , Ga has penetrated through most of the Ti film. In our case if we suppose N is extracted from the GaN without decomposing GaN , then an accumulation of N vacancies would be created in the GaN near the junction. Since N vacancies most likely act as donors, this region would be heavily doped n-GaN which provides the configuration needed for tunneling contacts. Thus annealing temperatures of about 500°C would be optimum for obtaining thermally stable $\text{Ti}/\text{Pt}/\text{Au}$ ohmic contacts but temperatures higher than that may lead to extensive reaction at the interface which obviously implies degrading of the sample.

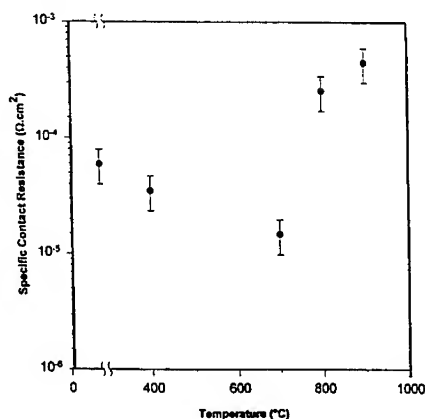


Figure 4. WSi_x specific contact resistivity on $\text{In}_{0.5}\text{Ga}_{0.5}\text{N}$ versus annealing temperature.

CONCLUSION

Processing of FET devices involve a high temperature annealing step for implant activation, typically $\geq 900^\circ\text{C}$. The stability of the $\text{WSi}_x/\text{In}_{0.5}\text{Ga}_{0.5}\text{N}$ contacts are high enough to allow dopant activation in HBT or FET processing. The contact degradation at higher annealing temperature was related to increased in the sheet resistance which in turn resulted from the degradation of the metal-semiconductor interface.

The AuBe/GaN contact system showed poor thermal stability while Au/Ge/Ni/GaN contact was thermally stable up to temperatures of 500°C . The Ti/Pt/Au contacts were found to remain substantially stable at $450\text{--}500^\circ\text{C}$. There is no penetration of Au into GaN which was prevented owing to the Pt diffusion barrier. These contacts exhibited better structural properties than Ti/Au contacts deposited on GaN.

The scope of future work in the field of $\text{WSi}_x/\text{InGaN}$ system is probably to experiment with the In concentration to lower the bandgap of InGaN. The contact resistance could be measured as a function of annealing temperature and the condition mechanisms and thermal stability.

ACKNOWLEDGMENTS

The work at UF is partially supported by an NSF grant through DMR (94-21109), an AASERT grant through USARO (J. M. Zavada) and a DOE URI administered through ONR (N00014-92-J-1895). The staff of the Microfabritech facility is greatly appreciated.

REFERENCES

1. H. Amano, M. Kito, X. Hiramatsu and I. Akasaki, Jpn. J. Appl. Phys. **28**, L2112 (1989)
2. S. Nakamura, T. Mukai and M. Seno, Jpn. J. Appl. Phys. **30**, L1998 (1991).
3. M. A. Khan, J. N. Kuznia, A. R. Bhattacharai and D. T. Olson, Appl. Phys. Lett. **63**, 1786 (1993).
4. M. A. Khan, A. Bhattacharai, J. N. Kuznia and D. T. Olson, Appl. Phys. Lett. **63**, 1214 (1993).
5. J. S. Foresi and T. D. Moustakas, Appl. Phys. Lett. **62**, 2859 (1993).
6. M. E. Lin, Z. Ma, F. Y. Huang, Z. F. Fan, L. H. Allen and H. Morkoc, Appl. Phys. Lett. **64**, 1003 (1994).
7. M. E. Lin, F. Y. Huang and H. Morkoc, Appl. Phys. Lett. **64**, 2557 (1994).
8. G. Stareev, H. Kunzel and G. Portmann, J. Appl. Phys. **74**, 7344 (1993).
9. A. Lahav, M. Genut, Materials Science and Engineering **B7**, 231 (1990).
10. B. M. Henry, A. E. Staton-Beran, V. Sharma, M. A. Crouch and S. S. Gill, Materials Res. Soc. Symp. Proc. **240**, 431 (1992).

Schottky Barrier Heights of Ni, Pt, Pd, and Au on n-type GaN

A.C. SCHMITZ*, A.T. PING*, M. ASIF KHAN**, and I. ADESIDA*

*Center for Compound Semiconductor Microelectronics, and Department of Electrical and Computer Engineering, University of Illinois, Urbana-Champaign, Illinois 61801

**APA Optics, Inc., Blaine, Minnesota 55449

ABSTRACT

Schottky barrier heights of Ni, Pt, Pd, and Au on n-type GaN were measured using current-voltage and capacitance-voltage techniques. Measurements from the I-V technique yielded barrier heights of 0.95, 1.01, 0.94, and 0.87 eV for Ni, Pt, Pd, and Au, respectively. Barrier heights of 1.13, 1.16, 1.07, and 0.98 eV, for Ni, Pt, Pd, and Au, respectively, were obtained using C-V measurements.

INTRODUCTION

There is significant interest in gallium nitride (GaN) and related compounds due to the wide band gaps which correspond to energy transitions in the visible wavelengths. This property makes these materials very useful for short wavelength light emitting diodes and laser diodes. Another area of potential application is high temperature transistors. For this application, high quality Schottky barrier contacts with adequate barrier heights are required for field effect transistors. These factors have prompted recent reports on the contact characteristics of GaN with various metals. Hacke et al. [1] reported a barrier height of 0.84 eV and an ideality of ~ 1.03 for Au using I-V measurements, with corresponding C-V measurements giving a barrier height of 0.94 eV. Binari et al. [2] reported an ideality factor of 1.28 for Ti/GaN contacts and Schottky barrier heights of 0.58 and 0.59 eV for Ti by I-V and C-V measurements, respectively. Work on Schottky barrier contacts have also been reported by Guo et al. [3] for Pd and Pt. The I-V and C-V characteristics yielded barrier heights of 1.03 and 1.04 eV, respectively, for Pd, and 0.91 and 0.94 eV, respectively, for Pt. The ideality factor measured by Guo et al. [3], however, was 1.14 for Pd and 1.21 for Pt. In this paper, we report our work on the measurement of Schottky barrier heights of various metals on n-GaN. The metals investigated were Ni, Pt, Pd, and Au. Current-voltage and capacitance-voltage measurements were carried out to determine ideality factors and barrier heights. The results obtained are compared with those previously reported by other authors [1-3].

EXPERIMENT

The Schottky barrier contacts in this work were patterned on 4 μm layers of GaN which was epitaxially grown by metal-organic chemical vapor deposition (MOCVD) on the (0001) surface

of sapphire substrates. Hall measurements revealed a bulk carrier concentration of $\sim 10^{17} \text{ cm}^{-3}$ due to unintentional doping. The room temperature electron mobility was measured to be $\sim 250 \text{ cm}^2/\text{V-s}$. A ohmic contact with $300 \mu\text{m}$ diameter openings was first patterned on the samples. The ohmic contact consisted of Ti/Al which were deposited by electron beam and thermal evaporation, respectively. The samples were then alloyed in an N_2 atmosphere using rapid thermal annealing (RTA). Schottky contacts of $250 \mu\text{m}$ diameter were patterned at the center of the ohmic contact openings using metal lift-off techniques. The exposed GaN surface was cleaned in the following sequence: descummed in an O_2 plasma asher, dipped in diluted HCl, rinsed in DI, and blown-dry with N_2 . Surface oxides formed in the plasma asher are removed by the HCl solution. The samples were then immediately transferred into an evaporator. Nickel, palladium, and platinum were each deposited by electron beam evaporation, while gold was deposited thermally. The Ni, Pd, and Au were deposited to thicknesses of 100 nm . The Pt, however, was deposited to a thickness of 50 nm due to thermal cracking of thicker layers. The I-V characteristics were measured using a four point technique with an HP4142 semiconductor parameter analyzer. An HP4280 was used for C-V measurements at a frequency of 1 MHz .

RESULTS AND DISCUSSION

The current-voltage measurements were analyzed using the thermionic emission theory. Accordingly, the current-voltage relationship is given by

$$I = I_s e^{q(V-IR)/nkT} \quad \text{for } V \gg kT/q \quad (1)$$

and

$$I_s = AA^{**} T^2 e^{-q\phi_b/kT} \quad (2)$$

where R is the series resistance, n is the ideality factor, T is the measurement temperature, A is the area of the diode, A^{**} is the effective Richardson constant, and ϕ_b is the effective barrier height. An effective electron mass of $m_n^* = 0.22m_0$ was used to determine the theoretical value of the Richardson constant which is $26.4 \text{ A cm}^{-2} \text{ K}^{-2}$ [4]. When R is small, a $\log I$ vs. V plot of the forward characteristics yields a linear region in which a fit can be used to calculate the barrier height and ideality factor from the y-intercept and slope, respectively. Figure 1 shows the forward characteristics ($\log I$ vs. V) of the four metals investigated in this work. For Ni, Pt, Pd, and Au, the barrier heights are 0.95 , 1.01 , 0.94 , and 0.87 eV , respectively, while the ideality factors are 1.04 , 1.05 , 1.04 , and 1.04 , respectively. The electron affinity, χ_s , is determined using the relation $\chi_s = \phi_m - \phi_b$. The metal work function, ϕ_m , is 5.15 eV for Ni, 5.65 eV for Pt, 5.12 eV for Pd, and 5.1 eV for Au [5]. Therefore, the electron affinity from I-V measurements for Ni, Pt, Pd, and Au are 4.20 , 4.64 , 4.18 , and 4.23 eV , respectively.

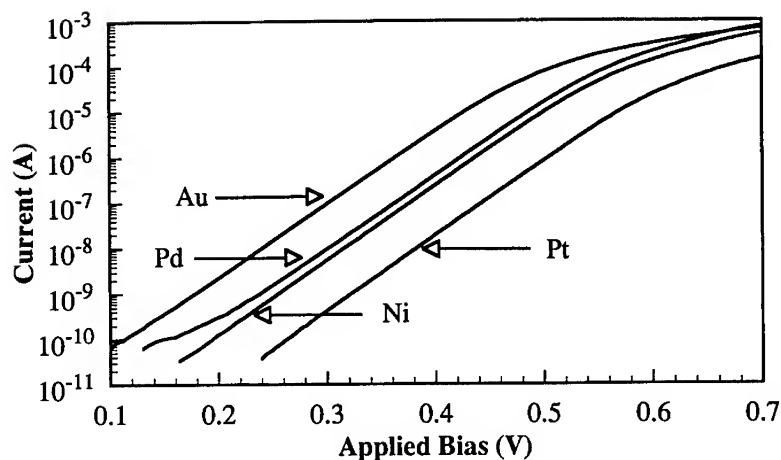


FIG. 1. Forward Log I vs. V characteristics for Ni, Pt, Pd, and Au Schottky barrier contacts.

The reverse I-V characteristics of the four metals are shown in Figure 2. The reverse bias leakage current for the Ni and Pd diodes were ~ 1 nA at -10 V. For the Pt and Au diodes, the leakage current at -10 V was ~ 1 μ A and ~ 100 nA, respectively. The I-V characteristics, however, were found to degrade once the reverse bias exceeded the breakdown voltage. In particular, the diodes were observed to have increased reverse bias current leakage and degraded forward characteristics. These observations were made for all the metals investigated in this work.

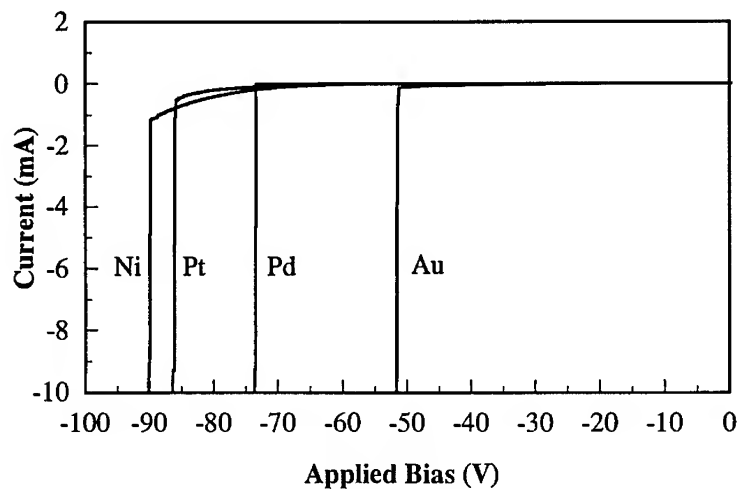


FIG. 2. Reverse bias characteristics of the Schottky barrier contacts.

The relationship between the capacitance and voltage is given by

$$C = A[\epsilon q N_d / 2(V_o - V)]^{1/2}. \quad (3)$$

Figure 3 shows a plot of the $1/C^2$ vs. V data for all four metals. From this plot, the ionized dopant concentration and built-in potential are calculated from the slope and x-intercept, respectively. The x intercept, or V_o , and the built-in potential, V_i , are related by $V_o = V_i - kT/q$. The effective barrier height can then be calculated by

$$\phi_b = V_n + V_i \quad (4)$$

where

$$V_n = (kT/q) \ln(N_c / N_d) \quad (5)$$

and $N_c = 2(2\pi m_n^* kT / h^2)^{3/2}$ is the conduction band effective density of states. Using these equations, the C-V measurements yielded a barrier height of 1.13 eV for Ni, 1.16 eV for Pt, 1.07 eV for Pd, and 0.98 eV for Au. These and the other quantities determined in this work are listed in Table I.

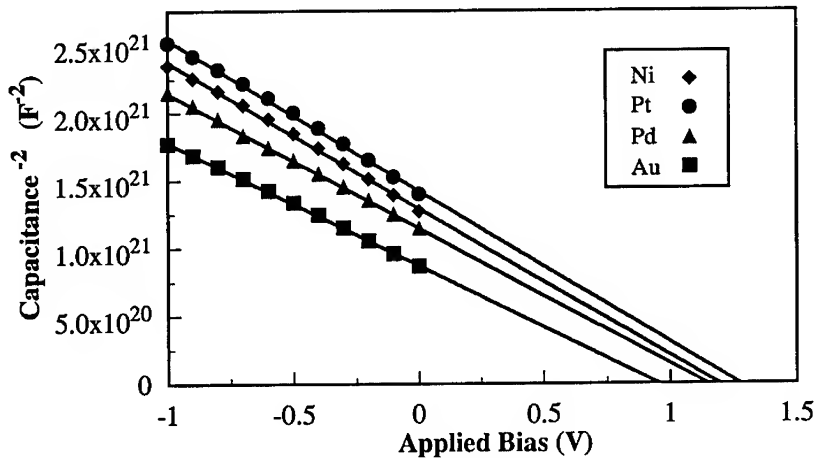


FIG. 3. Capacitance-voltage characteristics of the Ni, Pt, Pd, and Au Schottky barrier contacts on n-type GaN.

Discrepancies between the barrier heights determined from C-V and I-V are often attributed to image force barrier lowering. However, the differences for the results presented in this paper are too large to be accounted for in this manner. The ideality factor and barrier heights for Au obtained in this work agree with that obtained by Hacke et al. [1] for n-GaN with the same level of doping. They have also noted the disparity between the C-V and I-V barrier height measurements which was attributed largely to a thin interfacial oxide layer.

SUMMARY

The Schottky barrier heights of Ni, Pt, Pd, and Au on n-type GaN were presented. Both I-V and C-V measurements were taken and compared. The effective Schottky barrier heights for Ni, Pt, Pd, and Au were 0.95, 1.01, 0.94, and 0.87 eV, respectively, from I-V measurements and 1.13, 1.16, 1.07, and 0.98 eV, respectively, from C-V measurements. The ideality factors are close to unity which is an indication of carrier transport by thermionic emission.

TABLE I. Summary of Schottky characteristics of Ni, Pt, Pd, and Au on n-type GaN.

	Ni		Pt		Pd		Au	
	I-V	C-V	I-V	C-V	I-V	C-V	I-V	C-V
Barrier Height ϕ_b (eV)	0.95	1.13	1.01	1.16	0.94	1.07	0.87	0.98
Ideality, n	1.04	-----	1.05	-----	1.04	-----	1.04	-----
Carrier Conc. N_d (cm ⁻³)	-----	6.5E+16	-----	4.4E+16	-----	6.0E+16	-----	6.7E+16
Electron Affinity χ_s (eV)	4.2	4.02	4.64	4.49	4.18	4.05	4.23	4.12
Built-in Potential V_i (V)	0.87	1.05	0.93	1.08	0.86	0.99	0.79	0.90

ACKNOWLEDGMENTS

The material work at APA Optics was supported by Air Force Office of Scientific Research under Contract NO. F46920-93-C-0059 and the work at the University of Illinois was supported by NSF Grant ECS 95-21671.

REFERENCES

1. P. Hacke, T. Detchprohm, K. Hiramatsu, and N. Sawaki, Appl. Phys. Lett. **63**, pp. 2672-2678 (1993)
2. S.C. Binari, H.B. Dietrich, G. Kelner, L.B. Rowland, K. Doverspike, and D.K. Gaskill, Elect. Lett., **30**, pp. 909-910 (1994)
3. J.D. Guo, M.S. Feng, R.J. Guo, F.M. Pan, and C.Y. Chang, Appl. Phys. Lett. **67**, pp. 2657-2659 (1995)
4. S. Strite and H. Morkoç, J. Vac. Sci. Technol. **B10**, pp. 1237-1266 (1992)
5. D.R. Lide, CRC Handbook of Chemistry and Physics, CRC, Boca Raton, 1992, p. 12-108.

SCHOTTKY BARRIERS ON p-GaN

N.I. KUZNETSOV, E.V. KALININA, V.A. SOLOVIEV* and V.A. DMITRIEV**

* A.F. Ioffe Institute and Cree Research EED, 26 Polytechnicheskaya Str., St. Petersburg, 194021 Russia, EED@cree.spb.su

** Cree Research, Inc., 2810 Meridian Parkway, Durham, NC 27713 USA

ABSTRACT

Schottky barriers were formed on p-GaN. p-GaN layers doped with Mg were grown by metalorganic chemical vapor deposition (MOCVD). 6H-SiC wafers were used as substrates. The barriers were made by vacuum thermal evaporation of Au. Capacitance-voltage (C-V) and current-voltage (I-V) characteristics of the barriers were investigated. The concentration of the ionized acceptors in the p-layers was measured to be about $\sim 10^{17} \text{ cm}^{-3}$. The barrier height was determined to be 2.48 eV by C - V measurements at room temperature. The forward current flow mechanism through the barriers is discussed.

INTRODUCTION

Recently extensive study has been done on Schottky barriers formed on group III nitrides [1-3]. The parameters of Au Schottky barriers to n-GaN were studied in detail [1,2]. In paper [2] we reported the characteristics of Au barriers formed on n-GaN layers grown on SiC substrates: barrier height was determined to be 1.03 eV using both C-V and I - V characteristics. The electron affinity for GaN was calculated to be 4.1 eV using the Au-n-GaN barrier characteristics (both from C - V and I - V data). Much less information is available on Schottky barriers to p-type A³N materials. M.A. Khan et al [4] used Ti/Au Schottky barriers formed on p-GaN to fabricate a photodetector, but barrier characteristics were not published. In this paper, the electrical characteristics of Au Schottky barriers formed on p-GaN layers are reported.

EXPERIMENTAL PROCEDURE

GaN layers were grown by MOCVD on SiC substrates at Cree Research, Inc. [5]. The substrates used were n-type 6H-SiC wafers. GaN was deposited on the (0001)Si face of the substrate. First a Si-doped n-GaN layer about 2 μm thick was grown. The donor concentration N_d in the layer was $\sim 2 \times 10^{18} \text{ cm}^{-3}$. Then a Mg-doped GaN p-layer about 1 μm thick was grown on top.

Schottky barriers were formed by vacuum thermal evaporation of high purity Au on samples which were previously etched in a KOH-water solution for 2 min and then boiled in deionized water. Before evaporation, the gold was cleaned in organic solvents and acids. The gold was evaporated in a vacuum of $\sim 3 \times 10^{-3} \text{ Pa}$ through shadow masks. The area of the Schottky contact was $1 \times 10^{-3} \text{ cm}^2$ and the thickness of the evaporated metal ranged from 0.1 to 0.15 μm . The thickness of evaporated metal and the effective area of the Schottky contact were measured by electron microscopy using electron beam induced current (EBIC) and back scattered electron modes. Pd was evaporated on the

perimeter of the samples to form an ohmic contact to p-GaN. A planar device geometry (Fig. 1) was used.

The C-V measurements were performed using a computer controlled system at a test frequency of 1 MHz and a test signal of 20 mV rms. The I-V characteristics were measured in the temperature range from 300 to 600 K. The measurements were done in a cryostat where the sample temperature was maintained with an accuracy of 0.1 K.

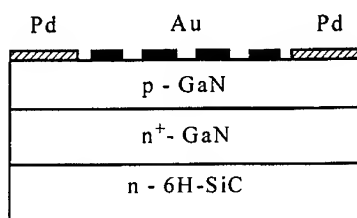


Fig.1. Cross section of a wafer with the Au Schottky barriers and ohmic contact formed on p-GaN.

RESULTS AND DISCUSSION

Capacitance - voltage characteristics

The C-V characteristics were linear when plotted in C^{-2} - V coordinates (Fig. 2). This fact indicates that the doping depth profile was uniform and that the barrier height was not dependent on applied voltage.

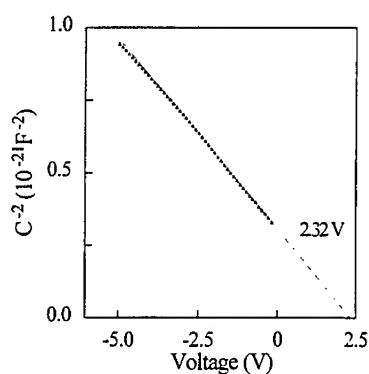


Fig.2. Capacitance - voltage characteristic for Au-p-GaN (1 MHz, 300 K).

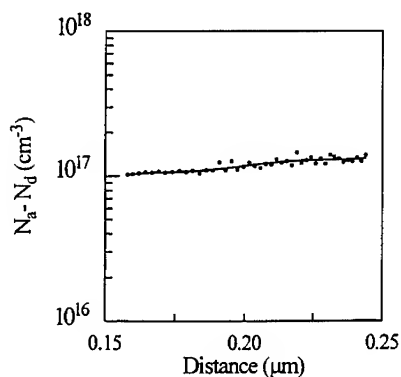


Fig.3. Concentration depth profile.

In this case, the well-known equations were used to determine the barrier characteristics and impurity concentration in the semiconductor [6]:

$$C^{-2} = \frac{2(V+V_c)}{S^2 q \epsilon_s N_a} \quad (1)$$

$$N_a = \frac{2}{\epsilon_s q} \left[- \frac{dV}{d\left(\frac{1}{C^2}\right)} \right] \quad (2)$$

where V - the applied voltage, V_c - the cut-off voltage of the C-V characteristic, ϵ_s - the dielectric constant of the semiconductor, N_a - the concentration of ionized acceptors and S - the effective contact area. The effective contact area of the barrier measured using EBIC was determined to be close to the metal area measured by optical microscopy. This fact indicates a good mechanical contact between the metal and semiconductor. The concentration of ionized acceptors N_a was determined using C-V data to be about $1 \times 10^{17} \text{ cm}^{-3}$ (Fig. 3). The barrier characteristics were calculated using the equations:

$$V_{bi} = V_c + \frac{kT}{q} \quad (3)$$

$$\phi_{bp} = qV_c + E_f + kT \quad (4)$$

where V_{bi} - the barrier built-in potential, ϕ_{bp} - the barrier height, and E_f - the difference in the energies between the top of the valance band and the Fermi level. The cut-off voltage was extracted from the C-V measurements to be 2.32 V (see Fig. 2). E_f was estimated to be 0.13 eV. The calculations gave $V_{bi} = 2.35$ V and $\phi_{bp} = 2.48$ eV. According to Schottky's theory [7], the barrier height may be determined by:

$$\phi_{bp} = E_g - \phi_m + \chi_s \quad (5)$$

where E_g is the band gap energy (for GaN $E_g \sim 3.4$ eV, 300 K), ϕ_m is the work function of the metal ($\phi_{m \text{ Au}} = 5.1$ eV [8]) and χ_s is the semiconductor electron affinity. Assuming that the Fermi level in GaN is not pinned [9], we calculated that $\chi_s = 4.17$ eV. This value is close to the GaN electron affinity value of 4.1 eV calculated for Au-n-GaN barrier characteristics [2].

The sum of the barrier heights for barriers formed on samples having n- and p-conductivity must be equal to the band gap width of the semiconductor:

$$\phi_{bn} + \phi_{bp} = E_g \quad (6)$$

For Au Schottky barriers formed on n-GaN, the height was found to be $\phi_{bn} = 1.03$ eV [2]. According to (6) we calculated $E_g \text{ GaN}$ to be 3.51 eV, which is close to the experimental value of 3.4 eV measured by optics.

Current - voltage characteristics

The leakage current was 100 μ A at a reverse voltage of 10 V at room temperature. The forward I-V characteristics at different temperatures are shown in Fig. 4. At a forward voltage ranging from ~ 3 kT/q to ~ 1 V, straight lines were obtained in log (I) - V coordinates for currents ranging 4 orders of magnitude. The ideality factor $\eta = qdV/kTd(\ln I)$ was found to be temperature dependent (Fig. 5). The ideality factor ranged from 2.0 to 1.27 with temperature changes from 300 to 600 K. It was found that the ideality factor may be described by:

$$\eta = 1 + \left(\frac{T_0}{T} \right)^2 \quad (7)$$

where $T_0 = 304$ K. Data with a similar ideality factor temperature dependence has been observed for Schottky barriers formed on Si and GaAs and was attributed to carrier tunneling through the barrier [10]. However, the background carrier concentration was determined to be too small (10^{17} cm $^{-3}$) making the carrier tunneling through the An-p-GaN barrier unlikely. As known, the value of the ideality factor is determined by the nature of the current through the barrier. It is close to 1.0 if the current is due to thermionic emission. A possible reason for deviation from ideal behavior of the Schottky barrier is due to carrier recombination [7]. In the case of pure recombination current, the ideality factor is equal 2.0 [7]. The effect of recombination is more pronounced at low temperatures. We propose that in our case the current transport was due to both recombination and thermionic emission. We assume that these two mechanisms act simultaneously.

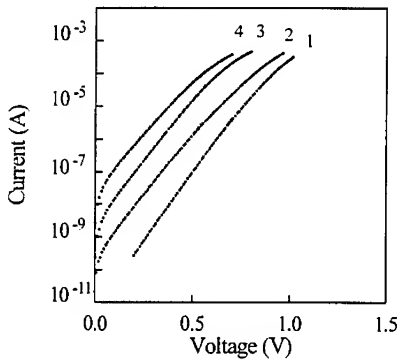


Fig.4. Forward I-V characteristics for a Au-p-GaN barrier: 1 - 300 K, 2 - 400 K, 3 - 500 K, 4 - 600 K.

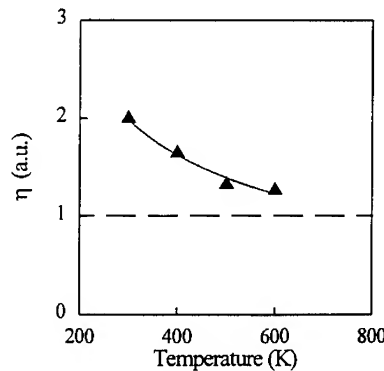


Fig.5. Dependence of the ideality factor on temperature.

SUMMARY

Au Schottky barriers were formed on p-GaN. The barrier height was determined to be 2.48 eV by C-V measurements at room temperature. The sum of this barrier height and the Au-n-GaN barrier height of 1.03 eV determined previously equals 3.51 eV which is close to the GaN band gap of 3.4 eV. The forward current ideality factor was found to be temperature dependent and may be expressed as $\eta = 1 + (T_0/T)^2$, where $T_0 = 304$ K. We propose that the current flow is due to both recombination of carriers in the depletion regions through deep centers and thermionic emission of carriers. We assume that these two mechanisms act simultaneously.

ACKNOWLEDGMENTS

We gratefully acknowledge work of K.G. Irvine in the growth of the p-GaN.

REFERENCES

1. P. Hacke, T. Detchprohm, K. Hiramatsu, and N. Sawaki, Appl. Phys. Lett. **63**, 2676 (1993); M.R.H. Khan, T. Detchprohm, P. Hacke, K. Hiramatsu and N. Sawaki, 2 Int. High Temperature Electronics Conference, North Carolina, USA, **2**, p. 231 (1994).
2. E.V. Kalinina, N.I. Kuznetsov, V.A. Dmitriev, K.G. Irvine and C.H. Carter, Jr., accepted to Journal of Electronic Materials.
3. J.D. Guo, M.S. Feng, R.J. Guo, F.M. Pan, and C.Y. Chang, Appl. Phys. Lett. **67**, 2657 (1995).
4. M.A. Khan, I.N. Kuznia, D.T. Olson, M. Blasiagame and A.R. Bhattara, Appl. Phys. Lett. **63**, p. 2455 (1993).
5. V.A. Dmitriev, K.G. Irvine, J.A. Edmond, G.E. Bulman, C.H. Carter, Jr., A.S. Zubrilov, I.P. Nikitina, V.I. Nikolaev, A.I. Babanin, Y.V. Melnik, E.V. Kalinina and V.E. Sizov, in Proceedings of the 21st. Int. Symp. Compound Semiconductors, San Diego, CA, 1994, Inst. Phys. Conf. Ser. No141, edited by H. Goronkin and V. Mishra (IOP, Bristol, 1995) pp. 497-502.
6. S.M. Sze, Physics of Semiconductor Devices, 2nd ed (Wiley, New York, 1981).
7. E.M. Rhoderick, Metal - Semiconductor Contacts (Clarendon Press, Oxford, 1978).
8. H.B. Michaelson, J.Res. Dev. **22**, p. 72 (1978).
9. J.S. Foresi and T.D. Moustakas, Appl. Phys. Lett. **62**, p. 2859 (1993).
10. C.R. Crowell and V.L. Rideout, Solid State Electron. **12**, p. 89 (1969).

METALLURGICAL STUDY OF CONTACTS TO GALLIUM NITRIDE

S. E. MOHNEY*, B. P. LUTHER†, and T. N. JACKSON‡

*Department of Materials Science and Engineering

†Department of Electrical Engineering

The Pennsylvania State University, University Park, PA 16802

M. A. KHAN, APA Optics, Blaine, MN 55449

ABSTRACT

Thermally stable contacts to GaN that also have desirable electrical characteristics are required for the further development of optoelectronic and high temperature devices based on GaN. To make improvements on existing contacts or to develop new ones, information on the metallurgy of potential contact systems is needed. In this work, the Metal-GaN ternary phase equilibria and the contact metallurgy are examined for Ti, Re, and Ni. Annealed contacts of these metals have been examined with x-ray diffraction and/or x-ray photoelectron spectroscopy, and the observed metallurgical reactions are discussed in light of estimated or experimentally determined Metal-GaN phase diagrams. Particular attention is paid to the gas phase equilibria and the role of the annealing environment on the metallurgical reactions. Finally, the consequences of this work for the design of thermally stable contacts are considered.

INTRODUCTION

Researchers of contacts to the other III-V semiconductors have long recognized the utility of Metal-III-V phase diagrams for designing thermally stable electrical contacts and for better understanding the reactions that occur when metal contacts are not in thermodynamic equilibrium with the semiconductor [1-4]. Unfortunately, no Metal-GaN phase diagrams are available in the literature. Thus, there is a lack of information on the metallurgy of the Metal/GaN systems just when it could prove extremely valuable: during the early stages of development of electrical contacts to GaN. We have previously estimated the phase equilibria for the Transition Metal-GaN systems through thermodynamic calculations [5]. In this work, we discuss in greater detail the contact metallurgy of one metal from each of three groups in the periodic table: Ti from the early transition metals, Re from the middle transition metals, and Ni from the late transition metals. The features of the contact metallurgy that may be important for the development of electrical contacts to GaN are emphasized, including the role of the gas phase equilibria and the effect of the annealing environment on the reactions in Metal/GaN contacts.

Ti/GaN CONTACTS

The early transition metals all form metal nitrides of considerable thermodynamic stability, some of which exist over a wide compositional range. They also form metal gallides, and Metal-GaN ternary phases have been reported for Ti [6], V [7-9], Nb [7], and Ta [7]. For those metals for which no ternary phases have been reported (Sc, Y, Zr, La, and Hf), sufficient thermodynamic data is available to estimate the M-GaN phase diagrams. The common feature of these diagrams is a tie-line between GaN and a metal nitride of nominal composition MN; thus, the MN phases are predicted to be in thermodynamic equilibrium with GaN over at least a portion of their ranges of homogeneity. Experimentally we have confirmed the existence of the TiN-GaN tie through a phase equilibria study of pressed powder samples annealed at 800 °C, and the relevant portion of the phase diagram from this study is shown in

Fig. 1. Because of the stability of the MN/GaN interface, MN phases such as TiN could be directly deposited onto GaN to form thermally stable contacts for high temperature electronics, provided the electrical characteristics of such a contact are satisfactory. Some of the early transition metal nitrides have already been used in microelectronics, and many of them have been reported to have resistivities below 50 m Ω -cm (TiN, ZrN, and HfN [10]) and work functions below 4 eV (TiN, ZrN, VN, and NbN [11]). In fact, these nitrides have already attracted attention as ohmic to *n*-type GaN, partly because of the anticipated dependence of the Schottky barrier height on the work function of the metal [12, 13].

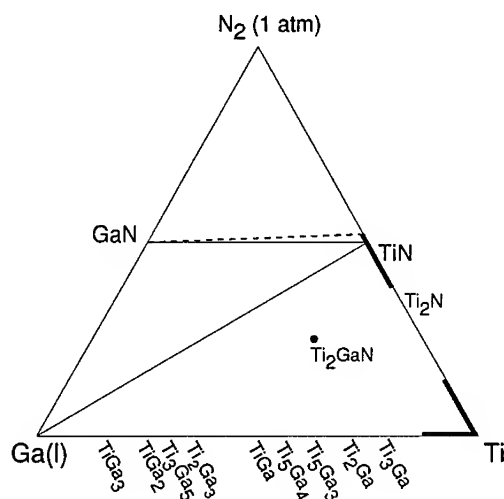


Figure 1. Tie-lines in the Ti-Ga-N system at 800 °C from the phase diagram experiment.

The great stability of the early transition metal nitrides also influences the way that early transition metal contacts may interact with their environment during annealing. The diagram of Fig. 1 can be used to discuss the role of the N_2 partial pressure in the annealing environment on the metallurgical reactions in Ti/GaN contacts. According to the diagram, if a N_2 pressure of 1 atm were continuously maintained over the contact, the Ti/GaN contact would actually be thermodynamically favored to extract nitrogen from the annealing environment, ultimately resulting in a TiN/GaN contact. This result is expected since only TiN and GaN are simultaneously in equilibrium with N_2 gas at 1 atm (the pressure represented in the nitrogen corner of the hypothetical diagram). The contact would therefore come to equilibrium with GaN without any net consumption of GaN through reaction with the metal. However, there may be competition between nitrogen incorporation into the film and metallurgical reaction at the non-equilibrium Ti/GaN interface during the intermediate stages of reaction.

On the other hand, if the exchange of elements with the annealing environment is insignificant, a Ti contact would react with GaN to ultimately form TiN and liquid Ga on the remaining GaN. This situation could occur when contacts are annealed under a lesser N_2 partial pressure or when the incorporation of nitrogen from the environment is kinetically hindered. This situation is the "closed system" case that has been described previously for the final equilibrium reaction products for other Metal/III-V contacts [1-4].

Our experimental investigation examines this issue. Titanium films 100 nm thick were evaporated onto *n*-type GaN cleaned in 5 % HF for 1 min prior to deposition. Two annealing environments were examined: Ar gas and N₂ gas at 1 atm. On *n*-type GaN ($n = 6.8 \times 10^{16} \text{ cm}^{-3}$), annealing times and temperatures that resulted in a change from rectifying to linear I-V characteristics of the Ti/GaN contacts were identified, and they were found to be the same regardless of the annealing environment. Metallurgical studies of these contacts were then conducted by XPS depth profiling. Profiles for a sample that was not annealed (Fig. 2a) and samples annealed in N₂ (Fig. 2b) and Ar (Fig. 2c) are shown for one of these annealing conditions (700 °C for 1 h).

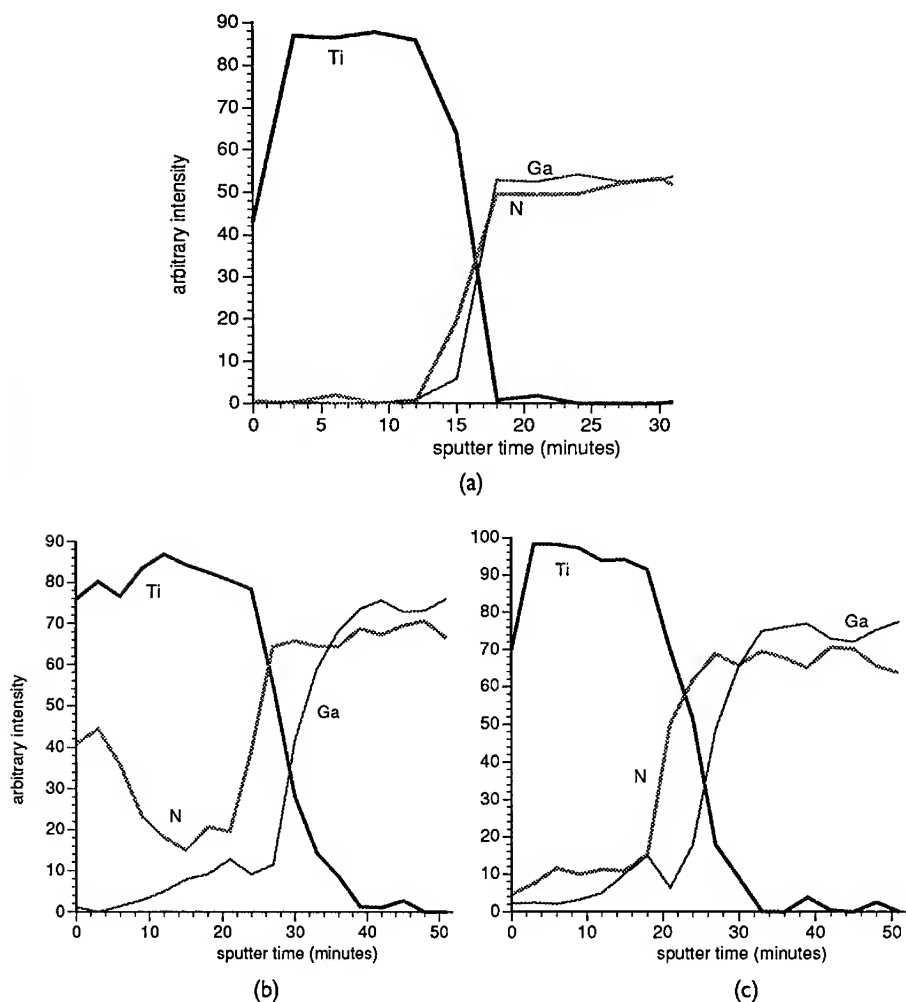


Figure 2. XPS depth profile for Ti/GaN contacts (a) as-deposited and annealed at 700 °C for 1 h in (b) N₂ gas and (c) Ar. Some oxygen contamination (not shown) was also detected in the annealed and as-deposited films.

It is interesting to note the nitrogen incorporation at the contact surface for the contact annealed in N_2 but not for the contact annealed in Ar. The interfacial region at the Ti/GaN interface, however, appears very similar for both samples. Hence, reaction at the N_2 gas/Ti and Ti/GaN interfaces occur at comparable rates, and the similar reaction at the Ti/GaN interface appears to be responsible for the change in the electrical characteristics in both samples. However, there is still a difference in these contacts from the point of view of long-term thermal stability. The contact annealed in N_2 gas has less Ti remaining to react with and consume the underlying GaN upon continued exposure to elevated temperatures, since much of the Ti has already been nitrided by the annealing environment.

Re/GaN CONTACTS

Both W and Re are expected to be in thermodynamic equilibrium with GaN at room temperature and at 600 °C. The W-Ga and Re-Ga binary phase diagrams are characterized by an absence of intermediate phases under atmospheric pressure and negligible miscibility between liquid Ga and the metals. Although metal nitrides have been reported, but none of them are expected to be stable at 600 °C under 1 atm or lower N_2 pressures. The calculated Re-Ga-N diagram at 600 °C is shown in Fig. 3.

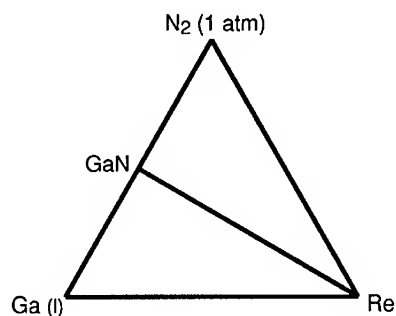


Figure 3. Calculated Re-Ga-N diagram at 600 °C.

Our study of annealed Re/GaN contacts is consistent with these calculations. Sputtered Re films 50 nm thick were deposited on polycrystalline GaN and annealed at 600 °C for 12 h in flowing N_2 gas. The films were examined by glancing angle x-ray diffraction before and after annealing, and in each case, only Re and GaN were observed. Based on thermodynamic arguments, the N_2 partial pressure in the annealing environment should not influence the metallurgical stability of the Re/GaN contact unless the N_2 partial pressure at which bare GaN decomposes is approached.

Ni/GaN CONTACTS

The near noble transition metals (Ni, Pd, and Pt) have been widely used in contacts to other III-V semiconductors and have recently been used in contacts to GaN. There is particular interest in these metals because of their high work functions and the anticipated dependence of the Schottky barrier height on the work function of the metal [12, 13]. These Metal-Ga-N systems are characterized the absence of reported metal nitrides that are equilibrium phases un-

der typical processing conditions for contacts. However, these metals form many metal gallides, some of which have been demonstrated to have desirable properties for use in contacts to other III-V semiconductors [14]. No ternary phases have been reported in these systems, and attempts to synthesize ternary phases in the Ni-Ga-N system met with failure [15].

Phase equilibria in these systems has been estimated and found to vary with temperature [5]; however, the distinguishing characteristic of these diagrams is the presence of tie-lines between the metal gallides and GaN, with no tie-line between the metal and GaN at elevated temperatures. In contrast to the early transition metals on GaN, loss rather than incorporation of nitrogen from the environment is expected to be important for the late transition metal contacts to GaN.

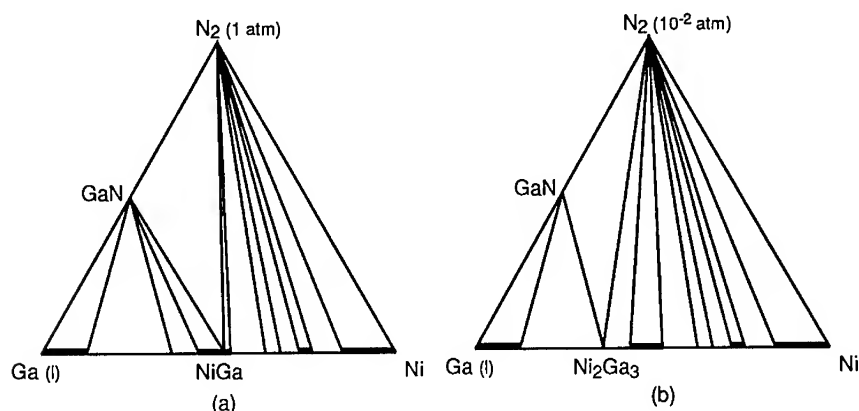


Figure 4. Calculated Ni-Ga-N diagram at 600 °C. The nitrogen corner of the diagram represents (a) N_2 at 1 atm and (b) 10^{-2} atm pressure.

The Ni-Ga-N diagram has been calculated at 600 °C [5] using experimentally determined thermodynamic data for the Ni-Ga binary system at 600 °C from [16] and data for GaN from Karpinski and Porowski [17]. At 600 °C, a tie-triangle between NiGa, GaN, and N_2 gas at 1 atm is predicted, as shown in Fig. 4a. Assuming that the Ni contact is much thinner than the underlying GaN, the phase diagram predicts that Ni/GaN is favored to react until the entire contact is ultimately converted to NiGa/GaN under 1 atm of N_2 . Nitrogen gas would be released during this reaction, even in an annealing environment of 1 atm N_2 . If the N_2 partial pressure in the annealing environment is reduced to 10^{-2} atm, however, the phase diagram should be redrawn for a N_2 pressure of 10^{-2} atm at the top corner. NiGa is no longer in equilibrium with GaN under the reduced N_2 partial pressure, and a tie-triangle is found between Ni_2Ga_3 , GaN, and N_2 gas at 10^{-2} atm. This diagram is shown in Fig. 4b. In this case, the reaction would be driven further due to the lower N_2 partial pressure, and thermodynamic equilibrium would not be achieved until all of the Ni contact was converted to Ni_2Ga_3 . A further decrease in the N_2 partial pressure to 2×10^{-4} atm places a tie-triangle between the gas phase, GaN, and liquid Ga with 5 atomic % Ni dissolved in it. For comparison, GaN in the absence of Ni is not expected to decompose until the N_2 partial pressure is below 2×10^{-5} atm at 600 °C, based on the thermodynamic data for GaN from Karpinski and Porowski [17]. It is important to note that although errors in the experimentally determined thermodynamic data could result in errors in the predicted tie-lines in the Ni-Ga-N diagrams, the trends discussed in this section should be preserved.

The predictions for the reaction of Ni/GaN contacts under reduced partial pressures of N₂ are qualitatively consistent with the study of Ni films on GaN by Bermudez *et al.* [18], who used Auger electron spectroscopy, electron energy loss spectroscopy, ultraviolet photoemission spectroscopy, and low energy electron diffraction to analyze their films in vacuum. They observed chemical interaction of the Ni with GaN even near room temperature, as well as desorption of nitrogen from the film surface accompanied by extensive intermixing of Ni and Ga at 600 °C.

CONCLUSIONS

From estimated Metal-Ga-N phase diagrams, trends in the equilibrium reaction products of Metal/GaN contacts are predicted based on the position of the metal in the periodic table. For the early transition metals, MN phases are predicted to be in thermodynamic equilibrium with GaN, and their stability influences the interaction of early transition metal contacts with the annealing environment. There is a strong driving force for these metals to be nitrided under 1 atm N₂ gas, and for Ti/GaN contacts, this reaction is observed to compete with the reaction at the non-equilibrium Ti/GaN interface. Some of the transition metals in the middle of the periodic table (Re and W) are predicted to be in thermodynamic equilibrium with GaN, even at elevated temperatures, consistent our experimental investigation of annealed Re/GaN contacts. For the late transition metals, particularly the near noble transition metals, loss of nitrogen to the annealing environment becomes an important issue, and the reaction products of these annealed Metal/GaN contacts are predicted to be metal gallides and N₂ gas.

ACKNOWLEDGMENTS

This work was supported by ARPA through AFOSR grant F49620-95-1-0516. The authors also wish to thank V. Bojan for assistance with the XPS and S. Sinharoy for donating GaN films for the early stages of this work.

REFERENCES

1. T. Sands, *J. Metals* **38**, 31 (1986).
2. J. R. Lince and R. S. Williams, *Thin Solid Films* **137**, 251 (1986).
3. R. Beyers, K. B. Kim, and R. Sinclair, *J. Appl. Phys.* **61**, 2195 (1987).
4. J.-C. Lin, K.-C. Hsieh, K. J. Schulz, and Y. A. Chang, *J. Mater. Res.* **3**, 148 (1988).
5. S. E. Mohny and X. Lin, submitted to *J. Electron. Mater.*
6. W. Jeitschko, H. Nowotny, and F. Benesovsky, *Mh. Chem.* **95**, 178 (1964).
7. W. Jeitschko, H. Nowotny, and F. Benesovsky, *Mh. Chem.* **95**, 156 (1964).
8. W. Jeitschko, H. Nowotny, and F. Benesovsky, *Mh. Chem.* **95**, 1212 (1964).
9. H. Boller, *Mh. Chem.* **102**, 431 (1971).
10. L. E. Toth, *Transition Metal Carbides and Nitrides*, edited by J. L. Margrave (Academic Press, New York, 1971).
11. V. S. Fomenko and G. V. Samsonov, *Handbook of Thermionic Properties* (Plenum Press Data Division, New York, 1966).
12. J. S. Foresi and T. D. Moustakas, *Appl. Phys. Lett.* **62**, 2859 (1993).
13. S. Kurtin, T. C. McGill, and C. A. Mead, *Phys. Rev. Lett.* **22**, 1433 (1969).
14. C.-H. Jan, Ph.D. Thesis, University of Wisconsin-Madison (1990).
15. H. H. Stadelmaier, *Z. Metallkde.* **52**, 758 (1961).
16. J. N. Pratt and J. M. Bird, *J. Phase Equilibria* **14**, 465 (1993).
17. J. Karpinski and S. Porowski, *J. Cryst. Growth* **66**, 11 (1984).
18. V. M. Bermudez, R. Kaplan, M. A. Khan, and J. N. Kuznia, *Phys. Rev. B* **48**, 2436 (1993).

CALCULATIONS OF THE SPECIFIC RESISTANCE OF CONTACTS TO III-V NITRIDE COMPOUNDS

P.A. Barnes and X-J Zhang, Department of Physics, Auburn University, AL 36849-5311
M.L. Lovejoy, T.J. Drummond, H.P. Hjalmarson, M. Crawford, R.J. Shul, J.C. Zolper
Sandia National Laboratories, Albuquerque, NM 87185

ABSTRACT

We present calculations of the specific contact resistance for metals to GaN. Our calculations include a correct determination of the Fermi level taking into account the effect of the degenerate doping levels, required in creating tunneling ohmic contacts. Using a recently reported improved WKB approximation suitable in representing the depletion width at the metal-semiconductor interface, and a two band $\mathbf{k} \cdot \mathbf{p}$ model for the effective masses, specific contact resistance was determined as a function of doping concentration. The specific contact resistance was calculated using the best data available for barrier heights, effective masses and dielectric coefficients for GaN. Because the barrier height at the metal-semiconductor interface has a very large effect on the contact resistance and the available data is sketchy or uncertain, the effect of varying the barrier height on the calculated specific contact resistance was investigated. Further, since the III-V nitrides are being considered for high temperature device applications, the specific contact resistance was also determined as a function of temperature.

INTRODUCTION

The III-V nitrides are promising materials for short wavelength light emitting diodes (LED's) and semiconductor lasers because of their wide direct band gaps, ranging from $E_g = 1.97$ eV for InN [1], $E_g = 3.45$ eV for GaN [2], to $E_g = 6.03$ eV for AlN [1]. In this paper we calculate Fermi levels, specific contact resistance and related parameters useful in modeling for device applications. The data presented is restricted to GaN due to its being the most studied of the III-V nitrides, and space restrictions. In order to account for all possible doping levels, we calculated Fermi levels of GaN with a method valid for both non degenerate doping and degenerate doping, which is then used in the determination of specific contact resistance for assumed barrier heights. The results are general and therefore a helpful reference for both theoretical and experimental researchers working on GaN.

FERMI LEVELS

The fundamental relationship used to calculate the Fermi level is the charge neutrality equation. [3]

$$p - n + N_d^+ - N_a^- = 0 \quad (1)$$

in which the usual notation is used. For the degenerate doping levels the full half-order Fermi integral should be used in solving Eq. (1) for the Fermi level, viz.,

$$F_{1/2}(\eta) = \frac{2}{\sqrt{\pi}} \int_0^\infty \frac{x^{1/2}}{1 + \exp(x - \eta)} dx \quad (2)$$

$$\text{with} \quad \eta_c = (E_F - E_c) / kT; \quad \eta_v = (E_v - E_F) / kT. \quad (3)$$

For non-degenerate doping the Fermi integral is approximated with the usual Boltzmann approximation,

$$u = F_{1/2}(\eta) \approx \exp(\eta) \quad \text{or} \quad \eta = \ln u \quad \text{for } (\eta \leq -3) \quad (4)$$

but for degenerate doping, a correction term $f(u)$, due to Nilsson[4], is added to the non-degenerate expression for η . Nilsson's $f(u)$ covers the whole range of doping from non-degenerate to degenerate concentrations and is given by:

$$f(u) = u \left[64 + 0.05524u(64 + \sqrt{u}) \right]^{-1/4} \quad (5)$$

Nilsson's equation is used in our calculation of Fermi levels. The temperature dependence of the bandgap was also accounted for, [1], for both Fermi level and contact resistance calculations.

CONTACT RESISTANCE MODEL

Electrical access to semiconductor devices is gained through metal-semiconductor (MS) ohmic contacts, the resistance of which must be small so that the power dissipated in the contact is negligible compared with the semiconductor junction power. So-called ohmic contacts are in reality tunneling Schottky contacts with near linear IV characteristics.

The behavior of an electron transported across the potential barrier is described by a wave function $\Psi(x)$ which can be numerically determined with the Schrodinger equation

$$\frac{d}{dx} \left[\frac{1}{m(x)} \frac{d\Psi(x)}{dx} \right] + \frac{8\pi^2}{h^2} [E - qV(x)]\Psi(x) = 0 \quad (6)$$

in which $m(x)$ and E are the effective mass and energy of the electron crossing the MS barrier.

In a one band model, $m(x)$ is a constant, m_n^* (estimated); but for a more realistic two band model [7]

$$m(x) = m_c \left[\frac{E_g + E - V(x)}{E_g} \right] \quad \text{with} \quad m(0) = m_n^* \quad (7)$$

m_c is a constant (called the tunneling mass), and E_g is the band gap of the semiconductor.

Many authors use the WKB approximation to calculate the tunneling probability. However, the conventional WKB method is not appropriate for potentials with an abrupt discontinuity, which is characteristic of a metal-semiconductor interface. Furthermore, incident particles with energies greater than the barrier peak energy are treated as if emitted over the barrier unimpeded by quantum mechanical reflection, resulting in large errors in the calculated transmission coefficient.

An improved WKB method reported by Betser et. al., [8] which is applicable above, below, and near the potential peak, gives the tunneling probability valid in all regions of the barrier.

This improved WKB calculation yields a result which is indistinguishable from a numerical integration of the Schrodinger equation, and therefore is chosen in our calculation for its accuracy and simplicity.

The contact resistance was determined by taking the derivative of the total current density which flows between the metal and semiconductor [9].

$$J = \frac{4\pi q m_e kT}{h^3} \int_0^\infty T(E) \ln \left(\frac{1 + \exp\left(\frac{E_{FC} - E}{kT}\right)}{1 + \exp\left(\frac{E_{FC} - E - qV}{kT}\right)} \right) dE \quad (8)$$

and thus the specific contact resistance, r_c , is expressed as [10]

$$\frac{1}{r_c} \equiv \left[\frac{dJ}{dV} \right]_{V \rightarrow 0} = \frac{4\pi m_e q^2}{h^3} \int_0^\infty \frac{T(E)}{1 + \exp\left(\frac{E - E_{FC}}{kT}\right)} dE \quad (9)$$

In both equations, $E_{FC} = E_F - E_C$ is the difference between the Fermi level and the conduction band edge.

RESULTS AND DISCUSSION

With the methods discussed earlier, we calculated the Fermi levels of GaN as a function of temperature in the range 10 to 1000K and doping concentration in the range 10^{17} to 10^{21} cm^{-3} , to cover possible working temperatures and impurity concentrations for contact fabrication and device applications. These calculations indicate, that for n-type GaN the material becomes degenerate if the impurity concentration is higher than 10^{18} cm^{-3} at 300K. While for p-GaN, degeneracy requires a higher doping concentration, which is close to 10^{19} cm^{-3} . These differences reflect the difference in effective masses of electrons and holes in GaN. Parameters used in the calculation were $m_n = 0.2m_0$, $m_p = 1.0m_0$, $\epsilon_s = 9.2\epsilon_0$ [1], [11], [14].

The improved WKB method was used to calculate the transmission probability and contact resistance using the Fermi level results discussed above. The results for both the one band model and two band model were compared, indicating that the resistance calculated for the one band model is consistently larger, by up to a factor of 2, compared to the two band model. In the following discussion, we will consider the two band model only.

Reliable barrier height information is not available for the III-V nitrides consequently we used the observed barrier height distributions for the usual III-V materials as a guide. It is observed that barrier heights in these materials are clustered around $E_b = 1/3 E_g$ for one doping type leading to $E_b = 2/3 E_g$ for the other polarity. For completeness, a barrier height equal to one half the bandgap was also chosen. The results, shown in Figs. 1 and 2, verify that the contact resistance depends dramatically on barrier height in these wide band-gap materials.

For the high barrier heights used for GaN, it is difficult to make the contact ohmic even at a doping concentration as high as 10^{20} cm^{-3} for both p- and n-type materials as indicated in Figs. 1 and 2. With decreasing doping concentration, contact resistance increases drastically and is definitely non-ohmic for the doping lower than about 10^{18} cm^{-3} for every barrier height value used for GaN.

We also compared the temperature dependence of contact resistance for n- and p-type GaN. Results are normalized to the resistance value at 300K as shown in Figs. 3 and 4. It is easily seen that the resistance drops as temperature increases due to the increasing contribution from thermionic emission. Changes in effective mass with temperature and doping were not considered. The temperature dependence of the contact resistance is also critically dependent on the doping concentration. The higher the doping concentration, the less dependent the contact resistance is on the temperature as the tunneling probability increases and becomes less temperature sensitive. At the other end of the temperature scale, however, the contact resistance

Contact Resistance of n-GaN

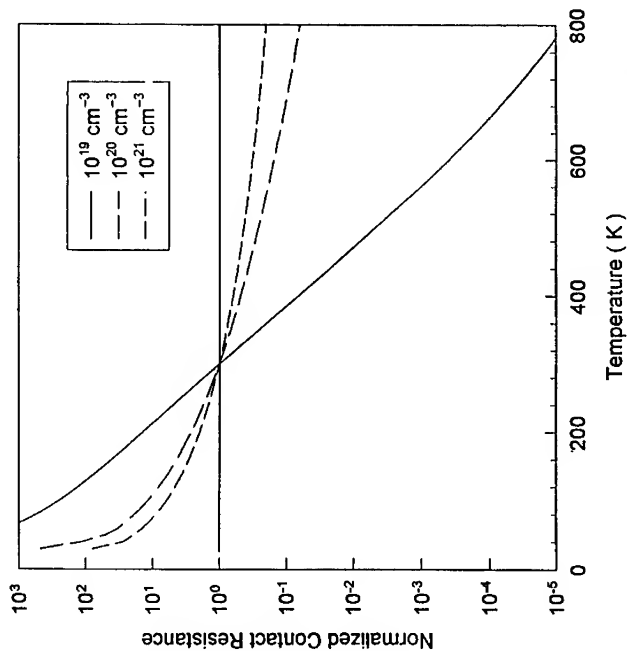


Fig. 3 Contact resistance of n-GaN normalized to the values at 300K for three different doping concentrations. Two band model is used and barrier height is taken to be 1.7 eV.

Contact Resistance of p-GaN

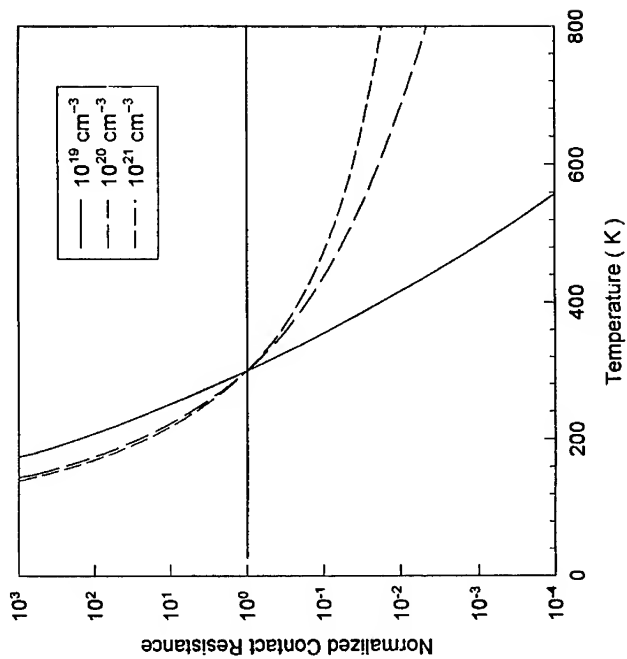


Fig. 4 Contact resistance of p-GaN normalized to the values at 300K for three different doping concentrations. Two band model is used and barrier height is taken to be 1.7 eV.

Contact Resistance of n-GaN

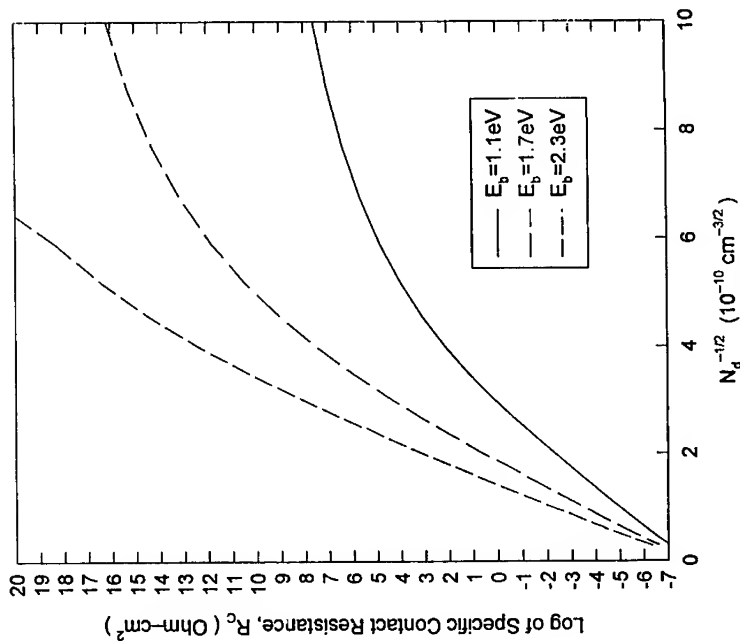


Fig. 1 Contact resistance vs. the inverse square root of doping concentration for n-GaN at 300K. The results corresponding to three different values of barrier height are compared. Two band model is used.

Contact Resistance of p-GaN

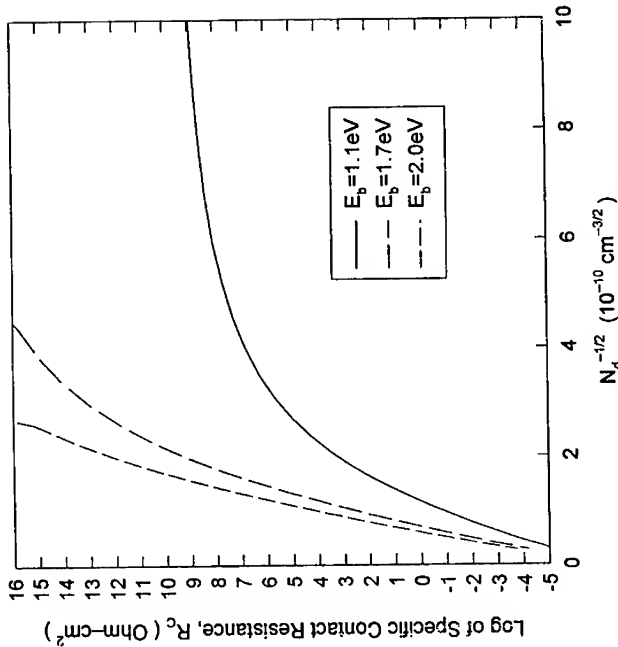


Fig. 2 Contact resistance vs. the inverse square root of doping concentration for p-GaN at 300K. The results corresponding to three different values of barrier height are compared. Two band model is used.

would increase greatly as the temperature decreases toward 0°K, no matter what value the doping concentration is.

CONCLUSION

We have calculated the Fermi levels for p and n-type GaN with degenerate and non-degenerate doping. The Fermi levels were then used to calculate the specific contact resistance, r_c , of contacts to both materials. The dependence of contact resistance on doping concentration, barrier height and temperature were also obtained and shown graphically. The calculated contact resistance, r_c , will undoubtedly change with improved data for the effective mass and barrier height. Improved data for the barrier height of metals on the nitrides, E_b , effective masses, m^* , and dielectric constants, ϵ_s , are needed. Changes in effective mass change the location of the intrinsic energy with respect to the conduction and valence band edges but have very little effect on the Fermi energy. However, large changes can be expected for calculated values of the contact resistance r_c , because the tunneling probability is very sensitive to the magnitude of the tunneling effective mass, the dielectric coefficient and the barrier height. This can be seen in the Padovani and Stratton model [5] for heavily doped, tunneling MS interfaces which predicts that the contact resistance will vary according to

$$r_c \propto \exp(E_b \cdot \sqrt{m^* \epsilon_s} / N) \quad (10)$$

where N is the number of ionized donors or acceptors. Low resistance ohmic contacts to the wide band-gap III-V nitrides will be difficult to fabricate and may require compositional grading [12] as described by Woodall et al, or tunneling superlattice contacts as described by Lin et al [13].

ACKNOWLEDGMENT

The work at Auburn University was supported by Sandia National Laboratories Grant # AI-7673. The continuing support of Thomas Zipperian is gratefully acknowledged.

REFERENCES

1. Q. Guo and A. Yoshida, *Jpn. J. Appl. Phys.* **33**, 2453 (1994)
2. P.B. Perry and R.F. Rutz, *Appl Phys. Letts.*, **33**, 319 (1978)
3. R.F. Pierret, *Advanced Semiconductor Fundamentals*, Addison-Wesley, 1987.
4. N.G. Nilsson, *Appl. Phys. Lett.* **33**, 653 (1978)
5. F.A. Padovani and R. Stratton, *Solid State Electron* **9**, 695 (1966)
6. E.H. Rhoderick, *Metal-Semiconductor Contacts*, Clarendon Press, Oxford, 1980.
7. E.O. Kane, *Physics of III-V Compounds 1*, Academic Press, New York, 1966.
8. Y. Betser, A. Fenigstein, J. Salzman, D. Rotter, *IEEE Journal of Quantum Electronics*. **30**, 1995 (1994).
9. A.T. Fromhold, *Quantum Mechanics for Applied Physics and Engineering*, Academic Press, New York, 1981.
10. J. Crofton and P.A. Barnes, *J. Appl. Phys.* **69** (11), 7660 (1991).
11. S. Strite and H. Morkoc, *J. Vac. Sci. Technol.* **B 10**(4), 1237 (1992).
12. J.M. Woodall, J.L. Freeouf, G.D. Pettit, T. Jackson and P. Kirchner, *J. Vac. Sci. Technol.* **19** (3), 626 (1981)
13. M.E. Lin, F.Y. Huang, H. Morkoc, *Appl. Phys. Letts.*, **64** (19), 2557 (1994)
14. C.P. Foley and T.L. Tansley, *Phys. Rev. B*, **33**, No.2, 1430 (1986)

Ohmic contacts to Si-implanted and un-implanted n-type GaN

J. BROWN, J. RAMER, K. ZHENG, L.F. LESTER, S.D. HERSEE, J. ZOLPER*

Center for High Technology Materials, University of New Mexico, Albuquerque, NM 87131

*Sandia National Laboratories, Albuquerque, NM 87

ABSTRACT

We report on ohmic contacts to Si-implanted and un-implanted n-type GaN on sapphire. A ring shaped contact design avoids the need to isolate the contact structures by additional implantation or etching. Metal layers of Al and Ti/Al were investigated. On un-implanted GaN, post metalization annealing was performed in an RTA for 30 seconds in N₂ at temperatures of 700, 800, and 900°C. A minimum specific contact resistance (r_c) of $1.4 \times 10^{-5} \Omega\text{-cm}^2$ was measured for Ti/Al at an annealing temperature of 800°C. Although these values are reasonably low, variations of 95% in specific contact resistance were measured within a 500 μm distance on the wafer. These results are most likely caused by the presence of compensating hydrogen. Specific contact resistance variation was reduced from 95% to 10% by annealing at 900°C prior to metalization. On Si-implanted GaN, un-annealed ohmic contacts were formed with Ti/Al metalization. The implant activation anneal of 1120°C generates nitrogen vacancies that leave the surface heavily n-type, which makes un-annealed ohmic contacts with low contact resistivity possible.

INTRODUCTION

Obtaining stable, low resistance ohmic contacts is essential for the fabrication of most practical semiconductor devices. For GaN and other highly ionic semiconductors, evidence suggests that contact barrier heights depend directly on the difference between the work function of the metal and the electron affinity of the semiconductor [1]. Consequently, of the common metals used in semiconductor processing, we expect Al and Ti to form ohmic contacts to n-type GaN fairly easily due to their relatively small work functions [2,3]. The quality of ohmic contacts, however, will be greatly influenced by the condition of the semiconductor surface prior to metalization as well as heat treatment of the material after the contacts have been formed. In this paper we present the results of our investigations of the formation of ohmic contacts to Si-implanted and un-implanted n-type GaN. Surface preparation, pre-metalization and post-metalization treatments are discussed.

EXPERIMENT

Annealed Ohmic Contacts to Undoped GaN

Metal was deposited by evaporation at 5×10^{-7} - 10^{-6} Torr. Ring shaped contacts were then formed using a photolithography and liftoff process. The ring shaped contact design avoids the need to isolate the contact structures by additional implantation or etching. For a large ring to gap-spacing ratio, the ring contact geometry reduces to the standard transmission line model (TLM) structure [4]. For practical ring radii (200 μm) and spacings (5-45 μm), though, small, geometrical correction factors are necessary to compensate for the difference between the TLM and ring layouts.

Our studies indicate that, while Al forms an ohmic contact to undoped n-type GaN, the specific contact resistance for this metalization is very high. This is probably due to the presence of an oxide layer on the GaN surface which reacts with the Al to form insulating Al_2O_3 . Furthermore, Al on GaN 'balls' or forms into puddles when annealed at temperatures above the melting pointing of Al (660°C) requiring the presence of either a 'wetting' metalization below or a 'capping' metalization above the Al. Consequently, contacts of Al only to GaN are undesirable.

Metal layers of Ti/Al deposited on $4\text{ }\mu\text{m}$ thick undoped, n-type GaN [5] were also investigated with Ti thicknesses of 150, 300, and $500\text{ }\text{\AA}$ covered with $2000\text{ }\text{\AA}$ of Al. Ohmic contacts to undoped n-type GaN are obtained with each of the above Ti/Al metalizations after rapid thermal annealing (RTA). As-deposited metal contacts exhibited Schottky behavior or extremely large contact resistance. Heat treatment was performed in a RTA system for 30 seconds in N_2 at temperatures of 700, 800, and 900°C . Lower temperatures were investigated, but gave r_c results that were generally inferior. The specific contact resistance varies with annealing temperature as indicated in Fig. 1 below. A minimum specific contact resistance of $1.4 \times 10^{-5}\text{ }\Omega\text{-cm}^2$ is reached with the $300\text{ }\text{\AA}$ Ti metalization at an annealing temperature of 800°C . From our study, the optimum titanium thickness is $300\text{ }\text{\AA}$. We do not observe any significant alloying of the annealed Ti/Al metalization into the GaN as measured by surface profilometry after stripping of the metalization in HF and H_2SO_4 .

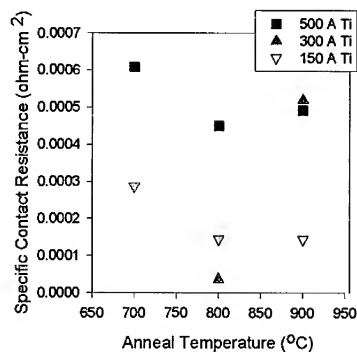


Figure 1. Specific Contact Resistance, r_c , vs. Anneal Temp for three different Ti thicknesses in a Ti/Al metalization on GaN. The Al thickness is $2000\text{ }\text{\AA}$. The optimum Ti thickness is $300\text{ }\text{\AA}$ and the optimum anneal temperature is 800°C .

Variation in specific contact resistance across samples is observed for all of the metalizations examined. Typical TLM data that we obtained is shown in Fig. 2. In this figure, the data denoted by circles was taken from a site adjacent to the site designated by squares. The sheet resistances (R_{sh}), which are found from the slopes of the lines through the data, are the same for both sites, but the contact resistances, which are found from the intercepts, differ significantly. The contact resistance is indicative of properties of the surface, whereas the sheet resistance is a characteristic of the bulk semiconductor. Although it is not immediately obvious why the surface electrical properties should vary so dramatically, any variation at the surface will probably not be reflected by sheet resistance measurements due to the thick GaN layer ($4\text{ }\mu\text{m}$). Donor-compensating hydrogen in the GaN [6] and inadequate pre-metalization surface treatment are two conditions that could have an adverse effect on the GaN surface. Since improvement in the

contact resistance is observed using a NH_4OH :DI pre-metalization dip, our surface treatment is probably sufficient. This fact leaves hydrogen as the probable cause of the non-uniformity, a conclusion supported by the noticeable drop in sheet resistance after further annealing at 800°C . In his studies of p-type GaN grown by MOCVD, Nakamura [7] found that 20 min. anneals in nitrogen at temperatures above 500°C were effective in driving out H_2 and improving the conductivity (sheet resistance) of GaN. It is reasonable to assume that since the annealing time used in our work is only 30 sec. that a higher temperature would be needed to drive out the hydrogen.

The reason for the drop in contact resistance as the anneal temperature is increased from 700 to 800°C is not certain. Titanium, which is known to getter hydrogen [8], could be acting as a catalyst in the removal of H_2 , which would in turn increase the electron concentration at the surface and reduce the contact resistance. Alternatively, r_c could be decreasing due to a deeper alloy of the Ti/Al metalization into the semiconductor.

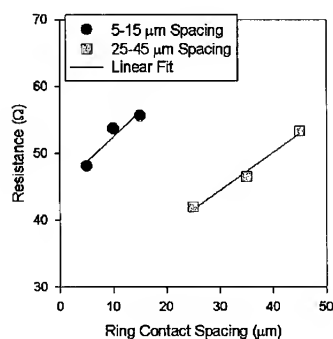


Figure 2. Resistance between ring-shaped contacts as a function of the gap between contacts. Variation in the contact resistance can be seen from the y-axis intercepts and slopes of the fitted lines, respectively.

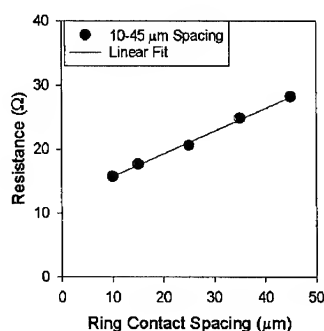


Figure 3. The resistance between contacts vs. the spacing for GaN sample pre-annealed at 900°C for 30 sec. before Ti/Al metalization. The improvement in uniformity can be seen by the fact that the various gap spacings fall on the same line.

Due to the belief that hydrogen is present in the material, we decided to investigate the influence of high temperature annealing of the wafer prior to metal evaporation. At the very least, this technique should liberate hydrogen near the surface and increase the conductivity in that region. Without the anneal, it is possible that the contact metalization itself may trap the hydrogen in the GaN. The results of our pre-metalizations anneal study are shown in Fig. 3. Both the uniformity of the specific contact resistance across the sample and the curve fit to the data are significantly improved by pre-annealing the GaN piece at 900°C in flowing nitrogen. This supports our theory that hydrogen compensation can influence ohmic contact formation in undoped GaN. Secondary ion mass spectroscopy (SIMS) analysis of our GaN material was performed to determine the hydrogen concentration. However, the hydrogen concentration that we expect to be present in the material (about 10^{17} cm^{-3} or lower) is extremely difficult to detect by this or any other technique and the results were inconclusive.

In subsequent Ti/Al contact experiments on other GaN wafers, we have found that high temperature annealing does not always prevent sheet resistance or contact resistance non-uniformities in undoped GaN. Variations in the material thickness or defect concentration could also be affecting the ohmic contact results. Nevertheless, we treat the pre-anneal as a preliminary step to eliminate unwanted hydrogen given the good chance that it is present in MOCVD-grown GaN.

Non-Annealed Ohmic Contacts to Si Implanted GaN

To obtain more control over the electronic properties of GaN, as opposed to relying on the reproducibility of unintentionally doped GaN, silicon donor implantation has also been studied. In addition, the implant increases the electron concentration at the near surface, therefore improving the tunneling process involved in forming an ohmic contact to n-type GaN. A two-step implant was performed with doses of $5 \times 10^{14} \text{ cm}^{-2}$ and $7.5 \times 10^{14} \text{ cm}^{-2}$ and energies of 40 and 100 keV, respectively on 4 μm thick GaN grown on both a-plane and c-plane sapphire. This double implant is intended to give approximately $3 \times 10^{19} \text{ cm}^{-3}$ donor atom concentration through the first 3500 Å of the material. We expect about 10% activation of the Si donors given previous results on implanted EMCORE material. The implant activation anneal employed a temperature of 1120°C for 15 sec in flowing N_2 .

The sheet resistance of the GaN does not change appreciably after the implant due to the thickness of the epilayer as compared to the implant depth. This ratio is about 10:1. Typical sheet resistances of the a- and c-plane material are about 1500-2000 Ω/square and 6000-7000 Ω/square , respectively.

Our experiments on Si-implanted material show that un-annealed Ti/Al ohmic contacts with low specific contact resistances are possible. The lowest r_c that we obtained for un-annealed contacts is $1.0 \times 10^{-5} \Omega\text{-cm}^2$. This same metalization deposited on un-implanted material yields Schottky or rectifying characteristics when annealing is not used. This result implies that the implantation and/or activation anneal process leaves the top surface of the GaN very heavily n-type. To determine whether the Si donors or the 1120°C anneal are responsible for the high electron concentration at the surface, we compared the contact resistance of a Ti/Al contact on an un-annealed, un-implanted GaN wafer and an 1120°C annealed, but un-implanted sample. The non-alloyed contact on the un-annealed sample was Schottky as usual, but the non-alloyed contact on the 1120°C wafer was ohmic with a contact resistance of $1.3 \times 10^{-3} \Omega\text{-cm}^2$ (see Fig. 6, wafer 110A result). Clearly, the annealing increases the electron concentration at the surface. The most probable mechanism is through desorption of nitrogen [9] from the GaN at high temperature leaving nitrogen vacancies that behave as donors in GaN [10].

After the 1120°C anneal for 15 sec. in N_2 , we do not observe Ga puddled on the surface either optically or in a scanning electron microscope (SEM). If any Ga were left on the surface, however, the contact resistance should be very sensitive to the surface chemical treatment used before metal deposition. A wafer clean that uses a corrosive 1:1 $\text{H}_2\text{SO}_4\text{:H}_2\text{O}_2$ acid etch intended to remove Ga left on the surface after the high temperature anneal does not appear to change the quality of the ohmic contact significantly as shown in Figs. 4 and 5. The r_c results shown in Fig. 4 and 5 also indicate that any potential oxide left by the anneal is better removed by NH_4OH than by HCl .

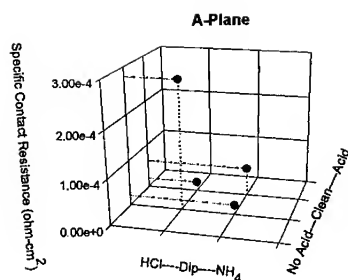


Figure 4. The specific contact resistance of Ti/Al non-alloyed contacts to Si-implanted GaN grown on a-plane sapphire (wafer 184a) as a function of wafer clean (acid-etch or no etch) and the surface treatment (NH₄OH or HCl) just prior to placing the material in the metal evaporator.

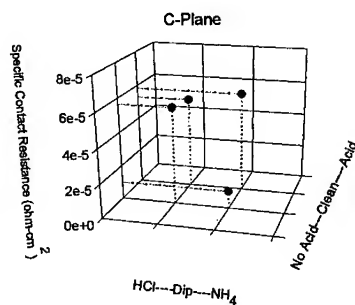


Figure 5. The specific contact resistance of Ti/Al non-alloyed contacts to Si-implanted GaN grown on c-plane sapphire (wafer 184c) as a function of wafer clean (acid-etch or no etch) and the surface treatment (NH₄OH or HCl) just prior to placing the material in the metal evaporator.

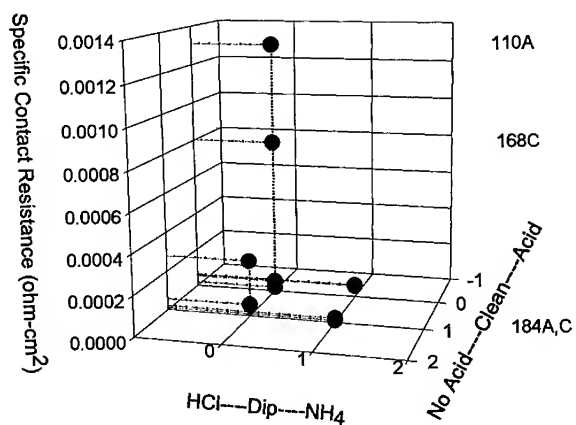


Figure 6. The specific contact resistance data contained in Figs 4 and 5 compared to two other samples. 110A is un-implanted and annealed at 1120°C prior to metalization and 168c is Si implanted and annealed at 1120°C.

CONCLUSIONS

Specific contact resistances of $1.4 \times 10^{-5} \Omega\text{-cm}^2$ have been obtained for a 300 Å Ti/2000 Å Al metalization annealed at 800°C for 30 seconds in N_2 . We have observed that pre-annealing of undoped, n-type GaN at 900°C for 30 seconds improves the uniformity of the specific contact resistance across the material. We attribute this result to release of compensating hydrogen during the high temperature pre-processing anneal. For both Si-implanted and un-implanted GaN, annealing at 1120°C in flowing N_2 for 15 seconds prior to processing yields ohmic contacts for as-deposited (un-annealed) Ti/Al metalizations. This result is explained by the creation of nitrogen vacancies, which are known to behave as donors, at the surface of the GaN. For p-type MOCVD grown III-N's where a high temperature anneal is commonly used to drive out compensating hydrogen, a capping film may be necessary to avoid compensation of acceptors due to nitrogen vacancies at the near surface.

ACKNOWLEDGMENTS

This work was supported by the ARPA Optoelectronics Materials Center under grant # MDA 972-94-1-0003, the National Science Foundation under a CAREER grant # ECS-9501785, and Sandia National Laboratories under the SURP program. The portion of this work performed at Sandia National Laboratories was supported by the US Department of Energy under contract no. DE-AC04-94AL85000.

REFERENCES

1. J. S. Foresi, and T. D. Moustakas, *Appl. Phys. Lett.* **62**, 2859 (1993).
2. M. E. Lin, Z. Ma, F. Y. Huang, Z. F. Fan, L. H. Allen, and H. Morkoc, *Appl. Phys. Lett.* **64**, 1003 (1994).
3. S. C. Binari, H. B. Dietrich, G. Kelner, L. B. Rowland, K. Doverspike, and D. K. Gaskill, *Electron. Lett.* **30**, 909 (1994).
4. G. S. Marlow and M. B. Das, *Solid St. Electron.* **25**, 91 (1982).
5. S. D. Hersee, J. Ramer, K. Zheng, C. Kranenberg, K. Malloy, M. Banas, and M. Goorsky, to be published in *J. Of Electronic Materials*, November 1995.
6. J. A. Van Vechten, J. D. Zook, R. D. Horning, and B. Goldenberg, *Jpn. J. Appl. Phys.* **31**, 3662 (1992).
7. S. Nakamura, N. Iwasa, M. Senoh, and T. Mukai, *Jpn. J. Appl. Phys.* **31**, L1258 (1992).
8. J. D. Fast, *Interaction of Metals and Gases*, MacMillan, New York, 1971, Chapter 1.
9. C. J. Sun, P. Kung, A. Saxler, H. Ohsato, E. Bigan, M. Razeghi, and D. K. Gaskill, *J. Appl. Phys.* **76**, 236 (1994).
10. S. Strite and H. Morkoc, *J. Vac. Sci. Technol. B* **10**(4), 1237 (1992).

OHMIC CONTACT FORMATION TO DOPED GaN

L. L. Smith, M. D. Bremser, E. P. Carlson, T. W. Weeks, Jr., Y. Huang*, M. J. Kim*, R. W. Carpenter*, and R. F. Davis

Department of Materials Science and Engineering, North Carolina State University, Raleigh, NC 27695-7907

*Center for Solid State Science, Arizona State University, Tempe, AZ 85287-1704

ABSTRACT

Ohmic contact strategies for n- and p-type GaN have been investigated electrically, chemically, and microstructurally using transmission line measurements, high-resolution EELS and cross-sectional TEM, respectively. The contributions to contact performance from work function differences, carrier concentrations, annealing treatments, and interface metallurgy have been examined. The contact materials of Ti, TiN, Au, and Au/Mg were deposited via electron beam evaporation; Al was deposited via thermal evaporation. As-deposited Al and TiN contacts to highly doped n-GaN were ohmic, with room-temperature specific contact resistivities of $8.6 \times 10^{-5} \Omega\text{-cm}^2$ and $2.5 \times 10^{-5} \Omega\text{-cm}^2$ respectively. The Ti contacts developed low-resistivity ohmic behavior as a result of annealing; TiN contacts also improved with further heat treatment. For p-GaN, Au became ohmic with annealing, while Au/Mg contacts were ohmic in the as-deposited condition. The performance, structure, and composition of different contact schemes varied widely from system to system. An integrated analysis of the results of this study is presented below and coupled with a discussion of the most appropriate contact systems for both n- and p-type GaN.

INTRODUCTION

The majority of successful ohmic contact systems that have so far been implemented with the more conventional compound semiconductors such as GaAs and InP have relied upon alloying (liquid-phase reaction) or sintering (solid-phase reaction) via post-deposition annealing treatments, and/or the presence of high carrier concentrations near the interface [1-4]. Another consideration involves the Schottky-Mott-Bardeen (SMB) model of semiconductor interfaces [5,6]. The III-V nitride compounds are more ionically bonded than their phosphide and arsenide counterparts, as a result of larger electronegativity differences between the component elements. According to the observations of Kurtin *et al.* [7], this fact indicates that the barrier heights of contacts to the nitrides should be more dependent on the contact material than is the case with the more conventional and more covalent semiconductors such as Si, GaAs, InP, SiC, etc. [8]. Such behavior has indeed been observed for the metals investigated to date in the work of Foresi and Moustakas [9,10], Hacke *et al.* [11,12], Binari *et al.* [13], and the present authors, and is receiving increasing attention.

Contact metals and processing schemes for the present study were chosen on the basis of the considerations described above. Efforts were made to minimize barrier heights through work function contributions, and to increase carrier concentrations at the contact interfaces through metallurgical reaction and addition of dopant impurities. The nitride-forming metals Al and Ti were compared as contacts to n-GaN, and a comparison was also made between elemental Ti and TiN as a contact metal. The contact metals deposited on p-GaN were Au and a Au/Mg/Au multilayer contact.

EXPERIMENTAL

The substrates used for III-nitride film growth were 6H-SiC wafers supplied by Cree Research, Inc. Two growth methods have been used for the deposition of III-N films for these contacts studies: ECR plasma-enhanced gas-source molecular beam epitaxy (MBE) and metal-organic vapor phase epitaxy (MOVPE). The dopants of Ge and Si were introduced via MBE and MOVPE respectively to achieve n-type material. The p-type GaN described here was grown via

MBE, using Mg as the acceptor impurity ($p=1 \times 10^{18} \text{ cm}^{-3}$). Dopant levels and carrier concentrations for the n-GaN films varied. The nitride films were cleaned with a 50:50 HCl:H₂O dip and carefully pulled dry from the solution, prior to deposition of the metals. Any remaining cleaning solution was blown dry with N₂. Where the equipment used for metallization provided the capability, the GaN samples were also thermally desorbed in vacuum at 700°C for 15 min prior to metal deposition.

The Al layers were deposited in a conventional thermal evaporator; the Ti, Au and Au/Mg/Au layers were deposited by means of electron beam evaporation. Titanium nitride was grown by means of ion beam-assisted deposition (IBAD), using electron beam evaporation of Ti and purified N₂ activated by a Kaufman-type ion gun. Both the Ti and the TiN growth were performed at a substrate temperature of 350°C and a deposition rate of 10-15 Å/min. All other metallizations were performed at room temperature. After deposition, I-V measurements were taken using tungsten probe tips and an HP 4145C Semiconductor Parameter Analyzer. Annealing treatments for most of the samples were performed in a flowing N₂ atmosphere at successively higher temperatures using a Heatpulse 410 rapid thermal annealing (RTA) furnace. The TLM measurements were taken using the method described by Reeves and Harrison [14]. The mathematical assumptions and pattern geometry inherent in this model yield values for ρ_c that represent an upper limit; thus, the measured values are conservative assessments of performance. Analytical and high-resolution transmission electron microscopy were performed on the contact-GaN interfaces; conditions for the study were reported previously [15].

RESULTS AND DISCUSSION

Al contacts on n-GaN

Aluminum contacts (single Al layers 2500 Å thick) deposited on Ge-doped n-GaN ($n=5 \times 10^{19} \text{ cm}^{-3}$) were ohmic and exhibited low contact resistivity in the as-deposited condition. The I-V relationship of the Al contacts on Ge:GaN was completely linear; from TLM measurements, the contact resistivity ρ_c at room temperature was found to be $8.6 \times 10^{-5} \Omega \cdot \text{cm}^2$. These results compare very favorably with those reported by Foresi and Moustakas [9,10], and, more recently, Lin *et al.* [16], who obtained ρ_c values of $1 \times 10^{-3} \Omega \cdot \text{cm}^2$ and approximately $1 \Omega \cdot \text{cm}^2$ respectively. In both cases, the carrier concentration of the unintentionally doped n-type GaN used was $\sim 10^{17} \text{ cm}^{-3}$. However, as noted above, the n-GaN films used in the present study for these Al contact measurements were highly doped and thus had characteristics favorable for low-resistivity contact formation. The samples were annealed at 200, 350, 450, 550, and 650°C for 3 min at each temperature; TLM measurements were performed after every heat treatment. The effect of this heat treatment on the contact resistivity is plotted in Figure 1. From room temperature through 450°C, the behavior of the Al contacts was essentially unchanged from the as-deposited condition. However, the 550°C and 650°C anneals resulted in an overall increase of contact resistivity, reaching $2 \times 10^{-3} \Omega \cdot \text{cm}^2$ after annealing to 650°C.

The Al film as initially deposited was polycrystalline with quasi-columnar growth, which was oriented randomly with respect to the GaN surface. Annealing resulted in grain growth in the Al layer, but no change in the random orientation with respect to the GaN lattice. In addition, this analysis also revealed that a new phase formed at the Al/GaN interface as a result of heat treatment. Cross-sectional TEM images of the interface, both as-deposited and annealed at 650°C for 3 min, are shown in Figure 2. These second phase particles at the interface consisted of Al and N; they did not form a continuous layer and ranged in size from about 50-800 Å. Smaller particles of the same phase were found farther into the Al layer, about 10-100 Å in size. The appearance of this interfacial phase as a result of annealing correlated with an increase in contact resistivity, which suggests the formation of a higher-resistivity material at the interface, namely AlN [15]. Spectroscopic analysis via EELS revealed the presence of nitrogen in the Al layer, but no appreciable amounts of Ga. Some oxygen was also found in the Al layer, though at this time it is not clear how much of this oxygen originated at the GaN surface prior to metal deposition and how

much of it was incorporated into the Al film during thermal evaporation in a non-UHV environment.

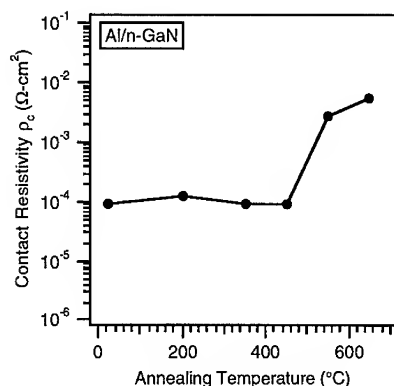


Figure 1. Room-temperature specific contact resistivity, ρ_c , of Al/n-GaN contacts as a function of annealing temperature.

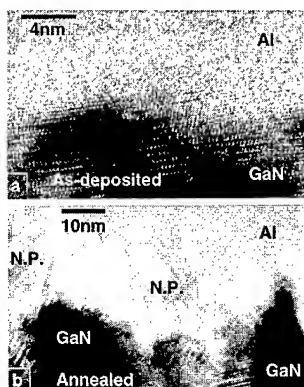


Figure 2. High-resolution TEM images of an Al/GaN interface, (a) as-deposited; (b) annealed at 650°C for 3 min. A new Al and N-containing crystalline phase formed at the Al/GaN interface as a result of annealing. N.P.=new phase.

Ti and TiN contacts on n-GaN

The as-deposited Ti contacts on Si-doped, MOVPE-grown n-GaN ($n=1.2 \times 10^{18} \text{ cm}^{-3}$) exhibited rectifying behavior and high resistance. The TiN contacts deposited on GaN of two different carrier concentrations ($n=1.2 \times 10^{18} \text{ cm}^{-3}$ and $n=7.4 \times 10^{18} \text{ cm}^{-3}$); were ohmic in the as-deposited condition, though the higher-doped samples showed substantially lower resistance in current-voltage measurements. For the lower-doped n-GaN, TLM measurements yielded as-deposited ρ_c values of $650 \Omega\cdot\text{cm}^2$. The very high resistivities in the as-deposited Ti/n-GaN and TiN/n-GaN ($n=1.2 \times 10^{18} \text{ cm}^{-3}$) contacts decreased sharply in response to annealing, as shown in Figure 3. After the 600°C anneal, the Ti contacts lost most of their rectifying character and the overall resistance decreased markedly. With subsequent anneal steps through 900°C, the ρ_c of both contacts dropped substantially; the TiN contacts reached $1.1 \times 10^{-2} \Omega\cdot\text{cm}^2$ and the Ti contacts reached $9.9 \times 10^{-3} \Omega\cdot\text{cm}^2$. The TiN contacts on the more highly doped GaN ($n=7.4 \times 10^{18} \text{ cm}^{-3}$) exhibited low- ρ_c behavior in the as-deposited condition; TLM measurements revealed a low room temperature specific contact resistivity of $2.5 \times 10^{-5} \Omega\cdot\text{cm}^2$. In contrast to the

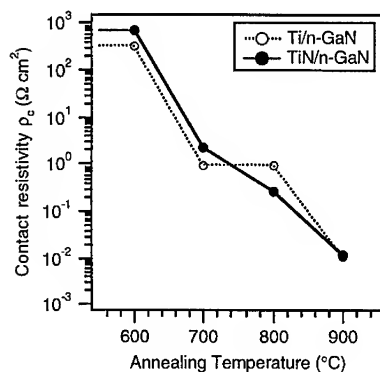


Figure 3. Specific contact resistivity ρ_c of Ti/n-GaN and TiN/n-GaN contacts ($n=1.2 \times 10^{18} \text{ cm}^{-3}$) as a function of annealing temperature, showing substantial decrease in ρ_c as a result of heat treatment.

TiN contacts on the lower-doped GaN, the already low- ρ_c behavior did not change as a result of annealing treatment.

TiN is metallic in electrical behavior, in contrast to the insulating nitride formed by Al. Both AlN and TiN have highly negative free energies of formation and are therefore thermodynamically favored. As described in the preceding section, the nitridation of Al at the contact interface results in increasing resistivity. By comparison, the formation of metallic TiN at the contact interface is expected to improve contact characteristics; a substantial decrease in ρ_c as a function of annealing was indeed observed. The role of Ti nitridation in the formation of low-resistivity Ti-containing contacts to n-GaN has been discussed by Lin *et al.* [16]. The results of the present study indicate that high-temperature annealing benefits both Ti and TiN contacts. The roles played by microstructural changes and loss of N from the GaN at high temperatures are being investigated by means of cross-sectional, high-resolution TEM analysis, currently underway.

Au contacts on Mg:GaN

The as-deposited Au/p-GaN contacts were rectifying. They exhibited linearly ohmic I-V behavior after annealing at sufficiently high temperatures ($>650^\circ\text{C}$). Annealing at 800°C for 10 minutes, after earlier anneals at lower temperatures, resulted in a ρ_c of $53\ \Omega\cdot\text{cm}^2$. This change in contact behavior, shown in Figure 4(a), was associated with some visible roughening of the Au surface, indicative of interfacial roughening, and noticeable intermixing of the metallic elements at the interface was observed in Auger depth-profiling analysis. Cross-sectional microstructural characterization by means of TEM revealed that the Au layer (2500 Å thick) was polycrystalline as-deposited, and while grain growth in the Au film occurred during annealing, no particular crystallographic orientation or relationship was observed between the Au and the GaN.

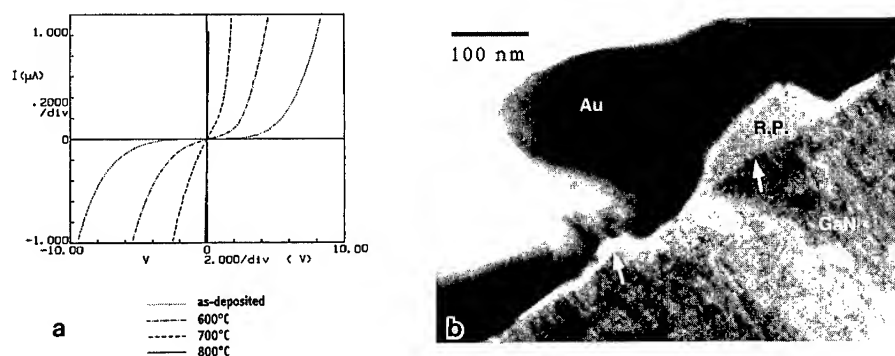


Figure 4. (a) I-V behavior of Au/p-GaN contacts as a function of annealing temperature, showing transition to ohmic behavior. (b) High-resolution X-TEM image of Au/GaN interface, annealed at 800°C for 10 min, showing formation of amorphous phase as a result of high-temperature annealing. R.P. = reaction product.

High-resolution images showed that interfacial reaction did indeed occur as a result of annealing at high temperature. Figure 4(b) shows the formation of an amorphous phase at the annealed Au-GaN interface. In the preparation of TEM specimens, it was observed that there was poor adhesion of the Au to the GaN surface in both the as-deposited and annealed conditions. Some cavities were also seen at the interface, which almost certainly contributed to the poor adhesion. Spectroscopic analysis by means of EELS revealed the presence of nitrogen throughout the Au

layer; compositional characterization of the amorphous regions revealed the presence of Au, Ga, and N.

Au/Mg/Au contacts on p-GaN

A three-layer Au/Mg/Au (320 Å/320 Å/1700 Å) contact system was deposited on Mg-doped GaN by means of electron beam evaporation. In contrast to the Au single-layer contacts, the Au/Mg/Au contacts, having a 320 Å Au layer in direct contact with the GaN surface followed by the Mg layer, were linearly ohmic in the as-deposited condition. Contact resistivity measurements yielded a room-temperature ρ_c of 214 $\Omega\cdot\text{cm}^2$. This behavior remained essentially unchanged after heat treatments of 575°C and 650°C, for 15 s each. After further annealing at 725°C for 15 s, the contacts became substantially more resistive.

As was observed for the Au/p-GaN contact samples, there was poor adhesion of the metal layers to the GaN surface in both the as-deposited and annealed conditions. However, it was possible to obtain some TEM images of the contact interface. Figure 5 shows the presence of Mg metal in direct contact with the GaN in a sample annealed at 725°C for 15 s. In the as-deposited contact, the initial 320 Å Au layer was found to be continuous, thus the change in microstructure was a result of the annealing process. While Mg serves as an acceptor impurity in GaN and thus should help to dope the p-GaN surface, elemental Mg metal has a low work function ($\phi_{\text{Mg}}=3.7$ eV) and thus as a contact metal would contribute to a higher barrier at the interface in comparison to the high work function Au ($\phi_{\text{Au}}=5.3$ eV). This barrier effect is believed to be the cause of the increase in contact resistance as a result of annealing.

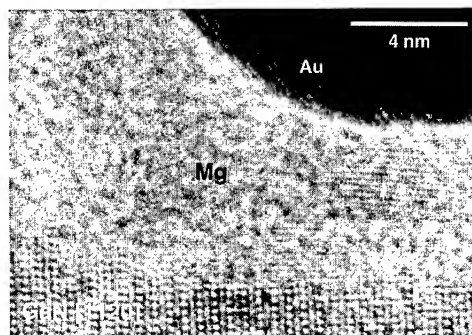


Figure 5. High-resolution TEM image of Au/Mg/Au/p-GaN interface, annealed at 725°C for 15 s, showing the presence of Mg metal in direct contact with the GaN surface.

CONCLUSIONS

The work conducted in this study to date has shown that it is possible to form metal contacts with ohmic, linear I-V behavior to both n-type and p-type GaN films. The Al contacts on highly doped n-type GaN had very good low-resistivity characteristics and remained stable to at least 450°C. At higher temperatures, the ρ_c of the Al contacts increased as a result of interfacial AlN formation. Both the Ti and the TiN contacts to n-GaN ($n=1.2\times10^{18}$ cm^{-3}) showed substantial drops in ρ_c as a result of high-temperature annealing, while TiN on more highly doped GaN ($n=7.4\times10^{18}$ cm^{-3}) showed thermally stable, low- ρ_c behavior. Gold contacts to p-GaN were rectifying in the as-deposited condition, and became linearly ohmic as a result of high-temperature annealing. A multilayered Au/Mg/Au contact to p-GaN was ohmic in the as-deposited condition. However, it increased in resistivity as a result of heat treatment. Further characterization of the Ti and TiN contacts, particularly the microstructural information obtained from cross-sectional TEM analysis, will yield greater understanding of the chemical and structural contributions to low- ρ_c contact behavior. Additional investigation of the addition of dopant impurities to contact metals is recommended. Further progress towards the goal of achieving low- ρ_c performance is needed, especially for p-type GaN.

ACKNOWLEDGEMENTS

The authors express their thanks to C. Wang and J. O'Sullivan (NCSU) for helpful discussions and assistance with the deposition processes, and to CREE Research for supplying the SiC wafers used in this work. This research was supported by the Office of Naval Research, Contract No. N00014-92-J-1720 (NCSU), and the National Science Foundation, Grant DMR-91-15680 (ASU).

REFERENCES

1. V.L. Rideout, *Solid-St. Electron.* **18** 541 (1975).
2. R. Williams, *Modern GaAs Processing Techniques* (Artech House, Norwood, MA, 1990) pp. 211-227.
3. T. C. Shen, G. B. Gao, H. Morkoç, *J. Vac. Sci. Technol. B* **10**(5) 2113 (1992).
4. E.D. Marshall and M. Murakami, in *Contacts to Semiconductors*, edited by L.J. Brillson (Noyes, Park Ridge, NJ, 1993) pp.1-66.
5. H.K. Henisch, *Semiconductor Contacts*, (Clarendon Press, Oxford, 1984) pp. 43-71.
6. E.H. Rhoderick and R.H. Williams, *Metal-Semiconductor Contacts*, 2nd ed. (Oxford University Press, New York, 1988), pp. 11-17.
7. S. Kurtin, T.C. McGill and C.A. Mead, *Phys. Rev. Lett.* **22**(26) 1433 (1969).
8. L.L. Smith and R.F. Davis, in *Properties of Group III Nitrides*, EMIS DataReview Series No. 11, ed. by J.H. Edgar (INSPEC, Institution of Electrical Engineers, London, 1994) pp. 288-292.
9. J.S. Foresi, M.S. Thesis, Boston University, 1992.
10. J.S. Foresi and T.D. Moustakas, *Appl. Phys. Lett.* **62**(22) 2859 (1993).
11. P. Hacke, T. Detchprohm, K. Hiramatsu, and N. Sawaki, *Appl. Phys. Lett.* **63**(19) 2676 (1993).
12. M.R.H. Khan, T. Detchprohm, P. Hacke, K. Hiramatsu, and N. Sawaki, *J. Phys. D* **28** 1169 (1995).
13. S.C. Binari, H.B. Dietrich, and G. Kelner, *Electronics Lett.* **30**(11) 909 (1994).
14. G.K. Reeves and H.B. Harrison, *IEEE Electron Device Lett.* **EDL-3** 111 (1982).
15. Y. Huang, L. Smith, M. J. Kim, R. W. Carpenter and R. F. Davis in *Evolution of Thin-Film and Surface Structure and Morphology*, edited by B. G. Demczyk, E. D. Williams, E. Garfunkel, B. M. Clemens, and J. E. Cuomo (Mat. Res. Soc. Proc. **355**, Pittsburgh, PA, 1995) pp. 433-439.
16. M.E. Lin, Z. Ma, F.Y. Huang, Z.F. Fan, L.H. Allen, and H. Morkoç, *Appl. Phys. Lett.* **64**(8) 1003 (1994).

Part XI
Devices

FABRICATION AND PROPERTIES OF AlGaIn/GaInN DOUBLE HETEROSTRUCTURE GROWN ON 6H-SiC(0001)_{Si}

Hiroshi AMANO, Shigetoshi SOTA, Masaki NISHIKAWA, Masato YOSHIDA, Makoto KAWAGUCHI, Masahiro OHTA, Hiromitsu SAKAI and Isamu AKASAKI
Department of Electrical and Electronic Engineering, Meijo University, 1-501 Shiogamaguchi, Tempaku-ku, Nagoya 468, Japan

ABSTRACT

AlGaIn/GaInN double heterostructures (DH) were fabricated by metalorganic vapor phase epitaxy on the (0001)_{Si} 6H-SiC substrate. A cleaved edge shows a very flat surface with roughness on the order of one monolayer. Stimulated emission and laser action from the UV to blue region was observed by optical pumping at room temperature (RT). The threshold power density was 27KW/cm² which is smaller than that of the same structure grown on a sapphire (0001) substrate by a factor of four. A AlGaIn/GaInN DH UV light emitting diode, using undoped GaInN is fabricated. The power efficiency and spectra width of this LED is comparable or superior to that of an LED having the same structure but grown on sapphire.

INTRODUCTION

Special attention is paid to the group III nitrides because of their large and direct band-gaps ranging from 1.9eV to 6.2eV. Applications as new light sources and detectors in the short wavelength region are expected. Moreover, they are promising for application as high-power microwave devices because they also have high-thermal conductivity and large electron saturation velocity.

Significant pioneering work has been done in the early 1970s by Maruska and Tietjen [1], Pankove [2], and Maruska et al. [3] on the crystal growth, the characterization of basic properties, and the fabrication of the first MIS-type blue light emitting diode (LED) of GaN.

However, the difficulty in growing high-quality films due to the lack of substrate materials with lattice constant and thermal expansion coefficients close to those of group III nitrides, and the difficulty in obtaining p-type films have long prevented their use.

In 1986, we succeeded in growing high-quality GaN on sapphire substrate by metalorganic vapor phase epitaxy (MOVPE) using a low-temperature deposited AlN buffer layer [4]. Low-temperature deposited GaN buffer layer also showed similar effect [5]. In 1989, p-type GaN was realized for the first time by low-energy electron beam irradiation (LEEBI) treatment of MOVPE-grown Mg-doped highly resistive film [6]. P-type GaN has also been obtained by thermal treatment in hydrogen-free atmosphere [7]. Hydrogen passivation of the doped Mg is proposed [7-9].

Based upon the above mentioned findings together with the use of alloys to control the emission wavelength [10], bright blue light emitting diodes (LED) composed of group III nitrides have become commercially available [11-14].

One of the next steps may be the realization of laser diodes (LD). Dingle et al. reported, for the first time, stimulated emission (SE) and laser action by optical pumping from a GaN needle crystal at 4.2K with the threshold power density (P_{th}) of 0.3MW/cm² [15]. Cingolani et

al. reported the SE from a GaN needle crystal and epitaxial layers at up to 120K [16], with a P_{th} of about $3\text{MW}/\text{cm}^2$. They emphasized the origin of the SE is electron hole plasma (EHP). Some of the present authors reported the first room temperature SE from epitaxial GaN film grown on sapphire using an AlN buffer layer with P_{th} of $0.7\text{MW}/\text{cm}^2$ [17], and also claimed in the following papers that P_{th} can be reduced by using the double heterostructure (DH) for optical and carrier confinement [18-21]. In the case of GaN grown on sapphire, it is difficult to observe mode separation of the Fabry-Perot resonator due to the difficulty in fabricating resonator mirrors by cleavage. Yang et al. [22] reported mode separation in SE from GaN grown on sapphire. They made the resonator mirrors by polishing. Very recently, Zubrilov et al. [23] used $6\text{H-SiC}(0001)_{Si}$ as the substrate, from which, it is easy to make edge mirrors by cleavage, and observed the mode separation. Unfortunately, P_{th} for SE is higher than that of GaN grown on sapphire.

In this paper, we fabricate a group III nitride based DH for the reduction of P_{th} for SE and characterize the properties of edge mirrors. We also fabricate a DH LED to characterize the performance of the device on 6H-SiC .

EXPERIMENTS

Figure 1 schematically shows the structure of the DH. Mechanically polished $6\text{H-SiC}(0001)_{Si}$ is used as the substrate. TMGa, TMAI and TMIn were used as the organometallic source gases, while the NH_3 was used as the nitrogen source gas, respectively.

At first, an AlN layer about $0.1\mu\text{m}$ is grown. The effects of the AlN buffer layer on the growth of GaN on $6\text{H-SiC}(0001)$ had been already reported by T.W.Weeks,Jr., et al. [24] and F.A.Ponce et al. [25].

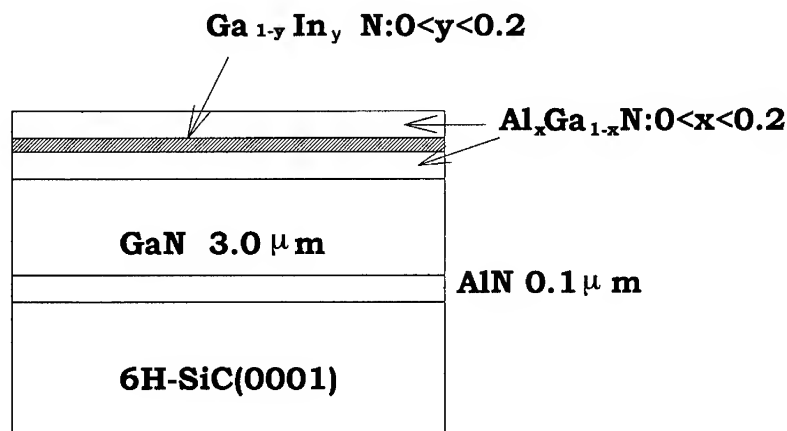


Fig.1 Structure of the DH for optical pumping measurement.

After growing undoped GaN layer about 2 μm thick, an $\text{Al}_x\text{Ga}_{1-x}\text{N}/\text{Ga}_{1-y}\text{In}_y\text{N}/\text{Al}_x\text{Ga}_{1-x}\text{N}$ DH was grown. The density of threading dislocation is about $2 \times 10^8 \text{cm}^{-2}$, which is comparable structures grown using an AlN buffer layer on the sapphire substrate.

Figure 2 shows a cross sectional transmission electron micrograph of the GaN/ $\text{Ga}_{0.9}\text{In}_{0.1}\text{N}$ double heterostructure. A clear and flat interface between GaN and GaInN can be observed. Full width at half maximum of the double crystal X-ray rocking curve from (0002) plane of GaN grown on 6H-SiC is about 116sec, which is almost the same as that of GaN grown on sapphire.

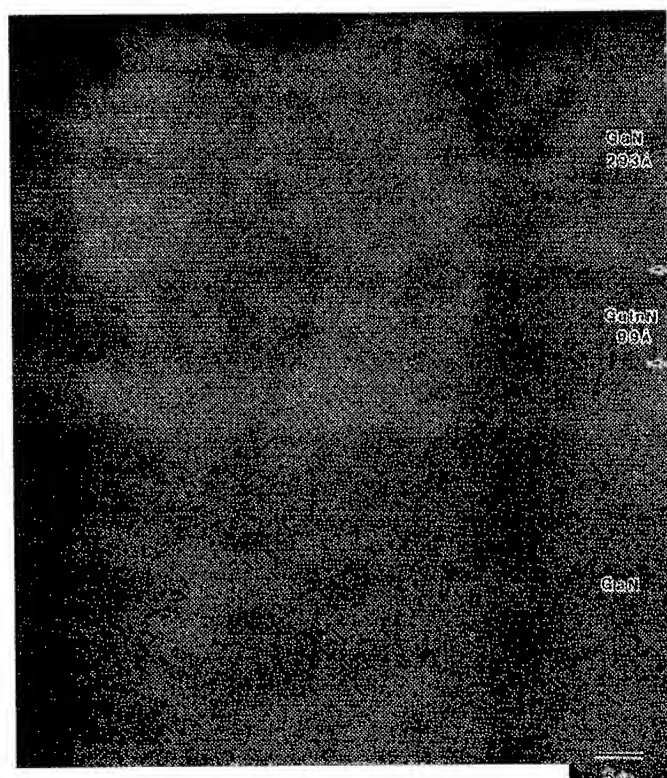


Fig.2 Cross sectional TEM photograph of the DH grown on 6H-SiC. InN molar fraction in GaInN active layer is 0.1.

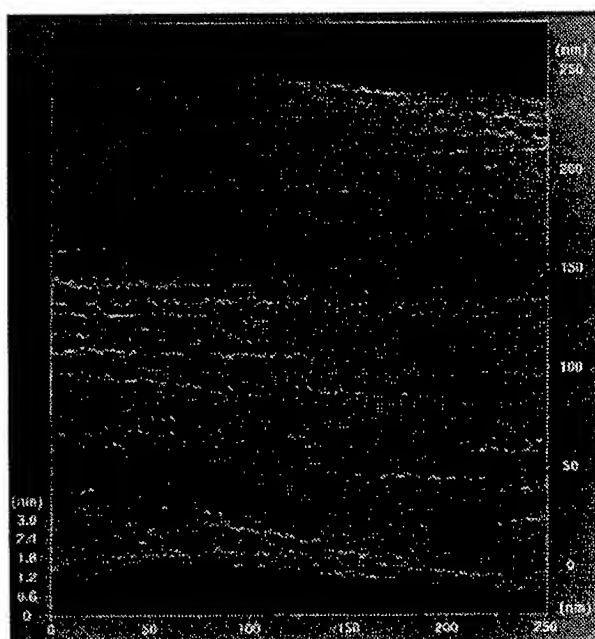


Fig. 3 AFM image of the cleaved edge of GaN grown on 6H-SiC.

Then the wafers were cut into narrow bars. The width of the bar is 0.5 to 1.0mm. Edge mirrors were made by cleavage. The cleaved face is $(10\bar{1}0)$ for both group III nitride and 6H-SiC. Flatness of the cleaved edge was characterized by atomic force microscopy (AFM). Figure 3 shows the AFM image of the cleaved edge of the GaN layer grown on 6H-SiC. The roughness is 0.267nm in average. Small undulation is also observed, the height of the peak to valley is 3 monolayers in maximum. From this result, it can be said that mirror facet is achieved by cleavage in case of 6H-SiC substrate.

Optical pumping was performed at room temperature using pulsed nitrogen laser with maximum power density of $0.2\text{MW}/\text{cm}^2$ as the excitation source. Neutral density filters were used to control the excitation power density. Fig.4 shows the configuration of the measurement of SE.

Figure 5 schematically shows the structure of the DH LED. In this case, a Si-doped $\text{Al}_{0.2}\text{Ga}_{0.8}\text{N}$ layer was used as the intermediate layer between the 6H-SiC and the nitride, thus making an electrical connection between the 6H-SiC and the nitride.

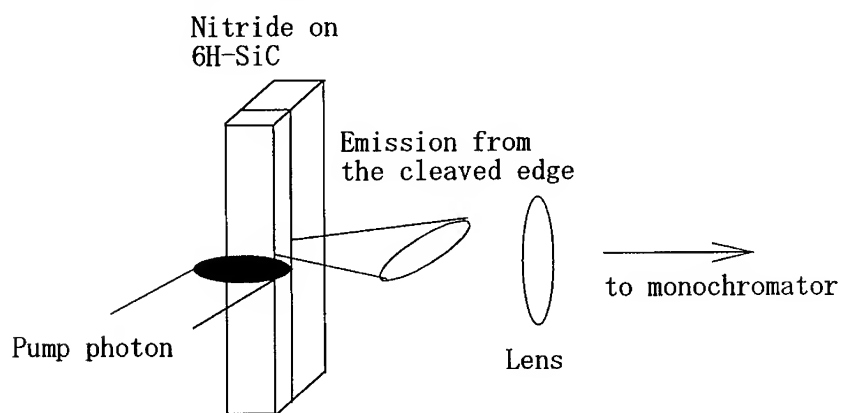


Fig.4 Configuration to measure the lasing characteristics of DH on 6H-SiC.

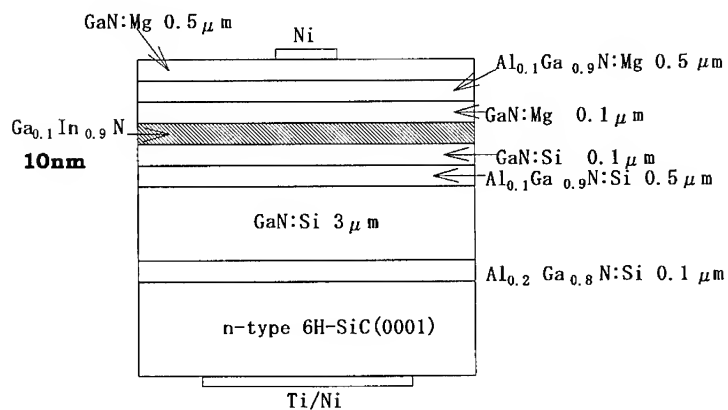


Fig.5 Structure of the DH LED.

RESULTS

Figures 6(a) and (b) show the spectra from the cleaved edge of the DH with different InN molar fractions in the active layer [26,27]. The excitation power density is $0.2\text{MW}/\text{cm}^2$ in both cases. Strong and narrow SE's are observed overlapped with the wide spontaneous emission. Beam divergence is very roughly $20^\circ \times 40^\circ$. Mode separation is also observed. The wavelength difference between mode is about 0.03nm and 0.02nm for fig.6 (a) and fig.6 (b), respectively, which are in close agreement with the resonator length and the refractive indices of DH. In fig.6(a), another wide mode with difference of about 0.5nm is also observed, which may be caused by resonance between cracks [22].

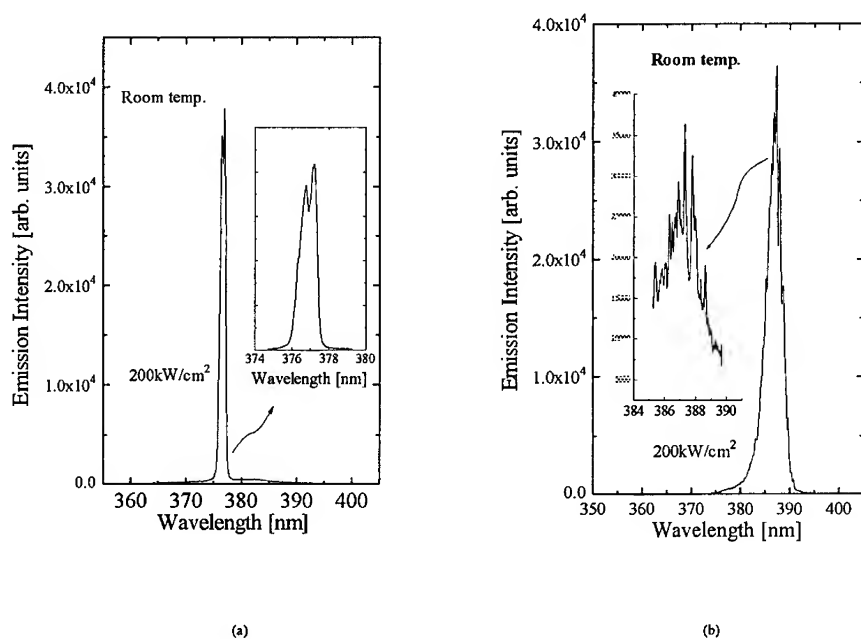


Fig.6 Spectra of SE from DH with low InN content of about 0.07(a), and medium InN content of about 0.1(b).

Figure 7 shows the dependence of the emission power from the DH of fig.4(a) on the excitation power density. Mode separation as shown in figs.6(a) and (b) and the steep rise of the emission power above P_{th} suggests that lasing might be present but a better clarified mode structure and a study of the far field pattern would be needed to verify lasing.. The P_{th} is $27\text{KW}/\text{cm}^2$, which is smaller than that from the same structure grown on sapphire (0001) by a

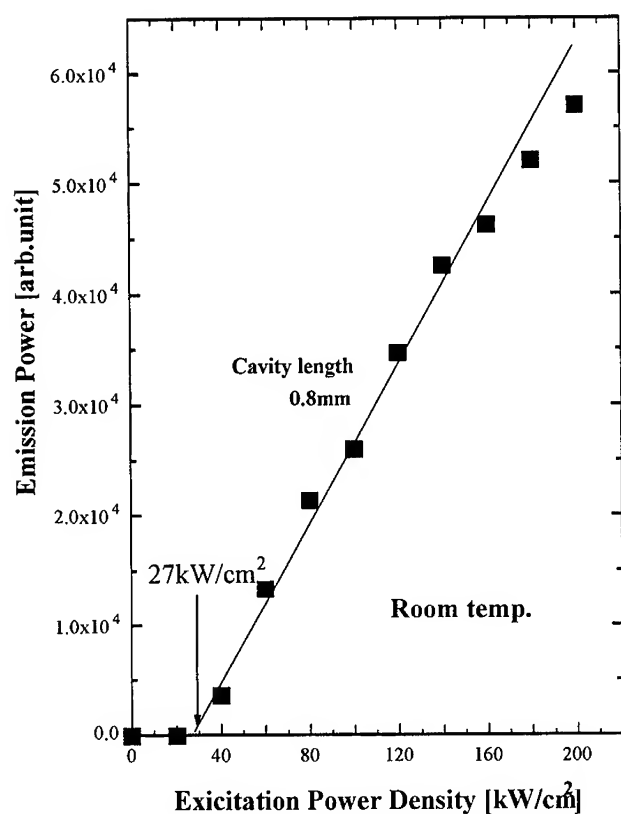


Fig.7 Intensity of total photon from DH as a function of excitation power density.

factor of four [28]. The corresponding current density is $7.4\text{KW}/\text{cm}^2$, which is realizable for current injection.

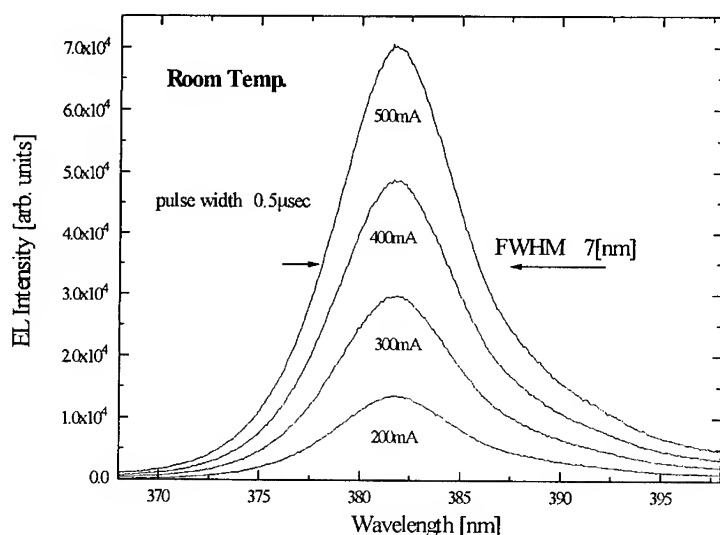


Fig. 8 EL spectra of DH LED shown in fig.5.

Figure 8 shows the EL spectrum at RT from DH LED shown in Fig.5. The power efficiency of this LED is 2-3%, which is comparable to those of LED having the same structure grown on sapphire. The spectrum width is about 7nm, which is close to or narrower than that of LED grown on sapphire.

CONCLUSION

High-quality group III nitride based DH can be grown on $6\text{H-SiC}(0001)_{\text{Si}}$ by MOVPE using AlN intermediate layer. Very low-threshold stimulated emission and laser action by optical pumping can be observed at room temperature. High performance DH LED is also fabricated. Therefore, 6H-SiC is promising as the substrate of the laser diode based on group III nitride.

ACKNOWLEDGEMENTS

This work was partly supported by the Ministry of Education, Science and Culture of Japan(contract Nos 06452114, 07505012 and 07650025), Research Foundation for Electrotechnology of Chubu, Nissan Science Foundation, Iketani Science and Technology Foundation and Daiko Foundation.

REFERENCES

1. H. P. Maruska and J. J. Tietjen, Appl. Phys. Lett., **15**, p.327 (1969).
2. J. I. Pankove, E. A. Miller, D. Richman and J. E. Berkeyheiser, J. Lumin., **4**, p.63 (1971).
3. H. P. Maruska, W. C. Rhines and D. A. Stevenson, Mat. Res. Bull., **7**, p.777(1972).
4. H. Amano, N. Sawaki, I. Akasaki and Y. Toyoda, Appl. Phys. Lett., **48**, p.353(1986).
5. S. Nakamura, Jpn. J. Appl. Phys., **30**, p.L1705 (1991).
6. H. Amano, M. Kito, K. Hiramatsu and I. Akasaki, Jpn. J. Appl. Phys., **28**, p.L2112(1989).
7. S. Nakamura, N. Iwasa, M. Senoh and T. Mukai, Jpn. J. Appl. Phys., **31**, p.1258(1992).
8. J. A. Van Vechten, J. D. Zook, R. D. Horning and B. Goldenberg, Jpn. J. Appl. Phys., **31**, p.3662(1992).
9. M. S. Brandt, J. W. Ager III, W. Götz, N. M. Johnson, J. S. Harris, R. J. Molnar and T. D. Moustakas, Appl. Phys. Lett., **64**, p.2264(1994).
10. N. Yoshimoto, T. Matsuoka, T. Sasaki and A. Katsui, Appl. Phys. Lett., **59**, p.2251(1991).
11. S. Nakamura, T. Mukai and M. Senoh, Appl. Phys. Lett., **64**, p.1687(1994).
12. S. Nakamura, T. Mukai and M. Senoh, J. Appl. Phys., **76**, p.8189(1994).
13. S. Nakamura, M. Senoh, N. Iwasa and S. Nagahata, Jpn. J. Appl. Phys., **34**, p.L797(1995).
14. M. Koike, N. Shibata, H. Kato, S. Yamasaki, N. Koike, H. Amano and I. Akasaki, Abstract of Topical Workshop on III-V Nitrides, Nagoya, Japan, September, p.C-2, (1995).
15. R. Dingle, K. L. Shaklee, R. F. Leheny and R. B. Zetterstrom, Appl. Phys. Lett., **19**, p.5(1971).
16. R. Cingolani, M. Ferrara and M. Lugara, Solid State Commun., **60**, p.705(1986).
17. H. Amano, T. Asahi and I. Akasaki, Jpn. J. Appl. Phys., **29**, p.L205(1990).
18. H. Amano, N. Watanabe, N. Koide and I. Akasaki, Jpn. J. Appl. Phys., **32**, L1000(1993).
19. H. Amano, T. Tanaka, Y. Kunii, K. Kato, S. T. Kim and I. Akasaki, Appl. Phys. Lett., **64** p.1377(1994).
20. S. T. Kim, H. Amano, I. Akasaki and N. Koide, Appl. Phys. Lett., **64**, p.1535(1994).
21. S. T. Kim, T. Tanaka, H. Amano and I. Akasaki, Mater. Sci. Eng., **B26**, p.L5(1994).
22. X. H. Yang, T. J. Schmidt, W. Shan, J. J. Song and B. Goldenberg, Appl. Phys. Lett., **66**, p.1(1995).
23. A. S. Zubrilov, V. I. Nikolaev, D. V. Tsvetkov, V. A. Dmitriev, K. G. Irvine, J. A. Edmond and C. H. Carter, Jr., Appl. Phys. Lett., **67**, p.533(1995).
24. T. W. Weeks, Jr., M. D. Bremser, K. S. Ailey, E. Carlson, W. G. Perry and R. F. Davis, Appl. Phys. Lett., **67**, p.401(1995).
25. F. A. Ponce, B. S. Krusor, J. S. Major, Jr., W. E. Plano and D. F. Welch, Appl. Phys. Lett., **67**, p.410(1995).
26. I. Akasaki and H. Amano, Proc. Int. Symp. Comp. Semicond. 22, Cheju, Korea, August 1995 (to be published).
27. I. Akasaki and H. Amano, 6th Int. Conf. SiC and Related Mater., Kyoto, Japan, September, 1995 (to be published).
28. I. Akasaki, H. Amano, N. Koide, M. Kotaki and K. Manabe, Physica B, **185**, p.428(1993).

InGaN LIGHT-EMITTING DIODES WITH QUANTUM-WELL STRUCTURES

SHUJI NAKAMURA

R&D Department, Nichia Chemical Industries, Ltd.,
491 Oka, Kaminaka, Anan, Tokushima 774, Japan
e-mail: shuji@nichia.co.jp

ABSTRACT

InGaN single-quantum-well-structure (SQW) light-emitting diodes (LEDs) with an emission wavelength between violet and orange were fabricated. The maximum on-axis luminous intensity of green LEDs was 12 cd and the external quantum efficiency was as high as 6.3 % at a forward current of 20 mA, while those of blue LEDs were 2 cd and 9.1 %, respectively. The peak wavelength and the full width at half-maximum of the green LEDs were 520 nm and 30 nm, respectively, while those of blue LEDs were 450 nm and 20 nm, respectively. The color of green InGaN SQW LEDs was greener than those of conventional GaP and AlInGaP LEDs.

INTRODUCTION

Much research has been done on high-brightness blue light-emitting diodes (LEDs) and laser diodes (LDs) for use in full-color displays, full-color indicators and light sources for lamps with the characteristics of high efficiency, high reliability and high speed. For these purposes, II-VI materials such as ZnSe [1], SiC [2] and III-V nitride semiconductors such as GaN [3] have been investigated intensively for a long time. However, it was impossible to obtain high-brightness blue LEDs with brightness over 1 cd and reliable LDs. Recent research on III-V nitrides has paved the way for the realization of high-quality crystals of GaN, AlGaIn and GaInN, and of p-type conduction in GaN and AlGaIn [4]. High-brightness blue LEDs have been fabricated on the basis of these results, and luminous intensities over 2 cd have been achieved [5]. These LEDs are now commercially available. In order to obtain blue and blue-green emission centers in these InGaIn/AlGaIn double-heterostructure (DH) LEDs, Zn doping into the InGaIn active layer was performed. Although these InGaIn/AlGaIn DH LEDs produced a high-power light output in the blue and blue-green region with a broad emission spectrum (full width at half-maximum (FWHM)=70nm), green or yellow LEDs which have peak wavelengths longer than 500 nm have not been fabricated. On the other hand, in conventional green GaP LEDs, the external quantum efficiency is only 0.1 % due to the indirect transition band-gap material and the peak wavelength is 555 nm (yellowish green) [6]. As another material for green emission devices, AlInGaP has been used. The present performance of green

AlInGaP LEDs is an emission wavelength of 570 nm (yellowish green) and maximum external quantum efficiency of 1% [6]. When the emission wavelength is reduced to the green region, the external quantum efficiency drops sharply because the band structure of AlInGaP approaches an indirect transition band structure. Therefore, high-brightness pure green LEDs, which have high efficiency of above 1 % at the peak wavelength between 510-530 nm with a narrow FWHM, have not been commercialized yet. Among II-VI materials, ZnSSe- and ZnCdSe-based materials have been intensively studied for use in green light-emitting devices, and much progress has been made recently. The recent performance of II-VI green LEDs is an output power of 1.3 mW, external quantum efficiency of 5.3 % at 10 mA and peak wavelength of 512 nm [7]. However, the lifetime of II-VI-based devices is still short, which prevents their commercialization at present.

Recently, high-brightness single-quantum-well-structure (SQW) blue, green and yellow InGaN LEDs with luminous intensity above 10 cd for green LEDs have been achieved and now commercialized [8,9]. Here, recent performance of III-V nitride based SQW LEDs is described.

EXPERIMENT

III-V nitride films were grown by the two-flow metalorganic chemical vapor deposition (MOCVD) method. Details of the two-flow MOCVD are described elsewhere [10]. The growth was conducted at atmospheric pressure. Sapphire with (0001) orientation (C face) and of two-inch diameter was used as a substrate. The growth conditions of each layer are described elsewhere [11].

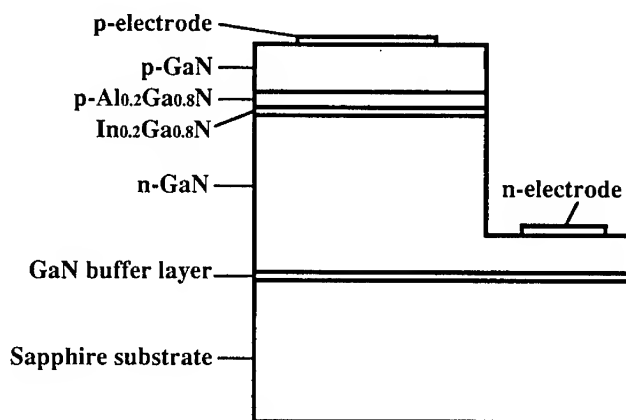


Fig.1. Structure of a blue SQW LED.

A blue LED device structure (Fig. 1) consists of a 300 Å GaN buffer layer grown at a low temperature (550 °C), a 4-μm-thick layer of n-type GaN:Si, a 20-Å-thick active layer of undoped In_{0.2}Ga_{0.8}N, a 1000-Å-thick layer of p-type Al_{0.2}Ga_{0.8}N:Mg, and a 0.5-μm-thick layer of p-type GaN:Mg. The active region forms a SQW structure consisting of a 20 Å In_{0.2}Ga_{0.8}N well layer sandwiched by 4 μm n-type GaN and 1000 Å p-type Al_{0.2}Ga_{0.8}N barrier layers. The indium mole fraction of the InGaN active layer was varied between 0.05 and 0.8 in order to change the peak wavelength of the InGaN SQW LEDs from blue to orange. Fabrication of LED chips was accomplished as follows. The surface of the p-type GaN layer was partially etched until the n-type GaN layer was exposed. Next, Ni/Au contact was evaporated onto the p-type GaN layer and a Ti/Al contact onto the n-type GaN layer. Then the wafer was cut into rectangles (350 μm x 350 μm). These chips were set on a lead frame, and were then molded. The characteristics of LEDs were measured under direct current (DC)-biased conditions at room temperature.

RESULTS AND DISCUSSION

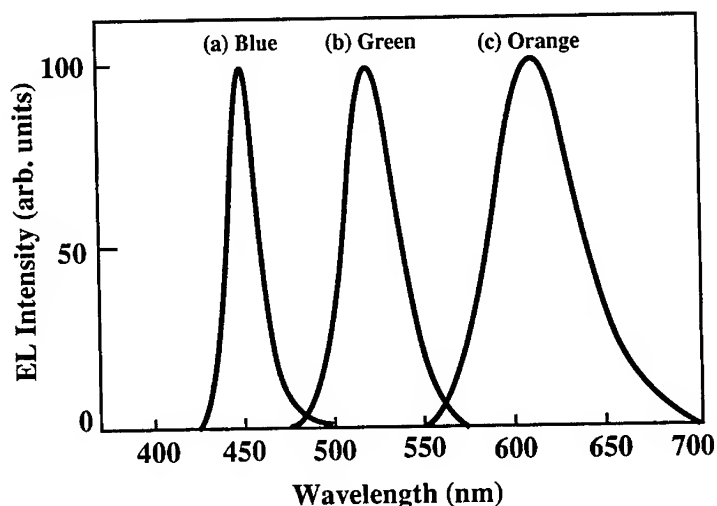


Fig.2. Electroluminescence of (a) blue, (b) green and (c) orange SQW LEDs at a forward current of 20 mA.

Figure 2 shows the typical EL of the blue, green and orange SQW LEDs with different indium mole fractions of the InGaN well layer at a forward current of 20 mA. The longest peak wavelength is 610 nm (orange). The peak wavelength and the FWHM of the typical blue SQW LEDs are 450 nm and 20 nm, respectively, those of green SQW LEDs 520 nm and 30 nm, respectively, and those of orange SQW LEDs 610 nm and 80 nm, respectively. When the peak wavelength becomes longer, the FWHM of the EL spectra increases, probably due to the strain between well and barrier layers of the SQW which is caused by the mismatch of the lattice and the thermal expansion coefficients between well and barrier layers.

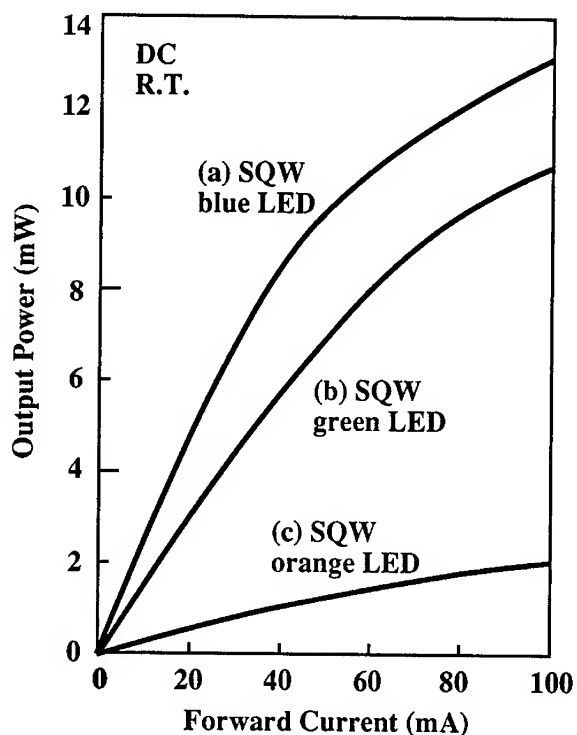


Fig.3. Output power of (a) blue, (b) green and (c) orange SQW LEDs as a function of forward current.

The output power of the SQW LEDs is shown as a function of the forward current in Fig.3. The output power of the blue SQW LEDs slightly increases sublinearly up to 40 mA as a function of the forward current. Above 60 mA, the output power almost saturates, probably due to the generation of heat. At 20 mA, the output power and the external quantum efficiency of blue SQW LEDs are 5 mW and 9.1 %, respectively, which are much higher than those of InGaN/AlGaIn DH LEDs (3 mW and 5.4 %). Those of the green SQW LEDs are 3 mW and 6.3 %, respectively, and those of orange SQW LEDs are 0.5 mW and 1.25 %, respectively. The output power of green and orange SQW LEDs is relatively small in comparison with that of blue SQW LEDs, probably due to poor crystal quality of the InGaIn well layer which has large lattice mismatch and difference in thermal expansion coefficients between well and barrier layers. The maximum on-axis luminous intensity of green SQW LEDs with 10° cone viewing angle is 12 cd at 20 mA. The conventional green GaP LED with a peak wavelength of 555 nm has an output power of 0.04 mW [6]. In comparison, the output power of green AlInGaP LEDs with a peak wavelength of 570 nm is 0.4 mW. Therefore, the output power of green InGaIn SQW LEDs is much higher than that of conventional yellowish green LEDs. Also, the luminous intensity of InGaIn green SQW LEDs (12 cd) is about 100 times higher than that of conventional green GaP LEDs (0.1 cd), and the color of InGaIn SQW LEDs is greener than those of conventional GaP and AlInGaP LEDs. A typical example of the I-V characteristics of the blue SQW LEDs shows that the forward voltage is 3.6 V at 20 mA.

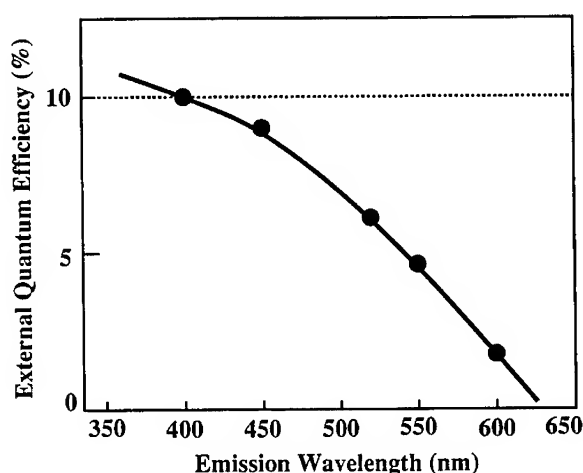


Fig.4. External quantum efficiency as a function of emission wavelength of InGaIn SQW LEDs.

Figure 4 shows the external quantum efficiency as a function of the emission wavelength of InGaN SQW LEDs. The external quantum efficiency of the SQW LEDs exceeds 10 % at the emission wavelengths shorter than 400 nm. When the emission wavelength exceeds 500 nm, the external quantum efficiency drops sharply because of the large strain between well and barrier layers.

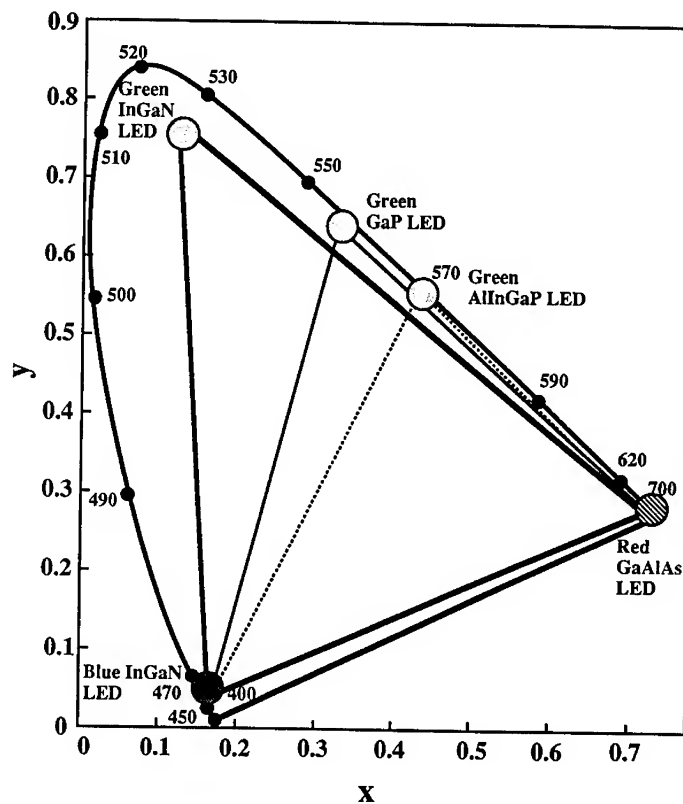


Fig.5. Chromaticity diagram in which blue InGaN SQW LED, green InGaN SQW LED, green GaP LED, green AlInGaP LED and red GaAlAs LED are shown.

Figure 5 is a chromaticity diagram in which blue and green InGa_N SQW LEDs are shown. Commercially available green GaP LEDs, green AlInGaP LEDs and red GaAlAs LEDs are also shown. The color range of light emitted by a full-color LED lamp in the chromaticity diagram is shown as the region inside each triangle which is drawn by connecting the positions of three primary color LED lamps in the diagram. Three color ranges (triangles) are shown for differences only in green LEDs (green InGa_N, green GaP and green AlInGaP LEDs). In this figure, the color range of lamps composed of three primary color LEDs, namely, a blue InGa_N SQW LED, green InGa_N SQW LED and red GaAlAs LED, is the widest compared with other color ranges obtained using a different green LED, such as green GaP LED and green AlInGaP LED. This means that the InGa_N blue and green SQW LEDs show much better color and color purity in comparison with other blue and green LEDs.

Table 1. Comparison of various red, green and blue LEDs at a forward current of 20 mA except II-VI based LEDs which were measured at a forward current of 10 mA.

Color	Material	Peak Wavelength(nm)	Luminous Intensity (mcd)	Output Power (μW)	External Quantum Efficiency(%)
Red	GaAlAs	660	2000	4800	13.0
Green	AlInGaP	570	1000	400	1.0
	GaP	555	100	40	0.1
	ZnTeSe *	512	4000	1300	5.3
	InGa _N	520	12000	3000	6.3
Blue	SiC	470	20	20	0.04
	ZnCdSe*	489	700	327	1.3
	InGa _N	450	2500	5000	9.1

Under a forward current of 20 mA

*Under a forward current of 10 mA

Table 1 shows the comparison of commercially available red, green and blue LEDs in terms of luminous intensity, output power and external quantum efficiency. This table shows that the peak wavelengths of green and blue InGaN SQW LEDs are much shorter than those of conventional green GaP and blue SiC LEDs. Also, the output power and the external quantum efficiency of III-V nitride LEDs are much higher than those of conventional green and blue LEDs and almost comparable to those of red GaAlAs LEDs. Judging from this table, InGaN SQW LEDs have the highest performance in terms of luminous intensity, output power and external quantum efficiency, compared with green and blue LEDs fabricated using other materials. As for II-VI materials, ZnTeSe DH green LEDs have been reported [7]. The output power, external quantum efficiency and peak wavelength of those II-VI LEDs are 1.3 mW, 5.3 % and 512 nm, respectively, at a forward current of 10 mA. In contrast, ZnCdSe DH blue LED has output power, external quantum efficiency and peak wavelength of 0.3 mW, 1.3 % and 489 nm, respectively, at a forward current of 10 mA. The lifetime of these II-VI based LEDs is still short, which prevents their commercialization at present.

SUMMARY

InGaN SQW LEDs with an emission wavelength between violet and orange were fabricated. The luminous intensity of green LEDs was 12 cd and the external quantum efficiency was as high as 6.3 % at a forward current of 20 mA at room temperature. The peak wavelength and the FWHM of the green LEDs were 520 nm and 30 nm, respectively, while those of blue LEDs were 450 nm and 20 nm, respectively. The color of green InGaN SQW LEDs was greener than those of conventional GaP and AlInGaP LEDs. Fabrication of practical visible LEDs in the range from blue to orange is possible using III-V nitride materials at present. The luminous intensity of green InGaN SQW LEDs (12 cd) was about 100 times higher than that of conventional green GaP LEDs (0.1 cd). By combining high-power and high-brightness blue InGaN SQW LED, green InGaN SQW LED and red GaAlAs LED, many kinds of applications, such as LED full-color displays and LED white lamps for use in place of light bulbs or fluorescent lamps, are now possible with characteristics of high reliability, high durability and low energy consumption. The III-V nitride green, blue, violet or uv LEDs with high reliability will be realized in the near future because high-quality III-V nitride films as well as high-power green, blue and uv LEDs with quantum well structures are already available.

REFERENCES

1. W. Xie, D. C. Grillo, R. L. Gunshor, M. Kobayashi, H. Jeon, J. Ding, A. V. Nurmikko, G. C. Hua, and N. Otsuka, *Appl. Phys. Lett.* **60**, 1999 (1992).
2. J. Edmond, H. Kong, and V. Dmitriev, *Inst. Phys. Conf. Ser.* **137**, 515 (1994).

3. J. I. Pankove, E. A. Miller, and J. E. Berkeyheiser, *RCA Review* **32**, 283 (1971).
4. H. Morkoç, S. Strite, G. B. Gao, M. E. Lin, B. Sverdlov, and M. Burns, *J. Appl. Phys.* **76**, 1363 (1994).
5. S. Nakamura, T. Mukai, and M. Senoh, *Appl. Phys. Lett.* **64**, 1687 (1994).
6. M. G. Craford, *Circuits & Devices*. September 24 (1992).
7. D. E. Eason, Z. Yu, W. C. Hughes, W. H. Roland, C. Boney, J. W. Cook, Jr., J. F. Schetzina, G. Cantwell, and W. C. Harasch, *Appl. Phys. Lett.* **66**, 115 (1995).
8. S. Nakamura, M. Senoh, N. Iwasa, and S. Nagahama, *Jpn. J. Appl. Phys.* **34**, L797 (1995).
9. S. Nakamura, M. Senoh, N. Iwasa, S. Nagahama, T. Yamada, and T. Mukai, *Jpn. J. Appl. Phys.* **34**, L1332 (1995).
10. S. Nakamura, *Jpn. J. Appl. Phys.* **30**, L1705 (1991).
11. S. Nakamura, M. Senoh, and T. Mukai, *Appl. Phys. Lett.* **62**, 2390 (1993).

LIGHT-EMITTING DEVICES BASED ON GALLIUM NITRIDE AND RELATED COMPOUND SEMICONDUCTORS

M. KOIKE*, N. SHIBATA*, S. YAMASAKI*, S. NAGAI*, S. ASAMI*, H. KATO*,
and N. KOIDE*,
H. AMANO**, and I. AKASAKI**

*New Market Technical Division, Toyoda Gosei Co., Ltd., Haruhi-cho, Nishikasugai-gun, Aichi 452, JAPAN

**Department of Electrical and Electronic Engineering, Meijo University, 1-501 Shiogamaguchi, Tempaku-ku, Nagoya 468, JAPAN

ABSTRACT

Asymmetric double heterostructures (ADH) of AlGaIn/GaN blue light emitting diodes (LEDs) and GaInN/GaN multiple quantum well (MQW) LEDs were fabricated by metalorganic vapor phase epitaxy (MOVPE). The ADH LEDs had spectral emissions peaking at 450 nm and the luminous intensity was 2.5 cd at 20 mA. The output power was 3.6 mW at 20mA and the external quantum efficiency was as high as 5.1 % at 20 mA. The GaInN/GaN MQW structure was grown successfully by MOVPE. Fine multi-layer structures 7 - 9 nm thick were detected by secondary ion mass spectroscopy and transmission electron microscopy (TEM). The dislocation density in the MQW was as high as $0.5\text{-}2 \times 10^9 \text{ cm}^{-2}$ by TEM. The optical efficiency of the MQW layer was higher than that of a bulk GaInN layer. The intensity of UV emission from MQW LEDs was greater than that of blue light from ADH blue LEDs. The UV emission increased as a super-linear function of injection current at -100°C .

INTRODUCTION

Gallium nitride (GaN) semiconductors have great potential for short wavelength devices such as light emitting diodes (LEDs), laser diodes (LDs), and photo diodes (PDs). To accommodate the peak wavelength of the emission spectra, AlGaIn, GaInN, and AlGaInN can be applied by adjusting the AlN and InN molar fraction of AlGaInN. High optical efficiency GaN grown by MOVPE was achieved by low temperature growth of an AlN buffer layer on a sapphire substrate [1-2]. In 1993, the brightest blue LEDs of wavelength 485 nm peak were metal-insulating GaN-n type (m-i-n) GaN structure LEDs emitting 200 mcd at 10 mA [3]. P-type conducting GaN was achieved for the first time through Mg-doping and low energy electron beam irradiation (LEEBI) treatment [4], followed by heat treatment [5]. The external quantum efficiency of GaN-based blue LEDs increased in 1992 [6] after the realization of p-type conversion technology.

In 1994, candela-class GaInN/AlGaIn DH LEDs were reported [7]. Since we reported p-n junction type GaN LEDs of which the external quantum efficiency was 1.5% in 1992 [6], we continued to increase the efficiency by applying homo p-i-n GaN LEDs, single heterostructure (SH) AlGaIn/GaN LEDs, and asymmetric double heterostructure AlGaIn/GaInN/GaN LEDs. Over the past three years, the brightness increased from 0.2 cd to 2.5 cd for the above mentioned p-n types of LEDs. The external quantum efficiency increased to 3.9 % at 20 mA as a result of the ADH AlGaIn/GaInN/GaN LEDs [8].

GaN-based quantum wells (QWs) have been intensively investigated for short wavelength light-emitting devices [9-13]. The advantages of QWs include lower threshold current density for LDs and reduced sensitivity to temperature. Previous research [10] was concerned mainly with quantum size effects, such as the shift of photoluminescence (PL) peak energy to higher energies. Quite recently, high efficient GaN-based single quantum wells (SQW) LED have been reported, which apply to visible light regions such as blue, green, and yellow LEDs [14].

In this paper, high efficiency GaN-based blue and UV LEDs including active layers of undoped GaInN/GaN MQW are reported. The superlattices of GaInN/GaN MQWs are evaluated by SIMS and TEM. The thickness and number of GaInN quantum wells are described in terms of the MQW optical efficiency.

EXPERIMENT

GaN epitaxial films were grown on a sapphire substrate by MOVPE using an AlN buffer layer. The Al, Ga, In, and N source gases were trimethylaluminum (TMA), trimethylgallium (TMG), trimethylindium (TMI), and ammonia (NH₃), respectively. Silane (SiH₄) was used as the Si source gas. The Mg source gas was bis(cyclopentadienyl)magnesium (bis-Cp₂Mg). Other growth conditions were the same as the previous report [8]. The Si-doped n⁺-GaN layer was approximately 5 μm thick and the carrier concentration was about 1×10¹⁸ cm⁻³. The emitting layer of GaInN was doped with donors or acceptors as recombination centers. The InN molar fraction of GaInN active layer was approximately 0.08. Mg-doped p-AlGaIn and p-GaN layers were deposited sequentially on the bulk GaInN or the GaInN/GaN MQW layers and were converted to p-type conduction by LEEBI treatment after the growth. The GaN-barrier and GaInN-well MQW was grown by controlling growth conditions for MOVPE such as the flow rate of gas sources and the growth temperature. Ohmic contacts to the p- and n-GaN were Au/Ni.

For evaluating the optical properties of GaInN bulk layer and GaInN/GaN QW layers, cathodoluminescence (CL) and PL measurements were applied mainly at room temperature. The penetration depth of the incident electrons was estimated to be around 100 nm at an accelerating voltage of 5 kV.

RESULTS

High efficient ADH blue LEDs

The ADH of p-AlGaIn/GaInN/n-GaN was fabricated for highly efficient blue LEDs. The detailed structure of the LED chip is shown in Fig. 1. The active layer of GaInN was doped with Zn, etc. Figure 2 shows the electroluminescence (EL) spectra of devices described in Fig. 1 at room temperature. The main peak wavelength was blue emission of 450 nm and the full width at half-maximum (FWHM) of the spectra was 70 nm at room temperature. Ultra-violet (UV) emissions also appeared in the peak wavelength of 385 nm as shown in Fig. 2. The intensity ratio of UV to blue emissions increased with increasing forward current. The UV emission originated from recombinations between shallow donors and the valence band. The multi-peak spectra of blue emission could be understood by the interference of blue light within the GaN-based epitaxial layers. The emission built up at about 1 mA and increased linearly with forward current up to about 25 mA. The luminous intensity was typically 2 cd at 20 mA at a viewing angle of 16° . The highest brightness was 2.5 cd at 20 mA and its total output power was 3.6 mW at 20 mA, 3.5 V. The external quantum efficiency was 5.1 % maximum. Figure 3 shows the current and voltage (I-V) characteristic of the ADH blue LED. The lowest forward voltage at 20 mA was 3.3 V and the reverse voltage at -10 μA was as high as -25V.

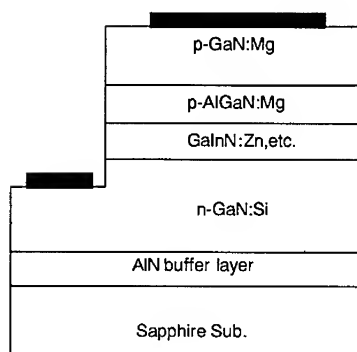


Fig. 1: Layer structure of ADH GaN-based blue LED

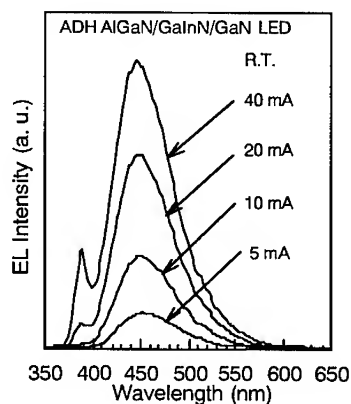


Fig. 2: EL spectra of ADH AlGaIn/GaInN/GaN LEDs

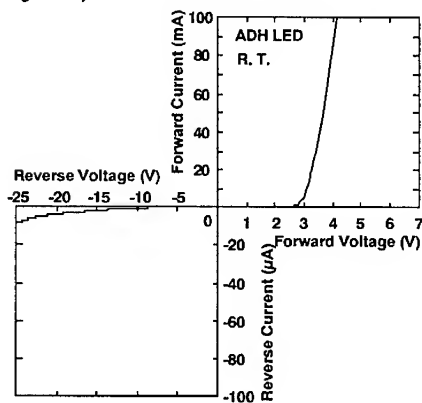


Fig. 3: I-V characteristics of ADH LEDs at R.T.

GaInN/GaN QW active layer

CL efficiency of the GaInN/GaN QW active layer was higher than that of the bulk GaInN layer. Figure 4 shows a schematic diagram of the GaInN/GaN MQWs for SIMS and CL measurement. Figure 5 shows the Ga, In, and N profiles in the MQW layer from a surface of the MQW layer in the direction of substrate taken by SIMS. The SIMS instrument was a CAMECA-ims-4f. In this case, the MQW layer was grown as six GaInN QWs, each 7 nm thick ($L_z=7$ nm) and seven GaN quantum barriers (QBs), each 9 nm thick ($L_B=9$ nm). The InN molar fraction of GaInN QWs was 0.08. The abruptness at the interface between the GaInN QW and the GaN QB was approximately 2 nm, as shown in Fig. 5.

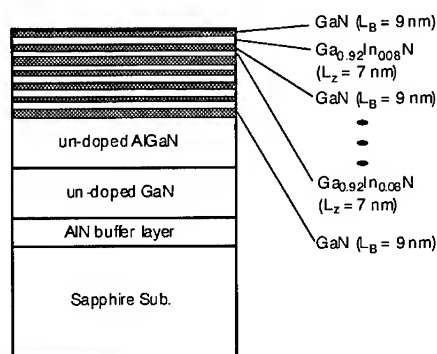


Fig. 4: Schematic diagram showing MQW.

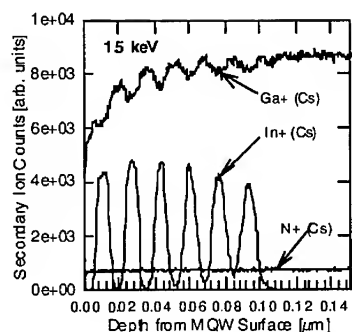


Fig. 5: In, Ga, N-depth profiles in GaInN/GaN MQW by SIMS analysis

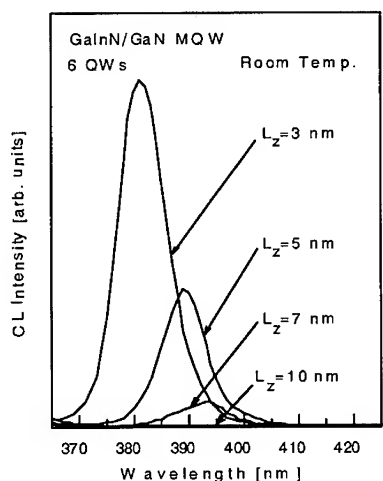


Fig. 6: CL spectra of GaInN/GaN MQW with different quantum well thickness.

Based on the abruptness of InN molar fraction, we decreased the QW thickness from 10 to 3 nm. Figure 6 shows the CL spectra of the MQWs with changing well thickness. The UV emission due to band edge recombination increased and the peak wavelength became short with decreasing well thickness. The peak shift towards higher energy as a result of decreasing the well thickness could be understood by quantum size effects [10].

Active layer GaInN/GaN MQWs were applied to the DH LED as shown in Fig. 7, which was similar to that of DH stripe lasers diodes. UV light was emitted from the edge face. Stripe windows were made in SiO₂ films evaporated on top faces. The stripe widths (W) were 5, 10, and 30 μm. The stripe lengths (L) were 200, 300, 500, and 1000 μm. Figure 8 shows the TEM bright field image of a cross section of the MQW DH. The TEM image was taken with a JEM-4000EX microscope.

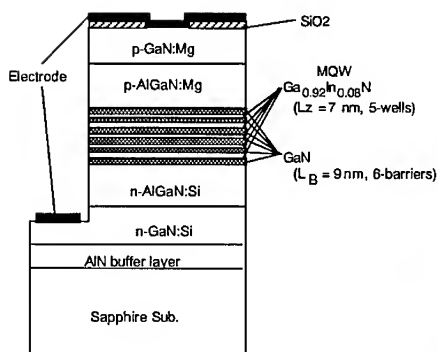
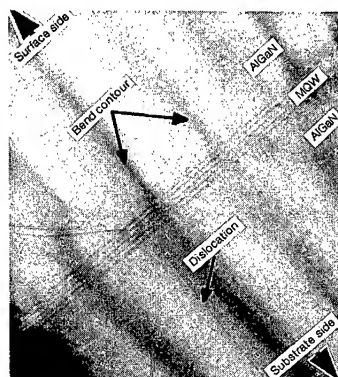


Fig. 7: Schematic diagram showing MQW heterostructure LED.



Acc. Voltage: 400 kV Thickness of TEM sample: 150 nm

Fig. 8: TEM micrograph showing MQW heterostructure layers and dislocations.

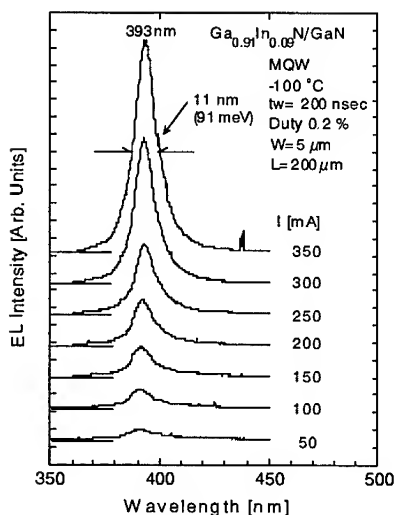


Fig. 9: EL spectra of MQW LED at -100°C .

intensity at room temperature as a function of the number of quantum wells. The well thickness of the MQWs was kept at constant so that the total well thickness increased with increasing number of QWs. The peak emissions from the MQW occurred at 386 nm. The indium mole fraction of the MQW was 0.08. The peak intensity of the QW DH LED with three QWs was one order of magnitude greater than that of the QW DH LED with 15 QWs at 20mA.

The GaInN QWs were observed as five dark layers in the TEM image. Dislocation lines propagated in a direction normal to the substrate. The dislocation density in the MQW was in the range of $0.5\text{-}2 \times 10^9 \text{ cm}^{-2}$.

Figure 9 shows the EL spectra at -100°C emitted from the MQW DH LED; $W=5 \mu\text{m}$, $L=200 \mu\text{m}$. The peak wavelength and FWHM was 393 nm and 11 nm (91 meV), respectively. Figure 10 shows light-current characteristics from an edge facet of the MQW DH LEDs. When the current was increased to 200 mA (200 kA/cm^2), the light output (L) increased as a super-linear function with the current (I) as shown in Fig. 10. However, the spectra did not show clearly the spectral narrowing that is a typical characteristic of laser operation.

As described above, we examined the QW thickness in terms of CL efficiency. The number of QWs also was studied by comparing the EL intensities of MQW DH LEDs with three, six, and 15 wells. Figure 11 shows the band edge EL

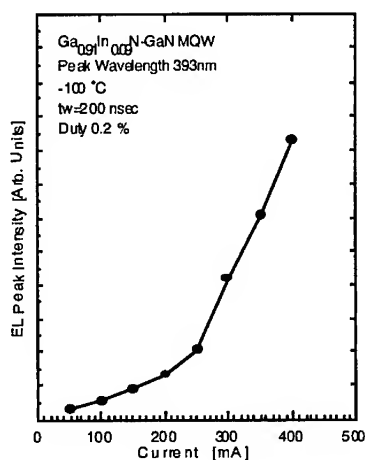


Fig. 10: EL peak intensity of MQW LED as a function of current at -100°C .

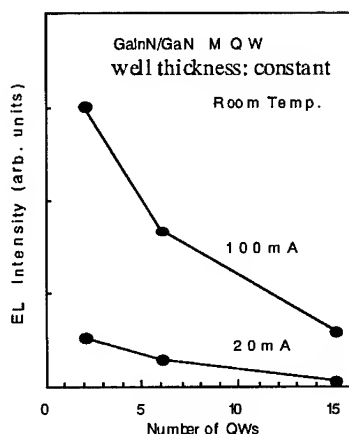


Fig. 11: EL peak intensity of MQW LED as a function of number of QWs at room temperature.

CONCLUSIONS

The very high efficiency GaN-based blue LEDs with 2.5 cd at 20 mA were fabricated by using a bulk GaInN light emitting layer which was doped with Zn, etc. The output power at 20 mA was approximately 3.7 mW and the external quantum efficiency was as high as 5.1% at room temperature. The high-quality $\text{Ga}_{0.92}\text{In}_{0.08}\text{N}/\text{GaN}$ MQW heterostructure was successfully fabricated with cladding layers of p-AlGaIn and n-AlGaIn by MOVPE. The fine superlattice structure was directly detected by TEM and SIMS analysis. The MQW extremely enhanced the optical efficiency in non-doped MQWs compared with bulk GaInN layer. GaInN/GaN MQW is consequently promising for the active layers of LEDs and LDs.

The UV emission from the MQW heterostructure diodes increased as a super-linear function with the current. Although the FWHM of the spectra did not become narrow with increased current, the active layer of GaInN/GaN MQWs indicated the possibility of lasing by current injection.

ACKNOWLEDGMENTS

The authors would like to thank "Japan Research and Development Corporation" for their R&D supports and helpful discussions.

REFERENCES

1. H. Amano, N. Sawaki, I. Akasaki, and Y. Toyoda, *Appl. Phys. Lett.* **48**, 353 (1986).
2. I. Akasaki, H. Amano, Y. Koide, K. Hiramatsu, and N. Sawaki, *J. Cryst. Growth* **98**, 209 (1989).
3. I. Akasaki, H. Amano, H. Murakami, M. Sassa, H. Kato, K. Manabe, *J. Cryst. Growth* **128**, 379 (1993).
4. H. Amano, M. Kito, K. Hiramatsu, and I. Akasaki, *Jpn. J. Appl. Phys.* **28**, L2112 (1989).
5. S. Nakamura, N. Iwata, M. Senoh, and T. Mukai, *Jpn. J. Appl. Phys.* **31**, 1258 (1992).
6. I. Akasaki, H. Amano, K. Itoh, N. Koide and K. Manabe, *Inst. Phys. Conf. Ser.* **129**, 851 (1992).
7. S. Nakamura, T. Mukai, and M. Senoh, *Appl. Phys. Lett.*, **64**, 1687 (1994).
8. M. Koike, N. Shibata, H. Kato, S. Yamasaki, N. Koide, H. Amano, and I. Akasaki, in "Topical Workshop on III-V Nitrides", Abstracts: C-2 (1995), to be published in proceedings.
9. M. A. Khan, R. A. Skogman, J. M. Van Hove, S. Krishnakutty, and R. M. Kolbas, *Appl. Phys. Lett.* **56**, 1257 (1990).
10. K. Itoh, T. Kawamoto, H. Amano, K. Hiramatsu, and I. Akasaki, *Jpn. J. Appl. Phys.* **30**, 1924 (1991).
11. S. Nakamura, T. Mukai, M. Senoh, S. Nagahama, and N. Iwasa, *J. Appl. Phys.* **74**, 3911 (1993).
12. I. Akasaki, H. Amano, and I. Suemune, 6th International Conference on Silicon Carbide and Related Materials-1995 (ICSCRM-95) Sept. 1995.
13. I. Akasaki and H. Amano, 22th International Symposium on Compound Semiconductors (ISCS-22) Aug. 1995.
14. S. Nakamura, M. Senoh, N. Iwasa, and S. Nagahama, *Jpn. J. Appl. Phys.* **34**, L797 (1995).

GROWTH OF SILICON-DOPED AND HIGH QUALITY, HIGHLY RESISTIVE GaN FOR FET APPLICATIONS

K. DOVERSPIKE*, A.E. WICKENDEN, S.C. BINARI, D.K. GASKILL, AND J.A. FREITAS**

Naval Research Laboratory, Washington DC 20375-5347

* currently at Hewlett Packard, San Jose, CA 95131

**Sachs/Freeman Associates Inc, Landover, MD 20785-5396

ABSTRACT

We have shown the ability to grow thin, high mobility, GaN channel layers on high quality, highly resistive GaN. The growth, characteristics, and device results of two types of MESFET structures were discussed. The first device structure consists of a 2000Å, $2 \times 10^{17} \text{cm}^{-3}$ Si-doped channel layer, grown on 3µm of highly resistive GaN, while the second structure (recessed-gate MESFET) had a 1000Å, $1 \times 10^{18} \text{cm}^{-3}$ Si-doped, n^+ capping layer deposited on a 2000Å, $2 \times 10^{17} \text{cm}^{-3}$ Si-doped channel layer. The first MESFET structure was operational at 500°C which is the highest reported operating temperature for a GaN device while the recessed-gate MESFET had a g_m as high as 41mS/mm, which is the highest reported value for a GaN MESFET.

INTRODUCTION

The GaN-based material system is of great interest, not only because of the recent high-efficiency blue and green LEDs, but also because of their potential in high temperature electronics, power electronics, and high power microwave devices[1]. GaN is an attractive material for these electronic applications because of the low thermal generation rates and high breakdown fields inherent in wide bandgap semiconductors. For the fabrication of high frequency FETs, thin high mobility semiconductor layers are required. The epitaxial growth of these active layers has historically required the use of appropriate buffer layers to spatially separate the active channel from defects and impurities which often lie at the epitaxial layer/substrate interface. In the case of GaN FETs, the "buffer layer" (thick highly resistive layer below the thin channel layer) takes on added importance due to the large lattice mismatch between GaN and sapphire which results in a highly defective region near the GaN/sapphire interface[2]. It is therefore necessary to grow a thick (>1µm), highly resistive GaN buffer layer upon which a high mobility FET channel layer can be grown. For GaN grown on sapphire, the unintentional electron concentration is typically in the mid- 10^{16}cm^{-3} or higher range, and the growth of highly resistive GaN is challenging. When highly resistive films are grown, it is often due to a high degree of compensation. For FET applications, it is essential to grow highly resistive films that are also of high quality in order to obtain high mobilities in the doped channel layer. In this paper, state-of-the-art GaN growth by low pressure organometallic vapor phase epitaxial (OMVPE) will be discussed with respect to the requirements of MESFET devices.

EXPERIMENTAL

An inductively heated, water cooled, vertical OMVPE reactor operated at 57torr was used for the growth as previously described in the literature[3]. The structures discussed in this paper were grown on a-plane (1120) sapphire substrates. A 200Å AlN nucleation layer was deposited at 450°C using triethylaluminum and ammonia(NH_3) as the reactant sources. The GaN films were grown using trimethylgallium(TMg) and NH_3 at a growth temperature of 1040°C. Disilane was used as the dopant source (8ppm in H_2)[4]. The 325nm line of a HeCd laser was used as the excitation source for the low temperature (6K) photoluminescence (PL) measurements. Double crystal x-ray diffractometry of the (0002) peak was used to assess film crystallinity, while Van der Pauw Hall measurements (2240G) were performed using a clover leaf geometry using In contacts. Capacitance-voltage (C-V) measurements were also performed using Pt/Au Schottky barriers. Details about the device fabrication have been previously described in the literature[5].

RESULTS AND DISCUSSION

Growth of highly resistive GaN

The growth of thin, high mobility GaN deposited directly on sapphire is not possible because of the large lattice mismatch between GaN and sapphire. Therefore, the first growth obstacle to be overcome before GaN FET structures can be grown is the ability to grow highly resistive GaN, which is also of high quality. Often times when the growth conditions are not optimized, highly resistive GaN can be grown. However, if this material is highly resistive because it is heavily compensated, then upon doping these films with Si, high mobilities are not obtained. We have been successful in obtaining high quality, highly resistive GaN by continuing to optimize parameters that we have previously shown to be critical for the growth of high quality GaN, e.g. nucleation layer temperature[6], nucleation layer thickness, NH_3/TMG ratio, and GaN growth temperature[3]. For the MESFET structures described in this paper, a-plane sapphire (1120) was used as the substrate because we have previously shown that for our growth conditions, we can more easily obtain high mobility GaN films on a-plane sapphire over a wider range of conditions than the corresponding growth on c-plane sapphire[3]. Irrespective of whether c-plane or a-plane sapphire is used as a substrate, the resulting GaN films are oriented with the c-plane parallel to the substrate.

Characterization of highly resistive GaN

Since it is difficult to make contacts to GaN when the carrier concentration is below low 10^{16}cm^{-3} , Hall measurements cannot be used to characterize these highly resistive films. X-ray rocking curves are also not very useful since the FWHM of the (0002) peak does not show a direct correlation with the electrical properties. For GaN films grown that are typically $3\mu\text{m}$ thick, the FWHM (typically 250-350 arcsec) does not track changes in mobilities, and cannot distinguish the difference between low mobility compensated films and higher quality films. In addition, the FWHM of the (0002) peak cannot distinguish the difference between films with a high background carrier concentration (mid- 10^{16}cm^{-3} or higher) or highly resistive films. The mobility of the doped channel layers grown on the highly resistive GaN thick buffer layer is a powerful characterization tool and gives some indication of the quality of the underlying highly resistive GaN layer (high quality highly resistive GaN exhibits higher mobilities when doped than highly compensated lower quality GaN). In the present study, the highly resistive GaN that was grown can support a two-point probe voltage of $>1000\text{V}$ without exhibiting breakdown. This does confirm that the GaN films are highly resistive (estimated to be approximately $10^{10}\Omega\text{-cm}$ from I-V measurements on samples with large area In contacts), but it cannot be used, however, to determine the difference between low quality heavily compensated GaN and high quality highly resistive GaN. Therefore, we have used low temperature photoluminescence to access the quality of the undoped GaN films. For unintentionally doped GaN whose background electron concentration is mid- 10^{16}cm^{-3} or higher, the dominant feature in the photoluminescence spectra is typically the exciton bound to a neutral donor. As shown in Figure 1, besides observing the exciton bound to a neutral donor, GaN free excitons are also observed at 3.4924 and 3.5052eV in a low temperature PL spectra of our undoped GaN. The fact that we observe free excitons in unintentionally doped material indicated that the highly resistive material is of high quality. Also shown in Figure 1 is a typical low temperature PL spectra of our Si-doped GaN which shows the exciton bound to a neutral donor at 3.4785eV. The intensity of the PL signal from the Si doped film is approximately 20 times stronger than the undoped film. In addition, there is only a small indication of the deep level 2.2eV band which is commonly observed in GaN films. The origin of this deep level is currently not known, but it may be associated with compensation in the GaN films involving deep donor states and shallow acceptor states[7].

Growth of MESFET structures

Once the ability to grow high quality highly resistive GaN had been demonstrated, a thin high mobility layer then needs to be deposited on this resistive GaN in order to fabricate MESFET devices. Without

able to grow high quality highly resistive GaN, and subsequently grow high mobility n-type doped layers using disilane as the dopant source[4]. Since having a high mobility layer in the MESFET device is important, we targeted a Si doping level of approximately $1-2 \times 10^{17} \text{ cm}^{-3}$ since this is a doping level that we can controllably achieve high mobility GaN films[8]. In the present paper, we report on two types of MESFET structures. The first consists of a 2000Å, $2 \times 10^{17} \text{ cm}^{-3}$ Si-doped channel layer grown on 3µm of highly resistive GaN, and the second structure has a similarly doped channel layer, but with an additional 1000Å, $1 \times 10^{18} \text{ cm}^{-3}$ Si-doped, n^+ capping layer. The n^+ layer was used to reduce the ohmic contact resistance as well as the source and drain access resistances.

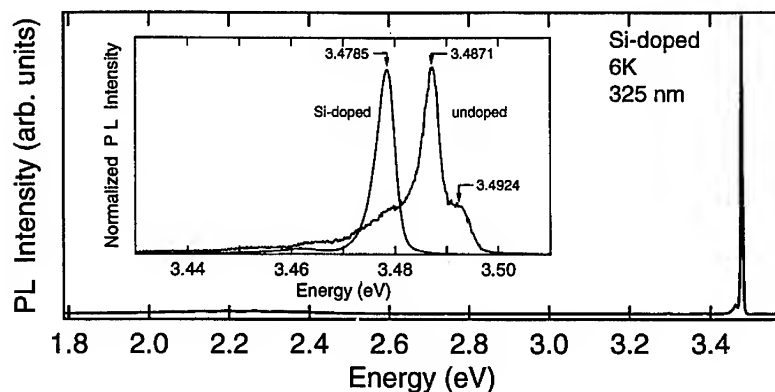


Figure 1. Low temperature (6K) photoluminescence spectra of a Si-doped GaN film and an undoped highly resistive GaN film (magnified 23X to normalize).

Characterization of MESFET structures

Hall measurements have been done in order to characterize these doped channel layers, and we have achieved room temperature mobilities up to approximately $600 \text{ cm}^2 \text{ V}^{-1} \text{ s}^{-1}$ for a 2500Å channel layer grown on 3µm of highly resistive GaN. The first MESFET structure whose device characteristics will be discussed in the present paper had a 300K Hall mobility of $410 \text{ cm}^2 \text{ V}^{-1} \text{ s}^{-1}$. A carrier concentration profile obtained from Schottky barrier capacitance-voltage (C-V) measurements from this Si-doped channel layer is shown in Figure 2. Previous SIMS analysis of the Si-doped channel layers indicates nearly complete activation of the silicon, when compared to electron concentrations obtained from Hall measurements[8]. Nearly complete activation of the silicon level is consistent with our variable temperature Hall measurements which give a donor ionization energy of 26meV for the Si-doped samples. This donor ionization energy is obtained simply by fitting the carrier concentration vs $1/T$, and assuming that twice the activation energy is the donor ionization energy. SIMS analysis also has shown a relatively sharp interface between the Si-doped channel layers and the highly resistive GaN which indicates that Si diffusion during the growth is minimal[8]. In the unintentionally doped, highly resistive GaN layer (below the channel layer) the Si level is below the detection limit of Si in the SIMS equipment (approximately $1-2 \times 10^{16} \text{ cm}^{-3}$).

Device Results

Details of the device fabrication can be found in a previously published paper[5]. The Si-doped MESFETs had a maximum transconductance of 23mS/mm and were completely pinched off at -11V. For a 0.9 µm gate length, the f_t and f_{max} were 5 and 11GHz. The elevated temperature performance is shown

in figure 3 which shows that at 400°C, the devices still have good pinch-off characteristics and a g_m of 10mS/mm. Although gate leakage prevented complete channel pinch-off at 500°C, the devices were still operational at this temperature and had a g_m of 8mS/mm. This is the highest operating temperature reported for a GaN device to date. Recessed-gate MESFETs were fabricated with the films that contained the $1 \times 10^{18} \text{ cm}^{-3}$ Si-doped, n^+ capping layer and had a g_m as high as 41mS/mm. This is the highest reported value for a GaN MESFET. Gate leakage currents were excessive due to the close proximity of the gate metal to the n^+ cap. For a 1.3 μm gate length, the f_t and f_{max} were 5 and 9GHz, respectively.

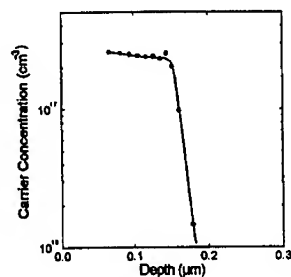


Figure 2. Carrier concentration profile obtained from C-V measurements on MESFET device.

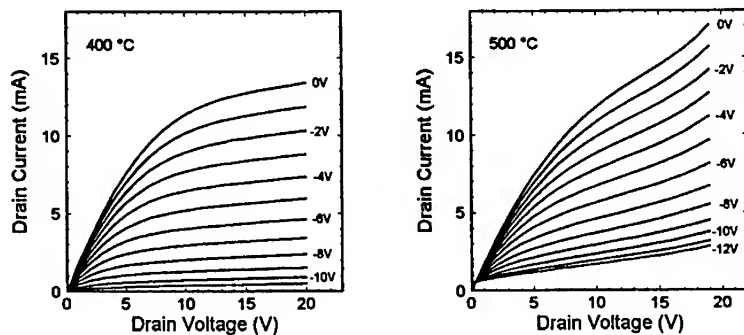


Figure 3. Drain characteristics of Si-doped MESFET device at 400 and 500C

SUMMARY

In this paper, we have reported on the ability to grow high quality, highly resistive GaN. We have observed free excitons in the low temperature photoluminescence spectra of this material and also have demonstrated the growth of high mobility channel layers (up to $600 \text{ cm}^2 \text{ V}^{-1} \text{ s}^{-1}$) on this highly resistive GaN. We were able to grow these high mobility layers, simply by doping with Si, and without changing the reactor conditions. MESFET devices have been fabricated from these structures and were operational up to 500°C. Recessed-gate MESFETs with a n^+ cap were also demonstrated.

REFERENCES

1. H.Morkoc, S.Strite, G.B.Gao, M.E.Lin, B.Sverdlov, and M.Burns, *J.Appl. Phys.* **76**,1363 (1994).
2. K.Hiramatsu, S.Itoh, H.Amano, I.Akasaki, N.Kuwano, T.Shiraishi, and K.Oki, *J. Crystal Growth*, **115**, 628 (1991).
3. K.Doverspike, L.B.Rowland, D.K.Gaskill, and J.A.Freitas, Jr., *J.Elect. Mat.*, **23**(12), 269 (1995).
4. L.B.Rowland, K.Doverspike, and D.K.Gaskill, *Appl. Phys. Lett.*, **66**(12),1495 (1995).
5. S.C.Binari, *Electrochemical Society Proceedings*, Vol. 95-21, pp. 136 (1994).
6. . L.B.Rowland, K.Doverspike, D.K.Gaskill, and J.A.Freitas, Jr., *Mater. Res.Soc. Proc.*, **339**, 477,1994.
7. E.R.Glaser, T.A.Kennedy, H.C.Crookham, J.A.Freitas, Jr., M.A.Khan, D.T.Olson, and J.N.Kuznia, *Appl. Phys.Lett.*, **63**,2673 (1993).
8. A.E.Wickenden, L.B.Rowland, K.Doverspike, D.K.Gaskill, J.A.Freitas, Jr., D.S.Simons, and P.H.Chi, submitted to *Elect. Mat.*

AlGaN/GaN/AlGaN double-heterojunction blue LEDs on 6H-SiC substrates

Hua-Shuang Kong, Michelle Leonard, Gary Bulman, Gerry Negley and John Edmond
Cree Research, Inc., Durham, N.C. 27713, USA

ABSTRACT

Blue LEDs with double-heterojunction (DH) have been produced in AlN-GaN system grown on n-type 6H-SiC substrates via metalorganic chemical vapor deposition (MOCVD). These devices employ a GaN active layer bordered by Mg doped p-type $\text{Al}_{0.1}\text{Ga}_{0.9}\text{N}$ and Si doped n-type $\text{Al}_{0.1}\text{Ga}_{0.9}\text{N}$. A vertical device design was utilized with a p-type Au contact centered on the chip top side for wire bonding. The backside contact to the SiC is Ni. The peak emission from these devices is 430 nm with a FWHM of 65 nm, producing a deep blue color. The output power is 1.7 mW at 20 mA which corresponds to an external quantum efficiency of 3%.

INTRODUCTION

The wurtzite polytypes of InN, GaN, and AlN form a continuous alloy system with direct band gaps. The band gap of this system ranges from 1.9 eV (InN) to 6.2 eV (AlN). Thus, optical devices fabricated in this system are capable of generating light from red to UV. In fact, InGaN-based LEDs with peak emissions from orange to UV have been demonstrated [1]. Furthermore, nitride blue LEDs have recently been commercialized, which proved the viability of the nitride system.

Two kinds of substrates were used in commercial nitride blue LEDs. They are sapphire and 6H-SiC. Sapphire substrates have 16% lattice mismatch with GaN and are insulating material. LEDs fabricated on sapphire substrates require two top side contacts to pass current through the p-n junction. On the other hand, SiC substrates have a lattice mismatch of 3.5% with GaN and is conductive which allows for the fabrication of a vertical device structure. In addition, SiC substrates have a high thermal conductivity of 5 W/cmK and have multi-cleavage planes. These properties are important for fabrication of laser diodes. Therefore, research efforts have been focused on epitaxial growth on SiC substrates at Cree Research. Epitaxial layers of GaN and AlGaN have been grown on 6H-SiC. They are smooth, featureless and crack-free. To obtain high brightness LEDs, AlGaN/GaN/AlGaN DH has been successfully grown on n-type 6H-SiC substrates. GaN:SiC-based blue LEDs are now in mass production. The LED output power of 1.7 mW at 20 mA was obtained. In this paper, optical and electrical characterizations of GaN epilayers and DH LEDs on 6H-SiC substrates will be presented and discussed.

EXPERIMENT

High quality GaN and AlGaN alloy thin films were epitaxially grown on 6H-SiC substrates with a diameter of 35 mm via MOCVD. The substrates were Si-face and n-type with typical resistivity of 0.02-0.04 $\Omega\cdot\text{cm}$. The growth temperature is in the range of 1000-1050 $^{\circ}\text{C}$. Si and Mg were doped into the nitride films as n- and p-type dopants, respectively. DH LED emission region was grown on Si-doped GaN layer. First, Si-doped, n-type $\text{Al}_{0.1}\text{Ga}_{0.9}\text{N}$ was grown. Then, GaN active layer and Mg-doped, p-type $\text{Al}_{0.1}\text{Ga}_{0.9}\text{N}$ were subsequently grown. Finally, a Mg-doped, p-type GaN was grown as p-type contact layer.

Room temperature photoluminescence (PL) was used to characterize n- and p-GaN. The excitation source was a 10 mW, 325 nm He-Cd laser. The laser spot size on samples was

approximately 50 μm in diameter. Al and Au were used as Ohmic contacts for measuring n- and p-type specific contact resistance, respectively. Secondary ion mass spectroscopy (SIMS) was used to determine atomic concentration of Mg in GaN epilayers. Conventional vertical geometry was utilized in LED fabrication. Ni and Au were used as Ohmic contacts for backside contact to SiC and for top side contact to Mg-doped GaN layer, respectively. The characteristics of LEDs were measured at room temperature and under DC bias.

RESULTS AND DISCUSSION

Characterization of GaN Epilayers

GaN epilayers grown on 6H-SiC substrates were controllably doped in the carrier concentration ranges of 10^{15} - 10^{19} cm^{-3} for n-type, and 10^{15} - $6 \times 10^{17} \text{ cm}^{-3}$ for p-type, respectively. Dislocation density as low as 10^8 cm^{-2} have been obtained as verified by plan-view transmission electron microscopy [2]. Al and Au were used as n- and p-type Ohmic contact, respectively, to study specific contact resistance. Arrays of transfer length measurement (TLM) structures were formed on electrically isolated n- and p-type GaN epilayers. The specific contact resistances were extracted from the resistance vs. contact spacing data. The best specific contact resistances measured so far were $2 \times 10^{-5} \Omega\text{-cm}^2$ for Ohmic contact on n-GaN and $3 \times 10^{-2} \Omega\text{-cm}^2$ for Ohmic contact on p-GaN, respectively. Figure 1 shows typical I-V characteristics of Ohmic contacts on n- (Figure 1a) and p-GaN (Figure 1b) epilayers.

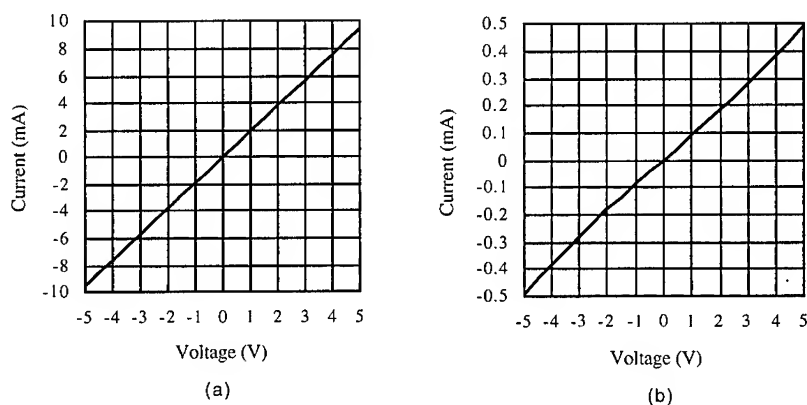


Figure 1. Current-voltage characteristics of (a) Al Ohmic contact on Si-doped GaN and (b) Au Ohmic contact on Mg-doped GaN.

Room temperature photoluminescence spectra of undoped and Mg-doped GaN films were measured. PL of undoped GaN epilayers exhibit an emission dominated by the band edge exciton of 3.41 eV (Figure 2a). The defect luminescence at 2.2 eV was not observed. PL spectra of a Mg-doped GaN epilayer is shown in Figure 2b. The peak emission is at 435.4 nm. The peak emission wavelength changes with Mg doping concentration as observed on Mg-doped GaN films grown on sapphire substrates by other researchers [3]. PL measurements were also

performed on undoped AlGaIn films. Al composition was in the range of 0-10%. No 2.2 eV defect emission was observed on any of these samples.

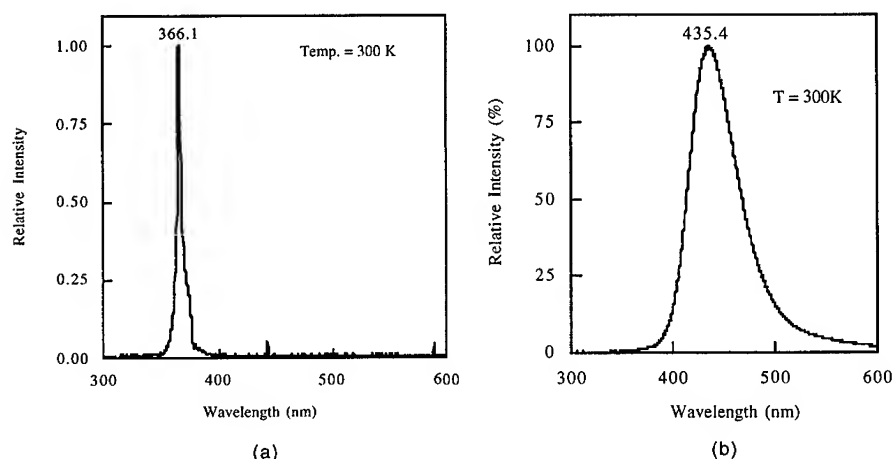


Figure 2. Room temperature photoluminescence spectra of (a) undoped GaN and (b) Mg-doped GaN.

Perkin-Elmer 6300 SIMS system was used in the analysis of Mg-doped GaN epilayers. Mg atomic concentration of as high as $4 \times 10^{20} \text{ cm}^{-3}$ was measured in GaN layer. By changing growth conditions, Mg doping levels can be well controlled and repeated. Figure 3 shows a SIMS depth profile of Mg-doped GaN epilayer with two doping levels. In the top layer which is about $0.9 \mu\text{m}$ thick, the Mg atomic concentration is about $1 \times 10^{20} \text{ cm}^{-3}$. The Mg concentrations remain quite constant through both Mg-doped epilayers.

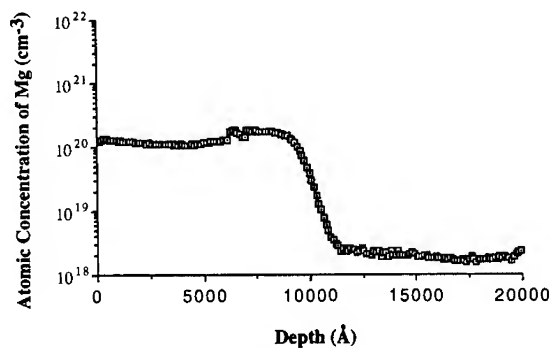


Figure 3. SIMS profile of a Mg-doped GaN epilayer with two doping levels grown on a 6H-SiC substrate.

Electrical and Optical Properties of Blue LEDs

A typical I-V characteristics of a LED chip is shown in Figure 4a. The forward voltage of the vertical device is typically in the range of 4-5 V at 20 mA. The output power of 1.7 mW at 20 mA was obtained. This corresponds to an external quantum efficiency of 3%. The LEDs emit a deep blue color. The emission spectra are shown in Figure 4b. The peak emission is 430 nm at a forward current up to 40 mA. The FWHM at 20 mA was measured to be 65 nm. Life test results indicate expected lifetimes in excess of 100,000 hours at 30 mA at room temperature.

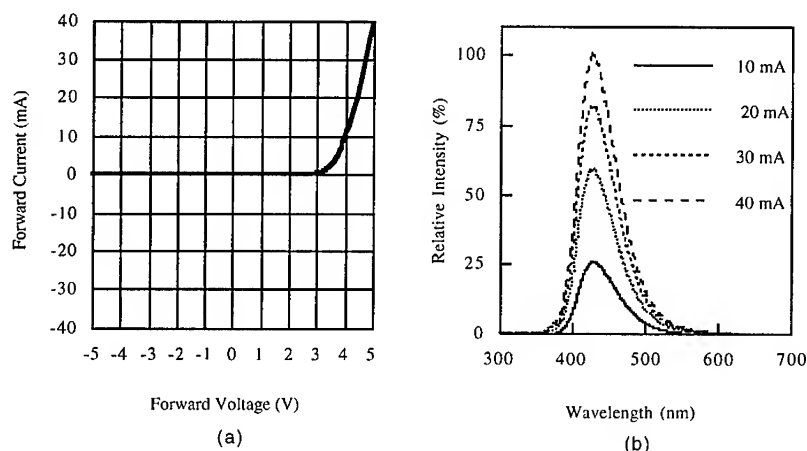


Figure 4. Characterization of DH blue LEDs on SiC substrates showing (a) typical I-V characteristics of a LED chip and (b) LED emission spectra with 10-40 mA drive current.

CONCLUSIONS

The growth of AlGaIn/GaN/AlGaIn DH LED structures on 6H-SiC substrates is now a routine process for mass production of high-brightness blue LEDs. These LEDs emit deep blue color with a peak wavelength of 430 nm. The output of 1.7 mW at 20 mA has been obtained. This corresponds to an external efficiency of 3%. The forward voltage at 20 mA is in the range of 4-5 V. Life test results indicate that the degradation is similar to other LED technologies.

ACKNOWLEDGEMENTS

This research was performed at Cree Research, Inc., and funded by Advanced Research Projects Agency under the contract number N00014-95-C-0038. This program was monitored by Office of Naval Research.

REFERENCES

1. S. Nakamura, Presentation A-2, Topical Workshop on III-V Nitrides, Sept. 21-23, 1995, Nagoya Congress Center, Nagoya, Japan.

2. J. Edmond, H.-S. Kong, M. Leonard, V. Dmitriev, K. Irvine and G. Bulman, Presentation A-3, Topical Workshop on III-V Nitrides, Sept. 21-23, 1995, Nagoya Congress Center, Nagoya, Japan.
3. H. Amano, M. Kitoh, K. Hiramatsu and I. Akasaki, J. Electrochem. Soc., **137**, p. 1639 (1990)

ELECTRIC BREAKDOWN IN NITRIDE PN JUNCTIONS

V.A. DMITRIEV*, N.I. KUZNETSOV**, K.G. IRVINE*, and C.H. CARTER, Jr.*

*Cree Research, Inc., 2810 Meridian Parkway, Durham, NC 27713 USA

**Cree Research Eastern European Division and A.F. Ioffe Institute,
26 Polytechnicheskaya Street, St. Petersburg, 194021 Russia

ABSTRACT

Electric breakdown of mesa terminated GaN and AlGaIn pn diodes was investigated. The nitride pn structures were grown on 6H-SiC (0001) wafers by metalorganic chemical vapor deposition (MOCVD). Mesa structures were fabricated by reactive ion etching (RIE). Capacitance-voltage (C-V) and current-voltage (I-V) characteristics of the pn junctions were measured. It was found that the junctions were linearly graded. Microplasmic breakdown was observed. The breakdown voltage for GaN and AlGaIn diodes ranged from 40 to 150 V and from 40 to 100 V, respectively. The electric breakdown field and temperature coefficient of the breakdown voltage were measured.

INTRODUCTION

Recently high quality GaN layers and pn structures were grown on SiC substrates [1,2]. It was shown that these structures have a high potential for light emitters. Edge electroluminescence of the structures was also investigated [3]. In this paper we report on the reverse current-voltage (I-V) characteristics of the nitride pn junctions. Two types of junctions were investigated: GaN pn junctions and AlGaIn pn junctions.

EXPERIMENT

Multilayer nitride structures were grown by MOCVD [1]. Substrates were 6H-SiC (0001) Cree wafers. Si and Mg were used as donor and acceptor dopants, respectively. The properties of GaN and AlGaIn layers grown on SiC substrates have been described elsewhere [1-4]. Mesa structures 100 - 300 μm diameter were fabricated by RIE [5]. Pd and Al were used as ohmic contacts for p-GaN and n-GaN, respectively. A planar device geometry was employed to prevent the effect of SiC/GaN heterojunctions on the experimental results. The C-V characteristics of the diodes were measured at a frequency of 1 MHz. The I-V characteristics were measured in the temperature range from 200 to 600 K. The position of the pn junction in the structure was determined by electron beam induced current (EBIC).

GaN pn junctions.

N-type and p-type GaN layers were grown subsequently in the same epitaxial run. Typical thicknesses for the n- and p-layer were $\sim 2 \mu\text{m}$ and $\sim 0.5 \mu\text{m}$, respectively. C-V characteristics of the diodes were linear when plotted in $V\text{-}C^{1/3}$ coordinates. This indicates that the pn junctions had a linear impurity distribution. The built-in voltage,

V_{bi} , determined by C-V measurements ranged from 2.2 to 2.6 V. The impurity gradient in the pn junction was calculated to be from 2×10^{22} to $2 \times 10^{23} \text{ cm}^{-4}$ for different samples.

The diodes had good rectifying I-V characteristics (Fig. 1). The reverse I-V characteristics showed an abrupt electric breakdown having a microplasmic nature. The breakdown voltage, V_b , ranged from 40 to 150 V. At reverse voltages less than breakdown voltage ($V < 0.9 \times V_b$), the leakage current density at room temperature was less than 10^{-2} A/cm^2 . Taking into account that the pn junctions were linearly graded, the strength of electric breakdown field was estimated using the well-known equation [6]:

$$V_b = \frac{2}{3} WE = \frac{4E^{1.5}}{3} \left(\frac{2\epsilon_s}{q} \right)^{0.5} (\alpha)^{-0.5} \quad (1)$$

where E is the strength of the electric breakdown field, W is the width of the space charge region at the breakdown voltage, ϵ_s is the dielectric constant of the semiconductor, and α is the impurity gradient. The values for W and α were extracted from C-V characteristics. Using equation (1), it was found that the strength of the electric breakdown field for the GaN pn junctions ranged from 1.5 to 3 MV/cm (Fig. 2). This value is approximately 4 times higher than the maximum breakdown field for a linearly graded GaAs pn junction at the same impurity gradient (see ref. [6]). The maximum breakdown field of 3 MV/cm was measured for an impurity gradient of $2 \times 10^{23} \text{ cm}^{-4}$. It was found that V_b increases with temperature. The temperature coefficient of V_b ranged from 1×10^{-2} to $2 \times 10^{-2} \text{ V/K}$ (Fig. 3).

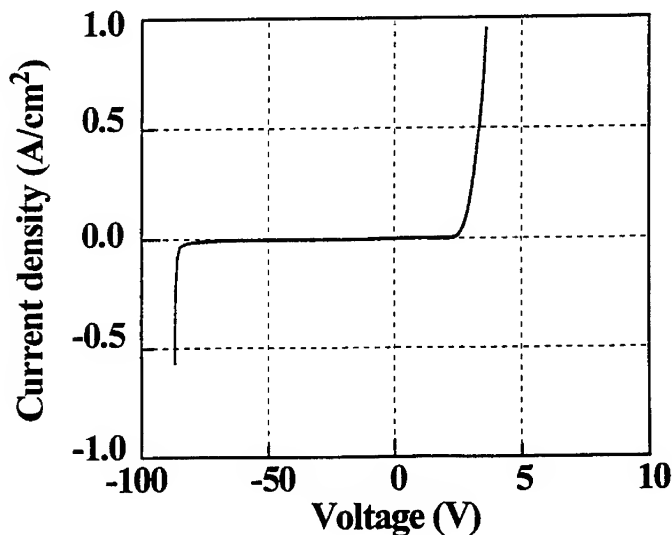


Figure 1. Current-voltage characteristics of a GaN pn diode (300 K).

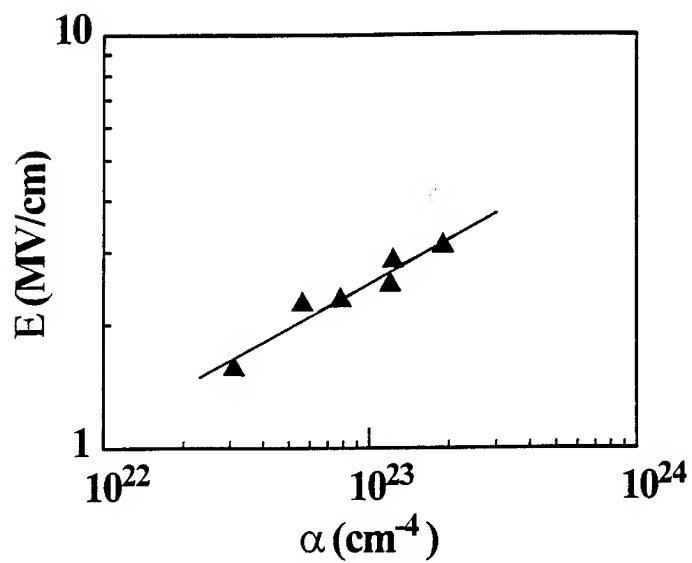


Figure 2. Breakdown field as a function of impurity gradient in a GaN pn junction.

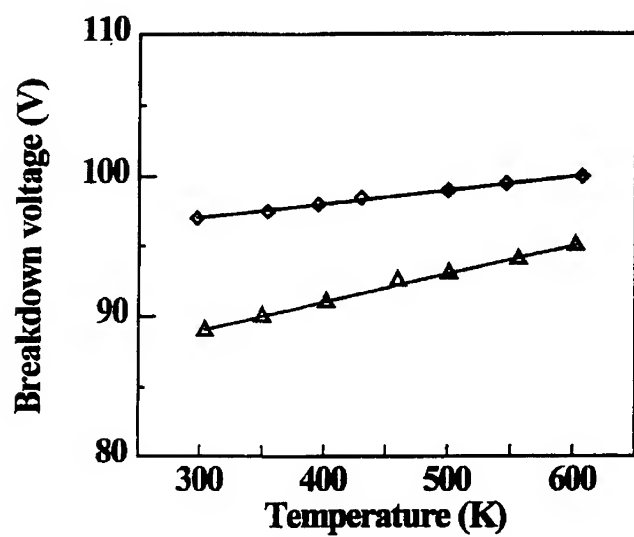


Figure 3. Temperature dependence of the breakdown voltage for two GaN pn structures.

AlGaIn pn junctions.

The structures investigated were as follows: n-GaN / n-AlGaIn / p-AlGaIn / p⁺-GaN. The structure was grown in a single epitaxial run. First, the n-GaN layer was grown and then the AlGaIn pn junction was formed. The AlN concentration in the alloy was from 2 to 8 mol.%. Thickness of the AlGaIn layers ranged from 0.1 to 0.5 μm . A p⁺-GaN cap layer about 0.5 μm thick was grown on the top of the AlGaIn pn junction. A detailed description of the structures was given in [2].

C-V characteristics indicated that these junctions were also linearly graded. Reverse I-V characteristics showed an abrupt breakdown at 40 - 100 V. The breakdown field was estimated to be not less than 2 MV/cm.

CONCLUSIONS

The electrical characteristics of GaN and AlGaIn pn junctions were investigated. The C-V characteristics showed that the junctions were linearly graded having an impurity gradient ranging from 2×10^{22} to $2 \times 10^{23} \text{ cm}^{-4}$. For GaN pn junctions, the built-in potential was from 2.2 to 2.6 V.

Reverse I-V characteristics showed an abrupt breakdown having a microplasmic nature. The breakdown voltage ranged from 40 to 150 V for GaN diodes and from 40 to 100 V for AlGaIn diodes. For GaN pn junctions, the breakdown electric field was measured to be 1-3 MV/cm depending on the impurity gradient in the junction. The temperature coefficient of the breakdown voltage was determined to be $\sim 10^{-2} \text{ V/K}$.

ACKNOWLEDGMENTS

The authors would like to thank K. Vassilevski, V. Sizov and E. Kalinina for help in sample preparation and V. Soloviev for EBIC measurements. This work was supported in part by the Advanced Research Projects Agency.

REFERENCES

1. V.A. Dmitriev, K.G. Irvine, J.A. Edmond, G.E. Bulman, C.H. Carter, Jr., A.S. Zubrilov, I.P. Nikitina, V.I. Nikolaev, A.I. Babanin, Yu.V. Melnik, E.V. Kalinina, and V.E. Sizov in Compound Semiconductors 1994, edited by H. Goronkin and U. Mishra (Inst. Phys. Conf. Ser. 141, Bristol: IOP Publishing, 1995) pp. 497-502.
2. V.A. Dmitriev, K.G. Irvine, C.H. Carter, Jr., A.S. Zubrilov, and D.V. Tsvetkov, Appl. Phys. Lett. **67**, p.115 (1995).
3. A.S. Zubrilov, D.V. Tsvetkov, V.I. Nikolaev, V.A. Soloviev, and V.A. Dmitriev, to be published in the Proceedings of the Int. Conf. on Silicon Carbide and Related Materials-1995.
4. I. Nikitina and V. Dmitriev in Compound Semiconductors 1994, edited by H. Goronkin and U. Mishra (Inst. Phys. Conf. Ser. 141, Bristol: IOP Publishing, 1995) pp. 431-436.
5. K.V. Vassilevski, V.E. Sizov, and A.I. Babanin, to be published in the Proceedings of the Int. Conf. on Silicon Carbide and Related Materials-1995.
6. S.M. Sze, Physics of Semiconductor Devices, 2nd ed. Wiley, New York, 1981, pp. 99-108.

RECENT PROGRESS IN AlGaN/GaN BASED OPTOELECTRONIC DEVICES

M. A. KHAN, Q. CHEN, C. J. SUN, J. W. YANG *, and M. S. SHUR **

* APA Optics, APA inc., 2950 N. E. 84th Lane, Blaine, MN 55449, USA

** Department of Electrical Engineering, University of Virginia, Charlottesville, VA 22903

ABSTRACT

We review our recent results on GaN based optoelectronic devices, which include InGaN-AlGaN Light Emitting Diodes (LEDs), GaN photoconductive, Schottky barrier, and *p-n* junction ultraviolet detectors, and optoelectronic AlGaN-GaN Heterostructure Field Effect Transistors. GaN-based optoelectronic devices cover a wide spectral range and demonstrate visible blind operation. A high quality of the epitaxial layers, the recent development of high performance GaN-based heterostructure field effect transistors, and transparent substrates make this material system uniquely suited for optoelectronic integrated circuits operating in visible and ultraviolet range.

I. INTRODUCTION

Unique optical and electronic properties of the GaN/AlGaN material system open up numerous opportunities for visible-blind optoelectronic devices. These devices have a high sensitivity and a large gain-bandwidth product and can be integrated with GaN/AlGaN field effect transistors which have already demonstrated an operation at microwave frequencies. A transparent sapphire substrate also makes AlGaN/GaN based devices uniquely suited for optoelectronic applications. Figure 1 compares the energy gaps of wide band gap semiconductor materials with the spectral sensitivity of a human eye. As seen, GaN and related materials (which include AlN, InN, and AlGaN and InGaN solid state solutions) span the range from visible to UV. Since these are direct gap materials, they are better suited for optoelectronic applications than SiC polytypes.

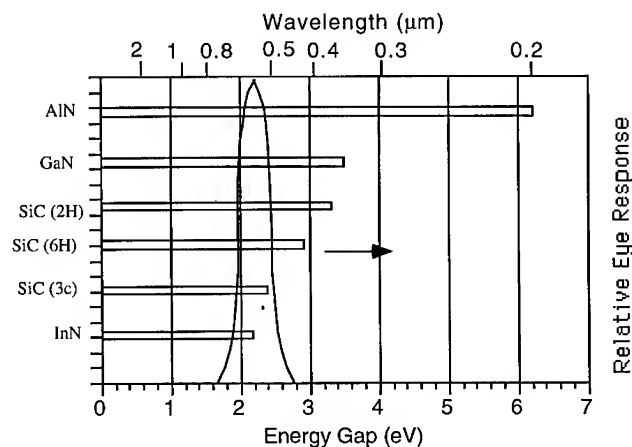


Figure 1: Energy gaps of wide band gap semiconductor materials with the spectral sensitivity of a human eye.

In this paper, we review our recent results on GaN based optoelectronic devices, which include, InGaN-AlGaN Light Emitting Diodes (LEDs), GaN *p-n* junction ultraviolet detectors, and optoelectronic AlGaN-GaN Heterostructure Field Effect Transistors.

II. EPITAXIAL LAYERS

All these devices use the epitaxial layers deposited using low pressure MOCVD over basal plane sapphire substrates. As reported elsewhere ^{1, 2, 3} we use triethylgallium, triethylaluminum and ammonia as the precursors for 'Ga', 'Al' and 'N'. Typical growth pressure and temperature are 76 torr and 1000 °C. As deposited the GaN layers are highly resistive with a carrier density well below 10^{15} cm^{-3} . The insulating GaN layers can be doped either *n*- or *p*-type using disilane (Si) or bis-Mg (Mg) as the dopants.

The single epilayers and the heterojunctions were characterized for their electrical and optical properties. The two dimensional electron gas at the AlGaIn/GaN heterointerface exhibits room temperature mobilities in excess of $1200 \text{ cm}^2/\text{V-sec}$ and over $5000 \text{ cm}^2/\text{V-sec}$ at 80 K. ^{3, 4}

III. PHOTOCONDUCTIVE, SCHOTTKY DIODE AND P-N JUNCTION DETECTORS

We fabricated GaN based photoconductive and photovoltaic ultraviolet (UV) detectors. ^{5, 6, 7} As an example, we show in Figure 2 the current-voltage curves for a *p-n* junction GaN UV detector. The doping level of the *p*- and the *n*-type layers in the junction region was around $5 \times 10^{16} \text{ cm}^{-3}$. A 1.5 V turn-on and a reverse breakdown in excess of 10 V is observed. Figure 3 shows the responsivity of this detector as a function of wavelength. As seen no photoresponse is observed for wavelengths larger than the band gap (365 nm). Below 365 nm, the responsivity is nearly independent of the wavelength indicating a very low surface recombination. This visible-blind detection feature was also observed for our GaN photoconductive and Schottky barrier detectors. ^{6, 7}

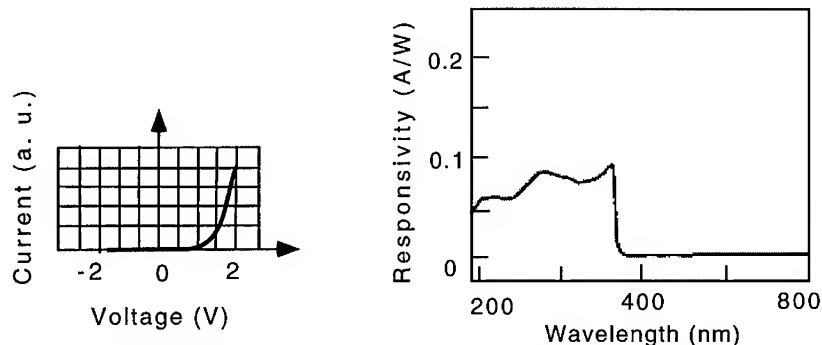


Figure 2: I-V curve of *p-n* junction GaN UV detector. ⁵

Figure 3: The photoresponsivity of GaN *p-n* junction versus wavelength. ⁵

IV. LIGHT EMITTING DIODES

Figure 4 we present the light emission from a GaN homojunction for a forward current of 20 mA across a 200x200 micron LED. ⁸ We have also demonstrated optically pumped stimulated emission from GaN ⁹ and InGaIn ¹⁰. These layers were deposited over basal plane sapphire substrates. A threshold power of around 1 MW/cm^2 was measured in each case. Figure 5 shows the vertical cavity photoluminescence signal from a GaN-InGaIn heterojunction as a function of wavelength using a pulsed nitrogen laser (337 nm) for pumping. As seen from the

figure, Fabry-Perot fringes are clearly visible on the spontaneous emission envelope. These indicate a high Q-value for the vertical cavity. The intensity of one of the modes increases superlinearly with an increase in the pump powers. From the dependence of the output power on the input power, we estimated a threshold for stimulated emission to be around 200-400 kW/cm² (a clear improvement compared to our previous results).

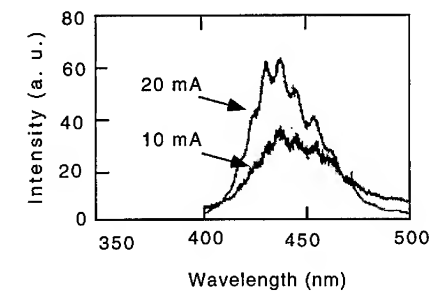


Figure 4: Emission spectrum of GaN homojunction LED at current of 20 mA. ⁸

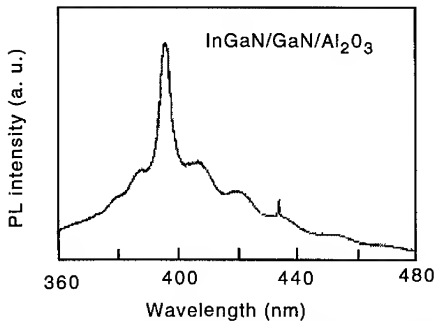


Figure 5: PL spectrum of InGaN/GaN/Al₂O₃ using pulsed N₂ laser as excitation source. ¹⁰

The sapphire substrates do not allow cleaving of parallel bars. The cubic spinel substrates allow for such cleaving. Therefore we have recently deposited high quality wurtzite GaN layers over cubic (111) spinel substrates. These were measured to have a stimulated emission threshold around 500 kW/cm² which is superior to the threshold value for similar films grown on sapphire substrates. These lateral cavities are well suited for studying optically and electrically pumped lasing.

V. OPTOELECTRONIC HETEROSTRUCTURE FIELD EFFECT TRANSISTORS (HFETs)

The HFET photodetector ¹¹ is based on a 0.2 micron gate AlGaIn/GaN HFET and utilizes a shift in the threshold voltage caused by the light generated carriers (see Figures 6 and 7).

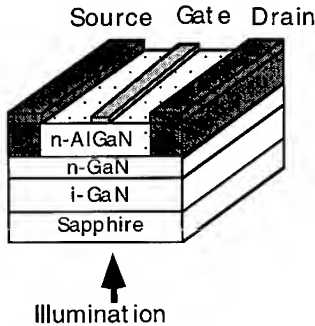


Figure 6: Schematic diagram of optoelectronic of AlGaIn/GaN HFETs. ¹¹

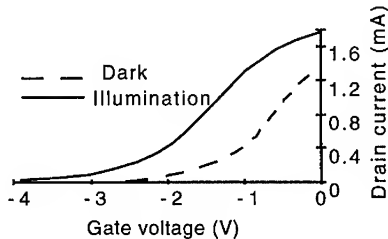


Figure 7: I-V characteristics of AlGaIn/GaN HFETs in the dark and under light. ¹¹

This shift is caused by trapped holes. Figure 8 compares the calculated values of the responsivity based on this model with the measured data.

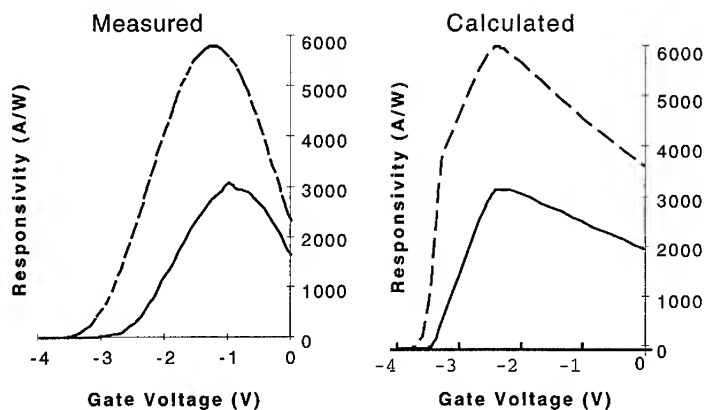


Figure 8: Measured and calculated dependencies of the AlGaIn/GaN responsivities on gate bias.¹¹ Dashed and solid curves refer to top and bottom illumination, respectively.

The response of AlGaIn/GaN Heterostructure Insulated Gate Field Effect Transistors (HIGFETs), see Figure 9, to light is different from that of AlGaIn/GaN HFETs. The HIGFET exhibits a low resistance state and a persisting high resistance state, before and after the application of a high drain voltage, respectively (see Figure 10). The device can be returned into the low resistance state by exposing it to optical radiation with sensitivity peaks at certain wavelengths (see Figures 11 and 12). Electron trapping in the gate insulator near the drain edge of the gate is a possible mechanism for this effect (see the insert in Figure 10).

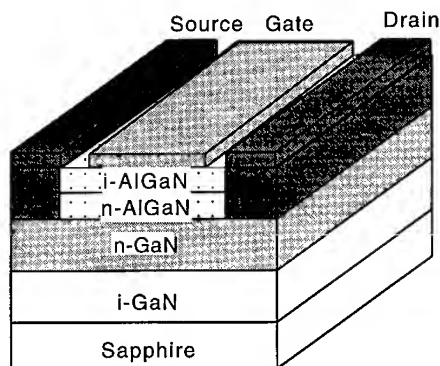


Figure 9: Schematic diagram of AlGaIn/GaN HIGFET.¹²

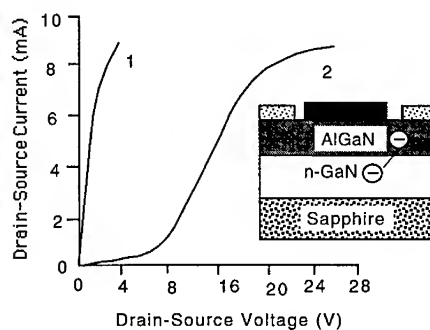


Figure 10: Current-voltage characteristic collapse. Curve 1 shows the on-state (before the application of a high drain bias). Curve 2 line shows the off-state (after the application of a high drain bias). The insert illustrates the suggested collapse mechanism which is the electron trapping in the barrier layer at the drain side of the gate.¹²

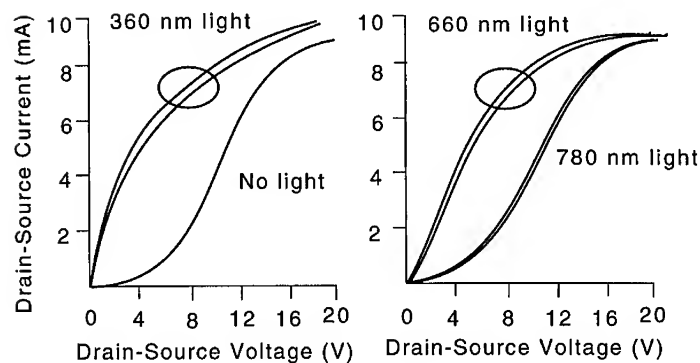


Figure 11: Current-voltage characteristics in the dark and under illumination. ¹²

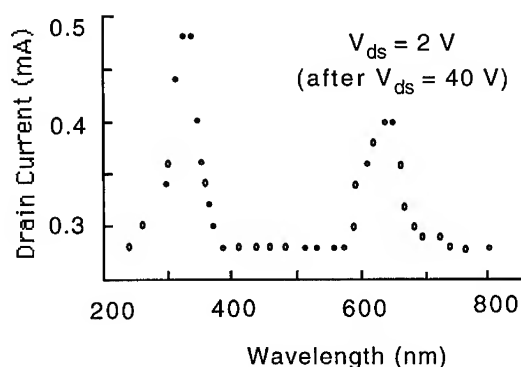


Figure 12: Dependence of the drain current on the wavelength of the optical radiation. ¹²

VI. CONCLUSIONS

GaN based optoelectronic devices include InGaN-AlGaN Light Emitting Diodes (LEDs), GaN photoconductive, Schottky barrier, and *p-n* junction ultraviolet detectors, and optoelectronic AlGaN-GaN Heterostructure Field Effect Transistors. These optoelectronic devices cover a wide spectral range. The GaN-based detectors demonstrate visible blind operation. A high quality of the epitaxial layers, the recent development of high performance GaN-based heterostructure field effect transistors, and transparent substrates makes this material system uniquely suited for optoelectronic integrated circuits operating in visible and ultraviolet range.

VII. ACKNOWLEDGMENT

This work has been partially supported by the Office of Naval Research (Project Monitor Max Yoder) and by the Army Research Office (Project Monitor John Zavada).

REFERENCES

- [1] M. A. Khan, J. M. Van Hove, J. N. Kuznia and D. T. Olson, "High Electron Mobility GaN/AlGa_N Heterostructures grown by LPMOCVD," *Appl. Phys. Lett.* 58, 2408 (1991).
- [2] M. A. Khan, J. N. Kuznia, J. M. Van Hove, N. Pan, and J. Carter, "Observation of a two-dimensional electron gas in low pressure MOCVD deposited GaN/AlGa_N heterojunctions," *Appl. Phys. Lett.*, 60, 3027 (1992)
- [3] M. A. Khan, Q. Chen, C. J. Sun, M. Shur, and B. Gelmont, "Two-dimensional electron gas in GaN-AlGa_N heterostructures deposited using trimethylamine-alane as the aluminum source in low pressure metalorganic chemical vapor deposition," *Appl. Phys. Lett.*, Vol. 67 (10), 1429 (1995).
- [4] M. S. Shur, B. Gelmont, and M. Asif Khan, High Electron Mobility in Two Dimensional Electrons Gas in AlGa_N/GaN Heterostructures, *J. Electronic Materials*, accepted for publication
- [5] M. A. Khan, Q. Chen, J. W. Yang, C. J. Sun, I. Adesida, A. T. Ping, and M. Shur, Processing and characterization of GaN-AlGa_N based electronic and optoelectronic devices, in *Proceedings of International Semiconductor Device Research Symposium*, Charlottesville, VA, Dec. 6-8, 1995, to be published
- [6] M. A. Khan, J. N. Kuznia, D. T. Olson, J. M. Van Hove, and L. Reitz, "High Responsivities photoconductive ultraviolet sensors based on insulating single crystal GaN layers," *Appl. Phys. Lett.*, 60, 2917 (1992).
- [7] M. Asif Khan, J. N. Kuznia, D. T. Olson, M. Blasingame and A. R. Bhattarai, "Schottky barrier photodetector based on Mg-doped p-type GaN films," *Appl. Phys. Lett.*, 63, 2455 (1993).
- [8] M. A. Khan, Q. Chen, R. A. Skogman, and J. N. Kuznia, "Violet LED's using high temperature RTA annealed p-type GaN Layers," *Appl. Phys. Lett.*, 66 (16), 2046 (1995).
- [9] M. A. Khan, J. M. Van Hove, D. T. Olson and J. N. Kuznia, "Vertical cavity, room temperature stimulated emission from photopumped GaN films deposited over sapphire substrates using LPMOCVD," *Appl. Phys. Lett.*, 58, 1515 (1991).
- [10] M. Asif Khan, S. Krishnakutty, R. A. Skogman, J. N. Kuznia, D. T. Olson and T. George, "Vertical Cavity Stimulated Emission from Photo-pumped InGa_N/GaN Heterojunctions at Room Temperature," *Appl. Phys. Lett.*, July 1994
- [11] M. A. Khan, M. S. Shur, Q. Chen, J. N. Kuznia, and C. J. Sun, *Electronics Letters*, 31, 398 (1995)
- [12] M. A. Khan, M. S. Shur, Q. C. Chen, and J. N. Kuznia, *Electronics Letters*, 30, 2175 (1994)

OPTICALLY PUMPED GaN-AlGa_N DOUBLE-HETEROSTRUCTURE LASERS GROWN BY ECR-GSMBE AND HVPE

P. A. Maki, R. J. Molnar, R. L. Aggarwal, Z.-L. Liao, and I. Melngailis
Lincoln Laboratory, Massachusetts Institute of Technology
Lexington, MA 02173-9108

ABSTRACT

We have observed laser emission with well-defined cavity modes in optically pumped GaN-Al_{0.1}Ga_{0.9}N double-heterostructure (DH) lasers. The laser structures were grown using an electron-cyclotron-resonance nitrogen-discharge source and gas-source molecular beam epitaxy (ECR-GSMBE) on thick ($\geq 10 \mu\text{m}$) GaN buffers grown by hydride vapor-phase epitaxy (HVPE) on c-plane sapphire. Transversely pumped cavities using a 337.1 nm nitrogen laser pump source exhibit a threshold pump fluence ranging from 0.15 to 0.3 mJ/cm² at 77 K, a linear light output above threshold, a lasing wavelength of 358 nm, and an estimated differential quantum efficiency of 1%. The room-temperature threshold is about 1.7 times higher. Longitudinal mode structure has been resolved in a shorter-cavity (23 μm) device at 77 K. The measured mode spacing of 0.56 nm corresponds to a group index of 5.0. Far-field measurements in a plane perpendicular to the plane of the heterostructure indicate a double-lobed pattern for a 1000 Å thick GaN active region, and a single lobe with a FWHM of 60° for a 4000 Å active region. The thick HVPE GaN buffer layer provides for a lattice-matched growth and results in improved nucleation in MBE, as indicated by a high-quality reflection-electron-diffraction pattern of the as-loaded wafers. The surface morphology of the MBE layers on the HVPE buffer shows improved optical smoothness as compared to layers grown directly on sapphire using a low-temperature, MBE-grown GaN buffer. Laser facets were formed either by saw cutting or cleaving of the GaN buffer and epilayer along crystal planes. Details of the material development and laser performance are described.

INTRODUCTION

The demonstration of efficient light emitting diodes in the group III-nitride material system [1] indicates that there is an excellent prospect for realizing diode lasers which span the visible to the ultraviolet. This would enable many low-cost applications based on diode lasers, such as optical data recording/reading, chemical sensing, and displays. While the development of efficient, long-lived diode lasers in this wavelength range is the eventual objective, optical pumping is a convenient technique for evaluating the optical properties of GaN laser structures without the added complications posed by electrical injection. Optically pumped lasing has been demonstrated [2-3], and there have been a number of reports of stimulated emission [4-8]; however, high threshold power densities observed in the optical pumping experiments indicate that the realization of a low threshold current density diode laser will require improvements in the material and laser structures.

We have found that a limiting factor in the gain characteristics of GaN is the surface morphology of the epitaxial film, which is intimately dependent on the substrate used for epitaxial growth. Morphology affects the gain by contributing a scattering factor as the optical mode is guided through the lasing medium. The strength of this scattering depends on the characteristic length scale of the surface ripple. Unfortunately, the length scale of surface ripple of GaN heteroepitaxially grown on (0001) sapphire, at least by ECR-MBE, contributes to high scattering losses in the guided mode for GaN/AlGa_N DHs in the UV wavelength range. This is true, at least in our experiments, despite the fact that the surfaces appear to be "mirror smooth" at visible wavelengths. These scattering losses should impact visible-wavelength lasers as well because of the wavelength reduction in the material due to the GaN refractive index.

Here, we demonstrate that the morphology of the epitaxial GaN film can be improved by using a GaN buffer grown by HVPE on (0001) sapphire as the starting substrate. The advantage of the HVPE buffer is that the morphology is optically smoother in the UV than for GaN material grown by ECR-MBE on sapphire using a low-temperature buffer (two-step process). The HVPE buffer enables homoepitaxial growth which replicates the starting surface morphology. The morphology of the HVPE buffer at present exhibits a variety of growth features characteristic of

the HVPE process, but by mechanically polishing these buffers, high-quality, planar surfaces can be obtained. It should be noted, however, that stimulated emission is observed from layers grown on both as-grown and polished surfaces. Using these buffers, we have observed, for the first time, optically pumped laser emission exhibiting cavity modes in GaN/AlGaIn DHs grown by ECR-MBE.

EXPERIMENTAL

The details of the HVPE process have been published elsewhere [9]. The HVPE buffers, initially $\sim 15\text{ }\mu\text{m}$ in thickness, grown on (0001) sapphire, are mechanically polished to remove growth hillocks with a resulting thickness of $\sim 8\text{ }\mu\text{m}$. The substrates are chemically cleaned using solvents and 1:1 $\text{H}_2\text{SO}_4 : \text{H}_2\text{O}_2$ to remove contaminants, and chemically etched with 1:1 $\text{H}_2\text{SO}_4 : \text{H}_3\text{PO}_4$ prior to loading into the MBE system.

The MBE system is a Varian gas-source modular GEN II, pumped by a 2200 l/s turbo-molecular pump, backed by a dry-pumping system. The nitrogen source is an ASTeX model AX4300 compact ECR source. Effusion sources are used for elemental gallium and aluminum. The substrates, typically 1 inch in diameter or a quadrant of a 2 inch wafer, are mounted in a nonbonded holder. These substrates, after loading in the MBE system, are heat cleaned in a nitrogen plasma.

Growth of the GaN/AlGaIn DH structure is initiated at the preferred GaN growth temperature, estimated to be 700 to 750 $^{\circ}\text{C}$, without the need for a low-temperature GaN buffer. Figures 1a and 1b show the reflection electron diffraction (RED) patterns after 100 \AA of GaN growth. The growth conditions, arrived at by a study of the GaN material quality and growth rates as a function of the ECR source parameters, substrate temperature, and N_2 mass flow, are as follows: ECR forward power of 40 to 60 W, N_2 mass flow of 3.3 sccm, and substrate thermocouple temperature of 950 $^{\circ}\text{C}$. These conditions result in 300 K Hall electron mobilities of 200 to 270 $\text{cm}^2/\text{V}\cdot\text{s}$ for GaN with $2 \times 10^{17}\text{ cm}^{-3}$ electron concentrations, grown on (0001) sapphire. These mobility values are typical for this growth method [10,11], and the growth conditions are assumed to be optimal for the laser structures. GaN growth rates are as high as 0.18 $\mu\text{m}/\text{h}$. The first DH grown consisted of a top cladding layer of $\text{Al}_{0.1}\text{Ga}_{0.9}\text{N}$, 1000 \AA thick, followed by the GaN active layer, 1000 \AA thick, and a bottom cladding layer of $\text{Al}_{0.1}\text{Ga}_{0.9}\text{N}$, 5000 \AA thick. In a second heterostructure, the active layer thickness was increased to 4000 \AA .



(a) $\langle 11\bar{2}0 \rangle$ orientation (b) $\langle 11\bar{0}0 \rangle$ orientation
Figure 1. RED patterns after 100 \AA of GaN growth.

RESULTS

Figure 2 shows a scanning electron micrograph (SEM) of the surface morphology of the DH laser grown on the polished HVPE substrate. For comparison, Figure 3 shows the surface

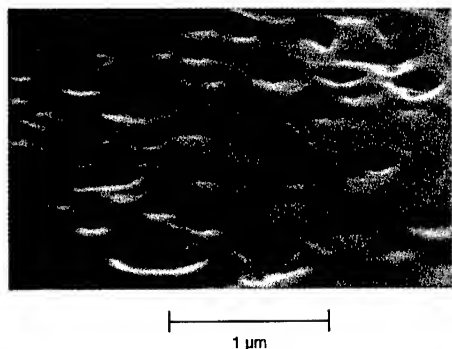


Figure 2. SEM of DH surface morphology grown on polished HVPE GaN buffer.

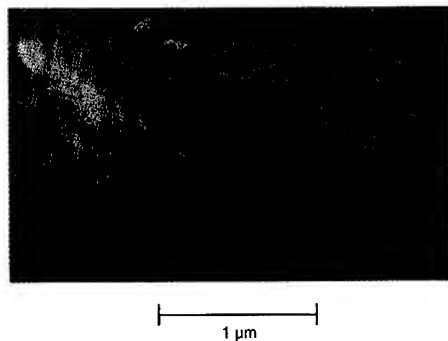


Figure 3. SEM of DH surface morphology grown directly on (0001) sapphire.

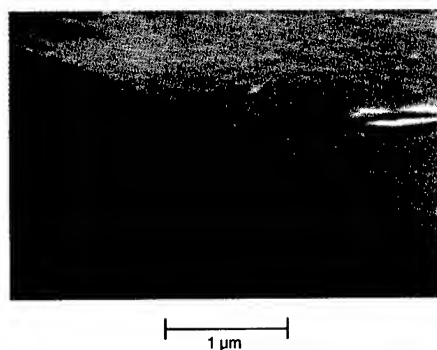


Figure 4. SEM of DH surface morphology grown on unpolished (as-grown) HVPE GaN buffer.

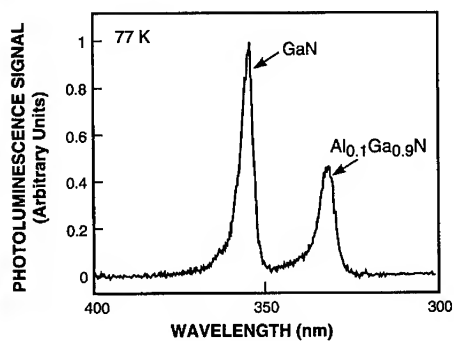


Figure 5. PL of DH grown on polished HVPE GaN buffer. Backscattering geometry from surface.

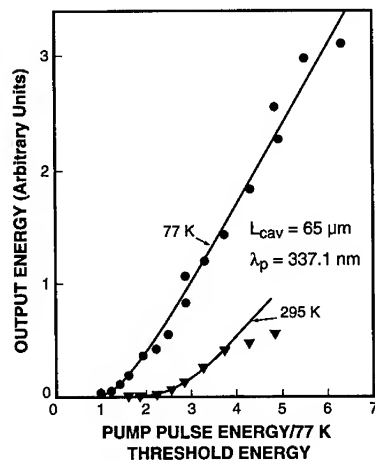


Figure 6 (right). Transversely optically pumped edge emission output energy as a function of normalized pump pulse energy at 77 and 295 K for DH grown on polished HVPE GaN buffer (65 μm long cavity, saw-cut facets).

morphology of the DH waveguide grown on (0001) sapphire using the two-step process with a 100 Å thick low-temperature GaN buffer. While both surfaces are textured, the fine-grain morphology observed in layers grown directly on sapphire by ECR-MBE is absent in layers grown on the HVPE buffer. The remaining features of the material grown on the HVPE buffer may result from the polishing and cleaning processes prior to growth, and are not necessarily due to growth-induced defects. This is supported by the morphology obtained by growth on unpolished HVPE buffers, as shown in Figure 4, where the scalloped pattern of the polished GaN buffers is absent.

Figure 5 shows the 77 K photoluminescence (PL) spectrum of the DH on the polished HVPE GaN buffer obtained in a backscattering geometry using a 266 nm radiation from a frequency-quadrupled Q-switched Nd:YAG laser. The PL intensity and linewidths are greatly improved over those of the DH grown directly on sapphire.

Figure 6 shows the output energy as a function of pump fluence of a 65 µm long cavity, at 77 and 300 K. Both curves show a threshold and a linear dependence above threshold, characteristic of stimulated emission. Based on the focused pump beam spot size of 2×0.2 mm, the calculated pump fluence is 0.3 mJ/cm² at 77 K, and 0.5 mJ/cm² at 300 K. The optical modes for this cavity length, however, could not be resolved. The 77 K emission spectrum from a shorter, saw-cut, 23 µm cavity is shown in Figure 7, where the cavity modes are clearly visible. The measured mode spacing of 0.56 nm corresponds to a group refractive index of 5.0, which is in agreement with the refractive index data of GaN [12].

Measurements of the far-field radiation pattern of the laser indicated a double-lobed intensity pattern in the plane perpendicular to the plane of the heterostructure, indicative of poor confinement of the optical field to the 1000 Å thick GaN active layer. In order to improve the mode confinement, a second structure was grown with a 4000 Å thick GaN active layer, this time on an unpolished HVPE buffer. The laser cavity was formed by breaking along the GaN cleavage planes of the thick buffer. The resulting intensity vs pump characteristic and the layer structure are shown in Figure 8 for a 1 mm long cavity at 77 K. The emission spectrum near threshold and above threshold is shown in Figure 9. No attempt has yet been made to resolve mode structure with a short cavity for this heterostructure. The calculated threshold fluence is 0.15 mJ/cm² (threshold pump power of 0.25 MW/cm²). The far-field pattern shown in Figure 10 exhibits an angular width (FWHM) of 60°, which is consistent with the 4000 Å thick active layer. Based on the far-field pattern, and measurements of the output energy of the laser, the estimated external quantum efficiency is 1%.

DISCUSSION

Thick GaN buffers, grown by HVPE, have proven to be effective as substrates for the overgrowth of GaN and AlGaIn by ECR-GSMBE. The RED patterns of the GaN films demonstrate high-quality crystalline structure and growth initiation behavior. Compared to the MBE growth of GaN directly on sapphire, the use of these buffers has resulted in improvements in both the morphology and the optical properties of the material, as illustrated by the results in Figures 2 and 5. At present, the main limitation of the method for device applications is the surface morphology of the as-grown HVPE GaN, which exhibits significant nonplanarity, due to the presence of growth hillocks. Mechanical polishing is an effective way to planarize the surface, and the resulting surface quality after chemical preparation is sufficient for growth. Further development work on this process is required to obtain a smoother morphology which will reduce scattering effects and result in lower laser thresholds. The surface quality of structures grown on as-grown HVPE buffers is also sufficient to obtain laser quality material, but the large-scale HVPE growth hillocks interfere with subsequent lithography steps.

A second advantage of the thick GaN buffer grown by HVPE is that the cleavage of the epilayer along the GaN cleavage planes is enhanced due to the greater thickness of material. This can overcome the fact that the GaN cleavage planes for (0001) growth are rotated by 30° from the sapphire cleavage planes. An SEM of this type of cleaving is shown in Figure 4. As indicated by the results of Figures 8 and 9, an effective optical cavity can be formed by cleaving the thick GaN buffer. Compared to thin GaN films on sapphire, the thick GaN buffer can also provide a lower series resistance contact for a laser. In addition, if the GaN buffer could be separated from the

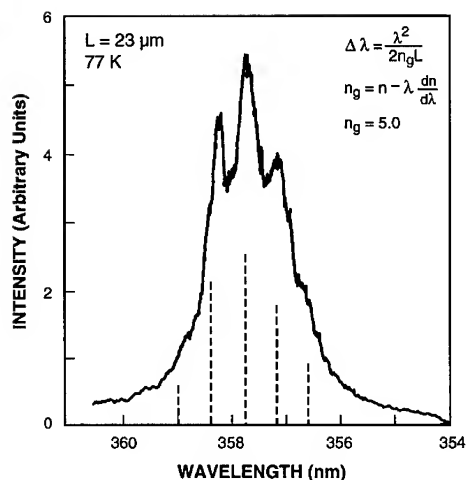


Figure 7. Emission spectrum of 23 μm long cavity at 77 K (saw-cut facets). Vertical dashed lines indicate mode positions (mode spacing 0.56 nm).

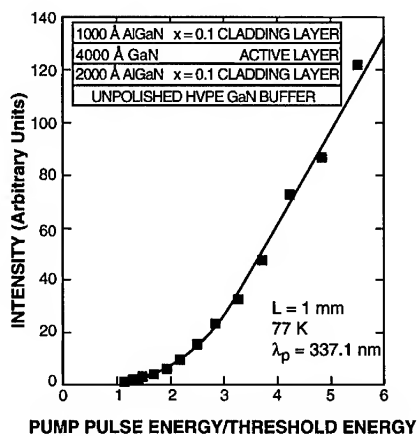


Figure 8. Transversely pumped edge emission output energy as a function of normalized pump pulse energy at 77 K for DH grown on unpolished HVPE GaN buffer (1 mm long cavity, cleaved facets). Inset indicates structure.

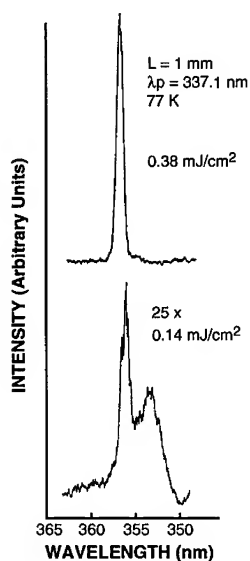


Figure 9. Emission spectrum at threshold ($E_p = 0.14 \text{ mJ/cm}^2$) and above threshold ($E_p = 0.38 \text{ mJ/cm}^2$) for DH (Figure 8) grown on unpolished HVPE GaN buffer (cleaved facets).

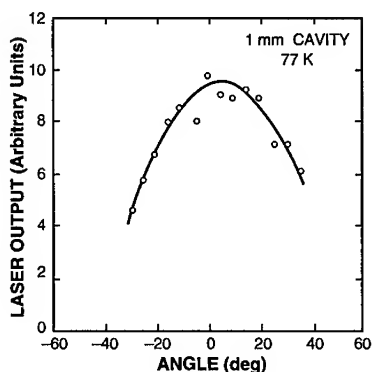


Figure 10. Emission far-field output beam profile of DH (Figure 8) grown on unpolished HVPE GaN buffer (cleaved facets).

sapphire to yield a free-standing device film, this would be an added advantage in diode laser fabrication.

The threshold pump power observed for the GaN/AlGaIn DHs is higher than, but comparable to, the value reported by Akasaki et al. [5] for optically pumped GaN films grown by OMVPE. These results suggest that the optical quality of the ECR-MBE material may be comparable to OMVPE material for laser applications.

As indicated by the far-field patterns, the optical field is poorly confined in the thinner GaN active layer, suggesting that the thicker active layers are required for effective confinement, due to the small index difference between GaN and $\text{Al}_{0.1}\text{Ga}_{0.9}\text{N}$. For the 4000 Å thick active layer, the spontaneous emission intensity is significantly reduced above threshold, suggesting that the tail of the optical field into the GaN buffer has been reduced. To our knowledge, this is the first report of far-field patterns from GaN DH laser structures and illustrates some of the problems that will arise with the design of a diode laser.

The observation of the mode structure for the 23 μm cavity laser is of interest because we believe it to be the first report of optical mode spacing that is consistent both with the physical cavity length and with independent data on the refractive index of GaN.

CONCLUSION

The use of HVPE buffers as substrates has enabled the convincing demonstration of laser action with mode structure for GaN/AlGaIn DHs grown by ECR-GSMBE. This establishes the feasibility of using HVPE GaN buffers, grown on sapphire, as substitutes for bulk GaN substrates. The results also indicate that ECR-MBE has potential as a technique for the development of GaN/AlGaIn diode lasers.

ACKNOWLEDGMENT

We thank D. B. Hoyt and J. L. Daneu for their invaluable technical assistance. This work was supported by the U. S. Department of the Air Force.

Opinions, interpretations, conclusions, and recommendations are those of the author and are not necessarily endorsed by the United States Air Force.

REFERENCES

1. S. Nakamura, T. Mukai, and M. Senoh, *Appl. Phys. Lett.* **64**, 1678 (1994).
2. X. H. Yang, T. J. Schmidt, W. Shan, J. J. Song, and B. Goldenbert, *Appl. Phys. Lett.* **66**, 1 (1995).
3. A. S. Zubrilov, V. I. Nikolaev, D. V. Tsvetkov, V. A. Dmitriev, K. G. Irvine, J. A. Edmond, and C. H. Carter, Jr., *Appl. Phys. Lett.* **67**, 533 (1995).
4. H. Amano, T. Asahi, and I. Akasaki, *Jpn. J. Appl. Phys.* **29**, 205 (1990).
5. I. Akasaki, H. Amano, N. Koide, M. Kotaki, and K. Manabe, *Physica B* **185**, 428 (1993).
6. H. Amano, N. Watanabe, N. Koide, and I. Akasaki, *Jpn. J. Appl. Phys.* **32**, 1000 (1993).
7. M. A. Khan, S. Krishnankutty, R. A. Skogman, J. N. Kuznia, D. T. Olson, and T. George, *Appl. Phys. Lett.* **65**, 520 (1994).
8. K. Yung, J. Yee, J. Koo, M. Rubin, N. Newman, and J. Ross, *Appl. Phys. Lett.* **64**, 1135 (1994).
9. R. J. Molnar, K. B. Nichols, P. Maki, E. R. Brown, and I. Melngailis, *Mater. Res. Soc. Symp. Proc.* **378**, 479 (1995).
10. M. E. Lin, B. Sverdlov, G. L. Zhou, and H. Morkoç, *Appl. Phys. Lett.* **62**, 3479 (1993).
11. R. J. Molnar, R. Singh, and T. D. Moustakas, *J. Electron. Mater.* **24**, 275 (1995).
12. E. Ejder, *Phys. Status Solidi* **6**, 445 (1971).

ANALYSIS OF WURTZITE GaN/AlGaN QUANTUM WELL LASERS FROM FIRST-PRINCIPLES CALCULATIONS

T. UENOYAMA and M. SUZUKI

Central Research Laboratories, Matsushita Electric Industrial Co., Ltd.,
3-4 Hikaridai, Seika-cho Souraku-gun Kyoto 619-02, Japan, takeshi@crl.mei.co.jp

ABSTRACT

Optical gain of wurtzite GaN/AlGaN quantum wells has been studied from a first-principles calculation using the $\mathbf{k} \cdot \mathbf{p}$ method. Most of the parameters in the $\mathbf{k} \cdot \mathbf{p}$ method were determined by fitting the band structures by the first-principles calculation. Owing to the small spin-orbit splitting energies of the wurtzite GaN and AlN, the optical gain has been calculated using the 6×6 Hamiltonian for the valence band. It is found that the large hole effective masses and the small spin-orbit splitting cause the higher threshold current density of wurtzite GaN/AlGaN quantum well lasers.

INTRODUCTION

Since high efficient short wavelength light emitting diodes (LEDs)¹ were successfully fabricated recently using wurtzite GaN and related nitrides, the study of their laser diodes has been performed vigorously. Generally, most optical and transport phenomena in semiconductor devices involve only a small region of k -space centered around a particular wave number k_0 which is an extremum. As a result, the physics of these systems is governed by the band structure in the immediate vicinity of k_0 . The $\mathbf{k} \cdot \mathbf{p}$ method is an appropriate approach not only to determine the electronic states but also to design quantum devices. The parameters in the $\mathbf{k} \cdot \mathbf{p}$ method are usually determined from measurements but the most of them for the Group-III nitrides have not been measured yet. Recently, we have derived the unknown parameters of the $\mathbf{k} \cdot \mathbf{p}$ method of GaN and AlN by fitting the energy dispersions in terms of the first-principles calculations². In this paper, we have investigated the optical gain of wurtzite GaN/AlGaN quantum well structure using the $\mathbf{k} \cdot \mathbf{p}$ method with the parameters based on first-principles calculation. The detailed derivation of the parameters has been discussed in ref. 2. Since the spin-orbit splitting energies are less than 20 meV for AlN and GaN, we should construct the 6×6 effective Hamiltonian and have studied the valence subband structures, to analyze the optical gain. It is found that the large hole effective masses and the small spin-orbit splitting cause the higher threshold current density of wurtzite GaN/AlGaN quantum well laser diodes.

OPTICAL GAIN FROM FIRST-PRINCIPLES CALCULATIONS

The N atom has such a strong electron affinity that the valence charges of GaN and AlN tend to be localized. Therefore, a conventional pseudo-potential method based on the plane wave is not adequate. We have used the full-potential linearized augmented plane wave (FLAPW) method³, within the local density functional approximation (LDA)⁴. Generally, the LDA gives a reduced energy-gap, but the LDA wavefunctions are not so different from the corrected ones. Therefore, the mixing among the bands would be given correctly as long as the energy-gap was large. The $\mathbf{k} \cdot \mathbf{p}$ Hamiltonian for the band edge

near the Γ point of wurtzite structure is given by,

$$\mathbf{H}(\mathbf{k}) = \begin{pmatrix} \mathbf{H}_{cc} & \mathbf{H}_{cv} \\ \mathbf{H}_{cv}^\dagger & \mathbf{H}_{vv} \end{pmatrix}. \quad (1)$$

\mathbf{H}_{cv} indicates the direct interaction between the conduction band minimum (CBM) and the valence band maximum (VBM). \mathbf{H}_{cc} and \mathbf{H}_{vv} indicate the conduction band and the valence band without the interaction between CBM and VBM, respectively. The interactions with the other bands were treated as the second order perturbation. \mathbf{H}_{cv} is given by,

$$\mathbf{H}_{cv} = \begin{pmatrix} Q & 0 & R & 0 & Q^* & 0 \\ 0 & Q & 0 & R & 0 & Q^* \end{pmatrix}, \quad (2)$$

where

$$Q = \frac{1}{\sqrt{2}} \frac{\hbar}{m_0} \langle S|p_x|X \rangle (k_x + ik_y) = \frac{1}{\sqrt{2}} P_1 (k_x + ik_y),$$

$$R = \frac{\hbar}{m_0} \langle S|p_z|Z \rangle k_z = P_{||} k_z.$$

Note that \mathbf{H}_{cv} includes $\langle S|p_i|i \rangle (i = x, y, z)$, which is related to the dipole matrix element. Owing to the large energy-gaps of GaN and AlN, the 8×8 Hamiltonian can be splitted into the 2×2 Hamiltonian \mathbf{H}'_{cc} for the conduction bands and the 6×6 Hamiltonian \mathbf{H}'_{vv} for the valence bands. \mathbf{H}_{cv} was renormalized into the matrix elements of \mathbf{H}'_{cc} and \mathbf{H}'_{vv} . They are given by,

$$\mathbf{H}'_{cc} = \begin{pmatrix} E_c & 0 \\ 0 & E_c \end{pmatrix}, \quad (3)$$

$$\mathbf{H}'_{vv} = \begin{pmatrix} F & 0 & -H^* & 0 & K^* & 0 \\ 0 & G & \Delta & -H^* & 0 & K^* \\ -H & \Delta & \lambda & 0 & I^* & 0 \\ 0 & -H & 0 & \lambda & \Delta & I^* \\ K & 0 & I & \Delta & G & 0 \\ 0 & K & 0 & I & 0 & F \end{pmatrix}, \quad (4)$$

where

$$E_c = E_s^0 + \frac{\hbar^2 k_z^2}{2m_e^{\parallel}} + \frac{\hbar^2 k_{\perp}^2}{2m_e^{\perp}},$$

$$F = \Delta_1 + \Delta_2 + \lambda + \theta, \quad G = \Delta_1 - \Delta_2 + \lambda + \theta,$$

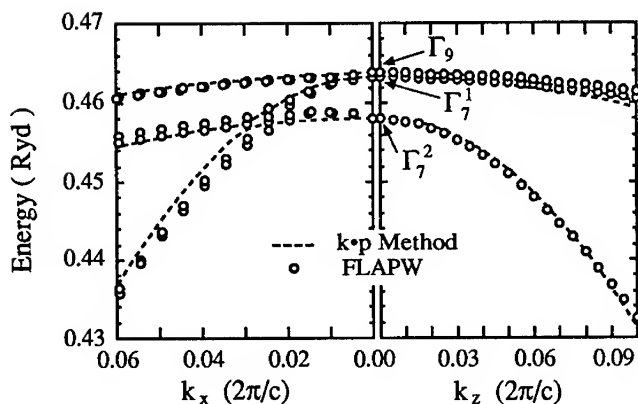


Fig. 1. Valence band structures of GaN by $\mathbf{k} \cdot \mathbf{p}$ method and FLAPW.

$$H = iA_6k_zk_+ - A_7k_+, \quad I = iA_6k_zk_+ + A_7k_+,$$

$$K = A_5k_+^2, \quad \Delta = \sqrt{2}\Delta_3, \quad \lambda = E_p^0 + A_1k_z^2 + A_2k_\perp^2,$$

$$\theta = A_3k_z^2 + A_4k_\perp^2, \quad k_\pm = k_x \pm ik_y, \quad k_\perp^2 = k_x^2 + k_y^2.$$

Δ_1 and $\Delta_{2,3}$ represent the crystal-field and spin-orbit splitting energies, respectively. A_i correspond to the Luttinger parameters in the zincblende crystals. Then, the parameters in \mathbf{H}'_{cc} and \mathbf{H}'_{vv} were determined independently, by reproducing the band structures near the band edge. The valence band structure, fitted by the $\mathbf{k} \cdot \mathbf{p}$ method (dashed lines) is shown in Fig. 1. The open circles are result from the FLAPW method. The parameters in the $\mathbf{k} \cdot \mathbf{p}$ calculation are indicated in Table 1. \parallel and \perp mean the directions parallel and perpendicular to the c -axis, respectively. The effective hole masses of GaN from the A_i are $m_{\Gamma_9}^\parallel = 1.1$, $m_{\Gamma_9}^\perp = 1.65$ and very heavy. There are three bands, labeled Γ_9 , Γ_7^1 , and Γ_7^2 at the Γ point. These eigenstates can be approximately expressed by,

$$|\Gamma_9 \pm \frac{3}{2}\rangle = |X \pm iY, \pm \frac{1}{2}\rangle$$

$$|\Gamma_7^1 \pm \frac{1}{2}\rangle \sim |X \pm iY, \mp \frac{1}{2}\rangle$$

$$|\Gamma_7^2 \pm \frac{1}{2}\rangle \sim |Z, \pm \frac{1}{2}\rangle,$$

due to $\Delta_{so} \sim 0$. Therefore, in the k_z direction, the conduction band is strongly coupled with the only Γ_7^2 state through $k_z p_z$ perturbation and it causes the only Γ_7^2 hole mass to be light. On the other hand, in the k_x direction, the conduction band is strongly coupled with the mixed state $(|\Gamma_9 \pm \frac{3}{2}\rangle + |\Gamma_7^1 \mp \frac{1}{2}\rangle \sim |X\rangle)$. Then, only one mixed band at the finite wavenumber has small effective hole mass.

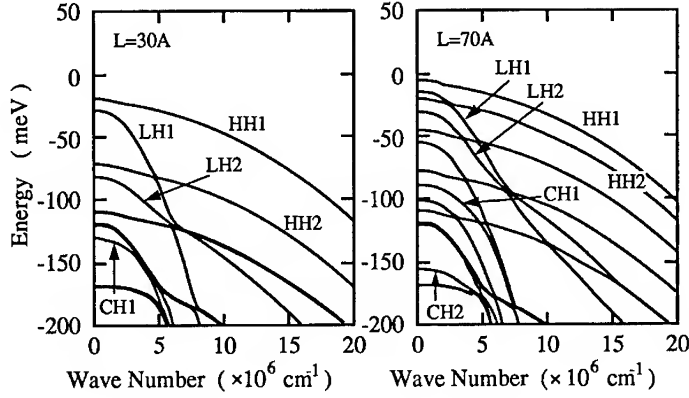


Fig. 2. Subband structures in k_x - k_y plane.

When the heterojunction is perpendicular to the c -axis, k_z becomes an operator in H'_{cc} and H'_{vv} . The subband structures are evaluated by solving the matrix differential eigenvalue problems. We have explained the method to solve it in detail in ref. 5. Figure 2(a),(b) show the valence subband structures of GaN/Al_{0.2}Ga_{0.8}N quantum well with the well length $L = 30$ Å and $L = 70$ Å, respectively. The parameters in the calculation are shown in the Table 1. The band off-sets and the other parameters in ternary layer are

Table I. Electron effective masses, the square of the momentum matrix elements, Luttinger-like valence band parameters and splitting energies. m_e^i , A_i and Δ_i are in units of m_0 , $\text{Ryd}\hbar^2/2m_0$, $\hbar^2/2m_0$ and meV, respectively.

	m_e^{\parallel}	m_e^{\perp}	P_{\parallel}^2	P_{\perp}^2
AlN	0.33	0.25		
GaN	0.20	0.18	0.96	1.13

	A_1	A_2	A_3	A_4	A_5	A_6	A_7	Δ_1	Δ_2	Δ_3
AlN	-3.95	-0.27	3.68	-1.84	-1.95	-2.91	0	-58.5	6.8	6.8
GaN	-6.56	-0.91	5.65	-2.83	-3.13	-4.86	0	72.9	5.2	5.2

determined by the virtual crystal approximation. The band off-set ΔE_v between GaN and AlN was 0.82 eV by the first-principles calculation. This value is merely derived from the difference in energy of the Γ_9 s between GaN and AlN. Here we labeled the subbands as HH_i (Γ_9 :heavy hole), LH_i (Γ_7^1 :light hole) and CH_i (Γ_7^2 :crystal field splitting), whose naming

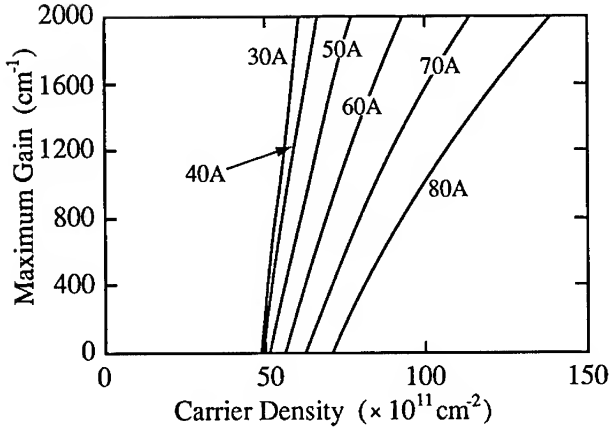


Fig. 3. Maximum gain as a function of carrier density.

corresponds to the case in k_x - k_y plane. Note here that the subband energy dispersions have a clear trace of the bulk ones due to the fact that the point group of the quantum well structure is still the same C_{6v} as the bulk. Since the hole masses of Γ_9 and Γ_7^1 are almost same along the k_z direction, the subband wavefunctions of HH_i and LH_i become almost same as well. Therefore, the mixing through A_5 between HH_i and LH_i with the same indices of the subbands is strong but the other mixings are very weak. As a result, there are strong mixings but the nonparabolicities of the dispersion are weak. The hole masses of HH_i and LH_i in the $k_x - k_y$ plane cannot be less than those of bulk. As for the CH subbands, the only CH_1 is a bound state in Fig.2(a) and is mixed with LH_2 through A_6 . Thus, the density of states (DOS) of the only LH_2 is enhanced. When the well length is increased, the CH_2 subband also becomes a bound state in the well. The mixing between CH_2 and LH_1 makes the DOS of the LH_1 enhanced, as shown in Fig. 2(b). Generally, these properties would be observed for the other Group-III nitrides materials since the spin-orbit coupling is negligible in a N atom⁵.

Since we have derived the values of the dipole matrix elements and subband energies with the eigenfunctions, the optical gain can be calculated by,

$$g(\omega) = \frac{\bar{n}2\pi}{c\hbar} \sum_{n,m} \sum_{k_{\perp}} |\langle c, n, k_{\perp} | \frac{e}{m_0 c} \vec{A} \cdot \vec{p} | v, m, k_{\perp} \rangle|^2 \times (f_c(E_{n,k_{\perp}}^c) + f_v(E_{m,k_{\perp}}^v) - 1) \delta(\omega - E_{n,k_{\perp}}^c - E_{m,k_{\perp}}^v) \quad (5)$$

\bar{n} is index number of the active layer. n, m are the subband indices of the conduction and valence bands, respectively. f_c, f_v are electron and hole distribution functions. Figure 3 shows the maximum gain of TE mode as a function of the carrier density in the wells, varying the well length from 30 to 70 Å. The other parameters are as same as in the calculation of the subbands. When the well length is beyond 50 Å, the transparent carrier

density becomes extremely increased. The reason is that the CH_2 subband becomes the bound state in the well and the DOS of the LH_1 subband is enhanced. The threshold carrier density of GaN/AlGaIn quantum well lasers would be two times or more than that of the conventional ones, if their cavity losses and the optical confinements could be assumed to be same. This is mainly caused by the large hole effective masses and the small spin-orbit splitting energy of the GaN/AlGaIn quantum well.

CONCLUSIONS

We have studied on the optical gain of wurtzite GaN/AlGaIn quantum wells, from the first-principles calculation by way of the $k \cdot p$ method. According to the calculated parameters, the wurtzite GaN/AlGaIn quantum well structure has the large hole effective masses and the small spin-orbit splitting energy. It causes the higher carrier density to obtain the enough optical gain. To overcome this problem, the excitonic effect, proposed by the author⁶, might be useful. Since the wide-gap materials have large exciton binding energies, excitonic effect can realize large optical gain with small carrier density, by adding a localized state in the energy-gap.

ACKNOWLEDGMENTS

We are grateful to Dr. H. Ogawa of Matsushita Central Research Laboratories for his continual encouragement, and to Dr. S. Kamiyama for the help of coding a program for optical gain calculation. Thanks are also due to Emeritus Professor A. Yanase of University of Osaka Prefecture for providing us with his FLAPW program.

REFERENCES

- 1 I. Akasaki, H. Amano, K. Itoh, N. Koide, and K. Manabe, *Inst. Phys. Conf. ser.*, **129**, (1992) 851. ; S. Nakamura, M. Senoh, and T. Mukai, *Jpn. J. Appl. phys.*, **28**, (1991) L1708.
- 2 M. Suzuki, T. Uenoyama, and A. Yanase, *Phys. Rev. B* **52** (1995) 8132. ; M. Suzuki and T. Uenoyama: submitted to *Jpn. J. Appl. Phys.*
- 3 E. Wimmer, H. Krakauer, M. Weinert and A. J. Freeman, *Phys. Rev. B* **24** (1981) 864.
- 4 O. Gunnarson and B. I. Lundqvist, *Phys. Rev. B* **13** (1976) 4274.
- 5 T. Uenoyama and M. Suzuki, *Appl. Phys. Lett.* **67** (1995) 2527.
- 6 T. Uenoyama, *Phys. Rev. B* **51**, (1995) 10228.

ROOM-TEMPERATURE LIFE TEST OF NICHIA AlGaN/InGaN/GaN
BLUE LIGHT EMITTING DIODES

MAREK OSIŃSKI*, CHRISTOPHER J. HELMS**, NIEL BERG**, DANIEL L. BARTON**, AND B. SCOTT PHILLIPS*

*Center for High Technology Materials, University of New Mexico, Albuquerque, New Mexico 87131-6081, USA, osinski@chtm.unm.edu

**Sandia National Laboratories, P.O.Box 5800, Albuquerque, New Mexico 87185-0527, USA

ABSTRACT

We report on the current status of room-temperature life testing of Nichia NLPB-500 blue light emitting diodes. So far, two tests have been completed. During the first 1000-h test, a constant current of 20 mA was maintained in all devices. During the second 1650 h test, groups of 3 or 4 devices were driven at currents ranging from 20 mA to 70 mA. Very little degradation has been observed in devices driven at normal conditions (20-30 mA), with a noticeable increase in degradation rate above 60 mA.

INTRODUCTION

Short-wavelength visible light-emitting optoelectronic devices are needed for a wide range of commercial applications, including high-density optical data storage, full-color displays, underwater communications, photolithography, *etc.* For example, the current trend in both magneto-optic and photorefractive storage is to shift the recording and reading wavelengths towards green/blue, as the storage density increases quadratically with decreasing wavelength.

Until very recently, efforts to develop short-wavelength visible light sources concentrated on either II-VI materials, or second harmonic frequency doubling of GaAs/AlGaAs lasers. The situation has changed dramatically following the commercial introduction by Nichia Chemical Industries of high-brightness blue LEDs, based on gallium nitride and related compounds InGaN/AlGaN [1]. The Nichia diodes are 100 times brighter than SiC blue LEDs available previously on the market. These developments, combined with reports of serious degradation problems in II-VI lasers, demonstrate that group-III nitrides represent the most promising family of semiconductor materials for short-wavelength optoelectronic devices. These materials combine a wide, direct bandgap with refractory properties and high physical strength. By controlling the active region composition, group-III nitrides can emit light from deep UV to orange.

A major problem encountered in epitaxial growth of group-III nitrides is the lack of suitable substrates that match the nitrides in lattice constant and in thermal expansion coefficient. Large lattice mismatch between GaN and sapphire, used as a substrate in Nichia blue LEDs, raises concern about the possible negative impact of defects on device lifetime.

So far, no studies of degradation in Nichia blue LEDs under normal cw operating conditions have been reported. In this paper, we describe the performance of the diodes under room-temperature cw low-to-moderate current excitation.

LIFE TESTING SETUP

The life test fixtures were assembled at Sandia National Laboratories. All LEDs were mounted inside a large environmental chamber maintained at a constant temperature of 23 °C. The light output of each LED is sampled by a separate optical fiber connected to its own photovoltaic detector located outside the chamber. The LED-to-fiber connection is both mechanically stable and light-tight, eliminating intensity variations due to mechanical misalignments and ambient light. The system uses a switching device to select a single detector's current, which is fed to a meter for automated reading of each LED's output.

Two separate driving circuits were used in the first life test, one based on op-amps, the other on current-limiting resistors. Each circuit was powered by a supply which maintained a constant output voltage. Currents through each LED were held approximately constant by two different methods. In the op-amp circuit, there was a current feedback loop for each LED which regulated LED drive current. In the resistor circuit, a current limiting resistor was placed in each parallel leg of the circuit to prevent excessive current through any one LED should any legs become short circuited. The simple resistor circuit is being compared to the more complicated op-amp circuit because life testing of the LEDs also relies on the consistent performance of each circuit component during the test. The op-amp circuit theoretically provides better current regulation, but it may prove to be less reliable during sustained life testing.

The test was fully computer controlled, with data automatically gathered every 12 hours or at the operator's request.

Eighteen Nichia NLPB-500 LEDs (numbered 1-18 for the test) were from a new "improved" batch (4B0001). The test also used two devices (numbered 19 and 20) from batch S403024, acquired a year earlier. Two additional "improved" devices (labeled A, B) were left untested to serve as controls. The LEDs were placed in cw operation after pre-test power measurements had been taken on all 20 devices. Ten LEDs were tested in the resistor circuit, and ten in the op-amp circuit.

The pre-test and post-test LED power measurements were computer automated. The conversion of photodetector current into optical power was made assuming a center wavelength of 450 nm.

ROOM-TEMPERATURE 20-mA TEST

The first test began on May 3, 1995, and ran for 1000 hours under normal operating conditions (20 mA cw current at 23 °C), ending on June 13, 1995. Fig. 1 shows the relative luminous intensity from all 20 devices tested, normalized to their initial readings. The thick line represents the chamber temperature. Two periods of increased temperature during the test are reflected in the intensity traces. The general trend for the 18 newer LEDs was for the output intensity to increase at a faster rate within the first 50 h, and then at a slower rate over the remainder of the test. The output intensity of the two older LEDs increased within the first 50 h, and then decreased during the remainder of the test. No hard failures were observed during this 1000-h test. Post-test LED power measurements were compared to pre-test data. This was done to study whether the intensity changes observed during the life test were due to changes in LED performance or some

other factor, such as a change in coupling efficiency from the LED to the monitoring fiber.

To study the apparent increase in relative LED intensity observed, two older LEDs were tested at 100-h and 25-h cycle times. To collect their output power at a constant temperature, the devices were placed in an integrating sphere inside the environmental chamber. These short-cycle tests showed that the output of the older LEDs did initially increase, just as it had in the first 1000-h life test.

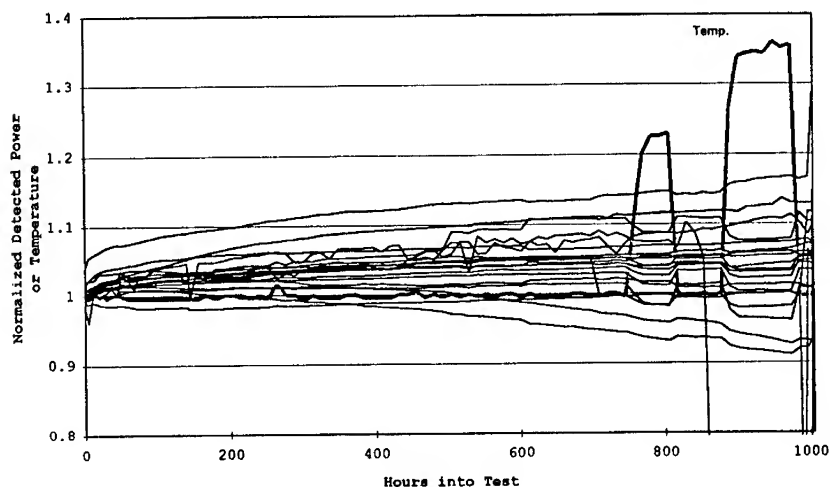


Fig. 1. Time evolution of the output of 20 Nichia LEDs subjected to a constant-current (20 mA) room-temperature test for 1000 h.

ROOM-TEMPERATURE TEST AT VARIOUS CONSTANT CURRENTS

The output power from all devices was measured after the first 1000-h life test. Subsequently, a new set of cw testing conditions was chosen, aimed at accelerating the degradation processes in some devices under test. The previously tested eighteen devices from the new batch were divided into six groups of three. Each group was driven at one of six current levels: 20, 30, 40, 50, 60, or 70 mA. Of the two older devices, one (#19) was subjected to a high current of 70 mA, and the other (#20) remained driven at 20 mA. The maximum current level of 70 mA is close to the condition producing a maximum cw output power from the LEDs. At 80 mA, we observed the onset on thermal rollover, with slightly decreased output. We therefore expected the current of 70 mA to be sufficiently high to cause measurable degradation after a few hundred hours.

The second test began on August 17, 1995. Readouts of LED current, LED voltage, and detector current were automatically generated every 12 hours. This test continued for 1650 h and was completed on October 25, 1995.

The relative intensity of one of the older-generation devices (#19) dropped to about half of its initial value after approximately 250 h and this device removed from the test on August 28, 1995. In this case, the high current (70 mA) had indeed caused a rapid failure. The remaining devices driven at the same current level, however, have performed much better: After a relatively fast drop in their relative intensity (10-15% over the first 750 h), their degradation rate has slowed (see Fig. 2).

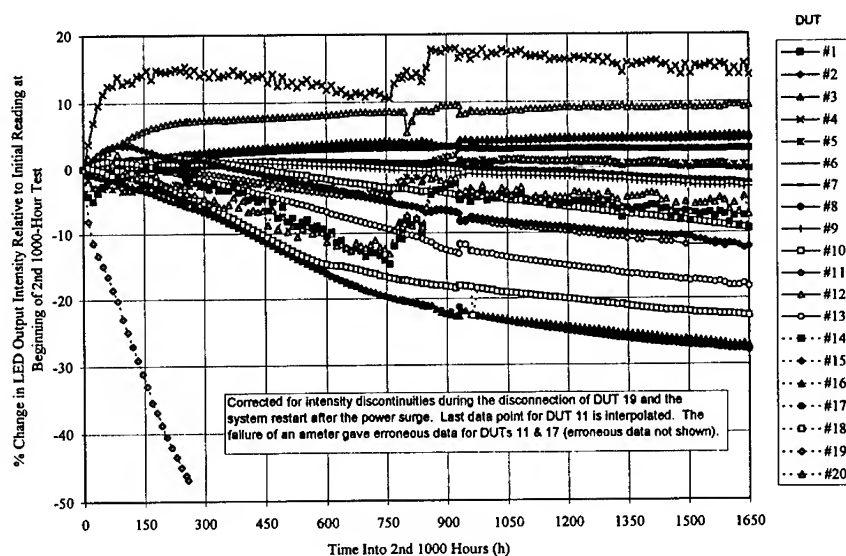


Fig. 2. Time evolution of the output of the same devices as those used in the first 1000-h life test, now subjected to various constant currents (20 to 70 mA in groups of 3-4 devices) at 23 °C for an additional 1650 h.

DISCUSSION AND CONCLUSIONS

Our first two life tests of Nichia blue LEDs, with the cumulative test time of 2650 h, failed to inflict significant degradation on any of the devices driven at currents smaller than 60 mA. As a matter of fact, the output intensity in many devices continued to increase, rather than decrease. These results indicate that Nichia devices exhibit a remarkable longevity in spite of their high density of defects [2,3]. We are conducting for a third test that will involve stepping up the ambient temperature, in addition to 20- to 70-mA driving currents. To identify the main degradation mechanisms, we will follow up with failure analysis of devices whose relative intensity drops below 50% of its original level during any one phase of testing.

ACKNOWLEDGMENTS

This work is supported by ARPA Optoelectronic Materials Center. A part of this work performed at Sandia National Laboratories is also supported by the US Department of Energy under the contract DE-AC04-94AL85000. The authors are grateful to Paul Royer and Rich Anderson, both of Sandia National Laboratories, for their support and encouragement, and to Miss Katarzyna Jezierska for her apt technical assistance.

REFERENCES

1. S. Nakamura, T. Mukai, and M. Senoh, *Appl. Phys. Lett.* **64** (13), pp. 1687-1689 (1994); S. Nakamura, *J. Cryst. Growth* **145**, pp. 911-917 (1994); S. Nakamura, *J. Vac. Sci. & Technol. A* **13**, 705 (1995).
2. S. D. Lester, F. A. Ponce, M. G. Craford, and D. A. Steigerwald, *Appl. Phys. Lett.* **66** (10), pp. 1249-1251 (1995).
3. D. L. Barton, J. Zeller, B. S. Phillips, P.-C. Chiu, S. Askar, D.-S. Lee, M. Osinski and K. J. Malloy, 1995 (33rd Annual) IEEE International Reliability Physics Proc., Las Vegas, NV, 4-6 April 1995, pp. 191-199.

ELECTRICAL PROPERTIES OF NICHIA AlGaN/InGaN/GaN BLUE LEDs IN A WIDE CURRENT/TEMPERATURE RANGE

JOACHIM ZELLER, PETR G. ELISEEV*, PHILIPPE SARTORI**, PIOTR PERLIN***, and MAREK OSIŃSKI

Center for High Technology Materials, University of New Mexico, Albuquerque, NM 87131-6081

*On leave from P. N. Lebedev Physics Institute, Russian Academy of Sciences, Moscow, Russia

**On leave from Ecole Nationale Supérieure des Télécommunications, Paris, France

***On leave from High Pressure Research Center, Warsaw, Poland

ABSTRACT

Studies of electrical characteristics of nitride-based light emitting diodes (LEDs) are of interest as they can shed light on carrier transport across the p - n heterojunction. In addition, they provide a convenient way of investigating degradation processes associated with high electrical stress. We present electrical characteristics of Nichia NLPB500 blue LEDs based on AlGaN/InGaN/GaN material system in the temperature range of 9-340 K. Two components of current are identified. High-density current stress leads to diode degradation by shunt formation caused by metal electromigration. At 8 K, blue emission was observed at currents as small as 20 nA.

INTRODUCTION

Wide-bandgap semiconductors GaN and InGaN are promising materials for application as laser active media in the emission range from visible to UV. Carrier injection across a heterojunction is of great interest as the most convenient technique for pumping the active material. So far, electrical characteristics of GaN-based diodes have not been extensively investigated, and carrier transport mechanism has not been well identified. In this paper, we discuss electrical properties of high-brightness Nichia NLPB500 AlGaN/InGaN/GaN double-heterostructure blue LEDs grown on sapphire substrate [1], with emphasis on carrier transport through the diode. Carriers injected into the active region can recombine radiatively, resulting in an efficient blue emission related to impurity centers at intermediate currents, and UV band-edge-related emission at high currents. Previously, we have identified the mechanism of photopumped visible emission in these devices at room temperature (RT) and at 20 K as radiative transitions involving three acceptor levels related to Zn impurity, combined with series of local (configuration-coordinate) phonon-replicas [2].

EXPERIMENT

The LED structure [1] is shown schematically in Fig. 1. Both electrical contacts are situated at upper side of the diode chip, with insulating sapphire substrate at the bottom side. The junction area is typically $4.6 \times 10^{-4} \text{ cm}^2$. The active $\text{In}_x\text{Ga}_{1-x}\text{N}$ layer ($x = 0.06$) is codoped with Zn and Si and is $\sim 50 \text{ nm}$ thick. Mg-doped nitrides form the p -side of the diode with $0.15\text{-}\mu\text{m}$ -thick $\text{Al}_{0.15}\text{Ga}_{0.85}\text{N}$ cladding and $0.5\text{-}\mu\text{m}$ -thick GaN contact layers. Two groups of devices were studied - "old generation" LEDs acquired in early 1994 (lot S403024) and "new generation" LEDs acquired a year later (lot 4B0001). Several devices were tested at different conditions of electrical load, including dc measurements of I - V characteristics in a wide temperature range and stress-testing under high-bias electrical pulses. Electrical characteristics were studied in the range of 9 - 340 K, with no total freeze-out of the diode conductance even at the lowest temperatures. Direct-current I - V measurements were performed using an HP 4140B picoamperometer, which enables the measurements down to the level of 10^{-15} A . For the temperature measurements above 80 K, the diode was fixed inside a micro refrigeration device (MMR Technologies, model K2001) which can cool the sample down to 80 K using Joule-Thompson effect. Lower temperatures were attained using a closed-cycle refrigerator (CTI-Cryogenics, model 22). Typical range of dc forward bias voltages was

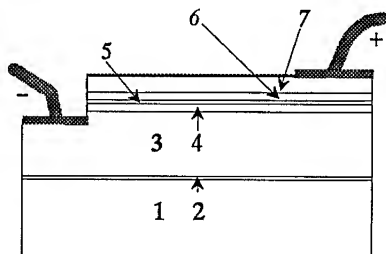


Fig. 1. Sketch of the Nichia NLPB-500 DH blue LED with InGaN active layer (after [1]):

- 1 - Sapphire substrate,
- 2 - GaN buffer layer (30 nm),
- 3 - $n\text{-Ga}\text{N}:\text{Si}$ layer (4000 nm),
- 4 - $n\text{-Al}_{0.15}\text{Ga}_{0.85}\text{N}:\text{Si}$ layer (150 nm),
- 5 - $\text{In}_{0.06}\text{Ga}_{0.94}\text{N}:\text{Zn}, \text{Si}$ emitting layer (50 nm),
- 6 - $p\text{-Al}_{0.15}\text{Ga}_{0.85}\text{N}:\text{Mg}$ layer (150 nm),
- 7 - $p\text{-Ga}\text{N}:\text{Mg}$ layer (500 nm)

0 - 5 V, giving a maximum current of ~100 mA. High-bias tests were performed using 100-ns forward-current pulses with 1 kHz repetition rate and amplitudes exceeding 1.5 A.

The diode characteristics are relatively stable up to moderately high-bias pulses, but above 1.5 A some changes may be detected by electrical and electroluminescent measurements. Minor and partially reversible diode damage manifested itself in changes in reverse-bias I - V curves and small changes in the light emission efficiency. Some devices became heavily degraded (great loss of light emission efficiency) under forward-bias overload (at current pulse amplitudes significantly larger than 1.5 A). Failure analysis was performed on these devices in order to identify defects responsible for the degradation [3].

RESULTS

Low-current I - V characteristics

Fig. 2 shows typical I - V curves taken at temperatures of 9, 81, 170 and 340 K. In the voltage range between 0.6 V and 2.8 V, the slope on semilog plot appears to be temperature independent, indicating that the dominant carrier transport mechanism is not thermally assisted. Instead, a tunneling process seems to dominate in this voltage range. We represent this portion of the I - V characteristic by the following approximate expression

$$I = I_0 \exp(eV/E_0), \quad (1)$$

where V is the diode voltage. At 340 K, the slope corresponds to the energy parameter $E_0 = 180$ meV. The parameter E_0 changes only by 4% in the temperature range of 80-340 K. As shown in Fig. 2, the pre-exponential factor I_0 demonstrates some temperature dependence, and it can be expressed in the form of $I_0 = I_{01} \exp(T/T_0)$, with $T_0 = 66$ K in the range 77 - 340 K. Above 200 K, the temperature dependence can be also represented in thermal-activation (Arrhenius-type) form of $I_0 = I_{02} \exp(-E_a/kT)$, with $E_a = 80$ meV and $I_{02} \approx 10^{13}$ A. Note that although the 9 K curve represents a new generation sample, the low-current slope of the I - V characteristic is very close to that of the other curves in Fig. 2. The parameter E_0 slightly increases with decreasing temperature, with maximum increment of ~20%.

At lowest temperatures, we have observed visible emission at very small currents. The smallest current at which light could still be seen by eye was only 20 nA, with the diode temperature of 8 K. The device was emitting from the entire junction area, indicating that the junction is the main contributor to chip resistivity, preventing any current crowding even at lowest temperatures.

Moderate-current I - V characteristics

In the voltage range of 2.9 - 3.6 V, the I - V curves are influenced by two factors, namely, by a change in the dominant carrier transport mechanism across the injecting junction, and by an increasing contribution of the series resistance to the diode voltage. The change in carrier injection mechanism is reflected in a slight increase of the I - V curve slope in the semilog-scale above $V = 3$ V, where the forward bias of the junction appears to approach the diffusion potential of the junction (cf. Fig. 2). This additional current

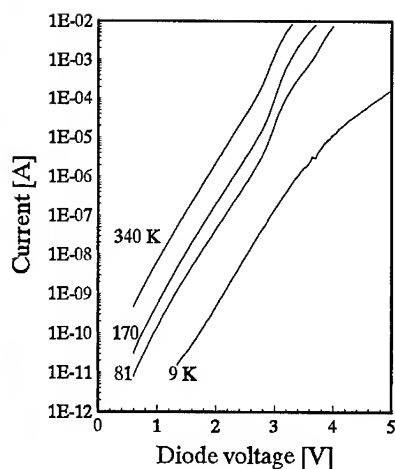


Fig.2. I - V characteristics of unstressed LEDs at different temperatures: #124 ("new generation") at 9 K and #48 ("old generation") at 81, 170 and 340 K.

component may be extracted by subtracting the temperature-independent-slope component, extrapolated from the low-current region, from the total current (see Fig. 3). This operation gives an exponential function of the type represented by Eq. (1), but with different parameters.

In general, the diode voltage can be expressed in the following form

$$V = IR_s + V_j, \quad (2)$$

where R_s is the series resistance and V_j is the junction voltage, controlling numerous current components that combine into the total current

$$I = \sum_{i=0} I_i \exp(eV_j/E_i), \quad (3)$$

with different parameters I_i and E_i attributed to each component. The differential resistance of the diode is

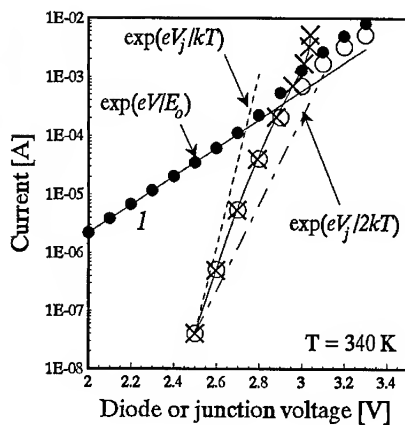


Fig.3. Analysis of intermediate-range I - V characteristics of unstressed LED #48 at 340 K:

Dots - experimental points of current versus diode voltage,
Line 1 - low current component ($E_o = 180$ meV),
Circles - difference between dot-points and line 1 (second current component versus diode voltage),
Crosses - second current component versus junction voltage,
Dashed lines - exponential functions $E_o = kT$ and $E_o = 2kT$.

$$dV/dI = R_s + dV/dI, \quad (4)$$

In the case of a single exponential function in Eq. (3), the differential resistance may be represented as follows

$$dV/dI = R_s + E_0/eI. \quad (5)$$

The voltage drop across the series resistance R_s of the diode can then be estimated using a plot of the differential resistance versus the inverse of the forward current. The extrapolation of the straight line to zero value of $1/I$ gives the value of R_s . The slope of the dV/dI plot gives the quantity E_0 . Thus, this technique allows us to identify the exponential function of type (1) when both voltage drops across the junction and across the passive regions contribute to the diode voltage. It gives the series resistance value if the extrapolation to $1/I = 0$ corresponds to an unambiguous straight line over the whole scale. If the straight-line approximation is not possible, this may be an indication that several components of current may have comparable magnitudes.

The differential-resistance-vs- $1/I$ plot was nonlinear in the case of helium-temperature measurements, and a simple interpretation could not be invoked, most probably due to diode heating at moderate currents. On the other hand, the determination of R_s seemed to be possible above 80 K, and the temperature dependence of R_s was obtained. The series resistance is $\sim 400 \Omega$ at 80 K and goes down along with the temperature increase, reaching the minimum of 15-30 Ω near RT. Above RT, it increases again. This non-monotonic behavior of R_s may be explained by the influence of temperature on the equilibrium carrier density (causing a decrease of resistivity with increasing temperature) and by the influence of temperature on carrier mobility (causing an increase of passive material resistivity above RT, where the carrier density remains practically constant).

The next step in our analysis of the I - V characteristics was identification of the intermediate-current component as one related to visible emission from the diode. A fraction of the I - V curve measured at 340 K is shown in Fig. 3 for the range of V from 2.0 to 3.3 V. The low-current "tunneling" component is approximated by an exponential function with $E_0 \approx 180$ meV and extrapolated into the intermediate-current range. Open circles show the second current component which is obtained by subtraction of the first one from the total current. When the voltage drop on the series resistance is subtracted from the diode voltage V , the plot of this current component versus the junction voltage V_j seems to be closer to a simple exponential function, with the slope corresponding to the energy parameter E_1 of 44-48 meV. As shown in Fig. 3, this curve is contained between characteristic exponential functions of the slope kT and $2kT$, which suggests the involvement of thermal diffusion transport across the junction barrier in contrast to tunnel transport at lower bias. Similar procedure for component identification was performed at other temperatures. At $T = 290$ K, the total current is divided into two components with energy parameters $E_0 \approx 182$ meV and $E_1 \approx 57.5$ meV ($2.3kT$). At 90 K, it is also possible to identify intermediate current component, with energy parameters $E_0 \approx 187$ meV and $E_1 \approx 59$ meV ($7.6 kT$). Thus, the intermediate-current component has the slope weakly dependent on temperature (from 59 meV at 90 K to ~ 46 meV at 340 K). This indicates that at least at low temperature the transport mechanism is not a simple thermal diffusion, but it is obstructed by a penetration through some residual barrier ("thermo-tunneling" mechanism). The intermediate current component seems to be related to blue emission occurring above $V = 2.8$ V. At very low temperatures, the blue emission is also seen above 2.8 V, but a second current component cannot be easily identified.

High-current stress

LEDs subjected to 100 ns, 1 kHz current pulses with amplitudes up to 1.5 A manifest minor changes in electrical characteristics which can be interpreted in terms of the micro-shunt formation resulting from localized overheating by high-density current. The main signatures of this process are a decrease in the zero-bias differential resistance and an increase in the reverse-bias current. At forward bias, the low-current part of the I - V curve is also affected by the stress. Fig.4 shows the effect of stress on this part of

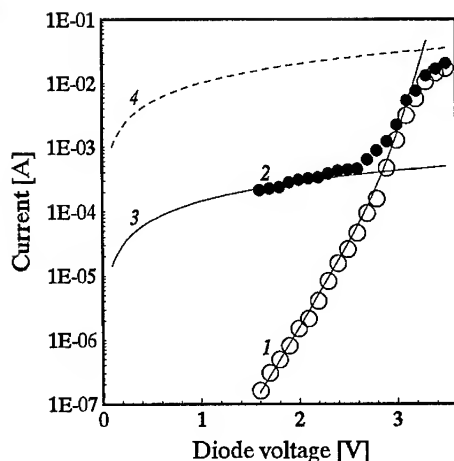


Fig. 4. Typical change of I - V characteristics of blue LEDs induced by high-current stress:
 1 - unstressed LED #48,
 2 (dots) - stressed LED #45,
 3 - current via shunt of 7 kOhm resistance,
 4 - current limited by series resistance.

the I - V characteristic. The I - V curve of a stressed device is located between the lines representing the shunting and series resistances, i.e., the diode current can not be smaller than supplied by the shunt bridges and larger than limited by series resistance. When the added shunt resistance is larger than 7-8 k Ω , it is manifested mostly at bias below 2.7 - 2.9 V, hence there is only minor degradation of the light emission at higher bias. Smaller shunt resistance can inflict noticeable degradation of the L - I characteristics, as summarized in Table 1. The stressed sample was tested under high-current pulses during ~1 h. Degraded samples were created by accidental overload for less than a minute. The latter behave like shortened diodes, but with no sign of damage to contacts; thus, the damage is associated with internal diode properties and not with the electrode wires.

Table 1. Results of high-current tests

Sample	Stress conditions	Estimated shunt resistance, k Ω
Unstressed	None	>10 ⁶
Stressed	Up to 1.5 A 100-ns pulses	5 - 8
Degraded	Pulses over 1.8 A, >100ns	0.001-0.020

DISCUSSION AND CONCLUSIONS

Analysis of electrical characteristics of blue LEDs, and especially those measured at low temperatures, indicates that the radiative current flows through the junction by a tunneling process rather than by thermally-activated diffusion. To provide the Zn-related blue luminescence at low junction voltage (below the diffusion potential), tunneling to impurity levels from conductive states at the opposite side of the junction has to occur. As Zn-related centers have large capture cross-section for electrons, it is possible that the blue emission occurs in the space-charge region by radiative capture of electrons, tunneling from the wide-bandgap n -side. At higher voltages, this type of emission is admixed to normal Zn-related emission in the bulk that occurs when carriers are injected across the junction into the active region.

The absence of a total conductance freezing even at 8 K may be explained by a degenerate state of all layers involved in current conduction. Such a state can be expected at the n -side with 10¹⁹ cm⁻³ shallow

donors. With respect to the *p*-side, such assumption cannot be easily made, as Mg acceptors introduce rather deep levels (~180 meV above the valence-band edge). The maximum hole density in *p*-GaN is usually estimated to be only $(3-7) \times 10^{17} \text{ cm}^{-3}$, which is much less than the effective valence-band density of states. However, it has been also established that the low-temperature resistivity does not strongly freeze-out either in *n*-GaN [4] or in *p*-InGaN [5], approaching some "floor" value. It was concluded in Ref. [4] that significant fraction of electron transport takes place by hopping in the compensation centers, leading to low mobility as compared to normal conduction electrons. This process becomes dominant at lower temperatures. The residual density of holes in the low-temperature limit (13 K) in Mg-doped $\text{In}_{0.09}\text{Ga}_{0.91}\text{N}$ was found to be $\sim 10^{16} \text{ cm}^{-3}$ [5]. We expect a similar behavior in *p*-GaN and *p*-AlGaIn. In these materials, like in the *n*-type materials, there is a high density of background donors. They are overcompensated with a high density of acceptors, so both kinds of centers are surrounded with numerous centers of the opposite type. Possibly, such a situation occurs also in the space-charge region of the junction, so non-injection transport through the junction (of tunneling or mixed thermo-tunneling types) is related to the residual low-temperature conductivity in bulk materials.

Diode degradation under high-current stress occurs via the formation of shunting defects in the junction region, and as described in Ref. [3], the electromigration of contact metals may be responsible for such phenomenon. The micro-shunts cause the luminescence degradation by creating parallel leakage paths, which decreases the fraction of the uniform junction current in the total current of the diode. Degree of degradation can be represented by the shunt resistance of stressed diode. It is 5 - 10 k Ω in stressed devices (moderate influence on the luminescence performance) but can drop to a few Ω in heavily degraded devices. In the latter case, the luminescence is suppressed because the diode current passes through the shunting bridges instead of the junction.

In conclusion, we have studied the electrical characteristics of AlGaIn/InGaIn/GaN double-heterostructure LEDs over a wide range of temperatures and current densities. Dominant low-density current component through the junction has been identified to be of tunneling type with a logarithmic slope weakly dependent on temperature. Another current component appearing at higher voltages seems to be related to efficient blue light emission via Zn-related centers. Light emission was observed at the lowest temperature (8 K) and at very small current (20 nA).

ACKNOWLEDGMENTS

This work was supported by ARPA Optoelectronic Materials Center and New Energy and Industrial Technology Development Organization (NEDO) of Japan. The authors are grateful to Prof. Kevin Malloy of the University of New Mexico for his assistance with experimental setup.

REFERENCES

1. S. Nakamura, T. Mukai, and M. Senoh, Appl. Phys. Lett. **64** (13), pp. 1687-1689 (1994); S. Nakamura, J. Cryst. Growth **145**, pp. 911-917 (1994); S. Nakamura, J. Vac. Sci. & Technol. **A13**, 705 (1995).
2. M. Osiński and P. G. Eliseev, Abstracts, Topical Workshop on III-V Nitrides, Nagoya, Japan, 21-23 Sept. 1995, Paper C-5; P. G. Eliseev, M. Osiński, B. S. Phillips, P.-C. Chiu, G. Mohs, B. Fluegel, H. Giessen, and N. Peyghambarian, Conf. Proc., LEOS '95 8th Annual Meeting, San Francisco, CA, Oct. 30 - Nov. 2, 1995, Paper OMP4.3, Vol. 2, pp. 104-105.
3. D. L. Barton, J. Zeller, B. S. Phillips, P.-C. Chiu, S. Askar, D.-S. Lee, M. Osiński and K. J. Malloy, 1995 (33rd Annual) IEEE International Reliability Physics Proc., Las Vegas, NV, 4-6 April 1995, pp. 191-199.
4. R. J. Molnar, T. Lei, and T. D. Moustakas, Appl. Phys. Lett. **62** (1), pp. 72-74 (1993).
5. S. Yamasaki, S. Asamu, N. Shibata, M. Koike, K. Manabe, T. Tanaka, H. Amano, and I. Akasaki, Appl. Phys. Lett. **66** (9), pp. 1112-1113 (1995).

Correlation of surface morphology and optical properties of GaN by conventional and selective-area MOCVD

X. Li, A. M. Jones, S. D. Roh, D. A. Turnbull, E. E. Reuter, S. Q. Gu, S. G. Bishop and J. J. Coleman
Microelectronics Laboratory, University of Illinois, Urbana, IL 61801

ABSTRACT

We have studied GaN films grown by atmospheric pressure metalorganic chemical vapor deposition (MOCVD) on sapphire substrates using different buffer layer structures. Surface morphology was characterized by scanning electron microscopy (SEM). Optical properties were measured using photoluminescence (PL), cathodoluminescence (CL) spectroscopy and cathodoluminescence wavelength imaging (CLWI) method. It is found that the hexagonal pit-like defects in morphology are associated with the D-A/e-A transition band in the PL and CL spectra. The same correlation of morphology with optical properties is observed for the GaN films grown by selective area epitaxy (SAE). In addition, the possibility of improving optical quality by SAE is investigated. The SAE depth profile is simulated for the first time, and satisfactory results are obtained.

INTRODUCTION

The GaN based III-V nitride semiconductor system is an interesting, challenging and technically important one because of its potential applications in optical devices operating in the blue and UV wavelength range and electronic devices operating under high frequency and high power conditions. Considerable effort has been devoted to crystal growth and device fabrication in this system, as reviewed recently by several groups.¹ However, efforts in optimizing growth conditions including developing new buffer layer structures and exploring new substrates are indispensable in order to reduce the strain due to lattice mismatch and thus reduce defect density. Understanding the native defects, impurities, dislocations and dopants is also important in order to produce efficient, reliable and reproducible devices. We report, in this paper, the correlation of surface morphology with optical properties through the study of GaN films grown on different buffer layers and by selective area epitaxy.

EXPERIMENT

GaN films were grown using (0001) sapphire substrates by vertical atmospheric pressure MOCVD. Please refer to our previous paper for details of the growth conditions.² Briefly, trimethylgallium (TMG), trimethylaluminum (TMA) and ammonia (NH₃) were used as the Ga, Al and N sources, respectively. H₂ was used as a carrier gas. Buffer layers, varying from a single GaN, a single AlN and a double buffer layer consisting of GaN and AlN, were grown at 560°C. The epilayer growth temperature was ~1040°C. Selective area epitaxy (SAE) was done using conventional photo-lithography methods.³ The growth mask used consisted of 50, 75, 100 and 125 μ m stripe openings separated by 500 μ m center to center spacing. The patterned samples were immediately placed in the MOCVD reactor where they were heated under NH₃ until the

temperature reached $\sim 1020^{\circ}\text{C}$ when the GaN growth took place. Film morphology was characterized by scanning electron microscopy (SEM). The optical properties were examined by photoluminescence (PL) and cathodoluminescence (CL) spectroscopy. PL measurements were taken using a 325 nm HeCd laser as the excitation source and detected by a GaAs PMT. The CL was collected by a parabolic mirror, and detected by a GaAs PMT.

RESULTS AND DISCUSSIONS

1. PL, CL and CLWI study of GaN films grown on different buffer layers

Under the experimental conditions described in detail in our previous paper,² a single buffer layer of GaN leads to a opaque (hazy) surface with many hexagonal pit-like defects of sub- μm size distributed uniformly across the whole surface, as shown by the scanning electron microscopy (SEM) image in Fig. 1a. A single buffer layer of AlN yields an extremely non-

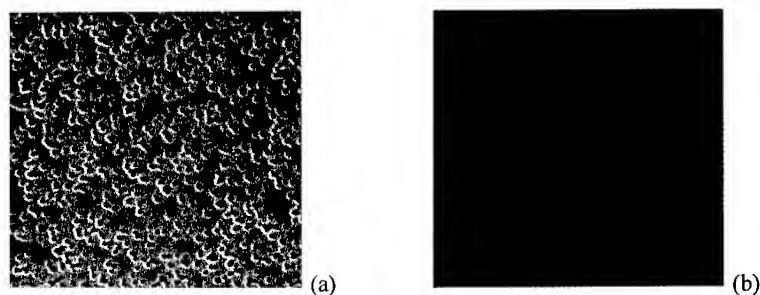


Fig 1 SEM images ($60\ \mu\text{m} \times 60\ \mu\text{m}$) for a $0.7\ \mu\text{m}$ thick GaN film grown on (a) an optimized single GaN buffer layer and (b) a double buffer layer consisting of GaN and AlN. The SEM image of the GaN film grown on a single AlN buffer layer was similar to (a) in the center area and (b) in the outer area.

uniform surface, with morphology ranging from defect-free in the outer areas to hexagonal defects in the center. In contrast, the double buffer layer structure, consisting of $200\ \text{\AA}$ of GaN and $500\ \text{\AA}$ of AlN, leads to near featureless SEM image (Fig. 1b). When the thickness is increased to $3\ \mu\text{m}$, the SEM image becomes entirely featureless.

In order to study the correlation of morphology with emission centers microscopically, we have mapped out the GaN films using cathodoluminescence wavelength imaging (CLWI). To our knowledge, this is the first report on CLWI of GaN films. In CLWI, the wavelength at which there is a peak in the intensity of a luminescence spectrum, is determined as a function of spatial position, and a color or gray scale image directly mapping these wavelengths is generated.⁴ CLWI has been found particularly useful for the characterization of strained-layer systems.^{5,6} We have performed preliminary CLWI study of our GaN films grown on sapphire substrates. In general, inhomogeneous patterns are observed using CLWI for GaN films including the ones grown on the double buffer layer, indicating the optical non-uniformity of the film. Shown in Fig. 2a and Fig. 2b are the CL images taken at the near-band-edge emission wavelength (370 nm) for the films in Fig. 1a and Fig. 1b, respectively. As can be seen that the inhomogeneity, evidenced as intensity contrast in the image, increases as the film surface morphology becomes rougher. The dark spots

in Fig. 3a correspond to the pits in the SEM images while no obvious correlation can be found for the less bright spots in Fig. 2b.

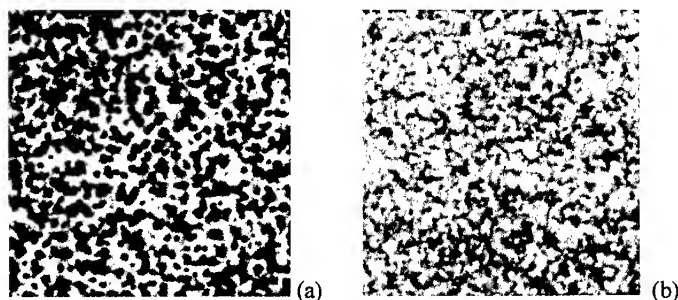


Fig. 2 (a) and (b) are CL images ($45\ \mu\text{m} \times 45\ \mu\text{m}$) taken at the near-band-edge emission wavelength (370 nm) for the films in Fig. 1a and Fig. 1b, respectively.

We have also performed photoluminescence (PL) and cathodoluminescence (CL) spectroscopic studies on GaN films grown on different buffer layers. As shown in Fig. 3, for a $2.7\ \mu\text{m}$ thick GaN film grown on the double buffer layer, the PL spectrum obtained at 5K shows a strong and sharp (FWHM = 4.7 meV) exciton peak at 3.484 eV and a high energy shoulder peak at 3.490 eV. They are identified as the neutral donor bound exciton and the free exciton, respectively.⁷ Virtually no peaks are found in the energy range corresponding to the D-A or e-A pair recombination band.^{7,8} The yellow band centered around 2.2 eV is found to be more than two orders of magnitude weaker than the exciton peak. For a thinner film ($0.7\ \mu\text{m}$), which shows only a few more hexagonal pits than the thick film, the e-A and D-A transition becomes visible. In addition, the exciton peak is broadened, and a shoulder on the low energy side appears (Fig. 3 inset). This low energy shoulder is attributed to be the acceptor bound exciton peak. Not much variation in peak intensity and bandwidth is observed for PL or CL spectra taken at different positions across the film.

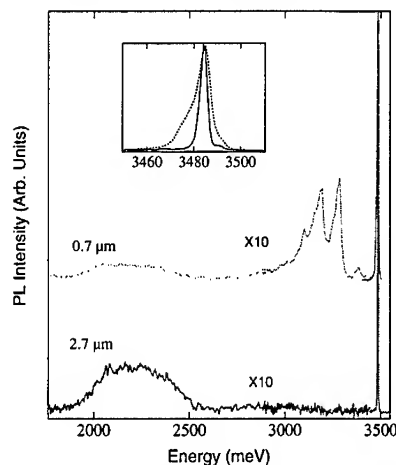


Fig. 3 The PL spectra of a $2.7\ \mu\text{m}$ (solid line) and a $0.7\ \mu\text{m}$ (dotted line) thick GaN films grown on the double buffer layer. Vertical scale at energies lower than 3450 meV is magnified by 10 times. Inset shows the near-band-edge emission (normalized).

The GaN films grown on a single GaN buffer layer show stronger D-A/e-A band in comparison to those grown on the double buffer layer. However, the exciton peak shows similar peak-width and intensity. It appears that the hexagonal pit-like defects (Fig. 1a) do not degrade the near-band edge emission but only enhance the D-A/e-A transition.

For the GaN film grown on a single AlN buffer layer where nonuniform morphology is found across the surface, several interesting features are revealed. First, the spectra taken at dif-

ferent positions on the sample show variations in peak positions across the sample surface (Fig. 4), consistent with the non-uniform morphology. The exciton peak shifts to lower energy by as

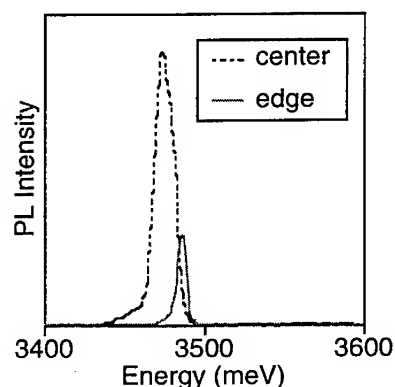


Fig. 4 PL spectra (5K) taken at two positions of a 0.7 μm thick GaN film grown on a single AlN buffer layer.

peak from the center area (opaque) is more than twice as strong as that from the edge (transparent area). This is not intuitive because the macroscopically better surface morphology does not show stronger luminescence. This may imply that some high quality material that can yield strong luminescence, is concealed in between the small pits in the apparently defective material. This is analogous to improving material quality by selective area growth. The selective area growth is thought to accommodate lattice mismatch by confining the defects to the interfaces and thus prevent dislocations from propagation to or generation at the surface.^{10,11,12}

2. SAE of GaN

Selective area epitaxy (SAE) is an attractive growth technique that enables growing epitaxial layers in selected regions of a wafer. It is achieved by using an inhibition dielectric mask of SiO_2 or SiN_x patterned by conventional photolithography. Ideally, growth takes place only on unmasked regions. This technique makes it possible to fabricate devices with different wavelengths on the same wafer for integrated optoelectronic applications and greatly simplifies the subsequent processing. The flexibility and reproducibility of SAE are important for device performance. The potential of SAE in the preparation of optoelectronic devices demonstrated in GaAs and InP based compound semiconductors will definitely draw attention to the research on this topic in GaN based materials. In addition, the lack of a suitable wet etching method for GaN material makes SAE an important technique for practical device fabrication in this system.

Only very preliminary experiments were reported so far on the SAE of GaN system.^{13,14,15} We have performed SAE of GaN on GaN/sapphire, AlGaN/Sapphire and AlN/GaN/Sapphire substrates by atmospheric pressure MOCVD. GaN growth shows excellent selectivity on GaN/Sapphire substrates, as reported previously^{13,14}, as well as on all other substrates examined, using SiO_2 stripes defined by conventional photolithography.

We have found that growth conditions are critical to the morphology and thus optical properties of the selectively grown films. When the same V/III ratio is used as in broad area

growth, the edges of the selective growth windows show poor morphology with many pit-like defects, as shown in Fig. 5a. This edge effect has been removed (Fig. 5b) by increasing the V/III ratio by 25%. This suggests that the excess supply of gallium (Ga) species at the edges, due to

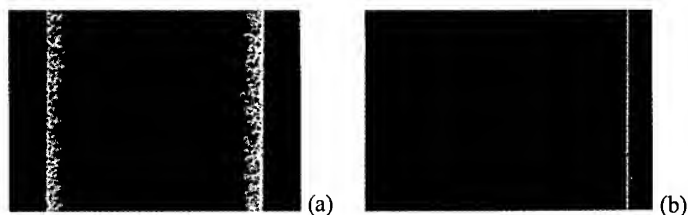


Fig. 5 SEM images of a 125 μm oxide opening grown with (a) 4 slm and (b) 5 slm NH_3 flow.

diffusion from the oxide mask region, reduces the V/III ratio locally and thus deteriorates the surface morphology. PL spectra obtained on these SAE samples indicate that the poor morphology leads to stronger D-A/e-A band, accompanied by a stronger acceptor bound exciton peak. This result verifies that the pit-like defects are associated with the D-A/e-A transition band. However, even the good morphology film grown by SAE still shows more D-A/e-A transitions than those from broad area growth. In contrast, when the V/III ratio was increased by 25% during the GaN broad area growth on a single GaN buffer layer, the exciton peak becomes even stronger than that of the featureless films. This is probably because the higher V/III ratio improved morphology at the boundaries of the pits (no growth or less growth areas), as is the case for SAE grown films. The growth on a single GaN buffer layer is analogous to a maskless SAE. This result suggests that the patterned widths need to be reduced to the dimension of the hexagonal pits which is on the order of sub- μm , in order for the SAE films to obtain optical quality superior to the broad area grown films. The dependence of stress relief through SAE on the patterned width has been reported before for other systems.^{10,11,12}

We have observed ridge growth on oxide defined stripes of 50 - 200 μm width. Growth thickness profiles, were obtained using conventional profilometry and are shown by the solid line in Fig. 6. No substrate orientation dependence of the growth profile is found for the size range we studied. In addition to the experimental work, we have performed, for the first time, some simulations using a computational diffusion model³. This model utilizes diffusion equations and boundary conditions derived from basic MOCVD theory, with self-consistent reaction parameters derived from experimental results, to predict the concentration of each column III constituent throughout the concentration boundary layer. Solutions to these equations are found using the two dimensional, finite element method. The simulated growth profiles for GaN stripes using this model are shown in Fig. 6 by the dotted lines. It can be seen that good agreement between the experimental and the predicted results was observed. This model can also predict the composition profiles of ternary or quaternary alloys.³ The success of

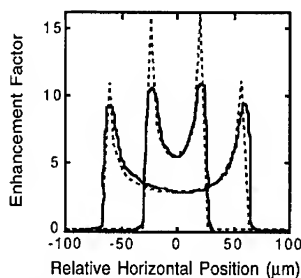


Fig. 6 Comparison of predicted (dotted line) and measured (solid line) growth thickness profiles for 50 and 125 μm GaN stripe openings. Broad area growth thickness has an enhancement factor of 1.

this model allows us to predict the selective growth thickness for more complex structures and design device structures accordingly.

CONCLUSIONS

We have studied the GaN films grown on sapphire substrates using different buffer layer structures by PL, CL spectroscopy and CLWI method. Those grown on the double buffer layer demonstrated better optical qualities than those grown on single GaN or AlN buffer layers. It was found that the hexagonal pit-like defects in morphology are associated with the D-A or e-A pair recombination band emission in the PL and CL spectra. The same correlation of morphology with optical properties was observed for the GaN films grown by SAE. It was also observed that higher V/III ratio has to be used for SAE than that for broad area growth in order to obtain smooth morphology at the growth boundaries. In addition, the SAE depth profile was simulated for the first time, and good agreement with the experimental results was found.

REFERENCES

- 1 (a) H. Morkoc, S. Strite, G. B. Gao, M. E. Lin, B. Sverdlov et al., *J. Appl. Phys.* **76**, 1363 (1994).
 (b) S. Strite, M. E. Lin, and H. Morkoc, *Thin Sol. Films* **231**, 197 (1993); S. Strite and H. Morkoc, *J. Vac. Sci. Technol. B* **10**, 1237 (1992). (c) R. F. Davis, *Proc. IEEE* **79**, 702 (1991). (d) J. H. Edgar, *J. Mater. Res.* **7**, 235 (1992). (e) J. I. Pankove, *Mater. Res. Soc. Symp. Proc.* **162**, 515 (1990). (f) D. Elwell and M. M. Elwell, *Prog. Cryst. Growth Charact.* **17**, 53 (1988).
- 2 X. Li, D. V. Forbes, S. Q. Gu, D. A. Turnbull, S. G. Bishop and J. J. Coleman, *J. Electron. Mater.* **24**, 1711 (1995).
- 3 A. M. Jones, M. L. Osowski, R. M. Lammert, J. A. Dantzig, and J. J. Coleman, *J. Electron. Mater.* **24**, 1631 (1995).
- 4 M. Grundmann, J. Christen, D. Bimberg, A. Hashimoto, T. Fukunaga, and N. Watanabe, *Appl. Phys. Lett.* **58**, 2090 (1991).
- 5 K. Rammohan, D. H. Rich, R. S. Goldman, J. Chen, H. H. Wieder, and K. L. Kavanagh, *Appl. Phys. Lett.* **66**, 869 (1995).
- 6 J. Christen, M. Grundmann, and D. Bimberg, *J. Vac. Sci. & Technol. B* **9**, 2358 (1991).
- 7 D. A. Turnbull et al., unpublished.
- 8 F. Fischer, C. Wetzel, E. E. Haller, and B. K. Meyer, *Appl. Phys. Lett.* **67**, 1298 (1995).
- 9 L. J. Gray, M. F. Chrisholm, and T. Kaplan, *Appl. Phys. Lett.* **66**, 1924 (1995) and references therein.
- 10 M. Yamaguchi, M. Tachikawa, M. Sugo, S. Kondo, and Y. Itoh, *Appl. Phys. Lett.* **56**, 27 (1990).
- 11 T. Ohashi, *J. Mater. Res.* **7**, 3032 (1992).
- 12 N. H. Karam, V. Haven, S. M. Vernon, N. El-Marsry, E. H. Lingunis, and N. Haegel, *J. Cryst. Growth* **107**, 129 (1991).
- 13 I. Akasaki and H. Amano, *J. Electrochem. Soc.* **141**, 2266 (1994).
- 14 Y. Kato, S. Kitamura, K. Haramatsu, and N. Sawaki, *J. Cryst. Growth* **144**, 133 (1994).
- 15 M. Nagahara, S. Miyoshi, H. Yaguchi, K. Onabe, Y. Shiraki, and R. Ito, *J. Cryst. Growth* **145**, 197 (1994); *Jpn. J. Appl. Phys.* part 1, **33**, 694 (1994).

LIGHT EMISSION PROPERTIES OF GaN-BASED DOUBLE HETEROSTRUCTURES AND QUANTUM WELLS

D.A.S. LOEBER*, J.M. REDWING**, N.G. ANDERSON*, and M.A. TISCHLER**

* Department of Electrical and Computer Engineering, University of Massachusetts at Amherst, Amherst, MA 01003

** Advanced Technology Materials, Inc., 7 Commerce Drive, Danbury, CT 06810

ABSTRACT

Edge emission characteristics of optically pumped GaN-AlGa_N double heterostructures and quantum wells are examined. The samples, which were grown by metalorganic vapor phase epitaxy, are photoexcited with light from a pulsed nitrogen laser. The pump light is focused to a narrow stripe on the sample surface, oriented perpendicular to a cleaved edge, and the edge luminescence is collected and analyzed. We first compare emission characteristics of highly excited GaN-AlGa_N double heterostructures grown simultaneously on SiC and sapphire substrates. Polarization resolved spectral properties of edge luminescence from both structures is studied as a function of pump intensity and excitation stripe length. Characteristics indicative of stimulated emission are observed, particularly in the sample grown on SiC. We then present results demonstrating laser emission from a GaN-AlGa_N separate-confinement quantum-well heterostructure. At high pump intensities, band edge emission from the quantum well exhibits five narrow (~1 Å) modes which are evenly spaced by 10 Å to within the resolution of the spectrometer. This represents the first demonstration of laser action in a GaN-based quantum-well structure.

INTRODUCTION

The III-V nitrides are important candidate materials for short-wavelength optical emitters. Light-emitting diodes based on InGa_N have been reported [1,2] and are commercially available. While injection lasers based on the III-V nitrides have yet to be realized, recent results from a number of groups bode well for GaN-based lasers. Photoluminescence features characteristic of stimulated emission, such as line narrowing and superlinear input/output power dependence at high intensity, have been observed in GaN [3-5] and InGa_N [6] films, InGa_N-AlGa_N [7] and GaN-AlGa_N double heterostructures [8], and GaN-AlGa_N superlattices [9]. Laser modes have been clearly observed in the edge emission from optically pumped GaN films grown on sapphire [10] and SiC [11] substrates. Most recently, we have demonstrated an optically pumped GaN-AlGa_N vertical-cavity surface emitting laser grown on sapphire [12].

In this work, we study the polarization and spectral properties of edge luminescence from optically excited GaN-AlGa_N double heterostructures and quantum wells. The excitation geometry and high excitation intensities used in these experiments are selected to provide information relevant to laser structures. Our results include what we believe to be the first observation of laser action from a III-V nitride quantum-well heterostructure.

CRYSTAL GROWTH AND OPTICAL CHARACTERIZATION

The samples studied in this work were grown by metalorganic vapor phase epitaxy (MOVPE) in a vertical reactor operating at 100 Torr. Trimethylgallium (TMGa), trimethylaluminum (TMAI), and ammonia were used as precursors, with H₂ as the carrier gas. In all samples, growth of the GaN and AlGa_N layers was performed at 1100°C following deposition of a 150 Å AlN buffer layer at 550°C.

Two types of structures were grown: The first is a double heterostructure consisting of a 750 Å GaN active layer sandwiched between a 0.2 μm Al_{0.15}Ga_{0.85}N cap layer and a 3 μm Al_{0.15}Ga_{0.85}N lower cladding layer. This double heterostructure was grown simultaneously on a 6H-SiC substrate and a (0001) c-plane sapphire substrate. The second is a step-index separate-confinement quantum-well heterostructure grown on a 6H-SiC substrate. The active region of this structure consists of a 150 Å GaN quantum well sandwiched between 300 Å Al_{0.07}Ga_{0.93}N

waveguide layers, which is in turn sandwiched between a $0.2\text{ }\mu\text{m}$ $\text{Al}_{0.15}\text{Ga}_{0.85}\text{N}$ cap layer and a $3\text{ }\mu\text{m}$ $\text{Al}_{0.15}\text{Ga}_{0.85}\text{N}$ lower cladding layer.

High-intensity ($\sim\text{MW}/\text{cm}^2$) photoluminescence experiments were performed using focused light from a nitrogen laser. A somewhat unusual excitation geometry was used, in which the sample was excited in a variable-length rectangular stripe with a width of approximately $50\text{ }\mu\text{m}$. In this configuration, the stripe length is determined by the position of a shadow plate which is mounted on a micrometer-controlled translator and positioned partially in the pump beam. Apertures and a cylindrical lens are used to achieve narrow stripe width. The sample is oriented such that the pump light is incident normal to the sample surface and the excitation stripe intersects the cleaved sample edge at a right angle. The excitation stripe is colinear with the input axis of the spectrometer in this configuration.

Light emanating from the cleaved sample edge was focused into a 0.64m monochromator, after passing through a polarization analyzer at the input slit, and dispersed by a UV diffraction grating into a cooled S-1 photomultiplier tube. Excitation pulse energies were measured using a pyroelectric detector and a photodiode. Pump power densities were calculated from the measured pulse energy, the $50\text{ }\mu\text{m}$ stripe width, the measured stripe length, and the 0.8 ns pulse duration specified by the manufacturer of our laser. Pump intensities reported in this work represent incident power densities at the sample surface.

RESULTS AND DISCUSSION

Edge Emission from GaN-AlGaN Double Heterostructures

Polarization-resolved edge emission spectra obtained at a pump intensity of $10\text{ MW}/\text{cm}^2$ are shown in Fig. 1 for double heterostructures grown on SiC and sapphire (hereafter DH/SiC and DH/sapphire, respectively). These spectra were obtained using a $100\text{ }\mu\text{m}$ excitation stripe. Note that the emission for the DH/SiC sample (left) is much more intense than that of the

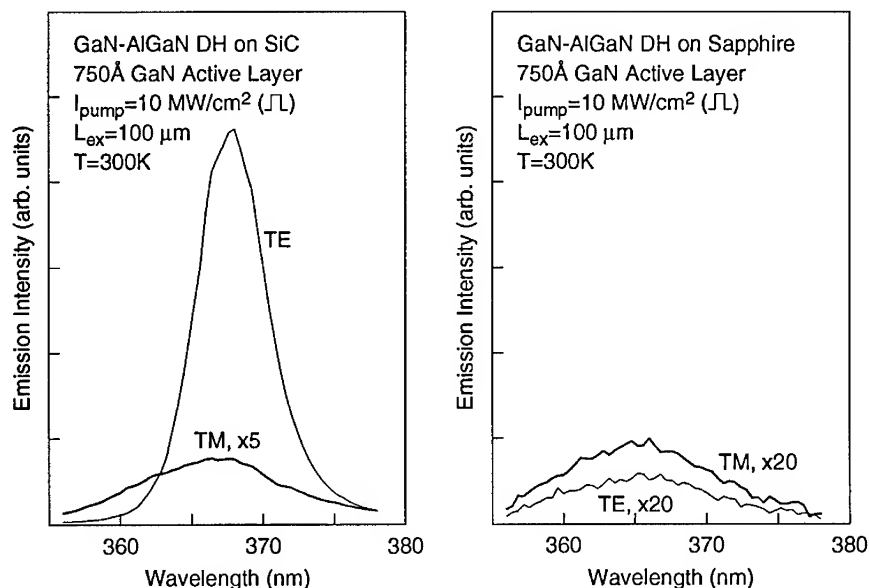


Fig. 1 Polarization-resolved edge-emission spectra for $\text{GaN-Al}_{0.15}\text{Ga}_{0.85}\text{N}$ double heterostructures grown simultaneously on SiC (left) and sapphire (right) substrates.

DH/sapphire sample (right) grown in the same run, and that the DH/SiC emission is strongly TE polarized (note multiplication factors). The ratio of peak intensities for TE and TM emission (i.e. with the electric-field vector within and normal to the layer plane, respectively) is $\sim 9:1$ at this pump intensity and excitation stripe length in the DH/SiC sample. The dependence of this ratio on pump intensity is explored further for this sample in Fig. 2, which shows peak emission intensity as a function of pump intensity for both polarizations. The emission intensity clearly exhibits a threshold behavior near a pump intensity of 5 MW/cm^2 , above which the output intensity increases rapidly and becomes strongly TE polarized. Similar behavior, while much less pronounced, was also observed for the DH/sapphire sample (data not shown).

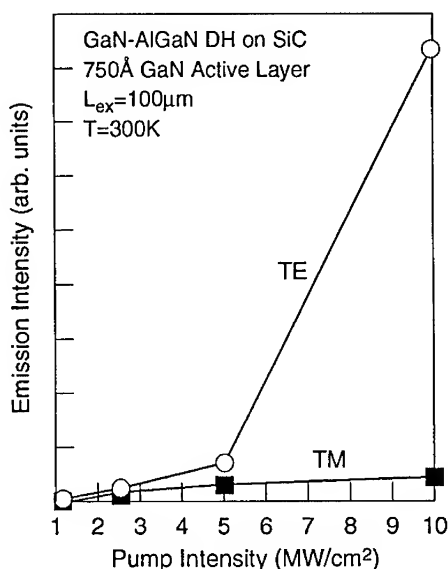


Fig. 2 Polarization-resolved peak emission intensity for edge luminescence from a GaN-Al_{0.15}Ga_{0.85}N double heterostructure grown on a SiC substrate.

The effects of both pump intensity and excitation stripe length on the TE-polarized edge emission spectra are explored for the DH/SiC and DH/sapphire samples in Fig. 3. Results for the DH/SiC sample (left) will be discussed first. Spectrum (a) was obtained at a pump intensity of 10 MW/cm^2 and an excitation stripe length of $200 \mu\text{m}$. Halving either the pump intensity (spectrum (b)) or the excitation stripe length (spectrum (c)) has significant and qualitatively similar effects: The luminescence intensity is substantially reduced, the spectrum is blue shifted, and significant spectral broadening occurs. Stripe length also has a substantial effect on the polarization ratio: The TE:TM polarization ratio at a pump intensity of 10 MW/cm^2 increases from $9:1$ to $130:1$ as the stripe length is increased from $100 \mu\text{m}$ to $200 \mu\text{m}$ (data not shown). Similar behavior, albeit less pronounced again, is observed for the DH/sapphire sample (right). Spectrum (a) was obtained at a pump intensity of 30 MW/cm^2 and an excitation stripe length of $200 \mu\text{m}$. Reducing the pump intensity by a factor of 3 (spectrum (b)) or halving the excitation stripe length (spectrum (c)) clearly reduces the emission intensity in a nonlinear way and broadens and blue shifts the spectrum.

These results, particularly for the DH/SiC sample, are strongly suggestive of stimulated emission. Output intensities increase in a superlinear fashion, the emission becomes strongly polarized, and spectral narrowing is clearly observed with increasing pump intensity in these highly excited structures. That similar behavior is observed with increases in excitation stripe length strengthens this conclusion, since it provides direct evidence of optical gain along the stripe.

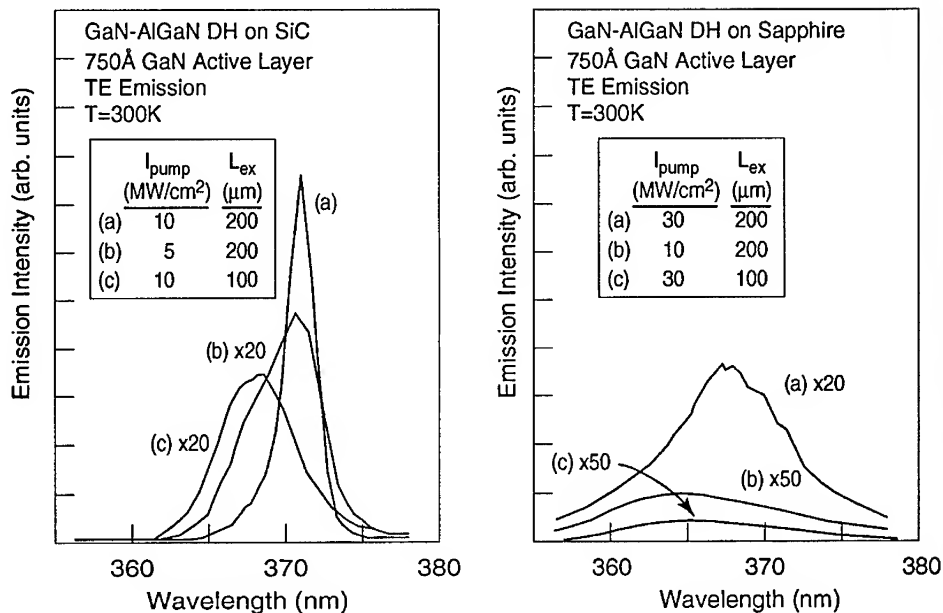


Fig. 3 TE-polarized edge-emission spectra for GaN-Al_{0.15}Ga_{0.85}N double heterostructures, grown on SiC (left) and sapphire (right) substrates, obtained at various photoexcitation intensities and excitation stripe lengths. (Note multiplication factors.) Increases in either photoexcitation intensity or excitation stripe length yield superlinear intensity increases and spectral narrowing, particularly in the sample grown on the SiC substrate.

Laser Emission from a GaN-AlGaN Quantum Well Structure

Experiments similar to those described above were performed on the separate confinement quantum-well heterostructure (SCQWH). Standard surface photoluminescence spectra were also obtained for this structure, however, and will be discussed first. In Fig. 4 (lower trace), we show the spectrum of unpolarized surface luminescence for this sample obtained at low excitation intensity using a CW HeCd laser as a pump source. A strong feature peaked just below 360 nm is clearly evident, and presumably originates from the fundamental transitions in the GaN quantum well. This feature is peaked at a slightly shorter wavelength than the emission from the double heterostructures discussed above, as can be expected from small compressive strain and quantum-confinement effects in the 150Å well. The position of the shorter wavelength (~340 nm) feature in this spectrum is consistent with emission from the Al_{0.07}Ga_{0.93}N waveguide layers.

Under sufficiently high excitation, using the pulsed nitrogen laser and the excitation stripe geometry, sharp features evolve from the low energy side of the quantum well photoluminescence peak. The emission spectrum obtained at a pump intensity of 15 MW/cm², shown in Fig. 4 (upper trace), exhibits five sharp (~1Å) lines which are evenly spaced by 10Å to within the resolution of the spectrometer. This linewidth and spacing is consistent with Fabry-Perot mode structure in a short-cavity edge-emitting laser. The emission is strongly TE polarized, with the TE:TM polarization ratio exceeding 100:1 at this pump intensity.

We examined the pump-intensity dependence of the emission spectrum for this structure, and found positions and spacing of the modes to be stable over a wide range of pump intensities. We also studied the dependence of the TE polarized emission intensity on pump intensity. Output

intensities, integrated over the full quantum-well emission spectrum (from 356 nm to 374 nm), are shown in Fig. 5 for pump intensities ranging from 5 to 14 MW/cm². A sharp threshold clearly exists at 11 MW/cm². The emergence of sharp, evenly spaced, highly-polarized peaks above a clear photoexcitation threshold is strong evidence that the SCQWH sample is lasing at pump intensities above 11 MW/cm².

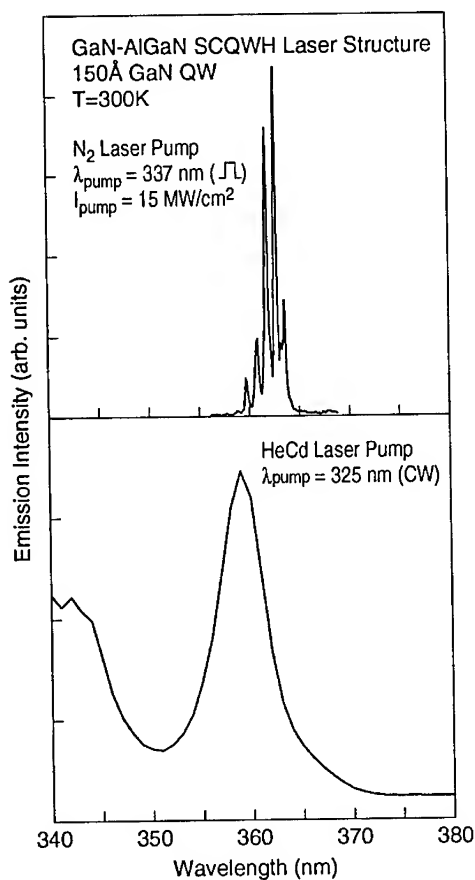


Fig. 4 Photoluminescence from a GaN-AlGaN SCQWH structure obtained from the sample edge at high photoexcitation (upper trace) and from the sample surface at low photoexcitation (lower trace). At high excitation, five narrow ($\sim 1\text{\AA}$) lines spaced evenly by 10\AA emerge from the quantum well photoluminescence peak near 360 nm.

The 10\AA spacing of the modes observed in the emission spectrum at high excitation levels corresponds to a cavity length in the $15\text{--}20\text{ }\mu\text{m}$ range, depending on the wavelength-dependent refractive index assumed for this SCQWH structure. Since we did not intentionally create a cavity, we assume that the Fabry-Perot modes must be arising from a cavity created by parallel cracks in the epitaxial film and perhaps the cleaved sample edge. Similar results were observed for a bulk GaN film grown on SiC by Zubrilov and co-workers [11].

CONCLUSIONS

In conclusion, we have investigated the polarization and spectral properties of edge luminescence from GaN-AlGaIn heterostructures grown by MOVPE and optically excited using a stripe geometry. Double heterostructures grown simultaneously on SiC and sapphire were studied, and the sample grown on SiC showed superior emission characteristics. Large nonlinear increases in output intensity and TE:TM output polarization ratio with increasing pump intensity were observed above a well defined excitation threshold, and were accompanied by substantial spectral narrowing. These emission characteristics are strongly suggestive of stimulated emission, particularly since similar trends were observed with increasing excitation stripe length. We also examined edge emission from a separate-confinement quantum well heterostructure with a 150Å quantum well. Five sharp ($\sim 1\text{\AA}$), evenly spaced (10Å), highly TE-polarized (TE:TM>100:1) modes emerge from the low energy side of the luminescence spectrum at excitation intensities above a well defined threshold. We believe that this is the first demonstration of laser emission reported for a III-V nitride quantum-well structure.

ACKNOWLEDGEMENT

The authors thank the National Science Foundation for their support of the portions of this work carried out at the University of Massachusetts at Amherst (NSF Grant ECS-9414510).

REFERENCES

1. S. Nakamura, T. Mukai, M. Senoh., Appl. Phys. Lett. **64**, 1687 (1995).
2. S. Nakamura, M. Senoh, N. Iwasa, and S. Nagahama, Appl. Phys. Lett. **67**, 1868 (1995).
3. H. Amano, T. Asahi, and I. Akasaki, Jpn. J. Appl. Phys. **29**, L205 (1990).
4. M.A. Kahn, D.T. Olsen, J.M. Van Hove, J.N. Kuznia, Appl. Phys. Lett. **58**, 1515 (1991).
5. K. Yung, J. Lee, J. Koo, M. Rubin, N. Newman, and J. Ross, Appl. Phys. Lett. **64**, 1135 (1994).
6. M.A. Kahn, S. Krishnankutty, R.A. Skogman, J.N. Kuznia, D.T. Olson, and T. George, Appl. Phys. Lett. **65**, 520 (1995).
7. H. Amano, T. Tanaka, Y. Kunii, K. Kato, S.T. Kim, and I. Akasaki, Appl. Phys. Lett. **64**, 1377 (1994).
8. S.T. Kim, H. Amano, I. Akasaki, and N. Koide, Appl. Phys. Lett. **64**, 1535 (1994).
9. D.A.S. Loeber, J.M. Redwing, M.A. Tischler, and N.G. Anderson, *Electronic Materials Conference*, Charlottesville, June 22, 1995.
10. X.H. Yang, T.J. Schmidt, W. Shan, J.J. Song, and B. Goldenberg, Appl. Phys. Lett. **66**, 1 (1995).
11. A.S. Zubrilov, V.I. Nikolaev, D.V. Tsvetkov, V.A. Dmitriev, K.G. Irvine, J.A. Edmond, and C.H. Carter, Jr., Appl. Phys. Lett. **67**, 533 (1995).
12. J.M. Redwing, D.A.S. Loeber, M.A. Tischler, N.G. Anderson, and J.S. Flynn, submitted for publication in Appl. Phys. Lett.

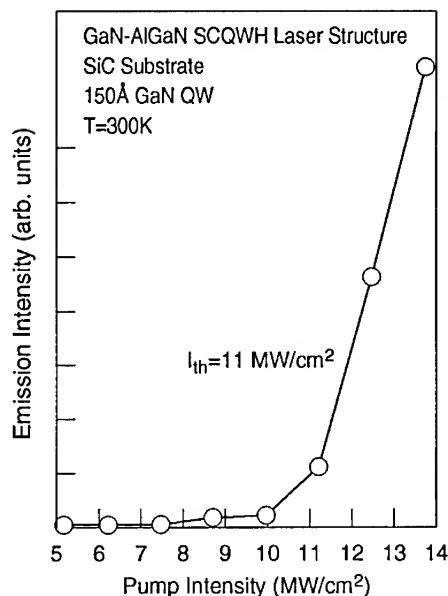


Fig. 5 Integrated intensity of edge photoluminescence from a highly excited GaN-AlGaIn SCQWH structure. A clear threshold is evident near a pump intensity of 11 MW/cm².

SPECTRAL RESPONSE OF GAN P-N JUNCTION PHOTOVOLTAIC STRUCTURES

D. WALKER, X. ZHANG, P. KUNG, A. SAXLER, J. XU, AND M. RAZEGHI.
Northwestern University, Center for Quantum Devices, EECS Department, Evanston, IL 60208

ABSTRACT

GaN ultraviolet photovoltaic and photoconductive detectors were grown on sapphire substrates by metalorganic chemical vapor deposition. The spectral response was analyzed considering the detector structure of a p-n junction connected back-to-back with a Schottky barrier. Based on the one-dimensional model of abrupt p-n junctions, the diffusion length of minority carriers was derived to be about 0.1 μm in n-GaN. To further characterize the n-GaN material, photoconductivity experiments have also been realized. The majority carrier lifetime of about 0.1 ms was obtained by analyzing the voltage-dependent responsivity of GaN photoconductors. The current-responsivity under a bias of 8 V was about 1 A/W.

INTRODUCTION

The III-V nitrides, with wide, direct bandgap, are attractive materials for developing high performance solar blind photodetectors in the UV region. These detectors have numerous applications such as the detection of solar UV rays reflected from orbiting craft, engine monitoring and flame detection, whenever there is a visible or infrared background.[1] In this paper we report the growth and characterization of GaN photovoltaic and photoconductive detectors.

EXPERIMENT

Material Growth and Characterization

The GaN epitaxial layers were grown in a metalorganic chemical vapor deposition reactor (MOCVD). Trimethylgallium, trimethylaluminum and ammonia were used as Ga, Al and N source materials, respectively. The Mg source, bis-cyclopentadienylmagnesium, was used as an acceptor dopant in GaN. The growth temperature was about 1000°C, and the growth rate was 0.5 - 1 $\mu\text{m}/\text{h}$. The carrier concentration for autodoped n-GaN was 10^{17} - 10^{18} cm^{-3} . The as-grown GaN:Mg layer was semi-insulating. After annealing in N_2 -ambient at the Mg in the layer was effectively "activated" to produce p-type GaN, with a typical carrier concentration of 10^{16} - 10^{17} cm^{-3} . Further details and characterization results have already been reported.[2-4] Optical evidence of the transformation to p-type GaN is seen in the photoluminescence data for the p-GaN film, as shown in Figure 1. The emission from p-type GaN was broadband and red-shifted with respect to the position of the peak for n-type GaN, because of the transition from the donor level to the acceptor level rather than from the donor level to the valence band.

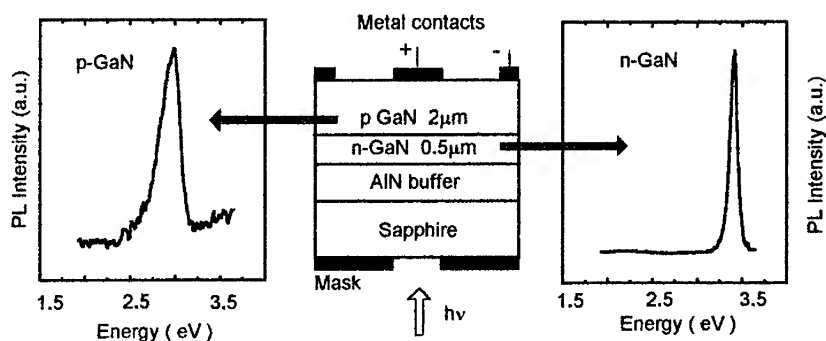


Figure 1. A schematic cross-section of the GaN photovoltaic structure with photoluminescence of the n- and p-type layers.

Photodetector Devices

Both a photodiode and a photoconductor were realized using GaN. The photodiode structure is shown in Figure 1. The substrate used was sapphire (00-1). The GaN homo p-n junction had a 0.5 μm thick n- GaN layer and a 2 μm thick p-GaN layer. The geometry of the contacts employed circumvents the difficulties in etching the top p-type GaN layer. Instead of the classical mesa structure, both of the indium contacts were put on the p-type layer. The small, center contact was in the path of illumination coming from the backside through the sapphire substrate. The much larger indium metal contact, which ran around the perimeter of the device, contacted the n-type layer through the p-type layer and was masked from the illumination. The separation distance of the contacts was on the order of 2 mm. Since the work function of indium is lower than that of p-GaN, Schottky contact characteristics for p-GaN are expected.[5]

Figure 2 shows the structure of the photoconductor. The substrate used was sapphire (01-2). The thickness of the AlN buffer layer and the n-GaN layer were 0.6 μm and 5 μm thick, respectively.

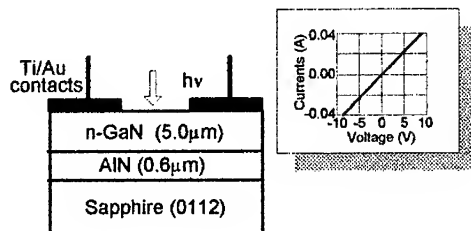


Figure 2. A schematic cross-section of the GaN photoconductive structure with photoluminescence of the n-type layer.

Ti/Au contacts were evaporated onto n-GaN for a thickness of 200 \AA and 1400 \AA , respectively. The stripe-contact pattern was made using standard photolithographic techniques. The distance between the two contacts was 950 μm . The resistance of the material between these contacts was

about 320 Ω . The I-V behavior of this device was linear in both the forward and reverse-bias cases.

Measurement Methods

The spectral responsivity was measured using a Xe lamp light, which was chopped at 400 Hz and focused into a monochromator. The GaN detector was placed at the exit slit of the monochromator, and a standard synchronous detection scheme was used to measure the detector signal. The optical power density at a given distance from the output slit of the monochromator was determined after a calibration of the optical system using detectors with known responsivities. We were then able to normalize the spectrum to account for the non uniform power output of the lamp at different wavelengths.

RESULTS

Figure 3 shows the spectral response of a GaN photovoltaic device. Two peaks of opposite signs are evident in this spectral response. A narrow, positive peak is observed at a shorter wavelength ($\lambda=362$ nm). The photovoltaic response showed a negative photovoltage at longer wavelengths, peaking at 375 nm. The spectral response of the photovoltaic structure can be interpreted by considering the absorption of light through successive layers, at the p-n and the metal-semiconductor junctions. First, the photons arrive at the sapphire substrate and are not absorbed, because sapphire is transparent for the photon energies considered here. AlN, the next layer that the photons pass through, acts as an optical filter and allows only photons with wavelengths greater than 200 nm to pass through, while absorbing those with wavelengths less than 200 nm. Of the UV radiation that can reach the n-GaN layer, the photons with wavelengths close to 200 nm are absorbed near the AlN surface and photons with wavelengths close to 365 nm, the cutoff wavelength of GaN, are absorbed near the p-n junction. The photogenerated carriers created shortly after the AlN interface cannot reach the depletion region of the p-n junction because the diffusion length of minority carriers is typically shorter than 0.1 μm . This explains why the spectral photoresponse is almost nonexistent until near the cut-off wavelength of GaN. Photons not absorbed near the p-n junction finally are absorbed near the metal contact, which forms a Schottky barrier junction with p-GaN. There are two contributions to the measured

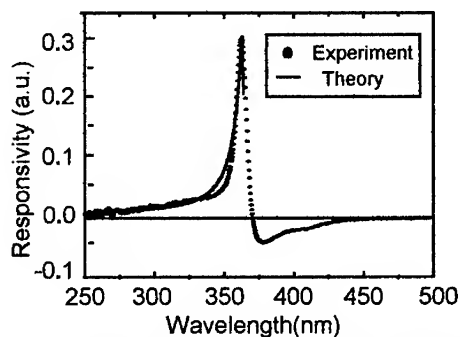


Figure 3. Spectral responsivity of GaN photovoltaic device.

photovoltage: one results from carriers swept across the p-n junction, the other from carriers swept across the Schottky junction. At wavelengths very close to 365 nm, the photogenerated carriers from the p-n junction are dominant, which leads to a large, narrow positive peak at 362 nm. In contrast, the photogenerated carriers from the Schottky barrier are dominant at slightly longer wavelengths. Thus, a relatively small, wide negative peak appears around 365 nm.

The peak positions and intensity are dependent on the thickness and doping levels of the n- and p-GaN materials. Using the one-dimensional model of abrupt p-n junctions and taking into account three UV absorption regions (p-GaN, n-GaN and p-n junction), the photoresponse near 362 nm was calculated and fit to the experimental data, as shown in Figure 3. Based on the theoretical analysis of the spectral response, the diffusion length of the minority carriers was derived to be about 0.1 μm . [6]

The current-voltage (I-V) characteristics of the detector show a forward bias turn-on voltage of about 4 V and a reverse bias breakdown voltage of -15 V. The series resistance is found to be about 60 Ω . The p-type layer provides the load resistance to the junction.

To further characterize the material which makes up the photodiode, an n-type photoconductor was grown and characterized to obtain information such as majority carrier lifetime and kinetics. The spectral response of the GaN photoconductive detector shows that the cutoff wavelength was about 365 nm. Figure 4 shows voltage-dependent current responsivity at given wavelength of 360 nm, where the peak of the spectral response is located.

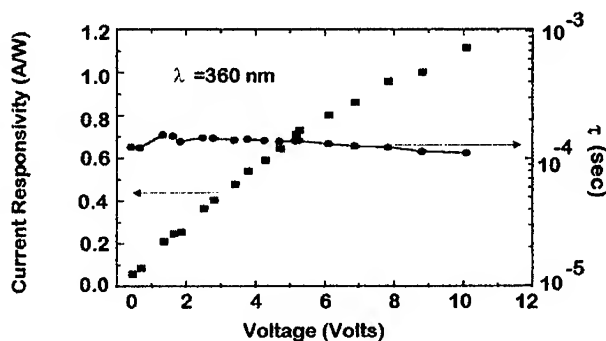


Figure 4. The Voltage-dependent current responsivity and lifetime of the GaN photoconductor.

The responsivity increases with applied voltage up to 6 V. Above 6 V, it saturates. Based on simple photoconductive theory, we estimated the carrier lifetime from the voltage-dependent responsivity to be about 0.1 ms, as shown in Figure 4. Upon further analysis of these photoconductors, it was found that there is a linear dependence of the photocurrent on the incident optical power and a logarithmic dependence of the responsivity on the frequency of the incident light.

CONCLUSIONS

Photodiodes and photoconductors were fabricated using GaN grown on sapphire by MOCVD. The spectral response of the photodiode was analyzed. The diffusion length of holes in the n-GaN layer was derived using the one-dimensional model of abrupt p-n junctions and found

to be about 0.1 μm . The cutoff wavelength for the photoconductor was about 365 nm at room temperature. Based on the voltage-dependent responsivity, a lifetime of electrons in n-GaN of 0.1 ms was estimated.

REFERENCES

1. H. Morkoç, S. Strite, G. B. Gao, M. E. Lin, B. Sverdlov and M. Burns. *J. Appl. Phys.* **76**, p. 1363 (1994).
2. C. J. Sun and M. Razeghi. *Appl. Phys. Lett.* **63**, p. 973 (1993).
3. C. J. Sun, P. Kung, A. Saxler, H. Ohsato and M. Razeghi. *Inst. Phys. Conf. Ser.* **137**, p. 425 (1993).
4. P. Kung, A. Saxler, X. Zhang, D. Walker, T.C. Wang, I. Ferguson and M. Razeghi. *Appl. Phys. Lett.* **66**, p. 2958 (1995).
5. J. S. Foresi and T. D. Moustakas. *Appl. Phys. Lett.* **62**, p. 2859 (1993).
6. X. Zhang, P. Kung, D. Walker, J. Piotrowski, A. Rogalski, A. Saxler and M. Razeghi. *Appl. Phys. Lett.* **67**, p. 2028 (1995).
7. M. Asif Khan, J. N. Kuznia, D. T. Olson, J. M. Van Hove and M. Blasingame. *Appl. Phys. Lett.* **60**, p. 2917 (1992).

AUTHOR INDEX

- Abernathy, C.R., 685, 751, 801, 825
 Adesida, I., 769, 831
 Agarwal, A.K., 157
 Ager, III, J., 417
 Aggarwal, R.L., 189, 919
 Ailey, K.S., 3
 Akasaki, Isamu, 351, 467, 577, 589,
 595, 619, 633, 697, 709, 869, 889
 Aktas, Ö., 527
 Alexis, J.P., 207, 411
 Amano, Hiroshi, 351, 467, 577, 589
 595, 619, 633, 697, 709, 869, 889
 Ambacher, O., 657
 Anderson, N.G., 949
 Arendt, M.F., 85
 Arlery, M., 393
 Asami, S., 889
 Ashby, C.I.H., 751
 Aspnes, D.E., 195, 405
 Augustine, G., 157
 Aulombard, R.L., 207, 411

 Bachem, K.-H., 393
 Bai, R., 55
 Bambha, N., 547
 Banas, Mike, 225, 583
 Bandic, Z.Z., 243
 Baranowski, J.M., 15, 351
 Barnak, John P., 739
 Barnes, P.A., 751, 849
 Barski, A., 145
 Barton, Daniel L., 931
 Beach, David B., 79
 Bechstedt, Friedhelm, 429
 Bedair, S.M., 213, 219, 273, 307
 Ben-Chorin, M., 467
 Benjamin, Mark C., 375, 739, 777
 Beresford, R., 55
 Berg, Niel, 931
 Bergman, J.P., 595, 709
 Berkstresser, G.W., 51
 Bernholz, J., 777
 Bhat, Ishwara, 497
 Binari, S.C., 897
 Bishop, S.G., 943
 Boćkowski, M., 15, 351
 Bosin, Andrea, 503, 515
 Botchkarev, A., 67, 175, 527, 565
 Bour, D.P., 443
 Bourret, A., 145, 393
 Boutros, K.S., 213, 219, 273, 307
 Bozeman, S.P., 777
 Brandle, C.D., 51
 Brandt, M.S., 657
 Brandt, O., 27, 607
 Bremser, Michael D., 3, 195, 405,
 667, 739, 777, 861
 Brener, I., 51

 Brennan, K.F., 479, 601, 733
 Briant, C., 55
 Briot, O., 207, 411
 Brock, W., 343
 Broom, R.F., 795
 Broser, I., 589
 Brown, E.R., 189
 Brown, Ian M., 691
 Brown, J., 763, 855
 Brown, K.A., 319
 Brown, S.W., 667
 Buchanan, D.N.E., 51
 Buczkowski, S.L., 237
 Bulman, Gary, 903

 Cappellini, Giancarlo, 429
 Carlos, W.E., 673
 Carlson, E.P., 861
 Carmalt, C.J., 85
 Carpenter, R.W., 861
 Carter, Jr, C.H., 909
 Cerny, C., 813
 Chai, B.H.T., 535
 Chen, B., 777
 Chen, C.H., 103, 443
 Chen, G.D., 527
 Chen, J.C., 703, 789
 Chen, N., 279
 Chen, Q., 913
 Chen, Y., 351
 Cheng, T.S., 535
 Chi, P.H., 679
 Chilukuri, R.K., 331
 Christman, Jim A., 739
 Chung, H.Y., 135
 Coleman, J.J., 943
 Constantine, C., 717
 Cook, Jr., J.W., 757
 Cowley, A.H., 85
 Craford, M.G., 103
 Crawley, J.A., 231

 Davis, P., 751
 Davis, Robert F., 3, 195, 331, 375,
 405, 667, 739, 777, 861
 Demeester, P., 231
 Detchprohm, T., 467, 577, 589
 Dharma-Wardana, M.W.C., 473
 Diener, J., 467
 Dmitriev, V.A., 295, 837, 909
 Domen, K., 61
 Dommann, A., 795
 Doverspike, K., 381, 405, 485,
 679, 697, 897
 Dovidenko, K., 387
 Drechsler, M., 467
 Driver, M.C., 157
 Drummond, T.J., 849

Dupuis, R.D., 183
 Durbha, A., 825

 Ebeling, K.J., 135
 Eckey, L., 491, 577, 589
 Eddy, Jr., C.R., 745
 Edmond, John, 903
 Edwards, N.V., 195, 405
 Ekerdt, J.G., 85
 Eliseev, Petr G., 937
 El-Masry, N.A., 213, 219, 273, 307
 Epperlein, P.W., 795
 Erickson, J.W., 363
 Evans, Keith R., 141, 527, 813

 Feldman, Bernard J., 691
 Ferry, D.K., 565
 Fertitta, K.G., 183
 Florentini, Vincenzo, 429, 435, 503, 515
 Fischer, S., 417, 491, 571
 Flynn, J.S., 201
 Fong, C.Y., 509
 Forner, T., 559
 Foxon, C.T., 535
 Freedman, Andrew, 73
 Freitas, Jr., J.A., 405, 485, 667, 897
 Freundt, Dirk, 91

 Gallagher, H., 535
 Gao, Y., 363
 Gaskill, D.K., 381, 405, 679, 697, 897
 Gassmann, A., 351
 Gil, B., 207, 411
 Glaser, E.R., 667, 673
 Goepfert, I.D., 151
 Goldenberg, B., 527
 Götz, W., 189, 443, 723
 Grudowski, P.A., 183
 Grzegory, I., 15, 351, 417
 Gu, S.Q., 943
 Gubanov, V.A., 509

 Hagerott Crawford, M., 801, 849
 Haller, E.E., 417, 491, 571
 Hangleiter, A., 559
 Härle, V., 559
 Harris, C., 709
 Hartford, Jr., E.H., 51
 Hawley, M.E., 261
 He, Y.W., 219, 273, 307
 Heitz, R., 491, 589, 613
 Hellman, E.S., 51
 Helms, Christopher J., 931
 Henderson, B., 535
 Hengehold, R.L., 813
 Hersee, Steve D., 225, 583, 763, 801, 855
 Hiramatsu, Kazumasa, 267, 467, 577, 589
 Hjalmarson, H.P., 849

 Ho, Wilson, 301, 319
 Hoffmann, A., 491, 577, 589, 613
 Hofmann, D.M., 619
 Holloway, P.H., 819, 825
 Holmes, A.L., 183
 Hopkins, R.H., 157
 Horino, K., 61
 Horton, M.N., 243
 Howard, A.J., 751, 801
 Hristakos, L., 343
 Hu, D.Q., 319
 Huang, Y., 861
 Huang, Z.C., 703, 789
 Hughes, W.C., 757
 Hwang, C.-Y., 369, 521

 Ikedo, T., 697
 Im, J.S., 559
 Imler, W., 103, 443
 Irvine, K.G., 295, 909

 Jackson, T.N., 843
 Jagannadham, K., 325
 Jakobson, M., 295
 Jeon, Chan-Wook, 313
 Jiang, H.X., 527
 Johnson, M.A.L., 757
 Johnson, N.M., 189, 443, 723
 Jones, A.C., 337
 Jones, A.M., 943
 Jones, Charles R., 141
 Jones, R.A., 85
 Jun, J., 15, 351

 Kalinina, E.V., 837
 Kamp, M., 135
 Kaplan, R., 697
 Kaspi, Ron, 141
 Kato, H., 889
 Kaufmann, U., 633
 Kawaguchi, Makoto, 869
 Kennedy, T.A., 667, 673
 Kern, R.S., 3, 405
 Khan, M. Asif, 769, 813, 819, 831, 843, 913
 Kidder, Jr., J.N., 249
 Kim, Ig-Hyeon, 313
 Kim, J.G., 547
 Kim, Kwiseon, 399, 455
 Kim, M.J., 861
 Kim, Seon-Hyo, 313
 Kim, W., 527
 King, Sean W., 375, 739, 777
 Kisielowski, Ch., 351
 Kistenmacher, T.J., 261
 Kitamura, Shota, 267
 Klein, B.M., 509
 Kolde, N., 889
 Kolke, M., 889
 Koleske, D.D., 679
 Kolnik, J., 479, 601, 733
 Kong, Hua-Shuang, 903

Korakakis, D., 151
 Kouvetakis, John, 79
 Kovalev, D., 619
 Kranenberg, C.F., 225
 Ku, Ja-Hum, 739
 Kuech, T.F., 97, 243, 255
 Kung, P., 625, 955
 Kunzer, M., 633
 Kuo, C.P., 103, 443
 Kuo, J.S., 249
 Kuramata, A., 61
 Kuznetsov, N.I., 837, 909

 Lamb, H.H., 331
 Lambrecht, Walter R.L., 375, 399, 455
 Landmesser, Georg, 91
 Lauhon, L., 301, 319
 Leavitt, R.P., 261
 Lee, J.W., 685, 825
 Lei, Ting, 141, 813
 Leonard, Michelle, 903
 Lester, L.F., 763, 855
 Leszczyński, M., 15
 Leuchtner, Robert, 343
 Lewis, L.J., 473
 Li, L.K., 169
 Li, X., 943
 Li, Y., 343, 369, 521
 Liao, Z.L., 189, 919
 Lillental-Weber, Zuzanna, 351
 Lin, J.Y., 527
 Lin, Shu-Han, 691
 Litton, C.W., 527
 Liu, Guangtian, 583
 Liu, H., 103, 405, 443, 547
 Liu, X., 351
 Loa, I., 491
 Loeber, D.A.S., 949
 Look, D.C., 527
 Loong, C.-K., 423
 Lovejoy, M.L., 849
 Lu, Hongqiang, 497
 Lu, Y., 369, 521
 Lundström, T., 595
 Lüth, Hans, 91
 Luther, B.P., 843

 MacKenzie, J.D., 685
 Maki, P.A., 919
 Malloy, Kevin, 583
 Manasreh, M.O., 553
 Marti, O., 135
 Martin, G.A., 67, 175
 Maruska, H. Paul, 301
 Matsuoka, Takashi, 39
 Mayer, M., 135
 Mayo, W.E., 369, 521
 McGill, T.C., 243
 McIntosh, F.G., 213, 219, 273, 307
 McLane, G.F., 717
 McMurran, Jeffrey, 79
 McIngaillis, I., 189, 919

 Meloni, F., 515
 Merz, C., 633
 Messham, R.L., 157
 Meyer, B.K., 467, 491, 577, 589, 613, 619
 Middleton, P.G., 231, 535
 Miglio, L., 435
 Miller, S.J., 819
 Miragliotta, Joseph, 541
 Mitchel, W., 201
 Moerman, I., 231
 Mohny, S.E., 843
 Mokov, E.N., 619
 Molnar, B., 745
 Molnar, R.J., 189, 919
 Monemar, B., 595, 709
 Monteiro, T., 619
 Morales, G., 151
 Morkoç, H., 67, 175, 527, 565
 Mott, D.B., 703, 789
 Moussa, M., 219, 273
 Moustakas, T.D., 111, 151, 163
 Müllhäuser, J.R., 607
 Myers, T.H., 237

 Nagai, S., 889
 Nakamura, Shuji, 673, 879
 Narayan, J., 325, 387
 Nayfeh, M.H., 67
 Negley, Gerry, 903
 Nelson, D., 295
 Nelson, J.S., 509
 Nemanich, Robert J., 375, 739, 777
 Neugebauer, Jörg, 645, 723
 Neumayer, Deborah A., 85
 Newman, N., 351
 Ng, H.K., 697
 Ng, H.M., 151
 Nicholls, J.F.H., 535
 Niebuhr, R., 393
 Nikolaev, V., 295
 Nilsson, S., 613
 Nishikawa, Masaki, 869
 Norris, Peter E., 301

 O'Donnell, K.P., 231, 535
 Oguzman, I.H., 479, 601, 733
 Ohta, Masahiro, 869
 Oktyabrsky, S., 387
 Osiriski, Marek, 931, 937

 Paine, D.C., 55
 Pakula, K., 15, 351
 Parikh, N., 195
 Park, R.M., 547
 Payne, J., 381
 Pearsall, T.P., 249
 Pearton, S.J., 685, 717, 751, 801, 807, 825
 Pelzmann, A., 135
 Pereira, E., 619
 Perkins, N.R., 243

Perlin, Piotr, 15, 937
 Perry, W.G., 3, 195, 667
 Phillips, B. Scott, 931
 Piner, E.L., 213, 219, 273, 307
 Ping, A.T., 769, 831
 Ploog, K.H., 27, 607
 Ponce, F.A., 183
 Porowski, S., 15, 351, 417
 Pressel, K., 491, 613

 Qian, W., 381

 Ramer, Jeff C., 225, 583, 763, 801, 855
 Rashkeev, Sergey N., 455
 Razeghi, M., 387, 625, 955
 Redwing, J.M., 201, 255, 949
 Reinacher, N.M., 657
 Ren, F., 825
 Reuter, E.E., 943
 Reynolds, D.C., 527
 Richards-Babb, M., 237
 Rieger, D.J., 751
 Rizzi, Angela, 91
 Roberts, J.C., 213, 219, 273, 307
 Roberts, J.S., 337
 Roberts, V., 337
 Robinson, Gary N., 73
 Rockett, A., 795
 Rogers, Jr., J.W., 249
 Roh, S.D., 943
 Rohrer, G.S., 381
 Romano, L.T., 189
 Rossner, U., 145
 Rossow, U., 405
 Rouviere, J.-L., 145, 393
 Rowland, L.B., 157, 381
 Rowland, Jr., W.H., 757
 Ruden, P.P., 479, 601, 733
 Rushworth, S., 337
 Ruvimov, S., 351

 Safvi, S.A., 255
 Sakai, Hiromitsu, 869
 Salagaj, T., 369
 Salvador, A., 175, 527, 565
 Sampath, A., 151
 Sartori, Philippe, 937
 Sato, Michio, 285
 Satta, A., 515
 Sawaki, Nobuhiko, 267
 Saxler, A., 201, 625, 955
 Schetzina, J.F., 123, 757
 Schloss, L., 351
 Schmidt, T.J., 527
 Schmitz, A.C., 769, 831
 Schneemeyer, L.F., 51
 Scholz, F., 559
 Schurman, M.J., 369, 521
 Segall, B., 399, 455
 Semendy, F., 547
 Serra, S., 435

 Shan, W., 527
 Sharma, A.K., 553
 Shen, H., 369
 Shibata, N., 889
 Shul, R.J., 685, 717, 751, 849
 Shur, M.S., 913
 Siegle, H., 577
 Siegrist, T., 51
 Silkowski, E., 813
 Simons, D.S., 679
 Singh, R., 163
 Sinharoy, S., 157
 Sitar, Z., 3
 Sitnikova, A., 295
 Skowronski, M., 381
 Smith, David J., 67, 79, 175
 Smith, Laura L., 739, 861
 Smith, M., 527
 Soejima, R., 61
 Soloviev, V.A., 837
 Song, J.J., 527
 Sota, Shigetoshi, 869
 Spencer, M.G., 279
 Stall, R.A., 369, 405, 521, 801
 Steigerwald, D., 103
 Sternschulte, H., 135
 Steude, G., 619
 Stevens, K.S., 55
 Strite, S., 795
 Stutzmann, M., 657
 Sudo, H., 61
 Sumakeris, J.J., 331
 Sun, C.J., 913
 Suski, T., 15, 351, 417
 Suzuki, M., 925
 Sverdlov, B.N., 67, 175, 565
 Swider, W., 351

 Tan, H.H., 807
 Tanahashi, T., 61
 Tanaka, S., 3
 Tang, X., 279
 Teisseyre, H., 15
 Tenelsen, Katrin, 429
 Thies, A., 135
 Thompson, W.H., 67
 Thomsen, C., 577
 Thon, A., 97
 Thrush, E.J., 231
 Thurian, P., 491, 577, 613
 Tian, Z.-J., 473
 Tischler, M.A., 201, 255, 949
 Trager-Cowan, C., 231, 535
 Trampert, A., 27
 Trexler, J.T., 819
 Tsen, K.T., 565
 Tsen, S.-C.Y., 67, 175
 Tsvetkov, D., 295
 Turnbull, D.A., 943

 Uenoyama, T., 925
 Ustin, Scott, 301, 319

Van de Walle, Chris G., 645, 723
Van der Stricht, W., 231
Vanderbilt, David, 503, 515
Vartuli, C.B., 685, 751, 801
Vispute, R.D., 325
Volm, D., 467, 619

Walker, D., 625, 955
Walukiewicz, W., 417, 571
Wang, C., 3
Wang, R., 479, 601, 733
Wang, W.I., 169
Wang, Y.J., 697
Ward, B.L., 777
Washburn, J., 351
Weber, E.R., 351
Weeks, Jr., T.W., 3, 405, 667, 861
Wetzel, C., 417, 491, 571
White, J.M., 85
Wickenden, A.E., 405, 485, 679,
897
Wickenden, Dennis K., 261, 541
Wiesmann, D., 51
Williams, J.S., 807
Wilson, R.G., 363, 685, 801
Wongchotiql, K., 279
Wraback, M., 369
Wright, A.F., 509
Wu, H., 325
Wysmolek, A., 15

Xavier, C., 619
Xu, J., 955

Yamasaki, S., 889
Yang, H., 27, 607
Yang, J.W., 913
Yang, X.H., 527
Yang, Z., 169
Yeo, Y.K., 813
Yoshida, Masato, 869
Yu, Zonghai, 237
Yuan, C., 801, 807

Zavada, J.M., 685
Zeller, Joachim, 937
Zhang, D.P., 279
Zhang, L., 763
Zhang, X., 625, 955
Zhang, X-J, 849
Zhang, Z., 777
Zheleva, T., 195
Zheng, Kang, 225, 583, 763, 855
Zheng, Youdou, 789
Zhu, Long D., 301
Zolper, J.C., 685, 801, 849, 855
Zubrilov, A., 295

SUBJECT INDEX

- acceptor(s), 633
 - bound exciton, 709
 - doping, 3
- active nitrogen, 73
- adduct reactions, 97, 103, 337
- AlGaInN quaternary alloys, 219, 363
- AlGa_N/Ga_N
 - heterostructures, 777
 - SCH structures, 527
- AlGa_N/InGa_N double heterostructure, 61
- AlGa_N thin films, 3, 15, 757
- AlIn_N, 685
- AlN, 157, 319, 325
 - single crystals, 613
- AlN/Ga_N interfaces, 515
- alternative precursors, 337
- ammonia as nitrogen source, 135, 169
- amorphous layers, 807
- annealing studies, 225, 703, 813, 855, 869
- asymmetric double heterostructures (ADH), 889
- atomic
 - force microscopy, 67, 225, 237, 751
 - layer epitaxy, 213, 249, 273, 307
- AuBe contacts, 825
- Au/Ge/Ni contacts, 825
- auger electron spectroscopy (AES), 751, 819
- background carrier concentration, 521
- band
 - edge energies, 553
 - offsets, 123, 455, 473, 515
 - structures, 455
- barrier height, 837
- BCl₃, 757
- biaxial compression, 411
- boron nitride, 399, 429
- bowing parameter, 195
- breakdown voltage, 909
- buffer layer
 - growth, 225
 - recrystallization, 307
- bulk
 - GaN epitaxy, 337
 - single crystals, 15
- capacitance-voltage (C-V), 831, 837
- carbon
 - as an impurity, 685
 - doping of AlN, 279
- carrier
 - gas effects, 261
 - lifetime, 955
 - transport mechanisms, 937
- catalytic enhancement, 135
- cathodoluminescence, 195, 949
- charge density maps, 509
- cleaving, 61, 919
- Cl₂GaN₃, 79
- compensation and passivation, 645, 679
- complexes, 645
- concentration profiles, 255
- conductance, 467
- contact
 - interfaces, 861
 - metallurgy, 843
 - resistivity, 849, 861
- crystal polarity, 337
- cubic
 - boron nitride, 691
 - GaN, 27, 509, 607, 733
- current-voltage (I-V), 831, 837
- cyclotron resonance measurements, 467
- deep
 - donor states, 667
 - level transient spectroscopy (DLTS), 443
 - levels, 613, 703
- defect(s)
 - density reduction, 307
 - states, 435
- degradation, 931
- density-functional calculations, 515
- desorption
 - mass spectrometry, 141
 - rates, 141
- dielectric
 - constant, 515
 - function, 405, 601
- dimethylethylamine:alane (DMEA), 249
- dislocation
 - densities, 889
 - related defects, 589
- donor
 - acceptor pairs, 633
 - bound exciton, 709
- dot-patterns, 267
- double heterostructure devices, 213, 273, 657, 869, 889, 903, 909, 949
- double positioning boundaries, 175
- dry etch damage, 769
- dry etching, 717
- ECR-MBE, 145
- ECR plasma etching, 717, 751, 763
- effective mass, 473, 667, 697
- elastic constants, 399
- electrically detected magnetic resonance (EDMR), 657
- electric breakdown, 909
- electroluminescence detected magnetic resonance (ELDMR), 673

- electron
 - affinity, 777
 - cyclotron resonance, 697
 - phonon interaction, 565
 - spin resonance, 485, 691
 - transport, 679
- electronic
 - band structure, 473
 - properties, 745
- electroreflectance, 541
- energy density of states, 405
- epitaxial relationship, 387
- exciton(s)
 - fine structure, 455
 - line, 553
 - luminescence, 607
- excitonic recombination, 485, 709
- facet formation, 267
- Fermi level, 849
- field
 - effect transistors, 897, 913
 - emission, 777
- first-principle calculations, 645, 925
- free exciton, 559
- Fröhlich interaction, 565
- fundamental absorption edge, 553
- GaAsN, 285
- GaCl surface pretreatment, 189
- gallium vacancy, 645
- GaN bulk film growth, 189
- GaN/GaAs, 285
- GaN/SiC, 123
- Ga-rich regime, 111
- gas source MBE, 141, 145
- grazing-incidence XRD, 313
- green LEDs, 879
- growth
 - kinetics, 27
 - mechanisms, 207, 255
- Gunn effect, 789
- hafnium substrates, 55
- halide vapor phase epitaxy (HVPE), 243
- Hall electron mobility, 521
- heteroepitaxy, 351
- hexagonal pyramids, 393
- high
 - pressure growth, 15
 - resolution EELS, 91
 - resolution TEM, 387
 - temperature vapor phase epitaxy, 571
- hole transport, 479
- homoepitaxy, 15, 351
- hydrazoic acid, 73
- hydride vapor phase epitaxy (HVPE), 189, 919
- hydrogen, 645, 685, 725, 739, 763, 855
 - acceptor complex, 503
- etching, 745
 - passivation, 369, 503
 - vibrational frequencies, 503
- hydrostatic pressure, 417
- hyperfine structure, 691
- impact ionization, 733
- impurities, 521, 645, 679
- incorporation kinetics, 141
- infrared absorption, 691
- InGaAlN, 39
- InGaN alloys, 163, 213, 273, 813, 879, 913
- InGaN/GaN heterostructures, 183
- integrated heterostructure devices, 123
- interfacial reactions, 819
- inversion domain boundaries, 387, 393
- ion
 - beam assisted deposition, 313
 - channeling, 807
 - damage, 807
 - implantation, 795, 801, 807, 813
- ionization rate, 733
- k · p method, 925
- Keating model, 399
- kinetics, 207
- laser
 - emission, 949
 - mirrors, 763
- lattice
 - matched substrates, 39, 51, 55, 535
 - mismatch, 455
- LEDs, 497, 673, 879, 889, 903, 913, 931, 937
- life testing, 931
- light emitting diode, 61
- Lithium salt substrates, 535
- low
 - resistivity AlN, 279
 - temperature growth, 213
- luminescence, 417, 619
- macroscopic polarization, 515
- magnetic resonance, 673
- magneto-optic studies, 697
- MBE, 3, 27, 55, 67, 111, 123, 157, 163, 175, 237
- Me₂GaN₃, 85
- metal
 - contacts, 831
 - semiconductor-metal photoconductors, 789
 - thin films, 819
- metastable alloys, 285
- Mg
 - acceptors, 15
 - doping 111, 169, 443, 497, 527, 813
 - hydrogen complex, 723
 - implantation, 813
- MgAl₂O₄, 61

microplasmic breakdown, 909
 microstructure, 351
 MOCVD, 3, 39, 97, 103, 195, 201, 219, 255,
 267, 273, 279, 295, 497, 625, 869, 903
 modulation doped AlGaIn/GaN, 595
 molecular
 dynamics simulations, 435
 stream epitaxy, 307
 MOMBE, 91, 685
 momentum matrix element, 559
 Monte Carlo calculations, 479, 733
 morphology studies, 231
 mosaic dispersion, 261
 MOVPE, 3, 39, 97, 103, 195, 201, 219, 255,
 267, 273, 279, 295, 497, 625, 869, 903
 muffin-tin method, 473
 multiple
 -phonon excitations, 423
 quantum well structures, 889

 nanostructures, 295
 native defects, 625, 645
 NdGaO₃, 39
 negative
 differential resistivity, 789
 electron affinity, 777
 neutral singlet donor, 417
 neutron spectroscopy, 423
 nitridation step, 207
 nitrogen
 rf plasma source, 237
 vacancy, 509, 703
 nucleation, 27, 231, 237

 ohmic
 contacts, 825, 843, 849, 855, 861
 p-type contacts, 819
 OMVPE, 3, 39, 97, 103, 195, 201, 219, 255,
 267, 273, 279, 295, 497, 625, 869, 903
 on-surface cracking technique, 135
 open-core screw dislocations, 375
 optical
 absorption, 813
 cavity, 61
 devices, 273, 769
 gain, 925
 properties, 547, 943
 pumping, 919
 response, 455
 optically detected magnetic resonance
 (ODMR), 619, 633, 667
 oxidation, 739
 oxygen, 685
 donor level, 571

 parasitic reactions, 103
 Pendellosung fringes, 183
 phase
 equilibrium, 843
 separation, 163
 phonon
 density of states, 423
 sidebands, 491
 photoconductor, 789
 photoemission capacitance transient
 spectroscopy, 433
 photoluminescence
 excitation, 583
 spectroscopy (PL), 369, 485, 491, 595,
 607, 613, 633, 667, 795, 813, 943, 949
 photovoltaic devices, 955
 picosecond Raman spectroscopy, 565
 plasma
 assisted CVD, 691
 -assisted MOCVD, 285
 chemistry, 751
 etching, 745, 763
 processing, 343
 p-n junctions, 909, 955
 post-growth processing, 723
 power dependence bandgap, 583
 precursors, 73, 79, 91, 337
 preferential crystal orientation, 249
 pressure dependence, 103
 pseudopotential calculations, 135, 601, 733
 p-type
 doping, 151
 GaN, 369
 pulsed laser deposition, 325, 343
 pyramidal growth, 393

 quantification of stoichiometry, 363
 quantum
 efficiency, 559
 well structures, 123, 879, 925, 949
 quasiparticle band structure, 429
 quaternary alloys, 219

 radiative lifetime, 559, 607, 709
 Raman spectroscopy, 577
 rapid thermal annealing, 795, 801
 reactive ion etching, 717, 757, 769
 recombination dynamics, 485, 589, 673
 regrowth, 819
 residual stress, 411
 resistive films, 897
 rf plasma MBE, 547
 RHEED, 51, 145, 151

 ScAlMgO₄, 51
 scanning force microscopy, 375
 Schottky barrier, 831, 837, 913
 second-harmonic generation, 541
 seeded helium beams, 331
 selective area epitaxy, 267, 943
 self
 compensation, 169
 -consistent calculations, 595
 -limiting process, 267
 -nucleation, 261
 SiC/AlN band offset, 381
 SiC-cubic substrates, 301
 SiC-6H substrate, 3, 39, 151, 157, 195, 295,
 301, 667, 837, 869, 903

SiCl_4 , 769
 silicon
 doping, 443, 697, 897
 implantation, 855
 substrates, 67, 79, 243, 319, 325
 SIMS, 363
 single
 quantum well structure, 889
 -source precursor, 79, 85
 spectral response, 955
 spectroscopic ellipsometry, 405
 spinoidal decomposition, 163
 spin-orbit splitting, 405, 455
 spiral growth mechanisms, 375
 stacking
 faults, 111
 mismatch boundaries, 175
 stimulated emission, 61, 189, 869, 949
 strain
 -anneal process, 55
 effects, 411, 577, 667
 Stranski-Krastanov process, 225
 stream of light molecules, 331
 structural disorder, 435
 supersonic
 jet epitaxy, 301
 MBE, 319
 surface
 cleaning, 739
 morphology, 919, 943
 reactions, 91
 reconstruction, 151
 roughening, 111
 structure, 375

 thermal
 annealing, 225, 703, 813, 855
 stability, 825, 843
 threading dislocations, 175, 387
 tight binding calculations, 435, 509
 time resolved photoluminescence, 709
 Ti/Pt/Au contacts, 825
 transition metals, 491, 613
 transmission electron microscopy (TEM),
 145, 175
 triallylamine, 91
 triethylaluminum, 319
 two
 -dimensional electron gas, 595
 -phonon resonance, 541

 UV/O₃ oxidation, 739
 UV-photoemission, 777

 vertical reactor, 189, 231

 wet etching, 757
 wrong bonds, 435
 WSi contacts, 825

 x-ray
 diffraction, 51, 151, 225, 231
 photoemission spectroscopy (XPS), 73,
 85, 91, 381
 rocking curves, 183

 yellow luminescence, 15, 583, 625

 Zn doping, 15, 795
 ZnO substrates, 39, 535